Transactions of the ASME®

Journal of Heat Transfer

HEAT TRANSFER DIVISION
Chair, **G. P. PETERSON**
Vice Chair, **W. A. FIVELAND**
Past Chair, **O. A. PLUMB**
Secretary, **J. H. KIM**
Treasurer, **L. C. WITTE**
Technical Editor, **J. R. HOWELL (2000)**

Associate Technical Editors,
P. S. AYYASWAMY (2000)
C. BECKERMANN (2001)
R. D. BOYD (1999)
B. T. F. CHUNG (2001)
R. W. DOUGLASS (2000)
J.-C. HAN (2000)
D. A. KAMINSKI (2001)
M. KAVIANY (1999)
R. L. MAHAJAN (2001)
A. MAJUMDAR (2001)
M. P. MENGUC (2000)
T. TONG (1999)
D. A. ZUMBRUNNEN (2001)

BOARD ON COMMUNICATIONS
Chairman and Vice President
R. K. SHAH

OFFICERS OF THE ASME
President, **W. M. PHILLIPS**
Executive Director,
D. L. BELDEN
Treasurer,
J. A. MASON

PUBLISHING STAFF
Managing Director, Engineering
CHARLES W. BEARDSLEY

Director, Technical Publishing
PHILIP DI VIETRO

Managing Editor, Technical Publishing
CYNTHIA B. CLARK

Managing Editor, Transactions
CORNELIA MONAHAN

Production Coordinator
JUDITH SIERANT

Production Assistant
MARISOL ANDINO

Transactions of the ASME, Journal of Heat Transfer (ISSN 0022-1481) is published quarterly (Feb., May, Aug., Nov.) for $240.00 per year by The American Society of Mechanical Engineers, Three Park Avenue, New York, NY 10016. *Periodicals postage paid at New York, NY and additional* mailing offices. POSTMASTER: Send address changes to Transactions of the ASME, Journal of Heat Transfer, c/o THE AMERICAN SOCIETY OF MECHANICAL ENGINEERS, 22 Law Drive, Box 2300, Fairfield, NJ 07007-2300.
CHANGES OF ADDRESS must be received at Society headquarters seven weeks before they are to be effective. Please send old label and new address. **PRICES:** To *members, $40.00, annually: to nonmembers, $240.00.* Add $40.00 for postage to countries outside the United States and Canada.

STATEMENT from By-Laws. The Society shall not be responsible for statements or opinions advanced in papers or . . . printed in its publications (B7.1, Para. 3), **COPYRIGHT** © **1998** by The American Society of Mechanical Engineers. Authorization to photocopy material for internal or personal use under circumstances not falling within the fair use provisions of the Copyright Act is granted by ASME to libraries and other users registered with the Copyright Clearance Center (CCC) Transactional Reporting Service provided that the base fee of $3.00 per article is paid directly to CCC, 222 Rosewood Drive, Danvers, MA 01923. Request for special permission or bulk copying should be addressed to Reprints/Permission Department. **INDEXED** by Applied Mechanics Reviews and Engineering Information, Inc. Canadian Goods & Services Tax Registration #126148048.

Published Quarterly by The American Society of Mechanical Engineers

VOLUME 120 • NUMBER 4 • NOVEMBER 1998

TECHNICAL PAPERS

Special Section—Invited Papers on Opportunities in Heat Transfer Applications

Featured Section—Heat Transfer in Manufacturing

Analytical and Experimental Techniques

(Contents continued on Outside Back Cover)

This journal is printed on acid-free paper, which exceeds the ANSI Z39.48-1992 specification for permanence of paper and library materials.∞ ™

♻ 85% recycled content, including 10% post-consumer fibers.

Downloaded 04 Feb 2011 to 194.85.80.107. Redistribution subject to ASME license or copyright; see http://www.asme.org/terms/Terms_Use.cfm

(Contents continued)

Properties and Property Measurements

Conduction Heat Transfer

Forced Convection

Natural and Mixed Convection

Boiling and Condensation

Combustion

Heat Pipes

Heat Transfer Enhancement

TECHNICAL BRIEFS

(Contents continued on Inside Back Cover)

(Contents continued)

DISCUSSION

ANNOUNCEMENTS AND SPECIAL NOTES

Journal of Heat Transfer

Editorial

The November 1998 issue of the *Journal of Heat Transfer* marks a shift in our editorial policy. The Journal and the Heat Transfer Division have been criticized, rightly or wrongly, for not paying sufficient attention to the needs and interests of our industrial readers. We have addressed the issue in the past by attempting to enlist members of the Division who are from industry as Associate Editors of the Journal. However, it is often more difficult for our industrial colleagues to devote time to this activity given the differing reward structures in industry and academia.

This issue marks a different approach to industrial involvement. Because the field of heat transfer is extremely broad, the JHT Editorial Board has solicited papers that outline the unresolved problems that are found in particular heat transfer applications. The search for such papers began under the previous Technical Editor, Prof. Ray Viskanta, and we continue to seek such submissions. We have found it valuable to look for author teams involving one member from the academic community and another with industrial or commercial insight.

The first set of these papers is highlighted in this issue and deals with challenges, applications, and research needs concerning heat transfer in living systems; in aircraft brake systems; and in electronic packaging. These special articles are not meant to be reviews; in fact, the Journal generally does not entertain publication of review articles, as there are many other outlets for such papers. The articles in the special section are aimed instead at defining problems and challenges in particular fields of heat transfer application. We plan to highlight additional papers in future issues.

I would be remiss if I did not recognize the help of Prof. Yogesh Jaluria of Rutgers University. Yogesh, as Special Projects Editor, has been instrumental in soliciting these special articles and following through on the review process.

We hope these papers will prove helpful to those seeking new research opportunities in heat transfer, and that they will also show the growth of the field into challenging and exciting areas.

As an additional feature in this issue, we have grouped a number of papers into a special section on Manufacturing and Materials Processing to indicate the interest in this area of heat transfer application and research.

The Journal will continue to emphasize and publish articles that deal with fundamental advances in heat transfer, new physical insights, and novel experimental and analytical methods. This will always be the chief objective of JHT. We hope, however, that special papers that examine the many challenges and opportunities in the field will be of interest and help to our readers. We welcome response and comments on this question from our subscribers and readers.

John R. Howell
Technical Editor

K. R. Diller[1]
Biomedical Engineering Program
and Department of Mechanical Engineering,
The University of Texas at Austin,
ENS 612
Austin, TX 78712
e-mail: kdiller@mail.utexas.edu
Fellow ASME

T. P. Ryan
Valleylab, Inc.,
Research and Development,
5921 Longbow Drive,
Boulder, CO 80301

Heat Transfer in Living Systems: Current Opportunities

This paper presents an overview of the field of bioheat transfer. Topics covered include factors that distinguish heat transfer in living systems from inanimate systems, application areas in basic research and in clinical diagnosis and therapy, and our projection of where the field is headed and what are likely to be the most fertile opportunities for contributions by members of the heat transfer community.

Introduction

It has been 30 years since bioheat transfer has been defined as a discipline of focus within the engineering community. Initial applications targeted analysis of processes such as human thermoregulation, thermal-based surgical procedures, cryopreservation of living cells, and thermal burn injury. Over the ensuing years significant contributions have been made in the development of both clinical and laboratory instrumentation, physiological function models, and even analytical tools for the optimal design of tissue processing protocols. Complementary developments in computational capabilities and in cellular and molecular biology now provide opportunities for investigating and manipulating living systems at the mechanistic and baseline kinetics levels of physiological resolution. The state of the art has reached the point wherein there are unprecedented opportunities for contributions to the solution of problems in bioheat transfer. This paper presents a brief introduction to some of the areas which we consider to offer the greatest potential for integrating the tools of heat transfer analysis with the biological and medical sciences to address problems of impact and importance.

Heat transfer is important in living systems as it affects the temperature and its spatial distribution in tissues. The primary role of temperature is the regulation of a plethora of rate processes that govern all aspects of the life process. These thermally driven rate processes define the differences between sickness and health, injury and successful therapy, comfort and pain, and accurate and limited physiological diagnoses. Bioheat transfer analysis of living tissues is complicated by the fact that the thermal properties of most of them are nonhomogeneous and anisotropic, have large variations among inter and intraspecimen samples, often as a function of the history of the system, and are coupled to the general and local physiological states of the system. Consequently, it is difficult to build models of bioheat transfer processes that have broad general applicability. As experience has accrued in the field, it has become clear that for many specific applications it is necessary to include in the models considerable physiological detail, such as morphology of the local vascular network, in order to achieve an acceptable level of accuracy of prediction of transient thermal phenomena. For this reason, many bioheat transfer analyses are conducted by collaborative teams of bioengineering and life and medical scientists. Refinement of an experiment or model may require continuous input from a colleague well versed in subtle aspects of behavior of the biological system at the molecular, cellular, tissue, organ or organism level, as appropriate. In the absence of this kind of input it is easy for an engineer to design an experiment or model that is not relevant to the salient biological problem. In the same manner, many life scientists do not possess the design and analytical skills to develop a sophisticated approach to solving a biological problem that will have broad impact. Therefore, many successful bioheat transfer research programs are built around a team approach involving investigators from complementary disciplines.

Clinical outcomes of hyperthermal therapy depend on the understanding and application of heat transfer, assuming certain target temperatures are useful for treatment. Sustaining normal tissue temperatures surrounding the target tissue may be an important factor in the treatment to avoid irreversible damage. The distribution of blood flow is a barrier to homogeneous heating, and even if it is known in three dimensions prior to a treatment, may change significantly due to the reaction to the heating. Normal tissue perfusion may increase two to threefold, whereas pathological tissue with abnormal vasculature may have its perfusion shut down. In addition, the electrical properties and thermal properties of various tissues change as their temperatures are elevated. The percent of change depends on the tissue type and temperature achieved.

The quest for an ideal thermal treatment would thus require two major components. The first is the noninvasive imaging of the temperature field in real time, which is being done with magnetic resonance imaging (MRI) (Carter et al., 1998) and with diagnostic ultrasound (Simon et al., 1998). The second major component would be a steerable system to apply power in response to the differences in perfusion and tissue properties. Only under these conditions could tissue temperature homogeneity be assured. No clinical work has yet successfully integrated both systems into a viable thermal treatment apparatus.

Many bioheat transfer analysis problems have a dual objective of quantifying a transient temperature field within a tissue and of determining the associated effect of temperature excursions on life processes of interest. Mammalian systems exist within a very narrow band of normothermic temperatures. One area of bioheat transfer analysis deals with how the normothermic state is maintained within an extraordinarily complex physiological system in the presence of multiple redundant feedback control loops, coupling of processes across numerous energy domains, and compound transient boundary conditions. However, much of bioheat transfer deals with understanding and control of processes outside the normothermic range of states in conjunction with processes involving injury, diagnosis and/or therapy. Some of these processes may be initiated by humans under controlled conditions for predetermined objectives, whereas others occur in response to unplanned environmental events. Excursions from normothermia occur for both high and

---

[1] To whom correspondence should be addressed.

Contributed by the Heat Transfer Division for publication in the JOURNAL OF HEAT TRANSFER. Manuscript received by the Heat Transfer Division, July 2, 1998; revision received, Sept. 11, 1998. Keywords: Microwave, Radio Frequency, Therapeutic Ultrasound, Tissue Ablation, Tissue Models. Associate Technical Editor: Y. Jaluria.

low temperatures. In some cases it is desirable to use the excursion for purposes of irreversibly destroying tissue, such as in killing cancerous lesions. In other cases, it is desirable to conduct the thermal excursion so as to maximize the reversibility of the process, such as in cryopreservation of tissue for transplantation. In each case, control of the thermal kinetics via manipulation of the temperature in time and space is critical to successful implementation of the specific objective.

As experience has accrued on how to apply the mechanisms of thermal transport to control the kinetics that govern processes in living tissues, it has been possible to develop commercial applications based on the principles of bioheat transfer. The types of intellectual property involved in these applications include processes, apparatus, and even living materials which can be transplanted into the human body. It has been projected that the economic impact of bioengineering will place it among the most important engineering disciplines within the next two decades. Bioheat transfer will have an important role in that development, including diverse areas of application. Some of these application areas are already developing, as will be discussed in this paper, and others remain to be defined.

Bioheat Equation

A major distinguishing feature of heat transfer processes in living tissues is the influence on the temperature distribution of local perfusion of blood through the vascular network. For many conditions there is a significant difference in the temperature of blood and the tissue through which it flows. Consequently, convective heat transport will occur, altering the temperatures of both the blood and tissue. This perfusion-based heat transfer interaction is critical to a number of physiological processes such as thermoregulation and inflammation. The characteristics of the blood/tissue thermal interaction is a function of several parameters including the rate of perfusion and the vascular anatomy, which varies widely among the different tissues, organs of the body, and pathology. Effective understanding and modeling of bioheat transfer requires accurate data on the vascular anatomy, and designing experiments to obtain these data is an important and productive area of collaborative interaction between bioengineers and physiologists. The literature on mathematical modeling of bioheat transfer phenomena has been reviewed recently by Charney (1992), and this reference is highly recommended for readers desiring an in-depth presentation of the topic. The current review will present only an introductory discussion of the bioheat equation to cover some recent developments and to provide a background for the discussion of further application areas.

The rate of perfusion of blood through different tissues and organs varies over the time course of a normal day's activities, depending on factors such as physical activity, physiological stimulus, and environmental conditions. Further, many disease processes are characterized by alterations in blood perfusion, and some therapeutic interventions result in either an increase or decrease in blood flow in a target tissue. For these reasons, it is very useful in a clinical context to know what the absolute level of blood perfusion is within a given tissue. There are numerous techniques which have been developed for this purpose over the past several decades. In some of these techniques, the coupling between vascular perfusion and local tissue temperature is applied to advantage to assess the flow through local vessels. These measurements depend on an inverse solution of equations which model the thermal interaction between perfused blood and the surrounding tissue.

The seminal work on developing a quantitative basis for describing the thermal interaction between tissue and perfused blood was published 50 years ago by Pennes (1948). Pennes conducted a series of experiments to measure the temperature distribution as a function of radial position in the forearms of nine human subjects. A butt-junction thermocouple was passed completely through the arm via a needle inserted as a temporary guideway, with the two leads exiting on opposite sides of the arm. The subjects were unanesthetized so as to avoid the effects of anesthesia on blood perfusion. Following a period of normalization, the thermocouple was scanned transversely across the mediolateral axis to measure the temperature as a function of radial position within the interior of the arm. The environment

Nomenclature

a = Arrhenius rate constant, s^{-1}
A = Gausian coefficient at distance z, MHz
B = cooling rate, K/s
c = specific heat, J/(g.K)
C = concentration, mol/m^3
D = diameter of transducer, cm
E = **E** field, V/m
ΔE = activation energy, J/mol
f = frequency, A
h = convection coefficient, $W/(m^2.K)$
I = needle current, A
I_A = acoustic intensity, W/m^2
J = flux, $mol/(m^2.s)$
k = thermal conductivity, W/(m.K)
L_p = permeability to solvent (water), $m^3/(N.s)$
m = perfusion rate, $kg/(m^3.s)$
p = pressure, kPa
P = power deposition, W/m^3
r = radial position, m
R = universal gas constant, 8.31441, kJ/(kmol.K)
S = surface area, m^2
SAR = specific absorption rate, W/kg
t = time, s
T = temperature, K
U = overall heat transfer coefficient, $W/(m^2.K)$
v = molar volume, m^3/mol
$\mathbf{V}$ = mean vessel blood flow velocity, m/s
W = acoustic power, W
x = coordinate position, m
y = coordinate position, m
z = axial coordinate, m
α = amplitude attenuation for the catheter wall, Np/(m.MHz)
γ = nonlinear correction factor for attenuation ($1 \leq \gamma \leq 1.3$)
η = ultrasonic attenuation coefficient, Np/cm
ϵ^* = complex dielectric constant, farad/m
κ = electrical conductivity, Seimens/m
μ = ultrasonic intensity absorption coefficient, Np/cm
ϑ = current density, A/m^2
ρ = density, kg/m^3
π = osmotic pressure, kPa
σ = reflection coefficient
χ = thermal equilibrium length, m
Ψ = volume, m^3
ω = permeability to solute (at zero volume flow), mol/(N.s)
Ω = injury factor

Subscripts

a = arterial
b = blood
ex = extracellular
g = reference state
i = counter index
in = intracellular
o = initial
is = external casing
r = radial component
s = surface
o = spatial peak
S = solute
t = tissue
v = vessel
V = volume
z = longitudinal component
1 = coolant column
2 = external casing

in the experimental suite was kept thermally neutral during experiments. Pennes' data showed a temperature differential of three to four degrees between the skin and the interior of the arm, which he attributed to the effects of metabolic heat generation and heat transfer with arterial blood perfused through the microvasculature.

Pennes proposed a model to describe the effects of metabolism and blood perfusion on the energy balance within tissue. These two effects were incorporated into the standard thermal diffusion equation, which is written in its simplified form as

$$\rho c \frac{\partial T}{\partial t} = k\nabla^2 T + q_m + \dot{m}\rho_b c_b (T_a - T). \qquad (1)$$

Metabolic heat generation, q_m, is assumed to be homogeneously distributed throughout the tissue of interest as rate of energy deposition per unit volume. It is assumed that the blood perfusion effect is homogeneous and isotropic and that thermal equilibration occurs in the microcirculatory capillary bed. In this scenario, blood enters capillaries at the temperature of arterial blood, T_a, where heat exchange occurs to bring the temperature to that of the surrounding tissue, T. There is assumed to be no energy transfer either before or after the blood passes through the capillaries, so that the temperature at which it enters the venous circulation is that of the local tissue. The total energy exchange between blood and tissue is directly proportional to the density, ρ_b, specific heat, c_b, and perfusion rate, m, of blood through the tissue, and is described in terms of the change in sensible energy of the blood. This thermal transport model is analogous to the process of mass transport between blood and tissue, which is confined primarily to the capillary bed.

A major advantage of the Pennes model is that the added term to account for perfusion heat transfer is linear in temperature, which facilitates the solution of Eq. (1). Since the publication of this work the Pennes model has been adapted by many researchers for the analysis of a variety of bioheat transfer phenomena. These applications vary in physiological complexity from a simple homogeneous volume of tissue to thermal regulation of the entire human body (Wissler, 1961; 1985). As more scientists have evaluated the Pennes model for application in specific physiological systems it has become increasingly clear that many of the assumptions foundational to the model are not valid. For example, Chato (1980), Chen and Holmes (1980), and Weinbaum, et al. (1984) all demonstrated very convincingly that thermal equilibration between perfused blood and local tissue occurs in the precapillary arterioles and that by the time blood flows into vessels 60 μm in diameter and smaller, the equilibration process is complete. Therefore, no significant heat transfer occurs in the capillary bed; the exchange of heat occurs in the larger components of the vascular tree. The morphology of the vasculature is vastly different in these segments of the circulatory system (Zweifach, 1961). The capillary bed is characterized by a diffuse network of small vessels (less than 10 μm in diameter and 2 mm in length). The larger arterioles and venules that lead to and from the capillary bed lie in closely matched pairs with countercurrent blood flow. In this region heat transfer occurs between blood and tissue, and also between the warmer arriving arteriolar blood and the cooler returning venular blood. Plus, the very specific geometry of the vessels provides a directional bias to the local heat flow. This geometry varies considerably among the various organs of the body, which contributes to the need for specific models for the thermal effects of blood flow (as compared to the Pennes model, which incorporates no information concerning vascular geometry). It would appear as a consequence of these physiological realities that the validity of the Pennes model is questionable.

Many investigators have developed alternative models for the exchange of heat between blood and tissue. These models have accounted for the effects of vessel size (Chato, 1980: Chen and Holmes, 1980; Mooibroek and Lagendijk, 1991), countercurrent heat exchange (Mitchell and Meyers, 1968; Keller and Seiler, 1971; Baish, 1990; Mooibroek and Lagendijk, 1991; Huang et al., 1996), as well as a combination of partial countercurrent exchange and bleed-off perfusion (Weinbaum and Jiji, 1985). All of these models provided a larger degree of rigor in the analysis, but at the compromise of greater complexity and reduced generality. Some of these models have been the subject of considerable debate concerning their validity and range of appropriate application (Baish et al., 1986; Weinbaum and Jiji, 1987; Wissler, 1988a, 1988b). These studies also led to an increased appreciation of the necessity for a more explicit understanding of the local vascular morphology as it governs bioheat transfer, which has given rise to experimental studies to measure and characterize the three-dimensional architecture of the vasculature in tissues and organs of interest.

It is quite interesting that, in the context of the above studies to improve on the widely applied but questioned Pennes model, this year marked the 50th anniversary of the publication of Pennes' paper. For this occasion Wissler (1998) returned to Pennes' original data and analysis and reevaluated his work. The results of this analysis were published along with Pennes' original paper and an invited editorial (Nelson, 1998) in the *Journal of Applied Physiology.* Given the hindsight of five decades of advances in bioheat transfer plus greatly improved computational tools and better constitutive property data, Wissler's analysis pointed out further flaws in Pennes' work which had not been appreciated previously. However, he also showed that much of the criticism that has been directed toward the Pennes model is not justified, in that his improved computations with the model demonstrated a good standard of agreement with the experimental data. Thus, his conclusion is that "those who base their theoretical calculations on the Pennes model can be somewhat more confident that their starting equations are valid."

In conclusion, it should be clear that developing a more efficacious definition and application of the bioheat equation remains a topic of importance and an area ripe for potentially significant contributions. Readers desiring a more thorough understanding are referred to the primary literature and the review by Charney (1992) for details. The remainder of this paper will address a broad range of topics in bioheat transfer applications, with an emphasis on describing the current state of the art and providing an indication of where the field appears to be headed.

Thermally Driven Surgical Techniques

Surgical Energy Tools. Focused energy has been applied quite effectively as a tool for controlled tissue destruction in a broad spectrum of surgical procedures. In all cases the surgical process is coupled with changes in temperature to achieve the desired alterations in physiological state. As a tool in surgery, cutting and coagulating with a handset that delivers radio frequency (RF) energy is probably used in about 80–90 percent of all surgical cases worldwide. Although lasers are used infrequently in surgery, the primary application is for vaporizing tissue rather than for the general cutting and coagulation found at the skin incision of all open surgical procedures. The cutting is done using a blunt, rounded blade which when radio frequency (RF) energy is applied, easily glides through the tissue while simultaneously providing hemostasis. On a microscopic level, cells heat and burst in the vicinity of the blade and the speed of cutting depends not only on the tissue type and force applied by the surgeon, but also the power level and mode of the RF generator. When bleeding occurs, the surgeon switches to a coagulation mode, and the blade coagulates by applying a modulated duty cycle that causes arcs to the tissue to coagulate blood and seal small blood vessels. A large dispersive or ground electrode is attached to the patient's thigh.

In cutting or coagulation during surgery, the blade electrode or needle used by the surgeon has a much greater current density than the dispersive electrode due to surface area differences. As the blade is activated with RF, an arc is established and current is highly concentrated where the arc strikes tissue. Opposite to the direction of travel, the tissue has already been cut, thus biasing electric field lines in the tissue path in the direction of travel. In addition, the optimal waveform is a sine wave for cutting tissue. Cells adjacent to the scalpel are vaporized but thermal damage is very localized and shallow. Deviation from a continuous sine wave adds coagulation or hemostasis to the cutting. Coagulation of tissue is accomplished by arcing to the tissue in a high voltage, pulsed output. A charred black mass is formed during tissue protein denaturation (Pearce 1986).

The dispersive electrode is the large return pad placed on the patient's skin. The temperature rise at a point under the conductive pad in contact with the patient is estimated to be (Pearce, 1986)

$$T = \left(\frac{1}{\kappa \rho_t c_t}\right) J^2 t + T_o . \qquad (2)$$

Surface coagulation of tissue is accomplished during surgery for organs that bleed easily, such as the liver. One technique is to use RF coagulation delivered to the tissue in an argon beam. This procedure allows surface coagulation to be performed without contact with the tissue, which avoids sticking of the instrument to the tissue that causes further bleeding. This method is called fulguration, the conduction of a high-frequency electrical current to tissue via a plasma arc. The plasma current conduction is due to electron motion and is created by ionization of the surrounding (background) gas, which normally is air. The breakdown voltage is much greater for air than for argon, so argon is used advantageously for plasma coagulation. With air, the depth of damage for a noncontact application is 1.4–1.9 mm. With argon used as the background gas for the arcs, the depth of damage is 0.5–1.0 mm, accompanied by a much longer allowable distance from device to tissue of 12 mm versus 1.0 mm for air background.

Thermal Therapy Utilizing Hyperthermia Techniques. Hyperthermia is the elevation of tissue temperature to at least 43°C for an extended time period of 30 to 60 minutes. It is designed to be used primarily as an adjuvant therapy in conjunction with radiation and/or chemotherapeutic agents for cancer treatment. In hyperthermia treatments, large volumes of tissue are heated with one of the following energy sources: microwave, ultrasound, radio frequency, or conductive sources. The sources may be placed directly into the tissue or tumor (interstitially) for localized heating. Another modality is to treat superficial tumors transcutaneously with surface applicators that are in direct contact with the target region. These technologies utilize planar ultrasound (Ryan et al., 1992), microwave waveguides, or microstrip sources (Ryan et al., 1995). A more controllable version utilizes focused ultrasound applied transcutaneously that scans a precise focal zone around the target tissue. The scanning can be done with a mechanical system or with an electronically focused system where the beam is synthesized with a number of sources with phase and amplitude control.

Thermal Ablation Techniques. Thermal ablation techniques are autonomous and do not necessarily require any adjuvant therapy such as radiation or chemotherapy. To be successful these techniques strive to raise the tissue temperatures more rapidly and to higher target temperatures than hyperthermia, to more successfully treat with heat alone. Often the treatments are for benign disease and thus a failure to treat the entire treatment volume is less catastrophic than in cancer treatment. Since thermal therapy is intended to be autonomous, the activation times are much shorter than for hyperthermia and may range from seconds to minutes. In some cases the thermal treatments replace surgical procedures or may be performed during a surgery and replace a lengthy tissue removal procedure, to shrink or deactivate tissue without removal. In cases of cancer treatment an added margin of at least 1.0 cm is necessary and are only successful if the lesions are solitary and relatively small. For larger tumors multiple treatments may be required, and this complicates the dosage distribution and makes it more difficult to assure coverage of the total treatment volume plus a margin. The following interstitial sources are applied for thermal ablation: microwave, ultrasound, RF, laser, or cryoablation. These sources will be developed in the following pages.

Thermal Energy Sources

Therapeutic Radio Frequency (RF) Sources. RF energy applied to different anatomic sites has been applied since the early 1900s, when the early electrosurgical, spark gap generators called the ''Bovie'' were developed. Early lesioning took place in neurosurgical sites to ablate nerve structures to alleviate pain, muscle spasticity, epilepsy, involuntary movement, tremor, and other neurological disorders. More recently, by following anatomic maps of the brain and spinal cord in conjunction with stereotaxic guidance systems that place a probe precisely in the brain, specific structures can be treated. The treatment consisted of an initial test ablation of short duration in an awake patient, then the neurosurgeon would evaluate the change in the neurologic condition (such as lessening of a tremor) and whether the desired effect was achieved. If so, they would perform a second activation of longer duration to achieve permanence. This same procedure was also done in nerve roots of the spine to alleviate pain.

The method of heating with RF starts with alternating current flowing between two electrodes. The tissue impedance is a complex quantity with a real (resistive) component and an imaginary (reactive) component. The resistive or ionic component generates heat by Joule's law, and the reactive component allows for the exchange of energy stored in an electric or magnetic field. Interstitial RF systems operate between 100 kHz and 27 MHz. The lower limit avoids muscle stimulation (Kapp and Prionas, 1992).

RF sources are often simple hollow metal tubes inserted into tissue and require direct tissue contact. They can either be ganged for current to flow between all needles referenced to an external dispersive pad placed on the patient, or individual needles can be multiplexed to shape the heating field. The applicators are simple to fabricate and can be insulated from regions where no heating is intended. Disadvantages include the necessity of a parallel implant to insure a more homogeneous heating field, and the close spacing required due to the poor depth of penetration.

By applying a voltage between implanted needles, an RF current is induced in tissue resulting in joule heating. If the RF needles are implanted nearly parallel, power deposition and temperatures will tend to be uniform in the longitudinal direction. The SAR for an array of parallel RF electrodes is

$$\mathrm{SAR}(r) = \frac{(\kappa/\rho_t)}{8\pi^2 \omega^2 |\epsilon^*|^2} \left[\left(\sum_{i=1}^{m} \frac{I_i (x - x_i)^2}{r_i^2} + \sum_{i=1}^{m} \frac{I_i (y - y_i)^2}{r_i^2} \right)^2 \right] . \qquad (3)$$

Calculations were done in two dimensions with the assumptions of homogeneity in electrical and thermal properties and infinitely long needles to ignore the edge effects. Prior (1991) use the two-dimensional finite difference method to obtain the two-dimensional solution to the bioheat equation to model water-cooled RF sources. At 1.0-cm spacing between needles, a needle surface temperature of 49°C was necessary to encompass the array in the 42°C isotherm with no cooling. With cooling, the needle surface was brought down to 46°C, with the array inside the 43°C isotherm.

Therapeutic Ultrasound Sources. In ultrasound therapy, vibrational energy is propagated by the transducer as a mechanical wave by the motion of particles. Energy attenuates as it passes through tissue, of which part is absorbed and part is scattered to be absorbed elsewhere. There are viscous forces between particles that cause a lag between pressure and velocity, thus energy is lost during each cycle. This mechanism of energy absorption is called relaxation.

Simple piezoelectric devices of cylindrical shape that are poled in the radial mode launch an acoustic wave into tissue for therapeutic treatment. The elements are from 1.0 to 10.0 mm in diameter, and the larger sizes can be sectored for control of quadrants around the sources. The elements can be sectioned longitudinally to allow independent control along the source axis. No direct tissue contact is necessary for these devices, although a fluid coupling is necessary both for cooling of the lossy sources and acoustic coupling. In addition, the catheter or delivery tube partially absorbs the field. The small devices, which are high frequency, have a rapid fall-off of temperature and are rather delicate. The acoustic intensity distribution produced by the cylindrical source in a catheter is approximated by Diederich (1996):

$$I_A = \frac{I_s r_o}{r} e^{-2\alpha f^{\gamma}(r-r_o)} \tag{4}$$

and the power deposition is

$$P = 2\alpha f I_A . \tag{5}$$

If the devices are small in relation to a wavelength, the elements can have individual amplitude and phase control to shape power deposition (Buchanan and Hynynen, 1994). Volumetric power deposition is shown below with the assumptions that all attenuated power is absorbed, and that the acoustic properties of tissue remain unchanged during insonication.

The intensity of the ultrasonic field by focused ultrasonic transducers is (Kolios et al., 1996)

$$I_A(r, z) = \frac{8W_o}{\pi D_o^2} A(z) e^{-2\eta z} e^{(-8Ar^2)}/D_o^2 \tag{7}$$

so that the power is

$$P(r, z) = \mu I_{sp}(r, z) e^{-\eta z} . \tag{8}$$

These devices are able to be coupled to the body with fluid and focused deep into the tissue. The size, shape, and intensity of the focal zone is the result of the frequency, size, and radius of curvature of the spherical piezoelectric source. Due to the smallness of the focal zone, small zones of tissue are heated very rapidly to ablate without much thermal spread.

Therapeutic Microwave (MW) Sources. At frequencies above 300 MHz, tissue acts as a lossy dielectric, and the predominant mode of microwave propagation for electromagnetic waves is radiative, rather than conductive (Stauffer, 1998). Electromagnetic energy transforms into kinetic energy inside cells, forcing ionic conduction and vibration of water and protein molecule dipoles. By rotation of dipole molecules, conduction currents are formed, and losses are due to electrical resistance. Additionally, displacement currents are induced which cause further loss due to the viscosity in the cells (Johnson and Guy, 1972). Tissues of high water content (muscle, brain, organs, skin) have high absorption and low penetration. Tissues of low water content (fat, bone) have low absorption.

The microwave antenna embedded in a catheter in tissue forms an insulated antenna embedded in an electrically dense medium. The system can be treated as a generalized coaxial transmission line with the antenna surface acting as the inner conductor, the catheter as the insulator, and the tissue acting as an extensive outer conductor (Trembly, 1985). Small coaxial MW antennas can be designed to heat tissue through the catheter wall that they reside in. For best performance in dipole designs, the two half-sections are a quarter wavelength. Dipole antennas are typically designed for 433, 915, or 2450 MHz. The phase relationship of dipole antennas is such that they can be phase focused to move the power deposition pattern around in the target region without moving the sources. No direct tissue contact is required for the microwave sources. Modified designs include choke antennas that make the active length of the antenna less susceptible to depth of insertion in tissue (Ryan, 1991). Disadvantages of microwave antennas include losses in the feedline cables, impedance mismatches, standing waves along the antenna feedline, and inability to control power along the antenna length. Microwave sources are typically either resonant dipole, helical, or helical-dipole antennas (Ryan, 1991). These sources are typically placed as arrays to enhance the treatment volume covered.

The specific absorption rate (SAR) for dipole microwave antennas is discussed at length elsewhere (Trembly, 1985). The SAR is calculated as

$$\mathrm{SAR} = \frac{r}{2\rho} [|\mathbf{E}_r|^2 + |\mathbf{E}_z|^2]. \tag{9}$$

Since the typical array dimensions of 2 cm between antennas, in the form of a square, is comparable to the wavelength in tissue, there are strong phase coherence effects (Trembly et al., 1995). Phase focusing has been performed successfully in the human brain during microwave heating sessions (Ryan et al., 1991). A pair of antennas in phase at 915 MHz was shown to have maximum SAR at the midpoint between antennas, and thus will heat maximally in the target and not at the source (Trembly et al., 1991).

Helical antennas can be of varied geometry which will drastically alter the mode of propagation (Ryan, 1991). When the circumference of the helix is about a wavelength, the antenna operates in the end-fire mode, producing a circularly polarized beam directed along the axis of the helix (Astrahan et al., 1991). When the helix diameter is small compared to a wavelength as in thermal therapy applications, the antenna operates in the normal mode with most of the radiation normal to the axis of the device.

Surface cooling of the microwave sources will provide deeper penetration into tissue. Both air and water have been used for the cooling medium (Trembly et al., 1991). Gentile (1991) modeled a water-cooled antenna by neglecting the external casing or catheter since it was much smaller than a wavelength. The wave number of the irradiating tissue was determined by the cooling liquid. Total heat transfer coefficient U is calculated below with dependence on the catheter wall thickness and thermal conductivity.

$$U = \left[\left(\frac{r_2}{h r_1} \right) + \left(\frac{r^2}{k_{is}} \right) \ln \left(\frac{r_2}{r_1} \right) \right]^{-1} \tag{10}$$

Therapeutic Cryoablation Sources. As another technique for ablation of tissue, cryoablation has been applied to benign prostatic hypertrophy (BPH), myomas, uterus, and also to liver and prostate cancer. Extreme cold can cause cell death without compromising the structural integrity of the tissue. In addition, a test lesion can be made in some cases (i.e., cardiac), the effect evaluated, and the decision made whether to re-lesion for a permanent effect. Delivery systems are generally large and deliver liquid nitrogen to the probe site to freeze tissue. The iceball formed can be observed by ultrasound imaging, but the zone of coagulation necrosis lies typically within the zone of the −40°C isotherm. Often two freeze-thaw cycles are delivered.

Cryosurgery employs extremely low temperatures as a surgical tool for tissue destruction. Ice forms on the cryoprobe and propagates into tissue as a freeze front leading to localized tissue destruction. The transition stage between phases advances as the moving interface travels radially away from the source (Weill et al., 1993). For cancer treatment where large treatment volumes are required, a single probe in large tumors will not address a sufficient volume to be effective.

More recently smaller catheter-based steerable applicators have been used with the introduction of a new technology for clinical use. The system utilizes a room-temperature liquid refrigeration and adiabatic expansion of gases, the Joule-Thomson effect. One catheter lumen is reserved for a vacuum channel which facilitates evaporation and freezing of the tip. In this manner, smaller steerable devices that only cool at the tip can be placed percutaneously through blood vessels to work on the inner heart (Lewis and Dubuc, 1998) or other structures where ablation is required.

Clinically, cryoablation is used in a variety of anatomic sites, depending primarily on the size of the applicator and access to target sites. Some recent work in the brain utilized a 3-mm probe that had a 2-cm freezing tip to create 1.4-cm lesions. All lesioning was monitored by diagnostic ultrasound (Quigley et al., 1992). Ultrasound was found to consistently underestimate the lesion size. Monitoring the ice ball with ultrasound will overestimate the lesion size, since the kill zone is much lower than 0°C. In experiments in animals, it was found that a single freeze-thaw cycle resulted in a lesion diameter of 64 percent of the ice ball diameter. In a double cycle of freeze-thaw-freeze-thaw, the lesion diameter was 83 percent of the diameter seen on ultrasound (Dilley et al., 1993). A further discussion of cryoablation is presented in the subsequent section on cryopreservation.

Thermal Significance of Blood Vessels. Large blood vessels may be heat sources or heat sinks and are ignored by the bioheat equation. The directionality of flow is also ignored. To determine whether or not a vessel is thermally significant, the thermal equilibrium length was calculated. This work was done by Mooibroek and Lagendijk (1991) as follows:

$$\chi_{eq} = \left[\frac{\rho_b c_b}{8k_b}\right] V D_v^2 \left[\frac{3}{4} + \frac{k_b}{k_t} \ln\left(\frac{D_t}{D_v}\right)\right]. \qquad (11)$$

If a vessel length is smaller than the thermal equilibrium length, it is considered thermally significant and should not be ignored. Capillaries are in thermal equilibrium with their surroundings, whereas small arteries and veins experience significant heat transfer. Large arteries and veins experience very little heat transfer. Vessels range in size from capillaries (4 μm), arterioles (10 μm), venules (15 μm), large arteries (1500 μm), and large veins (3000 μm) to the aorta (5000 μm). The thermal equilibrium length, χ, for various categories of vessels is

Vessel	**Diameter (μm)**	**χ (m)**	**Percent of vascular volume of body**
Capillary	4	2×10^{-7}	6.6
Arterioles	10	5×10^{-6}	3
Venules	15	2×10^{-6}	12
Large arteries	1500	4	7
Large veins	3000	5	12
Aorta	5000		3

Specific Thermal Therapies

Transmyocardial Revascularization. For chronic heart disease of persons of poor surgical risk, transmyocardial revascularization can be done. With this technique, a CO_2 laser is used to bore 1-mm diameter holes numbering about 26 in the left ventricle wall in order to revascularize areas of ischemia to revitalize the tissue (Cooley et al., 1995). The exact mechanism is not understood at this time, although the direct perfusion of the ischemic area is accomplished as ventricular blood flows through the new channels of the myocardium. The clinical effect is to have patent channels in the myocardium, confirmed by histological studies (Horvath et al., 1995), and these channels connect to native vasculature (Cooley et al., 1995).

Skin Resurfacing. Several applications of wrinkle removal using skin resurfacing have been performed by laser irradiation. The laser is passed slowly over the target area to be reshaped, and the heat causes redistribution of the collagen layer. This will initially cause reddening, and over time, the resolution of wrinkles, deep lines, and acne scars.

Skin resurfacing is able to remove layers of skin of about 100 um without bleeding (Apfelberg, 1996). Combining short 1-ms pulses, much shorter than tissue thermal relaxation times, with high power (600 W), heat is dissipated during tissue vaporization, and little is conducted, keeping the tissue normothermic. Spot size is 2.25 mm with 300 mJ/spot. The computer moves the laser in a preprogrammed pattern. A CO_2 laser is absorbed in water and thus in tissue, 90 percent of the radiant energy is absorbed in the superficial 30 um. Skin ablation requires energy fluence of 5 J/cm^2. As tissue is vaporized, shrinkage of the remaining dermis is seen. Thus, during healing, the skin is smooth and tighter. Heat-induced collagen shrinkage occurs at 55–60°C (Dover and Hruza, 1996). The laser vaporization results in a persistent redness that lasts for months (Fulton, 1996). Thermal coagulation of collagen is an end point of a kinetic rate process of thermal damage which is linear with time and exponential with temperature. Collagen is naturally birefringent, that is, it appears bright when illuminated with 90-deg polarized light. Collagen loses this birefringence with temperature exposure and is an indicator of thermal damage (Pearce et al., 1993).

Myoma Treatment. Of the more than 600,000 hysterectomies done annually in the U.S., about 30 percent are performed due to the presence of myomas in the walls of the uterus. As the desire by women to avoid hysterectomy increases, a sound procedure is necessary to treat rather than remove the uterus. Surgical procedures that are minimally invasive include laparoscopic myomectomy, which presents great difficulties in suturing the cavity left by the myoma defect, as well as removing the myoma mass through the 10-mm trocar sites (Dubuisson et al., 1997). To obviate surgical removal, one method of treatment utilizes coagulation of the myomas and has been attempted with a variety of energy sources. An Nd:YAG laser has been used to achieve this by drilling holes in the myoma with the 600-μm fiber and treating to about a diameter of 5 mm per treatment site. Altogether a total of 75–100 punctures and activations were made in a 5-cm diameter myoma (Goldfarb, 1992). This took about 30 minutes. Shrinkage of 50–90 percent was achieved in the myomas, as evaluated by diagnostic ultrasound.

Another form of coagulative treatment utilizes bipolar needles comprised of long sharp parallel needles separated by about 5 mm. These needles are placed into the myoma and activated with RF energy at 70 W for 10 s. Multiple treatments are done at 3–5 mm spacing and therefore the entire myoma takes about 30 minutes to treat (Goldfarb, 1995). Second-look laparoscopy was used to follow up the patients. Many had adhesions, a reaction on the treated surface that can cause significant pain and discomfort. The problems underlying the technique are the lack of thermal dose information per treatment site, lack of attention to instrument trajectory, and surface coagulation as the only indicator of thermal damage. In fact, to avoid adhesions, the surface should be kept normothermic and subsurface temperatures should be kept below 95°C to avoid steam formation and popping that can cause mechanical damage.

Liver Treatment. Often metastases are found in the liver as isolated cancer nodules that can be treated using percutaneous procedures by radiologists, assisted by image guidance. Early treatment utilized RF where an electrode was placed in the nodule and then ablated by energy delivery. More modern techniques utilize RF energy that is temperature controlled to avoid steam formation and charring if the tissue is heated excessively. To enlarge the size of the lesion, special techniques such as cooling of the electrode (Goldberg et al., 1998), or infusion of saline (Livraghi et al., 1997), or hypertonic saline (Hoey et al., 1997) may enlarge the lesion without enlarging the size of the device. One problem with fluid infusion in tissue is the uncertainty of where it actually travels to (Goldberg and Gazelle, 1998; Livraghi et al., 1997). The clinical effect is coagulation necrosis of the lesion as imaged on CT or MRI. An extra rim of damage of about 10 mm is also added to ensure complete cancer obliteration. If successful, the necrotic zone due to the thermal treatment will cause localized cancer obliteration.

The liver is a common site for both primary and metastatic malignancies and focal treatments to the malignancy are appropriate for a number of patients. Percutaneous techniques go directly through the skin with only a small needle (18–20 gage) puncture and are guided by diagnostic ultrasound visualization where both the malignancy and needle are visible. At high power activations of RF energy, microbubbles form and steam is vented through the needle hub. Care must be taken to avoid an air embolus entering the bloodstream. A lesion of 1–2 cm in diameter is produced in liver, and thus for a larger target region, multiple needle passes are necessary (McGahan et al., 1993).

Many techniques have been attempted to increase the lesion size of coagulative necrosis without increasing applicator size or number of activations. For radiologists doing percutaneous procedures, a small 18-gage needle is the ideal size. To increase lesion size, long activation times have been done with temperature control at the needle tip to avoid charring and sticking to the tissue. Saline injection through the applicator increases lesion size by creating a virtual electrode, since saline is of higher electrical conductivity than tissue. Unfortunately, wherever the fluid travels the lesion will follow. Any ducts, vessels, or other physiological tracks, such as muscle fibers, may redirect the lesion (Goldberg and Gazelle, 1998). Another method is to cool the electrode and increase power. This approach has been shown to significantly increase lesion size without infusing fluid into the tissue. A third strategy is to pulse RF power, which also increases lesion size.

Other groups have utilized an Nd:YAG laser fiber placed in the liver to create a lesion. Lesions were increased in size by increasing time of activation, power, repetitions, and advancing the laser while activated. Time extension only helps to a certain degree, since as the tissue is charred, the laser cannot radiate due to increased internal scattering (Matsumoto et al., 1992).

An alternate treatment method is to use cryosurgery. Two freeze-thaw cycles are used with liquid nitrogen to kill tumors by cell destruction and obliteration of small blood vessels. Freezing for eight minute's duration is followed by 20 minutes of thawing prior to refreezing. The probe diameters are 6 or 10 mm (Ravikumar et al., 1994). The procedure is monitored with ultrasound. Local control is achieved in most patients and recurrence occurs outside of the treatment zone (Ravikumar et al., 1991). Ultrasound shows the progression of the iceball relative to the tumor margin and a margin of 10 mm is planned during the treatment, beyond the tumor margin (Ravikumar et al., 1994).

Breast Treatment. With the advent of more sensitive radiographic equipment and more frequent mammograms being done on women, breast lesions that are small and isolated are now more frequently encountered prior to growth and metastasis. If caught early, these lesions are considered solitary and if ablated, the patient can be cured (Robinson et al., 1998). Several attempts at using lasers as an energy source have been attempted. The laser is placed with a needle in the center of the lesion, the fiber is advanced, and the needle withdrawn. The laser is then kept on for several minutes to obliterate the lesions. Some studies have shown treatment failure and regrowth, probably due to lack of sufficient penetration of a single laser applicator.

Cardiac Ablation. For the condition of cardiac arrhythmias, heat is applied to ablate the tissue of the cardiac wall to produce irreversible damage. Often a minor test burn is given, the abnormality evaluated, and then a permanent lesion created. These devices enter percutaneously through the femoral artery and are steered under fluoroscopic guidance to the inner chambers of the heart. Various energy sources have been used in clinical trials to ablate these false ectopic sites and restore a normal heart rhythm. For ventricular tachycardia and atrial fibrillation, deeper lesions are required and thus microwave sources have been used to achieve deeper penetration in tissue (Berube and Liem, 1998).

Catheter ablation for cardiac tachyarrythmia has been used to replace a surgical procedure. Early techniques utilized a DC shock of 100–300 J from a defibrillator resulting in a peak voltage of 2–3 kV at the electrode surface. This resulted in an explosive flash and spark accompanied by a shock wave of 1–2 atm pressure. Delivery catheters were damaged and tissue ruptured. Alternatively, using RF, the voltage is less than 100 V, eliminating sparking and barotrauma (Huang et al., 1991).

Radio frequency electrodes can overheat the electrode-tissue interface since power falls off as $1/r^4$, away from the electrode source. The RF electrode heats resistively, unlike the microwave antenna which radiates an electromagnetic field into the surrounding tissue. The EM field heats by tissue friction and does not depend on the flow of current from the electrode to the tissue. Thus the microwave device can heat more deeply and access lesion structures that are not accessible to RF devices. A thin flexible helical antenna is used for the microwave energy delivery at 2540 MHz (Langberg et al., 1991; Berube and Liem, 1998). This treatment successfully interrupts atrial-ventricular conduction.

In treatment of cardiac vessels, a balloon with a laser is used to provide a heat treatment to a stenosis. A stainless steel coil in the balloon is heated with an Ar laser through reflection and absorption. The balloon heats the artery and expands the lumen with temperatures of 60–70°C for 20–30 s (Arai et al., 1991). Another technique of thermal angioplasty utilizes a microwave antenna at 2450 MHz. The microwave power is deposited directly in the vessel wall and heated using the following parameters: time of 30–60 s, balloon pressure of 2–5 atm, and balloon temperature of 50–115°C (Smith et al., 1992).

Endometrial Ablation. Endometrial ablation is a thermal treatment done for dysfunctional bleeding of the uterus. The endometrium is the inner lining of the uterus, and excessive bleeding can be debilitating for women. The only treatment offered prior to thermal therapy was a surgical procedure where a loop electrode was used to resect the endometrium, or a rollerball was used to ablate the endometrial surface. The complications and the significant surgical skills demanded by these procedures stimulated the search for an office-based thermal treatment. Several treatments have been developed, ranging from a microwave or cryoablation treatment currently in experimental studies to thermal balloon treatments just out of clinical trails.

One system utilizes a fluid filled balloon that is inserted transvaginally into the uterus and is inflated, thus compressing the target tissue. A heater is used to heat the fluid to 87°C, thereby heating the tissue by conduction. An alternate system also inflates, but with air, and has 12 independent conductive patches on the outside surface with a thermistor centered on each patch. In this manner, the patches deliver temperature regulated RF to the tissue to adjust to local blood flow variations and tissue thermal and electrical properties (Ryan et al., 1998). The clinical effect is the ablation and destruction of the endometrium and will result in less bleeding or potentially, amenhorrea (no bleeding).

Female Sterilization. Female sterilization is currently done by using a surgical procedure to tie or coagulate the fallopian tubes to prevent sperm and egg passage. Early in this century, technology had been applied to cauterize the tubes by using a ''hot poker,'' thus relying on thermal conduction to coagulate the tubes. More contemporary devices utilize microwaves with a dipole antenna and have been proven in a feline model (Trembly et al., 1998). The microwave catheter can be inserted transvaginally and thus obviates a surgical procedure. An alternate system utilizes two cylindrical electrodes on a catheter that fits into the lumen of the fallopian tube and applies energy such that the temperature between the electrodes is raised to 95 or 105°C. The system has been proven to be successful in a rabbit model (Hurst et al., 1998). The immediate clinical effect is the inflammatory response that due to swelling will close off the tube. The long-term effect is the fibrosis and scarring which will obliterate the tubal lumen.

Shoulder Capsule Treatment. Recently, several devices have appeared on the market for collagen shrinking of the shoulder capsule. These devices have an RF energy source and apply energy as a ball-type electrode is passed over the tissue surface under arthroscopic visualization. As the electrode applies energy to the surface that it is in contact with, the area visibly shrinks and is reshaped. This replaces more invasive therapy and the healing time is much shortened. The clinical effect is to shrink the capsule acutely and then additional shrinkage may take place over time. Athletes especially benefit from this treatment, and since the recovery time is rapid, their return to their sport is significantly hastened. Maximal shrinkage of 50 percent of collagen length occurred at 65°C (Naseef et al., 1997).

Prostate Treatment. A common benign condition in men is the hyperplasia or overgrowth of the prostatic tissue that begins to close off the urethra in the prostate, causing difficulty in urination and complete emptying the bladder. This condition is called benign prostatic hypertrophy (BPH). Surgery consists of taking a loop electrode, applying RF current, and cutting away the interior of the prostate under endoscopic guidance. An alternative is to apply RF to a roller barrel electrode to vaporize tissue (Patel et al., 1997). This alleviates the obstruction to urine flow, but nonetheless is a surgical procedure and has risks and potential complications including impotence and incontinence. As a replacement for surgery, a thermal treatment has been successful in clinical trials. Successful treatments are typically done transurethrally, that is through the urethra of the prostate by entering through the tip of the penis. Two microwave systems are currently approved for use that heat transurethrally to achieve 55°C or greater in the prostatic tissue. Because the urethra is in the location of maximal power density near the microwave antenna surface, cooling is done in the urethra to spare this structure. These systems require no penetration of the device through the urethral wall, but require careful monitoring of the urethra and rectal temperatures during the treatments. Since the treatment can be done in the doctor's office and requires no anesthesia, the complications and lack of surgical procedure make the application very promising.

There are several applications that use microwaves to treat the prostate from the inside-out, transurethrally. A flexible helical antenna is placed in a Foley catheter through the penis and into the prostate for the treatment. The catheter has lumens for urinary drainage, microwave antenna, and two temperature tracks that can be mapped. The applicator is capable of raising a cylinder of tissue ≥42°C. This cylinder measures 40 mm in height and 5 mm in radius (Astrahan et al., 1991). Another access region to the prostate is through the rectum. In this case a 4-cm long, 16-mm diameter applicator is water cooled to spare the rectal wall which would be in contact with the applicator (Stawarz et al., 1991).

For benign diseases as discussed above, some treatment of the intraprostatic tissue is required to effect some clinical relief by shrinking the prostate tissue and lessening the obstruction to urine flow. In the case of prostate cancer, most of the prostate must be heated to successfully prevent cancer recurrence. Montorsi et al. (1992) used microwaves applied transrectally to treat prostate cancer with the aim of bringing the prostate to 43.5°C, during ten treatments lasting 60 minutes. A catheter with thermocouples was placed in the urethra in the central prostate to monitor temperatures. Treatments were given twice a week for five weeks. This fits within the constraints of thermotolerance which specifies that if a treatment is given within three days of a prior treatment, heat shock protein alteration will cause the second heating to have almost no effect (Carper et al., 1987).

Other groups have combined transrectal and transurethral microwave applicators that can be phased to steer the power deposition pattern in the prostate (Yeh et al., 1994). Another transurethral applicator attempted to heat the entire prostate to 45°C while maintaining the urethra at the antenna surface at 45°C also. Ordinarily, to penetrate 10–15 mm from the urethra into the prostate, a temperature of 75–80°C would be found at the antenna and urethra surface. To alleviate this, cooling of the urethra was done with fluid during the application of microwave power (Devonec et al., 1991). Some studies have found that the coolant must be about 10°C (Martin et al., 1992). Another interesting system utilized a dipole antenna inside of a balloon catheter placed in the prostate. The balloon inflation compressed the prostate tissue and would probably lower the blood flow in the immediate vicinity. The balloon was filled with deionized fluid that was cooled to spare the urethra.

There are RF systems that also treat BPH. Since these systems need direct tissue contact, needles are placed through the urethra into the prostatic target tissue. One system places two needles through the urethra and then gives a temperature controlled treatment to a small zone of tissue. An adjustable sleeve allows tailoring of the length and position of the desiccation. The needles are retracted and the device turned 180 deg to treat the other hemispheres of the prostate. A total of six to eight treatments is made in each patient to achieve the clinical effect. Ultrasound has also been applied to the prostate transcutaneously with a focussed system or transrectally through a rectal applicator.

Cryoablation has been used in the prostate, especially for prostate cancer treatment. The device is applied transurethrally with urethral warming to preserve the urethra. The conductive system is limited in its tissue penetration and the resultant iceball is monitored by transrectal ultrasound. To achieve full prostate treatment, five probes are placed into the prostate percutaneously through the perineum. Liquid nitrogen is applied at −196°C to give an iceball of radius 2 cm. At 2–3 mm inside the iceball, a kill level of −20°C is reached (Lee et al., 1994).

Eye Treatment. A disk-shaped microwave antenna with a teflon offset from the eye has been designed for treating choroid melanoma (Finger, 1992). The tumor center was targeted to 42°C for 45 minutes. The maximum temperature at surface was 47–52°C, with a loss of about 1°C/mm axial entry into the eye.

A second 2450 MHz MW applicator utilized a copper ring as one conductor. This ring was water cooled to spare the surface from overheating. With MW only, the surface was 48°C, with a falloff of 1.5°C per mm depth and 39°C and 36.5°C temperatures at 6 and 12 mm depths, respectively. With cooling of 18°C fluid, the surface was 42°C, the maximum was at 6 mm (44°C), and at 12 mm the temperature was 42°C (Swift, 1990).

Laser irradiation has been used for ocular tumors. The normal eye has a transmission of more than 80 percent in the 500–950 nm band. Absorption decreases linearly from 70 percent at 450 nm to ten percent at 1000 nm. Reflection increases linearly from ten percent at 500 nm to 40 percent at 900 nm (Swaasand, 1989).

Focused ultrasound has been used for intraocular melanoma. It was found that tumors have high acoustic absorption, but the rest of the eye does not. The advantage of the applicator is that it is external to the eye (Coleman et al., 1986). Caution must be exercised since ultrasound can cause immediate cataracts if aimed at the lens. Focused ultrasound has been used also for glaucoma using a beam focal size of 0.4 mm diameter and 3.0 mm length at 4.6 MHz. The result of the heat treatment was a reduction in intraocular pressure (Silverman et al., 1991).

RF has also been used by placing a small electrode on the front of the eye and a larger dispersive electrode at the back. Tests were done on normal eyes for 45 minutes. No residual effects were found at 43–45°C, but scarring was found at 47°C (Liggett et al., 1990).

A novel way to reshape the cornea is with a microwave treatment to the eye. Heating was applied to reach the shrinkage temperature of collagen in the range 55–58°C using an open-ended coaxial near-field applicator at 2450 MHz. Cooling of the cornea surface was accomplished with flowing saline (Trembly and Keates, 1991). Other eye experimental work has investigated the biomechanical properties. Sporl et al. found that shrinkage occurs at 60–90°C, with the maximal extent of 57 percent is between 75–80°C (1996).

Finite Element Model for RF Treatment

Ablation of the endometrium has become a viable treatment for dysfunctional bleeding of the uterus in women. Recently there have been several attempts at applying heat treatments for thermal ablation in an office-based procedure that does not require surgery. This treatment is composed of utilizing either a hot fluid-filled balloon for conductive heating or RF patches on the outside of a balloon to make contact with the endometrial wall. The latter applies RF energy and deposits power in the superficial layers of the endometrium. The target depth of ablation is approximately 5 mm. Due to the wide variety of parameters that effect heating, a finite element model was created to predict temperature distribution and extent of thermal damage in the uterus. Some of the parameters studied include blood flow, heat source temperature, type of heat source, heat application time, blood vessel presence, temperature-dependent electrical properties, and perfusion.

Lesions produced by RF ablation depend on the temperature distribution resulting from the electric field distribution in the tissue layers. Although other works in the literature have modeled heating in tissue, the temperatures achieved were in the hyperthermia range of 40–55°C (Ryan, 1993), typically with temperatures limited to 45°C maximum. This limit simplified the model somewhat since the initial thermal and electrical properties of tissue remained substantially constant. The system being modeled raises tissue temperature into the range of 60–110°C, where tissue desiccates and electrical properties change substantially and nonlinearly (Dadd et al., 1996). In addition, if temperatures exceed 41°C, damage to living tissue is a function of both temperature elevation and duration of exposure (Sapareto and Dewey, 1984). Since values of electrical conductivity with changing temperatures at 500 kHz were not available, the electrical conductivity was measured over time at various temperatures to provide input to the model. Other works that assume changes in conductivity with temperature, assume that conductivity increases two percent/°C (Schwan and Foster, 1980), up to 100°C (Labonte, 1994).

Having a blood flow or perfusion term in the model, especially one that can be varied with time or temperature, is important. The tissue perfusion term is rate of mass flow of blood per unit mass of tissue. Flow is considered to occur at the capillary level and due to the convoluted nature of these capillary beds, causes it to be nondirectional (Patel et al., 1987). Blood perfusion is also a temperature-dependent function that can be rescaled due to tissue reaction to heating which will increase flow in normal but not in pathologic tissue, and decrease due to desiccation and capillary shutdown. In addition, our own experiments showed that blood coagulates at 60°C (Dadd et al., 1996).

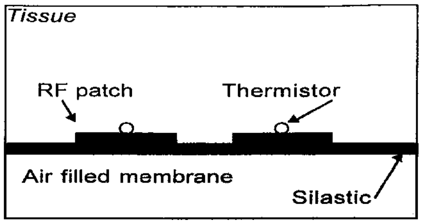

Fig. 1 A two-dimensional model of two RF electrodes with thermistors centrally located for temperature-controlled treatment. The silastic balloon is air filled.

A modeling code was developed (Humphries et al., 1997; Ryan et al., 1997) which allows thermal and electrical properties to vary with temperature, time, or location. It simulates both RF devices that deposit power in tissue and purely conductive heating devices. It is based on Pennes' bioheat equation (Pennes, 1948) as modified to include a term for the absorbed power:

$$\rho_t c_t \frac{\partial T}{\partial t} = k_t \nabla^2 T + q_m + q_p + \dot{m} \rho_b c_b (T_a - T). \quad (12)$$

The model incorporates spatial and thermal variations in the terms $\rho(r, T)$, $c(r, T)$, $k(r, T)$, $m(r, T)$, and $q_p(r, T)$.

Two devices presently in clinical trials have been modeled. The device requirements for treatment are to heat and ablate the endometrium, the inner lining of the uterus, with a single application of heat in under ten minutes. A cross section of the RF device as modeled in two dimensions is shown in Fig. 1. The silastic membrane in Fig. 1 has electrodes composed of thin copper patches, each with a central thermistor in contact with tissue. The electrodes are mounted on an air-filled membrane which, when inflated, may lower perfusion in adjacent tissue. RF current is multiplexed among the electrodes which share a common dispersive electrode mounted elsewhere on the body. The thermistors in the center of each electrode are controlled to 72°C or 75°C for four minutes, after a one minute heatup. Figure 2 is a model of a conductive endometrial ablation device. The central heater is held at 87°C, as measured by a thermocouple affixed to the wall of the heater. The fluid carries the heat to the tissue through the balloon wall. The heater takes one minute to reach target temperature and is then held constant at 87°C for eight minutes.

Figure 3 shows lines of constant potential for the device in Fig. 1. Since the system is multiplexed, only a single electrode is on. The right-hand electrode reshapes the electric field of the

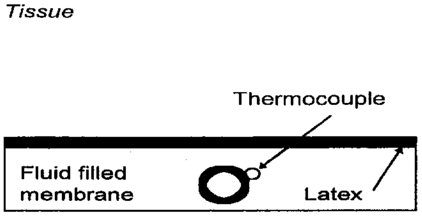

Fig. 2 A two-dimensional model of a conductive heating balloon with temperature control on the heater. The balloon is fluid filled.

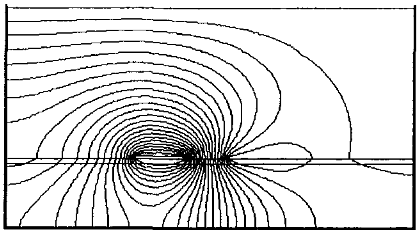

Fig. 3 Lines of constant potential in tissue for the case of one electrode on and one off

left electrode. Due to edge effects of the patches, the field is most intense in the gap between the electrodes. The electrodes are 8 mm width separated by 6 mm. Note the discontinuity of the electric field at the tissue-silastic and silastic-air interfaces.

Figure 4 shows temperature distributions when the two electrodes are multiplexed and controlled such that the central electrode temperatures are maintained at 75°C for 300 s. The target temperature is achieved in 60 s and held for an additional four minutes. Perfusion is constant at 3.34 $kg/m^3/s$. The dashed lines demarcate the insulating silicone layer with air filling the interior below the silicone. The electrodes ride on this layer as shown by the horizontal lines. Note the outer uterine wall achieves 40°C. The model incorporated $\kappa(T)$. We have shown that when heating beyond 60°C, the electrical conductivity of tissue changes enough to make a visible difference in the predicted temperature distribution. It has also been shown in clinical trials (Ryan et al., 1998) that as the electrodes heat tissue, electrical conductivity increases, and as temperatures begin to stabilize and plateau, so does the conductivity.

The temperature distribution shown in Fig. 5 is for a block of tissue containing a 2-mm diameter vessel. The two electrodes are the same as in Fig. 4. The perfusion is 3.34 $kg/m^3.s$. There is a 2-mm vessel denoted by the shaded circle. Mooibroek and Lagendijk (1991) showed that a vessel of this size will not equilibrate with the surrounding tissue over a short distance, thus the vessel is modeled as a constant temperature region.

Figure 6 shows results from a heating source with one minute of heatup and eight minutes of steady state as measured at the source, which is held at 87°C. Perfusion is 3.34 $kg/m^3.s$. The dashed line demarcates a latex membrane, below which is a fluid filled balloon with the conductive heater. The fluid is dextrose.

Figure 7 shows the temperature distribution as in Fig. 6, but with a 2-mm blood vessel embedded in tissue. Note the influence on the temperature distribution. Perfusion is 3.34 $kg/m^3.s$. Heating is for eight minutes, following a one-minute heatup to 87°C at the heating source.

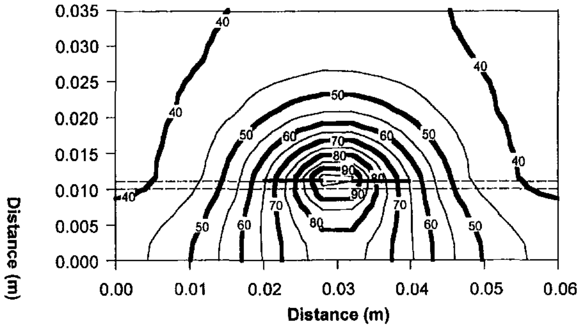

Fig. 4 Isotherms for two electrodes multiplexed and controlled such that the central electrode temperatures are maintained at 75°C for 300 s. The model incorporates $k_t(T)$. The layer of silicone is between the dashed lines. The two electrodes are represented by short horizontal lines. The electrodes are 8 mm in width separated by 6 mm.

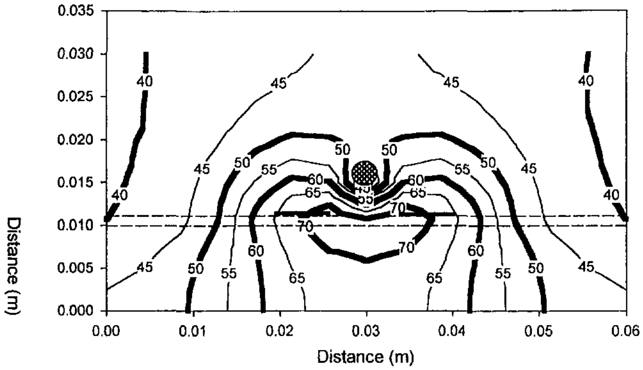

Fig. 5 Temperature distribution resulting from the two RF electrodes heating tissue perfused by a 2-mm diameter vessel

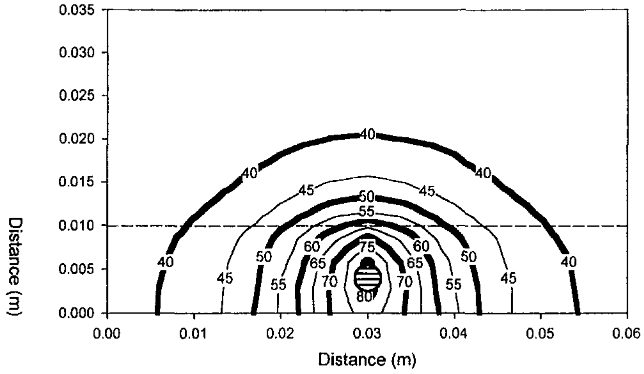

Fig. 6 Isotherms in nonperfused tissue model resulting from heating with a conductive source held at 87°C. The dashed line demarcates a latex membrane, below which is a fluid-filled balloon with the conductive heater.

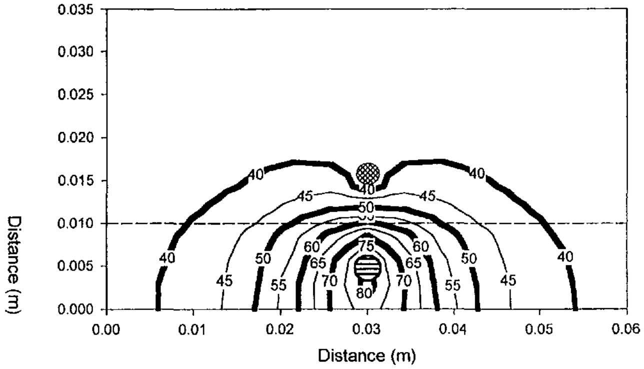

Fig. 7 Isotherms in the model tissue perfused with a 2-mm vessel resulting from heating with a conductive source held at 87°C. Perfusion rate is 3.34 $kg/m^3/s$. The dashed line demarcates a latex membrane, below which is a fluid-filled balloon with the conductive heater.

A versatile model should have the capability of inputting changing tissue parameters when temperatures are high enough to effect results, and thus will better predict tissue thermal events in biological systems. If the tissue is pathological and has different thermal properties or perfusion, these can be input. Trends show that as temperature rises, electrical conductivity increases, but not exactly as two percent/°C (Schwan and Foster, 1980) estimates predict. Conductivity values for muscle tissue actually decreased over time at 70°C and above (Dadd et al., 1996). Thermal doses of time and temperature affect various tissues differently, however, and depending on the temperature level, the tissue could be irreversibly altered. These results agree with work at lower frequencies (Moskowitz et al., 1995) that demonstrated the effects of irreversible damage. Only at lower temperatures did the electrical conductivity in tissue samples return to baseline values and show complete reversibility due to lack of damage by the thermal dose (Dadd et al., 1996). Lastly, since the damage integral is built into the code, we can track estimates of irreversible tissue damage due to the thermal history at each location in the mesh.

The development of the devices shown here can be greatly aided by numerical simulations that allow parameter changes such as material types and thicknesses, heat source temperatures, device dimensions, tissue properties, and others. The design process may be sped up by letting the model compare various designs prior to prototyping and bench testing. Hopefully, application of a good model may reduce time to commence clinical trials and make the devices available to the medical treatment community so that patients can ultimately benefit.

Cryopreservation

Living tissues may be frozen to deep subzero temperatures to create a state of suspended animation for indefinite periods and recovered with very minimal loss of viability and function. It is necessary to store tissues at below approximately −120°C so the kinetics of chemical reactions and ice nucleation become infinitesimally small. Successful cryopreservation protocols require that subject tissue be modified prior to cooling to subzero (C) temperatures by addition of a cryoprotective additive (CPA) either to protect against the injurious effects of ice formation or to block the formation of ice so that a glassy state results (vitrification).

Widespread interest has developed in exploiting cryopreservation as a means for reversibly banking a broad spectrum of tissues for transplantation. The seminal paper which first reported this work described the use of glycerol to freeze fowl sperm about 50 years ago (Polge et al., 1949). Successes were reported in succession for other types of tissues having rather simple cell structures, such as erythrocytes, gametes, and various cells obtained from primary cultures (Lovelock, 1953; Strumia et al., 1960; Whittingham et al., 1972). Most of these cryopreservation techniques were derived via largely empirical methods, and starting in the 1970s it came to be realized that the cryopreservation of more complex systems, such as multicellular tissues and whole organs, require a more rigorous scientific understanding of the mechanisms of the governing biophysical processes and cellular response to freezing and thawing. Since that time engineers have made significant contributions to the developing science of cryobiology, not the least of which has been to identify some of the key biophysical problems to be solved (McGrath and Diller, 1988).

Analysis of cryopreservation by freeze/thaw processes is based on addressing phenomena associated with the solidification of aqueous solutions and their resulting effects on embedded living cells surrounded by semipermeable membranes. When an aqueous solution freezes, water is sequestered into the solid ice phase, resulting in concentration of solutes in the residual liquid phase solution. If equilibrium is maintained between the liquid and solid phases, the coupling between temperature and solute concentration is described by the phase diagram for the solution. As shown in Fig. 8, as the temperature is depressed below 0°C the amount of solute in the liquid increases according to a function defined by the liquidus curve until the eutectic state is reached. Thus, cooling a biological tissue until ice is nucleated imposes an osmotic as well as thermal stress.

A consequence of the osmotic stress is that the individual cells in a tissue will lose intracellular water to the solute enriched environment (it is assumed that at subzero temperatures the time scales for transport of other molecular species will be negligible in comparison to that for water). The rate at which this mass transport occurs across the cell membrane is governed by the membrane permeability to water. This transport process has been modeled as a simple diffusion phenomenon (Mazur, 1963).

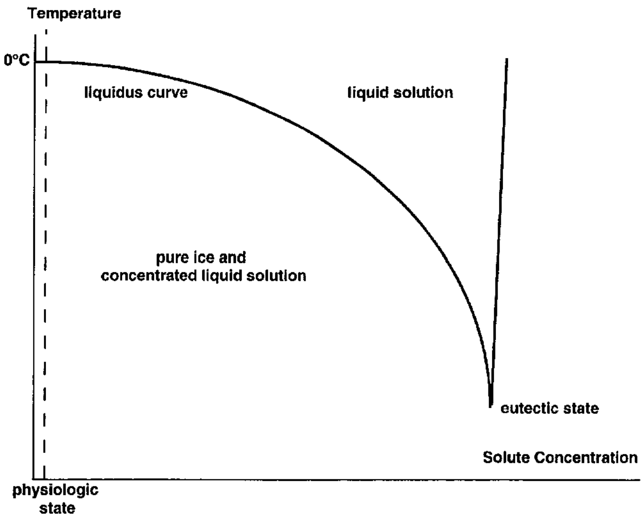

Fig. 8 ***Simplified representation of an aqueous equilibrium phase diagram.*** **Physiological solutions have solute concentrations that are quite small (about 300 mOsm) in comparison with the eutectic state. As freezing progresses the liquid phase concentration may increase by more than 20-fold, subjecting cells to intense osmotic stress.**

$$\frac{\partial \Psi}{\partial T} = -\frac{L_p SBRT}{v} \ln \left(\frac{p_{in}}{p_{ex}} \right) \qquad (13)$$

The Mazur equation predicts the change in the volume, Ψ, of a cell with temperature during freezing at a cooling rate of B in conjunction with the transport of water from within the cell in response to the osmotic differential developed across the membrane as solutes are concentrated during the solidification process. The rate of transport is dependent on the surface area, S, of the cell, the membrane permeability to water, L_p, the molar volume of water, v, and the ratio of intracellular to extracellular vapor pressures of water. Although the latter term is not a rigorous description of the driving potential for the transport process, it is easily replaced by the transmembrane differential in chemical potential or solution concentration.

Dehydration is not the only process by which equilibrium can be achieved between intracellular and extracellular water during freezing. Ice crystals may nucleate within the cell, forming intracellular ice (IIF). The occurrence of IIF is nearly always lethal to cells and is therefore to be avoided during cryopreservation. The balance between equilibration of water across the cell membrane by osmotic dehydration and by IIF is governed primarily by the magnitude of the cooling rate. As depicted in Fig. 9, at rapid cooling rates, there is little opportunity for water to escape from the interior of the cell as the extracellular solute concentration increases with progressive freezing. Eventually the conditions are satisfied for intracellular nucleation of ice crystals. At slow cooling rates, the cells are able to dehydrate as the extracellular solute concentration increases, and the intracellular water becomes frozen in the extracellular space. The resulting shrinkage of the cell can give rise to injurious chemical and mechanical stresses. In general, optimal survival from cryopreservation is achieved at intermediate cooling rates, the magnitude of which are dictated by the membrane permeability at subzero temperatures (Mazur, 1990).

The sensitivity of cells and tissues to both IIF and osmotic stress and dehydration can be modified substantially by the prefreezing additions of a CPA. As a consequence, virtually all practical cryopreservation procedures are based on the use of a

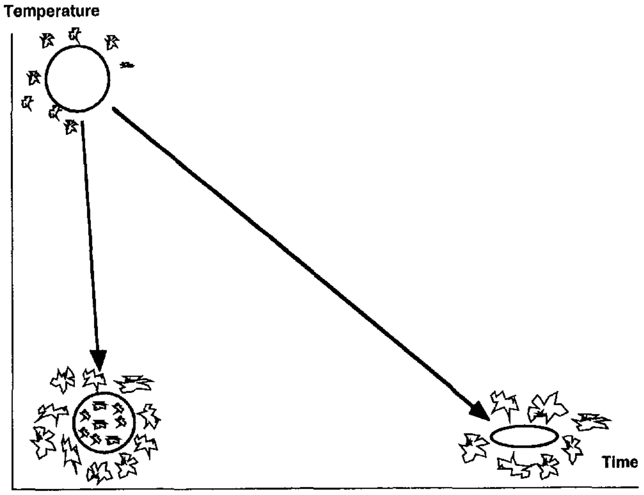

Fig. 9 **Schematic of the reaction of individual cells to extreme variations in the cooling rate during freezing. At rapid cooling rates dehydration of the cell is minimal, and intracellular ice forms. At slow cooling rate dehydration is extensive, resulting in loss of intracellular water and morphological distortion.**

CPA to which the cell membrane is permeable. During both the CPA addition and removal procedures and the freezing and thawing processes, the applied osmotic stress results in coupled transport between the CPA and water. This coupled process is typically described in terms of irreversible thermodynamics using a format defined by Kedem and Katchalsky in which the phenomenological coefficients are related directly to physically measurable properties of a cell membrane (Kedem and Katchalsky, 1958; McGrath, 1988). These equations are written as

$$J_V = L_p\Delta p - \sum_{i=1}^{n} \sigma_i \Delta\pi_i \qquad (14)$$

$$J_S = C_S(1 - \sigma)J_V + \omega_S\Delta\pi. \qquad (15)$$

L_p is the membrane permeability to water, ω the permeability to solute (CPA for applications in cryopreservation), and σ the coupling between the two flows (reflection coefficient). The average concentration of permeable solute between the extracellular and intracellular solutions is given by C_S, and the total volume flux and solute fluxes by J_V and J_S, respectively. Equation (14) shows a provision for volume flow occurring under the action of multiple solutes.

An alternative, more generalized formulation of this type of phenomenon was also posed by Katchalsky in terms of network thermodynamics (Oster et al., 1973). The network thermodynamic model has been applied successfully to the analysis of the cellular response to freezing processes (Diller, 1988a; Diller et al., 1988; deFreitas et al., 1998). It can readily be applied for inverse solution to quantify the transport coefficients from either freezing data or CPA addition data (Diller et al., 1988; Walsh et al., 1997).

The preceding models hold for the analysis of individual cells. However, many important biological systems of interest for cryopreservation consist of organized tissues which have a three-dimensional geometry that exerts a significant effect on the osmotic behavior. For these systems transport occurs not only across the individual cell membranes, but the interstitial volume is also involved in both the transport and storage of water and CPA. In this case the model must be expanded to include both parallel and serial transport and storage for all mobile chemical species. Network thermodynamics provides an effective modeling format for describing these processes.

The cryopreservation of whole organs, which is still in the research stage, will demand even more complex coupled thermal and chemical transport analyses. CPAs are added and removed via perfusion through the vascular network, and this hydrodynamic flow is coupled to the osmotic, diffusional, and viscoelastic energy domains of the organ. The network thermodynamic approach to modeling is very well suited to analysis of these coupled multidomain processes and has been applied successfully to the design of CPA perfusion protocols (Lachenbruch et al., 1998).

It is well documented that the permeability of cell membranes to water and to CPA is a strong function of the cell species, and that for all species it is a function of temperature (McGrath, 1988). For example, the water permeability among various species may vary by a factor of 10^3 or greater. In general, membranes are significantly more permeable to water than to common CPAs, although the opposite case may also occur under unusual conditions (Walsh et al., 1998). As the temperature is reduced, the permeability is depressed dramatically. For most practical purposes, at temperatures below the range of about −20 to −30°C the impedance to membrane transport becomes so high that there can be very little molecular exchange between the intracellular and extracellular compartments.

One of the major challenges in applying models for cell membrane transport during freezing has been developing instrumentation to measure the permeability to water and CPAs at subzero temperatures, both in the presence and absence of ice. The approach which has proven to be most successful is to follow visually on a light microscope the transient size of individual cells or tissues when they are subjected to controlled osmotic stress created either by freezing the specimen (Diller and Cravalho, 1970; Diller, 1982, 1988b) or by changing the chemical environment (McGrath, 1985; Walcerz and Diller, 1991). An effective step change in the concentration of the extracellular solution is produced when ice is nucleated in the extracellular medium, and the temperature is subsequently held constant for the duration of the experiment, or when a new bathing medium are perfused rapidly through the specimen chamber on the stage while the cells or tissues is physically immobilized. By both procedures the concentration of the environmental solution is altered from an initial concentration to a final well-defined state, and the change in cell volume with time can be measured by direct microscopic observation. The two-dimensional cross-sectional areas of the cells in the micrographs are quantified via digital image analysis and extrapolated to three-dimensional volumes based on an assumption of a consistent geometric morphology throughout the process. These experiments are repeated serially at different temperatures to generate a series of transient volume curves as shown in Fig. 10 for pancreas islets (deFreitas et al., 1997), a multicellular mammalian tissue. A $2M$ solution of the CPA dimethyl sulfoxide (Me_2SO) was introduced stepwise into the perfusion cryostage to control the osmotic environment of the islets. An initial

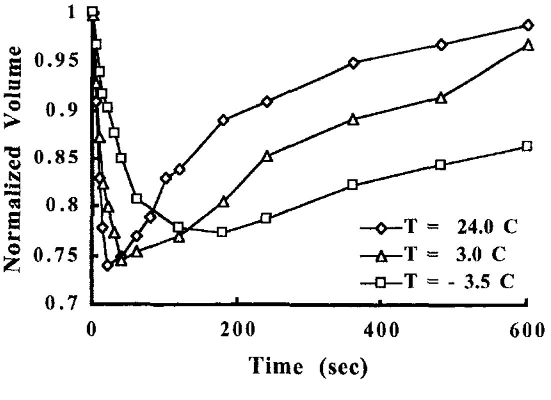

Fig. 10 **The osmotic response of human pancreas islets to exposure to a 2*M* solution of dimethyl sulfoxide at the indicated temperatures**

shrinkage is measured as water leaves the cells more rapidly than the Me_2SO can enter. As time progresses the islet reaches a minimum volume and then begins to swell as Me_2SO and water enter the cell. The design of protocols for addition and removal of CPAs to tissues is an important and challenging step in developing effective cryopreservation methods. A rational design process is dependent on being able to measure the constitutive transport properties of the tissue of interest and having a model which can be applied to optimize the osmotic process, minimizing stresses (which are potentially lethal) on the cells.

Thus, the utility of the transient volume data is to provide a data base from which Eqs. (13)–(15) can be applied to determine the constitutive transport properties for a cell or tissue of interest by inverse solution techniques. Property values are identified at each temperature for which experimental data exist, and the data for each property are used to fit an Arrhenius-type function to characterize the temperature coefficient (McGrath, 1988). Equation (16) shows a typical formulation used for this purpose.

$$L_p(T) = L_{p,g}(T_g)\exp\left[\frac{\Delta E}{R}\left(\frac{1}{T}-\frac{1}{T_g}\right)\right] \tag{16}$$

Experiments for many different cell types have shown that the Arrhenius expression provides a model that describes the temperature dependence of the tissue transport properties well (McGrath, 1988).

In order to fully interpret the transient osmotic data described above, it is necessary to determine the fraction of the cell contents which is unable to cross the cell membrane under the types of osmotic stress encountered during cryopreservation. This component of the cytoplasm is often referred to as the osmotically inactive volume. It can be measured by conducting a series of experiments in which cells are exposed to increasing concentrations of impermeable solute and measuring the equilibrium volume at each state. These volumes are then plotted as a function of reciprocal solute concentration and extrapolated to the intercept of the ordinate, which indicates the volume which the cell would assume without injury when exposed to an infinitely large solute concentration. The complementary normalized fraction is a measure of the initial amount of intracellular water which can participate in the response to extracellular osmotic stress. The data is displayed on a Boyle-van't Hoff plot (Levin, 1988).

A fundamental issue in the analysis of cryopreservation processes that has only recently begun to be addressed via rigorous quantitative modeling is the osmotic behavior of frozen cells during the thawing process. It has now been demonstrated by application of a model based on Eq. (13) that there are combinations of freeze/thaw protocols for which the warming rate may be the governing component of the thermal history in determining the mechanism and extent of injury (Kasharin and Karlsson, 1998). The design of optimal cryoprocessing protocols may therefore require an analysis of the effect on a tissue of interest of the complete thermal history, including both cooling and warming.

Ice nucleation can be avoided by doping the biological specimen with a high concentration of chemicals to induce a vitreous state (Fahy, 1988). The chemicals act to raise the glass transition temperature to a high value which can be reached at cooling rates consistent with standard refrigeration systems. Two major problems involving transport processes remain to be solved before vitrification can be applied to the cryopreservation of whole organs. One is the process by which a four to five molar solution equilibrates with the entire volume of an organ, including all the constituent cells. Since this high concentration of CPA can be toxic to cells, the addition process is preferably effected at a low temperature such as 4°C to reduce the rates of injurious chemical reactions. In addition, the duration of exposure to the CPA prior to further cooling should be minimized to limit the accrued reaction time. However, the tradeoff to lowering the temperature is caused by the thermal coefficient of viscosity, which makes it much more difficult to effect the perfusion of CPA solution through the vascular systems of an organ and the diffusion from the vascular lumen through the interstitial tissue and into the individual cells. Optimal design is dependent upon balancing the coupled hydrodynamic, osmotic and viscoelastic reaction of the organ to the perfusion process with the biochemical toxic reactions (Lachenbruch et al., 1998).

The foregoing discussion indicates the importance of the combined osmotic and thermal history at the local cellular level in determining the response to cryopreservation, including the type and extent of injury which may occur. For a given combination of cell type and CPA composition and concentration, the post-thaw viability achieved is governed by the thermal history of the process. The cooling rate determines the frozen state for storage, and the warming rate determines the manifestation of the frozen state on the final level of viability. In general there are two extremes of behavior during freezing. For relatively slow cooling rates the rate at which the extracellular solute concentration increases will have a time scale comparable with that for the osmotic dehydration of the cell at high subzero temperatures. Therefore, the cell will lose a considerable fraction of its water and experience extensive dehydration as indicated in Fig. 8. This large loss of volume is known to damage cells by one or more molecular level mechanisms which have not been fully identified (Mazur, 1990). Increasing the concentration of CPA will provide an osmotic buffer against this type of dehydration-induced injury, as well as possibly providing other means of protection. Alternatively, when the cooling rate is rapid, the temperature is reduced much more rapidly than the cell can respond osmotically (because the membrane permeability becomes greatly reduced at low temperatures as will be explained subsequently). Therefore, there is no opportunity for intracellular water to osmotically equilibrate with the extracellular water which is being progressively diminished in concentration. When the transmembrane water disequilibrium (as manifested in terms of liquid phase supercooling) reaches a critical value, the conditions will be satisfied for nucleation of ice in the intracellular volume. It is important to note that the cell membrane acts as a barrier to the growth of a continuous ice phase between the intracellular and extracellular compartments. The crystalline structure of intracellular ice will be considerably smaller than that of extracellular ice owing to the greater extent of supercooling prior to nucleation. Consequently, the propensity for recrystallization will be relatively large in the intracellular volume, and this process has been demonstrated to be nearly universally lethal to cells.

The combination of different injury mechanisms associated with rapid and slow cooling rates during freezing gives rise to a two factor theory of cryoinjury (Steoponkus, 1984; Mazur, 1990). Between the extremes of rapid and slow cooling there will be a range of intermediate rates at which survival will be maximized. The magnitude and breadth of this range is defined uniquely for each cell type as a function of its membrane permeability and sensitivity to injury. Cryopreservation protocols are targeted to produce a cooling process which lies within the optimal range of this survival signature which will produce the highest possible biological function following thawing. The design of a cryopreservation protocol for a given cell type must take into account the combined effects of the CPA composition and concentration plus the cooling and warming rates.

The above analysis of the freezing process is presented from the perspective of the local thermal history for an individual cell. However, practical cryopreservation procedures are conducted either on tissues and organs of finite macroscopic dimensions or on containers of solutions of cells or microscopic tissue suspensions. The consequence is that although the governing mass transport processes occur across microscopic scale dimensions (a single membrane and the associated boundary layers may be less than 0.1 μm), the governing heat transport occurs on a scale measured in millimeters or centimeters. It is this macroscopic heat transfer that drives all components of the cryopreservation process. Because of the macroscopic dimensions and the restriction that the refrigeration source be applied only at the external boundary of the systems during cooling, there can be significant spatial gradients in cooling rate manifested within the system. Also, in general the cooling rate will not be constant over the entire cooling process. The cooling rate should be defined over the range of temperatures most important to determining the frozen state of a cell. The critical temperature range is defined as that for which transport occurs across the cell membrane and for which intracellular ice formation (IIF) is most probable. Analysis of this process involves solution of the classic Stefan moving boundary problem. For the freezing of biological systems it is most important to accurately determine the cooling at high subzero temperatures within the mushy zone (Kurz and Fisher, 1992) during which the primary membrane transport processes occur. It is precisely this range of temperatures for which simplifying assumptions concerning the pattern of latent heat release are frequently made in order to render the mathematical solution more tractable. Therefore, it is important to match as well as possible the coupling between temperature and changing solute concentration as defined by the phase diagram. Only when the actual process physics are matched can the cooling rate for the critical temperature range be described accurately. The combination of a nonlinear pattern of latent heat release with temperature and the often complex system geometry dictates that the governing heat transport equations be solved via numerical methods. The thermal histories calculated may then be correlated with the cooling rates on the survival signature and with the membrane mass transport equations, such as Eq. (13), to predict the biological response of a given tissue to a defined boundary cooling protocol (Hayes et al., 1988).

Another analysis problem to be addressed in cryopreservation is that of thermal stresses in an organ that has been vitrified. Although the constitutive properties are yet to be measured, it is apparent that a biological tissue with dimensions on the order of several centimeters will be subject to fracture at even moderate cooling rates below −120°C after a glass phase has formed (Fahy, 1990). A mechanical fracture of a whole organ will render it useless for subsequent transplantation. It is important to measure the viscoelastic properties of biological materials loaded with high concentrations of CPA over the temperature range between the glass transition and storage temperatures (usually at or near liquid nitrogen temperature at −196°C). Complementary to the property measurements is a need for a thermal stress analysis that can be applied with versatility of geometric details. Rubinsky et al. (1980) have developed an initial model for how mechanical stresses may develop in the interior of an organ during solidification and the subsequent cooling process. Different organs have widely divergent shapes and sizes, and constitutive property data for frozen and vitrified tissues are practically nonexistent. In addition, an organ is likely to be preserved in a container of fluid with which it will be coupled thermally and mechanically. Factors which can be considered in a process design are: manipulation of the boundary thermal protocol, shape of the overall container into which an organ is placed, and coordination of the pattern of distributed internal deposition with cooling at the boundary.

Recent innovative experiments by Fowler and Toner (1998) have demonstrated that it is possible at the micro (cellular) scale to melt and recool cells containing intracellular ice at a rate that can produce a vitrified state without the introduction of the CPA to block the initial ice nucleation event. The frozen specimen is irradiated with a laser wavelength that is absorbed preferentially by the cell cytoplasm over the extracellular solution. For a solution of individual cells having characteristic diameters of about 6 μm, warming rates on the order of 10^{11} °C/s can be achieved within the cells, while the extracellular matrix remains frozen. When the heating process is terminated in an approximate step-wise manner after 7 ns, heat transfer from the extracellular matrix to the cells produces an intracellular cooling rate of about 10^6 °C/s, which is adequate to produce a glass state in an aqueous solution. The vitrified cells may then be warmed rapidly to suprafreezing temperatures (>0°C) without nucleation and with no measured injury. If this process is to realize broad clinical or commercial application, there is considerable engineering work to be accomplished in scale-up from these microscopic level processes to applications in larger tissue and organ systems.

Since the initial achievements in the cryopreservation of cells, many applications have been developed in both the biological and medical fields. There are now numerous for-profit concerns that have developed successful techniques for preserving human tissues for subsequent transplantation. Many of these corporations use proprietary processing protocols to preserve specific tissues, and the number of commercial participants in this field has been growing steadily over the past ten years. In like manner, there are many for-profit and not-for-profit groups which are marketing the cryopreservation of a very broad spectrum of nonhuman tissues. Some of the more prominent applications involve mammalian and amphibian gametes, tissue culture collections, and plant germplasm. A potentially important new area of application will be the cryopreservation of living materials manufactured by the tissue engineering techniques which are being developed (Nerem and Sambanis, 1995). Bioartificial systems such as skin and organs that contain living cells will require a technology for maintaining them in a viable but latent state between the time of manufacture and implementation in a clinical setting. Cryopreservation provides a tool of suitable potential for meeting this unique need, but the processing protocols will have to be designed to ensure successful storage and recovery for each type of manufactured tissue.

All of the foregoing discussion has been devoted to cryopreservation, for which the objective is to maximize the survival of cells from the frozen state to ensure their living function after thawing. The antithesis of this work is cryosurgery, for which the objective is to maximize destruction of a target tissue in situ. Cryosurgery has long been practiced as an effective means for killing surface lesions, and recently it has been adopted more widely as a tool for treating internal tumors that are difficult to resect mechanically (Onik and Rubinsky, 1988). Much of the recent gains in the successful application of cryosurgery are due to the development of new imaging methods that enable the surgeon to follow the growth of the solid-liquid interface, to which the zone of cellular destruction is coupled, in real time during the freezing process. The initial imaging methodology adapted for this purpose was ultrasonography (Onik et al., 1984). Subsequently, other imaging modalities that can be coupled to the transient temperature field are being developed, including NMR (Rubinsky et al., 1993) and spectroscopy (Otten et al., 1998). Advances in cryosurgical probes that provide more effective removal of heat from tissues via enhanced thermal transport mechanisms have also contributed to the recent growth in cryosurgery (Baust and Chang, 1995). Finally, over the past decade there has been a steady advance in understanding the mechanisms by which freezing and thawing act to cause tissue death as a function of the thermal parameters of the solidification process and tissue properties. Many of these fundamental advances have resulted from the application of bioengineering analysis of the tissue freezing process (Rubinsky and Pegg, 1988; Bischof and Rubinsky, 1993; Pazhayannur and Bischof, 1997), which portends the potential for engineering to further contribute to the field of cryosurgery.

Thermal Injury and Protection

Thermal injury occurs as a consequence of exposure to environmental conditions that are severe enough to drive tissue temperature outside the range at which normal life processes can exist. As a consequence there are alterations to biomolecules, which in most cases are irreversible resulting in injury. Common examples are burns and frostbite. It has recently been discovered that under some kinds of moderate thermal stress that is subthreshold to injury, cells produce molecules which render temporary protection against levels of many types of stress (thermal, mechanical, chemical, etc.) that would normally cause injury. These protective molecules are called heat shock proteins, and they are the subject of widespread investigation to identify the kinetics of their expression and function and to develop applications in which they may be induced either before or even after a traumatic event.

The most commonly encountered type of thermal injury is the burn. Accidental burns are encountered most frequently in domestic and industrial settings as well as many other venues of activity. Most burns result from the propagation of heat inward into tissues as result of contact at the surface (skin) with a hot solid, liquid, or vapor. One exception is electrical burns in which the tissue temperature is elevated owing to I^2R dissipation of electrical energy when a voltage is applied. In this case, the primary source of heating is internal since the impedance of muscle is higher than of skin and fat.

It is generally assumed that thermal burns can be modeled as a simple Arrhenius rate process such that

$$\frac{d\Omega}{dt} = a \exp\left(-\frac{\Delta E}{RT}\right). \tag{17}$$

This model was first posed for predicting the severity of a burn as a function of the temperature and time of exposure at the skin surface by Moritz and Henriques (Henriques, 1947; Henriques and Moritz, 1947; Moritz and Henriques, 1947) shortly after World War II. They also performed experiments to determine threshold conditions for eliciting first and second degree burns in humans and applied this data to determine values for the scaling constant and activation energy in their Arrhenius model. Their experiments were conducted at temperatures between 44°C and 70°C and exposure times between 1 and 25,000 seconds. The model parameter values are $a = 3.1 \times 10^{98}\ \mathrm{s}^{-1}$ and $\Delta E = 6.28 \times 10^5$ kJ/mol. Over the ensuing 50 years many subsequent investigators have modeled this process (Büttner, 1951a; Stoll, 1960; Weaver and Stoll, 1969; Takata, 1974) and made experimental measurements of threshold burn conditions in human (Stoll and Green, 1959; Stoll and Chianta, 1968; Lawrence and Bull, 1976), animal (Büttner, 1951b; Ross and Diller, 1976), and cellular and molecular (Moussa et al., 1977, 1979) systems. Although a considerable body of literature has been accrued, there is by no means a consensus on how to accurately predict the occurrence of thermal injury over the wide range of conditions that cause burns.

Thermal Property Measurements

As has been indicated in the foregoing sections, one of the major challenges of bioheat transfer is measurement of the transport properties of living tissues. There are a number of compounding factors that add to the difficulty of determining these properties in biosystems over standard engineering materials. Anisotropy is encountered frequently in biomaterials. Variation among specimens of the same species can be large, as well as within a single animal or plant. Electrical, thermal, and perfusion properties of pathologic tissue may also differ from normal tissue in various disease states. In addition, in rapidly growing malignant tissue, the interior may be liquid and the boundary encapsulated by a well-perfused margin of neovasculature that will shut down if exposed to heat.

The intrinsic thermal transport properties in vivo can be influenced quite strongly by local perfusion of blood, and perfusion, under some conditions, is strongly influenced by the local and environmental state and history. This effect was discussed in the section dealing with the bioheat equation, but it can be a source of major challenge when attempting to measure thermal conductivity of living tissues. On the other hand, the ability to measure tissue thermal properties presents an opportunity to assess the state of blood perfusion by inverse solution of the bioheat equation. Data on blood perfusion can be of great clinical significance for both diagnostic and therapeutic applications. As a consequence there is a growing interest in being able to make thermal measurements simply and reliably, and the potential for commercial exploitation of successful techniques is large.

In addition to the foregoing tissue-specific difficulties in measuring thermal properties, there is a further problem in designing instrumentation to acquire the requisite experimental data. Many engineering materials can to fabricated to a geometry advantageous to matching with the boundary conditions of an inverse solution model used to determine property values. Instrumentation can be placed at strategic locations to monitor temperatures and heat flows without compromise to the integrity of the material. In general, these opportunities do not exist with living tissues. Tissues cannot be readily conformed to the geometry of a thermal conductivity apparatus, with the exception of fluids that can be removed from the body for testing. Some property measurement techniques are based on inserting thermal probes into the interior of a specimen. Although variations of this method have been adapted for biological tissues (Chato, 1968; Bowman et al., 1975; Balasubramaniam and Bowman, 1977; Valvano et al., 1984), they may cause changes in the local physiological state in association with the trauma of introducing a foreign body. Even tissues evaluated in vitro (removed from the body) are altered by the insertion of probes owing to their mechanical viscoelastic behavior and the difficulty of ensuring adequate thermal contact between instruments and the specimen (Valvano, 1992). Obvious considerations of pain and discomfort are important for applications of in vivo (in the body) measurements in patients. As a consequence, invasive procedures for measuring thermal properties must be viewed as undesirable, and a primary current thrust in research is to develop techniques for effective assessments of thermal conductivity and diffusivity, and where appropriate, local blood perfusion via techniques which can be effected from the surface of the specimen. The remainder of this section will deal with recent advances in thermal property measurements in living tissues, with a stress on minimally invasive techniques and applications to determining local blood perfusion through tissues. This problem is an area of bioheat transfer that has significant potential for the development of new intellectual property and commercial activity directed to the health care market.

Until recently virtually all techniques for measurement of the thermal properties of tissues have been made with the embedded thermistor technique first described by Chato (1968). This technique is based on a small thermistor placed in the interior of a homogeneous body so that it can function both as a measured heat source to create a temperature gradient in the system, and as a thermal probe having a well-defined geometrical arrangement with the energy source. After a period during which the thermistor comes to thermal equilibrium with the surrounding tissue, a step input in power is effected by applying a voltage across the thermistor leads. A control circuit maintains the probe temperature at a constant increment above the initial value, and the transient power input necessary to maintain this differential is monitored. The rate at which power input diminishes over time can be related directly to the thermal diffusivity of the surrounding medium, and the extrapolated steady-state value is related to the thermal conductivity.

The elegant simplicity of the single probe and complementary analysis make the technique nicely suited for measuring properties in situ. Some of the inaccuracies associated with the early implementation of the technique, such as the effects of probe geometry, temperature gradients in the probe and limitations of process control, have been addressed effectively by Bowman, Valvano and colleagues (Balasubramaniam and Bowman, 1977; Valvano et al., 1984). The technique can also be adapted to measurements over wide ranges of temperatures (Valvano et al., 1985; Bai and Pegg, 1991). However, the primary drawback of this technique of being invasive to tissue cannot be eliminated. Therefore, current efforts tend to be focused on devising a technique that is minimally invasive (Patel et al., 1987).

A number of approaches have been studied to combine introducing the thermal perturbation and also monitor the resulting transient temperature from the surface using a thermopile and copper plate sandwich (Holti and Mitchell, 1979), a thin resistor (Castellana et al., 1983) and a thermistor (Walsh and Bowman, 1984). Although the principle of coupling both the heat source and temperature into a single surface probe is promising, the above embodiments suffered from limitations in the accuracy in which the actual heat flux into the tissue could be measured, and from the effects of variable thermal contact resistance between the probe and the surface.

An important application of thermal property measurement techniques is to assess the rate of blood flow in a tissue. Thermal modeling of the heat transfer in tissue, using the bioheat transfer equation, permits the quantification of tissue perfusion from thermal property measurements (Bowman, 1985). For many years the rate clearance of an increment of heat introduced into tissue (thermal clearance technique) has been applied to estimate blood perfusion through a target tissue (Eberhart et al., 1980). The technique is used clinically to determine cardiac perfusion by introducing a probe into the coronary circulation via a catheter. The probe has the capability for injecting a bolus of cold liquid into a vessel and incorporates a thermistor to monitor the transient local temperature as the thermal perturbation caused by the bolus diffuses. Although this system provides information related to blood perfusion, it is highly invasive and inappropriate for many applications. However, it is consistent with established cardiac catheterization protocols to access the circulatory system of the heart, and there are possibilities for improving the system performance by better temperature measurement and modeling.

Bowman and colleagues have developed a thermal diffusion probe (TDP) with two thermistors embedded at the tip of a flexible catheter (Delhomme et al., 1992; Klar et al., 1995). The distal thermistor is heated to a small increment ($\sim$2°C) above the tissue baseline temperature, while the proximal sensor monitors and compensates for tissue baseline temperature fluctuations. The power dissipated by the heated thermistor (0.005–0.01 W) provides a measure of the tissue's ability to carry heat by both thermal conduction within the tissue and by thermal convection due to tissue blood flow (Balasubramaniam and Bowman, 1977; Bowman, 1985). Numerous studies have validated this technique to quantify blood throughout the physiologic range. Klar et al. (1997) showed that the TDP and the H_2 clearance methods were highly correlated ($R = 0.941$, $p < 0.001$) over the range of liver flows tested (10–90 ml/min-100 g). Also, the TDP method correlated well with the total liver flow, as measured by Doppler ultrasound ($R = 0.902$, $p < 0.05$).

The TDP probe has been used to monitor hepatic microcirculation in transplant patients intraoperatively and continuing seven days postoperative, after which time the probes are extracted transcutaneously (Klar, et al., 1996). The average liver perfusion in four out of seven patients in the study who had normal graft function recovered within one day from a low perfusion (70 ± 20 ml/min-100 g) measured intraoperatively to 92 ± 17 ml/min-100 g. Patients with primary graft failure, whose hepatic perfusion was low (34–50 ml/min-100 g), did not recover before retransplantation. In a related study of 29 patients, Klar et al. (1997) showed that liver perfusion rates measured intraoperatively at less than 60 ml/min-100 g predicted the occurrence of primary graft failure in patients that required retransplantation ($n = 5$). Thus, the TDP presents a potential for providing data on the state of perfusion that has significant potential of improving the outcome of organ transplants.

Tom Diller and colleagues (Michner et al., 1991; Scott et al., 1998) have developed a noninvasive thermal technique for measuring blood perfusion in tissue that is based on a surface probe that appears to overcome the foregoing limitations. The concept for the operation of the probe is to combine heat flux and temperature measurements with a model for the effect of blood perfusion on tissue thermal behavior to obtain an estimate of the local state of flow. The probe incorporates a type K foil thermocouple and a thermopile fabricated into a thin sheet sandwiched between two layers of Kapton to protect the sensor. The cross section of the probe is about 3.5 cm × 2.8 cm, and the thermal capacitance is quite small to facilitate following both transient temperatures and heat fluxes. A stream of air at room temperature is impinged against the outside of the probe to generate the heat flux through the probe with the underlying tissue. One of the advantages of this design is that the tissue is not exposed to a high temperature in order to create the temperature gradient necessary to produce a measurable response. A significant increase in the operating effectiveness was achieved when a thin layer of aluminum was added to the outer surface of the probe and the air supply was directed to increase the heat transfer coefficient to about 700 $\mathrm{W/m^2\,K}$. A sensitivity analysis has demonstrated that the heat flux provides a much more effective parameter than temperature for determining the blood perfusion through underlying tissue. This work shows that there is a promising potential for building a thermally based noninvasive probe for measuring blood perfusion. Successful development could lead to significant clinical and commercial impact.

Potential Future Developments

In recent years there has been a shift in the focus of biomedical research from an emphasis on whole systems and organs (macroscopic level) to an understanding of underlying mechanisms in cellular and molecular systems (microscopic level). Accompanying this change in focus has been the development of the field of ''translational research'' with the objective of taking discoveries made at the laboratory bench to practical application in the clinic. Much of this change is driven by dramatic new discoveries in molecular biology, microinstrumentation, and computational capabilities. Bioheat transfer is also undergoing a similar transition enabled by the new molecular and microsciences.

As has been described in the foregoing sections, considerable progress has been made in measuring, modeling, and manipulating thermal processes in systemic tissues and organs. Many of these processes are governed by the kinetics of transport phenomena and biochemical transformations in cells and molecules, which are then integrated over whole tissues, organs and organisms to be manifested as familiar physiological behaviors. A new generation of diagnoses and therapies is being pursued based on being able to manipulate these kinetic processes in cells and molecules. For example, as mentioned earlier, a family of unique molecules have been identified that are produced by cells when placed under limited thermal stress. These molecules are termed heat shock proteins (HSP), and are expressed by a rate process in response to temperatures above a minimum threshold to activate the process, but less than a higher threshold above which irreversible damage occurs (Perdrizet, 1995). Therefore it is anticipated that research and development in bioheat transfer will also experience a change toward focusing on systems and processes at a more microscopic scale (Chato and Lee, 1998).

After HSP are expressed they afford protection against subsequent transient stress originating in several different energy domains, including thermal, mechanical, chemical, toxic, and others. Based on this function, HSP can have effective and broad prophylactic function. In this context HSP are often considered as an endogenous drug that can be effective in its targeted function, but with minimal undesirable side effects. If this prophylactic function can be designed and manipulated via optimal thermal processing to induce HSP expression prior to exposure to a trauma, such as elective surgery, it then becomes possible to precondition a targeted tissue or organ to better withstand the stress of the anticipated trauma. The obvious result is reduced morbidity and mortality, with commensurate decreases in pain, recovery times, and medical costs. Some investigators have found indications that HSP induction can even have a therapeutic benefit if the induction is soon enough following the occurrence of a traumatic event.

Clearly, HSP hold the potential for producing major positive changes in the delivery of medical care. A key to the effective exploitation of HSP is to gain a rigorous model of the expression kinetics within various specific cells and tissues, which then could be coupled to design control of thermal boundary conditions and energy source distribution and intensities to produce the desired protective results in a target tissue. Success in this endeavor will require the collaboration of experts in bioheat transfer, molecular biology, and clinical medicine disciplines.

A further area of important exploration in the field of thermal bioengineering is to identify the cellular and molecular basis of high and low-temperature inducing of tissue injury. There have for decades been many studies into the phenomena of thermal causation of tissue damage, but the current understanding is founded to a large extent on empirical descriptions of the governing processes. This type of fundamental information is crucial to the development of more efficacious therapeutic methods that can target the actual sites of injury in cells and molecules. As an example, recent studies have helped to clarify changes to the cell plasma membrane that greatly alter its selective permeability as a consequence of electrical burn injuries. Equipped with this understanding, strategies are being devised whereby the membranes can be healed to reverse the injury, which is a therapeutic approach that was impossible to design prior to identifying the mechanisms of cellular damage.

In summary, the advances in bioheat transfer over the past several decades have been significant and many. However, owing both to our accrued understanding of unique features of heat transfer processes in living tissues and to seminal advances in complementary biological and clinical sciences, there is now a greater scientific and commercial potential to be explored in bioheat transfer than has ever been the case. We anticipate that this field will attract many new and experienced researchers in the coming years and that there will result important advances in both the basic science and clinical applications of heat transfer in living systems.

Acknowledgments

This paper was prepared with the support (to KRD) of Texas Advanced Research Program grant no. 003658-158, National Science Foundation grants no. CTS-9632378 and no. DBI-9512746, and the Joe J. King Professorship in Engineering at the University of Texas at Austin.

References

Apfelberg, D. B., 1996, "The Ultrapulse Carbon Dioxide laser with Computer Pattern Generator Automatic Scanner for Facial Cosmetic Surgery and Resurfacing," *Annals of Plastic Surgery*, Vol. 36, pp. 522–529.

Arai, T., Sakurada, M., Miyamoto, A., Mizuno, K., Arakawa, K., Shibuya, T., Kurita, A., Nakamura, K., Kikuchi, K., Utsumi, A., Akai, Y., and Takeuchi, K., 1991, "Laser Hot Balloon Catheter for Stenotic Coronary Diseases," *Lasers and Electrooptics*, Vol. 19, pp. 1770–1771.

Astrahan, M., Imanaka, K., Jozsef, G., Ameye, F., Baert, L., Sapozink, M. D., Boyd, S., and Pertivich, Z., 1991, "Heating Characteristics of a Helical Microwave Applicator for Transurethral Hyperthermia of Benign Prostatic Hyperplasia," *International Journal of Hyperthermia*, Vol. 7, pp. 141–155.

Bai, X., and Pegg, D. E., 1991, "Thermal Property Measurement on Biological Materials at Subzero Temperatures," ASME *Journal of Biomechanical Engineering*, Vol. 113, pp. 423–429.

Baish, J. W., 1990, "Heat Transport by Countercurrent Blood Vessels in the Presence of an Arbitrary Temperature Gradient," ASME *Journal of Biomechanical Engineering*, Vol. 112, pp. 207–211.

Baish, J. W., Ayyaswamy, P. S., and Foster, K. R., 1986, "Heat Transport Mechanisms in Vascular Tissues: A Model Comparison," ASME *Journal of Biomechanical Engineering*, Vol. 108, pp. 324–331.

Balasubramaniam, T. A., and Bowman, H. F., 1977, "Thermal Conductivity and Thermal Diffusivity of Biomaterials: A Simultaneous Measurement Technique," ASME *Journal of Biomechanical Engineering*, Vol. 99, pp. 148–154.

Baust, J. G., and Chang, Z., 1995, "Underlying Mechanisms of Damage and New Concept in Cryosurgical Instrumentation," *Cryosurgery: Mechanism and Applications*, IIR Press, Paris, pp. 21–36.

Berube, D., and Liem, L. B., 1998, "Microwave Catheter Ablation for the Treatment of Atrial Flutter," *Proceedings of Surgical Applications of Energy*, T. P. Ryan, ed., Vol. 3249, SPIE Press, Bellingham, WA.

Bischof, J. C., and Rubinsky, B., 1993, "Microscale Heat and Mass Transfer of Vascular and Intracellular Freezing in the Liver," ASME Journal of Heat Transfer, Vol. 115, pp. 1029–1035.

Bowman, H. F., 1985, "Estimation of Tissue Blood Flow," *Heat Transfer in Medicine and Biology: Analysis and Application*, Vol. I, A. Shitzer and R. Eberhart, eds. Plenum Press, New York, pp. 193–230.

Bowman, H. F., Cravalho, E. G., and Woods, M., 1975, "Theory, Measurement, and Applications of Thermal Properties of Biomaterials," *Annual Review of Biophysics and Bioengineering*, Vol. 4, pp. 43–80.

Buchanan, M. T., and Hynynen, K., 1994, "Design and Experimental Evaluation of an Intracavitary Ultrasound Phased Array System for Hyperthermia," *IEEE Transactions on Biomedical Engineering*, Vol. 41, pp. 1178–1187.

Büttner, K., 1951a, "Effects of Extreme Heat and Cold on Human Skin. I. Analysis of Temperature Changes Caused by Different Kinds of Heat Application," *Journal of Applied Physiology*, Vol. 3, pp. 691–702.

Büttner, K., 1951b, "Effects of Extreme Heat and Cold on Human Skin. II. Surface Temperature, Pain and Heat Conductivity in Experiments with Radiant Heat," *Journal of Applied Physiology*, Vol. 3, pp. 691–702.

Carper, S. W., Duffy, J. J., and Gerner, E. W., 1987, "Heat Shock Proteins in Thermotolerance and Other Cellular Processes," *Cancer Research*, Vol. 47, pp. 5249–5256.

Castellana, F. S., Skalak, R., Cho, J. M., and Case, R. B., 1983, "Steady-State Analysis and Evaluation of a New Thermal Sensor for Surface Measurements of Tissue Perfusion," *Annals of Biomedical Engineering*, Vol. 11, pp. 101–115.

Carter, D. L., MacFall, J. R., Clegg, S. T., Wan, X., Prescott, D. M., Charles, H. C., and Samulski, T. V., 1998, "Magnetic Resonance Thermometry During Hyperthermia for High-Grade Glioma," *International Journal of Radiation Oncology, Biology and Physics*, Vol. 40, pp. 815–822.

Charney, C. K., Weinbaum, S., and Levin, R. L., 1990, "An Evaluation of the Weinbaum-Jiji Bioheat Equation for Normal and Hyperthermic Conditions," ASME *Journal of Biomechanical Engineering*, Vol. 112, pp. 80–87.

Charney, C. K., 1992, "Mathematical Models of Bioheat Transfer," *Advances in Heat Transfer*, Vol. 22, pp. 19–155.

Chato, J. C., 1968, "A Method for the Measurement of the Thermal Properties of Biological Materials," *Thermal Problems in Biotechnology*, J. C. Chato, ed., ASME, New York, pp. 16–25.

Chato, J. C., 1980, "Heat Transfer to Blood Vessels," ASME *Journal of Biomechanical Engineering*, Vol. 102, pp. 110–118.

Chato, J. C., and Lee, R., 1998, "The Future of Biothermal Engineering," *Annals New York Academy of Sciences*, Vol. 858, pp. 1–20.

Chen, M. M., and Holmes, K. R., 1980, "Microvascular Contributions in Tissue Heat Transfer," *Annals New York Academy of Sciences*, Vol. 335, pp. 137–150.

Coleman, D. J., Lizzi, F. L., Burgess, S. E. P., Silverman, R. H., Smith, M. E., Driller, J., Rosado, A., Ellsworth, R. M., Haik, B. G., Abramson, D. H., and McCormick, B., 1986, "Ultrasonic Hyperthermia and Radiation in the Management of Intraocular Malignant Melanoma," *American Journal of Ophthalmology*, Vol. 101, pp. 635–642.

Cooley, D. A., Frazier, O. H., Kadipasaoglu, K. A., Pehlivanoglu, S., Shannon, R. L., and Angelini, P., 1994, "Transmyocardial Laser Revascularization: Anatomic Evidence of Long-Term Channel Patency," *Texas Heart Institute Journal*, Vol. 21, pp. 220–224.

Dadd, J. S., Ryan, T. P., and Platt, R. C., 1996, "Tissue Impedance As a Function of Temperature and Time," *Biomedical and Scientific Instrumentation*, Vol. 32, pp. 205–214.

Delhomme, G., Dittmar, A., Newman, W. H., Bowman, H. F., and Jouvet, M., 1992, "Thermal Diffusion Probes for Tissue Blood Flow Measurements," *Sensors and Actuators*, Vol. 6, pp. 87–90.

Devonec, M., Berger, N., and Perrin, P., 1991, "Transurethral Microwave Heating of the Prostate–or from Hyperthermia to Thermotherapy," *Journal of Endourology*, Vol. 5, pp. 129–135.

Diederich, C. J., 1996, "Ultrasound Applicators with Integrated Catheter-Cooling for Interstitial Hyperthermia: Theory and Preliminary Experiments," *International Journal of Hyperthermia*, Vol. 12, pp. 279–297.

Diller, K. R., 1982, "Quantitative Low Temperature Optical Microscopy of Biological Systems," *Journal of Microscopy*, Vol. 126, pp. 9–28.

Diller, K. R., 1988a, "Energy Based Network Modeling for Cryobiology," *Low Temperature Biotechnology: Emerging Applications and Engineering Contributions*, J. J. McGrath and K. R. Diller, eds., ASME, New York, pp. 189–202.

Diller, K. R., 1988b, "Cryomicroscopy," *Low Temperature Biotechnology: Emerging Applications and Engineering Contributions,* J. J. McGrath and K. R. Diller, eds., ASME, New York, pp. 347–362.

Diller, K. R., 1992, "Modeling of Bioheat Transfer Processes at High and Low Temperatures," *Advances in Heat Transfer,* Vol. 22, pp. 157–357.

Diller, K. R., ed., 1998, "Biotransport: Heat and Mass transfer in Living Systems," *Annals New York Academy of Sciences,* Vol. 858, pp. 1–319.

Diller, K. R., Beaman, J. J., Montoya, J. P., and Breedfeld, P. C., 1988, "Network Thermodynamic Modeling with Bond Graphs for Membrane Transport During Cell Freezing," ASME JOURNAL OF HEAT TRANSFER, Vol. 110, pp. 938–945.

Diller, K. R., and Cravalho, E. G., 1970, "A Cryomicroscope for the Study of Freezing and Thawing Processes in Biological Cells," *Cryobiology,* Vol. 7, pp. 191–199.

Dilley, A. V., Dy, D. Y., Walters, A., Copeland, S., Gillies, A. E., Morris, R. W., Gibb, D. B., Cook, T. A., and Morris, D. L., 1993, "Laboratory and Animal Model Evaluation of the Cryotech LCS 2000 in Hepatic Cryotherapy," *Cryobiology,* Vol. 30, pp. 74–85.

Dover, J. S., and Hruza, G. J., 1996, "Laser Skin Resurfacing," *Seminars in Cutaneous Medicine and Surgery,* Vol. 15, pp. 177–188.

Dubuisson, J. B., Chapron, C., Fauconnier, A., and Kreiker, G., 1997, "Laparoscopic Myomectomy and Myolysis," *Current Opinions in Obstetrics and Gynecology,* Vol. 9, pp. 233–238.

Eberhart, R. C., Shitzer, A., and Hernandez, E. J., 1980, "Thermal Dilution Methods: Estimation of Tissue Blood Flow and Metabolism," *Annals New York Academy of Sciences,* Vol. 335, pp. 107–132.

Fahy, G. M., 1988, "Vitrification," *Low Temperature Biotechnology: Emerging Applications and Engineering Contributions,* J. J. McGrath and K. R. Diller, eds., ASME, New York, pp. 113–146.

Fahy, G. M., 1990, "Physical Problems with the Vitrification of Large Biological Systems," *Cryobiology,* Vol. 27, pp. 492–510.

Finger, P. T., Smith, P. D., Paglione, R. W., and Perry, H. D., 1990, "Transscleral Microwave Cyclodestruction," *Investigative Ophthalmology and Visual Science,* Vol. 31, pp. 2151–2155.

Fowler, A. J. and Toner, M., 1998, "Prevention of Hemolysis in Rapidly Frozen Erythrocytes by Using a Laser Pulse," *Annals New York Academy of Sciences,* Vol. 858, pp. 245–252.

deFreitas, R. C., Diller, K. R., Lakey, J. R. T., and Rajotte, R. V., 1997, "Osmotic Behavior and Transport Properties of Human Islets in a Dimethyl Sulfoxide Solution," *Cryobiology,* Vol. 35, pp. 230–239.

de Freitas, R. C., Diller, K. R., Lachenbruch, C. A., and Merchant, F. A., 1998, "Network Thermodynamic Model of Coupled Transport in a Multicellular Tissue—The Islet of Langerhans," *Annals New York Academy of Sciences,* Vol. 858, pp. 191–204.

Fulton, J. E., 1996, "Dermabrasion, Chemabrasion, and Laserabrasion," *Dermatological Surgery,* Vol. 22, pp. 619–628.

Gentile, D. B., Gori, F., and Leoncini, M., 1991, "Electromagnetic and Thermal Models of a Water-Cooled Dipole Radiating in a Biological Tissue," *IEEE Transactions on Biomedical Engineering,* Vol. 38, pp. 98–103.

Goldberg, S. N., and Gazelle, G. S., 1998, "Advances in Radiofrequency Tumor Ablation Therapy: Technical Considerations, Strategies for Increasing Coagulation Necrosis Volume, and Preliminary Results," *Proceedings of Surgical Applications of Energy,* T. P. Ryan, ed., Vol. 3249, SPIE Press, Bellingham, WA.

Goldfarb, H. A., 1992, "Nd:YAG Laser Laparoscopic Coagulation of Symptomatic Myomas," *Journal of Reproductive Medicine,* Vol. 37, pp. 636–638.

Goldfarb, H. A., 1993, "Bipolar Laparoscopic Needles for Myoma Coagulation," *Journal of American Association of Gynecologic Laparoscopists,* Vol. 4, pp. 425–433.

Hayes, L. J., Diller, K. R., Chang, H. J., and Lee, H. S., 1988, "Prediction of Local Cooling Rates and Cell Survival During the Freezing of Cylindrical Specimens," *Cryobiology,* Vol. 25, pp. 67–82.

Henriques, F. C., 1947, "Studies of Thermal Injury. V. The Predictability and the Significance of Thermally Induced Rate Processes Leading to Irreversible Epidermal Injury," *Archives of Pathology,* Vol. 5, pp. 489–502.

Henriques, F. C., and Moritz, A. R., 1947, "Studies of Thermal Injury. I. The Conduction of Heat to and Through Skin and the Temperatures Attained Therein. A Theoretical and Experimental Investigation," *American Journal of Pathology,* Vol. 23, pp. 531–549.

Hoey, M. F., Mulier, P. M., Leveillee, R. J., and Hulbert, J. C., 1997, "Transurethral Prostate Ablation with Saline Electrode Allows Controlled Production of Larger Lesions than Conventional Lesions," *Journal of Endourology,* Vol. 4, pp. 279–284.

Holti, G., and Mitchell, K. W., 1979, "Estimation of the Nutrient Skin Blood Flow Using a Non-Invasive Segmented Thermal Clearance Probe," *Non-Invasive Physiological Measurements,* Vol. 1, E. P. Rolfe, ed., Academic Press, London, pp. 113–123.

Horvath, K. A., Smith, W. J., Laurence, R. G., Schoen, F. J., Appleyard, R. F., and Cohn, L. H., 1995, "Recovery and Viability of an Acute Myocardial Infarct after Transmyocardial Laser Revascularization," *Journal of American College of Cardiology,* Vol. 25, pp. 258–263.

Huang, H. W., Chen, Z. P., and Roemer, R. B., 1996, "A Counter Current Vascular Network Model of Heat Transfer in Tissues," ASME *Journal of Biomechanical Engineering,* Vol. 118, pp. 120–129.

Huang, S. K. S., Graham, A. R., Lee, M. A., Ring, M. E., Gorman, G. D., and Schiffman, R., 1991, "Comparison of Catheter Ablation using Radiofrequency Versus Direct Current Energy: Biophysical, Electrophysiologic and Pathologic Observations," *Journal American College Cardiology,* Vol. 18, pp. 1091–1097.

Humphries, S., Platt, R. C., and Ryan, T. P., 1997, "Finite-Element Codes To Model Electrical Heating and Non-Linear Transport In Biological Media," *Advances In Heat And Mass Transfer in Biotechnology,* HTD-Vol. 355/BED-Vol. 37, ASME, New York, pp. 131–134.

Hurst, B. S., Ryan, T. P., Thomsen, S., and Lawes, K., 1998, "Computer-Controlled Bipolar Endotubal Sterilization is Successful in a Rabbit Model," in press.

Jiji, L. M., Weinbaum, S., and Lemons, D. E., 1984, "Theory and Experiment for the Effect of Vascular Microstructure on Surface Tissue Heat Transfer. Part II. Model Formulation and Solution," ASME *Journal of Biomechanical Engineering,* Vol. 106, pp. 331–341.

Johnson, C. S., and Guy, A. W., 1972, "Non-ionizing Wave Effects in Biological Materials and Systems," *Proceedings of the IEEE,* Vol. 60, pp. 692–718.

Kapp, D. S., and Prionas, S. D., 1992, "Experience with Radiofrequency-Local Current Field Interstitial Hyperthermia: Biological Rationale, Equipment Development, and Clinical Results," *Interstitial Hyperthermia,* Handl-Zeller ed., Springer-Verlag, Austria, pp. 95–119.

Kasharin, A. V., and Karlsson, J. O. M., 1998, "Analysis of Mass Transport during Warming of Cryopreserved Cells," *Annals New York Academy of Sciences,* Vol. 858, pp. 163–174.

Kedem, O., and Katchalsky, A., 1958, "Thermodynamic Analysis of Permeability of Biological Membranes to Nonelectrolytes," *Biochimica et Biophysica Acta,* Vol. 27, pp. 229–246.

Klar, T., Kraus, M., Bleyl, J., Newman, W. H., Bowman, H. F., von Kummer, R., Otto, G., and Herfarth, C., 1995, "Thermodiffusion as a Novel Method for Continuous Monitoring of the Hepatic Microcirculation after Liver Transplantation," *Transplantation Proceedings,* Vol. 27, pp. 2610–2612.

Klar, T., Kraus, M., Bredt, B., Osswald, N., Senninger, C., Herfarth, C., and Otto, G., 1996, "First Clinical Realization of Continuous Monitoring of Liver Microcirculation after Transplantation by Thermodiffusion," *Transplantation International,* Vol. 9, pp. S140–S143.

Klar, T., Kraus, J., Bleyl, B., Newman, W. H., Bowman, H. F., Hofmann, W., von Kummer, R., Otto, G., and Herfarth, C., 1997, "Thermodiffusion for Continuous Quantification of Hepatic Microcirculation—Validation and Potentials in Liver Transplantation," *Transplantation,* submitted for publication.

Kolios, M. K., Sherar, M. D., and Hunt, J. W., 1996, "Blood Flow Cooling and Ultrasonic Lesion Formation," *Medical Physics,* Vol. 23, pp. 1287–1298.

Kress, R., and Roemer, R. B., 1987, "A Comparative Analysis of Thermal Blood Perfusion Measurement Techniques," ASME *Journal of Biomechanical Engineering,* Vol. 109, pp. 218–225.

Kurz, W., and Fisher, D. J., 1992, *Fundamentals of Solidification,* 3rd Ed., Trans Tech Publications, Aedermannsdorf, Switzerland.

Labonte, S., 1994, "Numerical Model for Radio-Frequency Ablation of the Endocardium and Its Experimental Validation," *IEEE Transactions on Biomedical Engineering,* Vol. 41, pp. 108–115.

Lachenbruch, C. A., Pegg, D. E., and Diller, K. R., 1998, "Sensitivity of Kidney Perfusion Protocol Design to Physical and Physiological Parameters," *Annals New York Academy of Sciences,* Vol. 858, pp. 298–309.

Langberg, J. L., Wonnell, T., Chin, M. C., Finkbeiner, W., Scheinman, M., and Stauffer, P., 1991, "Catheter Ablation of the Atrioventricular Junction using a Helical Microwave Antenna: A Novel Means of Coupling Energy to the Endocardium," *PACE,* Vol. 14, pp. 2105–2113.

Lawrence, J. C., and Bull, J. P., 1976, "Thermal Conditions Which Cause Skin Burns," *Journal of the Institute of Mechanical Engineers, Engineering in Medicine,* Vol. 5, pp. 61–63.

Lee, F., Bahn, D. K., McHugh, T. A., Onik, G. M., and Lee, F. T., 1994, "US Guided Percutaneous Cryoablation of Prostate Cancer," *Radiology,* Vol. 192, pp. 769–776.

Levin, R. L., 1988, "Osmotic Behavior of Cells During Freezing and Thawing," *Low Temperature Biotechnology: Emerging Applications and Engineering Contributions,* J. J. McGrath and K. R. Diller, eds., ASME, New York, pp. 177–188.

Lewis, J. W., and Dubuc, M., 1998, "Catheter Application of Cryogenic Temperatures Inside the Heart," *Proceedings of Surgical Applications of Energy,* T. P. Ryan, ed., Vol. 3249, SPIE Press, Bellingham, WA.

Liggett, P. E., Pince, K. J., Astrahan, M., Rao, N., and Perrovich, Z., 1990, "Localized Current Field Hyperthermia: Effect on Ocular Tissue," *International Journal of Hyperthermia,* Vol. 6, pp. 517–527.

Livraghi, T., Goldberg, S. N., Monti, F., Bizzini, A., Lazzaroni, S., Meloni, F., Pellicano, S., Solbiati, L., and Gazelle, G. S., 1997, "Saline Enhances Radio-Frequency Tissue Ablation in the Treatment of Liver Metastases," *Radiology,* Vol. 202, pp. 205–210.

Lovelock, J. E., 1953, "The Mechanism of the Protective Action of Glycerol Against Haemolysis by Freezing and Thawing," *Biochimica et Biophysica Acta,* Vol. 11, pp. 28–36.

Martin, G. T., Haddad, M. G., Cravalho, E. G., and Bowman, H. F., 1992, "Thermal Model for the Local Microwave Hyperthermia Treatment of Benign Prostatic Hyperplasia," *IEEE Transactions on Biomedical Engineering,* Vol. 39, pp. 836–844.

Matsumoto, R., Selig, A. M., Colucci, V. M., and Jolesz, F. A., 1992, "Interstitial Nd:YAG Laser Ablation in Normal Rabbit Liver," *Lasers in Surgery and Medicine,* Vol. 12, pp. 650–658.

Mazur, P., 1963, "Kinetics of Water Loss from Cells at Subzero Temperatures and the Likelihood of Intracellular Freezing," *Journal of General Physiology,* Vol. 47, pp. 347–369.

Mazur, P., 1990, "Equilibrium, Quasi-Equilibrium and Nonequilibrium Freezing of Mammalian Embryos," *Cell Biophysics,* Vol. 17, pp. 53–92.

McGahan, J. P., Schneider, P., Brock, J. M., and Tesluk, H., 1993, ''Treatment of Liver Tumors by Percutaneous Radiofrequency Electrocautery,'' *Seminars in Interventional Radiology,* Vol. 10, pp. 143–149.

McGrath, J. J., 1985, ''A Microscope Diffusion Chamber for the Determination of the Equilibrium and Non-Equilibrium Response of Individual Cells,'' *Journal of Microscopy,* Vol. 139, pp. 249–263.

McGrath, J. J., 1988, ''Membrane Transport Properties,'' *Low Temperature Biotechnology: Emerging Applications and Engineering Contributions,* J. J. McGrath and K. R. Diller, eds., ASME, New York, pp. 273–330.

McGrath, J. J., and Diller, K. R., eds., 1988, ''Low Temperature Biotechnology: Emerging Applications and Engineering Contributions,'' ASME, New York, pp. 1–380.

Michner, M., Hager, J. M., Terrell, J. P., Veit, H., and Diller, T. E., 1991, ''Noninvasive Blood Perfusion Measurement with a Heat Flux Microsensor,'' *Advances in Biological Heat and Mass Transfer,* HTD-Vol. 189/BED-Vol. 18, ASME, New York, pp. 9–14.

Mitchell, J. W., and Myers, G. E., 1968, ''An Analytical Model of the Counter-current Heat Exchange Phenomena,'' *Biophysical Journal,* Vol. 8, pp. 897–911.

Montorsi, F., Guazzoni, G., Colombo, R., Galli, L., Bergamaschi, F., and Rigatti, P., 1992, ''Transurethral Microwave Hyperthermia for Advanced Prostate Cancer: Long Term Clinical Results,'' *Journal of Urology,* Vol. 148, pp. 342–345.

Mooibroek, J., and Lagendijk, J. J. W., 1991, ''A Fast and Simple Algorithm for the Calculation of Convective Heat Transfer by Large Vessels in 3-Dimensional Inhomogeneous Tissue,'' *IEEE Transactions on Biomedical Engineering,* Vol. 38, pp. 490–501.

Moritz, A. R., and Henriques, F. C., 1947, ''Studies of Thermal Injury. II. The Relative Importance of Time and Surface Temperature in the Causation of Cutaneous Burns,'' *American Journal of Pathology,* Vol. 23, pp. 695–720.

Moskowitz, M. J., Ryan, T. P., Paulsen, K. D., and Mitchell, S. E., 1995, ''Clinical Implementation of Electrical Impedance Tomography with Hyperthermia,'' *International Journal of Hyperthermia,* Vol. 11, pp. 141–149.

Moussa, N. A., McGrath, J. J., Cravalho, E. G., and Asimacopoulos, P. J., 1977, ''Kinetics of Thermal Injury in Cells,'' ASME *Journal of Biomechanical Engineering,* Vol. 99, pp. 155–159.

Moussa, N. A., Tell, E. N., and Cravalho, E. G., 1979, ''Time Progression of Hemolysis of Erythrocyte Populations Exposed to Supraphysiological Temperatures,'' ASME *Journal of Biomechanical Engineering,* Vol. 101, pp. 213–217.

Naseek, G. S., Fostre, T. E., Trauner, K., Solhpour, S., Anderson, R. R., and Zarins, B., 1997, ''The Thermal Properties of Bovine Joint Capsule, The Basic Science of Laser and Radiofrequency-Induced Capsular Shrinkage,'' *American Journal of Sports Medicine,* Vol. 25, pp. 670–674.

Nelson, D. A., 1998, ''Invited Editorial on 'Pennes' 1948 Paper Revisited,'' ' *Journal of Applied Physiology,* Vol. 85, pp. 2–3.

Nerem, R. M., and Sambanis, A., 1995, ''Tissue Engineering: From Biology to Biological Substitutes,'' *Tissue Engineering,* Vol. 1, pp. 3–13.

Onik, G., Gilbert, J., Hoddick, W., Filly, R., Callen, P., Rubinsky, B., and Christianson, M., 1984, ''Ultrasonic Characteristics of Frozen Liver,'' *Cryobiology,* Vol. 21, pp. 331–335.

Onik, G., and Rubinsky, B., 1988, ''Cryosurgery: New Developments in Understanding and Technique,'' *Low Temperature Biotechnology: Emerging Applications and Engineering Contributions,* J. J. McGrath and K. R. Diller, eds., ASME, New York, pp. 57–80.

Oster, G. F., Perelson, A. S., and Katchalsky, A., 1973, ''Network Thermodynamic Modelling of Biophysical Systems,'' *Quarterly Reviews of Biophysics,* Vol. 6, pp. 1–134.

Otten, D. M., Rubinsky, B., Cheong, W.-F., and Benaron, D. A., 1998, ''Ice Front Propagation Monitoring in Tissue by the Use of Visible-Light Spectroscopy,'' *Applied Optics,* Vol. 37, pp. 6006–6010.

Patel, P. A., Valvano, J. W., Pearce, J. A., Prahl, S. A., and Denham, C. R., 1987, ''A Self-Heated Thermistor Technique to Measure Effective Thermal Properties from the Tissue Surface,'' ASME *Journal of Biomechanical Engineering,* Vol. 109, pp. 330–335.

Patel, P., Fuchs, G. J., Guitierrez-Aceves, J., and Ryan, T. P., 1997, ''Prostate Heating Patterns Comparing Electrosurgical Transurethral Resection and Vaporization: A Prospective Randomized Study,'' *Journal of Urology,* Vol. 157, pp. 169–172.

Pazhayannur, P. V., and Bischof, J. C., 1997, ''Measurement and Simulation of Water Transport During Freezing in Mammalian Liver Tissue,'' ASME *Journal of Biomechanical Engineering,* Vol. 119, pp. 269–277.

Pearce, J. A., 1986, *Electrosurgery,* Chapman and Hall, London.

Pearce, J., Thomsen, S., Vijverberg, H., and McMurray, T., 1993, ''Kinetics for Birefringence Changes in Thermally Coagulated Rat Skin Collagen,'' *Lasers in Otolaryngology, Dermatology, and Tissue Welding,* Vol. 1876, pp. 180–186.

Pennes, H. H., 1948, ''Analysis of Tissue and Arterial Blood Temperatures in the Resting Forearm,'' *Journal of Applied Physiology,* Vol. 1, pp. 93–122 (republished for the 50th anniversary issue of *JAP,* Vol. 85, pp. 5–34).

Perdrizet, G. A., 1995, ''Heat Shock and Tissue Protection,'' *New Horizons,* Vol. 3, pp. 312–320.

Pitt, R. E., 1992, ''Thermodynamics and Intracellular Ice Formation,'' *Advances in Low-Temperature Biology,* Vol. 1, P. L. Steponkus, ed., JAI Press, London, pp. 63–100.

Platt, R. C., 1998, ''Argon Plasma Electrosurgical Coagulation,'' 1998, submitted for publication.

Polge, C., Smith, A. U., and Parkes, A. S., 1949, ''Revival of Spermatozoa After Vitrification and Dehydration at Low Temperatures,'' *Nature,* Vol. 164, p. 666.

Quigley, M. R., Loesch, D. V., Shih, T., Marquardt, M., Lupetin, A., and Maroon, J. C., 1992, ''Intracranial Cryosurgery in a Canine Model: A Pilot Study,'' *Surgical Neurology,* Vol. 38, pp. 101–105.

Ravikumar, T. S., Kane, R., Cady, B., Jenkins, R., Clouse, M., and Steele, G., 1991, ''A Five Year Study of Cryosurgery in the Treatment of Liver Tumors,'' *Archives Surgery,* Vol. 126, pp. 1520–1524.

Ravikumar, T. S., Buenaventura, S., Salem, R. R., and D'Andrea, B., 1994, ''Intraoperative Ultrasonography of Liver: Detection of Occult Liver Tumors and Treatment by Cryosurgery,'' *Cancer Detection and Prevention,* Vol. 18, pp. 131–138.

Robinson, D. S., Parel, J. M., Denham, D. B., Gonzalez-Cirrre, X., Manns, F., Milne, P. J., Schachner, R. D., Herron, A. J., Comander, J., and Hauptmann, G., 1998, ''Interstitial Laser Hyperthermia Model Development for Minimally Invasive Therapy of Breast Carcinoma,'' *Journal of American College of Surgeons,* Vol. 186, pp. 284–292.

Ross, D. C., and Diller, K. R., 1976, ''An Experimental Investigation of Burn Injury in Living Tissue,'' ASME Journal of Heat Transfer, Vol. 98, pp. 292–296.

Rubinsky, B., Cravalho, E. G., and Mikic, B., 1980, ''Thermal Stresses in Frozen Organs,'' *Cryobiology,* Vol. 17, pp. 66–73.

Rubinsky, B., Gilbert, J. C., Onik, G. M., Roos, H. S., Wong, S. T. S., and Brennan, K. M., 1993, ''Monitoring Cryosurgery in the Brain and in the Prostate with Proton NMR,'' *Cryobiology,* Vol. 30, pp. 191–199.

Rubinsky, B. and Pegg, D. E., 1989, ''A Mathematical Model for the Freezing Process in Biological Tissue,'' *Proceedings of the Royal Society of London,* Vol. B234, pp. 343–358.

Ryan, T. P., 1991, ''Comparison of Six Microwave Antennas for Hyperthermia Treatment of Cancer: SAR Results for Single Antennas and Arrays,'' *International Journal of Radiation Oncology, Biology and Physics,* Vol. 21, pp. 403–413.

Ryan, T. P., Backus, V. L., and Coughlin, C. T., 1995, ''Large Stationary Microstrip Arrays for Superficial Microwave Hyperthermia at 433 MHz: SAR Analysis and Clinical Data,'' *International Journal of Hyperthermia,* Vol. 11, pp. 187–209.

Ryan, T. P., Colacchio, T. A., Douple, E. B., Strohbehn, J. W., and Coughlin, C. T., 1992, ''Techniques for Intraoperative Hyperthermia with Ultrasound: The Dartmouth Experience with 19 Patients,'' *International Journal of Hyperthermia,* Vol. 8, pp. 404–421.

Ryan, T. P., Garza-Leal, J., Thomsen, S., Iglasias-Benavidas, J., Vancaillie, T. G., Vidal, O., and Lawes, K., 1997, ''Comparison of Thermal and Multielectrode Balloons for Endometrial Ablation.'' Annual Meeting, American Association of Gynecologic Laparoscopists, Seattle, WA.

Ryan, T. P., Hoopes, P. J., Taylor, J. H., Strohbehn, J. W., Roberts, D. W., Douple, E. B., and Coughlin, C. T., 1991, ''Experimental Brain Hyperthermia: Techniques for Heat Delivery and Thermotherapy,'' *International Journal of Radiation Oncology, Biology and Physics,* Vol. 20, pp. 739–750.

Ryan, T. P., Platt, R. C., and Humphries, S., 1998, ''Finite Element Model for Endometrial Ablation Systems,'' *Proceedings of Surgical Applications of Energy,* T. P. Ryan, ed., Vol. 3249, SPIE Press, Bellingham, WA.

Ryan, T. P., Platt, R. C., Dadd, J. S., and Humphries, S., 1997, ''Tissue Electrical Properties as a Function of Thermal Dose for Use in a Finite Element Model,'' *Advances In Heat And Mass Transfer In Biotechnology,* HTD-Vol. 355/BED-Vol. 37, ASME, New York, pp. 167–171.

Saparetto, S. A., and Dewey, W. C., 1984, ''Thermal Dose Determination in Cancer Therapy,'' *International Journal of Radiation Oncology, Biology and Physics,* Vol. 10, pp. 787–800.

Schwan, H. P., and Foster, K. R., 1980, ''RF-Field Interactions with Biological Systems: Electrical Properties and Biophysical Mechanisms,'' *Proceedings of the IEEE,* Vol. 68, pp. 104–113.

Scott, E. P., Robinson, P. S., and Diller, T. E., 1998, ''Development of Methodologies for the Estimation of Blood Perfusion Using a Minimally Invasive Thermal Probe,'' *Measurement Science and Technology,* Vol. 9, pp. 888–897.

Shitzer, A., and Eberhart, R. C., eds., 1985, *Heat Transfer in Medicine and Biology: Analysis and Applications,* Vols. 1 and 2, Plenum Press, New York.

Simon, C., Van Baren, P., and Ebbini, E. S., 1998, ''Two-Dimensional Temperature Estimation using Diagnostic Ultrasound,'' *IEEE Transactions on Ultrasonics, Ferroelectrics, and Frequency Control,* Vol. 45, pp. 1088–1099.

Silverman, R. H., Vogelsang, B., Rondeau, M. J., and Coleman, D. J., 1991, ''Therapeutic Ultrasound for the Treatment of Glaucoma,'' *American Journal of Ophthalmology,* Vol. 111, pp. 327–337.

Smith, D. L., Walinsky, P., Martinez-Hernandez, A., Rosen, A., Syterzer, F., and Kosman, Z., 1992, ''Microwave Thermal Balloon Angioplasty in the Normal Rabbit,'' *American Heart Journal,* Vol. 123, pp. 1516–1521.

Sporl, E., Genth, U., Schmalfuss, K., and Seiler, T., 1996, ''Thermomechanical Behavior of the Cornea,'' *Journal of Ophthalmology,* Vol. 5, pp. 322–327.

Stauffer, P. R., 1998, ''Implantable Microwave Antennas for Thermal Therapy,'' *Proceedings of Surgical Applications of Energy,* T. P. Ryan, ed., Vol. 3249, SPIE Press, Bellingham, WA.

Stawarz, B., Szmigielski, S., Ogrodnik, J., Astrahan, M., and Petrovich, Z., ''A Comparison of Transurethral and Transrectal Microwave Hyperthermia in Poor Surgical Risk Benign Prostatic Hyperplasia Patients,'' *Journal of Urology,* Vol. 146, pp. 353–357.

Steponkus, P. L., 1984, ''The Role of the Plasma Membrane in Freezing Injury and Cold Acclimation,'' *Annual Review of Plant Physiology,* Vol. 35, pp. 543–584.

Stoll, A. M., 1960, ''A Computer Solution for Determination of Thermal Tissue Damage Integrals from Experimental Data,'' *Institute of Radio Engineers Transactions on Medical Electronics,* Vol. 7, pp. 355–358.

Stoll, A. M., and Chianta, M. A., 1968, "Burn Production and Prevention in Convective and Radiant Heat Transfer," *Aerospace Medicine*, Vol. 39, pp. 1232–1238.

Stoll, A. M., and Green, L. C., 1959, "Relationship Between Pain and Tissue Damage due to Thermal Radiation," *Journal of Applied Physiology*, Vol. 14, pp. 373–382.

Strumia, M. M., Clawell, L. S., and Strumia, P. V., 1960, "The Preservation of Blood for Transfusion," *Journal of Laboratory and Clinical Medicine*, Vol. 56, pp. 576–593.

Svaasand, L. O., Gomer, C. J., and Profio, A. E., 1989, "Laser-Induced Hyperthermia of Ocular Tumors," *Applied Physics*, Vol. 28, pp. 2280–2287.

Swift, P. S., Stauffer, P. R., Fries, P. D., Kaleta-Michaels, S., Murray, T., Sneed, P. K., Phillips, T. L., and Char, D. H., 1990, "Microwave Hyperthermia for Choroidal Melanoma in Rabbits," *Investigative Ophthalmology and Visual Science*, Vol. 31, pp. 1754–1760.

Takata, A. N., 1974, "Development of Criterion for Skin Burns," *Aerospace Medicine*, Vol. 45, pp. 634–637.

Toner, M., 1993, "Nucleation of Ice Crystals Inside Biological Cells," *Advances in Low-Temperature Biology*, Vol. 2, P. L. Steponkus, ed., JAI Press, London, pp. 1–52.

Trembly, B. S., 1985, "The Effects of Driving Frequency and Antenna Length on Power Deposition Within a Microwave Antenna Array Used for Hyperthermia," *IEEE Transactions on Biomedical Engineering*, Vol. 32, pp. 152–157.

Trembly, B. S., Douple, E. B., and Hoopes, P. J., 1991, "The Effect of Air Cooling on the Radial Temperature Distribution of a Single Microwave Hyperthermia Antenna In-Vivo," *International Journal of Hyperthermia*, Vol. 7, pp. 343–354.

Trembly, B. S., Douple, E. B., Ryan, T. P., and Hoopes, P. J., 1995, "Effect of Phase Modulation on the Temperature Distribution of a Microwave Hyperthermia Antenna Array In Vivo," *International Journal of Hyperthermia*, Vol. 10, pp. 691–705.

Trembly, B. S., and Keates, R. H., 1991, "Combined Microwave Heating and Surface Cooling of the Cornea," *IEEE Transactions on Biomedical Engineering*, Vol. 38, pp. 85–91.

Trembly, B. S., Manganiello, P., and Hoopes, J., 1998, "Microwave Occlusion of the Rabbit Uterine Horn," *Proceedings of Surgical Applications of Energy*, T. P. Ryan, ed., Vol. 3249, SPIE Press, Bellingham, WA.

Trembly, B. S., Ryan, T. P., and Strohbehn, J. W., 1991, "Physics of Microwave Hyperthermia," *Hyperthermia and Oncology*, Urano and Douple eds., VSP, Vol. 3, pp. 11–98.

Valvano, J. W., 1992, "Temperature Measurements," *Advances in Heat Transfer*, Vol. 22, pp. 359–436.

Valvano, J. W., Allen, J. T., and Bowman, H. F., 1984, "The Simultaneous Measurement of Thermal Conductivity, Thermal Diffusivity and Perfusion in Small Volumes of Tissue," ASME *Journal of Biomechanical Engineering*, Vol. 106, pp. 192–197.

Valvano, J. W., Cochran, J. R., and Diller, K. R., 1985, "Thermal Conductivity and Diffusivity of Biomaterials Measured with Self-heated Thermistors," *International Journal of Thermophysics*, Vol. 6, pp. 301–311.

Walcerz, D. B. and Diller, K. R., 1991, "Quantitative Light Microscopy of Combined Perfusion and Freezing Processes," *Journal of Microscopy*, Vol. 161, pp. 297–311.

Walsh, J. R., Diller, K. R. and Brand, J. J., 1997, "Osmomechanical Behavior of Plant Cells Across Regions of Elastic and Osmotic Stress," *Advances in Heat and Mass Transfer in Biotechnology*, HTD-355/BED-37, ASME, New York, pp. 15–23.

Walsh, J. R., Diller, K. R., and Brand, J. J., 1998, "Measurement and Simulation of Water Transport in Algal Cells," ASME *Journal of Biomechanical Engineering*, submitted for publication.

Walsh, J. T., and Bowman, H. F., 1984, "A Noninvasive Technique for Quantifying Tissue Perfusion," *Advances in Bioengineering*, R. L. Spilker, ed., ASME, New York, pp. 5–6.

Weaver, J. A., and Stoll, A. M., 1967, "Mathematical Model of Skin Exposed to Thermal Radiation," *Aerospace Medicine*, Vol. 40, pp. 24–30.

Weill, A., Shitzer, A., and Bar-Joseph, P., 1993, "Finite Element Analysis of the Temperature Field Around Two Adjacent Cryo-Probes," ASME *Journal of Biomechanical Engineering*, Vol. 115, pp. 374–379.

Weinbaum, S. and Jiji, L. M., 1987, discussion of papers by Wissler and Baish et al. concerning "The Weinbaum-Jiji Bioheat Equation," ASME *Journal of Biomechanical Engineering*, Vol. 109, pp. 234–237.

Weinbaum, S., Jiji, L. M., and Lemons, D. E., 1984, "Theory and Experiment for the Effect of Vascular Microstructure on Surface Tissue Heat Transfer. Part I. Anatomical Foundation and Model Conceptualization," ASME *Journal of Biomechanical Engineering*, Vol. 106, pp. 321–330.

Whittingham, D. G., Leibo, S. P., and Mazur, P., 1972, "Survival of Mouse Embryos Frozen to −196°C and −296°C," *Science*, Vol. 178, pp. 411–414.

Wissler, E. H. 1961, "Steady State Temperature Distribution in Man," *Journal of Applied Physiology*, Vol. 16, pp. 734–740.

Wissler, E. H., 1985, "Mathematical Simulation of Human Thermal Behavior Using Whole-Body Models," *Heat Transfer in Medicine and Biology*, Vol. 1, A. Shitzer and R. C. Eberhart, eds., Plenum Press, New York, pp. 325–373.

Wissler, E. H., 1987a, "Comments on the New Bioheat Equation Proposed by Weinbaum and Jiji," ASME *Journal of Biomechanical Engineering*, Vol. 109, pp. 226–233.

Wissler, E. H., 1987b, "Comments on Weinbaum and Jiji's Discussion of Their Proposed Bioheat Equation," ASME *Journal of Biomechanical Engineering*, Vol. 109, pp. 355–356.

Wissler, E. H., 1998, "Pennes' 1948 Paper Revisited," *Journal of Applied Physiology*, Vol. 85, pp. 35–41.

Yeh, M. M., Trembly, B. S., Douple, E. B., Ryan, T. P., Hoopes, P. J., Jonsson, E., and Heaney, J. A., 1994, "Theoretical and Experimental Analysis of Air Cooling for Intracavitary Microwave Hyperthermia Applicators," *IEEE Transactions on Biomedical Engineering*, Vol. 41, pp. 874–882.

Zweifach, B. W., 1961 *Functional Behavior of the Microcirculation*, Charles C. Thomas Publisher, Springfield, IL.

A Review of Recent Developments in Some Practical Aspects of Air-Cooled Electronic Packages

S. Sathe
Manager, Thermal & Mechanical
Analysis Group,
IBM Corporation,
Microelectronics Division,
1701 North Street,
Endicott, NY 13760
e-mail: sanjeev@us.ibm.com

B. Sammakia
Director IEEC and
Professor of Mechanical Engineering,
T. J. Watson School of Engineering,
State University of New York,
Binghamton, NY 13902-6000
e-mail: bahgat@binghamton.edu

The recent emphasis on low-cost high-end servers and desktop workstations has resulted in a renewed interest in the development of high-performance air-cooled systems. A new generation of advanced heat sink designs capable of dissipating up to 10^5 W/m^2 have been proposed and developed. Better manufacturing tolerances, lower defects, and an improved understanding of card and enclosure effects have been attained and shown to be critical to achieving the desired thermal performance. Advanced internal thermal enhancements, encompassing high thermal conductivity adhesives and greases have also been implemented. This review article covers recent developments in heat sink designs and applications intended for high-end high-power dissipation systems. A review of recent studies of card effects in the thermal enhancement of electronic packages is also presented. In certain applications the card heat-sinking effect can play a major role in the thermal management of a package, accounting for more than 50 percent of the total power dissipation of the package.

Introduction

During the past several years there have been significant changes in the packaging of electronic equipment, and particularly in the packaging of computer systems. This change started with the shift from central mainframes to distributed computing, and from bi-polar chips to CMOS. These changes had a profound impact on the thermal management schemes used in such systems. Bi-polar-based mainframes had been mostly watercooled. The power dissipation in those systems had been consistently increasing over the years. Elaborate cooling schemes had been developed and implemented, with increasing complexity, for each new generation. The primary concerns for these mainframes were performance and reliability. When the paradigm shift to CMOS-based systems took place, there was the additional emphasis of reduced cost in all aspects of the system which resulted in a preference for air cooled systems whenever the application requirements allowed it. The shift to distributed computing also meant that systems needed to be installed in offices and could not be exclusively housed in air-conditioned computer centers with cooling water connections. This increased emphasis on air cooling revived the need for advanced heat sinks that can handle significant heat flux densities at a reasonable junction temperature. The first section of this paper deals with recent developments in advanced air-cooled heat sinks.

Another aspect of thermal management in air-cooled systems that has gained relevence over the past few years is the role of the printed circuit board or card in the overall thermal performance of the system. The true thermal performance of the system cannot be determined without accounting for the card effects. Consider, for example, an application with a single processor on a sparsely populated card, with few other heat dissipating devices on the card. The card may then act as a very effective heat sink. On the other hand, consider the same processor on a card that is densly populated with other heat dissipating devices. In the latter case the card would not be an effective heat sink. Obviously the requirements for the thermal management scheme and for the heat sink design for the same processor is different depending upon the card population. There are also several other card design parameters that affect the heat sink design. These include card thickness, the number and thickness of power planes, resign material, card to card pitch and single or double-sided applications. Card effects and their impact upon thermal management and heat sink design are discussed in the second section of this paper.

Heat Sinks in Air-Cooled Electronic Devices

In view of the proliferation of office environment computing, air-cooling has gained considerable attention. Due to the poor thermal properties of air compared with water, it becomes necessary to resort to using extented surfaces, commonly termed as heat sinks. Even in the high-end servers or supercomputer products, air-cooling is gaining grounds due to the lower hardware cost and higher reliability.

The use of heat sinks to improve the heat transfer rate from a module has to be implemented with great care. The increased surface area usually requires an increase in the air pressure drop in that region, and if there are other paths for the air to flow through at a lower pressure drop, the resulting air starvation in the "enhanced" region may actually result in a lower heat transfer rate. Careful analysis or testing is therefore necessary under the actual system condition to ensure effectiveness of the design.

The following sections mainly focus on heat sinks categorized based on single or multiple flow-through heat sinks, impingement heat sinks, heat sink optimization, novel heat sink materials or structures and natural convection heat sinks. Emphasis is placed on recent developments in the areas of electronic packaging. For a comprehensive and detailed review of heat sink design fundamentals the reader is referred to Kraus and Bar-Cohen (1995).

Flow Through or Serially Cooled Heat Sinks. Flow through heat sinks refers to heat sinks wherein the flow enters the heat sink from one end and travels more or less in a straight

---

Contributed by the Heat Transfer Division for publication in the JOURNAL OF HEAT TRANSFER. Manuscript received by the Heat Transfer Division, July 12, 1998; revision received, Oct. 8, 1998. Keywords: Cooling, Electronics, Enhancement, Heat Transfer, Packaging, Temperature, Thermal. Associate Technical Editor: Y. Jaluria.

line to exit from the other end. One of the simplest, and most cost-effective heat sink designs used is the linearly extruded aluminum heat sink. These heat sinks can be extruded to a maximum fin density ratio (the height to width spacing between fins) of approximately 5 to 1. This limit is a result of manufacturing costs and tolerance control, as described by Kiley and Soule (1990). Such heat sinks are commonly used for many applications, but are limited to relatively low-power dissipation due to the limitation of total surface area per volume. Higher aspect ratios of up to 25 or more can be attained by using epoxy-bonded fin heat sinks. These heat sinks consist of an extruded or machined base, which is flat on the module-facing side and grooved on the fin side. The fins are then epoxied into the grooves. The epoxy interface does, however, add a thermal resistance to the system. This difficulty can be overcome by brazing or soldering the fins to the base, resulting in reduced overall resistance at a higher cost, Kiley and Soule (1990) and Soule (1993). Both aluminum and copper can be used to construct this type of heat sink, depending on the system requirements and allowable overall weight.

Pin-fin heat sinks are also commonly used and have the added advantage of not requiring specific positioning relative to flow direction. Pin-fin heat sinks can be manufactured either by starting with a linearly extruded parallel plate heat sink and then cutting the plates to form the pins, or by building them using more costly specialized techniques such as epoxy bonding, brazing and soldering as described above. Round pins or other cross-section shapes can also be manufactured using casting. Other less commonly used heat sinks included folded-fin heat sinks where sheet metal .005 to .08 cm (.002 to .032 inches thick) is corrugated to form fins. A maximum density of about 24 fins per inch is attainable.

For parallel plate heat sinks it is important to design the heat sink accounting for all air flow paths, since the air can bypass the heat sink if other low-resistance paths exist. Sparrow and Kadle (1986) studied the effect of tip to shroud clearance on the resulting heat transfer. In this experimental study the flow was turbulent, and the clearance above the fins was parametrically varied. It was determined that the heat transfer dropped significantly for increased clearance above the fins.

For clearances of 10, 20, and 30 percent of the fin height it was determined that the heat transfer rate was 85, 74, and 64 percent of the no-clearance case. In another study Kadle and Sparrow (1986) measured and analyzed the heat transfer rates from shrouded parallel plate heat sinks to a turbulent air stream. Average Nusselt numbers were determined by complementary use of the experimental and analytical results and were found to compare well with the widely used Petukhov-Popov correlation (e.g., Holman, 1981). Figure 1 shows the Nusselt number as a function of the Reynolds number where

Nu = hD/k
h = heat transfer coefficient

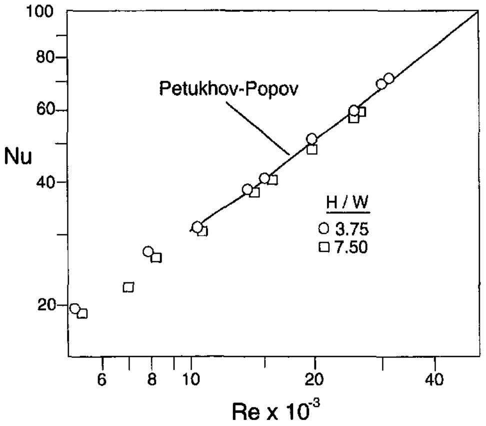

Fig. 1 Average Nusselt numbers versus Reynolds number (Holman, 1981)

D = $4HW/2(H + W)$ = hydraulic diameter
H = fin height
W = channel width between fins
k = thermal conductivity
Re = Reynolds number based on the hydraulic diameter.

For channels with very high aspect ratio, $H \gg W$, the hydraulic diameter D approximately equals $2W$. The heat transfer coefficient can then be maximized by minimizing W. This results in very narrow channels with a very high aspect ratio, a large pressure drop across the heat sink and laminar flow, Re < 2100. The limitation on narrowing the channel is basically the high-pressure drop required to drive the flow. Tuckerman and Pease (1981) designed a silicon micro heat sink based upon this principle and were able to dissipate very high heat flux levels, 790 W/cm^2 with an associated water temperature rise of 70°C. Based upon the same principle (microchannels), Goldberg (1984) proposed a laminar flow copper heat sink for air-cooling capable of delivering heat flux in excess of 25 W/cm^2 at the chip level with an associated air temperature rise of 60°C.

Mahalingham and Andrews (1988) conducted an extensive experimental study of microchannel Silicon heat sinks with air as the cooling medium. Two channel widths were studied, .025 and .0127 cm with corresponding fin heights of 0.17 and 0.114 cm. The resulting aspect ratios were therefore 6.8 and 9. The heat sinks were built by machining the Silicon and then housing it to prevent air leakage. The resulting heat sinks resembled a miniature extruded straight finned heat sink. Temperature and pressure drop measurements were taken at the inlet and exit sections of the heat sinks. The pressure drop was found to increase linearly with the air flow rate for the range investigated. A simplified noncompressible flow analysis (Mach number

Nomenclature

b = distance between adjacent printed circuit boards, m
d = depth of the printed circuit board, m
D = $4HW/2(H + W)$ = hydraulic diameter, m
g = gravitational acceleration, m/s^2
Gr = Grashof number
h_b = height of the printed circuit board, m
h = heat transfer coefficient, W/m^{2}K
H = heat sink fin height, m
k = thermal conductivity, W/mK
l = characteristic length = $n(h_b, s)$
L = heat sink base length, m
n = number of stacked printed circuit boards
Nu = hD/k
Nu$_{\mathrm{PCB}}$ = $qb/\lambda(T_{\mathrm{PCB}} - T_0)$
Pr = Prandtl number = $Cp\mu/k$
T_0 = surrounding air temperature of the cabinet, K
T_{PCB} = maximum printed circuit board temperature, K
q = total power dissipation in the card/m^2 $2dh$, W
s = free space between two adjacent stacked printed circuit boards, m
S = optimal spacing, m
W = channel width between fins
Ra = Pr $g\beta qb^5/(\upsilon^2 l\lambda)$
Re = Reynolds number based on hydraulic diameter
β = thermal expansion coefficient of air, K^{-1}
λ = thermal conductivity of air, W m^{-1} K^{-1}

<0.3) was introduced, and the results of the analysis were in good agreement with the measurements.

Mahaney and Vader (1993) performed an experimental and numerical study of a multichip high aspect ratio heat sink with laminar flow. Good agreement was found between the experimental measurements and the numerical results for both overall pressure drop and heat transfer rates from the heat sink. The effects of power variation from chip to chip was investigated numerically. Different heat sink materials were also evaluated.

Another type of heat sink that is gaining popularity is the pin-fin heat sink. These heat sinks are not sensitive to flow direction like parallel plate heat sinks, and they can be used in both flow through as well as impingement configurations. There are two common configurations of the fins relative to the flow field, in line or staggered. The flow is fairly complex for these configurations since it is constantly attaching to and seperating from the fins, and if there is a fin-tip clearance then additional complexities arise due to transverse flow component (in the direction of the axis of the fins) which is superimposed on the main flow. Sparrow and Ramsey (1978) and Sparrow et al. (1980) conducted experimental studies on in line and staggered pin fin arrays, with various pin-tip clearance. Pressure drops were measured across the arrays and heat transfer was measured by applying the analogy between heat and mass transfer to mass transfer coefficients measured via the Napthaline sublimation technique. For most of the cases studied, the row by row heat transfer coefficient was found to vary only in the initial rows, and attained a fully developed value by about the fourth row. The fully developed heat transfer coefficients were also found to be insensitive to the pin height, that is to tip clearance, for a given channel. The coefficients increased moderately as the fin height increased (and thus the clearance decreased). The pressure drop, however, was very sensitive to the fin height. It was also found that in line arrays had a lower heat transfer coefficient, but also had a lower associated pressure drop across the heat sink, probably due to increased air bypass.

Metzger et al. (1983) and Steuber and Metzger (1986) conducted a similar extensive experimental investigation of the heat transfer and pressure loss from partial length pin fins in high aspect ratio rectangular ducts. Twenty-five different pin fin array configurations were studied and documented. The primary findings were similar, heat transfer coefficients were higher for fins extending the entire height of the channel; however, the associated pressure drop was also higher. A flow through cooled heat sink using miniature pins was reported by Minakami et al. (1992). The side length of the copper pins was only 0.19 mm, manufactured by etching. It was found that the pin-spacing in the flow direction, optimal for thermal performance was about 4.5 pin diameters. The heat transfer increased monotonically as the transverse fin pitch decreased, with an associated penalty in pressure drop increase.

Multiple Heat Sink Arrays in Flow-Through Situations. The previous section examined the single flow-through heat sink. In many instances, an array of single-chip modules may need heat sinks mounted to each module. In this case, not only the heat sink dimensions itself, but also the bypass gaps are of importance. Not much work has been carried out in this area to determine the characteristics of such systems. Typically the difficulty in computational diagnosis or characterization arises because the flow may be laminar or transitional in the gaps in between the fins, but fully turbulent within the gaps between the heat sinks. Moreover, there may be vortex shedding as the flow exits one heat sink and enters another heat sink.

In one related study, Matsushima and Takehiko (1992) investigated the heat transfer and pressure drop characteristics of finned heat sink arrays. The heat sink base was 22 mm × 22 mm with a total sink height of 17.6 mm. The array consisted of five columns and up to 12 rows arranged in an in-line fashion. A thorough investigation was done to evaluate the effects of different fin geometries, package spacing (heat sink to heat sink spacing), air flows and placing of obstacles between heat sinks to promote mixing and also effects of missing heat sinks in the array. It was found that the heat transfer coefficients for the packages downstream did not show a noticeable difference for different heat sinks investigated, and the air heat-up seemed to be the primary contributor to the thermal resistance. The heat transfer coefficients for the upstream heat sinks changed more compared with the downstream heat sinks. Also it seemed helpful to have a missing package in front of a high-powered component due to the enhanced mixing created by a missing package. Azar (1992) studied the effect of in-line, staggered and a circuit pack layout on the performance of multiple thin-fin high aspect ratio heat sink arrangements. The fin thickness was 0.4 mm and the channel gap was 1.1 mm. It was found that the component layout on the circuit board did not significantly affect thermal performance of the heat sink under the conditions tested, as long as the flow through is not adversely affected by the component layout.

More research is required to characterize such systems and have a database readily available for electronic designers to be able to select heat sinks and predict the chip junction performance of heat sinks in an array. Future work is also needed in optimization of fin spacings and gaps between heat sinks to maximize heat transfer from an array of heat sinks.

Impingement Air Cooling. Some of the difficulties arising in flow through heat sinks relate to the pressure field in the actual system, and the air temperature rise due to upstream power dissipation. A heat sink designed for general use and tested for specific flow rate and inlet air temperatures may end up in a system where the air reaches the heat sink at a significantly higher temperature and may even bypass the heat sink if the path of least resistance lies around the heat sink instead of through it. A possible method to overcome these difficulties is to use air impingement, where the air is ducted directly to the heat sink and forced through it. The flow rate and air inlet temperature are then known more precisely. This approach is costly in that it requires specific manifold, heat sink, stiffeners, and more complex assembly for each application. Impingement also requires some additional space in the z-dimension (perpendicular to the boards) to allow for the manifolds and ducts channeling the flow. The advantages, however, are very significant, particularly for high-power applications using air cooling.

When characteristic dimension of the base of the heat sink is larger than the heat sink height, impingement usually reduces the pressure drop drastically, and if the nozzle size is properly chosen, the thermal performance can be comparable with a much lower pressure drop in a similar flow through heat sink (Sathe et al., 1995). Another advantage of impingement heat sinks is that fresh air can be ducted directly to the heat sinks without the temperature rise associated with flow through or serial cooling wherein the air passes from one module to another. The penalty to be paid is the increased height perpendicular to the heat sink base to accomodate the nozzle. This results in a less dense board spacing. Most of the impingement applications use pin-fins, as in Dunn et al. (1981), however, some utilize straight fins as in Sathe et al. (1995).

One of the earliest applications in electronic packaging of multichip modules, using air impingement for thermal management is the IBM 4381 system as described in Dunn et al. (1981) and Biskeborn et al. (1984). In that application the system consisted of 22 modules with up to 36 chips per module, each chip dissipating up to 3.6 W. The heat sink is attached to a ceramic cap which also served as a hermetic seal for the module. The flip chip (c4-controlled collapse chip connection) design required a thermal grease to attach the chips to the cap thermally. Overall internal and external thermal resistances were determined to be 9°C/W and 8°C/W, respectively (Oktay et al., 1983). Recently Sathe et al. (1997) modeled the 4381 heat

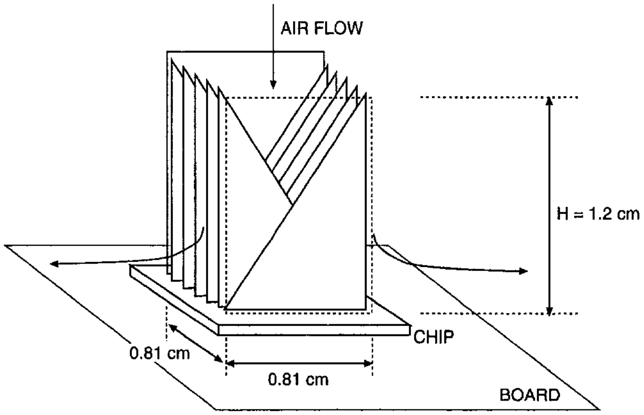

Fig. 2 Schematic perspective view of the impingement heat sink. The tip of the triangular fins can be folded to provide constant fin spacing. The prototype dimensions are shown in the figure (Hilbert et al., 1990).

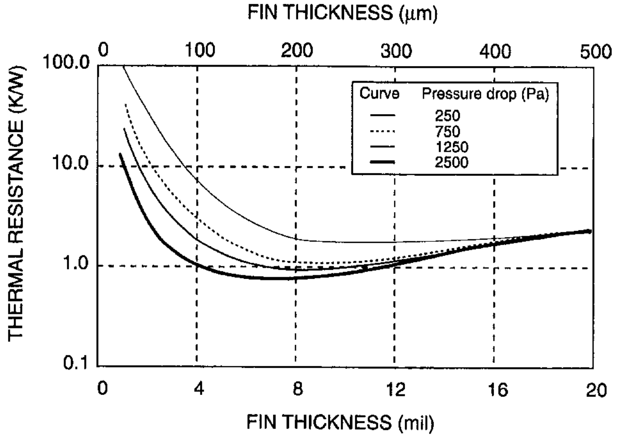

Fig. 3 Theoretical optimization of the fin thickness at different operating pressures for heat sink design in Fig. 2. The optimal fin thickness depends upon the pressure drop (Hilbert et al., 1990).

sink using CFD techniques and obtained good agreement with the experimental pressure drop and heat transfer performance. Based on the study, improvements were made in the heat sink by baffling and redistributing the flow (Sathe and Tai, 1992) to obtain better flow in the corner regions. McPhee et al. (1990), Fitch (1991), and Heng and Pei (1991) described the design for the air impingement design used in the VAX 9000 family of computers. In this design the chips dissipating up to 30 W each are back bonded to a copper base plate used as a heat spreader, which in turn is bonded to a pin-fin heat sink.

Bartilson (1991) presented the results of a numerical and experimental study of a miniature air impingement pin-fin heat sink. In this design air is brought in parallel to the printed circuit boards (PCBs), then turned 90 deg to impinge, through an opening in the PCB, into the pin-fin heat sink. This eliminates the additional spacing required for heat sinks between the PCBs. The heat sinks were 9.45 mm width × 9.45 mm length × 2 mm fin height, with a square pin of dimension only 0.305 × 0.305 mm, manufactured by etching. A thermal resistance of 4.5°C/W was reported at a jet velocity of 30 m/s, obtained through a 5 mm jet. Pressure drops were not reported but are believed to be within 200 N/m^2 of water based on the entire system air-cooling design.

Hilbert et al. (1990) investigated a unique heat sink design, comprised of interleaved fins, which formed narrow high-aspect ratio channels. Figure 2 is a schematic of the heat sink. In this design the channel width is equal to the fin thickness, t, since each fin is used to space the adjacent channel. Air impinged near the center of the heat sink and the flow was laminar. The external thermal resistance was reported as a function of t, at various pressure drops across the heat sink as shown in Fig. 3. The minimum in external thermal resistance was found to occur at $t = .0127$ cm. for a pressure drop of 2500 Pa. As t is increased the heat transfer area decreases and the boundary layer thickness also increases, both of which reduce the heat transfer. As t is decreased below optimum, the flow rate decreases due to increased drag.

Sathe et al. (1995) presented numerical and experimental results for a high-performance heat sink with a novel fin shape shown in Fig. 4. The stepped cuts reduced the central stagnation zone and increased heat transfer inspite of losing fin area. An external thermal resistance (R_{ext}) of 0.03 C/W was obtained on a 84 mm × 127 mm heat sink base at 140 cubic feet per minute, CFM (0.066 m^3/s), at 0.4 in. water pressure drop. The pressure drop and heat t transfer performance of this heat sink is better than some of the water-cooled technologies used in main-frame computers. The fin thickness and the channel gaps were 0.5 mm and 0.8 mm, respectively, and were determined from an optimization program. The heat sink was manufactured using stamped sheets brazed to a base with grooves to locate the sheets.

Recently, "fan-heat sinks" have been gaining popularity in the cooling of uniprocessors. These are small fans attached typically to pin-fin heat sinks, such that the air more or less impinges on the heat sink. Not too many quantitative studies are reported on the fan-heat sink performance or optimization. The fan-heat sink idea is not viable for multiprocessors where each processor uses a fan-heat sink due to the increased chance of failure by using many fans. There is much potential of conducting research in fan-heat sinks. It is difficult to perform numerical analysis on this topic due to the proximity of the heat sink to the fan and swirling, turbulent flow emerging out of the fan and impinging on the complex geometrical arrangement of the heat sink. Wirtz et al. (1997) report experimental results on the thermal performance of model fan-sink assemblies consisting of a small axial flow fan impinging air on a square array of pin fins. Mansuria and Kamath (1994) compared the performance of pin-fins, radial plate fins, and longitudinal plate fin with assembled fans. The radial units showed the lowest thermal resistance for a fixed pressure drop.

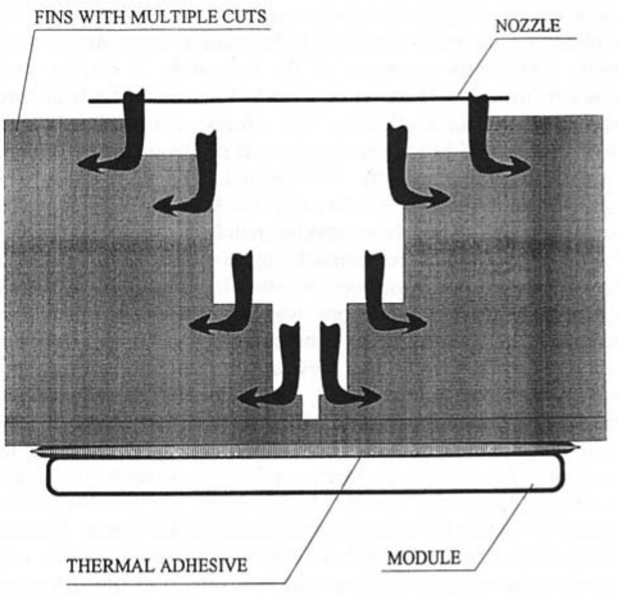

Fig. 4 Schematic diagram of the impingement heat sink (Sathe et al., 1995)

Heat Sink Optimization

The problem of heat sink optimization entails maximizing the thermal performance while meeting other constraints such as flow rate, pressure drop, heat sink envelope and heat sink weight. An increase in surface area can be achieved by packing more fins for a given fin height. Increasing the number of fins by reducing channel gap increases the pressure drop, while by reducing fin thickness, fin efficiency suffers. Hence, as may be expected, optimal number of fins exists. The most important system parameters are the flow rate and the pressure drop. Most studies optimize for a constant flow rate and only a few address the pressure drop constraint that exist in actual systems. Thus studies that do not consider the pressure drop in the optimization do not address the needs of the electronics industry.

Constans et al. (1994) developed a design tool to study pin-fin sink optimization. A conduction model was developed for the heat transfer within the pins and boundary conditions were applied using empirical relations for the heat transfer coefficient. The ellipsoid algorithm was used to predict the minimized temperature, with the outputs as fin height, width, and spacing. The pressure drop was not considered in the optimization and was not estimated for the optimized heat sink.

Tahat et al. (1994) performed an experimental optimization of a ducted flow-through heat sink. The circular pin material was aluminum, with a fixed diameter and pin height of 6.35 mm and 60 mm, respectively, in both in-line and staggered configurations on a 300 mm × 170 mm base. The number of pins was varied. It was found that the optimal pin spacing in the transverse direction was between 1 mm and 3 mm and the longitudinal spacing was about 7.8 mm for both staggered and in-line arrays to obtain the maximum heat transfer rate. Pressure drop data were reported but was not considered in the optimization.

A study more relevant to electronic cooling situations was performed by Azar and Mandrone (1994). Circular pin heat sinks with base dimension 3.175 × 3.175 cm and 1.27 cm pin height were considered in the experimental study. Since the air was allowed to bypass the heat sink it was found that increasing the pin density at first increased the heat transfer but a further increase in pin density reduced the heat transfer due to greater air bypass, thus reaching an optimal density. Results were reported mostly for a pin diameter of 0.09 in. (2.29 mm) for different upstream air speeds. Pressure drops were not reported, however, it is expected that when sufficient bypass space exists, more or less similar air-speeds upstream of the heat sink will produce similar pressure drops if the velocity measurements are made sufficiently upstream of the heat sink. A similar study was performed by Wirtz et al. (1994) for straight fin heat sinks instead of pin-fin heat sinks. The effects of fin density on the flow bypass and hence on the thermal performance of the heat sink were experimentally investigated. The heat sinks were made of aluminum with a fixed fin thickness of 2.33 mm. The fin height was varied from approximately 8 mm to 32 mm and the number of fins were changed from 6 to 9 to 12 fins to obtain flow bypasses. A rigorous optimization for straight fin heat sinks under fully ducted conditions was analytically performed by Knight et al. (1991). The constraints on the optimization of heat transfer rates were the pressure drop, pumping work, heat sink width, length, and height. The output of the scheme was the fin and channel gaps for which the thermal resistance was computed and a minimum value was obtained by changing the number of fins and the fin-to-channel thickness ratio. The results were experimentally verified by changing the number of fins from 6 to 12 fins for a fixed-fin thickness of 3.175 mm. Shaukatullah et al. (1996) reported an experimental optimization study of pin-fin arrays in cross flow with low velocities. Pin-fin arrays from 4 × 4 to 8 × 8, heights from 5 to 25 mm and pin width from 1.5 to 2.5 mm were studied. Results showed that a different optimal heat sink design existed for every flow velocity. All results are for a 25 mm base.

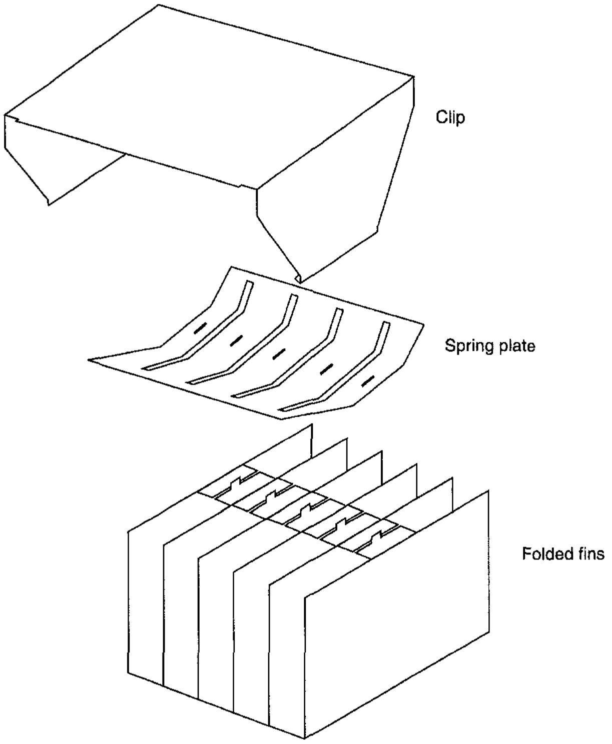

Fig. 5 Exploded view of the spring-loaded, folded-fin heat sink (Mok, 1994)

Ledezma et al. (1996) reported an optimization study for a pin-fin impingement heat sink similar to that described by Sathe et al. (1993). It is shown that the heat sink resistance can be minimized by selecting the appropriate pin-fin spacing (s) for an array of square pin-fins on a square bases, $s/L = 0.81\ \mathrm{Pr}^{-0.25}\ \mathrm{Re}^{-0.32}$, where L is the base dimension. Pressure drop was not reported and is not relevant if the drop through the heat sink is much smaller than that in the rest of the computer system, which includes filters, grilles, louvers, bends and turns, nozzles, etc.

New Heat Sink Materials or Structures

Most commonly used heat sink materials are aluminum and copper, with aluminum being the most used. In certain high-performance applications, it is desirable to increase the surface area by reducing fin thickness. For low fin thicknesses, of a fraction of a mm, copper fins may have advantage over aluminum due to higher fin efficiencies. However, copper is approximately three times as dense as aluminum, making heat sink support and attachment a challenge. In thicker fins, there is not much impactable difference in fin efficiencies. This section describes the use of heat sink materials other than aluminum or copper and also heat sinks other than straight finned or pin-fins with square or circular cross sections.

Vogel (1994) described a 7.62 × 7.62 × 3.81 cm heat sink capable of dissipating 100 W in a 150 fpm (0.765 m/s) air velocity with a 0.04 in. (10 $\mathrm{N/m^2}$) water pressure drop with fins made of copper attached to a graphite base .317 cm with a thermal conductivity of 800 W/mK to spread the heat out, with a resulting external thermal resistance of 0.53°C/W. The heat source was 1.27 × 1.27 cm at the center of the heat sink. The use of the conventional copper base instead of graphite yielded a resistance of 0.48°C/W, but the weight of the composite heat sink was 50 percent smaller than the copper heat sink.

Mok (1994) experimentally measured the thermal performance of a unique folded U-shaped fins made of sheet metal as shown in Fig. 5. For a 59 mm × 59 mm base size, data was

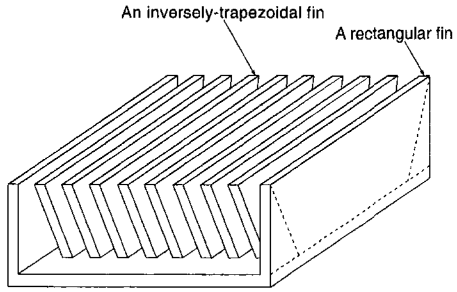

Fig. 6 IT heat sink external appearance. The IT heat sink consists of inversely trapezoidal fins, except for ends. Both end fins are rectangular (Kitajo et al., 1992).

reported for 15 mm and 25 mm fin heights. The heat sink was situated in a channel 123 mm wide so that bypass was allowed. The interface resistance between the fins and the base plate was about 0.05°C/W to 0.13°C/W using a ZnO filled grease. With a fin thickness of 0.6 mm and gap of 3.6 mm, the thermal resistance and pressure drop were about 0.75°C/W and 1.25 Pa for a velocity of 2 m/s for a 25 mm tall fin. The fins were aluminum 1100-H12 sheets.

A novel inversely trapezoidal fin (shown in Fig. 6) performance was reported by Kitajo et al. (1992). A 60 × 60 × 17 mm heat sink was tested. The straight-fin heat sink with fin thickness of 0.8 mm yielded 0.8°C/W at 3 m/s with 26 fins. The trapezoidal fin shape gave a 20 percent better thermal performance, attributed to the retaining of the flow inside the heat sink area instead of lifting off of the flow towards the top. They also changed the number of fins to study the bypass effect. It was found that at 1 m/s, the optimal number of fins for the minimum resistance is about 17, while at 3 and 5 m/s the optimal numbers are 22 and 26, respectively.

Chapman et al. (1994) experimentally compared the performance of novel elliptical cross-section pin-fins with regular extruded heat sinks. It was found that for a 58 mm × 58 mm 25.4 mm heat sink, the straight-fin heat sink performed the best under both open and ducted configurations. The pin-fins heat sink and the straight fin had approximately the same surface area.

Morega and Bejan (1994) showed that a 15 percent enhancement could be obtained by increasing the thickness of the fin in the flow direction. Though not reported, this feature is expected to increase the pressure drop, due to the narrowing of the channels. From the practical viewpoint their other investigation in the same paper appears more attractive, wherein they report a 30 percent enhancement by using a fin height that increases along the flow direction. The penalty to be paid is the package space due to the increased heat sink height near the exit. Brown et al. (1993), tested magnesium (M1A) and aluminum (6063-T5) heat sinks to compare the performance. The heat sinks were pin fins with a height of 2.54 cm (1 in.) and a pin diameter of 0.127 cm. Air speeds from 0 to 7 m/s were investigated. The performance difference between the two alloys was reported not to be significant, yet the advantage of using magnesium alloy is the weight reduction. It is anticipated, however, that for high-performance application which need large surface areas, the fin thicknesses are smaller than 1 mm, and the difference in the alloys will be quite significant due to larger differences in fin efficiencies.

Natural Convection From Heat Sinks

Due to the proliferation of hand-held, portable, and laptop computers, passive cooling is gaining more importance. The module level heat fluxes in the laptop computers are expected to be of the order of 0.5 W/cm^2 by 2000. The challenge is to use a heat sink that is not too large (z height of the heat sink will have to be less than 0.5 in. to be accomodated in a laptop). Fans are not permitted since they drain the battery power very quickly, and hence a novel heat sink operating under natural convection would be required.

A review of the vendor literature on heat sinks reveals that most of the heat sinks designed for natural convection are either stamped or extruded. The stamped heat sink products are typically light weight and for low-power applications and are cheaper than the extruded heat sinks. The authors are not aware of any quantitative studies related to the stamped heat sinks that can be manufactured in a large variety of shapes; which makes methodical analysis somewhat difficult. However, such studies need to be undertaken. Typically the data presented for the extruded heat sinks is for the vertical position, (the heat sink base is vertical). The heat transfer under such conditions can be approximately predicted using correlations for natural convective heat transfer between vertical flat plates. Also an optimal spacing exists, since very close spacing can choke the flow, but large spacing may yield lower surface areas. For horizontal orientations, pin-fin heat sinks are more suitable since the flow can access the heat sink from all four sides and rise at the center versus access from only two sides. Limited literature exists on natural convection in pin-fins. Aihara et al. (1990) presented the results of an experimental study of the free convective heat transfer from 59 types of pin-fin dissipators, all with a vertical base plate. A wide range of pin density was investigated, ranging from 1.08 to 10.58 pins/cm^2. The surface emissivity of the surfaces was 0.9 for air. The average heat transfer coefficient for a single pin array was found to correlate well with the Nusselt number and the Grashoff number based upon the effective length of the pin fin array. The relation of the Nusselt number to the Grashoff number was shown to be similar to that for a vertical flat plate. A recent study by Fisher and Torrance (1998) explored free convection in a vertical pin-fin heat sink in a chimney system. For electronic packaging applications, the optimal heat sink porosities were generally greater than 90 percent. The chimney effect increased local heat transfer. Interestingly, when optimized, both pin-fin and straight plate-fin heat sinks were shown to produce roughly equivalent thermal performance.

Elenbass (1942) reported an expression for the optimal spacing for natural convection between parallel plates as $S = (50H \text{ Gr Pr})**0.25$ where H is the plate height, Gr is the Grashof number based on the plate spacing, and Pr is the Prandtl number. Morrison (1992) extended the above optimization of Elenbass to account for the U-shaped fin channel which is only roughly approximated by infinite parallel vertical walls, so that both the fin height and length are accounted for, and thus is realistic. The effect of fin spacing and fin thickness on the thermal performance was presented. Radiation heat transfer can play a significant role in enhancing the heat transfer from heat sinks operating in natural convection. However, besides using surface treatments to increase the emissivity, not much has been studied about shape factors to enhance radiation.

Mertol (1993) evaluated different heat sink options for a 20 W application specific integrated circuit (ASIC) module for both natural and forced convection. A conduction model of the fins was used and empirical convection coefficients were applied as boundary conditions. A heat sink with 38 mm fin height, 43 mm length, 52 mm width with 9 fins separated by 4.5 mm could cool the ASIC package to 125°C with a 50°C ambient temperature.

Fisher et al. (1997) presented an analysis for the optimization of a natural draft heat sink system consisting of a vertical, parallel plate isothermal heat sink with a chimney. The size of the overall system is constrained. A ridge of maximum total heat transfer is observed with respect to the plate spacing and heat sink height.

Card Effects

Conduction in the printed circuit board and convection from it to the surrounding air are highly dependent upon the layout of the board, and upon the geometry and location of the power dissipating components on the board. The relative importance of card effects varies considerably depending upon the thermal management scheme used and the specific application conditions. For low-power dissipation applications where natural or mixed convection is used, card effects could be significant, and the effective thermal conductivity of the board could be very significant in determining the system thermal performance. In applications where the board is closely packed with heated components and where forced convection is used, board effects play a minor role compared to conditions inside the power dissipating modules themselves, which determine the module internal thermal resistance. Due to the complexity of solving the conjugate problem, and due to the relative insignificance of card effects in mid to high-end systems, there have been few studies of card effects. With the proliferation of uniprocessor machines, card effects are beginning to assume more significance.

Malhammer (1991) studied the heat dissipation limits for five different plastic and ceramic packages mounted to boards and cooled by natural, mixed, and forced convection. Several different card lay-ups were investigated with varying copper content and thermal conductivity. The performance of the different packages was numerically studied, and a methodology established for calculating the "territory surface," which is the area on the card around the heated module, that is effective in dissipating heat from that specific module. For natural convection the card is generally found to be an effective heat spreader. In forced convection, however, the card effects are shown to be small compared to the module configuration and internal thermal resistance. This analysis methodology can serve as an early approximate thermal design tool, for low-end applications designed to be cooled with natural convection.

An extensive experimental study of surface-mount components on printed circuit boards (PCBs) with different copper content was conducted by Shaukatullah and Gaynes (1994). One of the objectives of the study was to evaluate and compare the effect of the effective PCB thermal conductivity for different types of packages. The packages were all 28 mm 208-leaded plastic packages with copper and alloy 42 leadframes, plastic with exposed heat spreader, and metal quad flat packs. Two different types of PCBs were studied, one with a single signal distribution layer on the module side, and another with 2 additional internal copper planes. The primary findings are that for components with high-thermal resistance, such as those with alloy 42, the thermal conductivity of the card plays a minor role. On the other hand for metal packages with relatively low-thermal resistance a strong dependance on card thermal conductivity was shown to exist. The sensitivity to card thermal conductivity was also found to decrease in forced convection, since more of the power is dissipated directly from the module, particularly at higher velocities, similar to earlier findings (Malhammer, 1991).

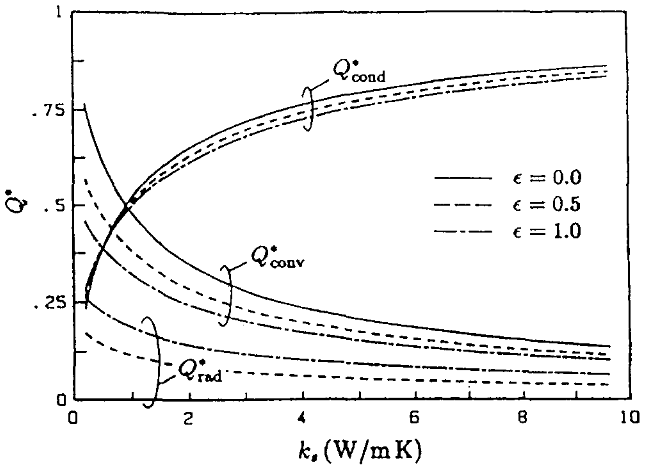

Fig. 7 Dimensionless heat dissipation from the downstream heat source by means of conduction, convection, and radiation (Lee, 1991).

The conjugate heat transfer problem including conduction in the board as well as convection and radiation to the surroundings was studied by Lee et al. (1991). An analytical/numerical model was used to calculate the temperature distributions in a test circuit board with flush-mounted heat sources. The numerical algorithm used combines an analytical boundary layer solution with a finite-volume solid-body solution. The boundary layer solution is based upon a linearized form of the boundary layer equations for laminar flow over a flat plate with a flux specified boundary condition. The effect of thermal conductivity and surface emissivity of the board were investigated for various air flow rates and different power dissipation levels for the heated components. The main objective of the study was to parametrically study the relative importance of conduction in the board, radiation, and convection. For the range of parameters studied it was determined that a change in the thermal conductivity of the board leads to the largest change in the Nusselt number. Board conductivity values in the range of 2 to 54 W/mK were examined. As the thermal conductivity was increased beyond 20 W/mK the rate of increase in Nu was found to decrease slowly as the thermal resistance in the boundary layer begins to increase. A change in board thermal emissivity between 0 and 1 was found to provide an increase in Nu of approximately 50 percent, which is twice the the change in Nu provided by increasing the air flow velocity from 0.5 m/s to 1 m/s. Figure 7 shows a comparison of the relative effects of conduction, convection, and radiation for a range of power dissipation Q^*, an air flow velocity of 0.5 m/s and three different surface emissivity levels, 0, 0.5, and 1.

Graham and Witzman (1987) proposed an analytical correlation to be used as a design tool, accounting for package size and PCB participation in the heat transfer process. In this study the external thermal resistance was determined experimentally and the conduction equation was solved to evaluate the heat flow in the component and the board. The experiments covered a broad range of component package styles including leadless ceramic chip carriers, plastic-leaded chip carriers, c-Quads (c-shaped leads), pin grid arrays, ceramic dual in-line and plastic dual in-line. Air velocities between 1 and 5 m/s were evaluated. For sparsely populated circuit boards where the distance between modules exceeded the package dimensions, it was shown that the total package thermal resistance varies with the square root of the circuit board conductivity. This simple analysis can be used as a preliminary design guide for deciding upon an adequate thermal management scheme.

The temperature rise of printed circuit boards in natural convection was studied by Birnbreier (1981). In this experimental study the temperature of a printed circuit board was measured at various locations for a power dissipation range of 0.5 to 5 W per board. The boards had discrete resistors as a source of power, and teflon blocks to simulate larger modules on the board. The spacing between adjacent boards was varied from 13.6 mm to 59.4 mm. Measurements were taken after steady-state conditions had been reached. Figure 8 shows a comparison of the experimentally measured heat transfer from the printed circuit board to the results for smooth channels reported by Aung et al. (1972). Where

$\mathrm{Nu}_{\mathrm{PCB}} = qb/\lambda(T_{\mathrm{PCB}} - T_0)$
$\mathrm{Ra} = \mathrm{Pr}\, g\beta q b^5/(\upsilon^2 l \lambda)$
q = Total heat flux in board/$2dh_b$, W/m^2
b = channel spacing

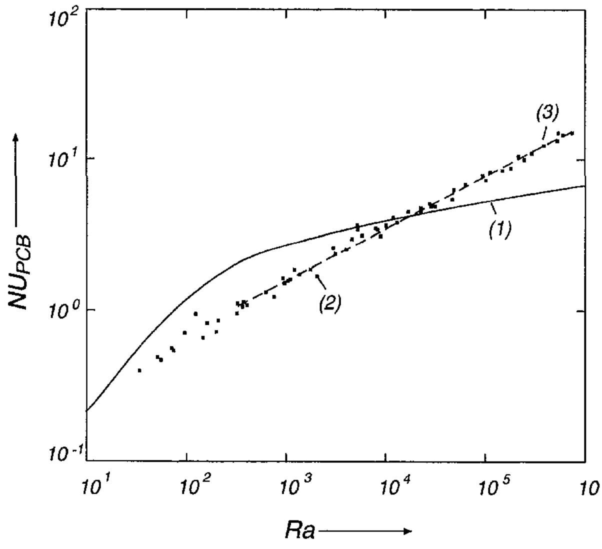

Fig. 8 Plot of Nusselt number for maximum P. C. board temperature versus Rayleigh number

d = depth of the printed circuit board, m
h_b = height of the printed circuit board, m
$l = n(h_b + s)$.

The data shown in Fig. 8 were found to follow:

$$\mathrm{Nu} = 0.2\ \mathrm{Ra}^{0.31}. \qquad (1)$$

The differences between Eq. (1) above and the data by Aung et al. (1972) was attributed to radiation effects at high Ra numbers, and due to the flow obstacles at low Ra numbers.

Other studies of the board conductivity effects have been conducted. Gale (1982) performed a numerical study of the thermal resistance of PCBs with various inner structures and concluded that the placement of a ground plane as near to the heat dissipating source as possible will significantly reduce the thermal resistance of the board. This is due to the spreading effect of the ground plane before heat is transferred through the low thermal conductivity resin layers of the board. For boards that are densely packed with heat dissipating components this spreading effect would not be as effective. Hamilton (1976) completed a numerical study of the effect of PCB thermal conductivity on the thermal performance of dual inline packages (DIP) devices. It was shown that increasing the DIP area, the card area, the board thermal conductivity, and/or the convective heat transfer coefficient results in improved thermal performance for the DIP. Azar et al. (1994) performed a numerical study of the effect of board thermal conductivity on the thermal performance of electronic packages in natural convection. The board had a three by three array of components and was mounted vertically in a channel. Increasing the thermal conductivity of the board by threefold resulted in a 17 percent reduction in internal thermal resistance. Optimum conditions were found around a 900 mil spacing between modules and at a board thermal conductivity of 13.6 W/mK.

Takubo et al. (1993) report the results of a numerical and experimental study of the thermal resistance of a Tape Carrier Package, TCP. The effect of using thermal vias to conduct heat through the board to a copper heat spreader on the opposite side is shown to result in a significant improvement in the thermal performance of the package.

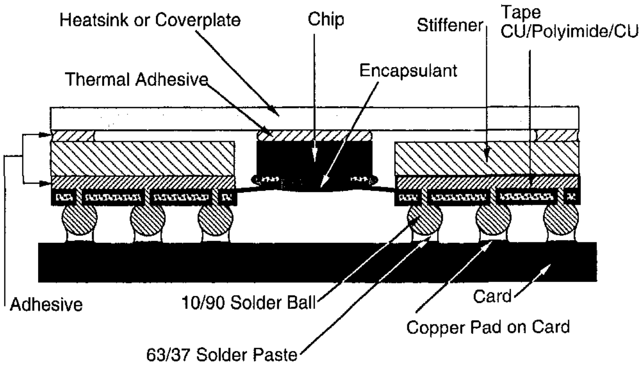

Fig. 9 Schematic cross section of a TBGA module

In a recent study Sathe and Sammakia (1996) presented the results of a detailed experimental and numerical study of the thermal performance of a Tape Ball Grid Array (TBGA) organic chip carrier. The package was a flip chip area array BGA package, with a heat sink attached to the chip as shown in Fig. 9. The experimental data consisted of temperature measurements at various locations in the module and on the card. The numerical model was a conjugate three-dimensional model, accounting for conduction in the package and card, and convection to the surrounding air. Radiation effects were also included in the model. Both natural and forced convection regimes were investigated, and a detailed study of the effects of the card thickness, area, and configuration (number of copper power planes in the card) was conducted.

It was shown that the effect of the number of power distribution planes upon the chip junction temperature is very significant. Three cases were studied, 0, 1, and 2 power planes. The power planes consist of a solid layer of copper 0.36 μm thick. The results for a chip dissipating 4 W are shown in Fig. 10. The incoming air flow velocity ranged from 0 to 3.8 m/s. At all air flow rates, the effect of power planes in the card is seen to be significant. The temperature difference between one and two power planes is seen to be almost 10°C, and the difference between two and zero power planes is about 35°C. Also shown in the figure are results of a turbulent model for the two power plane configuration, and the experimental measurements of the chip junction temperatures. The experimental measurements are seen to be in reasonably good agreement with the laminar model at low air flow rates and the turbulent model at the higher velocities.

Figure 11 shows the chip junction temperature as a function of the chip power dissipation for the same three configurations of 0, 1, and 2 power planes. All of the results here are for a natural convection flow. Here also the effect of power planes in the card are shown to be very significant. At 10 W the chip

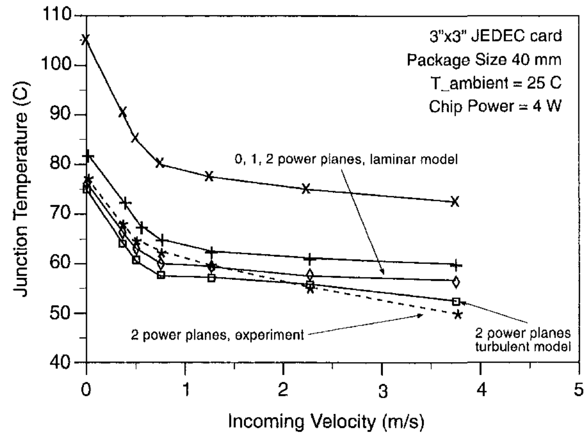

Fig. 10 Chip junction temperatures as a function of incoming air velocities. Numerical results are shown for a card with 0, 1, and 2 power planes. Also shown are experimental measurements for a card with two power planes (Sathe and Sammakia, 1996).

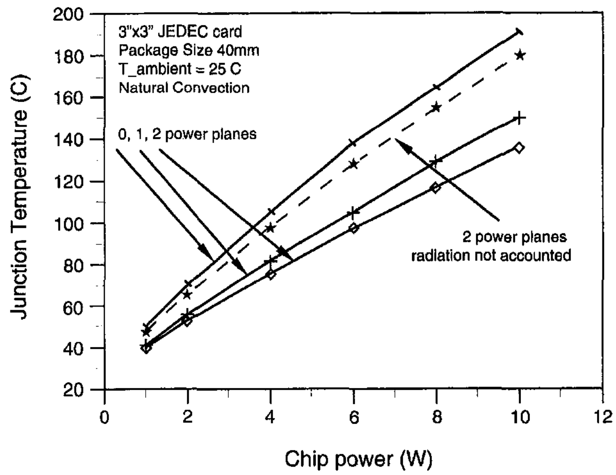

Fig. 11 Chip junction temperatures as a function of chip power levels in natural convection. Numerical results are shown for a card with 0, 1 and 2 power planes. Effect of radiation is shown for a card with two power planes (Sathe and Sammakia, 1996).

junction temperature for a card with 2 power planes could be as much as 55°C lower than a card with no power planes. Even at 1 W the difference could be as high as 10°C. This significant difference in temperature effects not only package performance but also reliability. The temperature difference is not only at the chip junction, but across the entire module. Figure (12) shows the temperature profile from the top of the module to the bottom of the card. The circumstance of a card with no power planes is seen to have the most severe temperature gradient. This gradient would be applied across the module and card for hundreds or perhaps thousands of times during the life of the package. This effects the reliability of the solder interconnections as well as all of the interfaces in the package.

Conclusions and Future Directions

There are several key areas related to thermal enhancement of air-cooled electronic packages that need to be addressed. One such area is heat sinks in an array. More research is required to characterize such systems and have a database readily available for electronic designers to be able to select heat sinks and predict the chip junction performance of heat sinks in an array.

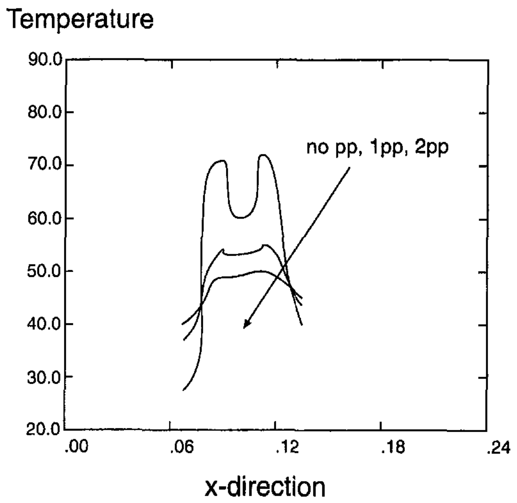

Fig. 12 Temperature distributions at the center line of the card and the module. Results are shown for 3″ × 3″ cards with 0, 1, and 2 power planes. All results are shown for an incoming air-flow velocity of 0.81 m/s and chip power = 4W (Sathe and Sammakia, 1996).

Future work is also needed in optimization of fin spacings and gaps between heat sinks to maximize heat transfer from an array of heat sinks. Another key area is heat sink optimization. Most studies optimize for a constant flow rate and only a few address pressure drop as a constraint. Thus most studies do not address the needs of the electronics industry as far as optimization of heat sinks is concerned since pressure drop determines blower size and power, and this also effects acoustics for the whole system. The stamped heat sink products are typically light weight and used for low-power applications and are cheaper than the extruded heat sinks. The authors are not aware of any quantitative studies related to the stamped heat sinks that can be manufactured in a large variety of shapes, this makes analysis and design very difficult. This is also true of studies exploring the pin fin heat sinks in natural convection. In natural convection applications radiation can be a significant factor in determining the operating temperature. However, besides using surface treatments to increase the emissivity, not much has been studied about shape factors to enhance radiation. In summary considerable work needs to be done in the area of heat sink research. The trend towards miniaturization continues, and even though technology shifts from bipolar to CMOS have dropped the power dissipation, the trend within the CMOS technology is that of increasing power density. Another trend to be taken note of is the proliferation of high-speed office environment computers needing air-cooling.

Another area where additional research needs to be done is in determining card effects upon the overall thermal performance of the system. Card effects are often neglected or misrepresented in the analyses performed during system design. A typical occurrence is that testing is performed to determine the thermal performance of a system, using a test card which is intended to represent the final product. There are, however, frequent design changes made to the functional cards, often very late in the design cycle, that may in turn result in significant deviations from the test results. Algorithms for the representation of complex card structures need to be developed. Cards are often complex multilayer structures with alternating power and signal planes. A detailed representation of every layer is not practical and often not necessary, provided appropriate simplifications can be developed and used.

References

Aihara, T., Maruyama, S., and Kobayakawa, S., 1990, "Free convective/radiative heat transfer from pin-fin arrays with a vertical base plate (general representation of heat transfer performance)," *Int. J. Heat Mass Transfer,* Vol. 33, No. 6, pp. 1223–1232.

Aung, W., Fletcher, L. S., and Sernas, V., 1972, "Developing Laminar Free Convection Between Vertical Flat Plates with Asymmetric Heating," *Int J Heat Mass Transfer,* Vol. 15.

Azar, K., and Mandrone, C. D., 1994, "Effect of Pin-Fin Density of the Thermal Performance of Unshrouded Pin-Fin Heat Sinks," ASME *Journal of Electronic Packaging,* Vol. 116, pp. 306–309.

Azar, K., McLeod, R. S., and Caron, R. E., 1992, "Narrow Channel Heat Sink for High Powered Electronic Components," *Proc. Eighth IEEE SEMITHERM Conf.,* Piscataway, NJ, pp. 12–19.

Azar, K., Pan, S. S., Parry, J., and Rosten, H., 1994, "Effect of Circuit Board Parameters on Thermal Performance of Electronic Components in Natural Convection Cooling," *Tenth IEEE Semi-Therm,* San Jose, CA, Feb. 1–3, p. 32.

Bartilson, B. W., 1991, "Air jet impingement on a miniature pin-fin heat sink," ASME WAM, Atlanta, GA, Dec., paper no. 91-WA-EEP-41.

Birnbreier, H., 1981, "Experimental Investigations on the Temperature Rise of Printed Circuit Boards in Open Cabinets with Natural Ventilation," ASME HTD-Vol. 20, pp. 19–23.

Biskeborn, R. G., Horvath, J. L., and Hultmark, E. B., 1984, "Integral cap heat sink assembly for the IBM 4381 processor," 1984, *Proc. of the Fourth Annual Intl. Electronic Packaging Society Conf.,* Baltimore, MD, pp. 468–474.

Brown, J. F., Lisabeth, R., and Shirazi, S. A., 1993, "Magnesium Heat Sink Evaluations," SAE Special Publication, No. 962, pp. 27–36.

Chapman, C. L., Lee, S., and Schmidt, W. L., 1994, "Thermal Performance of an Elliptical Pin-Fin Heat Sink," *Proc. Tenth IEEE SEMI-Therm Symposium,* pp. 24–31.

Constans, E. W., Belegundu, A. D., and Kulkarni, A. K., 1994, "Optimization of a Pin-Fin Heat Sink: A Design Tool," *CAE/CAD Application to Electronic Packaging,* ASME EEP-Vol. 9, pp. 25–32.

Dunn, R. M., Schulman, M., and Timko, N., 1981, "Electronic circuit module cooling," United States Patent No. 4,277186, Aug. 13.

Elenbaas, W., 1942, "Heat Dissipation of Parallel Plates by Free Convection," *Physica*, Vol. 9, No. 1.

Fisher, T. S., Torrance, K. E., and Sikka, K. K., 1997, "Analysis and Optimization of a Natural Draft Heat Sink System," *IEEE Transactions on Components, Packaging and Manufacturing Technology*, Part A, Vol. 20, pp. 111–119.

Fisher, T. S., and Torrance, K. E., 1998, "Free Convection Limits for Pin-Fin Cooling," ASME JOURNAL OF HEAT TRANSFER, Vol. 120, pp. 633–640.

Fitch, J. S., 1990, "A one dimensional thermal model for the VAX 9000 multichip units," *Thermal modeling and design of electronic systems and devices*, Wirtz, R. A. and G. L. Lehmann, eds., ASME WAM, Dallas, TX, HTD-Vol 153, pp. 59–64.

Gale, H. E., 1982, "Printed wiring Board Z axis Thermal Resistance Reduction," *Second Annual International Packaging Conference, IEPS Proceedings*, Nov. 15–17, pp. 296–306.

Goldberg, N., 1984, "Narrow channel forced air heat sink," *IEEE transactions on components, hybrids, and manufacturing technology*, Vol. CHMT-7, No. 1, Mar.

Graham, K., and Witzman, S., 1987, "Analytical Correlation of Thermal Design of Electronic Packages," *Proc. of the International Symposium on Cooling Electronic Equipment*, Honolulu, HI, pp. 249–264.

Hamilton, J. L., 1976, "On the Effect of the Circuit Boards' Thermal Conductivity in The Thermal Performance of a Circuit Package Employing a DIP Device," ASME 76-WA/HT-30.

Heng, S., and Pei, J., 1991, "Air impingement cooled pin-fin heat sink formultichip unit," *Proc. National electronic packaging and production conference*, Vol. 2, Des Plaines, IL.

Hilbert, C., Sommerfeldt, S., Gupta, O., and Herrell, D. J., 1990, "High Performance Air Cooled Heat Sinks for Integrated Circuits," *IEEE Transaction on Components, Hybrids and Manufacturing Technology*, Vol. 13, No. 4, Dec.

Holman, J. P., 1981, *Heat Transfer*, 5th Ed., McGraw-Hill, New York.

Kadle, D. S., and Sparrow, E. M., 1986, "Numerical and experimental study of turbulent heat transfer and fluid flow in longitudinal fin arrays," ASME JOURNAL OF HEAT TRANSFER, Vol. 108, p. 16.

Kiley, R. F., and Soule, C. A., 1990, "Engineered heat sinks," *Powertechnics Magazine*, July.

Kitajo, S., Takeda, Y., Kurokawa, Y., and Ohta, T., 1992, "Development of a High Performance Air-Cooled Heat Sink for Multi-Chip Modules," *Eighth IEEE Semi-Therm Symposium*, Austin, TX. pp. 119–124.

Knight, R. W., Goodling, J. S., and Gross, B. E., 1992, "Optimal Thermal Design of Air-Cooled Forced Convection Heat Sinks—Experimental Verification," *IEEE Intersociety Conference on Thermal Phenomena*, Piscataway, NJ, pp. 206–212.

Knight, R. W., Goodling, J. S., and Hall, D. J., 1991, "Optimal Thermal Design of Forced Convection Heat Sinks—Analytical," ASME *Journal of Electronic Packaging*, Vol. 113, pp. 313–321.

Kraus, A. D., and Bar-Cohen, A., 1995, *Design and analysis of heat sinks*, John Wiley and Sons, New York.

Ledezma, G., Morega, A. M., and Bejan, A., 1996, "Optimal Spacing Between Pin Fins With Impinging Flow," ASME JOURNAL OF HEAT TRANSFER, Vol. 118, pp. 570–577.

Lee, S., Culham, J. R., and Yovanovich, M. M., 1991, "Parametric Investigation of Conjugate Heat Transfer from Microelectronic Circuit Boards Under Mixed Convection Cooling," *IEPS Conf. Proceedings*, Vol. 1, San Diego, CA, Sept., pp. 428–446.

Lee, S., Lemczyk, T. F., and Yovanovich, M. M., 1992, "Analysis of Thermal Vias in High Density Interconnect Technology," *Eighth annual IEEE Semiconductor thermal measurement and management symposium*, Feb. 3–5, Austin, TX.

Mahalingam, M., and Andrews, J., 1988, "High performance air cooling for microelectronics," *Cooling Technology for Electronic Equipment*, W. Aung, ed., Hemisphere, Washington, DC.

Mahaney, H. V., and Vader, D. T., 1993, "Predicted and measured performance of an advanced laminated heat sink formulti-chip modules," *Enhanced Cooling Techniques for Electronics Applications*, ASME, New York, pp. 49–57.

Malhammer, A., 1991, "Heat Dissipation Limits for Components Cooled by the PCB surface," *IEPS Conf. Proceedings*, Vol. 1, San Diego, CA, Sept., pp. 304–311.

Mansuria, M. S., and Kamath, V., 1994, "Design Optimization of a High Performance Heat Sink/Fan Assembly," ASME *Heat Transfer Development; Heat Transfer in Electronic Systems*, Vol. 292, pp. 95–104.

Matsushima, H., and Yanagida, T., 1992, "Heat Transfer from Finned LSI Packages in a Channel between Circuit Boards," *Heat Transfer Japanese Research*, Vol. 21, No. 2, pp. 165–176.

McPhee, J. M., O'Toole, T. S., and Yedvabny, M., 1990, "Cooling the VAX 9000," *Electro/90*, Conference Record, Boston, MA, pp. 288–292.

Mertol, A., 1993, "Optimization of Extruded Type External Heat Sink for Multichip Module," ASME *Journal of Electronic Packaging*, Vol. 115, pp. 440–444.

Metzger, D. E., Fan, C. S., and Pennington, J. W., 1983, "Heat transfer and flow friction characteristics of very rough transverse ribbed surfaces with and without pin fins," *Proceedings of the ASME-JSME Thermal engineering joint conference*, Vol. 1, pp. 429–436.

Minakami, K., Mochizuki, S., Murata, A., and Yagi, Y., 1992, High Performance Air-Cooling for LSIs Utilizing a Pin Fin Heat Sink, Paper No. 92-WA/EEP-5, ASME Winter Annual Meeting, Anaheim, CA.

Mok, L., 1994, "Thermal Management of Silicon-based Multichip Modules," *Proc. Tenth IEEE Semitherm Symposium*, Piscataway, NJ, pp. 59–63.

Morega, M., and Bejan, A., 1994, "Plate-fins with Variable Thickness and Height for Air-Cooled Electronic Modules," *Int. J. Heat and Mass Transfer*, Vol. 37, Suppl. 1, pp. 433–445.

Morrison, A. T., 1992, "Optimization of Heat Sink Fin Geometries for Heat Sinks in Natural Convection," *Proc. Intersociety Conference on Thermal Phenomena*, pp. 145–148.

Oktay, S., Dessauer, B., and Horvath, J. L., 1983, "New internal and external cooling enhancements for the IBM 4381 module," *ICCD 83, Proc. of the IEEE Intl. conference on computer design: VLSI in Computers*, Port Chester, NJ.

Sathe, S. B., and Tai, C., 1994, "Pin Fin Heat Sink Impingement Cooling Enhancement Using Flow Baffles," *IBM Technical Disclosure Bulletin*, Vol. 37, No. 2A, Feb., pp. 275–276.

Sathe, S. B., Kelkar, K. M., Karki, K. C., Tai, C., Lamb, C. R., and Patankar, S. V., 1997, "Numerical Prediction of Flow and Heat Transfer in an Impingement Heat Sink," ASME *Journal of Electronic Packaging*, Vol. 119, pp. 58–63.

Sathe, S. B., Sammakia, B. G., Wong, A. C., and Mahaney, H. V., 1995, A Numerical Study of a High Performance Air-Cooled Impingement Heat Sink," *Proc. National Heat Transfer Conference*, Portland, OR, ASME HTD-Vol. 303, pp. 43–53.

Sathe, S. B., and Sammakia, B. G., 1996, "A numerical study of the thermal performance of a tape ball grid array (TBGA) package," ASME HTD-Vol. 329, pp. 83–93, also accepted for publication in the ASME *Journal of Electronic Packaging*.

Shaukatullah, H., and Gaynes, M. A., 1994, "Experimental Determination of the Effect of Printed Circuit Card on the Thermal Performance of Surface Mount Electronic Packages," *Tenth annual IEEE Semiconductor thermal measurement and management symposium*, Feb. 1–3, San Jose, CA.

Shaukatullah, H., Storr, W. R., Hanse, B. J., and Gaynes, M. A., 1996, "Design and Optimization of Pin Fin Heat Sinks for Low Velocity Applications," *12th IEEE SEMI-THERM Symposium Proceedings*, pp. 151–163.

Soule, C. A., 1993, "Air and liquid cooled techniques for high power density components," *Power conversions and intelligent motion*, Vol. 19, No. 11.

Sparrow, E. M., and Kadle, D. S., 1986, "Effect of Tip-to-shroud Clearance on Turbulent Heat Transfer From a Shrouded, Longitudinal Fin Array," ASME JOURNAL OF HEAT TRANSFER, Vol. 108, p. 519.

Sparrow, E. M., Niethammer, J. E., and Chaboki, A., 1982, "Heat Transfer and Pressure Drop Characteristics of Arrays of Rectangular Modules Encountered in Electronic Equipment," *Int. J. Heat Mass Transfer*, Vol. 25, No. 7, pp. 961–973.

Sparrow, E. M., and Ramsey, J. W., 1978, "Heat Transfer and Pressure Drop For a Staggered Wall-attached Array of Cylinders With Tip Clearance," *Int. J. Heat and Mass Transfer*, Vol. 21, pp. 1369–1377.

Sparrow, E. M., Ramsey, J. W., and Altemani, C. A. C., 1980, "Experiments on in-line pin fin arrays and performance: Comparisons with staggered arrays," ASME JOURNAL OF HEAT TRANSFER, Vol. 102, pp. 44–50.

Sparrow, E. M., Vemuri, S. B., and Kadle, D. S., 1983, "Enhanced and local heat transfer, pressure drop, and flow visualization for arrays of block like electronic components," *Int. J. Heat and Mass Transfer*, Vol. 26, No. 5, pp. 689–699.

Steuber, G. D., and Metzger, D. E., 1986, "Heat Transfer and Pressure Loss Performance for Families of Partial Length Pin Fin Arrays In High Aspect Ratio Rectangular Ducts," *Proceedings of the Eighth International Heat Transfer Conference*, pp. 2915–2920.

Tahat, M. A., Babus'Haq, R. F., and Probert, S. D., 1994, "Forced Steady State Convections From Pin-Fin Array," *Applied Energy*, Vol. 48, No. 4, pp. 335–351.

Takubo, C., Tazawa, H., Yoshida, A., Hirata, S., Hiruta, Y., and Sudo, T., 1993, "A Remarkable Thermal Resistance Reduction In A Tape Carrier Package on a Printed Circuit Board," *ITAP Proceedings*, pp. 44–51.

Tuckerman, D. B., and Pease, R. F. W., 1981, "High Performance Heat Sinking for VLSI," *IEEE Electron Dev. Letters*, Vol. EDL-2, No. 5, pp. 126–129.

Vogel, M. R., 1994, "Thermal Performance of Air-Cooled Hybrid Heat Sinks for a Low Velocity Environment," *Proc. Tenth IEEE Semitherm Symposium*, pp. 17–22.

Wirtz, R. A., Chen, W., and Zhou, R., 1994, "Effect of Flow Bypass on the Performance of Longitudinal Fin Heat Sinks," ASME *Journal of Electronic Packaging*, Vol. 116, pp. 206–211.

Wirtz, R. A., Sohal, R., and Wang, H., 1997, "Thermal Performance of Pin-Fin Fan-Sink Assemblies," ASME *Journal of Electronic Packaging*, Vol. 119, pp. 26–31.

Fundamental Issues and Recent Advancements in Analysis of Aircraft Brake Natural Convective Cooling

M. P. Dyko
Research and Technology,
Aircraft Braking Systems Corporation,
Akron, OH 44306
Mem. ASME

K. Vafai[1]
Department of Mechanical Engineering,
The Ohio State University,
Columbus, OH 43210
vafai.1@osu.edu
Fellow ASME

A heightened awareness of the importance of natural convective cooling as a driving factor in design and thermal management of aircraft braking systems has emerged in recent years. As a result, increased attention is being devoted to understanding the buoyancy-driven flow and heat transfer occurring within the complex air passageways formed by the wheel and brake components, including the interaction of the internal and external flow fields. Through application of contemporary computational methods in conjunction with thorough experimentation, robust numerical simulations of these three-dimensional processes have been developed and validated. This has provided insight into the fundamental physical mechanisms underlying the flow and yielded the tools necessary for efficient optimization of the cooling process to improve overall thermal performance. In the present work, a brief overview of aircraft brake thermal considerations and formulation of the convection cooling problem are provided. This is followed by a review of studies of natural convection within closed and open-ended annuli and the closely related investigation of inboard and outboard subdomains of the braking system. Relevant studies of natural convection in open rectangular cavities are also discussed. Both experimental and numerical results obtained to date are addressed, with emphasis given to the characteristics of the flow field and the effects of changes in geometric parameters on flow and heat transfer. Findings of a concurrent numerical and experimental investigation of natural convection within the wheel and brake assembly are presented. These results provide, for the first time, a description of the three-dimensional aircraft braking system cooling flow field.

Introduction

The combined worldwide sales of wheels and brakes for transport, commuter, business, and military aircraft now exceeds one billion dollars annually. A large segment of the aircraft in the world commercial fleet fly short-haul routes which require rapid cooling of the brakes after landing in order to prevent operational delays. Forced convection air flow is sometimes utilized to reduce cooling times, but there are significant penalties associated with the axle mounted fans employed for this purpose including increased weight and higher cost. For this reason, cooling by means of buoyancy-induced air flow is relied upon in most cases. It is recognized that augmentation of heat dissipation through enhanced natural convection heat transfer offers the potential to increase aircraft revenue flying time and in some cases eliminate the need for axle fans. Current trends in aircraft brake performance requirements of shorter aircraft turnaround time (Currey, 1988), increased heat sink energy loading, and lighter weight (Greenbank, 1991) have resulted in greater focus on maximizing heat loss from the system. As an important step toward developing production design methods to improve cooling performance, numerical simulations of braking system natural convection flow fields as described in this paper have been developed and employed in cooling optimization studies.

In an aircraft wheel and brake assembly, which is shown schematically in Fig. 1, multiple carbon-carbon composite or metallic rotating and stationary disks are grouped together in a subassembly known as the brake heat sink or brake stack. The frictional force necessary to stop the aircraft is developed at the interfaces between the rotors and stators when they are clamped together by the brake pistons, which in nearly all designs are actuated hydraulically. During the main braking event following touchdown, a major portion of the aircraft kinetic energy is converted to thermal energy at these friction interfaces and absorbed by the rotors and stators. After this brake application and subsequent lower speed applications during taxi-in to the gate, the aircraft comes to a stop and remains stationary for a relatively long period. During this time, a significant amount of the heat sink stored energy is removed directly by natural convection air flow in the annular space between the brake stack and wheel as well in the regions adjacent to the ends of the brake stack/frame subassembly. Brake stack heat is also transferred directly and indirectly by thermal radiation and conduction to surrounding components such as the wheel, piston housing subassembly, and axle, which in turn dissipate heat to the surroundings. Radiation heat loss also occurs directly from the brake stack to the environment. Natural convection currents that develop in the open annular cavity formed by the wheel outboard surfaces are responsible for much of the total heat dissipated by the wheel. The combined processes of energy absorption, redistribution, and dissipation determine the overall system thermal response, which to a significant degree is dependent on natural convection.

During brake application, the average rate of energy absorption is much greater than the combined rate of heat loss from the brake disks due to convection, radiation, and conduction. Therefore the mean temperature of the heat sink at the end of the stop is essentially a function of the thermal capacitance of

---

[1] To whom correspondence should be addressed.

Contributed by the Heat Transfer Division for publication in the JOURNAL OF HEAT TRANSFER. Manuscript received by the Heat Transfer Division, June 25, 1998. Keywords: Augmentation, Computational, Conjugate, Experimental, Heat Transfer, Natural Convection. Associate Technical Editor: Y. Jaluria.

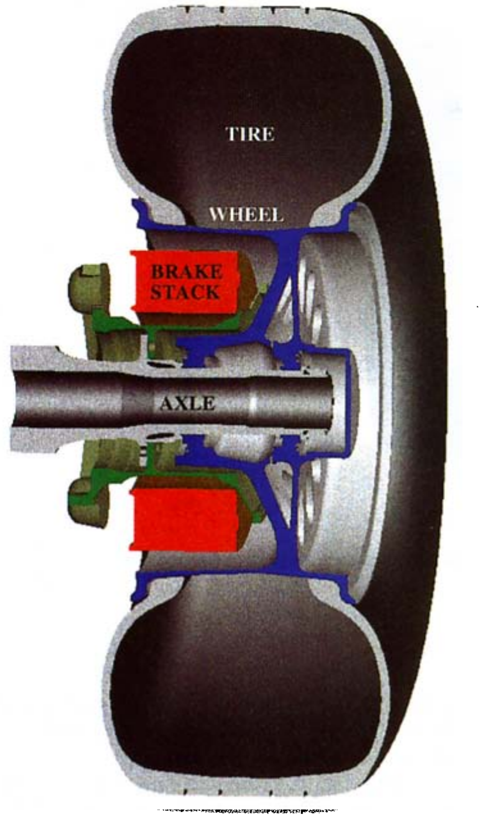

Fig. 1 Schematic of an aircraft wheel and brake assembly, axle, and tire

the heat sink, the total energy absorbed by the brake, and the initial temperature of the brake disks. For steel disk-type aircraft brakes, which have been in widespread use for over 35 years, heat sink mean temperatures up to approximately 1400°F are possible during short-haul commercial operation, while temperatures exceeding the melting point of the friction material can occur locally for the rejected take-off condition. Carbon-carbon composite brake disks were first introduced in the 1960s and are now commonly used, offering much greater energy absorption capability per pound than steel. The thermal environment for carbon brakes is more severe than steel, with heat sink mean temperatures as high as approximately 1800°F occurring under conditions of heavy usage. Peak temperatures at the carbon disk friction interfaces may exceed 3500°F under worst-case conditions.

The high temperatures attained by the heat sink require careful implementation of system thermal management methods in order to prevent strength loss and/or damage of the braking system and landing gear components. The US Patent literature dealing with thermal barrier technology and other methods developed specifically for controlling aircraft brake heat transfer is substantial, highlighting the major challenges that are present. Examples of thermal management features commonly incorporated into the braking system include wheel ventilation holes to promote convection cooling, heat shields to reduce radiation heat transfer to the wheel and axle, beam-type wheel drive keys to reduce heat conduction into the wheel, and insulators to minimize conduction into the piston housing subassembly and axle. In general, the number and types of thermal barriers are selected to reduce heating of the components surrounding the brake stack to acceptable levels while at the same time maintaining sufficient cooling of the brake stack.

Examples of thermally related problems due to insufficient heat capacity, thermal barrier protection, or cooling include release of wheel fusible plugs (which prevents overpressurization of the tire) at unacceptably low energy levels, strength reduction of the aluminum wheel, degradation of hydraulic seals and hydraulic fluid properties, deterioration of tire rubber, and damage to the axle. Under conditions involving misuse of the brakes, tire fire can occur and heat-related failures leading to leakage of hydraulic fluid and subsequent fluid fire

Nomenclature

b = annular gap width = $r_o - r_i$
c_p = specific heat of fluid
c_{pw} = specific heat of solid wall
$\mathbf{e}$ = unit gravitational vector = $\cos\theta\mathbf{e}_1 - \sin\theta\mathbf{e}_2$
g = gravitational acceleration
$\mathbf{g}$ = gravitational vector = $-g\mathbf{e}$
h = heat transfer coefficient
k = turbulent kinetic energy
L = length to radius ratio = l_2/r_i
l_c = characteristic length
l_e = length of extended computational domain
l_1 = length of wheel outboard cavity
l_2 = length of brake stack
l_3 = distance between brake stack and z datum
Nu = Nusselt number = hr_o/λ
Nu_{av} = average Nusselt number
Pr = Prandtl number = ν/α
Pr_t = turbulent Prandtl number
n = outward normal from surface
p = pressure
q = applied heat flux
R = radius ratio = r_o/r_i
Ra = Rayleigh number based on annular gap width = $g\beta(T_i - T_{\mathrm{ref}})b^3/\alpha\nu$
Ra_{ro} = Rayleigh number based on outer radius = $g\beta(T_i - T_{\mathrm{ref}})r_o^3/\alpha\nu$
Ra_{ri} = Rayleigh number based on inner radius = $g\beta(T_i - T_{\mathrm{ref}})r_i^3/\alpha\nu$
Ra_{ro}^{*} = modified Rayleigh number = $g\beta qr_o^4/\lambda\alpha\nu$
r = radial coordinate
r_e = radius of extended computational domain
r_i = radius of inner cylinder
r_{ih} = radius of wheel hub
r_o = radius of outer cylinder
r_s = inner radius of brake stack end wall
T = temperature
T_i = temperature at surface of inner cylinder
T_{ref} = reference temperature
T_w = temperature of solid wall
T_∞ = ambient temperature
t_w = thickness of wheel web
U = characteristic velocity = $(\alpha/r_o)\sqrt{\mathrm{Ra}_r^{*}\,\mathrm{Pr}}$
u_r = radial velocity
u_θ = angular velocity
u_z = axial velocity
$\mathbf{u}$ = velocity vector
z = axial coordinate

Greek Symbols

α = thermal diffusivity
β = volume expansion coefficient
δ = height of the wall element
ε = dissipation of turbulent kinetic energy
κ = Von Karman constant
λ = thermal conductivity of fluid
λ_{eff} = effective thermal conductivity
λ_t = turbulent thermal conductivity
λ_w = thermal conductivity of wall
μ = dynamic viscosity
μ_{eff} = effective viscosity
μ_t = turbulent viscosity
ν = kinematic viscosity
θ = angular coordinate
τ = stress tensor
τ_{eff} = effective stress tensor

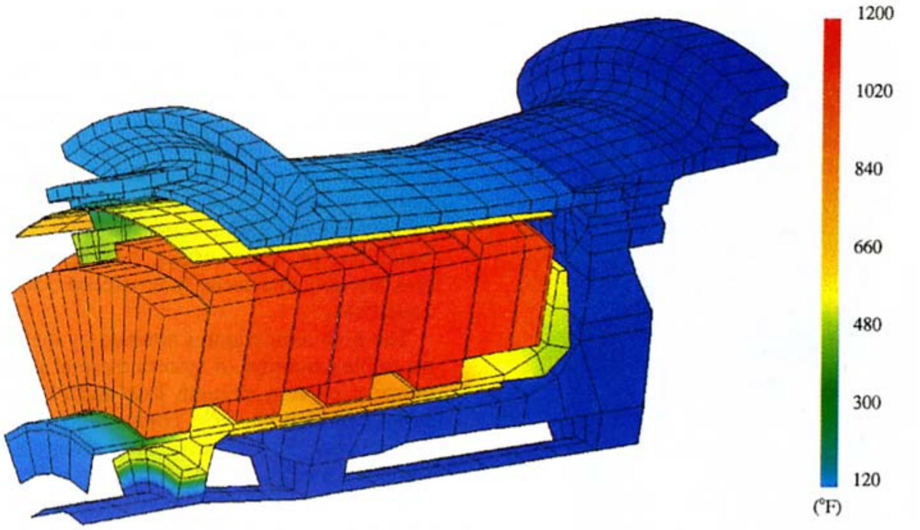

Fig. 2 Wheel and brake temperature distribution eight minutes after a high energy stop (from Dyko and Chung, 1990)

are possible, thus posing a potential threat to safety. Hence, in addition to directly affecting aircraft turnaround time which is a critical performance parameter, the influence of natural convection cooling on overall system thermal behavior profoundly impacts the reliability and safety of the braking system. In addition to these issues, a major objective in the design of aircraft braking systems is to minimize assembly weight. Reducing the weight of the braking system increases the difficulty of the thermal management problem and makes it imperative to understand the net benefits to be obtained from altering the design for increased convective heat loss. Our increased understanding of natural convection cooling for fundamental braking system geometries positively impacts each of the above cited issues.

To help ensure that a new design will meet thermal requirements and to analyze changes to existing designs, numerical heat transfer models are employed to predict the transient temperature distributions within wheel and brake components. Computer codes tailored specifically for simulation of braking system multimode heat transfer are used by the manufacturers of aircraft brakes. Typically, thermal network principles which are analogous to resistance-capacitance electrical networks and can be flexibly applied to a wide range of wheel and brake configurations are followed. The finite element method has also been applied to the multicomponent braking system heat transfer problem with good success (Dyko and Chung, 1990), offering greater resolution of thermal gradients within the individual components. An example of wheel and brake temperature distributions calculated with this method is provided in Fig. 2 for a time of eight minutes after a high-energy braking event. With both the thermal network and finite element models, peak temperatures and cooling times for established brake configurations can be predicted quite accurately. However, the heat transfer coefficient relations employed in convective boundary conditions have traditionally been empirically based and thus restrict the ability to study the effects of changes in geometry on convection cooling. Therefore, it is necessary to analyze the braking system natural convection air flow and temperature fields to obtain improved predictions of heat transfer for new designs and to better evaluate design changes for increased cooling rates. Convective heat transfer correlations for the different regions of the braking system have been successfully developed from results of recent numerical and experimental studies of brake stack/wheel subdomain and wheel and brake assembly flow fields that are described herein. An example of results obtained by integrating the correlations into a thermal model of the braking system and the close agreement of these results with experimental data is presented in a later section. A summary of the available correlations is provided in Table 1.

The aircraft wheel and brake assembly shown schematically in Fig. 1 is comprised of the brake stack and brake frame, wheel inboard and outboard halves, and piston housing subassembly. These components are supported by the axle which attaches to the landing gear strut. It is evident from this diagram that the air passages within the braking system consist primarily of (a) an open-ended horizontal annulus bounded at its inner diameter by the brake stack and at its outer diameter by the wheel (brake stack/wheel subdomain), (b) an open-ended horizontal annular cavity formed by the wheel outboard surfaces (wheel outboard subdomain), and (c) connecting regions between these two subdomains defined by the wheel web ventilation passages (distributed circumferentially around the web) and the web itself. The system is

Table 1 Summary of available Nusselt number correlations for the braking system

Wheel Outboard Region

$$(1.27 \times 10^9 \leq \mathrm{Ra}_{ro}^* \leq 5.05 \times 10^9)$$

$$\mathrm{Nu}_{av} = 0.0136\,(\mathrm{Ra}_{ro}^*)^{0.376} \quad \text{(outer cylinder)} \tag{29}$$

$$\mathrm{Nu}_{av} = 0.0133\,(\mathrm{Ra}_{ro}^*)^{0.379} \quad \text{(end wall)} \tag{30}$$

$$\mathrm{Nu}_{av} = 0.0113\,(\mathrm{Ra}_{ro}^*)^{0.381} \quad \text{(inner cylinder)} \tag{31}$$

$$\mathrm{Nu}_{av} = 0.0119\,(\mathrm{Ra}_{ro}^*)^{0.378} \quad \text{(inner cylinder tip)} \tag{32}$$

$$\mathrm{Nu}_{av} = 0.0131\,(\mathrm{Ra}_{ro}^*)^{0.378} \quad \text{(cavity)} \tag{33}$$

Brake Stack

$$\mathrm{Nu}_{av} = 0.134\,(\mathrm{Ra}_{ro}^*)^{0.264}\text{: } 7.09 \times 10^8 \leq \mathrm{Ra}_{ro}^* \leq 4.76 \times 10^9 \tag{34}$$

$$\mathrm{Nu}_{av} = 0.2\,(\mathrm{Ra}_{ri})^{0.14}(1 - 0.705L)[1 + 27.74(R - 1)]\text{:} \quad \mathrm{Ra}_{ri} < 1 \times 10^5 \tag{35}$$

$$\mathrm{Nu}_{av} = 0.2\,(\mathrm{Ra}_{ri})^{0.174}(1 - 0.525L)[1 + 28.01(R - 1)]\text{:} \quad 1 \times 10^5 \leq \mathrm{Ra}_{ri} \leq 1 \times 10^6 \tag{36}$$

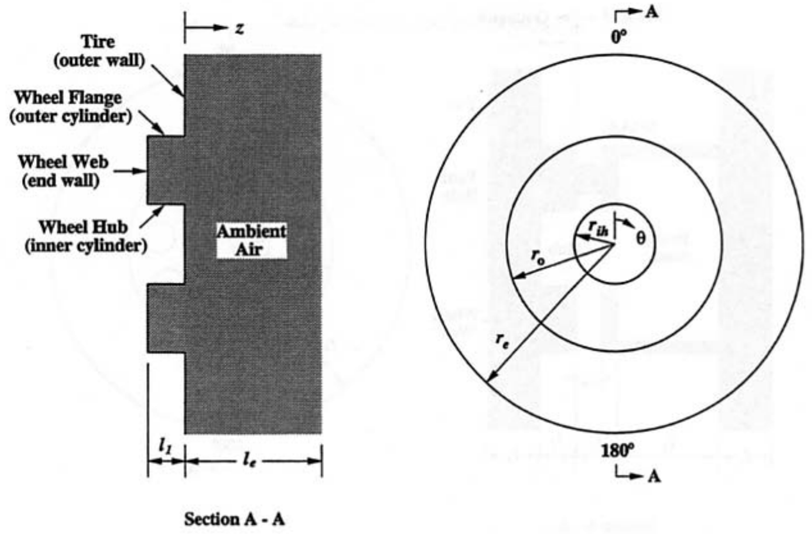

Fig. 3 Wheel outboard subdomain

cooled by ambient air outside the assembly, which enters the internal regions through the open ends of the brake stack/wheel and wheel outboard subdomains. The air subsequently gains energy from the brake stack and from surrounding wheel and brake components which are heated by the stack, and returns to the external region through these open ends. For the purposes of convective heat transfer analysis, the cooling passage geometries associated with the wheel and brake assembly are modeled for the general case as wheel outboard and brake stack/wheel subdomains and the overall wheel and brake assembly domain as shown in Figs. 3–5. From these geometries, it is apparent that studies of natural convection within the wheel outboard, brake stack/wheel, and overall wheel and brake assembly (combined inboard and outboard) regions have their basis in the more fundamental investigation of buoyancy-driven flow and heat transfer within closed and open-ended horizontal annuli.

As discussed in this paper, the fundamental work pertaining to basic horizontal annuli has recently been expanded to consider the higher Rayleigh numbers associated with an aircraft brake, annulus aspect ratios corresponding to actual wheel and brake geometries, conjugate heat transfer, thermal boundary conditions more closely representative of a braking system, and the simultaneous interaction of wheel outboard and brake stack/wheel flow fields with each other and the external flow field. These fundamental and practical advancements have resulted in a much more realistic simulation of three-dimensional aircraft braking system buoyancy induced cooling. Several significant challenges associated with optimizing aircraft brake cooling still lie ahead, however. These include incorporating more detailed design features into the wheel and brake assembly simulation and establishing the braking system design trade-offs associated with enhanced cooling configurations.

The review section of this paper, which follows presentation of the governing equations and boundary conditions, is divided into two main parts. The first part (Fundamental Advancements) addresses pertinent fundamental studies which lay the groundwork for the practical experimental and numerical work discussed in the second part (Braking System Subdomains). Following this, results of the current investigation of natural convection within the overall wheel and brake assembly are presented (Wheel and Brake Assembly). The fundamental work provides the reader with a solid understanding of the underlying

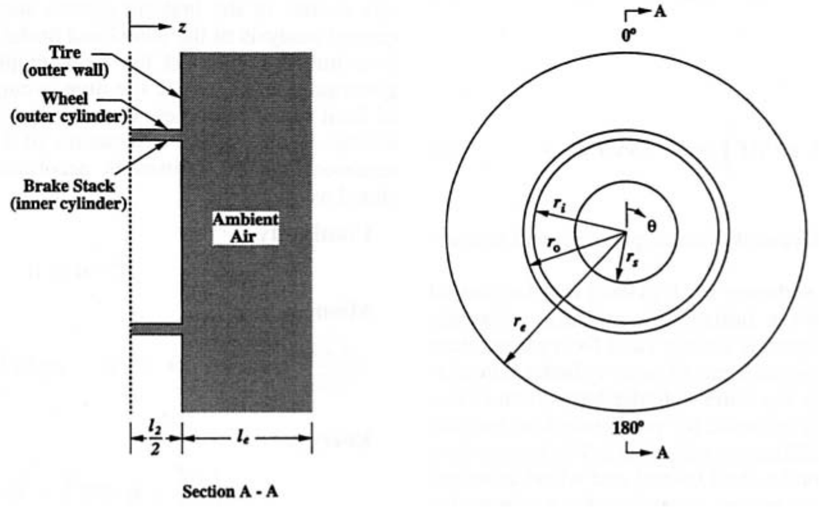

Fig. 4 Brake stack/wheel subdomain

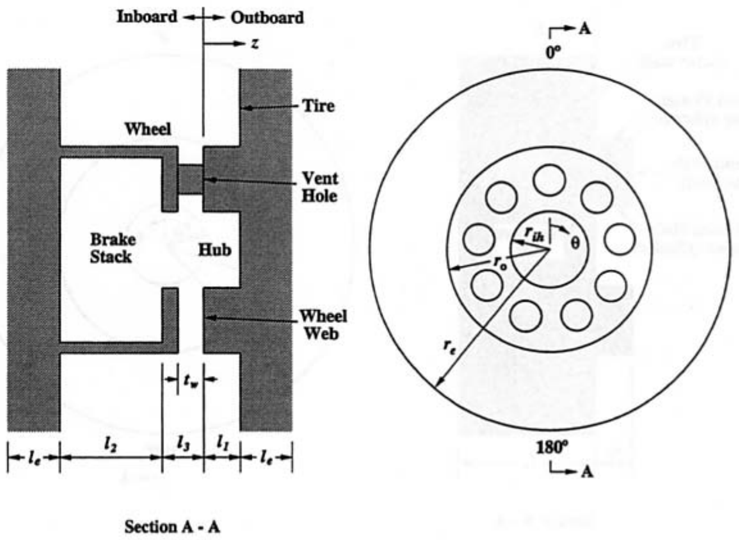

Fig. 5 Wheel and brake assembly domain

convective flow processes prior to attempting to understand the more complicated flows associated with the actual braking system geometry.

Governing Equations

In order to clearly distinguish fundamental characteristics of the three-dimensional cooling flows and efficiently analyze the effects of changes in geometry on cooling performance, it is usually assumed that (a) the fluid is Newtonian, (b) viscous dissipation is negligible, and (c) in accordance with the Boussinesq approximation, density is constant except when it directly causes buoyancy forces. Based on these assumptions, the governing equations can be written as follows.

Continuity.

$$\nabla \cdot \mathbf{u} = 0 \tag{1}$$

Momentum.

$$\rho\left(\frac{\partial \mathbf{u}}{\partial t} + \mathbf{u} \cdot \nabla \mathbf{u}\right) = -\nabla p - \rho \mathbf{g} \beta (T - T_\infty) + \nabla \cdot \tau \tag{2}$$

Energy.

$$\rho c_p \left(\frac{\partial T}{\partial t} + \mathbf{u} \cdot \nabla T\right) = \nabla \cdot (\lambda \nabla T) \tag{3}$$

where $\mathbf{u}$, p, and T, are the velocity vector, pressure, and temperature, respectively.

It has been shown by Mahoney et al. (1986) that for natural convection of gases between horizontal concentric cylinders, the Boussinesq approximation is strictly valid for a temperature difference ratio (defined as the inner to outer cylinder temperature difference divided by the outer cylinder temperature) less than 0.1 and is reasonably accurate for predicting heat transfer rates up to a temperature difference ratio of 0.2. The temperature difference ratios for the brake stack/wheel and wheel outboard subdomains of the braking system meet the above criteria for validity of the Boussinesq approximation for a wide range of typical brake operating conditions. Furthermore, the agreement of results from numerical models which employ this approximation with test data is very good as shown in Vafai et al. (1997) and Desai and Vafai (1996) for the brake stack/wheel and wheel outboard subdomains, respectively. Under severe brake operating conditions the Boussinesq approximation is not strictly satisfied, but agreement of the numerical model results with test data is nonetheless still good as shown in these same references. Therefore, over a wide range of operating conditions of interest, the Boussinesq approximation is valid for the braking system application.

Depending on the Rayleigh number and geometric conditions, turbulent flow and heat transfer can be encountered during the brake cool down period. Direct numerical simulation (DNS) of turbulent natural convection using Eqs. (1)–(3) requires an extremely large number of grids to resolve the small scale flow features and, consequently, an extremely large core memory size and CPU time. This approach is impractical for the aircraft brake cooling problem which is three-dimensional, includes calculations in an extended computational domain, and requires reasonable computational efficiency in order to investigate design changes for enhanced cooling performance. Accurate calculation of the turbulent natural convection for engineering purposes can be made using turbulence models, however. In previous studies of the braking system subdomains as well as the current analysis of the wheel and brake assembly flow field, the $k-\varepsilon$ turbulence model has been employed. In this case, the governing equations are the time-averaged Reynolds equations of fluid motion and heat transfer along with the equations for kinetic energy k and dissipation of kinetic energy ε. These equations can be written in accordance with the previously stated assumptions as

Continuity.

$$\nabla \cdot \bar{\mathbf{u}} = 0 \tag{4}$$

Momentum.

$$\rho\left(\frac{\partial \bar{\mathbf{u}}}{\partial t} + \bar{\mathbf{u}} \cdot \nabla \bar{\mathbf{u}}\right) = -\nabla \bar{p} - \rho \mathbf{g} \beta (\bar{T} - T_\infty) + \nabla \cdot \tau_{\text{eff}} \tag{5}$$

Energy.

$$\rho c_p \left(\frac{\partial \bar{T}}{\partial t} + \bar{\mathbf{u}} \cdot \nabla \bar{T}\right) = \nabla \cdot (\lambda_{\text{eff}} \nabla \bar{T}) \tag{6}$$

Kinetic Energy.

$$\rho\left(\frac{\partial k}{\partial t} + \bar{\mathbf{u}}\cdot\nabla k\right) = \nabla\cdot\left(\frac{\mu_t}{\sigma_k}\nabla k\right) + \frac{\mu_t}{\mathrm{Pr}_t}\mathbf{g}\beta\nabla\bar{T} + \mu_t\Phi - \rho\varepsilon \quad (7)$$

Dissipation.

$$\rho\left(\frac{\partial \varepsilon}{\partial t} + \bar{\mathbf{u}}\cdot\nabla \varepsilon\right) = \nabla\cdot\left(\frac{\mu_t}{\sigma_\varepsilon}\nabla \varepsilon\right) + c_1(1 - c_3)\frac{\varepsilon}{k}\frac{\mu_t}{\mathrm{Pr}_t}\mathbf{g}\beta\nabla\bar{T} + c_1\frac{\varepsilon}{k}\mu_t\Phi - \rho c_2\frac{\varepsilon^2}{k} \quad (8)$$

The standard $k-\varepsilon$ method used to model flow in the high Reynolds number core region cannot be used to model the effects of viscosity on the turbulence field in the viscous sublayer, and therefore an auxiliary treatment of the near-wall region is needed. A number of approaches to near-wall modeling including the law-of-the-wall technique, use of a one equation model near the wall and a two equation model away from it, and a low Reynolds number variant of the $k-\varepsilon$ turbulence model have been developed. The latter two methods may be more accurate than the law-of-the-wall technique, but require a very fine mesh to accurately resolve the sharp gradients of the flow variables in the near-wall region, which can lead to excessive computational cost. A near-wall modeling methodology that was applied to forced flows involving strong and subtle flow reversal by Haroutunian and Engelman (1991) and found to be more accurate than the $k-\varepsilon$ model using standard wall functions is employed in the present study. In this scheme, the mean flow equations are solved throughout the computational domain. The $k-\varepsilon$ model, however, is applied only up to and excluding a single layer of specialized elements located between the physical boundary and the fully turbulent outer flow field. In order to accurately resolve the local flow profiles, these wall elements employ specialized interpolation functions which are based on universal near-wall profiles and are functions of the characteristic turbulence Reynolds number. The turbulent diffusivity in the near-wall region is calculated using Van Driest's mixing length approach.

To more accurately calculate the temperature distributions within the thermally conductive wheel and brake components, the conjugate heat transfer problem is solved. Depending on whether the flow is laminar or turbulent, either Eqs. (1)–(3) or Eqs. (4)–(8), respectively, are solved in conjunction with the energy equation in the solid components, which is

$$\rho_w c_{pw}\frac{\partial T}{\partial t} = \nabla\cdot(\lambda_w\nabla T). \quad (9)$$

The temperature in Eq. (9) represents the temperature in the solid components, while the temperature in Eqs. (2), (3), and (5)–(8) is that of the fluid.

In the present study of turbulent natural convection within the wheel and brake assembly, the following nondimensional form of Eqs. (4)–(9) was employed (for brevity, the overbars indicating averaged values and the asterisks denoting the nondimensional quantities will be dropped, except for Ra^*_{ro}, from here on)

Fluid.

Continuity.

$$\nabla\cdot\mathbf{u} = 0 \quad (10)$$

Momentum.

$$\sqrt{\frac{\mathrm{Ra}^*_{ro}}{\mathrm{Pr}}}\left(\frac{\partial\mathbf{u}}{\partial t} + \mathbf{u}\cdot\nabla\mathbf{u}\right) = -\nabla p - \sqrt{\frac{\mathrm{Ra}^*_{ro}}{\mathrm{Pr}}}\mathbf{e}T + \nabla\cdot\tau_{\mathrm{eff}} \quad (11)$$

Energy.

$$\sqrt{\mathrm{Ra}^*_{ro}\,\mathrm{Pr}}\left(\frac{\partial T}{\partial t} + \mathbf{u}\cdot\nabla T\right) = \nabla\cdot(\lambda_{\mathrm{eff}}\nabla T) \quad (12)$$

Kinetic Energy.

$$\sqrt{\frac{\mathrm{Ra}^*_{ro}}{\mathrm{Pr}}}\left(\frac{\partial k}{\partial t} + \mathbf{u}\cdot\nabla k\right) = \nabla\cdot\left(\frac{\mu_t}{\sigma_k}\nabla k\right) + \frac{\mu_t}{\mathrm{Pr}_t}\mathbf{e}\nabla T + \mu_t\Phi - \sqrt{\frac{\mathrm{Ra}^*_{ro}}{\mathrm{Pr}}}\varepsilon \quad (13)$$

Dissipation.

$$\sqrt{\frac{\mathrm{Ra}^*_{ro}}{\mathrm{Pr}}}\left(\frac{\partial \varepsilon}{\partial t} + \mathbf{u}\cdot\nabla \varepsilon\right) = \nabla\cdot\left(\frac{\mu_t}{\sigma_\varepsilon}\nabla \varepsilon\right) + c_1(1 - c_3)\frac{\varepsilon}{k}\frac{\mu_t}{\mathrm{Pr}_t}\mathbf{e}\nabla T + c_1\frac{\varepsilon}{k}\mu_t\Phi - c_2\sqrt{\frac{\mathrm{Ra}^*_{ro}}{\mathrm{Pr}}}\frac{\varepsilon^2}{k} \quad (14)$$

Solid.

Conduction.

$$\sqrt{\mathrm{Ra}^*_{ro}\,\mathrm{Pr}}\left(\frac{\rho_w c_{pw}}{\rho c_p}\right)\frac{\partial T}{\partial t} = \left(\frac{\lambda_w}{\lambda}\right)\nabla^2 T \quad (15)$$

The nondimensional variables in the above equations are based on the following transformations:

$$r^* = \frac{r}{r_o},\quad z^* = \frac{z}{r_o},\quad u_i^* = \frac{u_i}{U},\quad t^* = \frac{tU}{r_o},\quad T^* = \frac{T - T_\infty}{(qr_o/\lambda)},$$

$$p^* = \frac{pr_o}{\mu U},\quad k^* = \frac{k}{U^2},\quad \varepsilon^* = \frac{\varepsilon}{(U^3/r_o)},\quad \Phi^* = \frac{\Phi}{(U^2/r_o^2)}$$

where the characteristic velocity of the flow is $U = (\alpha/r_o)\sqrt{\mathrm{Ra}^*_{ro}\,\mathrm{Pr}}$. Furthermore, the nondimensional turbulent and effective viscosities and turbulent and effective conductivities are

$$\mu_t^* = c_\mu\left(\frac{k^{*2}}{\varepsilon^*}\right)\sqrt{\frac{\mathrm{Ra}^*_{ro}}{\mathrm{Pr}}},\quad \mu^*_{\mathrm{eff}} = 1 + \mu_t^*$$

$$\lambda_t^* = \left(\frac{\mu_t^*}{\mathrm{Pr}_t}\right)\mathrm{Pr},\quad \lambda^*_{\mathrm{eff}} = 1 + \lambda_t^*.$$

The empirical constants in the above equations are taken as $c_1 = 1.44$, $c_2 = 1.92$, $c_3 = 1.44$, $c_\mu = 0.09$, $\sigma_k = 1.0$, $\sigma_\varepsilon = 1.3$, and $\mathrm{Pr}_t = 1.0$. Except for c_3, these constants are well established from experimental data for turbulent forced convection flows. Sensitivity studies were conducted to determine the effects of c_3 on the calculated results. It was found that there was very little variation in the heat transfer results and flow variables for a significant variation in c_3.

In Eqs. (11)–(15), the modified Rayleigh number Ra^*_{ro} is defined as

$$\mathrm{Ra}^*_{ro} = \frac{g\beta q r_o^4}{\lambda\alpha\nu}. \quad (16)$$

In previous studies of natural convection within closed and open-ended horizontal annuli involving a prescribed inner cylinder temperature T_i, Rayleigh numbers of the following form have been employed:

$$\mathrm{Ra} = \frac{g\beta(T_i - T_{\mathrm{ref}})l_c^3}{\alpha\nu}. \tag{17}$$

The Rayleigh number Ra referred to in later sections of this paper is based on the Eq. (17) definition, with characteristic length l_c corresponding to the annular gap width $r_o - r_i$. The Rayleigh numbers Ra_{r_o} and Ra_{r_i} found in later sections are also based on Eq. (17), but with l_c corresponding to the outer cylinder radius r_o and inner cylinder radius r_i, respectively.

Boundary Conditions

Solid Walls. At all stationary and impermeable boundaries of the fluid computational domain, the three components of velocity are set to zero to satisfy the no-slip condition

$$u_r = u_\theta = u_z = 0. \tag{18}$$

In studies of closed or open annulus natural convection where the fundamental aspects of the flow and heat transfer are of primary interest, the various solid boundaries are either set to a uniform temperature, subject to a uniform heat flux, or defined to be insulated. These basic thermal boundary conditions are specified as follows:

$$T = T_w \quad \text{(uniform temperature surface)} \tag{19}$$

$$-\lambda\frac{\partial T}{\partial n} = q \quad \text{(uniform heat flux surface)} \tag{20}$$

$$\frac{\partial T}{\partial n} = 0 \quad \text{(adiabatic surface)} \tag{21}$$

where n is the direction normal to the surface.

In a conjugate analysis of a braking system subdomain or of the overall wheel and brake assembly flow field, appropriate values of heat flux are usually applied to the wheel and brake solid components. These are intended to represent the heating of these components resulting either directly from frictional conversion of kinetic energy to thermal energy within the brake stack, or indirectly from conduction and radiation heat transfer to the wheel from the brake stack. The heat flux condition is written as

$$-\lambda_w\frac{\partial T}{\partial n} = q. \tag{22}$$

In the conjugate model, the following conditions are always satisfied at the interfaces of the solid components and the fluid:

$$T|_w = T|_f, \quad \left(\frac{\lambda_w}{\lambda}\right)\frac{\partial T}{\partial n}\bigg|_w = \frac{\partial T}{\partial n}\bigg|_f. \tag{23}$$

In the turbulent modeling approach previously described, the equations for k and ε are not solved in the specialized wall elements immediately adjacent to each impermeable wall. Therefore, the boundary conditions for these variables are applied at the first grid point away from the wall as prescribed by Eq. (24),

$$\frac{\partial k}{\partial n} = 0, \quad \varepsilon = \frac{(c_\mu k)^{1.5}}{\kappa\delta}. \tag{24}$$

Symmetry Planes. In cases where the natural convection flow and temperatures fields are symmetric about the vertical plane passing through the axis of the cylinders, the computational domain can be restricted to one side of this plane. The symmetry boundary condition applied at this plane requires that the component of velocity in the θ-direction and gradients of the remaining variables in the θ-direction are zero there. This assumption was justified in the present study based on the symmetry of the experimental results as well as comparisons with the results of simulations covering the entire domain. The boundary conditions at the angular symmetry plane are expressed as

$$\frac{\partial u_r}{\partial\theta} = u_\theta = \frac{\partial u_z}{\partial\theta} = \frac{\partial T}{\partial\theta} = \frac{\partial k}{\partial\theta} = \frac{\partial\varepsilon}{\partial\theta} = 0 \quad \text{at} \quad \theta = 0, \pi. \tag{25}$$

For the narrow gap brake stack/wheel subdomain modeled as shown in Fig. 4, the flow and temperature fields are assumed to be symmetric about the midaxial vertical plane. Therefore, the annulus and extended computational domain on one side of this plane is considered. The validity of this assumption has been confirmed in previous experimental studies of narrow gap open annuli such as that by Vafai et al. (1997). For the brake stack/wheel subdomain, the boundary conditions at the midaxial symmetry plane are

$$\frac{\partial u_r}{\partial z} = \frac{\partial u_\theta}{\partial z} = u_z = \frac{\partial T}{\partial z} = \frac{\partial k}{\partial z} = \frac{\partial\varepsilon}{\partial z} = 0 \quad \text{at} \quad z = 0. \tag{26}$$

Far Field. An extended computational domain is employed to overcome the difficulty in specifying boundary conditions at the open ends of the annular region without overconstraining the problem. This approach permits investigation of the complex interactions occurring between the fluid internal to the annulus and the external fluid in the vicinity of the open end. The issues involved in using an extended domain are addressed in more detail later on.

There are two pertinent choices for the far-field boundary conditions that can be used in an implicit numerical scheme which simultaneously incorporates the boundary and internal points into the solution algorithm at each time step. These are (Vafai and Ettefagh, 1990b)

$$\xi = 0, \quad T = T_\infty \quad \text{(Dirichlet)}$$

$$\frac{\partial\xi}{\partial n} = 0, \quad \frac{\partial T}{\partial n} = 0 \quad \text{(Neumann)}$$

where ξ in the above expressions represents either u_r, u_θ, u_z, k, or ε. Utilizing all Dirichlet conditions is physically valid only for very large extensions of the outer boundaries, which results in a substantial number of grid points and correspondingly large computational requirements. In previous open annulus and aircraft braking system subdomain studies, either all Neumann-type far-field boundary conditions or a combination of Dirichlet and Neumann conditions have been employed. The latter approach was adopted in the present study of the wheel and brake assembly flow field. Through numerical experimentation, it was determined that this provides a good approximation of the far-field conditions without an excessively large computational domain and without sacrificing the accuracy of the solution within the internal flow region or the near outer flow field. The size of the extended domain in the present study was set such that further extensions in the radial and axial directions produced negligible change in the results. The far-field boundary conditions used in the present study of the wheel and brake assembly flow domain, which is shown schematically in Fig. 5, are as follows:

$$\frac{\partial u_r}{\partial r} = \frac{\partial u_\theta}{\partial r} = u_z = \frac{\partial T}{\partial r} = \frac{\partial k}{\partial r} = \frac{\partial\varepsilon}{\partial r} = 0 \quad \text{at} \quad r = r_e \tag{27}$$

$$u_r = u_\theta = \frac{\partial u_z}{\partial z} = \frac{\partial k}{\partial z} = \frac{\partial\varepsilon}{\partial z} = 0,$$

$$T = T_\infty \quad \text{at} \quad z = l_1 + l_e \quad \text{and} \quad z = -l_2 - l_3 - l_e. \tag{28}$$

Fundamental Advancements

In this section, three categories of research which together provide a theoretical foundation for the study of buoyancy-induced cooling of an aircraft braking system are reviewed. The results of published studies of three-dimensional natural convection in cylindrical annuli with closed ends are discussed first. Comparison of this information with the results for open-ended annuli and braking system subdomains reviewed later underscores the substantial changes in the flow field and temperature distribution brought about by removing the impermeable end walls and thereby allowing the internal fluid to communicate with the ambient domain. It is also seen that the two cases are similar in some respects, provided certain conditions are met. A discussion of selected investigations of natural convection in a basic open rectangular cavity and several important aspects of this problem that are pertinent to convection within an open annulus is presented afterwards. It has been shown that the physical processes associated with interaction of the fluid internal to the cavity with the external flow field are very similar for the open rectangular cavity and open annulus geometries. Finally, the existing research work pertaining to three-dimensional buoyancy-induced flow and heat transfer within open cylindrical annuli, which is more closely representative of that within an actual aircraft braking system, is reviewed. The overview of fundamental research activity in this section, together with a review of studies more specifically related to three-dimensional flow and heat transfer within the wheel outboard, brake stack/wheel, and combined inboard and outboard flow domains presented later, is intended to provide a comprehensive framework for understanding and analyzing natural convection cooling of an aircraft braking system.

Closed Cylindrical Annuli. Buoyancy-induced flow and heat transfer in the annular space between concentric cylinders has been of interest to many researchers due to its many technological applications such as nuclear reactors, inert gas insulated electrical cables, solar receivers, thermal storage systems and, recently, aircraft brakes. Depending on the Rayleigh number and outer to inner cylinder radius ratio R, various types of laminar flow structures can arise in the core region of a sufficiently long horizontal annulus containing air. These structures were identified in some of the earlier experimental treatments of the problem. Liu et al. (1961) performed experiments using a heated inner cylinder and cooled outer cylinder to determine overall heat transfer correlations for R within the range of 1.15 to 7.5 using air, water, and silicone oil. For $R = 1.15$ with air and using tobacco smoke for visualization of flow patterns, they qualitatively described the transition from unicellular crescent shaped flow to a multicellular pattern in the top portion of the annulus as Rayleigh number was increased beyond a critical value. With further increase in Rayleigh number, the angular extent of the counter-rotating cells in the multicellular pattern increased and they began to oscillate slowly about the vertical. It was concluded that the upper region of a narrow gap annulus behaves like a ''fluid heated from below'' between horizontal plates, with Bénard type instabilities occurring at Rayleigh numbers in the range of $\mathrm{Ra} = 1600$ to 2000.

A photographic study of annulus flow patterns was conducted by Bishop and Carley (1966) using air as the fluid medium. Uniform inner cylinder temperature was achieved by a vapor condensing method and flow visualization in the annular space was accomplished by transverse illumination after introduction of tobacco smoke. Two types of stable unicellular flow patterns were observed: the crescent eddy pattern for R up to 2.45, and the kidney shaped pattern for the largest R studied of 3.69. The period and amplitude of flow oscillations observed for $R = 3.69$ at higher Rayleigh numbers were reported. In experiments conducted by Grigull and Hauf (1966), a Mach-Zehnder interferometer and cigarette smoke were used for visualization of temperature and flow fields, respectively, in air. Their results revealed the existence of a three-dimensional spiral flow in the upper portion of the annulus for moderate R and increased Rayleigh number. Powe, et al. (1969) conducted experiments using an apparatus similar to that of Bishop and Carley (1966). Based on their results and those of previous investigators, they showed the existence of four laminar convective regimes in a closed horizontal annulus containing air: a *unicellular steady* regime for small Rayleigh number and any value of R, a *multicellular* regime for higher Rayleigh numbers and $R < 1.24$ (small gap annulus), a *spiral flow* regime for higher Rayleigh numbers and R between 1.24 and 1.71 (moderate gap annulus), and an *oscillating* regime for high Rayleigh number and $R > 1.71$ (large gap annulus). In a later numerical and experimental study by Kuehn and Goldstein (1976) the development of steady unicellular recirculating flow patterns in the core region of a large gap annulus, starting at low Rayleigh numbers where heat transfer occurs primarily by conduction and progressing to higher Rayleigh numbers where thin boundary layers are present on the inner and outer cylinders, was described for air. It was found that the center of rotation of the flow moves upward in the annulus with increased Rayleigh number.

The numerical studies of laminar natural convection between concentric cylinders have mainly concentrated on two-dimensional flow in the core region of long annuli and, to a much lesser extent, three-dimensional flow in shorter annuli with closed ends. A three-dimensional analysis is required for an annulus with finite axial length since the viscous shearing effect of the end walls affects the convection in the axial direction. Certain types of secondary flows which arise due to thermal instability, such as spiral flow in a moderate gap annulus, also require a three-dimensional analysis. Ozoe et al. (1979) conducted a numerical and experimental investigation of a vertically oriented annulus heated on the bottom end wall and cooled on the top wall. Their results showed that the stable flow consists of identical roll cells with axes oriented along radial lines within a single horizontal plane. The number of cells in the annulus was equal to the even integer nearest to the average circumference divided by the height. The effects of annulus inclination for the same problem were later investigated numerically and experimentally by Ozoe et al. (1981). The three-dimensional governing equations were formulated in terms of vorticity and vector potential and solved by the finite difference method. Numerical calculations were performed for Prandtl number of 10. They reported that, as the heated surface is inclined from the lower horizontal position, the mean Nusselt number at first decreases as the circulation pattern changes from a symmetrical array of roll cells to distorted and oblique roll cells to a single circulation. With further inclination, the mean Nusselt number increases until going through a maximum and then decreases to unity as the heated surface reaches the upper horizontal position.

Takata et al. (1984) numerically and experimentally studied the effects of inclining a large-gap closed annulus having a heated inner cylinder and cooled outer cylinder for a fluid with Prandtl number of 5000. The vorticity-vector potential form of the three-dimensional governing equations was solved using the SOR procedure. Flow visualization was accomplished using glycerol as the working fluid and suspended aluminum powder as a seeding material. The results of this investigation indicated that a co-axial double helix flow pattern is present adjacent to each end wall inside the horizontal annulus. For the horizontal orientation, the flow has a relatively small component of axial velocity. When the annulus is tilted, the axial velocity increases considerably and a more distorted co-axial double helix is present. It was found that while the maximum local Nusselt numbers show a strong dependence on the inclination angle, the average Nusselt number increases only slightly as the inclination increases. Three-dimensional numerical simulations of natural convection in a moderate gap horizontal annulus were conducted by Rao et al. (1985), also for a fluid with Prandtl number of 5000. They found that a spiral-type flow was present in the upper portion of the annulus in conjunction with nearly two dimensional flow in the lower regions. The structure of the flow pattern was confirmed by an experimental visualization study using glycerol as the working fluid. It was seen from the experimental and numerical results that for this high Prandtl number the number of spiral vortices tends to increase as Rayleigh number is increased.

A three-dimensional numerical study of natural convection in a large-gap closed horizontal annulus filled with air was performed by Fusegi and Farouk (1986) using the vorticity-velocity formulation. The length of the annulus was chosen to be small so that the influence of the end walls was evident in the fluid motion. Double helical roll structures qualitatively similar to that reported by Takata et al. (1984) were calculated. Transient three-dimensional buoyancy-driven flow and heat transfer in a large-gap closed horizontal annulus was numerically investigated by Vafai and Ettefagh (1991a). Calculations were performed for a Prandtl number corresponding to that of air, and therefore the results are of greater practical applicability than previous studies at much higher Prandtl numbers. The results showed that a core region in which the temperature distribution remains unchanged and the flow is essentially two-dimensional is present at the mid-axis of the annulus, provided the length to outer radius ratio is adequately large. The effects of the axial impermeable boundaries were shown to be characterized by retardation of the flow field through the viscous shearing force in regions near the end walls. Accordingly, the local Nusselt number experiences a reduction at the end walls. The transient development of the flow and temperature fields as a result of sudden heating of the inner cylinder was presented.

A numerical and experimental investigation of the development of three-dimensional buoyancy-induced flow and temperature fields in moderate and large-gap closed horizontal annuli was conducted by Dyko et al. (1999). It was shown that in a moderate gap annulus, the natural convective flow at low Rayleigh numbers is similar to that in a large gap annulus, with crescent-shaped flow patterns (r-θ plane) in the core region and a rotating cell (r-z plane) located in the upper portion of the annulus at each end wall. As Rayleigh number is increased above a critical value, however, an integral number of transverse spiral vortex pairs forms between the end vortices in the moderate gap annulus due to thermal instability. The size of the inner vortical cells was shown to depend on the natural size predicted by stability theory for an infinitely long annulus, the increase in Rayleigh number above the critical value, and the length of the annulus. The Nusselt number distribution in the upper part of the annulus was found to be significantly influenced by the vortex structures. The results of the investigation by Dyko et al. (1999) showed that in a sufficiently long large-gap annulus, three stable flow regions coexist at higher Rayleigh numbers. First, a three-dimensional recirculating flow consisting of a transverse vortex in the upper portion of the annulus and a double helical flow structure below this sets up next to each end wall. In the core region, the thermal field retains the characteristics of that associated with two-dimensional flow. Finally, between the end wall and core zones a third region is present in which the primary flow circulation takes place in the axial planes in conjunction with much lower speed axial flow. For a large-gap annulus filled with a high Prandtl number fluid, it was shown that the crescent-shaped flow patterns present at low Rayleigh numbers change to symmetric unicellular structures with centers of rotation near the top of the annulus as Rayleigh number is increased. Longitudinal roll cells are positioned at the top of the annulus for the larger Rayleigh number flows. The numerical results presented by Dyko et al. (1999) were shown to be in excellent agreement with the experimental results for both Prandtl numbers studied.

A numerical study of the effects of an inner cylinder geometric perturbation on three-dimensional natural convection in a closed horizontal annulus was performed by Iyer and Vafai (1997). The fundamental structure of the flow field and the heat transfer characteristics associated with this geometry were analyzed and compared with that of the regular annulus without any perturbation. The effect of variation of a number of key geometric parameters of the perturbation on the overall heat transfer was also presented. Iyer and Vafai (1998) also conducted a detailed study of buoyancy-induced flow and heat transfer in a closed horizontal annulus having multiple geometric perturbations on the inner cylinder. The flow field structures corresponding to different numbers of perturbations and pertinent geometric variations were analyzed, and heat transfer effects were studied by analyzing local and average Nusselt numbers. As was the case for the single perturbation, the flow field was found to evolve from the entrainment of flow by the heated vertical portion of the perturbation. As more perturbations were added, the flow field changed in a regular and recurring manner. Qualitative similarities in the local Nusselt number distributions for different numbers of perturbations were also observed. The results showed that the overall heat transfer rate increases substantially with introduction of multiple perturbations of the size considered.

The number of experimental and numerical studies of buoyancy-induced turbulent flow in annular geometries, which is pertinent to aircraft brakes due to the high Rayleigh numbers that are attained, is very limited. Kuehn and Goldstein (1978) conducted an experimental study of the influence of Rayleigh number and eccentricity on natural convection between two horizontal isothermal cylinders. Results for the concentric cylinder case using nitrogen showed that the flow first becomes unsteady in the plume above the inner cylinder, and that with further increases in Rayleigh number this becomes turbulent. The turbulence in the plume is transported to the top of the outer cylinder and decays as the flow proceeds downward along the outer cylinder to the lower half of the annulus. The flow in the bottom half of the annulus remains laminar and is virtually steady. The transition to turbulent flow in the annulus of $R = 2.6$ that was studied occurred for $\mathrm{Ra} > 10^6$. An experimental study of turbulent natural convection of helium between horizontal concentric cylinders maintained at cryogenic temperatures was conducted by Bishop (1988). Time-averaged temperature profiles and overall heat transfer rates were obtained for Rayleigh numbers in the range of $\mathrm{Ra} = 6 \times 10^6$ to 2×10^9 and expansion numbers ($\beta\Delta T$) from 0.20 to 1.0. The study was conducted for an annulus with a radius ratio of $R = 3.36$. The heat transfer rate was found to be dependent on both the expansion number and the Rayleigh number. Using the same basic test apparatus and fluid but with an annulus of $R = 4.85$, McLeod and Bishop (1989) presented time-dependent temperature data and discussed the spatial extent of turbulence in the annulus as well as the postulated flow structures based on these measurements. In these experiments, the inner and outer cylinders were maintained at cryogenic temperatures. It was determined that increasing the expansion number from 0.25 to 1.0 results in a more turbulent flow structure and increased heat transfer, which further substantiated the conclusion of Bishop (1988) that the expansion number, in addition to Rayleigh number, should be accounted for in calculating the heat transfer rate.

A numerical study of turbulent natural convection in a large-gap annular geometry was conducted by Farouk and Guceri (1982). They carried out two-dimensional simulations over the Rayleigh number range of $\mathrm{Ra} = 10^6$ to 10^7 using the $k-\varepsilon$ turbulence model. The differential equations for time-averaged vorticity, stream function, temperature, turbulent kinetic energy, and dissipation rate of turbulent kinetic energy were solved using a finite difference technique. The results were found to be in good agreement with the available experimental data in the literature. The direct numerical simulation (DNS) of three-dimensional turbulent flow within closed annuli, which is a taxing computational task owing to the fine mesh resolution and time step size necessary to capture the details of the small scale eddies, has recently become more practical due to the development of supercomputers. Morita et al. (1990) demonstrated the applicability of DNS to the problem of three-dimensional, unsteady, turbulent natural convection in an annulus. Fukuda et al. (1990) carried out the DNS for a large-gap annulus using the explicit leap-frog scheme and the approximation of periodic boundary conditions in the axial direction. Analyses were conducted for Rayleigh numbers up to $\mathrm{Ra} = 6 \times 10^5$. The results were verified by comparison with experimentally obtained time averaged velocity and temperature profiles and turbulence quantities such as intensities of velocity and temperature fluctuations. The DNS captured the general trend of the stable flow pattern changing to a periodic and then irregular turbulent flow. Three-dimensional DNS and LES (large eddy simulation) of turbulent flow was performed for Rayleigh numbers up to $\mathrm{Ra} = 1.18 \times 10^9$ by Fukuda et al. (1991) using the explicit finite difference method. Their results were found to be in good agreement with experimental data from other investigators.

Turbulent natural convection in a horizontal annulus was numerically investigated for a wide range of parameters ($10^6 < \mathrm{Ra} < 10^9$, $0.01 < \mathrm{Pr} < 5000$, $1.5 < R < 11$) by Desai and Vafai (1994). Discretization of the time averaged governing equations was achieved using a finite element method based on the Galerkin method of weighted residuals, and the $k-\varepsilon$ turbulence model was applied. A comprehensive analysis was presented for the effects of varying Rayleigh number and Prandtl number on the time-averaged flow and temperature fields and Nusselt numbers, as well as the effect of R on isotherms and Nusselt numbers. The heat transfer rates were found to be substantially higher than those for laminar flow. The heat transfer decreased with an increase in R for the same Rayleigh number. As Prandtl number was increased, the turbulent viscosity decreased indicating lower levels of turbulence at the same Rayleigh number. The mean cavity Nusselt number increased with higher Prandtl number up to $\mathrm{Pr} = 100$ for $\mathrm{Ra} = 10^8$ and $R = 2.6$. Transition to turbulence was delayed for fluids with Prandtl numbers of 1000 and 5000, however, which resulted in lower heat transfer at the same Rayleigh number since the flow was still in the laminar regime. Desai and Vafai (1994) also provided results from a three-dimensional model to show the influence of the end walls on the natural convection. The local Nusselt number experienced a drastic decrease at the end walls. As in the laminar case studied by Vafai and Ettefagh (1991a), it was shown that if the annulus is sufficiently long, there exists a core region over a substantial length of the annulus in which a two-dimensional approximation can be made. Good agreement between results from this investigation and those of previous experimental and numerical studies was shown.

Open Rectangular Cavities. Natural convection in open-ended structures has been an active area of research in recent years, with most of the studies dealing numerically with two-dimensional open rectangular cavities. The interest in this problem stems from applications such as cooling of electronic equipment, energy conservation in buildings, fire research, and solar receiver systems. The open rectangular cavity studies have provided valuable insight into the coupling of the internal and external flow fields and have served as a stepping stone toward the more recent treatment of the open annulus. Investigations have been conducted to ascertain the effects of parameters such as Rayleigh number (Le Quere et al., 1981; Penot, 1982; Chan and Tien, 1983, 1985a, b, 1986; Humphrey and To, 1986; Vafai and Ettefagh, 1990a; Skok et al., 1991; Mohamad, 1995), Prandtl number (Bejan and Kimura, 1981; Vafai and Ettefagh, 1990a), cavity aspect ratio (Le Quere et al., 1981; Humphrey and To, 1986; Vafai and Ettefagh, 1990a; Mohamad, 1995), and cavity inclination (Le Quere et al., 1981; Penot, 1982; Humphrey and To, 1986; Mohamad, 1995) on the open rectangular cavity flow and thermal fields and heat transfer. The effects of partially obstructing the opening have also been examined (Hess and Henze, 1984; Abib and Jaluria, 1988; Miyamoto et al., 1989). Various types of thermal boundary conditions such as all walls heated or only the back wall heated have been employed. Although these conditions affect the local flow and temperature fields, they do not substantially alter the basic flow mechanisms, which have been identified by Vafai and Ettefagh (1990a). Additional features of the outer and inner domain interactions are discussed in Ettefagh and Vafai (1988) and Ettefagh et al. (1991). An examination of the literature pertaining to open rectangular cavities is of interest in the present work because several key aspects of thermally driven flow in open rectangular cavities are also of importance in the open annulus case as related to the wheel outboard, brake stack/wheel, and wheel and brake assembly configurations.

One of the main difficulties encountered in the analysis of buoyancy-driven flow in open cavities is the specification of appropriate boundary conditions at the open ends, where physical conditions are unknown. In the numerical investigation by Le Quere et al. (1981) of an open rectangular cavity with uniform temperature walls, this was overcome by utilizing a short extended computational domain. Numerical tests were performed in which the position of the extended boundaries and the conditions set at these locations were varied. They stated that the flow and heat transfer inside the cavity were not affected by these conditions if the boundary of the extended domain is positioned two cavity heights or more from the aperture plane. It should be noted that in later studies by Vafai and Ettefagh (1990a, b) of a rectangular cavity open on both ends, it was determined that a much larger extension is required for the results inside the cavity not to be affected by the far-field conditions. Using the finite difference method, Le Quere et al. (1981) performed simulations over a range of Grashof numbers (based on the aperture plane dimension) from 10^4 to 3×10^7. For a cavity of aspect ratio $a/c = 1$ with Grashof number of 10^5, where a is the cavity width and c the cavity height, the flow was found to be steady and entered the cavity along the bottom $\frac{2}{3}$ of the aperture plane while exiting back to the ambient along the upper $\frac{1}{3}$ of this plane. For the conditions studied, flow recirculation did not arise in the cavity. At Grashof numbers exceeding 10^7, the flow became noticeably unsteady and localized recirculation zones formed along the bottom of the cavity. A periodic recirculating process in the top half of the aperture plane was also present.

Chan and Tien (1985b) compared two methods of addressing the problem of unknown physical conditions at the aperture plane: use of an extended computational domain and restriction of the computations to within the cavity. The motivation for the latter approach is savings of memory and computational time. In their numerical analysis of a square open cavity with heated back wall using the second approach, the temperatures of fluid entering the cavity were set to the ambient value and the temperatures of fluid exiting the cavity satisfied the upwind condition assuming conduction to be small relative to convection. The gradient of vertical velocity was set to zero at the opening and the horizontal velocity was determined by the continuity equation. With conditions at the cavity opening thus set, it was found that the isotherms were not predicted as accurately at lower Rayleigh numbers, which is when conduction is dominant. At higher Rayleigh numbers heat transfer was predicted fairly well, but certain flow characteristics such as the turn and separation around the lower corner were missed.

In a shallow cavity, the heat transfer rate and flow patterns are affected less by the manner the open boundaries are set because of the large distance between open and closed ends. Using the simplified approach of confining computations to within the cavity, Chan and Tien (1985b) performed numerical calculations for a shallow cavity heated at the back wall over the Rayleigh number range of 10^3 to 10^6. At lower Rayleigh numbers, they found that the effect of the open boundary does not penetrate very far into the cavity, and a core region exists in which the velocity field is everywhere parallel to the horizontal walls. As Rayleigh number is increased, the effects of the open boundary extend further into the cavity and the core region begins to disappear. A boundary layer forms at the vertical heated wall and the fluid heated by this wall accelerates at first gradually and then rapidly as it moves along the upper wall and exits the open end. Based on comparison of the numerical results with test data obtained by Chan and Tien (1983) using LDV and a thermocouple probe, it was concluded that the numerical model was adequate for predicting the basic flow patterns and heat transfer characteristics within a shallow open cavity. Both the numerical and experimental results showed that the flow remains "unicellular" throughout with no recirculation or secondary cell. The experimental results also showed that the exiting flow, which is driven by the heated cavity, was not strong enough to form a buoyant jet for Rayleigh numbers even as high as approximately 10^6 to 10^7. Instead, a wall plume rose up the vertical wall above the opening entraining fluid from the surroundings in the process. In the case where the fluid was thermally stratified the incoming flow approached horizontally, while in the case of no stratification it was expected to approach radially toward the lower part of the opening. It was therefore concluded that the incoming flow is significantly affected by the external conditions.

Buoyancy-induced convection in open-ended rectangular cavities was analyzed by Vafai and Ettefagh (1990a) for Rayleigh numbers in the range of 10^3 to 5×10^5. A thorough examination of the transient behavior of the flow and temperature fields and the effects of varying Rayleigh number, Prandtl number, temperature ratio between the upper and lower blocks, and cavity aspect ratio on the flow and temperature fields and heat transfer was presented in this study. It was determined that the size of the enlarged domain had to be at least 60 times the height of the cavity for higher Rayleigh numbers to eliminate the effects of the far-field solution on the flow field and heat transfer inside the cavity and near its opening, which is far greater than that anticipated by previous researchers. The results of this study showed that at lower Rayleigh numbers the heated fluid rises in a buoyant plume into the ambient domain as it leaves the cavity. As a result of this *ejection* mechanism, which is caused by energy transfer from the internal cavity surfaces to the fluid, the colder ambient fluid enters the cavity to replace the departing hot fluid. The departing fluid leaves at a higher velocity than the incoming fluid, and therefore it occupies a smaller portion of the aperture plane due to conservation of mass. As Rayleigh number is increased, the heated fluid exits at higher velocities due to greater buoyancy force and the colder fluid is sucked further into the cavity at higher speed. In the upper part of the cavity, the horizontal temperature gradient decreases with increasing Rayleigh number resulting in a thermally stratified region along the upper wall. While the ejection mechanism results in upward flow that is opposite the direction of the gravity field, the *suction* mechanism caused by the fluid filling the void left by the departing plume causes a parallel horizontal flow along the lower wall of the cavity. The horizontal flow along the lower wall experiences significant buoyancy forces. These two effects give rise to an instability mechanism described in detail by Vafai and Ettefagh (1990b). As Rayleigh number is increased more, the cold fluid penetrates even further into the cavity and a thermal boundary layer forms along the lower wall. In addition, the outgoing fluid rises up much faster resulting in a thinner thermal boundary layer along the wall outside the cavity. As a result of this thinner boundary layer, which is responsible for most of the heat transfer to the ambient fluid, the temperature of the plume decreases. At the highest Rayleigh number studied, a circulating flow region is formed inside the cavity due to the viscous interaction of the incoming and outgoing flows.

Open Cylindrical Annuli. Natural convection in horizontal cylindrical annuli open on one or both ends, which is representative of that which occurs in the actual aircraft braking system wheel outboard and brake stack/wheel regions, respectively, has only very recently been studied. While the open annulus geometry has some similarities to that of the closed annulus, there are some substantial differences in flow behavior due to axial transport effects induced by the open ends in conjunction with the buoyancy-driven flow in each axial plane of the cavity. Also, in contrast to the open rectangular cavity which can be analyzed using a two-dimensional model, the open annular cavity flows are strongly three-dimensional because of these effects and as such cannot even be approximated with a two-dimensional model. The first treatment of the open annular cavity problem was by Vafai and Ettefagh (1991b), who studied transient laminar natural convection in a horizontal annulus open on both ends with the inner cylinder heated and outer cylinder cooled. The ADI and extrapolated Jacobi schemes were employed to solve the vorticity-vector potential form of the time-dependent governing equations and an extended computational domain was utilized to properly account for the open boundaries. Calculations were performed for Rayleigh numbers of $\mathrm{Ra}_{ro} = 4.3 \times 10^3$ and 10^4.

The results of this study showed that flow inside the open annulus is comprised of recirculation in each axial plane driven by the heated inner and cooled outer cylinders in conjunction with axial movement due to interaction of the internal fluid with the external fluid. Near the open ends, the strength of the recirculation decreases and the axial velocity increases. The isotherms are spaced much closer to the inner cylinder at the aperture plane and therefore the heat transfer from the inner cylinder is considerably enhanced there. The heat transfer over the upper part of the outer cylinder is also greater at the opening. The existence of a core region in which the temperature field can be approximated as two-dimensional for Rayleigh numbers less than $\mathrm{Ra}_{ro} = 10^4$, provided the annulus is sufficiently long, was revealed. It was found that this approximation is not valid for the flow field, however, which is different from a closed annulus where both the flow and temperature fields are nearly two-dimensional in the core region as shown by Vafai and Ettefagh (1991a). In both the closed and open annulus studies, the extent of the core region was found to decrease with increased Rayleigh number. The transient development of the open annulus flow and temperature fields resulting from sudden heating of the inner cylinder was also investigated by Vafai and Ettefagh (1991b). It was observed that the errors for a two-dimensional assumption in the midportion of the annulus are less at earlier times during the transient development of the flow and temperature fields.

In another study, Ettefagh and Vafai (1991) showed that the strong coupling effects between the flow inside and outside the open annulus resulted in the three physical and fundamental transport mechanisms of *ejection, mixing,* and *suction,* which are similar to those in an open rectangular cavity. At the aperture plane, the recirculation pattern inside the annulus is no longer present and the heated fluid around the outer cylinder rises radially in the axial plane. Hot fluid exits the annulus at both the top of the outer cylinder and bottom of the inner cylinder due to the *ejection* mechanism, which is caused by energy transfer from the inner cylinder surface to the fluid. Cold fluid from the surroundings is drawn into the annulus at the top of the inner cylinder and bottom of the outer cylinder as a result of the *suction* mechanism caused by replacement of the fluid lost from the annulus. The velocity of fluid leaving the annulus at the top of the outer cylinder is significantly higher than that of fluid entering along the top of inner cylinder. However, fluid entering the annulus along the lower part of the outer cylinder is approximately at the same velocity as that exiting along the bottom of the inner cylinder. In the external region immediately adjacent to the aperture plane, *mixing* of the fluid departing from the annulus along the lower part of the inner cylinder with the cold fluid entering the annulus along the top of the inner cylinder occurs. This mixing mechanism has a direct influence in increasing the temperature of the surrounding fluid.

The results of the study by Ettefagh and Vafai (1991) also showed that at the lower Rayleigh number of $\mathrm{Ra}_{ro} = 4.3 \times 10^3$, the magnitude of the inner cylinder local Nusselt number at the aperture plane is greater than its value at the core region by a factor of 2 at the top of the annulus and a factor of 3 at the bottom of the annulus. Also, at the top of the annulus the outer cylinder local Nusselt number at the aperture plane is 2.4 times greater than its value at the core region, while at the bottom of the annulus it is three times less than at the midaxial plane. Within ±60 deg of the top of the annulus the outer cylinder local Nusselt number at the aperture plane is greater than at the core region, while below this region it is less than at the midaxis. An increase in Rayleigh number was shown to cause a sharp increase in the rate of heat transfer in the vicinity of the aperture plane.

Turbulent natural convection in a narrow-gap horizontal annulus open on both ends was recently investigated numerically and experimentally by Vafai et al. (1997). This study provided, for the first time, a description of the turbulent buoyancy-induced flow and a quantitative evaluation of the effects of varying geometric parameters on heat transfer in a narrow gap open annulus. As discussed later in the brake stack/wheel subdomain section of this paper, the results of this study revealed some of the basic differences between flow in a narrow-gap open annulus and that in a wider-gap open annulus. Natural convective air flow in the narrow open-ended annulus between a heated inner drum and cooled outer cylinder was studied experimentally by Braun et al. (1997). Visualization of the flow inside the annulus and mapping of the inner and outer cylinder temperature distributions was performed over a range of Rayleigh numbers in which the stable laminar flow transitions to a higher strength unstable laminar flow. An aluminum inner cylinder and Lucite outer enclosure were employed in the experiments. By filling the outer enclosure with an oil having the same refractive index as Lucite, an undistorted sheet of laser light could be introduced into the annulus to illuminate particles entrained in the natural convection currents. At the lower Rayleigh number studied of $\mathrm{Ra} = 6.6 \times 10^3$, it was determined from photographic images of the flow patterns that the air enters the lower regions of the annulus and is drawn inward toward the midaxial plane. At the same time, portions of the flow proceed circumferentially upward. At the midaxial plane, the remaining air moves circumferentially into the upper region of the annulus and then reverses axial direction. At the higher Rayleigh number studied of $\mathrm{Ra} = 1.6 \times 10^4$, the flow in the upper portion of the narrow gap annulus became unstable.

Braking System Subdomains

Wheel Outboard Region. As illustrated in Fig. 3, the wheel outboard subdomain is modeled as a wide-gap annulus of small axial length open to the ambient surroundings on one end and closed on the other. The outer cylinder, inner cylinder, and end wall of the annulus correspond to the wheel outboard flange, wheel hub, and wheel web, respectively. A numerical investigation of laminar natural convection for fundamental geometries of this type was performed by Desai and Vafai (1992) using the Galerkin method of finite element formulation. In this study, fundamental thermal boundary conditions consisting of a uniform temperature cold outer cylinder, uniform temperature hot inner cylinder, and an adiabatic end wall were employed. The effects of Rayleigh number and inner cylinder length were studied. Results of the investigation showed that at a Rayleigh number of $\mathrm{Ra}_{ro} = 10^4$, the effect of the closed end wall is to retard the flow coming into the cavity through the aperture plane. At a Rayleigh number of $\mathrm{Ra}_{ro} = 10^6$, the closed end wall causes the formation of two spirally rotating cells inside the cavity, separated by an axially stagnant flow region. At both the low and high Rayleigh numbers, there is a considerable enhancement in heat transfer in the vicinity of the open end. It was found that reducing the length of the inner cylinder causes higher heat transfer rates from the inner cylinder for both low and high Rayleigh number cases. This is a result of the higher velocities associated with the annular cavity having a shorter inner cylinder and the stagnant region occupying a smaller portion of the cavity which causes better interaction of the ambient fluid with the cavity fluid. The transient three-dimensional natural convection flow and heat transfer associated with this geometry was also investigated by Desai and Vafai (1993). The numerical results showed the evolution of the natural convection flow field in the annulus and its immediate surroundings resulting from sudden heating of the inner cylinder.

The annular cavity with one end open to the ambient surroundings has been studied experimentally and numerically by Desai and Vafai (1996) for high Rayleigh number conditions resulting in turbulent natural convection. This work provided, for the first time, validated heat transfer data for high Rayleigh number buoyancy-induced flows in open annular cavities. In the experimental portion of this investigation, a test section with aluminum inner and outer cylinders and an aluminum end wall was employed. A constant heat flux was applied to each of these components. Local surface temperature measurements were made to determine heat transfer characteristics of the convective flow. Nusselt number correlations were developed and presented for individual components of the cavity as well as the entire cavity over the Rayleigh number range of $\mathrm{Ra}^*_{ro} = 1.27 \times 10^9$ to 5.05×10^9. These correlations are given in Eqs. (29)–(33)

$$\mathrm{Nu}_{av} = 0.0136(\mathrm{Ra}^*_{ro})^{0.376} \quad \text{(outer cylinder)} \tag{29}$$

$$\mathrm{Nu}_{av} = 0.0133(\mathrm{Ra}^*_{ro})^{0.379} \quad \text{(end wall)} \tag{30}$$

$$\mathrm{Nu}_{av} = 0.0113(\mathrm{Ra}^*_{ro})^{0.381} \quad \text{(inner cylinder)} \tag{31}$$

$$\mathrm{Nu}_{av} = 0.0119(\mathrm{Ra}^*_{ro})^{0.378} \quad \text{(inner cylinder tip)} \tag{32}$$

$$\mathrm{Nu}_{av} = 0.0131(\mathrm{Ra}^*_{ro})^{0.378} \quad \text{(cavity).} \tag{33}$$

In the numerical part of the study, the $k-\varepsilon$ model was employed for simulating turbulent characteristics of the convective flow and the conjugate problem was solved to account for heat conduction in the walls of the cavity. Good agreement between the numerical and experimental results was shown. It was found that the fluid enters the lower half of the annular cavity axially due to the suction mechanism. Some of this fluid becomes entrained in the boundary layers on the inner and outer cylinders, while the remainder proceeds axially toward the cavity end wall and then rises in a boundary layer along this wall. In the upper part of the cavity, the fluid motion is characterized primarily by the rising plume from the top of the inner cylinder and the strong axial outflow of the heated fluid. The fluid is ejected from the top of the cavity as a buoyant jet. There is also a region of outflow immediately below the inner cylinder and inflow just above it.

In the study by Desai et al. (1996), the influence of various geometric parameters on the turbulent flow characteristics and heat transfer of the open annular cavity geometry was investigated numerically. Four different pertinent geometries were analyzed and thermal performance in terms of average surface temperature and Nusselt number were compared. The configurations studied can be classified as equally extended inner and outer cylinders, no outer cylinder, extended inner cylinder, and conical inner cylinder. The same total heat input was applied to each configuration in order to evaluate their relative thermal performance. It was found that changing the inner cylinder shape from cylindrical to conical improves the penetration of ambient air into the cavity and therefore improves the cooling characteristics. The average surface temperature of the configuration with a conical inner cylinder was approximately the same as the equally extended inner and outer cylinder design in spite of the reduced surface area. It was also shown that eliminating the outer cylinder results in the highest heat transfer rates from the cavity because of the improved interaction with the ambient air. However, the surface temperatures are highest because of the reduced surface area. The extended inner cylinder configuration resulted in the lowest surface temperatures, mainly because it had the greatest surface area.

Brake Stack/Wheel Region. The brake stack/wheel inboard subdomain is represented by a narrow gap annulus open at both ends to the ambient as shown in Fig. 4. The inner and outer cylinders correspond to the aircraft brake stack and wheel, respectively. An experimental and numerical study of turbulent buoyancy-induced flow in a narrow-gap open-ended annulus was performed for the first time by Vafai et al. (1997). A test section with aluminum inner and outer cylinders and aluminum vertical walls on either side of the inner cylinder was employed in the experiments. The aluminum end walls extended radially from $r = r_s$ to $r = r_i$ (Fig. 4). A constant heat flux was applied to the inner cylinder and vertical end walls using electrical heaters. Experiments were conducted over the range of Rayleigh numbers from $\mathrm{Ra}^*_{ro} = 7.09 \times 10^8$ to 4.76×10^9. Temperature distributions of the component surfaces resulting from the buoyancy-driven air flow occurring in the gap between the inner and outer cylinder and in the external region adjacent to the end walls were recorded. These were utilized for development of average Nusselt number relations, description of the thermal behavior, and validation of the numerical model, results of which compare very well with the experimental data. Smoke flow visualization using laser illumination was performed to illustrate flow patterns in the vicinity of the open ends. A Nusselt number correlation for the inner cylinder and its two vertical end walls which applies over the previously mentioned Rayleigh number range was developed and is given in Eq. (34)

$$\mathrm{Nu}_{av} = 0.134(\mathrm{Ra}^*_{ro})^{0.264}. \tag{34}$$

In the numerical part of the narrow-gap annulus study, the three-dimensional governing equations were discretized using a finite element formulation and the k–ε model was utilized for simulation of the turbulent flow. From the conjugate numerical results and flow visualization experiments, the latter of which qualitatively confirmed pertinent features of the numerically calculated flow field, the structure of turbulent flow within the annulus was determined. It was shown that the bulk flow is characterized by suction of cold fluid into approximately the lower two-thirds of the aperture plane and ejection of hot fluid at the top as a high-speed buoyant jet. The maximum axial penetration of fluid entering the annulus is at the lowermost angular position and the penetration diminishes in the upward direction. The fluid pathlines in the axial planes of the annulus are concentric circles, indicating a flow pattern similar to that in a narrow channel. As the fluid rises to the top portion of the annulus it reverses axial direction and then leaves the annulus. Fluid rising along the vertical faces adjacent to the inner cylinder becomes entrained in this buoyant flow exiting from the top of the annulus.

From the results of this study, it is seen that there are some major differences in flow characteristics compared to the wheel outboard cavity turbulent flow field previously described. These include the occurrence of channel type flow between the inner and outer cylinders of the narrow annulus as opposed to the free surface type boundary layer flow present in the much wider annular gap of the wheel outboard region, and an absence of the buoyant plume rising from the inner cylinder which is a prominent feature of the wider gap cavity flow. In addition, there is no localized inflow of ambient air above the inner cylinder or outflow below the inner cylinder, which are present in the wider gap cavity. Although the flow behavior in a narrow gap annulus is markedly different in many respects from that in a large-gap open annular cavity, in both cases the interaction between the inner and outer flow fields has been shown to result in locally enhanced heat transfer near the open ends.

In order to identify geometric parameters of the narrow-gap open annulus that are important to improved cooling performance, the effects of variations in inner to outer cylinder annular gap width and inner cylinder length were investigated by Vafai et al. (1997). For the baseline case, an outer-to-inner cylinder radius ratio of $R = 1.1$ and an inner cylinder length-to-radius ratio of $L = 0.5$ were chosen. Two configurations having the baseline inner cylinder length but radius ratios of $R = 1.075$ and $R = 1.05$, respectively, and two configurations having the baseline radius ratio but length-to-radius ratios of $L = 0.375$ and $L = 0.25$, respectively, were also modeled. The studies were carried out up to a Rayleigh number of $\mathrm{Ra}_{ri} = 1 \times 10^6$. At any given Rayleigh number, it was found that the average inner cylinder Nusselt number decreases with a decrease in the gap size between the inner and outer cylinders. The average Nusselt number decreased by approximately 60 percent and 80 percent for radius ratios of $R = 1.075$ and $R = 1.05$, respectively, compared to baseline. For $L = 0.25$, the average Nusselt number was higher than that for the baseline case of $L = 0.5$ up to a Rayleigh number of about $\mathrm{Ra}_{ri} = 6 \times 10^5$, and was lower than baseline above this Rayleigh number. Similar behavior was calculated for $L = 0.375$, except the change in trends occurred at about $\mathrm{Ra}_{ri} = 2 \times 10^5$. It was thus found that at lower Rayleigh numbers reduced length results in greater interaction of the internal and external flows and increased Nusselt number. At higher Rayleigh numbers where the axial penetration of the higher velocity inflow is much greater, the increase in Nusselt number is caused by increased length which results in a higher heat transfer area. These results suggest that an optimum inner cylinder length exists for a given operating condition at which convection heat transfer can be maximized. Correlations for the inner cylinder Nusselt number as a function of Rayleigh number, inner cylinder length to radius ratio, and outer to inner cylinder radius ratio were developed and are provided in Eqs. (35) and (36).

$$\mathrm{Nu}_{av} = 0.2(\mathrm{Ra}_{ri})^{0.14}(1 - 0.705L)[1 + 27.74(R - 1)]: \quad \mathrm{Ra}_{ri} < 1 \times 10^5 \tag{35}$$

$$\mathrm{Nu}_{av} = 0.2(\mathrm{Ra}_{ri})^{0.174}(1 - 0.525L)[1 + 28.01(R - 1)]: \quad 1 \times 10^5 \le \mathrm{Ra}_{ri} \le 1 \times 10^6 \tag{36}$$

Wheel and Brake Assembly

The wheel and brake assembly internal flow regions are comprised of (a) a narrow gap brake stack/wheel annulus which is open to the ambient on the inboard end and bounded on the outboard end by the air space between the stack and wheel web, (b) a wide gap wheel outboard annular cavity which is open to the ambient on the outboard end, and (c) ventilation passages in the wheel web which connect the inboard and outboard regions as shown in Fig. 5. A numerical and experimental investigation of turbulent natural convection in this geometry has recently been performed and the results are introduced in this section. A test section representing the geometry shown in Fig. 5 was employed in the experimental part of this study. Experiments were performed over a range of Rayleigh numbers which encompasses most of the range of aircraft brake operating conditions. Temperature distributions within the wheel and brake components were recorded for use in development of average Nusselt number relations and validation of the numerical model. The numerical results were found to be in excellent agreement with the experimental data. Visualization of the natural convection flow patterns using incense smoke was also performed using the experimental test section. From these tests, the primary features of the flow field predicted by the numerical model were qualitatively verified. Nusselt number correlations for the brake stack were developed from the experimental results. These correlations are of the form

$$\mathrm{Nu}_{av} = A(\mathrm{Ra}^*_{ro})^B \quad (37)$$

where A and B vary from 0.091 to 0.154 and 0.256 to 0.281, respectively, depending on the Rayleigh number range.

In the numerical portion of the investigation, an extended computational domain was utilized to implement the virtually unknown boundary conditions at the open ends. The governing equations (Eqs. (10)–(15)) and the relevant boundary conditions were discretized using a finite element formulation based on the Galerkin method of weighted residuals. The system of discretized equations was solved using a segregated approach in which the global matrix is decomposed into smaller submatrices each associated with only one of the independent variables. The submatrices were solved sequentially using the conjugate gradient and conjugate residual methods for the nonsymmetric and symmetric equation systems, respectively. Convergence of these iterative schemes was assumed to have been achieved when the relative change of each independent variable between successive iterations was less than 0.001.

To ensure the numerical results were not dependent on the grid size, a mesh refinement procedure was adopted in which results for different grid distributions were compared. In this procedure, the number of grid points in the radial direction was first successively increased while the angular and axial grid points were held constant. Keeping the number of axial grid points the same, the number of angular grid points was then successively increased using the grid size in the radial direction obtained from the previous step. With the angular and radial grid sizes thus established, the number of grids in the axial direction was then successively increased. Finally, the number of grids in all three directions were increased to determine the grid size which yielded grid-independent results.

A constant heat flux was applied to the thermally conductive solid elements which form the cylindrical wall and vertical end faces of the brake stack to represent the heat generation within the stack. A reduced value of heat flux was applied to the conductive aluminum wheel elements to account for heating of the wheel by conduction and radiation from the brake stack. To a very reasonable approximation, the aircraft tire surface can be considered to be adiabatic. Therefore, in the numerical model Eq. (21) was applied at the vertical surfaces of the tire facing the open flow region.

The natural convection flow is driven by the temperature differences between the heated surfaces of the wheel and brake assembly and the cooler ambient air. Heat is transferred from these surfaces to air within the internal passageways of the assembly, which produces convective currents due to density gradients which arise in the air. The heated vertical surfaces of the brake stack and wheel hub that are exposed directly to the ambient air induce currents external to the assembly which interact with the air leaving the inboard and outboard annular openings. Particle paths obtained from the numerical model are shown in Figs. 6 and 7 for a Rayleigh number of $\mathrm{Ra}^*_{ro} = 3 \times 10^9$. These paths represent the trajectories of massless fluid particles injected into the flow field immediately outside the brake stack/wheel and wheel outboard cavities at positions within the lower (Fig. 6) and middle to upper regions (Fig. 7) of these cavities. The radial positions of the particle release points ($0.55 \le r \le 1.1$, $\Delta r = 0.05$ at the inboard end and $0.1 \le r \le 1.1$, $\Delta r = 0.1$ at the outboard end) were chosen to encompass the annular opening and heated vertical surface at each end of the assembly. In Fig. 6, the particles which enter the lower portion of the brake stack/wheel annulus or wheel outboard cavity are numbered. It should be noted that the letters a and b designate the release points and end positions, respectively, of the particles. For example, 1a is the release point of particle 1 and 1b is the end position of particle 1. In Figs. 6–8, the physical boundary between the fluid and solid domains is superimposed on the numerical results. In the following discussion of results, the angular position θ is based on a cylindrical coordinate system in which the z-direction corresponds to the axis of the brake stack and $\theta = 0$ deg is at the uppermost vertical location (see Fig. 5).

As seen in Fig. 6(*a*), the suction mechanism draws air axially inward through the brake stack/wheel annulus aperture plane at $\theta = 160$ deg. One of the particles entering the annulus (particle 5) is seen to eventually become entrained in the circumferentially upward flow in the annulus, while the other particles (1, 2, 3, and 4) continue inward until reaching the gap between the brake stack and wheel web, and then rise circumferentially upward along the wheel web. In the upper part of this gap, two of the particles (1 and 2) enter the $\theta = 0$ deg wheel web ventilation passage and are ejected from the wheel outboard cavity in a buoyant stream. The other two particles (3 and 4) pass through the $\theta = 40$ deg ventilation passage and then become entrained in the fluid leaving the top of the wheel outboard cavity. The single particle remaining on the inboard side (particle 5) rises circumferentially in the space between the brake stack and wheel, reverses axial direction, and then proceeds to the brake stack/wheel annulus aperture plane where it is ejected from the top of the annulus in another buoyant stream. The particles introduced at the inboard end of the assembly at $\theta = 160$ deg which do not enter the annulus (for $0.55 \le r \le 0.85$) become entrained in the boundary layer rising along the vertical heated face of the brake stack (Fig. 6(*a*)). This air curves around the obstructing axle surface, rises above the axle in a buoyant plume, and becomes entrained in the air exiting the top of the brake stack/wheel annulus.

The air entering the wheel outboard cavity at $\theta = 160$ deg is drawn axially inward due to the suction mechanism as seen in Fig. 6(*b*). Part of this air (particles 8, 9, 10, and 11) is drawn through the $\theta = 160$ deg ventilation passage, where it subsequently gains energy from the heated brake stack and rises circumferentially upward. Most of this air continues until reaching the upper part of the brake stack, at which point it proceeds axially inboard through the brake stack/wheel gap until finally exiting on the inboard side of the assembly (particles 8, 9, and 10). A smaller portion of the air, however, flows back into the wheel outboard cavity through the $\theta = 0$ deg wheel ventilation passage, and then exits the cavity (particle 11). The air which enters the wheel outboard cavity at $\theta = 160$ deg but does not pass through any of the ventilation passages (particles 6, 7, and 12) becomes entrained in the boundary layers along the wheel outboard cavity surfaces and rises to the top region of the cavity before exiting to the ambient. As shown in Fig. 6(*b*), the air rising alongside the heated vertical face of the wheel hub is drawn slightly inward toward the wheel web due to the local suction effect above the hub. It continues upward and becomes entrained in the buoyant air stream leaving the $\theta = 0$ deg wheel web passage.

The air entering the brake stack/wheel annular gap at $\theta = 140$ deg (Fig. 6(*c*)) does not penetrate quite as far axially as that entering at $\theta = 160$ deg (Fig. 6(*a*)). As a result, all of the particles entering the brake stack/wheel gap at $\theta = 140$ deg (particles 13, 14, 15, 16, and 17) rise circumferentially to the top of the gap and then proceed in the opposite axial direction until exiting the annulus. Thus, it is seen from Figs. 6(*a*) and 6(*c*) that as the angular position of the particle release point is decreased from $\theta = 160$ deg to $\theta = 140$ deg, the particles *originating* from the inboard side no longer cross over to the outboard side through the upper ventilation passages.

The portion of air entering the wheel outboard cavity at $\theta = 140$ deg which crosses over to the inboard side of the wheel web (particles 21, 22, and 23) does so through the $\theta = 120$ deg ventilation passage as seen in Fig. 6(*d*). Instead of most of this air exiting the brake stack/wheel annulus on the inboard side, as it does when introduced at $\theta = 160$ deg (Fig. 6(*b*)),

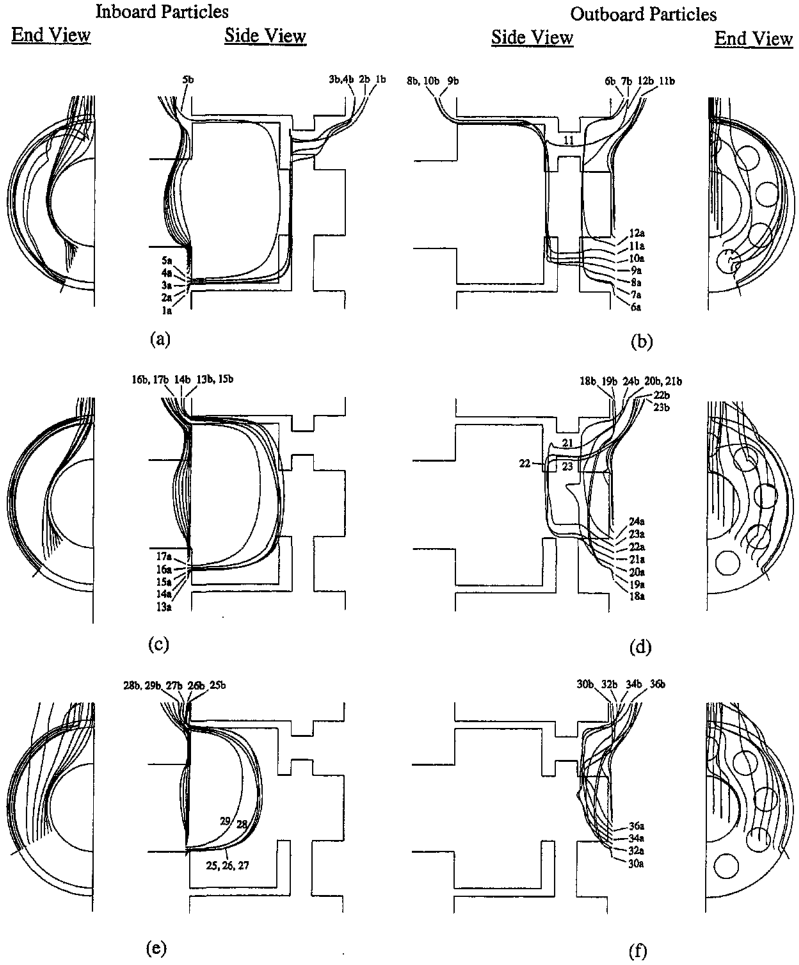

Fig. 6 Trajectories of particles released in the lower portion of the braking system inboard and outboard regions at (a) and (b) θ = 160 deg, (c) and (d) θ = 140 deg, and (e) and (f) θ = 120 deg for $\mathrm{Ra}_{ro}^{*} = 3 \times 10^{9}$

all of the air now crosses back over to the wheel outboard cavity through the $\theta = 0$ deg (particle 21) and $\theta = 40$ deg (particles 22 and 23) passages (Fig. 6(*d*)). Therefore, it is seen that by reducing the outboard particle release point from $\theta = 160$ deg to $\theta = 140$ deg, the ensuing flow routes through the wheel web ventilation passages change dramatically.

With a further decrease in release position to $\theta = 120$ deg, the axial penetration of particles introduced on the inboard side of the assembly (particles 25, 26, 27, 28, and 29) decreases further, as seen in Fig. 6(*e*). The air entering the wheel outboard cavity at $\theta = 120$ deg no longer passes through any of the ventilation passages (Fig. 6(*f*)). Instead, all of this air becomes entrained in the boundary layers on the wheel surfaces, rises upward, and exits the cavity.

The trajectories of particles released at $\theta = 90$ deg, 60 deg, and 30 deg are shown in Figs. 7(*a*), 7(*b*), and 7(*c*), respectively. As the circumferential release point is decreased from $\theta = 120$ deg to $\theta = 90$ deg, the axial penetration of both the inboard and outboard particles diminishes even further as seen by comparing Figs. 6(*e*) and 6(*f*) with Fig. 7(*a*). In Fig. 7(*a*), it is seen that the air rising along the vertical face of the brake stack does not enter the brake stack/wheel annulus at angular positions less than approximately $\theta = 60$ deg. The air entering between $\theta = 90$ deg and $\theta = 60$ deg travels a relatively short distance before exiting near the top of the annular gap. Particles introduced at angular positions of $\theta = 60$ deg and $\theta = 30$ deg do not enter the brake stack/wheel annulus but rise past the open end instead, as seen in Figs. 7(*b*) and 7(*c*), respectively. On the outboard side of the assembly at $\theta = 60$ deg, ambient air penetrates into the wheel cavity only a small distance before reversing axial direction and exiting the wheel outboard cavity (Fig. 7(*b*)). At $\theta = 30$ deg, the ambient air no longer enters the wheel outboard cavity (Fig. 7(*c*)). As seen in Figs. 6 and 7, the ventilation passages in the wheel web are utilized only by the air originally entering the lower portions of the braking system inboard and outboard annular openings.

A vector plot of the natural convection velocity field at the angular symmetry plane is provided in Fig. 8(*a*) for $\mathrm{Ra}_{ro}^{*} = 3 \times 10^{9}$. The local influx of ambient air into the bottom of the brake stack/wheel annulus and the velocity profiles of air flowing axially through the bottom of this annulus are clearly seen. As this air progresses toward the outboard end of the brake stack, the axial velocity decreases due to some of the air becoming entrained in the circumferentially upward flow in the annulus. At the top of the annulus, a stagnant region is seen to be present near the outboard end of the stack. On the inboard side of this stagnant region, the axial velocity increases rapidly with decreasing distance from the annulus inboard opening as more of the air rising in the annulus collects at the top and proceeds toward the opening. The air exits the top of the brake stack/wheel annulus in a high-speed buoyant jet, which entrains the heated air rising from the upper vertical face of the stack. On the outboard side of the stagnant region, the air in the top portion of the gap between the brake stack and wheel web enters the uppermost wheel web ventilation passage and then exits the entire assembly as a high speed buoyant jet of air. The air at

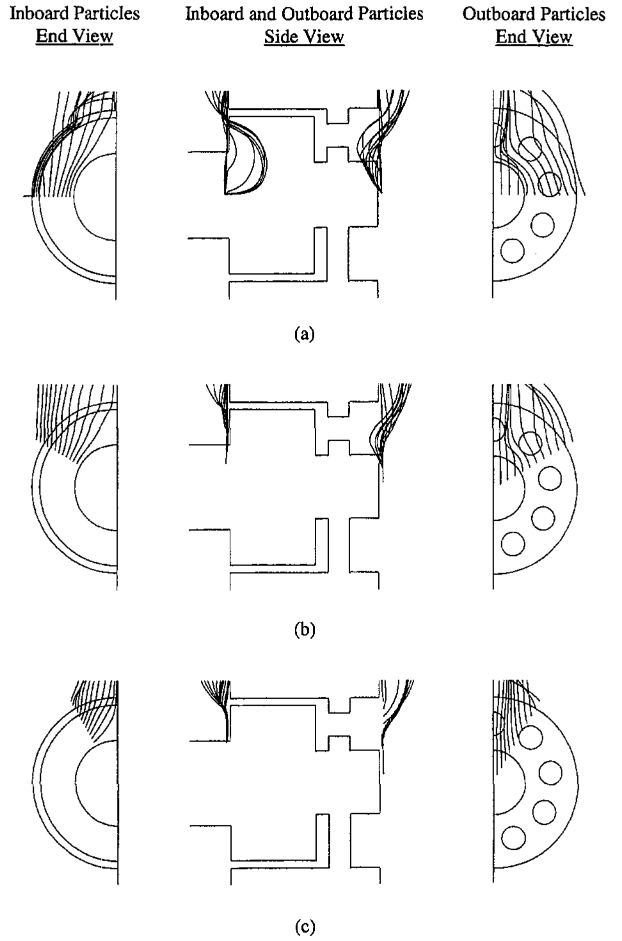

Fig. 7 **Trajectories of particles released in the middle and upper portions of the braking system inboard and outboard regions at (*a*) θ = 90 deg, (*b*) θ = 60 deg, and (*c*) θ = 30 deg for Ra$_{ro}^*$ = 3 × 10^9**

the top of the wheel outboard cavity and that rising from the surfaces of the wheel hub become entrained in this jet. The buoyant jet at the upper portion of the brake stack/wheel annulus, which is characteristic of open cavity flows, and that exiting from the uppermost wheel web ventilation passage are the most prominent features of the braking system flow field.

The isotherms in the angular symmetry plane calculated numerically for Ra$_{ro}^*$ = 3 × 10^9 are shown in Fig. 8(*b*). The suction of cold ambient air into the bottom of the brake stack/wheel annulus and the increasing thermal boundary layer thickness as the air proceeds axially toward the end of the brake stack are evident in the isotherms. The inflow of cold air from the annulus into the gap between the brake stack and wheel web is also apparent. The increase in thermal boundary layer thickness along the lower part of the brake stack vertical surface facing the inboard ambient region and along the wheel hub vertical surface facing the outboard ambient region is distinctly seen. The significant distortion of isotherms adjacent to the top of the brake stack/wheel annulus open end reflect the presence of the buoyant jet leaving the annulus. Likewise, at the top of the outboard end of the assembly the distorted isotherms are indicative of the buoyant jet leaving the uppermost wheel web ventilation passage. The isotherms next to the surfaces in the bottom of the brake stack/wheel annulus and the bottom of the wheel outboard cavity are spaced relatively close together compared to corresponding locations at the top of the assembly. This is indicative of the higher heat transfer rates at the bottom locations which results from thermal boundary layer development and the increase in bulk temperature of the air as it rises within the heated annular regions of the assembly. The numerically calculated temperatures of the wheel and brake components were found to be in excellent agreement with those obtained experimentally.

Based on the presented detailed aspects of the flow field and temperature distribution, a number of overall attributes can be cited. For example, it has been determined that ambient air is drawn into the narrow gap brake stack/wheel annulus and large gap wheel outboard annular cavity over roughly the lower two-thirds of the open ends, and heated air is ejected to the ambient across approximately the upper one-third of these openings. This was confirmed by plotting the axial velocities at the inboard and outboard aperture planes. Since the incoming air occupies a much larger segment of the annulus opening than the outgoing air, its velocity is lower due to conservation of mass. It was shown that a portion of the ambient air entering the bottom of the brake stack/wheel and wheel outboard annular openings flows through the wheel web ventilation passages, while the air entering in the

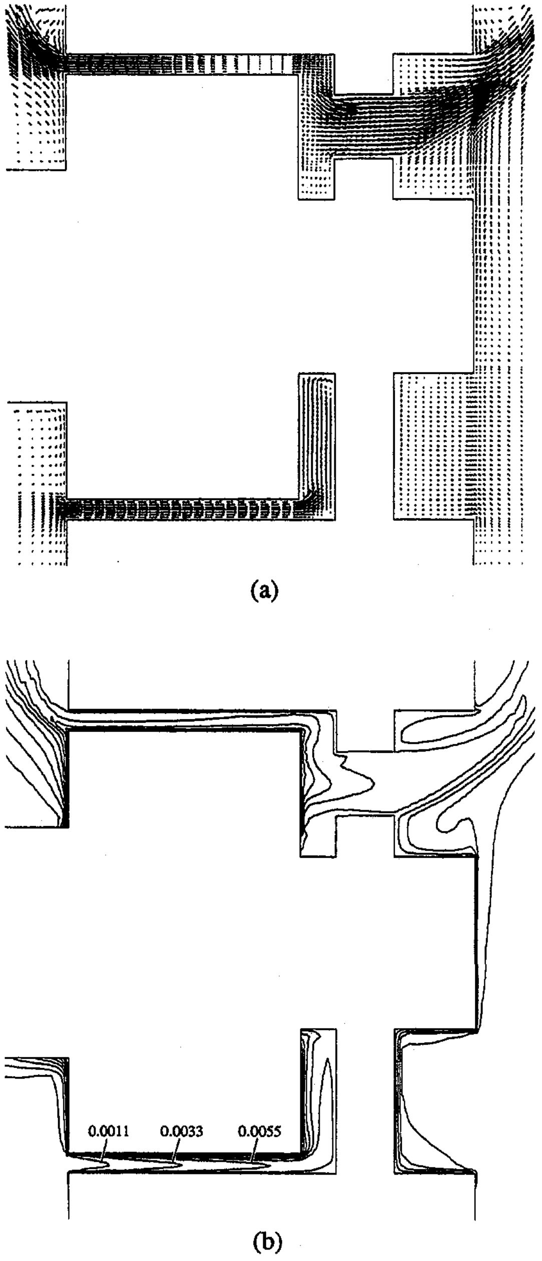

Fig. 8 **Natural convection in the angular symmetry plane for Ra$_{ro}^*$ = 3 × 10^9; (*a*) velocity field, (*b*) isotherms**

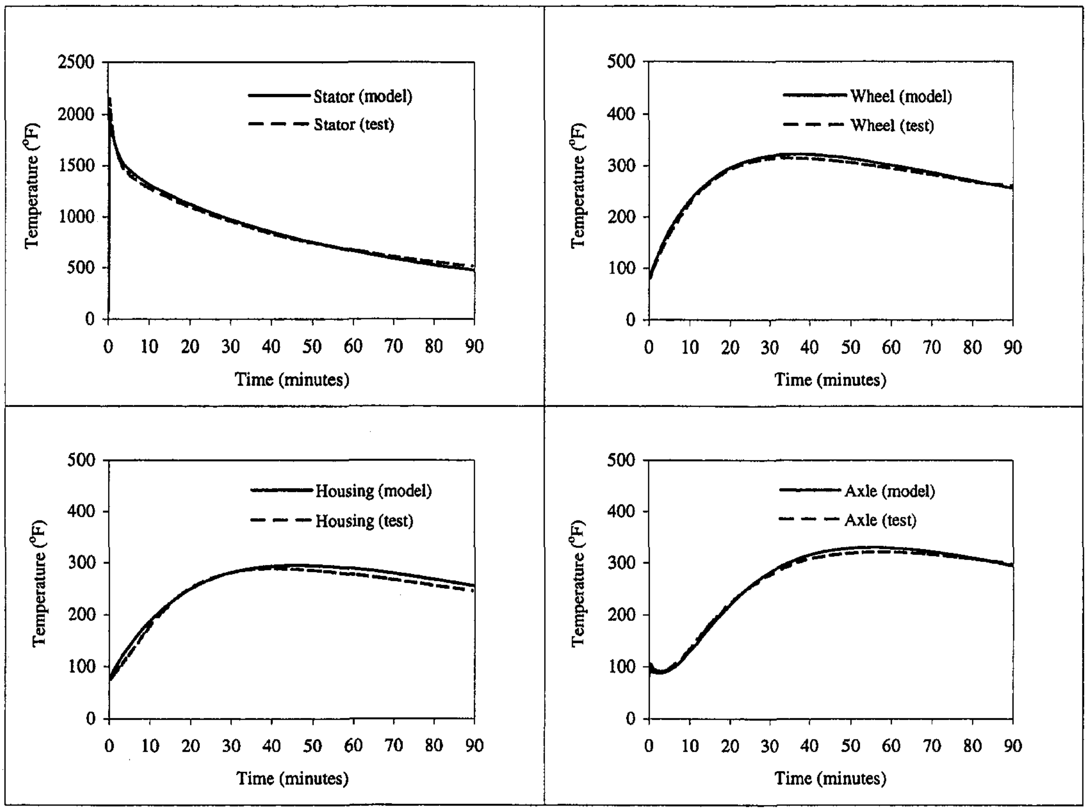

Fig. 9 Comparison of calculated temperature responses of aircraft braking system components with experimental data

middle portion of these openings does not. The primary features of the braking system natural convection flow field seen in the numerical results were confirmed in the flow visualization studies, where the previously described air inflow and outflow boundaries, strong buoyant outflow of air at the top of the annular cavities, and crossover of air from the outboard to inboard and inboard to outboard sides of the wheel web were observed.

The results of the experimental and numerical investigations of the wheel and brake assembly domain and the braking system subdomains were utilized to develop convective heat transfer coefficient relationships for different regions of the braking system as a function of Rayleigh number and the primary geometric parameters. These relationships were integrated into a braking system thermal analysis code developed and employed by Aircraft Braking Systems Corporation. An example of results obtained from this code using the convection coefficient relationships is presented in Fig. 9, which shows the calculated temperature responses of critical components of the aircraft wheel and brake after a braking event. Measured temperature responses obtained from a dynamometer test using full-scale braking system hardware are also plotted in Fig. 9. The braking system thermal model results are seen to be in excellent agreement with the experimental data, further verifying the convective heat transfer results from the studies of the wheel and brake assembly domain and braking system subdomains.

Summary

This work has discussed the practical significance of the brake cooling problem and has reviewed both fundamental considerations and recent developments in analysis of aircraft brake natural convection. The recent investigations of geometries and thermal conditions relevant to the aircraft braking system have arisen from a nearly complete absence of studies focused on this application only a decade ago. Numerical simulations of the wheel and brake assembly natural convection flow field have been developed and are now being utilized in industry for cooling optimization, thereby reducing the need for costly experimentation. A great deal has been learned about the characteristics of the buoyancy-induced flow and heat transfer, and progress has been made toward defining more efficient thermal designs. However, there are still unanswered questions concerning enhanced cooling design trade-offs and the effects of more detailed geometric features on cooling performance. It is expected that this will foster considerable continuing activity in this field.

The presented numerical and experimental investigation has established in detail the basic structure of natural convection flow within the aircraft wheel and brake assembly and shown that the physical mechanisms underlying buoyancy-induced flow in basic open-ended annuli are also strongly present in the braking system. The bulk flow is characterized by suction of air into the middle and lower regions of the narrow gap brake stack/wheel annulus and wide gap wheel outboard annular cavity, overall upward movement as the air is heated by the brake stack and wheel surfaces, outflow of air over roughly the top one-third of the inboard and outboard annular openings, and ejection of hot air from the top of the brake stack/wheel annulus and uppermost wheel web ventilation passage in separate strong buoyant jets. The wheel web ventilation passages connecting the inboard and outboard regions are utilized only by the air originally entering the bottom of the inboard and outboard annular openings. The primary features of the flow field and the temperature distribution in the wheel and brake components resulting from the buoyancy-induced flow were verified experimentally. Results of the numerical and experimental investigation were utilized to develop convective heat transfer relationships for different regions of the braking system. The results from a thermal model of the braking system which employed these relationships were found to be in excellent agreement with experimental data obtained from full scale braking system hardware.

Acknowledgments

The authors gratefully acknowledge and appreciate the support of Aircraft Braking Systems Corporation for the past few years.

References

Abib, A. H., and Jaluria, Y., 1988, "Numerical Simulation of the Buoyancy-Induced Flow in a Partially Open Enclosure," *Numerical Heat Transfer,* Vol. 14, pp. 235–254.

Bejan, A., and Kimura, S., 1981, "Penetration of Free Convection Into a Lateral Cavity," *Journal of Fluid Mechanics,* Vol. 103, pp. 465–478.

Bishop, E. H., and Carley, C. T., 1966, "Photographic Studies of Natural Convection Between Concentric Cylinders," *Proceedings of the 1966 Heat Transfer and Fluid Mechanics Institute,* pp. 63–78.

Bishop, E. H., 1988, "Heat Transfer by Natural Convection of Helium Between Horizontal Isothermal Concentric Cylinders at Cryogenic Temperature," ASME Journal of Heat Transfer, Vol. 110, pp. 109–115.

Braun, M. J., Daniels, C. C., Dyko, M. P., and Krga, V., 1997, "Temperature Distribution and Flow Characteristics of a Concentric Horizontal Cylinder Configuration," *Proceedings of the 1997 ASME Fluids Engineering Division Summer Meeting,* Paper No. FEDSM-3088.

Chan, Y. L., and Tien, C. L., 1983, "Laminar Natural Convection in Shallow Open Cavities," *Natural Convection in Enclosures,* HTD-Vol. 26, ASME, New York, pp. 77–82.

Chan, Y. L., and Tien, C. L., 1985a, "A Numerical Study of Two-Dimensional Natural Convection in Square Open Cavities," *Numerical Heat Transfer,* Vol. 8, pp. 65–80.

Chan, Y. L., and Tien, C. L., 1985b, "A Numerical Study of Two-Dimensional Laminar Natural Convection in Shallow Open Cavities," *International Journal of Heat and Mass Transfer,* Vol. 28, pp. 603–612.

Chan, Y. L., and Tien, C. L., 1986, "Laminar Natural Convection in Shallow Open Cavities," ASME Journal of Heat Transfer, Vol. 108, pp. 305–309.

Clark, S. K., and Dodge, R. N., 1984, "Heat Generation in Aircraft Tires Under Braked Rolling Conditions," NASA Contractor Report 3768.

Currey, N. S., 1988, "Aircraft Landing Gear Design: Principles and Practices," AIAA Education Series, pp. 137–173.

Desai, C. P., and Vafai, K., 1992, "Three-Dimensional Buoyancy Induced Flow and Heat Transfer Around the Wheel Outboard of an Aircraft," *International Journal of Heat and Fluid Flow,* Vol. 13, pp. 50–64.

Desai, C. P., and Vafai, K., 1993, "Investigation of the Temporal Thermal Performance of the Wheel Outboard of an Aircraft," *Journal of Thermophysics and Heat Transfer,* Vol. 7, pp. 377–384.

Desai, C. P., and Vafai, K., 1994, "An Investigation and Comparative Analysis of Two- and Three-Dimensional Turbulent Natural Convection in a Horizontal Annulus," *International Journal of Heat and Mass Transfer,* Vol. 37, pp. 2475–2504.

Desai, C. P., and Vafai, K., 1996, "Experimental and Numerical Study of Buoyancy-Induced Flow and Heat Transfer in an Open Annular Cavity," *International Journal of Heat and Mass Transfer,* Vol. 39, pp. 2053–2066.

Desai, C. P., Vafai, K., and Dyko, M. P., 1996, "Heat Transfer Optimization Within Open-Ended Annular Cavities," *Journal of Thermophysics and Heat Transfer,* Vol. 11, pp. 121–124.

Dyko, M. P., and Chung, B. T. F., 1990, "Finite Element Thermal Model of an Aircraft Wheel and Carbon Brake Assembly," *SAE Transactions, Journal of Aerospace,* Paper No. 901909.

Dyko, M. P., Vafai, K., and Mojtabi, A. K., 1999, "A Numerical and Experimental Investigation of Stability of Natural Convective Flows Within a Horizontal Annulus," *Journal of Fluid Mechanics,* in press.

Ettefagh, J., and Vafai, K., 1988, "Natural Convection in Open-Ended Cavities With a Porous Obstructing Medium," *International Journal of Heat and Mass Transfer,* Vol. 31, pp. 673–693.

Ettefagh, J., and Vafai, K., 1991, "An Investigation of Ejection, Mixing, and Suction Mechanisms in an Open-Ended Horizontal Annulus," ASME Journal of Heat Transfer, Vol. 113, pp. 1025–1028.

Ettefagh, J., Vafai, K., and Kim, S. J., 1991, "Non-Darcian Effects in Open-Ended Cavities Filled With a Porous Medium," ASME Journal of Heat Transfer, Vol. 113, pp. 747–756.

Farouk, B., and Guceri, S. I., 1982, "Laminar and Turbulent Natural Convection in the Annulus Between Horizontal Concentric Cylinders," ASME Journal of Heat Transfer, Vol. 104, pp. 631–636.

Fukuda, K., Yasutomi, M., and Hasegawa, S., 1990, "Analytical and Experimental Study on Turbulent Natural Convection in a Horizontal Annulus," *International Journal of Heat and Mass Transfer,* Vol. 33, pp. 629–639.

Fukuda, K., Yasutomi, M., Taniguchi, N., Morita, K., and Hasegawa, S., 1991, "Direct Simulation and Large Eddy Simulation of Turbulent Natural Convection in Horizontal Annulus," *Memoirs of Faculty of Engineering–Kyushu University,* Vol. 51, pp. 355–369.

Fusegi, T., and Farouk, B., 1986, "A Three-Dimensional Study of Natural Convection in the Annulus Between Horizontal Concentric Cylinders," *Proceedings of the Eighth International Heat Transfer Conference,* Vol. 4, pp. 1575–1580.

Greenbank, S. J., 1991, "Landing Gear–The Aircraft Requirement," *Proceedings of The Institution of Mechanical Engineers, Part G: Journal of Aerospace Engineering,* Vol. 205, pp. 27–34.

Grigull, U., and Hauf, W., 1966, "Natural Convection in Horizontal Cylindrical Annuli," *Proceedings of the Third International Heat Transfer Conference,* Vol. 2, pp. 182–195.

Haroutunian, V., and Engelman, M. S., 1991, "On Modeling Wall-Bound Turbulent Flows Using Specialized Near-Wall Finite Elements and the Standard k–ε Model," *Advances in Numerical Simulation of Turbulent Flows,* FED-Vol. 117, ASME, New York, pp. 97–105.

Hess, C. F., and Henze, R. H., 1984, "Experimental Investigation of Natural Convection Losses From Open Cavities," ASME Journal of Heat Transfer, Vol. 106, pp. 333–338.

Humphrey, J. A. C., and To, W. M., 1986, "Numerical Simulation of Buoyant, Turbulent Flow–II. Free and Mixed Convection in a Heated Cavity," *International Journal of Heat and Mass Transfer,* Vol. 29, pp. 593–610.

Iyer, S. V., and Vafai, K., 1997, "Effects of a Geometric Perturbation on Buoyancy Induced Flow and Heat Transfer in a Cylindrical Annulus," *International Journal of Heat and Mass Transfer,* Vol. 40, pp. 2901–2911.

Iyer, S. V., and Vafai, K., 1998, "Buoyancy Induced Flow and Heat Transfer in a Cylindrical Annulus With Multiple Perturbations," *International Journal of Heat and Mass Transfer,* Vol. 41, pp. 3025–3035.

Kuehn, T. H., and Goldstein, R. J., 1976, "An Experimental and Theoretical Study of Natural Convection in the Annulus Between Horizontal Concentric Cylinders," *Journal of Fluid Mechanics,* Vol. 74, pp. 695–719.

Kuehn, T. H., and Goldstein, R. J., 1978, "An Experimental Study of Natural Convection Heat Transfer in Concentric and Eccentric Horizontal Cylindrical Annuli," ASME Journal of Heat Transfer, Vol. 100, pp. 635–640.

Le Quere, P., Humphrey, J. A. C., and Sherman, F. S., 1981, "Numerical Calculation of Thermally Driven Two-Dimensional Unsteady Natural Convection Flow in Cavities of Rectangular Cross-Section," *Numerical Heat Transfer,* Vol. 4, pp. 249–283.

Liu, C., Mueller, W. K., and Landis, F., 1961, "Natural Convection Heat Transfer in Long Horizontal Cylindrical Annuli," *International Developments in Heat Transfer,* Part V, pp. 976–984.

Mahoney, D. N., Kumar, R., and Bishop, E. H., 1986, "Numerical Investigation of Variable Property Effects on Laminar Natural Convection of Gases Between Two Horizontal Isothermal Concentric Cylinders," ASME Journal of Heat Transfer, Vol. 108, pp. 783–789.

McLeod, A. E., and Bishop, E. H., 1989, "Turbulent Natural Convection of Gases in Horizontal Cylindrical Annuli at Cryogenic Temperatures," *International Journal of Heat and Mass Transfer,* Vol. 32, pp. 1967–1978.

Miyamoto,·M., Kuehn, T. H., Goldstein, R. J., and Katoh, Y., 1989, "Two-Dimensional Laminar Natural Convection Heat Transfer From a Fully or Partially Open Square Cavity," *Numerical Heat Transfer,* Part A, Vol. 15, pp. 411–430.

Mohamad, A. A., 1995, "Natural Convection in Open Cavities and Slots," *Numerical Heat Transfer,* Part A, Vol. 27, pp. 705–716.

Morita, K., Nakamura, Y., Taniguchi, N., Fukuda, K., and Hasegawa, S., 1990, "Unsteady Three-Dimensional Behavior of Natural Convection in Horizontal Annulus–Validity of Direct Numerical Simulation of Turbulent Natural Convection," *Journal of the Atomic Energy Society of Japan,* Vol. 32, pp. 719–727.

Ozoe, H., Okamato, T., and Churchill, S. W., 1979, "Natural Convection in a Vertical Annular Space Heated From Below," *Heat Transfer–Japanese Research,* Vol. 8, pp. 82–93.

Ozoe, H., Shibata, T., and Churchill, S. W., 1981, "Natural Convection in an Inclined Circular Cylindrical Annulus Heated and Cooled On Its End Plates," *International Journal of Heat and Mass Transfer,* Vol. 24, pp. 727–737.

Penot, F., 1982, "Numerical Calculation of Two-Dimensional Natural Convection in Isothermal Open Cavities," *Numerical Heat Transfer,* Vol. 5, pp. 421–437.

Powe, R. E., Carley, C. T., and Bishop, E. H., 1969, "Free Convective Flow Patterns in Cylindrical Annuli," ASME Journal of Heat Transfer, Vol. 91, pp. 310–314.

Rao, Y. F., Miki, Y., Fukuda, K., Takata, Y., and Hasegawa, S., 1985, "Flow Patterns of Natural Convection in Horizontal Cylindrical Annuli," *International Journal of Heat and Mass Transfer,* Vol. 28, pp. 705–714.

Skok, H., Ramadhyani, S., and Schoenhals, R. J., 1991, "Natural Convection in a Side-Facing Open Cavity," *International Journal of Heat and Mass Transfer,* Vol. 12, pp. 36–45.

Takata, Y., Iwashige, K., Fukuda, K., and Hasegawa, S., 1984, "Three-Dimensional Natural Convection in An Inclined Cylindrical Annulus," *International Journal of Heat and Mass Transfer,* Vol. 27, pp. 747–754.

Vafai, K., and Ettefagh, J., 1990a, "The Effects of Sharp Corners on Buoyancy-Driven Flows with Particular Emphasis on Outer Boundaries," *International Journal of Heat and Mass Transfer,* Vol. 33, pp. 2311–2328.

Vafai, K., and Ettefagh, J., 1990b, "Thermal and Fluid Flow Instabilities in Buoyancy-Driven Flows in Open-Ended Cavities," *International Journal of Heat and Mass Transfer,* Vol. 33, pp. 2329–2344.

Vafai, K., and Ettefagh, J., 1991a, "An Investigation of Transient Three-Dimensional Buoyancy-Driven Flow and Heat Transfer in a Closed Horizontal Annulus," *International Journal of Heat and Mass Transfer,* Vol. 34, pp. 2555–2570.

Vafai, K., and Ettefagh, J., 1991b, "Axial Transport Effects on Natural Convection Inside of an Open-Ended Annulus," ASME Journal of Heat Transfer, Vol. 113, pp. 627–634.

Vafai, K., Desai, C. P., Iyer, S. V., and Dyko, M. P., 1997, "Buoyancy-Induced Convection in a Narrow Open-Ended Annulus," ASME Journal of Heat Transfer, Vol. 119, pp. 483–494.

Analysis of Unsteady Heat and Mass Transfer During the Modified Chemical Vapor Deposition Process

K. S. Park
Graduate Student

M. Choi
Associate Professor,
e-mail: mchoi@plaza.snu.ac.kr,
Mem. ASME.

Department of Mechanical Engineering,
Seoul National University,
Seoul 151-742, Korea

An analysis of unsteady heat and mass transfer in the modified chemical vapor deposition has been carried out. It is found that the commonly used quasi-steady-state assumption could be used to predict the overall efficiency of particle deposition; however, the assumption would not be valid near the inlet region where tapered deposition occurs. The present unsteady calculations have been found to be capable of predicting the detailed deposition profile correctly even from the inlet region where further optimization is needed at a practical situation. The present results have also been compared with existing experimental data and were in good agreement. It is noted that previous quasi-steady calculation resulted in a significant difference in the deposition profile near the inlet region. The effects of time-varying torch speeds were also studied. The case of a linearly varying torch speed resulted in a much shorter tapered entry than the case of a constant torch speed.

Introduction

In the MCVD (modified chemical vapor deposition) process (MacChesney et al., 1974) which is currently utilized to manufacture high quality optical fibers, chemical reagents flow in a rotating fused silica tube which is heated by a slowly traversing oxy-hydrogen torch. As the torch moves, the gases are heated and chemical reactions take place. This results in the formation of glassy particles, which drift along with gases and deposit on the cold surface ahead of the torch due to the temperature gradient between gases and tube wall (Thermophoresis; Simpkins et al., 1979). Since the refractive index profile should be controlled by varying chemical compositions for each sweep, the torch should traverse several times to obtain the desired variation of refractive index. After the desired layers are deposited, the tube is collapsed into a solid rod, which is called a preform of an optical fiber. The preform is then drawn to produce a typical 125 μm diameter optical fiber. Since the deposited film is tapered near the torch starting region (this must be removed for a high-quality final product), every effort should be made to reduce the tapered entry section.

Simpkins et al. (1979) have made clear that the main mechanism of particle deposition in MCVD is thermophoresis. Walker et al. (1980) studied thermophoretic particle transport numerically and experimentally and presented the correlation between overall efficiency and minimum temperature. Laser-enhanced MCVD was investigated by Wang et al. (1985) and Morse et al. (1986). A study of chemical kinetics and silica aerosol dynamics has been carried out by Kim and Pratsinis (1988). Fiebig et al. (1988) and Choi and Park (1994) investigated the method of using an annular tube and showed that this method could remarkably reduce the tapered entry section. Three-dimensional effects due to tube rotation and buoyancy have been studied by Choi et al. (1990) and Lin et al. (1992). Park and Choi (1994) proposed a two-torch model which considered repeatedly traversing torch and discussed the effect of torch speed and tube wall thickness. Cho and Choi (1995) measured the axial variation of deposited film thickness and tube wall temperatures. The effects of chemical reactions have been studied by Joh et al. (1993).

A quasi-steady assumption has been used in previous studies, and requires constant operating conditions. Even though the constant operating conditions are satisfied, a quasi-steady assumption may not be valid near the inlet region where nonuniform deposition occurs. An unsteady analysis should be carried out to predict the deposition accurately near the torch starting region. Moreover, a prediction of the deposition profile when the torch speed varies with time as in real practice calls for a full unsteady calculation of heat and mass transfer, which is our present subject. This unsteady calculation can also test the validity of quasi-steady modeling used in the previous studies.

For the present unsteady calculation, the quartz tube is included in the calculation domain and the effects of chemical reaction and variable properties of fluid and tube are also included. The effects of torch speed variation with time on deposition performance are also examined.

Analysis

The mixture of chemical reagents flows in the rotating tube, as shown in Fig. 1. It has been shown (Lin et al., 1992) that for normal rotational speeds (60 ~ 120 rpm) uniform deposition in the circumferential direction can be assumed. The axisymmetric, two-dimensional unsteady analysis, including chemical reaction and variable properties of fluid and tube, is done. The present work describes a complex, coupled, heat and mass transfer problem including conduction in the solid tube wall, convection in gases and temperature-dependent thermophoretic particle transport with unsteady wall temperatures that are not known a priori but to be determined. Therefore, computation domain includes a gas flow inside the tube and a tube itself. Finite volume method has been applied to solve unsteady governing equations.

The unsteady governing equations for gases are

Contributed by the Heat Transfer Division for publication in the JOURNAL OF HEAT TRANSFER. Manuscript received by the Heat Transfer Division, Mar. 24, 1997; revision received, Mar. 13, 1998. Keywords: Heat Transfer, Mass Transfer, Materials, Unsteady, Vapor Deposition. Associate Technical Editor: M. Modest.

continuity

$$\frac{R_i}{L}\frac{V_{\mathrm{torch}}}{U_0}\frac{\partial \rho'}{\partial t'} + \frac{R_i}{L}\frac{\partial}{\partial x'}(\rho' u') + \frac{1}{r'}\frac{\partial}{\partial r'}(r'\rho' v') = 0 \quad (1)$$

momentum

$$\frac{R_i}{L}\frac{V_{\mathrm{torch}}}{U_0}\rho'\frac{\partial u'}{\partial t'} + \frac{R_i}{L}\rho' u'\frac{\partial u'}{\partial x'} + \rho' v'\frac{\partial u'}{\partial r'} = -\frac{R_i}{L}\frac{\partial p'}{\partial x'}$$
$$+ \frac{2}{\mathrm{Re}}\left\{\frac{2}{3}\frac{R_i}{L}\frac{\partial}{\partial x'}\left[\mu'\left(2\frac{R_i}{L}\frac{\partial u'}{\partial x'} - \frac{\partial v'}{\partial r'} - \frac{v'}{r'}\right)\right]\right.$$
$$\left. + \frac{1}{r'}\frac{\partial}{\partial r'}\left[r'\mu'\left(\frac{\partial u'}{\partial r'} + \frac{R_i}{L}\frac{\partial v'}{\partial x'}\right)\right]\right\} \quad (2a)$$

$$\frac{R_i}{L}\frac{V_{\mathrm{torch}}}{U_0}\rho'\frac{\partial v'}{\partial t'} + \frac{R_i}{L}\rho' u'\frac{\partial v'}{\partial x'} + \rho' v'\frac{\partial v'}{\partial r'}$$
$$= -\frac{\partial p'}{\partial r'} + \frac{2}{\mathrm{Re}}\left\{\frac{R_i}{L}\frac{\partial}{\partial x'}\left[\mu'\left(\frac{\partial u'}{\partial r'} + \frac{R_i}{L}\frac{\partial v'}{\partial x'}\right)\right]\right.$$
$$+ \frac{2}{3r'}\frac{\partial}{\partial r'}\left[r'\mu'\left(2\frac{\partial v'}{\partial r'} - \frac{R_i}{L}\frac{\partial u'}{\partial x'} - \frac{v'}{r'}\right)\right]$$
$$\left. + \frac{2\mu'}{3r'}\left(\frac{R_i}{L}\frac{\partial u'}{\partial x'} + \frac{\partial v'}{\partial r'} - \frac{2v'}{r'}\right)\right\} \quad (2b)$$

energy

$$\frac{R_i}{L}\frac{V_{\mathrm{torch}}}{U_0}\rho' c_p'\frac{\partial T'}{\partial t'} + \frac{R_i}{L}\rho' c_p' u'\frac{\partial T'}{\partial x'} + \rho' c_p' v'\frac{\partial T'}{\partial r'}$$
$$= \frac{2}{\mathrm{Pe}_T}\left\{\left(\frac{R_i}{L}\right)^2\frac{\partial}{\partial x'}\left(k'\frac{\partial T'}{\partial x'}\right) + \frac{1}{r'}\frac{\partial}{\partial r'}\left(r'k'\frac{\partial T'}{\partial r'}\right)\right\}$$
$$+ \frac{Y_{\mathrm{SiCl_4},0}R_i}{c_{p,0}U_0(T_{\max} - T_0)}r'_{\mathrm{SiCl_4}}\Delta H_{\mathrm{SiCl_4}} \quad (3)$$

species

$$\frac{R_i}{L}\frac{V_{\mathrm{torch}}}{U_0}\rho'\frac{\partial Y_i'}{\partial t'} + \frac{R_i}{L}\rho' u'\frac{\partial Y_i'}{\partial x'} + \rho' v'\frac{\partial Y_i'}{\partial r'}$$
$$= \frac{2}{\mathrm{Pe}_D}\left\{\left(\frac{R_i}{L}\right)^2\frac{\partial}{\partial x'}\left(\rho' D_i'\frac{\partial Y_i'}{\partial x'}\right)\right.$$
$$\left. + \frac{1}{r'}\frac{\partial}{\partial r'}\left(r'\rho' D_i'\frac{\partial Y_i'}{\partial r'}\right)\right\} + \frac{\nu_i'' R_i}{U_0}r'_{\mathrm{SiCl_4}}\frac{M_i}{M_{\mathrm{SiCl_4}}} \quad (4)$$

where Y_i', D_i' and M_i denote dimensionless mass fraction, dimensionless diffusion coefficient and molecular weight of species i ($SiCl_4$, O_2, Cl_2), respectively. $\Delta H_{\mathrm{SiCl_4}}$ represents the reaction enthalpy and $r'_{\mathrm{SiCl_4}}$ is the nondimensionalized reaction rate

Nomenclature

c_p = specific heat at constant pressure of gas
c_p' = $c_p/c_{p,0}$
D_i = diffusion coefficient of species i ($SiCl_4$, O_2, Cl_2)
D_i' = $D_i/D_{i,0}$
E = deposition efficiency
E_a = activation energy
$\Delta H_{\mathrm{SiCl_4}}$ = enthalpy of formation of $SiCl_4$ ((J/kg))
h = convection heat transfer coefficient
K = thermophoretic coefficient
k = thermal conductivity
k' = k/k_0
k_B = Boltzmann's constant
k_{cond}, k_{rad} = thermal conductivities due to pure conduction and radiation
L = length of quartz tube
m = mass
M_i = molecular weight of species i ($SiCl_4$, O_2, SiO_2, Cl_2)
n = refractive index of quartz
Pe_D = Peclet number for mass transfer ($2U_0R_i/D_{i,0}$)
Pe_T = Peclet number for heat transfer ($2\rho_0 c_{p,0}U_0R_i/k_0$)
p = pressure
p' = dimensionless pressure ($p/\rho_0U_0^2$)
$q_{\max}$ = maximum heat flux
r = radial coordinate
r' = dimensionless radial coordinate (r/R_i)
R_G = universal gas constant
R_i, R_o = inner and outer radii of tube
Re = Reynolds number ($2\rho_0U_0R_i/\mu_0$)
$r_{\mathrm{SiCl_4}}$ = reaction rate of $SiCl_4$ oxidation ((Kg/m^{3}s))
$r'_{\mathrm{SiCl_4}}$ = $r_{\mathrm{SiCl_4}}/(\rho_0Y_{\mathrm{SiCl_4},0})$
t = time
t' = dimensionless time ($t/(L/V_{\mathrm{torch}})$)
T = temperature
T' = dimensionless temperature ($(T - T_0)/(T_{\max} - T_0)$)
$T_{\max}$ = maximum temperature on the outer surface of the tube
T_0 = inlet temperature
T_∞ = ambient temperature
u = axial velocity of gas
u' = dimensionless axial velocity of gas (u/U_0)
v = radial velocity of gas
v' = dimensionless radial velocity of gas (v/U_0)
U_0 = averaged inlet velocity of gas
u_T = axial thermophoretic velocity ($-K\nu(\partial/\partial x)(\ln T)$)
u_T' = u_T/U_0
v_T = radial thermophoretic velocity ($-K\nu(\partial/\partial r)(\ln T)$)
v_T' = v_T/U_0
V_{torch} = torch speed
x = axial coordinate
x' = dimensionless axial coordinate (x/L)
x_0 = axial location where the temperatures are observed.
x_{rel} = relative location with respect to torch
x_{start} = torch starting location
x_{torch} = torch location
x_{travel} = torch moving distance
Y_i = mass fraction of species i
Y_i' = dimensionless mass fraction of species i($Y_i/Y_{\mathrm{SiCl_4},0}$)

Greek symbols

α = Rosseland mean absorption coefficient
δ = deposition thickness
λ = coefficient for heat flux distribution
μ = viscosity
μ' = μ/μ_0
ν = dynamic viscosity
ν'' = stoichiometric coefficient
ρ = density
ρ' = ρ/ρ_0
σ = Stefan-Boltzmann constant

Superscript

$'$ = dimensionless parameters

Subscripts

0 = properties at inlet
i = species ($SiCl_4$, O_2, Cl_2)
solid = properties of quartz tube

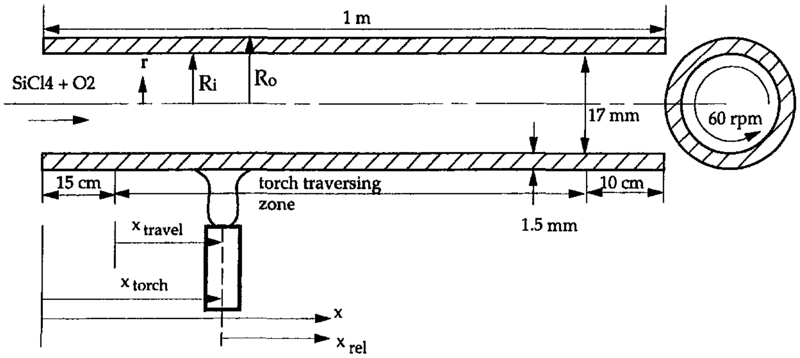

Fig. 1 Schematic diagram of the MCVD system

of oxidation of SiCl$_4$. Powers (1978) suggested the following equation:

$$r_{\mathrm{SiCl}_4} = (k_{0+k_1}\rho Y_{\mathrm{O}_2})e^{-E_a/R_GT}\rho Y_{\mathrm{SiCl}_4} \tag{5}$$

where E_a, k_0 and k_1 denote activation energy and reaction rate constants, respectively. When the reaction equation is expressed as the form $\Sigma\ \nu_i''A_i = 0$, A_i is the chemical species and ν_i'' represents the stoichiometric coefficient which is positive for reactants.

Since SiO$_2$ is in the form of particles, diffusion is negligible compared with thermophoresis (Simpkins et al., 1979; Walker et al., 1980). The following equation has been used to solve the mass fraction of particles.

$$\frac{R_i}{L}\frac{V_{\mathrm{torch}}}{U_0}\rho'\frac{\partial Y'_{\mathrm{SiO}_2}}{\partial t'} + \frac{R_i}{L}\rho'(u' + u'_T)\frac{\partial Y'_{\mathrm{SiO}_2}}{\partial x'} \tag{6}$$

$$+ \rho'(v' + v'_T)\frac{\partial Y'_{\mathrm{SiO}_2}}{\partial r'} = \frac{\nu''_{\mathrm{SiO}_2}R_i}{U_0} r'_{\mathrm{SiCl}_4}\frac{M_{\mathrm{SiO}_2}}{M_{\mathrm{SiCl}_4}}.$$

The boundary conditions are

$$x' = 0 \quad : \quad u' = 2(1 - r'^2), \quad v' = 0, \quad T' = 0$$

$$Y'_{\mathrm{SiCl}_4} = 1, \quad Y'_{\mathrm{O}_2} = (1 - Y_{\mathrm{SiCl}_4,0})/Y_{\mathrm{SiCl}_4,0}, \quad Y'_{\mathrm{SiO}_2} = Y'_{\mathrm{Cl}_2} = 0$$

$$x' = 1 \quad : \quad \partial^2(u', v', T', \quad Y'_{\mathrm{SiCl}_4}, Y'_{\mathrm{O}_2}, Y'_{\mathrm{Cl}_2})/\partial x'^2 = 0$$

$$r' = 0 \quad : \quad \partial(u', v', T', Y'_{\mathrm{SiCl}_4}, Y'_{\mathrm{O}_2}, Y'_{\mathrm{SiO}_2}, Y'_{\mathrm{Cl}_2})/\partial r' = 0$$

$$r' = 1 \quad : \quad u' = v' = 0, \quad \partial(Y'_{\mathrm{SiCl}_4}, Y'_{\mathrm{O}_2}, Y'_{\mathrm{Cl}_2})/\partial r' = 0 \tag{7}$$

and continuity of temperature and heat flux.

In the present study, the temperature distribution of tube wall is not known a priori, but should be determined by solving the following equation:

$$\frac{R_i}{L}\frac{V_{\mathrm{torch}}}{U_0}(\rho'c'_p)_{\mathrm{solid}}\frac{\partial T'}{\partial t'} = \frac{2}{\mathrm{Pe}_T}\left\{\left(\frac{R_i}{L}\right)^2\frac{\partial}{\partial x'}\left(k'_{\mathrm{solid}}\frac{\partial T'}{\partial x'}\right)\right.$$

$$\left. + \frac{1}{r'}\frac{\partial}{\partial r'}\left(r'k'_{\mathrm{solid}}\frac{\partial T'}{\partial r'}\right)\right\}. \tag{8}$$

To calculate the solid wall temperature as torch moves, the localized heating from the torch is modeled using a heat flux boundary condition on the outer wall of the tube:

$$r = R_o \quad : \quad q_{\max}\exp(-\lambda^2[x - x_{\mathrm{torch}}]^2)$$

$$= k\partial T/\partial r + h(T - T_\infty) + \epsilon\sigma(T^4 - T_\infty^4) \tag{9}$$

where x_{torch} is the torch location and h is the temperature-dependent heat transfer coefficient on the rotating cylinder (Farouk and Ball, 1985). Two parameters, λ and $q_{\max}$, characterize the width and the maximum value of the heating profile (Park and Choi, 1994). ϵ is the emissivity of the quartz tube which is calculated from a band approximation (Siegel and Howell, 1992), with the assumption that the quartz is transparent below 4.5 μm wavelength and behaves like a black body above 4.5 μm wavelength (Son, 1992).

In studies of optical fiber drawing, Homsy and Walker (1979) and Paek and Runk (1978) considered the effect of radiation in a silica solid rod by using the Rosseland diffusion approximation (Siegel and Howell, 1992). The same approximation is utilized in the present study:

$$k = k_{\mathrm{cond}} + k_{\mathrm{rad}} = k_{\mathrm{cond}} + 16n^2\sigma T^3/3\alpha \tag{10}$$

where the Rosseland mean absorption coefficient, α, and the refractive index, n, take the values of 4 cm^{-1} and 1.5 (Homsy and Walker, 1979; Paek and Runk, 1978).

Since the inlet SiCl$_4$ mass fraction is relatively large (approximately 0.6), all properties in the present study are calculated based on inlet composition, and properties are assumed to depend on local temperature. The flow rate (Q_T) and density (ρ) are calculated as follows:

$$Q_T = (Q_{\mathrm{O}_2}p_{\mathrm{O}_2}M_{\mathrm{O}_2}/R_GT + \dot{m}_{\mathrm{SiCl}_4})/\rho \tag{11}$$

$$\rho = p/(R_GT \sum_{i\ \mathrm{species}} Y_i/M_i). \tag{12}$$

For the mixture viscosity, conductivity, and diffusivity, experimental values are used when available (Weast and Arstle, 1981; Irvine and Liely, 1984), otherwise the following equations are utilized (Rosner, 1986; Bird et al., 1960):

$$\mu = 5(\pi m k_BT)^{1/2}/16(\pi\sigma^2)\Omega_\mu \tag{13}$$

$$k = 15\bar{R}\mu[1 + 4(\overline{C_p}/\bar{R} - 5/2)/15]/4M \tag{14}$$

$$\mu_{\mathrm{mix}} \approx \sum_{i\ \mathrm{species}} M_i^{1/2}X_i\mu_i / \sum_{i\ \mathrm{species}} M_i^{1/2}\mu_i \tag{15}$$

$$k_{\mathrm{mix}} \approx \sum_{i\ \mathrm{species}} M_i^{1/3}X_ik_i / \sum_{i\ \mathrm{species}} M_k^{1/3}k_i \tag{16}$$

where Ω_μ and σ are computed from the following equations:

$$\Omega_\mu = 1.22(k_BT/\epsilon)^{-0.16} \tag{17}$$

$$\sigma = 2.44(T_c/p_c)^{1/3} \tag{18}$$

$$\epsilon/k_B = 0.77T_c. \tag{19}$$

The critical temperature, T_c, and pressure, p_c, of SiCl$_4$ are 508.15 K and 3.593 MPa, respectively. Enthalpy of reaction for SiCl$_4$ is taken from JANAF thermodynamic tables (Chase et al., 1986).

Deposition thickness, $\delta(x, t)$, may be calculated from the mass flux onto the inner surface of tube, as follows:

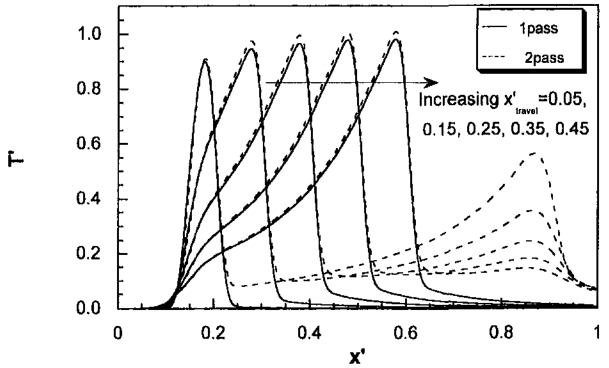

Fig. 2 Distributions of tube wall (outer surface) temperature in the absolute axial coordinate for different torch locations (different times)

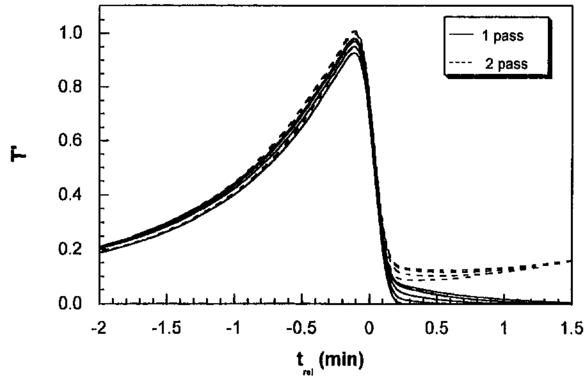

Fig. 3 Temporal variations of tube wall temperature at fixed points

$$\delta(x, t) = \int_0^t [-\rho Y_{SiO_2} K\nu \partial \ln T/\partial r]_{r=R_i} d\tilde{t}/\rho_{solid}. \quad (21)$$

Deposition efficiency can be calculated from the ratio of deposited SiO_2 moles to inlet $SiCl_4$ moles.

$$E_D(t) = 2M_{SiCl_4} \int_0^L \int_0^t [\quad (22)$$

$$-\rho Y_{SiO_2} K\nu \partial \ln T/\partial r]_{r=R_i} d\tilde{t} dx/\rho_0 Y_{SiCl_4,0} U_0 R_o t M_{SiO_2}$$

Numerical calculations have been performed using the finite volume technique with SIMPLE algorithm (Patankar, 1980). Grid sensitivity tests were carried out for several axially nonuniform grid systems; maximum axial grid space, Δx_{max}, minimum axial grid space, Δx_{min}, radial grid space Δr and time interval Δt are tested in the rage of 2.5 ~ 5 mm, 0.5 ~ 1 mm, 0.5 ~ 1 mm, $\frac{1}{3}$ ~ 1 sec, respectively. Grid spaces chosen are Δx_{max} = 5 mm, Δx_{min} = 1 mm, Δr = 0.7 mm and Δt = 1 sec. Deposition thickness in this grid system differs from denser grid system (Δx_{max} = 2.5 mm, Δx_{min} = 0.5 mm, Δr = 0.7 mm and $\Delta t = \frac{1}{3}$ sec) by less than one percent. Due to steep changes resulting from the chemical reaction, the grids near the reaction zone should be denser. Therefore, nonuniform grids are regenerated each time with the torch movement.

Results and Discussion

The present unsteady calculations of wall temperature and deposition profile were compared with available experimental data. Calculation conditions are identical to the experimental conditions of Cho and Choi (1995). The flow rate of carrier gas, O_2, is 2 l/min, the mass rate of $SiCl_4$ is 3.91 g/min and the inlet mass fraction of $SiCl_4$ is 0.6. The torch moves axially at a constant speed of 20 cm/min. The spatial wall temperature variations at several different times (different torch locations, $x'_{travel} = x_{travel}/L$) as the torch moves are shown in Fig. 2. As shown in Fig. 2, the maximum wall temperature when the torch is near the starting region is lower than that when torch moves far from the inlet region because the region behind the torch starting position ($x < x_{start}$) is not heated. The solid and dashed lines represent temperature distributions for the first pass and second pass of the torch traverse, respectively. The wall temperature distribution ahead of the torch for the second pass is higher than that of the first pass, and there exists an axial region where the wall temperature increases ahead of the torch. This is a consequence of the residual heat from the first pass. This temperature increase was predicted by a two-torch model suggested by Park and Choi (1994) and confirmed by the measurement of Cho and Choi (1995).

Figure 3 shows transient wall temperatures at several different axial locations (different x_o's) using the relative time, $t_{rel} = (x_o - x_{torch})/V_{torch} = (x_o - (V_{torch}t + x_{start}))/V_{torch}$ where x_o is the absolute distance of the axial location of interest from the origin. Zero value in t_{rel} corresponds to the time when the torch arrives at the axial location of interest, i.e., x_0, positive t_{rel}'s for times before the torch arrives at x_0 and negative t_{rel}'s for times after the torch passes over x_0. At all points, the temperature histories expressed with respect to the relative time coordinate seemed to fit reasonably into a single curve. Walker et al. (1980) and Cho and Choi (1995) expressed the measured wall temperature history by the same method described above. The fact that temperature variations with time for different points have a similar form supports the quasi-steady assumption used in previous studies; however, this does not necessarily guarantee quasi-steadiness. The quasi-steadiness can be satisfied only if the distribution of spatial temperature at different times show an identical form. It is noted that the measurement of spatial temperature distributions at different times is a difficult task, therefore, it has not yet been done.

To see this in the present unsteady analysis, the same data of Fig. 2 over the entire tube at several different times (different x_{travel}'s) are replotted in Fig. 4 using the relative coordinate that moves with the torch, $x'_{rel} = (x - x_{torch})/L$. In this figure, x'_{travel} represents the nondimensionalized distance travelled by the torch from its initial position by a tube length (L), which in turn expresses the elapsed time of torch movement if divided by the torch speed. Each curve in Fig. 4 shows the entire spatial distribution of wall temperature at the given time while each curve in Fig. 3 represents the temperature history of the tube wall at the given axial location. At early times (or, small x_{travel}'s), wall temperature distributions in the region behind the torch do not fall onto a single curve even though they are expressed in the relative coordinate. On the other hand, wall

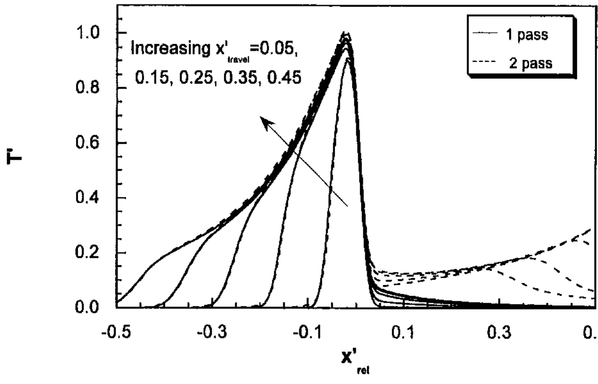

Fig. 4 Distributions of tube wall (outer surface) temperature in the relative axial coordinate for different torch locations (different times)

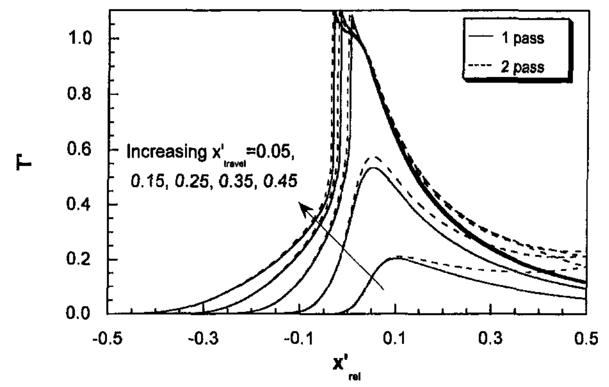

Fig. 5 Distributions of tube center temperature in the relative axial coordinate for different torch locations (different times)

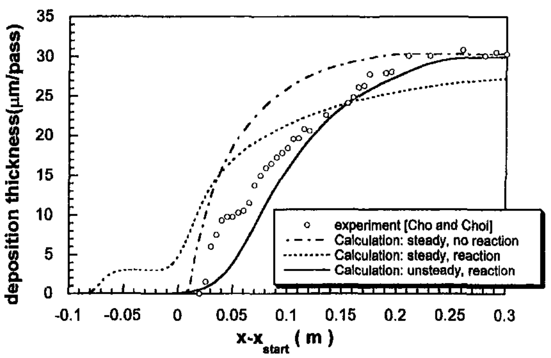

Fig. 7 Comparisons of deposition thickness variations in the axial direction (average deposition thickness of four passes, circles: experiment (Cho and Choi), lines: calculation)

temperature distributions seem to approach the one curve as torch moves farther from the torch starting position (at later times or large x_{travel}'s). This fact implies that the quasi-steady-state assumption can be valid only after the torch has moved by an appreciable distance; for example, beyond x_{travel} equal to 0.2 ~ 0.3 m. Therefore, we conclude that the assumption of a quasi-steady state cannot be used at early times (or small x_{travel}'s). We also note that discrepancies between predictions and measurements near the inlet region shown in the paper of Cho and Choi (1995) would have been caused by applying the quasi-steady assumption to the entire process. One of the present objectives of this study is to correctly predict the deposition profile of the entire tube including the inlet region. The precise prediction of the deposition profile especially near the inlet region is important to optimize process parameters and reduce the undesired taper region.

Figure 5 shows the gas temperature distributions at the centerline for several different times (different x_{travel}'s). Because the gas receives the energy from wall which is convected to the zone ahead of the torch, it takes a longer time to reach the quasi-steady state, as compared with the wall. This explains again the fact that the existing quasi-steady model could not precisely predict the deposition profile but could only roughly estimate the deposition efficiency (Walker et al., 1980; Park and Choi, 1994).

In Fig. 6, the validity of the unsteady analysis is examined by comparing the unsteady calculations with previous experimental and quasi-steady results. Previous results (both experimental and numerical) are the temperature histories at the given axial location. Therefore, the results of the present unsteady analysis are also plotted in Fig. 6 using the same relative time coordinate adopted in Fig. 3; circles and lines do not represent temperature distribution along the tube, but temporal variations of the given axial location. Unsteady results are almost the same as those of the steady calculations and experiments. It is reiterated that agreement shown in this figure does not guarantee the validity of the quasi-steady assumption (see Figs. 4 and 5). This agreement only means that temporal variation of wall temperature at certain location ($x_0 = 0.25$ m) behaves like quasi-steady. If the measurements of spatial temperature distributions over the entire tube wall were made and plotted as in Fig. 4, the unsteady effects would have been clearly seen. Deposition profile was measured over the entire tube (Cho and Choi; (1995)) and it will be shown in Fig. 7 that unsteady calculation gives superior agreement with experimental data to steady calculation. Since overall efficiency can be expressed as a function of minimum temperature in the case of sufficient reactions (Walker et al., 1980; Park and Choi, 1994), a proper prediction of wall temperature is a prerequisite condition for a correct estimation of efficiency.

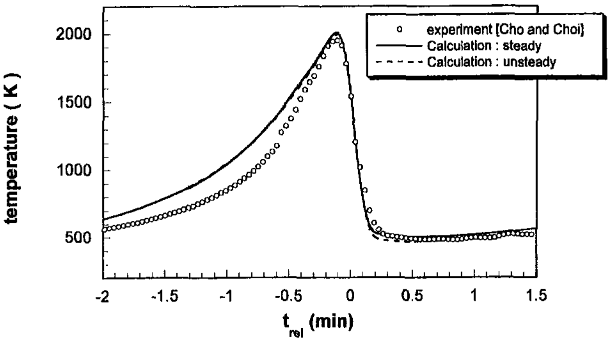

Fig. 6 Temporal variations of tube wall (outer surface) temperature at $x_0 = 0.25$ m

Deposition profiles are also compared in Fig. 7. In quasi-steady modeling, two cases are studied. In the first case (dotted curve in Fig. 7), mass diffusion and chemical reaction are included to calculate the deposition flux (Kim and Pratsinis, 1988; Joh et al., 1993; Choi et al., 1995). In the second case (dashed and dotted curve), only flow and temperature without chemical reaction and mass diffusion are calculated, and deposition efficiency is calculated from particle trajectories (Walker et al., 1980; Park and Choi, 1994). The value of 0.55 is used as the thermophoretic coefficient for the first case (Talbot et al., 1980; Kim and Pratsinis, 1988; Joh et al., 1993). For the second case in which mass diffusion and chemical reaction are excluded, a value of 0.9 is used as the thermophoretic coefficient because the use of higher value could compensate the neglected deposition caused by the omission of diffusion and the chemical reaction of $SiCl_4$. The value of 0.9 has been used in previous modelings without chemical reaction and mass diffusion (Walker et al., 1980; Lin et al., 1992; Park and Choi, 1994). This compensation can also be supported from the fact that calculated efficiencies with a higher thermophoretic coefficient are in good agreement with the experimental measurements of Walker et al. (1980) and Cho and Choi (1995).

In the case of quasi-steady modeling with chemical reaction and mass diffusion, some particles are deposited behind the torch starting position because quasi-steady modeling assumes the same established temperature profile even at the torch starting position. Since chemical reaction raises the gas temperature behind the torch above the maximum wall temperature in the case of high $SiCl_4$ loading, particles can be generated and deposited behind the torch. In the case with no diffusion and chemical reaction (dashed and dotted curve), there exist distinct discrepancies between the prediction and the measurement near the torch starting position; however, good agreement is obtained when torch travels downstream. The unsteady calculation with chemical reaction and mass diffusion (solid line) results in the

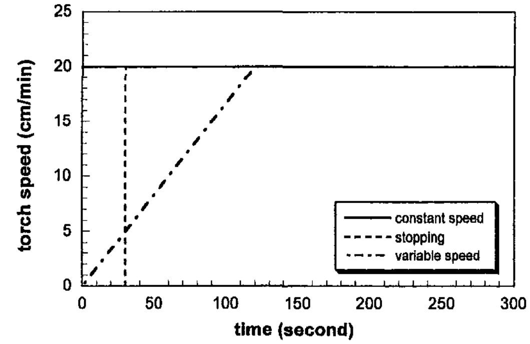

Fig. 8 Variations of torch speed considered in the study

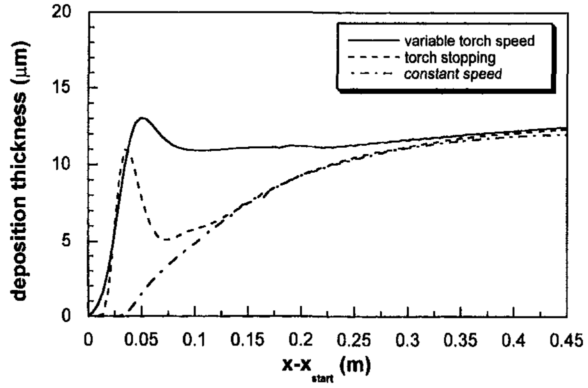

Fig. 10 Effect of torch speed on deposition thickness variation in axial direction (second pass case, x_{travel} = 0.45 m)

best agreement with the experiments over the entire region. The present unsteady analysis shows the correct prediction of the deposition profile from the inlet region.

The unsteady analysis is also capable of predicting the temperature field and deposition profile for time varying conditions that are used in actual practice. In this study, three different cases of torch speed variations were examined as shown in Fig. 8. In the first case, the torch speed maintains a constant value (20 cm/min). In the second case, the speed increases stepwise to a prescribed value (20 cm/min) after stopping the torch for some interval (30 seconds), whereas in the third case it increases linearly for a duration of 120 seconds.

Figure 9 shows the deposition profile variation as the torch moves. In the case of a variable torch speed (linearly varying case: second case in Fig. 8), the deposited mass near the torch starting position increases due to the longer duration of torch heating (smaller torch speeds in times less than 120's than the constant speed case), and thus the tapered entry region is greatly reduced. In Fig. 10, effects of various torch speeds on deposition performance are shown. The case of linear torch-speed variation has resulted in a much shorter tapered entry than the other cases, which indicates that the unsteady calculations can be used to optimize the torch speed variations in order to enhance the deposition performance and reduce the entry taper region.

Conclusions

A numerical analysis of unsteady heat and mass transfer has been carried out for the modified chemical vapor deposition. The present unsteady calculations of wall temperature and deposition profile were compared with the existing experimental data and were in good agreement.

It has been proved that the quasi-steady assumption of tube temperature is restricted to a zone which is removed from the torch starting position by an appreciable distance. The quasi-steady assumption for the tube wall is achieved at a shorter distance than that for gases. A steady calculation which assumes the identical temperature distribution with respect to the coordinate moving with torch cannot precisely predict the deposition profile near torch starting region where nonuniform (tapered) deposition occurs. Unsteady calculations predicted the deposition profile correctly in the entire region.

The effects of torch speed variation on deposition performance have also been examined. Three cases of torch speed variations were studied. In the first case, the torch speed maintains a constant value. In the second case, the speed increases stepwise to a prescribed value after stopping the torch for some interval, whereas in the third case it increases linearly from the beginning. The third case has resulted in a much shorter tapered entry than the other cases, which indicates that the unsteady analysis can be used to optimize the torch speed variations in order to enhance deposition performance.

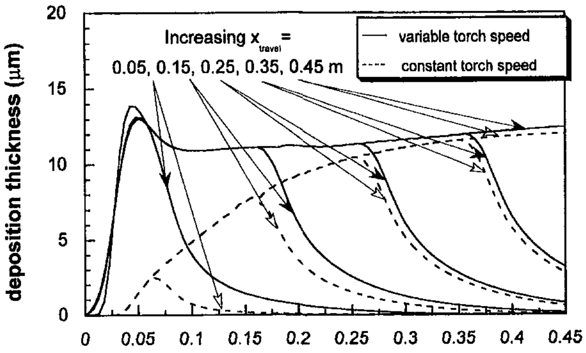

Fig. 9 Comparison of deposition thickness variations in the axial direction for different torch speed variations (second pass case)

Acknowledgments

Support from Korea Science & Engineering Foundation (project #961-1008-071-2) is gratefully acknowledged. Authors are also thankful to the Ministry of Education, Korea, for the partial support at the early stage of this work.

References

Bird, R. B., Stewart, W. E., and Lightfoot, E. N., 1960, *Transport Phenomena*, John Wiley and Sons, New York.

Chase, M. W., Jr., Davies, C. A., Downey, J. R., Jr., Frurip, D. J., McDonald, R. A., and Syverund, A. N., 1986, *JANAF Thermochemical Tables*, American Institute of Physics, New York.

Cho, J., and Choi, M., 1995, "An Experimental Study of Heat Transfer and Particle Deposition for the Modified Chemical Vapor Deposition," ASME JOURNAL OF HEAT TRANSFER, Vol. 117, pp. 1036–1041.

Choi, M., Lin, Y. T., and Greif, R., 1990, "Analysis of Buoyancy and Tube Rotation Relative to MCVD Process," ASME JOURNAL OF HEAT TRANSFER, Vol. 112, pp. 1063–1069.

Choi, M., Park, K. S., and Cho, J., 1995, "Modelling of Chemical Vapor Deposition for Optical Fiber Manufacture," *Optical and Quantum Electronics*, Vol. 27, pp. 327–335.

Choi, M., and Park, K. S., 1994, "Effects of Annular Jet in Inside Vapor Deposition with Applications to Optical Fiber Manufacture," *Heat Transfer 1994*, Vol. 7, 10th International Heat Transfer Conference at Brighton, England, Aug. 14–18, pp. 209–214.

Farouk, B., and Ball, K. S., 1985, "Convective Flow around a Rotating Isothermal Cylinder," *International Journal of Heat and Mass Transfer*, Vol. 28, No. 10, pp. 1921–1935.

Fiebig, M., Hilgenstock, M., and Rieman, H. A., 1988, "The Modified Chemical Vapor Deposition Process in a Concentric Annulus," *Aerosol Science and Technology*, Vol. 9, pp. 237–249.

Homsy, G. M., and Walker, K. L., 1979, "Heat Transfer in Laser Drawing of Optical Fibers," *Glass Technology*, Vol. 20, No. 1, pp. 20–26.

Irvine, T. F., and Liely, P. E., Jr., 1984, *Steam and Gas Tables with Computer Equations*, Academic Press, San Diego, CA, pp. 161–165.

Joh, S., Greif, R., and Lin, Y. T., 1993, "A Study of the Effects of Chemical Reaction on the Modified Chemical Vapor Deposition (MCVD) Process," *Journal of Materials Processing and Manufacturing Science*, Vol. 1, pp. 369–386.

Kim, K. S., and Pratsinis, S. E., 1988, "Manufacture of Optical waveguide preforms by MCVD," *AIChE Journal*, Vol. 34, pp. 912–920.

Lin, Y. T., Choi, M., and Greif, R., 1992, "A Three-Dimensional Analysis of Particle Deposition for the Modified Chemical Vapor Deposition (MCVD) Process," ASME JOURNAL OF HEAT TRANSFER, Vol. 114, pp. 735–742.

MacChesney, J. B., O'Connor, P. B., and Presby, H. M., 1974, "A new technique for preparation of low loss and graded index optical fibers," *Proc. IEEE*, Vol. 62, pp. 1278–1279.

Morse, T. F., DiGiovanni, D., Chen, Y. W., and Cippola, J. W., Jr., 1986, "Laser Enhancement of Thermophoretic Deposition Process," *Journal of Lightwave Technology*, LT-4, No. 2, pp. 151–155.

Paek, U. C., and Runk, R. B., 1978, "Physical Behavior of the Neck-down Region during Furnace Drawing Silica Fibers," *Journal of Applied Physics*, Vol. 49, No. 8, pp. 4417–4423.

Park, K. S., and Choi, M., 1994, "Conjugate Heat Transfer and Particle Deposition Process: Effect of Torch Speed and Solid Layer," *International Journal of Heat and Mass Transfer*, Vol. 37, No. 11, pp. 1593–1603.

Patankar, S. V., 1980, *Numerical Heat Transfer and Fluid Flow*, Hemisphere, Washington, DC.

Powers, D. R., 1978, "Kinetics of $SiCl_4$, Oxidation," *Journal of American Ceramic Society*, Vol. 61, pp. 295–297.

Rosner, D. E., 1986, *Transport Process in Chemically Reacting Flow Systems*, Butterworth, Stoneham, MA.

Siegel, R. and Howell, J. R., 1992, *Thermal Radiation Heat Transfer*, 3rd ed., Hemisphere, Washington, DC.

Simpkins, P. G., Kosinski, S. G., and MacChesney, J. B., 1979, "Thermophoresis: The Mass Transfer Mechanism in MCVD," *Journal of Applied Physics*, Vol. 50, pp. 5676–5681.

Son, J., 1992, "An Analysis of Radiation Heat Transfer in Rapid Annealing System," M. S. thesis, Seoul National University, Seoul, Korea.

Talbot, L., Cheng, R. K., Schefer, R. W., and Willis, D. R., 1980, "Thermophoresis of Particles in a Heated Boundary Layer," ASME *Journal of Fluid Mechanics*, Vol. 101, pp. 737–758.

Walker, K. L., Geyling, F. T., and Nagel, S. R., 1980, "Thermophoresis Deposition of Small Particles in the Modified Chemical Vapor Deposition (MCVD) Process," *Journal of American Ceramic Society*, Vol. 63, pp. 552–558.

Wang, C. W., Morse, T. F., and Cippola, J. W., Jr., 1985, "Laser Induced Natural Convection and Thermophoresis," ASME JOURNAL OF HEAT TRANSFER, Vol. 107, pp. 161–167.

Weast, R. C., and Arstle, M. J., 1981, *CRC Handbook of Chemistry and Physics*, 61st Ed., CRC Press, Boca Raton, FL.

H. Zhang
Assistant Professor,
Department of Mechanical Engineering,
State University of New York
at Stony Brook,
Stony Brook, NY 11794-2300
e-mail: hzhang@thermsa.eng.sunysb.edu
Assoc. Mem. ASME

L. L. Zheng
Research Scientist,
Department of Materials Science and
Engineering,
State University of New York
at Stony Brook,
Stony Brook, NY 11794-2275
e-mail: lzheng@thermsa.eng.sunysb.edu

V. Prasad
Professor,
Department of Mechanical Engineering,
State University of New York
at Stony Brook,
Stony Brook, NY 11794-2300
e-mail: prasad@thermsa.eng.sunysb.edu
Fellow ASME

D. J. Larson, Jr.
Professor,
Department of Materials Science and
Engineering,
State University of New York
at Stony Brook,
Stony Brook, NY 11794-2275
e-mail: dlarson@ccmail.sunysb.edu

Local and Global Simulations of Bridgman and Liquid-Encapsulated Czochralski Crystal Growth

A curvilinear finite volume-based numerical methodology has been developed that can be effectively used for simulation of the Bridgman and Czochralski (Cz) crystal growth processes. New features of grid generation have been devised and added to the original formulation (Zhang et al., 1995, 1996) to make it suitable for global modeling. The numerical model can account for convection in both the melt and the gas phases, convection/radiation in the furnace, and conduction in all solid components. Results for Bridgman growth show that the flow pattern and interface shape strongly depend on thermal conductivities of the crystal, melt, and ampoule materials. Transient simulations have been performed for the growth of Bismuth crystal in a Bridgman-Stockbarger system and the growth of GaAs crystal using liquid-encapsulated Czochralski (LEC) technique. This is the first time that a global high-pressure LEC model is able to account for convective flows and heat transfer and predict the interface shape and its dynamics.

Introduction

Single crystals of certain elements and compounds are the basic materials for the production of electronic, optoelectronic, and many other devices. These materials are also crucial to photovoltaic, laser, sensor, and fiber optic applications. One of the common techniques for single crystal growth is a variant of the original Bridgman method (see Fig. 1(*a*)). It is well known that the temperature distribution in the crystal and the shape of the solid/liquid interface significantly influence the crystal quality in a Bridgman growth. A flat interface or an interface that is slightly convex toward the melt is most desirable to produce better quality crystals (Glicksman et al., 1986).

Numerous computational studies of the vertical Bridgman growth have been performed in recent years (Brown, 1988; Dupret and Bogaert, 1994). Adornato and Brown (1987) used a transient finite element/Newton method to study the details of convection and solute segregation for compound semiconductors under the quasi-steady condition. Later, Kim and Brown (1991) extended this model to describe a fully transient process, and investigated the effects of Rayleigh number on the interface shape and dopant concentration distributions. Koai et al. (1994) used a commercial code, ABAQUS, to simulate the global Bridgman growth system based on the quasi-steady assumption. Deviating from others they took into account the deflection of the melt/crystal interface. In their work, a convex interface was obtained by redesigning the crucible as well as the radial heat flux in the system for GaAs growth. Recently, Liang and Lan (1996) have developed a three-dimensional finite volume/Newton method to study the effect of small deviations from axisymmetric Bridgman system on the flow pattern and radial solute segregation. On the other hand, Ouyang and Shyy (1996) have developed a finite volume scheme and a two-level patching strategy to perform the global simulation for a Bridgman system. In this scheme, level 1 accounts for the entire configuration and is referred to as the global model, while level 2 concentrates on the ampoule region, called the local model; level 1 supplying the boundary conditions to level 2 via a linear interpolation. Kuppurao and Derby (1997) used a model similar to that of Kim and Brown (1991) to analyze the effect of support materials and ampoule geometry on the shape of the solidification interface. Although major advancements have been brought by these studies on Bridgman growth and our understanding of interface shape formation has greatly improved, several important issues remain unclear. For example, most published results claim that the two-cell structure is the only flow pattern that can exist in a Bridgman system and the interface shape will be concave towards the melt during the growth. The reported studies do not show the possibility of one-cell pattern and under what conditions the two-cell structure will break down. This is a key area of the present investigation and it is shown that the melt in an axisymmetric Bridgman system can have a single cell flow structure.

Contributed by the Heat Transfer Division for publication in the JOURNAL OF HEAT TRANSFER. Manuscript received by the Heat Transfer Division, May 1, 1997; revision received, Mar. 9, 1998. Keywords: Materials Processing and Manufacturing Process, Moving Boundaries, Phase-Change Phenomena. Associate Technical Editor: T. Bergman.

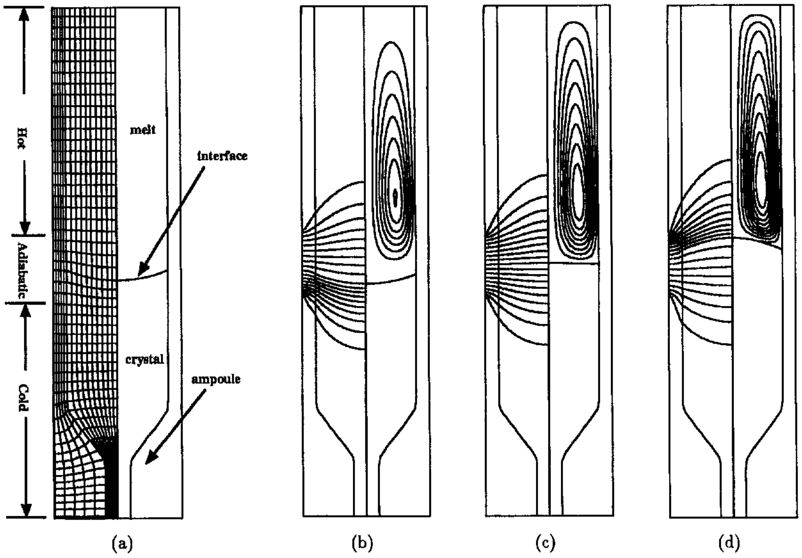

Fig. 1(*a*) Schematic of Bridgman growth system, Gr = 10^5, Pr = 0.015, $(T_f - T_c)/(T_h - T_f) = 1.0$, $\rho_s/\rho_l = 1.0$, $C_{ps}/C_{pl} = 1.0$, $k_a/k_l = 1.0$, $\rho_a/\rho_l = 1.0$, $C_{pa}/C_{pl} = 1.0$, and temperature and stream function contours for (*b*) $k_s/k_l = 0.5$, (*c*) $k_s/k_l = 1.0$, and (*d*) $k_s/k_l = 2.0$

Although several methods have been devised to manufacture silicon single crystals, the Cz and LEC methods have virtually dominated the entire production of single crystals for the microelectronics industry. A typical configuration of the LEC furnace is shown in Fig. 7(*a*). During growth, the heater radiates heat towards a crucible containing the molten material, and the crystal releases heat from its surface by convection and radiation to the surrounding gases and the furnace walls. The melt surface also loses heat by conduction and radiation through the encapsulant layer and convection at the encapsulant surface. The shape and dynamics of the crystal/melt interface therefore depend on energy transport in the entire furnace. Conduction, convection, and radiation all play important roles in the growth process. Global modeling that includes all components of the system and all important physical phenomena, is therefore necessary to understand the dynamics of the LEC process.

Both commercial packages and in-house codes have been used in the past to simulate the global Cz and LEC growth. Baumgartl et al. (1993) employed a finite element package, ABAQUS, to model global radiation and conduction heat transfer in an industrial LEC furnace. To improve the prediction of temperature field in the melt, they employed a finite volume package, STAR-CD, and combined it iteratively with the conduction/radiation solver. Santailler et al. (1996) employed two finite element packages, FIDAP and MARC, to simulate the global heat transfer in a LEC furnace. In both papers, the shape of the melt/crystal interface was prescribed, and no solidification and free-surface calculations were made. Kinney and Brown (1993) have developed an integrated hydrodynamic thermal-capillary model (IHTCM) based on the finite element/Newton method to simulate the global Cz growth of silicon. Dupret and van den Bogaert (1994) have also developed a global finite element model to simulate both the Cz and LEC growth. However, gas convection has not been considered by any one of these models. Indeed, to our knowledge no global simulation has been reported thus far that can account for both

Nomenclature

A = surface area, m^2
b = reference length, m
Bi = Biot number
C_p = specific heat, J/kgK
F = function
G = orthogonality function, Gebhart factor
g = gravity, m^2/s
g_l = function
Gr = Grashof number
h = heat transfer coefficient, W/m^2
H_1 = solid/melt interface height, m
H_2 = free surface height, m
I = integral
Ja = Jacobian
k = thermal conductivity, W/(mK)
M = grid inertial coefficient
N = number of surfaces
p = pressure, Pa
Pr = Prandtl number
q''' = heat source, W/m^3
r = radial distance, m
Rr = radius ratio
Ste = Stefan number
T = temperature, K
t = time, s
u = velocity in axial direction, m/s
v = velocity in radial direction, m/s
V_m = melt volume, m^3
V_p = pull rate, m/s
W = weight function
x = axial distance, m
λ = positive coefficient
Λ = positive coefficient
ξ, η = curvilinear coordinates
ρ = density, kg/m^3
ϵ = emissivity
σ = Stefan-Boltzmann constant
μ = dynamic viscosity, kg/(ms)
ν = kinematic viscosity, m^2/s
Θ = dimensionless temperature

Subscripts

a = ampoule
c = cold
eff = effective
f = freezing temperature
g = grid
h = hot
i = initial
k = surface
l = melt
m = inertia
o = reference, orthogonal
r = radiation
s = crystal
turb = turbulent
w = weight
ξ, η = curvilinear coordinates

Superscripts

$-$ = dimensionless

the convective and radiative heat transfer in gas and melt phases together with solidification.

In this paper, three major steps have been taken to develop a curvilinear finite volume-based numerical methodology and perform global simulation of the crystal growth processes. First, the effect of the crystal and ampoule materials, the thermal boundary conditions and the shape of the furnace on interface shape and its movement has been examined for a Bridgman system. Second, dynamic simulations of a real Bridgman-Stockbarger system have been performed to study the interface dynamics of directional solidification of Bismuth. Finally, a global simulation of LEC growth of GaAs crystal is performed. The primary goal of this paper is to demonstrate that the curvilinear finite volume-based method with multizone adaptive grid generation can be successfully used for both local and global modeling of a variety of crystal growth processes with varying level of system and physical complexities. The results demonstrate that the growth dynamics can significantly change when the melt is allowed to thermally interact with the other components of the system.

Mathematical Model

Conservation equations for transport in the melt, ambient gas, and solid in a two-dimensional axisymmetric system can be written in the dimensionless form as follows:

Continuity:

$$\frac{\partial}{\partial t}(\bar{\rho}) + \frac{\partial}{\partial x}(\bar{\rho} u) + \frac{1}{r}\frac{\partial}{\partial r}(r\bar{\rho} v) = 0. \tag{1}$$

Conservation of Momentum:

$$\frac{\partial}{\partial t}(\bar{\rho} u) + \frac{\partial}{\partial x}(\bar{\rho} uu) + \frac{1}{r}\frac{\partial}{\partial r}(r\bar{\rho} vu) = \frac{\partial}{\partial x}\left(\bar{\mu}_{\mathrm{eff}}\frac{\partial u}{\partial x}\right) + \frac{1}{r}\frac{\partial}{\partial r}\left(r\bar{\mu}_{\mathrm{eff}}\frac{\partial u}{\partial r}\right) - \frac{\partial p}{\partial x} + \mathrm{Gr}\,\bar{\rho}\Theta + S_{\mathrm{turb}}, \tag{2}$$

$$\frac{\partial}{\partial t}(\bar{\rho} v) + \frac{\partial}{\partial x}(\bar{\rho} uv) + \frac{1}{r}\frac{\partial}{\partial r}(r\bar{\rho} vv) = \frac{\partial}{\partial x}\left(\bar{\mu}_{\mathrm{eff}}\frac{\partial v}{\partial x}\right) + \frac{1}{r}\frac{\partial}{\partial r}\left(r\bar{\mu}_{\mathrm{eff}}\frac{\partial v}{\partial r}\right) - \frac{\partial p}{\partial r} - \frac{v}{r^2} + S_{\mathrm{turb}}. \tag{3}$$

Conservation of Energy:

$$\frac{\partial}{\partial t}(\bar{\rho}\bar{C}_p\Theta) + \frac{\partial}{\partial x}(\bar{\rho}\bar{C}_p u\Theta) + \frac{1}{r}\frac{\partial}{\partial r}(r\bar{\rho}\bar{C}_p v\Theta) = \frac{\partial}{\partial x}\left(\frac{\bar{k}_{\mathrm{eff}}}{\mathrm{Pr}}\frac{\partial\Theta}{\partial r}\right) + \frac{1}{r}\frac{\partial}{\partial r}\left(r\frac{\bar{k}_{\mathrm{eff}}}{\mathrm{Pr}}\frac{\partial\Theta}{\partial r}\right) + S_{\mathrm{turb}} + \dot{q}''', \tag{4}$$

where Gr and Pr are the phase Grashof and Prandtl numbers (zero for solid), respectively, $\dot{q}'''$ is the heat source term, and S_{turb} is the source term for turbulence, and $\bar{\mu}_{\mathrm{eff}}$ is the effective dimensionless viscosity.

The following scales have been used to nondimensionalize the governing Eqs. (1)–(4); length: b, velocity: ν_o/b, pressure: $\rho_o\nu_o^2/b^2$, time: b^2/ν_o, density: ρ_o, dynamic viscosity: μ_o, conductivity: k_o, specific heat: C_{po}, and temperature: $\Theta = (T - T_f)/(T_h - T_f)$; where the subscript "$o$" refers to the melt properties at a reference temperature. The quantities with overbars in Eqs. (1)–(4) represent dimensionless properties. Equations (1)–(4) can be used for global multiphase, multicomponent domain with the provision to account for local properties changing across the zone boundaries, and their movements.

For a pure material, solidification is assumed to take place at a fixed fusion temperature and the solid and liquid phases are separated by a sharp interface. There are two fundamental relations that must be satisfied at this interface. First, the temperature at the solid-liquid interface is continuous. Secondly, the interface must move to satisfy energy balance locally, which defines the interface position and motion as (Zhang and Prasad, 1995):

$$\frac{\partial H_1}{\partial t} = \left[1 + \left(\frac{\partial H_1}{\partial r}\right)^2\right]\frac{\mathrm{Ste}}{\mathrm{Pr}}\left(\frac{k_s}{k_l}\frac{\partial\Theta_s}{\partial x} - \frac{\partial\Theta_l}{\partial x}\right), \tag{5}$$

where $x = H_1(r, t)$ is the solid/melt interface height. The above formulation is suitable for calculations of the moving interface shape with time. In Eq. (5), $\mathrm{Ste} = C_{pl}(T_h - T_f)/h_f$ is the Stefan number.

The thermal boundary condition along the ampoule wall during a Bridgman growth is taken as

$$[\partial\Theta/\partial r]_a = \mathrm{Bi}[\Theta - \Theta_a], \tag{6}$$

where $\mathrm{Bi} = h_a b/k_a$, is Biot number defined to include radiative, conductive, and convective heat transfer between the ampoule and the furnace wall, and Θ_a is the furnace temperature which may vary axially. Here, we assume that the temperature difference between the ampoule and the furnace is small so that the radiative contribution can be linearized. A temperature profile obtained from the experiments can be fitted for a finite value of Bi (Adornato and Brown, 1987). In this paper, $\mathrm{Bi} = \infty$ is used in the hot and cold zones and $\mathrm{Bi} = 0$ is taken for the gradient region.

Denoting the free surface position as $x = H_2(r, t)$, the shapes of the crystal/melt are determined by solving following equations simultaneously with governing equations:

$$\frac{\partial^2 H_2/\partial r^2}{[1 + (\partial H_2/\partial r)^2]^{3/2}} + \frac{\partial H_2/\partial r}{r[1 + (\partial H_2/\partial r)^2]^{1/2}} = \mathrm{Bo}(H_2 - \lambda), \tag{7}$$

and the parameter, λ, can be calculated from the melt conservation constrain

$$\int_0^{Rr} H_1 r dr + \int_{Rr}^{1} H_2 r dr = \frac{V_m(t)}{2\pi}, \tag{8}$$

where H_2 is the height of the free surface, $V_m(t)$ is the volume of the melt, and Rr is the crystal-to-crucible radius ratio. Two boundary conditions are required to solve the shape of the free surface. At the tri-junction, the meniscus pins to the edge of the crystal, and at the junction between free surface and crucible wall, a 90 deg contact angle is assumed in view of the weak influence of the shape of the crucible meniscus on heat transfer. Using Eq. (8) as the constrain condition, a nonlinear ODE solver is developed based on the Newton-Raphson scheme to solve the shape of the free surface. A total of 500 nodes on the free surface is used to determine its shape in our simulations. Two-dimensional grids are then regenerated adaptively and constrained by this interface. The pulling velocity is calculated by retaining the meniscus angle as a constant value. A meniscus angle of 45°C is employed in our simulations.

Multizone Adaptive Curvilinear Finite Volume Scheme

Zhang and co-workers (1996) have developed a high-resolution computer model MASTRAPP based on multizone adaptive grid generation (MAGG) and curvilinear finite volume (CFV) discretization to simulate the transport phenomena associated with materials processes. The model uses a generalized governing equation for two-dimensional transient processes involving diffusion and convection with moving interfaces. Details can be found in Zhang and Moallemi (1995) and Zhang et al. (1996). Only new features of grid generation related to dynamical simulation are presented here for brevity.

The MAGG scheme distributes a fixed number of grid points in the computational domain such that grid line $\eta = \eta_l$ corresponds to the interface between the zones. The grid distribution is adjusted following the movement of the internal boundaries; the grids inside a single zone can move freely in two-dimensional space and the grids on the interface are only permitted to move along the interface curve. The grids are generated by solving the constrained optimization problems or by solving the optimization of the following augmented functionals:

$$I = \iint (F + \Lambda_l g_l) d\xi d\eta, \tag{9}$$

where g_l's are implicit functions of ξ and η, and define the interfaces for constant η_l values, and Λ_l is the Lagrange multipliers. F is the kernel of the functional which is referred to as the overall "performance function" of the optimization problem. F is a linear combination of the smoothness, F_s, orthogonality, F_o, weighted cell area, F_w, and inertia, F_m of the grids,

$$F_s = \left(\frac{x_\xi^2 + x_\eta^2 + y_\xi^2 + y_\eta^2}{\mathrm{Ja}} \right), \tag{10}$$

$$F_o = G(x_\xi x_\eta + y_\xi y_\eta)^2, \tag{11}$$

$$F_w = W\,\mathrm{Ja}^2, \tag{12}$$

$$F_m = M(u_g^2 + v_g^2), \tag{13}$$

where W and G are the weighting functions that are to be specified to control the grid areas and orthogonality, respectively; M is the inertia coefficient; u_g, v_g are the grid speeds; and Ja is the Jacobian, $\mathrm{Ja} = x_\xi y_\eta - x_\eta y_\xi$.

A set of equations can be derived by applying the Euler-Lagrange equation on Eq. (9) subjected to the constraints of internal interfaces. The interface position and its derivatives are determined using an accurate curve-fitting procedure in order to preserve its shape, while the grid points move along it (Zhang and Moallemi, 1995).

It is always a difficult task to find a weighting function that is suitable for complex multiphase systems. In this paper, the weighting functions of $W = \mathrm{Ja}_i^{-2}$ and $G = \mathrm{Ja}_i^3$ are employed and the grids generated are found to be generally suitable for dynamic simulations of crystal growth. Here, Ja_i is the Jacobian of the initial grids which are generated block by block in a multiblock fashion. The initial grids are then modified by the MAGG algorithm using the above weighting function.

The solution procedure can be described as follows. After generating the initial grids, the finite volume solver is employed to predict the velocity and temperature fields. Once the converged flow fields have been obtained, the solidification and free-surface interfaces are updated based on the energy balance and stress balance, respectively. The iteration is continued until the interface(s) stops moving. Since the defect in the crystal can be related to thermal stresses generated during the growth, von Mises stress distribution in the crystal is important. The location with high thermal stress is the place where higher defect density is expected. The finite element stress solver has therefore been developed and called to predict the stress distribution in the solid (Zou et al., 1996). Until this point, the system of governing equations is solved within one time step. The domain boundaries and boundary conditions for the process are subjected to changes using the information obtained from the current and/or previous time-steps. After the geometric configuration has been determined, the grids are regenerated. The process repeats until the required time-step has been reached.

Numerical Accuracy

The numerical scheme has been validated against the experimental and numerical results by simulating natural convection in an eccentric annulus, liquid metal solidification in a rectangular cavity, and many others (Zhang et al., 1996). The main feature developed in this paper has been verified by comparing predictions with one-dimensional analytical solutions for the solid-liquid phase-change problem (Carslaw and Jaeger, 1959). The predicted solid-liquid interface location is within four percent of the analytical interface position for all cases. A comparison of the interface position, and maximum and minimum values of stream function for Bridgman growth simulations using 102 × 62, 202 × 82, and 302 × 102 mesh showed less than three percent variation. The grid of 102 × 62 has been employed in the simulations presented here. A time-step of ten seconds has been used in the calculations based on a series of calculations for varying time-steps.

A comparison of the interface position, and maximum and minimum values of the stream function, was also made for global simulations of Czochralski growth using 82 × 42, 122 × 62 mesh, and 202 × 102 mesh. Grid independent results can be obtained if the Grashof numbers is low ($\mathrm{Gr}_g = 10^6$ and $\mathrm{Gr} = 10^5$). However, the results obtained for low Grashof numbers do not represent the industrial growth conditions. We have therefore used much higher parameters in this paper that are closer to real conditions. Many more grids are required for grid independent results for $\mathrm{Gr}_g = 10^{10}$ and $\mathrm{Gr}_l = 10^7$. However, the present results show general behavior and demonstrate that the present scheme can be used for these simulations. A parallel code is therefore being developed to simulate this system for high Grashof numbers.

Simulation of Bridgman Growth

A typical configuration of vertical Bridgman furnace is shown in Fig. 1(*a*). The molten material is contained in a cylindrical ampoule at the bottom of which solidification starts by a crystal seed. The environment consists of a hot zone, an insulated region, and a cold zone. During the growth, the ampoule is slowly moved downward, and the temperature distribution induced by the external environment shifts upward accordingly. The melt solidifies progressively until the crystal is completely formed. The solution procedure for dynamic simulation can be described as follows:

1 First, the temperature distribution and flow field in the solid, melt and ampoule, and the shape of the solid/melt interface are given as initial conditions.

2 The temperature profile at the ampoule wall moves at a rate, V_p, and a new temperature profile at the wall is obtained accordingly.

3 New interface line is computed using $H^{n+1} = H^n + (\partial H/\partial t)^n \Delta t$.

4 Converged flow field and temperature distribution are predicted using the new interface.

5 The velocity of the grid point movements are calculated thereafter.

6 The procedure is repeated starting from (2).

A major advantage of the Bridgman growth is that the solid crystal is located under the melt. The thermal conditions of low temperature at the bottom and high temperature at the top provide a stable thermal stratification with respect to natural convection. In practice, however, a curved solidification interface is found because of a difference between the thermal conductivities of the solid and liquid phases. This introduces a radial temperature gradient.

As noted earlier, most of the numerical studies on the vertical Bridgman growth focus on predicting results for a special furnace and a particular crystal material. The role of thermophysical properties of the growth materials and ampoule, boundary conditions, and convective heat transfer are not clarified in a general manner. To address these issues, we have selected a set of baseline parameters. The interface position is predicted for this set of parameters and a parametric study is then performed to examine the effects of varying governing parameters. The baseline parameters used for present simulations are: $\mathrm{Gr} = 10^5$, $\mathrm{Pr} = 0.015$, $(T_f - T_c)/(T_h - T_f) = 1.0$, $k_s/k_l = 1.0$, $\rho_s/\rho_l = 1.0$, $C_{ps}/C_{pl} = 1.0$, $k_a/k_l = 1.0$, $\rho_a/\rho_l = 1.0$, $C_{pa}/C_{pl} = 1.0$. The stream function, temperature distribution, and interface location for baseline parameters are shown in Fig. 1(*c*). An almost flat interface is obtained in this case.

The effect of the ratio of solid-to-melt thermal conductivity on interface shape and its movement are investigated for three different values of k_s/k_l, 0.5, 1.0, and 2.0, as shown in Figs. 1(*b*)–(*d*), respectively. It is seen that the interface shape changes from convex to concave as k_s/k_l decreases. The velocity field becomes weaker when the ratio of k_s/k_l increases. The conic section of the furnace does not affect the interface shape in this case.

The effect of the ampoule material on interface shape is considered next. Variations of the local heat flux over the side wall of the furnace for three different values of k_a/k_l, 5.0, 1.0, and 0.2, are presented in Fig. 2. The heat fluxes are located in the narrow region just outside of the gradient region. An almost flat interface has been obtained for all three cases. As the value of k_a/k_l increases, the local heat flux near the wall increases. However, most heat does not participate the solidification process. The heat, instead, dissipates directly from the hot zone to cold zone through the wall of the ampoule directly. The combined effect of ampoule and crystal materials on interface shape is presented in Fig. 3. If the thermal conductivity ratio of ampoule material to melt is small, the distortions in the temperature profile and interface shape reduce (flatter interface) as shown in the figure. With respect to the stream function contours, the recirculation velocities are weaker when the temperature gradient in the crystal is small. The reduction of the convective flow can be attributed to the weak buoyancy effect induced by weaker thermal gradients inside the molten liquid. A low value of k_a/k_l is therefore favorable for growing crystal as far as the interface shape and convective effects are concerned. However, it may have some effect on the pull rate since the solidification rate will decrease because of reduced heat transfer through the ampoule wall.

The effect of crucible conic angle and growth stage on interface shape and its movement is shown in Figs. 4(*a*)–(*c*). A constant cold temperature has been assumed here. The interface profile and flow pattern when the solidification takes place in the conic section (Figs. 4(*a*)–(*c*)) are quite different from that in the constant diameter section (Figs. 3(*a*)–(*d*)). Figures 4(*a*)–(*c*) show that the interface shape changes from convex to concave during the growth when $k_s/k_l = 0.5$ and $k_a/k_l = 0.1$. The temperature distribution on the bottom of the furnace is important in this case since it can change the thermal condition inside the molten material and solid significantly and directly affect the growth rate and the crystal quality. The rate of heat transfer varies with the crucible conic angle dramatically since the heat can be lost through both the side and the bottom of the furnace whereas when the solidification front has moved up, the solidified crystal adds to the thermal resistance in the lower portion. As observed in Fig. 4(*a*), the flow pattern in the beginning of the growth exhibits a single cell structure, while it changes to a two-cell structure as the growth proceeds (Figs. 4(*b*)–(*c*)).

Figures 3(*d*) and 4(*c*) display the flow pattern in the region far away from the conic zone. Interestingly, two different flow patterns have been observed: a single cell structure in Fig. 3(*d*) and two cell structure in Fig. 4(*c*). This reveals that the flow field is weakened when the value of k_a/k_l drops from 0.2 to 0.1.

To perform the simulation, it requires approximately one hour and 30 minutes of CPU time on a single node of IBM SP2 computer.

Dynamic Simulation of Bridgman-Stockbarger Growth

Having discussed the growth in a conventional Bridgman system, we shift our attention to the Bridgman-Stockbarger system. In what follows, we will present a dynamic simulation of directional solidification for Bismuth. The geometric configuration and thermophysical properties of Bismuth are given in Zheng et al. (1997). To handle the dynamical simulation for the Bridgman-Stockbarger configuration, a structured multiblock scheme in conjunction with the MAGG algorithm has

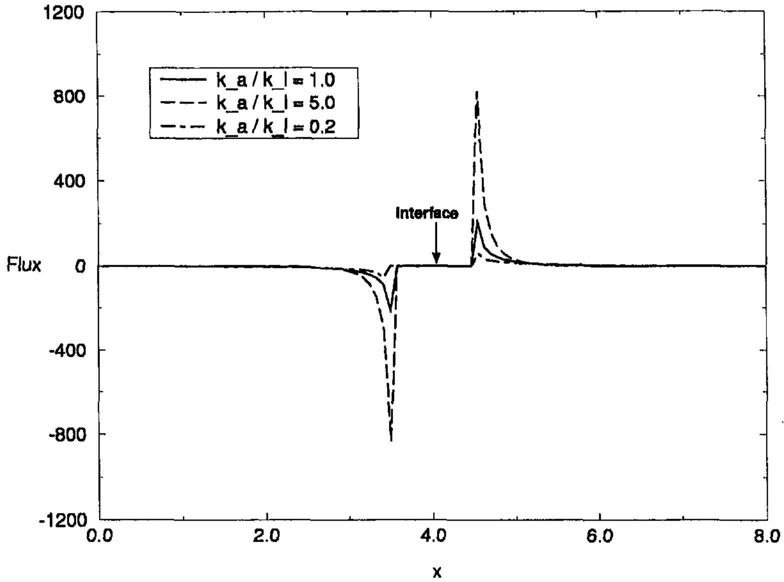

Fig. 2 Variation of local heat flux over the side wall of the furnace for $\mathrm{Gr} = 10^5$, $\mathrm{Pr} = 0.015$, $(T_f - T_c)/(T_h - T_f) = 1.0$, $k_s/k_l = 1.0$, $\rho_s/\rho_l = 1.0$, $C_{ps}/C_{pl} = 1.0$, $\rho_a/\rho_l = 1.0$, $C_{pa}/C_{pl} = 1.0$, and $k_a/k_l = 5.0$, 1.0, and 0.2

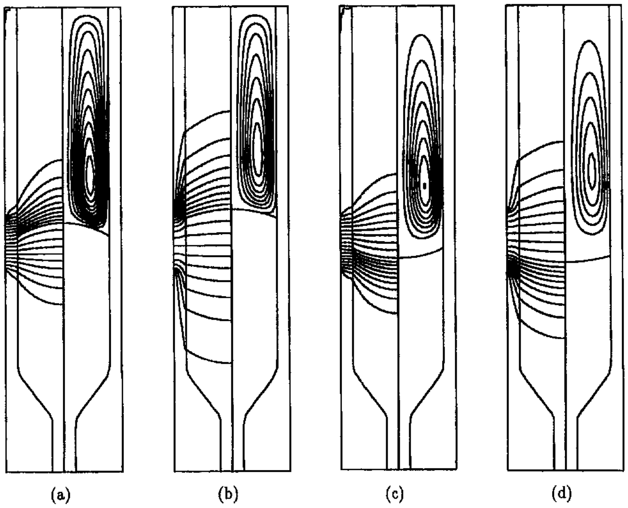

Fig. 3 Temperature and stream function contours for Gr = 10^5, Pr = 0.015, $(T_f - T_c)/(T_h - T_f) = 1.0$, $\rho_s/\rho_l = 1.0$, $C_{ps}/C_{pl} = 1.0$, $k_s/k_l = 2.0$, $\rho_a/\rho_l = 1.0$, $C_{pa}/C_{pl} = 1.0$, and (*a*) $k_s/k_l = 2.0$, $k_a/k_l = 5.0$; (*b*) $k_s/k_l = 2.0$, $k_a/k_l = 0.2$; (*c*) $k_s/k_l = 0.5$, $k_a/k_l = 5.0$; and (*d*) $k_s/k_l = 0.5$, $k_a/k_l = 0.2$

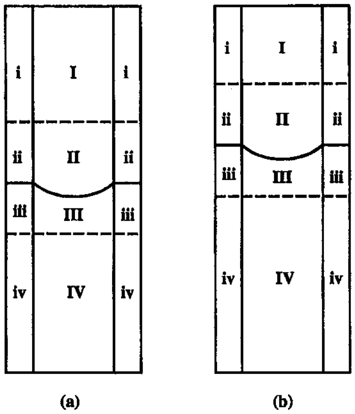

Fig. 5 Schematic of interface movement in a crystal growth system: (*a*) at the beginning, and (*b*) during the growth

been developed to avoid the stretching and compression of grids. A Bridgman-Stockbarger system can be divided into four blocks (Fig. 5(*a*)) and grids in each block can be generated and moved adaptively independent of other blocks. Block I consists of the cold zone of the furnace, blocks II and III consist of the gradient region, and block IV consists of the hot zone. The total lengths of blocks II and III remain constant during the growth. Block I on the other hand, becomes longer and block IV becomes shorter as the solidification front moves upward. An equal number of grids moves out of block I and reenters block IV as the crystal is grown. The efficiency and accuracy of the dynamic simulation of Bridgman-type growth can be improved by using this algorithm.

Figure 6 shows the distributions of the temperature and stream function at Grashof number of 10^5, Prandtl number of 0.015, and pulling velocity of 5 cm/h. The diameter of the crystal is 6 mm. The flow pattern of a two-cell structure is observed in Fig. 6(*b*) and (*c*). One large and strong cell rotating in a counterclockwise direction exists in the region between the hot and adiabatic zones. A small and weak cell rotating in a clockwise direction is produced directly above the solidification interface. Although the ratios of the conductivities, $k_s/k_l \approx 0.5$ and $k_a/k_l \approx 0.1$, are similar to those used in Fig. 4(*c*), the length of the gradient zone is longer in this case. The temperature gradients in the solid and the liquid crystals are smaller and therefore an almost flat interface toward the melt has been predicted in both cases. The heat flux vectors are shown in the left hand of Fig. 6(*a*). The heat flux enters the melt phase from the hot zone above the adiabatic region, passes through the solid/melt interface, and exits from the cold zone just below the adiabatic region. The heat flux in the ampoule is very small due to low conductivity of the ampoule material. Owing to the relatively larger length of the adiabatic region, the heat flux vectors are quite uniform above the interface and the interface is therefore fairly flat.

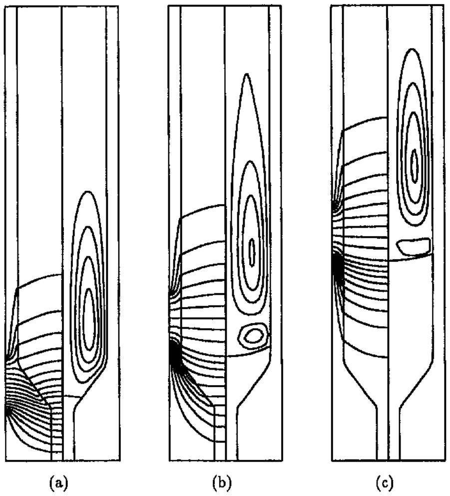

Fig. 4 Temperature and stream function contours: Gr = 10^5, Pr = 0.015, $(T_f - T_c)/(T_h - T_f) = 1.0$, $\rho_s/\rho_l = 1.0$, $C_{ps}/C_{pl} = 1.0$, $k_a/k_l = 1.0$, $C_{pa}/C_{pl} = 1.0$, $\rho_a/\rho_l = 0.1$, and $k_s/k_l = 0.5$

Global Simulation of GaAs Growth

Fundamentally, the Cz process consists of freezing material from a molten pool contained in a crucible, onto the end of a single crystal "seed" of the same material. The material thus frozen replicates the single-crystal structure of the seed, and consequently, a small seed becomes a large crystal. In the case of III-V compounds, an encapsulant layer of a highly viscous melt (generally B_2O_3) is placed over the compound melt to prohibit the escape of the volatile component, e.g., Arsenic in the case of GaAs. This growth technique is referred to as the LEC process. Gallium arsenide crystals can be grown at either atmospheric or a higher pressure since the equilibrium vapor pressure at its freezing temperature is about 0.9 atm.

Two issues are critical for global simulation of Cz or LEC growth. One is the accurate simulation of the convective heat transfer with solidification and free surfaces, and the other is the inclusion of the radiation heat transfer between all components (Dupret et al., 1990; Maruyama and Aihara, 1994; Tsukada et al., 1995). Because of the difficulty in solving highly nonlinear radiation equations and lack of experimental data on thermophysical properties, only radiation exchange among surfaces has been considered for crystal growth modeling (Ramachandran et al., 1985; Dupret and van den Bogaert, 1994). In this paper we have employed the numerical scheme developed for convective heat transfer with solidification and free surfaces (Zhang et al., 1996), combined with the radiation model developed by Ramachandran and Dudukovic (1985) to simulate the global LEC growth of GaAs crystal. The radiative heat flux for gray surface *j* is determined from radiant energy considerations. For exchange between gray surfaces, the radiation heat transfer per unit surface area q''_r for a control volume of surface designated by subscript *j*, can be calculated as

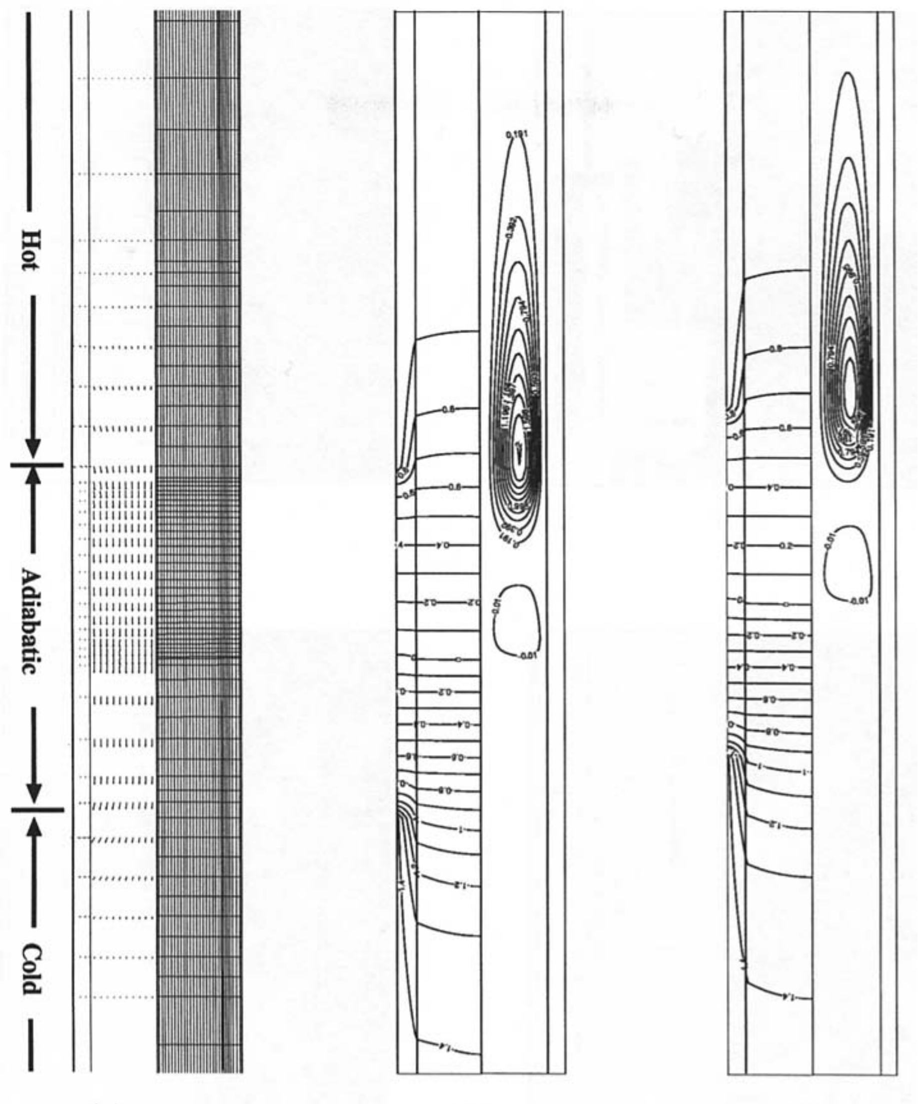

(a) (b) (c)

Fig. 6 (*a*) Initial grids and heat flux field, and temperature and stream function distributions during directional solidification with pulling velocity u_p = 5 cm/h for Gr = 10^5 at time (*b*) t = 0 s and (*c*) t = 200 s, where k_s = 7.86 W/m°C, k_l = 14.1 W/m°C, and k_a = 1.0 W/m°C

$$q''_{r,j} = \epsilon_j \sigma T_j^4 - \frac{1}{A_j} \sum_{i=1}^{N} G_{i,j} \epsilon_i \sigma T_i^4 A_i, \qquad (14)$$

where ϵ is the emissivity, σ is Stefan-Boltzmann constant, $G_{i,j}$ is the Gebhart factor representing the fraction of the radiation emitting from surface i which is absorbed by surface j, and N is the total number of radiating surfaces present in the system.

A typical grid distribution used for the present simulation is shown in Fig. 7(*a*). The geometric configuration of the furnace has been taken from Fainberg et al. (1997) and the thermophysical properties are obtained from CRC handbook (Lide, 1995). The furnace is considered to be filled with Argon gas at 1 MPa. In this simulation the diameter of the crystal is kept constant, while allowing the pull rate to change accordingly. The dimensionless temperature is defined by $\Theta = (T - T_f)/(T_f - T_c)$, where T_f is the melting temperature of GaAs, 1511 K, and T_c is the temperature at the furnace wall, 300 K. The thermophysical properties of the crystal, graphite, steel, and other materials are obtained from Baumgartl et al. (1993). The gas Grashof number based on the crucible radius is equal to 10^{10} in the calculation, and the gas flow inside the furnace is expected to be turbulent. The gas turbulence is modeled through the conventional $k-\epsilon$ model with appropriate wall functions to properly account for the near wall flows. The density of the gas is evaluated from an ideal gas equation of state, e.g., $\rho = P/RT$. The flow in the melt is considered to be laminar, and the melt Grashof number of 10^7 is used. During the growth, the total number of grids remains constant, and the number of grids in most solid components keep unchanged. However, the grids in the crystal increases as the crystal grows larger, and some of the nodes in the gas phase migrate to the crystal. An interpolation scheme has been applied to accomplish the grid migration.

Velocity and temperature fields in the melt, gas, crystal and furnace components for three different heights of the crystal are presented in Fig. 7(*b*)–(*d*). The figures also show von Mises stress in the grown crystal. In Fig. 7(*b*), the largest recirculation is generated in the region that includes the heater, graphite baffle, and vertical insulating shield. The gas flows downward along the side of the furnace walls and releases a large amount of heat that was originally gained from the heater into the furnace, gas flowing upward along the heater. A large temperature difference between the heater and cold furnace walls and a large vertical size of the furnace make the buoyancy recirculation strong. This recirculating flow reduces the heater

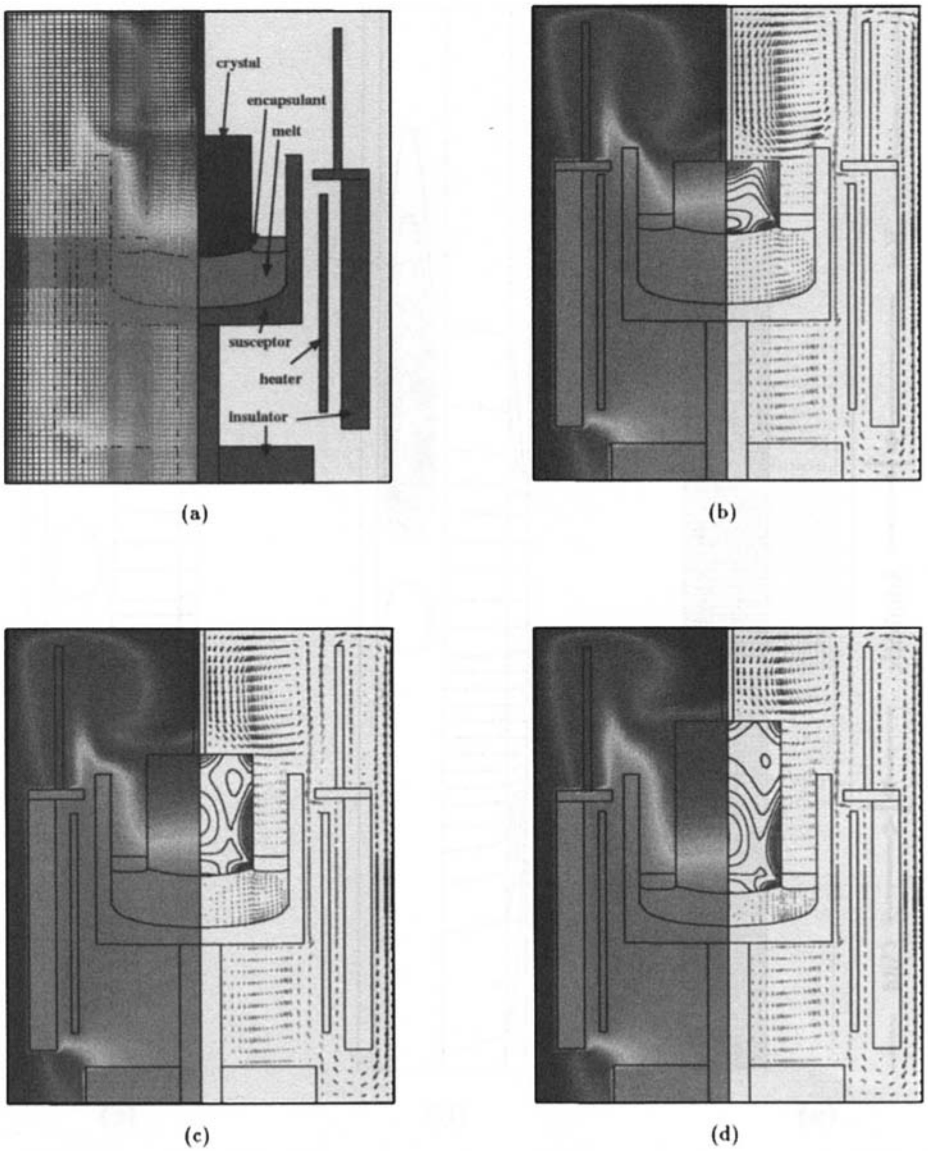

Fig. 7 Velocity, temperature, and von Mises stress fields in the crystal for a global simulation of GaAs growth with $Gr_g = 10^{10}$ and $Gr_l = 10^7$: (*a*) schematic and grid distribution, and represented for different crystal heights (*b*) 50 mm, (*c*) 80 mm, and (*d*) 110 mm

efficiency. Due to strong buoyancy effects, the gas with high velocities exits from the gap between the graphite insulator and the susceptor. This gas jet is observed to have high temperatures in all three figures, and it acts like a heat shield in the furnace which makes the original design of the graphite baffle less effective. The gas flow plays a key role in determining the local heat transfer in the vicinity of the crystal which is crucial for the quality of the final crystal.

The second largest convective cell is generated in the region that includes the crystal, seed shaft, part of the crucible, and graphite baffle. The gas flows downward along the seed shaft, which is cooled by water. This downward gas takes heat away from a part of the crystal. A small recirculating secondary cell sits on top of the crystal as shown in Figs. 7(*b*) and (*c*). The recirculation between the crystal and crucible plays an important role in heat transfer and stress distribution on the side of the crystal. The von Mises thermal stress distribution is greatly influenced by gas convection. During growth, the flow pattern in this region is changed dramatically, and the stress distribution is changed accordingly. The interface shape remains concave towards the crystal for all three heights.

Approximately six hours of CPU time on a single node of IBM SP2 computer is required to perform these calculations.

Conclusion

The effect of the crystal and ampoule materials, thermal boundary conditions, and shape of the furnace on interface shape and melt flow pattern have been studied for a Bridgman growth system. The numerical results reveal that a convex interface towards the melt is formed when the conductivity ratio of solid to melt is greater than unity, while an almost flat interface shape is obtained for $k_s = k_l$. In the Bridgman system, both a single-cell structure and the two-cell structure can be formed depending on the ampoule material and the size of the furnace gradient region. For the system we have studied, the benefits of flatter interface, weaker convection, and reduced heat lost through the ampoule have been achieved by lowering the ampoule thermal conductivity and/or widening the gradient region. However, the flow pattern changes from a single cell structure to two cell structure. It should be noted that the shape of the conic section can also play an important role during the growth.

A convex interface shape is expected during the seeding and a concave interface shape is formed as the growth proceeds.

Global simulations of LEC GaAs growth have also been performed. New features of grid generation have been devised and added to the original formulation to make it suitable for global modeling. The grids are able to follow the domain change due to the movement of the crystal/melt solidification interface and the free surface, reduction in the melt height, and increase in the crystal length. This is the first time that a dynamical global model is able to account for convection in both the melt and the gas phases. The drawback of the unknown boundary conditions in a local model can be certainly improved by using this kind of global model. The computational results demonstrate that the distributions of the temperature and von Mises stress in the crystal change with time, and the interface shape varies accordingly. This information can allow us to detect the crystal defect formation instantaneously. Dynamic simulations are essential to accurately predict the heat transfer and interface dynamics in this complicated Cz growth system. The simulation performed for Cz crystal growth process are based on an industrial design. Our results show that the extra built-in baffle does not have any significant impact on preventing the system heat loss from the wall since a naturally formed high temperature gas jet acts as a heat shield in parallel to the external baffle. This information provides some insights of the flow behavior inside the Cz furnace system, and can help in design of the next generation furnace.

Acknowledgments

This research has been supported by AFOSR/DARPA through Consortium for Crystal Growth Research, and Microgravity Sciences and Applications Program of NASA (Grant #NCC8-100).

References

Adornato, P. M., and Brown, R. A., 1987, "Convection and Segregation in Directional Solidification of Dilute and Non-dilute Binary Alloys: Effects of Ampoule and Furnace Design," *J. Crystal Growth,* Vol. 80, pp. 155–190.

Baumgartl, J., Bune, A., Koai, K., and Müller, G., 1993, "Global Simulation of Heat Transport, Including Melt Convection in a Czochralski Crystal Growth Process—Combined Finite Element/Finite Volume Approach," *Materials Science and Engineering,* Vol. A173, pp. 9–13.

Brown, R. A., 1988, "Theory of Transport Processes in Single Crystal Growth from the Melt," *AIChE J.,* Vol. 34, No. 6, pp. 881–911.

Carslaw, H. S., and Jaeger, J. C., 1959, *Conduction of Heat in Solids,* Oxford University Press, London.

Dupret, F., and van den Bogaert, N., 1994, "Modelling Bridgman and Czochralski Growth," *Handbook of Crystal Growth,* Vol. 2b, D. T. J. Hurle, ed., North-Holland, New York.

Dupret, F., Necodeme, P., Ryckmans, Y., Wouters, P., and Crochet, M. J., 1990, "Global Modeling of Heat and Mass Transfer in Crystal Growth Furnaces," *Int. J. Heat Mass Transfer,* Vol. 33, pp. 1849–1871.

Fainberg, J., Leister, H.-J., and Müller, G., 1997, "Numerical Simulation of the LEC-growth of GaAs Crystals with Account of High Pressure Gas Convection," *J. Crystal Growth,* Vol. 180, pp. 517–523.

Glicksman, M. E., Coriell, S. R., and McFadden, G. B., 1986, "Interaction of Flows with the Crystal-Melt Interface," *Ann. Rev. Fluid Mech.,* Vol. 18, pp. 307–335.

Liang, M. C., and Lan, C. W., 1996, "Three-dimensional Convection and Solute Segregation in Vertical Bridgman Crystal Growth," *J. Crystal Growth,* Vol. 167, pp. 320–332.

Lide, D. R., 1995, *Handbook of Chemistry and Physics,* 76th Ed., CRC Press, New York.

Kim, D. H., and Brown, R. A., 1991, "Modelling of the Dynamics of HgCdTe Growth by the Vertical Bridgman Method," *J. Crystal Growth,* Vol. 114, pp. 441–434.

Kinney, T. A., and Brown, R. A., 1993, "Application of Turbulence Modeling to the Integrated Hydrodynamic Thermal-Capillary Model of Czochralski Crystal Growth of Silicon," *J. Crystal Growth,* Vol. 132, 551–574.

Koai, K., Sonnenberg, K., and Wenzl, H., 1994, "Influence of Crucible Support and Radial Heating on the Interface Shape during Vertical Bridgman GaAs Growth," *J. Crystal Growth,* Vol. 137, pp. 59–63.

Maruyama, S., and Aihara, T., 1994, "Radiation Heat Transfer of a Czochralski Growth Furnace with Arbitrary Specular and Diffuse Surfaces," *Int. J. Heat Mass Transfer,* Vol. 37, pp. 1723–1731.

Ouyang, H., and Shyy, W., 1996, "Multizone Simulation of the Bridgman Growth Process of β-NiAl Crystal," *Int. J. Heat Mass Transfer,* Vol. 39, No. 10, pp. 2039–2051.

Ramachandran, P. A., and Dudukovic, M. P., 1985, "Simulation of Temperature Distribution in Crystals Grown by Czochralski Method," *J. Crystal Growth,* Vol. 71, pp. 399–408.

Santailler, J. L., Duffar, T., Theodore, F., Boiton, P., Barat, C., Angelier, B., Giacommentti, N., Dusserre, P., and Nabot, J. P., 1996, "Some Features of Two Commercial Softwares for the Modeling of Bulk Crystal Growth Processes," *2nd Int. Conf. on Modeling in Crystal Growth,* Durbuy, Belguim.

Tsukada, T., Kakinoki, K., Hozawa, M., and Imaishi, N., 1995, "Effect of Internal Radiation within Crystal and Melt on Czochralski Crystal Growth of Oxide," *Int. J. Heat Mass Transfer,* Vol. 38, No. 15, pp. 2707–2714.

Zhang, H., and Moallemi, M. K., 1995, "A Multizone Adaptive Grid Generation Technique for Simulation of Moving and Free Boundary Problems," *Num. Heat Transfer,* Vol. B27, pp. 255–276.

Zhang, H., and Prasad, V., 1995, "A Multizone Adaptive Process Model for Crystal Growth at Low and High Pressures," *J. Crystal Growth,* Vol. 155, pp. 47–65.

Zhang, H., Prasad, V., and Moallemi, M. K., 1996, "A Numerical Algorithm Using Multizone Adaptive Grid Generation for Multiphase Transport Processes with Moving and free Boundaries," *Num. Heat Transfer,* Vol. B29, pp. 399–421.

Zheng, L., and Larson, D. J., Jr., 1997, "Thermoelectric Effects on Interface Demarcation and Directional Solidification in Bismuth," *J. Crystal Growth,* Vol. 180, pp. 293–304.

Zou, Y. F., Zhang, H., and Prasad, V., 1996, "Dynamics of melt-crystal interface and thermal stresses in Czochralski crystal growth processes," *J. Crystal Growth,* Vol. 166, pp. 476–482.

H. Zhang
Assistant Professor,
Department of Mechanical Engineering,
State University of New York,
Stony Brook, NY 11794-2300
e-mail: hzhang@thermsa.eng.sunysb.edu
Mem. ASME

L. L. Zheng
Research Scientist,
Department of Materials
Science and Engineering,
State University of New York,
Stony Brook, NY 11794-2275
e-mail: lzheng@thermsa.eng.sunysb.edu

V. Prasad
Professor,
Department of Mechanical Engineering,
State University of New York,
Stony Brook, NY 11794-2300
e-mail: prasad@thermsa.eng.sunysb.edu
Fellow ASME

D. J. Larson, Jr.
Professor,
Department of Materials Science
and Engineering,
State University of New York,
Stony Brook, NY 11794-2275
e-mail: dlarson@ccmail.sunysb.edu

Diameter-Controlled Czochralski Growth of Silicon Crystals

A thermal-capillary dynamic model for Czochralski (Cz) growth of silicon single crystal is presented that accounts for convection in the melt, conduction in the crystal, and radiation from the melt free surface and crystal. The shapes of the crystal/melt interface, moving crystal, and free surface are governed by the balance of energy and stresses. Decrease of the melt volume as the crystal is grown is also considered. A control algorithm based on the adjustment of the pull rate and/or crucible wall temperature has been developed. The diameter of the crystal can remain constant or vary with time based on the strategies implemented to control the growth process.

Introduction

The growth of silicon single crystals and other semiconductor materials is the basis for electronic device fabrication. Although several methods have been devised to grow silicon crystals, the Czochralski (Cz) method has virtually dominated the entire production of single crystals for microelectronics industry (Shimura, 1989; Hurle and Cockayne, 1994). The popularity of this method comes from its ability to meet the stringent requirements for purity, doping, electrical and mechanical properties, and crystallographic perfection. Fundamentally, the Cz process consists of freezing material from a melt contained in a quartz crucible, onto the end of a single crystal ''seed'' of the same material. The material thus frozen replicates the single-crystal structure of the seed, and consequently, a small seed becomes a large crystal. Detailed discussions on growing semiconductor crystals using the Cz method can be found in several books and review articles (Brown, 1986; Müller, 1988; Dupret and Van den Bogaert, 1994; Prasad et al., 1997).

Heat transfer plays a vital role in Czochralski crystal growth process. Indeed, the convective transport in the melt is closely coupled with the radiation in the Cz growth system. For Si growth, the melt surface is maintained at a temperature above 1410°C while the walls of the furnace are cooled by recirculating water at around room temperature. The crystal and other components of the furnace also participate in radiation exchange making the transport phenomena in a Cz system quite complex. Generally, the recirculating flow in the melt is caused and varied by a combination of four basic modes of convection:

- natural convection due to buoyancy force,
- Marangoni convection due to temperature-dependent surface tension,
- forced convection due to crystal and crucible rotations, and
- forced convection due to crystal pulling and reduction in the melt height.

Batchwise simulations of Cz growth, taking into account the reduction in melt height and increase in crystal length, have been reported by Derby et al. (Derby and Brown, 1986, 1987; Derby et al., 1987). A dynamic thermal-capillary model (DTCM) was developed based on a finite element/Newton method. They observed that an uncontrolled growth leads to a steadily increasing or decreasing diameter because of the continually changing configuration of the melt. Using a proportional/integral controller, an almost cylindrical crystal shape was maintained in their study. This was a local model which did not consider convection in the melt. The work was later extended by Atherton et al. (1987) to develop a semi-global model including self-consistent calculations of the view factors and radiative fluxes. The model was further improved upon by Thomas et al. (1989) to simulate the liquid-encapsulated Czochralski (LEC) growth of GaAs crystals; the encapsulated layer, crucible support, and heater were all included in the system. Again, only the temperature equation was solved and the diffusion model was justified based on the argument that the convective heat transport was not important for the growth of GaAs in the presence of a strong axial magnetic field. Later, more sophisticated global simulations were performed by Kinney et al.

Contributed by the Heat Transfer Division for publication in the JOURNAL OF HEAT TRANSFER. Manuscript received by the Heat Transfer Division, Nov. 3, 1997; revision received, Aug. 18, 1998. Keywords: Control, Crystal Growth, Heat Transfer, Modeling, Moving Boundaries. Associate Technical Editor: C. Beckermann.

(1993) that included convective effects. However, the calculations were limited to a constant diameter crystal only.

Local and global models have been also developed by Dupret and co-workers (Dupret et al., 1990; Van den Bogaert and Dupret, 1997a, b) for Cz and LEC growth. A diameter-controlled local model was iterated with a global model to perform simulations for Cz growth of Germanium crystals. The model was claimed to be accurate and efficient for radiative heat transfer calculations and local/global iterations. Again, only the temperature equation was solved.

A high-resolution numerical scheme based on multizone adaptive grid generation (MAGG) and curvilinear finite volume discretization (MASTRAPP) has been developed recently by Zhang and co-workers to model the materials processes with moving phase-change interfaces and free surfaces. Extensive dynamic local and global simulations of Cz and LEC growth have been performed using the MASTRAPP-based model (Zhang and Prasad, 1995; Zhang et al., 1996b, c, 1997; Zou et al., 1996). The model is able to consider all interior components of the furnace and coupled convection and radiation heat transfer in the crystal, melt and gas phases. The model is capable of predicting the heat transfer in the furnace, crystal/melt interface shape and its dynamics, macrosegregation and stress prediction in the crystal. However, all of these simulations are based on a constant diameter growth, although dynamic growth has also been considered, e.g., the drop in melt level with the growth of crystal.

In the present work, a local diameter-controlled model is developed that considers convection in the melt with and without an applied magnetic field. The geometric flexibility for change in the crystal diameter and interface shape is achieved through the use of multizone adaptive grid generation scheme (Zhang and Moallemi, 1995). The diameter of the crystal, and the shapes of the crystal/melt solidification interface and free surface are calculated simultaneously with the temperature and flow fields in both the crystal and the melt, and thermal stresses in the crystal. Cz growth, both with and without diameter control has been simulated, and it is demonstrated that the change in crystal diameter depends on the pull rate and crucible wall temperature. A wavy or a cylindrical shape of the crystal can be obtained by using a simple control algorithm. The dynamic response of the system has been examined using both a diffusion model and a convection model with and without an applied magnetic field.

Mathematical Model

To formulate the Cz problem, the following assumptions have been made: (1) the melt flow is incompressible, laminar, and axisymmetric; (2) the melt is a Newtonian fluid; (3) the thermophysical properties are constant in various phases; (4) the density and specific heat are the same for the crystal and the melt; and (5) the Boussinesq approximation is applicable. Conservation equations for transport processes can then be written in dimensionless form as follows.

Continuity in the Melt:

$$\frac{\partial u}{\partial x} + \frac{1}{r}\frac{\partial}{\partial r}(rv) = 0. \tag{1}$$

Conservation of Momentum in the Melt:

$$\frac{\partial u}{\partial t} + \frac{\partial}{\partial x}(uu) + \frac{1}{r}\frac{\partial}{\partial r}(rvu) = \frac{\partial^2 u}{\partial x^2} + \frac{1}{r}\frac{\partial}{\partial r}\left(r\frac{\partial u}{\partial r}\right) - \frac{\partial p}{\partial x} + \mathrm{Gr}\,\Theta + F_x. \tag{2}$$

$$\frac{\partial v}{\partial t} + \frac{\partial}{\partial x}(uv) + \frac{1}{r}\frac{\partial}{\partial r}(rvv) = \frac{\partial^2 v}{\partial x^2} + \frac{1}{r}\frac{\partial}{\partial r}\left(r\frac{\partial v}{\partial r}\right) - \frac{\partial p}{\partial r} - \frac{v}{r^2} + \frac{w^2}{r} + F_r. \tag{3}$$

Nomenclature

b = crucible radius, m
B = magnetic induction, T (tesla)
Bi = Biot number, $\epsilon\sigma(T^2 + T_a^2)(T + T_a)b/k_s$
Bo = Bond number, $\rho g b^2/\sigma_s$
C_p = specific heat, J/kgK
F = Lorentz force, N/m^3
g_P = proportional gain
g_I = integral gain
G = shear modulus, Pa
Gr = Grashof number, $g\beta b^3(T_w - T_f)/\nu^2$
H_1 = solid/melt interface height, m
H_2 = free-surface height, m
Ha = Hartmann number, $Bb(\sigma_e/\mu)^{1/2}$
h_f = latent heat, J/kg
$\mathbf{J}$ = current density, A/m^2
k = thermal conductivity, W/mK
k_P = proportional parameter
k_I = integral parameter
Ma = Marangoni number, $(\partial\sigma_s/\partial T)(T_w - T_f)b/\mu\alpha$
n = normal direction
p = pressure, Pa
Pe = Peclet number, Gr Pr/Ha^2
Pr = Prandtl number, ν/α
r = radial coordinate
Re = Reynolds number, $\Omega b^2/\nu$
Rr = radius ratio, r_s/b
Ste = Stefan number, $C_{ps}(T_w - T_f)/h_f$
T = temperature, K
t = time, s
u = velocity in axial direction, m/s
u_p = pull rate, m/s
v = velocity in radial direction, m/s
V_m = melt volume, m^3
w = velocity in azimuthal direction, m/s
x = axial coordinate

Greek symbols

β = volume expansion coefficient, 1/K
ϵ = emissivity
λ = parameter
μ = dynamic viscosity, kg/ms
ν = kinematic viscosity, m^2/s Poisson's ratio
Ω = rotation rate, 1/s
ϕ_J = meniscus angle
ϕ_o = wetting angle
Ψ = electric current stream function
ρ = density, kg/m^3
σ = Stefan-Boltzman constant, W/m^2 K^4
σ_e = electrical conductivity, 1/Ω m
σ_s = surface tension, N/m
τ = tangential direction
Θ = dimensionless temperature, $\dfrac{T - T_\infty}{Tw - T_\infty}$

Subscripts

a = ambient
c = crucible
f = freezing temperature
fs = free surface
i = index
int = interface
J = tri-junction, melt/crystal/gas environment
m = melt
r = radial direction
s = solid
set = set value
t = top
x = axial direction
w = wall
θ = azimuthal direction

Superscripts

* = dimensional

$$\frac{\partial w}{\partial t} + \frac{\partial}{\partial x}(uw) + \frac{1}{r}\frac{\partial}{\partial r}(rvw) = \frac{\partial^2 w}{\partial x^2} + \frac{1}{r}\frac{\partial}{\partial r}\left(r\frac{\partial w}{\partial r}\right) - \frac{w}{r^2} - \frac{vw}{r} + F_\theta . \quad (4)$$

Conservation of Energy in the Melt:

$$\frac{\partial \Theta}{\partial t} + \frac{\partial}{\partial x}(u\Theta) + \frac{1}{r}\frac{\partial}{\partial r}(rv\Theta) = \frac{1}{\mathrm{Pr}}\left[\frac{\partial^2 \Theta}{\partial x^2} + \frac{1}{r}\frac{\partial}{\partial r}\left(r\frac{\partial \Theta}{\partial r}\right)\right] . \quad (5)$$

Conservation of Energy in the Crystal:

$$\frac{\partial \Theta}{\partial t} + u_p\frac{\partial \Theta}{\partial x} = \frac{1}{\mathrm{Pr}}\frac{k_s}{k_m}\left[\frac{\partial^{2\mu}}{\partial x^2} + \frac{1}{r}\frac{\partial}{\partial r}\left(r\frac{\partial \Theta}{\partial r}\right)\right] , \quad (6)$$

where u, v, and w are the non-dimensional velocities in x, r, and θ directions, respectively, and Θ is the nondimensional temperature. The following scales have been used to nondimensionalize the governing Eqs. (1)–(5); length: b, velocity: ν/b, pressure: $\rho\nu^2/b^2$, time: b^2/ν, and temperature: $\Theta = (T - T_a)/(T_w - T_a)$, where T_w is the wall temperature and T_a is the ambient temperature.

The dimensionless parameters $\mathrm{Gr} = g\beta b^3(T_w - T_f)/\nu^2$ and $\mathrm{Pr} = \nu/\alpha$ are the Grashof and Prandtl numbers, respectively. F_x, F_r, and F_θ refer to the components of the Lorentz force due to an applied magnetic field. For an axial magnetic field with induction free approximation (Sabhapathy and Salcudean, 1991; Baumgartl et al., 1993; Langlois et al., 1993),

$$F_x = 0, \quad (7)$$

$$F_r = -\mathrm{Ha}^2 v, \quad (8)$$

$$F_\theta = -\mathrm{Ha}^2 \frac{\partial \Psi}{\partial x} , \quad (9)$$

where $\mathrm{Ha} = Bb(\sigma_e/\mu)^{1/2}$ is the Hartmann number, B is the magnetic induction, and σ_e is the electric conductivity.

The electric current stream function equation can then be written as

$$\frac{\partial}{\partial x}\left(\frac{1}{r}\frac{\partial \Psi}{\partial x}\right) + \frac{\partial}{\partial r}\left(\frac{1}{r}\frac{\partial \Psi}{\partial r}\right) = \frac{\partial w}{\partial x} . \quad (10)$$

The electric current stream function is equal to zero on all boundaries except the crystal/melt interface. However, the electric current in the crystal has been neglected since molten Si is an electrical conductor ($\sigma_{em} = 1.2 \times 10^6\ \Omega^{-1}\ \mathrm{m}^{-1}$) and the solid Si is a semiconductor ($\sigma_{es} = 5.8 \times 10^4\ \Omega^{-1}\ \mathrm{m}^{-1}$). A small error may be introduced by this assumption according to Sabhapathy and Salcudean (1991).

Solidification of a pure substance is modeled with a fixed fusion temperation T_f, implying that the solid and liquid phases are separated by a sharp interface, $s(x, r, t) = H_1(r, t) - x = 0$, where H_1 is the dimensionless height of the crystal/melt interface. An expression for the movement of the crystal/melt interface can be obtained as follows (Zhang and Prasad, 1995):

$$\frac{\partial H_1}{\partial t} - u_p(t) = \frac{\mathrm{Ste}}{\mathrm{Pr}}\left(\frac{k_s}{k_m}\frac{\partial \Theta_s}{\partial n} - \frac{\partial \Theta_m}{\partial n}\right)\left[1 + \left(\frac{\partial H_1}{\partial r}\right)^2\right] , \quad (11)$$

where $u_p(t)$ is the pull rate and $\mathrm{Ste} = C_{ps}(T_w - T_f)/h_f$ is the Stefan number of the melt. This equation is based on the assumption that the crystal and melt are not separated at the trijunction.

Denoting the free-surface position as $x = H_2(r, t)$, the height of the free surface can be determined by solving the following equation:

$$\frac{\partial^2 H_2/\partial r^2}{[1 + (\partial H_2/\partial r)^2]^{3/2}} + \frac{\partial H_2/\partial r}{r[1 + (\partial H_2/\partial r)^2]^{1/2}} = \mathrm{Bo}(H_2 - \lambda), \quad (12)$$

where $\mathrm{Bo} = \rho g b^2/\sigma_s$ is the Bond number, and the parameter, λ, can be calculated from the melt conservation constraint,

$$\int_0^{Rr} H_1 r dr + \int_{Rr}^1 H_2 r dr = \frac{V_m(t)}{2\pi} , \quad (13)$$

where $V_m(t)$ is the volume of the melt, and $Rr = r_s/b$ is the radius ratio. Two boundary conditions are needed to solve for the shape of the free surface, which are as follows: At the trijunction, the meniscus is considered to be pinned to the edge of the crystal, and at the junction between the free surface and crucible wall, a 90-deg contact angle is assumed in view of the weak influence of the shape of the crucible meniscus on heat transfer.

The dynamic response of the crystal radius at the triple-point can be obtained from (Surek et al., 1980; Derby and Brown, 1987; Irizarry-Rivera and Seider, 1997):

$$\frac{\partial r_J}{\partial x} = -\frac{1}{u_p}\frac{\partial r_J}{\partial t} , \quad (14)$$

$$\frac{\partial r_J}{\partial t} = \left[u_p - \left.\frac{\partial H_2}{\partial t}\right|_{r=Rr}\right] \tan(\phi_J - \phi_o) \quad (15)$$

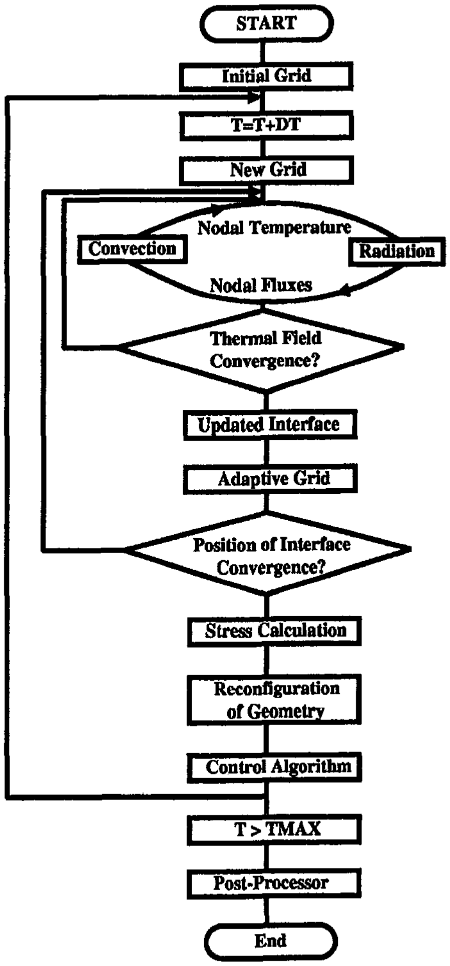

Fig. 1 Flow chart for MASTRAPP-based scheme

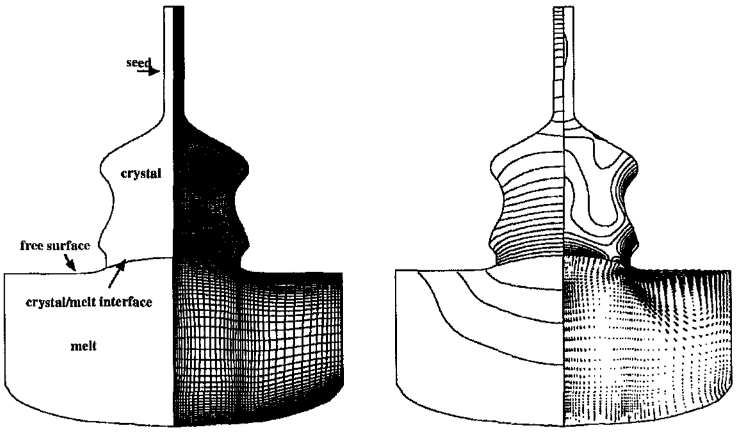

(a) (b)

Fig. 2 (*a*) Grid distribution, and (*b*) temperature, stress and flow fields during the batchwise simulations of Cz growth for Gr = 10^6, Ma = −100, $\mathrm{Re}_s = 2.0 \times 10^3$, $\mathrm{Re}_c = -5.0 \times 10^2$ and Ha = 0. The shape of the crystal is predefined, and the crucible wall temperature is taken as $\Theta_w = 1$ while the pull rate is adjusted during the growth.

where ϕ_J is the dynamic angle between the meniscus and the vertical direction, and ϕ_o is the equilibrium wetting angle between the meniscus and the crystal wall. For Si growth, ϕ_o is generally taken as 11 deg (Hurle and Cockayne, 1994). However, the single-valued representation of the meniscus imposes a restriction on the predictions when the crystal grows inward at an angle greater than the equilibrium wetting angle of 11 deg. When this happens, the meniscus folds over such that the shape becomes double-valued in r and the representation of the meniscus fails. An angle of 45 deg is, therefore, used for the current simulations in which the shape of the crystal will change significantly.

Some of the other boundary conditions for the problem under consideration include: top and side wall of the crystal,

$$u = u_p, \quad v = 0, \quad w = \mathrm{Re}_s r,$$

$$-\frac{\partial \Theta_s}{\partial n} = \mathrm{Bi}_s(\Theta_s - \Theta_a); \qquad (16)$$

crystal/melt interface,

$$u = u_{\mathrm{int}}, \quad v = v_{\mathrm{int}}, \quad w = \mathrm{Re}_s r, \quad \Theta = 0; \qquad (17)$$

free surface,

$$u = \frac{\partial H_2}{\partial t} + v\frac{\partial H_2}{\partial r}, \quad \frac{\partial v}{\partial n} - \frac{\partial u}{\partial \tau} = \frac{\mathrm{Ma}}{\mathrm{Pr}}\frac{\partial \Theta}{\partial n},$$

$$-\frac{k_{fs}}{k_s}\frac{\partial \Theta_{fs}}{\partial n} = \mathrm{Bi}_{fs}(\Theta_{fs} - \Theta_a); \qquad (18)$$

bottom and side wall of the crucible,

$$u = v = 0, \quad w = \mathrm{Re}_c r, \quad \Theta = \Theta_w; \qquad (19)$$

where $\mathrm{Re}_s = \Omega_s b^2/\nu$ and $\mathrm{Re}_c = \Omega_c b^2/\nu$ are the crystal and crucible-rotation Reynolds numbers, respectively, $\mathrm{Ma} = (\partial\sigma_s/\partial T)(T_w - T_f)b/\mu\alpha$ is the Marangoni number, Θ_w is the dimensionless temperature of the crucible wall, and u_{int} and v_{int} are the interface velocity components in x and r-directions, respectively. The radiative heat loss has been considered from the side wall of the crystal and the melt free surface with radiation Biot number, $\mathrm{Bi} = \epsilon\sigma(T^2 + T_a^2)(T + T_a)b/k_s$.

Table 1 Thermophysical properties and parameters for Si growth (Prasad et al., 1997)

Properties of Si melt	
Density (kg/m^3)	2420
Thermal conductivity (W/mK)	64
Specific heat (J/kgK)	1000
Kinematic viscosity (m^2/s)	5.0×10^{-7}
Coefficient of thermal expansion (/K)	1.41×10^{-5}
Electrical conductivity (S/m)	1.2×10^{6}
Emissivity	0.15
Latent heat of solidification (kJ/kg)	1800
Freezing temperature (°C)	1410
Wall temperature (°C)	1560
Ambient temperature (°C)	200
Surface tension (N/m)	0.72
Properties of Si solid	
Thermal conductivity (W/mK)	22
Electrical conductivity (S/m)	5.8×10^{4}
Emissivity	0.75

The control strategy is demonstrated by regulating the pull rate or crucible wall temperature with a servo-controller obtained by taking the time derivative of a conventional proportional-integral (PI) feedback control equation (Stephanopoulos, 1984; Gevelber and Stephanopoulos, 1987). If the pull rate is a control parameter, the control equation can be written (Derby and Brown, 1986 and 1987) as

$$\frac{\partial u_p}{\partial t} = g_p\frac{\partial r_J}{\partial t} + g_i(r_J - r_{\mathrm{set}}) \qquad (20)$$

where g_p is the proportional gain and g_i is the integral gain of the controller, and r_{set} is the set-point value for the crystal radius. This type of controller is often used in practice where the deviation quantity $(r_J - r_{\mathrm{set}})$ is determined by an analysis of the weight gain of the crystal, as monitored by a load cell connected to the pull shaft (Hurle et al., 1990).

Equation (15) together with Eq. (20) reduces to

$$\frac{\partial u_p}{\partial t} = g_p\left[u_p - \left.\frac{\partial H_2}{\partial t}\right|_{r=Rr}\right]\tan(\phi_J - \phi_o) + g_i(r_J - r_{\mathrm{set}}) \qquad (21)$$

for a small value of $\phi_J - \phi_o$, $\tan(\phi_J - \phi_o) \approx \phi_J - \phi_o$. The above equation can be simplified as follows:

$$u_p = u_p + k_p(\phi_J - \phi_o) + k_i(r_J - r_{\mathrm{set}}). \qquad (22)$$

Equation (22) can be used as a controller to adjust the pull rate during growth. Similar equations can be developed for the crucible wall temperature or heater power.

Numerical Scheme

Here we employ a high-resolution computer model developed by Zhang and co-workers based on multizone adaptive grid generation (MAGG) and curvilinear finite volume (CFV) discretization to simulate the transport phenomena associated with complex materials processes (Zhang and Moallemi, 1995; Zhang et al., 1996a). In this scheme, the computational domain

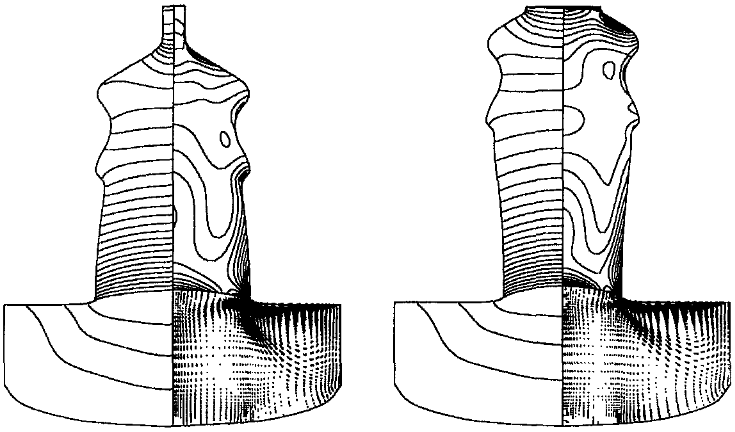

(a) $u_p = 10$ and $\Theta_w = 1$ (b) $u_p = 15$ and $\Theta_w = 1$

Fig. 3 Temperature, stress, and flow fields during the batchwise simulations of Cz growth for Gr = 10^6, Ma = −100, $Re_s = 2.0 \times 10^3$, $Re_c = -5.0 \times 10^2$, and Ha = 0 with two different pull rates and fixed crucible wall temperature $\Theta_w = 1$

is permitted to consist of various materials in different phases with significantly different thermophysical and transport properties. The model uses a generalized governing equation for transient processes involving diffusion and convection, thereby allowing a single formulation for materials processes with or without phase change.

The MAGG scheme is based on constrained adaptive optimization of grid characteristics: smoothness, orthogonality, concentration, and grid inertia (Zhang and Moallemi, 1995). This scheme is able to preserve internal interfaces and make them coincide with some grid lines. The scheme also allows grids to move adaptively as the solutions progress and/or domains

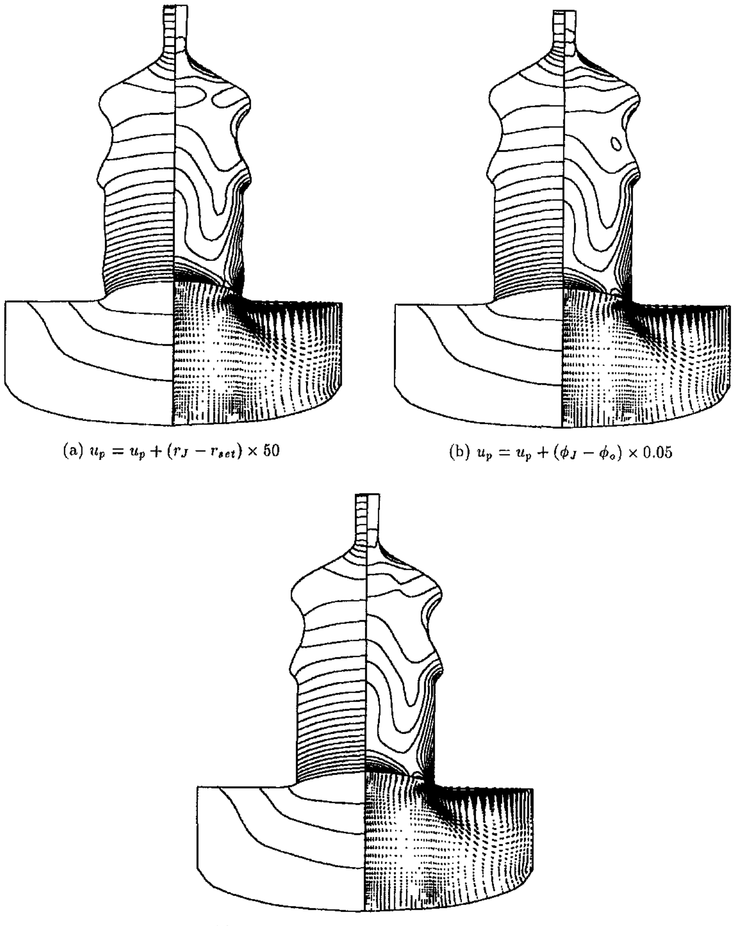

(a) $u_p = u_p + (r_J - r_{set}) \times 50$ (b) $u_p = u_p + (\phi_J - \phi_o) \times 0.05$

(c) $u_p = u_p + (r_J - r_{set}) \times 50 + (\phi_J - \phi_o) \times 0.05$

Fig. 4 Batchwise simulations of Cz growth: crystal radius vs the pull rate with a constant crucible wall temperature $\Theta_w = 1$ for Gr = 10^6, Ma = −100, $Re_s = 2.0 \times 10^3$, $Re_c = -5.0 \times 10^2$, and Ha = 0

change. The generated grids are always smooth and orthogonal, maintaining slope continuity, and cluster in the regions of interfaces/free surfaces and large gradients. The CFV approach is based on flux discretization in the physical domain. A nonorthogonal curvilinear finite volume discretization based on a nonstaggered grid is employed (Zhang et al., 1996a). The algorithm for fluid flow calculations is based on the solutions of a pressure equation to obtain the pressure field and a pressure-correction equation to correct the predicted velocities. A momentum interpolation scheme is employed in the discretization of pressure and pressure-correction equations.

For thermal stress calculations, a finite element module is coupled with the flow solver. The curvilinear grids generated by MAGG are used as control volumes in the finite volume solver and control elements in the finite element solver. In the finite element module, the element stiffness matrix is calculated for every element and then assembled into the global stiffness matrix. Gaussian quadrature is used to perform the integration. As the time needed for stress calculation is much smaller than that for the transport calculations, a direct solver can be effectively used. A detailed discussion on the coupled FVM-FEM scheme for thermal transport and stress calculations can be found in Zou et al. (1996).

The solution procedure of the MASTRAPP based computer algorithm is presented in Fig. 1. After generating the initial grids, the finite volume solver is employed to predict the velocity, temperature, and concentration fields. After the converged flow fields have been obtained, the solidification interface and free surface are updated based on energy balance and stress balance, respectively. The iteration is continued until the interface(s) stops moving. The finite element stress solver is then called to predict the stress distribution in the solid. Through a control algorithm, the domain boundaries and boundary conditions for the process are adjusted based on the information obtained from the current results and solutions obtained from the previous time steps. After the geometric configuration has been determined, the nodes can be rearranged based on a new domain.

The movement of the solidification interface is determined by Eq. (11). An explicit scheme is used to calculate the interface movement. Since the interface movement is very slow in the case of crystal growth, no appreciable error is introduced by the explicit scheme. The shape and location of the free surface is determined by Eq. (12) with two boundary conditions and the volume constraint condition (13). A nonlinear ordinary differential equation solver for Eq. (12) is developed, based on the Newton-Raphson scheme, to solve the shape of the free surface. This solver, independent of the two-dimensional transport calculations, allows us to use a large number of nodes (e.g., 500 or more) to predict the meniscus accurately and efficiently. One-dimensional nodes serve as trace particles on the free surface, and two-dimensional grids are then regenerated adaptively and constrained by the free surface. An accurate prediction of the meniscus angle is critically important to determine the crystal shape. Following this procedure, a large number of trace particles (>500) are also assigned on the side of the crystal. As the crystal is pulled, trace particles move upward, and a new trace particle is created at the triple-point at each time step. Using this scheme, the shape of the crystal can be tracked dynamically. The coupling between the trace particles on the surface of the crystal and two-dimensional mesh is again achieved implicitly through the MAGG scheme.

The algorithm has been validated against the experimental and numerical results by simulating one-dimensional solid-liquid phase change (Carslaw and Jaeger, 1959), two-dimensional natural convection in an eccentric annulus, liquid metal solidification in a rectangular cavity, and many other transport and phase change problems (Moallemi and Zhang, 1994; Zhang et al., 1996a). The code, MASTRAPP, has also been validated against experimental and numerical results for vertical Bridgman growth (Zheng et al., 1997) and Czochralski melt flow (Prasad et al., 1997).

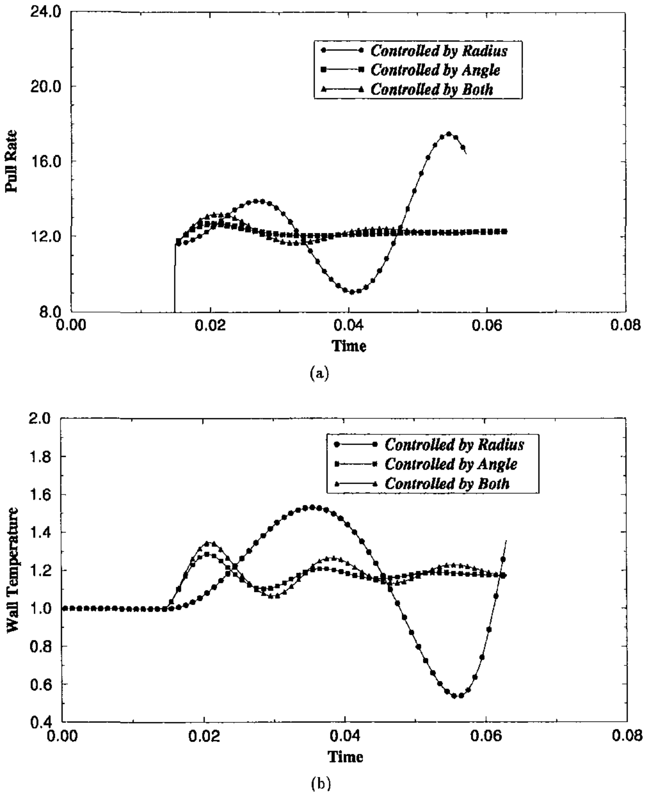

Fig. 5 (*a*) Pull rate and (*b*) crucible wall temperature as functions of time for batchwise Cz growth simulation with control

A comparison of the interface position, and maximum and minimum values of stream function was made using 152 × 42 and 192 × 82 meshes. Differences between the results using different grids are within five percent for Gr = 10^6, Ma = -100, Bo = 500, Re_s = 2000, Re_c = -500, and Ha = 100 with meniscus angle of 45 deg. A larger number of grids is required for higher values of these parameters. For example, 192 × 82 mesh is required for the case of Gr = 10^6, Ma = -100, Bo = 500, Re_s = 2000, Re_c = -500, and Ha = 200 with meniscus angle of 45 deg. A time step, $\Delta t = 0.001$ is required for 152 × 42 mesh to obtain a grid-independent result, while $\Delta t = 0.00025$ is taken for 192 × 82 mesh. A 152 × 42 mesh and $\Delta t = 0.0005$ are used for most of the present calculations. The CPU time for a transient simulation of 500 time steps with 152 × 42 mesh is about one hour on IBM SP2 computer using only one node.

Results and Discussion

Figure 2(*a*) shows the grid distribution at the beginning of the simulation, and Fig. 2(*b*) shows the numerical result. The left-hand side of Fig. 2(*b*) represents the temperature contours and the right-hand side shows the velocity field in the melt as well as the von Mises stress contours in the crystal obtained by a linear elastic stress model. These results are based on the shear modulus of Si crystal, $G = 3.51 \times 10^{10}$ Pa, Poisson's ratio of crystal, $\nu = 0.25$, and thermal expansion coefficients of Si melt, $\beta_m = 1.32 \times 10^{-4}$ 1/K and crystal, $\beta_s = 5.6 \times 10^{-6}$ 1/K. The operating parameters are Gr = 10^6, Ma = -100, Bo = 500, Re_s = 2000, Re_c = -500, and Ha = 0. The other thermophysical properties and parameters for Si crystals are shown in Table 1. The time step of $\Delta t = 0.0005$ (50*s* if b = 0.127 m) is used. The shape of the crystal is predescribed. The crucible wall temperature, $\Theta_w = 1$, is used and the pull rate, $u_p(t)$, is estimated by (Zhang and Prasad, 1995),

$$u_p(t) = -(1 - Rr^2)\left\{\frac{\mathrm{Ste}}{\mathrm{Pr}}\left(\frac{k_s}{k_m}\frac{\partial\theta_s}{\partial n} - \frac{\partial\theta_m}{\partial n}\right) \times \left[1 + \left(\frac{\partial H_1}{\partial r}\right)^2\right]\right\}\Bigg|_{r=Rr}, \quad (23)$$

$u_p = 11.6$ (5.8 cm/h if $b = 0.127$ m) is obtained for the present case. One strong cell located under the free surface is due to the combined effects of buoyancy and Marangoni convection, and one cell located directly under the crystal is due to the crystal rotation. The flow recirculation in the bottom portion of the melt is due to the combined effects of the crucible rotation and buoyancy force. The temperature difference between the contour lines is 0.25 (37.5°C), while the von Mises stress between the two contour lines is 1.0 MPa. The maximum thermal stress is located at the melt/crystal interface.

Based on previous results, two pull rates $u_p = 10$ and 15 are used to examine the uncontrolled growth. For the case in which the pull rate and crucible wall temperature are fixed, the variation of the crystal diameter with time depends on the pull rate, as shown in Figs. 3(a) and (b). In Fig. 3(a) ($u_p = 10$), the crystal diameter increases quickly in the beginning and more slowly at the end. The heat loss from the crystal increases as the diameter of the crystal becomes large, while in the meantime, the heat gain decreases as the melt level drops since the crucible wall temperature is not allowed to change. The combined effects favor the stabilization of the growth diameter. In Fig. 3(b) ($u_p = 15$), the diameter of the crystal decreases slowly. Heat loss both from the crystal and the melt tends to decrease. A stabilized growth may or may not be obtained in this case. In reality, a portion of the crucible wall is located above the melt, so that the meniscus and a portion of the crystal may be heated by the crucible wall. Results may therefore be quite different. It can be concluded that a constant diameter of the crystal cannot be obtained by fixing the pull rate and crucible wall temperature. In both cases, the temperature distributions in the crystal near the interface are similar since the radiative heat transfer dominates in this area. The stress fields do not show any significant difference between the two cases since the temperature field and interface shape are almost identical.

Growth with a simple control algorithm is examined next. Two control parameters are commonly used in the industrial growth of silicon, the pull rate, and heater power. For the pull-rate controlled growth, as shown in Fig. 4(a–c), three different algorithms for control are examined: diameter control, meniscus angle control, and both together. The time histories of the pull rate are presented in Fig. 5(a). The rate of pulling oscillates and the growth cannot continue after about 0.07 dimensionless time (≈ two hours if $b = 0.127$ m) due to a negative growth rate. The shape of the crystal is wavy as shown in Fig. 4(a). On the other hand, an almost cylindrical shape of the crystal is

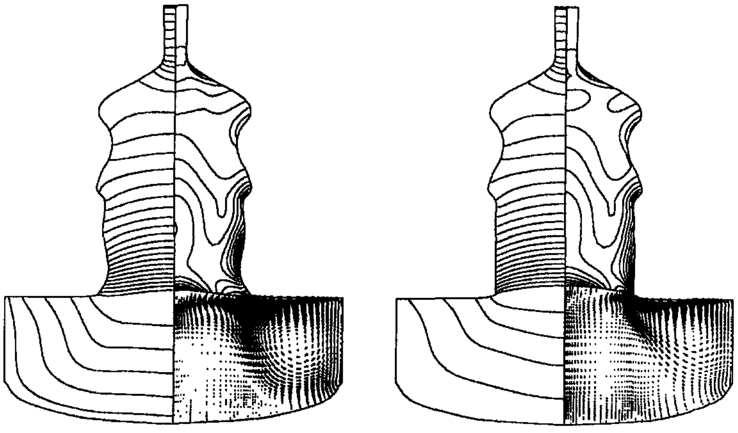

(a) $\Theta_w = \Theta_w + (r_J - r_{set}) \times 2.0$ (b) $\Theta_w = \Theta_w + (\phi_J - \phi_o) \times 0.005$

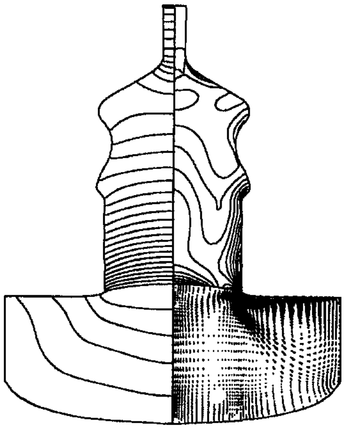

(c) $\Theta_w = \Theta_w + (r_J - r_{set}) \times 2.0 + (\phi_J - \phi_o) \times 0.005$

Fig. 6 Batchwise simulations of Cz growth: crystal radius vs crucible wall temperature with a constant pull rate $u_p = 10$ for $Gr = 10^6$, $Ma = -100$, $Re_s = 2.0 \times 10^3$, $Re_c = -5.0 \times 10^2$, and $Ha = 0$

obtained by the meniscus angle controlled growth. However, the desired radius is not guaranteed. Successful growth can be achieved by controlling both the radius and meniscus angle, as shown in Fig. 5(*a*).

The present algorithm has also been examined using the crucible wall temperature control. Undamped oscillations occur when the radius is controlled, and a successful growth can be achieved only when both the radius and meniscus angle are controlled, as shown in Figs. 6 and 5(*b*). The initial oscillations are caused partially by the drop in the pull rate from the initial value of 11.6 to 10. In Figs. 5(*a*) and 5(*b*), oscillations of about 8 percent and 15 percent are obtained for the pull rate and crucible wall temperature controlled growth, respectively. It is worth mentioning that the accurate measurement of the crystal radius and meniscus angle are difficult in practice. Instead, information on crystal weight and melt level is much easier to obtain. The correlation between this information and the diameter and meniscus angle can be obtained based on the analytical formulation of Irizarry-Rivera and Seider (1997). A control algorithm based on the crystal weight and melt level will be built and examined in the future.

The heat gain and loss at the melt/crystal interface and free surface for the combined controlled growth in Figs. 4(*c*) and 6(*c*) are examined in Fig. 7. The heat gain and loss are equal for the case in Fig. 4(*c*). In fact, an energy balance of 0.1 percent is one of our convergence criteria. The total gain and loss at any given time are not equal for the case in Fig. 6(*c*), as shown in Fig. 7. This heat imbalance requires the change of crucible wall temperature and hence the temperature of the melt, as is the common practice in industry.

Figure 8(*a*) shows the dynamic responses of the pull rate controlled growth of a diffusion model, a convection model, and a model including the effects of an imposed magnetic field (Ha = 100) using the same controller gains. The curves are close to each other indicating that the dynamic responses are similar for all three cases. Figure 8(*b*) shows the dynamic responses of the crucible wall temperature controlled growth for the above three cases. Results are different. In predictions made by the diffusion model, oscillations have been damped quickly ($\tau \approx b^2/\alpha_m = 0.015b^2/\nu$) whereas in the melt convection model, they dampen much more slowly. However, the controller gains we used will play an important role in dampening the oscillations. No conclusion can therefore be made whether the system will be more stable or not using a diffusion model or convection model. As the magnetic field is strengthened, the solution asymptotically approaches the diffusion case. The important parameter reflecting the ratio of convective to diffusive heat transfer is the thermal Peclet number, Pe. From the scaling analysis, the Peclet number, Pe = Gr Pr/Ha^2, can be used without considering the crystal and crucible rotational Reynolds numbers. For Gr = 10^6, Pr = 0.015, and Ha = 100,

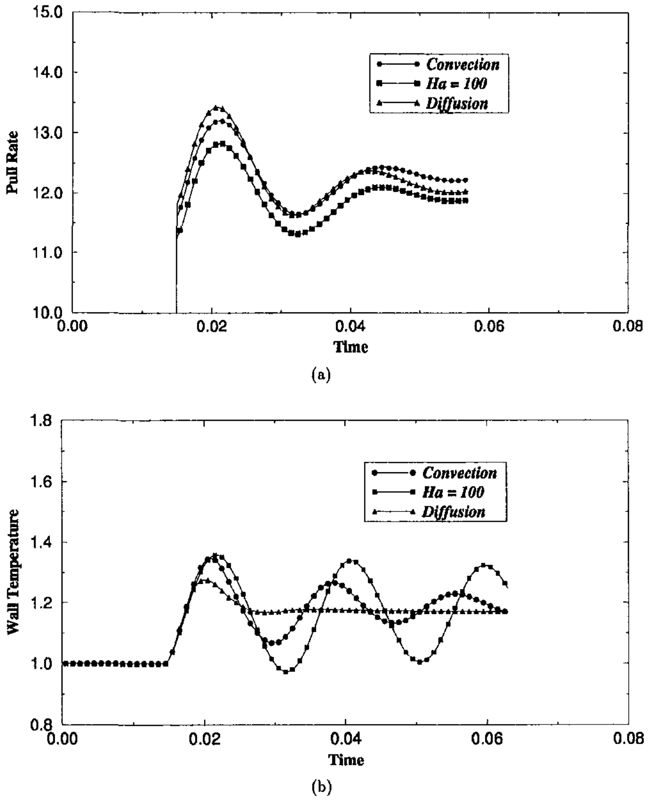

Fig. 8 (*a*) Pull rate and (*b*) crucible wall temperature as functions of time for batchwise Cz growth simulation using convection with and without magnetic field as well as a diffusion model

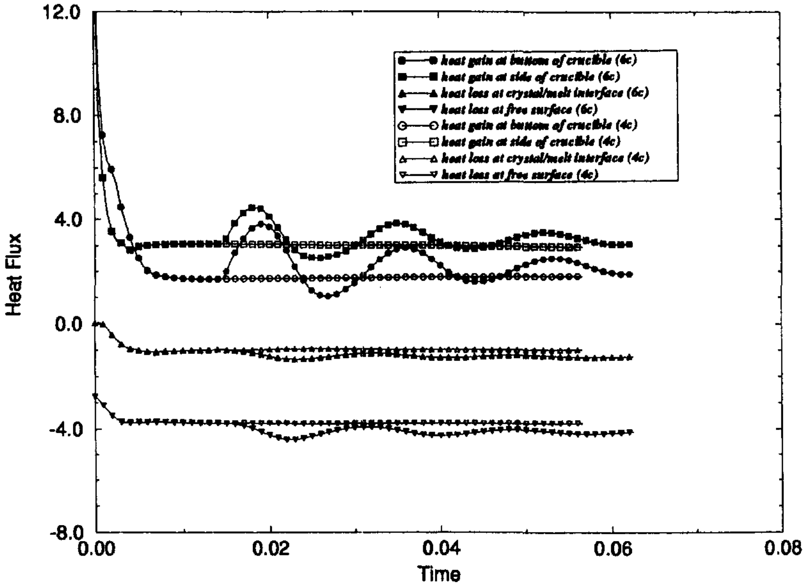

Fig. 7 Heat gain and loss at the interfaces as functions of time for batchwise Cz growth simulation with control, corresponding to Fig. 4(c) and 6(c)

the Peclet number is 1.5, therefore the convective heat transfer cannot be totally damped. However, for a high magnetic field, Ha = 500, the convective heat transfer is negligible (Pe = 0.06).

Conclusion

A thermal-capillary dynamic model is presented for complex moving-boundary problems of Czochralski (Cz) crystal growth of silicon, which accounts for convection in the melt, conduction in the crystal, and radiation on the free surface and the crystal surface. The shapes of the crystal/melt interface, moving crystal, and free surface are determined by energy and stress balances. A reduction in melt volume is also considered. Simulations are performed using constant values of the pull rate and crucible wall temperature. Numerical studies show that the crystal diameter will grow larger if the pull rate is lower and grow smaller if the pull rate is higher. However, a constant diameter crystal cannot be grown without a proper control since the melt volume decreases and the crystal grows longer. Thermal stress distribution based on the linear elastic model has also been presented. The thermal stresses in the crystal are determined by the solidification interface shape, the crystal shape and thermal gradient in the crystal. The heat gains and losses on the bottom and side of crucible, crystal interface, and free surface have been calculated.

Similar flow patterns and temperature distributions in the melt have been predicted for all cases studied in this paper. Three different control algorithms have been built and tested using the dynamic model we have developed. This is the first time that a dynamic Cz growth with control has been presented considering convection in the melt. Undamped oscillations of the shape of the crystal are obtained if the growth is controlled by the radius. Oscillations can be dampened if the growth is controlled by the meniscus angle or by a combination of the radius and angle. The dynamic response of the controlled Cz growth is examined by a diffusion model, a convection model, and a convection model with an axial magnetic field using the same controller gains. For the pull rate controlled growth, the conclusion obtained from the diffusion model can be extended to the convection model. For the wall temperature controlled growth, the results using an axial magnetic field are also close to the diffusion case if $Gr\, Pr/Ha^2 < 1.0$, and are close to the convection case if $Gr\, Pr/Ha^2 > 1.0$. However, it should be noted that the present calculations are performed for only low values of Grashof number and other parameters, and the convection effects may become important at high Grashof number. Further extension of this work may provide insights into this issue.

Acknowledgments

This research was supported by AFOSR/DARPA Consortium for Crystal Growth Research and Microgravity Sciences Program of NASA. Acknowledgements are also due to D. F. Bliss of USAF Research Lab. at Hanscom, Y. F. Chen, and M. A. Gevelber of Boston University for helpful discussions.

References

Atherton, L. J., Derby, J. J., and Brown, R. A., 1987, "Radiative Heat Exchange in Czochralski Crystal Growth," *Journal of Crystal Growth,* Vol. 84, pp. 57–78.

Baumgartl, J., Hubert, A., and Müller, G., 1993, "The Use of Magnetohydrodynamic Effects to Investigate Fluid Flow in Electrically Conducting Melts," *Physics and Fluids,* Vol. A5, pp. 3280–3289.

Brown, R. A., 1986, "Interactions between Convection, Segregation and Interface Morphology," *Advanced Crystal Growth,* Prentice-Hall, Englewood Cliffs, NJ, pp. 3–94.

Derby, J. J., and Brown, R. A., 1986, "Thermal-Capillary Analysis of Czochralski and Liquid Encapsulated Czochralski Crystal Growth II. Processing Strategies," *Journal of Crystal Growth,* Vol. 74, pp. 604–624.

Derby, J. J., and Brown, R. A., 1987, "On the Dynamics of Czochralski Crystal Growth," *Journal of Crystal Growth,* Vol. 83, pp. 137–151.

Derby, J. J., Atherton, L. J., Thomas, P. D., and Brown, R. A., 1987, "Finite Element Methods for Analysis of the Dynamics and Control of Czochralski Crystal Growth," *Journal of Scientific Computing,* Vol. 2, No. 4, pp. 297–343.

Dupret, F., Necodeme, P., Ryckmans, Y., Wouters, P., and Crochet, M. J., 1990, "Global Modeling of Heat and Mass Transfer in Crystal Growth Furnaces," *International Journal of Heat and Mass Transfer,* Vol. 33, pp. 1849–1871.

Dupret, F., and Van den Bogaert, N., 1994, "Modelling Bridgman and Czochralski Growth," *Handbook of Crystal Growth,* Vol. 2b, D. T. J. Hurle, ed., North-Holland, New York.

Gevelber, M. A., and Stephanopoulos, G., 1987, "Dynamics and Control of the Czochralski Process," *Journal of Crystal Growth,* Vol. 84, pp. 647–668.

Hurle, D. T. J., Joyce, G. C., Ghassempoory, M., Crowley, A. B., and Stern, E. J., 1990, "The Dynamics of Czochralski Growth," *Journal of Crystal Growth,* Vol. 100, pp. 11–25.

Hurle, D. T. J., and Cockayne, B., 1994, "Czochralski Growth," *Handbook of Crystal Growth,* Vol. 2a, D. T. J. Hurle, ed., North-Holland, New York, pp. 99–211.

Irizarry-Rivera, R., and Seider, W. D., 1997, "Model-Predictive Control of the Czochralski Crystallization Process Part I. Conduction-Dominated Melt," *Journal of Crystal Growth,* Vol. 178, pp. 593–611.

Kinney, T. A., Bornside, D. E., and Brown, R. A., 1993, "Quantitative Assessment of an Integrated Hydrodynamic Thermal-Capillary Model for Large-Diameter Czochralski Growth of Silicon: Comparison of Predicted Temperature Field with Experiment," *Journal of Crystal Growth,* Vol. 126, pp. 413–434.

Langlois, W. E., Kim, K. M., and Walker, J. S., 1993, "Hydromagnetic Flows and Effects on Czochralski Silicon Crystals," *Journal of Crystal Growth,* Vol. 126, pp. 352–372.

Moallemi, M. K., and Zhang, H., 1994, "A General Numerical Procedure for Multilayer Multistep IC Process Simulation," *IEEE Transactions on Computer-Aided Design of Integrated Circuits and Systems,* Vol. 13, No. 11, pp. 1379–1390.

Müller, G., 1988, "Convection and inhomogeneities in crystal growth from melt," *Crystals,* Vol. 12, Springer-Verlag, Berlin.

Nunes, E. M., Naraghi, M. H. N., Zhang, H., and Prasad, V., 1996, "Combined Radiative-Convection Modeling for Materials Processes: Application to Crystal Growth," *ASME Proceedings of the 31st National Heat Transfer Conference,* HTD-Vol. 323, Houston, TX, pp. 27–37.

Prasad, V., Zhang, H., and Anselmo, A., 1997, "Transport Phenomena in Czochralski Crystal Growth Processes," *Advances in Heat Transfer,* Vol. 30, Academic Press, New York, pp. 313–435.

Sabhapathy, P., and Salcudean, M. E., 1991, "Numerical Study of Czochralski Growth of Silicon in an Axisymmetric Magnetic Field," *Journal of Crystal Growth,* Vol. 113, pp. 164–180.

Shimura, F., 1989, *Semiconductor Silicon Crystal Technology,* Academic Press, New York.

Stephanopoulos, G., 1884, *Chemical Process Control,* Prentice-Hall, Englewood Cliffs, NJ.

Surek, T., Coriell, S. R., and Chalmers, B., 1980, "The Growth of Shaped Crystals from the Melt," *Journal of Crystal Growth,* Vol. 50, pp. 21–32.

Thomas, P. D., Derby, J. J., Atherton, L. J., Brown, R. A., and Wargo, M. J., 1989, "Dynamics of Liquid-Encapsulated Czochralski Growth of Gallium Arsenide Comparing Model with Experiment," *J. Crystal Growth,* Vol. 96, pp. 135–152.

Van den Bogaert, N., and Dupret, F., 1997, "Dynamic Global Simulation of the Czochralski Process I. Principles of the Method," *Journal of Crystal Growth,* Vol. 171, pp. 65–76.

Van den Bogaert, N., and Dupret, F., 1997, "Dynamic Global Simulation of the Czochralski Process II. Analysis of the Growth of a Germanium Crystal," *Journal of Crystal Growth,* Vol. 171, pp. 77–93.

Zhang, H., and Moallemi, M. K., 1995, "A Multizone Adaptive Grid Generation Technique for Simulation of Moving and Free Boundary Problems," *Numerical Heat Transfer,* Vol. B27, pp. 255–276.

Zhang, H., and Prasad, V., 1995, "A Multizone Adaptive Process Model for Crystal Growth at Low and High Pressures," *Journal of Crystal Growth,* Vol. 155, pp. 47–65.

Zhang, H., Prasad, V., and Moallemi, M. K., 1996a, "A Numerical Algorithm Using Multizone Adaptive Grid Generation for Multiphase Transport Processes with Moving and Free Boundaries," *Numerical Heat Transfer,* Vol. B29, pp. 399–421.

Zhang, H., Prasad, V., and Bliss, D. F., 1996b, "Transport Phenomena in High Pressure Crystal Growth Systems for III-V Compounds," *Journal of Crystal Growth,* Vol. 169, pp. 250–260.

Zhang, H., Prasad, V., and Bliss, D., 1996c, "Transport Phenomena in a High Pressure Crystal Growth System: In-situ Synthesis for InP Melt," *Journal of Crystal Growth,* Vol. 177, pp. 196–206.

Zhang, H., Zheng, L. L., Prasad, V., and Larson, D. F., Jr., 1998, "Local and Global Simulations of Bridgman and Czochralski Crystal Growth," ASME JOURNAL OF HEAT TRANSFER, Vol. 120, pp. 865–873.

Zou, Y. F., Zhang, H., and Prasad, V., 1996, "Dynamics of Melt-Crystal Interface and Thermal Stresses in Czochralski Crystal Growth Processes," *Journal of Crystal Growth,* Vol. 166, pp. 476–482.

Melting and Resolidification of a Subcooled Mixed Powder Bed With Moving Gaussian Heat Source

Yuwen Zhang

A. Faghri[1]
Fellow ASME

Department of Mechanical Engineering,
University of Connecticut,
Storrs, CT 06269-3139

Melting of a subcooled powder bed that contains a mixture of two powders with significantly different melting points under a moving Gaussian heat source was investigated numerically. Shrinkage induced by the density change on the melting process was taken into account in the physical model. The problem is formulated using a temperature transforming model and solved by the finite difference method. The results show that the effect of surface heat loss due to convection and radiation is not negligible regardless of whether the shrinkage phenomena is considered. The decrease of moving heat source intensity will result in decrease of the sintering depth and the volume of the liquid pool. The increase of the scanning velocity will decrease the sintering depth and the location and shape of the liquid pool is affected significantly.

1 Introduction

Selective Laser Sintering (SLS) is an emerging technology in which three-dimensional parts are built using CAD data. SLS of metal powder involves fabrication of near full density objects from powder via melting and resolidification induced by a directed laser beam (generally CO_2 or YAG). Heat transfer models of SLS are important because the final quality of the product depends on prediction and control of the powder bed temperature distribution. Some existing heat transfer models concerning SLS in the literature (Sun and Beaman, 1995; Williams et al., 1996) consider the heat transfer mechanism in the powder bed as a pure conduction problem, which is oversimplified. For sintering of polymer powder, which has little crystallinity and a nearly zero latent heat of fusion, Kandis and Bergman (1997) presented an experimental investigation and a numerical prediction. For sintering of metal powder, the latent heat of fusion is usually very large and therefore melting and resolidification phenomena have significant effect on the temperature distribution in the parts and powder, residual stress, and the final quality of the parts. Melting during the SLS process is significantly different from the normal melting phenomena because the volume fraction of gas(es) in the powder decreases from a value as large as 0.5 to nearly zero after melting. Therefore a significant change of density accompanies the melting process.

Fundamentals of melting and solidification phenomena and applications have been intensively investigated during the past three decades and detailed reviews are available in the existing literature, such as Viskanta (1983) and Yao and Prusa (1989). The change of density of phase-change materials (PCMs) associated with the melting and solidification process is usually not taken into account except by a few researchers (Eckert and Drake, 1972; Crank, 1956; Carslaw and Jaeger, 1959; Conti, 1995). Shrinkage formation due to density change during the solidification process in a two-dimensional cavity was investigated numerically by Kim and Ro (1993). They concluded that the density change played a more important role than convection in the solidification process.

Shah (1994) experimentally investigated melting of a single column of solder particle (eutectic Sn-Pb) held vertically inside a glass tube. A compressive load was applied on the top of the column and the bottom of the surface was heated by a heater at a specified temperature. The problem is also formulated using an enthalpy model and solved using a finite difference method. Manzur et al. (1996) and Bunnell (1995) proposed the use of a powder mixture containing two powders with significantly different melting points, in which only the low melting point powder will be molten and resolidified during the SLS process. The solid particles of the high melting point powder will move with the liquid of the low melting point metal and become part of the fully densified part. The present authors (Zhang and Faghri, 1998) analytically solved a one-dimensional melting problem in a powder bed containing mixture of the powder under a boundary condition of the second kind. The results showed that the shrinkage effect on the melting of the powder bed is not negligible. In fact, the laser beam used in the SLS process is usually Gaussian and moves with a velocity. The powder particles in the powder bed go through a melting and resolidification process upon motion of the laser beam. The melting and resolidification process in the powder bed is investigated in this paper.

2 Thermal Properties

Thermal property evaluation is very important in the prediction of melting and resolidification of the powder bed. It should be noted that there are three components in the powder bed: low melting point powder, high melting point powder, and gas(es). For sake of simplicity, it is assumed that the thermal properties of the low melting point powder are the same for both liquid and solid phase. The contribution of each component on the thermal properties of the powder bed is determined by their volume weighted fractions.

After the powder bed is molten, the gas(es) is driven from the powder bed by shrinkage so that fully densified parts can be formed after resolidification. Therefore, the thermal properties of the liquid pool or resolidified part can be expressed as

$$\rho_p = \phi\rho_L + (1-\phi)\rho_H \tag{1}$$

$$(\rho c_p)_p = \phi\rho_L c_{pL} + (1-\phi)\rho_H c_{pH} \tag{2}$$

---

[1] Corresponding author.

Contributed by the Heat Transfer Division for publication in the JOURNAL OF HEAT TRANSFER. Manuscript received by the Heat Transfer Division, Nov. 20, 1997; revision received, Mar. 11, 1998. Keywords: Heat Transfer, Melting, Solidification. Associate Technical Editor: M. Kaviany.

$$k_p = \phi k_L + (1 - \phi)k_H. \quad (3)$$

Before melting, gas(es) exists in the gap between powder particles. It is straightforward to express the density and heat capacity of the unsintered powder bed as

$$\begin{aligned}\rho_s &= (1 - \epsilon_s)\rho_p + \epsilon_s\rho_g \\ &= (1 - \epsilon_s)[\phi\rho_L + (1 - \phi)\rho_H] + \epsilon_s\rho_g \quad (4)\end{aligned}$$

$$\begin{aligned}(\rho c_p)_s &= (1 - \epsilon_s)(\rho c_p)_p + \epsilon_s(\rho c_p)_g \\ &= (1 - \epsilon_s)[\phi\rho_L c_{pL} + (1 - \phi)\rho_H c_{pH}] + \epsilon_s(\rho c_p)_g. \quad (5)\end{aligned}$$

The orders of magnitude of the typical metal powder thermal properties, such as aluminum and iron, and gas(es) are as follows:

$$\rho_L \sim \rho_H \sim 10^3 \text{ kg/m}^3, \quad \rho_g \sim 1 \text{ kg/m}^3$$

$$k_L \sim k_H \sim 10^2 \text{ W/mK}, \quad k_g \sim 10^{-2} \text{ W/mK}$$

$$c_{pL} \sim c_{pH} \sim 10^2 \text{ J/kgK}, \quad c_{pg} \sim 1 \text{ J/kgK}.$$

Thus, the contributions of the gas(es) to the density and heat capacity of the powder bed are negligible. The thermal properties of the powder bed before sintering are therefore expressed as

$$\rho_s = (1 - \epsilon)\rho_p = (1 - \epsilon_s)[\phi\rho_L + (1 - \phi)\rho_H] \quad (6)$$

$$\begin{aligned}(\rho c_p)_s &= (1 - \epsilon)(\rho c_p)_p \\ &= (1 - \epsilon_s)[\phi\rho_L c_{pL} + (1 - \phi)\rho_H c_{pH}]. \quad (7)\end{aligned}$$

Specification of the thermal conductivity of the powder bed before sintering is very complicated. The effective thermal conductivity of the powder depends on the arrangement of the particles in the powder bed and the order of magnitude of the thermal conductivities of the gas(es) and the particle. Contact between the particles also plays a significant role on the value of the thermal conductivity. For the case of large thermal conductivity ratio, k_p/k_g, the empirical correlation proposed by Hadley (1986) appears to be the best correlation since it agreed with the experimental data very well. Therefore, the effective thermal conductivity of the powder bed before sintering will be calculated by the following correlation (Hadley, 1986):

$$\begin{aligned}\frac{k_{\text{eff}}}{k_g} &= (1 - \alpha_0)\frac{\epsilon f_0 + k_p/k_g(1 - \epsilon f_0)}{1 - \epsilon(1 - f_0) + k_p/k_g\epsilon(1 - f_0)} \\ &\quad + \alpha_0\frac{2(k_p/k_g)^2(1 - \epsilon) + (1 + 2\epsilon)k_p/k_g}{(2 + \epsilon)k_p/k_g + 1 - \epsilon} \quad (8)\end{aligned}$$

where

$$f_0 = 0.8 + 0.1\epsilon \quad (8a)$$

$$\log \alpha_0 = \begin{cases} -4.898\epsilon & 0 \le \epsilon \le 0.0827 \\ -0.405 - 3.154(\epsilon - 0.0827) & 0.0827 \le \epsilon \le 0.298. \\ -1.084 - 6.778(\epsilon - 0.298) & 0.298 \le \epsilon \le 0.580 \end{cases} \quad (8b)$$

For a typical value of porosity, $\epsilon = 0.4$, the curve of k_{eff}/k_g versus k_p/k_g is plotted in Fig. 1. As can be seen, the thermal resistance of the gas(es) and particles in the powder bed is neither parallel arrangement nor series arrangement (Kaviany, 1995). For the case of low k_p/k_g, such as sintering of nonmetal powder, parallel thermal resistance can provide a good prediction (Kandis and Bergman, 1997). However, for sintering of metal powder, where k_p/k_g has an order of magnitude of 10^3, the effective thermal conductivity must be calculated by Hadley's (1986) correlation.

3 Governing Equations

The physical model of the problem under consideration is shown in Fig. 2. A powder bed, which contains two powders

Nomenclature

b = moving heat source half width (m)
Bi = Biot number, hb/k_H
C = dimensionless heat capacity, C^0/C_H^0
C^0 = heat capacity, ρc_p (W/m^{3}K)
c_p = specific heat (W/kg°C)
h = convective heat transfer coefficient (W/m^{2}K)
h_{sl} = latent heat of melting or solidification (J/kg)
I_0 = heat source intensity at the center of the heat source (W/m^2)
k = thermal conductivity (W/m°C)
K = dimensionless thermal conductivity, k/k_H
K_0 = modified Bessel function of second kind of order zero
N_i = dimensionless moving heat source intensity, $\alpha_a I_0 b/[k_H(T_m^0 - T_i^0)]$
N_R = radiation number, $\epsilon\sigma(T_m^0 - T_i^0)^3 b/k_H$
N_t = temperature ratio for radiation, $T_m^0/(T_m^0 - T_i^0)$
Q = strength of line heat source (W/m)
s = solid-liquid interface location (m)
s_0 = location of surface (m)
s_{st} = sintered depth (m)
Sc = subcooling parameter, $C_H^0(T_m^0 - T_i^0)/(\rho_L h_{sl})$
T = dimensionless temperature, $(T^0 - T_m^0)/(T_m^0 - T_i^0)$
t = false time (s)
T^0 = temperature (°C)
u = heat source moving velocity (m/s)
U = dimensionless heat source moving velocity, ub/α_H
V = volume (m^3)
w = velocity of liquid phase (m/s)
W = dimensionless velocity of the liquid phase, wb/α_H
x = moving horizontal coordinate, $x' - ut$ (m)
X = dimensionless moving horizontal coordinate, x/b
x' = fixed horizontal coordinate (m)
z = vertical coordinate (m)
Z = dimensionless vertical coordinate, z/b
z' = fixed vertical coordinate (m)

Greek letters

α = thermal diffusivity (m^2/s)
ΔT^0 = one-half of phase-change temperature range (K)
ΔT = one-half of dimensionless phase-change temperature range
ϵ = volume fraction of gas(es) (porosity for unsintered powder), $V_g/(V_g + V_L + V_H)$
ϵ_e = emissivity of surface
η = dimensionless solid-liquid interface location, s/b
η_0 = dimensionless location of the surface, s_0/b
η_{st} = dimensionless sintered depth, s_{st}/b
ρ = density (kg/m^3)
σ = Stefan-Boltzmann constant, 5.67×10^{-8} W/(m^{2}K^4)
τ = false dimensionless time, $\alpha_H t/b^2$
ϕ = volume percentage of low melting point powder, $V_L/(V_L + V_H)$

Subscripts

eff = effective
g = gas(es)
H = high melting point powder
i = initial
L = low melting point powder
m = melting point
p = sintered parts
s = solid

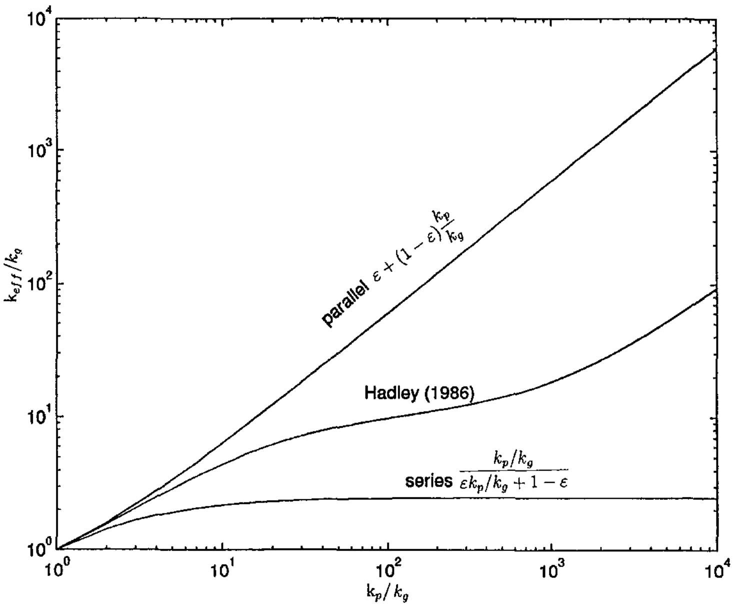

Fig. 1 Effective thermal conductivity

with significantly different melting points, with a uniform initial temperature, T_i, below the melting point of the low melting point powder, T_m, is in a half-space, $z > 0$. A Gaussian heat source moves along the surface of the semi-infinite body with a constant velocity, u. The problem is assumed to be two-dimensional although the actual SLS process of metal powder is a three-dimensional melting and resolidification problem. It is economical to investigate a two-dimensional problem before the complete three-dimensional process is considered. As the powder interacts with the heat source, the temperature of the powder bed will be brought up to the melting point of the low melting point metal powder which then begins to melt. The level of the melted powder bed lowers since the low melting point powder is molten and the high melting point alone cannot sustain the powder bed to keep its density unchanged. After the heat source moves away, the liquid pool cools and resolidifies to form the fully densified part. It should be noted that the temperature of the powder bed will never reach the melting point of the high melting point powder and therefore only the low melting point powder melts and resolidifies.

The heat source travels with a constant velocity, u, along the surface of the powder bed, which is a typical moving heat source problem (Eckert and Drake, 1972). If the powder bed is sufficiently large compared with the size of the heat source, which is in the 10^{-3} m order of magnitude, a quasi-steady-state occurs. The system appears to be in steady-state from the standpoint of the observer located in and traveling with the heat source. This paper will focus on the quasi-steady-state solution only.

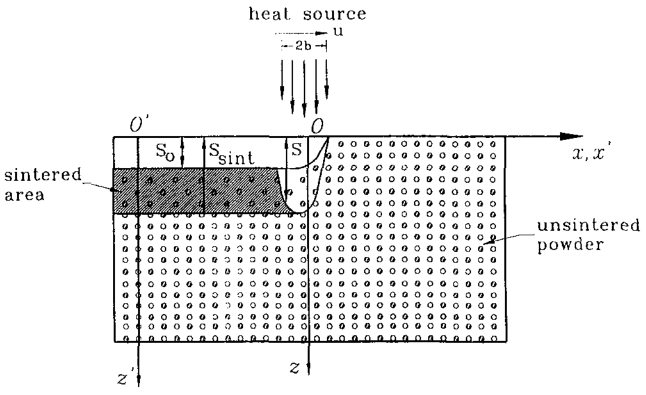

Fig. 2 Physical model

The temperature transforming model using a fixed grid method (Cao and Faghri, 1990a) will be employed to describe the melting/resolidification in the powder bed with a moving heat source. This model assumes that the melting and solidification process occurs over a range of phase-change temperatures from $(T_m^0 - \delta T^0)$ to $(T_m^0 + \delta T^0)$, but it can also be successfully used to simulate the melting and solidification process occurring at a single temperature. This model has the advantage of eliminating the time-step and grid size limitations that are normally encountered in other fixed grid methods.

In the fixed coordinate system (x', z'), the governing equation is written as

$$\frac{\partial(C^0T^0)}{\partial t} + w\frac{\partial(C^0T^0)}{\partial z'} = \frac{\partial}{\partial x'}\left(k\frac{\partial T^0}{\partial x'}\right) + \frac{\partial}{\partial z'}\left(k\frac{\partial T^0}{\partial z'}\right) - \left(\frac{\partial S^0}{\partial t} + w\frac{\partial S^0}{\partial z'}\right) \quad (9)$$

where w in Eq. (9) is the velocity induced by the shrinkage of the powder bed (Zhang and Faghri, 1998). It is evident that $w \equiv 0$ in the powder bed unsintered region. In the liquid phase, the velocity induced by shrinkage is expressed as (Zhang and Faghri, 1998):

$$w = \begin{cases} \epsilon\dfrac{\partial s}{\partial t} & z' \le s, \quad \text{liquid phase} \\ 0 & z' > s, \quad \text{solid phase (sintered or unsintered)} \end{cases} \quad (10)$$

where $s = s(x, t)$ is the position of the solid-liquid interface.

The effective heat capacity of the powder bed, C^0, can be expressed as

$$C^0(T^0) = \begin{cases} (1-\epsilon)(\rho c_p)_p & T^0 < T_m^0 - \Delta T^0 \\ (1-\epsilon)(\rho c_p)_p + (1-\epsilon)\phi\dfrac{\rho_L h_{sl}}{2\Delta T^0} & \\ T_m^0 - \Delta T^0 < T^0 < T_m^0 + \Delta T^0 & \\ (1-\epsilon)(\rho c_p)_p & T^0 > T_m^0 + \Delta T^0 \end{cases} \quad (11)$$

and S^0 in Eq. (9) is defined as

Table 1 The sintering parameters applied in numerical calculation

ϵ_s	0.4	ϕ	0.4
K_{LH}	2.9	C_{LH}	0.7
N_i	$0.2 \sim 0.4$	U	$0.05 \sim 0.1$
N_R	$0, 4.2 \times 10^{-4}$	Bi	$0, 7.4 \times 10^{-5}$
T_∞	-1	N_t	1.5
Sc	2		

$$S^0(T^0) = \begin{cases} 0 & T^0 < T_m^0 - \Delta T^0 \\ \frac{1}{2}(1-\epsilon)\phi\rho_L h_{sl} & \\ & T_m^0 - \Delta T^0 < T^0 < T_m^0 + \Delta T^0 \\ (1-\epsilon)\phi\rho_L h_{sl} & T^0 > T_m^0 + \Delta T^0 \end{cases} \quad (12)$$

The thermal conductivity of the powder bed is calculated by

$$k = \begin{cases} k_{\text{eff}} & T^0 < T_m^0 - \Delta T^0 \\ k_{\text{eff}} + \dfrac{k_p - k_{\text{eff}}}{2\Delta T^0}(T^0 - T_m^0 + \Delta T^0) & \\ & T_m^0 - \Delta T^0 < T^0 < T_m^0 + \Delta T^0 \\ k_p & T^0 > T_m^0 + \Delta T^0 \end{cases} \quad (13)$$

where k_{eff} and k_p are obtained from Eqs. (8) and (3) respectively.

It should be noted that the volume fraction of gas(es), ϵ, appears in Eqs. (11)–(13). Since a fully densified part is assumed to be obtained after sintering, it is reasonable to set $\epsilon = 0$ in the liquid phase and the sintered region while set $\epsilon = \epsilon_s$ in the unsintered region.

An analysis in a fixed coordinate system, (x', z') is difficult for this problem and therefore it is convenient to study it in a moving coordinate system where the origin is fixed at the center of heat source. Imagine an observer riding along with the moving heat source at a speed u. The powder bed will travel by at the same speed $-u$. If we fix a moving coordinate system (x, z) to the center of the beam, the system will appear in reference to the fixed coordinate system as shown in Fig. 1. The relationship between fixed and moving coordinate systems are expressed as

$$x = x' - ut$$

$$z = z'. \quad (14)$$

Substituting Eq. (14) into Eq. (10), the liquid-phase velocity induced by shrinkage in the moving coordinate system is

$$w = \begin{cases} \epsilon\left(\dfrac{\partial s}{\partial t} - u\dfrac{\partial s}{\partial x}\right) & z \le s, \quad \text{liquid phase} \\ 0 & z > s, \quad \text{solid phase} \end{cases} \quad (15)$$

The governing equation in the moving coordinate system is obtained by substituting Eqs. (14), (15) into Eq. (9), i.e.,

$$\frac{\partial(C^0T^0)}{\partial t} - u\frac{\partial(C^0T^0)}{\partial x} + w\frac{\partial(C^0T^0)}{\partial z} = \frac{\partial}{\partial x}\left(k\frac{\partial T^0}{\partial x}\right) + \frac{\partial}{\partial z}\left(k\frac{\partial T^0}{\partial z}\right) - \left(\frac{\partial S^0}{\partial t} - u\frac{\partial S^0}{\partial x} + w\frac{\partial S^0}{\partial z}\right). \quad (16)$$

At quasi-steady state, the transient terms in Eqs. (15)–(16) can be dropped, i.e.,

$$w = \begin{cases} -\epsilon_s u\dfrac{\partial s_{st}}{\partial x} & z \le s_{st}, \quad \text{liquid phase} \\ 0 & z > s_{st}, \quad \text{solid phase} \end{cases} \quad (17)$$

$$-u\frac{\partial(C^0T^0)}{\partial x} + w\frac{\partial(C^0T^0)}{\partial z} = \frac{\partial}{\partial x}\left(k\frac{\partial T^0}{\partial x}\right) + \frac{\partial}{\partial z}\left(k\frac{\partial T^0}{\partial z}\right) - \left(-u\frac{\partial S^0}{\partial x} + w\frac{\partial S^0}{\partial z}\right). \quad (18)$$

The initial and boundary conditions of the problem are

$$-k\frac{\partial T^0}{\partial z} = \alpha_a I_0 \exp\left(-\frac{x^2}{b^2}\right) - \epsilon_e\sigma[T^{0^4} - T_\infty^{0^4}] - h(T^0 - T_\infty^0) \quad z = s_0(x) \quad (19)$$

$$T^0 = T_i^0, \quad z \to \infty, \quad -\infty \le x \le \infty \quad (20)$$

$$T^0 = T_i^0, \quad |x| \to \infty, \quad 0 \le z \le \infty. \quad (21)$$

It should be noted that the surface of the powder lowers after melting and the shape of the surface is described by $s_0(x)$. The determination of $s_0(x)$ is straightforward if the horizontal motion in the liquid pool is neglected (Zhang and Faghri, 1998), i.e.,

$$s_0(x) = \epsilon_s s_{st}(x). \quad (22)$$

By defining the following dimensionless variables

$$T = \frac{T^0 - T_m^0}{T_m^0 - T_i^0} \quad \Delta T = \frac{\Delta T^0}{T_m^0 - T_i^0}$$

$$X = \frac{x}{b} \quad Z = \frac{z}{b} \quad \eta = \frac{s}{b} \quad \eta_0 = \frac{s_0}{b}$$

$$C = \frac{C^0}{(\rho c_p)_H} \quad C_L = \frac{(\rho c_p)_L}{(\rho c_p)_H} \quad K = \frac{k}{k_H} \quad K_{\text{eff}} = \frac{k_{\text{eff}}}{k_H}$$

$$K_p = \frac{k_p}{k_H} \quad K_L = \frac{k_L}{k_H}$$

$$K_g = \frac{k_g}{k_H} \quad S = \frac{S^0}{C_H^0(T_m^0 - T_i^0)} \quad Sc = \frac{C_H^0(T_m^0 - T_i^0)}{\rho_L h_{sl}}$$

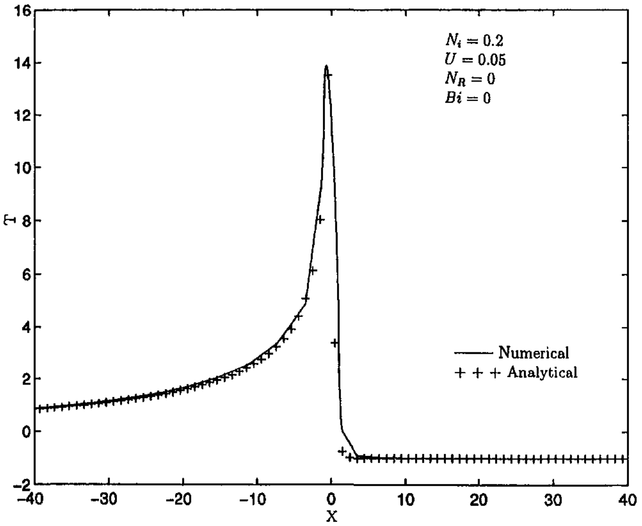

Fig. 3 Comparison between analytical and numerical results without phase change

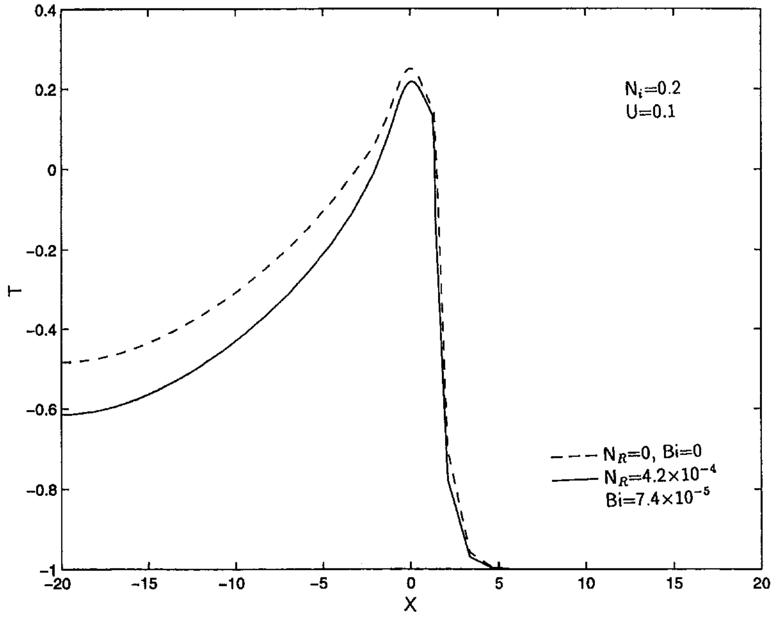

Fig. 4 Effect of surface boundary condition on the surface temperature (without shrinkage)

$$U = \frac{ub}{\alpha_H} \quad W = \frac{wb}{\alpha_H}$$

$$N_i = \frac{\alpha_a I_0 b}{k_H(T_m^0 - T_i^0)} \quad \mathrm{Bi} = \frac{hb}{k_H} \quad N_R = \frac{\epsilon_e \sigma (T_m^0 - T_i^0)^3 b}{k_H}$$

$$N_t = \frac{T_m^0}{T_m^0 - T_i^0}, \tag{23}$$

the nondimensional governing equations are obtained.

$$-U\frac{\partial(CT)}{\partial X} + W\frac{\partial(CT)}{\partial Z} = \frac{\partial}{\partial X}\left(K\frac{\partial T}{\partial X}\right) + \frac{\partial}{\partial Z}\left(K\frac{\partial T}{\partial Z}\right) - \left(-U\frac{\partial S}{\partial X} + W\frac{\partial S}{\partial Z}\right) \tag{24}$$

$$W = \begin{cases} -\epsilon_s U \dfrac{\partial \eta_{st}}{\partial X} & Z \le \eta_{st}, \quad \text{liquid phase} \\ 0 & Z > \eta_{st}, \quad \text{solid phase} \end{cases} \tag{25}$$

$$S = \begin{cases} 0 & T < -\Delta T \\ \dfrac{(1-\epsilon)\phi C_L}{2Sc} & -\Delta T < T < \Delta T \\ \dfrac{(1-\epsilon)\phi C_L}{Sc} T & > \Delta T \end{cases} \tag{26}$$

$$C = \begin{cases} (1-\epsilon)(\phi C_L + 1 - \phi) & T < -\Delta T \\ (1-\epsilon)(\phi C_L + 1 - \phi) + (1-\epsilon)\phi \dfrac{C_L}{2Sc\Delta T} & -\Delta T < T < \Delta T \\ (1-\epsilon)(\phi C_L + 1 - \phi) & T > \Delta T \end{cases} \tag{27}$$

$$K = \begin{cases} K_{\mathrm{eff}} & T < -\Delta T \\ K_{\mathrm{eff}} + \dfrac{K_p - K_{\mathrm{eff}}}{2\Delta T}(T + \Delta T) & -\Delta T < T < \Delta T \\ K_p & T > \Delta T \end{cases} \tag{28}$$

where

$$K_{\mathrm{eff}} = K_g(1-\alpha_0)\frac{\epsilon f_0 + (K_p/K_g)(1-\epsilon f_0)}{1 - \epsilon(1-f_0) + (K_p/K_g)\epsilon(1-f_0)} + K_g\alpha_0\frac{2(K_p/K_g)^2(1-\epsilon) + (1+2\epsilon)(K_p/K_g)}{(2+\epsilon)(K_p/K_g) + 1 - \epsilon} \tag{28a}$$

$$K_p = \phi K_L + (1-\phi) \tag{28b}$$

$$T = -1, \quad 0 \le z \le \infty, \quad -\infty \le x \le \infty, \quad \tau = 0 \tag{29}$$

$$-K\frac{\partial T}{\partial Z} = N_i \exp(-X^2) - N_R[(T + N_t)^4 - (T_\infty + N_t)^4] - \mathrm{Bi}(T - T_\infty), \quad Z = S_0(X) \tag{30}$$

$$T = -1, \quad Z \to \infty, \quad -\infty \le X \le \infty, \quad \tau > 0 \tag{31}$$

$$T = -1, \quad |X| \to \infty, \quad 0 \le Z \le \infty, \quad \tau > 0 \tag{32}$$

$$S_0(X) = \epsilon_s S(X). \tag{33}$$

4 Numerical Solution

The melting and resolidification problem has been specified by Eqs. (24)–(33). The problem is steady-state in the moving coordinate system. However, it is very difficult to solve the steady-state problem directly since the location of the solid-liquid interface and the upper surface of the powder bed is unknown a priori. Therefore, a false transient method is employed. In this methodology, a false transient term is added to the governing Eq. (24) and the steady-state is obtained when the temperature distribution does not vary with the false time. In order to accelerate convergence, the initial temperature distribution for a specific case can be set as the converged temperature distribution for a similar case. Equation (24), with the false transient term added, can be solved by a finite difference method described by Patankar (1980). In this methodology, the discretization equations are obtained by applying the conservation laws over a finite size control volume surrounding the grid node and integrating the equation over the control volume. The resulting scheme has the form

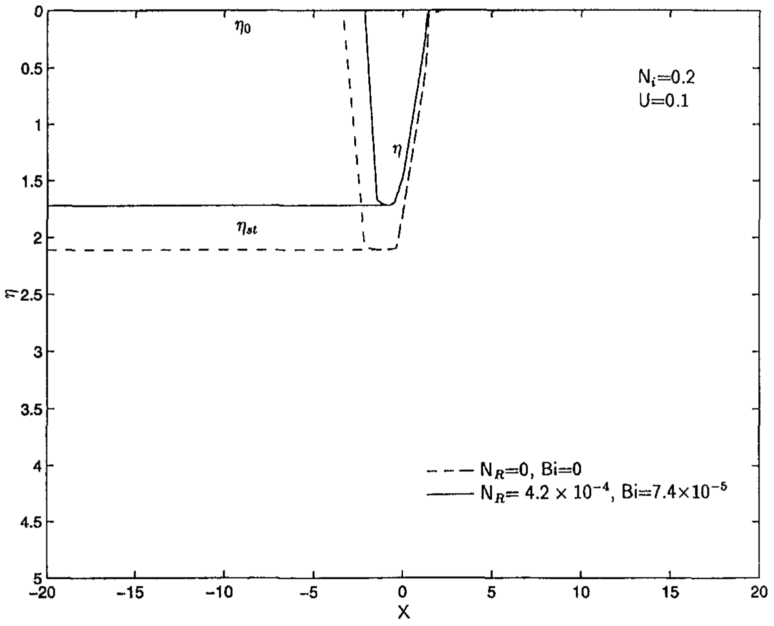

Fig. 5 Effect of surface boundary condition on the shape of solid-liquid interface (without shrinkage)

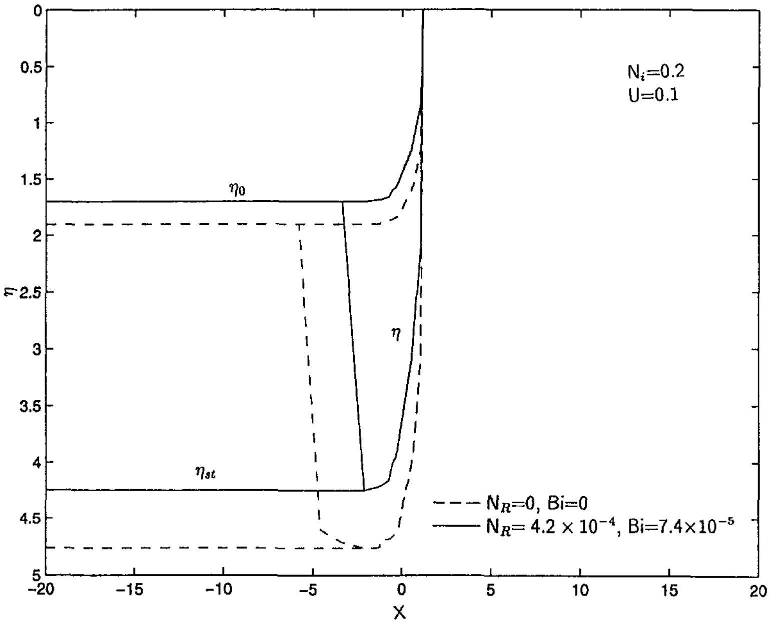

Fig. 6 Interfaces of sintering process

$$a_P T_P = a_E T_E + a_W T_W + a_T T_T + a_B T_B + b \tag{34}$$

where the coefficients in Eq. (34) can be found in Patankar (1980).

The beauty of the temperature transforming model (Cao and Faghri, 1990a), like other fixed grid models, is that the location of the solid-liquid interface is determined by the temperature distribution and therefore the interface does not need to be tracked in the calculation. However, for melting and resolidification in the SLS process, the upper surface of the powder bed is moving downward, which creates another moving interface. Thus, the powder bed, which includes unsintered powder, a liquid pool, and sintered part, has an irregular shape which is difficult to describe by the Cartesian coordinate system moving with the heat source. This irregular geometric shape can be transformed to a rectangular shape by employing a body-fitted coordinate transformation (Kim and Ro, 1993), but the energy equation of the problem will become very complex. A simpler method, which is used in this paper, is to employ the computational region expansion method (Patankar, 1980). In this methodology, the calculation region is the entire powder bed even though the powder bed shrank after sintering. In order to simulate the existence of the empty space created by shrinkage of the powder bed after sintering, it is assumed that the thermal conductivity in the empty space is equal to zero and an additional source term method (Patankar, 1980) accounts for the boundary conditions at the upper surface of the powder bed.

Since Eq. (24) is a nonlinear equation, iteration is needed. During the iteration process, some underrelaxation is necessary. The relaxation factor used in this method is 0.1 ~ 0.2. In order

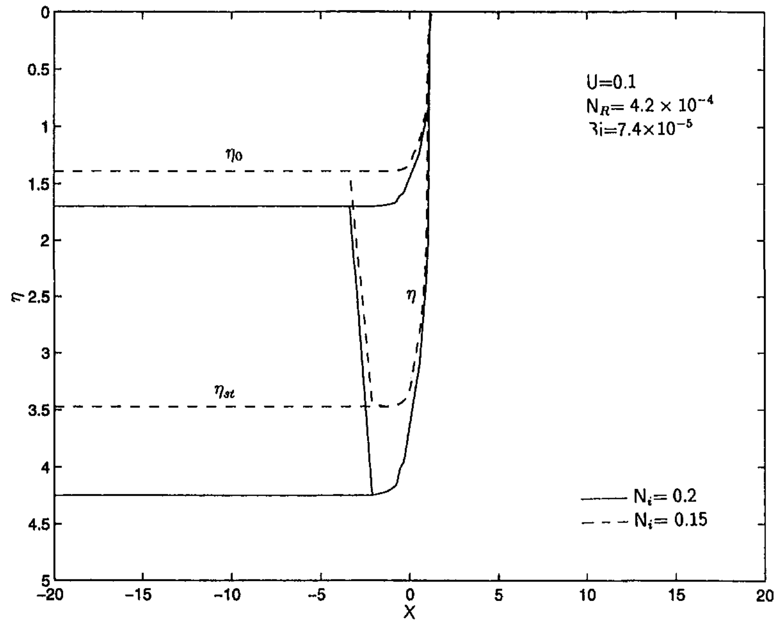

Fig. 7 Effect of scanning velocity on sintering process

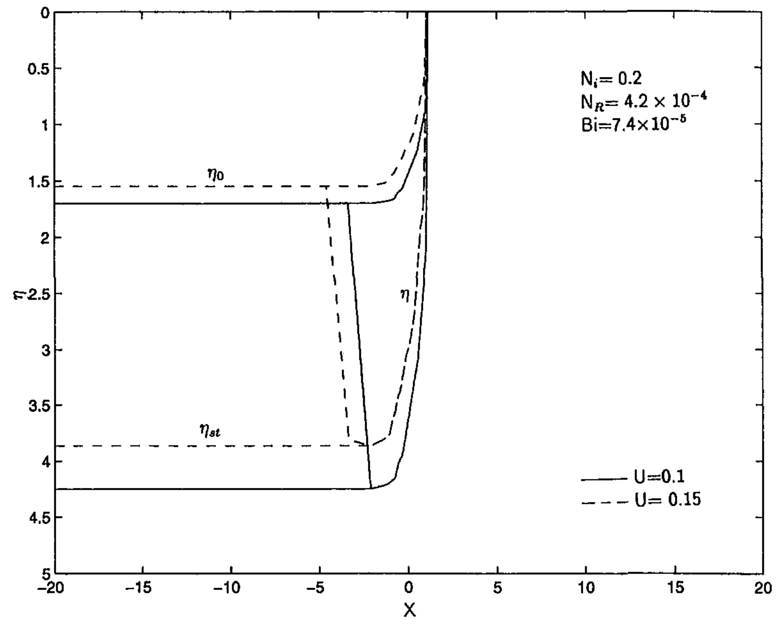

Fig. 8 Effect of heat source power on the sintering process

to simulate the melting and resolidification process occurring at a single temperature, a very small dimensionless phase-change temperature range, $\Delta T = 0.01$, is used in the calculation. In order to simulate melting and resolidification in a half-space $z > 0$, the calculation area must be large enough so that the effect of the calculation area on the interface shape and temperature distribution can be eliminated. The calculation area must be large enough so that the sintering of a semi-infinite powder bed may be simulated. The calculations were carried out for a nonuniform grid of 62 nodes in the x-direction and 42 nodes in the Z direction with a false dimensionless time step of $\Delta\tau = 10^{-4}$. Finer grid sizes and smaller false time steps were also used in the calculations, but their results did not provide a noticeable difference with the present grid size and time step.

5 Results and Discussions

The porosity of the unsintered powder bed plays a significant role since the thermal properties of the powder bed depend on the value of the porosity. For uniform-size spherical particles, the porosities are independent of the particle size and only depend on the arrangement of the particles in the powder bed. The smallest porosity is for the close-pack face-centered cubic arrangement, which gives a porosity of 0.259. In reality, random packing is usually the case, which gives the porosity of 0.37–0.43. Therefore, the porosity of the unsintered powder bed will be approximated as 0.4. The other parameters of sintering are determined by analyzing a real sintering process of the Al-Fe system performed by Manzur et al. (1996). The parameters are listed in Table 1.

In order to verify the validity of the simulation model, the calculation is initially made with pure conduction in powder bed with moving heat source. The pure conduction problem is achieved by setting the volume fraction of the low melting point powder, ϕ, to be zero so that the melting and resolidification do not occur. The steady-state surface temperature obtained by numerical solution is compared with the temperature distribution caused by a moving line heat source. The surface temperature obtained by both methods is plotted in Fig. 3. The temperature expression of a semi-infinite body with a moving line heat source is (Carslow and Jaeger, 1959)

$$T^0 - T_i^0 = \frac{Q}{\pi k_{\mathrm{eff}}} \exp\left(-\frac{ux}{2\alpha_{\mathrm{eff}}}\right) K_0\left[\frac{u\sqrt{x^2 + z^2}}{2\alpha_{\mathrm{eff}}}\right]. \quad (35)$$

In this particular case, the heat source is assumed to be top-hat (uniform distribution) instead of Gaussian distribution because the latter results in the energy spread in a wide width. For the top-hat distribution, the equivalent heat source intensity is expressed as

$$I_0 = \frac{Q}{2b}.$$

The nondimensional form of Eq. (35) is obtained by substituting Eq. (23) into Eq. (35), i.e.,

$$T + 1 = \frac{2N_i}{\pi K_{\mathrm{eff}}} \exp\left(-\frac{(1-\epsilon)UX}{2K_{\mathrm{eff}}}\right) \times K_0\left[\frac{(1-\epsilon)U\sqrt{X^2 + Z^2}}{2K_{\mathrm{eff}}}\right]. \quad (36)$$

In order to simulate the conduction problem in the powder under a moving line heat source, the boundary condition described by Eq. (30) should be replaced by the following equation:

$$-K\frac{\partial T}{\partial Z} = \begin{cases} N_i & Z = 0, \quad |X| \le 1, \quad \tau > 0 \\ 0 & Z = 0, \quad |X| > 1, \quad \tau > 0. \end{cases} \quad (30a)$$

As can be seen from Fig. 3, the overall agreement between the two solutions is very good except at the locations near $x = 0$. This discrepancy of the two results is due to the nature of heat source modeled in analytical and numerical solution. The analytical result is that the temperature distribution is caused by a infinitesimal heat source at $x = 0$, while the numerical temperature distribution result is caused by a finite width heat source of with dimensionless width of 2. Considering the different models, the agreement between the numerical and analytical solutions is very good at all locations.

Since most of the surface is exposed to the environment, heat will be lost by natural convection and radiation. Cao and Faghri (1990b) investigated thermal protection from an intense localized moving heat flux using phase-change materials and concluded that the effect of heat loss at the surface can be neglected. The difference between their work and the present paper is that the shrinkage phenomena were not considered due to the different application. When shrinkage phenomena are ignored, the effect of surface boundary condition on the surface temperature and the shape of solid-liquid interface are shown in Figs. 4 and 5, respectively. When shrinkage phenomena are ignored, it should be mentioned that the thermal conductivities of the powder bed cannot be calculated by Eq. (28) because the volume fraction of gas(es) remains unchanged after sintering. When the low melting point powder is molten, the contact area between the two powders is significantly increased and therefore it is expected that the effective thermal conductivity of the mixture of low melting point liquid metal and high melting point powder is higher than that before melting. The thermal conductivity of liquid is therefore calculated by using a parallel arrangement, i.e.,

$$K = (1-\epsilon)K_p \quad T > \Delta T. \quad (37)$$

The thermal conductivity in the mushy zone is then calculated by

$$K = K_{\mathrm{eff}} + \frac{(1-\epsilon)K_p - K_{\mathrm{eff}}}{2\Delta T}(T + \Delta T)$$
$$-\Delta T < T < \Delta T. \quad (38)$$

As can be seen, the effect of surface heat loss on both surface temperature and shape of sintering interface are not negligible. On the region of $X < 0$, where the surface temperature is higher than that of $X > 0$, the surface temperature decreases with the surface heat loss. However, at locations of $X > 0$, surface heat losses have very small effect on the surface temperature. The depth of the liquid pool and the sintering depth are more shallow when the surface heat loss is taken into account. This implies that the surface heat loss due to natural convection and radiation is not negligible for sintering of a metal powder bed. It should be noted that this conclusion is different from that of Cao and Faghri (1990b) where they concluded that the surface heat loss due to radiation and convection are negligible. This is because the heat loss in the area within the moving heat source, where the temperature is highest, was not taken into account in Cao and Faghri (1990b) due to different assumptions.

Figure 6 shows the effect of surface heat loss on the sintering process accounting for shrinkage. It can be seen that neglecting of surface heat loss will result in an overprediction of the sintering depth and the shape and volume of the liquid pool. The effect of surface heat loss is more significant for the case when shrinkage is taken into account than that for the case when shrinkage is ignored. Compared with the case without shrinkage, the most significant difference is that the surface of the powder bed lowers after being scanned by the moving heat source. This is due to shrinkage of the powder bed during the sintering process, which is required to form a fully densified part. The sintering depth is significantly larger than that of the case without shrinkage since the shrinkage induced an additional interface motion and the thermal conductivity of the liquid pool is greater than that for the case without shrinkage.

The effect of the moving heat source intensity on the sintering process is shown in Fig. 7. It can be seen that the sintering depth is decreased by a decrease of the moving heat source intensity. The liquid pool for the lower intensity is shallower and narrower than that at higher intensity. However, the location of the right side of the liquid pool is almost unaffected by the intensity. The effect of the scanning velocity of the moving heat source is shown in Fig. 8. It can be seen that the sintering depth is decreased with increase of the scanning velocity. It can be seen that the sintering depth decreases with increase of the scanning velocity. The liquid pool at higher scanning velocity is wider than that at lower scanning velocity. The entire right side of the liquid pool moves slightly toward the opposite direction of the heat source motion while the motion of the entire left side of the liquid pool is more significant.

6 Conclusion

Melting and resolidification of a powder mixture under moving heat flux heating is investigated numerically. The velocity induced by the shrinkage is taking into account in the physical model. The problem is formulated using a temperature transforming model and solved by the finite difference method. The results show that the effect of surface heat loss due to convection and radiation is not negligible regardless of whether the shrinkage phenomena is considered. The decrease of moving heat source intensity will result in decrease of the sintering depth and the volume of the liquid pool. The increase of the scanning velocity will decrease the sintering depth and the location and shape of the liquid pool is affected significantly. The physical model and results of this paper paves the way to simulate the complicated three-dimensional SLS process.

References

Bunnell, D. E., 1995, "Fundamentals of Selective Laser Sintering of Metals," Ph.D. thesis of the University of Texas at Austin, Austin, TX.

Cao, Y., and Faghri, A., 1990a, "A Numerical Analysis of Phase Change Problems Including Natural Convection," ASME JOURNAL OF HEAT TRANSFER, Vol. 112, pp. 812–816.

Cao, Y., and Faghri, A., 1990b, "Thermal protection from intense localized moving heat fluxes using phase-change materials," *Int. J. Heat Mass Transfer,* Vol. 33, pp. 127–138.

Conti, M., 1995, "Planar Solidification of a Finite Slab: Effect of the Pressure Dependence of the Freezing Point," *Int. J. Heat Mass Transfer,* Vol. 38, pp. 65–70.

Crank, J., 1956, *The Mathematics of Diffusion,* Clarendon, Oxford, UK.

Carslaw, H. S., and Jaeger, J. C., 1959, *Conduction of Heat in Solids,* Clarendon, Oxford, UK.

Eckert, E. R. G., and Drake, R. M., 1972, *Analysis of Heat and Mass Transfer,* McGraw-Hill, London.

Hadley, G. R., 1986, "Thermal Conductivity of Packed Metal Powders," *Int. J. Heat Mass Transfer,* Vol. 29, pp. 909–920.

Kandis, M., and Bergman, T. L., 1997, "Observation, Prediction, and Correlation of Geometric Shape Evolution Induced by Non-Isothermal Sintering of Polymer Powder," ASME JOURNAL OF HEAT TRANSFER, Vol. 119, pp. 824–831.

Kaviany, M., 1995, *Principles of Heat Transfer in Porous Media,* 2nd Ed., Springer-Verlag, New York.

Kim, C.-J., and Ro, S. T., 1993, "Shrinkage Formation During the Solidification Process in an Open Rectangular Cavity," ASME JOURNAL OF HEAT TRANSFER, Vol. 115, pp. 1078–1081.

Manzur, T., DeMaria, T., Chen, W., and Roychoudhuri, C., 1996, "Potential Role of High Power Laser Diode in Manufacturing," presented at SPIE Photonics West Conference, San Jose, CA.

Patankar, S. V., 1980, *Numerical Heat Transfer and Fluid Flow,* McGraw-Hill, New York.

Shah, A. A., 1994, "Thermomechanical Compressive Melting of Solder Particles," M.S. thesis, University of Texas at Austin, Austin, TX.

Sun, M. M., and Beaman, J. J., 1995, "A Three Dimensional Model for Selective Laser Sintering," *Proceeding of Solid Freeform Fabrication Symposium 1995,* pp. 102–109.

Viskanta, R., 1983, "Phase Change Heat Transfer," *Solar Heat Storage: Latent Heat Materials,* G. A. Lane, ed., CRC Press, Boca Raton, FL.

Williams, J., Miller, D., and Deckard, C., 1996, "Selective Laser Sintering Part Strength as Function of Andrew Number, Scan Rate and Spot Size," *Proceeding of Solid Freeform Fabrication Symposium 1996,* pp. 549–557.

Yao, L. C., and Prusa, J., 1989, "Melting and Freezing," *Advances in Heat Transfer,* Vol. 25, pp. 1–96.

Zhang, Y., and Faghri, A., 1998, "Melting of a Subcooled Mixed Powder Bed with Constant Heat Flux Heating," *Int. J. Heat Mass Transfer,* submitted for publication.

Transient Elastic and Viscoelastic Thermal Stresses During Laser Drilling of Ceramics

M. F. Modest
Department of Mechanical Engineering,
The Pennsylvania State University,
University Park, PA 16802
Fellow ASME

Lasers appear to be particularly well suited to drill and shape hard and brittle ceramics, which are almost impossible to netshape to tight tolerances, and are presently machined in industry only by diamond grinding. Unfortunately, the large, focussed heat fluxes that allow the ready melting and ablation of material, also result in large localized thermal stresses within the narrow heat-affected zone, which can lead to microcracks, significant decrease in bending strength, and even catastrophic failure. In order to assess the where, when, and what stresses occur during laser drilling, that are responsible for cracks and decrease in strength, elastic and viscoelastic stress models have been incorporated into our two-dimensional drilling code. The code is able to predict temporal temperature fields as well as the receding solid surface during CW or pulsed laser drilling. Using the resulting drill geometry and temperature field, elastic stresses as well as viscoelastic stresses are calculated as they develop and decay during the drilling process. The viscosity of the ceramic is treated as temperature-dependent, limiting viscoelastic effects to a thin layer near the ablation front where the ceramic has softened.

Introduction

Nearly all ceramics can be efficiently drilled, scribed, or cut with a laser, although massive problems remain that are poorly, or not at all, understood. These problems include thermal stress, redeposition of evaporated or liquified material, poor surface finish, undesirable hole and groove tapers, etc. It is well known that laser irradiation causes damage in ceramics due to thermal stresses, resulting in microcracks and, often, catastrophic failure; in all cases laser processing severely reduces the bending strength of the ceramic (Copley et al., 1983; Yamamoto and Yamamoto, 1987; deBastiani, Modest, and Stubican, 1990).

Criteria for stress failure of ceramics have been discussed in detail by Hasselman and Singh (1986). They note that ceramic materials will exhibit creep by diffusional processes at levels of temperature at which vacancy concentrations and mobility become appreciable. These temperatures correspond to about 0.5 to 0.7 × T_{melt} of the material. At the fast heating rates during laser machining severe compressive stresses develop, and creep rates fast enough to effect appreciable stress relaxation may not occur until somewhat higher temperature levels are reached; however, experimental evidence suggests that such rapid stress relaxation does occur before the material melts or decomposes. Extrapolating data for alumina given by Hasselman (1967) to a temperature just below the melting point ($T \approx 2300$ K) gives a thermal stress relaxation time of only 30 μs. While creep may reduce the probability of failure by thermal stresses during the heating up of the ceramics, the resulting stress relaxation would be expected to lead to very strong tensile stresses during cooldown, which in turn could cause the generation of microcracks, overall weakening of the material's mechanical strength, or catastrophic failure.

Data on creep behavior have been obtained by a number of investigators for a number of ceramic materials, although no creep properties appear to have been measured for temperatures approaching the melting/decomposition point, which are needed to fully understand the laser shaping process. For example, creep rates for alumina at 1500°C have been determined by Folweiler (1961); Lane et al. (1988) measured creep rates for sintered α-SiC, finding rates of $\sim 10^{-7}$/s at 1750°C and 200 MPa. Assuming that these data can be extrapolated to the melting/decomposition point, plastic deformation accompanied by thermal stress relaxation is to be expected during laser shaping of ceramics. This was confirmed by Gross et al. (1991), who investigated crack formation during laser (CO_2 and Nd:YAG) drilling of thin silicon wafers. The existence of a plastically deformed zone was shown by etch pit studies. Radial cracks, terminating at the deformed zone boundary, were observed as well as circumferential cracks following the boundary of the deformed zone; both types of cracks confirming, at least qualitatively, the nature of the expected stresses in the presence of creep prior to melting.

Most analytical investigations have been limited to thermoelastic bodies, using a one-dimensional analysis or commercial finite element programs. Hasselman et al. (1980, 1981) and Singh et al. (1981) investigated analytically the transient thermal stress field in a one-dimensional slab subjected to external radiation, with internal absorption of this irradiation. They found that greatest tensile stresses occurred in slabs of medium optical thickness ($\tau_L \sim 3 - 5$). A similar analysis for an opaque slab was made by Bradley (1988), and a procedure to describe the total strain energy at fracture due to thermal stresses is given.

Sumi et al. (1987) give an analytical/numerical solution for transient stresses for a simplified three-dimensional problem in which a local square surface heat source moves in the x-direction across an infinite flat x-y plane plate. The resulting stresses turn out to be mostly compressive stresses with some small tensile stresses. However, the tensile stresses occur near the (unrealistically abrupt) edge of the heat source and are, thus, exaggerated.

Very few theoretical investigations have addressed thermal stresses accompanied by creep. Guan and Cao (1993) predicted

---

Contributed by the Heat Transfer Division for publication in the JOURNAL OF HEAT TRANSFER. Manuscript received by the Heat Transfer Division, Dec. 30, 1997; revision received, June 29, 1998. Keywords: Ablation, Heat Transfer, Laser, Numerical Methods, Stress. Associate Technical Editor: D. Zumbrunnen.

residual stresses during welding of thin plates using a two-dimensional elastoplastic finite element model. Ferrari and Harding (1992) modeled the residual thermal stress field for a one-dimensional sphere with several plasma-sprayed ceramic coatings, finding moderate compressive stresses in the radial direction, but large tensile stresses in the transverse direction.

Gross et al. (1991) investigated crack formation during laser (CO_2 and Nd:YAG) drilling of thin silicon wafers. They developed a simple one-dimensional model incorporating compressive plastic deformation to predict thermal stresses in the wafer. The predictions indicate that, during cool-down, residual circumferential stresses are tensile in the deformed zone and compressive outside. Radial thermal stresses are tensile everywhere with a maximum at the deformed zone boundary. Radial cracks, terminating at the deformed zone boundary, were observed as well as circumferential cracks following the boundary of the deformed zone; both types of cracks confirming, at least qualitatively, the nature of the predicted stresses. Bahr et al. (1993) presented a one-dimensional transient model to predict thermal stresses inside an opaque solid irradiated by a short laser pulse. At high temperatures the material was allowed to deform visco-elastically as a Maxwell body. Results show that compressive stresses build up until—over a small range of temperature and a short period of time—stress relaxation takes place due to creep. During cool-down the solid behaves elastically again, resulting in tensile stresses throughout the heat-affected zone, which extends a few hundred μm for a 100 ms pulse, but only a few μm for a 1 ms pulse. Interestingly, for shorter pulses the tensile stresses are not only limited to a shallower depth, but they are also of much smaller magnitude.

In the present paper our two-dimensional drilling code is being augmented by an elastic and viscoelastic stress model to predict thermal stresses as they develop and decay during CW and pulsed laser drilling of ceramics.

Theoretical Background

To make analyses for the thermal and the stress problems tractable, a number of limiting and simplifying assumptions need to be made. Assumptions for the heat transfer problem are identical to those in previous papers of the author (1996, 1997), and are very briefly given here:

1 The solid is isotropic, has constant density, and the material is opaque, i.e., the laser beam does not penetrate appreciably into the solid.

2 Change of phase from solid to vapor (or decomposition products) occurs in a single step with a rate governed by a simple Arrhenius relation, modeled through a "heat of removal," Δh_{re} (Modest, 1996).

3 The evaporated material does not interfere with the incoming laser beam (or is removed by an external gas jet).

4 Heat losses by convection and radiation (on top surface and sidewalls) are negligible (Modest, 1997; Modest and Abakaians, 1986).

5 Multiple reflections of laser radiation within the groove are neglected, restricting the present model to shallow holes, holes with steep sidewalls, or materials with high absorptivities (Bang et al., 1991, 1992, 1993).

6 Heat transfer is unaffected by thermal expansion (always true for ceramics as shown by a simple order-of-magnitude analysis).

7 Inertia effects are negligible during stress development (always true for opaque ceramics, but may become questionable for semitransparent ceramics subject to ns laser pulses).

Heat Transfer. The transient heat conduction equation for a solid plate of thickness D, irradiated by a Gaussian laser beam may be expressed in terms of temperature T as (see Fig. 1)

$$\rho c \frac{\partial T}{\partial \bar{t}} = \nabla\cdot(k\nabla T) = \frac{1}{\bar{r}}\frac{\partial}{\partial \bar{r}}\left(k\bar{r}\frac{\partial T}{\partial \bar{r}}\right) + \frac{\partial}{\partial \bar{z}}\left(k\frac{\partial T}{\partial \bar{z}}\right), \qquad (1)$$

subject to the boundary conditions

$$\bar{r} = 0: \frac{\partial T}{\partial \bar{r}} = 0 \qquad (2a)$$

$$\bar{r} \to \infty: T \to T_\infty \qquad (2b)$$

$$\bar{z} = 0: \alpha\mathbf{F}\cdot\hat{\mathbf{n}} = -\hat{\mathbf{n}}\cdot(k\nabla T) + v_n\rho\Delta h_{re} \qquad (2c)$$

Nomenclature

A = viscoelasticity factor as defined in Eq. (14)
b = stress constant defined in Eq. (14)
c = specific heat of ceramic (J/kg K)
C_1 = preexponential factor for ablation rate, Eq. (3) (m/s)
$\mathbf{C}$ = viscoelasticity tensor defined in Eq. (14)
D = thickness of ceramic workpiece (m)
E = decomposition energy (J/kg)
$\mathbf{F}$ = laser irradiation vector (W/m^2)
F_0 = laser irradiation at center of beam ($r = 0$) (W/m^2)
G = shear modulus ($= \mu$, Lamé's constant) (Pa)
k = thermal conductivity of ceramic (W/m K)
$\dot{m}''$ = material removal rate (kg/m^{2}s)
$\hat{\mathbf{n}}$ = unit surface normal pointing into workpiece
N_k = conduction-to-irradiation parameter, Eq. (5)
Q, $\bar{Q}$ = (nondimensional) activation energy for creep (J/kg)
r, $\bar{r}$ = (nondimensional) radial coordinate (m)
$\bar{R}$ = universal gas constant, (J/kmol K)
s, $\bar{s}$ = (nondimensional) hole depth, (m)
Ste = Stefan number, Eq. (5)
t, $\bar{t}$ = (nondimensional) time (s)
T = temperature, (K)
$\mathbf{u}$, $\bar{\mathbf{u}}$ = (nondimensional) displacement vector (m)
u, w = displacements in r and z directions, respectively
v_n = surface recession velocity (m/s)
w_0 = $1/e^2$ laser beam radius at focal plane (m)
z, $\bar{z}$ = (nondimensional) axial coordinate (m)
α = absorptance of ceramic at laser wavelength
α_v = coefficient of thermal expansion (K^{-1})
β = nondimensional creep rate
$\boldsymbol{\delta}$ = identity tensor
Δh_{re} = heat of removal (J/kg)
$\boldsymbol{\epsilon}$, $\bar{\boldsymbol{\epsilon}}$ = (nondimensional) strain tensor
μ = Lamé constant ($= G$, the shear modulus) (Pa)
ν = Poisson's ratio
η = viscosity of viscoelastic solid (kg/m s)
ρ = density of ceramic (kg/m^3)
$\boldsymbol{\sigma}$, $\bar{\boldsymbol{\sigma}}$ = (nondimensional) stress tensor (Pa)
ξ, ζ = computational coordinates
θ = nondimensional temperature

Subscripts

∞ = at ambient or far-away conditions
0 = at focal plane, at $r = 0$, or at $t = 0$
re = at removal temperature
r = r-component
z = z-component
θ = θ-component

Superscripts

$\bar{\ }$ = dimensional quantity
$\dot{\ }$ = time rate
(n) = at time step n

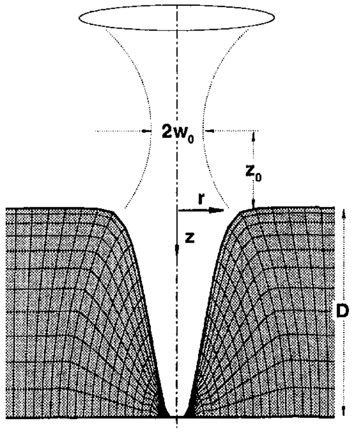

Fig. 1 Laser drilling setup and coordinate system

$$\bar{z} = D: \quad \frac{\partial T}{\partial \bar{z}} = 0, \tag{2d}$$

and an appropriate initial condition, such as

$$\bar{t} = 0: \quad T(\bar{r}, \bar{z}, \bar{t} = 0) = T_\infty \tag{2e}$$

$$\bar{s}(\bar{r}, \bar{t} = 0) = \bar{s}_0(\bar{r}), \tag{2f}$$

where ρ, c, k, and α are density, specific heat, thermal conductivity, and laser absorptance, respectively. Also, $\bar{r}$ is radial distance measured from the center of the laser beam, $\bar{z}$ is axial distance through the plate, and $\bar{s}$ is the local depth of a hole (i.e., the $\bar{z}$-coordinate of the top surface) and $\hat{\mathbf{n}}$ is a unit vector normal to the surface (pointing into the solid); v_n is the local surface recession velocity during drilling and it is assumed that the solid is originally at a uniform temperature T_∞; $\mathbf{F}$ is energy intensity distribution for a focussed Gaussian laser beam with a waist w_0 at the focal plane $\bar{z}_0$ (some quantities have been barred to distinguish the present dimensional quantities from the nondimensional ones introduced below).

Boundary conditions (2) are sufficient to solve Eq. (1) for the temperature if the shape of the hole, $\bar{s}$, is already established ($v_n = 0$) or if v_n is otherwise known. We will assume in this paper that the ablation and/or decomposition of the solid material is governed by a simple reaction equation of the Arrhenius type, i.e., the rate of mass loss per unit area is described by

$$\dot{m}'' = \rho v_n = \rho C_1 e^{-E/\bar{R}T}, \tag{3}$$

where E is the decomposition energy, $\bar{R}$ is the universal gas constant, and C_1 is a pre-exponential factor that depends on the nature of the ablation process.

The governing equations and boundary conditions are nondimensionalized using the 86 percent beam radius at the focal point, w_0:

$$r = \bar{r}/w_0; \quad z = \bar{z}/w_0; \quad t = \frac{k_{\mathrm{re}}\bar{t}}{\rho c_{\mathrm{re}} w_0^2}; \quad s = \bar{s}/w_0;$$

$$\theta = \frac{T - T_\infty}{T_{\mathrm{re}} - T_\infty}, \tag{4}$$

leading to two basic nondimensional parameters governing the laser/material interaction:

$$N_k = \frac{k_{\mathrm{re}}(T_{\mathrm{re}} - T_\infty)}{F_0 w_0}; \quad \mathrm{Ste} = \frac{\Delta h_{\mathrm{re}}}{c_{\mathrm{re}}(T_{\mathrm{re}} - T_\infty)}. \tag{5}$$

Boundary-fitted coordinates are employed in the numerical solution, i.e., the physical domain (r, z), is transformed to a uniformly spaced rectangular coordinate region (ξ, ζ). Detailed discussions of the heat transfer analysis and the numerical implementation are given by Modest (1996), (general development for a moving laser) and Modest (1997) (details on through-cutting and drilling).

Thermal Stresses. The extreme temperature gradients that occur during laser machining (in space and in time) result in extreme nonuniformities in the local thermal expansion of material (strain) which in turn cause strong thermal stresses. While under most conditions ceramics may be considered elastic, during (thermal) laser drilling there will be a thin zone near the receding interface (and at extremely high temperature) over which significant creep may occur. To assess the importance of this nonelastic zone on the overall thermal stress development, the present analysis includes a simple linear viscoelastic model (Maxwell body). The deviatoric stress-strain relation for a Maxwell body is (Boley and Weiner, 1960)

$$\dot{\bar{\mathbf{e}}} = \frac{1}{2\mu}\dot{\bar{\mathbf{s}}} + \frac{1}{2\eta}\bar{\mathbf{s}}, \tag{6}$$

where $\bar{\mathbf{e}}$ and $\bar{\mathbf{s}}$ are the dimensional deviatoric strain and stress tensors, respectively, μ is one of Lamé's constants ($= G$, the shear modulus), and η is the viscosity of the viscoelastic solid, which—unlike all other properties—is assumed to be temperature-dependent, since for ceramics its value changes by many orders of magnitude between room temperature and ablation/decomposition temperature. The viscosity-temperature dependence of $\bar{\mathbf{e}}$ is known from creep studies to follow an Arrhenius relationship (e.g., Lane et al., 1988), i.e.,

$$\frac{1}{\eta} = Ae^{-\bar{Q}/\bar{R}T} = \frac{1}{\eta_{\mathrm{re}}} e^{-\bar{Q}/\bar{R}T_{\mathrm{re}}(1-T_{\mathrm{re}}/T)}, \tag{7}$$

where $\bar{Q}$ is the activation energy, A is a pre-exponential factor, and η_{re} is the viscosity at the material's removal temperature. The complete stress-strain relation for a Maxwell body may then be stated (Boley and Weiner, 1960) in nondimensional form as

$$\dot{\boldsymbol{\sigma}} + \beta(\theta)\boldsymbol{\sigma} = \dot{\boldsymbol{\epsilon}} + \boldsymbol{\delta}\left[\frac{3\nu}{1-2\nu}\dot{\epsilon} - \frac{1+\nu}{1-2\nu}\dot{\theta} + \frac{1+\nu}{1-2\nu}\beta(\theta)(\epsilon - \theta)\right] \tag{8}$$

$$\boldsymbol{\epsilon} = \tfrac{1}{2}(\nabla\mathbf{u} + \nabla\mathbf{u}^T); \ \epsilon = \tfrac{1}{3}\,\mathrm{trace}\,(\boldsymbol{\epsilon}) \tag{9}$$

where

$$\boldsymbol{\sigma} = \frac{\bar{\boldsymbol{\sigma}}}{2\mu\alpha_v(T_{\mathrm{re}} - T_\infty)}, \quad \boldsymbol{\epsilon} = \frac{\bar{\boldsymbol{\epsilon}}}{\alpha_v(T_{\mathrm{re}} - T_\infty)},$$

$$\mathbf{u} = \frac{\bar{\mathbf{u}}}{w_0\alpha_v(T_{\mathrm{re}} - T_\infty)}, \tag{10a}$$

$$\beta(\theta) = \frac{\rho c_{\mathrm{re}} w_0^2 \mu}{k_{\mathrm{re}}\eta(T)} = \beta_{\mathrm{re}} e^{-Q(1-T_{\mathrm{re}}/T)}, \quad Q = \frac{\bar{Q}}{\bar{R}T_{\mathrm{re}}}, \tag{10b}$$

with ξ varying along lines essentially parallel to top and bottom surfaces and ζ perpendicular to them (as indicated in Fig. 1); nondimensional time, coordinates, and temperature have already been defined in Eq. (4). Here $\bar{\boldsymbol{\sigma}}$ and $\bar{\boldsymbol{\epsilon}}$ are stress and strain tensors, respectively, $\boldsymbol{\delta}$ is the identity tensor, $\bar{\mathbf{u}}$ is the displacement vector, α_v is the coefficient of thermal expansion, ν is Poisson's ratio, and the dot upon a symbol denotes differentiation with respect to time. Equation (8) requires initial conditions for $\boldsymbol{\sigma}$ and $\boldsymbol{\epsilon}$; we will here assume that the solid is initially unstressed and unstrained:

$$t = 0: \boldsymbol{\sigma} = 0; \quad \mathbf{u} = 0. \tag{11}$$

Because of the temperature dependence of the viscosity, or β, it is inconvenient to substitute Eq. (8) into the equilibrium condition $\nabla \cdot \boldsymbol{\sigma} = 0$ (since stress cannot be eliminated). Since a numerical solution will be attempted, the time derivatives will first be eliminated through a simple implicit finite difference (as is done in the solution of Eq. (1)), i.e.,

$$\dot{\theta} = \frac{\theta^{(n)} - \theta^{(n-1)}}{\Delta t}, \text{ etc.,} \tag{12}$$

where the superscript (n) denotes the nth time step. Equation (8) may then be rewritten as

$$\boldsymbol{\sigma}^{(n)} = A^{(n)}(\boldsymbol{\epsilon}^{(n)} - \boldsymbol{\delta}\epsilon^{(n)}) + \boldsymbol{\delta}b(\epsilon^{(n)} - \theta^{(n)}) + \mathbf{C}^{(n)} \tag{13}$$

$$A^{(n)}(\theta) = \frac{1}{1 + \beta^{(n)}\Delta t}; \quad b = \frac{1 + \nu}{1 - 2\nu},$$

$$\mathbf{C}^{(n)} = A^{(n)}[\boldsymbol{\sigma} - \boldsymbol{\epsilon} + \boldsymbol{\delta}\epsilon - \boldsymbol{\delta}b(\epsilon - \theta)]^{(n-1)}. \tag{14}$$

Note that Eq. (13) reduces to the thermoelastic case for infinite viscosity ($\beta \rightarrow 0 : A \rightarrow 1, \mathbf{C} \rightarrow \mathbf{O}$).

For the two-dimensional axisymmetric problem at hand, Eq. (13) in longhand becomes

$$\epsilon_{rr} = \frac{\partial u}{\partial r}, \quad \epsilon_{\theta\theta} = \frac{u}{r}, \quad \epsilon_{zz} = \frac{\partial w}{\partial z}, \tag{15a}$$

$$\epsilon_{rz} = \frac{1}{2}\left(\frac{\partial u}{\partial z} + \frac{\partial w}{\partial r}\right), \quad \epsilon_{r\theta} = \epsilon_{\theta z} = 0, \tag{15b}$$

$$\sigma_{rr} = A\frac{\partial u}{\partial r} + \frac{1}{3}(b - A)\left(\frac{\partial u}{\partial r} + \frac{u}{r} + \frac{\partial w}{\partial z}\right) - b\theta + C_{rr} \tag{16a}$$

$$\sigma_{\theta\theta} = A\frac{u}{r} + \frac{1}{3}(b - A)\left(\frac{\partial u}{\partial r} + \frac{u}{r} + \frac{\partial w}{\partial z}\right) - b\theta + C_{\theta\theta} \tag{16b}$$

$$\sigma_{zz} = A\frac{\partial w}{\partial z} + \frac{1}{3}(b - A)\left(\frac{\partial u}{\partial r} + \frac{u}{r} + \frac{\partial w}{\partial z}\right) - b\theta + C_{zz} \tag{16c}$$

$$\sigma_{rz} = \frac{A}{2}\left(\frac{\partial u}{\partial z} + \frac{\partial w}{\partial r}\right) + C_{rz} \tag{16d}$$

and the equilibrium conditions reduce to

$$\frac{\partial \sigma_{rr}}{\partial r} + \frac{\partial \sigma_{rz}}{\partial z} + \frac{1}{r}(\sigma_{rr} - \sigma_{\theta\theta}) = 0, \tag{17a}$$

$$\frac{\partial \sigma_{rz}}{\partial r} + \frac{\partial \sigma_{zz}}{\partial z} + \frac{1}{r}\sigma_{rz} = 0. \tag{17b}$$

For simplicity, the superscript (n) has been dropped from these equations. Equation (17) is a set of elliptic equations in the unknown displacements u and w, thus requiring boundary conditions along the bounding surface of the volume under consideration. Assuming zero traction on top and bottom surfaces ($\boldsymbol{\sigma} \cdot \hat{\mathbf{n}} = 0$), and zero displacement far away from the laser leads to

$$r = 0: \quad u = 0, \frac{\partial w}{\partial r} = 0 \tag{18a}$$

$$r \rightarrow \infty: \quad u = w = 0 \tag{18b}$$

$$z = 0: \quad \sigma_{rr}n_r + \sigma_{rz}n_z = 0, \quad \sigma_{rz}n_r + \sigma_{zz}n_z = 0 \tag{18c}$$

$$z = D: \quad \sigma_{rz} = \sigma_{zz} = 0. \tag{18d}$$

In Eq. (18d) use has been made of the fact that the bottom surface is always perpendicular to the z-axis. For very thick specimens Eq. (18d) may be replaced by a no-displacement condition far enough into the medium (actually, in the numerical implementation, here and for boundary condition (18b), we use the fact that displacement decays as $1/r^2$ far away from a point source).

After substituting Eqs. (16) into (17), the equations are transformed from physical coordinates (r, z, t) to computational coordinates (ξ, ζ, τ), followed by finite differencing (Roy and Modest, 1993). This results in extremely long and tedious relations, which will not be reproduced here. Special consideration must be given to the top and bottom boundaries because of the out-of-plane derivatives. These are taken care of by integrating Eqs. (17) over the half-nodes near the surface, eliminating out-of-plane derivatives through the use of Eqs. (18c) and (18d). Another trouble spot is the triangular node at the bottom of a hole once it forms (see Fig. 1), which is dealt with by integrating Eqs. (17) over the triangular element (in physical coordinates). Finally, the evaluation of $\mathbf{C}$ requires special attention. Recall that Eq. (8) was finite-differenced in time before transformation to computational coordinates: values at the previous time step must be evaluated at the same *physical* coordinates. Therefore, if the computational coordinates move with speed ξ_t, ζ_t,

$$\mathbf{C}^{*(n-1)}(r^{(n)}, z^{(n)}) = \mathbf{C}^{*(n-1)}(r^{(n-1)}, z^{(n-1)}) - \left[\xi_t \frac{\partial \mathbf{C}^*}{\partial \xi} + \zeta_t \frac{\partial \mathbf{C}^*}{\partial \zeta}\right]^{(n-1)}(r^{(n-1)}, z^{(n-1)})\Delta t, \tag{19a}$$

$$\mathbf{C}^* = \boldsymbol{\sigma} - \boldsymbol{\epsilon} + \boldsymbol{\delta}\epsilon - \boldsymbol{\delta}b(\epsilon - \theta). \tag{19b}$$

The result is a set of two equations for each of the $N_\xi \times N_\zeta$ nodes making up the overall grid (assuming no burn-through). In nine-point stencil form this may be written as

$$\mathbf{p} \cdot \mathbf{u}_{ik} + \mathbf{n} \cdot \mathbf{u}_{i,k+1} + \mathbf{ne} \cdot \mathbf{u}_{i+1,k+1} + \mathbf{e} \cdot \mathbf{u}_{i+1,k} + \mathbf{se} \cdot \mathbf{u}_{i+1,k-1} + \mathbf{s} \cdot \mathbf{u}_{i,k-1} + \mathbf{sw} \cdot \mathbf{u}_{i-1,k-1} + \mathbf{w} \cdot \mathbf{u}_{i-1,k} + \mathbf{nw} \cdot \mathbf{u}_{i-1,k+1} = \mathbf{f}, \tag{20}$$

where each of the $\mathbf{p}$, $\mathbf{n}$, etc., are 2×2 tensors. The set of simultaneous Eqs. (20) may be inverted in a number of ways. Since temperature varies fastest in the ζ-direction, we ordered Eq. (20) into a block-tridiagonal system for constant ξ, which was solved directly, and iteratively swept over ξ using successive overrelaxation. This works reasonably well, but will be improved before implementation in the three-dimensional laser machining problem. Note that, for the thermoelastic case, Eq. (20) needs to be solved only at times of interest while, for the viscoelastic case, an inversion must be carried out after every time step. However, using the previous time step as an initial guess causes very rapid convergence.

Results and Discussion

In order to assess the development of thermal stresses, and the importance of viscoelastic effects, several drilling operations on α-SiC were simulated, using silicon carbide physical properties from Ramanathan and Modest (1990) (all taken at removal temperatures of $T_{re} = 3000$ K, which gives good agreement with variable property calculations) and Edington et al. (1975): $k_{re} = 20$ W/mK, $\rho c_{re} = 5 \times 10^6$ J/m^{3}K, $\Delta h_{rc} \simeq 12.1$ MJ/kg, $\alpha_v = 10^{-6}$/K; $E = 400$ GPa, $\nu = 0.17$; and the viscoelastic properties were determined from a curve fit of data given by Lane et al. (1988) as $A = 5.30 \times 10^{14}$/(MPa s) and $\bar{Q} = 840$ kJ/mol. Laser parameters were typical values for a CO_2 laser (such as the one in our laboratory), using a $w_0 = 175$ μm and an average absorbed power of $\alpha P = 500$ W. Several CW and pulsed laser drilling events have been simulated, including a cool-down period after the laser has been turned off, all on large wafers with a thickness of 0.7 mm ($= 4w_0$). Results are shown in terms of principle stresses which, for the two-dimensional axisymmetric case, are

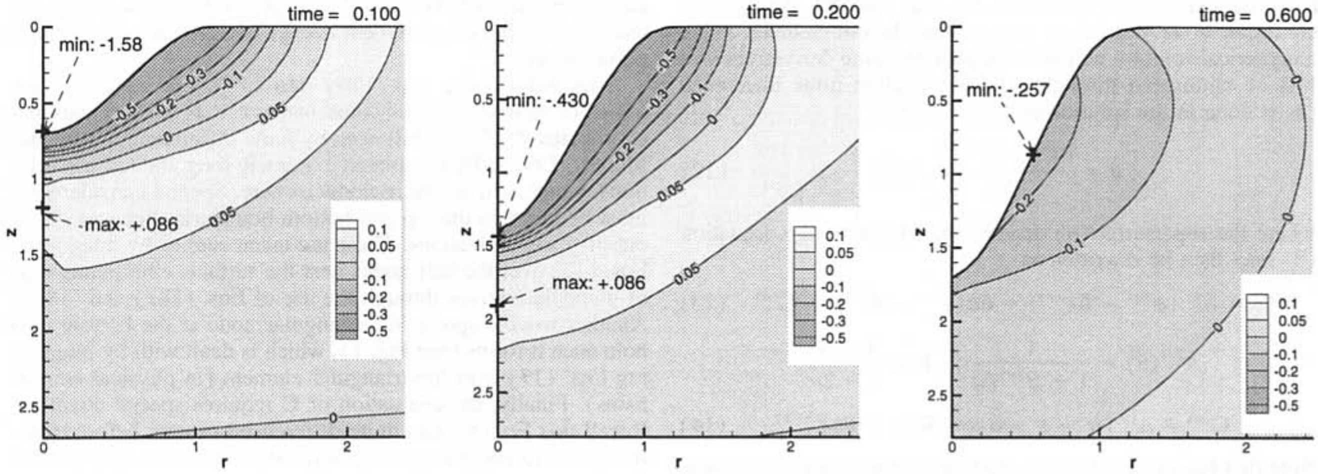

Fig. 2 Hoop stress development during CW CO_2 laser drilling of SiC; thermoelastic body (time $<$ 0.25: heating/drilling; time $>$ 0.25: cooling)

$$\sigma_{1,2} = \frac{1}{2}\left[\sigma_{rr} + \sigma_{zz} \pm \sqrt{(\sigma_{rr} - \sigma_{zz})^2 + 4\sigma_{rz}^2}\right],$$

$$\sigma_3 = \sigma_{\theta\theta}. \tag{21}$$

Figures 2 and 3 are sequences of frames showing the development of principal stresses for an elastic body during CW drilling (up to a nondimensional time of $t = 0.25$, or $\bar{t} \simeq 2$ ms), and cool-down after the laser is turned off at $t = 0.25$. Figure 2 shows hoop stresses ($\sigma_1 = \sigma_{\theta\theta}$), while Fig. 3 depicts the stress σ_2 perpendicular to the principal plane more or less parallel to the top surface (i.e., σ_{zz} at large r); the third principal stress was found to be always compressive (with maximum values of $\bar{\sigma}_3 \simeq -1.3$ GPa). As expected, strong compressive hoop stresses develop near the surface of the hole (up to $\bar{\sigma}_1 \simeq -1.3$ GPa), however, not strong enough to cause serious damage; σ_2 is close to zero at the surface due to the no-load boundary conditions. Interestingly, substantial tensile stresses in both the σ_1 and σ_2 directions develop parallel to the hole surface inside the material (up to values of about +0.1 or 80 MPa). While these tensile stresses are barely sufficient to cause substantial damage at room temperature, the effects may be more pronounced at elevated temperatures. On a *qualitative* level the results explain beautifully the damage we have routinely observed when scribing α-SiC with our CW CO_2 laser (see, e.g., Fig. 4, which shows α-SiC scribed at 1 cm/s and CW power of 600 W).

Similar observations are made when the laser operates in pulsed mode, here assumed to be running at 500 Hz (2 ms pulse time, or $t = 0.25$) with a 25 percent duty cycle (500 μs on-time $= \bar{t}_{p,\mathrm{on}}$). The frames in Fig. 5 show the hoop stresses just before ($t = 0.06 < t_{p,\mathrm{on}} = 0.0625$) the end of several laser pulses. As in the CW case substantial tensile stresses are seen to form inside the medium parallel to the hole surface, with the maximum tensile stresses below the rim of the hole (at $\bar{r} \simeq 1w_0$).

Finally, the effects of viscoelasticity are shown in Fig. 6, which shows the viscoelastic case equivalent to the frames in Fig. 3. Not surprisingly, the compressive stresses (hoop and radial) near the surface are substantially reduced (from a maximum of $\simeq -1.3$ GPa to approximately -400 MPa). This is accompanied by a strong buildup of compressive normal stresses just below the surface, as seen from Fig. 6. Also, the below-surface tensile stresses are increased substantially in the viscoelastic material (by approximately 50 percent), making the failure depicted in Fig. 4 much more likely. During cooling the viscoelastic material contracts, producing very strong tensile stresses in all three principal directions very close to the surface (up to values of $\sigma = 0.8$ or $\bar{\sigma} \simeq 600$ MPa), in particular near the hole's rim. Viscoelasticity during pulsed drilling, at least for the conditions and extrapolated properties employed here, always only affects the immediate vicinity of the surface. The

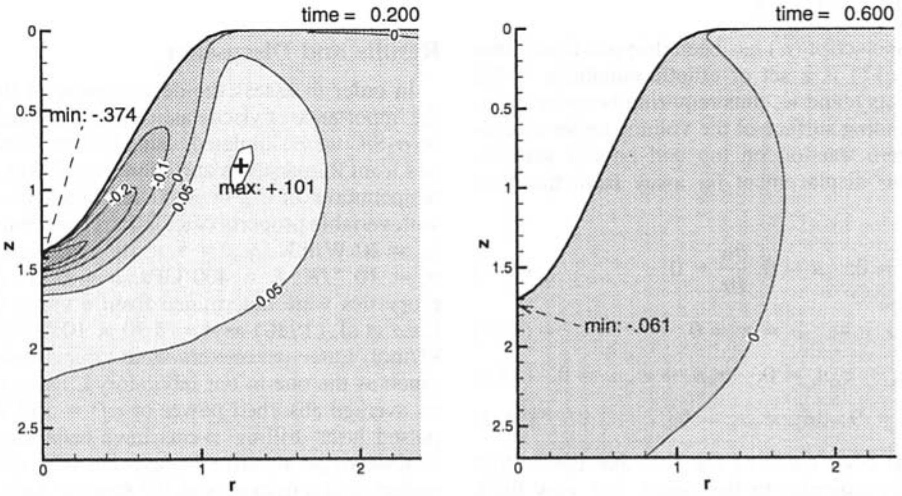

Fig. 3 Principal stresses (approx. normal to top surface) during CW CO_2 laser drilling of SiC; thermoelastic body (time $<$ 0.25: heating/drilling; time $>$ 0.25: cooling)

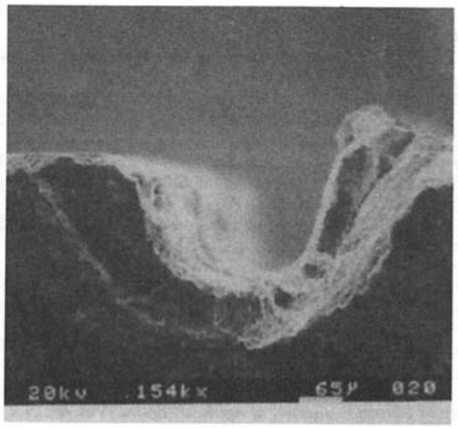

Fig. 4 SEM cross section of CW CO$_2$ laser scribed of α-SiC (power = 600 W, scan velocity = 1 cm/s)

effects do not seem to propagate into the material; therefore, one may assume that this layer will simply spall off during drilling. However, some very preliminary acoustic emission experiments in our laboratory for alumina indicate that crack formation primarily occurs immediately after the laser is turned off and during cool-down. Perhaps it is the combination of strong tensile stresses at the surface and the internal layer of tensile stresses that cause cracks to occur (although one also needs to keep in mind that alumina, unlike SiC, melts and resolidifies, thus generating a much thicker creep zone).

The reasons for the thin tensile stress surface layer are obvious from Fig. 7, which shows Eq. (7) and temperature versus depth at two locations, i.e., near the center and the rim of a typical hole: the temperature drops off so rapidly that after 3 μm (center) to 10 μm (rim) the viscoelasticity has decreased by three orders of magnitude and, for a typical time of 1 ms, has become negligible, i.e., $1/\mu \gg t/\eta$ (see Eq. (6)).

Conclusions

To assess the *where, when,* and *what* stresses occur during CW and pulsed laser drilling of ceramics, elastic and viscoelastic stress models have been incorporated into our two-dimensional drilling code. Simulations have been performed to predict temporal temperature fields, the receding solid surface during CW or pulsed laser drilling of thin ceramic wafers, and—based on these results—elastic stresses as well as viscoelastic stresses as they develop and decay during the drilling process. It was observed that during drilling substantial hoop and normal tensile stresses develop over a thick layer below and parallel to the surface, which may be the cause for experimentally observed subsurface cracks. It was also found that viscoelastic effects

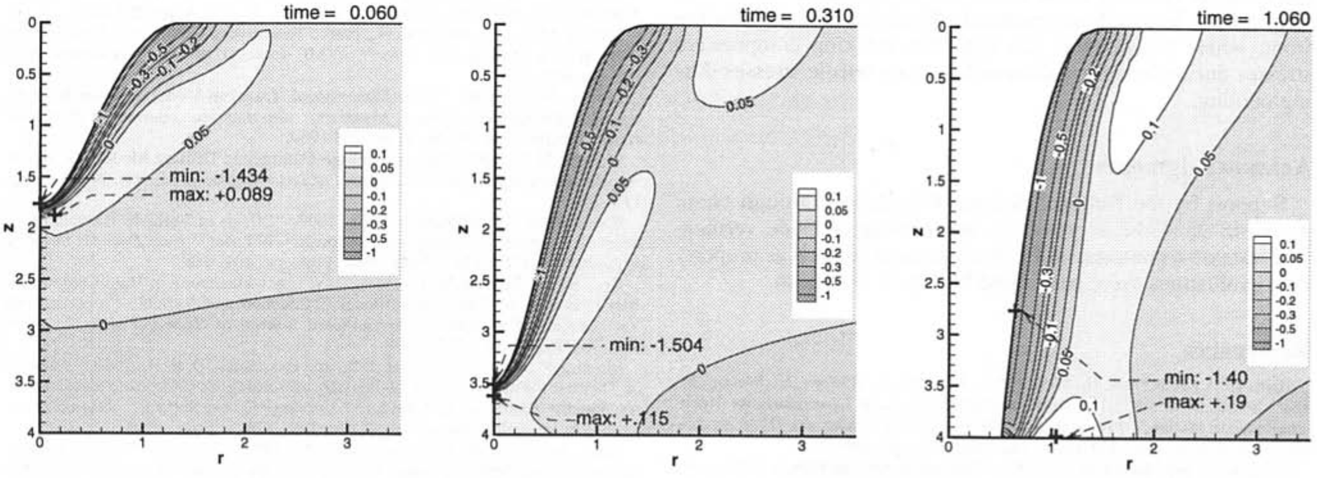

Fig. 5 Hoop stress development during pulsed CO$_2$ laser drilling of SiC; thermoelastic body (time = 0.06: near end of first pulse; time = 0.31: near end of second pulse; time = 1.06: near end of fifth pulse)

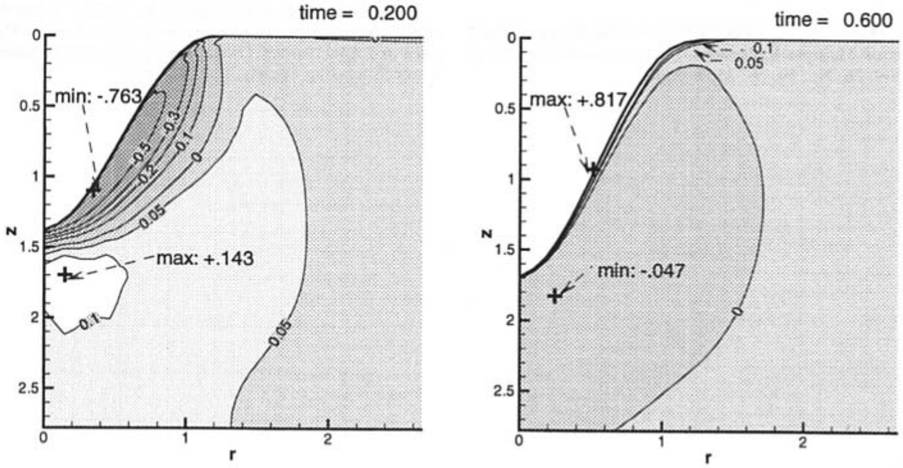

Fig. 6 Effects of viscoelasticity on hoop stresses during CW CO$_2$ laser drilling of SiC (time $<$ 0.25: heating/drilling; time $>$ 0.25: cooling)

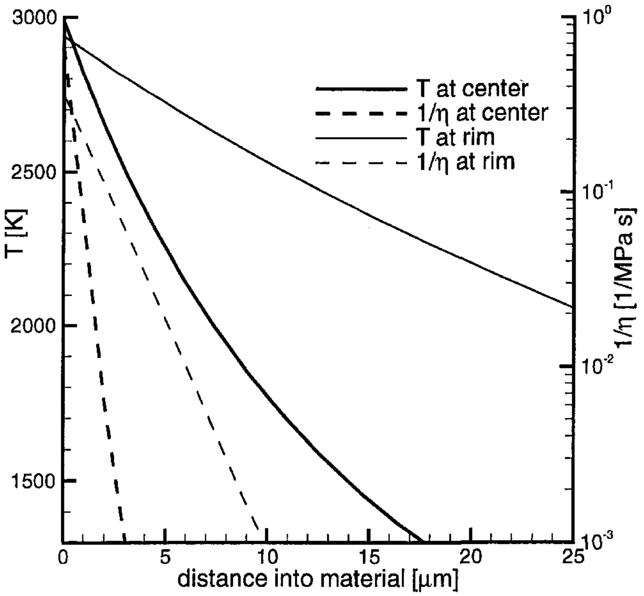

Fig. 7 Decay of temperature and viscoelasticity into substrate during pulsed laser drilling of SiC

(treating the viscosity of the ceramic as temperature-dependent) were mostly limited to an extremely thin layer near the ablation front, where the ceramic has softened, relaxing compressive stresses during heating, followed by strong tensile stresses during cooling.

Acknowledgments

Support by the National Science Foundation through Grant no. CMS-9634744 is gratefully acknowledged. Code verification tests on a commercial FEM stress code, as well as property data evaluations were performed by Mr. T. Mallison.

References

Bahr, H.-A., Schultrich, B., Weim, H.-J., Pflugbeil, I., Rüdiger, E., Wetzig, K., and Menzel, S., 1993, "Thermoschockrißbildung durch Laserinduzierte Hochtemperaturrelaxation," *Proceedings of Vortragsveranstaltung des DVM-Arbeitskreises Bruchvorgänge, Karlsruhe,* Germany, Feb., pp. 149–157.

Bang, S. Y., and Modest, M. F., 1991, "Multiple Reflection Effects on Evaporative Cutting With a Moving CW Laser," ASME JOURNAL OF HEAT TRANSFER, Vol. 113, pp. 663–669.

Bang, S. Y., and Modest, M. F., 1992, "Evaporative Scribing with a Moving CW Laser—Effects of Multiple Reflections and Beam Polarization," *Proceedings of ICALEO '91, Laser Materials Processing,* Vol. 74, San Jose, CA, pp. 288–304.

Bang, S. Y., Roy, S., and Modest, M. F., 1993, "CW Laser Machining of Hard Ceramics—Part II: Effects of Multiple Reflections," *International Journal of Heat and Mass Transfer,* Vol. 36, No. 14, pp. 3529–3540.

Boley, B. A., and Weiner, J. H., 1960, *Theory of Thermal Stresses,* John Wiley and Sons, New York.

Bradley, F., 1988, "Thermoelastic Analysis of Radiation-Heating Thermal Shock," *High Temperature Technology,* Vol. 6, No. 2, pp. 63–72.

Copley, S. W., Wallace, R. J., and Bass, M., 1983, "Laser Shaping of Materials," E. A. Metzbower, ed, *Lasers in Materials Processing,* American Society for Metals, Metals Park, Ohio.

DeBastiani, D., Modest, M. F., and Stubican, V. S., 1990, "Mechanisms of Reactions During CO_2-Laser Processing of Silicon Carbide," *Journal of the American Ceramic Society,* Vol. 73, No. 7, pp. 1947–1952.

Edington, J. W., Rowcliffe, D. J., and Henshall, J. L., 1975, "The Mechanical Properties of Silicon Nitride and Silicon Carbide Part I: Materials and Strength," *Powder Metallurgy International,* Vol. 7, No. 2, pp. 82–96.

Ferrari, M., and Harding, J. H., 1992, "Thermal Stress Field in Plasma-Sprayed Ceramic Coatings," ASME *Journal of Energy Resources Technology,* Vol. 114, pp. 105–109.

Folweiler, R. C., 1961, "Creep Behavior of Pore-Free Polycrystalline Allumimum Oxide," *Journal of Applied Physics,* Vol. 32, No. 5, pp. 773–778.

Gross, T. S., Hening, S. D., and Watt, D. W., 1991, "Crack Formation during Laser Cutting of Silicon," *Journal of Applied Physics,* Vol. 69, No. 2, pp. 983–989.

Guan, Q., and Cao, Y., 1993, "Verification of FE Programs for Welding Thermal Strain—Stress Analysis Using High Temperature Moiré Measurement," *Journal of the International Institute of Welding,* Vol. 31, No. 1, pp. 344–347.

Hasselman, D. P. H., and Singh, J. P., 1986, "Criteria for the Thermal Stress Failure of Brittle Structural Ceramics," *Thermal Stresses I,* R. B. Hetnarski, ed., North-Holland, New York, Chapter 4.

Hasselman, D. P. H., Thomas, J. R., Kamat, M. P., and Satyamurthy, K., 1980, "Thermal Stress Analysis of Partially Absorbing Brittle Ceramics Subjected to Symmetric Radiation Heating," *Journal of the American Ceramic Society,* Vol. 63, Nos. 1–2, pp. 21–25.

Hasselman, D. P. H., 1967, "Approximate Theory of Thermal Stress Resistance of Brittle Ceramics Involving Creep," *Journal of the American Ceramic Society,* Vol. 50, pp. 454–457.

Lane, J. E., Carter, C. H., and Davis, R. F., 1988, "Kinetics and Mechanisms of High-Temperature Creep in Silicon Carbide: III, Sintered α-Silicon Carbide," *Journal of the American Ceramic Society,* Vol. 71, No. 4, pp. 281–295.

Modest, M. F., and Abakians, H., 1986, "Evaporative Cutting of a Semi-Infinite Body With a Moving CW Laser," ASME JOURNAL OF HEAT TRANSFER, Vol. 108, pp. 602–607.

Modest, M. F., 1996, "Three-Dimensional, Transient Model for Laser Machining of Ablating/Decomposing Materials," *International Journal of Heat and Mass Transfer,* Vol. 39, No. 2, pp. 221–234.

Modest, M. F., 1997, "Laser Through-Cutting and Drilling Models for Ablating/Decomposing Materials," *Journal of Laser Applications,* Vol. 9, No. 3, pp. 137–146.

Ramanathan, S., and Modest, M. F., 1990, "Effects of Variable Thermal Properties on Evaporative Cutting with a Moving CW Laser," *Heat Transfer in Space Systems,* Vol. HTD-135, ASME, New York, pp. 101–108.

Roy, S., and Modest, M. F., 1993, "CW Laser Machining of Hard Ceramics—Part I: Effects of Three-Dimensional Conduction and Variable Properties and Various Laser Parameters," *International Journal of Heat and Mass Transfer,* Vol. 36, No. 14, pp. 3515–3528.

Singh, J. P., Sumi, N., Thomas, J. R., and Hasselman, D. P. H., 1981, "Analysis of Thermal Stress Resistance of Partially Absorbing Ceramic Plate Subjected to Asymmetric Radiation, II: Convective Cooling at Front Surface," *Journal of the American Ceramic Society,* Vol. 64, pp. 169–173.

Sumi, N., Hetnarski, R. B., and Noda, N., 1987, "Transient Thermal Stresses due to a Local Source of Heat Moving over the Surface of an Infinite Elastic Slab," *Journal of Thermal Stresses,* Vol. 10, pp. 83–96.

Thomas, J. R., Singh, J. P., and Hasselman, D. P. H., 1981, "Analysis of Thermal Stress Resistance of Partially Absorbing Ceramic Plate Subjected to Asymmetric Radiation, I: Convective Cooling at Rear Surface," *Journal of the American Ceramic Society,* Vol. 64, No. 3, pp. 163–173.

Yamamoto, J., and Yamamoto, Y., 1987, "Laser Machining of Silicon Nitride," *International Conference on Laser Advanced Materials Processing—Science and Applications,* Osaka, Japan, High Temperature Society of Japan, Japan Laser Processing Society, pp. 297–302.

Transient Thermal Response of a Rotating Cylindrical Silicon Nitride Workpiece Subjected to a Translating Laser Heat Source, Part I: Comparison of Surface Temperature Measurements With Theoretical Results

J. C. Rozzi

F. E. Pfefferkorn

F. P. Incropera
Fellow ASME

Y. C. Shin

Laser Assisted Materials
Processing Laboratory,
School of Mechanical Engineering,
Purdue University,
1288 Mechanical Engineering Building,
West Lafayette, IN 47907-1288

Laser-assisted machining (LAM), in which the material is locally heated by an intense laser source prior to material removal, provides an alternative machining process with the potential to yield higher material removal rates, as well as improved control of workpiece properties and geometry, for difficult-to-machine materials such as structural ceramics. To assess the feasibility of the LAM process and to obtain an improved understanding of governing physical phenomena, a laser assisted machining facility was developed and used to experimentally investigate the thermal response of a rotating silicon nitride workpiece heated by a translating CO_2 laser. Using a focused laser pyrometer, surface temperature history measurements were made to determine the effect of rotational and translational speed, as well as the laser beam diameter and power, on thermal conditions. The experimental results are in good agreement with predictions based on a transient three-dimensional numerical simulation of the heating process. With increasing workpiece rotational speed, temperatures in proximity to the laser spot decrease, while those at circumferential locations further removed from the laser increase. Near-laser temperatures decrease with increasing beam diameter, while energy deposition by the laser and, correspondingly, workpiece surface temperatures increase with decreasing laser translational speed and increasing laser power. In a companion paper (Rozzi et al., 1998), the detailed numerical model is used to further elucidate thermal conditions associated with laser heating and to assess the merit of a simple, analytical model which is better suited for on-line process control.

Introduction

Although much has been done to establish the efficacy of the laser machining of ceramic materials (Modest and Abakians, 1986; Wallace and Copley, 1989; Roy and Modest, 1993), comparatively little has been done to assess an alternative laser-*assisted* machining (LAM) process. Unlike laser machining, which uses an intense laser for material removal by melting or sublimation of the workpiece, in LAM the laser is used to change the ceramic deformation behavior from brittle to ductile for material removal with a conventional cutting tool. Although the feasibility of this hybrid machining process has been demonstrated (König and Zaboklici, 1993), underlying physical mechanisms are not well understood and a comprehensive thermomechanical model of the heating and material removal processes has yet to be developed and validated through comparisons with experimental results. These deficiencies must be addressed if intelligent control schemes capable of optimizing LAM processes are to be established.

Previous investigators have conducted plasma and laser-assisted machining of various advanced ceramic materials, including zirconia, alumina, and, silicon nitride. The studies suffer from exiguous characterizations of experimental conditions and temperature measurement techniques and do not mention the development of a process model. For example, Uehara and Takeshita (1986) and Kitagawa and Maekawa (1990) conducted experiments with various ceramic materials, but did not specify the location of temperature measurement and, in the latter case, the measurement technique. Studies by König and Wageman (1991) and König and Zaboklici (1993) focused on the laser-assisted machining of silicon nitride using CO_2 (10.6 μm) and Nd:YAG (1.06 μm) lasers. Less power was required to effectively heat silicon nitride using the Nd:YAG laser. Although the implication is that the silicon nitride surfaces were spectral, with more energy being absorbed at the lower wavelength, no mention was made of surface radiative properties.

Several investigators (Davis et al., 1986; Festa et al., 1993; Koai et al., 1993) have studied localized heat treatment of various materials using either laser or electron beams. The first two studies did not utilize temperature measurements for model validation. Rather, hardened steel parts were sectioned, etched and the hardened depth compared to simple thermal models through knowledge of the solid-state transformation temperature. Koai et al. (1993) did make surface temperature measure-

---

Contributed by the Heat Transfer Division for publication in the JOURNAL OF HEAT TRANSFER. Manuscript received by the Heat Transfer Division, Mar. 18, 1997; revision received, May 29, 1998. Keywords: High-Temperature Phenomena, Laser Processing, Materials Processing and Manufacturing Process. Associate Technical Editor: A. Lavine.

ments using a thermal imaging system in their experimental and numerical investigation of the hardening of steel cylinders using a CO_2 laser. While the authors indicate that the CO_2 laser power distribution was tailored empirically in response to changes in the surface absorptivity during heating, no mention of surface radiative properties was made with respect to surface temperature measurement.

The present study represents the first step in the systematic development of a thermomechanical model for LAM. Rotating cylindrical silicon nitride workpieces have been heated by a translating CO_2 laser and surface temperatures measured using a laser pyrometer. These measurements have been compared to predictions based on a transient, three-dimensional model which embodies pertinent physical features of the heating process.

Experimental Methods

The laser-assisted machining facility consists of a 1.5 kW CO_2 laser, a 60 hP computer numerically controlled (CNC) turret lathe, a water-cooled chiller, laser supply gases, and a laser assist gas. Beam emission from the CO_2 laser was controlled using a shutter which was activated within a CNC program. When the shutter was opened, the beam was directed to the lathe cavity by a series of three mirrors and, once received by mirror 4 (Fig. 1), was directed by mirrors 5, 6, and 7 toward the workpiece surface. By mechanically attaching the laser optics, excluding mirror 4, to the lathe tool turret, the laser output may be traversed in the axial direction of the workpiece. Flexible tubing was utilized between mirrors 4–5 to ensure beam containment during the experiments. The beam then passes through a focusing optic, which can provide a minimum beam diameter of 0.2 mm. During heating, a low-pressure laser assist gas (air) is forced into the cavity between the focusing optic and the laser exit location to protect the optic from debris. The vertical and angular positions of the beam output can be adjusted to alter the output beam diameter and adjust beam placement. All mirrors were cooled using chilled water. Mirror mounts and rigid tubing were constructed from MIC-6 black anodized aluminum. The workpiece rotational and laser translational speeds were specified using part programs written on the CNC controller, and lathe vibration was minimized using damping pads at each of the six lathe supports.

Cylindrical silicon nitride workpieces sintered with alumina and yttria, resulting in 90 wt% β-Si_3N_4 and 10 wt% Y-Si-Al-O-N glass (prior to recrystallization), were used in all of the heating experiments. The workpieces were of 8.46 mm diameter and 57.2 mm length, with 5.53 mm long hemispherical ends and were secured in the lathe chuck by means of a special adapter and holder assembly. Off-line measurements of surface radiative properties (Pfefferkorn, 1997) revealed that the workpiece could be reasonably approximated as an opaque and diffuse emitter and reflector.

The laser power was determined using simultaneous voltage and power measurements, respectively, from a power detector located within the rear mirror assembly of the laser cavity and a calorimeter, consisting of an aluminum alloy coated with an absorbing material ($\alpha_{10.6\mu m} \approx 0.97$). By measuring the voltage and power before and after the optics, respectively, heat losses to the seven cooled mirrors were implicitly considered. The accuracy of the calorimeter (Digital Power Probe Model 30/H3-C, Macken Instruments, Inc.) is ±4 percent + 2 W over the power range from 200 to 2200 W and includes a calibration constant, which accounts for free convection and radiation heat transfer from the calorimeter surface at a CO_2 laser power of 600 W. From a numerical model of the calorimeter, it was determined that application of the constant over the range of laser powers (200–1400 W) resulted in errors of less than ±1 percent, which are within the reported (±4 percent + 2 W) calorimeter accuracy.

The radial distribution of the laser heat flux may be assumed to be uniform or Gaussian (Rozzi et al., 1995), or it may be represented by the actual distribution. For the CO_2 laser used in this study, the distribution was obtained from manufacturer-supplied data and was fit with a ninth-order polynomial, where the maximum laser flux is given by

$$q''_{l,m} = \frac{P_l}{2\pi r_{l,p}^2 \int_0^{1.75} (r/r_{l,p}) f(r/r_{l,p}) d(r/r_{l,p})}, \qquad (1a)$$

$r_{l,p} = r_l/1.75$ is the radius of the beam plane containing 86.5 percent of the total laser power, and

$$f(r/r_{l,p}) = a_9 (r/r_{l,p})^9 + a_8 (r/r_{l,p})^8 + \ldots + a_0. \qquad (1b)$$

The characteristic mode shape of the laser corresponds to a combination of TEM_{00} and TEM_{01}, where TEM_{mn} designates the number of beam profile segmentations occurring along the m and n coordinate directions on a plane perpendicular to the beam propagation direction (Hect, 1987). Comparative calculations performed to assess the effect of mode shape on the predictions of this study indicate that the difference between surface

Nomenclature

c_p = specific heat at constant pressure, J/kg K
D = diameter, m
E = emissive power, W/m^2
G_{sur} = irradiation from the surroundings, W/m^2
H_j = nozzle-to-surface distance, m
h = convective heat transfer coefficient, W/m^{2}K
h_{rad} = radiative heat transfer coefficient, W/m^{2}K
k = thermal conductivity, W/m K
L_w = workpiece length, m
P_l = laser power, W
q''_{conv} = convective heat flux, W/m^2
q''_l = laser heat flux, W/m^2
$q''_{l,m}$ = maximum laser heat flux, W/m^2
r = radial coordinate, m
r_l = radius of the laser beam, m
r_w = workpiece radius, m
t = time, s
T = temperature, K
$\forall$ = volume, m^3
V_z = laser traverse velocity, m/s
z = axial coordinate, m
z_c = axial location of the laser center, m
$z_{c,o}$ = initial ($t = 0$) axial location of the laser center, m

Greek Symbols

α = thermal diffusivity, m^2/s; total absorptivity of workpiece surface
α_{sur} = absorptivity of the workpiece surface to irradiation from the surroundings
ϵ = emissivity of workpiece surface
ω = workpiece rotational speed, rad/s
ϕ = circumferential coordinate, rad
ϕ_c = circumferential location of the laser center, rad
λ = wavelength, μm
$\Delta\lambda$ = wavelength bandwidth, μm
ν = workpiece rotational speed, rpm
ρ = density, kg/m^3
σ = Stefan-Boltzmann constant, W/m^{2}K^4

Subscripts

∞ = ambient air conditions
c = source geometric center
conv = convection
env = environment
j = laser assist gas jet
l = laser
rad = radiation
sur = surroundings
w = workpiece
λ = spectral

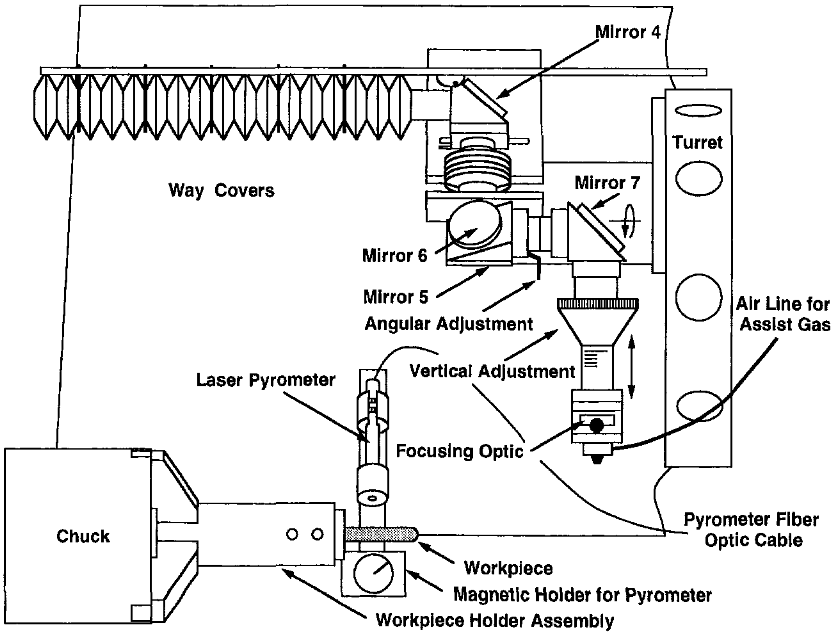

Fig. 1 CNC lathe cavity with the CO_2 laser optics, silicon nitride workpiece, and laser pyrometer

temperatures predicted for the TEM_{00} and TEM_{01} profiles may be as large as 170°C at the beam center. This difference experiences a pronounced decay to approximately 10°C with increasing circumferential distance from the laser center. Since comparisons between predicted and measured surface temperatures are made at locations well removed from the laser center, they are not affected by uncertainties in the precise form of the beam profile.

A fiber optic, single wavelength, laser pyrometer (PyroFiber® Model 865, Pyrometer Instrument Co.) was used to make simultaneous spectral emissivity and temperature measurements for temperatures exceeding 650°C over a portion of the workpiece surface which measured 0.3 mm in diameter. The operating wavelength (λ) of the laser pyrometer is 0.865 μm with a bandwidth ($\Delta\lambda$) of 0.055 μm, and details relating to calibration and implementation are provided by Pfefferkorn (1997). The pyrometer consists of a sensor head, electronics unit (EU), and two fiber optic connections, one of which transmits collected radiation from the workpiece surface and the other radiation emitted by a GaAs laser located in the EU. During a measurement sequence of 0.027 s: (i) radiation emitted by the heated workpiece surface was collected and stored in the EU; (ii) the GaAs laser was fired and the total radiation from the workpiece surface (emission plus reflected GaAs radiation) was collected; and (iii) assuming opaque, diffuse surface behavior, the spectral reflectivity and emissivity were calculated, along with the surface temperature.

The pyrometer was calibrated using a blackbody radiation source and a diffuse-white reflective standard constructed according to NIST laboratory specification SRS-99-020-M1. The sensor head was positioned 14 mm from the workpiece surface and was enclosed in a shield with a small aperture to eliminate background radiation. Complete details concerning the calibration and operation of the laser pyrometer are provided by Pfefferkorn (1997).

Experimental uncertainties were evaluated using a statistical analysis of the contributing factors. Measurement of the surface emissivity and blackbody temperature is influenced by errors in (i) the pyrometer-to-surface distance caused by improper placement of the pyrometer and workpiece out-of-roundness, (ii) the pyrometer angle relative to the surface normal, (iii) the axial and circumferential placement of the pyrometer, (iv) the workpiece rotational and laser translational speeds, and (v) the laser beam diameter and power. For nominal conditions, the 95 percent confidence interval for the surface temperature was based on the data scatter around a five-point moving average and corresponded to ±2.5 percent at 1500°C and ±5.5 percent at 700°C. Because the silicon nitride workpieces were obtained immediately after the sintering process, out-of-round measurements averaged approximately 0.4 mm and represented the largest contribution to the experimental uncertainty, as determined from the methodology of Kline and McClintock (1953).

Mathematical Model

For a rotating cylinder subjected to a translating laser source (Fig. 2), the following modified form of the heat equation accounts for transient three-dimensional conduction and circumferential advection in a cylindrical (r, ϕ, z) coordinate system.

$$\frac{1}{r}\frac{\partial}{\partial r}\left(kr\frac{\partial T}{\partial r}\right)+\frac{1}{r^2}\frac{\partial}{\partial \phi}\left(k\frac{\partial T}{\partial \phi}\right)+\frac{\partial}{\partial z}\left(k\frac{\partial T}{\partial z}\right)-\frac{\partial(\rho\omega c_p T)}{\partial \phi}=\frac{\partial(\rho c_p T)}{\partial t} \qquad (2)$$

The boundary condition at the workpiece surface ($r = r_w$) is of the form

$$k\left.\frac{\partial T}{\partial r}\right|_{r=r_w} = q''_{l,\mathrm{abs}} - q''_{\mathrm{conv}} - E(T) + \alpha_{\mathrm{sur}}G_{\mathrm{sur}}(T_{\mathrm{sur}}) \qquad (3a)$$

for $\sqrt{[r_w(\phi-\phi_c)]^2+(z-z_c)^2} \leq r_l$, or

$$k\left.\frac{\partial T}{\partial r}\right|_{r=r_w} = -q''_{\mathrm{conv}} - E(T) + \alpha_{\mathrm{sur}}G_{\mathrm{sur}}(T_{\mathrm{sur}}) \qquad (3b)$$

for $\sqrt{[r_w(\phi-\phi_c)]^2+(z-z_c)^2} > r_l$, where ($\phi_c$, z_c) specifies the location of the laser geometric center. In this formulation (Fig. 2), the laser beam is assumed to move at a fixed speed, V_z, in which case $z_c = V_z t + z_{c,o}$, where $z_{c,o}$ is the initial axial location of the laser center, and to be incident perpendicular to

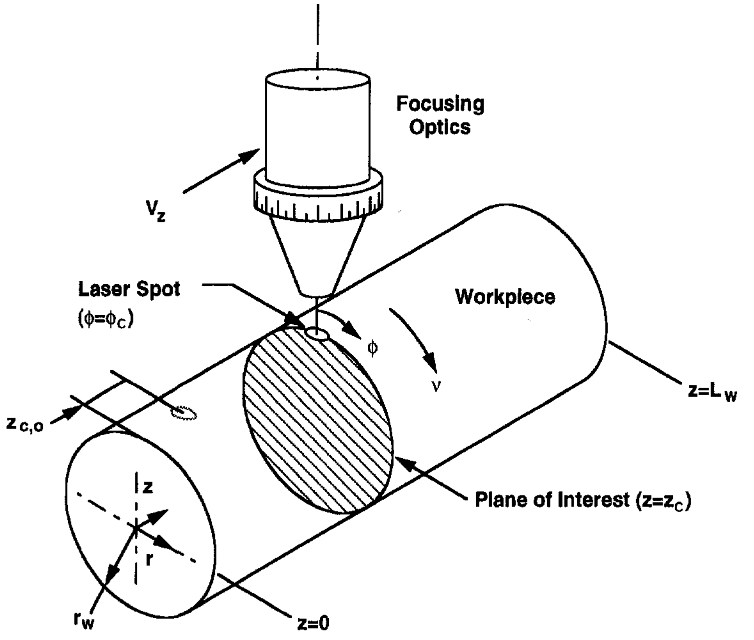

Fig. 2 Coordinate system for rotating workpiece with translating laser

the cylinder surface at a fixed circumferential location, ϕ_c. In addition, from radial symmetry at the centerline of the workpiece,

$$\left.\frac{\partial T}{\partial r}\right|_{r=0} = 0. \tag{4}$$

Allowing for convection and radiation at the end face corresponding to $z = 0$ and assuming enclosure of the workpiece by the chuck to provide an adiabatic surface at $z = L_w$, the corresponding boundary conditions are

$$k\left.\frac{\partial T}{\partial z}\right|_{z=0} = q''_{\text{conv}} + E(T) - \alpha_{\text{sur}}G_{\text{sur}}(T_{\text{sur}}) \tag{5}$$

$$k\left.\frac{\partial T}{\partial z}\right|_{z=L_w} = 0. \tag{6}$$

In the circumferential direction, boundary conditions correspond to continuity between temperatures and temperature gradients at ϕ and $\phi + 2\pi$. Hence,

$$T(r, \phi, z, t) = T(r, \phi + 2\pi, z, t), \tag{7}$$

$$\left.\frac{\partial T}{\partial \phi}\right|_{\phi} = \left.\frac{\partial T}{\partial \phi}\right|_{\phi+2\pi}. \tag{8}$$

At the initiation of laser heating, the workpiece is in thermal equilibrium with the surroundings.

$$T(r, \phi, z, 0) = T_\infty = T_{\text{sur}} \tag{9}$$

If the jet exit velocity of the laser assist gas is much higher than the workpiece surface speed, convection heat transfer in the jet impingement zone will not be significantly influenced by workpiece motion (Zumbrunnen, 1991). Hence, since nominal conditions of this study ($\nu = 1000$ rpm, $D_w = 8.46$ mm) correspond to a workpiece surface rotational velocity of 0.44 m/s and the gas assist exit velocity exceeds 100 m/s, the effects of surface motion may be neglected. For a gas assist jet diameter of $D_j = 1$ mm, the Reynolds number and dimensionless nozzle-to-surface distance were $\text{Re}_j = 15{,}900$ and $H_j/D_j = 10$, respectively. The corresponding radial variation of the local Nusselt number was determined from experimental results obtained by El-Genk et al. (1992). The maximum centerline value of the convection coefficient was $h_j = 3200$ W/m^{2}K. The jet center corresponded to the laser center (ϕ_c, z_c), and the extent of the jet interaction zone was determined by placing a few drops of ink at the jet geometric center on the surface of a stationary workpiece and measuring the pattern created by jet impingement. The extent of the interaction zone corresponded to $(\phi - \phi_c) \approx \pm 27$ deg, or $r_w(\phi - \phi_c) \approx \pm 2$ mm, and $(z - z_c) \approx \pm 5$ mm. Convective heat transfer from the workpiece surface to the gas assist jet was computed from the expression, $q''_{\text{conv},j} = h_j[T(r_w, \phi, z) - T_j]$, where $T_j \approx T_\infty$.

Convection coefficients on portions of the workpiece surface not exposed to the laser assist gas and on the workpiece free end were evaluated using the empirical correlations of Etemad (1955) and Richardson and Saunders (1963), respectively. The correlations presume the existence of mixed and forced convection at the cylindrical and end surfaces, respectively, of the workpiece. In all convection calculations, air properties were evaluated at a representative film temperature.

Touloukian (1967) and DeWitt and Nutter (1988) have provided measurements of the normal spectral emissivity of sintered and commercially supplied silicon nitride surfaces, respectively, over the wavelength range from 1 to 15 μm at approximately 1700 K. Both of the cited studies indicate variations in the normal, spectral emissivity ranging from 0.78 to 0.98. At the wavelength of laser irradiation ($\lambda = 10.6$ μm), Touloukian (1967) and DeWitt and Nutter (1988) recommend values of $\epsilon_l \approx 0.89$ and 0.82, respectively. Pfefferkorn (1997), who made reflectivity measurements on the opaque sintered silicon nitride surface of interest in the present study at a single wavelength of $\lambda = 0.865$ μm, found that the surface was a diffuse reflector and that the reflectivity was only weakly dependent on surface temperature over the range from 23 to 1500°C. The spectral hemispherical reflectivity ranged between 0.12 and 0.22, resulting in a spectral hemispherical absorptivity between 0.88 and 0.78, or an average value over the range corresponding to 0.83. While DeWitt and Nutter (1988) did not provide the experimental uncertainty of their measurements, the respective values for Toloukian (1967) and Pfefferkorn (1997) were ±8 percent and ±2.5 percent. Based on the experimental data provided by Touloukian (1967), and DeWitt and Nutter (1988), and the measurements of Pfefferkorn (1997), the absorptivity of the sintered silicon nitride workpiece surface at the wavelength of laser irradiation was assumed to be $\alpha_l \approx 0.83$.

Radiation exchange between the workpiece surface and the surroundings was modeled by assuming a small surface in a large enclosure, from which it follows that

$$E(T) - \alpha_{\text{sur}} G_{\text{sur}} \equiv q''_{\text{rad}} = h_{\text{rad}}[T(r_w, \phi, z) - T_{\text{sur}}], \quad (10a)$$

where diffuse and gray surface behavior is assumed ($\epsilon = \alpha_{\text{sur}} \approx 0.83$) and

$$h_{\text{rad}} = \epsilon\sigma[T(r_w, \phi, z)^2 + T^2_{\text{sur}}][T(r_w, \phi, z) + T_{\text{sur}}]. \quad (10b)$$

The implications of the gray surface approximation for the sintered workpiece surface and the accuracy of the assumed radiative property values were investigated by computing the total hemispherical emissivity and absorptivity. The assumed values of the emissivity (ϵ) and absorptivity to irradiation by the surroundings (α_{sur}) fell within the experimental uncertainty of the total hemispherical values calculated from the data of Touloukian (1967) for a sintered silicon nitride surface.

The numerical scheme used to solve Eqs. (2)–(9) is a control-volume method with fully implicit time-marching (Patankar, 1980). The computer algorithm uses a cyclic TDMA solver in the ϕ-direction, and a standard TDMA solver in the r and z-directions. The cyclic TDMA solver enables modeling of periodic problems in which the beginning and the end of the computational domain are equivalent. The computational domain and the corresponding meshes are similar to those used by Rozzi et al. (1995). Control volume sizes in the r-ϕ plane were selected by achieving agreement between two-dimensional computational results and the analytical solution of Gecim and Winer (1984).

Calculations were performed for conditions corresponding to those considered experimentally. However, although the workpiece consisted of YSiAlON sintered silicon nitride, for which temperature-dependent thermophysical property data are not available, the desire to account for temperature-dependent behavior necessitated the use of available properties for an MgO sintered silicon nitride ceramic. The thermal conductivity (Anonymous, 1976) and specific heat (Lange, 1973) were updated for changes in temperature at each iteration within a time-step. The radius and axial length of the computational domain were $r_w = 4.23$ mm and $L_w = 55$ mm, respectively. In the r and ϕ-directions, respectively, 32 and 52 nodes were employed. The spatial extent of control volumes in the z-direction was 0.3 mm for $0 < z < 24$ mm, 1 mm for $24 \leq z < 35$ mm, and 2 mm for $35 \leq z \leq 55$ mm, requiring a total of 103 nodes.

Laser heating was initiated at an axial location of $z_{c,o} = 5.1$ mm for which the volume of unheated material was equal to the volume of a hemispherical end on the actual workpiece. The calculations were marched in time until a distance of 15 mm had been traversed by the laser. The entire temperature field at a given time-step was considered converged if the energy balance was satisfied to less than 10^{-3}. Increasing the grid density or decreasing the convergence criterion resulted in no significant change in the temperature field. The calculations were performed on the IBM RISC/6000 Compute Cluster at the Purdue University Computing Center and required approximately 5.0×10^4 CPU seconds.

Experimental conditions of the study are given in Table 1, with ranges of workpiece rotational speed, laser traverse velocity, and laser beam power and diameter selected to verify the three-dimensional numerical model for representative LAM conditions. The experiments were conducted by (i) focusing the stationary pyrometer on a preselected measurement location using a measurement scale affixed to a silicon nitride alignment workpiece; (ii) securing the test workpiece in the holder and measuring the part out-of-roundness; (iii) initiating workpiece rotation; (iv) moving the laser optics with the shutter closed to the starting position; (v) simultaneously opening the shutter and traversing the laser with constant velocity, V_z, to the final position; and (vi) closing the shutter and moving the laser optics away from the workpiece. Steps (iii) through (vi) were accomplished using a computer program written for the CNC lathe. The laser pyrometer was utilized to measure the temperature history at five locations on the silicon nitride workpiece (Fig. 3) as the laser traversed in the axial direction and the workpiece rotated relative to the pyrometer.

Table 1 Summary of experimental operating conditions ($\Delta P_l \approx \pm 5$ W; $\Delta D_l \approx \pm 0.3$ mm)

Case	ν (rpm)	V_z (mm/min)	P_l (W)	D_l (mm)
1	1000	100	500	3
2	500	100	500	3
3	1500	100	500	3
4	1000	50	500	3
5	1000	200	500	3
6	1000	100	600	3
7	1000	100	400	3
8	1000	100	500	4

Comparison of Experimental and Theoretical Results

Figure 4 illustrates measured and predicted temperature histories at three axial locations (M1, M2, and M3) for nominal operating conditions. At each location, the temperature increases as the laser approaches, and the increase is attributable to workpiece conduction in the axial direction. The temperature reaches a maximum as the laser spot passes the r-ϕ plane of the measurement location, and subsequently decays, largely due to radial and longitudinal conduction of energy from the heated surface. Agreement between the measurements and predictions is excellent with the majority of the data falling within ±5 percent of the predictions, particularly as the laser passes.

Temperature histories at two circumferential locations (M2 and M5) are shown in Fig. 5 for the nominal operating conditions. At the location in closest proximity to the laser, the absorbed energy remains somewhat concentrated near the workpiece surface. However, with rotation away from the laser, energy is transferred by conduction to the inner region of the workpiece. Hence the magnitude of the surface temperature decreases with increasing ϕ, while the temperature history becomes flatter. Although a decline in the peak temperature is revealed by both the predictions and measurements, it is more pronounced for the predictions. The discrepancy may be due to inaccuracies in the high-temperature thermophysical property data of silicon nitride, particularly for the specific heat, which could result in an underprediction of advection in the ϕ-direction. The maximum surface temperature as the workpiece passes beneath the laser is in excess of 1900°C at which, after sufficient exposure, silicon nitride decomposes to silicon liquid and nitrogen gas (McColm, 1983). However, due to circumferential advection and radial conduction effects, the maximum time that the workpiece surface was above 1900°C corresponded to 0.006 seconds which precluded the occurrence of significant damage on the workpiece surface.

Both the measurements and predictions indicate that the rotational speed has only a small influence on the surface temperature history at location M2. However, as shown by Rozzi et al. (1997), the near and far-field surface temperatures decrease and increase, respectively, with increasing ν in an r-ϕ plane corresponding to the laser center. These trends are illustrated in Fig. 6, which provides the circumferential distribution of the surface temperature in an r-ϕ plane when the laser center is at

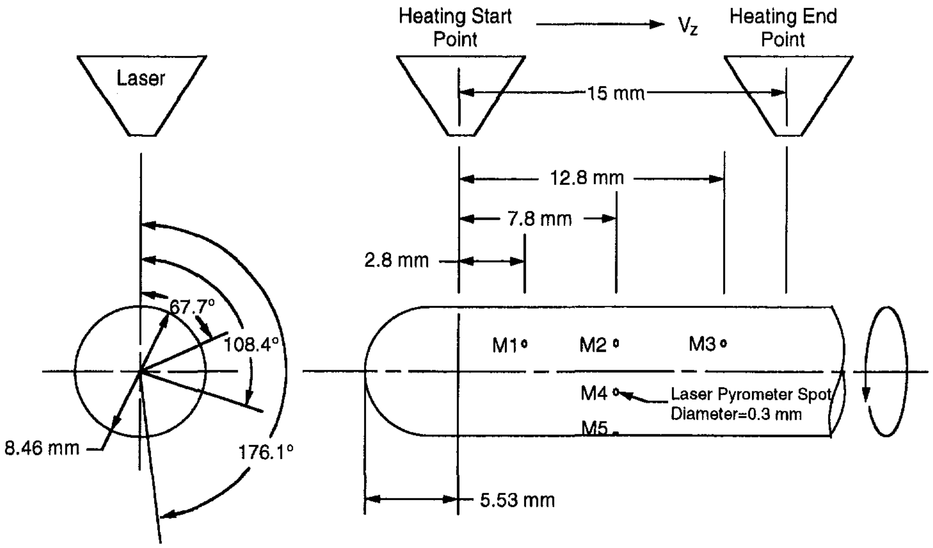

Fig. 3 Temperature measurement locations on the silicon nitride workpiece

z = 7.8 mm. This behavior causes an intersection of surface temperature distributions corresponding to the two values of ν. Existence of such an intersection is revealed both experimentally and numerically and may influence positioning of the cutting tool in a LAM operation. At ϕ locations preceding the intersection, both the magnitude and radial penetration of the workpiece temperatures decrease with increasing ν, requiring a smaller depth of cut. Conversely, at ϕ locations beyond the intersection, the surface temperature and radial temperature distribution are much less dependent on the value of ν, thereby lessening the restriction on depth of cut.

Increasing the laser traverse velocity, V_z, decreases the amount of energy deposited within the workpiece, as illustrated in Fig. 7. Hence, at a fixed axial location, the workpiece surface temperatures decrease as V_z increases. At the lowest laser translation speed (50 mm/min), there is significant disagreement between the predicted and measured temperature histories for $t > 15$ seconds. Recall that the axial extent of gas assist jet interaction was experimentally found to be approximately $z - z_c \approx \pm 5$ mm. Hence at $t \approx 16$ s in the numerical calculation for $V_z = 50$ mm/min, the gas assist jet will have completely passed location M2, thereby removing a significant surface heat removal mechanism, leaving only mixed convection, radiation, and conduction to decrease the temperature in the immediate vicinity of M2 (Rozzi et al., 1997). However, the measured decay of surface temperature with time exceeds that which can be accommodated by either or all of the remaining heat transfer mechanisms, suggesting that the ink measurements may have underestimated the extent of the gas assist jet interaction zone. While the jet heat transfer coefficient decreases with distance from the jet center, the surface temperature at location M2 for $V_z = 50$ mm/min is much larger than that for the nominal operating conditions ($V_z = 100$ mm/min), resulting in significantly higher jet convection heat transfer for $z < z_c$. Nevertheless, for LAM the temperature history in the near-laser region is most critical, and even for the lowest value of V_z, it is well predicted. Differences between peaks in the experimental and numerical surface temperature histories at the highest laser traverse velocity (200 mm/min) may be partially due to the finite time required to accelerate the tool turret from 0 to 200 mm/min, resulting in increased heating early in the laser traverse period.

As expected, decreasing the laser power (Fig. 8) or increasing the laser beam diameter decreases the surface temperature

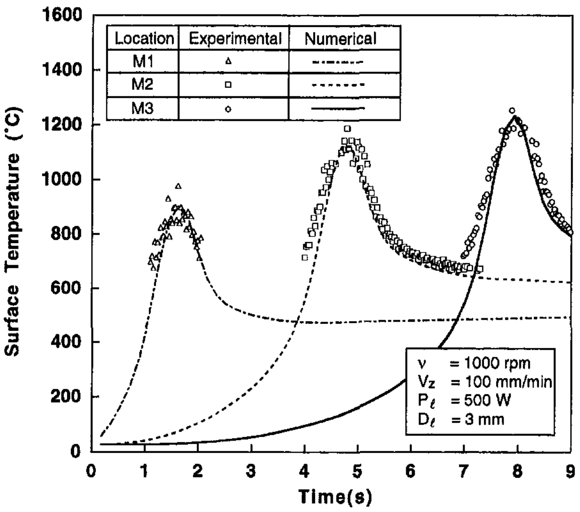

Fig. 4 Experimental and numerical surface temperature histories for nominal operating conditions at selected axial positions (M1, M2, and M3)

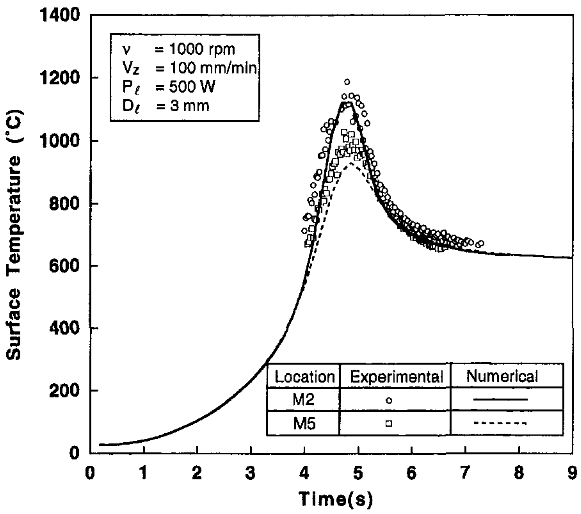

Fig. 5 Experimental and numerical surface temperature histories for nominal operating conditions at selected circumferential positions (M2 and M5)

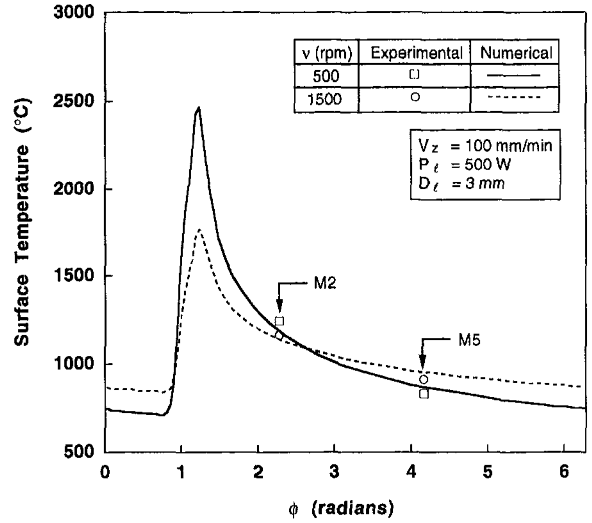

Fig. 6 Effect of workpiece rotational speed on experimental and numerical surface temperatures on the r-ϕ plane corresponding to the laser center at $z_c - z_{c,o} = 7.8$ mm

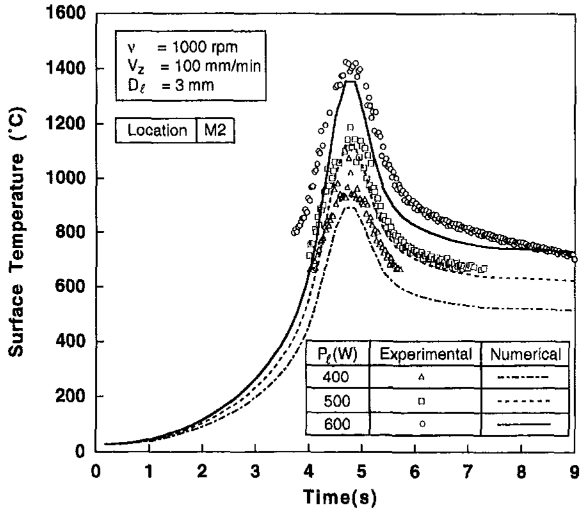

Fig. 8 Effect of laser power on experimental and numerical surface temperature histories at location M2

due to reduced energy deposition or decreased maximum laser heat flux, respectively. Again, the numerical predictions compare well with the experimental temperature histories, particularly as the laser passes the measurement plane.

Conclusions

Experimental data and three-dimensional numerical predictions have been presented for rotating silicon nitride workpieces heated by a translating CO_2 laser. Using a focused laser pyrometer, temperature histories were measured at selected locations on the workpiece surface for ranges of the workpiece rotational and laser translational speeds, as well as the laser beam diameter and power, corresponding to those anticipated in LAM. Numerical predictions were based on (i) use of temperature-dependent thermophysical properties; (ii) a manufacturer-supplied laser heat flux distribution; and (iii) treatment of convective heat transfer due to a laser gas assist jet.

For the laser traverse distance of this study, the experiments and the predictions revealed that near-laser quasi-steady conditions are not achieved, requiring characterization of the process as time-dependent. While significantly influencing near-laser surface temperatures, the effect of rotational speed on the surface temperature distribution decreases with increasing circumferential location from the laser spot. Near-laser temperatures decrease with increasing beam diameter, while energy deposition by the laser and, correspondingly, workpiece surface temperatures, increase with decreasing laser translational speed and increasing laser power. Increased advection in the circumferential direction is manifested by a reduction in the maximum surface temperature but an increase in temperature at locations well removed from the laser.

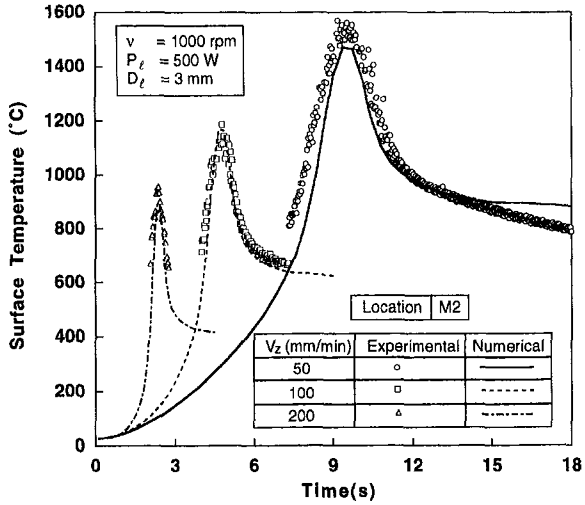

Fig. 7 Effect of laser translation velocity on experimental and numerical surface temperature histories at location M2

Acknowledgments

Support of this work by the National Science Foundation under Grant Number 9400654-CTS is gratefully acknowledged.

References

Anonymous, 1976, "Engineering Property Data on Selected Ceramics, Vol. 1, Nitrides," Battelle, Metals and Ceramics Information Center, Columbus Division, Columbus, Ohio, MCIC-HB-07-Vol. 1.

Davis, M., Kapadia, P., Dowden, J., Steen, W. M., and Courtney, C. H. G., 1986, "Heat Hardening of Metal Surfaces With a Scanning Laser Beam," *Journal of Applied Physics*, Vol. 19, pp. 1981–1997.

DeWitt, D. P., and Nutter, G. D., 1988, *Theory and Practice of Radiation Thermometry*, John Wiley and Sons, New York.

El-Genk, M. S., Huang, L., and Guo, Z., 1992, "Heat Transfer Between a Square Flat Plate and a Perpendicularly Impinging Circular Air Jet," *Proceedings of the 28th National Heat Transfer Conference and Exhibition*, M. B. Pate, and M. K. Jensen, eds., Vol. HTD-Vol. 202, Enhanced Heat Transfer, San Diego, California, pp. 33–38.

Etemad, G. A., 1955, "Free-Convection Heat Transfer From a Rotating Horizontal Cylinder to Ambient Air With Interferometric Study of Flow," ASME JOURNAL OF HEAT TRANSFER, Vol. 77, pp. 1283–1289.

Festa, R., Nenci, F., Manca, O., and Naso, V., 1993, "Thermal Design and Experimental Analysis of Laser and Electron Beam Hardening," ASME *Journal of Engineering for Industry*, Vol. 115, pp. 309–314.

Gecim, B., and Winer, W. O., 1984, "Steady Temperature in a Rotating Cylinder Subject to Surface Heating and Convective Cooling," ASME JOURNAL OF HEAT TRANSFER, Vol. 106, pp. 120–127.

Hect, E., 1987, *Optics*, Addison-Wesley, Reading, MA.

Kitagawa, T., and Maekawa, K., 1990, "Plasma Hot Machining for New Engineering Materials," *Wear*, Vol. 139, pp. 251–267.

Kline, S. J., and McClintock, F. A., 1953, "Describing Uncertainties in Single-Sample Experiments," *Mechanical Engineering*, Vol. 75, pp. 3–6.

Koai, K., Damaschek, R., and Bergmann, H. W., 1993, "Heat Transfer in Laser Hardening of Rotating Cylinders," *Proceedings of the Winter Annual Meeting of the ASME*, Vol. HTD-259, New Orleans, LA, pp. 1–8.

König, W., and Wageman, A., 1991, "Fine Machining of Advanced Ceramics," *Ceramics Today-Tomorrow's Ceramics*, P. Vincenzini, ed., Montecatini Terme, Italy, pp. 2769–2784.

König, W., and Zaboklici, A. K., 1993, "Laser Assisted Hot Machining of Ceramics and Composite Materials," National Institute of Science and Technology, NIST Special Publication 847.

Lange, F. F., 1972, "Dense Si_3N_4 and SiC: Some Critical Properties for Gas Turbine Application," ASME, New York, paper no. 72-GT-56.

McColm, I. J., 1983, *Ceramic Science for Materials Technologists,* Leonard Hill, New York.

Modest, M. F., and Abakians, H., 1986, "Heat Conduction in a Moving Semi-Infinite Solid Subjected to Pulsed Laser Irradiation," ASME JOURNAL OF HEAT TRANSFER, Vol. 108, pp. 597–601.

Patankar, S. V., 1980, *Numerical Heat Transfer and Fluid Flow,* Hemisphere, New York.

Pfefferkorn, F. E., 1997, "Laser Pyrometry: Non-Intrusive Temperature Measurement for Laser Assisted Machining of Ceramics," Master's thesis, Purdue University, West Lafayette, IN.

Richardson, P. D., and Saunders, O. A., 1963, "Studies of Flow and Heat Transfer Associated With a Rotating Disc," *Journal of Mechanical Engineering Science,* Vol. 5, pp. 336–342.

Roy, S., and Modest, M. F., 1993, "CW Laser Machining of Hard Ceramics—I. Effects of Three-Dimensional Conduction, Variable Properties and Various Laser Parameters," *International Journal of Heat and Mass Transfer,* Vol. 36, No. 14, pp. 3515–3528.

Rozzi, J. C., Krane, M. J. M., Incropera, F. P., and Shin, Y. C., 1995, "Numerical Prediction of Three-Dimensional Unsteady Temperatures in a Rotating Cylindrical Workpiece Subjected to Localized Heating by a Translating Laser Source," *Proceedings of the International Mechanical Engineering Congress and Exhibition,* Vol. HTD-Vol. 317-2, San Francisco, CA, pp. 399–411.

Rozzi, J. C., Incropera, F. P., and Shin, Y. C., 1998, "Transient Thermal Response of a Rotating Cylindrical Silicon Nitride Workpiece Subjected to a Translating Laser Heat Source: II-Parametric Effects and Assessment of a Simplified Model," ASME JOURNAL OF HEAT TRANSFER, Vol. 120, pp. 907–915.

Touloukian, Y. S., 1967, *Thermophysical Properties of High Temperature Solid Materials,* Macmillian, Purdue University, West Lafayette, IN.

Uehara, K., and Takeshita, H., 1986, "Cutting Ceramics with a Technique of Hot Machining," *Annals of the CIRP,* Vol. 35, pp. 55–58.

Wallace, R. J., and Copley, S. M., 1989, "Shaping Silicon Nitride With a Carbon Dioxide Laser by Overlapping Multiple Grooves," ASME *Journal of Engineering for Industry,* Vol. 111, pp. 315–321.

Zumbrunnen, D. A., 1991, "Convective Heat and Mass Transfer in the Stagnation Region of a Laminar Planar Jet Impinging on a Moving Surface," ASME JOURNAL OF HEAT TRANSFER, Vol. 113, pp. 563–570.

Transient Thermal Response of a Rotating Cylindrical Silicon Nitride Workpiece Subjected to a Translating Laser Heat Source, Part II: Parametric Effects and Assessment of a Simplified Model

J. C. Rozzi

F. P. Incropera
Fellow ASME

Y. C. Shin

Laser Assisted Materials
Processing Laboratory,
School of Mechanical Engineering,
Purdue University,
1288 Mechanical Engineering Building,
West Lafayette, IN 47907-1288

In a companion paper (Rozzi et al., 1998), experimental validation was provided for a transient three-dimensional numerical model of the process by which a rotating workpiece is heated with a translating laser beam. In this paper, the model is used to elucidate the effect of operating parameters on thermal conditions within the workpiece and to assess the applicability of an approximate analysis which is better suited for on-line process control. From detailed numerical simulations, it was determined that the thickness of a surface thermal layer decreases with increasing workpiece rotational speed and that the influence of axial conduction on the workpiece temperature distribution increases with decreasing laser translational velocity. Temperatures increase throughout the workpiece with increasing laser power, while the influence of increasing beam diameter is confined to decreasing near-surface temperatures. Temperature-dependent thermophysical properties and forced convection heat transfer to the laser gas assist jet were found to significantly influence the maximum temperature beneath the laser spot, while radiation exchange with the surroundings and mixed convection to the ambient air were negligible. The approximate model yielded relations for calculating the radial temperature distribution within an r-ϕ plane corresponding to the center of the laser source, and predictions were in reasonable agreement with results of the numerical simulation, particularly in a near-surface region corresponding to the depth of cut expected for laser-assisted machining.

Introduction

Advanced materials are increasingly being employed in many engineering systems, with ceramics used for components such as mechanical seals and bearings in both internal combustion and gas turbine engines. While such applications are growing, there has not been commensurate improvement in the ability to precisely and rapidly machine these materials. For structural ceramics, finish machining is necessary because of the distortion, contraction, limited formability, and lack of dimensional control achieved in net-shape manufacturing processes (König and Zaboklici, 1993). Grinding and diamond machining currently provide the only processing options (Stinton, 1988; Wobker and Tönshoff, 1993) and represent as much as 60 to 90 percent of the final product cost. Although laser evaporation has been proposed as a material removal process (Chryssolouris et al., 1989), surface microcracking and altered material composition are present in the heat-affected zone. Alternatively, in a hybrid, laser-assisted machining (LAM) process, the material is subjected to intense heating just before it is machined, thereby changing the material deformation behavior from brittle to ductile (without melting or sublimation) and providing for material removal by plastic deformation. Once fully developed, the LAM process is expected to yield higher material removal rates, reduced man and machine hours per part, an increased ability to precisely control part geometry, and substantial cost savings.

Although the effectiveness of LAM has been demonstrated (König and Zaboklici, 1993), the underlying physical mechanisms are not well understood, and a comprehensive thermomechanical model of the heating and material removal processes has yet to be developed and validated through comparisons with experimental results. Development of such a model would facilitate optimization and intelligent control of the LAM process.

Several thermal processes occur simultaneously during LAM and may influence the development of a control scheme. They include (i) laser irradiation and penetration of the absorbed heat flux; (ii) convection heat transfer from the rotating workpiece to the ambient air and to an impinging jet known as the laser gas assist; (iii) emission from the workpiece to the surroundings; (iv) radial, axial, and circumferential conduction through the workpiece; (v) energy advection out of the system with the heated chips; (vi) thermal energy generation associated with plastic work; and (vii) frictional heating and conduction heat transfer at the chip-tool interface.

Conduction heat transfer in a rotating cylinder has been considered by Kawashimo and Yamada (1978), Gecim and Winer

---

Contributed by the Heat Transfer Division for publication in the JOURNAL OF HEAT TRANSFER. Manuscript received by the Heat Transfer Division, Mar. 18, 1997; revision received, Dec. 19, 1997. Keywords: High-Temperature Phenomena, Laser Processing, and Materials Processing and Manufacturing Process. Associate Technical Editor: A. Lavine.

(1984), and Yuen (1984, 1994), who obtained analytical or semi-analytical solutions for two-dimensional steady-state temperature fields due to various surface heat flux distributions, with application to cold and hot rolling of strip steel. Koai et al. (1993) used the finite element method to determine the transient temperature field in a two-dimensional rotating cylinder subjected to laser hardening. However, in these studies, the heat equation did not include z-advection or z-conduction terms, which along with energy storage effects, can significantly influence the transient temperature distribution for a moving heat source.

An initial assessment of transient three-dimensional thermal conditions within a finite rotating cylinder subjected to a translating square laser source has been made (Rozzi et al., 1995). The nondimensional calculations and scaling analysis revealed that (i) with increasing workpiece rotational speed or laser translational velocity, there is a greater concentration of thermal energy near the surface of the workpiece, a reduction of bulk conduction into the workpiece, and a decrease in the maximum temperature on the workpiece surface; (ii) conduction in the axial direction has a significant effect on the quasi-steady temperature distribution, particularly for small values of the translational velocity; and (iii) surface mixed convection and radiation effects are negligible.

Using a three-dimensional numerical model described by Rozzi et al. (1998), the present study seeks to clarify the role of physical phenomena associated with LAM and, in particular, to determine the influence of operating conditions on the temperature distribution within the heated workpiece. An additional objective is to develop a simpler, more approximate model of the laser heating process which may be used to calculate the radial temperature distribution at various circumferential locations within an r-ϕ plane corresponding to the center of the laser source. Such a model would be useful for implementing on-line control of the LAM process.

Approximate Analysis

To formulate on-line control schemes for adjusting parameters such as workpiece rotational speed, cutting tool and laser feed rate, depth of cut, and laser diameter or power, knowledge of their effect on the near-surface temperature distribution at the cutting tool location is required. Although a detailed numerical simulation may be used to obtain the time-dependent temperature distribution throughout the heated workpiece, related computational requirements do not facilitate application to on-line process control. Furthermore, exact solutions of the governing partial differential equations and boundary conditions which approximate near-laser conditions may not apply at the cutting location and are in the form of Fourier series for which required summations could be excessive. To facilitate process control of LAM, an approximate thermal analysis has been used to obtain a set of algebraic equations for predicting the near-laser ($\phi - \phi_c \leq 3\pi/4$) radial transient temperature distribution in an r-ϕ plane corresponding to the laser center.

The approximate analysis is based on subdividing the workpiece into a thin outer region, within which radial and circumferential temperature gradients are significant near the laser spot, and an inner (core) region for which temperature gradients are negligible (Fig. 1). Such a delineation is consistent with results obtained from a three-dimensional numerical simulation of the heating process (Rozzi et al., 1998). As verified by a scaling analysis, within the outer region energy transfer in proximity to the laser spot is dominated by radial conduction and circumferential advection, while axial and circumferential conduction, as well as changes in thermal energy storage, are small. Although a z-direction temperature gradient exists within the inner region, its magnitude can be reasonably approximated as constant, allowing characterization of the inner region temperature exclusively in terms of its time variation. As a first approximation, it is also assumed that heating of the inner region is confined to $z < (z_c + D_l/2)$, in which case axial conduction from the heated core, $z < (z_c + D_l/2)$, to the unheated core, $z > (z_c + D_l/2)$, is neglected.

Inner Region Analysis. The inner region model is based on assuming that all of the absorbed laser radiation contributes to energy storage within that portion of the rotating workpiece which has been traversed by the laser (Fig. 2). The translating laser of diameter D_l is assumed to provide circumferentially

Nomenclature

A_c = workpiece cross-sectional area, m^2
A_1, A_2 = constants used for inner region model
B_1 = constant used for outer region model
c_p = specific heat at constant pressure, J/kg K
D = diameter, m
k = thermal conductivity, W/m K
L_w = workpiece length, m
P_l = laser power, W
Pe$_x$ = pseudo-Peclet number in x-direction
Pe$_z$ = pseudo-Peclet number in z-direction
Pe$_\phi$ = pseudo-Peclet number in ϕ-direction
q'' = absorbed laser heat flux, W/m^2
r = radial coordinate, m
r_l = radius of the laser beam, m
r_w = workpiece radius, m
t = time, s
$\hat{t}$ = dimensionless time, $V_z t/L_o$
T = temperature, K
$\forall$ = volume, m^3
V_x = x-direction velocity, m/s
V_z = laser traverse velocity, m/s
x = rectangular coordinate, m
$x' = x - D_l$, m
$\tilde{x}$ = dimensionless coordinate, x/D_l
y = rectangular coordinate, m
$\tilde{y}$ = dimensionless coordinate, y/δ_1
z = axial coordinate, m
z_c = axial location of the laser center, mm
$z_{c,o}$ = initial axial location of the laser center, mm

Greek Symbols

α = thermal diffusivity, m^2/s; absorptivity of the workpiece surface
δ = thickness of outer region, m
δ_1, δ_2 = thermal penetration thicknesses used in outer region model, mm
ϵ = emissivity of workpiece surface
ω = workpiece rotational speed, rad/s
ϕ = circumferential coordinate, rad
ϕ_c = circumferential location of the laser center, rad
$\vartheta = \theta_o(x, y, t) - \theta_i(t)$, K
$\tilde{\vartheta}$ = dimensionless temperature, $\vartheta/(q''_{l,\mathrm{abs},a} D_l/k)$
ν = workpiece rotational speed, rpm
ρ = density, kg/m^3
$\theta = T(x, y, t) - T_\infty$, K
$\hat{\theta}$ = dimensionless temperature, $\theta/(P_{l,\mathrm{abs}}/\rho c_p V_z A_c)$

Subscripts

a = average
abs = absorbed
∞ = ambient
c = source geometric center
i = inner region
l = laser
λ = spectral
m = maximum
o = initial ($t = 0$) or outer region
w = workpiece
r, ϕ, z = cylindrical coordinate directions
x, y = rectangular coordinate directions

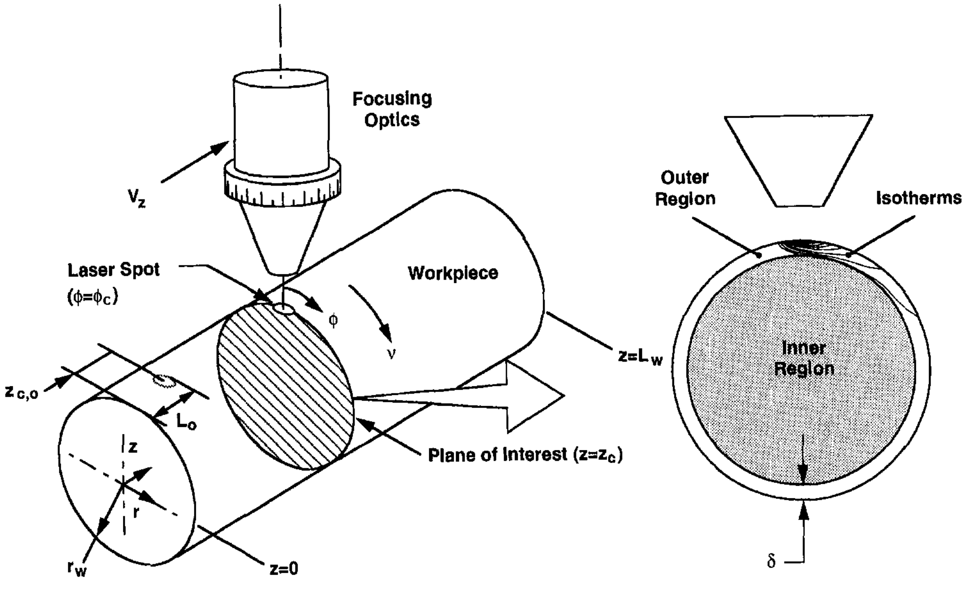

Fig. 1 Coordinate system for rotating workpiece with translating laser and r-ϕ plane detailing inner and outer regions of thermal energy storage

uniform heating, and the control volume about the heated material expands with the moving laser. As previously indicated, the heated material is assumed to be at a uniform, but time-varying, temperature, and conduction to the unheated portion of the workpiece, which is at the ambient temperature T_∞, is neglected.

Variation of the inner region temperature with time, $T_i(t)$, may be obtained by performing an energy balance on the control volume. The thermophysical properties are assumed constant, and surface heat losses are neglected. Hence, all of the laser heating is assumed to be manifested by thermal energy storage within the region enclosed by the control volume, and the energy balance yields

$$P_{l,\text{abs}} = \rho c_p \frac{d}{dt}[\forall(T_i - T_\infty)] \tag{1}$$

where $P_{l,\text{abs}}$ is the rate at which laser radiation is absorbed and $\forall = A_c(L_o + V_z t)$ is the volume of the heated region. The initial axial length of the control volume, $L_o = z_{c,o} + D_l/2$, corresponds to the distance from the end of the workpiece to the end of the band of laser heating. It follows that

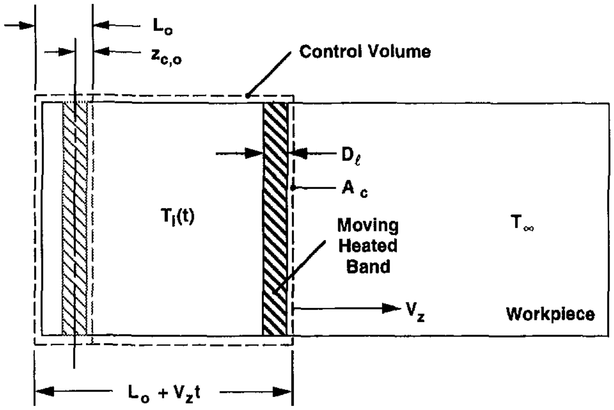

Fig. 2 Control volume used for the inner region model

$$P_{l,\text{abs}} - \rho c_p V_z A_c (T_i - T_\infty) = \rho c_p A_c (V_z t + L_o) \frac{dT_i}{dt} \tag{2}$$

or, introducing the reduced temperature, $\theta_i = T_i - T_\infty$, as well as the dimensionless temperature, $\hat{\theta}_i = \theta_i/(P_{l,\text{abs}}/\rho c_p V_z A_c)$, and time, $\hat{t} = V_z t/L_o$, Eq. (2) may be expressed as

$$(\hat{t} + 1)\frac{d\hat{\theta}_i}{d\hat{t}} = 1 - \hat{\theta}_i. \tag{3}$$

With the initial condition, $\hat{\theta}_i(0) = 0$, the solution to Eq. (3) is

$$\hat{\theta}_i(\hat{t}) = \frac{\hat{t}}{(\hat{t} + 1)}. \tag{4}$$

Equation (4) may be used to characterize the transient temperature history of the inner region within an r-ϕ plane that cuts through the center of the laser source (Fig. 1). However, because the analysis neglects energy absorbed by the outer region and surface heat losses, it will overestimate the inner region temperature and underestimate the time required to achieve a particular temperature. Hence, two adjustable constants, A_1 and A_2, are introduced to compensate for these effects, and Eq. (4) is expressed as

$$\hat{\theta}_i(\hat{t}) = \frac{A_1 \hat{t}}{(\hat{t} + A_2)}. \tag{5}$$

Values of A_1 and A_2, which are each of order unity, will be determined by comparing the results of the simplified model with predictions based on the more detailed, three-dimensional numerical model.

Outer Region Analysis. Although the process of interest corresponds to surface heating of a rotating workpiece, its influence on near-surface conditions for an r-ϕ plane encompassed by the laser spot may be approximated by the steady two-dimensional system shown in Fig. 3. Relative to a stationary coordinate system, absorption of the laser radiation is assumed to induce development of a surface thermal layer (the outer region), within which temperatures exceed that of the inner region. For conditions in close proximity to the laser spot, ($\phi - \phi_c \leq 3\pi/4$), and for small layer thicknesses ($\delta/r_w \ll 1$), the

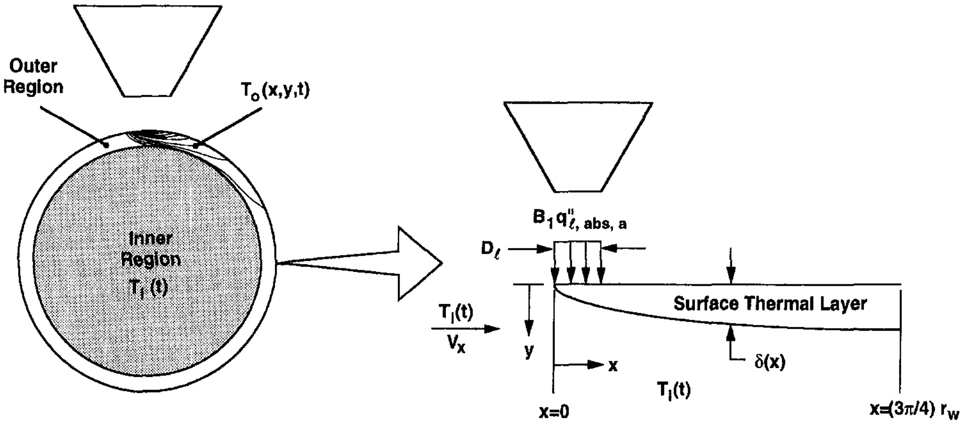

Fig. 3 Geometric approximation used for the outer region model

outer region can be represented in terms of Cartesian coordinates and characterized by a velocity of $V_x = r_w\omega$. Assuming complete dissipation of the thermal layer to occur within one revolution, the temperature at its leading edge ($x = 0$) corresponds to that of the inner region.

To obtain an appropriate form of the laser heat flux for the foregoing model, attention must be paid to the fact that any location on the rotating workpiece will pass through the laser beam many times as it traverses the surface. Hence, if $q''_{l,\mathrm{abs},a}$ represents the average absorbed flux of the laser beam, an adjustable correction factor $B_1 > 1$ must be applied to account for the actual periodicity of the heating process. Its value will be determined by comparing results of the simplified and three-dimensional models.

Thermal conditions may be represented by a reduced temperature of the form $\vartheta(x, y, t) = T_o(x, y, t) - T_i(t) = \theta_o(x, y, t) - \theta_i(t)$, where the time dependence for the outer region, $T_o(x, y, t)$, follows from that of the inner region, $T_i(t)$. From the approximate model depicted in Fig. 3, the energy equation for the outer region may be expressed as

$$\frac{\partial^2\vartheta}{\partial y^2} = \frac{V_x}{\alpha}\frac{\partial\vartheta}{\partial x}. \tag{6}$$

The boundary conditions are of the form

$$\vartheta(0, y, t) = 0 \tag{7a}$$

$$\left.\frac{\partial\vartheta}{\partial y}\right|_{y=0,0\le x\le D_l} = -\frac{B_1 q''_{l,\mathrm{abs},a}}{k}, \quad \left.\frac{\partial\vartheta}{\partial y}\right|_{y=0,x>D_l} = 0 \tag{7b, c}$$

$$\vartheta(x, \delta, t) = 0 \tag{7d}$$

where heat loss from the surface to the surroundings is neglected based on the near-laser scaling analysis of Rozzi et al. (1995). This assumption is reasonable for small to moderate process times ($t \le 3$ min) but breaks down with increasing time. The solution of Eqs. (6) and (7) may be obtained by superposition, where

$$\vartheta(x, y, t) = \vartheta_1(x, y, t) + \vartheta_2(x', y, t), \tag{8}$$

and $x' = x - D_l$. Substituting Eq. (8) into the governing differential equation and boundary conditions, the resulting equations are of the form

$$\frac{\partial^2\vartheta_1}{\partial y^2} = \frac{V_x}{\alpha}\frac{\partial\vartheta_1}{\partial x} \tag{9}$$

$$\vartheta_1(0, y, t) = 0 \tag{10a}$$

$$\left.\frac{\partial\vartheta_1}{\partial y}\right|_{x,y=0} = -\frac{B_1 q''_{l,\mathrm{abs},a}}{k} \tag{10b}$$

$$\vartheta_1(x, \delta_1, t) = 0 \tag{10c}$$

and

$$\frac{\partial^2\vartheta_2}{\partial y^2} = \frac{V_x}{\alpha}\frac{\partial\vartheta_2}{\partial x'} \tag{11}$$

$$\vartheta_2(0, y, t) = 0 \tag{12a}$$

$$\left.\frac{\partial\vartheta_2}{\partial y}\right|_{x',y=0} = \frac{B_1 q''_{l,\mathrm{abs},a}}{k} \tag{12b}$$

$$\vartheta_2(x', \delta_2, t) = 0. \tag{12c}$$

Solutions to Eqs. (9), (10) and (11), (12) may be substituted into Eq. (8) to obtain the temperature distribution in close proximity to the laser source.

To reduce the response time for on-line control, integral analyses are used to calculate the thermal layer thicknesses, δ_1 and δ_2, as a function of x. For $\vartheta_1(x, y, t)$, a third-order polynomial is used to approximate the temperature profile, and the following boundary conditions are used to determine the corresponding coefficients:

$$\vartheta_1(x, \delta_1(x), t) = 0 \tag{13a}$$

$$\left.\frac{\partial\vartheta_1}{\partial y}\right|_{x,y=0} = -\frac{B_1 q''_{l,\mathrm{abs},a}}{k}, \quad \left.\frac{\partial\vartheta_1}{\partial y}\right|_{x,y=\delta_1(x)} = 0,$$

$$\left.\frac{\partial^2\vartheta_1}{\partial y^2}\right|_{x,y=\delta_1(x)} = 0. \tag{13b, c, d}$$

The analysis yields a temperature profile of the form

$$\frac{\vartheta_1(x, y, t)}{\left(\dfrac{q''_{l,\mathrm{abs},a}D_l}{k}\right)} = B_1\left(\frac{x}{D_l}\right)\left(\frac{12}{\mathrm{Pe}_x}\right)^{1/2}\left[\frac{1}{3} - \left(\frac{y}{\delta_1(x)}\right) + \left(\frac{y}{\delta_1(x)}\right)^2 - \frac{1}{3}\left(\frac{y}{\delta_1(x)}\right)^3\right], \tag{14}$$

where

$$\frac{\delta_1(x)}{x} = \left(\frac{12}{\mathrm{Pe}_x}\right)^{1/2}. \tag{15}$$

Similarly, representing $\vartheta_2(x, y, t)$, by a third-order polynomial with boundary conditions

$$\vartheta_2(x', \delta_2(x'), t) = 0 \tag{16a}$$

$$\left.\frac{\partial \vartheta_2}{\partial y}\right|_{x', y=0} = \frac{B_1 q''_{l,\mathrm{abs},a}}{k}, \quad \left.\frac{\partial \vartheta_2}{\partial y}\right|_{x', y=\delta_2(x')} = 0,$$

$$\left.\frac{\partial^2 \vartheta_2}{\partial y^2}\right|_{x', y=\delta_2(x')} = 0 \tag{16b, c, d}$$

the integral analysis gives

$$\frac{\vartheta_2(x', y, t)}{\left(\dfrac{q''_{l,\mathrm{abs},a} D_l}{k}\right)} = -B_1\left(\frac{x'}{D_l}\right)\left(\frac{12}{\mathrm{Pe}_{x'}}\right)^{1/2}\left[\frac{1}{3} - \left(\frac{y}{\delta_2(x')}\right) + \left(\frac{y}{\delta_2(x')}\right)^2 - \frac{1}{3}\left(\frac{y}{\delta_2(x')}\right)^3\right], \tag{17}$$

where

$$\frac{\delta_2(x')}{x'} = \frac{\delta_2(x - D_l)}{x - D_l} = \left(\frac{12}{\mathrm{Pe}_{x-D_l}}\right)^{1/2}. \tag{18}$$

Substituting Eqs. (14), (15), (17), and (18) into Eq. (8) and introducing the dimensionless temperature, $\tilde{\vartheta} = \vartheta/(q''_{l,\mathrm{abs},a} D_l/k)$, distances, $\tilde{x} = x/D_l$ and $\tilde{y} = y/\delta_1$, and time, $\tilde{t} = V_z t/L_o$, the radial temperature distribution within an r-ϕ plane through the center of the laser source for $0 \le \tilde{x} \le (3\pi/4)(r_w/D_l)$ and $0 \le \tilde{y} \le 1$ may be expressed as

$$\tilde{\vartheta}(0 \le \tilde{x} \le 1, 0 \le \tilde{y} \le 1, \tilde{t}) = B_1 \tilde{x}\left(\frac{12}{\mathrm{Pe}_x}\right)^{1/2}\left[\frac{1}{3} - \tilde{y} + \tilde{y}^2 - \frac{\tilde{y}^3}{3}\right] \tag{19}$$

$$\tilde{\vartheta}\left(1 < \tilde{x} \le \left(\frac{\pi}{2}\right)\frac{r_w}{D_l}, 0 \le \tilde{y} \le \frac{\delta_2(x')}{\delta_1(x)}, \tilde{t}\right) = 2B_1\tilde{x}\left(\frac{3}{\mathrm{Pe}_x}\right)^{1/2}\left\{\begin{array}{l} \dfrac{1}{3}\left[1 - \left[1 - \left(\dfrac{1}{\tilde{x}}\right)\right]^{1/2}\right] \\ + \tilde{y}^2\left[1 - \left(\dfrac{(1/\tilde{x})}{1 - (1/\tilde{x})}\right)^{1/2}\right] \\ - \dfrac{\tilde{y}^3}{3}\left(\dfrac{1}{1 - (1/\tilde{x})}\right) \end{array}\right\} \tag{20}$$

$$\tilde{\vartheta}\left(1 < \tilde{x} \le \left(\frac{\pi}{2}\right)\frac{r_w}{D_l}, \frac{\delta_2(x')}{\delta_1(x)} < \tilde{y} \le 1, \tilde{t}\right) = B_1\tilde{x}\left(\frac{12}{\mathrm{Pe}_x}\right)^{1/2}\left[\frac{1}{3} - \tilde{y} + \tilde{y}^2 - \frac{\tilde{y}^3}{3}\right]. \tag{21}$$

The inner region corresponds to $0 \le \tilde{x} \le (3\pi/4)(r_w/D_l)$ and $1 < \tilde{y} \le r_w/\delta_1$, whose temperature is given by Eq. (5). The constant B_1 will be determined by using the approximate model to match predictions for the surface temperature distribution downstream of and in close proximity to the laser. In this region Eq. (20) reduces to

$$\tilde{\vartheta}\left(1 < \tilde{x} \le \left(\frac{\pi}{2}\right)\frac{r_w}{D_l}, \tilde{y} = 0, \tilde{t}\right) = 2B_1\tilde{x}\left(\frac{1}{3\mathrm{Pe}_x}\right)^{1/2}\left\{1 - \left[1 - \left(\frac{1}{\tilde{x}}\right)\right]^{1/2}\right\}. \tag{22}$$

Equations (5) and (19) through (22) completely characterize the near-laser temperature distribution in an r-ϕ plane that cuts through the center of the laser source and can be used to approximate the radial temperature distribution at a prospective cutting tool location.

Numerical Results

The conditions chosen for the numerical computations correspond to those in Rozzi et al. (1998). The values of ν and V_z represent a range of workpiece rotational speeds and laser translational velocities characteristic of actual machining conditions. The numerical results are presented in the form of r-ϕ and r-z temperature distributions in planes that cut through the center of the laser.

Temperature contours corresponding to three laser axial positions are shown in Fig. 4 for the nominal operating conditions ($\nu = 1000$ rpm, $V_z = 100$ mm/min, $P_l = 500$ W, $D_l = 3$ mm). Quasi-steady conditions are not achieved, as evidenced by the increase in the maximum surface temperature with increasing $z_c - z_{c,o}$. However, temperature gradients in the r-ϕ plane are nearly identical at all axial positions ($z_c - z_{c,o}$), suggesting self-similarity of the r-ϕ temperature distributions. Also, significant heat removal occurs after the laser has completely passed a particular z-location as evidenced by the near-surface r-z temperature contours.

Figure 5 indicates the influence of workpiece rotational speed, ν, on the temperature field at the end of the heated length ($z_c - z_{c,o} = 15$ mm). With V_z held constant, the radiant energy input is equivalent for each value of ν. However, as ν increases, circumferential advection becomes increasingly more important relative to radial conduction and the input energy is increasingly concentrated near the surface. Moreover, circumferential temperature gradients, as well as the maximum workpiece temperature, are reduced. Although the thickness of the surface layer in which radial temperature gradients are concentrated decreases, the inner region temperature distribution is not significantly influenced by increasing ν. In addition, axial temperature gradients in regions removed from the laser spot (the far-field) are relatively unaffected by increasing ν. With decreasing ν, however, there is a progressively larger concentration of input energy in the near-laser region and large temperature gradients in both the r and z-directions. Hence, in the near-field, energy transport is strongly influenced by conduction. Because V_z is a constant, the frequency with which the r-ϕ plane of interest is heated as it passes through the laser spot increases with increasing ν. The net effect is a small increase in surface temperature at circumferential locations far from the laser source.

Figure 6 demonstrates the influence of V_z on the workpiece temperature distribution. With ν fixed, temperature gradients in the r-ϕ plane are relatively unchanged. However, with increasing V_z, axial advection and conduction become comparable, causing a reduction in the maximum surface temperature, as well as forward propagation of the temperature field. This effect is manifested most prominently for the r-z plane.

In the approximate analysis, the inner region temperature was found to be directly proportional to the laser power. This result is confirmed by the numerical predictions. In the r-ϕ plane temperatures increase uniformly with increasing laser power, while near-laser temperature gradients in the r-z plane increase

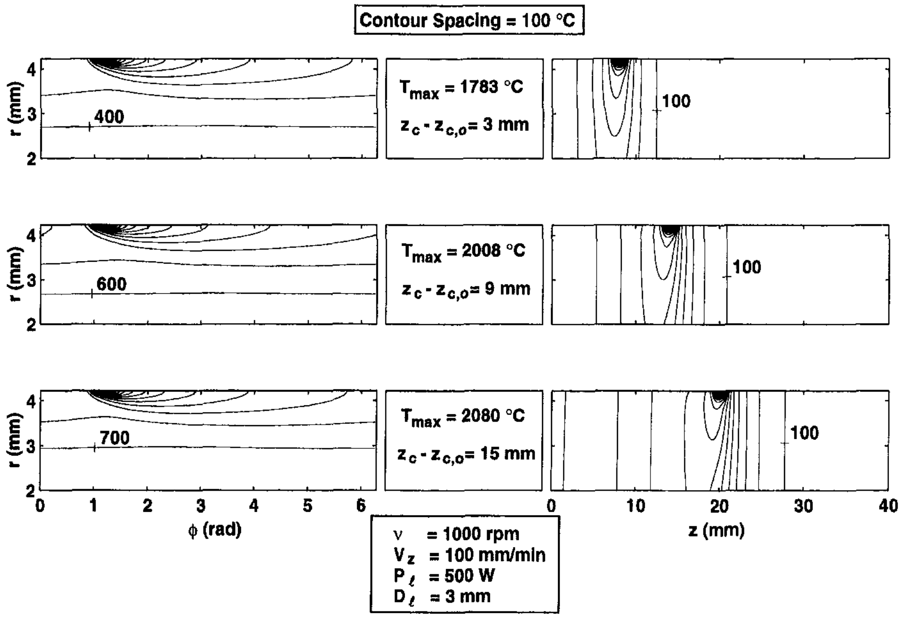

Fig. 4 Predicted temperature contours at selected laser axial positions for the nominal operating conditions

substantially. By increasing the laser beam diameter for a fixed laser power, the maximum laser heat flux decreases, with a corresponding reduction in the maximum temperature. Changes in the r-ϕ temperature distribution are confined to the outer region.

The influence of thermophysical properties and surface thermal conditions on the maximum temperature within the laser spot was also computed, and the results are illustrated in Fig. 7. Constant thermophysical properties were computed using a weighted average of the temperature-dependent relations for thermal conductivity and specific heat, resulting in values of $k_a = 20$ W/m K and $c_{p,a} = 1129$ J/kg K. Because $c_{p,a}$ is smaller than the actual high temperature value (~1500 J/kg K), the amount of thermal energy the material is able to store in the near-laser region is significantly reduced, causing an increase in the maximum workpiece surface temperature. Conversely, because k_a exceeds the high temperature value (~15 W/m K), more energy is transferred into the workpiece by conduction, with a corresponding decrease in the maximum surface temperature. Without mixed convection to the ambient, the maximum surface temperature undergoes a nondiscernible change, indicating that the effect is negligible relative to other near-laser heat transfer mechanisms. Similarly, excluding emission results in only a small change in the maximum temperature. However, by neglecting convection heat transfer to the gas assist jet for which heat transfer coefficients exceed 2000 W/m^2 K, there is a significant increase in the maximum surface temperature.

Results of the Approximate Analysis

The approximate model was developed to obtain simplified relations for on-line control of the laser-assisted machining process. However, the relations depend upon the coefficients A_1, A_2, and B_1, values of which will be inferred from a comparison with the numerical predictions.

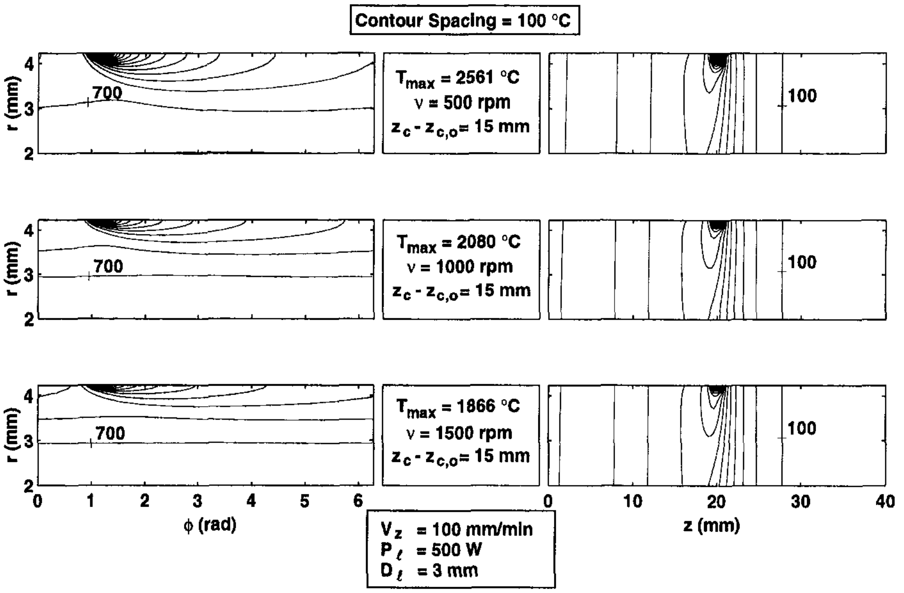

Fig. 5 Predicted temperature contours at z_c–$z_{c,o}$ = 15 mm for various workpiece rotational speeds

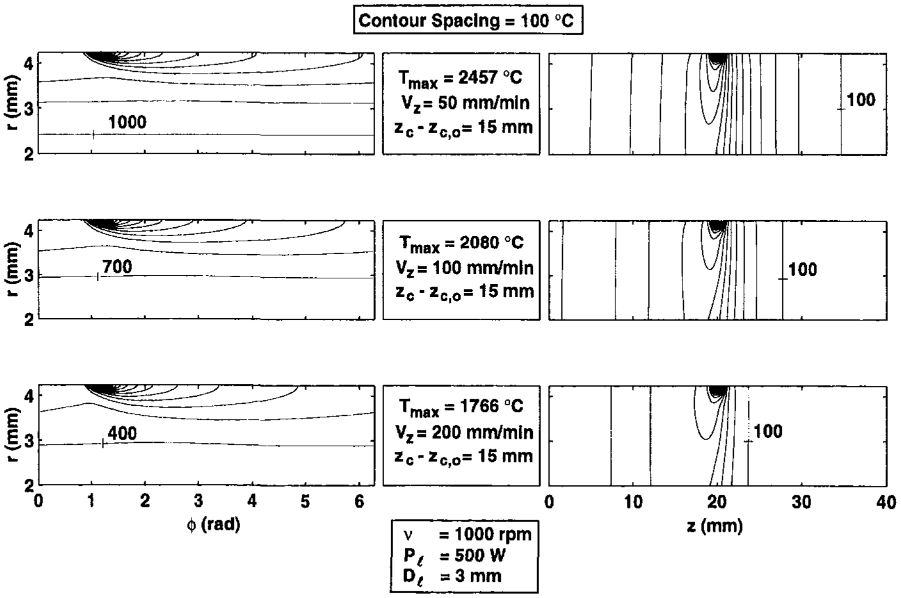

Fig. 6 Predicted temperature contours at $z_c-z_{c,o}$ = 15 mm for various laser translation velocities

Figure 8 illustrates the numerical data used to obtain the values of A_1 and A_2. For axial traverse distances, $z_c-z_{c,o}$, of 0, 3, 6, 9, 12, and 15 mm, which correspond to dimensionless times, $\hat{t}$, of 0, 0.455, 0.909, 1.364, 1.818, and 2.273, respectively, numerical predictions of the inner region temperatures were obtained for the nominal operating conditions. Each temperature represents an average over a region of the r-ϕ plane cutting through the center of the laser source of radius $0 < r \leq (r_w - \delta_1)$. Excellent agreement is obtained with predictions based on the approximate model for values of A_1 and A_2 equal to 0.64 and 0.5, respectively. The coefficient $B_1 = 2$ was found by comparing predictions based on Eq. (22) with numerical predictions of the surface temperature at circumferential locations corresponding to 40.6, 67.7, and 94.8 deg from the center of the laser source and dimensionless times of 0.455, 0.909, 1.364, 1.818, and 2.273 for the nominal operating conditions. The constants A_1, A_2, and B_1 are valid over the ranges of conditions investigated in this study ($\nu = 500$–1500 rpm, $V_z = 50$–200 mm/min, $P_l = 400$–600 W, $D_l = 3$–4 mm, $r_w = 4.23$–6 mm). Constant thermophysical properties were used in the approximate analysis and were calculated by averaging over the temperature range of interest and corresponded to values of $k_a = 20$ W/m K and $c_{p,a} = 1129$ J/kg K.

In Fig. 9, radial temperature distributions computed from the approximate model are compared to the corresponding predictions from the detailed three-dimensional transient numerical model for the nominal operating conditions at selected circumferential positions in the r-ϕ plane passing through the laser center at a particular z-location. With increasing $\phi-\phi_c$, both models predict a reduction in temperature at the workpiece surface and within a portion of the outer region. Both models also predict a crossover in the temperature distributions, beyond which temperatures at a particular radial location increase with increasing $\phi-\phi_c$. However, the three radial temperature distributions merge within a millimeter of the surface to an inner region temperature which is predicted to be uniform or to decrease with decreasing r for the approximate and numerical models, respectively. Reasonable agreement is obtained between the two models in much of the outer region for $\phi-\phi_c \gtrsim$

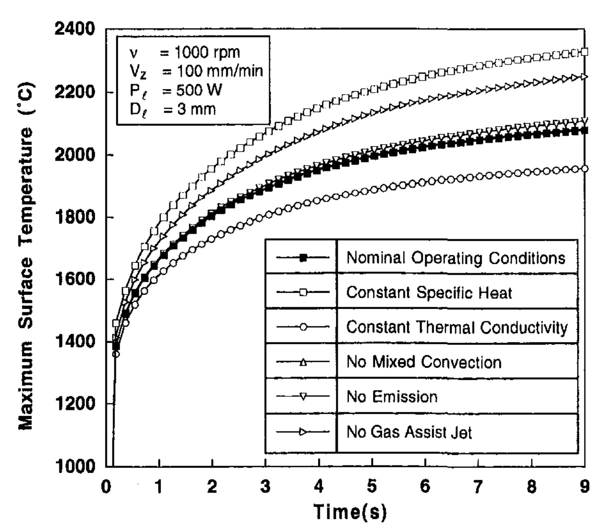

Fig. 7 Effect of surface heat exchange and thermophysical properties on the maximum workpiece surface temperature

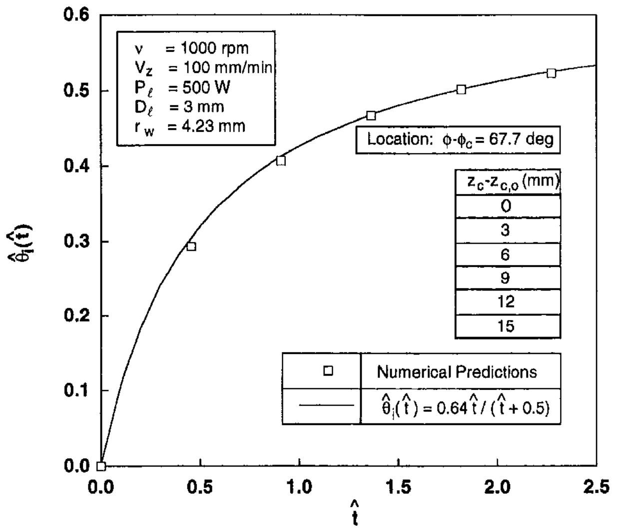

Fig. 8 Comparison of numerical predictions for nominal operating conditions used to obtain inner region model coefficients

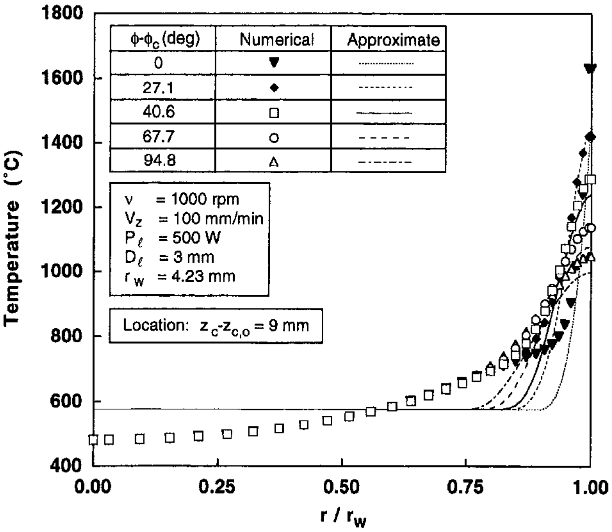

Fig. 9 Comparison of radial temperature distributions predicted numerically and by the approximate model for selected circumferential locations, $z_c - z_{c,o} = 9$ mm and the nominal conditions

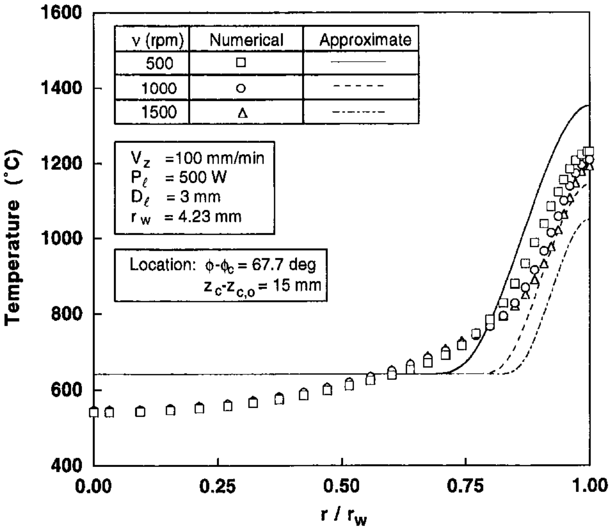

Fig. 11 Comparison of radial temperature distributions predicted numerically and by the approximate model for selected workpiece rotational speeds at $z_c - z_{c,o} = 15$ mm and $\phi - \phi_c = 67.7$ deg

27.1 deg, although consistent with the assumption of a uniform inner region temperature, the approximate model predicts a much sharper transition between the inner and outer regions. However, the uniform temperature predicted by the approximate model for the inner region provides a good measure of the average temperature associated with the radial variation predicted numerically. Poor and reasonable agreement is obtained at and beneath the workpiece surface, respectively, between the two models beneath the laser center location ($\phi - \phi_c = 0$ deg). Note that both models predict an increase in the outer region thickness with increasing $\phi - \phi_c$.

The ability of the approximate model to predict axial variations in the radial temperature distribution is shown in Fig. 10 along with predictions from the detailed numerical model. As illustrated by the variation of the inner region temperature with time (Fig. 8) and confirmed by the results of Fig. 10, temperatures in the r-ϕ plane corresponding to the laser center increase with increasing laser traverse distance (increasing heating time), but in an asymptotic manner leading to quasi-steady conditions. Also, the increase in the inner and outer region temperatures with time is nearly equivalent.

As shown in Fig. 5, surface temperatures in the r-ϕ plane at locations far from and close to the laser source increase and decrease, respectively, with increasing ν. However, as shown in Fig. 11, the approximate model cannot capture this complex phenomenon and significantly overpredicts the influence of ν on the radial temperature distribution. As indicated by the detailed numerical results (Fig. 5), the r-ϕ temperature distribution is not significantly influenced by changes in ν in regions removed from the laser source.

With decreasing laser traverse velocity, the time required for the laser to travel a prescribed distance increases, thereby increasing the influence of z-direction conduction on the temperature distribution. As heating effects propagate in the z-direction due to increased conduction, the volume of the heated workpiece increases (Fig. 6). However, because the inner region energy balance accounts only for control volume growth due to the traversing laser, the inner region temperature is overpredicted by the approximate model for low traverse velocities,

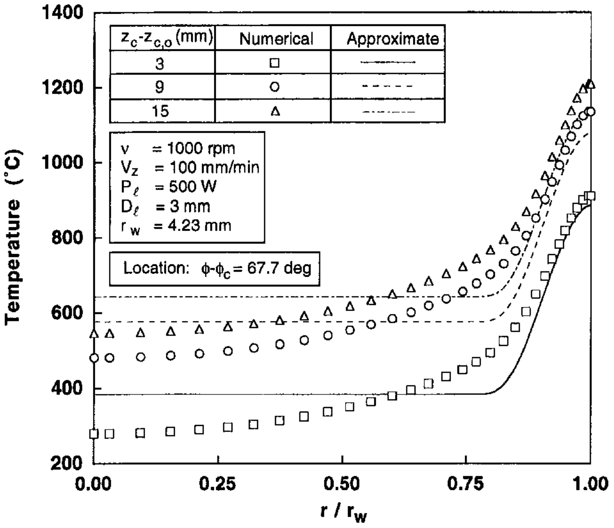

Fig. 10 Comparison of radial temperature distributions predicted numerically and by the approximate model for selected axial locations, $\phi - \phi_c = 67.7$ deg and the nominal conditions

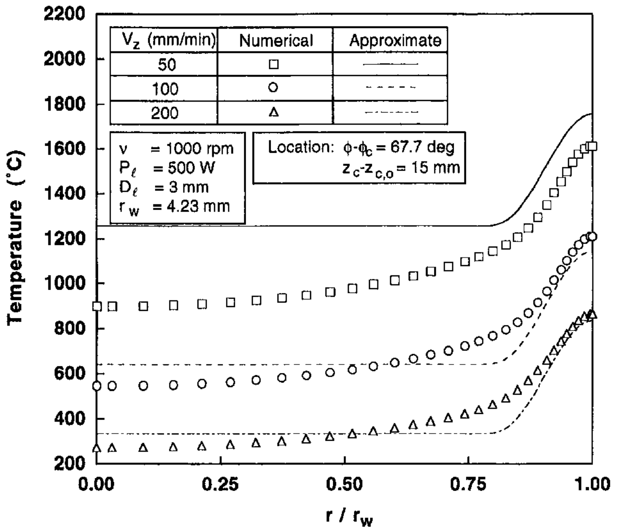

Fig. 12 Comparison of radial temperature distributions predicted numerically and by the approximate model for selected laser traverse velocities at $z_c - z_{c,o} = 15$ mm and $\phi - \phi_c = 67.7$ deg

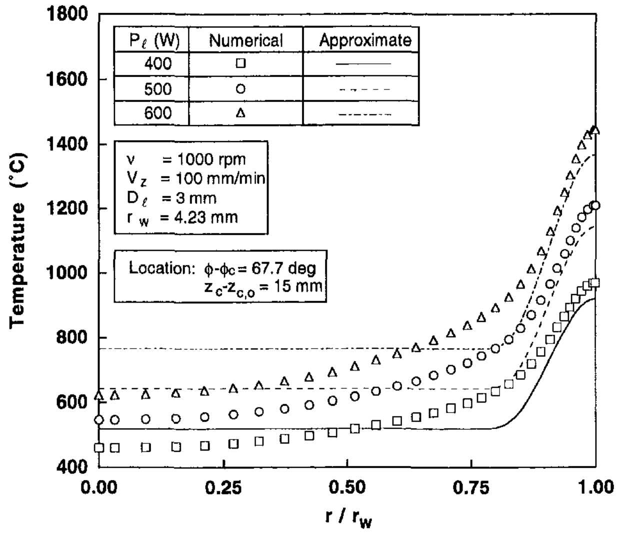

Fig. 13 Comparison of radial temperature distributions predicted numerically and by the approximate model for selected laser powers at $z_c - z_{c,o} = 15$ mm and $\phi - \phi_c = 67.7$ deg

as demonstrated in Fig. 12. Changes in the radial temperature distribution with increasing laser power, beam diameter, and workpiece radius are predicted with good to reasonable accuracy by the approximate model, and results for the effect of laser power are shown in Fig. 13. Temperatures decrease with decreasing power and increasing workpiece radius throughout the workpiece and with increasing beam diameter in the outer region.

Relative to applicability of the approximate model, it is noted that laser-assisted machining is likely to be restricted to depths of cut within approximately 0.5 mm of the workpiece surface. In this near-surface region, results from the approximate analysis are in reasonable agreement with those of the numerical model, suggesting that the approximate model may provide a useful tool for on-line process control.

Conclusions

A transient three-dimensional numerical simulation and an approximate two-zone model have been used to predict the thermal response of a rotating silicon nitride cylinder to an axially translating laser. Features of the numerical model include: (i) temperature-dependent thermophysical properties; (ii) a manufacturer-supplied laser heat flux distribution, and (iii) treatment of convective heat transfer due to a laser gas assist jet. The numerical model yielded the following conclusions: (i) the thermal layer thickness for an r-ϕ plane cutting through the center of the laser source decreases with increasing workpiece rotational speed; (ii) the influence of heat transfer by conduction in the z-direction increases with decreasing laser traverse velocity; (iii) local temperatures increase throughout the workpiece for increasing laser power; and (iv) outer region temperatures decrease with increasing beam diameter due to a diminished potential for near-laser conduction heat transfer. From the numerical simulations, it has also been found that, while mixed convection to the ambient air and surface emission to the surroundings are negligible, forced convection associated with a gas assist jet and changes in thermophysical properties can significantly influence the maximum surface temperature beneath the laser spot.

The approximate model of this study yielded relations for calculating the radial temperature distribution at various circumferential locations within an r-ϕ plane corresponding to the center of the laser source. Model predictions are generally in good agreement with those based on the more detailed numerical simulation, particularly in a near-surface region corresponding to the maximum depth of cut (~0.5 mm) expected for LAM. Hence, the approximate model provides a useful tool for assessing the effect of operating conditions on the subsurface temperature distribution, for establishing preferred process operating conditions, including cutting tool placement, and most importantly, for on-line process control.

Acknowledgments

Support of this work by the National Science Foundation under Grant Number 9400654-CTS is gratefully acknowledged. The first author would also like to thank Dr. M. J. M. Krane for many useful discussions during the course of this work.

References

Chryssolouris, G., Shonbeck, J., Choi, W., and Sheng, P., 1989, "Advances in Three-Dimensional Laser Machining," *Proceedings of the Winter Annual Meeting of the ASME,* E. S. Geskin, ed., Vol. PED-41, San Francisco, CA, pp. 1–7.

Gecim, B., and Winer, W. O., 1984, "Steady Temperature in a Rotating Cylinder Subject to Surface Heating and Convective Cooling," ASME JOURNAL OF HEAT TRANSFER, Vol. 106, pp. 120–127.

Kawashimo, K., and Yamada, T., 1978, "Temperature Distribution within a Rotating Cylindrical Body Heated and Cooled Locally on Its Peripheral Surface," *Bulletin of the Japan Society of Mechanical Engineers,* Vol. 21, pp. 266–272.

Koai, K., Damaschek, R., and Bergmann, H. W., 1993, "Heat Transfer in Laser Hardening of Rotating Cylinders," *Proceedings of the Winter Annual Meeting of the ASME,* Vol. HTD-259, New Orleans, LA, pp. 1–8.

König, W., and Zaboklici, A. K., 1993, "Laser Assisted Hot Machining of Ceramics and Composite Materials," National Institute of Science and Technology, NIST Special Publication 847.

Rozzi, J. C., Pfefferkorn, F. E., Incropera, F. P., and Shin, Y. C., 1998, "Transient Thermal Response of a Rotating Cylindrical Silicon Nitride Workpiece Subjected to a Translating Laser Heat Source: I—Comparison of Surface Temperature Measurements with Theoretical Results," ASME JOURNAL OF HEAT TRANSFER, Vol. 120, pp. 899–906.

Rozzi, J. C., Krane, M. J. M., Incropera, F. P., and Shin, Y. C., 1995, "Numerical Prediction of Three-Dimensional Unsteady Temperatures in a Rotating Cylindrical Workpiece Subjected to Localized Heating by a Translating Laser Source," *Proceedings of the International Mechanical Engineering Congress and Exhibition,* Vol. HTD-Vol. 317-2, San Francisco, CA, pp. 399–411.

Stinton, D. P., 1988, "Assessment of the State-of-the-Art in Machining and Surface Preparation of Ceramics," Oak Ridge National Laboratory, ORNL/TM-10791.

Wobker, H. G., and Tönshoff, H. K., 1993, "High Efficiency Grinding of Structural Ceramics," National Institute of Science and Technology, NIST Special Publication 847.

Yuen, W. Y. D., 1984, "On the Steady-State Temperature Distribution in a Rotating Cylinder Subject to Heating and Cooling Over Its Surface," ASME JOURNAL OF HEAT TRANSFER, Vol. 106, pp. 578–585.

Yuen, W. Y. D., 1994, "The Thermal Boundary Layer in a Rotating Cylinder Subject to Prescribed Surface Heat Fluxes," *International Journal of Heat and Mass Transfer,* Vol. 37, pp. 605–618.

Thermal Transport and Flow in High-Speed Optical Fiber Drawing

Zhilong Yin

Y. Jaluria
Fellow ASME

Department of Mechanical
and Aerospace Engineering,
Rutgers, The State University
of New Jersey,
New Brunswick, NJ 08903

The thermal transport associated with optical fiber drawing at relatively high drawing speeds, ranging up to around 15 m/s, has been numerically investigated. A conjugate problem involving the glass and the purge gas regions is solved. The transport in the preform/fiber is coupled, through the boundary conditions, with that in the purge gas, which is used to provide an inert environment in the furnace. The zonal method, which models radiative transport between finite zones in a participating medium, has been employed to compute the radiative heat transfer in the glass. The flow of glass due to the drawing process is modeled with a prescribed free-surface neck-down profile. The numerical results are compared with the few that are available in the literature. The effects of important physical variables such as draw speed, purge gas velocity and properties, furnace temperature, and preform diameter on the flow and the thermal field are investigated. It is found that the fiber drawing speed, the furnace temperature, and the preform diameter have significant effects on the temperature field in the preform/fiber, while the effects of the purge gas velocity and properties are relatively minor. The overall heating of the preform/fiber is largely due to radiative transport in the furnace and the changes needed in the furnace temperature distribution in order to heat the glass to its softening point at high speeds are determined.

1 Introduction

The drawing of an optical fiber is usually accomplished by feeding a cylindrical glass preform of appropriate purity and composition into a high-temperature furnace. After the preform is heated to a temperature exceeding its softening point, which is about 1900 K for fused silica glass (Paek and Runk, 1978), it is drawn into a fiber of about 125-μm diameter through a neck-down region. The optical and mechanical properties of the fiber strongly depend on the thermal transport in the furnace (Li, 1985). Therefore, a rigorous study of the flow and heat transfer during optical fiber drawing is desirable in order to optimize and control the fiber drawing process and the associated system.

Modeling of the optical fiber drawing process has been of considerable interest for about three decades. Glicksman (1968) carried out analytical and experimental studies on various aspects of the process, such as fiber spinning from molten melt and cooling of a moving fiber. Paek and Runk (1978) experimentally and numerically investigated the characteristics of the neck-down region of a glass preform. They assumed a heat flux distribution at the furnace and employed a very simple radiation model to determine the radiative heat input at the glass surface. Employing the Rosseland approximation for an optically thick medium, lumped axial velocity and temperature distributions, and a specified heat transfer coefficient at the preform/fiber surface, they studied the thermal transport during the optical fiber drawing process. Sayles and Caswell (1984) carried out a finite element analysis of the neck-down region. In their work, variable properties were considered, but the draw-down ratio (preform diameter/fiber diameter) was limited to about 10. Employing the absorption data given by Sayles (1982), Myers (1989) numerically modeled the drawing process using a one-dimensional model and constant properties, except for the viscosity which varies by several orders of magnitude during the drawing process (Fleming, 1964). The convective transport from the glass to the purge gas was neglected on the basis of an order of magnitude analysis, but an enclosure analysis was employed for the radiative exchange between the furnace and the preform/fiber. The Rosseland approximation was used to consider the radiative transport within the preform/fiber.

Recently, Lee and Jaluria (1995a, 1996), Roy Choudhury, and Jaluria (1998a, b), Kaminski (1995), and Yin and Jaluria (1997) have carried out more rigorous studies on the neck-down region. Lee and Jaluria (1995a, 1996) employed an enclosure analysis to compute the radiative heat exchange between the glass preform/fiber and the furnace. The surface of the preform/fiber was assumed to be diffuse and spectral, and a diameter-dependent emissivity based on the absorption coefficient information from Myers (1989) was used. The Rosseland approximation was used to consider the radiative transport within the preform/fiber. The convective heat transfer coefficient at the surface of the preform/fiber was specified using empirical correlations given by Paek and Runk (1978). The effect of variable properties and viscous dissipation on the neck-down region was thoroughly investigated. Roy Choudhury and Jaluria (1998a, b) improved on the study of Lee and Jaluria (1995a, 1996) by incorporating the solution of the momentum and energy equations of the purge gas into the modeling of the optical fiber drawing process. In their study, the heat transfer coefficient at the surface of the preform/fiber was computed by solving the conjugate problem which involves both the glass preform/fiber and the purge gas, but the radiation was still considered using the approach employed by Lee and Jaluria (1995a).

Roy Choudhury et al. (1985) developed a numerical scheme to determine the neck-down profile for a wide range of operating conditions. This paper, along with that by Roy Choudhury and Jaluria (1998a), consolidated most of the earlier portions of the overall problem, involving convection in the glass and in the purge gas, thermal radiation in the furnace, and profile determination. They obtained results on preform/fiber heating in the furnace for practical circum-

---

Contributed by the Heat Transfer Division for publication in the JOURNAL OF HEAT TRANSFER and presented at the AIAA/ASME Joint Thermophysics and Heat Transfer Conference, Albuquerque. Manuscript received by the Heat Transfer Division, Mar. 3, 1998; revision received, Sept. 1, 1998. Keywords: Conjugate, Forced Convection, Heat Transfer, Manufacturing, Radiation. Associate Technical Editor: D. Kaminski.

stances and determined the range of feasible operating conditions for fiber drawing. However, relatively low draw speeds, up to around 3 m/s, and small preform diameters, up to around 2 cm, were considered. The optically thick assumption was used to model radiation within the glass preform/fiber. It was shown in these studies that, even though radiation is the dominant mode of transport in the overall heating of the glass, convective transport becomes quite important near the end of the neck-down region because of the small contribution of radiation in this region resulting from the geometry. Thus, neglecting convection, as done by Myers (1989), can lead to substantial error in the prediction of the neck-down profile and the temperature distribution in the fiber.

Kaminski (1995) was among the first researchers to model the radiative heat transport in the neck-down region without using Rosseland approximation. In her study she employed the P_1 method to compute the radiative transport in the glass, but her model only considered the upper neck-down region where the diameter is relatively large, making the optically thick assumption fairly satisfactory. In addition she prescribed the flow velocities for both the glass and purge gas regions rather than solve the momentum equations. Yin and Jaluria (1997) employed the zonal method to consider the radiative heat transport inside the preform/fiber. But, in their study, only the radiative heat flux was investigated and the flow of glass and the purge gases was not considered. Ball et al. (1997) considered radiation in a glass jet using the discrete ordinates method to account for the directional nature of the radiation. The glass surface was treated as specular. However, only a small change in diameter was considered. The problem is much more involved for optical fiber drawing.

The optical fiber drawing process involves coupled convection, conduction, and radiation transport mechanisms. The first two modes of heat transfer have been studied in detail by the earlier researchers, but the radiation transport has left much room for improvement. In most of the earlier studies, the glass preform/fiber was assumed to be optically thick, either explicitly or implicitly, and when the enclosure analysis was used, the radiation from the glass preform/fiber was only considered to be influenced by the glass surface temperature. But in the real optical fiber drawing process, the optically thick condition is not satisfied, particularly in the lower neck-down region, and the radiation to and from the glass preform/fiber is a volume phenomenon which is determined by the temperature distribution in the preform/fiber. In addition, in the earlier studies, draw-down ratios of around 100, which

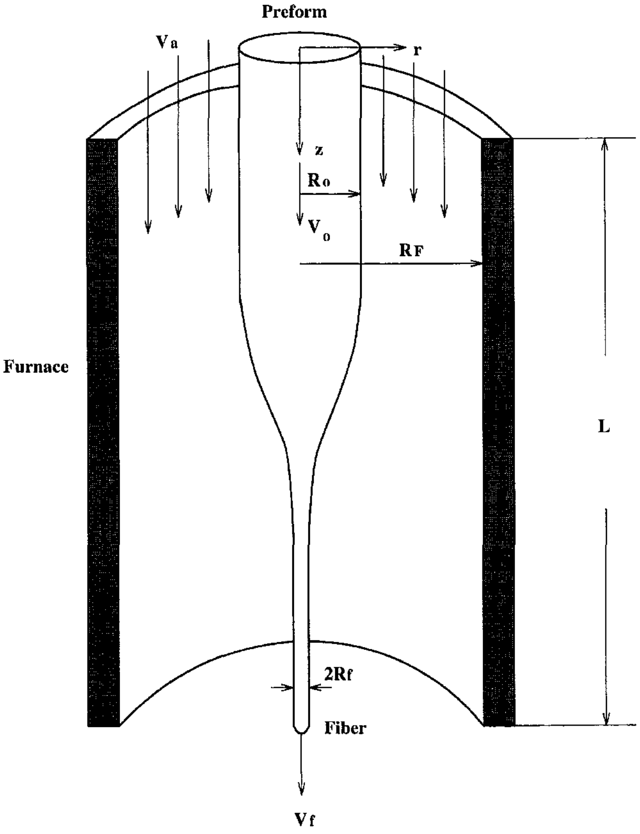

Fig. 1 Schematic diagram of the optical fiber drawing process with aiding purge gas flow

Nomenclature

A = area
a_λ = spectral absorption coefficient of glass
C_p = specific heat at constant pressure
D = diameter of preform, fiber or furnace
f = black body radiation fraction
$\overline{GG}$ = volume-volume direct exchange area
h = local convective heat transfer coefficient
J = radiosity
K = thermal conductivity
L = height of furnace
Nu = Nusselt number
n = refractive index of silica glass
n = normal direction to preform/gas interface
p = pressure
R = radius of preform, fiber, furnace
r = radial coordinate distance
S = distance
S_r = radiative source term
$\overline{SG}$ = surface-volume direct exchange area
T = temperature
T_{melt} = glass softening point, typically around 1900 K for silica glass
t = time
t^* = transformed time, t/R_0
U = nondimensional radial velocity
u = radial velocity
V = volume; nondimensional axial velocity
v = axial velocity
z = axial coordinate distance

Greek Symbols

β = nondimensional axial coordinate distance, z/L
η = nondimensional radial coordinate distance, $r/R(z)$
η_a = nondimensional radial coordinate distance in the purge gas, $r_a/R_F - R(z)$
θ = polar angle; nondimensional temperature
μ = dynamic viscosity
ν = kinematic viscosity
ρ = reflectivity; density
σ = Stefan-Boltzmann constant
Φ = viscous dissipation
Ψ = nondimensional streamfunction
Ω = nondimensional vorticity

Superscripts

i = inside surface of the preform
$'$ = first derivative with respect to z
$''$ = second derivative with respect to z

Subscripts

0 = preform at furnace entrance
a = purge gas
F = furnace
f = fiber

Table 1 Parameters used in the computation for validation of the zonal method

D_0 (cm)	D_f (cm)	D_F (cm)	L (cm)	V_f (m/s)	V_a (m/s)	T_0 (°C)	T_F (°C)
5	0.5	6	20	6	0.1	1600	2100

apply for preform diameters of around 1.25 cm, were considered. But with the increasing demand for optical fibers and the development of advanced drawing techniques, the preform diameters have increased steadily, currently being in the range of 5–10 cm. Consequently, the draw-down ratios have also increased significantly.

In the present study, a draw down ratio of 400, corresponding to a preform diameter of 5 cm and a fiber diameter of 125 μm, has been considered. The zonal method, rather than the Rosseland approximation for an optically thick medium, has been employed to compute the radiative heat transport in the glass preform/fiber. The surface is still taken as diffuse because of the simplicity of the diffuse approximation and earlier work which showed relatively small effect of specular modeling of radiative transport in typical draw circumstances (Yin, 1997). However, specular effects should be included for more accurate modeling and for certain applications involving highly polished preforms. A conjugate problem which involves coupled transport in the glass and the gas regions has been solved. The effects of different physical parameters, such as fiber drawing speed, purge gas velocity and properties, furnace temperature, and preform diameter, have been investigated. The focus is on large preform diameters, high draw speeds, incorporation of the zone model, and bringing together many of the separate elements of the problem that have been considered earlier.

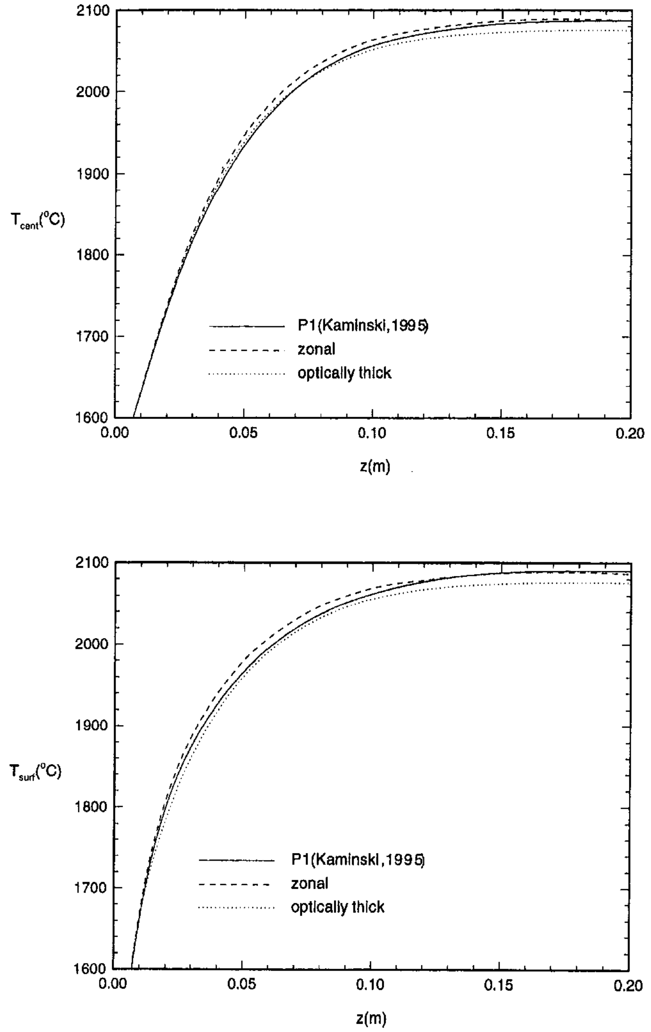

Fig. 2 Comparison of the temperature variations in the preform computed using the P_1 method, zonal method, and optically thick approximation. Here, T_{cent} is the centerline temperature and T_{surf} is the surface temperature.

2 Analysis

The transport process in the neck-down region includes the flow and heat transfer in both the glass and purge gas regions. The flow is assumed to be laminar because glass is a highly viscous liquid, even near its softening temperature, and the velocity of the purge gas is small. The heat transfer involves conduction, convection, and radiation. Because glass is semitransparent, the radiative energy absorbed by the glass comes from the glass surface, as well as from the surrounding glass. The glass preform has a streamwise variation in radius when it is drawn into a fiber, varying in diameter from 5–10 cm to around 125 μm in a vertical distance of about 30 cm. The neck-down profile depends on the drawing conditions, such as furnace temperature, drawing speed etc. In this study, however, a prescribed neck-down profile has been assumed, on the basis of results available in the literature, in order to simplify the modeling, substantially reduce computational times, and to focus on the effects of other parameters. It has been shown in earlier studies that though the neck-down profile is an important consideration in the problem, the use of a generic profile to represent variation from the preform to the fiber diameter captures most of the important effects quite satisfactorily. However, to simulate an actual system for design and optimization, the full problem, including profile determination, must be solved. The outer boundary of the glass in the neck-down region is a free surface where a zero-shear condition is assumed (Roy Choudhury et al., 1995). The purge gas inflow and outflow are taken in the same direction as the preform movement, as shown by Fig. 1.

2.1 Governing Equations.

For the optical fiber drawing process shown in Fig. 1, the heating and the flow are axisymmetric. Using cylindrical coordinates, the momentum and energy equations can be written for both the glass preform/fiber and the purge gas, which is assumed to be incompressible at the typical low flow rates employed in practice, as (Burmeister, 1983)

$$\frac{\partial v}{\partial z} + \frac{1}{r}\frac{\partial (ru)}{\partial r} = 0 \qquad (1)$$

$$\frac{\partial v}{\partial t} + u\frac{\partial v}{\partial r} + v\frac{\partial v}{\partial z} = -\frac{1}{\rho}\frac{\partial p}{\partial z} + \frac{1}{r}\frac{\partial}{\partial r}\left[r\nu\left(\frac{\partial v}{\partial r} + \frac{\partial u}{\partial z}\right)\right] + 2\frac{\partial}{\partial z}\left(\nu\frac{\partial v}{\partial z}\right) \qquad (2)$$

Table 2 Parameters used in the parametric study

D_0 (cm)	D_f (μm)	D_F (cm)	L (cm)	V_f (m/s)	V_a (m/s)	T_F (K)
5	125	7	30	5	0.1	2500

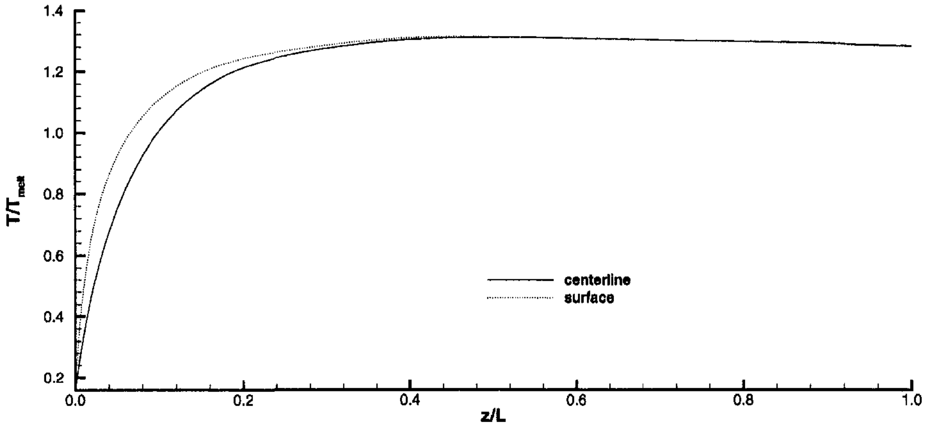

(a) $v_f = 5$ m/s

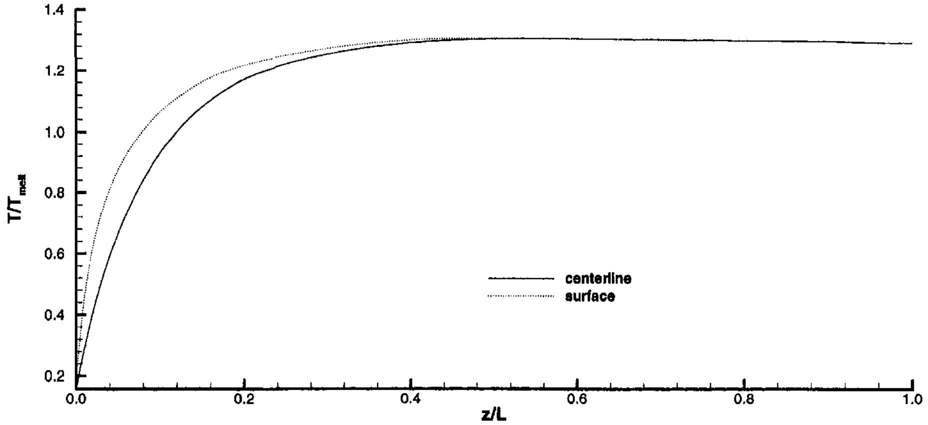

(b) $v_f = 10$ m/s

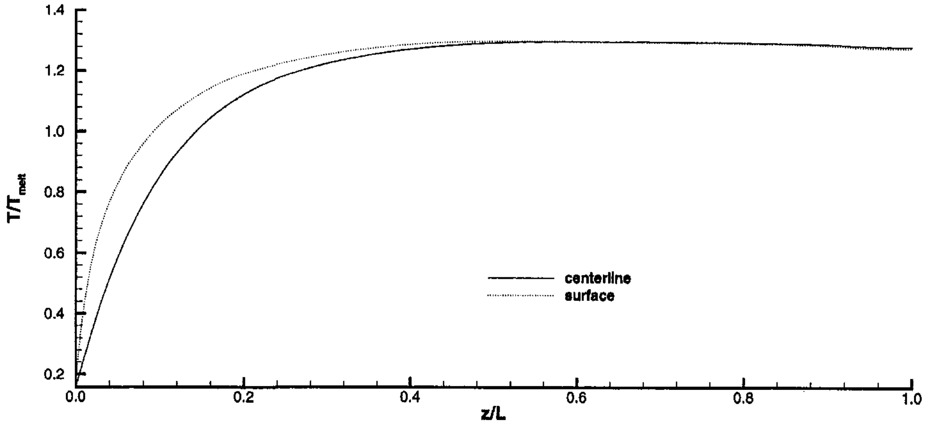

(c) $v_f = 15$ m/s

Fig. 3 Centerline and surface temperature distributions in the preform for different fiber drawing speeds

$$\frac{\partial u}{\partial t} + u\frac{\partial u}{\partial r} + v\frac{\partial u}{\partial z} = -\frac{1}{\rho}\frac{\partial p}{\partial r} + \frac{2}{r}\frac{\partial}{\partial r}\left(r\nu\frac{\partial u}{\partial r}\right) + \frac{\partial}{\partial z}\left[\nu\left(\frac{\partial v}{\partial r} + \frac{\partial u}{\partial z}\right)\right] - \frac{2\nu u}{r^2} \quad (3)$$

$$\rho C_p\left(\frac{\partial T}{\partial t} + u\frac{\partial T}{\partial r} + v\frac{\partial T}{\partial z}\right) = \frac{1}{r}\frac{\partial}{\partial r}\left(rK\frac{\partial T}{\partial r}\right) + \frac{\partial}{\partial z}\left(K\frac{\partial T}{\partial z}\right) + \Phi + S_r \quad (4)$$

where Φ is the viscous dissipation and is given as

$$\Phi = \mu\left\{2\left[\left(\frac{\partial u}{\partial r}\right)^2 + \left(\frac{u}{r}\right)^2 + \left(\frac{\partial v}{\partial z}\right)^2\right] + \left(\frac{\partial u}{\partial z} + \frac{\partial v}{\partial r}\right)^2\right\}. \quad (5)$$

S_r is the radiative source term which represents the rate of net gain of radiative energy per unit volume at any point due to the excess of absorbed radiation over that emitted. The radiative source term for the purge gas is zero since it is taken as nonpar-

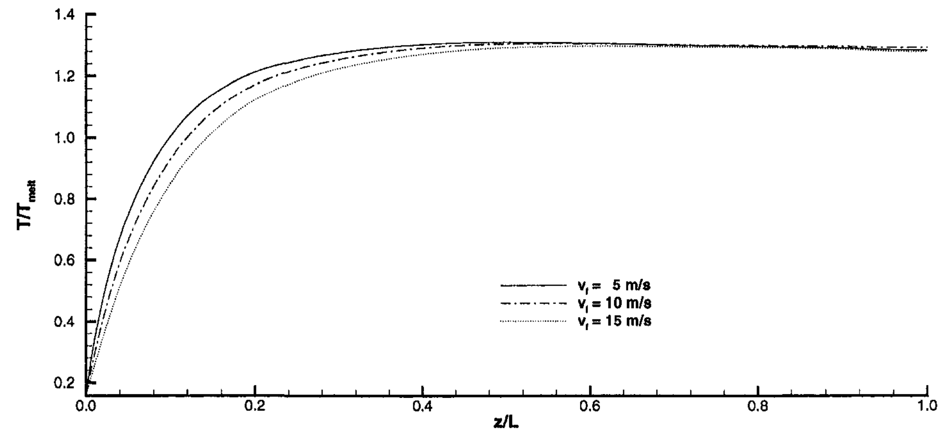

(a) Centerline temperature

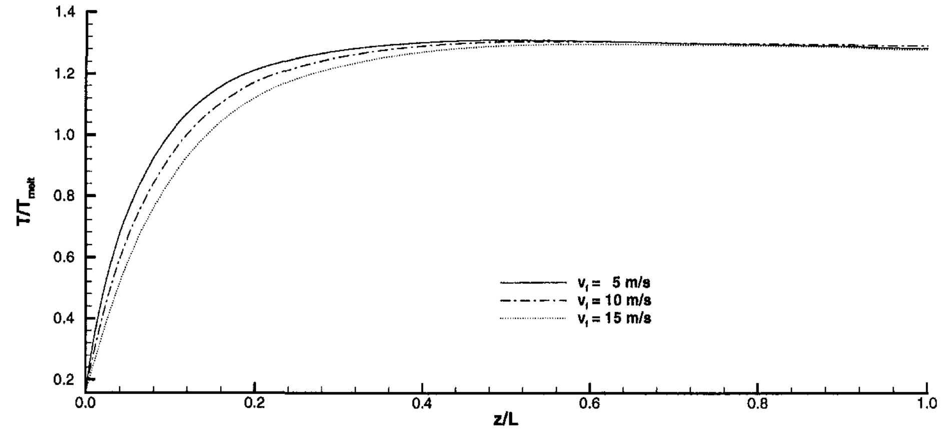

(b) Surface temperature

Fig. 4 Comparisons of preform temperature distributions for different fiber drawing speeds

ticipating. But the radiative source term for the glass preform/fiber is nonzero because glass emits and absorbs energy in certain wavelength bands. Therefore, in this study, only the radiative source term in the glass is considered. The details about the computation of this radiative source term is given later.

In a typical optical fiber drawing process, the viscosity and velocity of the purge gas are relatively small. Thus, viscous dissipation effects in the purge gas are negligible. But in the glass, viscous dissipation cannot be neglected, especially in the lower neck down region because the viscosity and velocity gradients are high (Lee and Jaluria, 1996). Buoyancy effects in the gas phase are neglected since the mixed convection parameter, $\mathrm{Gr}/\mathrm{Re}^2$, where Gr is the Grashof number and Re is the Reynolds number, both being based on furnace height, was estimated to be small for typical operating conditions. Also, earlier results have shown these effects to be small in the overall transport. Variable property effects in the gas are also small (Roy Choudhury, 1995). However, the variation of glass properties, particularly viscosity, cannot be neglected and is taken into account, employing the property data from Fleming (1964) and Myers (1989). The kinematic viscosity of glass ν is taken as $\nu(T) = 4545.45 \exp[32((T_{\mathrm{melt}}/T) - 1)]$. Thus, viscosity varies very strongly with temperature and changes by several orders of magnitude over the temperature range encountered in the furnace.

Based on the transformations proposed by Lee and Jaluria (1995b) and Roy, Choudhury, and Jaluria (1998b), the above governing equations are converted to nondimensional stream-function, vorticity, and energy equations, and the computational domain is converted to a cylindrical one. For the glass region, the transformed equations with pseudo-time t^* are given as

$$\frac{\partial\Psi}{\nu_0\partial t^*} = \left(\frac{R_0}{R}\right)^3 \frac{\partial}{\partial\eta}\left(\frac{1}{\eta}\frac{\partial\Psi}{\partial\eta}\right) + R'^2\eta\left(\frac{R_0}{R}\right)^3 \frac{\partial^2\Psi}{\partial\eta^2} + \left(2R'^2\left(\frac{R_0}{R}\right)^3 - R''R_0\left(\frac{R_0}{R}\right)^3\right)\frac{\partial\Psi}{\partial\eta} - 2R'\left(\frac{R_0}{R}\right)^2\left(\frac{R_0}{L}\right)\frac{\partial^2\Psi}{\partial\eta\partial\beta} + \frac{1}{\eta}\left(\frac{R_0}{R}\right)\left(\frac{R_0}{L}\right)^2\frac{\partial^2\Psi}{\partial\beta^2} + \Omega \quad (6)$$

$$\frac{\partial\Omega}{\partial t^*} + \frac{\upsilon_0 R_0}{R}\frac{\partial(U\Omega)}{\partial\eta} - \frac{\eta\upsilon_0 R_0 R'}{R}\frac{\partial(V\Omega)}{\partial\eta} + \frac{\upsilon_0 R_0}{L}\frac{\partial(V\Omega)}{\partial\beta} = \nu\left[\frac{R_0}{R^2}\frac{\partial}{\partial\eta}\left(\frac{1}{\eta}\frac{\partial(\eta\Omega)}{\partial\eta}\right) + \frac{\eta^2 R'^2 R_0}{R^2}\frac{\partial^2\Omega}{\partial\eta^2} - \frac{2\eta R' R_0}{RL}\frac{\partial^2\Omega}{\partial\eta\partial\beta} + \frac{R_0}{L^2}\frac{\partial^2\Omega}{\partial\beta^2} - \eta\left(\frac{R''R_0}{R} - 2R_0\left(\frac{R'}{R}\right)^2\right)\frac{\partial\Omega}{\partial\eta}\right] + \frac{R_0^2}{\upsilon_0}S_\nu \quad (7)$$

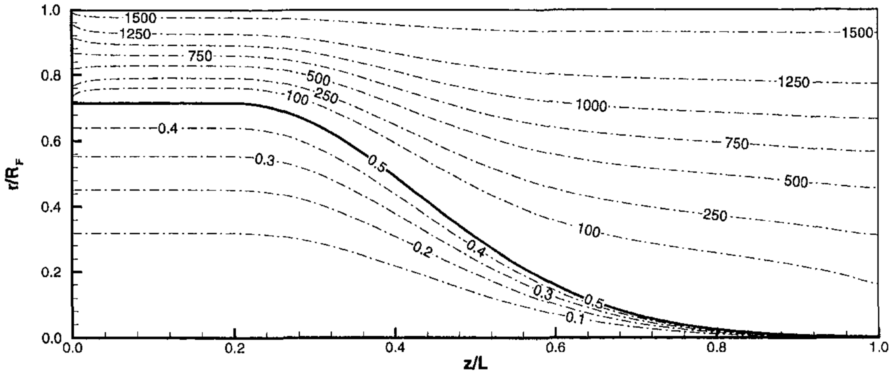

(a) $v_f = 5$ m/s

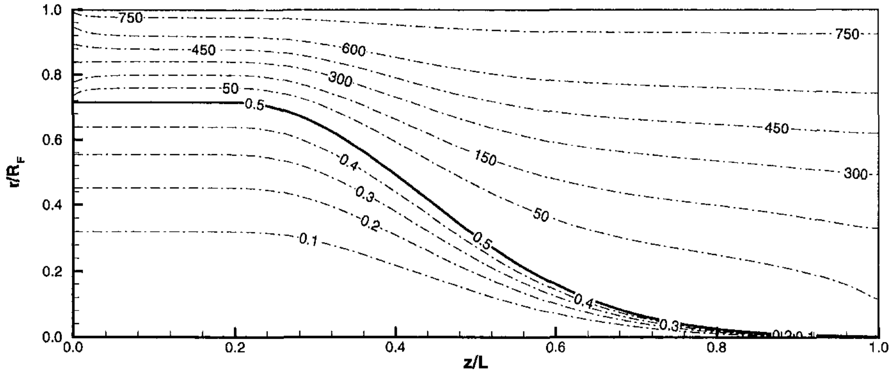

(b) $v_f = 10$ m/s

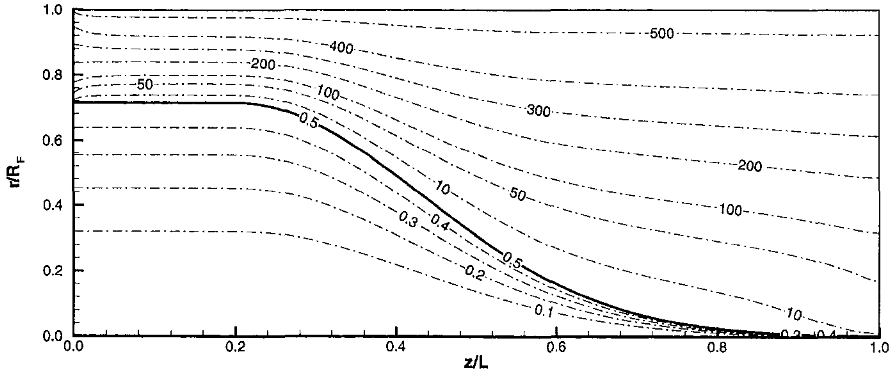

(c) $v_f = 15$ m/s

Fig. 5 Streamlines for different fiber drawing speeds

$$
\begin{aligned}
&\frac{\partial \theta}{\partial t^*} + \frac{v_0 R_0}{R\eta} \frac{\partial(\eta U \theta)}{\partial \eta} - \frac{v_0 \eta R' R_0}{R} \frac{\partial(V\theta)}{\partial \eta} + \frac{v_0 R_0}{L} \frac{\partial(V\theta)}{\partial \beta} \\
&= \frac{1}{\rho C_p} \left[\frac{R_0}{R^2 \eta} \frac{\partial}{\partial \eta} \left(\frac{\partial(K\eta\theta)}{\partial \eta} \right) + \frac{R_0}{L^2} \frac{\partial}{\partial \beta} \left(K \frac{\partial \theta}{\partial \beta} \right) \right. \\
&\quad - \frac{\eta R_0}{L} \frac{\partial}{\partial \beta} \left(\frac{KR'}{R} \frac{\partial \theta}{\partial \eta} \right) - \frac{\eta R' R_0}{LR} \frac{\partial}{\partial \eta} \left(K \frac{\partial \theta}{\partial \beta} \right) \\
&\quad \left. + \frac{\eta R'^2 R_0}{R^2} \frac{\partial}{\partial \eta} \left(K\eta \frac{\partial \theta}{\partial \eta} \right) \right] + \frac{R_0}{\rho C_p T_{\mathrm{melt}}} \Phi + \frac{R_0}{\rho C_p T_{\mathrm{melt}}} S_\nu \qquad (8)
\end{aligned}
$$

where S_ν represents the source term due to the variable viscosity and is given as

$$
\begin{aligned}
S_\nu &= \frac{\partial \nu}{\partial z} \left(2 \frac{\partial^2 u}{\partial r^2} + 2 \frac{\partial^2 u}{\partial z^2} + \frac{2}{r} \frac{\partial u}{\partial r} - \frac{2u}{r^2} \right) \\
&\quad - \frac{\partial \nu}{\partial r} \left[2 \frac{\partial^2 v}{\partial r^2} + 2 \frac{\partial^2 v}{\partial z^2} + \frac{1}{r} \left(\frac{\partial v}{\partial r} + \frac{\partial u}{\partial z} \right) \right] \\
&\quad + \left(\frac{\partial^2 \nu}{\partial z^2} - \frac{\partial^2 \nu}{\partial r^2} \right) \left(\frac{\partial u}{\partial z} + \frac{\partial v}{\partial r} \right) \\
&\quad + 2 \frac{\partial^2 \nu}{\partial r \partial z} \left(\frac{\partial u}{\partial r} - \frac{\partial v}{\partial z} \right). \qquad (9)
\end{aligned}
$$

For the purge gas region, the transformed equations are given as

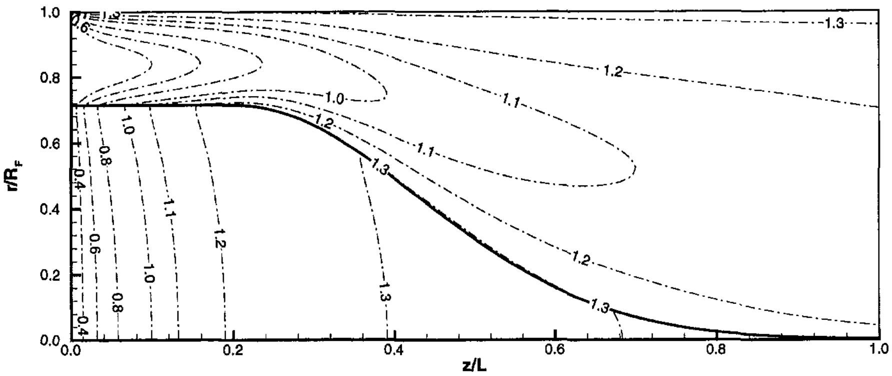

(a) $v_f = 5$ m/s

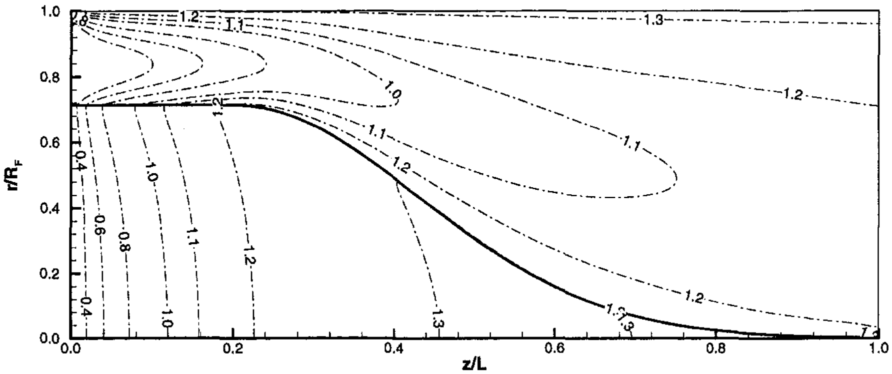

(b) $v_f = 10$ m/s

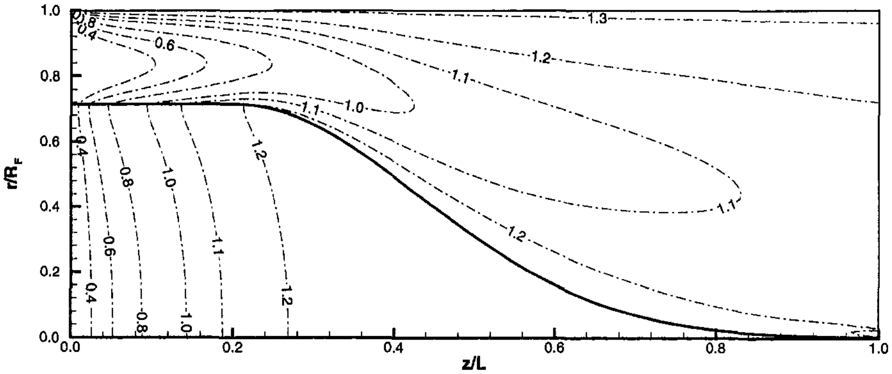

(c) $v_f = 15$ m/s

Fig. 6 Isotherms for different fiber drawing speeds

$$\frac{\partial \Psi_a}{v_0 \partial t^*} = \frac{R_0}{(k_8-\eta_a)R_a}\left[\left(\frac{R_0}{L}\right)^2 \frac{\partial^2\Psi_a}{\partial\beta^2} + \eta_a^2 R_a'^2 \left(\frac{R_0}{R_a^2}\right)^2 \frac{\partial^2\Psi_a}{\partial\eta_a^2} - 2\eta_a R_a' \frac{R_0^2}{R_a L}\frac{\partial}{\partial\beta}\left(\frac{\partial\Psi_a}{\partial\eta_a}\right)\right] + \left(\frac{R_0}{R_a}\right)^3 \frac{\partial}{\partial\eta_a}\left(\frac{1}{k_8-\eta_a}\frac{\partial\Psi_a}{\partial\eta_a}\right) + \frac{\eta_a}{(k_8-\eta_a)}\left(\frac{R_0}{R_a}\right)^2 \times\left(\frac{2R_a'^2R_0}{R_a} - R_a''R_0\right)\frac{\partial\Psi_a}{\partial\eta_a} + \Omega_a \tag{10}$$

$$\frac{\partial\Omega_a}{\partial t^*} - \frac{v_0R_0}{R_a}\frac{\partial(U_a\Omega_a)}{\partial\eta_a} - \frac{v_0\eta_a R_a' R_0}{R_a}\frac{\partial(V_a\Omega_a)}{\partial\eta_a} + \frac{v_0R_0}{L}\frac{\partial(V_a\Omega_a)}{\partial\beta} = \nu_a R_0\left\{\frac{\eta_a^2R_a'^2}{R_a^2}\frac{\partial^2\Omega_a}{\partial\eta_a^2} - \frac{2\eta_aR_a'}{R_aL}\frac{\partial^2\Omega_a}{\partial\eta_a\partial\beta} - \eta_a\left[\frac{R_a''}{R_a} - 2\left(\frac{R_a'}{R_a}\right)^2\right]\frac{\partial\Omega_a}{\partial\eta_a} + \frac{1}{R_a^2}\frac{\partial}{\partial\eta_a}\left[\frac{1}{(k_8-\eta_a)}\frac{\partial((k_8-\eta_a)\Omega_a)}{\partial\eta_a}\right] + \frac{1}{L^2}\frac{\partial^2\Omega_a}{\partial\beta^2}\right\} \tag{11}$$

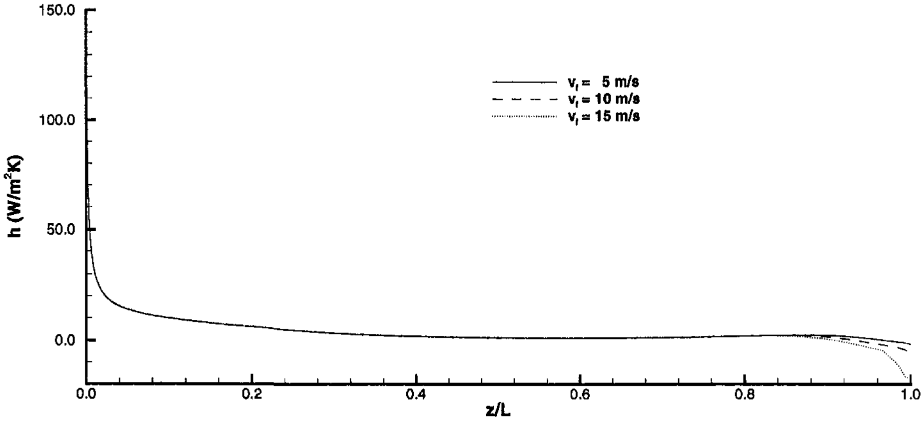

(a) Heat transfer coefficient

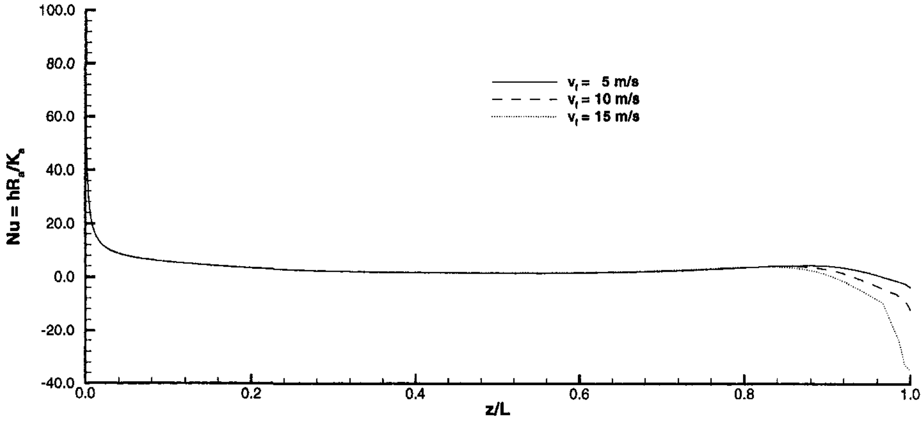

(b) Nusselt number

Fig. 7 **The computed heat transfer coefficient and the Nusselt number for different fiber drawing speeds**

$$\frac{\partial \theta_a}{\partial t^*} - \frac{v_0 R_0}{(k_8 - \eta_a) R_a} \frac{\partial[(k_8 - \eta_a) U_a \theta_a]}{\partial \eta_a} - \frac{v_0 \eta_a R'_a R_0}{R_a} \frac{\partial (V_a \theta_a)}{\partial \eta_a} + \frac{v_0 R_0}{L} \frac{\partial (V_a \theta_a)}{\partial \beta}$$
$$= \frac{R_0}{\rho_a C_{pa}} \left\{ \frac{1}{R_a^2 (k_8 - \eta_a)} \frac{\partial}{\partial \eta_a} \left[K_a (k_8 - \eta_a) \frac{\partial \theta_a}{\partial \eta_a} \right] + \frac{1}{L^2} \frac{\partial}{\partial \beta} \left(K_a \frac{\partial \theta_a}{\partial \beta} \right) - \frac{\eta_a}{L} \frac{\partial}{\partial \beta} \left(\frac{K_a R'_a}{R_a} \frac{\partial \theta_a}{\partial \eta_a} \right) - \frac{\eta_a R'_a}{L R_a} \frac{\partial}{\partial \eta_a} \left(K_a \frac{\partial \theta_a}{\partial \beta} \right) + \frac{\eta_a R_a'^2}{R_a^2} \frac{\partial}{\partial \eta_a} \left(K_a \eta_a \frac{\partial \theta_a}{\partial \eta_a} \right) \right\}, \quad (12)$$

where $k_8 = R_F / R_a$.

2.2 Boundary Conditions. The boundary conditions are the same as those used by Roy Choudhury and Jaluria (1998b) except for the thermal boundary condition at the interface between the preform/fiber and the purge gas. This condition has been modified and is given as

$$\theta(\eta = 1) = \theta_a(\eta_a = 1);$$
$$K \frac{\partial \theta}{\partial \mathbf{n}} (\eta = 1) = K_a \frac{\partial \theta_a}{\partial \mathbf{n}_a} (\eta_a = 1). \quad (13)$$

Symmetry conditions at the axis, no-shear at the glass-gas interface, and no-slip at the solid boundaries yield the remaining conditions. At the exit, the diffusion terms are set equal to zero for both the glass and the gas. For further details, the preceding references may be consulted.

3 Numerical Scheme

The above equations are solved using the finite difference method. All the equations are approximated by a second-order central differencing scheme, except for the convection terms for which a different second-order approximation is used (Lee and Jaluria, 1995b). Two discretization schemes have been used. The first one is for the transport equations (streamfunction, vorticity, and energy equations) and the second one is for the radiation analysis.

The discretization for the transport equations is based on the method proposed by Lee and Jaluria (1995b). A nonuniform grid has been employed. Finer grids are used wherever large velocity and temperature gradients are expected. Especially important is the temperature gradient in the glass preform/fiber, which affects the viscosity gradient significantly, because the glass viscosity is an exponential function of temperature. In general, finer grids are used in both the preform/fiber and the purge gas near the entrance and near the preform-gas interface, as well as in the purge gas near the furnace. The optimal grid

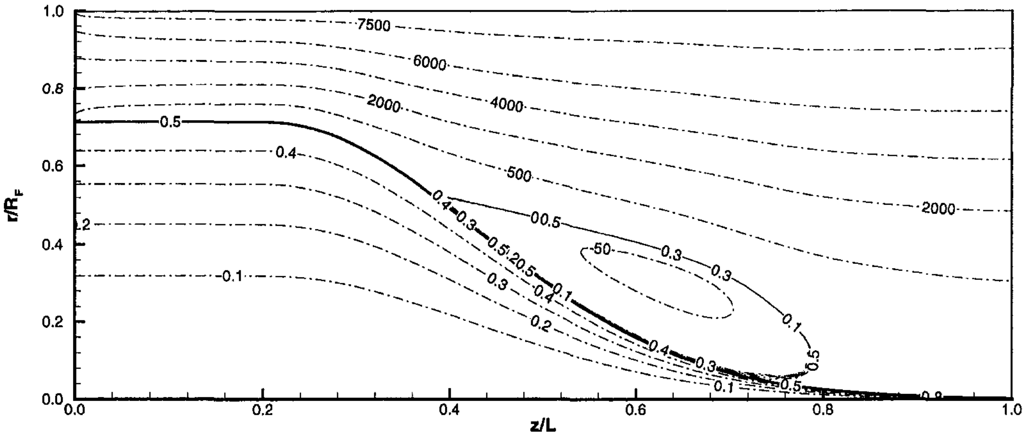

(a) Streamlines

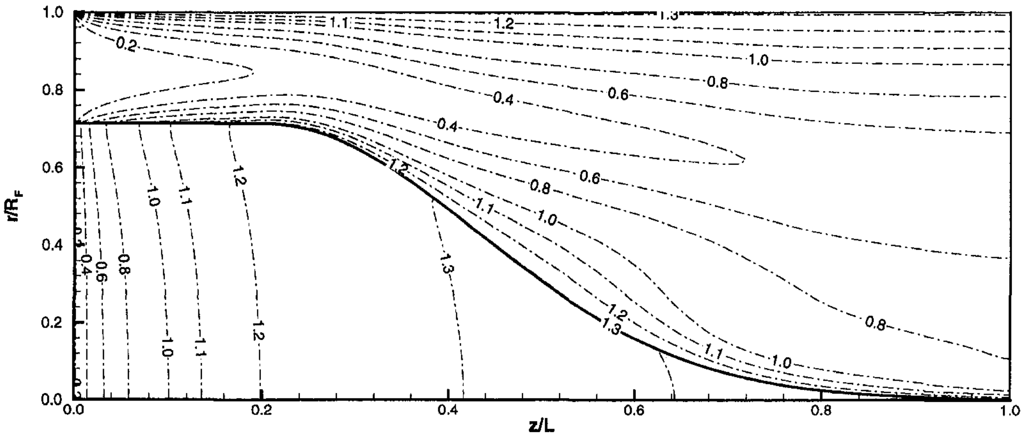

(b) Isotherms

Fig. 8 Streamlines and isotherms for v_a = 0.5 m/s

number, which refers to the grid spacing at which the results are not significantly affected by further grid refinement, is obtained by checking the numerical results. For a 5-cm diameter and 30-cm long preform/fiber in a 7-cm diameter furnace, the optimal grid number is obtained as 369 × 41 for the preform/fiber and 369 × 61 for the purge gas.

The discretization for the radiation is also nonuniform. Finer grids are used in the preform/fiber near the surface and near the two ends. The radial grid size increases parabolically from the surface to the center line. Similarly, the axial grid size also increases parabolically with the maximum size at midpoint. Due to the large amount of computational time involved, the grid size used for the radiation is much coarser than that used for the transport equations. But this coarse grid size is verified to be fine enough to produce grid-independent results. The optimal grid number is obtained by computational experiments. For a 5-cm diameter and 30-cm long preform/fiber, the optimal radiation grid is obtained as 31 × 6.

In the computation of the radiative source term, the preform/fiber surface is assumed to be diffuse (Yin and Jaluria, 1997; Kaminski, 1995). The radiative source term is computed using the zonal method. For a volume zone, k, in the preform/fiber, the radiative source term can be obtained as (Modest, 1993)

$$S_{rk} = \frac{1}{V_k}\sum_{l=1}^{M}\Big[\sum_{i}\overline{S_iG_k}(J^i_{i,l} - n^2\sigma T^4_k f_{k,l}) + \sum_{j\neq k}\overline{G_jG_k}n^2\sigma(T^4_j f_{j,l} - T^4_k f_{k,l})\Big] \qquad (14)$$

where the subscripts i and j denote the surface and volume zones, respectively. The radiosity on the inner surface of the preform/fiber, $J^i_{i,l}$, is computed using the approach proposed by Yin and Jaluria (1997). The surface-volume direct exchange area, $\overline{S_iG_k}$, and the volume-volume direct exchange area, $\overline{G_jG_k}$, are defined as (Modest, 1993)

$$\overline{S_iG_k} = \int_{A_i}\int_{V_k} a_\lambda \exp(-a_\lambda S_{ik}) \frac{\cos\theta_i}{\pi S^2_{ik}}\, dA_i\, dV_k \qquad (15)$$

$$\overline{G_jG_k} = \int_{V_j}\int_{V_k} \frac{a^2_\lambda \exp(-a_\lambda S_{jk})}{\pi S^2_{jk}}\, dV_j\, dV_k \qquad (16)$$

where a_λ is the spectral absorption coefficient of glass. Its value is taken from Myers (1989). The direct exchange areas are computed using Gaussian quadrature.

Because the radiation grid size is much coarser than that for the energy equation, the radiative source term at the grid points for the energy equation is obtained by linear interpolation from those at the radiation grid points.

The problem is solved sequentially in the false transient manner using the Alternate Direction Implicit (ADI) method. Successive Under Relaxation (SUR), with a relaxation parameter of around 0.1, is used for the temperature and vorticity to obtain convergence for this strongly nonlinear problem (Patankar, 1980; Jaluria and Torrance, 1986). The initial conditions are either taken as no flow, or as the results obtained from earlier runs for similar conditions. In all cases, it was ensured that the

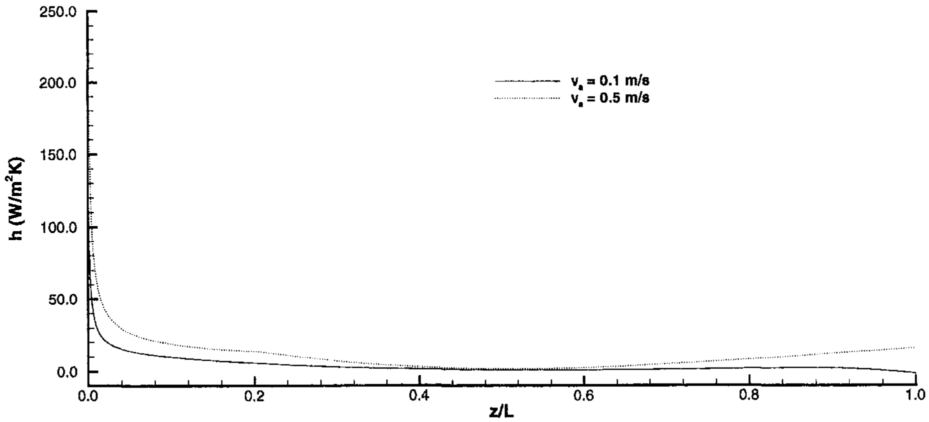

(a) Heat transfer coefficient

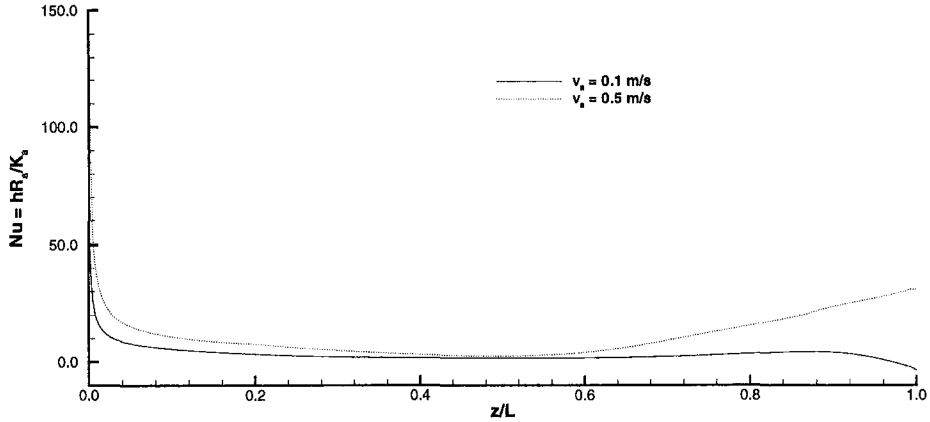

(b) Nusselt number

Fig. 9 The heat transfer coefficient and the Nusselt number for different purge gas velocities

steady-state results were essentially independent of the initial conditions employed. The nonlinear terms are generally linearized by using values from the previous time step. The major uncertainty in the results is introduced by the property data. If these are accurately known, the results have been found to agree very well with earlier experimental and numerical results on similar transport problems. The streamfunction equations for the preform/fiber and the purge gas are first solved, followed by an evaluation of the velocities from the definition of the streamfunction. With the velocity field obtained, the vorticity equations are solved. Finally, the energy equations for the preform/fiber and the purge gas are solved in a similar manner. Because of a specified neck-down profile, typical CPU times were of order 15–30 minutes on a Cray T90 computer. However, these go up to several hours if the profile is also to be determined.

4 Numerical Results and Discussion

4.1 Validation. In modeling the optical fiber drawing process, most of the numerical results (Lee and Jaluria, 1995a, 1996; Myers, 1989; Roy Choudhury and Jaluria, 1998a, b) are based on the Rosseland approximation. Only the results presented by Kaminski (1995) were obtained using the P_1 model, but it was still restricted to the upper neck-down region where the diameter is much larger than that of the fiber and the optically thick assumption is valid. Due to the lack of relevant results in the modeling of the optical fiber drawing process in terms of radiation, it is very difficult to validate the zonal method employed in the present study. In order to get a general idea of how well this method works, the results obtained are compared with those obtained by Kaminski (1995) and those computed using the optically thick approximation as employed by Lee and Jaluria (1995a, 1996) and Roy Choudhury and Jaluria (1998a, b). A cosinusoidal function is assumed for the neck-down profile in these calculations. The computational domain only covers the upper neck-down region with the neck-down starting at $z = 0$. The furnace temperature is assumed to be constant. The values given in Table 1 have been used in the computation (Kaminski, 1995).

The results obtained are presented in Fig. 2. It is seen that the results obtained using the zonal method agree closely with those obtained using the P_1 method (Kaminski, 1995). Due to the fact that the optically thick condition is satisfied in the case considered here, the results obtained using the optically thick approximation also agree well with those obtained using the zonal method and the P_1 method. Several comparisons were also made with experimental and numerical results in the literature on a variety of flow configurations (Roy Choudhury et al., 1995; Roy Choudhury and Jaluria, 1998b) to validate different aspects of this complicated numerical modeling problem. For relatively low draw speeds and small preform diameters, the comparisons with experimental results were found to be very good.

4.2 Parametric Study. Several physical and process parameters have been varied to study their effects on the thermal transport during the drawing of an optical fiber and to determine which parameters and physical effects dominate in the process. The ranges used are based on actual process variables and system parameters in typical practical situations at large draw speeds. For all these results, unless otherwise mentioned, the

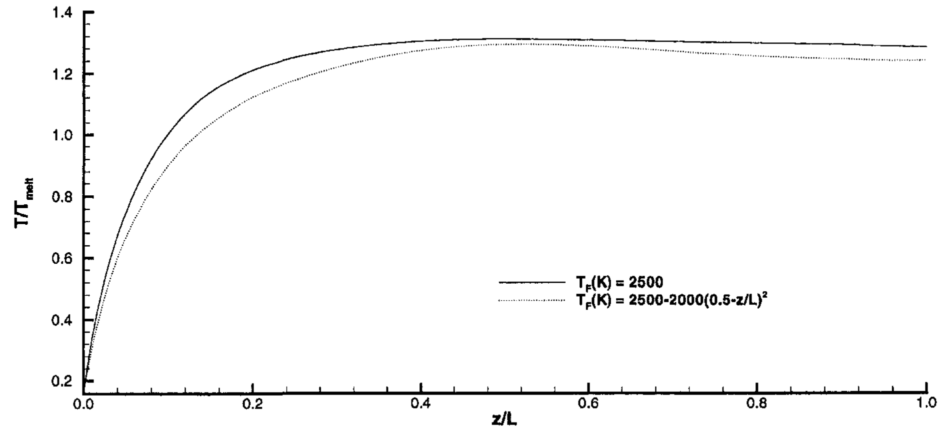

(a) Centerline temperature

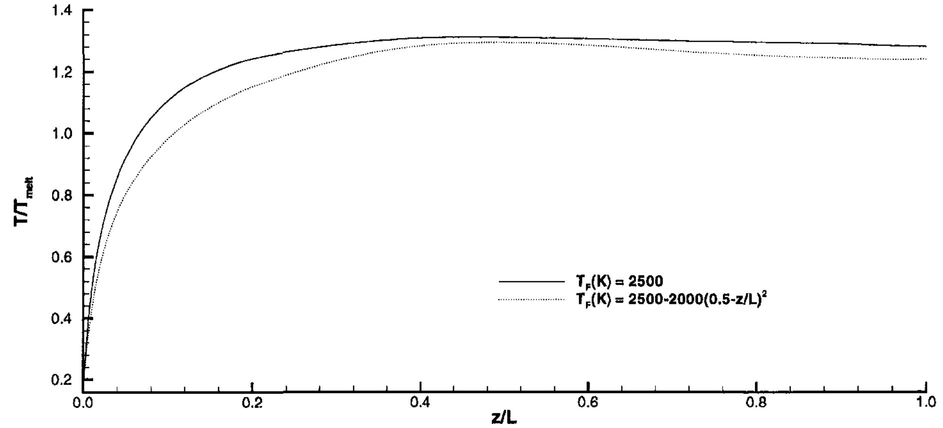

(b) Surface temperature

Fig. 10 Comparisons of preform temperature distributions for two different furnace wall temperature distributions

parameters in Table 2 have been used. The purge gas is taken as argon at constant properties. For the preform/fiber, variable properties taken from Fleming (1964) have been used. The purge gas inflow and outflow are in the same direction as the movement of the preform. Both the preform and the purge gas are assumed to enter the furnace at 300 K. The neck-down region is located between 0.3–0.9 of the furnace length and the neck-down profile is assumed to be a polynomial function with the maximum at $z = 0.3L$, as obtained from the literature (Lee and Jaluria, 1994). All the streamfunction and temperature results are plotted in their nondimensional forms.

Drawing Speed. The effect of the fiber drawing speed is first examined. The furnace is assumed to be isothermal at 2500 K, and the purge gas to enter the furnace at 0.1 m/s. Three different drawing speeds, i.e., 5, 10, and 15 m/s, are considered here. Figure 3 shows the centerline and surface temperature distributions in the preform/fiber. It is seen that in the lower neck-down region, the temperature is almost uniform in the radial direction, but in the upper neck-down region, the temperature difference is significant. The maximum difference lies between 100–300 K. This is mainly due to the larger diameter of the preform and relatively low thermal conductivity of glass.

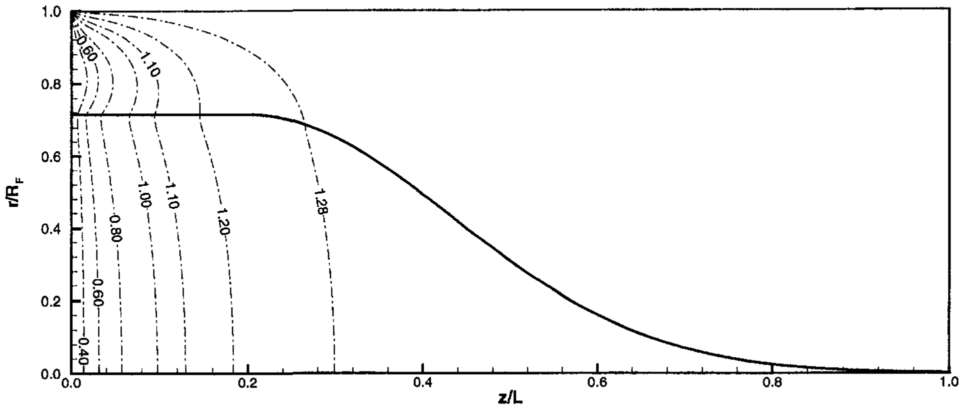

Fig. 11 Isotherms when Helium is used as the purge gas

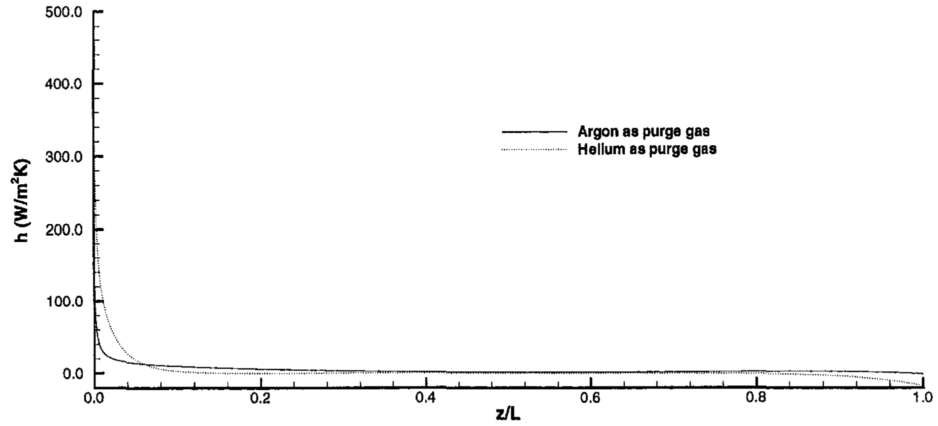

(a) Heat transfer coefficient

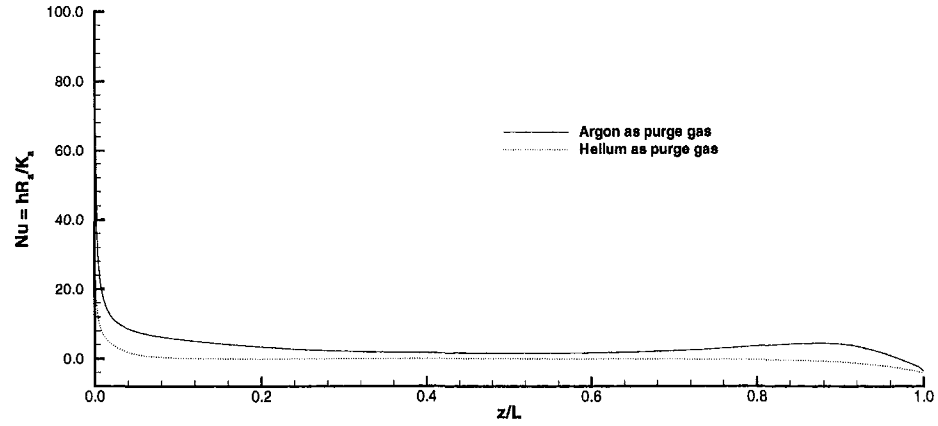

(b) Nusselt number

Fig. 12 The heat transfer coefficient and the Nusselt number for two different purge gases

When the drawing speed increases, the radial temperature difference also increases. Even though this appears to be a relatively small difference, it can have a substantial effect on viscosity because of the exponential dependence on temperature. This, in turn, affects the flow, as well as the defect generation. When the drawing speed increases, the radial temperature difference also increases. It must be noted that, with a speed increase, the profile also changes which will affect the results. However, the general shape has been seen, experimentally and numerically, to remain similar, with most change occurring near the end of neck down.

Figure 4 shows the effect of the drawing speed on the preform/fiber temperature variation with axial distance. It is obvious that, when the drawing speed increases, the preform takes a larger distance to get heated up to the softening point, but, the final temperature levels are fairly close. Also, the centerline temperature is affected more significantly than the surface temperature by the drawing speed. This explains why the radial temperature difference increases with the drawing speed, as mentioned previously.

Figure 5 shows the streamlines for three different drawing speeds while Fig. 6 shows the isotherms for the same drawing conditions. In Fig. 5, the reverse flow at the furnace exit indicated by Roy Choudhury and Jaluria (1998b) is not observed because, in the present computation, the purge gas velocity is much larger than that used in the earlier study (2.6412 cm/s). From the isotherms in Fig. 6, it is seen that when the drawing speed increases, heating the preform up to the same temperature level needs a greater axial distance, as expected. The purge gas is heated up to a lower temperature level, because it remains in the furnace for a shorter time due to the drag imparted by the preform/fiber.

Figure 7 shows the heat transfer coefficient and the Nusselt number distributions for different drawing speeds. It is seen that an increase in drawing speed has little effect on the heat transfer coefficient and the Nusselt number except in the region near the exit. This is because, when the drawing speed increases, the difference between the fiber and the purge gas velocities increases significantly in the region near the exit, while in the upper neck-down region, the change in the velocity difference is very small. Besides, near the exit, the heat transfer coefficient is negative, which means that the fiber is being heated by the purge gas. This occurs because at the exit the radiative loss from the fiber results in its temperature becoming lower than that of the purge gas.

Purge Gas Velocity. The effect of the purge gas velocity is studied by considering two different purge gas velocities at the entrance, i.e., 0.1 and 0.5 m/s. Other parameters are as specified in Table 2. The results are presented in Figs. 8 and 9. Figure 8 shows the streamlines and the isotherms. Unlike the flow field shown in Fig. 5, circulation arises in the purge gas outside the neck-down region due to the high velocity of the purge gas. Because of the existence of this circulation, the temperature of the purge gas outside the neck-down region is raised to a higher level. This is clearly indicated by the fact that, in the purge gas outside the neck-down region, the isotherms are shifted away from the preform/fiber. A comparison of the temperature distributions for two different purge gas velocities showed that an increase in the purge gas velocity had little effect on the temperature variations in the preform/fiber over the range of 0.1–0.5 m/s.

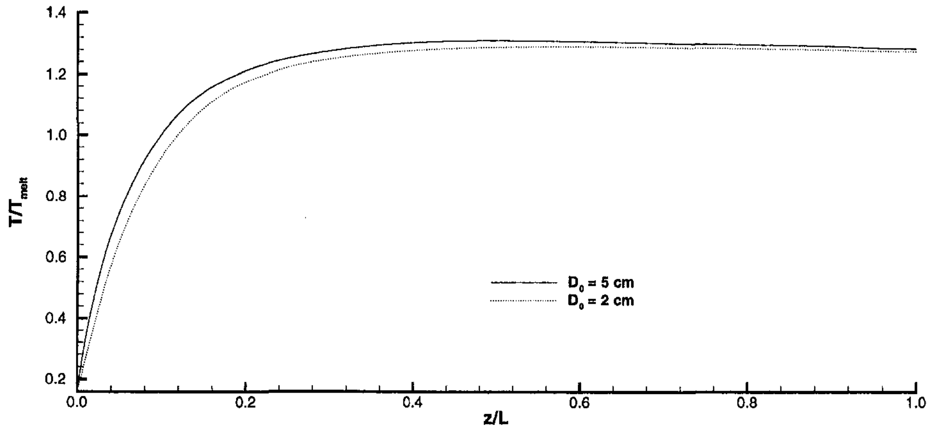

(a) Centerline temperature

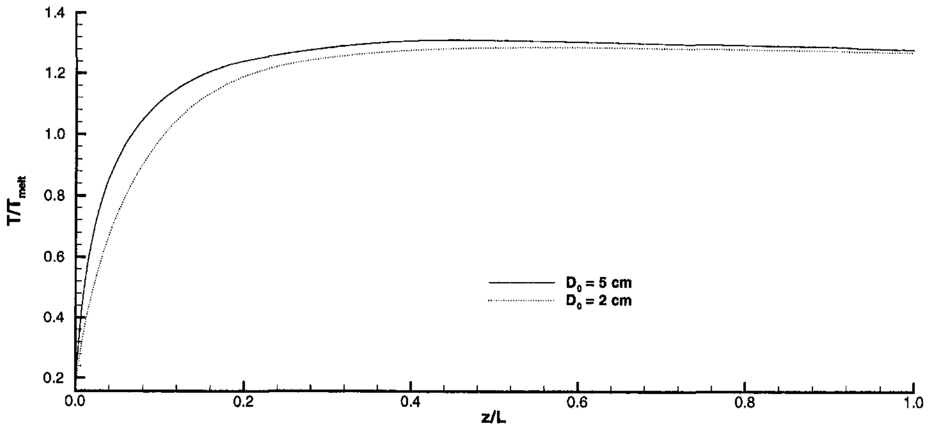

(b) Surface temperature

Fig. 13 Comparisons of preform temperature distributions for two different preform diameters

Figure 9 shows the heat transfer coefficient and the Nusselt number distributions for two different purge gas velocities. It is seen that, when the purge gas velocity increases, the heat transfer coefficient and the Nusselt number also increase, as expected. It is noted that near the exit, the heat transfer coefficient changes from negative to positive when purge gas velocity increases from 0.1 to 0.5 m/s. This means that at low velocities the purge gas heats the fiber near the exit while at high velocities the purge gas is heated by the fiber. Also, near the exit, convection becomes the dominant mode of heat transfer to and from the fiber because of the geometry of the domain and large distance from the heated region of the furnace wall.

Furnace Wall temperature. In order to investigate the effect of furnace wall temperature, two different furnace wall temperature distributions have been used, i.e., a constant temperature distribution of 2500 K and a parabolic temperature distribution with the maximum of 2500 K at the midpoint and 2000 K at both ends. Other parameters are specified in Table 2. The results are presented in Fig. 10, which shows the centerline and surface temperature distributions in the preform/fiber for the two different cases. As expected, the temperature level for the parabolic furnace wall temperature is noticeably lower than that for the constant furnace wall temperature. This means that the furnace wall temperature has a strong effect on the temperature distributions in the preform/fiber.

The heat transfer coefficient and the Nusselt number were also calculated for two cases. The plots clearly indicated that furnace wall temperature distribution has little effect on the convective heat transfer coefficient at the surface of the preform/fiber. This is because the furnace temperature only affects the convective heat transfer coefficient indirectly through the preform/fiber surface temperature, and the effect of the preform/fiber surface temperature on the convective heat transfer coefficient is expected to be weak.

Purge Gas. The effect of purge gas properties is investigated by considering helium and argon, because the former has a much larger thermal diffusivity than the latter. The results are presented in Figs. 11 and 12. Figure 11 shows the isotherms for helium, indicating the rapid heating up of the purge gas and the smaller temperature difference across the medium. These trends are quite different from those for argon (see Fig. 6). A comparison of the temperature variations in the preform/fiber with argon and helium as purge gases also showed that helium is quickly heated up to a temperature higher than that at the preform/fiber surface. Therefore, the preform/fiber gains heat from the helium so that its temperature becomes higher than that with argon. But, the difference was found to be quite small because, compared with thermal radiation, convection between the purge gas and the preform/fiber is not a very significant contributor to the overall heating.

Figure 12 compares the heat transfer coefficients and the Nusselt numbers for argon and helium. It is seen that near the entrance, helium has a much higher heat transfer coefficient, as expected from its higher thermal conductivity and rapid heating up, while in the rest of the region, both gases have almost the same heat transfer coefficient.

Preform Diameter. In order to study the effect of the preform diameter, a 2-cm diameter preform is considered and the results are compared with those for a 5-cm diameter preform.

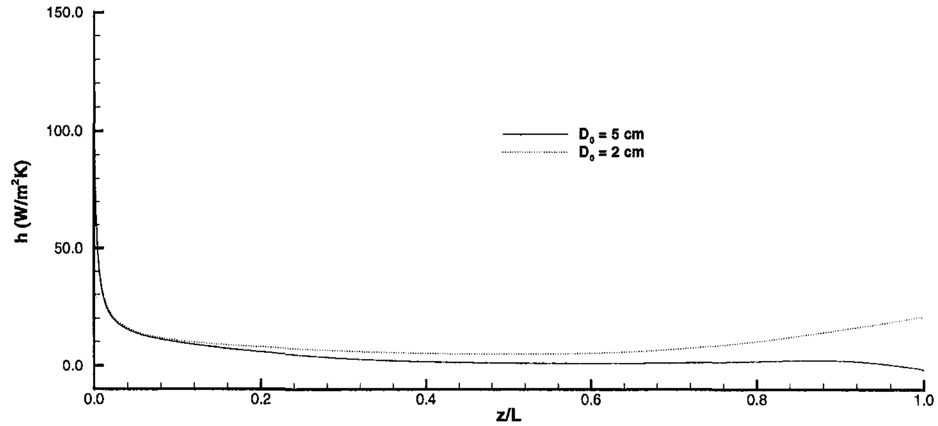

(a) Heat transfer coefficient

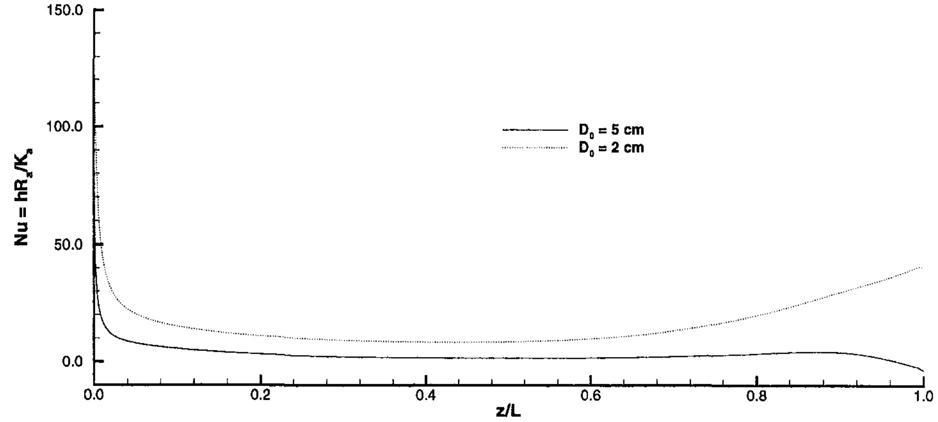

(b) Nusselt number

Fig. 14 The heat transfer coefficient and the Nusselt number for two different preform diameters

The results are presented in Figs. 13 and 14. Figure 13 shows the preform temperature distributions for two different diameter preforms. It is seen that the 2-cm diameter preform has a lower temperature level than the 5-cm diameter preform. This occurs because of three reasons. First, the 2-cm diameter preform has a smaller volume so that it absorbs less radiative energy. Secondly, the 2-cm diameter preform has a higher velocity for the same drawing speed so that it stays in the furnace for a shorter time. Thirdly, the 2-cm diameter preform has a larger purge gas flow rate due to the larger cross-sectional area between the furnace and the preform surface, resulting in stronger cooling from the purge gas.

Figure 14 shows the heat transfer coefficient and the Nusselt number for the two different diameter preforms. It is seen that the 2-cm diameter preform has a higher convective heat transfer coefficient. Because of the higher flow rate of purge gas for the 2-cm diameter preform, the purge gas is heated up to a lower temperature level. Therefore, the preform is cooled more strongly, resulting in a higher heat transfer coefficient. In addition, the 2-cm diameter preform has a higher velocity, also resulting in a higher heat transfer coefficient.

5 Conclusions

In the present study, a prescribed neck-down profile on the basis of results in the literature has been used. Different physical and process parameters, such as fiber drawing speed, purge gas velocity, furnace wall temperature, purge gas type, and preform diameter, have been varied to investigate their effects on the thermal transport and to determine the dominant parameters. Based on the results and discussion presented above, it is found that the fiber drawing speed, the furnace wall temperature and the preform diameter have significant influence on the preform/fiber temperature variation, while the purge gas velocity and type have a minor effect. An increase in the furnace temperature or preform diameter raises the preform/fiber temperature level, while an increase in the fiber drawing speed lowers the preform/fiber temperature level. Since an increase in the temperature level of the furnace is generally not desirable due to the adverse effect on the life of the heater and on the generation of defects in the fiber, an increase in the length of the heating zone of the furnace is preferred for supplying the energy input at higher draw speeds.

The convective heat transfer coefficient at the preform/fiber surface is affected mainly by the purge gas velocity and the preform diameter. When the purge gas velocity is increased or the preform diameter is decreased, the heat transfer coefficient is increased, as expected. The fiber drawing speed has very little effect on the heat transfer coefficient except in the region near the exit where the magnitude of the heat transfer coefficient is increased, though the values are negative, when the drawing speed is increased. Helium is found to lead to a higher heat transfer coefficient than argon in the region near the entrance due to the larger thermal conductivity of the former. The furnace wall temperature is found to have minor effect on the heat transfer coefficient at the preform/fiber surface. Though radiation is the dominant mode for the overall heating of the preform.fiber, convection is important near the end of the neck-down region because of reduced radiation there. Therefore, the results obtained on convection are valuable in the design and optimization of the furnace.

In this study, because the neck-down profile is prescribed, rather than numerically generated, the conclusions obtained here may be somewhat different from those obtained when the neck-down profile is generated for practical systems. However, the prescribed shape is based on actual measurements and simulation results in the literature. The effect of the dominant parameters need further study with the generation of the neck-down profiles. The current investigation provides a basis for that study.

Acknowledgments

The authors acknowledge the financial support provided by the National Science Foundation, under Grant Nos. DDM-92-13458 and DMI-96-33194, and the computing facilities provided by the Pittsburgh Supercomputing Center, Under Grant No. CBT920017P, for this work. Helpful discussions with Profs. C. E. Polymeropoulos and G. H. Sigel and with Dr. S. Roy Choudhury are also acknowledged.

References

Ball, K. S., Song, M., and Bergman, T. L., 1997, "A Model for Radiative and Convective Cooling of a Semitransparent Molten Glass Jet," *Proc. 1997 Nat. Heat Transfer Conf.*, ASME HTD-Vol. 347, pp. 231–240.

Burmeister, L. C., 1983, *Convective Heat Transfer*, John Wiley and Sons, New York.

Fleming, J. D., 1964, "Fused Silica Manual," Final Report for the U.S. Atomic Energy Commission, Oak Ridge, TN, Project No. B-153.

Glicksman, L. R., 1968, "The Dynamics of a Heated Free Jet of Variable Viscosity Liquid at Low Reynolds Numbers," ASME *Journal of Basic Engineering*, Vol. 90, pp. 343–354.

Jaluria, Y., and Torrance, K. E., 1986, *Computational Heat Transfer*, Taylor and Francis, Washington, DC.

Kaminski, D. A., 1995, "Thermal Transport in Optical Fiber Manufacturing," *Proceedings of the First International Symposium on Radiative Heat Transfer*, M. Pinar Menguc, ed., Begell House, New York, pp. 667–681.

Lee, S. H.-K., and Jaluria, Y., 1994, "The Effects of Variable Viscosity and Viscous Dissipation on the Flow and Thermal Transport during Optical Fiber Drawing," *Proceedings of 10th International Heat Transfer Conference*, Vol. 7, Taylor and Francis, Washington, DC, pp. 303–308.

Lee, S. H.-K., and Jaluria, Y., 1995a, "The Effects of Geometry and Temperature Variations on the Radiative Transport during Optical Fiber Drawing," *Journal of Material Processing and Manufacturing Science*, Vol. 3, pp. 317–331.

Lee, S. H.-K., and Jaluria, Y., 1995b, "Effects of Streamwise Convergence in Radius on the Laminar Forced Convection in Axisymmetric Ducts," *Numerical Heat Transfer*, Vol. 28, pp. 19–38.

Lee, S. H.-K., and Jaluria, Y., 1996, "Effects of Variable Properties and Viscous Dissipation During Optical Fiber Drawing," ASME JOURNAL OF HEAT TRANSFER, Vol. 118, pp. 350–358.

Li, T., ed., 1985, *Optical Fiber Communication, Vol. 1: Fiber Fabrication*, Academic Press, Orlando, FL.

Modest, M. F., 1993, *Radiative Heat Transfer*, McGraw-Hill, New York.

Myers, M. R., 1989, "A Model for Unsteady Analysis of Preform Drawing," *AIChE J.*, Vol. 35, pp. 592–602.

Paek, U. C., and Runk, R. B., 1978, "Physical Behavior of the Neck-down Region during Furnace Drawing of Silica Fibers," *Journal of Applied Physics*, Vol. 49, pp. 4417–4422.

Pantankar, S. V., 1980, *Numerical Heat Transfer and Fluid Flow*, Hemisphere, New York.

Roy Choudhury, S., 1995, "Thermal Transport in the Optical Fiber Drawing Process," Ph.D. Thesis, Rutgers University, New Brunswick, NJ.

Roy Choudhury, S., and Jaluria, Y., 1998a, "Practical Aspects in the Drawing of an Optical Fiber," *J. Mater. Res.*, Vol. 13, pp. 483–493.

Roy Choudhury, S., and Jaluria, Y., 1998b, "Thermal Transport Due to Material and Gas Flow in a Furnace for Drawing an Optical Fiber," *J. Mater. Res.*, Vol. 13, pp. 494–503.

Roy Choudhury, S., Jaluria, Y., and Lee, S. H.-K., 1995, "Generation of Neck-Down Profile for Furnace Drawing of Optical Fiber," *Proceedings of the ASME Heat Transfer Div.*, Vol. 306, ASME, New York, pp. 23–32.

Sayles, R., 1982, "A Finite Element Analysis of the Upper Jet Region of a Fiber Drawing Flow Field," Ph.D. Thesis, Brown University, Providence, RI.

Sayles, R., and Caswell, B. A., 1984, "A Finite Element Analysis of the Upper Jet Region of a Fiber Drawing Flow Field of a Temperature Sensitive Material," *International Journal of Heat and Mass Transfer*, Vol. 27, No. 1, pp. 57–67.

Yin, Z., 1997, "Numerical Investigation of Thermal Transport in Optical Fiber Drawing Processes," Ph.D. Thesis, Rutgers University, New Brunswick, NJ.

Yin, Z., and Jaluria, Y., 1997, "Zonal Method to Model Radiative Transport in an Optical Fiber Drawing Furnace," ASME JOURNAL OF HEAT TRANSFER, Vol. 119, No. 3, pp. 597–603.

M. Song
Department of Mechanical Engineering,
Dongguk University,
Seoul 100-715, Korea

K. S. Ball
Department of Mechanical Engineering,
The University of Texas at Austin,
Austin, TX 78712-1063
e-mail: kball@burst.me.utexas.edu
Mem. ASME

T. L. Bergman
Department of Mechanical Engineering,
The University of Connecticut,
Storrs, CT 06269-3139
Fellow ASME

A Model for Radiative Cooling of a Semitransparent Molten Glass Jet

A mathematical model for the radiative cooling of a semitransparent molten glass jet with temperature-dependent viscosity has been developed and is implemented numerically. The axial velocity and jet diameter variations along the length of the jet, the axial bulk mean temperature distributions, and the centerline-to-surface glass temperature distributions are determined for different processing conditions. Comparisons are also made between the semitransparent predictions, which are based on a spectral discrete ordinates model, and predictions for an opaque medium.

Introduction

Transfer of molten glass from location to location typically involves a pouring process, during which a stream of glass is driven by gravity and cooled by combined convective and radiative heat transfer. This study of the thermal and fluid mechanics aspects of glass pouring is motivated by the glass casting of vitrified, surplus weapons-grade plutonium (National Academy of Sciences, 1994; see also Marples, 1988, for a more general review of the vitrification of nuclear wastes). Here, plutonium is diluted into a solution of silicon oxide and metal oxides, and encapsulated within a small ''can'' that is approximately 75 mm in diameter and 425 mm in height. The cans containing vitrified plutonium are then suspended on a rack that is placed inside a larger ''canister,'' which is 600 mm in diameter and 3 m tall and initially at room temperature. To provide a proliferation barrier between the plutonium and the population at large, this ''can-in-canister'' structure is subsequently back filled with molten glass containing high-level radioactive waste. Finally, the rigidified glass logs are stockpiled and stored underground.

The canister filling operation is accomplished by a continuous pour of a thin stream (approximately 1 ~ 10 mm) of molten glass lasting 24 hours. As the glass cools, its viscosity increases by several orders of magnitude. The ability of high-level waste glass to fill the narrow passages between the cans, the rack, and the canister wall (especially at lower temperatures and correspondingly higher viscosities) is of paramount importance. Also, void formation within the glass log due to the entrapment of gas is undesirable. Gas can become trapped within the molten glass as a result of the gravity jet's impingement upon the glass pool within the canister; this entrainment process is highly dependent upon the viscosity of the jet (Ball et al., 1996; Gomon, 1997). To predict the glass viscosity during filling, a model has been developed to determine the temperature distribution within a molten glass jet. This study builds upon the existing literature involving (i) gravity-driven viscous jets and (ii) radiative-convective cooling of semitransparent media (in particular, glass).

One of the first studies to approximate the axial velocity distribution of a two-dimensional liquid was made by Taylor (1959). Similarity solutions for the flow field within an axisymmetric viscous gravity jet have been found under the assumptions of negligible surface tension and large Reynolds number (Wilson, 1986). Joseph et al. (1983) considered the effects of surface tension, but confined their attention to stable jets. Stability analyses, which take into account the interaction between the viscous jet and the ambient medium, have been reported only for nonaccelerating jets (Nayfeh, 1970; Sterling and Sleicher, 1975). The behavior of viscous gravity-driven jets with highly variable temperature-dependent viscosity has not been considered previously.

At high temperatures, glass is semitransparent to thermal radiation so that if the viscosity distribution within the jet is of interest, an appropriate radiation model must be applied within the glass. The model should account for the specularly reflecting boundaries, as well as the spectral dependence of the radiative properties of the glass (Lee and Jaluria, 1993; Song and Viskanta, 1996). Note that considerable attention has been recently directed to the development of thermal and hydrodynamic models to predict the coupled ''neck-down'' and temperature distribution within optical fibers during drawing—a process that is similar to the problem of interest here. Utilization of effective thermal conductivities to account for the volumetric emission and absorption of thermal radiation has been reported (Paek and Runk, 1978), as has detailed treatment of the surface-to-surface radiation (Lee and Jaluria, 1993). Kaminski (1995) developed the necessary boundary conditions to utilize the P_1 approximation within the neck-down region to account for the specularly reflecting boundaries of the glass-gas interface. Kaminski (1995) and Issa et al. (1995) reviewed various models for the optical fiber drawing process. More recently, Lee and Jaluria (1996) considered variable property effects and viscous dissipation in their model of the neck-down process, and Yin and Jaluira (1997) applied the zonal method to assess the validity of the widely used optically thick approximation for predictions of the radiative heat flux in the neck-down region.

In this study, a viscous gravity-driven molten glass jet that is cooled by convective and radiative heat transfer is modeled in order to predict the temperature (viscosity) of the glass at a region far downstream (tens of jet diameters) of the inlet. The velocity distribution is assumed to be one-dimensional (radial variations of the axial velocity are neglected), while the temperature distribution varies both axially (due to advection and diffusion) and radially (due to radiation and diffusion). The spectral variation of the glass properties is accounted for, as is the specular reflection at the glass-gas interface. To test the sensitivity of the results to conjugate effects involving the transparent

---

Contributed by the Heat Transfer Division for publication in the JOURNAL OF HEAT TRANSFER and presented at NHTC '97. Manuscript received by the Heat Transfer Division, Sept. 9, 1997; revision received, Mar. 30, 1998. Keywords: Jets, Materials Processing and Manufacturing Process, Radiation. Associate Technical Editor: P. Menguc.

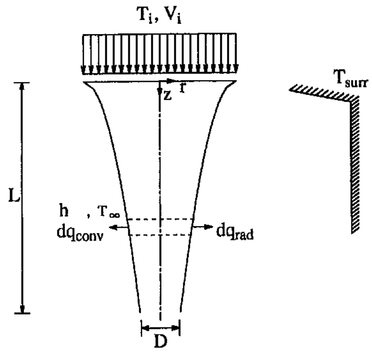

Fig. 1 Model geometry and coordinate system

gas, predictions are reported for cases in which various convective heat transfer coefficients are applied at the glass-gas interface.

Although experimental correlations are available for the heat transfer coefficient in the optical fiber drawing process (Paek and Kurkjian, 1975), they are based on assumptions of laminar flow with negligible buoyancy effects, which are typically encountered in cooling glass fibers (Glicksman, 1968a, 1968b). Note that in this study values of the convection heat transfer coefficient are assigned, rather than estimated via use of a correlation. At the slow pour rates and large length scales considered here, buoyancy effects in the ambient gas are very important and will be affected by conduction and radiation within the glass jet due to conjugate effects. Also, highly turbulent mixed convection occurs in the gas at the glass-gas interface (this has been verified experimentally using flow visualization studies). Moreover, the jet surface is one of neither uniform temperature nor uniform heat flux, and complicated recirculation patterns develop in the gas since the glass jet is flowing into a fixed container in the application of interest. Modest levels of thermal stratification may also develop within the gas held in the container, further affecting the gas phase velocities and in turn the value of h. No correlations exist to reliably predict the value of the heat transfer coefficient for this situation, and the values specified in this study span the range that is expected to exist.

Mathematical Models

A schematic of the model geometry is shown in Fig. 1 together with the coordinate system employed. A circular molten glass jet having a uniform inlet temperature, T_i, and velocity, V_i, enters the calculation domain at $z = 0$. As the jet travels downward, the stream of molten glass is accelerated by the gravity force (in excess of viscous drag), and the jet diameter decreases. The bulk mean temperature of the jet also decreases due to radiative heat transfer to the surroundings and convective cooling by the ambient gas. The temperatures of the ambient gas and surroundings are taken to be uniform and constant (300 K). The surroundings are assumed to be large relative to the jet (i.e., there are no near or far-field obstacles for radiative exchange outside the jet), corresponding to the filling of an empty canister.

Hydrodynamic Model. In the hydrodynamic analysis, it is assumed that the flow is incompressible, laminar, and axisymmetric. The radial distribution of axial velocity is assumed to be uniform at any given axial location since the shear stress exerted on the surface of the jet by the ambient gas is negligible. The assumption of a one-dimensional axial velocity profile is valid except very near the inlet, where the curvature of the jet surface in the axial direction is significant.

For a freely falling jet, the flow is stable (steady) and the occurrence of jet break-up is precluded under the assumption of negligible surface tension and negligible momentum of entrained ambient gas (Nayfeh, 1970). The assumption of a stable jet may not be justified at far downstream distances. For a constant velocity jet, the growth rate of disturbances is enhanced as surface tension increases and viscosity decreases (Sterling and Sleicher, 1975). Analytical methods to determine the break-up length of an accelerating and cooling jet are not yet available. If the cooling rate is sufficiently large along the jet, the glass stream can rigidify without break-up due to significantly increased viscosity.

Since glass can be treated as a Newtonian fluid above its transition temperature (Viskanta, 1994), the momentum equation to be solved for the axial velocity is

$$\rho V \frac{dV}{dz} = \frac{d}{dz}\left(2\mu \frac{dV}{dz}\right) - \frac{2\mu}{V}\left(\frac{dV}{dz}\right)^2 + \rho g. \qquad (1)$$

The first two terms on the RHS of Eq. (1) represent the internal viscous forces (Joseph et al., 1983), while the last term represents the body force. The momentum equation is strongly coupled with the energy equation through the temperature-dependent viscosity, which can vary by as much as two orders of magnitude over the range of temperatures of interest (700°C $\le T \le$ 1000°C). The appropriate boundary conditions for the momentum equation are

$$z = 0\colon V = V_i; \quad z = L\colon \frac{dV}{dz} = 0, \qquad (2)$$

i.e., the jet becomes fully developed hydrodynamically at the downstream boundary of the calculation domain. In order to justify the downstream hydrodynamic condition, predictions for

Nomenclature

A = cross-sectional area (m^2)
c = specific heat (J/kg·K)
D = jet diameter (m)
E = emissive power (W/m^2)
g = gravitational acceleration (m/s^2)
h = convective heat transfer coefficient (W/m^2·K)
I = radiative intensity (W/m^2·sr)
k = thermal conductivity (W/m·K)
L = jet length (m)
$\dot{m}$ = mass flow rate (kg/s)
n = refractive index
q_C = convective heat flux (W/m^2)
q_R = radiative heat flux (W/m^2)
R = jet radius (m)
r = radial coordinate (m)
T = temperature (°C)
$\bar{T}$ = bulk mean temperature (°C)
V = axial velocity (m/s)
$\dot{V}$ = volumetric flow rate (mm^3/s)
z = axial coordinate (m)

Greek symbols

ε = emissivity
θ = angle of incidence, transmission, or reflection
κ = absorption coefficient (m^{-1})
λ = wavelength (μm)
μ = viscosity (Pa·s)
ν = frequency (s^{-1})
ρ = density (kg/m^3) or reflectivity
Ω = solid angle (sr)

Subscripts

0 = band-averaged quantity
b = blackbody value
c = critical value or center
i = inlet
opaque = opaque medium
s = surface
surr = surroundings
ν = spectral quantity
∞ = ambient

different values of L were compared. The maximum difference (over the range $0 < z \leq 3$ m) between the predicted local velocities for $L = 3$ m and $L = 6$ m is less than 0.2 percent.

Conservation of mass relates the jet radius to the axial velocity:

$$\dot{m} = \pi R^2 \rho V. \tag{3}$$

Thus, the pour rate is proportional to the square of the inlet jet diameter if the inlet velocity is held fixed.

Thermal Model. The following assumptions are made in developing the thermal model: (i) the transport of thermal energy is steady and axisymmetric, (ii) axial diffusion and radiation heat transfer within the jet are negligible compared to the axial advection of thermal energy, (iii) the radial advection of thermal energy is negligible compared to the radial diffusion and radiation heat transfer, (iv) the medium emits and absorbs but does not scatter thermal radiation, (v) the medium is in local thermodynamic equilibrium, thus Planck's and Kirchhoff's laws are invoked, (vi) the spatial dimensions of the medium are much larger than the radiation wavelengths for the semitransparent band, i.e., the coherence effect is negligible, (vii) the refractive index of the medium is constant; therefore, refraction of radiation within the medium is absent, (viii) the interface between the medium and the ambient gas is optically smooth, and (ix) the convection heat transfer coefficient is uniform along the length of the jet. The second and third assumptions are valid since molten glass is characterized by a high Prandtl number, and the jet stream is relatively long and thin.

The equation describing the combined advective, diffusive, and radiative heat transfer within the jet is

$$\rho V c \frac{dT}{dz} = \frac{1}{r}\frac{d}{dr}\left(k\frac{dT}{dr}\right) - \nabla \cdot q_R. \tag{4}$$

The appropriate boundary conditions are

$$z = 0\colon T = T_i; \quad r = 0\colon \frac{dT}{dr} = 0 \tag{5a}$$

$r = R$:

$$-k\frac{dT}{dr} = h(T - T_\infty) + \varepsilon\sigma(T^4 - T^4_{\text{surr}})\frac{\displaystyle\int_{\text{opaque}} E_{b\nu}d\nu}{\displaystyle\int E_{b\nu}d\nu}. \tag{5b}$$

The first and second terms on the RHS of Eq. (5b) are, respectively, the convective cooling and the radiative cooling at the opaque wave frequency band. (For a semitransparent medium, only the opaque wave frequency band contributes to the surface heat flux; in effect there is no surface for transparent frequencies.)

In order to solve for the temperature field, the divergence of the radiative heat flux is determined from the radiative intensity:

$$\nabla \cdot q_R = \int_\nu \kappa_\nu\left(4\pi n^2 I_{b\nu} - \int_{4\pi} I_\nu d\Omega\right)d\nu. \tag{6}$$

The general form of the spectral radiative transfer equation can be written (Modest, 1993):

$$(\mathbf{\Omega}\cdot\nabla)I_\nu(r, z, \mathbf{\Omega}) = \kappa_\nu[I_{b\nu}(T, n) - I_\nu(r, z, \mathbf{\Omega})]. \tag{7}$$

Equations (4) and (7) are coupled through Eq. (6) and $I_{b\nu}$, which is determined from the medium temperature utilizing Planck's function. The boundary condition for Eq. (7) at the optically smooth bounding surfaces is

$$I_\nu(r, z, \mathbf{\Omega}) = [1 - \rho(\theta)]I_{b\nu}(T_{\text{surr}}, n) + \rho(\theta)I_\nu(r, z, \mathbf{\Omega}') \tag{8}$$

which applies for $\mathbf{\Omega}\cdot\mathbf{n} > 0$, where $\mathbf{n}$ is the inward normal at the interface, $\theta = \cos^{-1}(\mathbf{\Omega}\cdot\mathbf{n})$, and $\mathbf{\Omega}' = 2(\mathbf{\Omega}\cdot\mathbf{n})\mathbf{n} - \mathbf{\Omega}$.

When the radiation is refracted into the ambient gas from the glass jet, the angle of transmission approaches 90 deg as the incident angle increases toward the critical angle $\theta_c = \sin^{-1}(n^{-1})$. For an incident angle larger than θ_c, the outgoing radiation is totally reflected inward. The incoming radiation from the surrounding wall is concentrated into the solid angle associated with the transmission angles, all of which are smaller than θ_c. For an incident angle smaller than θ_c, the relation between the magnitudes of the incident and reflected radiative energy at the smooth interface is well represented by Fresnel's law under the assumption of a weakly absorbing medium. Taking Snell's and Fresnel's laws into account, the reflectivity in Eq. (8) is

$$\rho(\theta) = \begin{cases} 1 & \theta \geq \theta_c \\ \dfrac{1}{2}\left(\dfrac{\cos\theta - nP}{\cos\theta + nP}\right)^2 + \dfrac{1}{2}\left(\dfrac{n\cos\theta - P}{n\cos\theta + P}\right)^2 & \theta < \theta_c \end{cases} \tag{11}$$

where

$$P = \sqrt{1 - n^2\sin^2\theta}.$$

Solution Procedure

Due to the coupling between the flow and temperature fields, in particular the temperature dependent viscosity, an iterative solution procedure is employed. Specifically, the one-dimensional axial velocity distribution and two-dimensional temperature distribution are alternately determined, while the local viscosity is updated corresponding to the bulk mean temperature at a given axial location, defined as $\bar{T}(z) = \int T\rho V dA / \int \rho V dA$. At the start of the calculation, the axial velocity and jet diameter distributions are evaluated under the inviscid flow assumption from Eqs. (1) and (3). The solution procedure is considered converged when the maximum change in nodal temperature values is less than 0.01 percent.

Equations (1), (4), and (7) are solved using a standard finite volume method. In short, the computational domain is discretized into finite control volumes, and the governing differential equations are integrated over these control volumes to yield a set of coupled algebraic equations. The locations of the control surfaces for the axial velocity and temperature are staggered in the z-direction, and the geometric-mean formulation is used to evaluate the viscosity.

Since Eqs. (4) and (7) are strongly coupled, additional iterations are required to update the temperature and radiative intensity distributions simultaneously. Owing to the parabolic nature of the thermal energy equation, a marching procedure is used to solve Eqs. (4) and (7), in which the temperature and radiative intensity distributions at a given z-location are determined implicitly from the known upstream distributions through the additional iterations.

In order to approximate the directional distribution of the radiative intensity, the radiative transfer equation is discretized (directionally) using discrete ordinates, in addition to the spatial discretization. A detailed discussion regarding the solution method (and its validation) for the radiative intensity field having specularly reflecting boundaries is given by Song and Viskanta (1996). For all cases discussed here, the S_4-quadrature and the exponential-type interpolation scheme are applied. This approach was validated by Song and Viskanta (1996) by comparing the predicted radiative fluxes with those based upon the integral solution for one-dimensional radiative transfer within

Table 1 Thermophysical properties of simulated waste glass

ρ	c	k
2220	1240	1.82
	$\mu(\bar{T}) = 0.1 \exp(36.5 - 0.0491\,\bar{T} + 1.83 \times 10^{-5}\,\bar{T}^2)$	

a semitransparent plate, and was found to provide accurate results over a wide range of the relevant parameters.

The thermophysical properties are based upon measurements reported by Soper and Bickford (1982) for simulated nuclear waste glasses used for vitrification studies at the DOE Savannah River Site, and are given in Table 1. The viscosity data were measured over the temperature range 800–1200°C; the other properties are assumed to be constant. Since the optical properties of the simulated waste glasses are not known, the refractive index and absorption coefficients are assumed to be the same as soda-lime glass (Field and Viskanta, 1990; Rubin, 1985) and are given in Table 2. The refractive index is taken to be constant, while the variation of the absorption coefficient with temperature is assumed to be negligible compared to its variation with wavelength (Field, 1989). The spectral variation of the absorption coefficient is taken into account by utilizing a five band approximation over the wavelength range $\lambda \le 5\ \mu$m. The medium is considered to be opaque for $\lambda > 5\ \mu$m. Field and Viskanta (1990) found that the sensitivity of temperature predictions to the number of spectral bands is negligible when five or more bands are used to model the absorption coefficient.

Results and Discussion

Predictions of axial velocity, jet diameter, and temperature distributions are obtained for extensive ranges of the volumetric pour rate, inlet temperature, and convection heat transfer coefficients. For selected cases, the influences of inlet jet velocity and absorption coefficient for thermal radiation were also examined.

The results were generated using a 22 × 52 grid in the r and z-directions, respectively. The distribution of the nodes was not uniform, but was more compact near the jet surface and inlet to resolve the relatively steep spatial changes in the physical variables expected in these regions. The predicted temperatures using a 22 × 52 grid differed by less than one percent from those obtained using a 42 × 102 grid along the entire length of the jet, except in the immediate vicinity of the inlet (first 20 mm) where differences of less than five percent were observed. However, the assumption of a one-dimensional axial velocity profile breaks down very near the inlet (as discussed earlier), so the results are not meaningful there and grid independence was not pursued in this region.

The jet diameters at three different pour rates are shown in Fig. 2 for an inlet velocity of 0.1 m/s. A 50 percent reduction in jet diameter occurs within the first 20 mm from the inlet; further changes in diameter with increasing distance occur gradually. Thus, the assumption of one-dimensional velocity is valid over about 99 percent of the jet length. The jet diameters for different pour rates are nearly similar; exact similarity is achieved in the limit of inviscid flow with negligible inlet velocity, i.e., the Torricelli limit (Joseph et al., 1983). The small deviations in the similarity of the jet diameter profiles originate from the effects of the internal viscous force.

Table 2 Optical properties of soda-lime glass

λ	0~1.0	1.0~1.8	1.8~2.6	2.6~3.8	3.8~5.0
κ_0	27.5	43.1	29.9	291.0	4820.0
n			1.46		

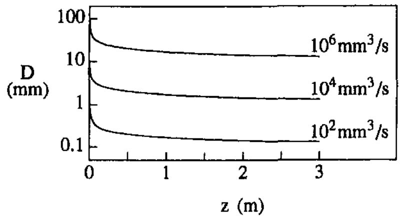

Fig. 2 Effect of pour rate on jet diameter (T_i = 1000°C, h = 50 W/m$^2\cdot$K and V_i = 0.1 m/s)

In Fig. 3, the axial velocity profiles with different inlet velocities are compared to the Torricelli limit $V = \sqrt{2gz}$. The lowest inlet temperature (highest viscosity) case considered is presented in Fig. 3, to provide the most conservative assessment of the effects of viscosity. When the inlet velocities are relatively small (0.01 and 0.1 m/s), the axial velocities follow the Torricelli limit to within one percent except for the first 50 mm near inlet, implying that viscous drag is not significant. In all cases, the gradient of axial velocity decreases with increasing z, diminishing the viscous drag.

Next, the axial temperature profiles are shown in Fig. 4 at three different pour rates. Among the parameters considered, the pour rate has the most significant effect on the cooling rate and consequently the bulk mean temperature gradient. The average (over the entire length of the jet) bulk mean temperature gradients are 2.7, 20.6, and 131 K/m when the pour rates are 10^6, 10^4, and 10^2 mm^3/s, respectively.

It is interesting to note that the axial velocities are not sensitive to changes in pour rate, despite the significant axial variation in the medium temperature and hence viscosity. (The viscosity of soda-lime glass increases by two orders of magnitude as the temperature drops from 1000°C to 700°C, which matches the temperature drop experienced by the jet for a pour rate of 10^2 mm^3/s). It can be concluded that the internal viscous drag does not exert a significant resistance to the acceleration of the jet by gravity. Near the inlet, the velocity gradients are significant but the viscosity is small; further downstream, the viscosity

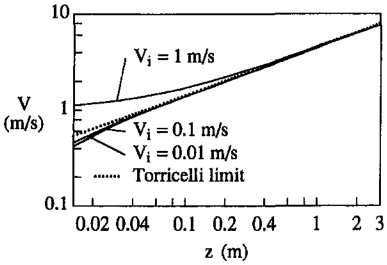

Fig. 3 Effect of V_i on axial velocity profiles ($\dot{V}$ = 10^4 mm^3/s, T_i = 800°C, h = 100 W/m$^2\cdot$K)

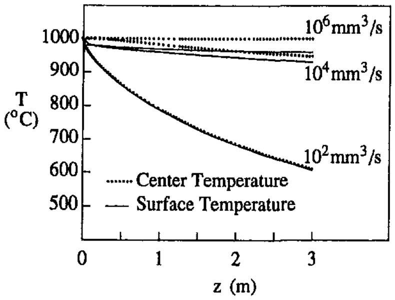

Fig. 4 Effect of pour rate on temperature profiles (T_i = 1000°C, h = 50 W/m$^2\cdot$K and V_i = 0.1 m/s)

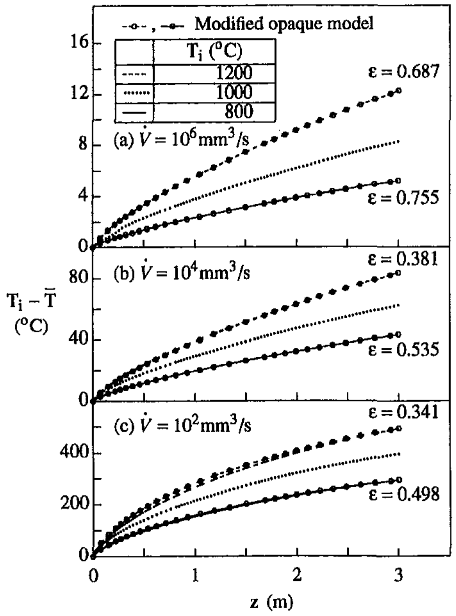

Fig. 5 Effect of T_i on bulk mean temperature drop (h = 50 W/m^2·K)

is large but the relatively small velocity gradients minimize the viscous drag.

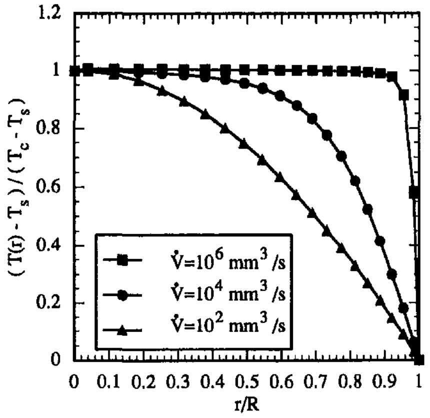

Fig. 7(*a*) Effect of $\dot{V}$ on radial temperature profiles at z = 107 mm (T_i = 1000°C and h = 50 W/m^2·K)

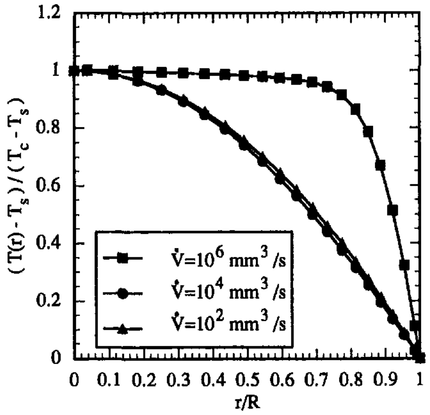

Fig. 7(*b*) Effect of $\dot{V}$ on radial temperature profiles at z = 3 m (T_i = 1000°C and h = 50 W/m^2·K)

The effects of inlet temperature on the bulk mean temperature and on the radial temperature difference are shown in Figs. 5 and 6, respectively, for a convection heat transfer coefficient of 50 W/(m^{2}K). (The data symbols in Figs. 5–6 and Figs. 8–9 are associated with predictions using a modified opaque model that utilizes an effective emissivity; these predictions will be discussed later.) The temperature variation within the jet evolves due to the interaction between the axial velocity (acceleration), the variation in jet diameter, and the combined diffusive, convective, and radiative heat transfer. Note that an increase of 200°C in inlet temperature from 1000°C is roughly equivalent to an increase of radiative heat flux by a factor of two. Due to the contribution of convective heat transfer, the corresponding increases in the average cooling rates are not as large as a factor of two, but approximately 44, 33, and 22 percent for pour rates of 10^6, 10^4, and 10^2 mm^3/s, respectively. Since the relative importance of radiative cooling over convective cooling decreases when the medium temperature is lower, the influence of inlet temperature is smaller when the pour rate is smaller (see Fig. 4). The temperature difference between the center

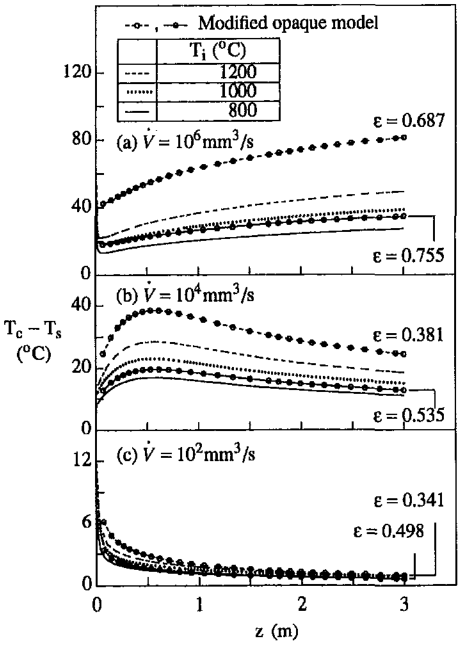

Fig. 6 Effect of T_i on radial temperature difference (h = 50 W/m^2·K)

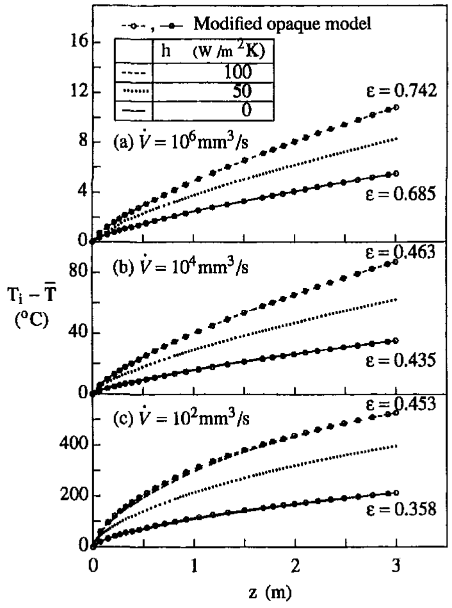

Fig. 8 Effect of h on bulk mean temperature drop (T_i = 1000°C)

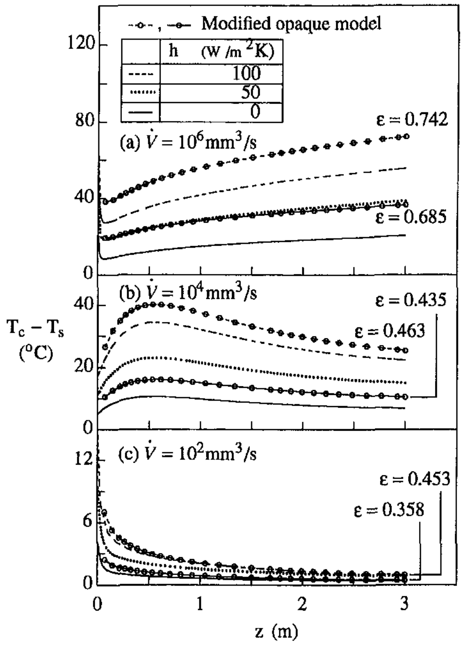

Fig. 9 Effect of h on radial temperature difference (T_i = 1000°C)

and the surface of the jet decreases as the pour rate decreases, due to the corresponding decrease in diameter seen in Fig. 2.

When the jet diameter is relatively large (Fig. 6(*a*)), the temperature at the centerline remains nearly the same as the inlet temperature for the entire jet length, while the surface temperature decreases. The optical radius of the jet in Fig. 6(*a*) is order of 100, and the radiative cooling is intense only near the surface. The resulting radial temperature nonuniformity is still developing at z = 3 m. The local minimum in the radial temperature difference very near the inlet is due to a local increase in the surface temperature, which is caused by the significant necking down of the jet and the resulting decrease in the heat removal rate through the surface. However, as noted earlier, two-dimensional effects dominate the neck-down region and must be included to adequately describe the complex thermal phenomena that occur there.

When the jet has an intermediate diameter (Fig. 6(*b*)), the maximum radial temperature difference occurs about 0.5 m downstream from the inlet. The optical radius of the jet in Fig. 6(*b*) is of order 10, and the radiative cooling is negligible along the center line but gradually increases toward the surface. Hence, the centerline temperature remains nearly the same as the inlet temperature between the inlet and the location of the maximum temperature difference. After the location of the maximum value, the centerline-to-surface temperature difference decreases as the cooling rate decreases.

For the cases where the jet diameter is relatively small (Fig. 6(*c*)), the maximum radial temperature difference occurs immediately after the inlet, since both the local heat flux at the surface and the jet diameter are greatest. The magnitude of the maximum radial temperature difference increases as the inlet temperature increases mainly due to the increase in the convective cooling. The changes due to a 200°C increase in inlet temperature from 1000°C are approximately 29, 26, and 21 percent for pour rates 10^6, 10^4, and 10^2 mm^3/s, respectively. The contribution of radiative cooling is negligible compared to the convective cooling away from the inlet as the medium temperature drops rapidly. The optical radius of the jet in Fig. 6(*c*) is of order unity, and the radiative intensity is only a fraction of that found in an opaque medium.

Radial temperature profiles (nondimensionalized by the local radial temperature difference $T_c - T_s$) are shown in Fig. 7 for the three cases considered in Fig. 6 with T_i = 1000°C. Two different axial locations are shown, one nearer to the jet inlet at z = 107 mm (Fig. 7(*a*)) and the other at z = 3 m (Fig. 7(*b*)). In all cases, there are significant radial temperature gradients throughout the jet, especially near the surface for the larger pour rates. The importance of optical thickness in the radial direction described above is evident; even for the case where the optical radius is of order 100 ($\dot{V} = 10^6$ mm^3/s), the optically thick assumption is not justified.

The effects of convection heat transfer on the bulk mean temperature and on the radial temperature nonuniformity are shown in Figs. 8 and 9, respectively, for an inlet temperature of 1000°C. The increases in average cooling rates are approximately 33, 42, and 44 percent when h is raised from 50 to 100 W/(m^{2}K) for pour rates of 10^6, 10^4, and 10^2 mm^3/s, respectively. The influence of convection heat transfer is more noticeable as the pour rate decreases, since the relative importance of radiative cooling decreases due to the relatively low medium temperatures (see Fig. 4). The changes in radial temperature difference caused by an increase in the convective heat transfer coefficient from 50 to 100 W/(m^{2}K) are approximately 57, 52, and 36 percent for pour rates 10^6, 10^4, and 10^2 mm^3/s, respectively. The influence of convection heat transfer is more prominent on the radial temperature nonuniformity than on the gradient of bulk mean temperature, when compared to the influence of inlet temperature. The change in the convection heat transfer coefficient directly affects the temperature gradient at the surface, while the change in the inlet temperature affects the convective heat transfer at the surface and the volumetric radiative cooling simultaneously.

The influence of semitransparent effects was examined by uniformly increasing the absorption coefficient for all wavelength bands, in the absence of convective cooling and with the inlet temperature fixed at 1200°C. The bulk mean temperature predictions are compared to the predictions using an opaque medium assumption in Fig. 10. The emissivity of the opaque wave frequency band for soda-lime glass, ε = 0.92 (Field and Viskanta, 1990), is used for the opaque predictions.

As the optical radius of the jet increases due to the increase in the absorption coefficient and/or due to the increase in the physical radius of the jet, the cooling rate of a semitransparent jet gradually approaches the cooling rate of an opaque jet. If the radial temperature variation were absent, this asymptotic approach would be monotonic. However, when the jet diameter

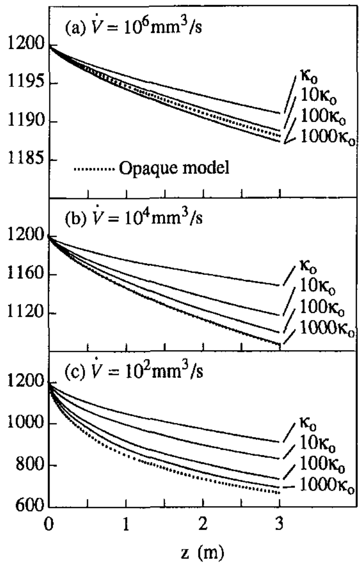

Fig. 10 Effect of absorption coefficient on bulk mean temperature drop (without convection)

is relatively large (Fig. 10(a)), the cooling rate of the semitransparent jet may exceed the cooling rate of the opaque jet due to the relatively large radial temperature gradient. The radiative heat flux at the surface may become larger than in the opaque jet since the radiative energy emitted by the hotter medium interior to the surface can contribute to the cooling of the jet. Here, the maximum cooling of the large-diameter jet is predicted when the absorption coefficients are larger than those of soda-lime glass by a factor of 190 in each band. The difference in cooling rates between the $190\kappa_0$ and $100\kappa_0$ cases is small (resulting in a 0.2°C temperature difference at $z = 3$m); hence the $190\kappa_0$ curve is not shown.

When the absorption coefficients are increased by larger factors (e.g., $1000\kappa_0$), the bulk mean temperature profile of the large-diameter jet approaches that of the opaque jet. Note that the results are not very sensitive to changes in the absorption coefficient in the range between $100\kappa_0$ and $1000\kappa_0$. Also, as the absorption coefficient increases, the spatial change in the radiative intensity becomes gradually steeper near the surface. For the smaller diameter jets, in which the radial temperature variations are likewise small, the semitransparent predictions approach the opaque case monotonically.

Finally, numerical experiments are conducted to examine the feasibility of using a modified opaque medium model, in which an effective emissivity is employed for a gray opaque medium under the assumption of a diffuse glass-gas interface. Predictions of the bulk mean temperature and the centerline-to-surface glass temperature differences using the modified opaque model are also shown in Figs. 5–6 and Figs. 8–9, as noted previously.

The effective emissivity values (reported in the figures) are determined by matching the mean temperature predicted by the opaque gray model to the mean temperature predicted by the semitransparent model at $z = 3$ m. When using these effective emissivity values, the decrease in the bulk mean temperature closely matches that of the semitransparent model for the entire length of the jet (Figs. 5 and 8). The discrepancies between the bulk mean temperatures predicted by the semitransparent and modified opaque models are less than two percent for all of the pour rates considered. The value of the matched effective emissivity is closer to the emissivity of the opaque wave frequency band (0.92) when the optical diameter of the jet is larger, i.e., when the physical diameter of the jet is larger due to a larger pour rate, or the glass temperature is lower due to a lower inlet temperature or due to a larger convection heat transfer coefficient.

In contrast to the close match in the bulk mean temperature, the errors in the centerline-to-surface glass temperature can be as large as 64 percent when the radiative cooling is most dominant (for the tested cases with $T_i = 1200$°C and $\dot{V} = 10^6$ mm^3/s). No consistent way to adjust the effective emissivity in the modified opaque model exists that will allow for the accurate predictions of both the radial and axial temperature variations. This is consistent with the observation by Yin and Jaluria (1997) that the optically thick approximation predicts the radiative heat flux satisfactorily for a range of axial temperature variation, but only when the radial temperature variation is small.

Viscosity Effects. As noted in the Introduction, the viscosity of the glass greatly influences the dynamics of the jet and its interaction with the rising glass pool that forms at the bottom of a canister during a filling operation (Gomon, 1997). A viscous jet may buckle when it first impacts a surface, depending upon its viscosity and fall height (Cruickshank and Munson, 1981). The jet may then begin to spiral near the region of impact, and if the viscosity is large enough, a considerable accumulation of fluid will develop in an unstable column below the jet. As this column of fluid buckles and collapses, the ambient gas is entrapped and/or entrained within the pool (Gomon, 1997), and in the case of a glass jet can be set into place with further cooling.

When considering molten glass jets, additional instabilities may be observed due to its highly temperature dependent viscosity. One unique phenomenon that has been observed is the formation of a "bird's nest," which develops when the viscosity of the glass jet rapidly increases, causing the bottom portion of the jet to rigidify and buckle over (Ball et al., 1997). This type of instability can occur with rapid cooling, when either the jet diameter is very small so that the entire jet rigidifies, or the jet diameter is large enough that significant radial temperature gradients develop, in which case a "hard shell" can form around an inner "soft core."

To illustrate the magnitude of the increase in viscosity that can be encountered in a molten glass jet as it is cooled, the case presented in Fig. 8(c) with $h = 100$ W/m$^2\cdot$K is considered (which resulted in the largest temperature change encountered in this study). At the inlet ($T_i = 1000$°C), the viscosity is 29.9 Pa·s (Table 1). At the bottom of the jet ($z = 3$ m) the bulk mean temperature is approximately 470°C, resulting in a viscosity of 3.85×10^6 Pa·s—an increase of five orders of magnitude. Because the behavior of the jet has been observed to be very sensitive to its temperature-dependent viscosity, accurate predictions of the cooling rates are vital to understanding the behavior of molten glass jets during pouring/filling operations.

Conclusion

Numerical predictions of the axial distributions of the jet diameter, bulk mean temperature, centerline-to-surface temperature difference, and axial velocity are presented for a glass jet undergoing combined radiative and convective cooling. The effects of varying the inlet velocity and temperature, volumetric pour rate, and convection heat transfer coefficient are included in the parametric studies. Two approaches are considered to describe the radiative heat transfer: a discrete ordinates semitransparent model using a five band approximation, and a diffuse gray opaque model using an effective emissivity. The latter model is found to provide reasonable accuracy for the axial bulk mean temperature profiles when the effective emissivity is adjusted, but significant differences exist between the predictions of the radial temperature distributions using the semitransparent and opaque models. Also, a priori determination of effective emissivity values poses significant difficulties. Thus, it is concluded that efforts to develop a modified opaque model for similar glass processing studies would be unproductive.

Acknowledgment

This paper was prepared with the support of the U.S. Department of Energy (DOE), Cooperative Agreement No. DE-FC04-95AL85832. However, any opinions, findings, conclusions, or recommendations expressed herein are those of the authors and do not necessarily reflect the views of DOE. This work was conducted through the Amarillo National Resource Center for Plutonium.

References

Ball, K. S., Song, M., Gomon, M., Silva, M. W., Taleff, E. M., Powers, B. M., and Bergman, T. L., 1996, "Canister Filling with a Molten Glass Jet," *Bulletin of the American Physical Society*, Vol. 41, p. 1749.

Ball, K. S., Song, M., Gomon, M., Silva, M. W., Taleff, E. M., Powers, B. M., and Bergman, T. L., 1997, "Canister Filling With a Molten Glass Jet," ASME JOURNAL OF HEAT TRANSFER, Vol. 119, p. 204.

Cruickshank, J. O., and Munson, B. R., 1981, "Viscous Fluid Buckling of Plane and Axisymmetric Jets," *Journal of Fluid Mechanics*, Vol. 113, 221–239.

Field, R. E., 1989, "Spectra Remote Sensing of the Temperature Distribution in Glass," Ph.D. thesis, Purdue University, West Lafayette, IN.

Field, R. E., and Viskanta, R., 1990, "Measurement and Prediction of the Dynamic Temperature Distributions in Soda-Lime Glass Plates," *Journal of the American Ceramic Society*, Vol. 73, pp. 2047–2053.

Glicksman, L. R., 1968a, "The Cooling of Glass Fibres," *Glass Technology*, Vol. 9, pp. 131–138.

Glicksman, L. R., 1968b, "The Dynamics of a Heated Free Jet of Variable Viscosity at Low Reynolds Numbers," ASME *Journal of Basic Engineering*, Vol. 90, pp. 343–354.

Gomon, M., 1997, "Experimental Study of Highly Viscous Impinging Jets," Masters thesis, University of Texas at Austin, Austin, TX.

Issa, J., Jaluria, Y., Polymeropoulos, C. E., and Yin, Z., 1995, "Radiation Heat Transfer Within an Optical Fiber Draw Tower Furnace," *Proceedings of 30th 1995 National Heat Transfer Conference*, Vol. 4, R. L. Mahajan, ed., ASME, New York, pp. 3–11.

Joseph, D. D., Nguyen, K., and Matta, J. E., 1983, "Jets into Liquid Under Gravity," *Journal of Fluid Mechanics*, Vol. 128, pp. 443–468.

Kaminski, D., 1995, "Thermal Transport in Optical Fiber Manufacturing," *Radiative Transfer-I: Proceedings of the First International Symposium on Radiation Transfer*, M. P. Menguc, ed., Begell House, New York, pp. 667–681.

Lee, S. H. K. and Jaluria, Y., 1993, "Radiative Transport in the Cylindrical Furnace for Optical Fiber Drawing," *Transport Phenomena in Nonconventional Manufacturing and Materials Processing*, C. L. Chan et al., eds., ASME, New York, pp. 43–58.

Lee, S. H. K., and Jaluria, Y., 1996, "Effects of Variable Properties and Viscous Dissipation During Optical Fiber Drawing," ASME JOURNAL OF HEAT TRANSFER, Vol. 118, pp. 350–358.

Marples, J. A. C., 1988, "The Preparation, Properties, and Disposal of Vitrified High Level Waste from Nuclear Fuel Reprocessing," *Glass Technology*, Vol. 29, pp. 230–247.

Modest, M. F., 1993, *Radiative Heat Transfer*, McGraw-Hill, New York.

National Academy of Sciences, 1994, *Management and Disposition of Excess Weapons Plutonium*, National Academy Press, Washington, DC.

Nayfeh, A. H., 1970, "Nonlinear Stability of a Liquid Jet," *Physics of Fluids*, Vol. 13, pp. 841–847.

Paek, U. C., and Kurkjian, C. R., 1975, "Calculation of Cooling Rate and Induced Stresses in Drawing of Optical Fibers," *Journal of the American Ceramic Society*, Vol. 58, pp. 330–335.

Paek, U. C., and Runk, R. B., 1978, "Physical Behavior of the Neck-Down Region During Furnace Drawing of Silica Fibers," *Journal of Applied Physics*, Vol. 49, pp. 4417–4422.

Rubin, M., 1985, "Optical Properties of Soda Lime Silica Glasses," *Solar Energy Materials*, Vol. 12, pp. 275–288.

Song, M., and Viskanta, R., 1996, "Discrete Ordinates Solution of Axisymmetric Radiative Transfer Within a Condensed Semitransparent Medium Having Specularly Reflecting Boundaries," *ASME Proceedings of the 31st National Heat Transfer Conference*, Vol. 3, R. D. Skocypec et al., ed., ASME, New York, pp. 55–62.

Soper, P. D., and Bickford, D. F., 1982, "Physical Properties of Frit 165/Waste Glasses," DPST-82-899, Technical Division–Savannah River Laboratory, Aiken, SC.

Sterling, A. M., and Sleicher, C. A., 1975, "The Instability of Capillary Jets," *Journal of Fluid Mechanics*, Vol. 68, pp. 477–495.

Taylor, G. I., 1959, "The Dynamics of Thin Sheets of Fluid, III. Disintegration of Fluid Sheets," *Proceedings of the Royal Society of London*, Vol. A253, pp. 313–321.

Viskanta, R., 1994, "Review of Three-Dimensional Mathematical Modeling of Glass Melting," *Journal of Non-Crystalline Solids*, Vol. 177, pp. 347–362.

Wilson, D. E., 1986, "A Similarity Solution for the Axisymmetric Viscous-Gravity Jet," *Physics of Fluids*, Vol. 29, pp. 632–639.

Yin, Z., and Jaluria, Y., 1997, "Zonal Method to Model Radiative Transport in an Optical Fiber Drawing Furnace," ASME JOURNAL OF HEAT TRANSFER, Vol. 119, 597–603.

Journal of
Heat Transfer

Technical
Note

Weakly Ionized Plasma Arc Heat Transfer Between Geometrically Dissimilar Electrodes

S. S. Sripada,[1] P. S. Ayyaswamy,[1] and I. M. Cohen[1]

A set of self-consistent conservation equations for the charged particle densities and the temperatures in a weakly ionized plasma between two dissimilar electrodes is numerically solved using an orthogonal body-fitted coordinate system. The electron number density and temperature variation in the discharge gap, and the results for the heat transfer to the anode are presented. Results have been developed for a configuration that commonly arises in microelectronic manufacturing—a thin cylindrical anode together with a planar cathode.

Nomenclature

A_i, B_i = constants in expression for ionization coefficient
a = accommodation coefficient
d = anode diameter
E = magnitude of electric field intensity
$\mathbf{E}$ = electric field intensity vector
e = electron charge
g = statistical weight
h = Planck's constant
I = current
$\mathbf{j}$ = species number flux
k = Boltzmann constant
l = length
m = mass
N = species number density
$\mathbf{n}$ = surface normal vector
P_i = ionization rate due to electron impact
P_t = thermal ionization rate
p = pressure
$\mathbf{q}$ = energy flux
(r, z) = cylindrical coordinates
$\mathbf{R}$ = position vector
R_c = external circuit resistance
R_t = three-body recombination rate
T = temperature (K)
V = electric potential

Greek Symbols

α_i = primary ionization coefficient
ϵ_0 = permittivity of free space
γ = three-body recombination coefficient
κ = thermal conductivity
μ = mobility
ϕ = work function
(ξ, η) = computational grid system

Subscripts

an = anode
ap = applied
c = conductive
d = discharge
e = electron
g = inter-electrode gap
i = ion, ionization
m = melting
n = neutral specie, surface normal
p = cathode plate
ref = reference
∞ = ambient

Superscripts

$*$ = nondimensional

Introduction

In many manufacturing processes, arc plasma heat transfer occurs between two dissimilar electrodes. High energy plasmas occur in such applications as arc welding and plasma spray coating. On the other hand, low energy plasmas are used in plasma processing in the microelectronics industry. Since electrode geometry significantly affects the electric field and the plasma transport, it is important to be able to correctly evaluate the heat transfer in such situations taking into account the geometrical variations. In this context, Jog et al. (1991, 1992) have studied the initial breakdown of the inter-electrode gap and the heat transfer to the tip of a wire in a wire-to-plane discharge. Qin (1997) numerically simulated the glow discharge between two dissimilar electrodes, a cylindrical anode and a planar cathode using a nonorthogonal body-fitted coordinate system based on elliptic grid generation (Knupp and Steinberg, 1993). The use of a nonorthogonal grid system, however, introduces cross-derivative terms which considerably complicate the numerical solution with attendant convergence difficulties. In this study, we have examined plasma arc heat transfer between two dissimilar electrodes taking into account Poisson's equation for the self-consistent electric potential. A set of continuum conservation equations for the charged particle densities and the heat

---

[1] Department of Mechanical Engineering and Applied Mechanics, University of Pennsylvania, Philadelphia, PA 19104-6315.

Contributed by the Heat Transfer Division for publication in the JOURNAL OF HEAT TRANSFER. Manuscript received by the Heat Transfer Division, Sept. 30, 1997; revision received, Sept. 15, 1998. Keywords: Heat Transfer, Melting, Phase Change, Plasma, Solidification. Associate Technical Editor: M. Modest.

fluxes in an arc plasma has been solved using an orthogonal grid system to minimize errors both grid based and those arising from approximate representations for boundary fluxes. We have presented results for a flat cathode and a spherical-tipped slender wire anode, a configuration that arises in many manufacturing processes.

Theory

A typical low-energy discharge may be characterized by a low-energy continuum description of a "weakly" ionized plasma. The plasma consists of three species: neutrals, ions (positive), and electrons. For such a continuum steady-state plasma, the governing equations are as follows. The number conservation equation is

$$\nabla \cdot \mathbf{j}_{e,i} = P_i(N_e) + P_t(N_e) - R_t(N_e), \tag{1}$$

where the electron and ion number fluxes are given by

$$\mathbf{j}_{e,i} = -\frac{\mu_{e,i}}{e} \nabla p_{e,i} \mp \mu_{e,i} N_{e,i} \mathbf{E},\ p_{e,i} = N_{e,i} k T_{e,i}. \tag{2}$$

The electron energy equation is

$$\nabla \cdot \mathbf{q}_e = -e\mathbf{j}_e \cdot \mathbf{E}, \quad \text{where} \quad \mathbf{q}_e = \tfrac{5}{2} k T_e \mathbf{j}_e - \kappa_e \nabla T_e. \tag{3}$$

The self-consistent electric field is given by Gauss' law

$$\nabla \cdot \mathbf{E} = \frac{e}{\epsilon_0}(N_i - N_e), \quad \text{where} \quad \mathbf{E} = -\nabla V. \tag{4}$$

$P_i(N_e)$ is the ionization rate due to electron impact (von Engel, 1965):

$$P_i = \alpha_i \mu_e E N_e, \text{ where } \alpha_i = A_i p \exp\left(\frac{-B_i p}{E}\right).$$

$P_t(N_e)$ is the thermal ionization rate, $R_t(N_e)$ is the three-body recombination rate. We employ the Saha equation (Mitchner and Kruger, Jr., 1973) to obtain the net ionization due to both thermal ionization and recombination,

$$P_t(N_e) - R_t(N_e) = \gamma\left[\frac{2g_i N_n}{g_n}\left(\frac{2\pi m_e k T_e}{h^2}\right)^{3/2} \exp\left(-\frac{eV_i}{kT_e}\right) - N_e N_i\right],$$

where the three-body recombination coefficient $\gamma = 1.09 \times 10^{-20} T_e^{-(9/2)} N_e$ (m^3/s) is a strong function of electron temperature (Hinnov and Hirschberg, 1962).

The heat flux from the plasma to the electrode has two major components, the work function energy flux and the conductive energy flux. For low-energy plasmas, all other modes of energy transport are likely to be negligible compared to these two components (Jog et al., 1992; Ayyaswamy et al., 1998). Incoming electrons at the anode release energy equivalent to the work function, ϕ, to the electrode surface. The net surface normal energy flux may be expressed as $q_n = a_e e \phi \mathbf{j}_e \cdot \mathbf{n}$, where $a_e = 0.9$ is the assumed electron accommodation coefficient for the anode surface (Wiedmann and Trumpler, 1946), and $\mathbf{n}$ is the surface normal vector. The conductive heat flux from the electrons is due to their thermal energy and is expressible as $q_c = -\kappa_e \nabla T_e \cdot \mathbf{n}$.

In this study, the above set of equations is solved in the axisymmetric cylindrical coordinate (r, z) system. In such an axisymmetric framework, the center of the circular planar cathode is located at $r = z = 0$ and the cathode radius is r_p. The spherical tip of the anode is represented by a spherical segment attached to a long slender cylinder (wire) of length l_{an} oriented along the z-axis. The tip is at a distance l_g, the gap length, from the center of the cathode plate. In the numerical simulation, the physical domain is truncated at a radius equal to that of the cathode plate which is taken to be much larger than the anode diameter so that the effect of the domain size on the transport to the anode is negligible. The boundary of the domain thus consists of the anode and its tip, the axis of symmetry, the cathode plate, and the outer periphery connecting the end of the anode to the outer edge of the cathode plate.

The boundary conditions may be stated as follows.

At the cathode plate ($0 \le r \le r_p$, $z = 0$)

$$N_{e,i} = N_0, \quad V = V_{\text{ap}} - I_{\text{an}} R_c, \quad T_e = T_\infty.$$

At the anode tip and on the lateral surface

$$N_{e,i} = N_0, \quad V = 0, \quad T_e = T_s.$$

At the axis of symmetry ($r = 0$, $0 \le z \le l_g$)

$$\frac{\partial N_{e,i}}{\partial r} = 0, \quad \frac{\partial V}{\partial r} = 0, \quad \frac{\partial T_e}{\partial r} = 0.$$

At the outer boundary

$$N_{e,i} = N_0, \quad \nabla V \cdot \mathbf{n} = 0, \quad \nabla T_e \cdot \mathbf{n} = 0.$$

Here, N_0 is the small ambient electron and ion density due to omnipresent background radiation. We consider the electrodes to be nearly perfect absorbing surfaces for the ionic species. The spherical tip of the anode is assumed to be at a constant prescribed temperature T_m, and the surface temperature T_s is assumed to decrease linearly along its axis beyond the spherical tip. I_{an} is the current collected at the anode and is expressed as

$$I_{\text{an}} = e \int_{\text{anode}} (\mathbf{j}_i - \mathbf{j}_e) \cdot d\mathbf{A}_{\text{an}}$$

where the integral is taken over the entire surface of the anode and $d\mathbf{A}_{\text{an}}$ is the elemental area vector.

The governing equations are nondimensionalized by the anode diameter d as the length scale, $\mu_e k T_\infty/(ed)$ as the velocity scale, kT_∞/e as the voltage scale, and the ambient temperature T_∞ as the temperature scale. The number densities have been nondimensionalized by the density N_{ref} that results in a Debye length equal to the chosen length scale d, that is, $N_{\text{ref}} = \epsilon_0 (kT_\infty / e^2 d^2)$. Next, we describe the numerical procedures adopted to solve the dimensionless equations.

Numerical Methodology

The chosen domain is irregular in that two of the four domain boundaries, the anode and the outer boundary, do not coincide with either of the (r, z) coordinate lines. We have generated a 41×41 *orthogonal* structured grid based on the solution of highly nonlinear coupled covariant Laplace equations (Ryskin and Leal, 1983; Eca, 1996) with the prescribed domain coordinates as boundary conditions. The finite volume method was used to discretize these equations, and an iterative algorithm is used for solution.

Since the arc heat transfer problem is axisymmetric but the (ξ, η) grid system is two-dimensional, the governing equations for the plasma are first written in the (r, z) coordinate system and *then* transformed to the computational (ξ, η) domain. A finite volume method was used in conjunction with the power-law scheme (Patankar, 1980) to discretize the partial differential equations.

A novel interpretation of the power-law scheme was necessary for use with the plasma equations. In the equations, the electric field, $\mathbf{E}$, plays the role of a convection "velocity" in the fluid dynamics sense. Therefore the ratio, $e\mathbf{E} \cdot \mathbf{t}_\zeta \Delta\zeta / kT_e$, the "electronic Peclet" number is used in lieu of the standard grid Peclet number. Here $\mathbf{t}_\zeta$ is the local tangent vector to the ζ

coordinate line where ζ may be either of (ξ, η) as appropriate. All dependent variables are colocated at the grid points.

The discretized equations are strongly nonlinear and coupled and were solved iteratively with severe under-relaxation. Due to the disparate velocity scales for the ions and electrons (electrons are orders of magnitude more mobile than ions, $\mu_e/\mu_i \sim 200$), relaxation parameters for the equations had to be suitably tailored to obtain a convergent solution. This required extensive numerical experimentation.

Numerical error in the simulation may stem from (i) grid generation, (ii) plasma equations discretization, (iii) the iterative solver, and (iv) machine error. Grid generation error from discretization and departure from orthogonality are $\sim 10^{-4}$ and ± 0.94 percent, respectively. Plasma equations discretization error is $\sim 10^{-4}$. The sensitivity of the solutions to grid coarseness was tested by performing the simulations on a variety of grids. The coarsest grid (21×21) failed to capture the sheath region satisfactorily. Using the finest grid, 61×61, changed the solutions by a maximum of 1.02 percent relative to the 41×41 grid.

The simulations were performed on a CRAY C90 at the Pittsburgh Supercomputing Center.

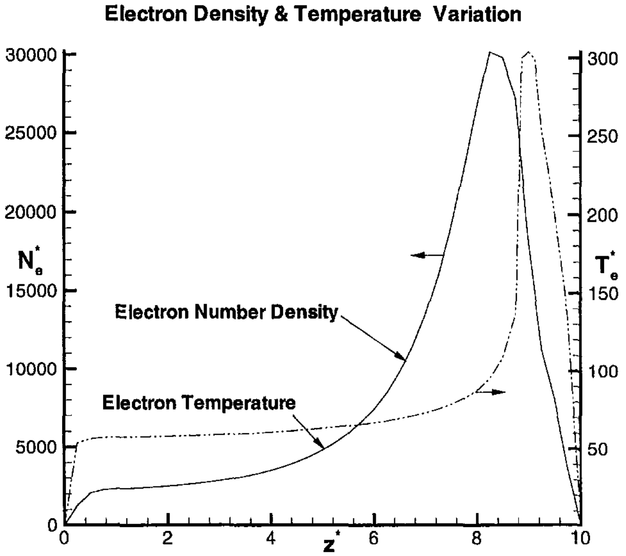

Fig. 1 Variation of normalized electron density and temperature along discharge axis

Results and Discussion

Numerical simulations were made for air as the medium with all the input parameters specified. The chosen values are typical of an EFO discharge used in the microelectronic industry. The parameters are: an applied voltage of -3000 V, an anode (wire) diameter $d = 1$ mil $= 25.4$ μm, a discharge gap $l_g = 10d$, an anode length $l_{an} = 30d$ from the anode tip, and the cathode plate radius $r_p = 40d$. The melting temperature of the anode material was prescribed to be $T_m = 1336$ K (this corresponds to a gold anode which is often used in microelectronic applications). The ambient reference temperature is $T_\infty = 300$ K, and the ambient pressure is 1 atmosphere which together specify the number density of neutrals $N_n = 2.44 \times 10^{25}$ m^{-3}. The small ambient ion density due to background radiation is taken to be $N_0 = 6 \times 10^8$ m^{-3}. The mobilities are $\mu_e = 3.48 \times 10^{-2}$ m^2(Vs)$^{-1}$ and $\mu_i = 1.7 \times 10^{-4}$ m^2 (Vs)$^{-1}$. These parameters result in a reference number density $N_{\text{ref}} = 2.22 \times 10^{15}$ m^{-3} and a reference voltage $V_{\text{ref}} = kT_\infty/e = 2.5875 \times 10^{-2}$ V. The ionization potential is taken to be 14.87 V. The outer circuit resistance was taken to be $R_c = 100$ kΩ. In the results presented in the following, all lengths (r, z) are nondimensionalized by d.

In Fig. 1 we present the variation of the nondimensional electron number density $N_e^* = N_e/N_{\text{ref}}$ along the discharge axis with the cathode at $z^* = 0$ and anode tip at $z^* = 10$. Due to the strong potential gradients near the anode surface the electric field intensity is high and impact ionization becomes a strong ionization source as electrons accelerate to large drift velocities near the anode. Thus there is a peak in the electron density near the anode. However, the strongly absorbing electrode boundary condition causes a severe gradient in the density at the anode. Since ions are generated at the same locations as electrons, an identical trend is seen for ions except for differences in gradients in the thin electrode sheaths.

In Fig. 1 we present the electron temperature variation along the symmetry axis. Due to the strong potential gradient at the anode, electrons undergo much stronger acceleration and thus assume large kinetic energies which is in turn reflected in the temperature. At the anode a constant temperature is prescribed which also acts as a strong energy-absorbing boundary condition. This is reflected in the temperature peak in the anode vicinity and the strong gradient. The gradient results in a large heat flux to the anode surface. As one moves away from the axis along the anode surface, the temperature gradient decreases in magnitude resulting in a decreasing heat flux. This is reflected in Fig. 2 where the variation of q^*, the dimensionless heat flux, with distance along the anode surface from the tip, is shown.

The heat flux is rendered dimensionless by $q_{\text{ref}} = kT_\infty(\mu_e N_{\text{ref}} V_{\text{ref}}/d)$ which is 3.2582×10^{-4} W/m^2 for the parameters considered. The minimum in the logarithmic heat flux variation appears at the "neck" of the anode where the segment of sphere is attached to the cylindrical portion of the anode. Beyond the spherical tip, there is enough ionization in the sheath to provide an energy flux to the anode surface albeit orders of magnitude lower than that in the vicinity of the tip. Moreover, it may be recalled that the anode surface temperature is assumed to decrease linearly along the anode axis beyond the spherical tip. For the chosen set of parameters, 0.104 W of thermal power is transferred to the anode from the plasma. Here, the bulge of the spherical tip acts like a shield against all energy driving gradients and explains the heat flux minimum. This is a novel result and indicates the crucial role played by electrode geometry in the determination of the heat flux from an arc plasma.

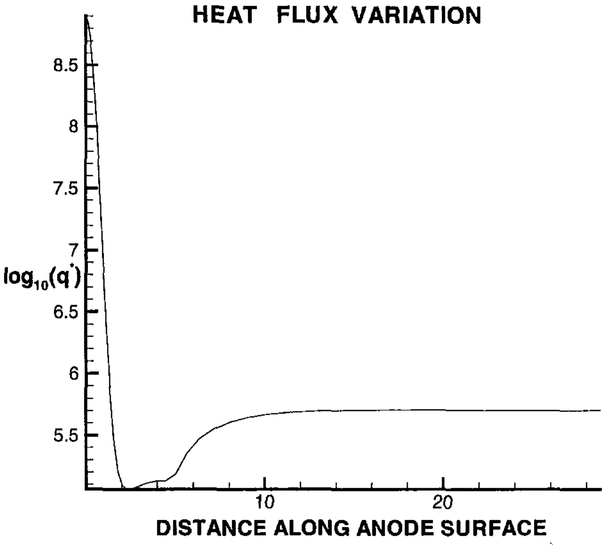

Fig. 2 Variation of nondimensional heat flux along anode surface

Conclusions

A numerical study of the heat transfer from a weakly ionized plasma between geometrically dissimilar electrodes that occurs in many manufacturing situations, and in particular in the microelectronics industry, has been described. An orthogonal body-fitted uniform grid system was generated to accurately model the plasma equations including geometrical variations in the domain. Results for the number densities, temperature, and heat flux were presented. A novel result of a minimum in the heat flux at the neck of the anode for the chosen electrode shape has also been presented.

Acknowledgments

The authors gratefully acknowledge support of this work by the National Science Foundation through NSF Grant CTS-94-21598, the Pittsburgh Supercomputing Center through Grant DMC890001P for use of the CRAY C90. and the University of Pennsylvania Research Foundation through grant of an IBM RS/6000 workstation on which much of the code development was undertaken. We also thank Prof. M. A. Jog, Department of Mechanical, Industrial, and Nuclear Engineering, University of Cincinnati, Cincinnati, OH, for stimulating discussions of some of the numerical methodology used in this study.

References

Ayyaswamy, P. S., Sripada, S. S., and Cohen, I. M., 1998, "Interfacial motion of a molten layer subject to plasma heating," *Fluid Dynamics at Interfaces*, W. Shyy, Cambridge University Press, New York, in press.

Eca, L., 1996, "2D orthogonal grid generation with boundary point distribution control," *J. Comp. Phys.*, Vol. 125, pp. 440–453.

Hinnov, E., and Hirschberg, J. G., 1962, "Electron-ion Recombination in Dense Plasmas," *Phys. Rev.*, Vol. 125, No. 3, pp. 795–801.

Jog, M. A., Cohen, I. M., and Ayyaswamy, P. S., 1991, "Breakdown of a Wire-to-plane Discharge," *Phys. Fluids B*, Vol. 3, pp. 3532–3536.

Jog, M. A., Cohen, I. M., and Ayyaswamy, P. S., 1992, "Electrode Heating in a Wire-to-plane Arc," *Phys. Fluids B*, Vol. 4, pp. 465–472.

Knupp, P., and Steinberg, S., 1993, *Fundamentals of Grid Generation*, CRC Press, Boca Raton, FL.

Mitchner, M., and Kruger, Jr., C. H., 1973, *Partially Ionized Gases*, John Wiley and Sons, New York.

Patankar, S. V., 1980, *Numerical Heat Transfer and Fluid Flow*, Hemisphere, Washington, DC.

Qin, W., 1997, "Numerical and Experimental Studies of Heat Transfer Phenomena in Microelectronic Packaging," Ph.D. thesis, University of Pennsylvania, Philadelphia, PA.

Ryskin, G., and Leal, L. G., 1983, "Orthogonal Mapping," *J. Comp. Phys.*, Vol. 50, pp. 71–100.

von Engel, A., 1965, *Ionized Gases*, 2nd Ed., Oxford University Press, London.

Wiedmann, M. L., and Trumpler, P. R., 1946, "Thermal Accommodation Coefficients," *Trans. ASME*, Vol. 68, pp. 57–64.

S. Andre
e-mail: sandre@ensem.u-nancy.fr

A. Degiovanni

L.E.M.T.A. CNRS UMR 7563,
B.P. 160,
2 Av. de la Foret de Haye,
54504 Vandoeuvre-les-Nancy
Cedex, France

A New Way of Solving Transient Radiative-Conductive Heat Transfer Problems

One-dimensional transient energy transfer by conduction and radiation is solved for a finite medium. The semitransparent layer emits, absorbs, and scatters radiation (participating medium). The coupled transfer is solved analytically by considering the well-known two-flux approximation, assuming linear transfer and using the Laplace transform. The semitransparent layer can then be modeled by a matrix transfer function. The accuracy of the solution is verified in the case of sharp thermal excitation by a heat pulse on the front face. It is shown that this general model is very accurate for simulating both the limiting cases of purely scattering and purely absorbing media. In the latter case, the same modeling is derived using the kernel substitution technique, and very good agreement is achieved compared with numerical simulations. The resulting computation times are very small, and suggest that such a model can be used in the inverse approach of thermal problems involving semitransparent materials.

Introduction

Combined conductive and radiative heat transfer cannot be ignored in modeling the thermal behavior of a semitransparent material (STM) like glass, polymers, paper and so forth. The main fields of research are:

- the thermal characterization of STM; i.e., separation of the purely radiative and conductive contributions to heat transfer under prescribed metrological conditions;
- the modeling of manufacturing or forming processes involving semitransparent materials; and
- the study of various insulating systems (thermal barriers for space vehicles, honeycomb structures, and so on).

The physical nature of radiative transfer, which must account for any spectral dependances of a medium's optical properties and of anisotropic scattering, generally leads to two limiting cases (Viskanta, 1982): (1) negligible absorption in comparison with scattering, and (2) negligible scattering in comparison with absorption. The more general case (3) studied in modeling the thermal behavior of STM is then to consider a medium that can emit, absorb, and scatter incident radiation through bulk matter interactions.

Many papers are available in the form of state-of-the-art reviews and/or textbooks (Özisik, 1973; Viskanta, 1982; Howell, 1988). A great number of works concern the solution of the radiative transfer equation (RTE) in all possible geometrical configurations. The main mathematical problem in purely radiative problems comes from the scattering term of the source function (angular dependence) and the broadening scope of each problem (strongly spectral dependence effects, multidimensional effects, inverse analysis, and so forth). Fewer works deal with combined conduction-radiation heat transfer, because of the mathematical difficulties arising from nonlinear coupling between the RTE and the energy equation. Among these, problems dealing with transient aspects are limited and, in a general way, imply some simplifications in the modeling of the radiative transfer. The present work does not escape this dilemma.

This paper presents an efficient solution to the one-dimensional conductive and radiative heat transfer problem in a participating medium. The approach is analytical, based on the differential approximation (Lick, 1965; Cess, 1966). It consists in obtaining a differential equation for the temperature field, instead of the natural integrodifferential energy equation. The solution is obtained under the linear transfer assumption and the two-flux approximation (model 3). When the Laplace transform is used, the problem is naturally formulated in terms of a matrix transfer (thermal quadrupole) linking the (temperature-heat flux) vectors at the boundaries of the system linearly. This concept is the extension of the thermal resistance concept in the steady state and is originally due to Degiovanni (1988) and Maillet (1998).

The first section provides a short, comprehensive introduction to the quadrupole concept. The equation governing the coupled heat transfer problem is given in Section 3. Section 4 presents the solution obtained in the general case of an absorbing, emitting, scattering medium (model 3). Section 5 briefly shows that the same treatment and formulation can be performed for purely absorbing-emitting media by the kernel substitution technique (model 2), and purely scattering media (model 1). The accuracy is tested in Section 6. The agreement of models 1 and 2 with numerical computations found in the literature is very good, and validates the new models. Attention will be given to the solutions generated by model 3. A comparison is made between (a) the results obtained with the general model when $\chi = 0$ (no absorption) and those of model 1, and (b) the results obtained with the general model 3 when $\sigma = 0$ (no scattering) and the exact analytical solution yielded by model 2. In this case, the validity of the Deissler model of radiative conductivity (Deissler, 1964), widely use by researchers in experimental work, is given. Section 8 will discuss the limitations of these models and various aspects concerning coupled heat transfer in participating media. An illustration will be given of the use of these models in the inverse approach (for parameter estimation) as applied to semitransparent walls. This is of great interest in the field of thermal characterization of semitransparent layers such as those encountered in numerous insulating materials, or between molds and tools in forming processes.

2 Quadrupole Concept

This section is a short introduction to the quadrupole representation of thermal systems as explained in Degiovanni's reference paper (1988) and in the book of Maillet et al. (1998).

Contributed by the Heat Transfer Division for publication in the JOURNAL OF HEAT TRANSFER. Manuscript received by the Heat Transfer Division, Oct. 22, 1996; revision received, June 1, 1998. Keywords: Radiation, Radiation Interactions, Transient and Unsteady Heat Transfer. Associate Technical Editor: T. Tong.

The thermal quadrupole is an extension of steady-state thermal resistance to the transient state. Its formulation for conductive heat transfer is easily obtained as follows:

A homogeneous "wall" (thickness e, diffusivity a) is considered, with one-directional transfer in the z-direction. There is no internal source in the medium, which is at thermal equilibrium at the initial time. The corresponding heat equation and initial conditions are

$$\begin{cases} \dfrac{\partial^2 T^*}{\partial z^{*2}} = \dfrac{1}{a}\dfrac{\partial T^*}{\partial t^*} & \text{for} \quad 0 < z^* < e \\ T^* = 0 & \text{for} \quad t^* = 0. \end{cases} \tag{1}$$

Let $\overline{\theta}_{\text{in}}$ and $\overline{\theta}_{\text{out}}$ be the Laplace transforms of temperature at $z^* = 0$ and $z^* = e$, and $\overline{\phi}_{\text{in}}$, $\overline{\phi}_{\text{out}}$ the Laplace transforms of the heat fluxes at $z^* = 0$ and $z^* = e$.

In a very general sense, there exists a linear relationship between input quantities ($\overline{\theta}_{\text{in}}$, $\overline{\phi}_{\text{in}}$) and the corresponding output quantities ($\overline{\theta}_{\text{out}}$, $\overline{\phi}_{\text{out}}$), since the problem is linear:

$$\begin{cases} \overline{\theta}_{\text{in}} = A_c\overline{\theta}_{\text{out}} + B_c\overline{\phi}_{\text{out}} \\ \overline{\phi}_{\text{in}} = C_c\overline{\theta}_{\text{out}} + D_c\overline{\phi}_{\text{out}} \end{cases} \tag{2}$$

where matrix $[\begin{smallmatrix} A_c & B_c \\ C_c & D_c \end{smallmatrix}]$ is the transfer matrix of the quadrupole that is associated with the wall as shown in Fig. 1.

After Laplace transform, system (1) becomes

$$\frac{\partial^2\overline{\theta}}{\partial z^{*2}} = \frac{p^*}{a}\overline{\theta} \tag{3}$$

where p^* is the Laplace parameter. The solution of this equation is

$$\overline{\theta} = K_1 sh(\alpha z^*) + K_2 ch(\alpha z^*) \quad \text{with} \quad \alpha^2 = p^*/a. \tag{4}$$

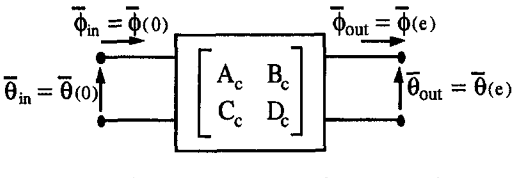

Fig. 1 Quadrupole for a conductive transfer

The flux q^* at abscissa z^* is associated with the temperature T^* at the same location:

$$q_c^* = -kS\frac{\partial T^*}{\partial z^*} \tag{5}$$

where k is the thermal conductivity of the wall and S the area of the plane surface that is considered for the z^*-transfer. After Laplace transform of this equation, considering Eq. (4), we get

$$\overline{\phi} = -kS\frac{\partial\overline{\theta}}{\partial z^*} = -kS\alpha(K_1 ch(\alpha z^*) + K_2 sh(\alpha z^*)). \tag{6}$$

Lastly, the constants K_1 and K_2 can easily be eliminated from Eqs. (4) and (6), written for $z^* = 0$ and for $z^* = e$, to provide the following input ($z^* = 0$)/output ($z^* = e$) equations:

$$\begin{cases} \overline{\theta}_{\text{in}} = ch(\alpha e)\overline{\theta}_{\text{out}} + \dfrac{1}{kS\alpha}sh(\alpha e)\overline{\phi}_{\text{out}} \\ \overline{\phi}_{\text{in}} = kS\alpha sh(\alpha e)\overline{\theta}_{\text{out}} + ch(\alpha e)\overline{\phi}_{\text{out}}. \end{cases} \tag{7}$$

The above pair of equations can be expressed in the following form:

$$\begin{bmatrix} \overline{\theta}_{\text{in}} \\ \overline{\phi}_{\text{in}} \end{bmatrix} = \begin{bmatrix} A_c & B_c \\ C_c & D_c \end{bmatrix} \begin{bmatrix} \overline{\theta}_{\text{out}} \\ \overline{\phi}_{\text{out}} \end{bmatrix} \quad \text{with:} \begin{cases} A_c = D_c = ch(\alpha e) \\ B_c = \dfrac{1}{kS\alpha}sh(\alpha e) \\ C_c = kS\alpha sh(\alpha e). \end{cases} \tag{8}$$

Figure 1 is a symbolic representation of the conductive wall-quadrupole. The electrical analogy is the same as for steady-

Nomenclature

A_i, B_i, C_i, D_i = matrix transfer coefficients of model i
a = intrinsic (phonic) diffusivity, (m^2/s)
Bi_1 = Biot number at $z = 0$, ($h_1 e/k$)
Bi_2 = Biot number at $z = 1$, ($h_2 e/k$)
C_p = specific heat (J $\cdot$ kg^{-1} $\cdot$ K^{-1})
e = slab thickness (m)
E_i = exponential integral function of order i
h_1, h_2 = heat transfer coefficient at $z = 0$ and $z = 1$, respectively (W $\cdot$ m^{-2} $\cdot$ K^{-1})
k = intrinsic thermal conductivity (W $\cdot$ m^{-1} $\cdot$ K^{-1})
L^* = intensity, radiant energy (W $\cdot$ m^{-2} $\cdot$ sr^{-1})
$L = \pi L^*/(4n^2\sigma_{\text{SB}}T_0^{*4})$, dimensionless intensity
$L^\circ(T)$ = blackbody intensity at temperature T
$N_{pl} = (k\beta_e/4n^2\sigma_{\text{SB}}T_0^{*3})$, gray conduction-to-radiation parameter or Planck number
n = refractive index
$p = e^2 \cdot p^*/a$ = dimensionless Laplace variable
p^* = Laplace variable
q_c^* = conductive heat flux (W $\cdot$ m^{-2})
q_r^* = radiative heat flux (W $\cdot$ m^{-2})
$q_r = q_r^*/4n^2\sigma_{\text{SB}}T_0^{*4}$, dimensionless radiative flux
Q = heat pulse surface density (J $\cdot$ m^{-2})
R_r = dimensionless radiative resistance
t^* = physical time (s)
$t = at^*/e^2$, dimensionless time
T^* = temperature (K)
T_0^* = reference temperature (K)
$T_0 = T_0^*/(Q/\rho C_p e)$, dimensionless reference temperature
z^* = space variable (m)

Greek Symbols

$\beta_e = \chi + \sigma$ = extinction coefficient (m^{-1})
χ = absorption coefficient (m^{-1})
ϵ_1, ϵ_2 = total emissivity of surfaces 1 and 2
ϕ = heat flux density (W $\cdot$ m^{-2})
ρ = density (kg $\cdot$ m^{-3})
ρ_1, ρ_2 = total reflectivity of surfaces 1 and 2
σ = scattering coefficient (m^{-1})
σ_{SB} = Stefan-Boltzmann constant
$\tau_0 = \beta_e \cdot e$ = gray optical thickness
$\theta = T - T_0 = (T^* - T_0^*)/(Q/\rho C_P e)$, dimensionless temperature
$\overline{\theta}$ = Laplace transform of θ
$\overline{\phi}$ = Laplace transform of heat flux q
$\omega = \sigma/\beta_e$ = scattering albedo

Superscripts

$+$ = refers to the forward direction
$-$ = refers to the backward direction
$*$ = refers to dimensional quantities

Subscripts

r = radiative quantity

state resistance: It can be shown (Maillet et al., 1998) that the quadrupole is equivalent to three impedances—accounting for the transient character of the problem—connected in a T-network.

3 Physical Model

The idealized problem under consideration is constructed in light of the following conditions:

1 finite medium,
2 emitting, absorbing, and scattering medium,
3 gray medium (both the absorption coefficient and refractive index are independent of wavelength),
4 the medium boundaries are opaque, and diffuse gray emissivities and reflectivities are assumed (only the case of perfectly black or perfectly reflecting walls will be considered in the applications shown in the present paper), and
5 the medium is initially at uniform temperature T_0^*, and receives a quantity of heat Q at time $t^* > 0$. This condition is responsible for the expression of the dimensionless temperature used to solve the problem.

The governing equation is

$$\rho C_p \frac{\partial T^*(z, t)}{\partial t^*} = -\frac{\partial q^*}{\partial z^*} \quad 0 < z^* < e \quad t^* \geq 0 \tag{9}$$

where q^* is the total energy flux, which is the sum of the conductive heat flux $q_c^* = -k[\partial T^*(z^*, t^*)/\partial z^*]$ and of the radiative flux q_r^*, which is responsible for the temperature coupling.

In dimensionless form, Eq. (9) becomes

$$\frac{\partial \theta}{\partial t} = \frac{\partial^2 \theta}{\partial z^2} - \frac{\tau_0 T_0}{N_{pl}} \frac{\partial q_r(z)}{\partial z} \quad 0 < z < 1 \quad t \geq 0. \tag{10}$$

θ is the temperature rise with respect to the initial temperature, normalized with respect to the adiabatic temperature. τ_0 and N_{pl} are based on the extinction coefficient $\beta_e = \chi + \sigma$, as shown in the Nomenclature.

At this point, the expression for the radiative flux need to be specified and the problem was treated analytically for two major operations: one approximation (depending on whether the participating or the purely absorbing-emitting medium is considered) along with the assumption of linear transfer.

4 Analytical Approach for the Participating Medium (Model 3)

4.1 Modified Integral Equation for the Radiative Flux.

Assumption of Linear Transfer: Our attention will be confined to relatively small input energy, i.e., to the case of phenomena that keep the energy transfer within the linear domain. This leads to small elevations of the temperature T^* above the reference temperature T_0^*, and the term $(1 + (\theta(z)/T_0))^4$ that will appear later in Eqs. (12) and (14) will thus be approximated by

$$\left(1 + \frac{\theta(z)}{T_0}\right)^4 = 1 + \frac{4 \cdot \theta(z)}{T_0}. \tag{11}$$

The Two-Flux Approximation: Isotropic scattering is considered in the forward and backward directions (Schuster-Schwarzschild approximation), but anisotropic scattering can also be considered through the modified two-flux approximation.

The RTE is expressed by the following two classical equations, given in nondimensional form:

$$\frac{dL^+}{dz} + M \cdot L^+ = N \cdot L^- + \frac{P}{4} \cdot \left(1 + \frac{\theta(z)}{T_0}\right)^4$$

$$\frac{dL^-}{dz} - M \cdot L^- = -N \cdot L^+ - \frac{P}{4} \cdot \left(1 + \frac{\theta(z)}{T_0}\right)^4 \tag{12a,b}$$

where

$$M = (2 \cdot \chi + \sigma) \cdot e; \quad N = \sigma \cdot e; \quad P = 2 \cdot \chi \cdot e.$$

In the framework of the two-flux approximation (isotropic Schuster-Schwarzschild), and only in this case, the three parameters M, N, and P are related by

$$M = N + P. \tag{13}$$

M can be regarded as the hemispherical extinction coefficient, N the hemispherical backwards scattering coefficient, and P the hemispherical absorption coefficient.

As is usually done, preference will be given to the coefficients ν, β and P, with $\nu^2 = M^2 - N^2$ and $\beta = \nu/(M + N) = \sqrt{(M - N)/(M + N)}$.

The solution of the above set of Eqs. (12) is then

$$L^+(z) = C_1 \cdot (1 - \beta) \cdot e^{\nu \cdot z} - (1 - \beta) \frac{P}{8\beta} \int_0^z \left(1 + \frac{\theta(z')}{T_0}\right)^4 \exp(\nu \cdot (z - z'))dz' + C_2 \cdot (1 + \beta) \cdot e^{-\nu \cdot z}$$
$$+ (1 + \beta) \frac{P}{8\beta} \int_0^z \left(1 + \frac{\theta(z')}{T_0}\right)^4 \exp(\nu \cdot (z' - z))dz'$$

$$L^-(z) = C_1 \cdot (1 + \beta) \cdot e^{\nu \cdot z}$$
$$- (1 + \beta) \frac{P}{8\beta} \int_0^z \left(1 + \frac{\theta(z')}{T_0}\right)^4 \exp(\nu \cdot (z - z'))dz'$$
$$+ C_2 \cdot (1 - \beta) \cdot e^{-\nu \cdot z} + (1 - \beta) \frac{P}{8\beta} \int_0^z \left(1 + \frac{\theta(z')}{T_0}\right)^4 \exp(\nu \cdot (z' - z))dz', \tag{14a,b}$$

where C_1 and C_2 are the integration constants obtained, thanks to the radiative boundary conditions (see Appendix A for their determination).

By stating that $q_r(z) = L^+(z) - L^-(z)$ and applying the linearization of the emission terms (Eq. (11)), we get the following expression for the radiative flux:

$$q_r(z) = -2\beta C_1 \cdot e^{\nu \cdot z} + 2\beta C_2 \cdot e^{-\nu \cdot z} + \frac{P}{4 \cdot \nu} (e^{\nu \cdot z} - e^{-\nu \cdot z})$$
$$+ \frac{P}{T_0} \left[\int_0^z \theta(z') \cdot \exp(\nu \cdot (z - z')) \cdot dz' + \int_0^z \theta(z') \cdot \exp(\nu \cdot (z' - z)) \cdot dz' \right]. \tag{15}$$

When Eq. (15) is substituted for $q_r(z)$ in the right term of Eq. (10), the following modified integrodifferential equation (MIDE) governing heat transfer results:

$$\frac{\partial^2\theta}{\partial z^2}-\frac{\partial\theta}{\partial t} = -\frac{\tau_0 T_0 \nu}{N_{pl}}\left[2\beta C_1 e^{\nu z}+2\beta C_2 e^{-\nu z}-\frac{P}{4\nu}(e^{\nu z}+e^{-\nu z}) - \frac{2P}{\nu T_0}\theta(z)+\frac{P}{T_0}\int_0^z \theta(z')\exp(\nu(z-z'))dz' - \frac{P}{T_0}\int_0^z\theta(z')\exp(\nu(z'-z))dz'\right]. \quad (16)$$

4.2 Differential Equation. The two-flux approximation makes the radiative flux having the property that

$$\frac{\partial^2 q_r}{\partial z^2} = \nu^2 q_r(z) + \frac{2P}{T_0}\frac{\partial\theta}{\partial z}. \quad (17)$$

Thus, differentiating the energy equation (Eq. (10)) twice yields

$$\frac{\partial^4\theta}{\partial z^4}-\frac{\partial^3\theta}{\partial z^2\partial t} = \frac{\tau_0 T_0}{N_{pl}}\frac{\partial}{\partial z}\left(\frac{\partial^2 q_r}{\partial z^2}\right). \quad (18)$$

Substituting Eq. (17) for the second-order derivative of the radiative flux yields

$$\frac{\partial^4\theta}{\partial z^4}-\frac{\partial^3\theta}{\partial z^2\partial t} = \frac{\tau_0\nu^2 T_0}{N_{pl}}\frac{\partial q_r(z)}{\partial z} + \frac{2P\tau_0}{N_{pl}}\frac{\partial^2\theta}{\partial z^2}. \quad (19)$$

At this point, the expression $\partial q_r(z)/\partial z$ appears along with partial derivatives of θ, as in Eq. (10). Thus, introducing Eq. (10) in Eq. (19) and applying the Laplace transform in time

$$\bar\theta(p) = \int_0^\infty \theta(t)\cdot\exp(-p\cdot t)\cdot dt$$

leads to the following differential equation

$$\frac{d^4\bar\theta}{dz^4} - \left(p + \frac{2P\cdot\tau_0}{N_{pl}} + \nu^2\right)\frac{d^2\bar\theta}{dz^2} + p\cdot\nu^2\bar\theta = 0. \quad (20)$$

4.3 Solution. The solution of this ordinary differential equation gives the Laplace transform of the temperature as a function of the position in the medium

$$\bar\theta(z) = \sum_{i=1}^{4}\alpha_i\cdot\exp(\gamma_i z), \quad (21)$$

where $\gamma_{1,2,3,4} = \pm[-b \pm \sqrt{b^2-4ac}/2a]^{1/2}$ with a, b, and c being the respective coefficients of the characteristic equation derived from Eq. (20).

The integration constants α_1, α_2, α_3, and α_4 are determined by a set of four equations.

- Two of them are obtained by requiring that the solution (21) satisfies the Laplace transform of the MIDE (16). This yields

$$\sum_{i=1}^{4} X_i\cdot\alpha_i = \left(\frac{P}{8\beta\nu} - I_1\right)\Big/ p = \Psi_1$$

$$\sum_{i=1}^{4} Y_i\cdot\alpha_i = \left(\frac{P}{8\beta\nu} - J_1\right)\Big/ p = \Psi_2 \quad (22a,b)$$

where the X_i's and Y_i's are defined in Appendix B.

- The other two equations are found either by solving the direct problem or by formulating the problem in terms of quadrupole, as follows.

Direct Problem: Introducing the thermal boundary conditions of the problem in the Laplace domain, we have

$$-\left.\frac{\partial\bar\theta}{\partial z}\right|_{z=0} + \frac{\tau_0 T_0}{N_{pl}}\bar q_r(0) = -\mathrm{Bi}_1\bar\theta(0) + \bar f_1(p) = \bar\phi(0)$$

$$-\left.\frac{\partial\bar\theta}{\partial z}\right|_{z=1} + \frac{\tau_0 T_0}{N_{pl}}\bar q_r(1) = \mathrm{Bi}_2\bar\theta(1) + \bar f_2(p) = \bar\phi(1) \quad (23a,b)$$

where f_1 and f_2 reflect any thermal solicitations there may be on either face of the boundaries as a function of time and where heat losses are considered on both sides of the sample. Of course, the analytical treatment is preserved only if the Laplace transforms of f_1 and f_2 remain "simple" functions of p.

Knowing the four constants, α_i's, the temperature or heat flux can be computed anywhere in the medium.

Quadrupole Formulation: The quadrupole representation is given here as it is an attractive and powerful tool in the analytical treatment of heat transfer problems in the transient state (Degiovanni, 1988; Maillet et al., 1998). Equation (20) can lead to a linear relationship between the temperature-heat flux column vectors (in Laplace domain) on the front ($z = 0$) and rear ($z = 1$) side of the STM slab. $\bar\phi(0)$ and $\bar\phi(1)$ correspond here to the right-hand term of Eqs. (23*a*,*b*).

$$\begin{bmatrix}\bar\theta(0)\\ \bar\phi(0)\end{bmatrix} = \begin{bmatrix}A & B\\ C & D\end{bmatrix}\begin{bmatrix}\bar\theta(1)\\ \bar\phi(1)\end{bmatrix} \quad (24a,b)$$

The matrix transfer coefficients A, B, C, and D are obtained as follows: Writing the input-output variables of the system, that is for $z = 0$ and $z = 1$, produces a set of four equations. Equation (21) easily gives two equations

$$\bar\theta(0) = \sum_{i=1}^{4}\alpha_i \quad (25a)$$

$$\bar\theta(1) = \sum_{i=1}^{4}\alpha_i\cdot\exp(\gamma_i). \quad (25b)$$

As the radiative and conductive components of the heat fluxes at the boundaries correspond to the input-output fluxes, two additional equations can be obtained. At $z = 0$, for example, we have

$$\bar\phi(0) = -\left.\frac{\partial\bar\theta}{\partial z}\right|_{z=0} + \frac{\tau_0 T_0}{N_{pl}}\bar q_r(0)$$

and using Eq. (15) to express $\bar q_r(0)$—with the integral terms being explicitly calculated by introducing the analytical expression for $\bar\theta(z)$ (Eq. (21))—we then obtain

$$\bar\phi(0) = \sum_{i=1}^{4}\alpha_i\cdot\gamma_i\cdot\delta_i \quad (25c)$$

and, in the same way,

$$\bar\phi(1) = \sum_{i=1}^{4}\alpha_i\cdot\gamma_i\cdot\delta_i\cdot\exp(\gamma_i) \quad (25d)$$

with

$$\delta_i = \left[\frac{2P\cdot\tau_0}{N_{pl}(\gamma_i^2-\nu^2)} - 1\right]. \quad (26)$$

This finally leads to a set of six equations, (22*a*,*b*) and (25*a*,*b*,*c*,*d*), that are linear combinations of the α_i's. The quadrupole formulation must lead to the two Eqs. (24*a*,*b*), from which we can find the four expressions of the coefficients A, B, C, D if one eliminates the four other unknowns α_i.

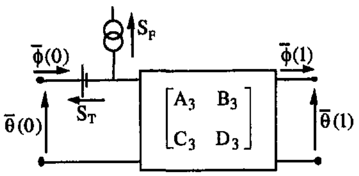

Fig. 2 Quadrupole for a participating semitransparent medium (model 3)

Equations (25*b*), (25*d*), (22*a*), and (22*b*) form the following linear system:

$$\begin{bmatrix} \bar{\theta}(1) \\ \bar{\phi}(1) \\ \Psi_1 \\ \Psi_2 \end{bmatrix} = \begin{bmatrix} e^{\gamma_1} & e^{\gamma_2} & e^{\gamma_3} & e^{\gamma_4} \\ \delta_1\gamma_1 e^{\gamma_1} & \delta_2\gamma_2 e^{\gamma_2} & \delta_3\gamma_3 e^{\gamma_3} & \delta_4\gamma_4 e^{\gamma_4} \\ X_1 & X_2 & X_3 & X_4 \\ Y_1 & Y_2 & Y_3 & Y_4 \end{bmatrix} \begin{bmatrix} \alpha_1 \\ \alpha_2 \\ \alpha_3 \\ \alpha_4 \end{bmatrix}$$

or $[O] = [M]\cdot[\alpha]$ where $[O]$ represents the output vector.

In the same way, Eqs. (25*a*) and (25*c*) can also be formulated as

$$\begin{bmatrix} \bar{\theta}(0) \\ \bar{\phi}(0) \end{bmatrix} = \begin{bmatrix} 1 & 1 & 1 & 1 \\ \delta_1\gamma_1 & \delta_2\gamma_2 & \delta_3\gamma_3 & \delta_4\gamma_4 \end{bmatrix} \begin{bmatrix} \alpha_1 \\ \alpha_2 \\ \alpha_3 \\ \alpha_4 \end{bmatrix}$$

or $[I] = [N]\cdot[\alpha]$, where $[I]$ is the input vector, leading to

$$[I] = [N]\cdot[M^{-1}]\cdot[O].$$

The problem of transient heat transfer by conduction and radiation together in a participating semitransparent layer is now reduced to the quadrupole form of Eq. (27). The solution is obtained by carrying out the calculations presented above using Matlab Inc. software, with a return to real space using the Stehfest (1970) algorithm.

$$\begin{bmatrix} \bar{\theta}(0) \\ \bar{\phi}(0) \end{bmatrix} = \begin{bmatrix} A_3 & B_3 \\ C_3 & D_3 \end{bmatrix} \begin{bmatrix} \bar{\theta}(1) \\ \bar{\phi}(1) \end{bmatrix} + \begin{bmatrix} S_T \\ S_F \end{bmatrix} \tag{27}$$

Subscript 3 is added for model 3. The presence of a column vector on the right side is due to the nonzero expression of the right-hand terms Ψ_1 and Ψ_2 of Eqs. (22). The symbolic representation of this matrix transfer formulation is given in Fig. 2. S_T and S_F behave as potential and current generators, respectively.

5 Analytical Approach for Absorbing-Emitting Medium (Model 2) and for Purely Scattering Medium (Model 1)

5.1 Absorbing-Emitting Medium (Model 2). The same analytical treatment as before can be applied for a purely absorbing-emitting medium. In this case, the analytical solution of the intensity balance equations, in dimensionless form, leads to the following integral expression for the radiative flux:

$$q_r(z) = 2\cdot L^+(0)\cdot E_3(\tau_0 z) - 2\cdot L^-(1)\cdot E_3(\tau_0(1-z)) + \frac{\tau_0}{2}\int_0^z \left(1 + \frac{\theta(z')}{T_0}\right)^4 E_2(\tau_0(z-z'))dz' - \frac{\tau_0}{2}\int_z^1 \left(1 + \frac{\theta(z')}{T_0}\right)^4 E_2(\tau_0(z'-z))dz'. \tag{28}$$

$L^+(0)$ and $L^-(1)$ are the dimensionless intensities given by the radiative limits under consideration (see Appendix A).

The main obstacle in providing a simplified answer to this problem is due to the presence of the exponential integral functions as the kernels of the integral terms of Eq. (28).

Carrier (1959) shows a technique in which an easily factored kernel replaces the original without serious loss of accuracy. This technique is generally referred as the differential approximation (Cess, 1966; Cogley et al., 1968). Applying this kernel substitution technique to a number of problems, he finds that reasonably accurate solutions are achieved when the substitute kernel duplicates at least three important features of the original kernel: the same singularity in the integration domain, the same area, and the same first moment. Applying this technique to radiative transfer problems, Lick (1965) found that an approximate kernel of the form $a\cdot\exp(-bz)$ can be substituted in Eq. (28) for the correct kernel $E_2(z)$, and also $(a/b)\cdot\exp(-bz)$ for the kernel $E_3(z)$, with a and b being, respectively, equal to $\frac{3}{4}$ and $\frac{3}{2}$.

By still considering the linear case (see Section 4.1), Eq. (28) now becomes

$$q_r(z) = L^+(0)\cdot e^{-\tau_0 z} - L^-(1)\cdot e^{-\tau_0(1-z)} - \frac{1}{4}(e^{-\tau_0 z} - e^{-\tau_0(1-z)}) + \frac{\tau_0}{T_0}\int_0^z \theta(z')\exp(-\tau_0(z-z'))dz' - \frac{\tau_0}{T_0}\int_z^1 \theta(z')\exp(-\tau_0(z'-z))dz'. \tag{29}$$

The variable τ_0 in Eq. (29) has now been changed to $(\frac{3}{2})\tau_0$ as a result of the kernel substitution. For the same reason, N_{pl} is now redefined as $(\frac{3}{2})N_{pl}$ in the problem. Appendix A gives the modified relations for the radiative equations at the limits.

It can be seen that this expression is similar to the one obtained for a participating medium in the two-flux approximation. It has the interesting feature expressed in Eq. (17). The same methodology can be used as in Section 4 to derive the quadrupole formulation of the problem (Appendix C gives the new expressions for the main mathematical equations of Section 4). Model 2 is represented symbolically in Fig. 3. A slight change can be seen in the fact that there is no additional vector on the right-hand side of Eqs. (A9) as it was for Eqs. (27). This is due to the null term in Eqs. (A7).

5.2 Purely Scattering Medium (Model 1). In this case, the heat and radiative balance equations are uncoupled, leading to the following theoretical model.

- Radiative transfer can be modeled by a simple resistance linking the radiative flux in the medium to the temperature difference between the two boundary surfaces. According to our nondimensional quantities and after linearization, it is easy to find from Eqs. (12*a,b*) and the radiative boundary Eqs. (A1) that

$$q_r = \frac{1}{T_0\left(\sigma\cdot e + \frac{1}{\epsilon_1} + \frac{1}{\epsilon_2} - 1\right)}\cdot(\theta(0) - \theta(1)).$$

This expression does not change when the Laplace transform is applied and the expression for the radiative resistance then becomes

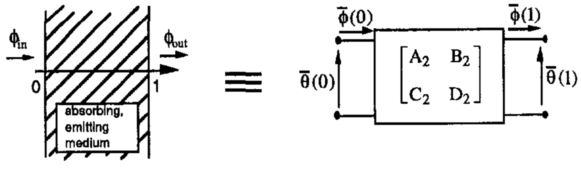

Fig. 3 Quadrupole for an absorbing-emitting semitransparent medium (model 2)

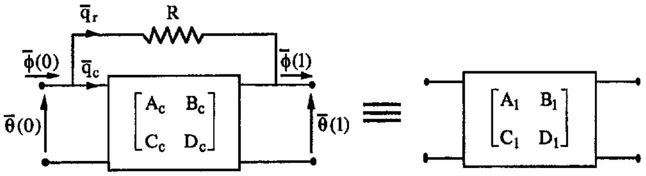

Fig. 4 Quadrupole for a purely scattering semitransparent medium (model 1)

$$R_r = T_0 \cdot \left(\sigma \cdot e + \frac{1}{\epsilon_1} + \frac{1}{\epsilon_2} - 1 \right) \tag{30}$$

- Conductive transfer is modeled (Section 2) in Laplace space by a matrix transfer which coefficients are

$$A_c = D_c = ch\sqrt{p}\,, \quad B_c = \frac{sh\sqrt{p}}{\sqrt{p}}\,, \quad C_c = \sqrt{p} \cdot sh\sqrt{p}\,.$$

The calculations must proceed carefully here, due to the use of dimensionless variables. The radiative flux q_r^* is normalized by $4n^2\sigma_{SB}T_0^{*4}$, but the expressions for A_c, B_c, C_c, and D_c of the purely conductive quadrupole are obtained for the conductive flux q_c^* normalized by $(Q \cdot a/e^2)$. Under these conditions, the agreement between the two current quantities requires that R_r be multiplied by the factor $(Q \cdot a/e^2 4n^2\sigma_{SB}T_0^{*4})$ which is nothing other than the ratio $N_{pl}/\tau_0 T_0$.

Thus the expression for the resistance that must be introduced in model 1 is

$$R = \frac{N_{pl}}{\tau_0} \cdot \left(\sigma \cdot e + \frac{1}{\epsilon_1} + \frac{1}{\epsilon_2} - 1 \right). \tag{31}$$

From the interaction between dimensioned and nondimensioned variables, R is no longer a radiative resistance but a radiative resistance divided by the conductive resistance, as attested by the proportionality with N_{pl}.

- Combining the two schemes, we get the following representation of the purely scattering case (model 1).

Resistance R is wired in parallel on the conductive quadrupole (Fig. 4) and the coefficients of the equivalent matrix transfer are

$$\begin{cases} A_1 = D_1 = \dfrac{B_c + R \cdot A_c}{B_c + R} \\[2ex] B_1 = \dfrac{B_c \cdot R}{B_c + R} \\[2ex] C_1 = \dfrac{A_c + D_c + R \cdot C_c - 2}{B_c + R} \end{cases}.$$

6 Computational Results

6.1 Validation of Analytical Models 2 and 3. In the test cases, the boundaries will always be considered as opaque, with diffuse emissivity equal to unity (nontransmissive black coating).

Table 1 Input data for simulations of Section 6.1

One-second square pulse $\dot{Q}$	50000 W/m^2
Heat capacity $\rho \cdot C_p$	2.2 10^6 J/m^3 K
Thermal conductivity k	1.5 W/mK
Reference temperature T_0^*	1000 K
Refractive index n	1.5
Emissivities ϵ_i	1
Biot number $\mathrm{Bi}_1 = \mathrm{Bi}_2$	1.51
Thickness of the slab e	0.01 m

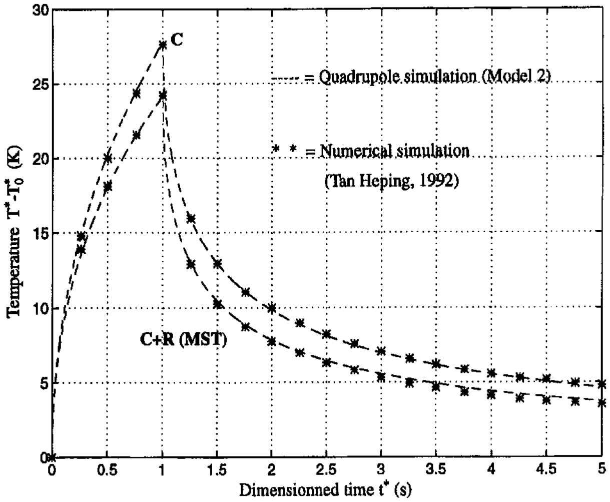

Fig. 5 Comparison between analytical (model 2) and numerical calculations. Front face thermal responses to a one-second square pulse of energy.

Validation of Model 2: The problem that will be considered is the temperature response on the front side of an absorbing STM sample subjected to a radiation pulse. This problem has been solved numerically by Tan Heping (1992) in the framework of a finite difference scheme applied to the energy equation, coupled to a Hottel's zonal method generalized by the ray-tracing method for solving the radiative transfer. The simulation conditions are given in Table 1. Two samples, one opaque and one semitransparent, are considered. The opaque sample serves as comparison for evaluating the level of radiative effects. The heat transfer in the semitransparent sample will be driven by conduction and radiation. The front-face time responses obtained by Tan Heping (1992) are reported in Fig. 5 with black asterisks (*).

The quadruple model 2 gives the coefficients of the quadrupole A_2, B_2, C_2, D_2, corresponding to the matrix transfer of an STM slab with opaque boundaries. To complete the modeling of the above test case, heat loss effects have only to be added and the type of excitation specified.

In the quadrupole technique, heat losses are described by the matrix transfer $[\begin{smallmatrix} 1 & 1/hS \\ 0 & 1 \end{smallmatrix}]$, which reduces to $\mathbf{H} = [\begin{smallmatrix} 1 & 0 \\ H & 1 \end{smallmatrix}]$ when the temperature variable used in the model is based on the difference $T^*(t) - T_0^*$, which is our case.

Considering equal heat transfer coefficients on both sides of the sample, the problem is expressed in the following matrix form:

$$\begin{bmatrix} \bar{\theta}(0) \\ \bar{\phi}(0) \end{bmatrix} = \begin{bmatrix} 1 & 0 \\ H & 1 \end{bmatrix} \begin{bmatrix} A_2 & B_2 \\ C_2 & D_2 \end{bmatrix} \begin{bmatrix} 1 & 0 \\ H & 1 \end{bmatrix} \begin{bmatrix} \bar{\theta}(1) \\ \bar{\phi}(1) \end{bmatrix}.$$

This can be written as $\mathbf{I} = \mathbf{H} \cdot \mathbf{M} \cdot \mathbf{HO} = \mathbf{M}'\mathbf{O}$ with $\mathbf{M}' = \mathbf{H} \cdot \mathbf{M} \cdot \mathbf{H}$, the new transfer matrix of coefficients $A' = A_2 + B_2 H$, $B' = B_2$, $C' = H(A_2 + D_2 + B_{2\mathrm{H}}) + C_2$, $D' = A'$ and $\mathbf{I}$, $\mathbf{O}$ denoting the input and output vectors.

Table 2 Gray band model for the numerical simulation

λ (mm)	n_k	χ_k $(m-1)$
0.5–2.7	1.5	10
2.7–4.5	1.5	1000
4.5–40.0	2.3	10000

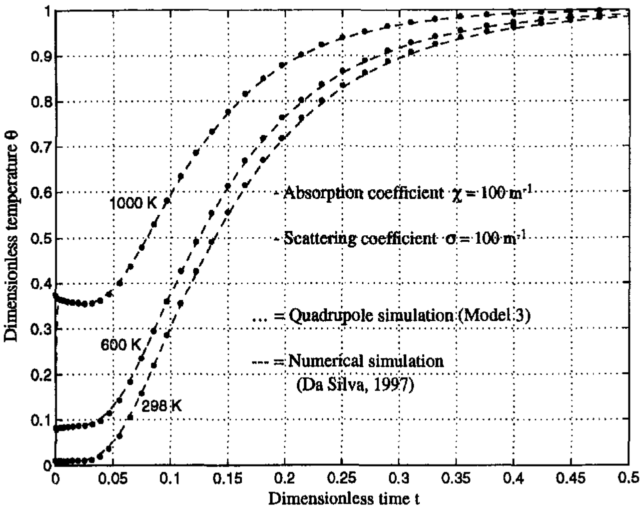

Fig. 6 Comparison between analytical (model 3) and numerical calculations. Rear face temperature responses to a flash excitation.

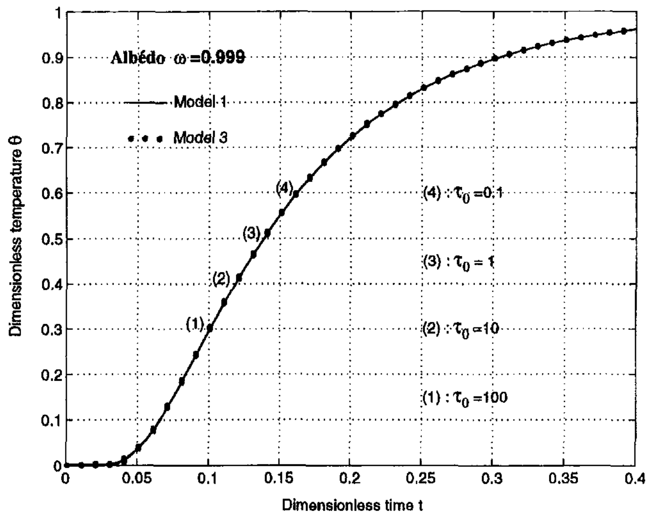

Fig. 7 Comparison between model 1 and model 3 in the case of reflecting walls

The perturbation is a one-second square pulse. The Laplace transform of the input flux is $\bar{\phi}(0) = (1 - e^{-dp})/p$, where d is the dimensionless time duration of the pulse. The output flux is $\bar{\phi}(1) = 0$ (no thermal perturbation on the rear face).

The front face response to an irradiation step is then computed by Eq. (32) below:

$$\bar{\theta}(0) = A'/(C'\bar{\phi}(0)). \qquad (32)$$

The numerical solution for the STM sample has been found for the nongray case with a model of three spectral bands, as reported in Table 2. In the quadrupole model, the index of refraction is taken to be equal to 1.5, and the equivalent gray absorption coefficient is found by making the maximum of the two curves meet exactly. We found that χ should be equal to 512 m^{-1}, and Fig. 5 shows that the analytical model fits very well with Tan Heping's results over the whole time period (curve $C + R$).

One conclusion of importance is that this analytical gray model (based on the kernel substitution technique) is able to perfectly fit nongray calculations as far as the "equivalent" gray absorption coefficient of the model is considered as a parameter to be estimated.

Lastly, one of the most important features of this analytical solution concerns the computation times, which are an average of 500 times smaller than those of same simulation runs made on the same computer with the numerical code. A simulation run (4000 time steps) takes 7.75 s of C.P.U time on a Sun Sparc 5 workstation.

Validation of Model 3: Figure 6 presents rear-face thermograms obtained for a participating medium subjected to an infinitely short pulse on its front face (flash method). Table 3 gives the simulation conditions for this case, studied numerically by Da Silva (1997). Solid line thermograms correspond to numerical simulations performed using a finite volume scheme for the energy equation and a discrete ordinate method for the radiative flux calculations. Isotropic scattering (phase function equal to 1) is considered. The gray absorption and scattering coefficient are both equal to 100 m^{-1}. Curve 2 (black points) is the thermogram obtained with model 3, where the scattering coefficient has been taken equal to 100 m^{-1} and the absorption coefficient to 75 m^{-1} (see explanations in Section 7). The agreement between numerical and analytical results is obvious.

Table 3 Input data for simulations of Section 6.1

Pulse of energy Q	3399 J/m^2
Heat capacity $\rho \cdot C_p$	1.7 10^6 J/m^3 K
Thermal conductivity k	1.38 W/mK
Reference temperature T_0^*	298-600-1000 K
Refractive index n	1.36
Emissivities ϵ_i	1
Biot number $Bi_1 = Bi_2$	0
Thickness of the slab e	0.002 m

6.2 Mutual Comparison Between Model 3 and Models 1 and 2.

Comparisons between the different models will be made on the basis of the rear-face temperature due to a heat pulse (flash method).

Numerical Comparison Between Models 1 and 3. Simulations were carried out in the case of reflecting (Fig. 7) and black surfaces (Figs. 8 and 9). During the simulation runs, two main input parameters (the thickness and the scattering coefficient) were set to cover a wide range of values. Table 4 gives the data used in these simulation runs.

Figures 7, 8, and 9 show that the two models are always in perfect agreement. For reasons of computational difficulties, the

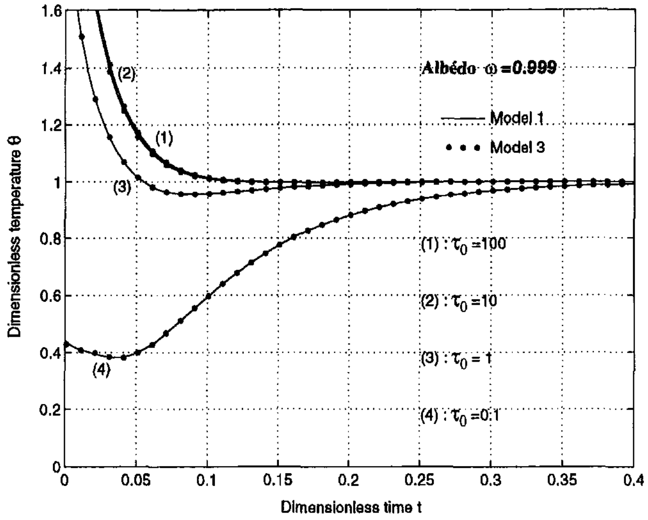

Fig. 8 Comparison between model 1 and model 3 in the case of black walls

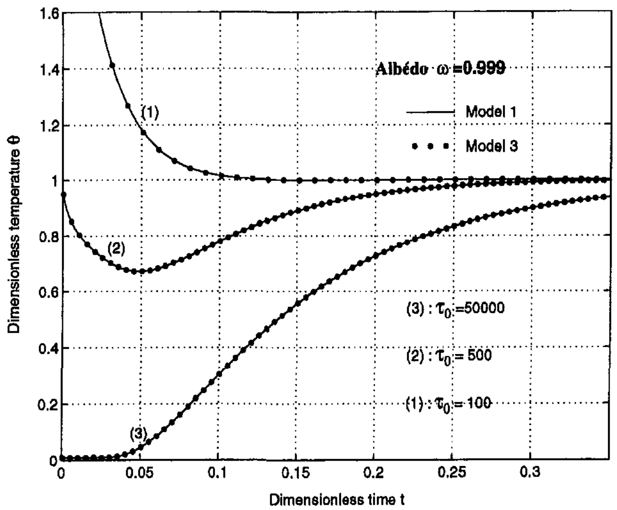

Fig. 9 Comparison between model 1 and model 3 in the case of black walls and very large optical thicknesses

albedo ω cannot be taken as exactly 1 to simulate a perfect scattering medium. In our simulations, it was set to 0.9999.

The analysis of the thermograms obtained in the case of reflecting boundaries (Fig. 7) is simple. Neither the boundaries nor the medium contribute to the radiative heat transfer. The thermograms reflect only the heat conduction mechanism. Due to the zero emissivities in relation (31), resistance R tends toward infinity and all the heat current flows through the conductive quadrupole (Fig. 4).

Figures 8 and 9 show the characteristics for black walls: a cold medium is considered, with small scattering coefficient, and its thickness is increased (Fig. 8). As the medium is highly transparent, the shape of the thermograms reflects a direct heat transfer between the two black walls. The thermograms for greater thicknesses are shown above those of lesser thickness only because of the normalization by $Q/\rho Ce$ applied to the temperature variable. Above optical thicknesses of the order of 10, the thickness effects tend to vanish; but the thermograms are not typical of an opaque material. This shows the fundamental difference between a purely scattering and partially absorbing radiative transfer, and the ambiguities that can result from misuse of the optical thickness criteria (see Section 7.2).

Starting at an optical thickness of 100 (curves 1 of Figs. 8 and 9), only the scattering coefficient is increased in Fig. 9. The agreement between the two models is perfect until the purely conductive limit is reached for an optical thickness of 50,000.

Validation for the Limiting Case of a Purely Absorbing Medium ($\omega = 0$). The validity of the general model (model 3) will now be demonstrated in the limiting case where $\sigma = 0$ (no scattering). Only the case of black walls will be examined, because it emphasizes certain aspects.

Table 4 Input data for simulations of Section 6.2

Pulse of energy Q	8600 J/m^2
Heat capacity $\rho \cdot C_p$	2.15 10^6 J/m^3 K
Thermal conductivity k	1 W/mK
Reference temperature T_0^*	800 K
Refractive index n	1
Emissivities ϵ_i	0 or 1
Biot number $Bi_1 = Bi_2$	0
Thickness of the slab e	from 0.004 to 4 m
Absorption or scattering coefficients χ or σ	from 23 m^{-1} to 23000 m^{-1}

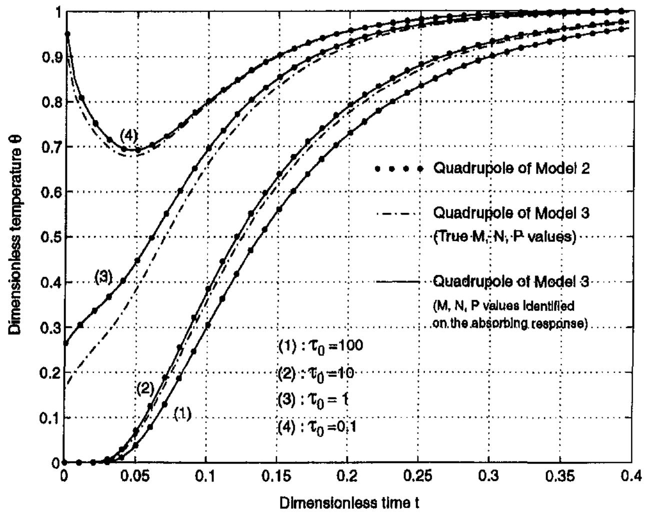

Fig. 10 Comparison between model 2 and model 3

The subject of this section will also be to study the application of the two-flux approximation (isotropic hemispherical intensities) to the absorbing medium. Figure 10 shows the thermograms (dashed and dotted curves) obtained with the two different models for four different optical thicknesses. The first conclusion should be that the general model 3 cannot correctly describe an absorbing medium, except for large optical thicknesses. This also holds for the case of reflecting walls, but is less apparent. Nevertheless, the similarity of the curves induced the authors to perform an inverse estimation of the parameters of model 3 on the thermograms generated by model 2 (dotted curves). The inversion process was performed simply, with a minimization tool provided by Matlab software and applied on the least-square criterion. The thermograms simulated with model 2 have been obtained for a thickness of 0.01 m and for the absorption coefficients reported in Table 5. The parameter estimation process carried out on these thermograms generates the three parameter values of model 3: M, N, P or rather χ, σ, $P = 2 \cdot \chi \cdot e$. The results of the identified parameters (i subscript) are reported in Table 6.

The quality of the estimation process was checked by comparing the residuals between the original thermogram (absorbing medium of model 2) and the thermogram obtained with model 3 with the estimated parameters of Table 6. They never exceed one percent, as attested by the agreement of the simulations presented in Fig. 10 (dotted curves compared to solid line curves). No random noise has been added to the test thermograms, because it is not the point here to study the inversion procedure (sensitivity analysis and robustness of the inversion).

The first remark is that the estimation process returns a null scattering coefficient. This proves that the two-flux model correctly describes a purely absorbing behavior. But of course this is not without influence on the estimated value of the absorbing coefficient, as will be seen later on.

The second remark is that the values found for P_i are strictly equal to $2 \cdot \chi_i \cdot e$. This is quite normal, since this relationship between P and χ (Eq. (13)) is part of the two-flux model.

Table 5

	Absorption coefficient χ (m^{-1})	Optical thickness τ_0
curve 4	10	0.1
curve 3	100	1
curve 2	1000	10
curve 1	10000	100

Table 6

	χ_i (m^{-1})	σ_i (m^{-1})	P_i
curve 4	7.4998	1.054 10^{-4}	0.15
curve 3	75.01	−0.0132	1.5002
curve 2	781.151	1.046 10^{-4}	15.626

The third comment is the most important. The estimated value of the absorption coefficient χ_i is equal to exactly $\frac{3}{4}$ of the input value. In other words, the value of χ that must be introduced in model 3 in order to simulate the perfectly absorbing medium must be 0.75 times the desired absorption coefficient. This is no chance occurrence. This factor of $\frac{4}{3}$ (or $\frac{3}{4}$) always appears when the two-flux method is applied to an absorbing medium and compared to P-1 or diffusion solutions. Generally, this is why researchers in radiative transfer consider that the two-flux method may only give good approximations for small optical thicknesses (Siegel and Howell, 1992, p. 789).

The first objection is that the two models also behave alike for strong optical thicknesses ($\tau_0 = 100$), as witnessed by curves 1 and 2 of Fig. 10. A rough justification for this can be seen in the slight discrepancy (3.8 percent) between the estimated value $\chi_i = 781.15$ and 0.75 times the input value of $\chi = 1000$, which is due to the fact that, in this particular case, the identification process is difficult because the sensitivity of the two models to the coefficient χ tends toward zero anyway.

The second objection is that the two-flux model perfectly describes the characteristics of a purely absorbing medium if the absorption coefficient input is corrected by a factor of $\frac{3}{4}$. This is valid for all optical thicknesses, for a wall in a thermal transient state and in presence of conduction (Fig. 10).

A few explanations for this can be found in analysing the angular distribution of the radiant intensity through an STM layer. To expedite the manual calculations, a linear temperature distribution is assumed within the layer. Figure 11 presents the angular dependence of the intensity for three different values of the optical thickness ($\tau_0 = 0.1, 1, 50$) calculated at location $z = 0.5$ in the medium (see Figs. 11(*a*), 11(*b*), 11(*c*)).

It is clear from these curves that the assumption of isotropic but different intensities in both the forward and backward hemispheres is more valid in the case of small and large optical thickness (Figs. 11(*a*), 11(*c*)). This is an effect of the one-dimensional geometry of the problem. An absorbing-emitting medium radiates energy isotropically. The boundaries emit energy isotropically. But this does not mean the intensity in the medium is isotropic.

Finally, this factor of $\frac{3}{4}$ that corrects χ in the two-flux model has to be applied for all optical thicknesses, simply because it encompasses both the radiative equilibrium approximation and the diffusion approximation (corrected by the emissive power jump at the boundaries (Deissler, 1964)). As it satisfies the two limiting cases, it is a good approximation in between. This should not be surprising, since it was first found in the theoretical works of many authors (Howell-Perlmutter, 1964; Deissler, 1964; Heaslet-Warming, 1965) that an interpolation formula of the form $1/(1/\epsilon_1 + 1/\epsilon_2 - 1 + 3\tau_0/4)$ for the radiative flux, led to good results for all optical thicknesses.

Heaslet and Warming (1965) report a maximum error of about three percent for the radiative flux, occurring near $\tau_0 = 0.4$. Deissler (1964) found that the calculated flux is within five percent of the exact solution for all values of τ_0.

From an experimental point of view, Banner (1990) shows the nead for $\frac{3}{4}$ factor in the two-flux model in order to match experimental results correctly. In a way, Tong and Tien (1983) also arrive at the same conclusion. They try to describe experimental data with both a classical two-flux conduction model and with a LAS (Linear Anisotropic Model) conduction model. The best agreement was obtained for the LAS model, which led to a radiative flux formula containing the factor $\frac{3}{4}$ to correct the optical thickness $\tau_0 = \beta_e \cdot e$.

In conclusion to this section, the use of this two-flux quadrupole model for participating media requires that the coefficients M, N, and P introduced in Section 4 follow the new relations $M = ((3/2)\chi + \sigma)\cdot e$; $N = \sigma \cdot e$; $P = (3/2)\cdot\chi\cdot e$.

7 Discussion

7.1 Limitations of the Model.

The Linear Assumption: To state the limitations of the analytical model clearly, we present simulations for the linear and nonlinear case (Fig. 12). The curves labelled (1-a, 1-n) are for the nonlinear case ($Q/\rho \cdot C_p \cdot e = 10$) and curves (2-a, 2-n) for the linear case ($Q/\rho \cdot C_p \cdot e = 0.1$): the input energy is varied by a factor of 100 from 860 J $\cdot$ m^{-2} to 86000 J $\cdot$ m^{-2} for a sample in same conditions as given by Table 4. The letter a or n stands either for the analytically or numerically calculated thermogram, respectively. Figure 12 demonstrates that the analytical model is not valid as long as the heat transfer is nonlinear: curve (1-a) differs largely from curve (1-n), which was obtained with the numerical code. At this point, it is interesting to note that the linear assumption is valid in almost all metrological systems, and especially in the flash method. With this new analytical model, and the efficiency of the calculations in terms of computational times, we may now engage an inverse approach to identify the true phonic diffusivity from an experimental thermogram. Furthermore, a sensitivity analysis should tell if a radiative parameter, namely an equivalent mean absorption coefficient, can be estimated on the same thermogram. This will be of great interest for researchers dealing with complex systems where reliable values of mean radiative parameters would

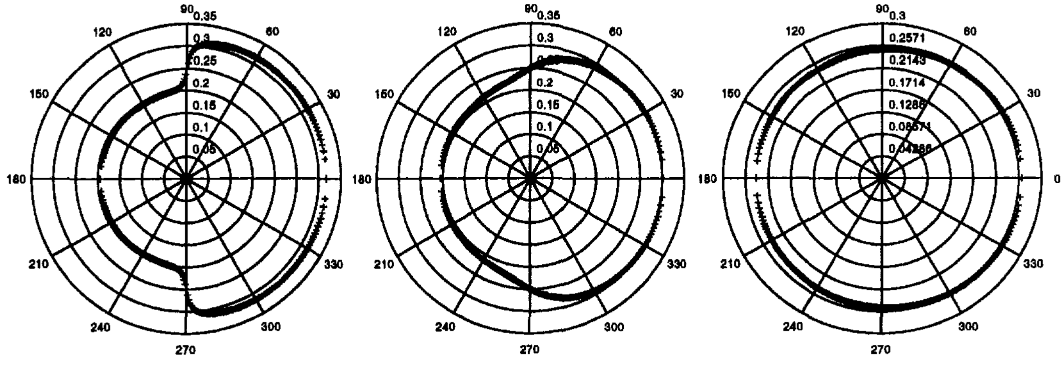

a- $\tau_0 = 0.1$ b- $\tau_0 = 1$ c- $\tau_0 = 100$

Fig. 11 Spatial intensity distributions for an absorbing-emitting ST medium for various optical thicknesses

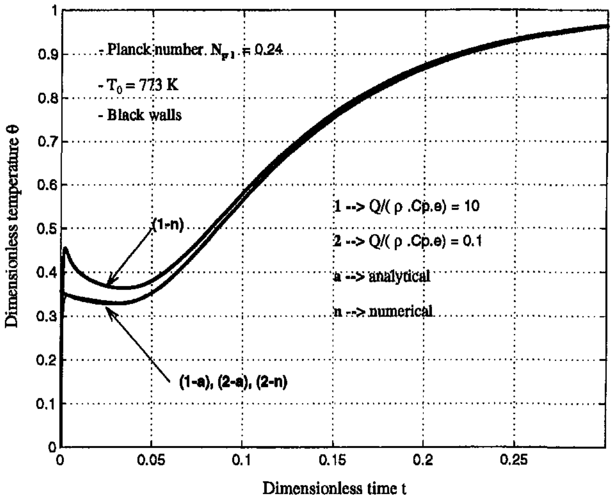

Fig. 12 Simulations of linear and nonlinear transfers. Limits of the analytical model.

avoid exhaustive nongray calculations or enhance the precision of gray calculations.

Gray Assumption: This last remark leads to a discussion of the gray approximation. There is a recurrent debate concerning the validity and choice of an equivalent gray absorption coefficient that can be assumed to describe the nongray behavior perfectly. The kernel substitution technique is interesting in that it mathematically defines the absorption coefficient that must be used, and the degree of approximation made in using it. A general mathematical result is that any kind of function can be expanded exactly into an infinite series of its moments. If the approximation of the exponential integral function by a pure exponential is made in truncating this series and matching the first two moments of the expansion, it can be strictly proven (Gilles et al., 1969) that the attenuation factor of the exponential is nothing other than the Rosseland mean coefficient. Gilles et al. discuss other average coefficients obtained by determining the coefficients of the new kernel, which is not based exclusively on the expansion of moments. The problem is then that there is no obvious criteria to determine which mean coefficient is most appropriate.

The first conclusion is that the Rosseland mean absorption coefficient is the exact absorption coefficient that must be used in the gray model, and the discrepancies with a nongray model are the result of the truncation of the moment expansion after only two terms.

The second conclusion has already been discussed in Section 6.1 where it is shown that there is no need to make nongray calculations, as this analytical model is able to restore the behavior of nongray materials. The "equivalent" absorption parameter is then considered as a parameter of the model that must first be determined by estimation methods.

7.2 From Large Optical Thickness-to-Thickness Effects and Diffusion Approximation. The simulations made using models 2 and 1 (or model 3 for both values of $\omega = 0$ or 1) reveal interesting features of the optical thickness criteria which might not have been investigated previously. A large optical thickness (of the order of 10 to 100) primarily means that there are no more thickness effects in the coupled conductive-radiative transfer, as can be seen in Fig. 8 (curves 1 and 2). Whatever the radiative transfer mechanisms are, the mean penetration distance is quite small compared to the characteristic dimension of the medium. Figure 13 illustrates this point:

- For a purely absorbant medium (curve 3) with a low extinction coefficient ($\beta_e = \chi = 23$ m^{-1}), a large optical thickness (10 or 100) means there are no thickness effects and temperature responses reflecting an enhanced heat transfer but due to a local heat diffusion mechanism. As these thermograms were obtained assuming no heat losses, the Parker model (Parker, 1961) can be used to identify the apparent diffusivity: $a_{\text{app}} = 0.139e^2/t^*_{1/2}$, in which the value 0.139 is the dimensionless time $t_{1/2}$ corresponding to the half-rise of the thermogram maximum. This half-rise time is 0.0181 and, by the interaction of the dimensionless variables, the ratio of the apparent to phonic conductivity is equal to the ratio of the dimensionless half-rise times. Thus $k_{\text{app}} = 0.139/0.0181 = 7.67$, since the phonic conductivity k was set equal to one.

  If we calculate the Rosseland radiative conductivity $k_r = 16\sigma T_0^{*3}/3\chi = 6.66$, we find that $k_{\text{app}} = k + k_r$, which confirms the diffusion character of the coupled heat transfer.
- For a purely scattering medium (curve 1 of Figs. 9 and 13) having the same small extinction coefficient ($\beta_e = \sigma = 23$ m^{-1}), a large optical thickness (10 or 100) means there are no thickness effects, but rather a completely different behavior towards the heat transfer. Energy is transferred by conduction and by a direct transfer between the two boundaries. For small $\beta_e = \sigma$, the Planck number N_{pl} is small and the heat transport is no longer a diffusion process. The diffusion limit is obtained if the scattering coefficient is increased greatly. Increasing the number of scattering particles decreases the scattering mean penetration distance $1_{m,s}$. When it is of the order of 1/50,000, the thermogram resemble a purely conductive thermogram, except for the slight jump on the rear-face temperature at short times. This is because, in the case of isotropic scattering, a particle emitted from one wall has very little chance of reaching the other wall. This jump is like a measure of the fraction of radiative energy transferred from one boundary to another. It is then interesting to note that the range of optical thicknesses for considering a local heat transfer mechanism differs widely between the two limiting cases of pure absorption or pure scattering.

The quadrupole representation explains these results simply if we consider how the resistance R (Eq. (31)) behaves in the scheme of Fig. 4. For small scattering optical thickness, $\sigma \cdot e$ is small enough so that the walls have an effect through the term $1/\epsilon_1 + 1/\epsilon_2 - 1$. As the thickness increases so that $\sigma \cdot e$ becomes much greater than $1/\epsilon_1 + 1/\epsilon_2 - 1$, then the resistance is blocked at the value of N_{pl}. If the scattering coefficient is now increased (curves 1 to 3 in Fig. 9), the resistance varies as N_{pl}, i.e., as σ, and can become large enough so that no more heat flux can

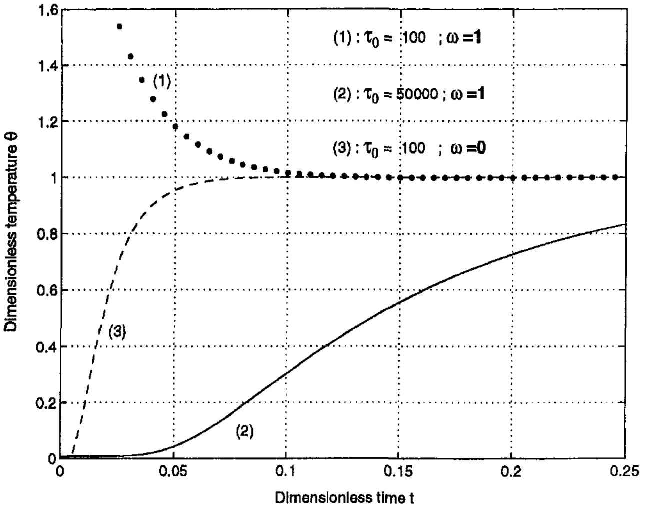

Fig. 13 Comparison of radiative behaviors at large values of τ_0 in the case of $\omega = 1$ and $\omega = 0$

pass through it: only the conductive quadrupole occurs in the heat transfer.

7.3 From Two-Flux Approximation to a Constitutive Equation for Semitransparent Layers. Our goal in this section is to gain greater insight into the possible uses of such an analytical model.

The two-flux approximation may seem to be a powerful limiting condition for a safe use of this model. The problem is then to establish, either experimentally or numerically, in which cases the scattering properties are such that the approximation holds (purely radiative analysis), and the interest of the present model is then restricted to direct calculations of transient coupled heat transfer.

Many papers have been written on the first topic (Daniel et al., 1979; Tong-Tien, 1980; Brewter-Tien, 1982; Mengüç-Viskanta, 1982) and it appears that, except for the case of interfaces within the medium, the usefulness of the two-flux approach has not been discredited in general (Brewster-Tien, 1982). Furthermore, Tong and Tien (1980) have pointed out that, although intermediate parameters may vary appreciably between the two-flux model and more precise models, the total predicted heat flux is usually very nearly the same for both cases. This conclusion is generally established when the only radiative transfer is examined, and we may expect this to be truer in the presence of conduction. This quadrupole formulation of the combined transient heat transfer in a participating medium is then interesting as concerns

- the accuracy of the model, shown in the two limiting cases of purely absorbing and purely scattering media (Section 6.2) and also in the case of a participating medium with isotropic scattering (Section 6.1),
- very short computation times, and
- the efficiency inherent in the quadrupole formulation, to adapt the model to any kind of thermal boundary conditions.

One possible feature of interest with such an analytical model is that it could help define a kind of constitutive equation for any kind of semitransparent layer. The predictions of the two-flux models are generally poor for acute single scattering anisotropy although modified or anisotropic two-flux models exist (Viskanta, 1982). This is inherent in the semi-isotropic assumption of the model which eliminates one parameter (the phase function) and the radiative model is governed only by two parameters (χ and σ are the two true parameters, M and N are the two parameters resulting of the two-flux formulation). The idea is then to leave M and N independent of each other and not mathematically related to the optical properties of the medium. Instead of determining the absorption coefficient, the scattering coefficient, and the mixture phase function from microscopic models and then calculating the thermal behavior in a coupled and generally difficult direct model, this efficient model (in terms of computation times) could allow an inverse analysis to identify the values of only two coefficients M and N that would reproduce the same thermal behavior when entered in a simple two-flux model. This process can be seen as similar to the calculation of scattering fractions for use in radiative flux models (Koenigsdorff et al., 1991), except that in this case the link with the physics is preserved: a microscopic model yields the mixture phase function which determines the backward scattering fraction for use in the two-flux model. In the present case, it is suggested that the three physical parameters characterizing the modified two-flux model be dropped, in favor of two global parameters M and N. These coefficients would then reflect the behavior of STM towards radiative transport, whatever the nature of the mechanisms involved. This was proven in Section 6.2 for the purely absorbing medium, and we expect this to be true for any kind of STM.

This conjecture must of course be verified. But it seems to be valid because first, the presence of absorption tends to distribute the intensity spatially; second, the presence of conduction smoothes the radiative effects on the temperature distribution; and third, for a purely scattering medium, model 1 has been used successfully. In a flash experiment, the radiative resistance is identified (Jeanmaire, 1992) together with the true thermal diffusivity of the STM, which is the quantity of interest.

Such a study will be the object of subsequent developments.

8 Conclusion

The transient one-directional conductive and radiative heat transfer in a participating medium has been modeled analytically in the framework of the two-flux model and in the case of a linear transfer. The analytical solution is obtained thanks to the differential approximation. The method has also been extended to a purely absorbing-emitting medium by use of a kernel substitution technique. An analytical model is also given for the purely scattering case. Both solutions receives a common formulation known as the quadrupole formulation which is a matrix transfer representation of the problem. This model has been used to predict the transient thermal response of scattering and purely absorbant material. The agreement has been found to be excellent in these two cases. Concerning the purely absorbant medium, one major finding is that the two-flux model can describe the absorbing behavior perfectly insofar as the value of the absorption coefficient is attenuated by a factor $\frac{3}{4}$ (determined in inverse analysis) compared with the desired value. Calculations, which require a Matlab program of less than 100 lines, are very efficient in terms of computation times and have proven to be in agreement with numerical solutions. The quadrupole representation of the solutions now can be extended to various problems involving a finite, participating medium with or without internal energy sources. As long as the layer boundaries are opaque, a great variety of thermal conditions can be studied, such as the thermal behavior of multilayered materials involving one or more semitransparent layers. The use of such models as reduction models could be powerful when combined to parameter estimation analysis.

References

Andre, S., and Degiovanni, A., 1995, "A Theoretical Study of the Transient Coupled Conduction and Radiation Heat Transfer in Glass. Phonic Diffusivity Measurements by the Flash Technique," *International Journal of Heat and Mass Transfer*, Vol. 38, No. 18, pp. 3401–3412.

Banner, D., 1990, "Propriétés Radiatives des Verres et des fontes de Silicates. Modélisation des transferts de chaleur," Thèse, Ecole Centrale de Paris.

Brewster, M. Q., and Tien, C. L., 1982, "Examination of the Two-Flux Model for Radiative Transfer in Particular Systems," *International Journal of Heat and Mass Transfer*, Vol. 25, No. 12, pp. 1905–1907.

Carrier, G. F., 1959, "Useful Approximations in Wiener-Hopf Problems," *Journal of Applied Physics*, Vol. 30, No. 11, pp. 1769–1774.

Cess, R. D., 1966, "On the Differential Approximation in Radiative Transfer," *Zeitschrift für Angewandte Mathemathik und Physik*, Vol. 17, pp. 776–781.

Cogley, J. C., Vincenti, W. G., and Gilles, S. E., 1968, "Differential Approximation for Radiative Transfer in a Nongrey Gas near Equilibrium," *AIAA Journal*, Vol. 3, pp. 155–553.

Daniel, K. J., Laurendeau, N. M., and Incropera, F. P., 1979, "Prediction of Radiation Absorption and Scattering in Turbid Water Bodies," ASME JOURNAL OF HEAT TRANSFER, Vol. 101, pp. 63–67.

Da Silva, Z. E., 1997, "Transferts Couplés Conduction/Rayonnement. Application de la Méthode Flash aux Milieux Semi-transparents." Thèse de Docteur de 3ème cycle, INSA Lyon.

Degiovanni, A., 1988, "Conduction dans un Mur Multicouche avec Sources: Extension de la Notion de Quadripôle," *International Journal of Heat and Mass Transfer*, Vol. 31, No. 3, pp. 553–557.

Deissler, R. G., 1964, "Diffusion Approximation for Thermal Radiation in Gases with Jump Boundary Condition," ASME JOURNAL OF HEAT TRANSFER, Vol. 86C, pp. 240–246.

Gilles, S. E., Cogley, J. C., and Vincenti, W. G., 1969, "A Substitute-Kernel Approximation for Radiative Transfer in a Nongrey Gas near Equilibrium, with Application to Radiative Acoustics," *International Journal of Heat and Mass Transfer*, Vol. 12, pp. 445–458.

Heaslet, M. A., and Warming, R. F., 1965, "Radiative Transport and Wall Temperature Slip in an Absorbing Planar Medium," *International Journal of Heat and Mass Transfer*, Vol. 8, pp. 979–994.

Heping, T., and Lallemand, M., 1989, "Transient Radiative-Conductive Heat Transfer in Flat Glasses Submitted to Temperature, Flux and Mixed Boundary

Conditions,'' *International Journal of Heat and Mass Transfer,* Vol. 32, pp. 795–810.

Heping, T., Maestre, B., and Lallemand, M., 1991, ''Transient and Steady-State Combined Heat Transfer in Semi-transparent Materials Subjected to a Pulse or a Step Irradiation,'' ASME JOURNAL OF HEAT TRANSFER, Vol. 113, pp. 166–173.

Howell, J. R., 1988, ''Thermal Radiation in Participating Media: The Past, the Present and Some Possible Futures,'' ASME JOURNAL OF HEAT TRANSFER, Vol. 110, pp. 1220–1229.

Howell, J. R., and Perlmutter, M., 1964, ''Monte Carlo Solution of Thermal Transfer Through Radiant Media Between Gray Walls,'' ASME JOURNAL OF HEAT TRANSFER, Vol. 86C, pp. 116–122.

Koenigsdorff, R., Miller, F., and Ziegler, R., 1991, ''Calculation of Scattering Fractions for Use in Radiative Flux Models,'' *International Journal of Heat and Mass Transfer,* Vol. 34, No. 10, pp. 2673–2676.

Jeanmaire, A., Martin, B., Billerey, D., and Degiovanni, A., 1992, ''A New Method for the Measurement of Thermal Conductivity of Semi-transparent Insulating Foams,'' Conference on Heat Transfer, July, Milano.

Lick, W., 1965, ''Transient Energy Transfer by Radiation and Conduction,'' *International Journal of Heat and Mass Transfer,* Vol. 8, pp. 119–127.

Maillet, D., Degiovanni, A., Batsale, J. C., Moyne, C., and André, S., 1998, *Thermal Quadrupoles: An Efficient Method for Solving the Heat Equation through Integral Transforms,* John Wiley and Sons, New York, to be published.

Mengüç, M. P., and Viskanta, R., 1982, ''Comparison of Radiative Transfer Approximations for Highly Forward Scattering Planar Medium,'' ASME paper 82-HT-17.

Özisik, M. N., 1973, *Radiative Transfer and Interactions with Conduction and Convection,* Wiley Interscience, New York.

Parker, W. J., Jenkins, R. J., Butler, C. P., and Abbot, G. L., 1961, ''Flash Method for Determining Thermal Diffusivity, Heat Capacity and Thermal Conductivity,'' *J. Appl. Phys.,* Vol. 32, pp. 1679–1684.

Siegel, R., and Howell, J. R., 1992, *Thermal Radiation Heat Transfer,* 3rd Ed., Hemisphere, Bristol, PA.

Stehfest, H., 1970, ''Remarks on Algorithm 368—Numerical Inversion of Laplace Transforms,'' *Comm. A.C.M,* Vol. 13, pp. 47–49.

Tong, T. W., and Tien, C. L., 1980, ''Resistance Network Representation of Radiative Heat Transfer with Particulate Scattering,'' *Journal of Quantitative Spectroscopy & Radiative Transfer,* Vol. 24, pp. 491–503.

Tong, T. W., and Tien, C. L., 1983, ''Radiative Heat Transfer in Fibrous Insulations—Part I: Analytical Study,'' ASME JOURNAL OF HEAT TRANSFER, Vol. 105, pp. 76–75.

Tong, T. W., Yang, Q. S., and Tien, C. L., 1983, ''Radiative Heat Transfer in Fibrous Insulations—Part II: Experimental Study,'' ASME JOURNAL OF HEAT TRANSFER, Vol. 105, pp. 76–81.

Viskanta, R., and Anderson, E. E., 1975, ''Heat Transfer in Semi-transparent Solids,'' *Advances in Heat Transfer,* Vol. 11, pp. 315–553.

Viskanta, R., 1982, ''Radiation Heat Transfer: Interaction with Conduction and Convection and Approximate Methods in Radiation,'' *Proceedings of the Seventh Int. Heat Transfer Conference,* München, HT-Vol. 1, pp. 103–121.

APPENDIX A

Participating Medium (Model 3)

For the specified radiative boundary conditions, the non-dimensional intensities are

$$L^+(0) = \frac{\epsilon_1}{4}\left(1 + \frac{\theta(0)}{T_0}\right)^4 + \rho_1 \cdot L^-(0)$$

$$L^-(1) = \frac{\epsilon_2}{4}\left(1 + \frac{\theta(1)}{T_0}\right)^4 + \rho_2 \cdot L^+(1). \tag{A1}$$

Substituting equations (14*a*,*b*) (respectively, at $z = 1$ and $z = 0$) for their equivalent on the right-hand side of the above equations, and applying the linearization, we get an algebraic system from which we can determine the two unknowns C_1 and C_2:

$$C_1 = I_1 + I_2 \cdot \theta(0) + I_3 \cdot \theta(1) + I_4 \int_0^1 \theta(z') \cdot \exp(\nu(1 - z'))dz' + I_5 \int_0^1 \theta(z') \cdot \exp(\nu(z' - 1))dz'$$

$$C_2 = J_1 + J_2 \cdot \theta(0) + J_3 \cdot \theta(1) + J_4 \int_0^1 \theta(z') \cdot \exp(\nu(1 - z'))dz' + J_5 \int_0^1 \theta(z') \cdot \exp(\nu(z' - 1))dz'$$

where I_i and J_i are constants equal to K_i/D and L_i/D, respectively, and

$$D = (\rho_1 + \rho_2) \cdot (1 - \beta^2) \cdot (e^{-\nu} - e^{\nu}) + (1 + \beta)^2 \cdot (e^{\nu} - \rho_1 \cdot \rho_2 \cdot e^{-\nu}) + (1 - \beta)^2 \cdot (\rho_1 \cdot \rho_2 \cdot e^{\nu} - e^{-\nu})$$

$$K_1 = -\frac{\epsilon_1}{4}[(1 - \beta)e^{-\nu} - \rho_2 \cdot (1 + \beta)e^{-\nu}] - \mathbf{F} \cdot [\rho_1 \cdot (1 - \beta) - (1 + \beta)]$$

$$K_2 = -\frac{\epsilon_1}{T_0}[(1 - \beta)e^{-\nu} - \rho_2 \cdot (1 + \beta)e^{-\nu}]$$

$$K_3 = -\frac{\epsilon_2}{T_0}[\rho_1 \cdot (1 - \beta) - (1 + \beta)]$$

$$K_4 = -\frac{P}{2\beta T_0}[(1 + \beta) - \rho_2 \cdot (1 - \beta)][\rho_1 \cdot (1 - \beta) - (1 + \beta)]$$

$$K_5 = -\frac{P}{2\beta T_0}[\rho_2 \cdot (1 + \beta) - (1 - \beta)][\rho_1 \cdot (1 - \beta) - (1 + \beta)].$$

$$L_1 = \frac{\epsilon_1}{4}[(1 + \beta)e^{\nu} - \rho_2 \cdot (1 - \beta)e^{\nu}] + \mathbf{F} \cdot [\rho_1 \cdot (1 + \beta) - (1 - \beta)]$$

$$L_2 = -\frac{\epsilon_1}{T_0}[\rho_2 \cdot (1 - \beta)e^{\nu} - (1 + \beta)e^{\nu}]$$

$$L_3 = \frac{\epsilon_2}{T_0}[\rho_1 \cdot (1 + \beta) - (1 - \beta)]$$

$$L_4 = \frac{P}{2\beta T_0}[(1 + \beta) - \rho_2 \cdot (1 - \beta)][\rho_1 \cdot (1 + \beta) - (1 - \beta)]$$

$$L_5 = \frac{P}{2\beta T_0}[\rho_2 \cdot (1 + \beta) - (1 - \beta)][\rho_1 \cdot (1 + \beta) - (1 - \beta)]$$

and

$$\mathbf{F} = \frac{\epsilon_2}{4} + \frac{P}{8\beta\nu}e^{\nu}((1 + \beta) - \rho_2 \cdot (1 - \beta)) - \frac{P}{8\beta\nu}e^{-\nu}(\rho_2 \cdot (1 + \beta) - (1 - \beta)) + \frac{P}{4\beta\nu} \cdot (\rho_2 - 1)$$

The Emitting-Absorbing Medium (Model 2)

For the specified radiative boundary conditions, the intensities are now (Özisik, 1973, p. 277):

$$L^+(0) = \frac{a_1 + b_1 \cdot a_2}{1 - b_1 \cdot b_2}$$

$$L^-(1) = \frac{a_2 + b_2 \cdot a_1}{1 - b_1 \cdot b_2} \tag{A2}$$

with, in nondimensional form,

$$a_1 = \frac{\epsilon_1}{4}\left(1 + \frac{\theta(0)}{T_0}\right)^4 + 2\rho_1 \int_0^1 \frac{\tau_0}{4}\left(1 + \frac{\theta(z')}{T_0}\right)^4 E_2(\tau_0 z'))dz'$$

$$a_2 = \frac{\epsilon_2}{4}\left(1 + \frac{\theta(1)}{T_0}\right)^4 + 2\rho_2 \int_0^1 \frac{\tau_0}{4}\left(1 + \frac{\theta(z')}{T_0}\right)^4 E_2(\tau_0(1 - z'))dz'$$

and

$$b_i = 2\rho_i E_3(\tau_0) \quad \text{for} \quad i = 1, 2.$$

Applying the same analytical treatment (linearization + kernel substitution) as was done with the radiative flux equation, one finds that the Laplace transforms of the intensities at the frontiers are

$$\bar{L}^+(0) = \frac{u_0}{p} + u_1 \cdot \overline{\theta(0)} + u_2 \cdot \overline{\theta(1)} + u_3 \int_0^1 \bar{\theta}(z')e^{-\tau_0 z'}dz' + u_4 \int_0^1 \bar{\theta}(z')e^{-\tau_0(1-z')}dz'$$

$$\bar{L}^-(1) = \frac{v_0}{p} + v_2 \cdot \overline{\theta(0)} + v_1 \cdot \overline{\theta(1)} + v_4 \int_0^1 \bar{\theta}(z')e^{-\tau_0 z'}dz' + v_3 \int_0^1 \bar{\theta}(z')e^{-\tau_0(1-z')}dz' \quad \text{(A3)}$$

with

$$u_0 = 1/4 \qquad u_1 = \frac{\epsilon_1}{T_0 \cdot w} \qquad u_2 = \frac{\epsilon_2 \rho_1 \cdot \exp(-\tau_0)}{T_0 w} \qquad u_3 = \frac{\rho_i \cdot \tau_0}{T_0 \cdot w} \qquad u_4 = \frac{\rho_1 \cdot \rho_2 \cdot \tau_0 \cdot \exp(-\tau_0)}{T_0 \cdot w}$$

$$v_0 = 1/4 = u_0 \qquad v_1 = \frac{\epsilon_2}{T_0 \cdot w} \qquad v_2 = \frac{\epsilon_i \cdot \rho_2 \cdot \exp(-\tau_0)}{T_0 \cdot w} \qquad v_3 = \frac{\rho_2 \cdot \tau_0}{T_0 \cdot w} \qquad v_4 = u_4$$

and $w = 1 - \rho_1 \cdot \rho_2 \cdot \exp(-2 \cdot \tau_0)$ and τ_0 is $\frac{3}{2}\chi \cdot e$.

APPENDIX B

Coefficients of Equations (14*a,b*) (Model 3)

$$X_i = I_2 + I_3 \cdot e^{\gamma_i} + I_4 \cdot \frac{e^{\gamma_i} - e^{\nu}}{\gamma_i - \nu} + I_5 \cdot \frac{e^{\gamma_i} - e^{-\nu}}{\gamma_i + \nu} + \frac{P}{2\beta T_0} \frac{1}{\gamma_i - \nu}$$

$$Y_i = J_2 + J_3 \cdot e^{\gamma_i} + J_4 \cdot \frac{e^{\gamma_i} - e^{\nu}}{\gamma_i - \nu} + J_5 \cdot \frac{e^{\gamma_i} - e^{-\nu}}{\gamma_i + \nu} - \frac{P}{2\beta T_0} \frac{1}{\gamma_i + \nu} \quad \text{(A4)}$$

Corresponding Coefficients for Model 2

$$X_i = u_1 + u_2 \cdot e^{\gamma_i} + u_3 \cdot \frac{e^{(\gamma_i - \tau_0)} - 1}{\gamma_i - \tau_0} + u_4 \cdot \frac{e^{\gamma_i} - e^{-\tau_0}}{\gamma_i + \tau_0} - \frac{\tau_0}{T_0} \frac{1}{\gamma_i - \tau_0}$$

$$Y_i = v_2 + v_1 \cdot e^{\gamma_i} + v_4 \cdot \frac{e^{(\gamma_i - \tau_0)} - 1}{\gamma_i - \tau_0} + v_3 \cdot \frac{e^{\gamma_i} - e^{-\tau_0}}{\gamma_i + \tau_0} + \frac{\tau_0}{T_0} \frac{e^{\gamma_i}}{\gamma_i - \tau_0} \quad \text{(A5)}$$

APPENDIX C

Derivation of Model 2: Main Equations

Former Eq. (20) is now

$$\frac{d^4\bar{\theta}}{dz^4} - \left(p + \frac{2P \cdot \tau_0}{N_{pl}} + \nu^2\right) \frac{d^2\bar{\theta}}{dz^2} + p \cdot \nu^2 \bar{\theta} = 0. \quad \text{(A6)}$$

Equations (22*a,b*), (26), and (27) becomes

$$\sum_{i=1}^{4} X_i \cdot \alpha_i = 0$$

$$\sum_{i=1}^{4} Y_i \cdot \alpha_i = 0 \quad \text{(A7)}$$

where the X_i's and Y_i's are defined in Eqs. (A5) above,

$$\delta_i = \left[\frac{2\tau_0^2}{N_{pl}(\gamma_i^2 - \tau_0^2)} - 1\right]. \quad \text{(A8)}$$

$$\begin{bmatrix} \bar{\theta}(0) \\ \bar{\phi}(0) \end{bmatrix} = \begin{bmatrix} A_2 & B_2 \\ C_2 & D_2 \end{bmatrix} \begin{bmatrix} \bar{\theta}(1) \\ \bar{\phi}(1) \end{bmatrix} \quad \text{(A9)}$$

One-Dimensional Phase Field Models With Adaptive Grids

J. F. McCarthy
BHP Co. Ltd.,
600 Bourke Street,
Melbourne, Victoria 3000,
Australia

The phase field method has been demonstrated to hold promise for enabling the physics at the microscale to be incorporated in macroscopic models of solidification. However, for quantitatively accurate simulations to be performed, it will be necessary to develop algorithms which enable the interface width to be made very small. Adaptive grid techniques offer a means of achieving this within practical computational limits. This paper investigates the solution of one-dimensional phase field models using an adaptive grid technique. Three problems are considered: (1) the classical Stefan model, (2) the case of a solid sphere in equilibrium with its melt, and (3) a modified Stefan model with a generalized kinetic undercooling term. The numerical results are compared with those obtained using a fixed grid algorithm. In general, the adaptive grid technique is shown to be far more efficient, but it requires some care in its implementation.

1 Introduction

Recent research efforts have led to the development of sophisticated computational techniques for modeling important metallurgical processes in solidification, including the details of microstructure formation at the dendritic scale. These techniques are applicable to a wide range of industrial processes; from ingot casting and the continuous casting of steel strip to the precision casting of single crystals for jet turbine blades. In fact, it has been estimated that, worldwide, as many as ten billion metallic dendrites are produced in industry every second during solidification (Rappaz and Kurz, 1995).

In the solidification of alloys (Rappaz, 1989), it is events on the smallest scales (e.g., the transport of heat and solute in the vicinity of dendrite tips) that lead to the microsegregation features of the final product (e.g., the size and shape of grains). However, it is these events which traditionally have been the hardest to incorporate in computer models because of the disparity between the scale of the events and the physical scale of the overall domain of interest. The true physical size of the width of the solid-liquid interface is of the order of 10^{-8} cm, while the overall domain of interest may vary between 10^{-1} cm for dendritic growth and 10^{2} cm for the casting of metals. It has been necessary to develop ad hoc rules relating microstructural parameters to the macroscopic temperature field. These rules are not adequate for a quantitative description of all relevant phenomena.

The "phase field method" (Boettinger et al., 1994; Caginalp, 1986; Caginalp and Socolovsky, 1994; Kobayashi, 1993; Warren and Boettinger, 1995; Wheeler et al., 1992, 1993a, b) is a technique which offers the hope of accurately coupling the micro and macroscales in solidification processes. It involves developing an equation for a phase field parameter, $\varphi(x, t)$, which characterizes the phase of the system at each position in space and time. This equation is then coupled with the macroscopic continuity equations for heat and/or solute transfer. In the original formulation of the method (cf. Caginalp, 1986), the phase field parameter is defined such that $\varphi = -1$ in solid regions, $\varphi = 1$ in liquid regions, and φ varies rapidly between -1 and 1 in a region of thickness ϵ at the solid-liquid interface. The interface itself is defined as being the level set where φ vanishes.

The equation for the phase field is derived using techniques from statistical mechanics and the theory of phase transitions. A Landau-Ginzburg free-energy functional is constructed for the whole system, depending on φ and any other thermodynamic variables (e.g., temperature, solute concentration). The system is assumed to evolve in such a way that it drives the free-energy functional towards its minimum. Using this formulation, it is possible to incorporate properties of the continuum model which are left out of classical (i.e., Stefan-type) models and which otherwise may have to be included in an ad hoc manner. For example, phase field models can incorporate the following features:

- an equilibrium Gibbs-Thompson relation between the temperature at the interface and the interface curvature,
- anisotropy in growth velocities,
- a finite interface thickness,
- certain supercooling and superheating effects, and
- interaction of the material and its interface with the boundary of the containing vessel.

Computer simulations (Kobayashi, 1993) performed using phase field models have shown many of the qualitative features of microstructure formation, such as the breakdown of planar and circular interfaces to cellular structures, the formation of dendritelike structures, the inclusion of liquid pockets, and Ostwald ripening and coarsening behavior. Indeed, these simulations, in both two and three dimensions, are quite stunning illustrations of the beautiful patterns which can arise in competitive growth situations. Other more detailed simulations have demonstrated a good quantitative agreement between the results of phase field models and the Ivantsov and microscopic solvability theories of dendrite tip growth.

From the computational viewpoint, the main advantages of the phase field method are

- it provides a simple, elegant description that embodies a rich variety of realistic physical growth phenomena, from stable crystal growth to dendritic growth to motion-by-mean curvature;
- it is not necessary to distinguish between the different phases in computations, i.e., front tracking is not required;
- all the physical parameters are clearly identified so that the equations can be used to obtain quantitatively reliable numbers; and
- computations involving self-intersections of the interface (e.g., in simulating the growth and coalescence of spherical grains) do not pose difficulties.

Contributed by the Heat Transfer Division for publication in the JOURNAL OF HEAT TRANSFER. Manuscript received by the Heat Transfer Division, Nov. 12, 1996; revision received, Jan. 16, 1998. Keywords: Modeling and Scaling, Moving Boundaries, Phase-Change Phenomena. Associate Technical Editor: S. Ramadhyani.

The two main challenges for the method are as follows:

1 **Resolving Fine Scales:** Although it has been demonstrated that the interfacial thickness ϵ in phase field models can be varied over a broad range without significant change in the results (provided that macroscopic physical parameters such as surface tension σ are kept close to the value of interest); detailed, accurate simulations of microscopic growth phenomena, sufficient for a proper test of theory, will still demand a very thin interface, beyond the practical computational limit for fixed grid algorithms. This will require the development of algorithms which combine the phase field method with adaptive grid techniques to finely resolve the region at the solid-liquid interface.

2 **Thermal Alloy Simulations:** To date, phase field simulations have been carried out with remarkable success for the solidification of pure substances and isothermal alloys, but there have been no simulations of thermal alloys (i.e., in which both the solute concentration and thermal fields are updated). There is no problem in formulating a phase field model for thermal alloys (Wheeler et al., 1993b; Caginalp and Xie, 1993). However, its computational solution gives rise to difficulties because the thermal field responds on a much faster time scale than the solute field. Once again, there is a need for the development of clever algorithms to overcome these difficulties.

In this paper we introduce the phase field model, verify its accuracy for a selection of classical models, and investigate the advantages of using adaptive grid techniques. All the simulations are for pure substances in one dimension. In the future, the intention is to extend this work to higher dimensions and to consider alloy models, especially for application to rapid solidification problems.

2 Solidification Models

Consider a material that may be in either of two phases, which we assume to be solid or liquid, occupying a region Ω in space. A basic problem, called the "modified" Stefan problem (Carslaw, 1959; Crank, 1984), is to find a temperature function $u(x, t)$ and an interface $\Gamma(t) \subset \Omega$ that satisfy the equations

$$u_t = K\Delta u \quad \text{in} \quad \Omega/\Gamma(t) \tag{1}$$

$$lv = -K\nabla u\cdot n]_+^- \quad \text{on} \quad \Gamma(t) \tag{2}$$

$$u = -\frac{\sigma}{[s]_E}\kappa - \alpha\frac{\sigma}{[s]_E}v \quad \text{on} \quad \Gamma(t) \tag{3}$$

where

l := latent heat per unit mass,
K := thermal conductivity,
σ := surface tension between two phases,
$[s]_E$:= entropy difference between phases per unit volume (N.B. $[s]_E = 4$ with the normalization used in this paper),
v := normal velocity,
κ := sum of principal curvatures at the particular point on the interface,
$\nabla u\cdot n]_+^-$:= jump in the normal component of the temperature gradient at the interface, and
α := kinetic undercooling coefficient.

The two terms in Eq. (3) correspond to the undercooling at the interface due to surface tension and curvature effects (i.e., $-(\sigma/[s]_E)\kappa$) and kinetic effects (i.e., $-\alpha(\sigma/[s]_E)v$). The kinetic undercooling effect is related to the attachment kinetics at the interface—the interface cannot progress unless enough driving force is provided for the atomic or molecular transfer between the melt and the growing solid. If kinetic effects are ignored, then Eq. (3) reduces to the well-known Gibbs-Thompson relation (Mullins, 1984) for a curved surface in equilibrium. If surface tension effects are neglected altogether (i.e., by setting $\sigma = 0$), then there is no undercooling at the interface and the interfacial temperature remains at the melting temperature (i.e., $u = 0$). This case is called the "classical" Stefan model. It incorporates heat diffusion and latent heat of fusion, but ignores undercooling effects, so that the sign of the temperature determines the phase of the material. Setting $\sigma = 0$ has the effect of eliminating an important length scale in the problem which is crucial in terms of the stability of the interface.

Both the classical and modified Stefan problems have been studied extensively. They are examples of a broad set of problems called free boundary problems (Crank, 1984). There are two basic approaches to solving free boundary problems:

1 *single domain methods,* in which the solid and liquid phases are considered to be a single domain with average quantities for the thermodynamic variables defined at each point in space.
2 *two-domain methods,* in which the solid and liquid phases are considered to be two separate domains with the governing equations for the thermodynamic variables formulated in each domain independently, and the solutions matched at the solid-liquid interface using conservation laws (and, in some cases, experimental relations) for the thermodynamic variables.

Two-domain methods often result in very difficult numerical algorithms and are typically used when tracking a sharp interface is of primary importance, i.e., for solidification of pure substances or for calculations of isolated cell or dendrite shapes. Single-domain methods are more suitable for modeling alloys because they naturally evolve a mushy zone, i.e., the solid-liquid interface has a finite width. However, they can also be interpreted as a means of approximating, with a smooth interface, any of the sharp-interface problems.

The phase field method is an example of a single-domain method. Where it differs from more established single domain methods, such as the enthalpy method (Swaminathan and Voller, 1993), is in the introduction of a new variable, the phase field φ, that is defined independently of temperature and composition, according to the underlying physics of the problem. The phase field equation is derived using Landau-Ginzburg theory (Landau and Lifshitz, 1959). This involves the construction of a free-energy functional, F, for the whole system in terms of φ and the other thermodynamic variables (e.g., temperature, u). For example,

$$F(\varphi, u) = \int dx\{\tfrac{1}{2}\zeta^2(\nabla\varphi)^2 + f(\varphi, u)\} \tag{4}$$

where ζ is a length scale and f is the free-energy density function.

In an equilibrium situation, the equation for the phase field would be obtained by minimizing the free-energy functional, i.e., by taking

$$-\frac{\delta F}{\delta\varphi} = 0. \tag{5}$$

In a nonequilibrium situation, it is assumed that φ is restored to equilibrium with a "force" which is proportional to the extent to which it is out of equilibrium, i.e., the phase field equation is obtained by taking

$$\alpha\zeta^2\varphi_t = -\frac{\delta F}{\delta\varphi} \tag{6}$$

where $\alpha\zeta^2$ is a relaxation time.

The free-energy functional, F, is not uniquely defined. The term involving $(\nabla\varphi)^2$ in Eq. (4) is the basic interaction term, but the free-energy density function f may be modified in many different ways, to incorporate different physics, while still retaining the features necessary for the model. One formulation which is commonly seen in the literature (cf. Caginalp, 1986), and which has been rigorously linked with sharp-interface models using formal matched asymptotics (Caginalp and Socolovsky, 1991), involves taking

$$f(\varphi, u) = \frac{1}{8a}(\varphi^2 - 1)^2 - 2u\varphi \tag{7}$$

which is a double-well potential term, with a depth measured by the parameter a, plus a term coupling u and φ. The double-well potential indicates a lower free-energy associated with the values $\varphi = \pm 1$ (i.e., pure solid or pure liquid) than with the intermediate values $-1 < \varphi < 1$ corresponding to transitional states.

In this case, the phase field equation becomes

$$\alpha\zeta^2\varphi_t = \zeta^2\Delta\varphi + \frac{1}{2a}\varphi(1 - \varphi^2) + 2u. \tag{8}$$

The solidification model is completed by coupling this with a simple energy balance equation, i.e.,

$$u_t + \frac{l}{2}\varphi_t = K\Delta u, \tag{9}$$

and by specifying appropriate initial and boundary conditions. Usually, the boundary conditions are chosen so that $\varphi = \varphi_\pm$ on the boundary, where φ_+ and φ_- are the largest and smallest roots of

$$(2a)^{-1}(\varphi - \varphi^3) + 2u = 0. \tag{10}$$

Another formulation for the free-energy density, introduced by Kobayashi (Kobayashi, 1993), is

$$f(\psi, u) = W\int_0^\psi p(p - 1)(p - \tfrac{1}{2} - m(u))dp \tag{11}$$

where W is a constant with units of energy per unit volume. This involves taking a different normalization for the phase field parameter, i.e., $\psi := \frac{1}{2}(\varphi + 1)$, so that the solid and liquid states are associated with $\psi = 0$ and $\psi = 1$, respectively. It also involves introducing a monotonic increasing function of u, $m(u)$, such that $m(u_M)$ is the freezing temperature of the material, and $|m| < \frac{1}{2}$.

The restriction $|m| < \frac{1}{2}$ ensures that the double-well potential has local minima at $\psi = 0$ and $\psi = 1$, and a local maximum at $\psi = \frac{1}{2} + m$. If $-\frac{1}{2} < m < 0$, i.e., $u < u_M$, then the global minimum of the energy density is at $\psi = 1$, and so the single-phase solid has the lowest energy. However, if $0 < m < \frac{1}{2}$, i.e., $u > u_M$, then the global minimum of the energy density is at $\psi = 0$, and so the single-phase liquid has the lowest energy.

For the Kobayashi potential, the phase field equation is

$$\alpha\zeta^2\psi_t = \zeta^2\Delta\psi + W\psi(1 - \psi)(\psi - \tfrac{1}{2} + m). \tag{12}$$

This can be compared with the previous phase field equation, Eq. (8), by making the change of variables $\varphi := 2\psi - 1$, in which case it becomes

$$\alpha\zeta^2\varphi_t = \zeta^2\Delta\varphi + \frac{W}{4}(\varphi(1 - \varphi^2) + 2m(1 - \varphi^2)). \tag{13}$$

The main difference is that the $2u$ term in Eq. (8) has been replaced by $2m(u)(1 - \varphi^2)$ in Eq. (13). Multiplying the temperature function by $(1 - \varphi^2)$ forces $\varphi = \pm 1$ at the boundaries (compare with Eq. (10)). Fixing the minima of the free-energy density in this way is convenient for the purpose of numerical computation. It has the effect of introducing additional artificial nonlinearities into the free energy, but this usually makes little difference in practice as long as the role of temperature outside of the interfacial region is negligible.

3 Computational Issues

The phase field model in the form of Eq. (8) and (9) has been rigorously analyzed by Caginalp using asymptotic analysis (Caginalp, 1989). It was shown that various classical sharp-interface models (e.g., Stefan, modified Stefan, Hele-Shaw, Cahn-Allen motion-by-mean curvature) all arise as limiting cases of the phase field equations. This was used to link the model parameters with macroscopic material parameters. For example if, in terms of macroscopic properties, $\epsilon := \zeta\alpha^{1/2}$ is the interface thickness and $\sigma := (2/3)\zeta a^{-(1/2)}$ is the interface tension, then by taking the limit $\epsilon \to 0$ (i.e., sharp-interface limit) and keeping σ fixed, the modified Stefan model can be recovered, along with the Gibbs-Thompson relation.

This procedure enables the parameters in the phase-field model to be chosen to give a quantitative model of solidification, with known material and growth parameters, so that comparisons can be made with experiment. By adjusting the parameters, the computations can be varied continuously from single-needle dendritic to faceted crystals. The patterns observed are the result of competition between diffusion, which tends to promote instabilities, and surface tension, which tends to suppress them.

Wheeler et al. (1993a) and Warren and Boettinger (1995) have demonstrated a good quantitative agreement between the results of phase field models and the Ivantsov and microscopic solvability theories of dendrite tip growth. These simulations were performed using a fixed grid algorithm, which limited the range of scales which could be accurately resolved. To take a value of the interfacial thickness ϵ equivalent to its physical value and still retain enough grid points at the interface to accurately evaluate the curvature (and, hence, the surface tension effect), would exceed the practical computational limits of fixed grid algorithms. This problem is exacerbated by the fact that the stiffness of the phase field equations is proportional to ϵ^{-2}. The success of phase field simulations, despite these limitations, confirms the finding of Caginalp and Socolovsky (1991) that ϵ can be spread dramatically without significant error, provided that the macroscopic physical parameters, such as surface tension σ, are kept close to the value of interest. The justification for this is that, while spreading the interface allows the latent heat to be released over a thicker region than in a real experiment, the same amount of latent heat is released and the temperature at the interface is the same, so that the difference should amount to a slight change in the diffusion constant. Physically, the surface tension is more critical than how the latent heat is released or the precise validity of the heat equation away from the interface.

It has been demonstrated that, for fixed grid algorithms of grid size Δr, a moderate stiffness and an adequate ratio for $\epsilon/\Delta r$ are more important than taking ϵ very small. In typical simulations, choosing $\epsilon/\Delta r \approx 1$ achieves an acceptable tradeoff between accuracy and processor time.

Nevertheless, to perform quantitatively accurate simulations at the scale of dendrite tips, it will be necessary to develop algorithms which enable ϵ to be made very small. This is a major challenge for the phase field method. The introduction of adaptive grid techniques would seem to be a promising avenue of research, since significant changes in the phase field variable only occur over a very small part of the domain. Adaptive grid techniques use nonuniform space grids and move the grid continuously in the space-time domain while the discretization of the PDE and the grid selection are intrinsically coupled.

In this paper we investigate solving one-dimensional phase field models using a moving-grid method which has been developed and implemented by Blom and Zegeling (1994). The method is based on a Lagrangian description of the PDE and a smoothed-equidistribution principle to define the grid positions at each time level, coupled with a spatial discretization method that automatically discretises the spatial part of the user-defined PDE following the method of lines approach. This means that

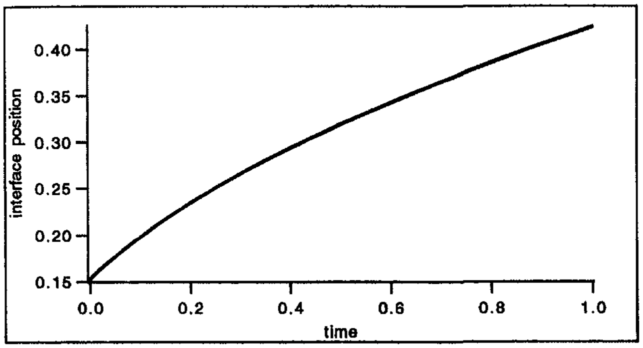

Fig. 1 Interface position versus time for the classical Stefan model: Comparison of the exact solution with the results obtained using an adaptive grid phase field algorithm with $N = 50$ and $N = 100$ grid points

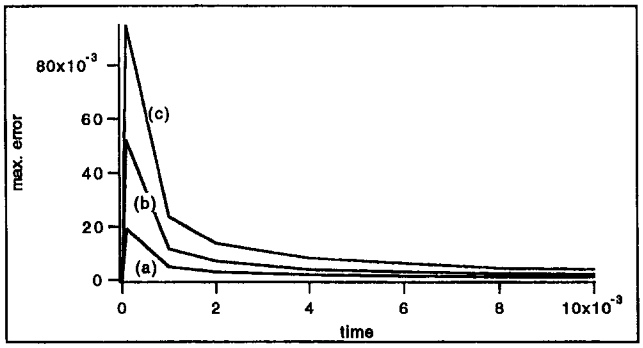

Fig. 3 Maximum error versus time for the classical Stefan model: Comparison of the results obtained using an adaptive grid phase field algorithm with (*a*) $N = 25$, (*b*) $N = 50$, and (*c*) $N = 100$ grid points

it is not necessary to explicitly track the interface, which is an important feature since, otherwise, one of the main advantages of the phase field method would be lost.

Moving-grid methods are solution-adaptive methods for time-dependent PDEs which move the spatial grid in time while the discretization of the PDE and the grid selection procedure are intrinsically coupled. Moving-grid methods use a fixed number of spatial grid points, without need of interpolation, and let them move with whatever fronts are present. Using these methods, if properly applied, can save up to a factor of 10 (in one dimension) or 100 (in two dimension) spatial grid points in the case of steep moving layers stemming from a convection-diffusion or reaction-diffusion system.

Our work is restricted to one dimension for illustrative purposes. Two-dimensional methods are more difficult to implement, but research is progressing rapidly in this area and many examples are already available in the literature (Zegeling, 1992; Zegeling, 1996; Huang and Russell, 1997; Huang and Russell, 1998).

The reader is referred to the paper of Blom and Zegeling (1994) for details of the one-dimensional moving-grid method used in this paper. Importantly, there are three parameters that should be specified by the user: a time-smoothing parameter τ, a spatial smoothing parameter λ, and a monitor regularising parameter η. The choice of parameters λ and η is not very critical; i.e., experiments have shown that a variation of these parameters does not result in a drastic change of performance. However, a wrong choice of τ can result in starting problems or the grid lagging behind. In this work, we chose the values $\lambda = 1.5$ and $\eta = 0.01$, as recommended in (Blom and Zegeling, 1994). The value of τ was chosen on a problem-dependent basis, after performing sensitivities, and was related to the time scale of the problem. We found that the recommended value of $\tau = .001$ was a good starting point for most problems.

The numerical results are compared with those obtained using a fixed grid PDE solver; i.e., PDECOL (Madsen, 1979), a general package to solve nonlinear PDEs that uses the method of lines with collocation in space. All computations were performed on a Silicon Graphics Indigo workstation.

4 Results

The problems are considered:

1 The Classical Stefan Model: This allows comparison of the results with an exact solution.

2 The Case of a Solid Sphere in Equilibrium With its Melt: This is a delicate, unstable state of equilibrium which provides a good test case for investigating the effect of changing the time parameter τ in the adaptive grid technique.

3 A Modified Stefan Model With a Generalized Kinetic Undercooling Term: This is an important practical case and is implemented using Kobayashi's energy density function in the phase field model, i.e., Eq. (13).

4.1 Classical Stefan Model. The classical Stefan model has an exact solution, $u^s(x, t)$ for $t \geq 0$ (cf. Carslaw, 1959)

$$
\begin{aligned}
u^s(x, t) &= C_1 \frac{[\operatorname{erf}(\beta/2) - \operatorname{erf}(x/(2\sqrt{t + t_0}))]}{\operatorname{erf}(\beta/2)} \quad \text{if} \quad x \leq s(t) \\
&= C_2 \frac{[\operatorname{erf}(\beta/2) - \operatorname{erf}(x/(2\sqrt{t + t_0}))]}{[1 - \operatorname{erf}(\beta/2)]} \quad \text{if} \quad x > s(t)
\end{aligned} \tag{14}
$$

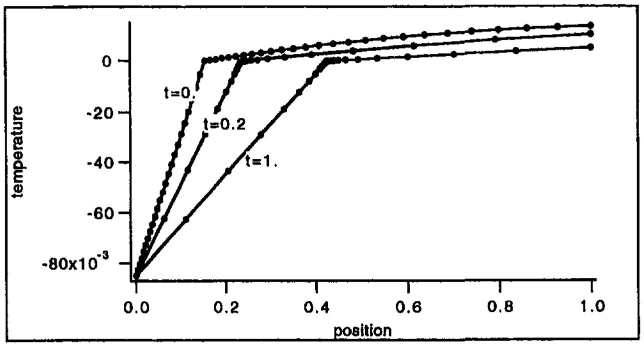

Fig. 2 Temperature profiles for the classical Stefan model calculated at times $t = 0$, $t = 0.2$ and $t = 1$: Comparison of the exact solution with the results obtained using an adaptive grid phase field algorithm with $N = 50$.

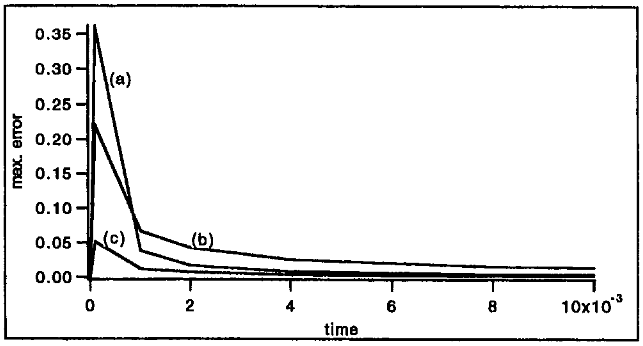

Fig. 4 Maximum error versus time for the classical Stefan model: Comparison of the results obtained using an adaptive grid phase field algorithm with $N = 50$ grid points and settings (*a*) $\tau = 10^{-5}$, logarithmic initial grid, (*b*) $\tau = 10^{-5}$, uniform initial grid, and (*c*) $\tau = 10^{-3}$, logarithmic initial grid.

where erf (x) is the error function, C_1 and C_2 are constants, and t_0 is the starting time. The interface $s(t)$ is given by

$$s(t) = \beta\sqrt{t + t_0} \tag{15}$$

where β is the solution of

$$\frac{2}{\sqrt{\pi}} e^{-\beta^2/4}[C_2/(1 - \text{erf}(\beta/2)) - C_1/\text{erf}(\beta/2)] - \beta = 0. \tag{16}$$

Our simulations were performed using the phase field model defined by Eqs. (8) and (9), setting $l = K = \alpha = 1$. Following Caginalp and Socolovsky (1994) we took $0 \le x \le 1$, $C_1 = -0.085$, $C_2 = -0.015$, $\beta = 0.396618$ and $t_0 = 0.15$. The boundary conditions were taken to be

$$\begin{aligned} \varphi(0, t) &= -1 \\ \varphi(1, t) &= +1 \\ u(0, t) &= C_1 \\ u(1, t) &= u^s(1, t), \quad \text{for} \quad t \ge 0. \end{aligned} \tag{17}$$

The initial conditions were taken to be

$$\begin{aligned} \varphi(x, 0) &= -1 \quad \text{if} \quad x \le s(t_0) \\ &= +1 \quad \text{if} \quad x > s(t_0) \\ u(x, 0) &= u^s(x, 0), \quad \text{for} \quad x \subset [0, 1]. \end{aligned} \tag{18}$$

The case considered corresponds to Experiment 5 in Caginalp and Socolovsky (1991). The parameters for the phase field equations were chosen to be $a = 0.0625$ and $\zeta = 0.002$, leading to an interface thickness of $\epsilon := \zeta a^{1/2} = 0.0005$ and a value for the surface tension of $\sigma := \frac{2}{3}\alpha a^{-(1/2)} = 0.00533$. With these values, and using the fixed grid algorithm PDECOL with 1000 grid intervals, the stiffness of the PDEs and the low grid resolution were such that the accuracy of the computations was destroyed before $t = 1$ was reached. The computations took 3330 CPU seconds. In contrast, using the adaptive grid algorithm with the total number of grid points N set equal to 25, 50, and 100, gave an acceptable solution in every case. The computational times were 4, 10, and 48 CPU seconds, respectively.

Figure 1 shows graphs of the calculated interface positions as a function of time for the cases $N = 50$ and $N = 100$, compared with the exact solution. The graphs are indistinguishable. The graph for $N = 25$ showed a very slight deviation from the exact solution and, to avoid confusion, has not been included in the figure.

Figure 2 shows temperature profiles calculated for the $N = 50$ case at times $t = 0$, 0.2 and 1, compared with the exact solution. Once again, the numerical results are indistinguishable from the exact solution. Note how the grid points cluster at the interface as the grid adapts to the solution gradients.

At each time step, a maximum error R was calculated according to

$$R(t) = \max\{|u(x, t) - u^s(x, t)|, x \subset [0, 1]\}. \tag{19}$$

Figure 3 shows R as a function of time for the three cases, $N = 25$, 50, and 100. This reveals that there are significant errors at very early times, i.e., $t < 0.002$, while the grid is adapting. For a particular choice of N, the size of these errors depends on factors such as the choice of the time parameter τ and the initial positions chosen for the grid points. For our computations, we chose $\tau = 10^{-5}$ and a logarithmic variation in the initial position of the grid points around the interface. Figure 4 compares the errors generated using these choices in the $N = 50$ case (cf. Graph (a)), with those generated using the choices (b) $\tau = 10^{-5}$, uniform initial grid and (c) $\tau = 10^{-3}$, logarithmic initial grid. To put the choice of τ in perspective, note that the time scale for this problem is related to $\epsilon/v_0 \approx 10^{-3}$, where ϵ is the interface width and v_0 is the initial velocity of the interface.

To further investigate the starting problems of the adaptive grid technique, we considered the case of a sphere in equilibrium with its melt; which is a delicate, unstable state of equilibrium, sensitive to the starting conditions.

4.2 Sphere in Equilibrium With its Melt.

The critical radius instability of a solid sphere in equilibrium with its melt is a well-known problem in materials science (Chalmers, 1977). Initially, both the solid and the melt are at a constant temperature u_0 given by the Gibbs-Thompson relation

$$u_0 = -\sigma_0\kappa_0/4 \tag{20}$$

where κ_0 is the sum of principal curvatures of the sphere. If the equilibrium is disturbed slightly, the material either melts or freezes. The growth of the sphere is strongly influenced by curvature, kinetic, and heat flow effects. The equilibrium is most delicate when l is small and K is large.

This is a three-dimensional problem, but because it is spherically symmetric, it can be parametrized in terms of one space variable x. Following Caginalp and Socolovsky (1991) we considered the three-dimensional computational region defined by $1 \le x \le 2$, with $K = 10$, $l = 0.1$, and $\alpha = 1$. The equilibrium position of the interface was chosen to be $r_0 = 3/2$, leading to an initial value of the curvature of $\kappa_0 = 2/r_0 = 4/3$. The surface tension was chosen to be $\sigma_0 = 0.15$; so, using Eq. (20), the initial temperature was $u_0 = -0.05$ everywhere. The boundary conditions for the temperature field were taken to be $u(1, t) = u(2, t) = u_0$, for $t \ge 0$. The initial and boundary conditions for the phase field were taken to be analogous to those used for the classical Stefan model (see Eqs. (17) and (18)).

Four cases were considered, depending on the initial position of the interface s_0, i.e., (a) $s_0 = 1.499$, (b) $s_0 = 1.5$, (c) $s_0 = 1.501$, and (d) $s_0 = 1.52$. For each case, five settings of the adaptive grid algorithm were tried: (i) $\tau = 10^{-3}$, $N = 100$, (ii) $\tau = 10^{-1}$, $N = 100$, (iii) $\tau = 10^{+3}$, $N = 100$, (iv) $\tau = 10^{+3}$, $N = 200$, and (v) $\tau = 10^{+3}$, $N = 500$. Setting $\tau = 10^{+3}$ in the adaptive grid algorithm effectively means that the grid is fixed, since it adapts over such a long time frame, so Experiments (iii)–(v) were investigating the effect of increasing the grid resolution for a fixed grid, while Experiments (i) and (ii) were investigating the effect of using a rapidly adapting grid. For this problem, it is difficult to set the time scale because the velocity of the interface is zero when the sphere is at the critical radius; i.e., $v = 0$ when $x = r_0$.

Figure 5 shows graphs of time as a function of the interface position for the four cases considered. The closer s_0 gets to the critical radius r_0, the more sensitive the results are to the settings of the parameter values in the algorithm. At the critical radius, when $s_0 = r_0$, some settings lead to freezing of the material, while others lead to melting. This sensitivity is further illustrated in Fig. 6, which shows the initial and final temperature profiles for Experiments (i)–(iii) for the critical case $s_0 = r_0$.

It appears from Fig. 5 that using an adaptive grid for this problem leads to errors near the critical instability. This is because the grid adapts too quickly to small changes in the computational solution, while the interface is only moving very slowly. It is better to use a fixed grid algorithm for this problem.

4.3 Modified Stefan Model.

The third problem considered was a modified Stefan model with a generalized kinetic undercooling term, u_{kin} (cf. Fabbri and Voller, 1995). Rather than taking

$$u_{\text{kin}} = -\alpha \frac{\sigma}{[s]_E} v \tag{21}$$

as in Eq. (3), the term is generalized to be

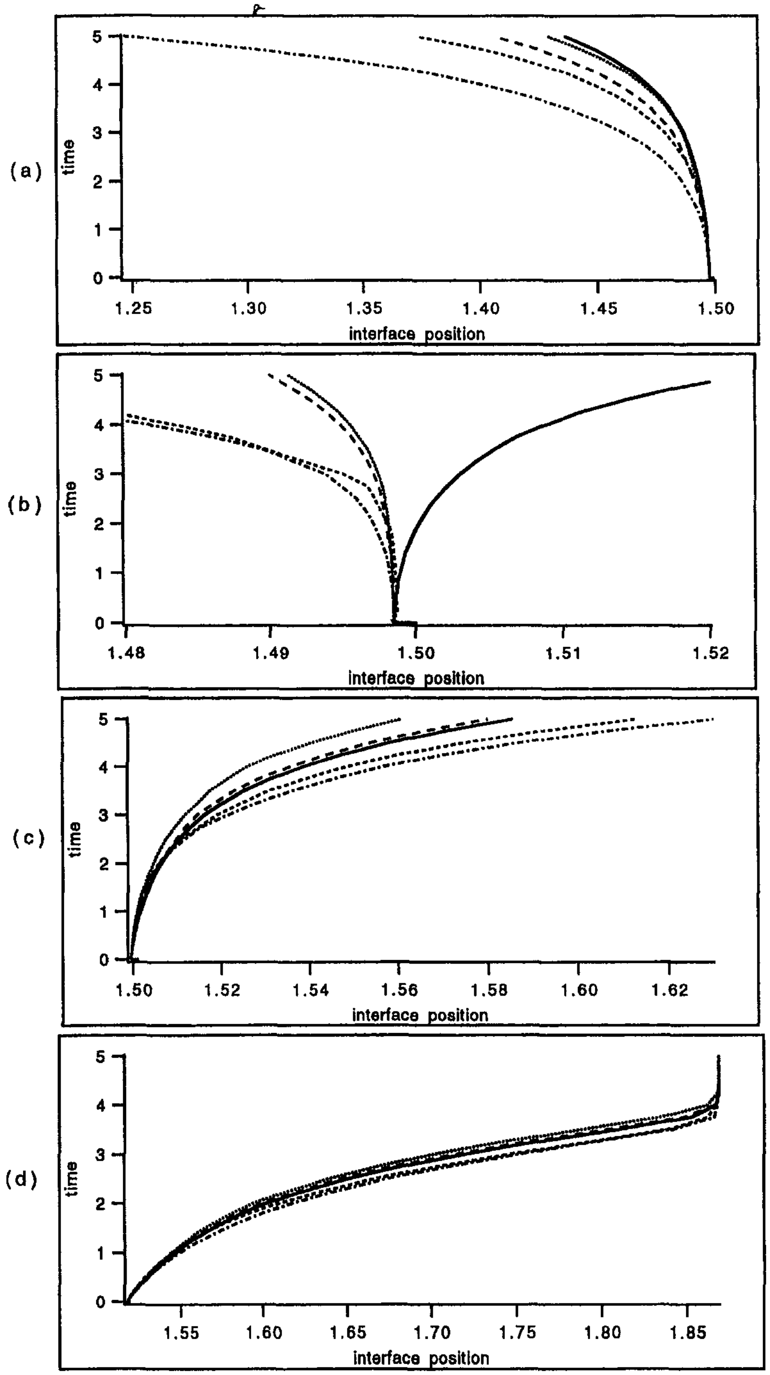

Fig. 5 Time versus interface position for the case of a solid sphere in equilibrium with its melt; (*a*) $s_0 = 1.499$, (*b*) $s_0 = 1.5$, (*c*) $s_0 = 1.501$, and (*d*) $s_0 = 1.52$: Comparison of the results obtained using an adaptive grid phase field algorithm with settings (i) $N = 100$, $\tau = 10^{-3}$ (dots/dashes), (ii) $N = 100$, $\tau = 10^{-1}$ (short dashes), (iii) $N = 100$, $\tau = 10^{+3}$ (solid), (iv) $N = 200$, $\tau = 10^{+3}$ (long dashes), and (v) $N = 500$, $\tau = 10^{+3}$ (dots).

$$u_{\mathrm{kin}} = -\Theta^b v^b, \tag{22}$$

where Θ is the kinetic coefficient and the exponent b is a parameter chosen according to the predominant interface kinetics during solidification (i.e., $b = 1$ for random kinetic attachment at the interface, and $b = \frac{1}{2}$ when the attachment kinetics is dictated by the development of defects in an otherwise perfect solid lattice).

In the context of the phase field model, this is accomplished by using the Kobayashi form of the potential, as in Eq. (13), with the function $m(u)$ defined to be

$$m(u) = \gamma |u|^{1/b} \operatorname{sgn}(u) \tag{23}$$

where γ is a constant. This leads to the relation

$$u_{\mathrm{kin}} = -\left(\frac{3\sigma\alpha}{4\gamma W}\right)^b v^b. \tag{24}$$

Following Fabbri and Voller (1995) for the computations, it is assumed that the slab has been solidified from $t = 0$ to $t = t_0$ according to the classical Stefan problem, i.e., Eqs. (14)–(16) with $C_1 = -0.085$, $C_2 = -0.015$, and $\beta = 0.396618$.

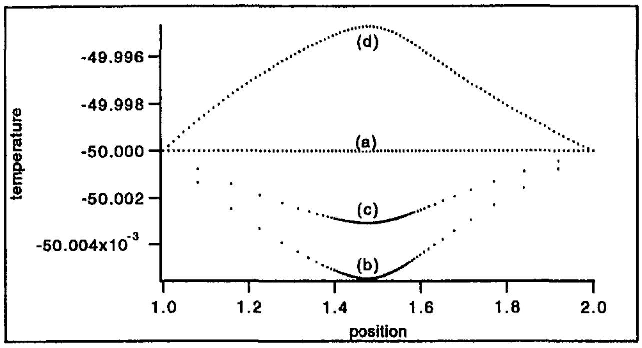

Fig. 6 Temperature profiles for the case of a solid sphere in equilibrium with its melt: (*a*) $t = 0$, (*b*) $t = 5$, $N = 100$, $\tau = 10^{-3}$, (*c*) $t = 5$, $N = 100$, $\tau = 10^{-1}$, and (*d*) $t = 5$, $N = 100$, $\tau = 10^{+3}$.

The kinetic undercooling effect is then suddenly triggered at $t = t_0$. For $t > t_0$, the problem is solved numerically with the desired values of Θ and b. The kinetic coefficient is given in terms of a temperature u^0 defined by

$$u^0 = -\Theta^b v_0^b \tag{25}$$

where v_0 is the interface velocity at $t = t_0$.

Four cases were considered: (a) $b = 1$, $\gamma = 6$, $u^0 = -0.01$, (b) $b = 1$, $\gamma = 6$, $u^0 = -0.08$, (c) $b = 0.5$, $\gamma = 100$, $u^0 = -0.01$, and (d) $b = 0.5$, $\gamma = 100$, $u^0 = -0.08$. The phase field model parameters were chosen to be $W = 8$ and $\zeta = 0.0025$. The value for the surface tension σ can then be evaluated using the expression due to Allen and Cahn (1979)

$$\sigma = \sqrt{2}\zeta \int_{-1}^{+1} \sqrt{f(\varphi, u)}\, d\varphi \tag{26}$$

which yields

$$\sigma = \frac{2\sqrt{2}}{3} \zeta \sqrt{W}. \tag{27}$$

The value of α is then obtained using Eqs. (24) and (25). The initial and boundary conditions for the phase field model were taken to be the same as those used for the classical Stefan problem in Section 4.1, but with the initial interface at $s_0 = \beta\sqrt{t_0} = 0.14$.

Each case was investigated using two different algorithms; (i) the adaptive grid technique with $N = 50$ and $\tau = \frac{1}{2}\zeta/v_0 \approx 2. \times 10^{-3}$, and (ii) the fixed grid method, PDECOL, with 1000 grid intervals. Figure 7 shows a comparison of the results for interface position as a function of time, for each case. Figure 8 shows graphs of interface temperature versus time. Figure 9 shows a comparison of temperature profiles obtained for Case

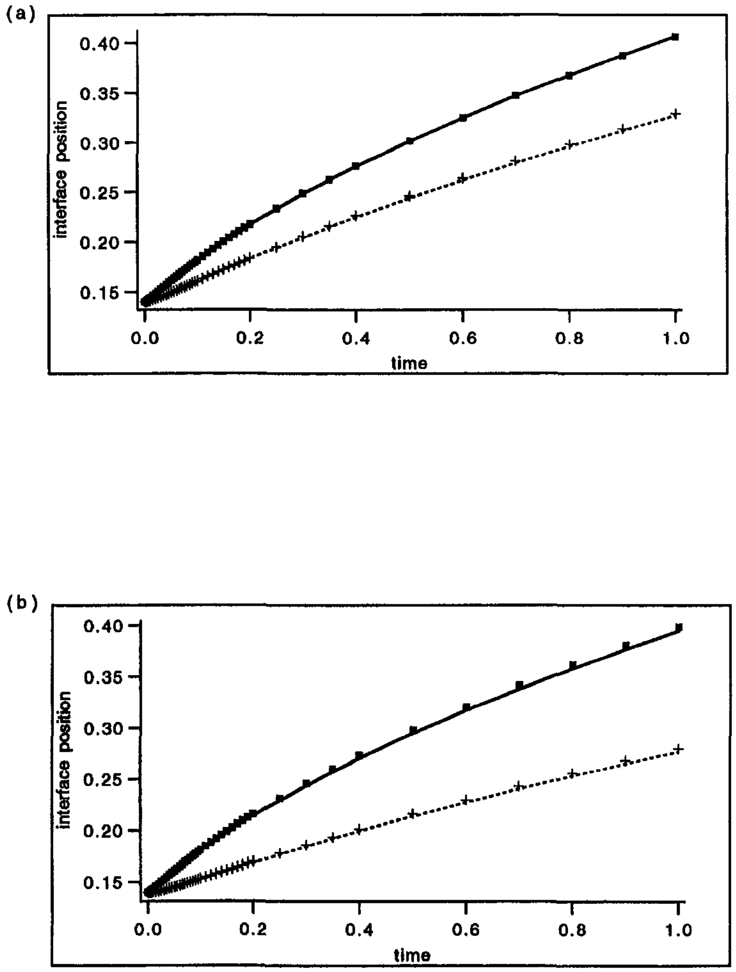

Fig. 7 Interface position versus time for the modified Stefan model: Comparison of the results obtained using an adaptive grid phase field algorithm and a fixed grid algorithm: (*a*) $b = 1$, $\gamma = 6$, $u^0 = -0.01$ (solid line and squares) and $u^0 = -0.08$ (dashed line and plusses), and (*b*) $b = 0.5$, $\gamma = 100$, $u^0 = -0.01$ (solid line and squares) and $u^0 = -0.08$ (dashed line and plusses).

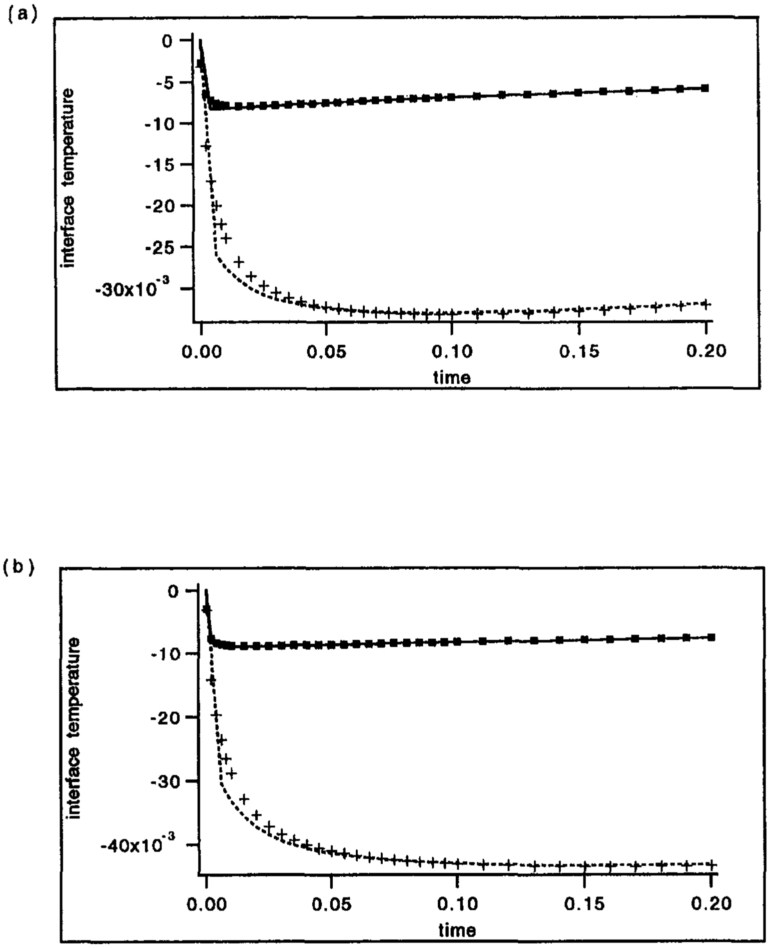

Fig. 8 Interface temperature versus time for the modified Stefan model (otherwise, as for Fig. 7)

(b) at times $t = 0$, 0.2 and 1. The agreement between the two algorithms is very good in each case, although slight deviations can be seen in the interface temperature at very early times (i.e., $t < 0.05$). The main difference between the two algorithms was that, on average, a speed up of about 200 times was achieved by using the adaptive grid technique.

5 Conclusion

The phase field method has been demonstrated to hold promise for enabling the physics at the microscale to be incorporated in macroscopic models of solidification. However, for quantitatively accurate simulations to be performed, it will be necessary to develop algorithms which enable the interface width to be made very small. Adaptive grid techniques offer a means of achieving this within practical computational limits.

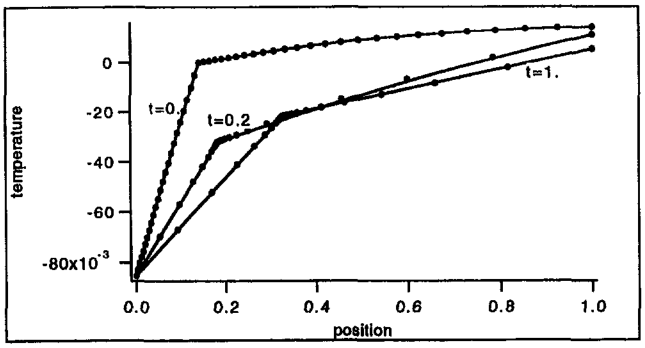

Fig. 9 Temperature profiles for the modified Stefan model with $b = 1$ and $u^0 = -0.08$, calculated at times $t = 0$, $t = 0.2$, and $t = 1$: Comparison of the results obtained using an adaptive grid phase field algorithm (dots) and a fixed grid algorithm (solid).

In this paper, investigations have been made of one-dimensional phase field models combined with an adaptive grid technique. Three problems were considered: (1) the classical Stefan model, (2) the case of a solid sphere in equilibrium with its melt, and (3) a modified Stefan model with a generalized kinetic undercooling term. The numerical results were compared with those obtained using a fixed grid algorithm. The results clearly demonstrate the computational advantages of using an adaptive grid technique, with speed-ups of the order of hundreds of times being achieved for comparable accuracy. To end on a cautionary note, adaptive grid techniques may require some extra care in their implementation, depending on factors such as the time scale of the problem and the degree of accuracy which is required at the earliest times, while the grid is adapting to the solution gradients.

References

Allen, S. M., and Cahan, J. W., 1979, "A Microscopic Theory for Antiphase Boundary Motion and its Application to Antiphase Domain Coarsening," *Acta. Metall.*, Vol. 27, pp. 1085–1095.

Blom, J. G., and Zegeling, P. A., 1994, "Algorithm 731: A Moving-Grid Interface for Systems of One-Dimensional Time-Dependent Partial Differential Equations," *ACM Transactions on Mathematical Software*, Vol. 20, pp. 194–214.

Boettinger, W. J., Wheeler, A. A., Murray, B. T., and McFadden, G. B., 1994, "Prediction Of Solute Trapping At High Solidification Rates Using A Diffuse

Interface Phase-Field Theory Of Alloy Solidification,'' *Mat. Sci. Eng. A,* Vol. 178, pp. 217–223.

Caginalp, G., 1986, ''An Analysis Of A Phase Field Model Of A Free Boundary,'' *Arch. Rat. Mech. Anal.,* Vol. 92, pp. 205–245.

Caginalp, G., 1989, ''Stefan And Hele-Shaw Type Models As Asymptotic Limits Of The Phase Field Equations,'' *Phys. Rev. A,* Vol. 39, pp. 5887–5896.

Caginalp, G., and Socolovsky, E. A., 1991, ''Computation Of Sharp Phase Boundaries By Spreading: The Planar And Spherically Symmetric Cases,'' *J. Comp. Phys.,* Vol. 95, pp. 85–100.

Caginalp, G., and Xie, W., 1993, ''Phase-Field and Sharp-Interface Alloy Models,'' *Phys. Rev. E,* Vol. 48, pp. 1897–1909.

Caginalp, G., and Socolovsky, E. A., 1994, ''Phase Field Computations of Single-Needle Crystals, Crystal Growth, and Motion by Mean Curvature,'' *SIAM J. Sci. Comput.,* Vol. 15, pp. 106–126.

Carslaw, H. S., and Jaeger, J. S., 1959, *Conduction of Heat in Solids,* Clarendon Press, Oxford.

Chalmers, B., 1977, *Principles of Solidification,* Krieger, New York.

Crank, J., 1984, *Free and Moving Boundary Problems,* Clarendon Press, Oxford.

Fabbri, M., and Voller, V. R., 1995, ''Numerical Solution of Plane Front Solidification with Kinetic Undercooling,'' *Num. Heat Transfer,* Vol. 27, pp. 467–486.

Huang, W., and Russell, R. D., 1997, ''A High Dimensional Moving Mesh Strategy,'' *Appl. Num. Math.,* Vol. 26, pp. 1–14.

Huang, W., and Russell, R. D., 1998, ''Moving Mesh Strategy Based Upon a Gradient Flow Equation for Two Dimensional Problems,'' *SIAM J. Sci. Comput.,* to appear.

Kobayashi, R., 1993, ''Modeling and Numerical Simulations of Dendritic Crystal Growth,'' *Physica D,* Vol. 63, pp. 410–423.

Landau, L., and Lifshitz, E., 1959, *Statistical Physics,* Pergamon, Oxford.

Madsen, N. K., and Sincovec, R. F., 1979, ''Algorithm 540 PDECOL, General Collocation Software for Partial Differential Equations,'' *ACM Transactions on Mathematical Software,* Vol. 5, pp. 326–351.

Mullins, W. W., 1984, ''Thermodynamic Equilibrium of a Crystal Sphere in a Fluid,'' *J. Chem. Phys.,* Vol. 81, pp. 1436–1442.

Rappaz, M., 1989, ''Modelling of Microstructure Formation in Solidification Processes,'' *International Materials Reviews,* Vol. 34, pp. 93–123.

Rappaz, M., and Kurz, W., 1995, ''Dendrites Solidified by Computer,'' *Nature,* Vol. 375, p. 103.

Swaminathan, C. R., and Voller, V. R., 1993, ''On the Enthalpy Method,'' *Int. J. Num. Meth. Heat Fluid Flow,* Vol. 3, pp. 233–244.

Warren, J. A., and Boettinger, W. J., 1995, ''Prediction of Dendritic Growth and Microsegregation Patterns in a Binary Alloy Using the Phase-Field Method,'' *Acta Metall. Mater.,* Vol. 43, pp. 689–703.

Wheeler, A. A., Boettinger, W. J., and McFadden, G. B., 1992, ''Phase-Field Model for Isothermal Phase Transitions in Binary Alloys,'' *Phys. Rev. A,* Vol. 45, pp. 7424–7439.

Wheeler, A. A., Murray, B. T., and Schaefer, R. J., 1993a, ''Computation of Dendrites Using a Phase Field Model,'' *Physica D,* Vol. 66, pp. 243–262.

Wheeler, A. A., Boettinger, W. J., and McFadden, G. B., 1993b, ''Phase-Field Model for Thermal Phase Transitions in Binary Alloys,'' *Phys. Rev. E,* Vol. 47, pp. 1893–1909.

Zegeling, P. A., 1992, ''Moving-Finite-Element Solution of a 2D Brine Transport Problem in a Porous Medium,'' *Advances in Computer Methods for Partial Differential Equations*–VII, R. Vichnevetsky, D. Knight, and G. Richter, eds., IMACS publication, pp. 845–851.

Zegeling, P. A., 1996, ''A Dynamically-Moving Adaptive Grid Method Based on a Smoothed Equidistribution Principle Along Coordinate Lines,'' *Proceedings of the 5th International Conference on Numerical Grid Generation in Computational Simulations,* B. K. Soni, J. F. Thompson, J. Hauser, and P. Eiseman, eds., Mississippi State University, Apr.

A Modified Temperature-Jump Method for the Transition and Low-Pressure Regime

T. Beikircher

N. Benz

Bayerisches Zentrum fur
Angewandte Energieforschung e.V.,
Domagkstr. 11,
D-80807 Munchen, Germany

W. Spirkl

Sektion Physik der Ludwig-Maximilians,
Universitat Munchen,
Amalienstr. 54,
D-80799 Munchen, Germany

For modeling the gas heat conduction at arbitrary Knudsen numbers and for a broad range of geometries, we propose a modified temperature-jump method. Within the modified approach, we make a distinction between an inner convex surface and an outer concave surface enclosing the inner surface. For problems, where only a single geometric length is involved, i.e., for large parallel plates, long concentric cylinders and concentric spheres, the new method coincides at any Knudsen number with the interpolation formula according to Sherman, and therefore also with the known solutions of the Boltzmann equation obtained by the four momenta method. For the general case, where more than one geometric length is involved, the modified temperature method is trivially correct in the limit of high pressure and identical with Knudsen's formula in the limit of low pressure. For intermediate pressure, where there is a lack of known solutions of the Boltzmann equation for general geometries, we present experimental data for the special two-dimensional plate-in-tube configuration and compare it with results of the modified temperature-jump method stating good agreement. The results match slightly better compared to the standard temperature method and significantly better compared to the interpolation formula according to Sherman. For arbitrary geometries and Knudsen numbers, the modified temperature method shows no principal restrictions and may be a simple approximative alternative to the solution of the Boltzmann equation, which is rather cumbersome.

Introduction

Gas heat conduction processes are commonly classified according to the Knudsen number Kn, which is defined as the ratio of the mean free path l_{free} to the characteristic geometric length d_{char} involved in the heat transport (Gombosi, 1994):

$$\text{Kn} := \frac{l_{\text{free}}}{d_{\text{char}}}, \qquad (1)$$

with

$$l_{\text{free}} = \frac{k_B \bar{T}_{\text{gas}}}{\sqrt{2}\sigma p}. \qquad (2)$$

Here p is the gas pressure, $\bar{T}_{\text{gas}}$ the mean gas temperature, σ the collision cross section, and k_B is the Boltzmann's constant. According to the value of the Knudsen number Kn and the gas pressure, respectively, four regimes of different gas conduction mechanisms are discerned (Saxena and Joshi, 1989), (see Fig. 1).

Above a certain critical pressure p_{cr}, depending on the geometry and the gas used, natural convection occurs. Heat is transported by a collective molecule movement, driven by buoyancy forces. The thermal conductivity is strongly increased if the gas pressure is raised.

For $p < p_{\text{cr}}$ and $\text{Kn} \ll 1$ the gas heat conduction is independent of pressure, which is referred to as the continuum regime. The independence of the gas pressure results from the proportionality of the heat flux to the product of the particle density n and l_{free}, the latter being proportional to $1/n$. Only gas-gas collisions are relevant, gas-wall collisions are negligible, and heat is transported in a diffusive way. The heat flux $\mathbf{q}$ can be easily calculated employing Fourier's law with a thermal conductivity λ_∞ which is independent of geometry and pressure (Kacac and Yener, 1985),

$$\mathbf{q} = -\lambda_\infty \cdot \nabla T, \qquad (3)$$

where the temperature field $T(\mathbf{r})$ is obtained using local energy conservation, which in the case of stationary heat conduction without sources reads

$$\nabla \cdot \mathbf{q} = 0. \qquad (4)$$

The boundary conditions are of the first type, i.e., they involve the local gas temperature but no derivatives,

$$\bar{T}_{\text{gas}}(\text{wall}) = T_{\text{wall}}, \qquad (5)$$

where $\bar{T}_{\text{gas}}(\text{wall})$ is the mean gas temperature at the wall with temperature T_{wall}.

For $\text{Kn} \approx 1$, in the transition regime, the calculation of the gas heat conduction is complicated by the fact that gas-wall and gas-gas collisions are similar in frequency. Gas heat conduction then depends on gas pressure and geometry, and on the heat exchange between gas and wall molecules. In principle, exact results can be obtained by solving the gas kinetic Boltzmann equation (Cercignani, 1988), which has turned out to be very tedious. Until now, only a couple of geometries have been calculated. For example Liu and Lees (1961, 1962) and Lees (1965) considered problems, where only a single geometric length is involved. An alternative treatment of the gas heat conduction is the temperature-jump method (Kennard, 1938; Eucken, 1938), but so far its application is confined to pressures near the continuum regime (Saxena and Joshi, 1989).

If $\text{Kn} \gg 1$, in the free molecule regime, gas-gas impacts are so rare that they can be neglected and the molecules are considered to travel freely between the walls. In this range of ballistic heat transport, the heat flux $\dot{Q}$ is proportional to the gas pressure p and can be calculated with Knudsen's formula (Knudsen, 1911; Scott, 1959) which is valid for a concave surface A_2 completely surrounding a convex surface A_1:

Contributed by the Heat Transfer Division for publication in the JOURNAL OF HEAT TRANSFER. Manuscript received by the Heat Transfer Division, Dec. 2, 1996; revision received, June 26, 1998. Keywords: Conduction, Cryogenics, Flow Transition, Thermophysical Properties. Associate Technical Editor: A. Lavine.

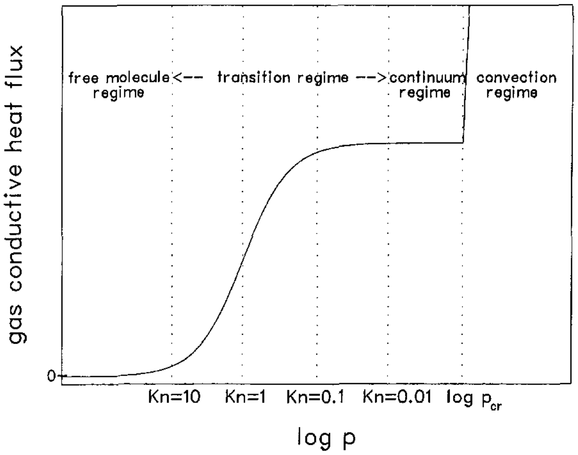

Fig. 1 Heat flux due to gas heat conduction in arbitrary units versus the Knudsen number, which is inversely proportional to the gas pressure

$$\dot{Q}_{\mathrm{FM}} = \left[\frac{1}{A_1}\cdot\frac{1}{\alpha_1} + \frac{1}{A_2}\cdot\left(\frac{1}{\alpha_2} - 1\right)\right]^{-1}\cdot\frac{(f+1)\cdot\sqrt{R_G}}{\sqrt{8\pi M\bar{T}_{\mathrm{gas}}}} \times p\cdot(T_1 - T_2). \quad (6)$$

Here A_i are the two areas the heat is transported between, T_i are their temperatures, f and M are the number of degrees-of-freedom and the mole mass of the gas molecules, R_G is the universal gas constant and, α_i are the accommodation coefficients, which are defined by

$$\alpha_i := \frac{T_{\mathrm{out},i} - T_{\mathrm{in},i}}{T_{\mathrm{wall},i} - T_{\mathrm{in},i}}, \quad \text{or} \quad \alpha_i = \frac{E_{\mathrm{out},i} - E_{\mathrm{in},i}}{E_{\mathrm{wall},i} - T_{\mathrm{in},i}}, \qquad (7)$$

and account for the incomplete temperature accommodation of the gas molecules to the wall temperature T_{wall}, when impinging with T_{in} and leaving with T_{out} (see also Fig. 2). $E_{k,i}$ are the corresponding energy fluxes carried by the molecules, the latter definition being the more modern one. For technical surfaces and monatomic gases, recently Demirel and Saxena (1996) proposed an improved correlation to calculate the accommodation coefficients, values for other gases can be taken from Saxena and Joshi (1989).

Finally, the numerical methods like direct Monte Carlo simulation have to be mentioned, which are powerful tools in treating heat conduction in rarefied gases, but do admittedly require much more calculating effort.

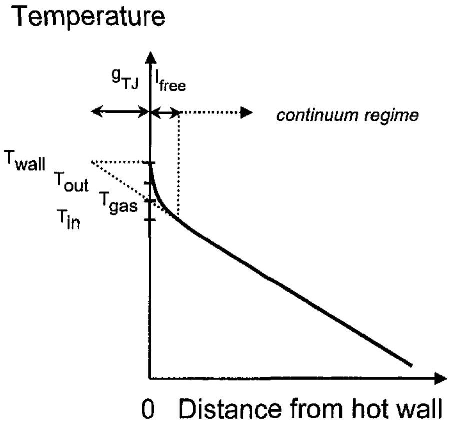

Fig. 2 Schematic of gas temperature distribution near the hot wall in the case of plane heat conduction in a moderately rarefied gas. At a distance in the order of magnitude of l_{free} from the wall, continuum-regime conditions can be supposed. The temperature-jump distance g_{TJ} can be interpreted as the distance, by which the wall has to be moved outwardly to achieve the temperature of the hot wall assuming the (in the plane case) linear bulk temperature distribution. An approximative expression for g_{TJ} is given by Eq. (9), the exact value can only be calculated by solving the Boltzmann equation.

Foundations of the Temperature-Jump Method

The temperature-jump method has been developed by Kennard (Kennard, 1938) and simultaneously by Eucken (Eucken, 1938) in analogy to Maxwell's theory for the velocity slip of a slightly rarefied gas at a resting wall. The calculations in the continuum regime assuming local thermal equilibrium according to Eqs. (3) and (4) are postulated to be valid also in the upper transition regime, i.e., for $0.01 < \mathrm{Kn} < 0.1$, if the boundary condition Eq. (5) is corrected for the effect of the gas-wall impacts,

$$\bar{T}_{\mathrm{gas}}(\mathrm{wall}) = T_{\mathrm{wall}} + g_{\mathrm{TJ}}\cdot\left(\frac{\partial\bar{T}_{\mathrm{gas}}}{\partial n}\right)_{\mathrm{wall}}, \qquad (8)$$

where n is the space coordinate normal to the wall surface directed into the gas and g_{TJ} is the temperature-jump distance, as shown in Fig. (2),

$$g_{\mathrm{TJ}} = \frac{2-\alpha}{\alpha}\cdot\frac{1}{\mathrm{Pr}}\cdot\frac{f+2}{f+1}\cdot l_{\mathrm{free}}$$
$$= \frac{2-\alpha}{\alpha}\sqrt{2\pi R_G M\bar{T}_{\mathrm{gas}}(\mathrm{wall})}\cdot\frac{\lambda_\infty}{(f+1)R_G p}, \qquad (9)$$

Nomenclature

Physical Quantities

α = thermal accommodation coefficient
d = length (m)
f = number of degrees-of-freedom
g_{TJ} = temperature-jump distance (m)
k = heat loss coefficient (WK^{-1})
κ = ratio of the heat capacities (adiabatic exponent)
Kn = Knudsen number
k_{B} = Boltzmann constant = $1.38\cdot 10^{-23}$ (JK^{-1})
λ = thermal conductivity ($\mathrm{W\,m^{-1}\,K^{-1}}$)
Λ = inverse thermal resistance ($\mathrm{W\,K^{-1}}$)
l_{free} = mean free path (m)
M = molecular mass ($\mathrm{kg\,mole^{-1}}$)
n = particle density ($\mathrm{m^{-3}}$)
p = gas pressure (Pa)
Pr = Prandtl number (1)
q = heat flux density ($\mathrm{Wm^{-2}}$)
$\dot{Q}$ = heat flux (W)
R_G = universal gas constant = 8.31 ($\mathrm{J\,mole^{-1}\,K^{-1}}$)
σ = collision cross section ($\mathrm{m^2}$)
T = temperature (K)
$\bar{T}$ = mean temperature (K)

Subscripts

char = characteristic
FM = referred to the free molecule regime
gas = gas
in = incoming molecules
inner = referred to the inner of the gas layer
mod = modified
out = outgoing molecules
plate = plate
ref = reference
TJ = according to the temperature-jump method
tube = tube
wall = wall
∞ = referred to continuum regime
1 = referred to the convex surface
2 = referred to the concave surface

where Pr is the Prandtl number. This boundary condition is of the third type, i.e., it involves the local gas temperature as well as its first derivative.

One can try to apply the temperature-jump boundary condition in conjunction with the assumption of local thermal equilibrium, even for the case where local thermal equilibrium is absent, i.e., for a non-negligible value of Kn. The validity of the temperature-jump method for Kn > 0.1 has been intensively discussed in the literature. Since the works of Lees and Liu (1961, 1962) and Lees (1965) it is known that the temperature-jump method is correct for parallel plates, while for concentric tubes and spheres it is erroneous and can produce deviations from the solution of the Boltzmann equation of up to +100 percent for $p \to 0$ and for complete accommodation. From this fact it was concluded that for geometries with strong curvatures the temperature-jump method is not applicable for Kn > 0.1, while a precise criterion is still missing.

There were some attempts to modify the temperature method and to expand its range of validity to larger Knudsen numbers: Deissler (1964) extended Eq. (9) for an additive term containing the curvature of the temperature field at the wall. Other authors (Payne, 1953; Loyalka and Ferziger, 1968) proposed slightly modified expressions for g_{TJ} obtained by comparison to solutions of the Boltzmann equation near the continuum regime. Recently, using the exact moment solutions of the Boltzmann equation an improved expression for g_{TJ} was obtained by Ivchenko et al. (1995). However, all these trials resulted in a maximum extension of the validity to Kn < 0.2, while for a larger Kn the temperature-jump method until now is not applicable.

Temperature Jump Method at Low Pressures

In the following, for two arbitrary surfaces A_l and A_2, we deduce an analytical expression for the heat flux $\dot{Q}_{p\to 0}$ exchanged in the limit of zero gas pressure, according to the temperature-jump method. From Eq. (8), substituting the normal derivative by means of Eq. (3) and integrating over A_i is obtained:

$$\int_{A_i} (T_{\text{wall}} - \bar{T}_{\text{gas}})\cdot dA_i = \frac{g_{\text{TJ}}^{(i)}}{\lambda_{\infty,i}} \int_{A_i} \dot{q}_{\text{TJ}}\cdot dA_i = \frac{g_{\text{TJ}}^{(i)}}{\lambda_{\infty,i}}\cdot \dot{Q}_{\text{TJ}}, \qquad (10)$$

where the index $i \in (1, 2)$ marks that the term has to be evaluated in the gas layer at the wall i. For $p \to 0$ the heat flux q must go to zero, in which case Eq. (3) requires that $\nabla \bar{T}_{\text{gas}} \to 0$. This implies that the mean gas temperature $\bar{T}_{\text{gas}}(\mathbf{r})|_{p\to 0} =: \bar{T}$ is independent of the location, so that the left side of Eq. (10) can be integrated to give

$$A_i \cdot (T_{\text{wall},i} - \bar{T}) = \frac{g_{\text{TJ}}^{(i)}}{\lambda_{\infty,i}} \dot{Q}_{TJ}|_{p\to 0}, \qquad (11)$$

which are two algebraic equations for $\bar{T}$ and $\dot{Q}_{TJ}|_{p\to 0}$. Solving for $\dot{Q}_{\text{TJ}}|_{p\to 0}$ yields

$$\dot{Q}_{\text{TJ}}|_{p\to 0} = \lambda_\infty(\bar{T})\cdot(T_{\text{wall},1} - T_{\text{wall},2})\cdot \frac{1}{\dfrac{g_{\text{TJ}}^{(2)}}{A_2} + \dfrac{g_{\text{TJ}}^{(1)}}{A_1}}. \qquad (12)$$

With the definition of g_{TJ} according to Eq. (9) and with the well-known identity (Eucken, 1938)

$$\lambda_\infty = \frac{5\pi}{128}\cdot(2f + 9)\cdot p \cdot \sqrt{\frac{8R_G}{\bar{T}\pi M}}\cdot l_{\text{free}} \qquad (13)$$

follows

$$\dot{Q}_{\text{TJ}}|_{p\to 0} = \left[\left(\frac{1}{\alpha_1} - \frac{1}{2}\right)\frac{1}{A_1} + \left(\frac{1}{\alpha_2} - \frac{1}{2}\right)\frac{1}{A_2}\right]^{-1}$$

$$\times \frac{(f+1)\cdot\sqrt{R_G}}{\sqrt{8\pi M\bar{T}}}\cdot p \cdot (T_1 - T_2), \qquad (14)$$

which is the desired general expression for $\dot{Q}_{\text{TJ}}|_{p\to 0}$ according to the temperature method as obtained for any geometry. Comparing Eq. (14) with the correct Knudsen formula, Eq. (6), yields

$$\frac{\dot{Q}_{\text{TJ}}|_{p\to 0}}{\dot{Q}_{\text{FM}}} = 1 + \frac{\alpha_1\alpha_2(A_2 - A_1)}{2\alpha_1 A_1 + 2\alpha_2 A_2 - \alpha_1\alpha_2(A_1 + A_2)}. \qquad (15)$$

Obviously, the error is zero, if $A_1 = A_2$, which is the desired quantitative criterion for the validity of the temperature method at low pressures. As a special case, this criterion explains the long-known validity of the temperature-jump method for parallel plates ($A_1 = A_2$) also in the free molecule limit.

In the case of complete accommodation, i.e., $\alpha_1 = \alpha_2 = 1$ Eq. (15) reads

$$\frac{\dot{Q}_{\text{TJ}}|_{p\to 0}}{\dot{Q}_{\text{FM}}} = 1 + \frac{A_2 - A_1}{A_1 + A_2}, \qquad (16)$$

which follows, that for concentric spheres and tubes at $p \to 0$, the heat flow is overestimated by a factor of 2, in full agreement with the observations of Liu and Lees (1962) and Lees (1965).

Modification of the Temperature-Jump Method

Comparing Eqs. (6) and (14), it can be seen that in the free-molecule regime, the error in the standard temperature-jump method results from the symmetric treatment of the two surfaces A_l and A_2. In the case of a small convex A_l and a large concave A_2, as most common in cryogenic systems, this produces incorrect results due to the fact that molecules having struck the outer wall A_2 possess a finite probability to reach again A_2 before striking A_1. On the other hand, a molecule leaving A_1 hits A_2 without multiple reflections (see Fig. 3). The consequence is an effective higher accommodation to the wall temperature T_2 due to the frequent impacts with A_2, which is not respected in the classical temperature method but is accounted for in Knudsen's formula. Consequently we modify Eq. (9) replacing at each wall $(2 - \alpha_i)/\alpha_i$ by

$\dfrac{2}{\alpha_1}$ on the convex A_1,

$$\text{and} \quad \frac{2 - 2\alpha_2}{\alpha_2} \quad \text{on the concave } A_2. \qquad (17)$$

With this modification in the free-molecule regime the temperature-jump method produces the same results as Knudsen's formula and therefore is correct for arbitrary shaped convex A_1 and concave A_2.

To check its validity in the transition regime we compare the results with known solutions of the Boltzmann equation, with the interpolation formula of Sherman, with the standard temperature method and with experimental results.

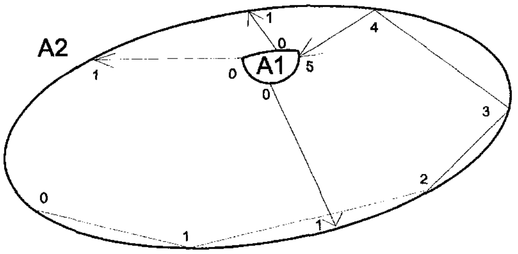

Fig. 3 Heat transfer in the free molecule regime between a convex surface A_1 and an enclosed concave surface A_2. Each molecule leaving A_1 hits A_2. Each molecule leaving A_2 may undergo multiple collisions with A_2 before impacting A_1 depending on the ratio of the areas A_1/A_2

A Single Geometric Length

For monatomic gases, small temperature differences and geometries, where a single geometric length is involved, analytical solutions of the Boltzmann equation have been known using two-sided Maxwell distributions in moment methods and assuming the Maxwell model for the intermolecular interaction (Liu and Lees, 1961; Liu and Lees, 1962; Lees, 1965). Recently the moment method has been extended to general interaction potentials by Ivchenko et al. (1993, 1994).

Since the work of Springer (1971) it is known that the moment solutions obtained by the Maxwell model can be represented in one single formula, the interpolation formula proposed by Sherman (1963):

$$\frac{1}{\dot{Q}} = \frac{1}{\dot{Q}_\infty} + \frac{1}{\dot{Q}_{\mathrm{FM}}}. \tag{18}$$

Here $\dot{Q}_\infty$ denotes the heat flux due to gas conduction in the limit of high pressure, i.e., in the continuum, and $\dot{Q}_{\mathrm{FM}}$ is calculated by Knudsen's formula, Eq. (6). Sherman's formula principally can be applied also to polyatomic gases, since the number of degrees-of-freedom is explicitly accounted for in $\dot{Q}_{\mathrm{FM}}$ and $\dot{Q}_\infty$.

In the following, in a manner quite similar to the consideration of the standard temperature method at low pressures, we show that for geometries where a single geometric length is involved, the modified temperature-jump method is identical to Eq. (18) and therefore also identical to the solution of the Boltzmann equation obtained by the momentum method of Liu and Lees (1961, 1962) and Lees (1965) for any Knudsen number. Due to the symmetry resulting from a geometry involving a single characteristic length, the gas temperature is constant along each area A_1 and A_2 and integration of Eq. (10) yields

$$\Delta T_i := T_{\mathrm{wall},i} - \bar{T}_{\mathrm{gas},i} = \frac{g_i^{(\mathrm{mod})}}{\lambda_{\infty,i} A_i} \cdot \dot{Q}_{\mathrm{TJ}}^{(\mathrm{mod})}, \tag{19}$$

with $g_i^{(\mathrm{mod})}$ as the temperature-jump distance of Eq. (9) modified according to Eq. (17). Assuming local equilibrium in the inner of the gas, for the temperature drop $\Delta T_{\mathrm{inner}}$ within the gas layer holds $\Delta T_{\mathrm{inner}} = \dot{Q}_{\mathrm{TJ}}^{(\mathrm{mod})}/\Lambda_\infty$. Here Λ_∞ is the inverse total thermal resistance of the configuration in the continuum regime and can be calculated by $\Lambda_\infty = \dot{Q}_\infty/\Delta T$, where $\Delta T = T_{\mathrm{wall},1} - T_{\mathrm{wall},2}$. On the other hand

$$\begin{aligned} \Delta T &= \Delta T_{\mathrm{inner}} + \Delta T_1 + \Delta T_2 \\ &= \dot{Q}_{\mathrm{TJ}}^{(\mathrm{mod})} \cdot \left(\frac{\Delta T}{\dot{Q}_\infty} + \frac{g_1^{(\mathrm{mod})}}{\lambda_{\infty,1} A_1} + \frac{g_2^{(\mathrm{mod})}}{\lambda_{\infty,2} A_2} \right). \end{aligned} \tag{20}$$

For small temperature differences, the temperature dependency of $\lambda_{\infty,i}$ and $g_i^{(\mathrm{mod})}$ can be neglected, and using Eq. (6), Sherman's interpolation formula is obtained for $\dot{Q}_{\mathrm{TJ}}^{\mathrm{mod}}$.

In the following, we compare the results of the standard and the modified temperature method for large concentric tubes, to get an insight in the errors of the standard method for curved geometries. Figure 4 shows the results for concentric tubes with different area (radius) ratios $A_1/A_2 = R_1/R_2$. We plot the ratio of the heat flux according to the standard method to the heat flux according to the modified method versus the Knudsen number, which, as for common concentric tubes, is defined as $\mathrm{Kn} := l_{\mathrm{free}}/R_1$, where R_1 is the radius of the inner tube. The accommodation is supposed to be total at both tubes.

It can be seen that for small Kn, both methods essentially produce the same results, the value of Kn where the deviations become visible getting smaller with increasing A_1/A_2. For larger Kn the deviations increase and tend to a maximum for $\mathrm{Kn} \rightarrow \infty$. Its value depends on the value of A_1/A_2, with a maximum deviation of +100 percent for $A_1/A_2 \rightarrow 0$.

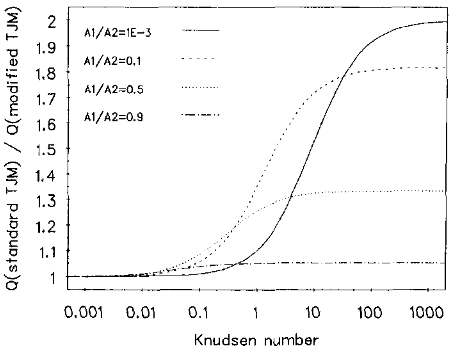

Fig. 4 Ratio of the heat fluxes according to the standard and the modified temperature-jump method versus the Knudsen number for two long concentric tubes with different ratios of their radii and areas, respectively

General Geometry

We showed that the modified temperature-jump method is correct in the limit of low pressures. On the other hand, it is trivial that it is correct in the limit of high pressures. We now investigate its validity in the transition regime. Due to the lack of closed-form solutions of the Boltzmann equation for geometries with more than a single geometric length involved, we compare the modified temperature-jump method with experimental data we obtained for a plate-in-tube configuration. This geometry has been used by Soddy and Berry (1910) and Umemura and Hakura (1974) to determine the accommodation coefficients in the free-molecule regime and is common for evacuated tube solar collectors (Beikircher and Spirkl, 1996).

The experimental setup is sketched in Fig. (5) and described in detail in Beikircher and Goldemund (1995, 1996). The thermal losses of an electrically heated aluminum plate (1200 mm × 100 mm × 7 mm) centered symmetrically in a glass tube (1500 mm length, 110 mm diameter) and filled with air were examined for pressures between 10^{-2} Pa and 10^4 Pa under steady-state conditions.

The temperatures of the plate and of the tube were controlled to 150°C and 30°C, respectively. The maximum spatial inhomogeneity of the temperature on the plate (tube) was 5 K (1 K), resulting in an error in the respective mean temperatures of below 0.5 K. From the electrical heating power, the gas conduction loss heat flux was obtained subtracting the background loss heat flux due to solid conduction and radiation which were measured at pressures below 10^{-2} Pa and amounted to about 30 W. Thereby, the electrical power was measured with an error of 1.4 percent and the error propagation law has been applied. The mean temperature of the plate was determined by 15 individually calibrated thermocouple sensors. The mean temperature of the glass tube was measured by five calibrated platinum resistance sensors. Two counter heaters at the long ends of the absorber plate avoid shunt losses via the heating wires and measuring leads.

Figure 6 compares the experimental and theoretical results for the gas heat conduction, which are presented by the pressure-dependent loss coefficient $k(p)$:

$$k(p) := \frac{\dot{Q}(p)}{A_{\mathrm{ref}}(T_{\mathrm{plate}} - T_{\mathrm{tube}})}, \tag{21}$$

where the reference area A_{ref} is chosen as the upper part of the plate surface, i.e., as the product of plate width and plate length. In the figure, experimental error bands have been calculated as plus and minus three standard deviations. The theoretical values shown are calculated for air by the standard and the modified temperature-jump method and by the interpolation formula, respectively. For the thermal accommodation coefficients of air, we used values from Saxena and Joshi (1989), that is 0.95 for the aluminum absorber and 0.86 for the glass tube.

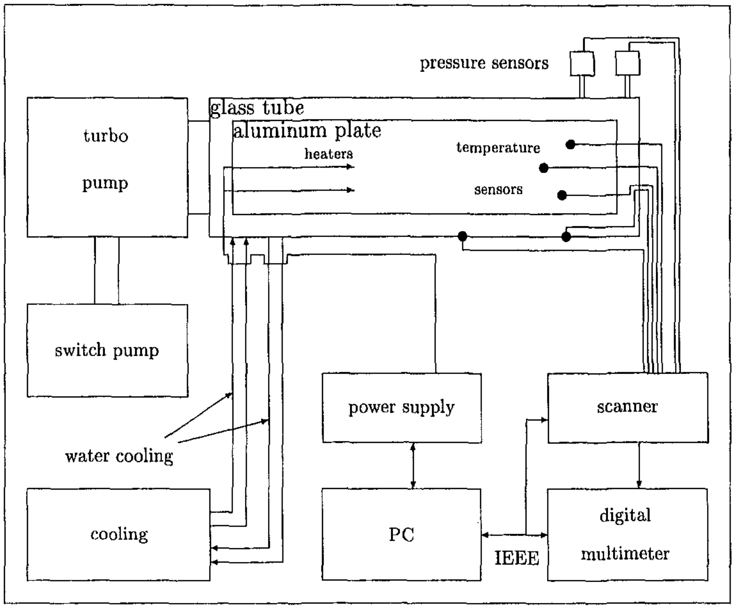

Fig. 5 The experimental setup

For all theoretical curves, the underestimation in the continuum regime is equal and systematic. It results from the heat losses at the rim which were neglected in the two-dimensional calculation (Beikircher and Spirkl, 1996). In the free-molecule regime, the rim losses can be neglected according to Eq. (6), because α_2, the accommodation coefficient for the system air/glass is close to unity (Saxena and Joshi, 1989).

From the experimental curve it can be seen that for a pressure of about 2 Pa, the heat flux is half of the heat flux in the continuum, which defines Kn = 1. Calculating l_{free} (2 Pa) for the typical length l_{free} has to be referred to, in the case of our apparatus 12 mm is obtained, while the smallest and largest distance between plate and tube amounts to 5 mm and 50 mm, respectively.

The results of the modified temperature-jump method fully agree with the measured data over the whole transition regime. The results of the interpolation formula significantly exceed the experimental error bounds, the calculated slope is too large, since the experimental curve averages over the different geometric lengths involved, which by construction cannot be accounted for by the interpolation formula (Beikircher, 1996). The results of the standard temperature-jump method fit the experimental data except of the two values at 1 and 5 Pa. According to Eq. (16), the standard method overestimates the real losses in the free molecule regime by about 20 percent due to the fact that in the experiment $A_1/A_2 = 1.5$. This cannot be resolved experimentally, but it is probable that the observed overestimation in the transition regime is caused by the same reason. The proposed modification removes the errors between 1 and 5 Pa, and is significantly closer to the measured data in the whole transition regime. However, the difference between modified and standard method is small in cases where the area ratio is near to unity.

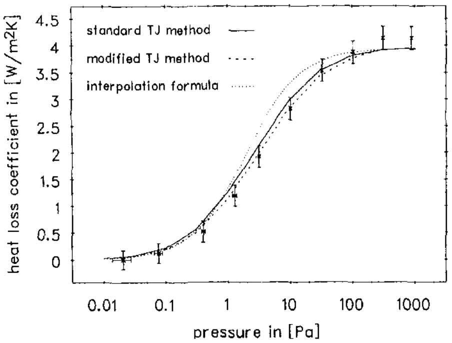

Fig. 6 Experimental versus theoretical results for the thermal loss coefficient due to gas heat conduction, *k*, of a plate-in-tube configuration

Conclusions

We modified the temperature-jump method and extended its validity to the free-molecule regime. In the transition regime, for geometries where only a single geometric length is involved, we analytically showed that the modified temperature-jump method is equivalent to the interpolation formula of Sherman, which implies the equivalence to solutions of the Boltzmann equation obtained by means of the four momenta method. For more complex geometries we proved the modified temperature-jump method to be correct in the limit of high as well as of low pressures. For intermediate pressures and the two-dimensional plate-in-tube configuration, we experimentally corroborated its validity in the entire transition regime while the Sherman interpolation fails. However, this does not prove that the modified temperature-jump method is valid in the transition regime for an arbitrary geometry. Comparisons to further experimental data or to numerical solutions of the Boltzmann equation are required. However, the proposed modification hopefully will raise the interest in the temperature-jump method, as a simple approximation method alternatively to the generally tedious solution of the Boltzmann equation.

References

Beikircher, T., and Goldemund, G., 1995, "Gas heat conduction in an evacuated tube solar collector," *Solar Energy*, Vol. 58, pp. 4–6.

Beikircher, T., and Spirkl, W., 1996, "Gas heat conduction in evacuated tube solar collectors," ASME *Journal of Solar Energy Engineering*, Vol. 118.

Beikircher, T., 1986, Gaswärmeleitung in evakuierten Sonnenkollektoren. Ph.D. thesis, Sektion Physik, Prof. Dr. J. Feldmann, Ludwig Maximilians Universität München.

Cercignani, C., 1988, *The Boltzmann equation and its applications*, Springer-Verlag, New York.

Deissler, R. G., 1964, "An analysis of second-order slip flow and temperature jump boundary conditions for rarefied gases, *Int. J. Heat Mass Transfer*, Vol. 7, pp. 681–694.

Demirel, Y., and Saxena, S. C., 1996, ''Heat transfer through a low-pressure gas enclosure as a thermal insulator: design and considerations,'' *Journal of Energy Research,* Vol. 20, pp. 327–338.

Eucken, A., 1938, *Lehrbuch der chemischen Physik.* Akademische Verlagsgesellschaft, Leipzig.

Gombosi, T. I., 1994, *Gaskinetic theory,* Cambridge University Press, Cambridge, UK.

Ivchenko, I. N., Loyalka, S. K., and Thompson, R. V., 1993, ''A method of solving the problem of heat transfer between two cylinders at arbitrary knudsen numbers,'' *Teplofiz. Vysok. Temp.,* Vol. 31.

Ivchenko, I. N., Loyalka, S. K., and Thompson, R. V., 1994, ''A method for solving linearized problems of the transfer theory for spherical geometry at arbitrary knudsen numbers,'' *Fluid Dynamics,* Vol. 29, No. 6.

Ivchenko, I. N., Loyalka, S. K., and Thompson, R. V., 1995, ''On the use of conservation laws in planar slip flow problems,'' *High temperature,* Vol. 33, No. 1.

Kacac, S., and Yener, Y., 1985, *Heat conduction,* Hemisphere Publishing Corporation and Springer Verlag, New York.

Kennard, E. H., 1938, *Kinetic theory of gases,* McGraw-Hill, New York.

Knudsen, M., 1911, ''Die molekulare Wärmeleitung der Gase und der Akkommodationskoeffizient,'' *Annalen der Physik,* Vol. 34, pp. 593–656.

Lees, L., 1965, ''Kinetic theory description of rarefied gas flow,'' *J. Soc. Indust. Appl. Math.,* Vol. 13, No. 1, pp. 278–311.

Liu, C. Y., and Lees, L., 1961, ''Kinetic theory description of plane compressible couette-flow,'' *Proceedings of the 2nd symposium on rarefied gas dynamics.*

Liu, C. Y., and Lees, L., 1962, ''Kinetic theory description of conductive heat transfer from a fine wire,'' *Physics of Fluids,* Vol. 5, No. 10, pp. 1137–1148.

Loyalka, S. K., and Ferziger, J. H., 1968, ''Model dependence of the temperature slip coefficient,'' *Physics of Fluids,* Vol. 11, No. 8, pp. 1668–1671.

Payne, H., 1953, ''Temperature jump and velocity slip at the boundary of a gas,'' *J. of Chemical Physics,* Vol. 21, No. 12, pp. 2127–2131.

Saxena, S. C., and Joshi, R. K., 1989, *Thermal accomodation and adsorption coefficients of gases,* Hemisphere, New York, 1989.

Scott, R. B., 1959, *Cryogenic Engineering,* D. van Nostrand, New York.

Sherman, F. S., 1963, ''Experiments in the transition regime,'' *Rarefied gas dynamics,* J. A. Laurmann, ed., Academic Press, New York.

Soddy, F., and Berry, A. J., 1910, *Proc. Roy. Soc. London,* Vol. A83, pp. 254–264.

Soddy, F., and Berry, A. J., 1911, *Proc. Royal Soc. London,* Vol. A84, pp. 576–585.

Springer, G. S., 1971, ''Heat transfer in rarefied gases,'' *Advances in heat transfer,* Vol. 7, pp. 163–218.

Umemura, K., and Hakura, M., 1974, *Nippon Kagaku Kaishi,* Vol. 3, pp. 439–444.

P. E. Phelan
Department of Mechanical and
Aerospace Engineering,
Arizona State University,
Tempe, Arizona 85287-6106
e-mail: phelan@asu.edu
Mem. ASME

R. C. Niemann
Argonne National Laboratory,
Energy Technology Division,
9700 South Cass Avenue, ET/335,
Argonne, IL 60439-4818
e-mail: RC_NIEMANN@QMGATE.ANL.GOV
Fellow ASME

Effective Thermal Conductivity of a Thin, Randomly Oriented Composite Material

The thermal conductivity of a randomly oriented composite material is modeled using a probabilistic approach in order to determine if a size effect exists for the thermal conductivity at small composite thicknesses. The numerical scheme employs a random number generator to position the filler elements, which have a relatively high thermal conductivity, within a matrix having a relatively low thermal conductivity. The results indicate that, below some threshold thickness, the composite thermal conductivity increases with decreasing thickness, while above the threshold the thermal conductivity is independent of thickness. The threshold thickness increases for increasing filler fraction and increasing k_f/k_m, the ratio between the filler and matrix thermal conductivities.

Introduction

Predicting the thermal, electrical, and mechanical properties of composite materials is very important to their application, since it is both time-consuming and expensive to measure these properties, given the wide possible ranges of filler and matrix materials, the filler orientation and dimensions, and the fraction of the total composite that is occupied by the filler. Numerous studies have been reported which describe methods for calculating the effective thermal (or electrical) conductivities for fiber-reinforced composites (see, e.g., Maewal et al., 1976; Han and Cosner, 1981; Peterson and Fletcher, 1987; and Mottram, 1992). However, apparently most, if not all, of these investigations focused on geometries in which the composite material was infinite in extent. Since the structure of fiber-reinforced composites is generally periodic, this allowed the use of a ''unit cell'' approach, in which the effective transport properties of an elemental cell containing representative properties of fiber and matrix material in an appropriate configuration, are the same as those of the composite medium as a whole. This approach works well, provided that the geometry of the actual composite material at hand is relatively large, so that it contains a sufficient number of the unit cells. This unit-cell approach, however, will not be applicable if the composite geometry is limited in at least one dimension, such that the unit cell cannot be truly representative of the entire composite structure.

Another class of composite materials is those in which the filler, such as the fibers in a fiber-reinforced composite, is randomly oriented throughout the matrix. Examples of this type of composite include in-plane randomly oriented fiber composites (Peterson and Fletcher, 1987), and thermally conductive compounds consisting of a grease or epoxy which contains a large number of small particles for enhancing the compound thermal conductivity, such as copper or silver particles. These thermally conductive compounds are generally applied as a thin layer between two solid materials in order to increase the thermal conduction across the interface. Hence, their geometry can be severely restricted in the thickness direction. It is anticipated that the effective compound thermal conductivity, k_{eff}, will be independent of thickness for sufficiently large thicknesses, but that k_{eff} will vary at smaller thicknesses.

This report is concerned with predicting k_{eff} for composites containing a randomly oriented filler material using a probabilistic approach. A range of filler and matrix thermal conductivities is examined. Specifically, our analysis determines the minimum thickness necessary to achieve the ''bulk'' value of k_{eff}, i.e., the minimum thickness needed to produce a k_{eff} that is independent of sample thickness.

Theoretical Approach

Due to the typical geometry of a thermal compound application, in which a thin layer of the compound is sandwiched between two solids, the two-dimensional model shown in Fig. 1 is employed. All elements are taken to be square-shaped for simplicity. The matrix elements, having a thermal conductivity k_m, are white, while the filler elements, having a thermal conductivity k_f, are shaded. The positions of the matrix elements are determined in a random procedure which is discussed below. The dimensions of each square element are $l \times l$. The thickness, H, is equal to the number of elements in the thickness direction, m, multiplied by l. The width, L, is equal to the number of elements in the width direction, n, multiplied by l. In all cases, $L \geq 2H$ in order to minimize any effects due to the left and right-hand boundaries. The composite is positioned between two solid materials having temperatures T_1 (upper) and T_0 (lower). Heat transfer between the solid materials and the composite is characterized by the heat transfer coefficients h_1 (upper) and h_0 (lower). For generality, a thermal contact conductance, h_c (not shown in Fig. 1), is assumed to exist between the filler elements and any of their neighboring elements.

Thermal Resistance Network. Since we are considering only steady-state heat transfer, it is expedient to model the thermal conduction through the composite material using a thermal resistance network. Figure 2 shows a small portion of this network near the lower left-hand corner of the composite. Each node represents the temperature of one of the elements in Fig. 1. The boundary conditions at the left and right-hand sides of the composite, at positions $j = 1$ and $j = n$, are taken to be insulated, so that no heat flows in those directions.

The thermal resistances surrounding the i, j node are shown in Fig. 2, where $R_{ij,U}$ is the ''upper'' resistance, $R_{ij,R}$ is the ''right'' resistance, $R_{ij,B}$ is the ''bottom'' resistance, and $R_{ij,L}$ is the ''left'' resistance. These resistances are determined by the two nodal elements which they straddle. For example, if the i, j node is a filler element, and the i, $j + 1$ node is a matrix element, $R_{ij,R}$ is given by

---

Contributed by the Heat Transfer Division for publication in the JOURNAL OF HEAT TRANSFER and presented at the '97 NHTC, Baltimore. Manuscript received by the Heat Transfer Division, Jan. 30, 1997; revision received, July 13, 1998. Keywords: Conduction, Numerical Methods, Thermophysical Properties. Associate Technical Editor: R. Boyd.

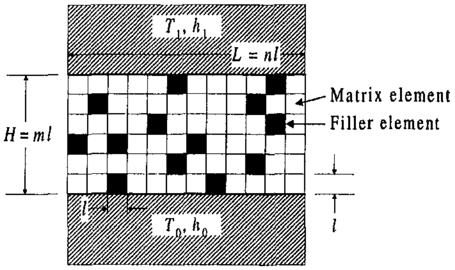

Fig. 1 Schematic thermal model of the two-dimensional, randomly oriented composite material

$$R_{ij,R} = R_{i,j} + R_{i,j+1} \tag{1}$$

where

$$R_{i,j} = \frac{1}{h_c l} + \frac{1}{2k_{i,j}} \tag{2}$$

and

$$R_{i,j+1} = \frac{1}{2k_{i,j+1}} \tag{3}$$

where in this case $k_{i,j} = k_f$ and $k_{i,j+1} = k_m$. Note that the thermal contact conductance, h_c, only appears where there is a filler element. If a filler element occupied the node $i, j + 1$ rather than a matrix element, than h_c would also appear in the expression for $R_{i,j+1}$. The other resistances surrounding the node i, j are determined in a completely analogous manner, except for the top ($i = 1$) and bottom ($i = m$) rows of the matrix, where the heat transfer coefficients h_1 and h_0 come into play, as shown for the bottom row in Fig. 2.

The system of linear equations is generated in a straightforward manner by summing up all the heat flows for each node and equating to zero. For example, for the i, j node located in the interior of the matrix, as shown in Fig. 2, we have

$$\frac{T_{i-1,j} - T_{i,j}}{R_{ij,U}} + \frac{T_{i,j}+1 - T_{i,j}}{R_{ij,R}} + \frac{T_{i+1,j} - T_{i,j}}{R_{ij,B}} + \frac{T_{i,j-1} - T_{i,j}}{R_{ij,L}} = 0. \tag{4}$$

One such equation can be written for each node, producing a system of equations of the form **Cx** = **B**, where **C** is an $(m \times n) \times (m \times n)$ coefficient matrix, **B** is a vector of length $m \times n$, and **x** is the output vector of length $m \times n$ which contains the nodal temperatures. This matrix equation is solved using LU decomposition (Press et al., 1992), where L represents "lower triangular" and U "upper triangular."

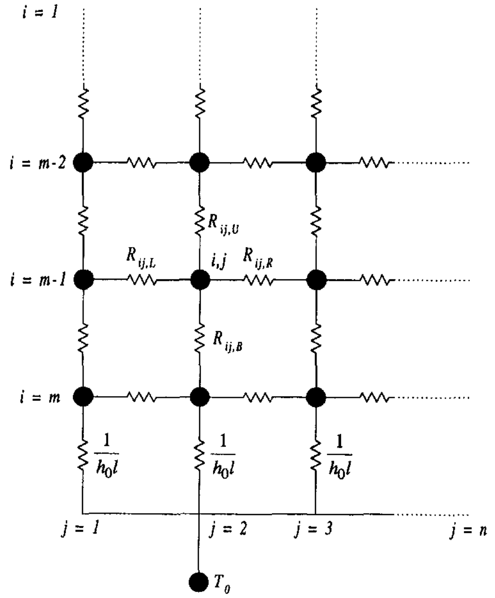

Fig. 2 Lower left-hand portion of the thermal resistance network

Determining the Positions of the Filler Elements. The total number of filler elements, n_f, is a function of the specified filler fraction, φ, where φ ranges between 0 and 1:

$$n_f = \varphi \times (m \times n) \tag{5}$$

where $p = m \times n$ is the total number of nodes. We employ a random number generator (Press et al., 1992) to determine which nodes are occupied by the filler. Since the output of the random number generator is between 0 and 1, we divide this range into p intervals,

$$0 < z < \frac{1}{p}, \frac{1}{p} \le z < \frac{2}{p}, \frac{2}{p} \le z < \frac{3}{p}, \ldots, \frac{p-1}{p} \le z < 1, \tag{6}$$

where each interval represents one node. The random number generator is then utilized to produce a random number between 0 and 1. The interval in which that number falls is assigned to be a filler node. This process is repeated until all n_f filler nodes are assigned. If, during the course of this procedure, two or more random numbers fall within the same interval, only the first such number is kept, since that node is already assigned to be a filler element. Any subsequent numbers falling within

Nomenclature

h_0, h_1 = heat transfer coefficients to the cold and hot thermal reservoirs, respectively (W m^{-2} K^{-1})

h_c = thermal contact conductance at the filler surface (W m^{-2} K^{-1})

H = composite thickness (m)

k_{eff} = effective composite thermal conductivity (W m^{-1} K^{-1})

k_f = filler thermal conductivity (W m^{-1} K^{-1})

k_m = matrix thermal conductivity (W m^{-1} K^{-1})

k_{mean} = mean composite thermal conductivity (W m^{-1} K^{-1})

l = element dimension (μm)

L = composite width (m)

m = number of cells (elements) in the thickness direction

n = number of cells (elements) in the width direction

n_f = total number of filler elements

q = total heat flow through the composite (W)

$R_{i,j}$ = thermal resistance of the i, j node, per unit length (m K W^{-1})

R_{tot} = total thermal resistance of the composite, per unit length (m K W^{-1})

T_0, T_1 = temperatures of cold and hot thermal reservoirs, respectively (K)

φ = filler fraction

the same interval are discarded, and additional random numbers are generated in order to ensure that exactly n_f nodes are occupied by filler elements.

Determining the Composite Thermal Conductivity. Determining k_{eff} for the composite material is actually not trivial, even once all the nodal temperatures have been determined. The reason lies in the highly anisotropic nature of the heat flow within the composite. Referring to Fig. 2, recall that the heat transfer coefficients to isothermal reservoirs, rather than the composite temperature itself, are specified at the upper and lower boundaries. If we assume the thermal resistances due to h_1, h_0, and the conduction within the composite are in series, we arrive at the following expression for the total thermal resistance, R_{tot}, between T_1 and T_0:

$$R_{\mathrm{tot}} = \frac{1}{h_1 L} + \frac{H}{k_{\mathrm{eff}} L} + \frac{1}{h_0 L}. \tag{7}$$

Intuitively, Eq. (7) seems reasonable, because we can imagine that we should be able to assign well-defined values for each of the three terms on the right-hand side of Eq. (7). However, in reality, for finite values of h_1 and h_0, there is no well-defined single temperature on the upper and lower boundaries of the composite, and hence the assumption implicit in Eq. (7) that these three resistances lie in series is not rigorously correct. This problem, however, is averted for the results reported here, since we take both h_1 and h_0 as tending towards infinity, which yields uniform upper and lower boundary temperatures for the composite. The resolution of this issue when h_1 and h_0 are assigned finite values is left for the future.

The composite thermal conductivity, k_{eff}, is determined here by first calculating R_{tot} using

$$R_{\mathrm{tot}} = \frac{T_1 - T_0}{q} \tag{8}$$

where q is the total heat flow through the composite. In practice, q is determined by summing all the individual nodal heat flows at either the upper or lower composite boundary, which must yield equal values of q. In fact, the consistency of the numerical scheme is checked by comparing q calculated at the upper boundary with that calculated at the lower boundary, and ensuring that the values are equivalent.

Finally, k_{eff} is determined by equating the value for R_{tot} calculated from Eq. (8) with Eq. (7), yielding

$$k_{\mathrm{eff}} = \frac{H}{L R_{\mathrm{tot}} - \frac{1}{h_1} - \frac{1}{h_0}}. \tag{9}$$

Once k_{eff} is calculated in this manner for a single set of random numbers, and hence filler positions, this procedure is repeated a number of times, with a new set of random numbers assigned for each repetition. This yields a distribution of k_{eff} values, from which a mean value of k_{eff} is calculated (k_{mean}). The value of most interest is k_{mean}, since that is what is most likely to occur in a real application. A total of 200 iterations are performed to determine k_{mean}. An example of the k_{eff} distribution for $\varphi = 0.20$, $m = 20$, $n = 40$, $k_m = 0.2$ W m^{-1} K^{-1}, and $k_f = 400$ W m^{-1} K^{-1} is shown in Fig. 3. These particular values of k_m and k_f correspond to a thermal grease matrix with copper particles serving as the filler. For this particular case, k_{mean} is 0.2975 W m^{-1} K^{-1}. It should be noted that the distribution in Fig. 3 is by no means typical. For larger values of φ, and/or small values of m, especially where $k_f \gg k_m$, occasional large values of k_{eff} result which skew the distributions towards the higher values. Such outlying points would presumably become less and less relevant as the total number of iterations is increased. However, in the interests of maintaining a reasonable computation time while achieving satisfactory accuracy, the number of iterations for the present results is fixed at 200. The error caused by this limitation, as well as from other sources, is discussed in the next section.

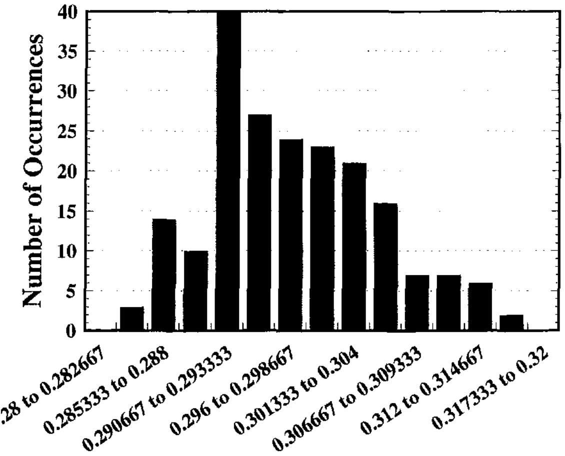

Fig. 3 Histogram of k_{eff} values for $k_m = 0.2$ W m^{-1} K^{-1}, $k_f = 400$ W m^{-1} K^{-1}, $\varphi = 0.20$, $m = 20$, $n = 40$, $h_0 = h_1 = h_c = 10^{30}$ W m^{-2} K^{-1}, and $l = 5$ μm

Numerical Uncertainty. There are essentially four contributions to error in our numerical scheme: (i) insufficient number of iterations to achieve a satisfactory distribution, (ii) insufficient L/H ratio to eliminate edge effects, (iii) errors originating from the random number generator, and (iv) roundoff and truncation errors. For (i), this error seems most severe where k_f differs greatly from k_m. A comparison between a test run of 1000 iterations with our standard run of 200 iterations indicates an error as high as ±10 percent. For (ii), sample calculations indicate that maintaining $L/H \gtrsim 2$ results in an error of less than ±1 percent. For (iii), the random number generator employed is satisfactory, according to Press et al. (1992), except for an extraordinarily high number of calls, on the order of 10^8. In the present case, the maximum number of calls is on the order of 10^5, so that we neglect any error due to the random number generator. Finally, for (iv), these errors are difficult to estimate, but are thought to be negligible compared with error (i). Therefore, the error caused by an insufficient number of iterations is the dominant contributor, and we thus estimate the total numerical uncertainty at ±10 percent.

Results and Discussion

The results shown below indicate the effects of filler fraction (φ), matrix and filler thermal conductivities (k_m and k_f), filler thermal contact conductance (h_c), and filler size l on the mean composite thermal conductivity (k_{mean}), as determined from an average of 200 iterations. In each case, the nondimensional thermal conductivity, k_{mean}/k_m, is plotted versus the nondimensional composite thickness, $m = H/l$. Where possible, however, the dimensional values of k_{mean} and H are also given on separate axes. All calculations are performed for $h_0 = h_1 = 10^{30}$ W m^{-2} K^{-1}, i.e., effectively infinite, $T_1 = 1$ K, and $T_0 = 0$ K. In each case the ratio L/H is at least two, and for smaller values of m, L/H is set at five so that edge effects due to the left and right boundaries can be neglected.

Effect of Filler Fraction (φ). Figure 4 presents k_{mean}/k_m as a function of φ. The matrix and filler thermal conductivities are $k_m = 0.2$ W m^{-1} K^{-1} and $k_f = 400$ W m^{-1} K^{-1}, respectively. These values correspond approximately to a matrix consisting of thermal grease, such as one of the Apiezon greases, and the filler consisting of copper particles, all at room temperature. Any effect of filler contact resistance is neglected here by taking $h_c = 10^{30}$ W m^{-2} K^{-1}.

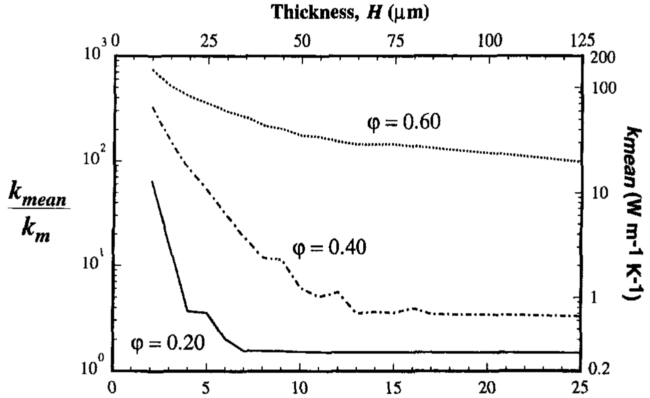

Fig. 4 Effect of varying fiber fraction φ on k_{mean}/k_m (k_m = 0.2 W m^{-1} K^{-1}, k_f = 400 W m^{-1} K^{-1}, $h_0 = h_1 = h_c = 10^{30}$ W m^{-2} K^{-1}, and l = 5 μm)

Figure 4 shows the anticipated results, in that at large thicknesses, the curves generally approach a horizontal asymptote which signifies that k_{mean}/k_m becomes independent of thickness at that point. At small thicknesses, k_{mean}/k_m tends to increase with decreasing thickness. Thus, each curve can be divided into two regions: the "small" region at lower thicknesses, where k_{mean}/k_m varies with thickness, and the "bulk" region at higher thicknesses, where k_{mean}/k_m is independent of thickness. The thickness at which the "bulk", or asymptotic, behavior is reached increases with increasing φ. For $\varphi = 0.20$, the boundary between the "small" and "bulk" regions occurs near $m = 7$, that is, for a composite thickness of only seven elements, or cells. The size of each element, $l \times l$, is determined by the average filler size, so that if the filler consists of solid copper particles, the "bulk" region is obtained for a thickness of seven copper particles. For $\varphi = 0.40$, the boundary between the two regions occurs near $m = 13$, and for $\varphi = 0.60$, the boundary apparently lies beyond $m = 25$. Therefore, the region in which the "small" size effect strongly impacts k_{mean}/k_m becomes much larger with increasing φ.

What causes k_{mean}/k_m to increase at small thicknesses? First of all, note that this trend is in agreement with a study on percolation in a unidirectional fiber composite consisting of perfectly conducting, circular fibers enmeshed within a nonconducting matrix (Joy and Strieder, 1979). Our model differs from the percolation model in that both the matrix and the filler have a finite conductivity, which allows conduction even without the percolation mechanism. However, we believe that a percolation type of mechanism is responsible for the enhanced thermal conduction at small thicknesses. It seems that as the thickness is decreased, there is a greater propensity for the filler particles to "line up," thus creating a relatively high thermal conductivity path, or thermal "short", which increases the overall composite thermal conductivity. The probability for this kind of filler alignment apparently decreases with increasing thickness, such that beyond some given thickness—the boundary between the "small" and "bulk" regions—none of these high thermal conductivity paths can occur, yielding a k_{mean}/k_m which is thereafter independent of composite thickness.

For consistency, the "bulk" values of k_{mean}/k_m calculated for large thicknesses should agree with standard estimates of the thermal conductivity of composite materials, given known values of φ, k_m, and k_f. Unfortunately, however, there is no single generally accepted formula that can be used to provide a reliable estimate of k_{mean}/k_m. Two approaches that provide upper and lower bounds to k_{mean}/k_m are to (i) assume the matrix and filler lie in series (lower bound), and (ii) assume the matrix and filler lie in parallel (upper bound) (Peterson and Fletcher, 1987). The corresponding relation for the series approximation is

$$\frac{k_{mean}}{k_m} = \frac{1}{\varphi \dfrac{k_m}{k_f} + (1 - \varphi)} \tag{10}$$

and that for the parallel approximation is

$$\frac{k_{mean}}{k_m} = \varphi \frac{k_f}{k_m} + (1 - \varphi). \tag{11}$$

A comparison of the values calculated from each of these relations, together with the bulk, or large thickness, values taken from Fig. 4, is provided in Table 1. It is seen that the bulk values taken from Fig. 4 always lie between the bounds calculated from Eqs. (10) and (11), thus demonstrating, as much as possible, the consistency of the present results for large thicknesses. Furthermore, Table 1 demonstrates a positive side benefit of the present approach: Following this statistical procedure, one can make much more precise estimates of k_{mean} for a randomly distributed composite, compared with the predictions of Eqs. (10) and (11).

So far, nothing has been said concerning any effect of element size, l, on k_{mean}/k_m. With reference to Eq. (2), l impacts the thermal resistance $R_{i,j}$ only in the term involving the filler contact conductance h_c. Therefore, where $h_c \to \infty$, as in the results in Fig. 4, changing l has no effect on k_{mean}/k_m. Later in this report, the effect of varying l for finite h_c will be evaluated.

Finally, note the small fluctuations in the curves in Fig. 4, which are especially apparent for the $\varphi = 0.20$ and $\varphi = 0.40$ curves. These fluctuations are the result of the probabilistic nature of our theoretical approach. As discussed above, there is some possibility, at small thicknesses, for the filler particles to align themselves to create a high thermal conductivity path. This can result in a value for k_{eff} that is a factor of 15 greater than k_{mean}, thus skewing the distribution and yielding a relatively high value for k_{mean}. Upon further investigation, it is revealed that this effect is somewhat dissipated by taking a greater number of iterations to determine k_{mean}. However, in an actual composite material, there is also some probability for the highly conducting particles to align themselves in this way, so that the fluctuations predicted by our theoretical model could also occur. Predicting exactly when and where such fluctuations will occur, however, is impossible because of the random nature of the composite.

Effect of k_m and k_f. The composite thermal conductivity k_{mean}/k_m is plotted versus nondimensional thickness for three values of k_f/k_m in Fig. 5. For each curve, $\varphi = 0.60$, $l = 5$ μm, and $h_0 = h_1 = h_c = 10^{30}$ W m^{-2} K^{-1}. The upper curve corresponds to a copper filler within a grease matrix, like the results in Fig. 4. The middle curve, where $k_m = 0.19$ W m^{-1} K^{-1} and $k_f = 46$ W m^{-1} K^{-1}, corresponds to a polyimide matrix with an alumina filler. The lowest curve, where $k_m = 0.3$ W m^{-1} K^{-1} and $k_f = 1.0$ W m^{-1} K^{-1}, corresponds to the G-10 composite, which consists of woven glass fibers within an epoxy matrix. Note, however, that since G-10 is a woven, not a random, composite, these results will not apply specifically to G-10. These three values of k_f/k_m are chosen to represent a broad range of thermal conductivities, while still being relevant for some practical applications.

Table 1 Limiting values of k_{mean}/k_m for the conditions shown in Fig. 4

φ	Bulk (from Fig. 4)	Series approximation	Parallel approximation
0.20	1.485	1.250	401.0
0.40	3.290	1.665	800.5
0.60	99.00	2.500	1200.5

Although all three curves indicate that k_{mean}/k_m increases with decreasing thickness, the effects on the two upper curves are most pronounced. For the lowest curve ($k_f/k_m = 3.3$), there is only a very slight increase in k_{mean}/k_m at lower thicknesses. Apparently, k_f/k_m must be sufficiently different from unity to achieve a significant size effect on k_{mean}/k_m at small thicknesses. Furthermore, the change in k_{mean}/k_m between its maximum and minimum values increases with increasing k_f/k_m. For the upper curve where $k_f/k_m = 2000$, k_{mean}/k_m changes by a factor of 7.5, while for the middle curve ($k_f/k_m = 242$), k_{mean}/k_m changes by only a factor of 4.5.

For the upper curve, the horizontal asymptote is still not reached for $m = 25$, indicating that the boundary between the "small" and "bulk" regions lies at still greater thicknesses. For the middle curve, the boundary occurs near $m = 12$, and for the lowest curve, at $m < 5$. Thus, it is clear that the greater the difference between k_m and k_f, as measured by the ratio k_f/k_m, the greater the thickness over which the size effect on k_{mean}/k_m is important.

Effect of Filler Contact Conductance (h_c) and Filler Size (l). Referring to Eq. (2), it is seen that h_c and l are present only in the denominator of the first term on the right-hand side. This suggests that the effects of these variables can be combined into a single nondimensional parameter. Maintaining consistency with the previous nondimensionalizations, we choose to multiply Eq. (2) by k_m, yielding the nondimensional parameter, h_cl/k_m, to describe the effects of h_c and l. Figure 6 shows the effect of varying this parameter on k_{mean}/k_m, for the same material properties as in Fig. 4, and for $\varphi = 0.40$. As anticipated, as h_c decreases (i.e., the thermal contact resistance between the filler particles and the matrix or other filler particles increases), k_{mean}/k_m decreases. For the thermal grease/copper particle combination considered here, the actual value of h_c at room temperature would probably be relatively high—perhaps close to 10^7 W m^{-2} K^{-1}, or even higher.

The effect of l on k_{mean}/k_m is perhaps less intuitive. As l decreases, that is, as h_cl/k_m decreases, there is less surface area for heat transfer between the filler particles and the matrix, and thus the overall thermal resistance of the composite increases, leading to a decreasing k_{mean}/k_m. Note, however, that since the composite thickness is also nondimensionalized by l, decreasing l decreases the composite thickness. In an application where the composite thickness and φ are fixed, decreasing l would necessitate a larger number of filler particles, and thus the effects of changing l would differ from those shown in Fig. 6.

Three of the curves in Fig. 6 display the size effect on k_{mean}/k_m at small thicknesses. However, one curve, that for $h_cl/k_m = 2.5$, is essentially flat. The reason for this can be understood by examining Eq. (2), the relation for $R_{i,j}$. For this value of h_cl/k_m, the resistance of the filler nodes is nearly the same as the resistance of the matrix nodes. Since the matrix nodes and filler nodes have approximately the same resistance, the distribution of filler nodes is insignificant, and hence there is no observable size effect on k_{mean}/k_m. This suggests that, if desired, the size effects on k_{mean}/k_m can be practically eliminated by a judicious choice of h_cl/k_m.

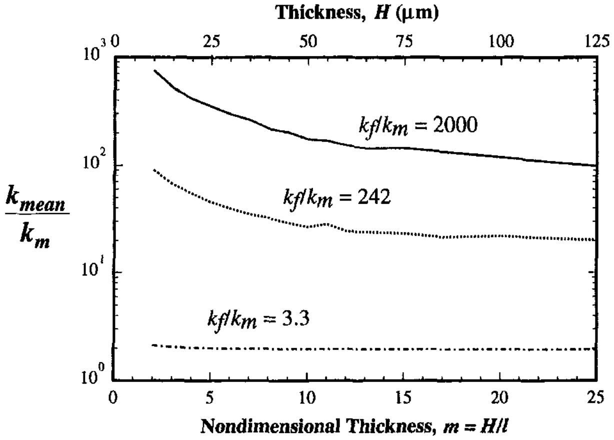

Fig. 5 Effect of varying fiber and matrix thermal conductivities on k_{mean}/k_m ($\varphi = 0.60$, $h_0 = h_1 = h_c = 10^{30}$ W m^{-2} K^{-1}, and $l = 5$ μm)

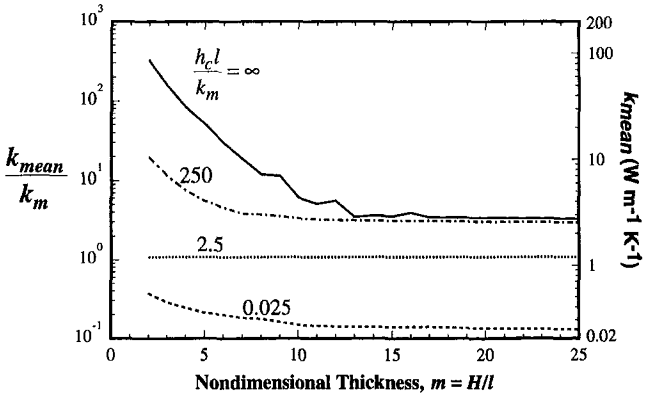

Fig. 6 Effect of varying the filler contact conductance and filler size on k_{mean}/k_m ($k_m = 0.2$ W m^{-1} K^{-1}, $k_f = 400$ W m^{-1} K^{-1}, $\varphi = 0.40$, and $h_0 = h_1 = 10^{30}$ W m^{-2} K^{-1})

Discussion

One simplifying feature of the present analysis is the assumption of square-shaped filler particles. In reality, the filler particles, especially in thermal compound applications, tend to be spherical, thus reducing the area of contact between touching particles and possibly reducing the size effect demonstrated here. For the future we can identify three unresolved matters concerning the thermal conductivity of thin, random composites: (i) the effect of spherical, or other nonsquare, particles on k_{mean}/k_m; (ii) the effect of finite h_0 and h_1 on k_{mean}/k_m; and (iii) experimental verification of the size effect on k_{mean}/k_m predicted by our model. Our forthcoming work will focus on these three areas, including an experiment on a commonly used thermal compound, in which the compound thickness will be carefully controlled and measured to produce thermal conductivity data that can be directly compared with our model.

Conclusions

A probabilistic model of the thermal conductivity of a two-component randomly oriented composite material indicates that a significant size effect exists for the thermal conductivity at small thicknesses. Specifically, below some threshold thickness beyond which the thermal conductivity is independent of thickness, the thermal conductivity increases with decreasing thickness. This effect appears to be due to the increased probability that for small thicknesses the filler particles, which have a relatively high thermal conductivity relative to the matrix, are able to align themselves in the thickness direction, thus providing a high-thermal-conductivity path which increases the overall composite conductivity. The threshold thickness below which the size effect is important increases with increasing filler fraction and increasing k_f/k_m, the ratio between the filler and matrix thermal conductivities.

Acknowledgments

One of the authors (P.E.P.) gratefully acknowledges the support of the National Science Foundation through an NSF CAREER Award (Grant No. CTS-9696003), and the financial support of the Hughes Electronics Corporation. Initial discussions with Prof. C. Y. Wang of the Pennsylvania State University are much appreciated.

References

Han, L. S., and Cosner, A. A., 1981, "Effective Thermal Conductivities of Fibrous Composites," ASME Journal of Heat Transfer, Vol. 103, pp. 387–392.

Joy, T., and Strieder, W., 1979, "Percolation in a Thin Ply of Unidirectional Composite," *Journal of Composite Materials,* Vol. 13, pp. 72–78.

Maewal, A., Bache, T. C., and Hegemier, G. A., 1976, "A Continuum Model for Diffusion in Laminated Composite Media," ASME Journal of Heat Transfer, Vol. 98, pp. 133–138.

Mottram, J. T., 1992, "Design Charts for the Thermal Conductivity of Continuous Fiber-Reinforced Composites," *Materials & Design,* Vol. 13, No. 5, pp. 279–284.

Peterson, G. P., and Fletcher, L. S., 1987, "A Review of Thermal Conductivity in Composite Materials," *AIAA 22nd Thermophysics Conference,* Paper No. AIAA-87-1586, Honolulu, HI, June 8–10.

Press, W. H., Teukolsky, S. A., Vetterling, W. T., and Flannery, B. P., 1992, *Numerical Recipes in Fortran,* 2nd Ed., Cambridge University Press, New York, pp. 34–42, 271.

Constructal Three-Dimensional Trees for Conduction Between a Volume and One Point

G. A. Ledezma
Harvard University,
Shriners Hospital Research Center,
Massachusetts General Hospital,
One Kendall Square, Building 1400W,
Cambridge, MA 02139
Assoc. Mem. ASME

A. Bejan
Department of Mechanical Engineering
and Materials Science,
Duke University,
Box 90300,
Durham, NC 27708-0300
Fellow ASME

This paper extends to three-dimensional heat conduction the geometric ''constructal'' method of minimizing the overall thermal resistance between a finite-size volume and a small heat sink. The volume contains (i) low-conductivity material that generates heat at every point, and (ii) a small amount of high-conductivity material that must be distributed optimally in space. The given volume is covered in a sequence of building blocks (volume sizes) that starts with the smallest volume element, and continues toward larger assemblies. It is shown that the overall shape of each building block can be optimized for minimal volume-to-point resistance. The relative thicknesses of the high-conductivity paths can also be optimized. These optima are developed analytically and numerically for the smallest elemental volume and the first assembly. The high-conductivity paths form a tree network that is completely deterministic.

Objective

The fundamental problem of minimizing geometrically the flow resistance between a volume and one point was initially proposed in the context of two-dimensional heat conduction through a composite material (Bejan, 1997a, b; Ledezma et al., 1997). It was assumed that the volume generates heat at every point in a material of low thermal conductivity (k_0). A fixed amount of high-conductivity (k_p) material was distributed through the volume to guide the generated heat to the heat sink. The problem of minimizing the volume-to-point thermal resistance consisted of optimizing geometrically the distribution of k_p material through the k_0 material. The remarkable property of the optimized architecture of the composite material is that the high-conductivity paths form a tree network in which every feature is deterministic. Equally important is the distribution of interstitial low-conductivity material: At every volume scale there is a balance between the temperature drops across the k_0 and k_p materials.

The key to solving this problem was the discovery that the shape of each finite-size element of the flow volume can be optimized such that the resistance to flow is minimal. This geometric optimization principle applies to any type of flow: heat, fluid, species, electricity. The optimal structure of the flow path—the tree network—was then *constructed* by putting together the shape-optimized building blocks, hence the ''constructal'' name for the geometric optimization method. In this way, macroscopic geometrical form (shape, structure) is *deduced* from a single principle: the minimization of flow resistance. At the same time, physics (theory, determinism) assumes the role of generating principle for the descriptions produced in the field of fractal geometry, i.e., the mechanism behind the truncated fractal algorithms that generate images that look like structures found in nature (e.g., botanical trees, river basins, lungs, vascularized tissues, lightning, neural dendrites, dendritic crystals).

The optimal volume-to-point heat flow is of fundamental interest in the geometric optimization of cooling schemes for small-scale electronic components. The state of the art in this engineering field is described by Peterson and Ortega (1990), Aung (1988), Kakac et al. (1993), Kim and Anand (1994), and Kim and Lee (1996). The cooling of electronics was the application that stimulated the first work on this problem (Bejan, 1997a). To make an analytical solution possible, the problem solved in Bejan (1997a) was formulated in an ideal set of circumstances: the volume and the resulting k_p architecture were *two-dimensional*, the ratio k_p/k_0 was orders of magnitude greater than 1, and the volume fraction occupied by the k_p material was much smaller than 1.

The objective of the work described in this paper was to minimize the volume-to-point thermal resistance in more realistic settings in which the simplifying assumptions of Bejan (1997a) do not apply. The most important new feature is the *three-dimensional* geometry of the volume. This feature complicates the search for the optimal architecture of the heat-flow paths, which is why it was necessary to conduct the search not only analytically but also numerically. In the first part of the paper, analytical results are developed for large values of the k_p/k_0 ratio and small values of the volume fraction of k_p material. In the second part, these material constraints are dropped, and the heat-flow paths are optimized numerically for minimal resistance.

Elemental Volume

Consider a cylindrical volume V_0 filled with material that generates heat volumetrically at the uniform rate q'''. The volume V_0 is fixed, but its shape (i.e., slenderness ratio H_0/L_0) is not. The boundary of V_0 is insulated, except for the cross-sectional area of diameter D_0 located in the plane $x = 0$, where the temperature is $T = 0$. The thermal conductivity of the V_0 material is k_0. The generated heat current ($q'''V_0$) is collected by a fiber of high conductivity material (k_p), and taken out through one end of the fiber ($x = 0$ in Fig. 1). The fiber diameter and length are D_0 and L_0. The volume of k_p material is also fixed, $V_{p,0} = (\pi/4)D_0^2L_0$. This constraint can be expressed as a volume fraction, which is fixed:

$$\phi_0 = \frac{V_{p,0}}{V_0} = \left(\frac{D_0}{H_0}\right)^2. \tag{1}$$

The objective of the composite-material design (k_0, k_p) is to accommodate the generation of heat in the fixed volume, while

---

Contributed by the Heat Transfer Division for publication in the JOURNAL OF HEAT TRANSFER. Manuscript received by the Heat Transfer Division, Dec. 30, 1997; revision received, June 24, 1998. Keywords: Conduction, Cooling, Electronics, Finned Surfaces, Heat Transfer, Thermodynamics. Associate Technical Editor: A. Majumdar.

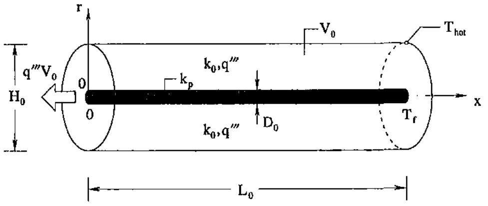

Fig. 1 The elemental volume

minimizing the peak temperature that occurs inside the volume. One feature that helps the design is the position chosen for the k_p fiber, which in Fig. 1 is on the x-axis. Another feature is the shape of the V_0 cylinder, which can be optimized as we show next. It is instructive to begin this study with the assumption that the following limits are valid:

$$\frac{k_p}{k_0} \gg 1 \tag{2}$$

$$\frac{H_0}{L_0} \ll 1 \tag{3}$$

$$\phi_0 \ll 1. \tag{4}$$

Their validity domain will be assessed at the end of this section. The advantage gained by invoking these limits is purely analytical: the conduction through the k_0 material is oriented almost radially, while the conduction through the k_p fiber is oriented in the x-direction. The hot-spot temperature (T_{hot}) is located in the end ring ($x = L_0$) of radius $r = H_0/2$. This temperature can be minimized by varying the aspect ratio H_0/L_0.

An analytical expression for T_{hot} is obtained by coupling the solution for radial conduction in the k_0 material with the solution for axial conduction in the k_p fiber. The k_0 conduction problem

$$\frac{1}{r}\frac{d}{dr}\left(r\frac{dT}{dr}\right) + \frac{q'''}{k_0} = 0 \tag{5}$$

$$\frac{dT}{dr} = 0 \quad \text{at} \quad r = \frac{H_0}{2} \tag{6}$$

$$T = T_f \quad \text{at} \quad r = \frac{D_0}{2} \tag{7}$$

can be solved to obtain the following expression for the total temperature difference in the radial direction, where $T(H_0/2) = T_{\text{hot}}$:

$$T_{\text{hot}} - T_f = \frac{q'''H_0^2}{16k_0}\left(2\ln\frac{H_0}{D_0} + \frac{D_0^2}{H_0^2} - 1\right). \tag{8}$$

Axial conduction in the k_p fiber is represented by the undirectional fin problem

$$k_p\frac{\pi}{4}D_0^2\frac{d^2T}{dx^2} + q' = 0 \tag{9}$$

$$T = 0 \quad \text{at} \quad x = 0 \tag{10}$$

$$\frac{dT}{dx} = 0 \quad \text{at} \quad x = L_0 \tag{11}$$

where q' is the rate of heat generation in each constant-x annulus, $q' = q'''(\pi/4)(H_0^2 - D_0^2)$. Note the heat sink temperature ($T = 0$) specified at the exit end ($x = 0$). Solving this second problem, and writing $T_f = T(L_0)$ for the fiber temperature in the plane where its end is insulated (i.e., in the plane of the hot spot) we obtain

$$T_f = \frac{q'''L_0^2}{2k_p}\left(\frac{H_0^2}{D_0^2} - 1\right). \tag{12}$$

The hot-spot temperature follows from combining Eqs. (8) and (12), and using the volume constraint

$$T_{\text{hot}} = a\frac{q'''H_0^2}{k_0} + b\frac{q'''V_0^2}{k_pH_0^4} \tag{13}$$

where

$$a(\phi_0) = \tfrac{1}{16}(-1 - \ln\phi_0 + \phi_0) \tag{14}$$

$$b(\phi_0) = \frac{8}{\pi^2}\left(\frac{1}{\phi_0} - 1\right). \tag{15}$$

The T_{hot} expression can be minimized with respect to H_0: we find that the optimal shape of the V_0 element is represented by

$$H_0 = \left(\frac{2b}{a}\frac{k_0}{k_p}\right)^{1/6} V_0^{1/3} \tag{16}$$

$$L_0 = \frac{4}{\pi}\left(\frac{a}{2b}\frac{k_p}{k_0}\right)^{1/3} V_0^{1/3} \tag{17}$$

$$\frac{H_0}{L_0} = \frac{\pi}{4}\left(\frac{2b}{a}\frac{k_0}{k_p}\right)^{1/2}. \tag{18}$$

The minimized hot-spot temperature $T_{\text{hot,min}}$ (or ΔT_0, for short) that corresponds to Eq. (16) is

$$\Delta T_0 = f_0\frac{q'''V_0^{2/3}}{k_0^{2/3}k_p^{1/3}} \tag{19}$$

where f_0 is the expression

Nomenclature

a, b, c = functions, Eqs. (14), (15), and (30)
D = diameter of k_p fiber, m
H = diameter of k_0 volume, m
f_0 = function, Eq. (20)
k_0 = low thermal conductivity, W/(m K)
k_p = high thermal conductivity, W/(m K)
$\tilde{k}$ = conductivity ratio, k_p/k_0
L = length of k_0 volume
n_1 = number of constituents in the first assembly
q' = heat generation rate per unit length, W/m
q''' = heat generation rate per unit volume, W/m^3
r = radial position, m
T = excess temperature, K
T_f = end temperature of k_p fiber, K
V = volume, m^3
V_p = volume of k_p material, m^3
x = longitudinal position, m
ΔT = peak excess temperature, K
ϕ = volume fraction of k_p material, V_p/V
$(\ )_{\text{hot}}$ = hot spot, peak excess temperature
$(\ )_{\text{min}}$ = minimal
$(\ )_{\text{opt}}$ = optimal
$(\ )_0$ = elemental volume
$(\ )_1$ = first assembly
$(\hat{\ })$ = dimensionless notation, Eqs. (31) and (48)
$(\tilde{\ })$ = dimensionless notation, Eq. (43)

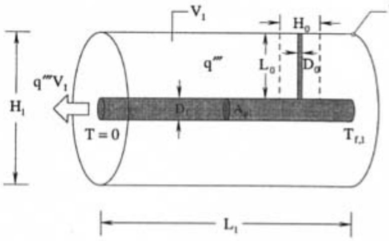

Fig. 2 The first assembly

$$f_0 = \frac{3}{4} 2^{-1/3} \pi^{-2/3} (-1 - \ln \phi_0 + \phi_0)^{2/3} \left(\frac{1}{\phi_0} - 1 \right)^{1/3}. \quad (20)$$

Looking back at the limits (2)–(4) assumed at the start of this analysis, we recognize, first, that when $\phi_0 \ll 1$ the functions a and b behave as $[\ln (1/\phi_0)]$ and $1/\phi_0$, respectively. In the same limit, the function f_0 increases monotonically as ϕ_0 decreases, which confirms the expectation that the minimized hot-spot temperature should increase as the amount of k_p material decreases. The second observation is that the ratio b/a increases monotonically as ϕ_0 decreases. In the limit $\phi_0 \ll 1$, the optimal ratio H_0/L_0 varies as $(\phi_0 k_p/k_0)^{-1/2}$. The slenderness assumption (3) is satisfied provided that ϕ_0 is not smaller than k_0/k_p. In summary, the optimized geometry described in this section satisfies assumption (2)–(4) when $k_0/k_p \ll \phi_0 \ll 1$.

First Assembly

We now consider the larger volume V_1 of diameter H_1 and length L_1 shown in Fig. 2. This volume is fixed, generates heat at every point, and is cooled by k_p inserts. The external surface is insulated, and the total heat current $q'''V_1$ is extracted through the left end of the central fiber (diameter D_1, length L_1). There are many (n_1) elemental systems of size V_0 inside V_1, and their function is to channel their heat currents ($q'''V_0$) into the central fiber,

$$V_1 \cong n_1 V_0. \quad (21)$$

This volume equivalence is approximate, because the radial cylinders V_0 do not fit perfectly inside V_1. An assembly such as Fig. 2 must be optimized numerically to obtain geometrically accurate results, as we illustrate in the second part of this paper. At this stage we continue on the approximate analytical path so that we may illustrate *the opportunity* to optimize the geometry of the assembly, i.e., the existence of tradeoffs with respect to assembly shape (H_1/L_1) and fiber thicknesses (D_1/D_0).

With reference to Fig. 2, we place $T_1 = 0$ at the left end of the central fiber (the heat sink), $T_1 = T_{f,1}$ at the opposite (insulated) end of the central fiber, and $T_{\text{hot},1}$ around the perimeter of the H_1 circle in the right-end plane. The temperature difference in the radial direction in the right-end plane is sustained by an elemental system of the kind optimized in the preceding section: $T_{\text{hot},1} - T_{f,1} = \Delta T_0$. The temperature difference along the central fiber can be estimated by solving the D_1-equivalent of Eqs. (9)–(11). The resulting expression for $T_{f,1}$ is the same as Eq. (12) with (D_1, H_1, L_1) in place of (D_0, H_0, L_0). Combining these results we obtain

$$T_{\text{hot},1} = \frac{q'''L_1^2}{2k_p} \left(\frac{H_1^2}{D_1^2} - 1 \right) + \frac{\pi^2}{64} \left(\frac{2b}{a} \right)^{2/3} \frac{q'''}{k_p} f_0 H_1^2. \quad (22)$$

The minimum of $T_{\text{hot},1}$ with respect to H_1 becomes visible after replacing L_1 with $(4/\pi)V_1/H_1^2$. Furthermore, in the first term on the right side of Eq. (22) we use $(H_1/D_1)^2 - 1 \cong (H_1/D_1)^2$, continuing in making the assumption that the amount if k_p material is sufficiently small. The optimal shape of the V_1 assembly is described by

$$H_1 = \frac{4}{\pi} 2^{1/2} f_0^{-1/4} \left(\frac{a}{2b} \right)^{1/6} \left(\frac{V_1}{D_1} \right)^{1/2} \quad (23)$$

$$L_1 = \frac{\pi}{8} f_0^{1/2} \left(\frac{2b}{a} \right)^{1/3} D_1 \quad (24)$$

$$\frac{H_1}{L_1} = \frac{32}{\pi^2} 2^{1/2} f_0^{-3/4} \left(\frac{a}{2b} \right)^{1/2} \frac{V_1^{1/2}}{D_1^{3/2}}. \quad (25)$$

The corresponding hot-spot temperature, $T_{\text{hot},1,\min} = \Delta T_1$,

$$\Delta T_1 = \frac{3}{2} f_0 \frac{q''' V_0^{2/3}}{k_0^{2/3} k_p^{1/3}} \quad (26)$$

is almost double the temperature difference across the elemental system, Eq. (19).

The number of elemental systems incorporated in V_1 is obtained by combining Eqs. (21), (23) and (24) with $V_1 = (\pi/4)H_1^2 L_1$ and the geometric assembly rule $H_1 = 2L_0$ (see Fig. 2). The result is

$$n_1 = 2 f_0^{1/2} \left(\frac{a}{2b} \right)^{1/3} \left(\frac{k_p}{k_0} \right)^{2/3} \frac{D_1}{V_0^{1/3}}. \quad (27)$$

The total volume of k_p material in the first assembly is

$$V_{p,1} = \frac{\pi}{4} D_1^2 L_1 + n_1 \frac{\pi}{4} D_0^2 L_0 \quad (28)$$

or, expressed as the volume fraction $\phi_1 = V_{p,1}/V_1$,

$$\phi_1 = \frac{\pi^2}{64} c^2 \hat{D}_1^2 + \frac{1}{c} \hat{D}_0^2 \quad (29)$$

where

$$c = \left(\frac{2b}{a} \frac{k_0}{k_p} \right)^{1/3}. \quad (30)$$

In Eq. (29) the fiber diameters are nondimensionalized based on the elemental length scale $V_0^{1/3}$:

$$(\hat{D}_0, \hat{D}_1) = \frac{(D_0, D_1)}{V_0^{1/3}}. \quad (31)$$

The overall thermal resistance of the first assembly follows from Eq. (26),

$$\frac{\Delta T_1 k_0}{q''' V_1^{2/3}} = \frac{3}{2^{5/3}} f_0^{2/3} \left(\frac{2b}{a} \right)^{2/9} \left(\frac{k_0}{k_p} \right)^{7/9} \hat{D}_1^{-2/3}. \quad (32)$$

This resistance blows up when $\hat{D}_1 \to 0$, that is, when the escape of the generated heat current is blocked by the central fiber. The resistance also blows up when the elemental fibers vanish ($\hat{D}_0 \to 0$): this effect is conveyed by f_0 and the group $2b/a$. The latter varies approximately as $(1/\phi_0)/\ln (1/\phi_0)$ where, cf. Eqs. (1) and (16),

$$\phi_0 = \hat{D}_0^2 \left(\frac{a}{2b} \right)^{1/3} \left(\frac{k_p}{k_0} \right)^{1/3}. \quad (33)$$

The fiber diameters $\hat{D}_0$ and $\hat{D}_1$ cannot both be made "large" to decrease the overall resistance (31). These diameters are constrained through the material constraint ϕ_1 = constant, Eq. (29), and can be selected optimally to minimize the overall resistance of the first assembly, Eq. (32).

After substituting $a(\phi_0)$ and $b(\phi_0)$ (namely, Eqs. (14) and (15)) and using the constraint (29), we can express the overall thermal resistance (32) as a function of ϕ_0 and $\hat{D}_0$:

$$R = (3/2)^{5/3}\pi^{-2/3}\tilde{k}^{-1}\left(\frac{1}{\phi_0} - 1\right)^{2/3} \times \left[\phi_1 - 2^{-8/3}\tilde{k}^{1/3}\pi^{2/3}\left(\frac{1}{\phi_0} - 1\right)^{-1/3} \times (-\ln \phi_0 + \phi_0 - 1)^{1/3}\hat{D}_0^2\right]^{-1/3} \qquad (34)$$

where $R = \Delta T_1 k_0/(q'''V_1^{2/3})$ and $\tilde{k} = k_p/k_0$. Next, we solve analytically $\partial R/\partial\hat{D}_0 = 0$, in which we use the expression $\phi_0 =$ function $(\hat{D}_0)$ provided by Eq. (33). We obtain an equation that is too long to be listed here,

$$\frac{\partial R}{\partial \hat{D}_0} = \text{function}\left(\phi_0, \hat{D}_0, \frac{\partial \phi_0}{\partial \hat{D}_0}\right) = 0. \qquad (35)$$

Equation (33) can be combined with Eqs. (14) and (15) to obtain the equation

$$\phi_0 - 2^{-8/3}\pi^{2/3}\tilde{k}^{1/3}\left(\frac{1}{\phi_0} - 1\right)^{-1/3} \times (-\ln \phi_0 + \phi_0 - 1)^{1/3}\hat{D}_0^2 = 0. \qquad (36)$$

Let Q be the left-hand side of this equation. Differentiating Q with respect to $\hat{D}_0$ we obtain a second equation that involves the same variables as Eq. (35):

$$\frac{\partial Q}{\partial \hat{D}_0} = \text{function}(\phi_0, \hat{D}_0, \partial\phi_0/\partial\hat{D}_0) = 0. \qquad (37)$$

The minimization of the overall thermal resistance of the first assembly with respect to $\hat{D}_1/\hat{D}_0$ consists of solving numerically the nonlinear set of Eqs. (35)–(37), for ϕ_0, $\hat{D}_0$ and $\partial\phi_0/\partial\hat{D}_0$. We used a Newton-Raphson method with a consistent tangent and line search, as described in Press et al. (1992). Equations (35)–(37) were solved for $0.001 \leq \phi_1 \leq 0.1$ and $\tilde{k} \geq 300$.

The calculated ϕ_0 and $\hat{D}_0$ values can be substituted into Eq. (29) to obtain the optimal ratio of fiber thicknesses, $(\hat{D}_1/\hat{D}_0)_{\text{opt}}$, or $(D_1/D_0)_{\text{opt}}$. The result is plotted as a function of ϕ_1 and $\tilde{k}$ in Fig. 3. The thickness ratio increases with conductivity ratio $\tilde{k}$.

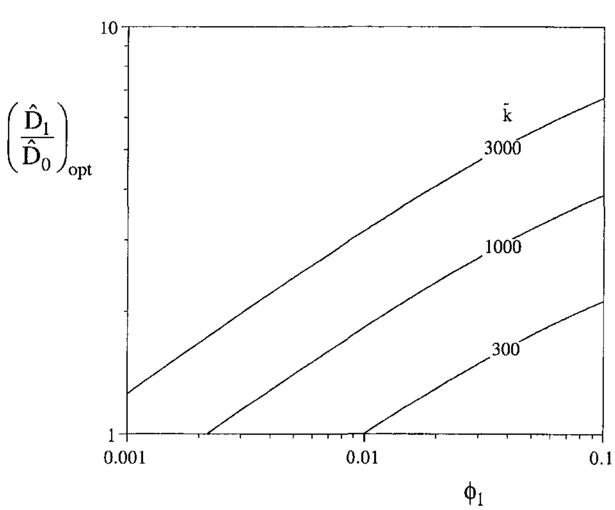

Fig. 3 **The ratio of the k_p-fiber thicknesses of the optimized first assembly**

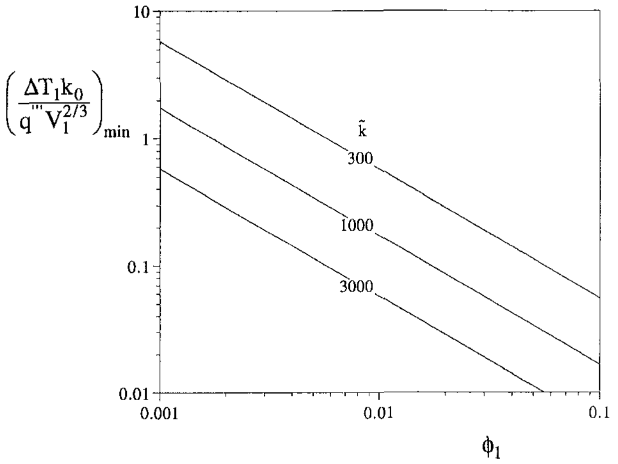

Fig. 4 **The minimized overall thermal resistance of the first assembly**

The effect of the volume fraction constraint ϕ_1 is relatively weaker. These trends are correlated within four percent by the following power law in the range $300 \leq \tilde{k} \leq 3000$ and $0.001 < \phi_1 < 0.1$,

$$\left(\frac{\hat{D}_1}{\hat{D}_0}\right)_{\text{opt}} = 0.279\phi_1^{0.344}\tilde{k}^{0.5}. \qquad (38)$$

The minimized thermal resistance that corresponds to the geometry optimized in Fig. 3 is reported in Fig. 4. As expected, the resistance decreases as the thermal conductivity of the inserts (k_p, or $\tilde{k}$) increases relative to the background conductivity k_0. The resistance also decreases as the volume fraction of the high-conductivity inserts increases. The results of Fig. 4 are correlated within six percent by the power law

$$\left(\frac{\Delta T_1 k_0}{q''' V_1^{2/3}}\right)_{\min} = \frac{1.641}{\phi_1 \tilde{k}}. \qquad (39)$$

Another feature of the optimized geometry is that the volume fraction calculated over one elemental volume ($\phi_{0,\text{opt}}$) is proportional to ϕ_1, but slightly smaller. In the (ϕ_1, $\tilde{k}$) range covered by the results of Fig. 3, this proportionality is expressed within six percent by

$$\phi_{0,\text{opt}} = 0.704\phi_1. \qquad (40)$$

The corresponding aspect ratio of the optimized first assembly is reported in Fig. 5. This figure is based on $n_1 \cong V_1/V_0$

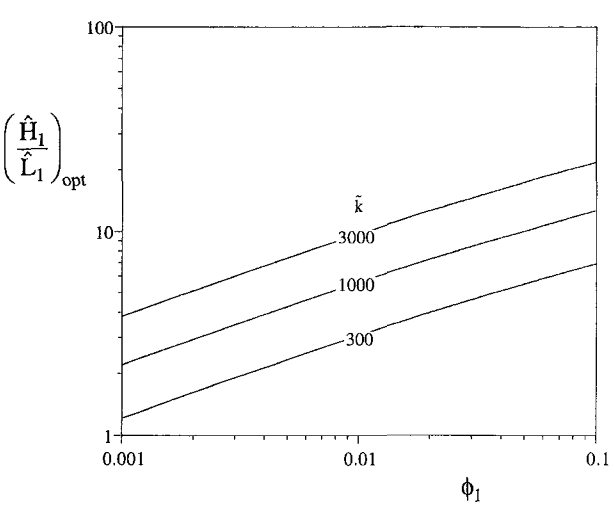

Fig. 5 **The geometric aspect ratio of the optimized first assembly**

and Eq. (25). The assembly becomes less slender when $\tilde{k}$ and ϕ_1 decrease. In the range $\tilde{k} > 300$ and $\phi_1 < 0.01$ these trends are correlated within one percent by the formula

$$\left(\frac{H_1}{L_1}\right)_{\text{opt}} = 1.144\phi_1^{0.404}\tilde{k}^{0.5}. \tag{41}$$

The corresponding number of constituents (elemental volumes V_0) assembled in V_1 is provided by Eq. (27). Figure 6 shows that the constituents become more numerous as the conductivity ratio increases. This trend is consistent with the aspect ratio of the elemental volume (H_0/L_0, Eq. (18)), which decreases as $\tilde{k}^{-1/2}$.

In summary, the optimized geometry of the first assembly is such that the high-conductivity fibers form a tree. The branches become thinner, their number increases, and the trunk (L_1) becomes shorter. As in the optimized elemental volumes Eqs. (16)–(20), every geometric feature of the first assembly is the result of a deterministic process of thermal resistance minimization.

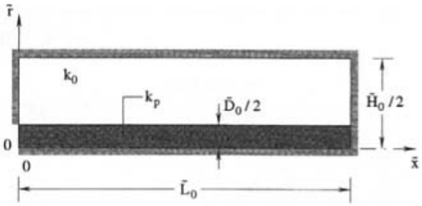

Fig. 7 The computational domain for the elemental volume

Numerical Optimization of the Elemental Volume

In the work described in this section we relaxed the simplifying assumptions (2)–(4), and simulated numerically the conduction of heat in the composite material shown in Fig. 1. The generation of heat occurs only in the background material of low conductivity k_0. Since the geometry is axisymmetric, we considered the two-dimensional computational domain defined in Fig. 7. The energy equation for steady conduction through the k_0 material is

$$\frac{1}{\tilde{r}}\frac{\partial}{\partial \tilde{r}}\left(\tilde{r}\frac{\partial \tilde{T}}{\partial \tilde{r}}\right) + \frac{\partial^2 \tilde{T}}{\partial \tilde{x}^2} + \frac{1}{1-\phi_0} = 0 \tag{42}$$

where

$$(\tilde{r}, \tilde{x}) = \frac{(r, x)}{V_0^{1/3}} \quad \tilde{T} = \frac{T - T(0, 0)}{q''' V_0^{2/3}/k_0}. \tag{43}$$

The corresponding equation for conduction in the k_p fiber is

$$\frac{1}{\tilde{r}}\frac{\partial}{\partial \tilde{r}}\left(\tilde{r}\frac{\partial \tilde{T}}{\partial \tilde{r}}\right) + \frac{\partial^2 \tilde{T}}{\partial \tilde{x}^2} = 0. \tag{44}$$

The total volume is fixed, $V_0 = (\pi/4)H_0^2L_0$. This constraint is the same as

$$\tilde{L}_0 = \frac{4/\pi}{\tilde{H}_0^2} \tag{45}$$

and means that the shape of the cylindrical volume is controlled by a single parameter, for example, $\tilde{H}_0$. The boundaries of the computational domain are adiabatic, except over the root of the k_p fiber (the heat sink) where we set $\tilde{T} = 0$.

We solved Eqs. (42) and (44) using a finite element code (FIDAP, 1993), which was tested and validated against our own finite difference code (Ledezma et al., 1997). For the actual geometric optimization work we used the finite element code because we needed a reliable and flexible solver capable of generating efficiently a large number of results, i.e., simulations for many geometries, one differing only slightly from the next. We chose quadrilateral elements with biquadratic interpolation functions. The grid was uniform in $\tilde{x}$ and nonuniform in $\tilde{r}$ so as to put more nodes near the interface between the high conductivity and the low conductivity material, where the steepest temperature gradients occur. The number of nodes in $\tilde{x}$ ranged between 41 and 75, while in the $\tilde{r}$ direction we needed between 35 and 89 nodes. We performed accuracy tests to determine that the meshes were fine enough so that the temperature results were insensitive to further mesh doubling in both $\tilde{r}$ and $\tilde{x}$.

The hot-spot temperature occurs on the rim of the disc situated the farthest from the heat sink ($\tilde{x} = \tilde{L}_0$, $\tilde{r} = \tilde{H}_0/2$). The results sampled in Figs. 8 and 9 confirm the theoretical points made in Section 2, namely, that the hot-spot temperature can be minimized with respect to the shape of the volume ($\tilde{H}_0$). We performed the optimization at constant ϕ_0 (Fig. 8) and at constant $\tilde{k}$ (Fig. 9).

The results obtained for the minimized hot-spot temperature ($\tilde{T}_{\min}$) are presented in Fig. 10. They are presented in relative terms, i.e., as a departure from the theoretical solution (19). Note that the dimensionless version of Eq. (19) is $\tilde{T}_{\min} = f_0/\tilde{k}^{1/3}$. Figure 10 shows that the numerical results depart from

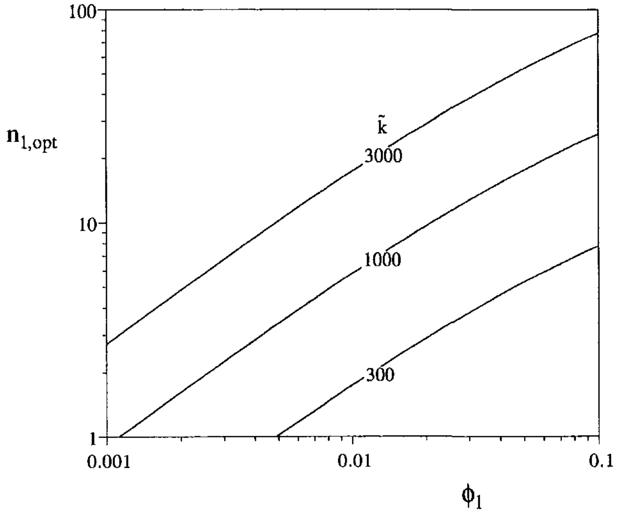

Fig. 6 The number of elemental volumes contained by the optimized first assembly

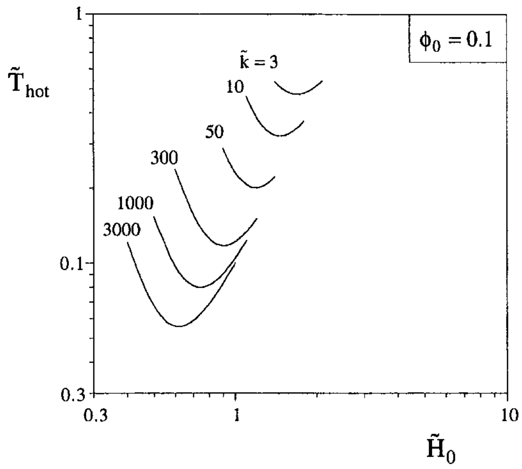

Fig. 8 Numerical results for the minimization of hot-spot temperature of the elemental volume when ϕ_0 is fixed

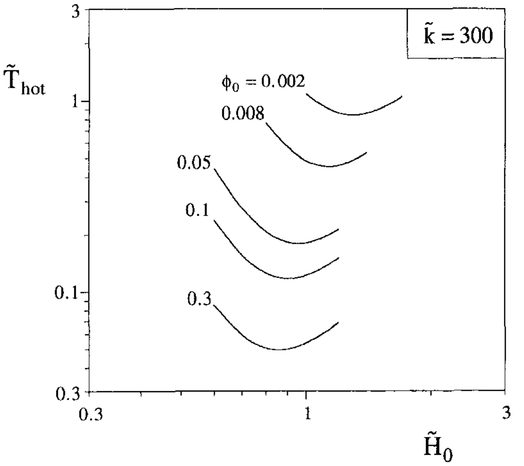

Fig. 9 Numerical results for the minimization of hot-spot temperature of the elemental volume when $\tilde{k}$ is fixed

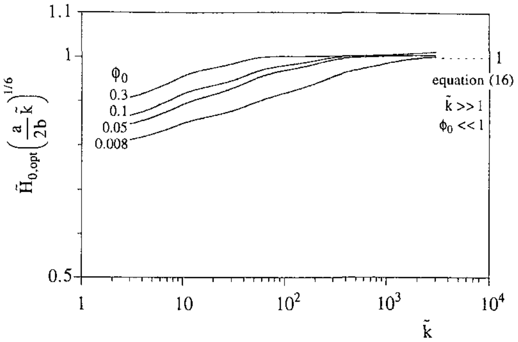

Fig. 11 Numerical results for the optimal shape of the elemental volume

Eq. (19) when ϕ_0 rises above 0.1. The effect of the conductivity ratio $\tilde{k}$ is much weaker.

The conductivity ratio $\tilde{k}$ has a stronger effect on the optimal shape of the elemental volume. Plotted on the ordinate of Fig. 11 is the numerical $\tilde{H}_{0,\mathrm{opt}}$ value divided by the theoretical estimate provided by Eq. (16). The latter assumes the dimensionless form $\tilde{H}_{0,\mathrm{opt}} = (2b/a\tilde{k})^{1/6}$. From Fig. 11 we learn that the theoretical results (Eqs. (16)–(20)) are sufficiently accurate when the order of magnitude of $\tilde{k}$ is greater than 10^2. Taken together, Figs. 10 and 11 establish the domain of validity of the theoretical results, and extend the geometric optimization results over a wider $(\tilde{k}, \phi_0)$ domain.

Numerical Optimization of the First Assembly

For the first assembly we chose the Cartesian configuration shown in Fig. 12, because in this configuration the mesh generation is much easier than in the cylindrical arrangement (Fig. 2). In addition, in Fig. 12 the elemental volumes "fit" inside the V_1 volume such that their number ($n_1 = V_1/V_0$) is an integer. The k_p fibers have square cross sections ($D_0 \times D_0$ and $D_1 \times D_1$). In this configuration we are constrained to using only two or four D_0 fibers in each plane perpendicular to the D_1 stem. Figure 12 corresponds to the case $n_1 = 4$, in which the four D_0 fibers are placed in a single plane.

The dimensionless formulation of the heat conduction equations for the k_0 and k_p regions of the Fig. 12 composite are, respectively,

$$\nabla^2\hat{T} + \frac{1}{1-\phi_1} = 0 \tag{46}$$

$$\nabla^2\hat{T} = 0 \tag{47}$$

where $\nabla^2 = \partial^2/\partial\hat{x}^2 + \partial^2/\partial\hat{y}^2 + \partial^2/\partial\hat{z}^2$, and the reference length scale is $V_1^{1/3} = (H_1^2 L_1)^{1/3}$:

$$(\hat{x}, \hat{y}, \hat{z}) = \frac{(x, y, z)}{V_1^{1/3}} \quad \hat{T} = \frac{T - T(0, 0, 0)}{q''' V_1^{2/3}/k_0}. \tag{48}$$

When $n_1 = 4$, the volume fraction allocated to k_p material ($\phi_1 = V_{p,1}/V_1$) is related to the assembly geometry through

$$\phi_1 = \frac{\hat{D}_1^2}{2}(\hat{L}_1 + \hat{D}_0) + 2\hat{D}_0^2(\hat{H}_1 - \hat{D}_1) \tag{49}$$

where $(\hat{D}_0, \hat{D}_1, \hat{H}_1, \hat{L}_1) = (D_0, D_1, H_1, L_1)/V_1^{1/3}$. The V_1 constraint reads $\hat{H}_1^2\hat{L}_1 = 1$.

Equations (46) and (47) were solved using the finite element method with trilinear interpolation functions. The mesh was nonuniform in all the directions such that more nodes were placed near the material interfaces where the steep gradients occur. The grid-independence of the solution was ensured by systematically increasing the number of nodes in each direction by 20 percent until the relative changes in the hot-spot temperature were less than 0.1 percent. Because of symmetry, it was sufficient to perform computations in only one of the four quadrants of each (x, z) plane.

The geometry of Fig. 12 has three degrees-of-freedom that are represented by the dimensionless numbers $\hat{H}_1$, n_1, and $\hat{D}_0$. The remaining dimensions of the assembly, $\hat{L}_1$ and $\hat{D}_1$, are furnished by the ϕ_1 and V_1 constraints, namely, Eq. (49) and $\hat{L}_1 = \hat{H}_1^{-2}$.

Figure 13 shows the approach to the minimization of $\hat{T}_{\mathrm{hot}}$, which is again located in the four corners that are the farthest from the origin (0, 0, 0) where the $D_1 \times D_1$ heat sink is located. At the optimum, however, the temperature of the closer four

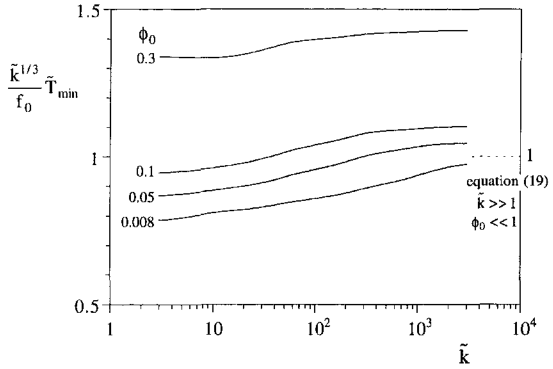

Fig. 10 Numerical results for the minimized hot-spot temperature of the elemental volume

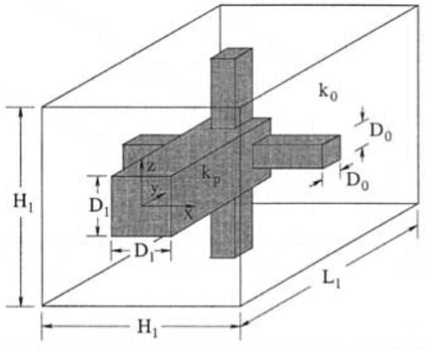

Fig. 12 The computational domain for a first assembly

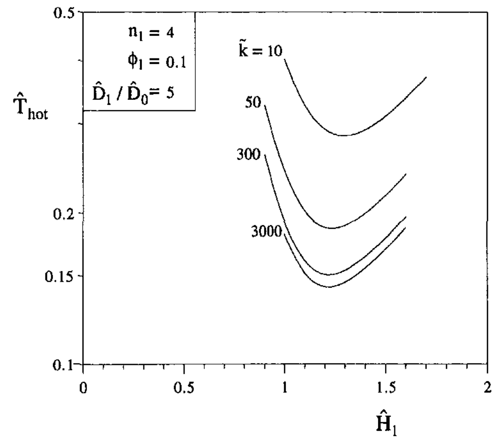

Fig. 13 Numerical results for the minimization of the hot-spot temperature of the first assembly of Fig. 12: the effect of changing the shape of the V_1 volume

corners (in the plane of the heat sink) is comparable with the hot-spot temperature. The optimization consisted of first holding n_1 and $\hat{D}_1/\hat{D}_0$ fixed, and varying the volume shape ($\hat{H}_1$). This first level of optimization is illustrated in Fig. 13. The minimum of $\hat{T}_{hot}$, with respect to $\hat{H}_1$ is relatively sharp, i.e., important.

At the second level of optimization, we repeated the work of Fig. 13 for other $\hat{D}_1/\hat{D}_0$ ratios, while continuing to hold n_1 fixed. Figure 14 is a summary of the results collected at the second level. Each point represents the minimum ($\hat{T}_{min}$, $\hat{H}_{1,opt}$) determined for a specified pair (ϕ_1, $\tilde{k}$) at the first level (Fig. 13). In Fig. 14, the lowest $\hat{T}_{min}$ value (namely, $\hat{T}_{min} = 0.183$) occurs at $(\hat{D}_1/\hat{D}_0)_{opt} = 3.41$, where $\hat{H}_{1,opt} = 1.22$ and $(H_1/L_1)_{opt} = 1.816$.

The important conclusion that is made evident by Fig. 14 is that the $\hat{D}_1/\hat{D}_0$ ratio has a very weak effect on the optimal performance, *provided* that the overall shape of the assembly has been optimized. In other words, deviations from the optimal internal distribution of high-conductivity material have relatively little effect on the overall performance as long as the system V_1 is ''constructed'' from elemental volumes, i.e., as long as the k_p material is *spread as a tree through a volume of optimal shape.*

The optimization can be refined by repeating the work sequence of Figs. 13 and 14 for other n_1 values, that is by varying the number of elemental volumes in the first assembly. We did this work for $n_1 = 2$ by holding the composite material parameters fixed at the values of Fig. 14 ($\tilde{k} = 50$, $\phi_1 = 0.1$). The $n_1 = 2$ assembly looks like the one shown in Fig. 12 except that there are only two diametrically opposed D_0-thick paths. In the k_p material constraint of Eq. (49), the factor 2 that multiplies the last term is replaced by 1.

The results of the double optimization procedure for $n_1 = 2$ are $\hat{T}_{min} = 0.180$, $(\hat{D}_1/\hat{D}_0)_{opt} = 4.44$, $(H_1/L_1)_{opt} = 1.95$ and $\hat{H}_{1,opt} = 1.249$. In conclusion, the $\hat{T}_{min}$ value shows that the performance of the first assembly with only two constituents is marginally better than in the case with four constituents, and, because n_1 cannot be smaller than 2, bifurcation (or dichotomy) emerges as a *result* of the optimization principle invoked throughout this paper. This deterministic approach to the bifurcation (or pairing) of the high conductivity paths reconfirms one of the main conclusions of the corresponding two-dimensional study (Bejan, 1997).

The first assemblies that we optimized ($n_1 = 4$ and $n_1 = 2$ (for $\tilde{k} = 50$ and $\phi_1 = 0.1$)) are close to the design of minimal resistance because their optimized dimensions are comparable in an order of magnitude sense with the approximate estimates provided by the analytical solution presented in the third section of this paper. Specifically, for $\tilde{k} = 50$ and $\phi_1 = 0.1$ the analytical solution predicts $(H_1/L_1)_{opt} = 3.2$, $\hat{H}_{1,opt} = 1.360$, $(\hat{D}_1/\hat{D}_0)_{opt} = 0.87$, and $\hat{T}_{min} = 0.33$ and $n_1 = 1.30$.

The Constructal Law of Structure Formation in Natural Flow Systems

In this study we have extended to three-dimensional heat conduction the geometric method of minimizing the thermal resistance between a volume and one point. The most important conclusion is that the overall shape of a finite-size volume can be selected such that its volume-to-point flow resistance is minimal. The existence of such a geometric optimum at other volume scales is responsible for the sequential assembling of optimized elements into larger volumes, and the emergence of a tree network of high conductivity paths.

We also found that when the amount of high-conductivity material is fixed, the overall thermal resistance is further minimized if the k_p-fiber diameters increase in an optimal proportion as the volumes (building blocks) become larger. This second geometric optimum is available beginning with the first assembly, however, its effect on the overall thermal resistance is less critical than that of the outer shape of the building block.

We demonstrated the existence of these optima by focusing on the first two steps of the volume construction sequence: the elemental volume (Fig. 1) and the first assembly (Figs. 2 and 12). In principle, this sequence can be continued toward assemblies of higher order, as was shown in the two-dimensional version of the volume-to-point flow problem (Bejan, 1997a). In practice, however, the increasing complexity of each new assembly prohibits the continuation of the analytical solution started here, and makes even more difficult the numerical simulation and optimization work that would be required. These complexities are due mainly to the fact that in a three-dimensional construction the building blocks do not fit perfectly in the assembly (e.g., Figs. 2 and 12).

The geometric optima determined in this paper are not the absolute best that can be determined in answer to the problem statement of minimizing the volume-to-point flow resistance. These optima are based on simplifying assumptions such as the round and square cross sections, the 90-deg angles between k_p fibers, and the fact that each fiber is straight. When these assumptions are relaxed, the number of degrees-of-freedom of the configuration increases, and features such as the confluence angles can be optimized as well. We documented this more general approach for the case of two-dimensional conduction (Ledezma et al., 1997), where we showed that the optimal angles are close to 90 deg, and that their optimization has a

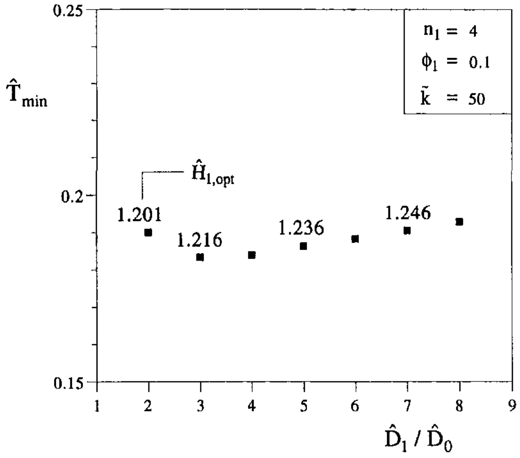

Fig. 14 The effect of the distribution of high-conductivity material ($\hat{D}_1/\hat{D}_0$) on the hot-spot temperature minimized already with respect to $\hat{H}_1$

very weak effect on the global volume-to-point resistance of each construct. The angles and the thickness ratio D_1/D_0 documented in this study are examples of ''internal'' features that have only a minor effect on the global performance of the system. Said another way, optimized configurations that are not identical internally have nearly the same global resistance, provided their external shapes have been optimized (which is why they all end up having k_p trees internally).

This observation is relevant to optimal-access paths in nature. If global performance subject to volume constraints is what counts, then the finest internal details of the flow path are not important. Important is that the large picture, overall performance, structure, and working mechanism can be described in purely deterministic fashion; that is, if *the constructal access-optimization principle is recognized as law.*

For systems with imposed steady flow, as in Bejan (1997a) and Ledezma et al. (1997), the constructal law may be summarized as follows: ''For a finite-size system to persist in time (to live), it must involve in such a way that it provides easier access to the imposed currents that flow through it.'' This statement has two parts. First, it recognizes the natural tendency of imposed currents to construct shapes, i.e., paths of optimal access through constrained open systems when there are at least two internal transport mechanisms available, one with high resistance and the other with significantly lower resistance. The second part of the statement accounts for the evolution (i.e., improvements) of these paths, which occurs in an identifiable direction that can be aligned with time itself.

If the system discharges itself to one point in unsteady fashion, then the constructal minimization of volume-to-point resistance is equivalent to the minimization of the time of discharge, or the maximization of the speed of approach to equilibrium (uniformity, zero flow, path). If the volume is unbounded, the constructs compound themselves and continue to spread indefinitely. Complexity continues to increase in time. Additional examples are the jet injected into a fluid reservoir, and the dendritic crystal that grows into a subcooled liquid. All the structured phenomena mentioned in the opening section of this paper, including the round cross section of the blood vessel and the proportionality between river width and depth, can be predicted based on the constructal theory of access optimization (Bejan, 1997b).

One of the reviewers of this paper noted that the assumption that an ''elemental'' building block exists makes sense from an engineering standpoint: Smaller blocks cannot be made in a given technological era. The reviewer also noted that it is possible to think that if the elemental k_p volume is redistributed as a tree through V_0 then the elemental resistance can be reduced further. This expectation is correct, and it rests on the results developed based on constructal theory for the first and higher-order constructs: The resistance drops when the k_p inserts are connected as a tree. Even if we proceed in this direction, from large to small, we must face the decision of where to stop. This process of making elemental volumes smaller and smaller cannot go on forever (ad infinitum), simply because the elemental k_p fibers must be of *finite length* in order to be recognized as ''fibers,'' and in order to be *connected* in their first construct. Transport at scales smaller than the elemental length is assured by the shapeless (disorganized) motion of the molecules—the k_0 material in this paper.

Natural volume-to-point (or point-to-volume) flows are organized similarly (Bejan, 1997b). The elemental volume with diffusion in the interstices is a universal feature in nature, and so is the development of external and internal similarity rules in the constructs that are situated at levels sufficiently high above the elemental level. In the constructs situated immediately above the elemental level the similarity rules break down—necessarily—in order to effect a relatively smooth transition from the self-similar higher constructs to the diffusion-filled elemental space.

All these observations are relevant to understanding why, contrary to Mandelbrot's (1982) claim, the geometry of nature is not fractal. It was pointed out in Bejan (1997b) that ''The *infinite* sequence of fracturing steps is the defining statement of fractal geometry; the noneuclidian dimension (Hausdorff) exists strictly in this limit (at infinity). When the sequence is cut off (quite arbitrarily) and made finite, the incomplete images printed on paper 'look like' patterns we see in Nature. This coincidence does not mean that natural patterns are fractal! The contrary is true: Everything shown to us by Nature, and everything done under the table by the fractal algorithm manipulator, supports empirically the view that the real image (e.g., sheet of paper, or sand sculpture) is euclidean. This is why the image can be distinguished (i.e., seen), because otherwise we would be seeing nothing but blurred images and shades of gray. Constructal theory is supported by the sharp euclidian images that we see, because the theory starts from the smallest (finite, elemental) building block, continues by predicting a finite sequence of assemblies, and displays its predictions in two, or three dimensions. The rules of geometric similarity between constructs of neighboring sizes are results (predictions), not assumptions. Along the way, the finite sequence of constructs also explains why the incomplete fractal sequences generated by the mathematician happen to look like natural patterns.''

Acknowledgment

This research project was sponsored by the National Science Foundation.

References

Aung, W., ed., 1988, *Cooling Technology for Electronic Equipment,* Hemisphere, New York.

Bejan, A., 1997a, ''Constructal-Theory Network of Conducting Paths for Cooling a Heat Generating Volume,'' *Int. J. Heat Mass Transfer,* Vol. 40, pp. 799–816.

Bejan, A., 1997b, *Advanced Engineering Thermodynamics,* 2nd Ed., John Wiley and Sons, New York.

FIDAP Theory Manual, 1993, Fluid Dynamics International, Evanston, IL, V.7.0.

Kim, S. H., and Anand, N. K., 1994, ''Laminar Developing Flow and Heat Transfer between a Series of Parallel Plates with Surface Mounted Discrete Heat Sources,'' *Int. J. Heat Mass Transfer,* Vol. 37, pp. 2231–2244.

Kim, S. J., and Lee, S. W., eds., 1996, *Air Cooling Technology for Electronic Equipment,* CRC Press, Boca Raton, FL.

Ledezma, G. A., Bejan, A., and Errera, M. R., 1997, ''Constructal Tree Networks for Heat Transfer,'' *J. Appl. Phys.,* Vol. 82, pp. 89–100.

Li, W., Kakac, S., Hatay, F. F., and Oskay, R., 1993, ''Experimental Study of Unsteady Forced Convection in a Duct with and without Arrays of Block-like Electronic Components,'' *Wärme-und Stoffübertragung,* Vol. 28, pp. 69–79.

Mandelbrot, B. B., 1982, *The Fractal Geometry of Nature,* Freeman, New York.

Peterson, G. P., and Ortega, A., 1990, ''Thermal Control of Electronic Equipment and Devices,'' *Adv. Heat Transfer,* Vol. 20, pp. 181–314.

Press, W. H., Vetterling, W. T., Teukolsky, S. A., and Flannery, B. P., 1992, *Numerical Recipes in C,* Cambridge University Press, New York.

N. Shahcheraghi
Post Graduate Researcher,
Mem. ASME

H. A. Dwyer
Professor,
Mem. ASME

Mechanical and Aeronautical
Engineering Department,
University of California,
Davis, CA 95616

Fluid Flow and Heat Transfer Over a Three-Dimensional Spherical Object in a Pipe

An incompressible viscous fluid flow with heat transfer over a spherical object inside a pipe is considered. The flow is made three-dimensional by an eccentric positioning of the sphere inside the pipe. The governing equations are solved by a numerical method which uses a finite volume formulation in a generalized body fitted coordinate system. An overset (Chimera) grid scheme is used to resolve the two geometries of the pipe and sphere. The results are compared to those of an external flow over a sphere, and the code is validated using such results in the intermediate Reynolds number range. The blockage effects are analyzed through evaluation of lift, drag, and heat transfer rate over the sphere. Also the change in the shear stress pattern is examined through evaluation of the local friction factor on a pipe wall and sphere surface.

Introduction

Incompressible, viscous, laminar pipe flow with heat transfer has a wide range of engineering and scientific applications. These applications include material and chemical processing, water and air distribution networks, and flow of biofluids in living organisms. Therefore, this problem has been the subject of investigation for many years. Analytical solutions are available for one-dimensional pipe flow with variations in the radial direction (Bird et al., 1960). However, more complicated cases with two and three-dimensional effects are the subject of ongoing research, and have not been completely resolved.

Another flow of great interest is that of an incompressible fluid with heat transfer over a three-dimensional object such as sphere. This type of flow has applications in various branches of combustion including droplet dynamics and vaporization, and particle migration. A large collection of work in this type of flow is gathered in the text by Clift et al. (1978). This work includes recent analytical, numerical, and experimental studies of various external flows over rigid and fluid spheres.

A particular class of problems is that of a sphere in a pipe flow, which is a combination of the two cases presented above. This class of flow is a realistic model for transport of particles through a pipe, or flow through a variety of regulating valves. Until now they have been solved by simplifying assumptions, which lead to either a pure pipe flow or an external flow over a sphere. Due to these assumptions important features of the flow are lost. For example, using external flow models for a sphere inside a pipe would ignore the important wall effects. Inversely, using pure pipe flow models would ignore the blockage effects of the sphere.

In this work a three-dimensional numerical simulation of a viscous laminar incompressible pipe flow with heat transfer over a sphere is presented. The sphere is placed off center to induce three-dimensional effects. Method of solution consists of a finite volume formulation of the incompressible continuity equations, Navier-Stokes equations, and the thermal energy equation (Dwyer, 1989). An overset (Chimera) type scheme is used in order to, effectively, resolve the geometry and flow features (Dwyer, 1985; Nirschl et al., 1994). This includes a major (background) cylindrical mesh for the pipe and a separate spherical (minor) mesh around the sphere.

In the following sections the problem statement is described, followed by method of solution and code validation results. Then, results for the stated problem are given and, finally, some concluding remarks are made.

Problem Statement

The basic problem consists of flow in a pipe of diameter, D_p, and length L, with $L/D_p = 5$. Inside the pipe there is a sphere of diameter, D_S, which is located at an eccentric distance, E, from the pipe center line, and $L/2$ from the pipe entrance (Fig. 1).

For $E = 0$, the flow is axisymmetric and can be solved as a two-dimensional problem. However, for $E > 0$, the flow becomes three-dimensional with a plane of symmetry that bisects both the sphere and the pipe cross-sectional areas (see Fig. 1). In this study $E = 0.2$ is used. The fluid is viscous and incompressible with constant properties, and the flow regime is assumed to be laminar. Pipe Reynolds number is defined as

$$\mathrm{Re}_p = \frac{U_a D_p}{\nu} .$$

For the purposes of comparison to available results of external flows, sphere Reynolds number is defined as

$$\mathrm{Re}_{s\infty} = \frac{U_\infty D_s}{\nu} .$$

Assuming a parabolic profile at the pipe inlet and $E = 0.2$, we get

$$U_\infty = 1.68 U_a .$$

Blockage ratio (BR) is defined as frontal area of the sphere divided by the cross-sectional area of the pipe and is expressed in terms of the pipe and sphere diameters,

$$BR = \frac{D_s^2}{D_p^2} .$$

In this study, two Re_p values of 25 and 125 are considered in combination with two blockage ratios of 4 percent and 16 percent. For the purposes of code validation, $\mathrm{Re}_{s\infty} = 10$ is used with BR = one percent, and $E = 0$.

The nondimensional temperature is defined as

Contributed by the Heat Transfer Division for publication in the JOURNAL OF HEAT TRANSFER. Manuscript received by the Heat Transfer Division, Feb. 22, 1996; revision received, May 18, 1998. Keywords: Enclosure Flows, Forced Convection, Numerical Methods. Associate Technical Editor: M. Kelleher.

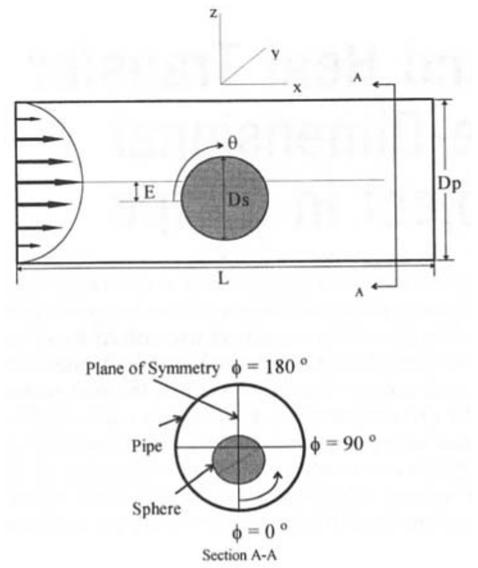

Fig. 1 Basic arrangement for three-dimensional flow over a sphere in a pipe

$$T = \frac{T_f - T_w}{T_s - T_w}.$$

In all cases considered here the sphere is at nondimensional temperature 1, while the entering fluid and pipe wall are at nondimensional temperature 0. For simplicity, all references to temperature from this point forward mean nondimensional temperature.

Initial and Boundary Conditions. At startup the fluid velocity and temperature are set to zero. The sphere is stationary with no slip at the surface and at a dimensionless temperature of 1. The flow evolves in time to reach a steady state. During this time there is no slip at the pipe wall. In addition, the dimensionless temperature at the pipe wall and for the entering fluid is kept constant (at zero).

Here, a mass-driven flow is assumed, therefore, the velocity is specified at the inlet and the pressure is specified at the outlet. At the pipe inlet a fully developed flow with parabolic velocity profile is specified. Then, outlet velocity and inlet pressure are solved assuming Neumann boundary conditions.

Solution Method

The governing equations for this problem are the low Mach number version of the incompressible continuity equation, Navier-Stokes equations, and the thermal energy equation. In dimensionless integral form, they are

$$\iint_s \mathbf{V}\cdot\mathbf{n}\,dA = 0$$

$$\frac{\partial}{\partial t}\iiint_v \mathbf{V}\,dV + \iiint \mathbf{V}\cdot\nabla\mathbf{V}\,dV = -\iint_s p\mathbf{n}\,dA + \frac{1}{\mathrm{Re}}\iint_s \mathbf{n}\cdot\bar{\bar{\tau}}\,dA$$

$$\frac{\partial}{\partial t}\iiint_v T\,dV + \iiint_v \mathbf{V}\cdot\mathbf{V}\,T\,dV = \frac{1}{\mathrm{Re\,Pr}}\iint_s (\nabla T)\cdot\mathbf{n}\,dA.$$

The Prandtl number, $\mathrm{Pr} = \nu/\alpha$, is set to unity in this study, therefore, the Peclet number is equal to the Reynolds number.

These equations are solved in three-dimensional generalized (body fitted) coordinates, finite volume formulation. The solution algorithm is described in detail by Dwyer (1989), and it will only be briefly outlined here. The three Cartesian components of velocity and temperature are marched in time using an implicit discretization of three momentum equations plus thermal energy equation. The pressure change or "correction" is solved in a Poisson equation, which results from application of continuity, and definition of a "velocity correction" potential function. The discrete system of linear equations is solved using a predictor-corrector, alternating direction implicit (ADI), solver.

Chimera Grid Scheme. The over-set (Chimera) grid scheme, Dougherty (1985), is a method in which different regions of the flow field have a separate mesh, depending on their geometric features. In this study separate grids are used for the pipe and the sphere. The major mesh is that of the pipe, and the sphere has the minor mesh (Fig. 2).

Holes and Fringe Points. Some points of the major mesh may fall on the interior of the sphere, where the fluid does not flow. Similarly, some points of the minor mesh may fall outside the flow region (the pipe). These points are called "holes." The holes are marked with hollow squares in Fig. 2. In order to prevent the governing equations from being solved at holes, the off diagonal coefficients and the right-hand side of the linear discrete equations are set to zero at these points.

The two separate meshes communicate by means of "fringe points." These are points in the flow region of each mesh that completely envelope the holes. They are found after all the holes are determined, by converting holes with a regular point

Nomenclature

A_s = sphere frontal area
BR = blockage ratio
C_D = sphere drag coefficient
C_L = sphere lift coefficient
D_p = pipe diameter
D_s = sphere diameter
E = sphere eccentric distance
f = local friction factor
F_D = drag force on sphere
F_L = lift force on sphere
h = heat transfer coefficient
k = fluid thermal conductivity
L = pipe length
Nu = overall Nusselt number
Nu_θ = local Nusselt number
$\mathbf{n}$ = area unit normal
Pr = fluid Prandtl number
P_s = sphere surface pressure
$P_{s\infty}$ = sphere normalized surface pressure
P_∞ = far field reference pressure
Re = Reynolds number
Re_p = pipe Reynolds number
$\mathrm{Re}_{s\infty}$ = sphere Reynolds number
T = dimensionless fluid temperature
T_f = dimensional fluid temperature
T_s = dimensional sphere surface temperature
T_w = dimensional pipe wall temperature
U_a = average pipe inlet flow velocity
U_∞ = pipe entrance velocity along sphere centerline
$\mathbf{V}$ = fluid velocity vector
x, y, z = Cartesian coordinates
x', y', z' = fringe point coordinates
α = fluid thermal diffusivity
ν = fluid kinematic viscosity
ρ = fluid density
$\bar{\bar{\tau}}$ = viscous stress tensor
τ_w = local shear stress

Subscripts

f = friction component
p = pressure component

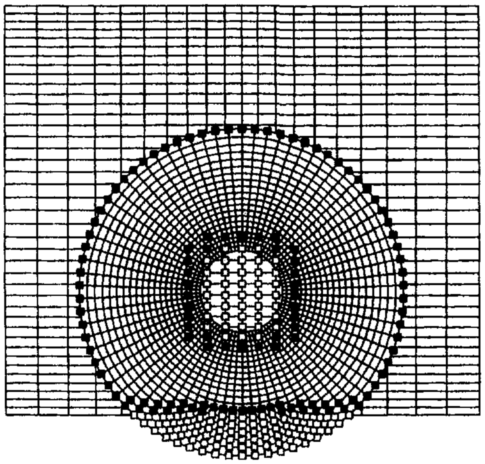

Fig. 2 Typical Chimera grid with holes (hollow squares) and fringe points (solid squares)

as a neighbor, to fringe points. Figure 2 shows a typical set of fringe points marked with solid squares.

Trilinear Interpolation Scheme. A Chimera scheme uses interpolation at the fringe points, in order to transfer data between the meshes. In this work a typical variable, g, is interpolated using a trilinear interpolation,

$$g(x', y', z') = a_1 + a_2x' + a_3y' + a_4z',$$

for given fringe point coordinates, x', y', z'. The coefficients, a_i, are found using Cramers rule. This is done by four simultaneous equations based on known values of g, and coordinates (x, y, z), at the four corners of the tetrahedron containing the point.

Lift, Drag, Shear Stress, and Heat Transfer. Forces exerted on the sphere by the fluid are, generally, lift and drag. The dimensionless form of these forces are lift coefficient, C_L, and drag coefficient, C_D, defined by

$$c_L = \frac{F_L}{1/2\rho U_\infty^2 A_s}, \quad c_D = \frac{F_D}{1/2\rho U_\infty^2 A_s}$$

where A_s is the sphere frontal area,

$$A_s = \pi R_s^2, \quad R_s = \text{sphere radius.}$$

F_L and F_D are the dimensional lift and drag forces given by integration of local pressure and viscous forces over the sphere surface given by

$$F_D = \iint_s (P + \tau_w)\bar{e}_x \cdot d\bar{A}$$

$$F_L = \iint_s (P + \tau_w)\bar{e}_z \cdot d\bar{A}$$

where e_x and e_z are unit vectors in the x and z-coordinate directions. Wall shear stress, τ_w, is given in terms of the local friction factor, f, defined by

$$f = \frac{8\tau_w}{\rho U_a^2}.$$

This factor is known as the Darcy friction factor in an unblocked pipe and is equal to $64/\mathrm{Re}_p$ in a laminar flow (White, 1994). The dimensionless heat transfer coefficient is the Nusselt number and is defined as

$$\mathrm{Nu} = \frac{hD_s}{k} = \frac{D_s}{(T_s - T_w)\iint_s dA} \iint_s (\nabla T)\cdot \mathbf{n} dA.$$

The integral is over the entire sphere surface area for the overall Nusselt number, Nu. For the local Nusselt number, Nu_θ, the integral is over individual cell area at the surface of the sphere.

Code Validation

To validate the computer program used in this work a well-known test case was run and the results were compared to the available data. The test case consists of a sphere centered along the center line of the pipe. The sphere to pipe diameter ratio was set to .1, which results in a small blockage ratio of one percent. The length, L, of the pipe was chosen to be twice its diameter, D_p. The pipe wall is at 10 sphere radii, and the pipe inlet and outlet are at 20 sphere radii. Grid densities are 21 × 21 × 21 for the pipe, and 31 × 21 × 31 for the sphere.

A parabolic velocity profile is specified at the inlet such that the sphere Reynolds number is $\mathrm{Re}_{s\infty} = 10$. At this Reynolds number, and given the distance of the pipe wall, the flow is closely approximated by an externally unbounded uniform flow over a sphere. This is a well-documented case and there are published data available for comparison (Clift et al., 1978).

The standard test is the sphere drag coefficient, C_D, which is the sum of the pressure and friction components, C_{Dp} and C_{Df}, respectively. The Nusselt number is a test of convective heat transfer and is compared with results from the work by Dandy and Dwyer (1990).

Table 1 shows a summary of the calculated results for the test case (sphere in a pipe flow), as compared to published results. Overall, drag and heat transfer values are in agreement with the published results within three percent.

Results

The results are presented for Re_p of 25 and 125 along with D_s/D_p of 0.2 and 0.4 (blockage ratios of 4 percent and 16 percent). The sphere is located off center at $E = 0.2D_p$, in order to induce a three-dimensional effect. The pipe length to diameter ratio is set to 5. The computational domain is half of the physical domain due the flow symmetry about the plane that bisects both the sphere and the pipe (symmetry plane, Fig. 1).

Re_p = 25 Case. The results for $\mathrm{Re}_p = 25$ with two D_s/D_p values of 0.2 and 0.4 are presented here. In these studies the grid densities are 21 × 21 × 31 both for the pipe and the sphere. At the entrance we specify a parabolic velocity profile, which results in $\mathrm{Re}_{s\infty} = 8.4$ and 16.8 for the two D_s/D_p values, respectively.

The dimensionless sphere surface pressure is defined by

$$P_{s\infty} = \frac{P_s - P_\infty}{1/2\rho U_\infty^2}$$

P_∞, is a reference pressure chosen on the outer grid surface in the sphere mesh, at 90 deg from the stagnation point, in the plane of symmetry.

Table 1 Test case drag coefficient and Nu

Case	C_{Dp}	C_{Df}	C_D	Nu
Present work	1.48	2.71	4.19	3.35
Published	1.52	2.77	4.29	3.45

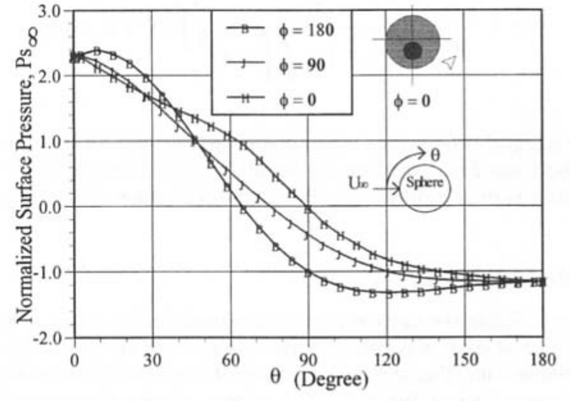

Fig. 3 Sphere surface pressure, $Re_p = 25$, $D_s/D_p = 0.4$

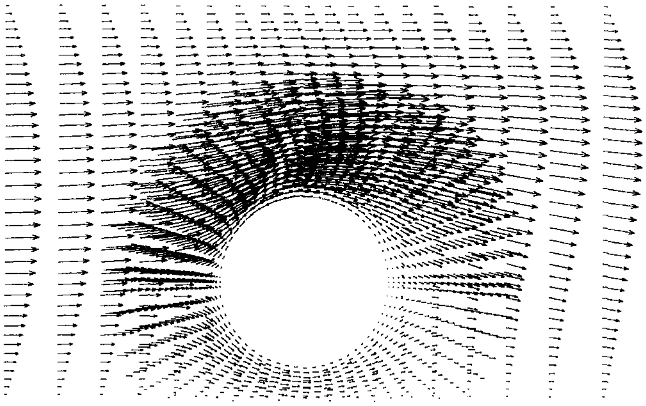

Fig. 5 Velocity vectors in the plane of symmetry, $Re_p = 25$, $D_s/D_p = 0.4$

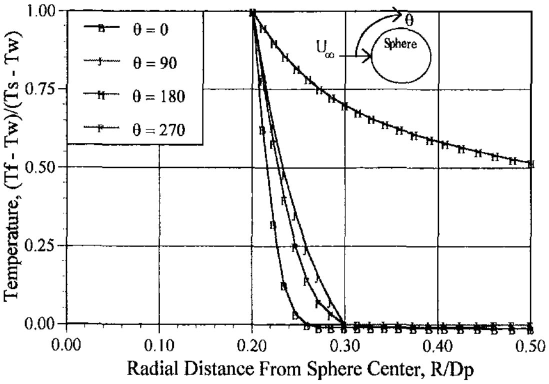

Fig. 6 Temperature along sphere radials at various angles in the plane of symmetry, $Re_p = 25$, $D_s/D_p = 0.4$

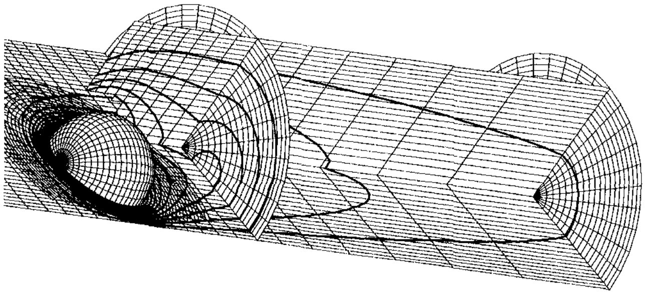

Fig. 7 Temperature contours around the sphere, $Re_p = 25$, $D_s/D_p = 0.4$

Figure 3 shows the normalized sphere surface pressure, $P_{s\infty}$ versus angle θ (from stagnation point) in three different planes (lower symmetry plane; $\phi = 0$, upper symmetry plane; $\phi = 180$, and the plane in between; $\phi = 90$) for the $Re_{s\infty} = 16.8$ case ($D_s/D_p = 0.4$). Compared to a uniform external flow, there are significant changes in the pressure field around the sphere. In the front the stagnation point is shifted approximately ten deg with maximum $P_{s\infty}$ of nearly 2.4. In an external flow stagnation $P_{s\infty}$ is less than 1.8 at $\theta = 0$. In the back there is less pressure recovery with $P_{s\infty}$ of almost -1.2, which is a typical value for $Re_{s\infty} = 100$ in an external flow. Combination of these two changes causes a higher pressure drag on the sphere.

In addition, the three-dimensional nature of the flow is evident by the difference of the surface pressure in the three different planes ($\phi = 0$, 90, and 180) around the sphere. Both the maximum ($\sim$2.4) and the minimum (~ -1.4) pressures occur in the $\phi = 180$ plane.

Heat transfer characteristics of this flow are given in Fig. 4 in terms of local Nusselt number, Nu_θ versus θ, over the sphere surface at various angles, for $D_s/D_p = 0.4$. The maximum is $\sim$6.3 at $\theta \sim 30$ deg, and the minimum is 2.0 at $\theta = 180$ deg. Local Nusselt number has three-dimensional variations as shown by three curves ($\phi = 0$, 90, and 180) around the sphere. The blockage has an interesting effect in the $\phi = 0$ plane, where flow retardation first lowers the Nusselt number ($\theta \leq 45$) and then an acceleration of the flow increases the Nusselt number ($\theta > 45$). This can result in the appearance of a new hot spot. Despite significant changes in the local Nusselt number, the overall Nusselt number (4.2) is close to that of a sphere in an external flow (Dandy and Dwyer, 1990).

Velocity vectors in the plane of symmetry are presented in Fig. 5. The parabolic velocity profile upstream of the sphere is changed downstream, where the wake of the sphere retards the lower half, and accelerates the upper half of the flow. Around the sphere flow is restricted near the pipe wall and continuity of mass forces an acceleration of the flow on the opposite side of the sphere. There are no separated flow regions as in the external flow case.

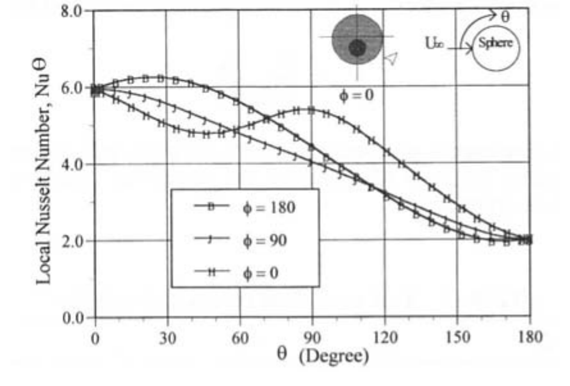

Fig. 4 Local Nu around the sphere at various angles, $Re_p = 25$, $D_s/D_p = 0.4$

Temperature variations at four different radials around the sphere, in the plane of symmetry, is given in Fig. 6 for $D_s/D_p = 0.4$. These curves which are chosen at $\theta = 0$, 90, 180, and 270 deg, confirm the results of Fig. 4 for the local Nusselt number. Temperature gradient near the sphere surface ($R/D_p = 0.2$) has its largest value at $\theta = 0$ and its smallest value at $\theta = 180$, with those at $\theta = 90$ and 270 in between the maximum and the minimum. Note that the $\theta = 270$ radial corresponds to the $\theta = 90$ in the $\phi = 0$ plane. Figure 7 shows temperature contours for the same case as Fig. 6. Asymmetry of the heat transfer is also evident based on the temperature contour patterns.

Table 2 Sphere lift, drag, and Nu, $Re_P = 25$

D_s/D_p	C_{Lp}	C_{Lf}	C_L	C_{Dp}	C_{Df}	C_D	Nu
0.2	0.34	0.29	0.63	2.35	3.72	6.07	3.1
0.4	0.55	0.33	0.88	2.39	2.31	4.70	4.2

Summary. A summary of the fluid dynamic forces and over all heat transfer performance of the flow is given in Table 2, in terms of C_L, C_D, and overall Nu. The lift and drag coefficient are broken down into their pressure and friction components, C_{Lp}, C_{Lf}, C_{Dp}, C_{Df}.

$Re_p = 125$ Case. For external flow over a sphere the flow separates at sphere Reynolds number larger than 20 and a new flow regime is encountered (Clift et al., 1978). Therefore, the pipe Reynolds number was increased to 125 with two D_s/D_p values of 0.2 and 0.4. The resulting sphere Reynolds numbers are 42 (for $D_s/D_p = 0.2$) and 84 (for $D_s/D_p = 0.4$). The grid densities are $21 \times 21 \times 41$ for both the pipe and the sphere in the $D_s/D_p = 0.2$ case, and $21 \times 21 \times 51$ for the pipe and $21 \times 21 \times 41$ for the sphere in the $D_s/D_p = 0.4$ case.

Figure 8 shows the normalized sphere surface pressure, $P_{s\infty}$ versus θ in three different planes ($\phi = 0$, 90, and 180) for the $Re_{s\infty} = 84$ case. The changes, compared to external flow results, are similar to the $Re_p = 25$ case, previously discussed. There is a shift in the stagnation pressure (~ 1.5 at θ of ~ 12 deg). However, the minimum of ~ -0.8 (at $\theta = 90$ deg) occurs closer to the front stagnation point and there is a more pronounced pressure recovery in the back of the sphere ($\theta > 90$ deg) in the $\phi = 180$ plane. Here, again the three-dimensional nature of the flow is shown by difference of surface pressure in the three different planes ($\phi = 0$, 90, and 180).

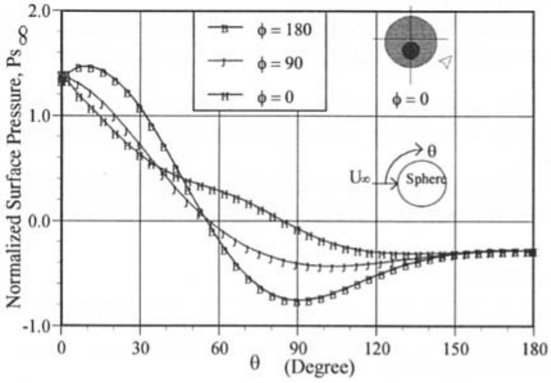

Fig. 8 Sphere surface pressure, $Re_p = 125$, $D_s/D_p = 0.4$

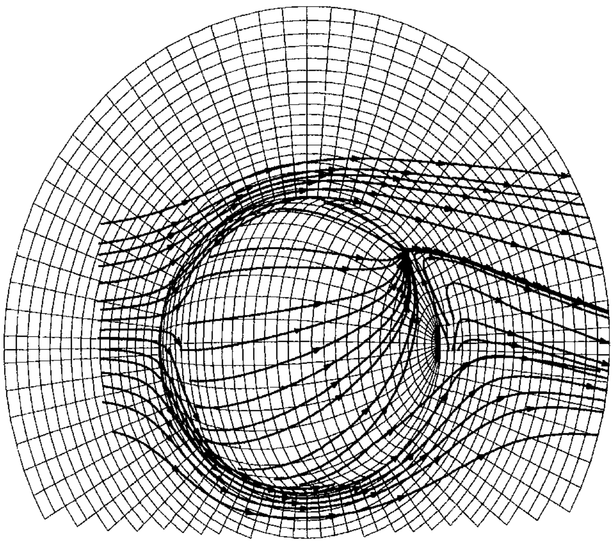

Fig. 9 Stream lines around the sphere, $Re_p = 125$, $D_s/D_p = 0.4$

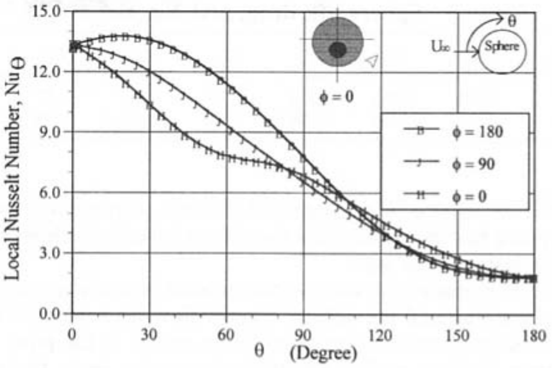

Fig. 10 Local Nu Around the sphere at various angles, $Re_p = 125$, $D_s/D_p = 0.4$

There are no recirculation zones around the sphere in either case ($Re_{s\infty} = 42$ or 84) despite the fact that the sphere Reynolds number is well above separation limit of $Re_{s\infty} = 20$ for an external flow. This delay in separation can be attributed to the favorable pressure gradient in the pipe along the flow direction. Figure 9 shows the stream lines around the sphere for the case with largest sphere Reynolds number ($Re_p = 125$, and $D_s/D_p = 0.4$). The stream lines show the absence of recirculation

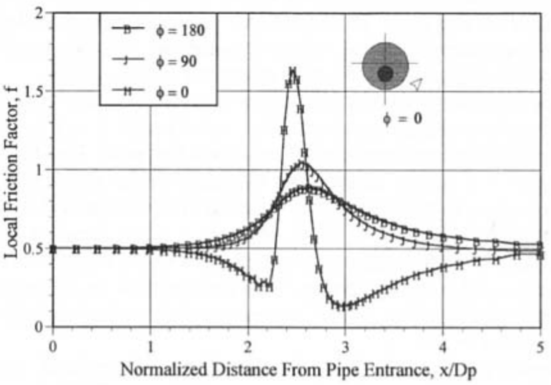

Fig. 11 Local friction factor along the pipe wall at various angles, $Re_p = 125$, $D_s/D_p = 0.4$

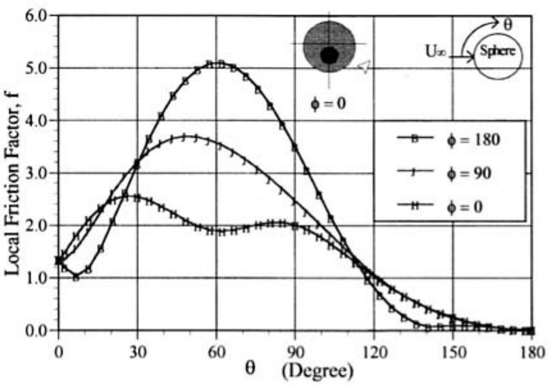

Fig. 12 Local friction factor on sphere surface at various angles, $Re_p = 125$, $D_s/D_p = 0.4$

Table 3 Sphere lift, drag, and Nu, $Re_P = 125$

D_s/D_p	C_{Lp}	C_{Lf}	C_L	C_{Dp}	C_{Df}	C_D	Nu
0.2	0.08	0.00	0.08	0.77	1.00	1.77	5.1
0.4	0.29	0.09	0.36	0.86	0.69	1.55	7.0

around the sphere. Also, note that the rear stagnation point on the sphere has moved towards the side of sphere which is closer to the center of the pipe.

The displacement of the stagnation point is due to asymmetry of pressure around the sphere. Slower flow near the pipe wall causes larger pressure compared to the center of the pipe. The pressure gradient pushes the stagnation point away from the wall and closer to the center of the pipe.

Local Nusselt number around the sphere, Nu_θ versus θ, for the $D_s/D_p = 0.4$ case, at various planes ($\phi = 0$, 90, and 180) is presented in Fig. 10. The maximum local Nu ~ 14 occurs at $\theta \sim 25$ deg in the $\phi = 180$ plane, and a minimum value of ~ 2 is common for all three planes at $\theta = 180$ deg. The shape of the curves are similar to the $Re_p = 25$ case, with the exception of the $\phi = 0$ curve, which no longer increases after the initial decrease. The overall sphere Nusselt numbers (5.1 for $D_s/D_p = 0.4$, and 7.0 for $D_s/D_p = 0.2$) are very close to the external flow case.

Another parameter of interest is the friction factor for the pipe and the sphere. This parameter is of particular importance in biological flows, where excessive shear stress can damage certain blood cells. The local pipe wall friction factor, f, is plotted along the pipe wall for the $D_s/D_p = 0.4$ case in Fig. 11, for the three planes ($\phi = 0$, 90, and 180). There, we see that f starts with a value of ~ 0.51 at the pipe entrance. This is the value for Darcy friction factor ($64/Re_p$) for an unblocked pipe and continues for a distance of nearly 1 pipe diameter from the entrance of the pipe. Therefore, we can conclude that the entrance boundary location, where a parabolic velocity profile is specified, is placed far enough upstream of the sphere.

The maximum shear stress on the pipe wall occurs very close to the sphere center location ($x/D_p = 2.5$) with $f \sim 1.6$, which is more than three times that of an unblocked pipe. This happens in the $\phi = 0$ plane, where flow blockage is the greatest.

Also, note that in this plane the shear stress initially decreases due to flow retardation. Then, there is a rapid increase to the maximum (~ 1.6) as the flow accelerates in the region between the pipe wall and the sphere. This acceleration is followed by a rapid deceleration, which brings the shear stress levels to a minimum (~ 0.1).

Figure 12 gives the local friction factor, f versus θ, around the sphere surface in the planes $\phi = 0$, 90, and 180 deg. The most dramatic change occurs in the $\phi = 180$ plane, where f starts at a value of ~ 1.3, initially decreases to ~ 1.0, and then increases to the overall maximum value of ~ 5. Therefore, the sphere sees shear stress as much as ten times that of an unblocked pipe at this flow rate. In the back of the sphere stress levels smoothly drop down to a minimum value of zero, as expected in an attached flow.

Summary. A summary of the fluid dynamic forces and overall heat transfer performance for this case is listed in Table 3, in terms of C_L, C_D, and overall Nu. The lift and drag coefficients are broken down into their pressure and friction components, C_{Lp}, C_{Lf}, C_{Dp}, C_{Df}.

Concluding Remarks

The following is a conclusive summary of the presented work:

1 Flow and heat transfer calculations over a three-dimensional spherical object in a pipe, at moderate Reynolds number range, were performed.

2 The solution method is a finite volume generalized coordinate formulation of the Low Mach number continuity, Navier-Stokes, and thermal energy equations.

3 An overset (Chimera) grid scheme is successfully used for the pipe and sphere meshes.

4 The solution method is validated using the external flow limit of the problem at one percent blockage ratio.

5 There is significant blockage effect at ratios larger than four percent.

6 The blockage results in a rise in the front stagnation pressure and a drop in the back stagnation pressure on the sphere with an overall effect of increased pressure drag.

7 The favorable pressure gradient along the pipe delays separation around the sphere.

8 Overall friction drag and Nusselt number over the sphere are not significantly changed compared to an external uniform flow.

9 The asymmetry of the flow induces a lifting force on the sphere. The lifting force is a function of sphere Reynolds number.

10 There is significant changes in the local shear stress levels on the pipe wall compared to those of an unblocked pipe.

References

Bird, R. B., Stewart, W. E., and Lightfoot, E. N., 1960, *Transport phenomena,* John Wiley and Sons, New York.

Clift, R., Grace, J. R., and Webber, M. E., 1978, *Bubbles, drops, and particles,* Academic Press, San Diego, CA.

Dandy, D. S., and Dwyer, H. A., 1990, "A sphere in shear flow at finite Reynolds number: effect of shear on particle lift, drag and heat transfer," *Journal of Fluid Mechanics,* Vol. 216, pp. 381–410.

Dougherty, F. C., 1985, "Development of a Chimera grid scheme with applications to unsteady problems," Ph.D. thesis, Stanford University, Stanford, CA.

Dwyer, H. A., 1989, "Calculation of droplet dynamics in high temperature environments," *Prog. Energy Combust. Sci.,* Vol. 15, pp. 131–158.

Nirschl, H., Dwyer, H. A., and Denk, V., 1994, "A Chimera grid scheme for calculation of particle flows," *Journal of Fluid Mechanics,* accepted for publication.

White, F. M., 1994, *Fluid Mechanics,* 3rd Ed., McGraw-Hill, New York.

L. B. Wang
School of Energy and Power Engineering,
Xi'an Jiaotong University,
Xi'an 710049, China

G. D. Jiang
Department of Mechanical Engineering,
Lanzhou Railway Institute,
Lanzhou 730070, China

W. Q. Tao
School of Energy and Power Engineering,
Xi'an Jiaotong University,
Xi'an 710049, China

H. Ozoe
Institute of Advanced Material Study,
Kyushu University 86,
Kasuga 816, Japan

Numerical Simulation on Heat Transfer and Fluid Flow Characteristics of Arrays With Nonuniform Plate Length Positioned Obliquely to the Flow Direction

The periodically fully developed laminar heat transfer and pressure drop of arrays with nonuniform plate length aligned at an angle (25 deg) to air direction have been investigated by numerical analysis in the Reynolds number range of 50–1700. The body-fitted coordinate system generated by the multisurface method was adopted to retain the corresponding periodic relation of the lines in physical and computational domains. The computations were carried out just in one cycle. Numerical results show that both the heat transfer and pressure drop increase with the increase in the length ratio of the long plate to the short plate, and decrease with the decrease in the ratio of transverse pitch to the longitudinal pitch. The numerical results exhibit good agreement with available experimental data.

Introduction

Flow interruption created in flow passages at periodic intervals is a popular mean for enhancing heat transfer. The louvered fin and offset fin surfaces are examples of its applications, which have been widely used in automobiles, chemical engineering, air conditioning, etc. Numerous experimental and numerical studies have been conducted on the heat transfer and pressure drop characteristics for such kind of surface configurations. It has been found experimentally that after passing though several cycles, typically four to six, the fluid flow and heat transfer become periodically fully developed (Yan et al., 1986; Lee, 1986; Zhang and Lang, 1989; Lue et al., 1992; Huang and Tao, 1993). In most engineering applications the cycle number in the flow direction is usually much larger than this value, therefore, the periodic fully developed fluid flow and heat transfer has received much attention in recent years. The heat transfer and fluid flow characters of a variety of interrupted plate arrays were numerically investigated by Sparrow et al. (1977), Sparrow and Liu (1979), Patankar et al. (1979), Patankar and Parakash (1981), Kajino (1986), Asako and Faghri (1988), Pang et al. (1990), and Wang and Tao (1995). The plate length in all these investigations was uniform.

The purposes of the present study are as follows: first, to carry out a numerical analysis of the heat transfer and fluid flow characteristics of arrays with nonuniform plate length by using multisurface grid generation method, so that the geometric boundaries of the plates can be simulated accurately; second, to perform a parametric study of the effect of Reynolds number, the ratio of plate length, and the ratio of transverse pitch to longitudinal one; and finally, to compare the numerical results of an average Nusselt number and friction factor with available experimental data.

Physical Model and Mathematical Formulation

The problem analyzed in this paper is schematically pictured in Fig. 1(*a*). As seen there, a two-dimensional array of nonuniform plate length with constant temperature T_w is positioned obliquely to the flow direction. The configuration studied can be specified by the following parameters: the periodic axial length L_p, the plate lengths L_1, L_2, the transverse space between the plates T_p, the oblique angle θ, and the plate thickness δ. The engineering background of this study is the heat transfer and fluid flow in louvered fins used in automobiles and other heat exchangers, where the fins are formed by slitting a continuous thin copper plate and then turning the slitted segments to an angle. In this case, $L_p = L_1 + L_2$. In order to make the laminar flow analysis consistent with the corresponding experimental work, the geometric parameters used in Huang and Tao (1993) are adopted in this paper, i.e., the plate thickness $\delta = 1.5$ mm, the oblique angle $\theta = 25$ deg, the short plate length $L_2 = 15$ mm, the ratio of $L_1/L_2 = 1.5$, 2.0, and 2.5, and the transverse pith $T_p = 20$, 25, and 30 mm. Thus nine configurations can be obtained (Table 1). For simplicity, a case number is assigned to each configuration. It is worth noting that the effects of the oblique angle to the heat transfer and friction factor were investigated in the work done by Zhang and Lang (1989). The results show that an oblique angle around 25 deg is the best choice in trading off heat transfer enhancement and pressure drop increment. The present study is focused on the effects of L_1/L_2 and T_p/L_p on heat transfer and friction factor characteristics of louvered fins.

The analysis is based on the following assumptions: (1) The fluid properties are constant; (2) the flow and heat transfer are in steady state, laminar, and periodically fully developed; and (3) the body force and the dissipation term are neglected.

The final computation domain is shown in Fig. 1(*b*). The fluid flow and heat transfer can be specified by the following equations with Cartesian tensor notation:

Contributed by the Heat Transfer Division for publication in the JOURNAL OF HEAT TRANSFER. Manuscript received by the Heat Transfer Division, Apr. 28, 1997; revision received, May 4, 1998. Keywords: Augmentation and Enhancement, Forced Convection, Numerical Methods. Associate Technical Editor: R. Douglass.

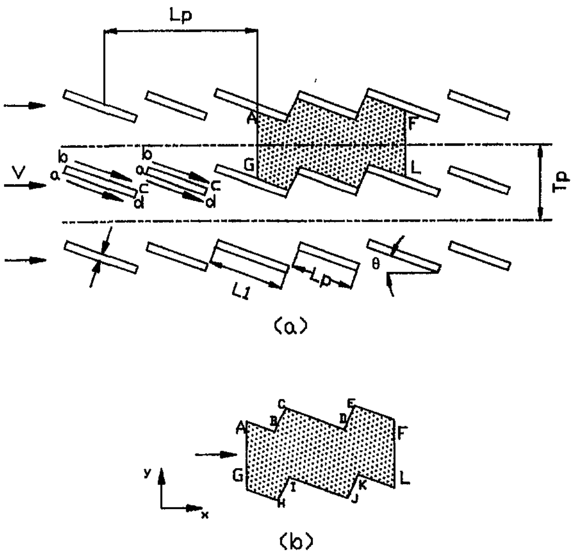

Fig. 1 Schematic diagram of the problem studied (*a*) plate array with nonuniform length, (*b*) computation domain

Continuity Equation:

$$\frac{\partial}{\partial x_i}(\rho u_i) = 0. \tag{1}$$

Momentum Equations:

$$\frac{\partial}{\partial x_i}(\rho u_i u_k) = \frac{\partial}{\partial x_i}\left(\mu \frac{\partial u_k}{\partial x_i}\right) - \frac{\partial p}{\partial x_k}, \; k = 1, 2. \tag{2}$$

Energy Equation:

$$\frac{\partial}{\partial x_i}(\rho c_p u_i T) = \frac{\partial}{\partial x_i}\left(\lambda \frac{\partial T}{\partial x_i}\right). \tag{3}$$

Boundary Conditions:

$$\begin{aligned} u(x, y)|_{AG} &= u(x, y)|_{FL} \\ v(x, y)|_{AG} &= v(x, y)|_{FL} \\ \Theta(x, y)|_{AG} &= \Theta(x, y)|_{FL} \end{aligned} \tag{4}$$

Table 1 Characteristics of configuration investigated (12 = 15 mm, theta = 25 deg)

Case	L_1, mm	T_b, mm	L_p, mm	L_1/L_2	T_p/L_p
1	37.5	30.0	52.5	2.5	0.571
2	30.0	30.0	45.0	2.0	0.667
3	22.5	30.0	37.5	1.5	0.800
4	37.5	25.0	52.5	2.5	0.476
5	30.0	25.0	45.0	2.0	0.556
6	22.5	25.0	37.5	1.5	0.667
7	37.5	20.0	52.5	2.5	0.381
8	30.0	20.0	45.0	2.0	0.444
9	22.5	20.0	37.5	1.5	0.533

$$\begin{aligned} u(x, y)|_{BC} &= u(x, y)|_{HI} \\ v(x, y)|_{BC} &= v(x, y)|_{HI} \\ T(x, y)|_{BC} &= T(x, y)|_{HI} \end{aligned} \tag{5}$$

$$\begin{aligned} u(x, y)|_{DE} &= u(x, y)|_{JK} \\ v(x, y)|_{DE} &= v(x, y)|_{JK} \\ T(x, y)|_{DE} &= T(x, y)|_{JK}. \end{aligned} \tag{6}$$

The boundary conditions at the surfaces of the solid plates are

$$\begin{aligned} u(x, y) &= 0 \\ v(x, y) &= 0 \\ T(x, y) &= T_w \end{aligned} \tag{7}$$

where the dimensionless temperature is defined as follows:

$$\Theta(x, y) = (T(x, y) - T_w)/(T_b(x) - T_w). \tag{8}$$

Attention is now turned to coordinate transformation and grid generation. The continuity equation and the conservation form of the transport equation for a general dependent variable in a generalized coordinate system (ξ, η) can be written as follows:

$$\frac{\partial}{\partial \xi}(\rho U) + \frac{\partial}{\partial \eta}(\rho V) = 0 \tag{9}$$

$$\frac{\partial}{\partial \xi}(\rho U \phi) + \frac{\partial}{\partial \eta}(\rho V \phi) = \frac{\partial}{\partial \xi}\left[\frac{\Gamma_\phi}{J}\left(\alpha \frac{\partial \phi}{\partial \xi} - \beta \frac{\partial \phi}{\partial \eta}\right)\right] + \frac{\partial}{\partial \eta}\left[\frac{\Gamma_\phi}{J}\left(-\beta \frac{\partial \phi}{\partial \xi} + \gamma \frac{\partial \phi}{\partial \eta}\right)\right] + J S_\phi \tag{10}$$

where S_ϕ is the source term in computational space and the contravariant velocities U, V are given as

Nomenclature

b = source term in discritization equations
f = per-cycle pressure drop factor
h_x = local heat transfer coefficient, W/m^2 °C
J = Jacobean of inverse coordinate transformation
L_p = streamwise length of one cycle, m
L = long plate length, m
$M_{r,\max}$ = relative maximum mass flow rate unbalance in one control volume
n = normal direction to plate surface
Nu = Nusselt number
p = pressure, P_a
Pr = Prandtl number
q = heat flux, W/m^2
q_x = local heat flux, W/m^2
Re = Reynolds number
T = temperature, °C
T_p = transverse spacing between two adjacent plates, m
T_b = bulk temperature, °C
T_w = wall temperature, °C
u_i = velocity components in Cartesian coordinates
U, V = contravariant velocity components in ξ and η-direction
x = distance from leading point along the plate surface
x_i = Cartesian coordinates

Greek Symbols

α, β, γ = metric coefficients of two coordinate systems
Γ = diffusion coefficient
δ = thickness of plate, m
θ = oblique angle, degree
Θ = dimensionless temperature, Eq. (8)
λ = thermal conductivity, W/m°C
ν = fluid kinematic viscosity, m^2/s
ξ, η = coordinates in transformed plane
ρ = fluid density, kg/m^3
ϕ = general dependent variable

Subscripts

m = mean
ξ, η = partial derivatives with respect to ξ and η
1 = long plate length
2 = short plate length

Superscripts

* = value of last iteration time

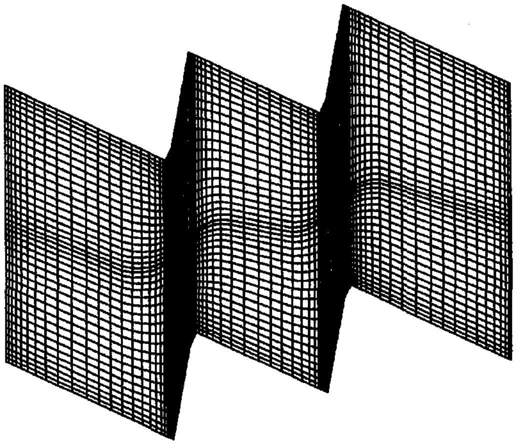

Fig. 2 Typical grid mesh

$$U = uy_\eta - vx_\eta, \quad V = vx_\xi - uy_\xi \tag{11}$$

$$J = x_\xi y_\eta - x_\eta y_\xi, \quad \beta = x_\xi x_\eta + y_\xi y_\eta \tag{12}$$

$$\alpha = x_\eta^2 + y_\eta^2, \quad \gamma = x_\xi^2 + y_\xi^2. \tag{13}$$

The grid generation scheme used in this paper is the multisurface transformation (Eiseman, 1979). This method can guarantee that the periodic counterparts of two corresponding surfaces in physical space are located at the periodically corresponding positions in computation space. The details of this method can be found in the references by Eiseman (1979, 1982, 1985) and will not be restated here. In the present study two intermediate surfaces are used. A typical grid generated by this method is shown in Fig. 2.

It should be noted that the sharp corners of the domain in physical space are not approximated with smooth curves to prevent singularities as this was done in Asako and Faghri (1986). In order to remove the internal grid skewness in multisurface transformation, the surfaces 1 and 4 in multisurface transformation are just extend to internal computational domain to a given small distance, and then the sharp corners of surfaces 1 and 4 are approximated with smooth curves. When the internal domain grid is generated, the boundary grids are taken as a part of the whole grid system according to the geometric relation. To prevent the singularities in the sharp corners, special care is taken in calculating the geometrical derivative such as x_ξ, y_ξ. The value of x_ξ, y_ξ at the points near the corner are calculated by the backward or forward difference according to the point position relative to the corner. The derivatives of x_ξ, y_ξ at the corner points are calculated by linear interpolation from the derivatives of the points aside.

Numerical Procedure

The discretization of the transport equations in the computational domain was performed on a staggered grid by using the finite volume approach. The convection-diffusion terms are treated by the power-law profiles of Patankar (1980). A SIMPLE-like solution algorithm in computational domain was adopted to deal with the linkage between pressure and velocities, the detail of which may be found in Shyy (1985) and Tao (1988). Because the grid is nonorthogonal, the pressure correction equations contain cross derivatives, which lead to a nine-point formulation. In this study the cross derivatives were incorporated into the source term, and a five-point solver was used to solve the algebraic equations.

As for the implementation of the periodic boundary conditions in the computational domain, the interpolation method proposed by Wang and Tao (1995) was used. For the η-direction, the following linear interpolation was used:

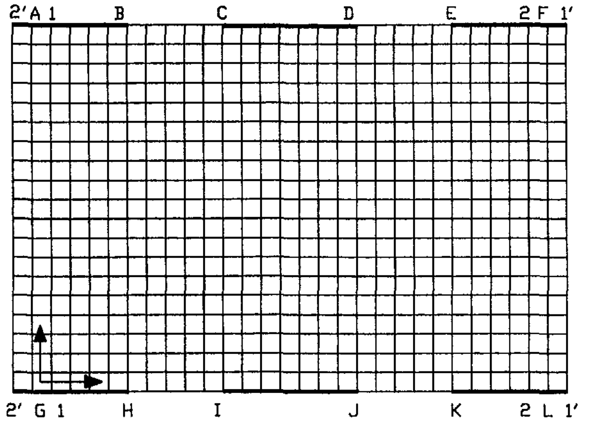

Fig. 3 Computational domain in computational space

$$\phi(i, 1) = \phi(i, M_1) = (\phi^*(i, 2) + \phi^*(i, M_2))/2 \qquad (i_G \le i \le i_L) \tag{14}$$

where "*" represents the previous iteration, and M_1, M_2 are the last and second to last indices in the η-direction. In the implementation of the periodic boundary conditions in ξ-direction, the following liner interpolation was used:

$$\phi(\xi_{A\text{-}G}, \eta) = \phi(\xi_{F\text{-}L}, \eta) = (\phi^*(\xi_{1\text{-}1}, \eta) + \phi^*(\xi_{2\text{-}2}, \eta))/2.0 \tag{15}$$

where $\xi_{1\text{-}1}$ and $\xi_{2\text{-}2}$ are positions corresponding to the lines 1-1 and 2-2 in Fig. 3. It should be noted that in order to restrict the

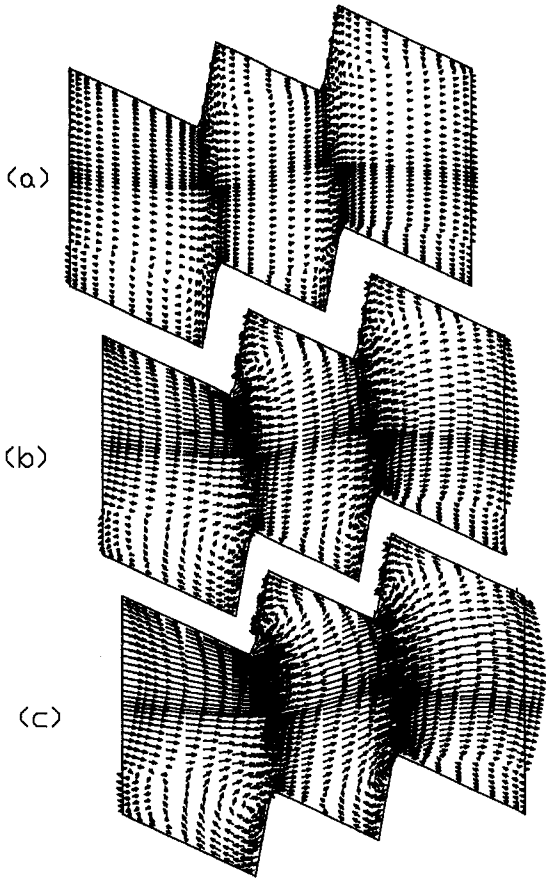

Fig. 4 Flow patterns at different Reynolds number, (*a*) Re = 200, (*b*) Re = 1000, (*c*) Re = 1700

computation to just one cycle, we adopted the linear interpolation method for the implementation of the periodic boundary condition, otherwise the computation domain must be extended in either the η and ξ direction. To overcome the drawback of this method—low order in accuracy—a grid system should be fine enough. As far as the temperature is concerned, the periodic condition is valid only for the dimensionless value. Thus, the interpolation values determined by Eq. (15) were taken as the dimensionless temperatures at the cycle inlet and outlet for the next iteration.

$$\Theta = \frac{1}{2}\left(\frac{T(\xi_{1\text{-}1}, \eta) - T_w}{T_b(\xi_{1\text{-}1}) - T_w} + \frac{T(\xi_{2\text{-}2}, \eta) - T_w}{T_b(\xi_{2\text{-}2}) - T_w}\right) \quad (16)$$

The local temperatures at the cycle inlet and outlet were calculated by

$$T(\xi_{AG}, \eta) = T_w + \Theta[T_b(\xi_{AG}) - T_w] \quad (17)$$

$$T(\xi_{FL}, \eta) = T_w + \Theta[T_b(\xi_{FL}) - T_w]. \quad (18)$$

Attention is now turned to the definitions of the local heat transfer coefficient, Nusselt number, and Reynolds number. The local heat transfer coefficient was determined by the following equation:

$$h_x = \frac{q_x}{(T_b(\xi_{FL}) - T_b(\xi_{AG}))/(\ln(T_w - T_b(\xi_{AG})) - \ln(T_w - T_b(\xi_{FL})))}. \quad (19)$$

The bulk temperature $T_b(\xi)$ was defined as

$$T_b = \int_{\eta_1}^{\eta_{M_1}} T(\xi, \eta)u(\xi, \eta)\sqrt{\alpha}d\eta \bigg/ \int_{\eta_1}^{\eta_{M_1}} u(\xi, \eta)\sqrt{\alpha}d\eta. \quad (20)$$

The local heat flux was computed by Fourier's law of heat conduction. The value of heat flux at the plate surface was determined by

$$q_{n_1} = -\lambda \left.\frac{\gamma T_\eta - \beta T_\xi}{J\sqrt{\gamma}}\right|_{\eta=\eta_1},$$

$$q_{n_2} = -\lambda \left.\frac{\gamma T_\eta - \beta T_\xi}{J\sqrt{\gamma}}\right|_{\eta=\eta_{M_1}}. \quad (21)$$

The average heat flux of the plate surface was determined by

$$q_m = \frac{\int_{\xi_A}^{\xi_B} q_{n_2}\sqrt{\gamma}\,d\xi + \int_{\xi_C}^{\xi_D} q_{n_2}\sqrt{\gamma}\,d\xi + \int_{\xi_E}^{\xi_F} q_{n_2}\sqrt{\gamma}\,d\xi + \int_{\xi_G}^{\xi_H} q_{n_2}\sqrt{\gamma}\,d\xi + \int_{\xi_I}^{\xi_J} q_{n_2}\sqrt{\gamma}\,d\xi + \int_{\xi_K}^{\xi_L} q_{n_2}\sqrt{\gamma}\,d\xi}{\int_{\xi_A}^{\xi_B} \sqrt{\gamma}\,d\xi + \int_{\xi_C}^{\xi_D} \sqrt{\gamma}\,d\xi + \int_{\xi_E}^{\xi_F} \sqrt{\gamma}\,d\xi + \int_{\xi_G}^{\xi_H} \sqrt{\gamma}\,d\xi + \int_{\xi_I}^{\xi_J} \sqrt{\gamma}\,d\xi + \int_{\xi_K}^{\xi_L} \sqrt{\gamma}\,d\xi}. \quad (22)$$

The plate-average heat transfer coefficient of one cycles was computed by

$$h_m = q_m/\{[T_b(\xi_{FL}) - T_b(\xi_{AG})]/[\ln[T_w - T_b(\xi_{AG})] - \ln[T_w - T_b(\xi_{FL})]]\}. \quad (23)$$

The Reynolds number and the plate-average Nusselt number were defined as

$$\mathrm{Re} = u_m L_2/\nu \quad \mathrm{Nu} = h_m L_2/\lambda \quad (24)$$

where the plate length, L_2 was taken as the characteristic dimension. The per-plate pressure drop factor of one cycle was determined from the following equation:

$$f = [p_m(\xi_{AG}) - p_m(\xi_{FL})]/(\rho u_m^2/2). \quad (25)$$

The velocity field convergence criterion used in this study was that the maximum mass flow rate unbalance in one control volume, $M_{r,\max}$. The value of $M_{r,\max}$ is calculated by

$$M_r = \mathrm{MAX}(|b|) \bigg/ \int_{\eta_1}^{\eta_{M_1}} \rho U(\xi_{AG}, \eta)d\eta \quad (26)$$

where b is the residual source term for a control volume in the computational domain. U is the controvariant velocity.

A preliminary computation was performed on two grid system (67×37, 101×61) to assure the grid independence of the numerical solution for the case 2, Re = 1700. The difference between the two solution of Nu was 2.87 percent and of f was 4.68 percent. As these differences were small, the grid numbers used in the computations for nine cases were basically in the region from 63×29 to 83×37. The convergent criterion is taken as $M_{r,\max} = 10^{-4}$. The iteration times needed to obtain a converged velocity field is usually less than 2500. All computations were performed for air (Pr = 0.7).

Results and Discussion

Flow Field. The velocity fields in Fig. 4 show how the flow pattern changes with increasing Reynolds number for case 1. The velocity fields plotted in Fig. 5 show how the flow pattern changes with increasing L_1/L_2 at the same Re = 1000. In Fig. 6, the effect of T_p on flow field at Re = 1500 is presented. It should be noted that the flow fields presented in the three figures are the ones within the computation domain shown in Fig. 1(*b*). There are three panels in each figure, among which the center panel is for the whole short plate (L_2), with the left and the right panels are the two parts for the long plate. To have a full sight of the flow field associated with the long plate the left part should be viewed as the extension of right part. The flow field characteristics shown in the three figures may be summarized as follows. First, for any cases studied, in the flow field at the leeward side of long plate, there are two recirculating zones, and at windward side of long plate as well as on both sides of the short plate there is only one recirculating zone. Among the two recirculating zones of the leeward side of the long plate, the circulation intensity of the zone near the end edge of the long plate is larger than the other one, which is positioned in the top-left region. For the cases with given T_p, L_1, and L_2, the increase in Re leads to the increase in recirculation intensity (Fig. 4). While the decrease in the ratio of transverse pitch to the longitudinal pitch leads to collapse of the two recirculation zones at the leeward side into one (Fig. 6), the same variation trend happens when the ratio of L_1/L_2 decreases, even the ratio of T_p/L_p increases at the same time (Fig. 5). This implies that the ratio of L_1/L_2 has a more significant effect on the flow field structure.

Friction Factor. The calculated friction factor for nine configurations is shown in Fig. 7. From these results the following features may be noted. First, in the low Reynolds number region (approximately less than 100), the variation of f with Re has the same trend as that of a fully developed laminar flow in a continuous duct, i.e., with the increase in Reynolds number, the value of f decreases. This is the flow region where the pressure drop is mainly caused by the surface friction effect. The form

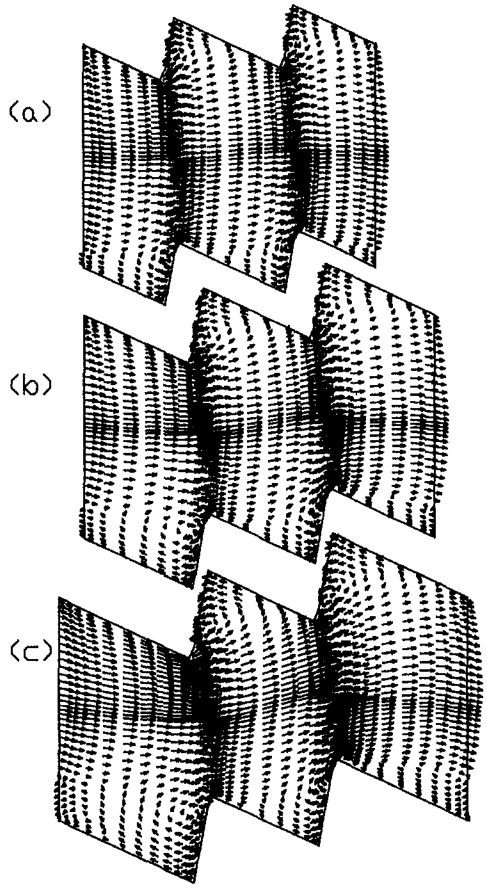

Fig. 5 Flow patterns at different L_1/L_2 (*a*) $L_1/L_2 = 1.5$, (*b*) $L_1/L_2 = 2.0$, (*c*) $L_1/L_2 = 2.5$

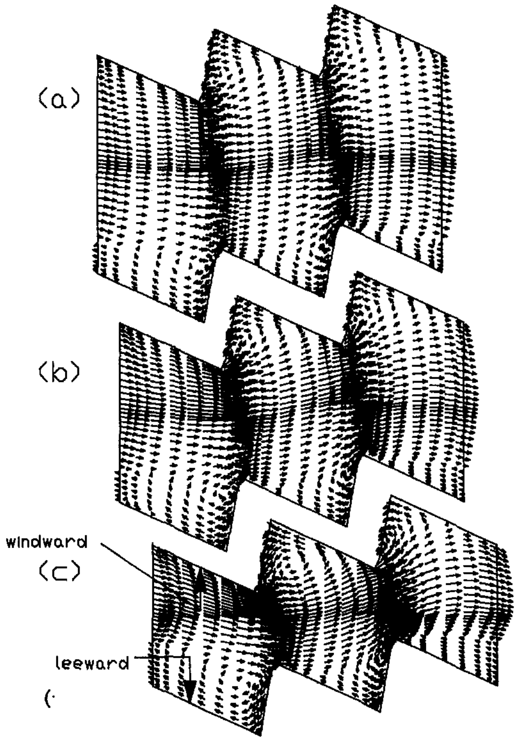

Fig. 6 Flow patterns at different T_p/L_p (*a*) $T_p/L_p = 0.667$, (*b*) $T_p/L_p = 0.556$, (*c*) $T_p/L_p = 0.444$

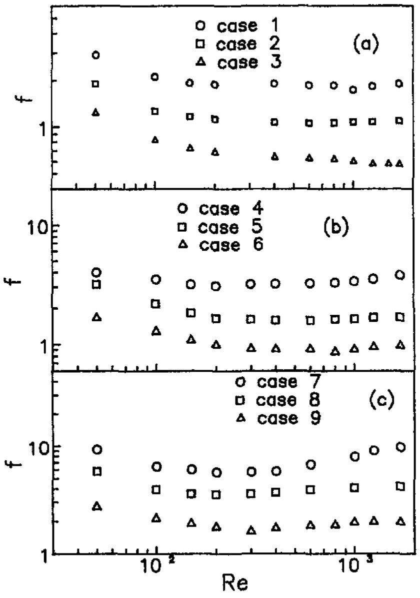

Fig. 7 Effect of L_1/L_2 on plate average Nusselt number

drag of the plate (including the inlet and outlet effects) gradually becomes significant with the further increase in Reynolds number, and finally, it becomes predominant, leading to a constant value of f for each case. From the nine cases studied, eight exhibit such kind of variation trend. However, for case 7, the friction factor keeps going high in the relatively large Reynolds number region. This may be associated with its configuration. Case 7 has the smallest value of T_p/L_p. Second, for the same value of L_1/L_2, the lower the value of T_p/L_p, the larger the value of f in the entire Reynolds number range studied (for example, cases 1, 4, and 7 in Figs. 7(*a*), (*b*), and (*c*)). This implies that even at very low Reynolds number (about 50), the form drag of the plate still has some effect on the total pressure drop of the cycle. Third, for the same value of T_p, with the increase of L_1/L_2, the value of f increases (for example, cases 1, 2, and 3 in Fig. 7(*a*)). This is because increase in L_1 leads to the increase in both friction effect and plate form drag, thus the total cycle pressure drop increases. For the eight cases stated

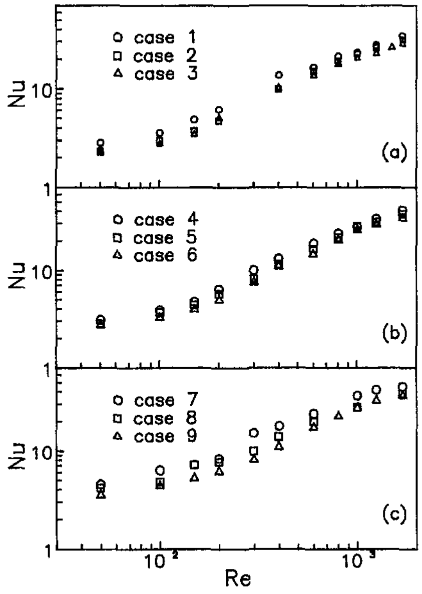

Fig. 8 Effect of L_1/L_2 on plate average Nusselt number

above, the starting Reynolds number beyond which the value of f becomes constant ranges from 150–300. For example for case 1, this Reynolds number is about 150, while for case 3, it increases to about 300.

Average Heat Transfer. The average heat transfer results are presented in Fig. 8 and 9, where the plate average Nusselt number is expressed as a function of Reynolds number. From these two figures, it can be seen that in the low Reynolds number region ($Re \leq 100$), the plate average Nusselt number increases slowly which shows the character of fully developed laminar heat transfer in a continuous duct. This variation trend was also revealed by Faghri and Asako (1988) and Pang et al. (1990). Beyond this Reynolds number region, the increase in the Reynolds number leads to an appreciable increase in the Nusselt number. For the cases of the same T_p, the larger the L_1, the higher the plate average Nusselt number. When L_1 is the same, the higher the T_p, the higher the Nusselt number (Fig. 9). This indicates the strong effect of the recirculating flow on heat transfer. However, if we compare Fig. 8 with Fig. 7, it can be seen that the configuration effect on f is much larger than that on the Nusselt number, an expected outcome from the theory of heat transfer enhancement.

Local Heat Transfer Characteristics. The local heat transfer coefficients of the windward and leeward surfaces are shown in Fig. 10 for cases 1, 2, and 3 at Re = 1000. In this figure, the leeward side consists of *ab* and *bc* segments (see Fig. 1(*a*)) and the windward side of the plate consists of *ad* and *dc* segments. The x coordinate in Fig. 10 is a local coordinate, which starts from point a, extends along the plate surface, and ends at point c for both the windward and leeward sides. It can be found that for the leeward surface, in the start region (*ab* segment), the local heat transfer coefficient has a very significant increase with x. The local heat transfer coefficient reaches its maximum at point b, where a boundary layer flow begins. It then rapidly decreases to a quite uniform value in a region about half of the plate length. This is because the boundary layer flow formed at the very beginning of the plate does not last long downward over the plate surface; rather it meets a counterdirection stream on the surface, mixes with it, and then deviates from the surface. The effect of the right bottom recirculating flow causes an increase of the local heat transfer coefficients. At the very end of the leeward surface, that is, at point c, the local heat transfer again reaches a maximum, basically because of the rushing-out effect of the fluid flow. As for the windward surface, for the most part, the local heat transfer coefficient increases with the distance from the leading edge. This is caused by the velocity acceleration effect occurring over the obliquely positioned plate. In the region adjacent to the end of the windward surface it has the same variation pattern as in the start region of the leeward surface.

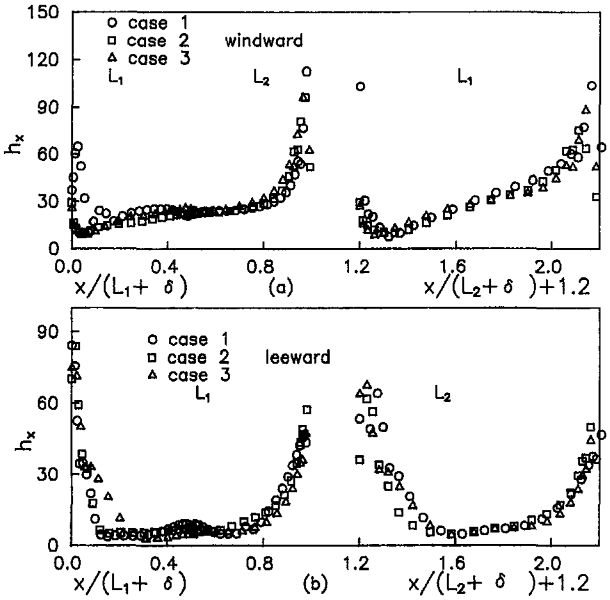

Fig. 10 Local heat transfer coefficient distribution for cases 1, 2, and 3, (Re = 1000), (*a*) windward, (*b*) leeward

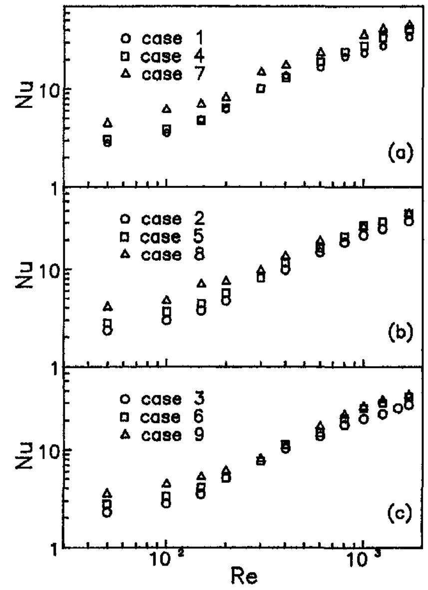

Fig. 9 Effect of T_p/L_p on plate average Nusselt number (*a*) $L_1/L_2 = 2.5$, (*b*) $L_1/L_2 = 2.0$, (*c*) $L_1/L_2 = 1.5$

The above-stated overall variation patterns of the local heat transfer coefficients for the windward and leeward surfaces hold for all the cases studied, with some differences mainly in qualitative level.

Comparison With Experimental Data. The numerical results are compared with the results of experiments made by Huang and Tao (1993). The comparison for the plate average Nusselt number are compared in Figs. 11, 12, and 13. Generally speaking, most of the numerical results are in good agreement with the experimental ones. However, it can be seen from Figs. 12 and 13 that the discrepancy between the numerical and experimental results gradually becomes larger with the increase in the Re, especially for the pressure-drop factor f for small T_p. This discrepancy of numerical results may be attributed to the local skewness of the grid network generated in this study. With the decrease in T_p, the local skewness of the grid network in connection region between two plates increases quite appreciably, possibly leading a larger numerical error. On the other hand, at the very low Reynolds number range (around 2×10^2), the discrepancy in the friction factor is often noticeable. This is believed partly because of the relative large measurement uncertainty at very low flow rate, for which the total pressure drop was often less than 1 mm.

The numerical results of the Nusselt number and friction factor were correlated by the least-square curve-fitting method, and Eq. (27) is obtained. The maximum deviations are 8.34 and 12.1 percent for the Nusselt number and friction factor, respectively.

$$Re = 50 - 400$$

$$Nu = 0.120\, Re^{0.663} (L_1/L_2)^{-0.172}\, (T_p/L_p)^{-1.03}$$

$$f = 1.235\, Re^{-0.25}\, (L_1/L_2)^{0.305} (T_p/L_p)^{-2.69}$$

$$Re = 600 - 1700$$

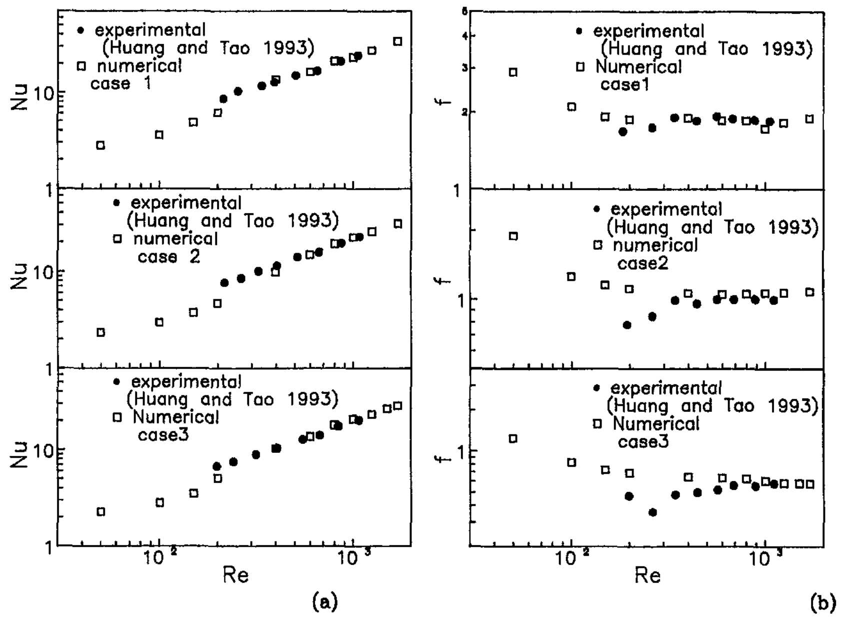

Fig. 11 Comparison of Nu-Re and *f*-Re with experiment data (cases 1, 2, and 3) (*a*) Nu versus Re, (*b*) *f* versus Re

$$\mathrm{Nu} = 0.133\ \mathrm{Re}^{0.712}(L_1/L_2)^{-0.149}(T_p/L_p)^{-0.747}$$

$$f = 0.118\ \mathrm{Re}^{0.102}(L_1/L_2)^{0.203}\ (T_p/L_p)^{-3.28}$$

$$L_1/L_2 = 1.5 - 2.5,\ T_p/L_p = 0.38 - 0.80,$$

$$\delta/T_p = 1/20 - 3/40,\ \theta = 25\ \mathrm{deg} \qquad (27)$$

Concluding Remarks

A parametric investigation on the fluid flow and heat transfer characteristics of the periodically fully developed flows in arrays with nonuniform plate length and oblique angle to the flow direction have been performed numerically by using the multisurface transformation for generation of the grid system. Comparisons between the numerical and experimental results are conducted, and quite good agreement is achieved. The numerical work not only extends the Reynolds number range within which both average heat transfer and pressure drop characteristics are known for the plate arrays studied, but also reveals the details of the related heat transfer and fluid flow processes. The following conclusions can be obtained from this study:

1 There are two recirculating zones in the flow field at the leeward side of the long plate and one recirculating zone at its windward side. With the decrease in T_p or L_1, the two recirculating zones at the leeward side gradually mixed up, and in that case along the most part of the long plate the velocity direction is opposite to the main flow direction.

2 With the increases in the Reynolds number and the ratio of L_1/L_2, both the friction factor and the Nusselt number increase, while at the same L_1/L_2, the decrease in T_p leads to the

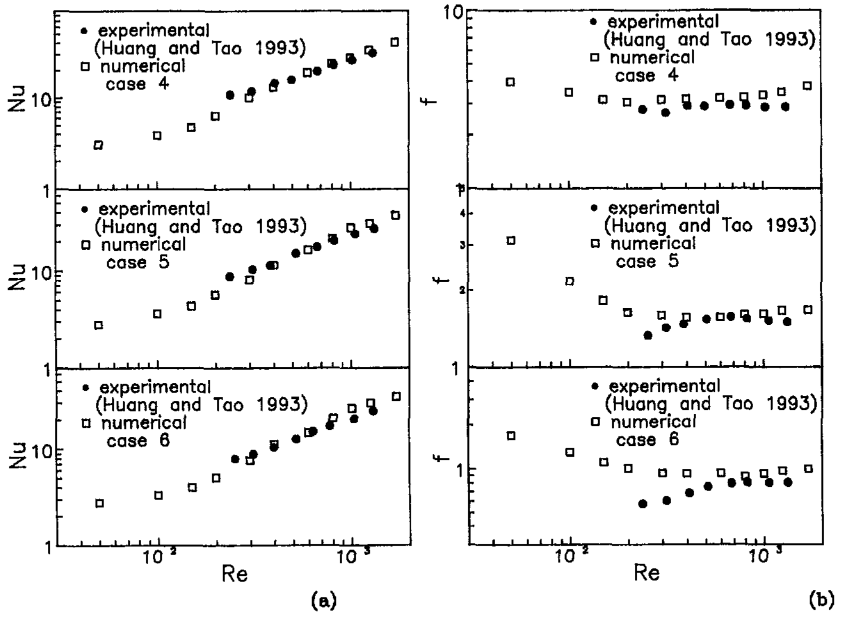

Fig. 12 Comparison of Nu-Re and *f*-Re with experiment data (cases 4, 5, and 6) (*a*) Nu versus Re, (*b*) *f* versus Re

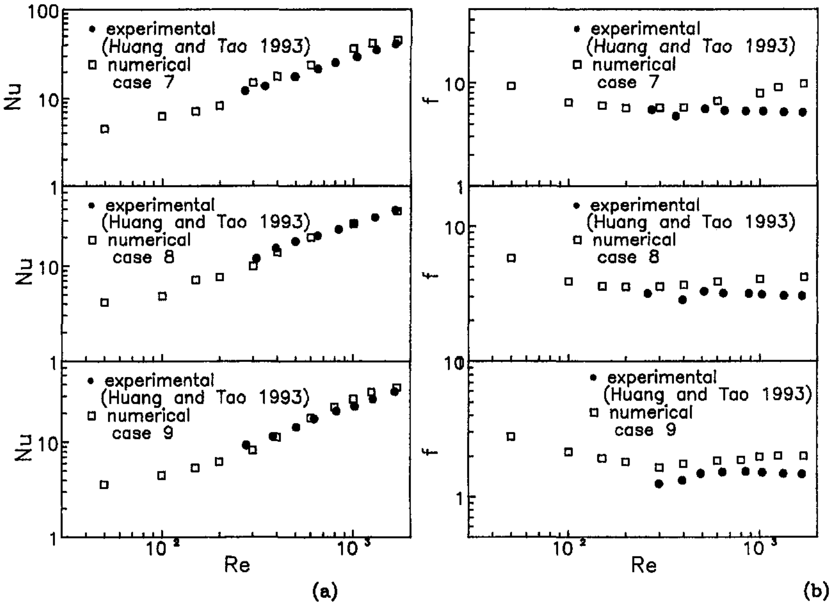

Fig. 13 Comparison of Nu-Re and *f*-Re with experiment data (cases 7, 8, and 9) (*a*) Nu versus Re (*b*) *f* versus Re

decrease in both heat transfer and friction factor. When the Reynolds number exceeds a certain value, the friction factor stops increasing with the Reynolds number, except for the smallest T_p/L_p.

3 In the very low Reynolds number region, typically less than 100, the fluid flow and heat transfer between the plates behave as an internal laminar flow in duct, characterized by the very weak dependency of the friction factor and Nusselt number on the Reynolds number, and the friction factor is almost inversely proportional to the Reynolds number.

Acknowledgment

This work was supported by the National Natural Science Foundation of China and the Special Foundation for Doctorate of National Educational Committee of China.

References

Amano, R. S., 1985, "A Numerical Study of Laminar and Turbulent Heat Transfer in a Periodically Corrugated Wall Channel," ASME JOURNAL OF HEAT TRANSFER, Vol. 107, pp. 564–569.

Asako, Y., and Faghri, M., 1988, "Heat Transfer and Fluid Flow Analysis for an Array of Interrupted Plates, Positioned Obliquely to the Flow Direction," *Proceedings of the Eighth International Heat Transfer Conference,* San Francisco, CA, Vol. 2, pp. 421–427.

Eiseman, P. R., 1979, "A Multi-surface Method of Coordinate Generation," *J. Comput. Phys.,* Vol. 33, pp. 118–150.

Eiseman, P. R., 1982, "Coordinate Generation with Precise Control over Mesh Properties," *J. Comput. Phys.,* Vol. 47, pp. 331–351.

Eiseman, P. R., 1895, "Grid Generation for Fluid Mechanics Computations," *Ann. Rev. Fluid Mech.,* Vol. 17, pp. 487–522.

Hiramastu, M., and Kajino, M., 1986, "Research and improvement of Automotive Radiators," *Internal Combustion Engine,* Vol. 25, pp. 21–28 (in Japanese).

Huang, H. Z., and Tao, W. Q., 1993, "An Experimental Study on Heat/Mass Transfer and Pressure Drop Characteristics for Array of Nonuniform Plate Length Positioned Obliquely to the Flow Direction," ASME JOURNAL OF HEAT TRANSFER, Vol. 115, pp. 568–575.

Lang, X. S., 1987, "An Experimental Study on Heat Transfer and Pressure Drop for an Array of Oblique Flat Plates Aligned with an Air Flow," Master's Thesis, Xi'an Jiaotong University, Xi'an, P. R. China.

Lee, Y. N., 1986, "Heat Transfer and Pressure Drop Characteristics of an Array of Plates Aligned at Angles to the Flow in a Rectangle Duct," *Int. J. Heat Mass Transfer,* Vol. 29, pp. 1553–1563.

Lee, Y., N., 1989, "Heat Transfer and Pressure Drop Characteristics of an Assembly of Partially Segmented Plates," ASME JOURNAL OF HEAT TRANSFER, Vol. 111, pp. 44–50.

Lue, S. S., Huang, H. Z., and Tao, Q. W., 1993, "Experimental Study on Heat Transfer and Pressure Drop Characteristics in the Developing and developed Regions for Arrays of Obliquely Positioned Plates of Non-uniform Length," *Experimental Thermal and Fluid Science,* Vol. Vol. 7, pp. 30–38.

Pang, K., Tao, W. Q., and Zhang, H. H., 1990, "Numerical Analysis of Fully Developed Fluid Flow and Heat Transfer for Arrays of Interrupted Plates Positioned Convergently-Divergently Along the Flow Direction," *Numerical Heat Transfer, Part A,* Vol. 18, pp. 309–342.

Patankar, S. V., Liu, C. H., and Sparrow, E. M., 1977, "Fully Developed Flow and Heat Transfer in Ducts Having Streamwise-Periodic Variation of Cross Sectional Area," ASME JOURNAL OF HEAT TRANSFER, Vol. 99, pp. 180–186.

Patankar, S. V., 1980, *Numerical Heat Transfer and Fluid Flow,* Hemisphere, Washington, D.C., p. 126.

Patankar, S. V., Prakash, C., 1981, "An Analysis of the Effect of Plate Thickness on Laminar Flow and Heat Transfer in Interrupted-Plate Passages," *Int. J. Heat Mass Transfer,* Vol. 24, pp. 1801–1810.

Shyy, W., 1986, "A General Coordinate System Method for Computing Heat Transfer Conference," *Proceedings of Eighth International Heat Transfer Conference,* San Francisco, CA, Vol. 2, pp. 397–401.

Sparrow, E. M., Baliga, B. R., and Patankar, S. V., 1977, "Heat Transfer and Fluid Flow Analysis of Interrupted-Wall Channel, With Application to Heat Exchanger" ASME JOURNAL OF HEAT TRANSFER, Vol. 99, pp. 4–11.

Sparrow, E. M., Liu, C. H., 1979, "Heat Transfer, Pressure-Drop, and Performance Relationships for In-Line, Staggered, and Continuous Plate Heat Exchanger," *Int. J. Heat Mass Transfer,* Vol. 22, pp. 1613–1625.

Tao, W. Q., 1988, "Numerical Heat Transfer," Xi'an Jiaotong University Press, Xi'an, China.

Wang, L. B., and Tao, W. Q., 1995, "Heat Transfer and Fluid Flow Characteristics of Plate Array Aligned at Angles to the Flow Direction," *Int. J. Heat Mass Transfer,* Vol. 38, pp. 3053–3063.

Xin, R. C., and Tao, W. Q., 1988, "Numerical Prediction of Laminar Flow and Heat Transfer in Wavy Channels of Uniform Cross-Sectional Area," *Numer. Heat Transfer,* Vol. 14, pp. 421–427.

Yan, X. J., Zhang, H. H., and Tao, W. Q., 1986, "An Experimental Investigation of Heat Transfer and Pressure Drop Performance for Arrays of Staggered Plates aligned with Air Flows," *Proceedings of Eighth International Heat Transfer Conference,* Vol. 4, pp. 2887–2896.

Zhang, H. H., and Lang, X. S., 1989, "The Experimental Investigation of Oblique Angles and Interrupted Plate Length for Louvered Fins in Compact Heat Exchanger," *Experimental Thermal and Fluid Science,* Vol. 2, pp. 100–106.

The Centerline Pressure and Cavity Shape of Horizontal Plane Choked Vapor Jets With Low Condensation Potential

T. J. Eden
Research Associate

T. F. Miller[1]
Research Associate

Applied Research Laboratory,
The Pennsylvania State University,
P. O. Box 30,
State College, PA 16804

H. R. Jacobs

College of Engineering,
Colorado State University,
Fort Collins, CO 80523
Fellow ASME

A study of plane, underexpanded, condensing vapor jets was undertaken using flash photography and a ventilated pressure probe. This study examined horizontal jets with much lower condensation driving potentials than have been previously studied. Photographic measurements of jet expansion angles, spread angles, cavity lengths, and cavity shapes were recorded and compared with numerical predictions using a parabolic, locally homogeneous flow model that had been modified to incorporate entrainment and condensation effects. When rendered dimensionless by the nozzle width rather than diameter, the plane condensation length agreed well with previously published round jet correlations for higher condensation driving potentials. At lower condensation driving potentials, the jets began to disperse, showing behavior similar to submerged air and energetic reacting vapor jets. Numerical predictions of condensation length were in good agreement over the entire range of measurement. Numerical predictions of vapor cavity shape were in reasonable agreement at higher condensation potentials but underpredicted the width of the vapor cavity at lower potentials. Pressure measurements showed the existence of periodic expansion/compression cells associated with underexpanded noncondensing gas jets. When these measurements were compared with similar measurements of air jets into quiescent water baths, the lengths of the initial steam vapor expansion/compression cells were substantially greater than those of the air jets, and the degree of pressure recovery over the cell length was substantially less.

Introduction

Vapor jets submerged in a liquid bath have several important applications in the nuclear, chemical, and metallurgical industries. The vapor suppression systems that are part of the safety system of some light water reactors work by injecting high-speed (sonic) vapor jets into a subcooled liquid pool (Kudo et al., 1974; Chun and Sonin, 1985). As subcooling (or the driving potential for condensation) is reduced, the potential for escape of uncondensed contaminated steam becomes a concern. Vapor jets are also important in steel making and in liquid metal combustors used in undersea energy systems (Hughes et al., 1983). In these applications, while chemical reaction produces large initial superheating of the vapor jet, the overall behavior of these jets are governed mainly by condensation requirements (Blake and Parnell, 1993; Cho et al., 1990). A common feature of these jets is their operation in a choked ($M_e = 1$), underexpanded condition where the exit-plane pressure of the jet exceeds the pressure in the surrounding liquid bath. Consequently, the jet must expand into the bath—producing a system of shock/expansion cells (Loth and Faeth, 1990) near the nozzle.

Although there is a limited amount of measured data available in the literature for condensing vapor jets injected into liquid (Kerney et al., 1972; Weimer et al., 1973; Young, 1975; Chan, 1982; Binford et al., 1968; Kudo et al., 1974), there is none in which the liquid bath subcooling is low. There are measurements with high initial jet superheating from chemical reaction (Blake and Parnell, 1993; Avery and Faeth, 1975), but these are limited to reaction/condensation lengths. Several of these studies were conducted with jets injected vertically to avoid the effects of buoyancy (Young, 1975; Chan, 1982; Binford et al., 1968; Kudo et al., 1974). The studies of vapor jets injected horizontally were limited to subcooled baths which produced short penetration (condensation) distances, thus allowing buoyancy forces to be neglected (Kerney et al., 1972; Weimer et al., 1973). Experimental data reported from these studies typically consisted of information taken from high-speed photographs of the vapor jet (vapor cavity shape and length), steam inlet pressure and temperature, ambient liquid pressure and temperature, and steam mass flow rate. While centerline pressure data are available for plane air jets injected into air and water, no comparable data are available for the condensing vapor jet.

When the bath subcooling and the condensation driving potential is low or when jet superheating is high (say from chemical reaction), the jet cavity volumes can become large—more like submerged jets of noncondensible gases (Surin et al., 1983). One of the goals of the present work is to obtain measurements of penetration (condensation) lengths, expansion angles, and shapes associated with the condensing vapor cavity in a low condensation driving potential situation caused here by bath temperatures approaching saturation. Figure 1 is a sketch showing the relationship between these parameters and the vapor jet. High-speed flash photography was used to determine the shape and length of the vapor cavity. An additional goal of the experimental work reported here was to provide pressure data for the near injector region of plane underexpanded condensing steam jets that are injected horizontally into slightly subcooled water.

Theoretical efforts at describing the condensing vapor jets have made use of similitude arguments (Blake and Parnell, 1992; Blake and McDonald, 1993) and numerical modeling

---

[1] To whom correspondence should be addressed.

Contributed by the Heat Transfer Division for publication in the JOURNAL OF HEAT TRANSFER. Manuscript received by the Heat Transfer Division, June 23, 1997; revision received, May 20, 1998. Keywords: Condensation, Jets, Modeling and Scaling, Multiphase Flows, Plumes. Associate Technical Editor: J.-C. Han.

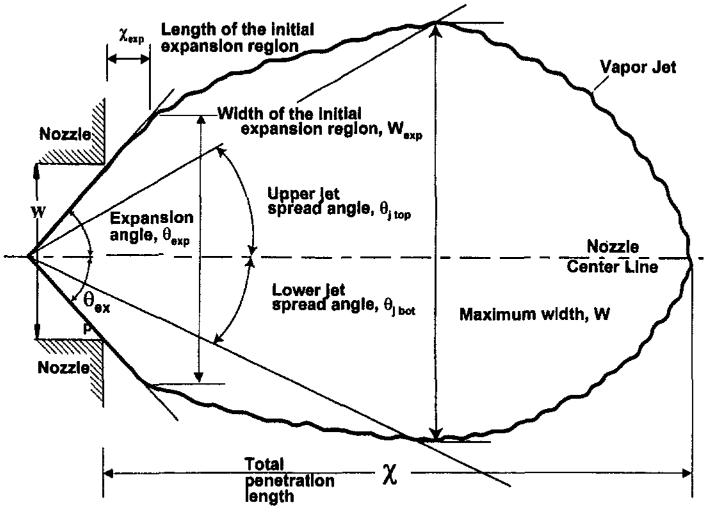

Fig. 1 Sketch showing the method for determining jet spread and expansion angles, and condensation lengths

(Chen and Faeth, 1982, 1983). Similitude arguments use dimensional analysis to extend existing empirical correlations. The numerical modeling efforts attempted to extend the k-ϵ-g model used for single-phase reacting jet applications. The studies of Blake and Parnell (1993) and earlier work of Chen and Faeth (1982) were limited to relatively small L/D_H (<15). The latter work of Chen and Faeth (1983) predicted reacting jet lengths that were shorter than those measured by Avery and Faeth (1975) for $50 \leq L/D_H \leq 82$. An additional objective of this paper is to present a numerical model which provides improved predictions of jet penetration length by more effectively modeling the effects of enhanced entrainment and condensation that occur with vapor jets.

Experimental Method

Apparatus. A sketch of the test apparatus is shown in Fig. 2 and more detailed specifications are available from Eden (1996). The main feature of the test apparatus was a rectangular fiberglass water tank 0.76 m wide, 0.9 m high, and 1.5 m long. The plane nozzle was mounted 38 cm above the bottom of the tank, and the depth of the water in the tank was maintained at 0.75 m. Overflow water was removed through a drain pipe. The design of the nozzle was similar to that used by Loth and Faeth (1989) for their air/water work. The plane nozzle had a slot height of 3 mm and width of 36 mm. A port was machined into the nozzle to allow access for measurement of the static pressure 2 mm upstream of the exit plane of the nozzle. The pressure tap was connected to a 0 to 1 MPa Heiss pressure gauge and a CEC 0-1.67 MPa pressure transducer.

The nozzle was connected to a steam plenum which provided a volume of 0.09 m^3 to minimize pressure oscillations in the steam at the highest flow rates (Kerney, 1970). A Heiss pressure gauge with a range of 0 to 1.67 MPa was used to monitor the internal plenum pressure measured by a CEC 0-2.34 MPa pressure transducer. Two type-K thermocouples measured the steam temperature inside the plenum. Slightly superheated steam was supplied by a Clayton Model E-202 steam generator. Steam pressure was controlled by a 1.67 MPa (gauge) dome regulator. For air jet runs, air was supplied at 9 ± 1°C from two large storage tanks with pressure controlled by a 2.34 MPa dome regulator.

Measurements and Test Conditions. A 30.5 cm diameter glass plate was mounted in the side of the tank to allow observation of the jet. A high-speed camera flash located above the jet with a light-reflecting surface on the tank opposite to the camera was used for photographing the jets. The flash photographs were taken using a Nikon model F-3 camera with a 60 mm micronikkor lens, and the f-stop set at f-8.

Nomenclature

A_D = jet nozzle area
B = condensation driving potential
C_p = specific heat
D = axisymmetric nozzle diameter
D_H = hydraulic diameter
F = empirical eddy viscosity constant
f = mixture fraction
g = acceleration due to gravity
h = enthalpy
h_{fg} = latent heat of vaporization
Ja = Jakob number
k-ϵ-g = turbulent kinetic energy-dissipation rate-square of mixture fraction fluctuations
L = jet length
L_c = characteristic jet dimension (D_H or w)
M = Mach number
$\dot{m}$ = mass flow rate
N = underexpansion ratio (P_e/P_∞)
P = pressure
Re = jet Reynolds number
Sc = Schmidt number
s = streamwise coordinate
u = streamwise velocity
w = nozzle width
W = dimensionless jet width (w/L_c)
$\dot{W}$ = droplet entrainment rate
v = transverse velocity
y = transverse coordinate
ρ = density
μ = viscosity
σ_f = turbulent Schmidt number
θ = jet deflection angle
γ_i = turbulence intermittency function
χ = dimensionless length (L/L_c)

Subscripts

e = nozzle exit plane
fs = saturated liquid
T = turbulent
∞ = bath
sat = saturation
jet = of the jet
v = vapor
l = liquid water
exp = expansion region

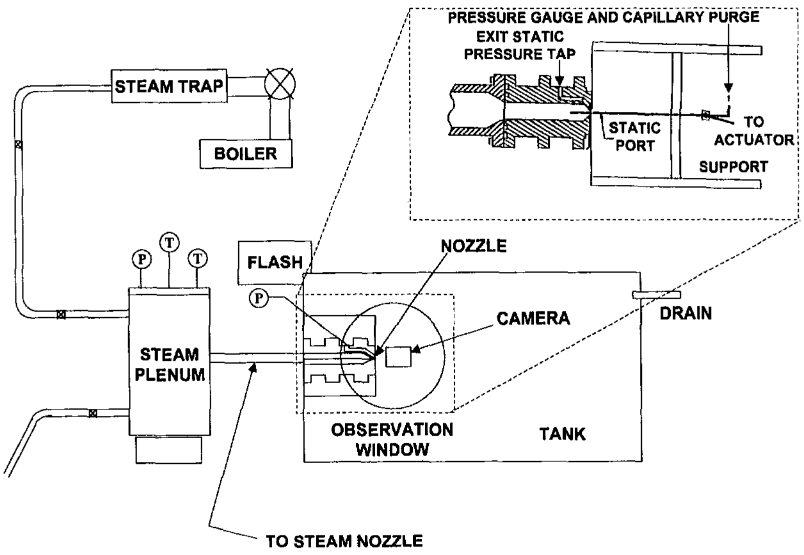

Fig. 2 Schematic of experimental test apparatus for the underexpanded steam jet study showing the ventilated pressure probe assembly

The static pressure along the axis of the jet was measured by a tap consisting of a 1.1 mm diameter, 127 mm long stainless steel tube. A static probe hole, 0.08 mm in diameter, was drilled in the side of the tube 102 mm from the upstream end of the tube. The tube was connected to a Heiss 0-0.8 MPa pressure gauge, a CEC 0-1.67 MPa pressure transducer, and a capillary purge. The pressure probe was connected to an actuator that positioned the probe along the jet axis. The movement of the actuator was controlled numerically, with an accuracy of ±0.2 mm. The pressure was observed with a Heiss vacuum/pressure gauge and data recorded with a CEC 0 to 1.67 MPa pressure transducer. For the tests, the probe traveled from six slot widths upstream to 15 slot widths downstream of the nozzle exit plane. Probe velocity was 0.3 mm/s and the pressure data were collected at 100 Hz. Pressure data were averaged over intervals of 0.1 seconds to provide a quasi-steady average static pressure at discrete locations. A capillary purge was used to prevent water from entering the probe. A microvalve was placed in the line to control the flow of high-pressure nitrogen and was opened until a slow stream of bubbles exited the probe, resulting in a pressure increase of less than 1.67 kPa in the probe.

Experiments were carried out for underexpansion ratios $N(P_e/P_\infty)$ of 2, 3, and 4. Theoretically, $N = 1.83$ corresponds to a choked condition for steam in a plane nozzle. The onset of the choked condition was evidenced by the transition of the jet from a "slugging/bubbling" type of operation to a more steady operation characterized by a loud high frequency noise. The water in the tank was heated to remove dissolved gases and allowed to cool overnight before testing. The static pressure and photographs were taken at several different water temperatures. Plenum pressure and temperature were monitored throughout with a standard deviation of two percent. Test conditions for this study are summarized in Table 1, which shows the condensation driving potential is $B = (h_{fs} - h_\infty)/(h_e - h_{fs})$, where h_{fs} is the enthalpy of the saturated liquid, h_∞ is the enthalpy of the bath, and h_e is the static enthalpy of the steam at the exit of the nozzle.

There were two main contributors to the uncertainty of the measurements: the steam supply and flow systems, and the method of determining the jet profiles. The uncertainty in the steam supply pressure system was ±19 percent, which was the principal uncertainty in pressure measurements as well. The profile of a steam jet at a given condition was determined from averaging the jet profiles from several photographs. The level of uncertainty for the jet profile was ±30 percent, for B^{-1} less than 55. The uncertainty for the jet profiles for B^{-1} greater than 55 was ±45 percent. The principal sources of uncertainty in the determination of B were from the measurements of the nozzle exit and bath temperatures (±4 percent).

Numerical Model

A numerical model of the underexpanded condensing jet that was rigorously derived by Eden (1996) combines the multiphase reacting jet model used by Lin (1990) and the single-phase buoyant jet model of Madni (1975). The set of governing equations is a parabolic form of the Navier-Stokes equations in a curvilinear coordinate system. The curvilinear coordinate system used an s-axis located along the jet trajectory (jet centerline), a y-axis oriented normal to it, and an angle θ representing an angle at any point between the trajectory tangent and the horizontal. As the algorithm marched along the s-axis, axisymmetric flow fields were determined at planes orthogonal to the jet centerline. The calculations began at the end of the expansion

Table 1 Summary of test conditions for underexpanded jets

Jet/Ambient	P_e/P_∞	$\dot{m}$ (kg/s)	$R_e/10^5$	ρ_∞/ρ_e	B^{-1}	u_e (m/s)
Steam/Water	2	0.064	1.4	858	8.1–81	530
	3	0.095	2.0	587	8.5–108	540
	4	0.113	2.6	448	9.7–161	490
Air/Water	2	0.100	1.6	337	—	325
	3	0.150	2.4	225	—	325
	4	0.195	3.2	169	—	320
Air/Air	2	0.100	1.6	0.4	—	325
	3	0.150	2.4	0.3	—	325
	4	0.195	3.2	0.2	—	320

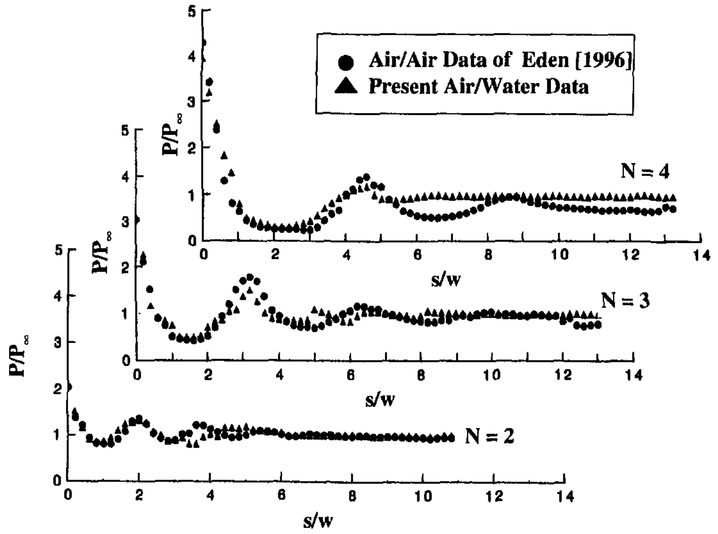

Fig. 3 Centerline static pressure measurements of an air jet into quiescent water for underexpansion ratios of P_e/P_∞ = 2, 3, and 4

and were marched in the streamwise direction after iteration to convergence at each streamwise location. The convergence condition for each streamwise step was when the flow reached the saturated liquid state at a mixture fraction of $f_{fs} = B/(1 + B)$. The mixture is a single-phase liquid for $f < f_{fs}$, and approaches the ambient liquid state as mixing continues and f approaches zero. The mixture fraction, f, is defined as the ratio of injected vapor mass flow rate to jet mass flow rate.

The jet centerline deflected due to the buoyant forces arising from the large difference between the densities of the vapor jet and the surrounding bath. The jet was treated as incompressible, with density effects included only in the buoyancy term. The conservation equations in terms of s, y, and θ are (Madni, 1975; Lin, 1990) as follows.

Continuity:

$$\frac{\partial}{\partial s}(u) + \frac{\partial}{\partial y}(v) = 0 \tag{1}$$

s-Momentum:

$$u\frac{\partial u}{\partial s} + v\frac{\partial u}{\partial y} = \frac{1}{\rho}\frac{\partial}{\partial y}\left((\mu + \mu_T)\frac{\partial u}{\partial y}\right) + \frac{\rho_\infty - \rho}{\rho_e} g \sin\theta \tag{2}$$

y-Momentum:

$$u^2\frac{\partial \theta}{\partial s} = \frac{\rho_\infty - \rho}{\rho_e} g \cos\theta \tag{3}$$

Mixture Fraction, f:

$$u\frac{\partial f}{\partial s} + v\frac{\partial f}{\partial y} = \frac{1}{\rho}\frac{\partial}{\partial y}\left(\left(\frac{\mu}{\mathrm{Sc}} + \frac{\mu_T}{\sigma_f}\right)\frac{\partial f}{\partial y}\right) \tag{4}$$

Madni and Pletcher (1975) modified Schetz's (1972) original model for the turbulent viscosity to account for intermittency effects:

$$\frac{\mu_T}{\rho} = \frac{2F\gamma_i}{w}\int_0^\infty |u_e - u| y dy \tag{5}$$

where F is an empirical constant equal to 0.012. The intermittency function, γ_i, is

$$\gamma_i = 1.0 \quad 0 \le \frac{y}{y_{1/2}} \le 0.8$$

$$\gamma_i = (0.5)^z \quad \frac{y}{y_{1/2}} > 0.8 \tag{6}$$

where $z = ((y/y_{1/2}) - 0.8)^{2.5}$ and $y_{1/2}$ is defined as the transverse distance from the jet centerline to the location where the velocity equals one-half the centerline velocity.

The locally homogeneous flow (LHF) model assumes infinite interphase transport rates so that both phases have the same velocity and are in thermodynamic equilibrium at each point in the flow. Because the velocities of the condensing vapor and entrained fluid are assumed to be equal, no knowledge of the interaction between the entrained drops and vapor is required. With these assumptions, the instantaneous properties at each point in the flow correspond to the state attained when an amount f (the mixture fraction) of injected vapor and 1-f of fluid from the surroundings at their initial states are mixed and brought to thermodynamic equilibrium at the local bath pressure. A tabulation of the steam tables along with the predicted mixture fraction were used to determine the jet enthalpy and composition. In the present model, mixing causes a reduction

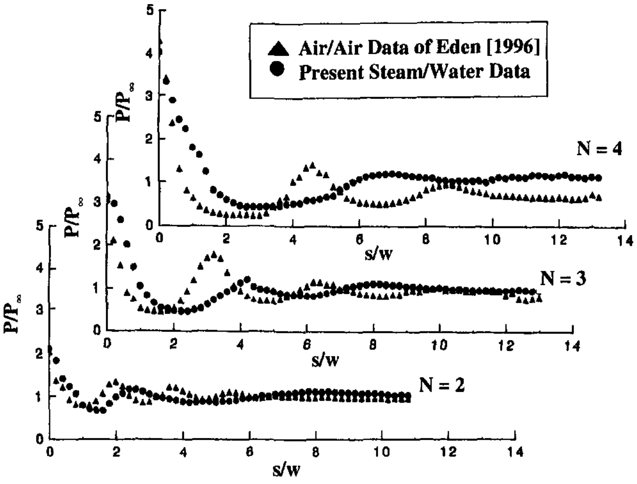

Fig. 4 Centerline static pressure measurements of a steam jet into quiescent water for underexpansion ratios of P_e/P_∞ = 2, 3, and 4

Table 2 Results from the photographic study of condensing steam jets

P_e/P_∞	T_b (°C)	B^{-1}	χ	$\chi_{\exp}$	$W_{\exp}/w$	$\theta_{\exp}$	θj_{top}	θj_{bot}
2	32.2	8.1	13.2	3.7	1.0	12.0	7.5	7.5
2	53.9	11.8	18.7	3.7	1.2	13.0	12.0	12.0
2	75.6	22.3	35.0	4.0	1.3	13.5	12.0	12.0
2	90.6	57.3	68.0	4.0	1.4	15.5	12.0	8.0
2	93	80.75	73.2	4.0	1.5	16.0	13.0	8.5
3	35.6	8.5	16.0	6.7	1.5	17.0	10.5	10.5
3	51.7	11.4	24.2	6.0	1.5	17.0	11.5	11.5
3	72.2	19.8	33.0	6.5	1.6	21.5	12.5	12.5
3	89.4	51.7	71.5	5.5	1.5	19.0	14.5	14.5
3	95	107.9	92.5	5.5	1.5	23.5	14.0	8.0
4	38.9	9.1	21.5	9.5	2.1	24.5	11.5	11.5
4	49	10.8	31.5	7.7	2.1	23.5	12.0	12.0
4	69.4	18.1	39.0	7.5	2.1	25.0	11.0	11.0
4	86.1	39.6	72.2	9.7	2.1	25.0	18.5	18.5
4	96.7	161.0	110.0	*	*	25.0	20.0	8.0

* Jet broke up before it could condense.

in the quality at constant temperature in the two-phase region (which is interpreted here as partial condensation). The entrained liquid results in increased density and reduced void fraction of the vapor when the mixture is brought to thermodynamic equilibrium.

The original model assumed that turbulent mixing governed both the rates of entrainment and of condensation. This form of the model substantially overpredicted the jet length because it had no mechanism to account for the entrainment of droplets and, consequently, underpredicted the mixing and entrainment rates. To correct this, the entrainment rate, $\dot{W}$ (divided by the steam mass flow rate), was used to determine the change in the mixture fraction produced by the additional entrained mass, $\Delta f = \dot{W}/\dot{m}_e$. Chawla's (1975, 1976) work provided a model for $\dot{W}$:

$$\dot{W} = 2w^2\rho_l\left(\frac{\lambda_m}{w}\right)^a \omega_c^b\left(\frac{\chi - \chi_o}{\chi_o}\right)u \exp\left(\frac{\chi_o w\alpha}{cu}\right) \tag{7}$$

where w is the nozzle width, λ_m is the wavelength of the maximum disturbance in the liquid/vapor interface, χ_o is the length required for the amplitude of a disturbance to become large enough to be sheared off, ω_c is a wave speed, and α is an amplification factor. Expressions for these parameters, as well as the empirical constants a, b, and c, are available in Chawla (1975, 1976) or Eden (1996).

The entrained drops are heated to saturation temperature by the jet vapor, thus reducing the vapor fraction of the jet. An energy balance can be written:

$$\Delta f \rho_l C_{p_l}(T_{\text{sat}} - T_\infty) = \Delta f_p(h_{fg} + \rho_v C_{p_v}(T_{\text{jet}} - T_{\text{sat}})) \tag{8}$$

where Δf_p is the modified change in mixture fraction. Solving for Δf_p, and assuming that $C_{p_v}(T_{\text{jet}} - T_{\text{sat}})$ is very much less than h_{fg}, yields an expression in terms of the Jakob number ($\text{Ja} = C_{pl}(T_{\text{sat}} - T_\infty)/h_{fg}$):

$$\Delta f_p = \Delta f\left(\frac{\rho_l}{\rho_v}\right)\text{Ja}. \tag{9}$$

Kutateladzes (1952) noted that the effects of bringing subcooled liquid up to the saturation temperature of the vapor required a modification of the Jakob number and proposed the following correlation:

$$\text{Ja}_m = C_o\left(\frac{\rho_l}{\rho_v}\right)^m \text{Ja} \tag{10}$$

where C_o and m are empirical constants. The Jakob number in

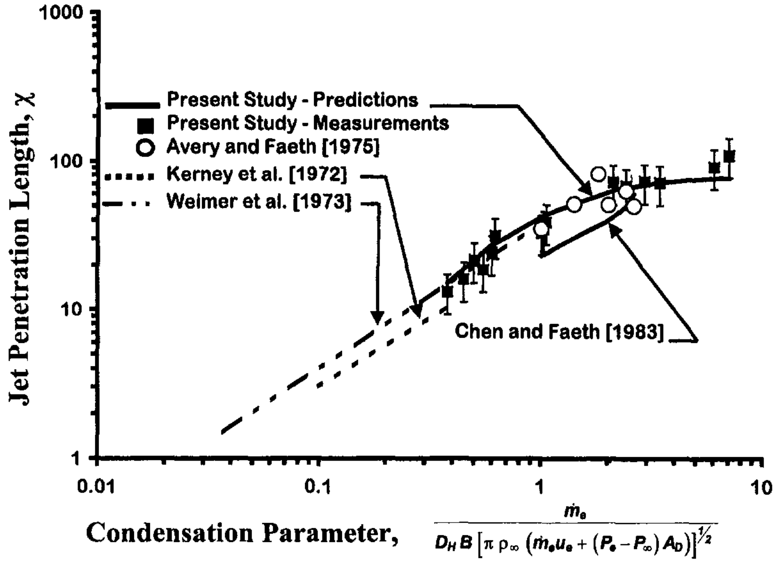

Fig. 5 Dependence of dimensionless jet penetration length on the dimensionless condensation parameter (error bars represent a 30 percent spread)

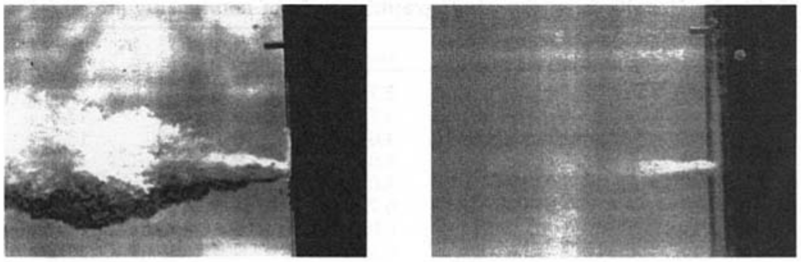
(a) (b)

Fig. 6 Photographs of condensing steam jets in water for $P_e/P_\infty = 4$ and (*a*) small condensation potential ($B = 0.09$) and (*b*) large condensation potential ($B = 0.23$)

Eq. (9) was replaced by the correlation, Eq. (10), where for this study C_o was set equal to unity and m was varied until the model yielded the best predictions ($m = 0.93$).

The equations were solved using an explicit DuFort-Frankel formulation with equal spacing in the radial direction and variable grid spacing in the axial direction. The solution at each axial location was based on the previous step. The model was exercised for each condition until a grid-independent solution was obtained. The number of nodes required for a grid-independent solution ranged from 175 to 219 in the radial direction and from 4800 to 11,800 in the axial direction for $B^{-1} = 8.1$ and 161, respectively.

The transport Eqs. (1) to (4) are first order with respect to s and require three initial conditions:

$$u(s_e, y) = u_e(y), \quad f(s_e, y) = f_e(y), \quad \theta(s_e) = \theta_e \quad (11)$$

where $u_e(y)$ and $f_e(y)$ are the initial velocity (plug) and mixture fraction (f_e equal unity) profiles, respectively, and θ_e is the initial angle between the jet centerline and the horizontal ($\theta_e = 0$). Weimer et al. (1973), Chen and Faeth (1982), Sun and Faeth (1986), and Chan and Kennedy (1975) used the "effective adapted jet" or "divergent nozzle" approximations to expand the flow from the injector exit conditions to the local bath pressure. However, these methods produce nonphysical initial conditions for condensable vapor. Instead, initial conditions for these calculations were determined from the measured exit pressures and temperatures and a method of characteristics (MOC) based near-injector treatment (Eden, 1996). Two boundary conditions were required for u and f, and a single boundary condition required for v:

$$\frac{\partial u}{\partial y}(s, 0) = \frac{\partial f}{\partial y}(s, 0) = 0, \quad v(s, 0) = 0$$

$$\lim_{y\to\infty} u = u_\infty, \quad \lim_{y\to\infty} f = f_\infty \quad (12)$$

where the ambient conditions $u_\infty(s)$ and $f_\infty(s)$ were set equal to zero for this study.

Results and Discussion

Centerline Pressure Measurements. Loth and Faeth (1990) verified the existence of shock cell structures in the expansion region of a choked air jet submerged in water. Upon leaving the nozzle, the jet is in an underexpanded condition and undergoes a Prandtl-Meyer expansion. The centerline static pressure of the jet decreases rapidly during the expansion, with a corresponding increase in width. The maximum jet width and velocity corresponds to the minimum static pressure. The centerline static pressure then increases, and the centerline velocity decreases as the jet experiences pressure recovery. In an isentropic flow, the pressure recovery is complete, with the centerline static pressure equal to the pressure at the exit plane of the injector. A shock occurs at this location, and the cycle of expansion and recovery repeats. In a real flow, viscous and entrainment effects lead to mixing with the ambient fluid which reduces the pressure recovery. This is particularly important for submerged gas jets because of the large mixing rates associated with the large density ratios between bath and jet (Chen and Faeth, 1982, 1983). The pressure recovery in each successive downstream shock cell is reduced until the mixing reaches the centerline of the jet, the static pressure is equal to the ambient

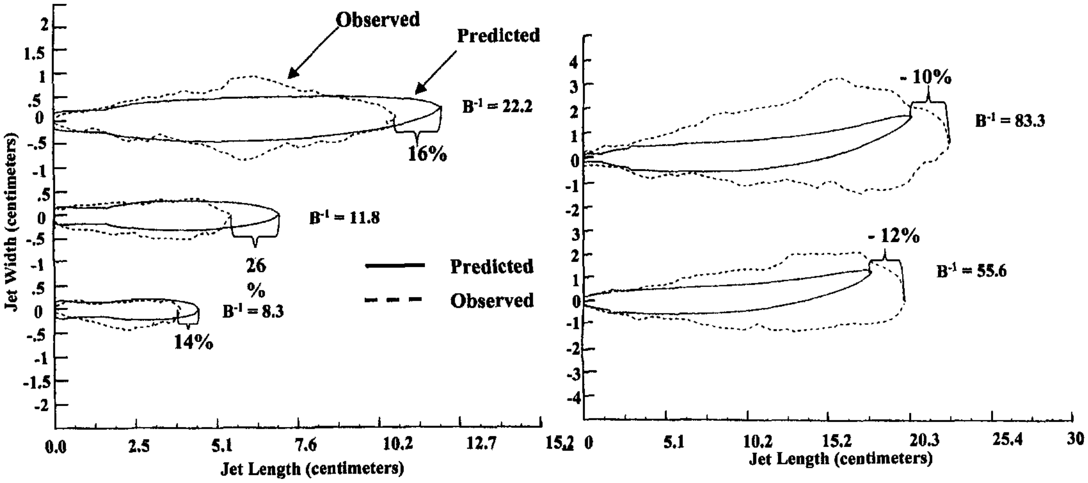

Fig. 7 Observed (dashed line) and predicted (solid line) vapor jet cavities for $P_e/P_\infty = 2$ and various condensation driving potentials

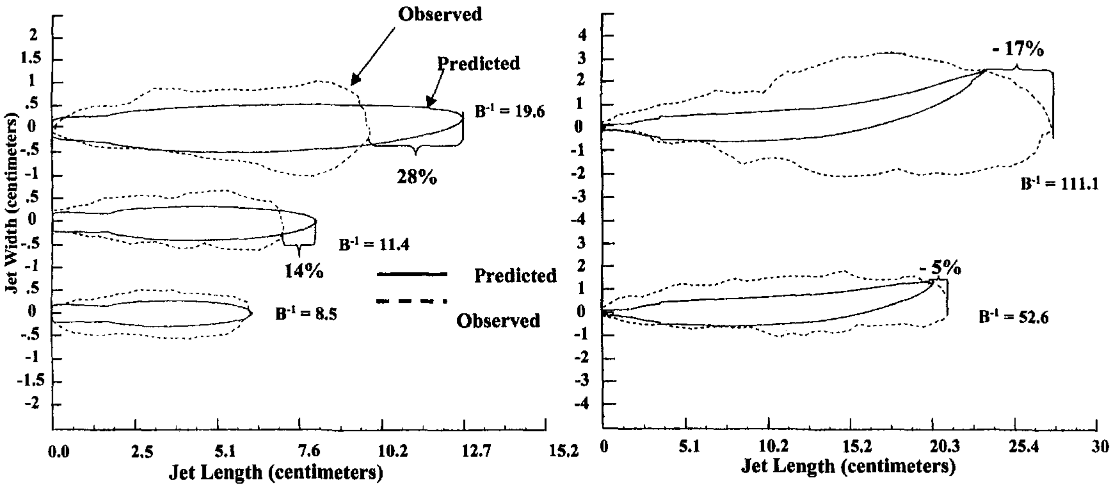

Fig. 8 Observed (dashed line) and predicted (solid line) vapor jet cavities for $P_e/P_\infty = 3$ and various condensation driving potentials

pressure, and the steam jet becomes a subsonic momentum-dominated constant-pressure jet.

Pressure measurements for underexpansion ratios of 2, 3, and 4 for a submerged air jet were made in order to compare with the condensing vapor jet. These are plotted in Fig. 3 along with the corresponding air-air data measured by Eden (1996) using the same test rig. Although the shock cell lengths are nearly the same, the centerline static pressures do not show the same level of recovery. This is due to the increased viscous shear losses at the air/water interface, losses associated with the entrainment and acceleration of liquid drops in the flow, and the work required for the air to expand against the water. Loth and Faeth's (1990) pressure measurements for submerged air jets showed very similar behavior relative to their air-air jets.

Pressure measurements were repeated for steam jets in water, and the results are shown plotted in Fig. 4 for underexpansion ratios of 2, 3, and 4. These results show that the oscillatory pressure behavior associated with a shock cell still exists for the condensing steam jet. The pressure recovery at the end of each expansion cell is much lower for the steam jets in water relative to the submerged air jets, and consequently, the number of cells is reduced for the steam jets. Some of the difference is attributed to the different mass flow rate of steam relative to air for the same underexpansion ratio. However, the principal cause of the greater pressure loss relative to the air/water cases was attributed to the condensation of the steam (Eden, 1996). Centerline pressure measurements were repeated for different bath temperatures and found to show good agreement amongst each other in spite of the differences in cavity size and shape further downstream of the nozzle.

Geometric Characteristics. Geometric measurements were obtained from the flash photographs of steam jets at the three underexpansion ratios and different bath temperatures and were made dimensionless by dividing by the height of the nozzle exit. Dimensionless data include χ, the total penetration length of the jet; χ_{exp}, the length of the first shock cell; W_{exp}, the width at the end of the initial expansion region; θ_{exp}, the spread angle of the expansion zone; $\theta_{j\mathrm{top}}$, the spread angle of the top of the jet; and $\theta_{j\mathrm{bot}}$, the spread angle of the bottom of the jet. The spread angle of the top and bottom of the jet was measured to help define the onset of the influence of buoyancy. The relationship between these parameters and the jet were shown in Fig. 1, with measurements summarized in Table 2. Note that at the lowest bath subcooling the jet dispersed before condensation was complete.

The underexpansion ratio and bath temperature determine the value of B. Increasing the value of B^{-1} (decreasing B), reduces

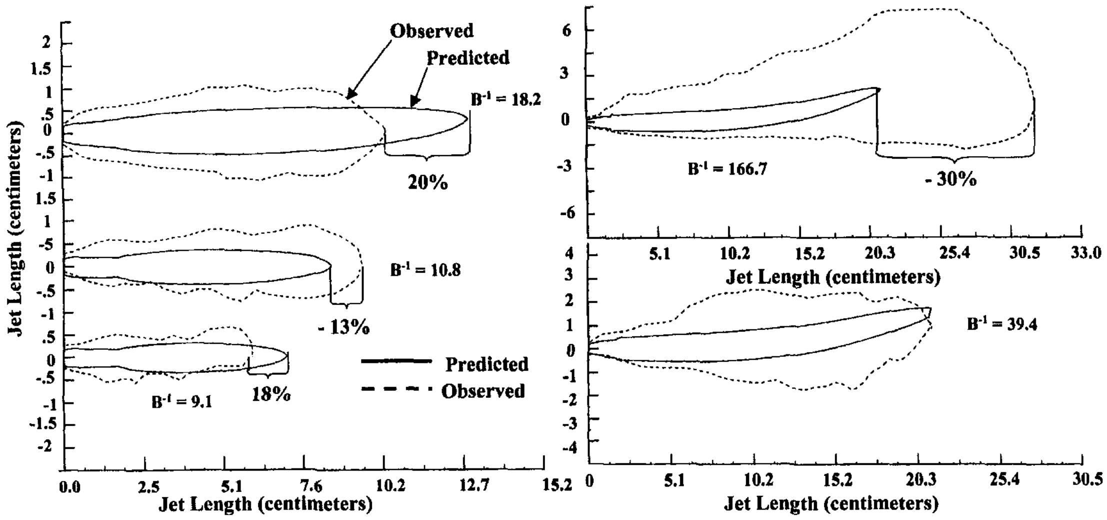

Fig. 9 Observed (dashed line) and predicted (solid line) vapor jet cavities for $P_e/P_\infty = 4$ and various condensation driving potentials

the condensation driving potential, and thus increases the jet penetration (condensation) length. The dimensionless penetration length is plotted in Fig. 5 along with the correlations determined by Kerney et al. (1972) and Weimer et al. (1973) for condensing round jets and the data of Avery and Faeth (1975) for reacting-condensing round jets. For χ less than 70, the measurements agree well with the correlation of Wiemer et al. (1973):

$$\chi = C\left\{\frac{\dot{m}_e}{D_H B[\pi\rho_\infty(\dot{m}_e u_e + (P_e - P_\infty)A_D)]^{1/2}}\right\} \quad (13)$$

which had a mean error of 20 percent relative to their measurements. The term in the curly brackets is defined here as the condensation parameter, and the normalizing length was the nozzle width (w) and the diameter (D) for the plane jets (measured here) and axisymmetric jets (measured by others), respectively. For the plane jets considered here, and for Wiemer et al.'s (1973) axisymmetric jets, $C = 35.5$ for χ less than 70.

For larger values of $\chi(>70)$ the condensation length deviates from the correlation—a behavior suggested by Avery and Faeth's (1975) measurements of a submerged reacting jet. Also plotted in Fig. 5 are predictions of the jet penetration length obtained from the model described here. Predicted lengths agree well with the measurements made here and the correlation of Weimer et al. (1973) over the range of the correlation's validity. At higher values of χ, the model predictions show the same trend as, and agree well with, the measurements in this region. This improvement in prediction relative to previous simulations (Chen and Faeth, 1983) results from the inclusion of the effect of enhanced entrainment rate and condensation.

Cavity Shapes. The spread angle of the jet is distinct from the angle of the initial expansion and is defined as the angle between the steam/water interface and the centerline of the nozzle. For χ greater than 50, the angle below the horizontal was less than the angle above—an indication of buoyant effects on the jet trajectory. Buoyant forces were clearly evidenced by jet centerline curvature for χ greater than 50 and underexpansion ratios of 3 and 4. The initial expansion angles are relatively constant for B^{-1} less than 70. Vapor bubbles which were attributed to boiling appeared on the nozzle face for B^{-1} values greater than 70 and made the determination of expansion angles at water temperatures approaching the saturation point difficult.

Steam jets operating in large subcooled conditions ($B^{-1} < 6$) appear as clouds of fine white mist where the steam/water interface is fairly well defined and the jet remains two-dimensional. For low subcooling, there is a dramatic change in the jet behavior because of the increased amount of liquid that is entrained. Large-scale structures are present in the jet, the steam/water interface becomes much more irregular, and the jet becomes more three-dimensional and behaves much like a submerged air jet. The differences in the structure of two steam jets at $N = 4$ are illustrated in Fig. 6 for $B^{-1} = 4$ and 11.

The shapes of the underexpanded steam jet cavities for several values of B^{-1} corresponding to $N = 2$ are shown in Fig. 7. The jet profiles predicted here agree well with experimental profiles at higher values of the condensation driving potential. Chen and Faeth's (1982) predicted jet profiles showed a rapid decrease in the jet width in the near nozzle region, which is typical of small B^{-1}. At intermediate values of B^{-1}, vapor jet cavities show an initial slight necking, followed by a fuller expansion. The steam jet had a relatively uniform interface for smaller values of B^{-1}; however, as B^{-1} increased the cavity interface became more irregular. For larger B^{-1}, the effects of buoyancy became more apparent as the cavity showed a tendency to curve up and started to show a fuller dispersion. Buoyancy causes the jet to become asymmetric, and at the large jet lengths the flow is no longer parabolic. Very wide vapor cavities are characteristic of air jets in water (Loth and Faeth, 1990), which vapor jets with very low condensation potential begin to mimic.

Cavity profiles at $N = 3$ and 4 are shown in Figs. 8 and 9, respectively. For larger values of B^{-1}, the discrepancy between the predicted and observed cavity widths became more pronounced. These comparisons show a trend towards greater discrepancy between numerical predictions and experimental observation as N is increased. The use of the locally homogeneous flow approximation becomes less appropriate with increasing underexpansion ratio and larger values of B^{-1}.

Conclusions

A study of underexpanded vapor jets with low condensation driving potential was undertaken using flash photography. The shapes of the vapor cavities were determined and compared with numerical predictions using a parabolic, locally homogeneous flow model with modifications for entrainment and condensation. For higher condensation potentials, the condensation length of the plane jets showed close agreement with published measurements of round vapor jets (when nondimensionalized using nozzle width rather than diameter). Vapor jets with low bath subcooling showed similar behavior to vapor jets with high vapor superheating (from chemical reaction). Predictions of jet penetration length were in good agreement over the entire range of measurements, and showed the proper deviation from published correlations at larger values of the condensation parameter. For lower condensation potential and/or underexpansion ratios, the observed vapor cavities were much wider than numerical predictions.

A ventilated pressure probe was used to measure static pressures along the axis of the condensing jet. Pressure measurements of the vapor jets showed the existence of the expansion/compression cells characteristic of the underexpanded shock cell structure seen in air/water jet combinations. The shock cell lengths of the condensing vapor jets were substantially longer, and the degree of pressure recovery substantially less than comparable submerged air jets. This was attributed to the combined effects of condensation of the vapor and evaporation of bath liquid as well as, to a lesser extent, the lower mass flow rate of steam relative to air operating at the same underexpansion ratio.

References

Avery, J. F., and Faeth, G. M., 1975, "Combustion of a Submerged Gaseous Oxidizer Jet in a Liquid Metal," *Fifteenth Symposium (International) on Combustion,* The Combustion Institute, Pittsburgh, PA, pp. 501–512.

Binford, F. T., Stanford, L. E., and Webster, C. C., 1968, "Nuclear Safety Program Annual Progress Report for Period Ending December 31, 1968," ONRL Report 4374, UC-80-Reactor Technology, pp. 234–250.

Blake, T. R., and McDonald, M., 1993, "An Examination of Flame Length Data from Vertical Turbulent Diffusion Flames," *Comb. and Flame,* Vol. 94, pp. 426–432.

Blake, T. R., and Parnell, L. A., 1992, "Dimensional Analysis and Similitude of Physicochemical Phenomena with Injection of a Gas Oxidizer into a Liquid Metal Fuel Bath," AIAA Paper 92-3140, 28th Joint Propulsion Conference, Nashville, TN.

Chan, K. C., 1982, "Dynamical Pressure Pulse in Steam Jet Condensation," *Int. J. of Multiphase Flow,* Vol. 8, pp. 11–20.

Chan, T. L., and Kennedy, J. F., 1975, "Submerged Buoyant Jets in Quiescent Fluids," *Journal of the Hydraulics Division,* Vol. 6, pp. 733–747.

Chawla, T. C., 1975, "Rate of Liquid Entrainment at the Gas-Liquid Interface of a Liquid Submerged Sonic Gas Jet," *Nuclear Science and Engineering,* Vol. 56, pp. 1–6.

Chen, L-D., and Faeth, G. M., 1982, "Condensation of Submerged Vapor Jets in Subcooled Liquids, Jets," ASME JOURNAL OF HEAT TRANSFER, Vol. 104, pp. 774–780.

Chen, L-D., and Faeth, G. M., 1983, "Structure of Turbulent Reacting Gas Jets Submerged in Liquid Metals," *Comb. Science Tech.,* Vol. 31, pp. 277–296.

Cho, D. H., Armstrong, D. R., and Bova, L., 1990, "Experimental Study of Reacting Gas Jets in Liquids: Heat Release Effects," *Chem. Engr. Science,* Vol. 45, pp. 423–435.

Chun, J. H., and Sonin, A. A., 1985, "Small-Scale Simulation of Vapor Discharges into Subcooled Liquid Pools," *Nuclear Engineering and Design,* Vol. 85, pp. 353–362.

Chuech, S. G., Lai, M. C., and Faeth, G. M., 1982, "Structure of Turbulent Sonic Underexpanded Free Jets," ASME JOURNAL OF HEAT TRANSFER, Vol. 104, pp. 774–780.

Eden, T. J., 1996, "Condensing Vapor Jets," Ph.D. thesis, The Pennsylvania State University, University Park, PA.

Hughes, T. G., Smith, R. B., and Kiely, D. H., 1983, "Stored Chemical Energy Propulsion Systems for Underwater Applications," *J. Energy,* Vol. 7, pp. 128–133.

Kataoka, I., and Ishii, M., 1982, "Mechanism and Correlation of Droplet Entrainment and Deposition in Annular Two-phase Flow," Argonne National Laboratory Report, ANL/RAS/LWR 82-44.

Kerney, P. J., Faeth, G. M., and Olson, D. R., 1972, "Penetration Characteristics of a Submerged Steam Jet," *AIChE Journal,* Vol. 18, pp. 548–553.

Kerney, P. J., 1970, "Characteristics of a Submerged Steam Jet," Ph.D. thesis, The Pennsylvania State University, University Park, PA.

Kudo, A., Egasu, T., and Toda, S., 1974, "Basic Study on Vapor Suppression," *Proceedings of the Fifth International Heat Transfer Conference,* Vol. 3, Tokyo, pp. 226–230.

Kutateladzes, S. S., 1952, "Heat Transfer During Condensation and Boiling," translated from a publication of *State Scientific and Technical Publishers of Literature and Machinery,* Moscow-Leningrad, as AEC-TR-3770.

Lin, T. F., 1990, "Modeling of Submerged Liquid Metal Combustion," 27th JANNAF Combustion Meeting, Nov. 5–9, Cheynne, WY.

Loth, E., and Faeth, G. M., 1990, "Structure of Plane Underexpanded Air Jets into Water," *AIChE Journal,* Vol. 36, No. 6, pp. 818–826.

Loth, E., and Faeth, G. M., 1989, "Structure of Underexpanded Round Air Jets Submerged in Water," *Int. J. of Multiphase Flow,* Vol. 15, Paper No. 4, pp. 589–603.

Madni, I. K., and Pletcher, R. H., 1995, "Prediction of Turbulent Jets in Coflowing and Quiescent Ambients," *Journal of Fluids Engineering,* Vol. 97, pp. 558–567.

Madni, I. K., 1975, "A Finite-Difference Analysis of Turbulent, Axisymmetric, Buoyant Jets and Plumes," Ph.D. thesis, Iowa State University, Ames, IA.

Schetz, J. A., 1972, "Free Turbulent Mixing in a Co-Flowing Stream," Proceedings of the Langley Working Conference of Free Turbulent Shear Flows, NASA SP-321, Vol. 1, pp. 259–276.

Sun, T-Y., and Faeth, G. M., 1986, "Structure of Turbulent Bubbly Jets-I. Methods and Centerline Properties," *Int. J. Multiphase Flow,* Vol. 12, pp. 99–117.

Surin, V. A., Evchenko, V. N., and Rubin, V. M., 1983, "Propagation of a Gas Jet in a Liquid," *Journal of Eng. Physics* (translated from Russian), Vol. 45, pp. 1091–1101.

Weimer, J. C., Faeth, G. M., and Olson, D. R., 1973, "Penetration of Vapor Jets Submerged in Subcooled Liquids," *AIChE Journal,* Vol. 19, pp. 552–558.

Young, R. J., 1975, "Interaction Between a High Velocity Vapor Jet and an External Coaxial Concurrent Water Flow," Ph.D. thesis, University of Notre Dame, South Bend, IN.

P. Cerisier

M. Jaeger

M. Medale

S. Rahal

IUSTI UMR CNRS 6595,
University of Provence,
13453 Marseille Cedex 13, France

Mechanical Coupling of Convective Rolls in a High Prandtl Number Fluid

Experimental and numerical studies (using the finite element method) were conducted in a rectangular vessel for a high Prandtl number fluid ($Pr = 880$ at 25°C). The pattern of convective rolls is perturbed by lateral heating of one of the smaller sides of the box. The wave number of the roll pattern is within a narrow range (± 10 percent at $R = 4.6R_c$ where R and R_c are the Rayleigh number and its critical value of Bénard convection). The formation of a large roll induced by the lateral heating causes a slight variation in the wave number of the rolls, accompanied by the disappearance of pairs of rolls, or single rolls, depending on the boundary conditions at the other small side of the enclosure. In all instances, this disappearance respects the mechanical coupling between the rolls. Temperature and velocity fields are assessed, as well as the heat transfer. The transient states observed during the experimentation are well reproduced by the two-dimensional numerical model developed for this study.

1 Introduction

Natural thermoconvection within an enclosure has been studied extensively in the last few decades, both in terms of fundamental understanding and practical applications. These studies focus on two basic features: (i) correlation between heat transfer, the physical properties of the fluid, the shape of the container, and the applied temperature field; (ii) determination of the hydrodynamic characteristics and description of the space-time behavior of the convective structures.

Rayleigh-Bénard (RB) convection appears in a fluid layer bounded by two flat horizontal surfaces heated uniformly from below and cooled from above. Close to the threshold, the structure most often observed is formed of rolls parallel to the smaller side of the rectangular enclosure. They correspond to a mechanical coupling given that the rolls revolve in opposite direction, i.e., they rotate in a gear-like fashion. When the temperature gradient increases, transitions then lead the system through different states and ultimately to a turbulent flow. This system is currently considered as the reference example for the study of dynamical regimes, turbulence and of the different processes that lead to these states (Koschmieder, 1993; Bergé et al., 1988; Manneville, 1990).

For a fixed value of the Prandtl number (Pr), Rayleigh-Bénard convection undergoes a number of discrete transitions, remaining in each regime for a finite range of Rayleigh number (R), which is the characteristic nondimensional number in this problem. A large number of studies were carried out to answer several questions. In which region of the (R, Pr) space does one observe two-dimensional rolls? Are they steady or not? What is the nature of the instabilities which lead from two-dimensional rolls to three-dimensional patterns?

A nonlinear analysis of the stability problem (Busse, 1978) gave a region of stable two-dimensional rolls which is often referred as the "Busse balloon" named after F. Busse who identified the different secondary instabilities (zig-zag, cross-rolls, knot, etc.) beyond which different types of convective states are observed. These states correspond either to steady roll patterns more complicated than the initially two-dimensional ones or to time-dependent ones which may be periodic or not.

An accurate experimental validation of the predicted stability diagram is not easy to carry out since the ideal geometry of the theory cannot be built. However, the predictions were confirmed experimentally at least qualitatively (Krishnamurti, 1970; Busse and Whitehead, 1971; Gollub et al., 1982; Kolodner et al., 1986; Kirchartz and Oertel, 1988; Croquette, 1989), both in the approximate location of the marginal stability and in the nature of each instability.

On the other hand, the thermoconvective flows inside a vertical enclosure submitted to a horizontal temperature gradient were extensively studied as a function of the same parameters (aspect ratio, fluid characteristics, and temperature difference). One has thus been able to observe stationary and nonstationary regimes, multiple-cell and single-cell structures depending on the magnitude of the temperature gradient (Stork and Muller, 1972; Chikhaoui, 1989; Daniels and Wang, 1994). In the case of narrow containers, the flow is initially made up of two shear layers. The structure then takes the form of transverse rolls which overlap the initial flow, given the intense shear. This is a generally recognized phenomenon.

The case of horizontal enclosures submitted to a horizontal temperature gradient has also been investigated. Here again, the motion generally consists of a main roll extending over the whole cavity. In the case of large aspect ratios (length/height), high shearing is produced, sometimes leading to secondary rolls to decrease the shear (Elder, 1965; Imberger, 1974; Patterson and Imberger, 1980; Simpkins and Chen, 1986; Wang and Daniels, 1994; Schoepf and Patterson, 1995).

The configuration of quasi-cubical enclosures (with low Prandtl fluid) with two heated walls was studied in recent years, notably in view of developing solar heating systems and improving the comfort of individual homes (Karyakin et al., 1988; Breton, 1989). From a theoretical point of view, Nield (1994) has examined the convection induced by an oblique temperature gradient applied to a shallow horizontal layer. To our knowledge, no research has been undertaken on the problems encountered when several heating surfaces induce different convective regimes which compete in distinct regions of the enclosure.

In this paper, we study convection of a large Prandtl number fluid in a horizontal rectangular cavity in which a vertical temperature gradient is initially applied (RB convection). A local-

---

Contributed by the Heat Transfer Division for publication in the JOURNAL OF OF HEAT TRANSFER. Manuscript received by the Heat Transfer Division, Oct. 20, 1997; revision received, June 2, 1998. Keywords: Experimental, Finite Element, Heat Transfer, Liquid, Natural Convection. Associate Technical Editor: P. Simpkins.

ized horizontal temperature gradient perpendicular to the axis of the rolls is then applied to the liquid by heating one of the lateral walls. The basic questions arising are: (i) How is the roll pattern modified by the additional heat transfer (produced by heating the lateral wall)? (ii) Do any new rolls appear at the heated lateral wall? (iii) How does the roll under the influence of the lateral heating interact with the already existing pattern? (iv) If the size of this roll increases, does it compress the roll pattern or does any roll disappear, in order to maintain a given bandwidth? (v) How are the velocity and temperature fields modified?

The paper is organized as follows. The experimental set-up is described in Section 2, whereas the experimental procedures are presented in the following one. Section 4 is devoted to the numerical model developed for this study. Both experimental and numerical results are presented and discussed in Section 5. Finally some conclusions are given in Section 6.

2 Experimental Set-Up

The vessel is a parallelepiped cavity ($12 \times 3 \times 1$ cm^3, cf. Fig. 1) filled with Rhodorsil 47V100 silicone oil, which physical properties are given in the Appendix (Prandtl number = 880 at 25°C). The walls are made of transparent "Lexan" polycarbonate, which physical properties are also given in the Appendix. The thickness of walls A and A' is 1 cm, that of C and C' is 0.3 cm, whereas that of B and B' (the other two lateral walls which are not shown in Fig. 1) is 1 cm. The walls have about the same thermal conductivity as oil. Therefore, the convection occurs in a box with moderate aspect ratios ($\Gamma_x = 12$, $\Gamma_y = 3$) between walls of moderate thermal conductivity. Under these conditions, the theoretical critical Rayleigh number R_c for the RB problem is approximately 1420 (Cerisier et al., 1997), which corresponds to $\Delta T_c = 1.55$°C for this oil at 30°C.

The horizontal walls C and C' are in contact with a heating and a cooling water flow at temperatures regulated by thermostatically controlled baths. In each of the two small lateral walls A and A', a copper parallelepiped ($5 \times 0.5 \times 0.5$ cm^3) is embedded horizontally. The part played by these copper rods is one of the following: (i) through a slight heating or cooling, one is able to impose the direction of rotation of the roll adjacent to the wall (when T_A, respectively, $T_{A'}$, is larger than the mean fluid temperature the flow is necessarily upwards, whereas it is downwards in the opposite case); (ii) through a higher heating of one of the rods (wall A in our study), one can generate a natural convection induced roll whose size depends on the strength of the heating.

In order to heat the wall A, an electric resistance is installed inside the copper part of this wall. On the other hand, one horizontal pipe containing a thermostatically controlled liquid flow is in the copper part of wall A' in order to produce a moderate cooling or heating. Under these conditions, the temperature of A' can be adjusted to $T_m = (T_C + T_{C'})/2$ or to a temperature slightly lower or higher than T_m. In the first case, the direction of rotation of the roll near A' wall is not imposed, it is free. In the second case, the flow direction is downward along A' whereas it is upward in the third case.

The temperatures in C and C' and in the copper part of A and A' are measured in steady states with 14 thermocouples (diameter = 0.5 mm, accuracy ± 0.05°C).

The flows are visualized in the vertical and horizontal planes using a laser sheet. The streamlines (steady states) and the trajectories (transient states) are made observable using small aluminum flakes dispersed in the liquid. The photographic exposure time is 45 sec. for steady states and 15 sec. for transient regimes.

3 Experimental Procedures

3.1 Series 1. In this case, Rayleigh-Bénard convection is studied in a non-"classical" box: the horizontal plates and the two opposite side walls have moderate thermal conductivity, whereas the two short side walls are made of copper, a good heat conductor. A vertical temperature gradient greater than the critical value is applied to the liquid layer and a roll pattern parallel to the small side walls A and A' is observed in the fluid layer (Fig. 2(a)). Note that the flow direction of the roll near A (or A') can be imposed by fixing T_A (or $T_{A'}$), whereas if the action of the vertical temperature gradient is considered alone, this roll is allowed to rotate in either direction. Thus, when A (or A') is warm, the flow is upward along A (or A') whereas it is downward when A (or A') is cold.

3.2 Series 2. First, a vertical temperature gradient is applied between C and C', as described in series 1. The stable RB roll pattern being established, the temperature of wall A is then increased to a fixed value. The size of the roll adjacent to wall A (which is either a new roll or an already existing one, see Section 5) increases and disturbs the existing RB roll pattern. When a steady regime is reached, T_A is again increased and so on. Figures 2(b–d) show the perturbed roll pattern obtained for three values of T_A (29.8°C, 44.4°C, and 60.9°C). It appears that the size of the roll adjacent to wall A increases and that of the other roll (RB rolls) stays nearly constant. Hence, the number of RB rolls decreases from ten (series 1: $T_A = 24$°C which nearly corresponds to the mean temperature of the oil) to nine ($T_A = 29.8$°C) then to seven ($T_A = 44.4$°C) and finally

Nomenclature

A, A' = sidewalls at the ends
B, B' = large vessel sidewalls
C, C' = bottom and top of the vessel
C_p = heat capacity
d = thickness of the silicone oil layer
g = acceleration of gravity
k = nondimensional wave number
Nu = Nusselt number
p = pressure
Pr = Prandtl number = $\mu_0 C_p/\lambda$
R = Rayleigh number = $\rho_0^2 C_p \beta g \Delta T d^3/\mu_0 \lambda$
RB = abbreviation of Rayleigh-Bénard
T = temperature
U = upward
D = downward
u, v, w = velocity components in x, y, z directions
x, y, z = Cartesian coordinates

Greek Symbols

β = thermal expansion coefficient
γ_i = coefficient of proportionality between Pr and Pi
Γ_i = aspect ratio in the i direction
ΔT = vertical temperature difference applied to the oil layer by the thermostatically regulated water flows
ϵ = distance from the threshold
λ = thermal conductivity
Λ = nondimensional wavelength
μ = dynamic viscosity
ν = kinematic viscosity
ρ = density

Subscripts

A, A' = sidewalls at the ends
B, B' = large sidewalls
C, C' = bottom and top of the vessel
c = critical value
co = cold wall
h = hot wall
mi = middle height
m = mean value
ref = reference scales
0 = value at $T = T_0$

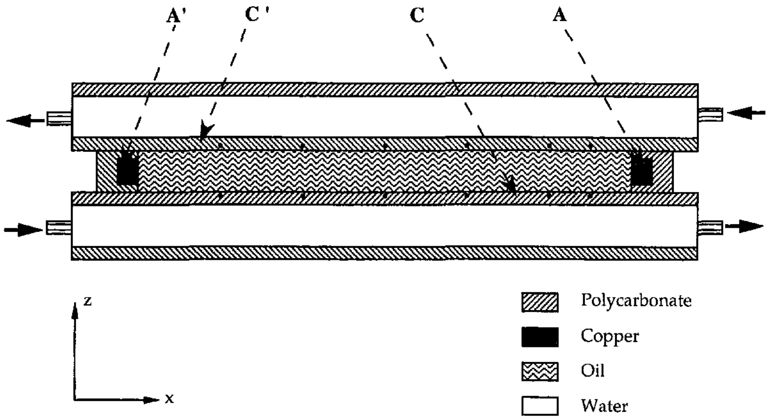

Fig. 1 Schematic of the apparatus. *A* and *A'* are the small lateral walls of the vessel. *C* and *C'* are the horizontal bottom and top surfaces. The black points in the walls show the thermocouples located at 1, 2, 4, 6, 8, and 10 cm from *A* and at 0.1 mm from the oil in the horizontal wall.

to five ($T_A = 60.9$°C). A detailed description of this phenomenon is given in Section 5.

In the following, RB rolls are numbered from A to A' starting from 1. If, during the experiment a new roll is created between the wall A and the roll 1, it is numbered 0. Various parameters must be considered for different initial conditions: (i) the value of the vertical temperature gradient (or Rayleigh number R) which imposes the initial number of rolls; (ii) the initial temperature of wall A which initially imposes the flow direction roll 1 (i.e., upward or downward); (iii) the initial temperature of wall A' with two different possibilities.

- $T_{A'} = T_m$: the wall A' does not impose any flow direction on its adjacent roll. The flow direction can be modified by a perturbation coming from the vessel (A for instance);
- $T_{A'}$ is different from T_m and, for instance, close to T_C or $T_{C'}$. In the first case the flow is upward along A' and it is downward in the second case; in both cases the flow direction is fixed and cannot be modified by any perturbation coming from A. The boundary condition imposes the flow direction on A' (provided that there are Rayleigh-Bénard rolls in this area).

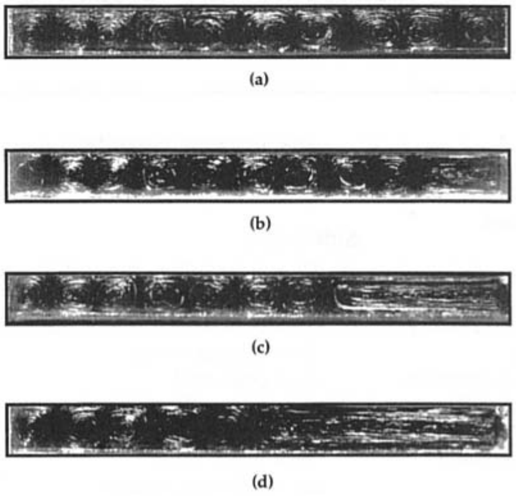

Fig. 2 Observed streamlines in the vertical median plane (case *U*, R = 4090) series 1: (*a*) T_A = 24°C; series 2: (*b*) T_A = 29.8°C—(*c*) T_A = 44.4°C—(*d*) T_A = 60.9°C

4 Numerical Method

Most of the numerical studies devoted to natural convection flows in parallelepiped enclosures have been carried out using models based on the finite difference method (De Vahl Davis and Jones, 1983; De Vahl Davis, 1983). More recently, spectral-type approaches have proved to be very effective for fine analysis of these flow types (Le Quere, 1991). On the other hand, the finite element method is gaining increasingly widespread use, since it offers the advantage of being able to take into account complex geometrical configurations (e.g., industrial applications). However, this last kind of model is also validated in well-understood configurations, such as natural convection in cavities, which have now been numerically studied by several authors (Bathe and Dong, 1987; Krishnan, 1985; Taylor and Ijam, 1979).

The finite element model that was developed in this work is formulated using primitive variables (velocity, pressure, temperature), and it is built following the conventional Bubnov-Galerkin approach (Carey and Oden, 1986). A variational statement is deduced from the set of equations describing the physical phenomena that come into play in this problem. This statement is spatially discretized using finite element approximation, and temporally with a finite difference scheme. One of the features of this model resides in the solution strategy, which consists of processing the mechanical and the thermal aspects of the problem alternately. This approach has long been in use for finite difference processing or finite volumes (Patankar and Spalding, 1972), and is now being extended to finite element solution of problems in fluid mechanics. In the case of this model, we have demonstrated its effectiveness on several natural convection systems (Jaeger et al., 1996).

4.1 Mathematical Model. For reasons of symmetry, the flow was studied only in the median vertical plane (O, x, z) of the enclosure, thus giving a two-dimensional model. This hypothesis has been validated experimentally for the horizontal enclosure studied in this work.

With the Boussinesq approximation, which is generally used to study natural convection in gases and liquids, the equations for the model are written (using the Cartesian coordinate system) as

- Flow

$$\frac{\partial u}{\partial x} + \frac{\partial w}{\partial z} = 0, \tag{1}$$

$$\frac{\partial u}{\partial t} + u\frac{\partial u}{\partial x} + w\frac{\partial u}{\partial z} = -\frac{1}{\rho_0}\frac{\partial p}{\partial x} + \frac{\partial}{\partial x}\left(2\frac{\mu}{\rho_0}\frac{\partial u}{\partial x}\right) + \frac{\partial}{\partial z}\left(\frac{\mu}{\rho_0}\left(\frac{\partial u}{\partial z} + \frac{\partial w}{\partial x}\right)\right), \quad (2)$$

$$\frac{\partial w}{\partial t} + u\frac{\partial w}{\partial x} + w\frac{\partial w}{\partial z} = -\frac{1}{\rho_0}\frac{\partial p}{\partial z} + \frac{\partial}{\partial x}\left(\frac{\mu}{\rho_0}\left(\frac{\partial u}{\partial z} + \frac{\partial w}{\partial x}\right)\right) + \frac{\partial}{\partial z}\left(2\frac{\mu}{\rho_0}\frac{\partial w}{\partial z}\right) - \beta(T - T_0)g, \quad (3)$$

- Heat transfer

$$\frac{\partial T}{\partial t} + u\frac{\partial T}{\partial x} + w\frac{\partial T}{\partial z} = \frac{\partial}{\partial x}\left(\frac{\lambda}{\rho_0 C_p}\frac{\partial T}{\partial x}\right) + \frac{\partial}{\partial z}\left(\frac{\lambda}{\rho_0 C_p}\frac{\partial T}{\partial z}\right), \quad (4)$$

where u and w are, respectively, the horizontal and vertical components of the velocity, p is the pressure and T is the temperature. The physical properties are the density ρ_0, the dynamic viscosity μ, the thermal expansion coefficient β, the thermal conductivity λ and the heat capacity C_p. The acceleration of gravity is designated by g.

Our aim was to simulate the thermoconvective flow in the cavity. Equations (1)–(3) are thus solved on a rectangular domain bounded by the horizontal and vertical walls of the cavity ($0 \le x \le 12$ cm; $0.3 \le z \le 1.3$ cm). The boundary conditions, expressing total adherence of the fluid onto the walls, are then written

$$u = w = 0 \quad \text{along walls } A, A', C, \text{ and } C'. \quad (5)$$

For the thermal study, the domain of interest is larger than for the flow computation. Indeed, it has to be extended to embody at least the horizontal walls, whose influence on thermal transfer is non-negligible. It should be noted that one of the particular features of this study resides in the material that makes up the walls (i.e., polycarbonate), which is neither entirely conductive nor entirely insulating in comparison with the oil used (47V100 silicone oil). This important aspect has to be taken into account in the numerical study. Indeed it has been shown that natural convection flows in cavities are considerably affected by the conductivity of the walls (Catton, 1972; Wang and Daniels, 1994). So the horizontal walls of the enclosure, which present a large exchange surface with the oil, are taken into account in the calculation of the heat transfer. On the other hand, the influence of the vertical walls, which present relatively little exchange surface with the oil, is neglected here. So the domain used to study the thermal exchange problem corresponds to the area encompassing the oil layer and the two horizontal walls ($0 \le x \le 12$ cm; $0 \le z \le 1.6$ cm).

The coherent boundary conditions for the selected domains are then as follows:

- temperature imposed by the thermostatically controlled baths running along the outer surface of the lower and upper walls

$$T = T_C \text{ for } z = 0 \quad \text{and} \quad T = T_{C'} \text{ for } z = 1.6 \text{ cm}; \quad (6)$$

- adiabatic boundary conditions along the vertical walls A and A' (in the case of no lateral heating the mean temperature of the oil is equal to that of the surrounding atmosphere)

$$\partial T/\partial x = 0 \text{ for } x = 0 \text{ and } x = 12 \text{ cm}. \quad (7)$$

When considering a lateral heating, the condition for wall A is modified locally at the heating element, whose temperature is imposed,

$$T = T_A \text{ along the copper rod}$$

$$(x = 12 \text{ cm}, 0.55 \text{ cm} < z < 1.05 \text{ cm}). \quad (8)$$

4.2 Validity of the Boussinesq Approximation. We have to discuss at this stage the validity of the Boussinesq approximation for that study. It is clear that with the magnitude of the lateral heating considered experimentally (30°C $< T_A <$ 110°C) one moves a certain distance from the regime in which the Boussinesq hypothesis has been validated.

In order to determine the matter of departure from this hypothesis, we can follow the method described by Paolucci and Chenoweth (1987) or by Ahlers (1980). This method is based on the work of Busse (1967) who introduced a parameter describing the departure from the Boussinesq approximation for laminar Bénard convection. This parameter is defined as

$$P = \sum_{i=0}^{4} \gamma_i P_i \quad (9)$$

with

$$\gamma_0 = \frac{\rho_{co} - \rho_h}{\rho_{mi}}, \quad \gamma_1 = \frac{\beta_h - \beta_{co}}{2\beta_{mi}}, \quad \gamma_2 = \frac{\nu_h - \nu_{co}}{\nu_{mi}},$$

$$\gamma_3 = \frac{\lambda_h - \lambda_{co}}{\lambda_{mi}}, \quad \gamma_4 = \frac{C_{P_h} - C_{P_{co}}}{C_{P_{mi}}} \quad (10)$$

where ν represents the kinematic viscosity and the P_i are functions of the Prandtl number (Busse, 1967). The subscripts h, co, and mi imply that the properties are evaluated at the hot wall, cold wall, and middle height temperature, respectively. Evaluating the γ_i for the silicone oil used (from the property behavior given by Rhône-Poulenc) shows that one has to take into account the influence of the temperature on the kinematic viscosity only. Hence, the parameter γ_2 is 10^2 times greater than the other γ_i; therefore it cannot be ignored in our study. To get a clear idea it should be pointed out that this oil is five times less viscous at 120°C than at 25°C. Following the approach proposed in Gray and Giorgini (1976), which is relevant for more general natural flows, one comes to the same observation.

In conclusion, to take into account the limitations of the Boussinesq model, we have simultaneously acted in two ways:

- we have considered the temperature dependance of the kinematic viscosity, which according to the data given by the silicone oil supplier (Rhône-Poulenc), obeys the following law

$$\nu = \mu/\rho_0 = 10^{10^{0.48}(223/T)^{1.41}} \quad (11)$$

with T in Kelvin and ν in centistokes. We have implemented this law in our numerical model which must then be understood as an extension of the Boussinesq approximation;
- the computations were restricted to the smallest values of the lateral heating considered experimentally, which induce however the destabilisation phenomenon under study ($T_A <$ 45°C).

4.3 Characteristic Nondimensional Parameters. In order to identify the nondimensional parameters involved in this study, we transform the set of Eqs. (1)–(4) in a nondimensional form. We define to this aim the following scaling:

$$\tilde{x} = \frac{x}{L_{\text{ref}}}; \quad \tilde{z} = \frac{z}{L_{\text{ref}}}; \quad \tilde{t} = \frac{t}{t_{\text{ref}}}; \quad \tilde{u} = \frac{u}{V_{\text{ref}}};$$

$$\tilde{w} = \frac{w}{V_{\text{ref}}}; \quad \tilde{p} = \frac{p}{p_{\text{ref}}}; \quad \tilde{T} = \frac{T - T_0}{\Delta T_{\text{ref}}}, \quad (12)$$

where the reference scales are chosen as

- $L_{\text{ref}} = d$ = thickness of the silicone oil layer;

- $\Delta T_{\mathrm{ref}} = \Delta T$ = vertical temperature difference applied to the oil layer by the thermostatically regulated water flows;
- $V_{\mathrm{ref}} = (\beta g \Delta T_{\mathrm{ref}} L_{\mathrm{ref}})^{1/2}$ = characteristic velocity of RB convection;
- $p_{\mathrm{ref}} = \mu_0 V_{\mathrm{ref}} / L_{\mathrm{ref}}$ with $\mu_0 = \mu\ (T = T_0)$;
- $t_{\mathrm{ref}} = V_{\mathrm{ref}} / L_{\mathrm{ref}}$.

The set of equations then takes the following nondimensional form

$$\frac{\partial \tilde{u}}{\partial \tilde{x}} + \frac{\partial \tilde{w}}{\partial \tilde{z}} = 0, \tag{13}$$

$$\sqrt{\frac{\mathrm{R}}{\mathrm{Pr}}}\left(\frac{\partial \tilde{u}}{\partial \tilde{t}} + \tilde{u}\,\frac{\partial \tilde{u}}{\partial \tilde{x}} + \tilde{w}\,\frac{\partial \tilde{u}}{\partial \tilde{z}}\right)$$

$$= -\frac{\partial \tilde{p}}{\partial \tilde{x}} + \frac{\partial}{\partial \tilde{x}}\left(2\,\frac{\mu}{\mu_0}\,\frac{\partial \tilde{u}}{\partial \tilde{x}}\right) + \frac{\partial}{\partial \tilde{z}}\left(\frac{\mu}{\mu_0}\left(\frac{\partial \tilde{u}}{\partial \tilde{z}} + \frac{\partial \tilde{w}}{\partial \tilde{x}}\right)\right), \tag{14}$$

$$\sqrt{\frac{\mathrm{R}}{\mathrm{Pr}}}\left(\frac{\partial \tilde{w}}{\partial \tilde{t}} + \tilde{u}\,\frac{\partial \tilde{w}}{\partial \tilde{x}} + \tilde{w}\,\frac{\partial \tilde{w}}{\partial \tilde{z}}\right)$$

$$= -\frac{\partial \tilde{p}}{\partial \tilde{z}} + \frac{\partial}{\partial \tilde{x}}\left(\frac{\mu}{\mu_0}\left(\frac{\partial \tilde{u}}{\partial \tilde{z}} + \frac{\partial \tilde{w}}{\partial \tilde{x}}\right)\right)$$

$$+ \frac{\partial}{\partial \tilde{z}}\left(2\,\frac{\mu}{\mu_0}\,\frac{\partial \tilde{w}}{\partial \tilde{z}}\right) - \tilde{T}\sqrt{\frac{\mathrm{R}}{\mathrm{Pr}}}, \tag{15}$$

$$\sqrt{\mathrm{R}\cdot\mathrm{Pr}}\left(\frac{\partial \tilde{T}}{\partial \tilde{t}} + \tilde{u}\,\frac{\partial \tilde{T}}{\partial \tilde{x}} + \tilde{w}\,\frac{\partial \tilde{T}}{\partial \tilde{z}}\right) = \left(\frac{\partial^2 \tilde{T}}{\partial \tilde{x}^2} + \frac{\partial^2 \tilde{T}}{\partial \tilde{z}^2}\right), \tag{16}$$

which shows that the characteristic nondimensional parameters involved in our problem are the Rayleigh number

$$\mathrm{R} = \frac{\rho_0^2 C_p \beta g \Delta T d^3}{\mu_0 \lambda}, \tag{17}$$

and the Prandtl number

$$\mathrm{Pr} = \frac{\mu_0 C_p}{\lambda}. \tag{18}$$

4.4 Finite Element Model. The method of weighted residuals is applied independently to the system of Eqs. (1)–(3) and to Eq. (4). One obtains then two separate variational statements for the flow and thermal problems which will be solved in a segregate manner.

The finite element model for the flow problem is based on a penalized formulation (Carey and Oden, 1986). It employs the six-node triangular element first developed by Bercovier and Pironneau (1979). On the other hand, the finite element model for the thermal problem uses a standard three-node triangular element of Lagrange type. Both problems are advanced in time with an implicit Euler scheme.

4.5 Solution Algorithm. Since the two problems are solved separately, their coupling has to be taken into account by the solution algorithm. For each time step, the thermal problem is solved first (since it is the driving force of the flow) given the velocity field obtained for the previous time step. Then, given these new values of the temperature, the fluid flow problem which is nonlinear is solved at its turn with an iterative Newton method. However, because of the segregated solving of the two problems, it is useless to make more than one or two iterations. In fact, although both problems use an implicit Euler scheme, the solution algorithm has a pronounced explicit nature. This can be overcome by iterating between the two problems inside each time step or by using sufficiently small time step to ensure convergence without iterating. Since we were also interested in the transient analysis of the physical phenomenon, we have opted for the second approach. When searching for stationary regimes, like in series 1 study, the value of the time step is increased on a regular basis, according to the advancement of the solution, up until a stationary solution can be processed. The loop on the time steps is then replaced by a loop on stationary solutions, ultimately producing the convergence of the two problems. For that stationary solution we most often use relaxation coefficients to update the unknowns.

4.6 Calculation Procedure. The aim is to produce numerical simulation of the destabilization of a Rayleigh-Bénard flow by lateral heating. We thus proceeded in two steps for each case studied. Initially, we sought to establish a stationary Rayleigh-Bénard flow induced by a purely vertical temperature gradient. This step corresponds to the experiments in series 1, described in Section 3.1. From this initial configuration, the lateral heating was then simulated by imposing the heating temperature T_A. This last step includes the analysis of the transient phase of the phenomenon which allows us to apprehend the mechanisms at play.

In both cases considered in the present work (case U: upward roll close to A, case D: downward roll close to A), the two corresponding stable states have been studied. The destabilization mechanism is found to behave quite differently, since the lateral heating increases the energy of the roll next to the heated wall in one case, whereas its energy is decreased in the other.

4.7 Convergence Study. Grid refinement study has been conducted both on the RB problem (series 1, case D) and the destabilization one (series 2, case D).

In the former, we have tested three uniform meshes, doubling successively the element number in each space direction. Thus the coarser one (MRB1) is built (in the oil layer) on 60 × 6 × 2 $T6$ (six-node triangular element), the medium one (MRB2) on 120 × 10 × 2 $T6$ and finally the finer one (MRB3) on 240 × 20 × 2 $T6$. The errors can be estimated through the vertical velocity component along the horizontal median axis plotted on Fig. 3(a). No discrepancy can be observed between the three meshes, since even the coarser one produces results with a satisfactory accuracy.

For the grid refinement study on the destabilization problem, we have started the analysis with the medium mesh previously described. Furthermore, three successive refinements in the last quarter of the box (where the destabilization phenomena numerically considered occurs) have been supplied. Each refinement step consists of doubling the element number in the horizontal direction leading to meshes of, respectively, 120 × 10 × 2 $T6$ (mesh MDS1 = mesh MRB2), 150 × 10 × 2 $T6$ (MDS2), 210 × 10 × 2 $T6$ (MDS3), and 330 × 10 × 2 $T6$ (MDS4) in the oil layer. For this study, the errors are estimated again through the vertical velocity component along the horizontal median axis but during the transient stage of the phenomenon (Fig. 3(c)). This introduces the second aspect of our convergence study concerning the choice of the time step. Computations have been carried out with three values ($\Delta t = 2s$, $\Delta t = 1s$, $\Delta t = 0.1s$) on the different meshes. Figure 3(c) shows the profiles obtained at $t = 2s$, $t = 50s$, and $t = 100s$ with the medium uniform mesh (MDS1). We have also reported in that figure the profiles obtained with the finest mesh (MDS4) and $\Delta t = 1s$. This demonstrates that a very good accuracy is reached with this last combination of spatial and temporal discretization. So it has been retained to provide all the following results presented in the paper.

5 Description of Phenomena, Results, and Discussion

All observed phenomena were two-dimensional, with the exception of the area very near the lateral walls B and B' ($\approx$1 to

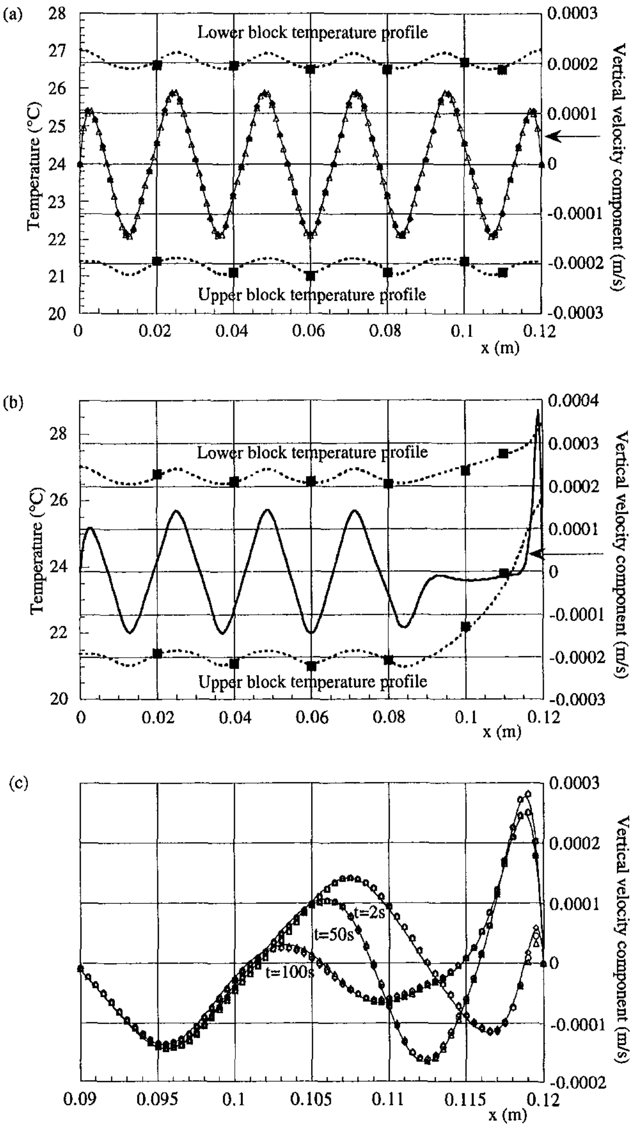

Fig. 3 Computed vertical component of the velocity in the horizontal median plane (z = 0.8 cm), and temperature in the horizontal median planes of horizontal walls C and C', as a function of the distance (x): (a) series 1 case U (♦ mesh MRB1, △ MRB2, - MRB3,); (b) stationary state of series 2, case U for T_A = 44.4°C; (c) transient stage of series 2, case D for T_A = 33.4°C (△ MDS1 Δt = 2s, ○ MDS1 Δt = 1s, ◇ MDS1 Δt = 0.1s, - MDS4 Δt = 1s); --- computed temperature, ■ measured temperature

2 mm on either side). The results are thus presented in the vertical longitudinal median plane.

5.1 Series 1. The temperature difference ΔT was set to a value ranging from 2°C to 7°C ($1.3\text{R}_c < \text{R} < 4.6\ \text{R}_c$). That corresponds to a system ranging from 12 to 8 rolls according to the value of R. Figure 2(a) shows such a pattern with ten rolls. In this example, the nondimensional wave number varies in the range 2.36–3.03 with a mean value of 2.61, the pattern being irregular owing to the thermal influence of the sidewalls A and A'. For 11 realizations the corresponding values are, respectively, 2.35–3.05 and 2.60. Figure 4 shows the marginal stability curve determined elsewhere (Cerisier et al., 1997), the experimental mean wave number and the minimum and maximum observed ones. It is clearly shown that the wave number decreases as R increases, in the same manner as in the experiments conducted between horizontal boundaries with very high thermal conductivity (Koschmieder, 1966; Leontiev and Kirdyashkin, 1968; Willis et al., 1972; Farhadieh and Tankin, 1974; Koschmieder and Pallas, 1974; Bühler et al., 1979). Koshmieder and Pallas (1974) quoted experimental results on wavelength variations as a function of R. Considering high Prandtl fluids (Pr > 350), they concluded that the nondimensional wavelength Λ increases with the distance to the threshold $\epsilon = (\text{R} - \text{R}_c)/\text{R}_c$. For small ϵ, Λ increases linearly with a mean slope of 0.1 ± 0.02 K^{-1} ($d\Lambda/d\epsilon$ was different in each experiment). We find a smaller value (0.05 K^{-1}) in the case of a ten roll pattern. The range of linearity, limited to a constant number of rolls, goes up to about 5 R_c, in agreement with experiments quoted previously (Koschmieder and Pallas, 1974). The bandwidth of the selected wavelength increases linearly from $\epsilon = 0$ to $\epsilon = 1.2$. A study for a vessel like ours has not yet been achieved; however, for an infinite layer, it has been shown (Schluter et al., 1965) that the bandwidth varies as $\epsilon^{1/2}$. In a finite vessel, it is known that the range of stable modes decreases. For $1.2 < \epsilon < 2$ the bandwidth fluctuates and for $\epsilon > 2$ it is constant in the investigated domain (up to $\epsilon \approx 5$). It is noteworthy for the understanding of series 2 experiments that the decrease of the wavelength for a acceptable agreement with the theoretical value $k_c = 2.6$ for an infinite layer with our boundary conditions (Cerisier et al., 1997).

The value of the numerically simulated wave number coincides quite closely with the experimental results. As an example, the flow structure and the corresponding isotherms computed for R = 4090 are depicted in Fig. 5. For this configuration, which corresponds to a Rayleigh number of 4090, we reach a system of ten rolls (or a mean wave number of 2.61), which corresponds to the experimental results. An interaction was observed between the horizontal walls and the temperature field in the fluid. It is particularly visible in Fig. 3(a), with the temperature values being represented in the median plane of both horizontal walls, in the case of upward rolls. The influence of the RB rolls is clearly visible, producing a sinusoidal distribution with an amplitude of approximately 0.25°C. Although the temperature difference remains roughly constant between C and C', these surfaces cannot be considered isothermal since they are in contact with the oil. The same remark holds true in the case of the downward rolls.

5.2 Series 2. All of the observed mechanisms are independent of the initial number of RB rolls (i.e., of the R value). For example, we give the results obtained with ten rolls (i.e., R = 2.9 R_c), and the rolls are numbered from 1 to 10, moving from wall A toward wall A'. As it has already been pointed out in Section 3.2, we must distinguish the upward rolls (U) and the downward rolls (D) along A and A'. It should be remembered that the actual induced process also depends on the type of thermal boundary conditions imposed at A'.

5.2.1 Roll 1 and 10 Initially Upward, Roll 10 Imposed (Not Reversible). In this case the lateral heating increases the energy of roll 1. The velocity field increases near wall A, with

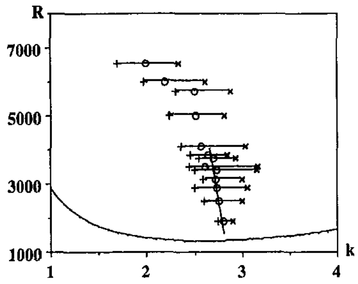

Fig. 4 Stability diagram of Rayleigh-Bénard convection between moderately heat conductoring horizontal boundaries. —: marginal stability curve (after Cerisier et al., 1998). ○: mean wave number; +: minimum observed wave number; ×: maximum observed wave number (present study).

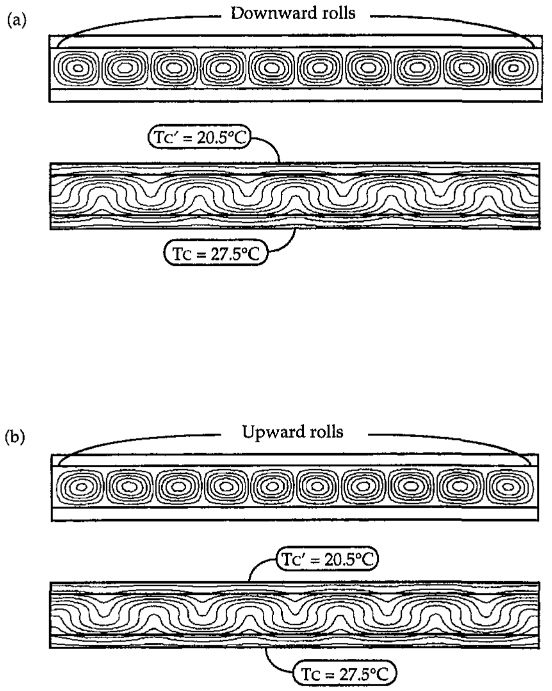

Fig. 5 Computed streamlines and isotherms (13 isotherms separated by an equal increment of 0.538°C between T_C and $T_{C'}$) for series 1 (R = 4090): (*a*) case *D*; (*b*) case *U*

the formation of a boundary layer in this area. This layer can be seen in Fig. 3(*b*), which shows the distribution of the vertical velocity component in the median plane of the oil layer at the end of the process (obtained numerically for T_A = 44.4°C). This increase in the energy of roll 1, which corresponds to the induced roll, also causes the roll size increase. This takes place to the detriment of the adjacent rolls which are compressed. The rolls near *A*′, however, remain unchanged (see Section 5.3 for the analysis of this phenomenon). The range of admissible wavelengths is, however, quite narrow (cf. Section 5.1). As a result, the compression cannot extend beyond a certain limit. Enhanced heating of *A* produces a new increase in the size of the induced roll, ultimately leading to the elimination of roll 2. Yet this new configuration remains unstable, since rolls 1 and 3 have opposite velocities at their interface. The mechanical coupling between the induced roll and the RB roll pattern can only be attained by the elimination of an additional roll (i.e., roll 3). The space freed up by the disappearance of this pair of rolls is then filled by the adjacent rolls which begin to expand, and by the induced rolls whose size goes on to increase.

This elimination of a pair of rolls is shown in the sequence of digitized photos (Fig. 6) which presents the evolution of the roll pattern during the transient regime for T_A = 44.4°C. It should be noted that these photographs actually represent a sequence of averaged transient states. To reveal the trajectories the photographic exposure time must be fairly long (i.e., 15 sec). On the other hand, Fig. 7(*a*) presents the computed streamlines of the same phenomenon, but with a different heating rate. Indeed, the wall temperature T_A = 44.4°C is applied throughout the whole process simulation. Thus the stationary state is reached more quickly than in the experiment. Nevertheless, one can see in comparing the Figs. 6 and 7(*a*) that the destabilization process is the same, letting us conclude that this process is not heating rate dependent.

This destabilization process can be summed up as follows:

- At the initial state, the rolls are in steady state, and thus turn in accordance with the mechanical coupling, with rolls 1 and 10 rising up at the walls (upward rolls).
- Following the increase in T_A (for instance from 24.°C to 33.4°C), roll 1 increases in size, to the detriment primarily of roll 2, which is progressively compressed. The size of this latter roll decreases and then eventually disappears (Figs. 6 and 7(*a*)).
- Rolls 1 and 3, which are now adjacent, turn in the same direction (counter clockwise in Fig. 7(*a*)). The intense shear at their interface produces the destruction of roll 3, or more precisely its assimilation in roll 1. After a brief period of turbulence at the interface (Figs. 6 and 7(*a*)), the trajectories are seen to rapidly rearrange, ultimately leading to the coalescence of the two structures. In the lower part of the adjacent roll, the streamlines do not rise toward the interface, but rather extend toward *A* and bond to roll 1. Likewise, in the upper part of the enclosure, the streamlines for roll 1 do not descend but rather bond to the adjacent roll. This second roll destruction lasts much less time ($\approx$1 mn) than the previous one ($\approx$9 mn).

At this stage, any sufficient increase in the heating of wall *A* reproduces the same cycle: compression of the RB roll pattern, disappearance of two rolls, extension of the system. In Figs. 2(*b*) and 2(*c*), the reduced number of rolls observed experimentally in the vertical median plane at steady regimes and for different values of T_A can be seen.

5.2.2 Roll 1 and 10 Initially Downward, Roll 10 Imposed (Not Reversible). In this case, the effect of the lateral heating at *A* is opposite to the movement of roll 1 (downward along *A*). Thus even very slight heating (2°C to 3°C above T_m) immediately leads to the formation of a small roll (induced roll) between the wall and roll 1. This new roll (numbered 0) moves upward along *A* and displays a gear like interaction with roll 1. As soon as T_A is about 8°C greater than T_m, the increase in roll 0 leads to the destruction of roll 1, and then of roll 2, following the process described for the previous configuration. The response of the system to this successive heating of *A* then follows a similar evolution: compression, disappearance of two other rolls, extension. In this latter case, however, the pairs disappear at rolls ($2i + 1$, $2i + 2$) with $i = 0, 1, 2, \ldots$.

The numerical simulation provides an accurate representation of this phenomenon. Notably, the evolution of the streamlines near wall *A* (Fig. 7(*b*)) clearly reveals the formation of the induced roll and then its growth to the detriment of the other rolls.

5.2.3 Roll 1 and 10 Initially Upward, Roll 10 Not Imposed (Reversible). If the increase in T_A occurs in stages and if the direction of rotation of the roll 10 is not imposed (i.e., it is reversible during the experiment), we observe rolls disappearing in a different manner: one by one. This phenomenon is rarely observed when there is a large number of remaining rolls (eight or nine in the enclosure), but it is commonly observed when the number of rolls is smaller (most likely due to the effect of weaker inertia).

5.3 Thermal Analysis. The temperature field for the stationary states (Figs. 3(*b*)) and 8(*a*)) expresses the coexistence of two different convective systems: (i) RB rolls generated by the vertical gradient, (ii) a roll induced by the lateral heating of wall *A*.

It should also be noted that the influence of each system remains limited to a distinct portion of the total cavity. In the zone filled with the induced roll, a heat flux is carried from wall *A* toward wall *C*′. In this latter area, the temperature increases and weakens the vertical gradient; when the lateral heating is high enough, this gradient is actually inverted (Fig. 9(*c*)). No RB convection can be observed in this part of the cavity. This action of the lateral heating is limited to the zone filled with the induced roll. Therefore, for both cases computed, the lateral heating does not affect the RB convection regime present in the other part of the cavity. For those configurations the

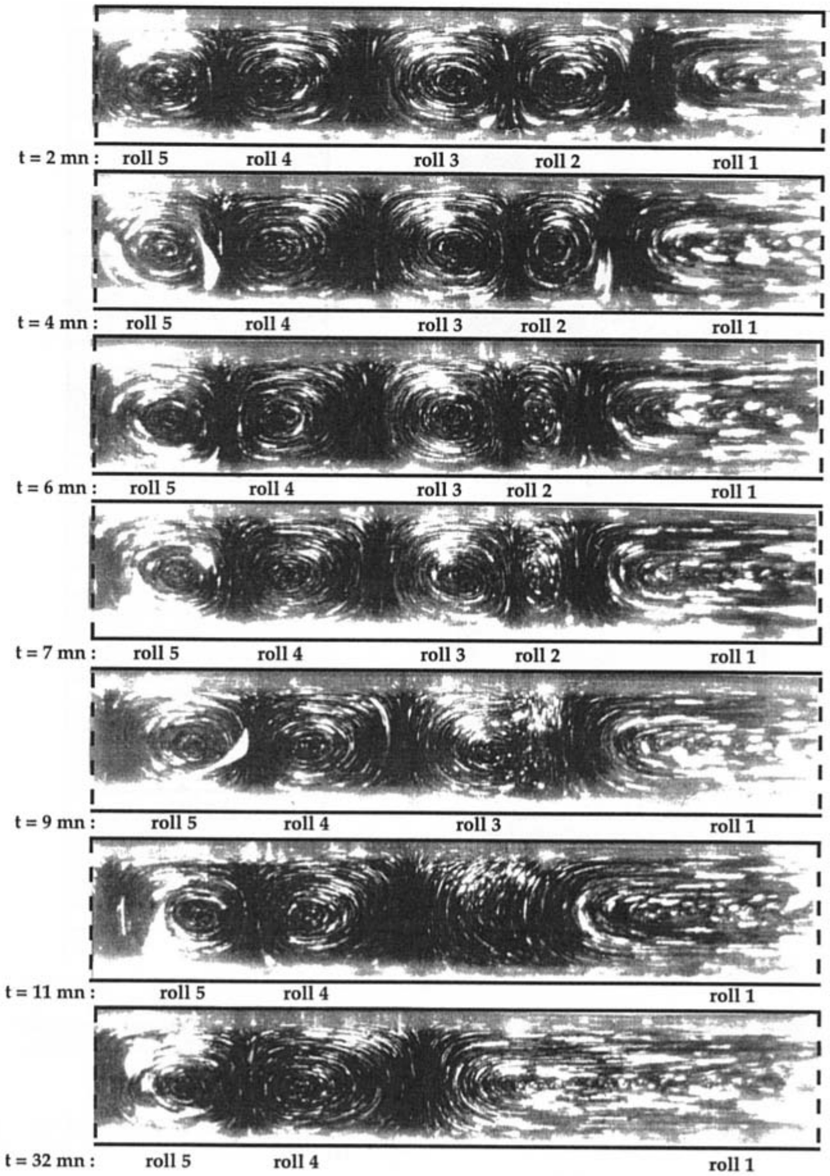

Fig. 6 Evolution of observed trajectories near wall *A* for T_A = 44.4°C in series 2 (R = 4090) case *U*, transient regime

numerical and experimental results coincide closely (Fig. 3(*b*)). This analysis holds true as long as the rotation of roll 10 is not imposed. In this case the heating of one lateral side can lead to the destruction of the RB roll close to the opposite side. This action is mostly a mechanical one (compression of the RB pattern). However, due to the shift of the remaining RB roll pattern, the temperature field is modified in the whole cavity.

The coexistence of these two convective systems is also visible in Figs. 9(*a*) and (*b*), which show the distribution of the Nusselt number (Nu) obtained numerically along the external surfaces of the horizontal blocks (which are in contact with the thermostatically controlled baths). In these figures, we have also plotted the Nu distribution along the median line through these two blocks for the initial RB regime. Even at this point, the influence of the convective rolls is clearly visible, producing a sinusoidal variation, with the maximum and minimum values corresponding to the boundaries of the rolls. These two distributions, however, are in opposite phases, with the highest Nusselt number for the lower wall at that point where the fluid descends, and the highest Nusselt number for the upper wall where the fluid rises.

When the lateral heating is applied, the shape of the curves is changed only in the zone influenced by the induced roll. In the case *U*, for the upper wall, the maximum value is multiplied by a factor of approximately 1.6, indicating the previously mentioned increase in heat transfer. For the lower wall, the curve presents a discontinuity roughly at $x = 11$ cm, which in fact corresponds to a vertical asymptote. To understand this phenomenon, one has to go back and review the definition of the Nusselt number

$$\mathrm{Nu} = \text{Total flux}/\text{Conductive flux} \qquad (19)$$

where the total flux is calculated on the outer surface of the wall when the oil flow in the enclosure has reached its stationary regime. The conductive flux corresponds to the flux calculated on the same line, but keeping the oil at rest. This latter configuration, which is simulated numerically by solving the heat conduction equation (zero velocity field), is thus used as a refer-

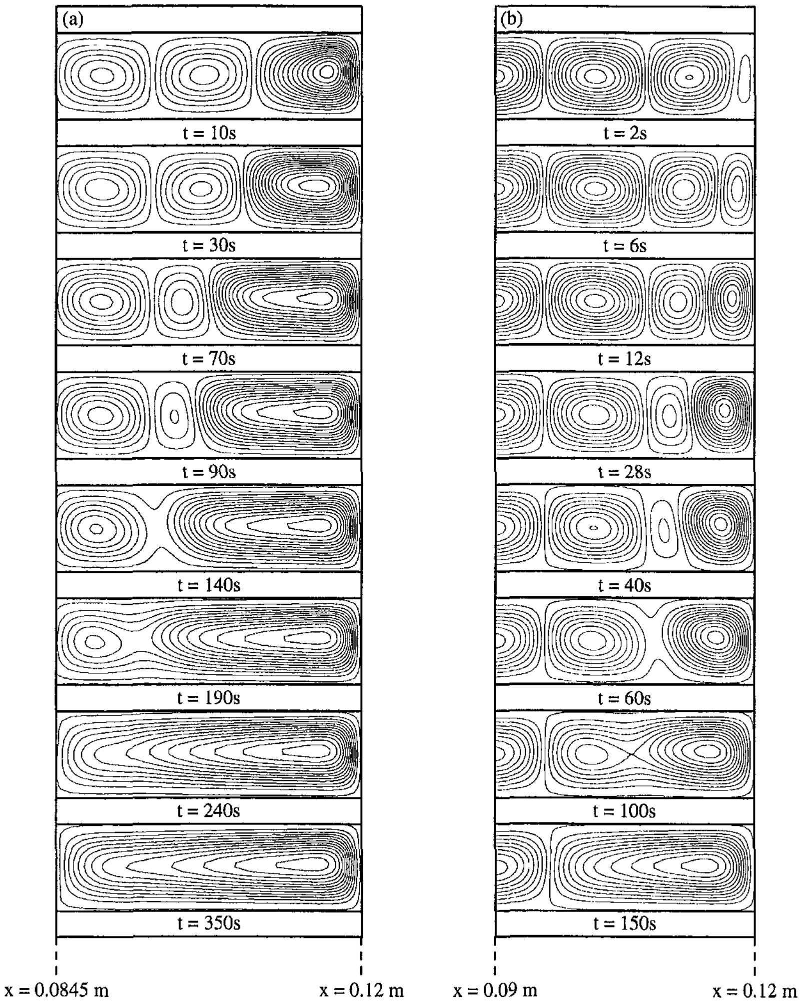

Fig. 7 Evolution of computed streamlines during the transient stage of the perturbation (close up of the container near wall *A*) in series 2 (R = 4090): (*a*) for T_A = 44.4°C case *U*; (*b*) for T_A = 33.4°C case *D*

ence to analyze the influence of the convective rolls on heat transfer. The Nusselt number is thus expressed as

$$\mathrm{Nu} = \left(\frac{\partial T}{\partial z}\right)_{cv} \Big/ \left(\frac{\partial T}{\partial z}\right)_{cd} \qquad (20)$$

where the subscripts cv and cd correspond, respectively, to the convective and conductive regimes. The vertical gradient $\partial T/\partial z$ is evaluated at $z = 0$ for the lower wall and at $z = 1.6$ cm for the upper one.

The temperature field for the reference conductive regime is shown on Fig. 8(*b*) for the case $T_A = 33.4$°C. The vertical gradient is negative everywhere, except in the zone adjacent to the vertical wall *A*, area beneath the copper heating element. The flow changes the shape of the temperature field (Fig. 8(*a*)). After having carried the hot fluid up to the upper wall, the roll induced by the lateral heating returns the cooled fluid toward the lower one. As a result, the zone with a positive vertical gradient is compressed toward the wall *A*. There is then a region in which the vertical gradient $\partial T/\partial z$ for the convective regime and for the reference conductive one have opposite signs, thus producing a negative Nusselt number (according to definition (20) of Nu). The distribution of $\partial T/\partial z$ along the outer surface of the lower wall (cf. Fig. 9(*c*)) confirms this result. It can be seen that the point where this quantity passes through zero is not the same for the two regimes, thus producing an infinite Nu value when the reference value passes through zero ($x \approx 11$ cm).

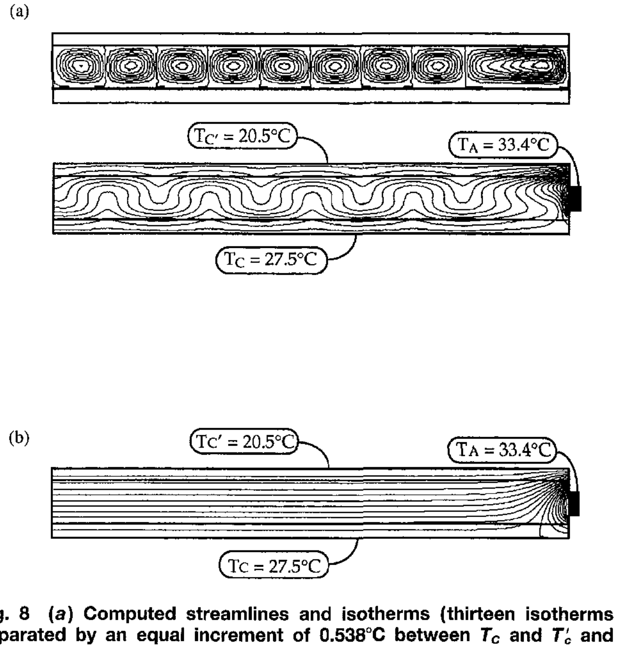

Fig. 8 (*a*) Computed streamlines and isotherms (thirteen isotherms separated by an equal increment of 0.538°C between T_C and T_C' and thirteen isotherms separated by an equal increment of 1.3°C between T_C and T_A) at stationary state for T_A = 33.4°C in series 2 (R = 4090) case *D*; (*b*) isotherms for the reference conductive regime

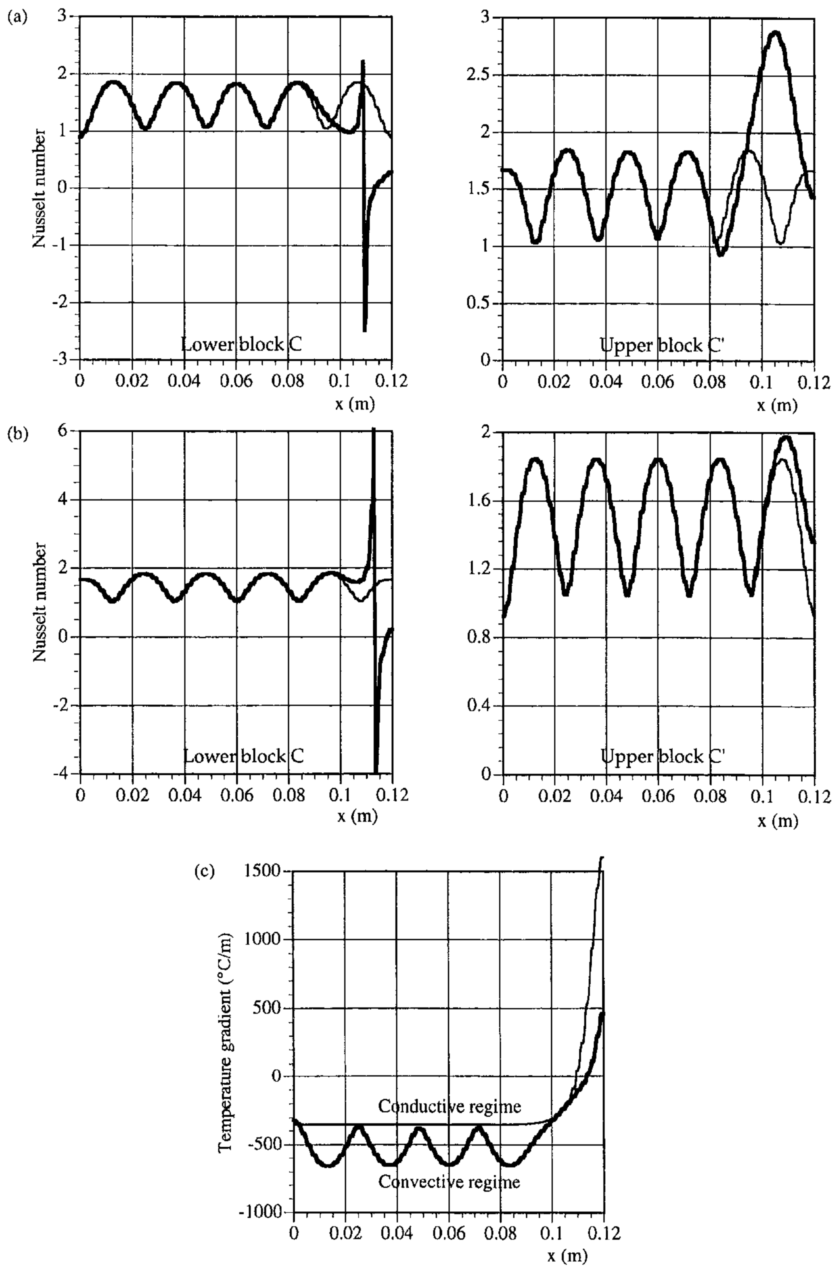

Fig. 9 (*a*) and (*b*): Comparison of computed Nusselt number distribution along the external face of horizontal blocks *C* and *C′* for series 1 and series 2 (bold line): (*a*) case *U* for T_A = 44.4°C; (*b*) case *D* for T_A = 33.4°C; (*c*) distribution of the computed vertical temperature gradient along the external face of the upper horizontal wall *C′*, for the conductive regime and the convective one, for T_A = 33.4°C in series 2 case *D*

6 Conclusion and Further Developments

The interaction of a RB roll pattern with a roll induced by a lateral heating has been analyzed. The increase in heat flux at the lateral wall produces an extension of the induced roll. This increase in the size of the induced roll is confronted with the nearly incompressible nature of the other RB rolls. This contradiction is overcome by the elimination of two rolls (in most cases) such that the gear-like effect between the rolls is maintained. Analysis of the thermal aspect of this phenomenon allowed us to link the destabilization process (disappearance of two rolls) and the competition of two convection regimes present in the problem. The finite element model developed for this study was found to describe the behavior of the natural convective flows both for steady and for transient regimes. It should also be noted that this numerical simulation is of considerable assistance in understanding the finer mechanisms involved in this problem. This study should be pursued experimentally to provide a more detailed description of the elimination of one or two rolls.

References

Ahlers, G., 1980, "Effect of Departures From the Oberbeck-Boussinesq Approximation on the Heat Transport of Horizontal Convecting Fluid Layers," *J. Fluid Mech.*, Vol. 98, pp. 137–148.

Bathe, K. J., and Dong, J., 1987, "Solution of Incompressible Viscous Fluid Flow with Heat Transfer Using ADINA-F," *Computer & Structures*, Vol. 26, pp. 17–31.

Bercovier, M., and Pironneau, O., 1979, "Error Estimates for Finite Element Solution of the Stokes Problem in the Primitive Variables," *Numer. Math.*, Vol. 33, pp. 211–224.

Berge, P., Pomeau, Y., and Vidal, Ch., 1988, *L'ordre dans le chaos*, Hermann, Paris.

Breton, J. L., 1989, "Similitude et stabilité des écoulements de convection naturelle dans une cavité fermée à haut nombre de Rayleigh (Pièce d'Habitation)," Thesis, Université Paul Sabatier, Toulouse, France.

Bühler, K., Kirchartz, K. R., and Oertel, H., 1979, "Steady Convection in a Horizontal Fluid Layer," *Acta Mech.*, Vol. 31, pp. 155–171.

Busse, F. H., 1967, "The Stability of Finite Amplitude Cellular Convection and Its Relation to an Extremum Principle," *J. Fluid Mech.*, Vol. 30, Part 4, pp. 625–649.

Busse, F. H., and Whitehead, J. A., 1971, "Instabilities of Convection Rolls in a High Prandtl Number Fluid," *J. Fluid Mech.*, Vol. 47, pp. 305–320.

Busse, F. H., 1978, "Non Linear Properties of Convection," *Rep. Prog. Phys.*, Vol. 41, pp. 1929–1967.

Carey, G. F., and Oden, J. T., 1986, *Finite Elements: Fluid Mechanics*, Vol. 6, Prentice-Hall, Englewood Cliffs, NJ.

Catton, I., 1972, "The Effect of Insulating Vertical Walls on the Onset of Motion in a Fluid Heated From Below," *Int. J. Heat and Mass Transfer*, Vol. 15, pp. 665–672.

Cerisier, P., Rahal, S., Cordonnier, J., and Lebon, G., 1998, "Thermal Influence of Boundaries on the Onset of Rayleigh-Bénard Convection," *Int. J. Heat and Mass Transfer*, Vol. 41, pp. 3309–3320.

Chikhaoui, A., 1989, "Stabilité des écoulements thermoconvectifs dans une couche fluide soumise à un gradient thermique horizontal," Thesis, Université d' Aix-Marseille II, France.

Croquette, V., 1989, "Convective Pattern Dynamics of Low Prandtl Number: Part I," *Contemp. Phys.*, Vol. 30, pp. 113–133.

Daniels, P. G., and Wang, P., 1994, "Numerical Study of Thermal Convection in Tall Laterally Heated Cavities," *Int. J. Heat and Mass Transfer*, Vol. 37, pp. 375–386.

De Vahl Davis, G., and Jones, I. P., 1983, "Natural Convection in a Square Cavity: A Comparison Exercise," *Int. J. Numerical Methods in Fluids*, Vol. 3, pp. 227–248.

De Vahl Davis, G., 1983, "Natural Convection of Air in a Square Cavity: A Bench Mark Numerical Solution," *Int. J. Numerical Methods in Fluids*, Vol. 3, pp. 249–264.

Elder, J. W., 1965, "Turbulence Free Convection in a Vertical Slot," *J. Fluid Mech.*, Vol. 23, pp. 99–111.

Farhadieh, R., and Tankin, R. S., 1974, "Interferometric Study of Two-Dimensional Bénard Convection Cells," *J. Fluid Mech.*, Vol. 66, pp. 739–752.

Gollub, J. P., Mc Carriar, A. R., and Steinman, J. F., 1982, "Convection Pattern Evolution and Secondary Instabilities," *J. Fluid Mech.*, Vol. 125, pp. 259–281.

Gray, D. D., and Giorgini, A., 1976, "The Validity of the Boussinesq Approximation for Liquids and Gases," *Int. J. Heat and Mass Transfer*, Vol. 19, pp. 545–551.

Imberger, J., 1974, "Natural Convection in a Shallow Cavity with Differentially Heated End Walls. Part 3. Experimental Results," *J. Fluid Mech.*, Vol. 65, pp. 247–260.

Jaeger, M., Medale, M., and Randriamampianina, A., 1996, "Numerical Modeling of Buoyancy-Driven Flows in a Rotating Cylindrical Cavity: Comparison of a Finite Element Model with a Spectral Model," *Numerical Heat Transfer, Part A*, Vol. 30, pp. 779–798.

Karyakin, Y. E., Sokovishin, YU. A., and Martynenko, O. G., 1988, "Transient Natural Convection in Triangular Enclosures," *Int. J. Heat and Mass Transfer*, Vol. 31, pp. 1759–1766.

Kirchartz, K. R., and Oertel, H., Jr., 1988, "Three-Dimensional Thermal Cellular Convection in Rectangular Boxes," *J. Fluid Mech.*, Vol. 192, pp. 249–186.

Kolodner, P., Walden, R. W., Passner, A., and Surko, C. M., 1986, "Rayleigh-Bénard Convection in an Intermediate-Aspect-Ratio Rectangular Container," *J. Fluid Mech.*, Vol. 163, pp. 195–226.

Koschmieder, E. L., 1996, "On Convection on a Uniformly Heated Plane," *Beitr. Phys. Atmos.*, Vol. 39, pp. 1–11.

Koschmieder, E. L., and Pallas, S. G., 1974, "Heat Transfer Through a Shallow, Horizontal Convecting Fluid Layer," *Int. J. Heat Mass Transfer*, Vol. 17, pp. 991–1002.

Koschmieder, E. L., 1974, "Bénard Convection," *Adv. Chem. Phys.*, Vol. 26, pp. 177–212.

Koschmieder, E. L., 1993, *Bénard Cells and Taylor Vortices*, Batchelor, ed. Cambridge University Press, Cambridge, UK.

Krishnamurti, R., 1970, "On the Transition to Turbulent Convection. Part 1. The Transition From Two- to Three Dimensional Flow," *J. Fluid Mech.*, Vol. 42, pp. 295–307.

Krishnan, R., 1985, "A Finite Element Approximation of the Bénard Problem," *Communications in Applied Numerical Methods*, Vol. 1, pp. 317–324.

Le Quere, P., 1991, "Accurate Solutions to the Square Thermally Driven Cavity at High Rayleigh Number," *Computer Fluids*, Vol. 20, No. 1, pp. 29–41.

Leontiev, A. J., and Kirdyashkin, A. G., 1968, "Experimental Study of Flow Patterns and Temperature Fields in Horizontal Free Convection Liquid Layers," *Int. J. Heat and Mass Transfer*, Vol. 11, pp. 1461–1466.

Manneville, P., 1990, *Dissipative Structures and Weak Turbulence*, Academic Press, London.

Nield, D. A., 1994, "Convection Induced by an Inclined Temperature Gradient in a Shallow Horizontal Layer," *Int. J. Heat and Fluid Flow*, Vol. 15, No. 2, pp. 157–162.

Paolucci, S., and Chenoweth, D. R., 1987, "Departures from the Boussinesq Approximation in Laminar Bénard Convection," *Phys. Fluids*, Vol. 30, pp. 1561–1564.

Patankar, S. V., and Spalding, D. B., 1972, "A Calculation Procedure for Heat, Mass and Momentum Transfert in Three Dimensional Parabolic Flows," *Int. J. Heat and Mass Transfer*, Vol. 15, pp. 1787–1806.

Patterson, C., and Imberger, J., 1980, "Unsteady Natural Convection in Rectangular Cavity," *J. Fluid Mech.*, Vol. 100, pp. 65–86.

Schlüter, A., Lortz, D., and Busse, F. M., 1965, "On the Stability of Steady Finite Amplitude Convection," *J. Fluid Mech.*, Vol. 23, pp. 129–144.

Schoepf, W. J., and Patterson, C., 1995, "Natural Convection in Side Heated Cavity: Visualization of the Initial Flow Features," *Fluid Mech.*, Vol. 295, pp. 357–379.

Simpkins, P. G., and Chen, K. S., 1986, "Convection in Horizontal Cavities," *J. Fluid Mech.*, Vol. 166, pp. 21–39.

Stork, K., and Müller, U., 1972, "Convection in Boxes: Experiments," *J. Fluid Mech.*, Vol. 54, pp. 599–611.

Taylor, C., and Ijam, A. Z., 1979, "A Finite Element Numerical Solution of Natural Convection in Enclosed Cavities," *Computer Methods in Applied Mechanics and Engineering*, Vol. 19, pp. 429–446.

Wang, P., and Daniels, P. G., 1994, "Numerical Study of Thermal Convection in Shallow Cavities with Conducting Boundaries," *Int. J. Heat and Mass Transfer*, Vol. 37, No. 3, pp. 387–399.

Willis, G. E., Deardorff, J. W., and Somerville, R. C., 1972, "Roll Diameter Dependence in Rayleigh Convection and Its Effect Upon the Heat Flux," *J. Fluid Mech.*, Vol. 54, pp. 351–368.

APPENDIX

Physical properties of Rhodorsil 47V100 silicone oil: $\rho_0 = 965\ \mathrm{kg \cdot m^{-3}}$; $\mu_0 = 9.65\ 10^{-2}\ \mathrm{N \cdot s \cdot m^{-2}}$; $\beta = 9.5\ 10^{-4}$; $C_p = 1460\ \mathrm{J \cdot kg^{-1} \cdot K^{-1}}$; $\lambda = 0.16\ \mathrm{W \cdot m^{-1} \cdot K^{-1}}$.

Physical properties of "Lexan" polycarbonate: $\rho = 1200\ \mathrm{kg \cdot m^{-3}}$; $C_p = 1170\ \mathrm{J \cdot kg^{-1} \cdot K^{-1}}$; $\lambda = 0.22\ \mathrm{W \cdot m^{-1} \cdot K^{-1}}$.

Physical properties of copper: $\rho = 8960\ \mathrm{kg \cdot m^{-3}}$; $C_p = 386\ \mathrm{J \cdot kg^{-1} \cdot K^{-1}}$; $\lambda = 398\ \mathrm{W \cdot m^{-1} \cdot K^{-1}}$.

P. Cadiou
University of Marne-la-Vallée,
Cité Descartes,
Bldg. Lavoisier,
Champs-sur-Marne,
F-77454 Marne-la-Vallée Cedex 2,
France

G. Desrayaud
INSSET,
University of Picardie,
48 rue Raspail,
BP 422,
F-02109 Saint-Quentin Cedex,
France

G. Lauriat
University of Marne-la-Vallée,
Cité Descartes,
Bldg. Lavoisier,
Champs-sur-Marne,
F-77454 Marne-la-Vallée Cedex 2,
France
e-mail: lauriat@univ-mlv.fr

Natural Convection in a Narrow Horizontal Annulus: The Effects of Thermal and Hydrodynamic Instabilities

Multicellular natural convective flows in narrow horizontal air-filled concentric annuli are considered numerically in this paper. The results show that the multiplicity of the multicellular upper flows reported in the literature can be credited to the existence of an imperfect bifurcation with two stable branches. The emergence and extinction of the buoyancy-driven cells have been proved to be identical on both branches. The appearance of another secondary flow, the origin of which is purely hydrodynamic and located within the crescent base flow at the vertical portions of the annulus, has also been evidenced at moderate values of the Rayleigh number. As Ra is increased a reverse transition from a multicellular structure to a unicellular pattern occurs through a gradual decrease in the number of cells. In addition, it is shown that shear-driven instabilities cannot develop for radius ratios larger than a value close to $R = 1.15$.

Introduction

Natural convection in horizontal concentric annuli has been a subject of interest to many studies during the last three decades because of its importance in a number of engineering applications. The basic two-dimensional steady flow which is observed at low Rayleigh numbers is characterized either by two crescent-shaped or by two kidney-shaped cells according to the value of the radius ratio R. The first pattern is observed for narrow annuli whereas the latter is found only for large radius ratios (Bishop and Carley, 1966). These two patterns present a symmetry with respect to the vertical centerline. The main difference between these two basic flow fields is in the shape of the central flow regions which become distorted into a kidney shape for the second flow structure. Powe et al. (1969) were the first to give a classification of free convective airflows according to the unsteady flow patterns exhibited at higher values of Ra (based on the annulus gap width). They showed experimentally that a three-dimensional thermal plume oscillates in the upper part of the annulus at values of R larger than 2. For intermediate values of R ($1.24 \leq R \leq 2$) a three-dimensional spiral motion exists in the up-flow region. This unsteady flow field has been experimentally and numerically confirmed by Rao et al. (1985) who also showed that this motion appears as transverse rolls in the longitudinal vertical upper plane. For the narrow annuli considered in the present study ($R < 1.24$), the two crescent unicellular base flows did not extend completely within the up-flow region at low Ra values. Unsteady flow which appears at higher Rayleigh numbers consists of one or more pairs of two-dimensional cells in the upper part of the annulus, outside the crescent base flows. These cells oscillate along the longitudinal axis. A bifurcation map showing the transition from the steady crescent base flows to the unsteady multicellular cells was given by Powe et al. (1969).

However, discrepancies among the results reported in the literature for narrow annuli are found (Rao et al., 1985; Fant et al., 1989; Cheddadi et al., 1992; Kim and Ro, 1994). Large differences are shown not only for the Ra values at which bifurcations occur but also in regard to a possible existence of hysteresis phenomena. For example, Kim and Ro (1994) and Fant et al. (1989) found a hysteresis numerically, whereas Rao et al. (1985) show only one type of multicellular flow. Cheddadi et al. (1992) presented two numerical solutions at the same Ra that depends on the initial conditions: the crescent base flow and a multicellular one. However, they failed to obtain multicellular flows experimentally. Rao et al. (1985) and Kim and Ro (1994) supported numerically the general trends presented by Powe et al. (1969); that is, the appearance of multicellular flow patterns in the upper part of narrow annuli. Furthermore, Rao et al. reported a transition of the steady upper cells to oscillatory motion at moderate Rayleigh numbers.

In horizontal annuli, the temperature gradient is both parallel and opposite to gravity at $\theta = 180$ deg as in the Rayleigh-Bénard problem but also perpendicular at $\theta = 90$ deg and 270 deg as in differentially heated vertical slots. Consequently, a fluid motion sets in whatever the value of the gradient is, in the form of two crescent eddies symmetric about the vertical centerline. These remarks suggest that thermal or Rayleigh-Bénard type of instabilities can occur in the upper horizontal portion of the annulus. Under certain conditions, hydrodynamic instability can also appear in the vertical portions like it is observed in vertical slots. A brief review of this second type of instability is given in what follows.

Using a linear stability analysis of steady two-dimensional natural convection of a fluid layer confined between differentially heated vertical plane walls, Korpela et al. (1973) reported that the flow is primarily unstable against purely hydrodynamic steady waves in the limit of zero Prandtl number. These secondary shear-driven instabilities are cross cells called "cat's eyes." Increases in Prandtl number lead to the appearance of buoyancy-driven oscillatory instabilities. The critical value of Pr determining which type of instabilities appears has been numerically determined to be around Pr = 12.7 by many authors. In slots of finite aspect ratio A (height over width) the vertical temperature gradient is an addi-

---

Contributed by the Heat Transfer Division for publication in the JOURNAL OF HEAT TRANSFER. Manuscript received by the Heat Transfer Division, Feb. 18, 1998; revision received, June 23, 1998. Keywords: Computational, Enclosure Flows, Heat Transfer, Instability, Natural Convection. Associate Technical Editor: R. Douglass.

tional parameter which has to be taken into account. Using numerical results and linear stability analysis, Roux et al. (1980) have demonstrated the existence of a zone of limited extent in the (Ra, A)-plane inside which steady cat's eyes can develop. This zone is only for aspect ratios larger than about $A = 11$ for air-filled cavities. This result was confirmed by the numerical studies of Lauriat (1980), Lauriat and Desrayaud (1985), and more recently by Le Quéré (1990) and Wakitani (1997). As Ra is further increased, a reverse transition from multicellular flow to unicellular flow occurs and this has been numerically and experimentally demonstrated by Roux et al. (1980), Lauriat (1980), Desrayaud (1987), and Chikhaoui et al. (1988).

It should be noted that this steady cat's eye zone seems to be much more complex than has been stated in the above referenced works. Le Quéré (1990) conducted a numerical study in a vertical cavity of aspect ratio $A = 16$ by gradually increasing or decreasing the Rayleigh number and he found a multiplicity of multicellular flows characterized by the number of cells. He showed a rather complex diagram of bifurcations based on the number of cells which exhibits hysteresis branches and a reverse transition to unicellular flow through a gradual decrease in the number of cells. More recently, Wakitani (1997) demonstrated the dependence of the multicellular structures on the initial conditions.

In a horizontal narrow annulus, Fant et al. (1989, 1990) numerically determined such hydrodynamic type of instability for the limit of zero Prandtl number fluid. These instabilities occur in the vertical portions of the annulus (inside the basic flow field) as like-rotating cells, and they can spread throughout the basic crescent-shaped cells. The first study (Fant et al., 1989) relates to an half-annulus of radius ratio $R = 1.09$. The critical value of the Grashof number was found to be around Gr = 10,060. Above the critical value, the flow develops a periodic motion of sequences of 4–5 cells inside the basic cells around the vertical portion of the annulus. These hydrodynamic instabilities are similar to those found by Korpela et al. (1973) in vertical slots for Prandtl number lower than Pr = 12.7. Fant et al. (1989) showed also that the variation of the critical Grashof number versus the radius ratio is scaled as $R \sim \mathrm{Gr}_c^{-0.30}$. They noticed that the number of cells at transition increased as the radius ratio decreased. Fant et al. (1990) solved the boundary layer equations in the limit of a zero-Prandtl-number fluid for narrow-gap annuli. They confirmed the magnitude of the critical Grashof number as well as the mode of instability. However, they found that the flow first develops a steady motion of seven cells which turns out to be unsteady at higher Gr numbers. A periodic motion with a sequence of 8–7–8–7 cells is then obtained. It is followed by a much more complex sequence of unsteady motions from perfectly periodic to chaotic behavior. It should be noticed that no upper cells were shown in these two studies since the limiting case of a zero Prandtl number was assumed. However, these cells were not detected by Rao et al. (1985) for an air-filled annulus of radius ratio $R = 1.175$ at Ra = 50,000.

The purpose of this paper is to study numerically the flow structure which develops both in horizontal and vertical regions of narrow air-filled annuli. The first part is devoted to the thermal instabilities observed in the top of the annulus and clarify, through the concept of imperfect bifurcation, the discrepancies found in the literature. Focusing next on hydrodynamic instabilities, it is shown that the basic flow field becomes multicellular and then returns to a unicellular structure when the Rayleigh number is gradually increased. Thus, a reverse transition of hydrodynamic instability occurs. Such instability only sets in for annuli having a radius ratio lower than $R = 1.15$.

Numerical Simulations

Governing Equations. Consider a horizontal air-filled annulus of inner and outer radii r_i' and r_o' as shown in Fig. 1. The surfaces of the cylinders are held at constant temperature T_i and T_o, respectively, with $T_i > T_o$. Only two-dimensional natural convection is considered in a plane perpendicular to the axis of the annulus. The cylindrical coordinate system is defined so that the r-axis is in the radial direction with the origin at the axis of the annulus and θ is the angular coordinate measured from the downward vertical. We consider laminar flows of a Newtonian fluid and assume that the Boussinesq approximation is valid. The governing equations are put into dimensionless forms by scaling length and time by the gap width $L = r_o' - r_i'$ and α/L, respectively. A dimensionless temperature difference is defined by $\Theta = (T - T_m)/\Delta T$, with $T_m = 0.5(T_i + T_o)$ and $\Delta T = (T_i - T_o)$ where T is the fluid temperature. The governing equations may be written in dimensionless form as

$$\frac{\partial}{\partial r}(fu) + \eta \frac{\partial v}{\partial \theta} = 0 \tag{1}$$

$$\frac{\partial}{\partial t}(fu) + \frac{\partial}{\partial r}(fuu) + \frac{\partial}{\partial \theta}(\eta v u) - \eta v^2$$
$$= -\mathrm{f}\,\frac{\partial \mathrm{P}}{\partial \mathrm{r}} - \mathrm{Ra}\,\mathrm{Pr} f \Theta \cos\theta + \mathrm{Pr}\left(\frac{\partial}{\partial r}\left[f\,\frac{\partial u}{\partial r}\right]\right.$$
$$\left. + \frac{\partial}{\partial \theta}\left[\frac{\eta^2}{f}\frac{\partial u}{\partial \theta}\right] - \frac{2\eta^2}{f}\frac{\partial v}{\partial \theta} - \frac{\eta^2}{f}u\right) \tag{2}$$

$$\frac{\partial}{\partial t}(fv) + \frac{\partial}{\partial r}(fuv) + \frac{\partial}{\partial \theta}(\eta v v) + \eta u v$$
$$= -\mathrm{f}\,\frac{\partial \mathrm{P}}{\partial \theta} + \mathrm{Ra}\,\mathrm{Pr} f \Theta \sin\theta + \mathrm{Pr}\left(\frac{\partial}{\partial r}\left[f\,\frac{\partial v}{\partial r}\right]\right.$$
$$\left. + \frac{\partial}{\partial \theta}\left[\frac{\eta^2}{f}\frac{\partial v}{\partial \theta}\right] + \frac{2\eta^2}{f}\frac{\partial u}{\partial \theta} - \frac{\eta^2}{f}v\right) \tag{3}$$

Nomenclature

g = acceleration due to gravity
Gr = Grashof number, Ra/Pr
L = gap width, $r_o' - r_i'$
Nu = local Nusselt number defined in Eq. (7)
$\overline{\mathrm{Nu}}$ = average Nusselt number defined in Eq. (8)
Pr = Prandtl number, ν/α
r = dimensionless radial coordinate
r_i = inner cylinder radius
r_o = outer cylinder radius
R = radius ratio, r_o/r_i
Ra = Rayleigh number, $g\beta L^3 \Delta T/\alpha\nu$
T_m = mean temperature, $0.5(T_i + T_o)$
u, v = radial and azimuthal velocity components

Greek Symbols

α = thermal diffusivity
β = coefficient of thermal expansion
ν = kinematic viscosity
θ = angular coordinate measured from downward vertical
ΔT = temperature difference, $T_i - T_o$

Superscript

$'$ = dimensional variables

Subscripts

i = inner cylinder
o = outer cylinder

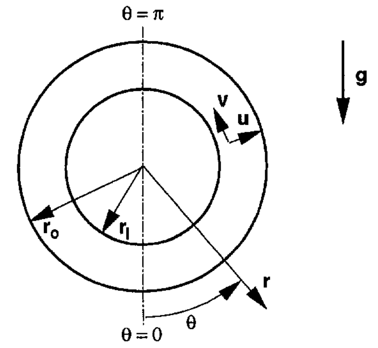

Fig. 1 Computational domain and coordinate system

$$\frac{\partial}{\partial t}(f\Theta) + \frac{\partial}{\partial r}(fu\Theta) + \frac{\partial}{\partial \theta}(\eta v\Theta) = \frac{\partial}{\partial r}\left[f\,\frac{\partial \Theta}{\partial r}\right] + \frac{\partial}{\partial \theta}\left[\frac{\eta^2}{f}\,\frac{\partial \Theta}{\partial \theta}\right] \quad (4)$$

with $\eta = R - 1$ and $f = f(r) = \eta r + 1$. The boundary conditions for the above system of equations are

$$\textit{Inner B.C.}\quad \text{at}\quad r = r_i \quad\text{and}\quad 0 \le \theta \le 2\pi,$$
$$\text{for}\quad u = v = 0 \quad \Theta = 0.5$$
$$\textit{Outer B.C.}\quad \text{at}\quad r = r_o \quad\text{and}\quad 0 \le \theta \le 2\pi,$$
$$\text{for}\quad u = v = 0 \quad \Theta = -0.5 \quad (5)$$

The motionless and isothermal solution used as the initial guess for computations is given by

$$\text{for } t = 0 \quad\text{at}\quad r_i \le r \le r_o \quad\text{and}\quad 0 \le \theta \le 2\pi,$$
$$u = v = 0 \quad \Theta = -0.5. \quad (6)$$

The nondimensional parameters Ra, Pr, and R are defined by

$$\mathrm{Ra} = g\beta L^3 \Delta T/\alpha\nu \quad \mathrm{Pr} = \nu/\alpha \quad R = r_o/r_i.$$

The Prandtl number considered here is that of the air, Pr = 0.7.

The local Nusselt number is defined as the ratio of the actual heat transfer to the conduction heat transfer and may be written as:

$$\mathrm{Nu}(r, \theta) = \ln R(u\Theta - \partial\Theta/\partial r)r \quad (7)$$

The mean Nusselt numbers at the inner and outer cylinders are defined as follows:

$$\overline{\mathrm{Nu}}_i = -\frac{r_i \ln R}{2\pi}\int_0^{2\pi}\left(\frac{\partial \Theta}{\partial r}\right)_{r=r_i} d\theta \quad (8)$$

$$\overline{\mathrm{Nu}}_o = -\frac{r_o \ln R}{2\pi}\int_0^{2\pi}\left(\frac{\partial \Theta}{\partial r}\right)_{r=r_o} d\theta \quad (9)$$

At steady state $\overline{\mathrm{Nu}}_i$ and $\overline{\mathrm{Nu}}_o$ are equal to $\overline{\mathrm{Nu}}$.

During the transient evolution of the flow field, a change from a unicellular to a multicellular pattern may occur after a rather long period during which the mean Nusselt numbers remain unchanged up to five digits. Figure 2 shows such a very long transient evolution of the flow from a subcritical state at Ra = 1900 to a supercritical state at Ra = 2000 for an annulus of radius ratio $R = 1.20$. Noticeable change in the value of the mean Nusselt numbers arises after a dimensionless time of about $t = 5$ (10,000 time steps) and the transition is achieved for t greater than about 12. This behavior has also been noticed by Rao et al. (1985). Thus, convergence criteria used to stop the computations must be carefully chosen. Indeed, very small values of these criteria have to be assumed, otherwise the temporal evolution can be interrupted before the transition to multicellular flow occurs. In fact, it appears that there is no best stopping criterion, and that it is preferable to fix the maximum number of time steps on the basis of physical considerations and computational costs, with careful and continuous attention to the evolution of the flow variables.

Solution Procedure. The two-dimensional governing equations were solved numerically in the primitive variable formulation by employing a finite volume method. The SIMPLER algorithm was used to treat the coupling between momentum and continuity. The transport terms in the momentum and energy equations were discretized using a second-order centered scheme. For the temporal evolution, an alternating directional implicit method was adopted to arrange the resulting set of algebraic equations in the tridiagonal form. An orthogonal, nonuniform, and staggered grid system was considered. The program was designed to take particular advantage of vector computers, like the CRAY C90.

Because of the large discrepancies found in the literature on flow characteristics and critical Rayleigh numbers, careful examination of the grid dependency of the results was made for a radius ratio $R = 1.20$ at Ra = 3000. A sample of mean Nusselt number at steady state and velocity maximum is reported in Table 1 for various grids. Comparisons with a commercial finite element code were also conducted. It can be noted that the grid in the angular direction was nonuniform with grid refinement at the upper part of the annulus. The number of grid points in the radial (n_r) and angular (n_θ) directions are given for a half-annulus. The following symmetric boundary conditions for a half-annulus have been adopted:

$$\frac{\partial u}{\partial \theta} = v = \frac{\partial \Theta}{\partial \theta} = 0 \quad\text{at}\quad \theta = 0 \text{ and } \pi. \quad (10)$$

A relative discrepancy less than one percent was obtained for a 19 × 146 grid compared to the finest grid when using the finite volume method. An excellent agreement between the finite element method and finite volume method is reported also (finite element method values are shown in parentheses in Table 1). In addition, the first bifurcation point was determined with both numerical codes (Table 2). The calculations performed for a half-annulus and various grid sizes resulted in a 2.5 percent change in the critical Rayleigh number. Its value is 1925 for the finest grid compared to 1920, which was found by using the finite element method with 25 × 146 elements (shown in parentheses in Table 2). When using the finite element method

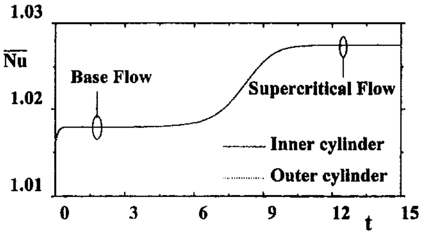

Fig. 2 Temporal evolution of the mean Nusselt numbers on outer and inner cylinders; Ra = 2000, $R = 1.20$, Pr = 0.7 (initial solution: Ra = 1900)

Table 1 Value of the mean Nusselt number and of the maximum of the velocity for various grids, $R = 1.20$, Ra = 3000, Pr = 0.7 (values reported in parentheses were obtained using a finite element method)

$n_r - n_\theta$	13–74	19–110	25–146	41–246
$\overline{\mathrm{Nu}}$	1.134 (1.109)	1.127 (1.116)	1.124 (1.118)	1.122 (–)
max $\sqrt{u^2 + v^2}$	23.37 (23.27)	23.86 (23.78)	24.03 (23.92)	24.06 (–)

Table 2 Critical Rayleigh numbers as a function of the grid size, $R = 1.20$, $Pr = 0.7$ (values reported in parentheses were obtained using a finite element method)

$n_r - n_\theta$	13–74	19–110	25–146	35–202
Ra	— (1950)	1880 (1935)	1915 (1920)	1925 (–)

or finite volume method, the transition was seen to occur from the unicellular crescent flow to a steady bicellular pattern with only one outer upper cell.

For thermal instabilities of air, which emerge as cells in the upper part of the annulus, computations were performed in a half-annulus for low Rayleigh numbers ($Ra < 5000$) at which symmetry about the vertical centerline can be assumed since the cells are motionless. The nodes of a 25×146 nonuniform mesh are concentrated near the top of the annulus to resolve adequately the first upper cell arising just after the critical bifurcation. This mesh density was selected for subsequent runs since it required significantly less computing resources without affecting the global accuracy of the results. A great number of nodes in the angular direction, especially at the top of the annulus, is particularly important in order to capture properly the appearance of the first thermal cells.

For hydrodynamic instabilities which appear at much higher Rayleigh numbers ($10{,}000 < Ra < 50{,}000$), the governing equations were solved within the entire annulus owing to the unsteadiness of the thermal cells, which oscillate right and left at the upper part of the annulus. The computations were then performed on a 31×240 uniform mesh and periodic boundary conditions were applied at $\theta = 0(2\pi)$.

Results

Thermal Instabilities. In a narrow horizontal concentric annulus with the inner cylinder temperature exceeding the outer, a natural convective flow sets in immediately in the form of two steady crescent rolls, symmetric about the vertical centerline. By increasing the Rayleigh number, a steady multicellular flow appears at the upper part of a narrow annulus. This flow structure is the result of amplification of thermal instabilities in a similar way to Rayleigh-Bénard cell development between horizontal planes. In the Rayleigh-Bénard problem, two branches of solution corresponding to steady clockwise and counterclockwise cell motions bifurcate from the hydrostatic solution at $Ra = Ra_c$. When conducting experiments, the probability of appearance of one of these perfectly symmetric solutions is almost the same because infinitesimal disturbances cannot be eliminated. On the other hand, the numerical disturbances (round-off errors) are negligibly small in comparison with the truncation errors, especially when using a finite volume method-method with a second-order accuracy in space integration. Therefore, while one branch is followed naturally through gradual increases in Ra, the other must be artificially aided. It is well established that the hydrostatic solution undergoes a pitchfork bifurcation at $Ra_c = 1708$ and the flow becomes oscillatory through the next bifurcation for small-Prandtl number fluids. The instabilities assume then the form of a wavy sinusoidal motion which propagates along the axis of the cell pattern.

In horizontal differentially heated annuli, the symmetry of the supercritical solutions on the two branches no longer holds because the pitchfork bifurcation degenerates into an imperfect bifurcation, at least for narrow annuli. In addition, the wall curvature modifies the bifurcation patterns found in the Rayleigh-Bénard problem. The two stable solutions are characterized by an upward (respectively, downward) radial velocity at the upper vertical centerline which in turn defines an upright (respectively, inverted) thermal plume within the top portion of the annulus. Such a behavior is depicted in Fig. 3 for a radius ratio $R = 1.04$ which shows the stable solutions on the two branches at the same Rayleigh number ($Ra = 3000$). The lack of symmetry between the two branches is clearly seen through the different number of cells built upon the main flow cell near the top of the annulus.

As it was noticed in a number of works dealing with hydrodynamic instabilities, initial conditions may determine which of the two stable branches of the imperfect bifurcation will be followed. This is in contrast to what was stated in other studies in which the different solutions were characterized by the number of cells within the top annulus region. One of the two branches is reached naturally through gradual increases in Rayleigh number from an initial value lower than Ra_c and using the converged solution as initial guess for the next Rayleigh number. The other branch is reached by using as an initial condition either a motionless and isothermal state or a slightly perturbed conductive temperature field (Cheddadi et al., 1994), and by abruptly increasing the Rayleigh number to a value substantially greater than Ra_c. For example, a perturbed temperature distribution such that

$$\Theta(r, \theta) = 0,5 - \frac{1}{\ln R}\cdot \ln\left[(R-1)\cdot r + 1\right] + \alpha \cdot \sin\left[\frac{\pi}{\ln R}\cdot \ln\left[(R-1)\cdot r + 1\right]\right]\cdot \cos \eta\theta \quad (11)$$

where α is an amplification coefficient and η a wavenumber, can be used as an initial condition.

In this case Ra_c can be determined by decreasing the Rayleigh number and the value obtained is almost the same as the one on the other bifurcation branch. Figure 4 presents the variation of the radial component of the velocity on both branches. This pattern evidences an imperfect bifurcation. Similar bifurcation diagrams have been obtained for various values of the radius ratio: $R = 1.08$, 1.12, 1.16, and 1.20. It should be noted that the critical Ra number increases slightly with an increase in R. The loss of symmetry of the solutions on the two branches is so weak that the Ra_c values for the two branches are almost indistinguishable, even at R value as large as $R = 1.20$ (Fig. 4). Although the present computations were carried out by using a Ra increment as small as 10 it was not possible to simulate hysteresis effects. If a further reduction in Ra increment is theoretically feasible, the computational costs are still tremendous, even by using supercomputers, because the time of integration required to obtain the transition from a multicellular to a unicellular mode increases dramatically when nearing the critical Rayleigh number. In Fig. 4, the solutions are shown with crosses (respectively, open symbols) on the A branch (respectively, D branch).

Table 3 Comparison of the critical Rayleigh numbers

R	1.04	1.08	1.12	1.16	1.20	$\sqrt{2}$	1.60
Present results	1735	1770	1810	1870	1915	—	—
Kim and Ro (1994)	—	—	—	—	1920	2150	2355
Correlation (12)	1728	1774	1820	1866	1912	2158	2372

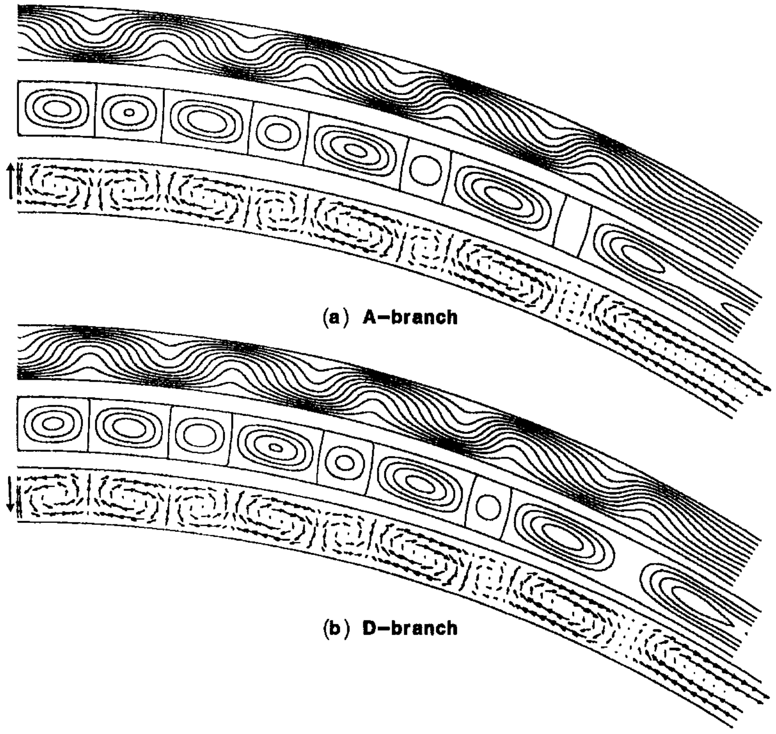

Fig. 3 Stationary isothermal patterns (−0.5 (0.1) 0.5), streamlines and velocity fields within the angular section 147.74 deg $< \theta <$ 180 deg at R = 1.04, Ra = 3000 and Pr = 0.7

On both branches, the birth of the cells upon the main flow cells is the same. Since the flow field is symmetric with respect to the center vertical, we consider only the right half-annulus where the crescent base flow is clockwise. If we assume that the cell next to the base flow is counterclockwise then the new eddy created by increasing Ra emerges from the base flow by separation. This separation process is generated by a competition between the buoyancy force and the viscous drag, as in the classical Rayleigh-Bénard problem. This new cell is then clockwise (like the base flow), and a stagnant zone starts to develop between them. Within this stagnant intercells zone, spreading out as the clockwise cell grows in strength with increases in Ra, one more cell appears. This cell is obviously counterclockwise owing to the driving viscous stresses between the cell streams which generate it. The process can go on downward until the curvature effect prevents a possible separation of the base flow. Decreases of the Rayleigh number leads to an inverse process with merging of cells up to the fading away of the uppermost cell. The multicellular motion degenerates then to a unicellular structure at a critical Rayleigh number very close to the Ra_c value obtained when increasing Ra.

From the present computations, a correlation equation for the critical Rayleigh number as a function of the radius ratio was found as

$$\mathrm{Ra}_c(R) = 552 + 1150R. \tag{12}$$

This correlation was obtained by increasing Ra from the stable unicellular flow pattern.

Hydrodynamic Instabilities. When increasing Ra secondary instabilities appear within the crescent base flow at small enough radius ratios. This second type of instabilities takes the form of unsteady cross cells which are axially oriented. These hydrodynamic instabilities are the result of the shear between the two counterflowing streams within the main flow cell.

Figure 5 presents the streamlines for various Rayleigh numbers for an annulus of radius ratio R = 1.12. A unicellular base flows is found at Ra = 6000. The cells at the top portion of the

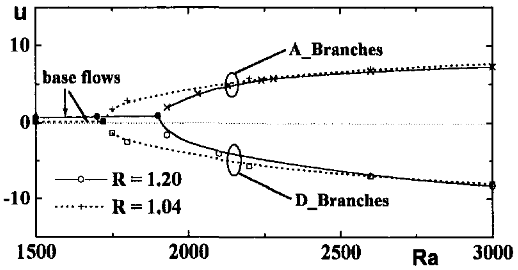

Fig. 4 Bifurcation diagram of the radial component of the velocity for R = 1.04 and 1.20 at $\{r = 0.5(r_i + r_o), \theta = \pi\}$, Pr = 0.7

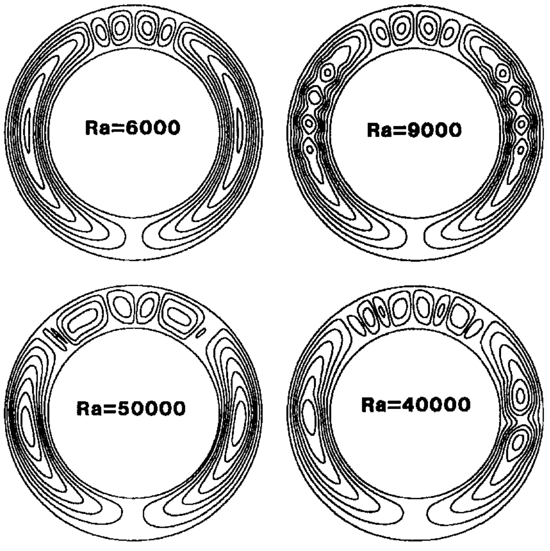

Fig. 5 Streamlines for various Rayleigh numbers (R = 1.12, Pr = 0.7)

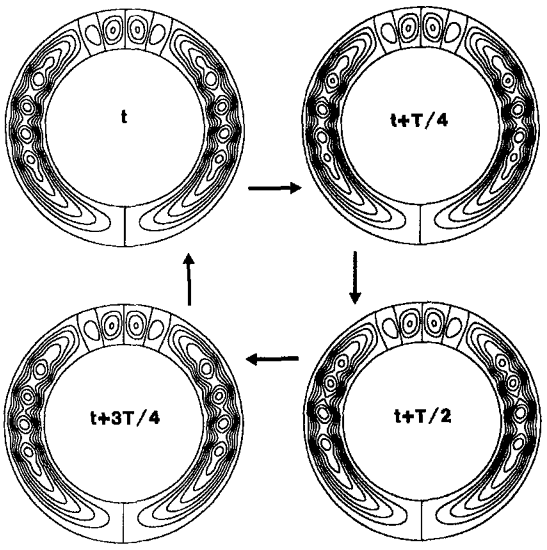

Fig. 6 Streamlines plotted at four equal intervals of one oscillation period with time progressing in the clockwise direction, Ra = 12000, R = 1.12, Pr = 0.7)

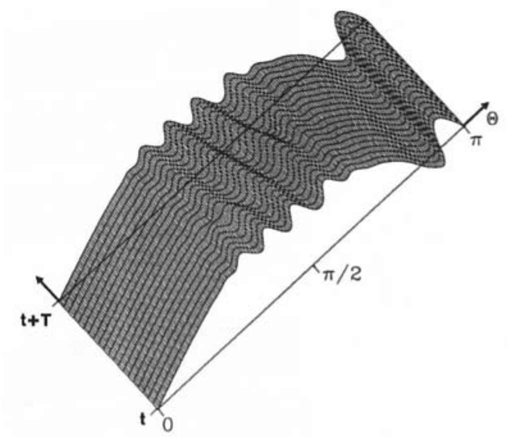

Fig. 8 Temporal evolution on half cylinder of the stream function at point $r = 0.5(r_i + r_o)$, (Ra = 12000, R = 1.12, Pr = 0.7)

annulus are then stationary. When increasing Ra, the base flow undergoes a multicellular structure as shown in Fig. 5 for Ra = 9000 and the cells come to oscillate with a perfectly time-periodic motion. At Ra = 40,000 the cells are unsteady within both top annulus portion and base flow. It should be noted that the amplitude of the fluctuations of the thermal cells and of the hydrodynamic cells are of same order of magnitude. At this Ra value, small time steps were used to accurately resolve the evolution of the flow and a very long integration time was required in order to accurately simulate the unsteady behavior of the oscillatory motion. Similarly to what is observed in vertical differentially heated slots, a reverse transition from multicellular to unicellular structure of the base flow is found when increasing Ra. For example, Fig. 5 shows that an increase in Ra up to 50,000 yields a unicellular base flow in an annulus with R = 1.12. However, the thermal cells at the top portion of the annulus were found to remain oscillatory in the range of Ra considered.

The periodic behavior of the flow is in contrast to the numerical results obtained by Fant et al. (1990) in the limit of a zero-Prandtl number fluid. They reported that the cell formation follows a sequence of type $(n, n + 1, n, n + 1)$ cells, the new cells originating alternatively during one period from the upper part or from the bottom part of the base flow, and otherwise from the top of the chain of cells or from the bottom. For an air-filled annulus, thermal cells are only located within the upper portion of the annulus, and during their oscillatory motion these cells push down the two main base cells. As a result, the upper thermal cells inhibit the development of the hydrodynamic cells at the bottom of the base flows. It follows that the sequence systematically presents only the same number of cells over a period, this number being a function of Ra and R. This is exemplified in Fig. 6 which shows four snapshots of streamlines equally time spaced during one period for R = 1.12 and Ra = 12,000. Figure 7 shows the periodic evolution of the stream function at $\theta = \pi/2$ and $\theta = \pi$ and the position of the four snapshots plotted in Fig. 6 are displayed over one period as open circles. The evolution over one period of the stream function at the middle of the annulus gap-width and from $\theta = 0$ to $\theta = \pi$ is shown in Fig. 8 for Ra = 12,000. As can be seen, the changes in size of the thermal cells (close to $\theta = \pi$) is almost negligible while growth and disappearance of the hydrodynamic cells are evident. At the beginning of the time period, the four cells corresponding to snapshot 1 in Fig. 6 are clearly shown. During the first half of the period, the smallest cell ($\theta < \pi/2$) vanishes while a cell appears and grows at the uppermost part of the base flow ($\theta > \pi/2$). When strengthening this cell pushes down the other cells and the result is that the bottom cell disappears gradually. At higher Ra, the number of hydrodynamic cells decreases and the amplitude of their oscillatory motion becomes much less than the amplitude of the thermal cells. The power spectrum of the stream function fluctuations displayed in Fig. 7 for Ra = 12,000 is shown in Fig. 9. The periodic nature of the hydrodynamic instabilities is clearly seen. To accurately calculate the fundamental frequency, $f = 0.42 \pm 0.02$, 120 time units or 35,000 time steps, representing about 50 periods, were used.

Figure 10 shows the streamlines for Ra = 15,000 and various radius ratios. Each of these solutions were obtained through

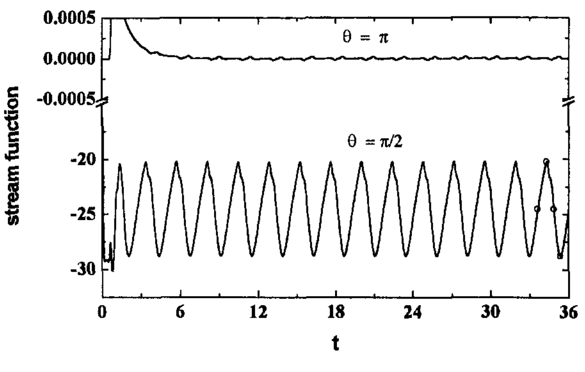

Fig. 7 Temporal evolution of the streamfunction at points $\{r = 0.5(r_i + r_o)\}$ and $\theta = \pi/2$ or π (Ra = 12000, R = 1.12, Pr = 0.7)

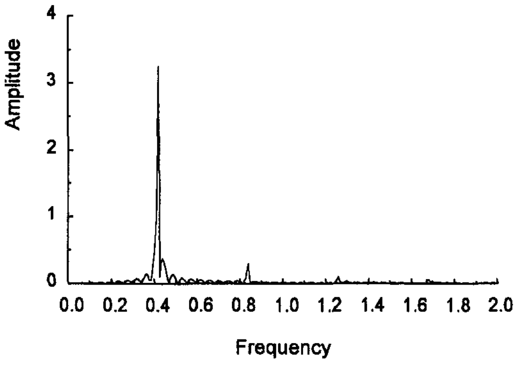

Fig. 9 Power spectrum of the stream function at $r = 0.5(r_i + r_o)$ and $\theta = \pi/2$ for Ra = 12,000 (R = 1.12, Pr = 0.7)

gradual increases in Ra, starting from a motionless and isothermal state as initial condition. The main conclusion which can be drawn from Fig. 10 is that hydrodynamic cells cannot develop when the radius ratio is greater than 1.15. The reason is that the curvature effect damps the amplification of hydrodynamic instabilities because the viscous stresses between the upward and downward flows decrease as R increases. This behavior is very similar to that was found in tall vertical cavities by Roux et al. (1980), Lauriat and Desrayaud (1985) and Le Quéré (1990). It is why Rao et al. (1985) did not detect hydrodynamic instabilities in an annulus with $R = 1.175$, even at a Rayleigh number as high as 50,000.

A diagram showing the flow structure of the different solutions calculated at various Ra and radius ratios is reproduced in Fig. 11. Unsteady calculations are presented through open square or circle when time periodic or chaotic motions were found. In agreement with the experimental flow pattern chart given by Powe et al. (1969), the present computations show that the Rayleigh number at which a transition to unsteady solutions first appears, increases by increasing the radius ratio. However, these critical Ra are lower than those determined experimentally. For example, a periodic motion was numerically simulated at Ra = 20,000 for $R = 1.16$ while the flow pattern chart of Powe et al. shows a transition from two-dimensional stable flow to two-dimensional multicellular but steady flow at a Ra value of the order of 32,000. The main other significance in Fig. 11 is to display that shear driven cells cannot develop in air-filled horizontal annuli if the radius ratio is greater than about $R = 1.15$. Also, a reverse transition to steady flows is clearly shown for Ra above the full line plotted in the R-Ra plane. As can be seen, the reverse transition to a unicellular basic flow pattern (together with chaotic motions of the thermal cells at the top of the annulus) is obtained at lower Ra when increasing the radius ratio. This finding is consistent with what has been found for tall vertical air-filled cavities. For $R \geq 1.15$, the transition to unsteady solutions are solely due to amplifications of the disturbances within the thermal cells.

Conclusions

Numerical investigations of multicellular natural convective flows in narrow horizontal air-filled concentric annuli have been carried out. Both thermal and hydrodynamic instabilities have been considered.

It has been first shown that the concept of imperfect bifurcation may explain the apparent multiplicity of the multicellular upper flows presented in the literature which, in fact, lie on two branches of a bifurcation. The hysteresis phenomena found in the literature are probably due to coarse grids and/or values of convergence criteria which are unsuitable to obtain the true solutions.

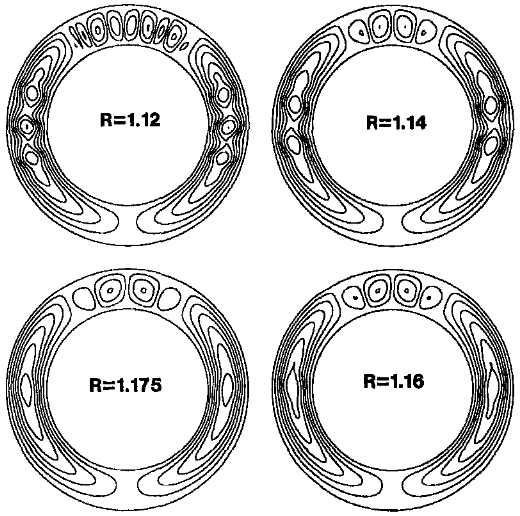

Fig. 10 Streamlines for various values of the radius ratio at the same Rayleigh number (Ra = 15,000, Pr = 0.7)

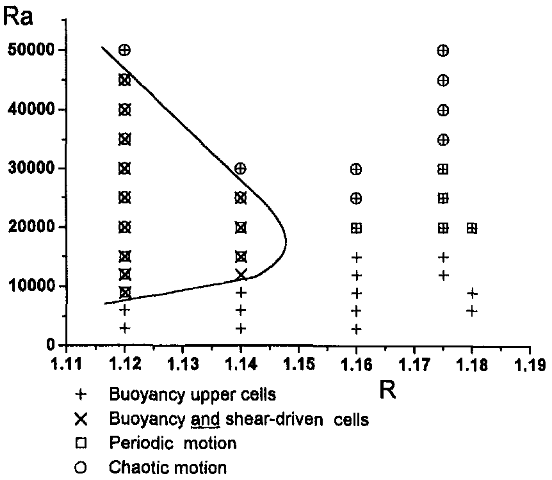

Fig. 11 Map of various kinds of multicellular flow patterns (Pr = 0.7)

Secondly, hydrodynamic instabilities have been simulated at moderate Rayleigh numbers. These instabilities set in as unsteady cross rolls inside the two crescent base flows. The perfect periodic motions are followed by a more complex behavior which is difficult to analyze owing to the very large computational times required. Nevertheless, a reverse transition from multicellular to unicellular base flows was evident as the Rayleigh number was increased. Furthermore, hydrodynamic cells cannot develop when the radius ratio is larger than $R = 1.15$. This finding is similar to what has been found in differentially heated vertical cavities of high aspect ratio.

Acknowledgments

Grant nos. 970174 and 981030 from the IDRIS-computer center (French National Institute for Advances in Scientific Computations) is gratefully acknowledged.

References

Bishop E. H., and Carley C. T., 1966, "Photographic Studies of Natural Convection between Concentric Cylinders," *Proc. Heat Transf. Fluid Mech. Inst.*, pp. 63–78.

Cheddadi A., Caltagirone J. P., Mojtabi A., and Vafai K., 1992, "Free Two-dimensional Convective Bifurcation in a Horizontal Annulus," ASME JOURNAL OF HEAT TRANSFER, Vol. 114, pp. 99–106.

Chikhaoui A., Marcillat J. F., and Sani R. L., 1988, "Successive Transitions in Thermal Convection within a Vertical Enclosure," *Natural Convection in Enclosures,* ASME HTD-Vol. 99, pp. 29–35.

Desrayaud G., 1987, "Analyse de stabilité linéaire dans un milieu semi-transparent. Détermination expérimentale des limites de stabilité dans un milieu transparent," thèse de doctorat ès sciences physiques.

Fant D. B., Rothmayer A., and Prusa J., 1989, "Natural Convective Flow Instability between Horizontal Concentric Cylinders," *Numerical Methods in Laminar and Turbulent Flow,* Vol. 6 Part 2, Pineridge Press, Swansea, UK, pp. 1047–1065.

Fant D. B., Prusa J., and Rothmayer A., 1990, "Unsteady Multi-Cellular Natural Convection in a Narrow Horizontal Cylindrical Annulus," ASME JOURNAL OF HEAT TRANSFER, Vol. 112, pp. 379–387.

Kim C. J., and Ro S. T., 1994, "Numerical Investigation on Bifurcative Natural Convection in an Air-Filled Horizontal Annulus," *10th Int. Heat Transfer Conference,* Vol. 7, pp. 85–90.

Korpela S. A., Gozum D., and Baxi C. B., 1973, "On the Stability of the Conduction Regime of Natural Convection in a Vertical Slot," *Int. J. Heat Mass Transfer,* Vol. 16, pp. 1683–1690.

Lauriat G., 1980, "Numerical Study of Natural Convection in a Narrow Cavity: An Examination of High Order Accurate Schemes," ASME Paper No. 80-HT-90.

Lauriat G., and Desrayaud G., 1985, ''Natural Convection in Air-Filled Cavities of High Aspect Ratios: Discrepancies between Experimental and Theoretical Results,'' ASME Paper No. 85-HT-37.

Le Quéré P., 1990, ''A Note on Multiple and Unsteady Solutions in Two-Dimensional Convection in Tall Cavity,'' ASME JOURNAL OF HEAT TRANSFER, Vol. 112, pp. 965–974.

Powe R. E., Carley C. T., and Bishop E. H., 1969, ''Free Convective Flow Patterns in Cylindrical Annuli,'' ASME JOURNAL OF HEAT TRANSFER, Vol. 91, pp. 310–314.

Rao Y., Miki Y., Fukuda K., Takata Y., and Hasegawa S., 1985, ''Flow Patterns of Natural Convection in Horizontal Cylindrical Annuli,'' *Int. J. Heat Mass Transfer,* Vol. 28, No. 3, pp. 705–714.

Roux B., Grondin J., Bontoux P., and de Vahl Davis G., 1980, ''Reverse Transition from Multicellular to Monocellular Motion in Vertical Fluid Layer,'' *Phys. Chem. Hydro.,* Vol. 3F, pp. 292–297.

Wakitani S., 1997, ''Development of Multicellular Solutions in Natural Convection in an Air-Filled Vertical Cavity,'' ASME JOURNAL OF HEAT TRANSFER, Vol. 119, pp. 97–101.

Toshio Tagawa

Hiroyuki Ozoe[1]

Institute of Advanced Material Study,
Kyushu University,
Kasuga 816, Japan

Enhanced Heat Transfer Rate Measured for Natural Convection in Liquid Gallium in a Cubical Enclosure Under a Static Magnetic Field

The heat transfer rate of natural convection in liquid gallium in a cubical enclosure was measured experimentally under an external magnetic field applied horizontally and parallel to the vertical heated wall and the opposing cooled wall of the enclosure. One vertical wall was heated with an electric heater and the opposing wall was cooled isothermally with running water. Experiments were conducted in the range of modified Rayleigh number from 1.85×10^6 to 4.76×10^6 and of Hartmann number from 0 to 573. The average Nusselt number was measured and found to increase when a moderate magnetic field was applied, but to decrease under a stronger magnetic field. This result means that the heat transfer rate has a maximum value at a certain moderate magnetic field, which supports our previous numerical analyses.

1 Introduction

Fumizawa (1980) and Takahashi et al. (1986) reported that the heat transfer rate of natural convection in liquid metals was enhanced by a moderate magnetic field. These findings called into question the conventional understanding that the heat transfer rate decreases under an external magnetic field because natural convection of electro-conducting fluids, such as liquid metals, is suppressed by the Lorentz force induced in liquid metals.

Ozoe and Okada (1989) recently reported that heat transfer rate of natural convection of liquid metal differs greatly depending on the direction of the applied magnetic field. They studied three cases of external magnetic fields, namely, horizontal and perpendicular to the heated wall (the *X*-direction), horizontal and parallel to the heated wall (the *Y*-direction), and vertical (the *Z*-direction). They (Okada and Ozoe, 1992) then measured the average heat transfer rate of natural convection of liquid gallium for a similar system with electric heating from one vertical wall and confirmed their previous computational results. Under the *X* or *Z*-directional magnetic field, the average heat transfer rate decreased with the strength of the magnetic field. However, under the *Y* directional magnetic field, a stronger magnetic field by one order of magnitude was required to suppress the average heat transfer rate by the same amount. This indicated the very weak suppressing effect of the *Y*-directional magnetic field. Furthermore, some of the experimental data for the *Y*-directional magnetic field suggested a slight increase in the heat transfer rate over the nonmagnetic case. However, the increase was within the limit of experimental uncertainty and could not be taken as a definite enhancement. Their system for applying the *Y*-directional magnetic field was similar in configuration to Fumizawa's experimental setup.

Tagawa and Ozoe (1997) carried out detailed three-dimensional numerical analyses for a similar system to that in Ozoe and Okada (1989) but for the *Y*-directional magnetic field (horizontal and parallel to the heated and cooled plates) and found enhancement of the heat transfer rate at some weak magnetic fields. They attributed the physical reason for this enhancement to Lorentz forces induced near the electrically insulated side walls. The present paper aims to support these theoretical findings by experimental measurements for a similar system.

2 Experimental Apparatus

A schematic diagram of the system is shown in Fig. 1. The system is similar in configuration to the previous experimental setup (Okada and Ozoe, 1992), but employs a much larger cubical enclosure in order to ascertain the apparent enhancement of heat transfer. Figure 2 shows a schematic diagram of the experimental apparatus, which consists of a cubical enclosure, an electromagnet, a gauss meter, a recorder, and a cold-water tank. One vertical wall of the cubical enclosure was heated by an electric heater and the opposing vertical wall was cooled by running water from a constant-temperature bath held at 32°C. The other four walls were made of plexiglas. The internal length of the sides of the cubical enclosure was 64 mm. The cubical enclosure was fixed centrally between two magnetic poles of 100 mm in diameter set 100 mm apart. The maximum strength of the electromagnet is 0.4 T for the 100 mm distance between the two magnetic poles. The uniformity of the magnetic field is as presented in Okada and Ozoe (1992). The direction of the magnetic field is horizontal and parallel to the heated and cooled walls (the *Y*-direction) as shown in Fig. 1.

Figure 3 shows details of the cubical enclosure. Three thermocouples were inserted into the heated copper wall at heights of 7, 32, and 57 mm from the bottom, and one thermocouple was inserted into the cooled copper wall at the central height (z = 32 mm). Both copper plates were 3 mm thick. Their surfaces were sprayed with teflon solution to prevent corrosion by liquid gallium. This teflon solution also acts as an electrical insulator between the copper plate and liquid gallium: the measured electrical resistance became zero after spraying the teflon solution. Hence, all six walls, including the four plexiglas walls, were electrically insulated. This electrically insulated boundary condition for the electric current density is the same as in the

---

[1] To whom correspondence should be addressed. e-mail: ozoe@cm.kyushu-u.ac.jp.

Contributed by the Heat Transfer Division for publication in the JOURNAL OF HEAT TRANSFER. Manuscript received by the Heat Transfer Division, Oct. 16, 1997; revision received, May 20, 1998. Keywords: Enhancement, Heat Transfer, Liquid Metals, Magnetic, Natural Convection. Associate Technical Editor: T. L. Bergman.

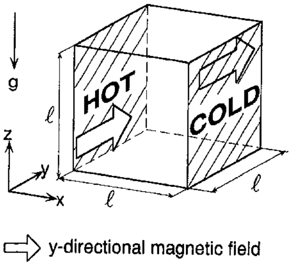

Fig. 1 Schematic diagram of system

numerical works (Ozoe and Okada, 1989; Tagawa and Ozoe, 1997). The cubical enclosure was placed in a box maintained at a constant temperature in order to minimize the heat loss from the enclosure.

3 Experimental Procedure

3.1 Evaluation of Heat Loss. One vertical wall of the cubical enclosure was heated with uniform flux by an electric heater, and the opposing vertical wall was cooled by running water at constant temperature. To estimate the net heat transfer rate in such a configuration, the heat loss from the cubical enclosure was evaluated by the method of Ozoe and Churchill (1973). The method is as follows.

A conduction experiment was carried out with the heated wall at the top, so that the experimental fluid was heated from above and cooled from below. Liquid gallium was used as the experimental fluid, and its physical properties were taken from Okada and Ozoe (1992). Figure 4 shows the relationship between the results of the conduction experiment (total heat supply) and Fourier's equation (conduction heat flux). The difference between the two lines is considered to be the heat loss. Subtracting the conduction heat from the total heat supply Q_{tot} gives the heat loss Q_{loss},

$$Q_{\text{loss}} = Q_{\text{tot}} - l^2 k_{\text{Ga}} \frac{\theta_h - \theta_c}{l} \tag{1}$$

where Q_{tot} indicates total heat supply from the electric heater. The heat loss Q_{loss} should depend solely on the hot wall temperature θ_h and can be represented as follows by least-square approximation for the data Q_{loss} versus θ_h:

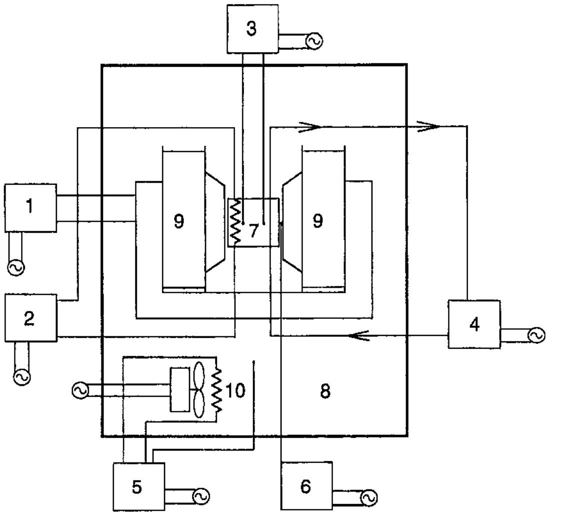

1. D. C. power source
2. D. C. power source
3. Strip-chart recorder
4. Constant temperature bath
5. P I D controller
6. Gauss meter
7. Cubical enclosure
8. Constant temperature box
9. Electromagnet
10. Heater and fun

Fig. 2 Schematic diagram of experimental apparatus

$$Q_{\text{loss}} = 0.5119\theta_h - 16.60. \tag{2}$$

Although the present experiments were conducted with the cube heated from a vertical wall and cooled from the opposing vertical wall, the heat loss Q_{loss} was assumed to be identical if the heated wall temperature is the same. This means that the heat loss Q_{loss} depends only on the heated wall temperature and not on the orientation. In the experiments with a heated vertical wall, the temperature at 32 mm height was employed as the representative θ_h. Then, the net heat flux Q_{net} is given by

$$Q_{\text{net}} = Q_{\text{tot}} - Q_{\text{loss}}. \tag{3}$$

3.2 Evaluation of the Average Nusselt Number. The average Nusselt number was defined as a ratio of the net heat flux Q_{net} to the conductive heat flux Q_{cond}.

Nomenclature

A = heat transfer area, (= l^2 in the present system), (m^2)
B_0 = magnetic flux density, (T) = (Wb/m^2) = (kg/($A \cdot s^2$))
c_p = specific heat of fluid, (J/(kg·K))
g = acceleration due to gravity, (m/s^2)
Gr = Grashof number = $g\beta(\theta_h - \theta_c)l^3/\nu^2$
Ha = Hartmann number = $(\sigma/\mu)^{1/2}B_0 l$
k = thermal conductivity of fluid, (W/(m·K))
l = distance between hot and cold walls, i.e., length of the sides of the cube, (m)
Nu = average Nusselt number = $Q_{\text{net}}/Q_{\text{cond}}$
Nu$_0$ = average Nusselt number in the absence of a magnetic field
Nu$_B$ = average Nusselt number under a magnetic field
Pr = Prandtl number = ν/α
q = heat flux density = Q_{net}/A, (J/(m^2·s))
Q_{cond} = conductive heat flux, (J/s)
Q_{loss} = heat loss, (J/s)
Q_{net} = net heat flux, (J/s)
Q_{tot} = total heat flux = $Q_{\text{net}} + Q_{\text{loss}}$, (J/s)
Ra = Rayleigh number = $g\beta(\theta_h - \theta_c)l^3/(\alpha\nu)$ = Gr·Pr
Ra* = modified Rayleigh number = $g\beta q l^4/(\alpha k \nu)$
t = time, (s)
X = coordinate
Y = coordinate
Z = coordinate

Greek Letters

α = thermal diffusivity of fluid = $\lambda/(\rho c_p)$, (m^2/s)
β = volumetric coefficient of expansion, (1/K)
$\Delta\theta$ = temperature difference between heated and cold walls, (K)
θ = temperature, (K)
θ_c = cold wall temperature, (K)
θ_h = hot wall temperature, (K)
μ = viscosity of fluid, (kg/(m·s))
ν = kinematic viscosity of fluid = μ/ρ, (m^2/s)
ρ = density of fluid, (kg/m^3)
σ = electric conductivity of fluid, (1/(Ω·m))

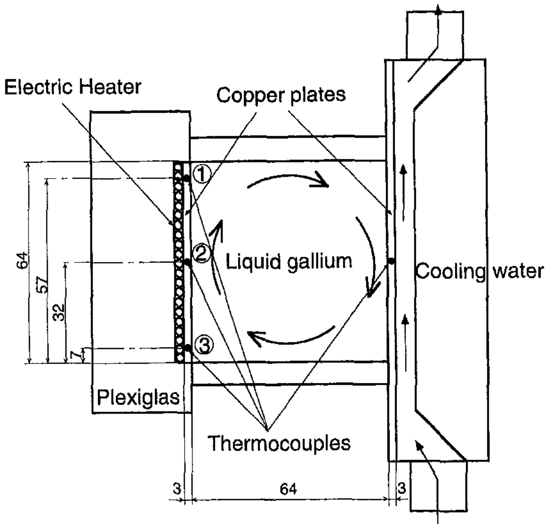

Fig. 3 Cubical convection enclosure

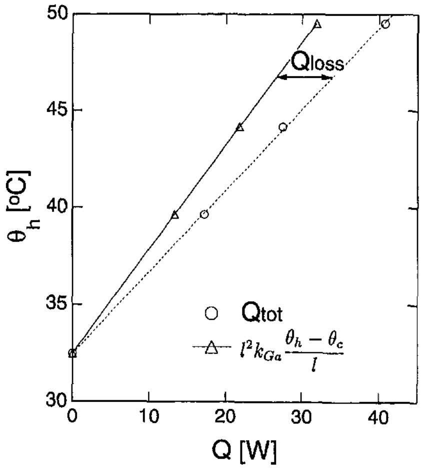

Fig. 4 Evaluation of heat loss

$$\mathrm{Nu} = Q_{\mathrm{net}}/Q_{\mathrm{cond}} \tag{4}$$

Q_{cond} was evaluated by the following procedure. First, the temperature profile on the heated wall was approximated by the following equation:

$$\theta_h(z) = az^2 + bz + c. \tag{5}$$

Coefficients a, b, and c were calculated from the measured temperatures at three points on the heated wall in the convection experiment. Then the equation of heat conduction was solved by finite difference computation for the fluid domain of a cubic enclosure under these temperature boundary conditions. These boundary conditions are as follows:

$$\theta = \theta_h(z), \quad \text{at} \quad x = 0$$

$$\theta = \theta_c = \text{constant}, \quad \text{at} \quad x = l$$

$$\frac{\partial \theta}{\partial y} = 0, \quad \text{at} \quad y = 0, l$$

$$\frac{\partial \theta}{\partial z} = 0, \quad \text{at} \quad z = 0, l.$$

Q_{cond} was calculated over the heated wall from this conduction temperature profile as follows:

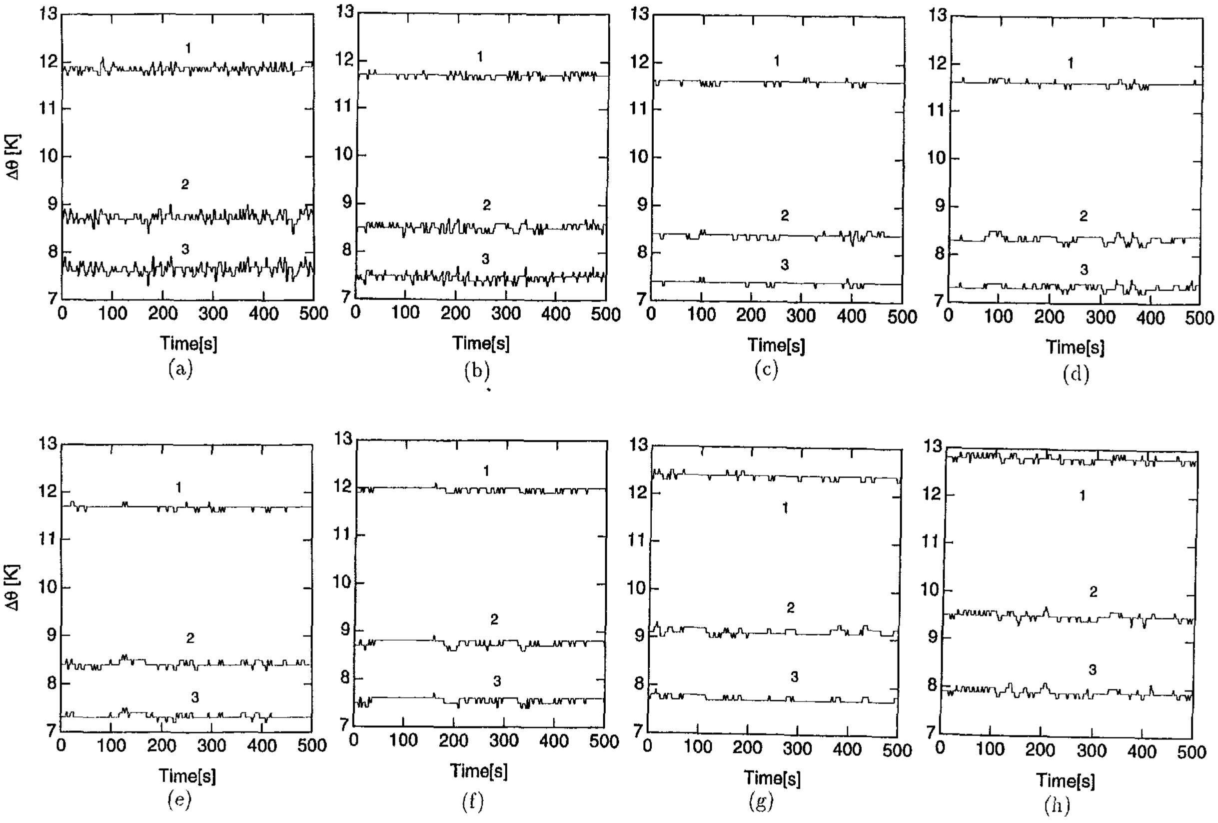

Fig. 5 Transient responses of the temperature difference between the heated and cold walls at Q_{tot} = 126.0 W: (*a*) 0.000 T, (*b*) 0.015 T, (*c*) 0.030 T, (*d*) 0.045 T, (*e*) 0.060 T, (*f*) 0.100 T, (*g*) 0.150 T, and (*h*) 0.200 T

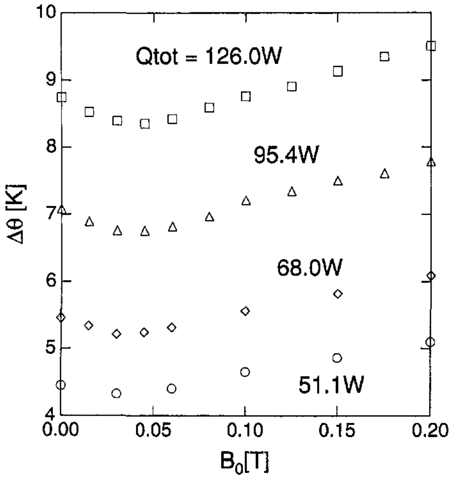

Fig. 6 Influence of the magnetic field on the temperature difference between the heated and the cold wall at the middle height (z = 32 mm)

$$Q_{\mathrm{cond}} = \int_0^l \int_0^l \left\{ -k\left(\frac{\partial\theta}{\partial x}\right)_{x=0} \right\} dydz. \qquad (6)$$

4 Experimental Results and Discussions

4.1 The Heat Transfer Rate Under External Magnetic Field. Figure 5 shows transient responses of the temperature difference between heated and cold walls at Q_{tot} = 126.0 W. The three thermocouples on the heated wall each represent a different profile in the vertical direction because of the uniform flux. These eight graphs are for different strengths of magnetic field. For example, the T.C. output at 57 mm from the bottom decreases from 11.8 K at 0 T to 11.6 K at 0.045 T, then increases to 12.8 K at 0.2 T. A similar tendency was obtained for the T.C. output at 32 mm and 7 mm. These suggest that the maximum heat transfer rate occurs at about 0.045 T.

Figure 5 also shows oscillation of temperature at any strength of the magnetic field. The oscillation was most remarkable at 0 T, and the amplitude of oscillation decreased upon applying the magnetic field. In comparison with our previous numerical result (Tagawa and Ozoe, 1997) this appears to correspond to the rectified flow under the magnetic field.

Time-averaged temperature differences at the middle height for 500 seconds in Fig. 5 are replotted in Fig. 6 versus the strength of magnetic field. The decrease in the temperature difference between the heated and cold walls under uniform flux heating suggests that the heat transfer rate increases under the moderate magnetic field.

Figure 7 shows a dimensionless replot of the present results for the average Nusselt number versus the Hartmann number with the modified Rayleigh number as a parameter. The average Nusselt number attained peak values at about Ha = 100. Figure 7 also shows that the Hartmann number corresponding to the maximum Nusselt numbers increases with the increase in the modified Rayleigh number. This tendency agrees with the Fumizawa's result (Fumizawa, 1980).

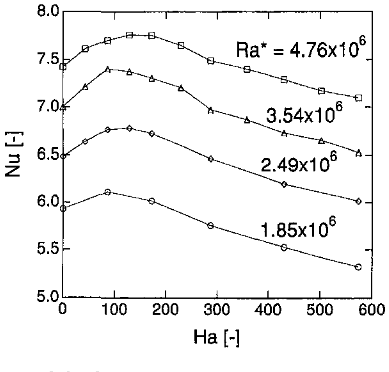

Fig. 7 Influence of the Hartmann number on the Nusselt number with the modified Rayleigh number as a parameter

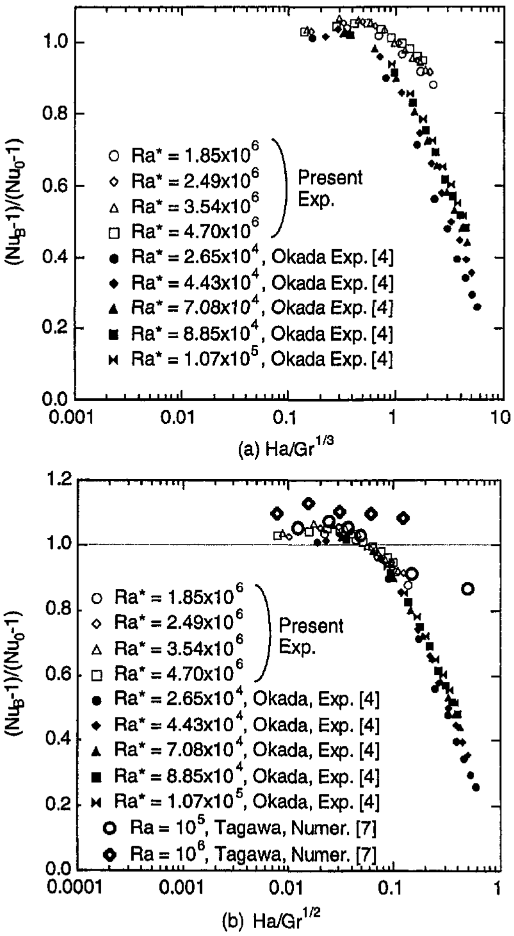

Fig. 8 Correlation of the present data and with the data of Okada and Ozoe (1992): (a) Ha/Gr$^{1/3}$ and (b) Ha/Gr$^{1/2}$

Natural convection in liquid metal in a cubical enclosure is in general three-dimensional and oscillatory. This tendency becomes more prominent with the increase in the Rayleigh number. Tagawa and Ozoe (1997) suggested that the three-dimensional flow is rectified and transformed into a two-dimensional flow whose velocity profile is uniform along the direction of the magnetic field. They suggested that this rectified flow appears to convect energy smoothly from the corresponding walls without fluctuating flow energy.

4.2 Data Correlation. Figure 8(a) shows a replot of the data of Okada and Ozoe (1992) with black symbols alongside the present results plotted with white symbols. These two data groups were aligned separately. These are replotted versus Ha/Gr$^{1/2}$ in Fig. 8(b), where almost all data are aligned in a single group.

Recently, Lykoudis (1996) considered the correlation of heat transfer rate of natural convection of liquid metal in a cubic enclosure using the data of Okada and Ozoe for the X-directional magnetic field and suggested that heat transfer rate was correlated closely with Ha/Gr$^{1/2.8}$ rather than with Ha/Gr$^{1/3}$. However, the present data for the Y-directional magnetic field could be correlated more smoothly with Ha/Gr$^{1/2}$.

Table 1 Experimental results and relative errors

Ra*	Ha	Nu	Rel. error Ra* [%]	Rel. error Ha [%]	Rel. error Nu [%]
1.85×10^6	0	5.93	6.04	—	12.4
	86	6.11		15.2	12.7
	172	6.01		16.3	12.4
	286	5.75		15.0	11.9
	430	5.53		17.5	11.4
	573	5.33		16.3	11.0
2.49×10^6	0	6.48	5.93	—	9.98
	43	6.63		17.5	10.2
	86	6.77		15.2	10.4
	129	6.78		17.5	10.3
	172	6.73		16.3	10.2
	286	6.46		15.0	9.83
	430	6.19		17.5	9.43
	573	6.02		16.3	9.10
3.54×10^6	0	7.00	5.87	—	7.64
	43	7.21		17.5	7.83
	86	7.40		15.2	7.98
	129	7.37		17.5	7.96
	172	7.31		16.3	7.88
	229	7.21		15.5	7.77
	286	6.97		15.0	7.55
	358	6.87		18.4	7.40
	430	6.73		17.5	7.26
	501	6.65		16.8	7.16
	573	6.53		16.3	7.01
4.76×10^6	0	7.42	5.84	—	6.11
	43	7.61		17.5	6.23
	86	7.70		15.2	6.30
	129	7.76		17.5	6.32
	172	7.75		16.3	6.28
	229	7.64		15.5	6.20
	286	7.49		15.0	6.10
	358	7.40		18.4	6.00
	430	7.29		17.5	5.90
	501	7.17		16.8	5.79
	573	7.09		16.3	5.72

4.3 Comparison With Numerical Results. Figure 8(*b*) compares the present results with previous experimental (Okada and Ozoe, 1992) and numerical results (Tagawa and Ozoe, 1997). Both experiments were carried out with uniform flux heating, and the numerical computation was for constant temperature heating. The experimental data were transformed to those of uniform wall temperature equivalence by $\mathrm{Ra}^* = \mathrm{Nu} \cdot \mathrm{Ra}$. The data greater than unity represent the enhancement of heat transfer rate by application of the external magnetic field. Agreement between experimental and numerical results is not satisfactory for higher regime of $\mathrm{Ha}/\mathrm{Gr}^{1/2}$. This will be studied further in future.

4.4 Discussion of Enhancement of Heat Transfer. The reason for the enhancement of the average rate of heat transfer was explained in Tagawa and Ozoe (1997) for natural convection of liquid metal under a static magnetic field in the *Y*-direction. Briefly, according to the numerical analyses, the induced electric current near the vertical side walls perpendicular to the *Y*-directional magnetic field is directed toward the center of each side wall. These electric currents and the *Y*-directional magnetic field induce Lorentz forces which assist the overall natural convection up along the heated wall and down along the cooled wall. The drag forces over the side walls appears to be canceled by these Lorentz forces, and the average heat transfer rate becomes higher than that without the magnetic field. When the flow becomes rectified at almost two-dimensional, the enhancement reaches its maximum.

5 Conclusions

The enhancement of the heat transfer rate formally predicted by Tagawa and Ozoe (1997) is clearly supported by the present experimental measurements for the natural convection in gallium in a cube heated and cooled from opposing vertical walls with the magnetic field horizontal and parallel to these walls. The standardized heat transfer rate was correlated well with a new dimensionless parameter $\mathrm{Ha}/\mathrm{Gr}^{1/2}$.

References

Fumizawa, M., 1980, "Natural Convection Experiment With Liquid NaK Under Transverse Magnetic Field," *J. Nuclear Science Technology*, Vol. 17, No. 2, pp. 98–105.

Lykoudis, P. S., 1996, "Natural Convection in a Cubic Enclosure in the Presence of a Horizontal Magnetic Field," ASME JOURNAL OF HEAT TRANSFER, Vol. 118, pp. 215–218.

Moffat, R. J., 1985, "Using Uncertainty Analysis in the Planning of an Experiment," *J. Fluids Eng.*, Vol. 107, pp. 173–178.

Okada, K., and Ozoe, H., 1992, "Experimental Heat Transfer Rates of Natural Convection of Molten Gallium Suppressed Under an External Magnetic Field in Either the *X*, *Y*, or *Z* Direction," ASME JOURNAL OF HEAT TRANSFER, Vol. 114, pp. 107–114.

Ozoe, H., and Churchill, S. W., 1973, "Hydrodynamic Stability and Natural Convection in Newtonian and Non-Newtonian Fluids Heated From Below," *AIChE Symp. Series, Heat Transfer*, No. 131, Vol. 69, pp. 126–133.

Ozoe, H., and Okada, K., 1989, "The Effect of the Direction of the External Magnetic Field on the Three-Dimensional Natural Convection in a Cubical Enclosure," *Int. J. Heat Mass Transfer*, Vol. 32, pp. 1939–1954.

Tagawa, T., and Ozoe, H., 1997, "Enhancement of Heat Transfer Rate by Application of a Static Magnetic Field During Natural Convection of Liquid Metal in a Cube," ASME JOURNAL OF HEAT TRANSFER, Vol. 119, pp. 265–271.

Takahashi, O., Nagase, N., Michiyoshi, I., and Takenaka, N., 1986, "Natural Convection Heat Transfer From a Vertical Cylindrical Heater to Liquid Metals Under Horizontal Magnetic Field," *Eighth Int. Heat Transfer Conference, San Francisco*, Vol. 3, pp. 1317–1322.

APPENDIX

Uncertainty Analysis

The estimated error ranges of various parameters involved in the present experiments are listed below. Following Moffat (1985) uncertainty analysis was applied for the dimensionless parameters such as the modified Rayleigh, Hartmann, and Nusselt numbers. These numbers are expressed as a product of terms, and the relative uncertainty is given as follows. If experimental result is

$$R = x_1^a x_2^b x_3^c \dots x_N^N \tag{7}$$

then

$$\frac{\delta R}{R} = \left\{ \left(a \frac{\delta x_1}{x_1} \right)^2 + \left(b \frac{\delta x_2}{x_2} \right)^2 + \dots + \left(N \frac{\delta x_N}{x_N} \right)^2 \right\}^{1/2} . \tag{8}$$

The following are the possible error ranges for both measured values and the correlated physical properties as listed in Okada and Ozoe (1992).

1 Temperature on the heated wall and cooled walls was measured with Cu-constantan thermocouples.
(*a*) Accuracy = ±(0.05 percent of temperature reading + 0.5°C)
(*b*) Reading error = ±0.05°C.
In total, $\delta\theta$ = ±(0.05 percent of temperature reading + 0.55°C) = ±0.57°C.

2 Heat flux measurement suffers from the following errors:
(*a*) Reading error = ±0.5 W.
(*b*) Heat loss correlation = ±0.29 W.
In total, $\delta Q_{\mathrm{net}} = \pm 0.79$ W.

3 Magnetic flux density B [T].
(*a*) Inaccuracy is ±2 percent of the full-scale range.
±0.0006 T for $0 \le B \le 0.03$ T.
±0.0020 T for $0.03 \le B \le 0.1$ T.
±0.0060 T for $0.1 \le B \le 0.3$ T.
(*b*) Reading error.
±0.0001 T for $0 \le B \le 0.03$ T.

±0.0001 T for $0.03 \leq B \leq 0.1$ T.
±0.0010 T for $0.1 \leq B \leq 0.3$ T.

(*c*) Nonuniformity of the magnetic field.

$\delta B = -12.6$ percent to 10.0 percent of readings

In total,

$\delta B = -12.6$ percent to 10.0 percent of readings ±0.0007 T for $0 \leq B \leq 0.03$ T.

$\delta B = -12.6$ percent to 10.0 percent of readings ±0.0021 T for $0.03 \leq B \leq 0.1$ T.

$\delta B = -12.6$ percent to 10.0 percent of readings ±0.0070 T for $0.1 \leq B \leq 0.3$ T.

The following errors were derived for the properties mentioned in Okada and Ozoe (1992).

4 Density, $\delta\rho = \pm 2.42$ kg/m^3.
5 Viscosity, $\delta\mu = \pm 1.09 \times 10^{-4}$ kg/(m·s).
6 Thermal conductivity, $\delta\lambda = \pm 0.14$ W/(m·K).
7 Volumetric coefficient of expansion, $\delta\beta = \pm 5.0 \times 10^{-8}$ 1/K.

The above inaccuracies are reflected in the dimensionless values in the table. Experimental results and the relative errors (percent) of the selected dimensionless numbers for each data are listed in Table 1.

R. Sangras

Z. Dai

G. M. Faeth[1]

Department of Aerospace Engineering,
The University of Michigan,
Ann Arbor, MI 48109-2140

Mixing Structure of Plane Self-Preserving Buoyant Turbulent Plumes

Measurements of the structure of plane buoyant turbulent plumes are described, emphasizing conditions in the fully developed (self-preserving) portion of the flow. Plumes were simulated using helium/air sources in a still and unstratified air environment. Mean and fluctuating mixture fractions were measured using laser-induced iodine fluorescence. Present measurements extended farther from the source (up to 155 source widths) and had more accurate specifications of plume buoyancy fluxes than past measurements and yielded narrower plume widths and different scaled mean and fluctuating mixture fractions near the plane of symmetry than previously thought. Measurements of probability density functions, temporal power spectra, and temporal integral scales of mixture fraction fluctuations are also reported.

Introduction

The structure and mixing properties of buoyant turbulent plumes in still and unstratified air environments are important fundamental problems that have attracted significant attention since the classical study of Rouse et al. (1952). Recent work has highlighted the need for a better understanding of buoyant turbulent plumes, however, in order to address turbulence/radiation and turbulence/buoyancy interactions (Faeth et al., 1989; Panchapakesan and Lumley, 1993). Thus, the overall objective of the present investigation was to extend recent measurements of round buoyant turbulent plumes (Dai and Faeth, 1996; Dai et al., 1994, 1995a, b) to consider plane buoyant turbulent plumes using similar methods. The fully developed region, where effects of the source have been lost and the properties of the flow become self-preserving, was emphasized because these conditions simplify reporting and interpreting measurements (Tennekes and Lumley, 1972), even though few practical buoyant turbulent plumes ever reach the self-preserving region.

Self-preserving buoyant turbulent plumes are reached when streamwise distances from the plume source are large compared to the characteristic source size (typically the source width and diameter for plane and round plumes, respectively) as a measure of conditions where effects of source disturbances have been lost. Another requirement is that streamwise distances must be large compared to the Morton length scale, l_M, as a measure of conditions where effects of source momentum have been lost and effects of buoyancy are dominant. The Morton length scale can be defined as follows for plane plumes having uniform source properties (List, 1982):

$$l_M/b = (\rho_o/\rho_\infty)u_o^2/(bu_og|\rho_o - \rho_\infty|/\rho_\infty)^{2/3} \qquad (1)$$

In Eq. (1), an absolute value has been used for the density difference in order to account for both rising and falling plumes; this practice will be adopted for the remainder of the article. A related parameter used to define source properties is the source Froude number, Fr, defined as follows:

$$\mathrm{Fr}^2 = \rho_ou_o^2/(2bg|\rho_\infty - \rho_o|) \qquad (2)$$

The final requirements for self-preserving flow are that $f \ll 1$, so that there is a linear relationship between mixture fraction and fluid density, and that the characteristic plume Reynolds number (Re_c, which will be defined later) is sufficiently large so that transport is dominated by turbulent rather than molecular effects. Once the flow satisfies these criteria, both mean and fluctuating properties satisfy the relatively simple scaling relationships of self-preserving behavior (List, 1982; Rouse et al., 1952).

In view of the increased generality of the findings, past studies of plane buoyant turbulent plumes emphasized the properties of the self-preserving region of the flow. These studies included Rouse et al. (1952), Lee and Emmons (1961), Harris (1967), Anwar (1967), Kotsovinos (1975, 1977), Kotsovinos and List (1977), and Ramaprian and Chandrasekhara (1985, 1989). The results of these studies are in reasonably good agreement; for example, appropriately scaled flow widths and mean mixture fractions near the plane of symmetry agree within 13 percent, which is comparable to anticipated experimental uncertainties. Whether these results actually represent self-preserving behavior still is questionable, however, because the measurements generally were limited to the region relatively close to the source $(x - x_o)/b \leq 65$ with values of $(x - x_o)/l_M$ as small as 2–3, aside from two exceptions to be discussed later. In contrast, Dai et al. (1994, 1995a, b) and Dai and Faeth (1996), only observe self-preserving behavior for round buoyant turbulent plumes farther from the source, $(x - x_o)/d > 80$ and $(x - x_o)/l_M > 12$, and found that flow widths were significantly smaller than earlier observations that were limited to the near source region with $(x - x_o)/d \leq 60$ and $(x - x_o)/l_M$ as small as 5–6. Another limitation of past studies of plane buoyant turbulent plumes is that measurements of turbulence properties are very limited for all these flows, and are nonexistent for gaseous plumes typical of many practical applications.

In view of these observations, the objective of the present investigation was to complete measurements of the mean and fluctuating mixture fraction properties of plane buoyant turbulent gaseous plumes in still gases, emphasizing conditions within the self-preserving region where the specific features of the source have been lost. Mixture fraction properties that were considered included mean and fluctuating values, probability density functions, temporal power spectra, and temporal integral scales. The experiments consisted of helium/air source flows in still air at normal temperature and pressure, in order to provide a straightforward specification of the buoyancy flux within the

---

[1] To whom correspondence should be addressed: Department of Aerospace Engineering, The University of Michigan, 3000 Francois-Xavier Bagnoud Building, 1320 Beale Avenue, Ann Arbor, MI 48109-2140. e-mail: gmfaeth@umich.edu. Fellow ASME.

Contributed by the Heat Transfer Division for publication in the JOURNAL OF HEAT TRANSFER and presented at the AIAA/ASME Thermophysics Heat Transfer Conference. Manuscript received by the Heat Transfer Division, Oct. 9, 1997; revision received, June 26, 1998. Keywords: Heat Transfer, Natural Convection, Nonintrusive Diagnostics, Plumes. Associate Technical Editor: P. Simpkins.

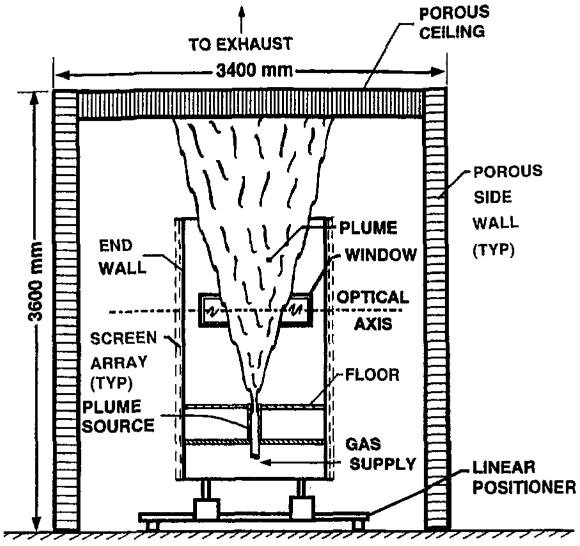

Fig. 1 Cross-sectional sketch of the plane buoyant turbulent plume apparatus

test plumes. Measurements of mixture fraction properties were carried out using laser-induced iodine fluorescence (LIF).

Experimental Methods

Apparatus. A sketch of the experimental apparatus appears in Fig. 1. In order to minimize room disturbances, the plumes were observed within a double enclosure contained within a large high-bay test area. The outer enclosure (3400 × 2000 × 3600 mm high) had porous side walls (the walls parallel to the source) and a porous ceiling made of filter material (Americal Air Filter, filter media pads, 102 mm thick). The filter material prevented flapping of the plume due to room disturbances as well as leakage of background light into the test enclosure. At the same time, the filter material allowed free inflow of air entrained by the plumes which controlled entrained air coflow effects, and free exhaust of the plume itself from the test enclosure. Varying the thickness of the filter material (by a factor of two) had negligible effect on plume properties. After leaving the test enclosure, the plume gases were captured in an upper hood near the ceiling of the laboratory, and were subsequently exhausted by a variable-flow blower. The upper hood was separated from the ceiling area of the plume enclosure so that there was no feedback between blower flow rates and plume properties, i.e., varying blower flow rates also had negligible effect on plume properties.

The test plume was centered at the plane of symmetry of the smaller inner enclosure. The source slot (876 mm long × 9.4 mm wide) was mounted at the center of the flat floor (876 mm long × 1220 mm wide) of the inner enclosure. The floor/slot assembly was mounted normal to end walls (1220 × 2440 mm high). The inner enclosure was completed by installing screen arrays (a pair of screens, 16 mesh × 0.28 mm wire diameter, separated by a distance of 38 mm) across the openings between the outer extremities of the two end walls. The use of screens to control room disturbances in this way was based on successful past use of similar methods by Gutmark and Wygnanski (1976) for plane-free turbulent jets and Dai et al. (1994, 1995a, b) and Dai and Faeth (1996) for round buoyant turbulent plumes. Other modifications of the inner enclosure were studied as follows: extended end walls, rounded contractions at the outer edge of the end walls and the floor to smooth the flow of entrained fluid, and various screen and honeycomb arrangements across the openings at the extremities of the end walls. None of these changes had an appreciable effect on plume properties, however, and they were eliminated in favor of the simplest effective approach for controlling room disturbances, as described earlier.

Optical access for measurements of plume properties was provided by fixed windows (914 mm wide × 203 mm high, mounted flush to the inner surfaces of the end walls), centered on the optical axis (nominally passing halfway between the end walls, roughly 2080 mm above the floor of the test enclosure). Various distances from the source were considered by mounting the source at different heights along the end walls. Horizontal traversing in the cross-stream direction was provided by mounting the entire floor/wall assembly on linear bearings so that it could be moved by a stepping-motor-driven linear positioner (5 μm positioning accuracy) in order to accommodate rigidly mounted instrumentation. Finally, various positions along the slot could be considered, to check for two-dimensionality, by shifting the floor/wall assembly along the linear bearing mount.

The gas supply system of the plume source involved mixing helium (commercial grade, 99.995 percent purity) and air (labo-

Nomenclature

b = source width
B_o = source buoyancy flux
d = source diameter
$E_f(n)$ = temporal power spectral density of f
f = mixture fraction
$F(y/(x-x_o))$ = scaled cross-stream distribution of $\bar{f}$ in the self-preserving region
Fr_o = source Froude number, Eq. (2)
g = acceleration of gravity
k_f = plume width coefficient based on $\bar{f}$, Eq. (9)
k_u = plume width coefficient based on $\bar{u}$
l_f = characteristic plume half-width based on $\bar{f}$, Eq. (10)
l_M = Morton length scale, Eq. (10)
l_u = characteristic plume half-width based on $\bar{u}$, analogous to Eq. (10)
$l_{1/2}$ = characteristic plume halfwidth where $\bar{f} = \bar{f}_c/2$
n = frequency
$\mathrm{PDF}(f)$ = probability density function of mixture fraction
Re_c = characteristic plume Reynolds number, Eq. (8)
Re_o = source Reynolds number, $2\bar{u}_o b/\nu_o$
u = streamwise velocity
$U(y/(x-x_o))$ = scaled cross-stream distribution of $\bar{u}$ in the self-preserving region
x = streamwise distance
y = cross stream distance
z = distance along slot from its mid-plane location
Z = slot length
ν = kinematic viscosity
ρ = density
τ_f = temporal integral scale of mixture fraction fluctuations

Subscripts

c = centerline value
o = initial value or virtual origin location
∞ = ambient value

Superscripts

$(\bar{\ })$ = time-averaged mean value
$(\bar{\ })'$ = root-mean-squared fluctuating value

ratory supply having a dewpoint less than 240 K). These flows were controlled by pressure regulators and metered using critical flow orifices in conjunction with absolute pressure gages (Heisse, Model CC, 0–2000 kPa range, 0.15 percent full-scale accuracy). The critical flow orifices were calibrated in turn by either wet test meters or a standard turbine flow meter (EG& G, Flow Technology, Model FT68AENA615A 1). After mixing, the source flows passed through beds of iodine flakes to provide iodine seeding for LIF measurements. The source flow then passed through four parallel lines having length-to-diameter ratios greater than 1200 to ensure uniform mixing. These flows subsequently entered the source manifold, passed through a bed of glass beads (0.5 mm bead diameter with bed dimensions of 876 mm long × 32 mm wide × 120 mm deep), a filter (3M, OCELLO, scouring pad, 876 mm long × 32 mm wide × 5 mm thick), and a contraction to a final slot width of 9.4 mm. All components in contact with the flow after seeding with iodine were either plastic or painted to avoid corrosion. The final plume flow in the exhaust blower was an exception because iodine concentrations at this point were less than 100 ppb and caused no corrosion problems.

Instrumentation. Mixture fractions were measured using laser-induced iodine fluorescence, similar to Dai et al. (1994). The LIF signal was produced by a focused argon-ion laser beam at 514.5 nm (measuring volume diameter at the e^{-2} points of 0.16 mm with a maximum optical power of roughly 1800 mW). This wavelength is absorbed by iodine and causes it to fluoresce at longer wavelengths in the visible. The laser beam was horizontal and directed normal to the plume source slot near its midpoint and roughly 2080 mm above the floor of the enclosure. The operation of the laser beam was monitored using two laser power meters that measured laser power before and after passing through the flow. Absorption of the laser beam was less than one percent and was even smaller for the fluorescence emissions, thus, it was not necessary to correct the LIF signal for effects of absorption.

The fluorescence signals were observed at right angles to the laser beam using f5:1 collecting lenses having diameters of 100 mm. The LIF signal was separated from light scattered at the laser line using long-pass optical filers (cut off wavelength of 530 nm). The resulting signal was measured with a detector (Hamamatsu, Model R269) with the detector aperture selected to provide a measuring volume length of 2 mm. The detector outputs were amplified and then low-pass filtered using sixth-order Chebychev filters to control alias signals. The detector signals were sampled using an a/d converter and then transferred to a computer for processing and storage. The detector signals were also monitored using a digital oscilloscope.

The LIF signals were calibrated based on measurements at the source exit by mixing the source flow with air to vary the mixture fraction. These tests showed that fluctuations of iodine seeding levels were less than one percent. The LIF signal was not saturated for present conditions and varied linearly with laser power. The LIF signals also varied linearly with the mixture fraction. These calibrations were checked periodically by diverting a portion of the source flow through a plastic tube whose exit was mounted temporarily just below the measurement location. Final processing of the data accounted for both absorption of the laser beam by iodine vapor and laser power variations.

Differential diffusion between the source of buoyancy in the source gas (helium) and the iodine vapor can be a significant source of error for LIF measurements. Effects of differential diffusion were evaluated using the approach of Stårner and Bilger (1983), noting that the binary diffusivities of helium and iodine in air at normal temperature and pressure are 70 and 8 mm^2/s (Bird et al., 1960). For conditions of present interest in the self-preserving region of the flows, local Reynolds numbers are reasonably large; ($\mathrm{Re}_c > 3700$ in the self-preserving portions of the flow, as discussed later); therefore, maximum errors of mean and fluctuating mixture fractions due to effects of differential diffusion were estimated to be less than 0.1 percent.

Table 1 Summary of plane buoyant turbulent plume test conditions[a]

Source properties	Case 1	Case 2
Helium concentration (percent by volume)	26.7	58.1
Density (kg/m^3)	0.894	0.581
Kinematic viscosity (mm^2/s)	21.5	34.7
Average velocity (mm/s)	887	1455
Buoyancy flux, B_o (m^3/s^3)	0.0188	0.0670
Density ratio, ρ_o/ρ_∞	0.770	0.500
Reynolds number, Re_o	780	790
Froude number, Fr_o	3.78	3.39
Morton length scale, l_M/b	8.6	6.4

[a] Helium/air source flow directed vertically upward in still air with an ambient pressure of 99 ± 0.5 kPa and temperature of 297 ± 0.5 K. Pure gas properties as follows: air density of 1.161 kg/m^3, air kinematic viscosity of 15.9 mm^2/s, helium density of 0.163 kg/m^3, and helium kinematic viscosity of 122.5 mm^2/s. Source slot width and length of 9.4 and 876 mm. Virtual origin based on $\bar{f}$ of $x_o/b = 0$ determined from present measurements in the range $(x - x_o)/b = 76$–155 and $(x - x_o)/l_M = 9$–21.

Experimental uncertainties (95 percent confidence) were found following Moffat (1982). Gradient broadening errors were small (less than one percent) at the locations where the measurements were made. Experimental uncertainties of source properties and distances from the source were also small (less than one percent). Signal sampling times were chosen to maintain experimental uncertainties near the plane of symmetry less than six and ten percent for mean and fluctuating mixture fractions, respectively, with both properties being repeatable well within these ranges. Corresponding experimental uncertainties of other flow properties reported here are as follows: 6 percent for $F(y/(x - x_o))$, 12 percent for $\bar{f}'/\bar{f}_c$, 10 percent for PDF(f), 40 percent for the low-frequency region $E_f(n)/(\tau_f \bar{f}'^2)$, and 35 percent for $B_o^{1/3}\tau_f/(x - x_o)$. These uncertainties were maintained at these values up to half the maximum value of the parameter (excluding the spike region of the PDF) but increased at smaller values roughly inversely proportional to the value of the parameter.

Test Conditions. The test conditions are summarized in Table 1. Two source flows were considered, having initial density ratios, $\rho_o/\rho_\infty = 0.770$ and 0.500. Source Froude numbers were kept near current estimates of asymptotic plane plume Froude numbers in order to enhance the development of the flow toward self-preserving conditions (Grella and Faeth, 1975; Liburdy and Faeth, 1978). In view of the large source flow rates of line plumes from a source having dimensions of 9.4 × 876 mm, it was difficult to maintain a large source Reynolds number, Re_o, at the same time. Thus, source Reynolds numbers were roughly equal to 800. The self-preserving regions were relatively far from the source, $(x - x_o)/b \geq 76$; therefore, locations of the virtual origins could not be distinguished from $x_o/b = 0$ within present experimental uncertainties.

Self-Preserving Scaling

The state relationship for density as a function of mixture fraction, assuming an ideal gas mixture, is as follows (Dai et al., 1994):

$$\rho = \rho_\infty/(1 - f(1 - \rho_\infty/\rho_o)). \tag{3}$$

Far from the source where the flow becomes self-preserving, Eq. (3) can be linearized as follows:

$$\rho = \rho_\infty + f\rho_\infty(1 - \rho_\infty/\rho_o),\ f \ll 1. \tag{4}$$

Present measurements consisted of mean and fluctuating mix-

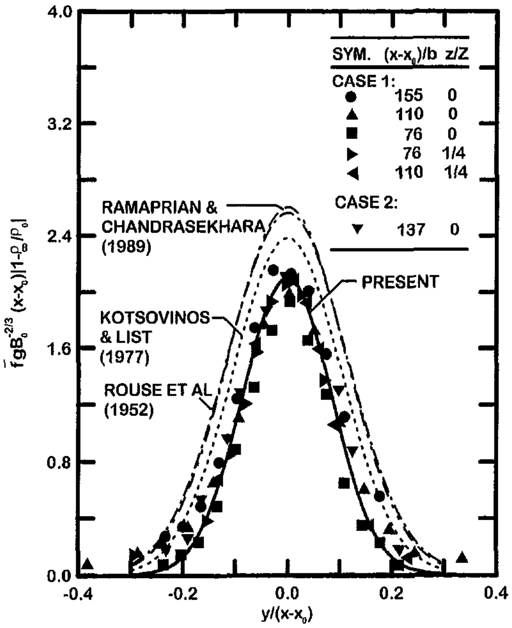

Fig. 2 Cross-stream distributions of mean mixture fractions in plane self-preserving buoyant turbulent plumes. Measurements of Rouse et al. (1952), Kotsovinos and List (1977), Ramaprian and Chandrasekhara (1989), and the present investigation.

ture fraction properties at various streamwise positions. Mean mixture fractions were then scaled in terms of self-preserving variables as follows (List, 1982):

$$F(y/(x-x_o)) = \bar{f}gB_o^{-2/3}(x-x_o)|1-\rho_\infty/\rho_o| \quad (5)$$

where $F(y/(x-x_o))$ represents an appropriately scaled cross-stream profile function of mean mixture fraction, which becomes a universal function far from the source where Eq. (4) applies. The source buoyancy flux, B_o, is a conserved scalar of the flow which can be written as follows for plane plumes having uniform source properties (List, 1982):

$$B_o = bu_og|\rho_o-\rho_\infty|/\rho_\infty. \quad (6)$$

The self-preserving relationship for streamwise mean velocity was not studied during the present investigation but velocity properties are useful to help define the turbulence properties of the plume. Thus, it should be noted that mean streamwise velocities within self-preserving plane buoyant turbulent plumes can be scaled as follows (List, 1982):

$$U(y/(x-x_o)) = \bar{u}/B_o^{1/3} \quad (7)$$

where $U(y/(x-x_o))$ is an appropriately scaled cross-stream profile function. The corresponding characteristic plume Reynolds number can be written as follows for self-preserving conditions:

$$\mathrm{Re}_c = \bar{u}_c l_u/\nu_\infty = U(0)B_o^{1/3}(x-x_o)/(k_u\nu_\infty) \quad (8)$$

where, for present purposes, values of k_u and $U(0)$ were taken from Rouse et al. (1952).

Results and Discussion

Mean Mixture Fractions. Distributions of mean mixture fractions in the self-preserving region of the flow will be considered first. Present measurements of cross-stream distributions of mean mixture fractions for the two sources are illustrated in Fig. 2. The scaling parameters of Eq. (5) have been used when plotting the figure so that the ordinate of the plot is equal to $F(y/(x-x_o))$. The results are plotted for $z/Z = 0$ and $\frac{1}{4}$ in order to evaluate the two-dimensionality of the flow; it is evident that there is little variation of flow properties with position along the source (in the z direction) confirming that flow properties are reasonably two-dimensional. Present measurements also yield the universal distributions within experiment uncertainties that are required for self-preserving flow, for $76 \le (x-x_o)/b \le 155$ and $9 \le (x-x_o)/l_M \le 21$ with flow aspect ratios $Z/(2l_f) \ge 2.6$. Measurements nearer to the source yielded broader distributions of scaled mean mixture fractions as will be discussed subsequently. Measurements were not undertaken farther from the source in order to avoid flow aspect ratios near unity that are affected by the presence of the end walls. Present conditions correspond to $3700 \le \mathrm{Re}_c \le 7500$, which are reasonably large for unconfined turbulent flows; for example, the companion study of self-preserving round buoyant turbulent plumes due to Dai et al. (1994, 1995a, b) achieved $2500 \le \mathrm{Re}_c \le 4200$.

Measurements of mean mixture fractions due to Rouse et al. (1952), Kotsovinos and List (1977), and Ramaprian and Chandrasekhara (1989) are also plotted in Fig. 2, for comparison with the present measurements (results from other past studies have not been plotted in order to avoid cluttering the figure but will be considered later). These distributions are seen to be significantly broader (up to 30 percent broader at the e^{-1} points of the distributions) and significantly larger near the plane of symmetry (up to 30 percent larger), than the present measurements. Reasons for these differences between past and present measurements will be discussed next, considering scaled widths and magnitudes of scaled mean mixture fraction distributions, in turn.

The larger scaled widths of the mean mixture fraction distributions of the earlier studies plotted in Fig. 2 than the present study are typical of conditions in the developing plume region before self-preserving behavior is achieved. As discussed earlier, this behavior is expected because the results of earlier studies involved *averages* of measurements for $8 \le (x-x_o)/b \le 65$ (possibly except for the classical findings of Rouse et al. (1952) where the range of the measurements in terms of $(x-x_o)/b$ cannot be specified because the sources used were a linear array of combusting jets) whereas Dai et al. (1994) only observed self-preserving behavior in round buoyant turbulent plumes farther from the source at $(x-x_o)/d > 80$. Corresponding flow development behavior for plane buoyant turbulent plumes can be quantified from the results given in Table 2. In this table, characteristic plume half-widths, $l_{1/2}/(x-x_o)$, are summarized as a function of scaled distance from the source, $(x-x_o)/b$, for the measurements of Kotsovinos (1975), Kotsovinos and List (1977), Ramaprian and Chandrasekhara (1989), and the present investigation. Present scaled flow widths are similar to the other studies near the source, in spite of significant differences in source properties, and characteristic plume half-widths tend to decrease with increas-

Table 2 Development of plane buoyant turbulent plumes[a]

Source	$(x-x_o)/b$	$l_{1/2}/(x-x_o)$
Present (developing region)	13	0.15
	50[b]	0.08
Present (self-preserving region)	76–155	0.08
Ramaprian and Chandrasekhara (1989)	24	0.14
	35	0.13
	55	0.13
Kotsovinos (1975), Kotsovinos and List (1977)	16	0.12
	38	0.12

[a] Plane buoyant turbulent plumes in still and unstratified environments. Entries are ordered chronologically.

[b] Not judged to be in self-preserving region because mixture fraction fluctuation intensity at the plane of symmetry was not equal to the self-preserving value of 47 percent.

ing distance from the source for all three studies. Present measurements, however, extend farther from the source with half-widths eventually reaching smaller asymptotic values than the rest. In fact, $l_{1/2}/(x - x_o) = 0.08$ for $50 \le (x - x_o)/b \le 155$ for the present measurements, providing rather strong evidence for the invariance of this property with streamwise distance. As noted in the table, however, self-preserving behavior is deferred until $(x - x_o)/b \ge 76$ for present test conditions because the distribution of mixture fraction fluctuations was still developing in the region $50 \le (x - x_o)/b \le 76$. Considering all this evidence, it seems reasonable to conclude that flow widths observed during the earlier studies plotted in Fig. 2 are larger than observed during the present study because they were not obtained far enough from the source to achieve fully self-preserving behavior.

The second issue concerning the mean mixture fraction distributions plotted in Fig. 2 is that present scaled values of mixture fractions are generally smaller than the rest. It is felt that these differences are caused by problems of finding B_o during the earlier studies, which all involved thermal plumes. In particular, B_o was accurately prescribed by the gas mixture at the source exit for the present study but had to be obtained by measurements of distributions of plume velocity and temperature properties for the other studies due to the difficulties of determining energy losses from the thermal plumes near the source. Measuring B_o from property distributions in plumes involves considerable uncertainties compared to the present approach, particularly because a significant portion of B_o is transported by the streamwise turbulent flux of species or energy (for composition and thermal plumes, respectively) which is difficult to measure accurately, e.g., Dai et al. (1995b) and George et al. (1977) find that the streamwise turbulent flux contributes 15–16 percent of B_o for round buoyant turbulent plumes with similar levels anticipated for plane buoyant turbulent plumes. Thus, it is not surprising that the measured scaled values of mean mixture fractions due to Rouse et al. (1952), where B_o is probably underestimated because the turbulent contribution to it was not measured and had to be ignored, are generally larger than the present measurements. In contrast, Ramaprian and Chandrasekhara (1989) and Kotsovinos and List (1977) report turbulence contributions to B_o of 18 and 38 percent, respectively, which differ considerably from each other whereas the latter differs considerably from the findings for round buoyant turbulent plumes. These differences clearly demonstrate the problems of accurately finding the turbulent flux of B_o, and thus the correct value of B_o needed to scale self-preserving flow properties, uncertainties of the determination of the mean flow contribution to B_o from distributions of mean properties aside. Taken together, these observations provide a reasonable explanation why present measurements of scaled mean mixture fractions in Fig. 2 are smaller than the rest.

Additional comparisons between present and earlier measurements will involve properties found from fits of the scaled mean mixture fraction distributions. Within the self-preserving region, present cross-stream distributions of mean mixture fractions in Fig. 2 are reasonably approximated by a Gaussian fit, similar to the results of Rouse et al. (1952), Kotsovinos and List (1977), and Ramaprian and Chandrasekhara (1989) also shown on the plot. This type of correlation can be expressed as follows:

$$F(y/(x - x_o)) = F(0) \exp\{-k_f^2(y/(x - x_o))^2\} \qquad (9)$$

where

$$k_f = (x - x_o)/l_f. \qquad (10)$$

Thus, l_f represents the characteristic plume radius where $\bar{f}/\bar{f}_c = e^{-1}$. The best fit of the present data in the self-preserving region yielded $F(0) = 2.10$, $k_f^2 = 70$ and, thus, $l_f/(x - x_o) = 0.120$. These parameters yielded the correlation of present observations illustrated in Fig. 2, which is seen to be a good representation of the measurements.

The present values of normalized streamwise distance required to reach self-preserving conditions within plane buoyant turbulent plumes are similar to the observations of Dai et al. (1994, 1995a, b) and Dai and Faeth (1996) for round buoyant turbulent plumes; however, they are generally larger than streamwise distances reached during past measurements of the self-preserving properties of plane buoyant turbulent plumes using a variety of sources. This behavior is quantified in Table 3, where the aspect ratio of the slot, Z/b, the range of streamwise distances, $(x - x_o)/b$, the smallest flow aspect ratio, $(Z/(2l_f))_{\min}$, the streamwise distance in terms of the Morton length scale, $(x - x_o)/l_M$, and the corresponding reported values of k_f^2, $l_f/(x - x_o)$ and $F(0)$ are summarized to the extent that they are known for the studies of Rouse et al. (1952), Lee and Emmons (1961), Harris (1967), Anwar (1968) and Kotsovinos and List (1977), Ramaprian and Chandrasekhara (1989), and the present investigation. The data summary of Table 3 shows that the most recent measurements of Ramaprian and Chandrasekhara (1989), Kotsovinos and List (1977), Anwar (1968), and Harris (1967) all involve relatively small values of $(x - x_o)/b$, and in some cases small $(x - x_o)/l_M$ and aspect ratios as well, so that broader flows in these instances, typical of flows developing toward self-preserving conditions, are not unexpected, as already discussed. The earlier studies of Lee and Emmons (1961) and to some extent Harris (1967), and Anwar (1968), however, were obtained at reasonably large distances from the source where self-preserving behavior should have been approached. Thus, in these cases, broader distributions of $\bar{f}$ probably resulted from plume disturbances, that invariably increase plume widths and are difficult to avoid far from the source for plane plumes due to their large source flows and extensive flow fields. The results of Rouse et al. (1952), where streamwise distances in terms of source widths and Morton length scales cannot be specified, may also be broad for similar reasons. Taken together, the studies summarized in Table 3 exhibit flow widths (based on l_f at conditions where $\bar{f}/\bar{f}_c = e^{-1}$) up to 36 percent larger, and scaled mean mixture fractions near the plane of symmetry up to 24 percent larger, than the present measurements. Such differences can have a significant impact on evaluation of turbulence models of buoyant turbulent plumes (Dai et al., 1994, 1995a, b) as well as on the interpretation of the stabilizing effects of surfaces on the mixing properties of buoyant turbulent wall plumes (Grella and Faeth, 1975; Liburdy and Faeth, 1978; Liburdy et al., 1979; Lai et al., 1986; Lai and Faeth, 1987a).

Mixture Fraction Fluctuations. Measurements of cross-stream distributions of rms mixture fraction fluctuations are plotted in Fig. 3. These results are plotted as $\bar{f}'/\bar{f}_c$ as a function of $y/(x - x_o)$, which corresponds to self-preserving scaling for buoyant turbulent plumes (Dai et al., 1994, 1995a, b). In addition to present measurements, for the same conditions as the results for $\bar{f}$ in Fig. 2, the measurements of Kotsovinos and List (1977) and Ramaprian and Chandrasekhara (1989) are also shown in this plot. The distributions of Kotsovinos and List (1977) and Ramaprian and Chandrasekhara (1989) are rather broad and exhibit a dip near the plane of symmetry much like the behavior of round buoyant turbulent plumes near the source (Dai et al., 1994) and the behavior of nonbuoyant round jets (Becker et al., 1967; Papanicolaou and List, 1987, 1988). Present results generally reach a maximum near the plane of symmetry, with no dip, which is similar to the behavior observed by Dai et al. (1994) for self-preserving round buoyant turbulent plumes. The differences between present findings concerning mixture fraction fluctuations and earlier results nearer to the source are not surprising because self-preserving behavior for turbulence properties generally requires self-preserving behavior for mean properties (Tennekes and Lumley, 1972). Present measurements within the self-preserving region can be cor-

Table 3 Summary of self-preserving properties of plane buoyant turbulent plumes[a]

Source	Medium	Z/b	$(x-x_o)/b$	$(Z/(2l_f))_{\min}$	$(x-x_o)/l_M$	k_f^2	$l_f/(x-x_o)$	$F(0)$	$(\overline{f}'/\overline{f})_c$
Present	gas	93	76–155	2.6	9–21	70	0.120	2.10	0.47
Ramaprian and Chandrasekhara (1989)	liquid	50	25–65	2.6	3–17	39	0.160	2.56	0.42
Kotsovinos and List (1977)	liquid	13	8–41	1.0	3–24	47	0.146	2.38	0.42
Anwar (1969)	liquid	60	50	3.9	—	41	0.156	2.57	—
Harris (1967)	liquid	—	70	—	—	38	0.163	2.30	—
Lee and Emmons (1961)	gas	138	140	—	—	—	0.156	—	—
Rouse et al. (1952)[b]	gas	—	—	—	—	41	0.156	2.60	—

[a] Plane buoyant turbulent plumes in still and unstratified environments. Range of streamwise distances are for conditions where quoted self-preserving properties were found from measurements over the cross section of the plumes. The entries are ordered chronologically.

[b] Source was a linear array of combusting round jets so that slot properties cannot be defined.

related reasonably well by the following expression which is also illustrated in Fig. 3:

$$\overline{f}'/\overline{f}_c = 0.47 \exp\{-25(y/(x-x_o))^{2.5}\}. \qquad (11)$$

The values of $(\overline{f}'/\overline{f})_c$ for Kotsovinos (1977), Ramaprian and Chandrasekhara (1985, 1989) and the present study, which are the only values available, are summarized in Table 3. The present value of 47 percent is significantly larger than the results of the other two studies, 42 percent, probably due to effects of flow development from relatively nonturbulent sources for the earlier studies. Present turbulence intensities of mixture fraction fluctuations near the plane of symmetry are also slightly larger than the value of 45 percent observed by Dai et al. (1994) at the axis of self-preserving round buoyant turbulent plumes but this difference is comparable to experimental uncertainties.

The absence of the dip near the center of mixture fraction fluctuation distributions for plane and round buoyant turbulent plumes is an interesting feature of free buoyant turbulent flows. In contrast, round and plane nonbuoyant turbulent jets have reduced mixture fraction fluctuations near the axis and plane of symmetry because turbulence production is small in this region because the mean mixture fraction gradient is smaller due to symmetry requirements (Becker et al., 1967; Papanicolaou and List, 1987, 1988). In spite of symmetry, however, effects of buoyancy provide a mechanism of turbulence production near the axis and plane of symmetry of round and plane plumes due to buoyant instability in the streamwise direction, i.e., the density always approaches the ambient density in the streamwise direction. As discussed by Dai et al. (1994), for round buoyant turbulent plumes, this instability is also responsible for larger mixture fraction fluctuations near the axis and plane of symmetry of round and plane plumes compared to nonbuoyant jets. Thus, the contribution of buoyancy to turbulence is appreciable in both round and plane buoyant turbulent plumes.

Probability Density Functions. Mixture fractions are limited to the finite range, 0–1, and cannot exhibit the simple Gaussian behavior typical of velocity probability density functions in turbulent flows. Representative plots of the PDF(f) of the present self-preserving plane buoyant turbulent plumes are illustrated in Fig. 4. These results are for the case 1 source at various cross-stream distances and $x/b = 110$. The measurements are compared with predictions of the clipped-Gaussian and beta function distributions which are frequently used to represent PDF(f) for modeling purposes (Lockwood and Naguib, 1975). Both these distributions are defined by two moments, $\overline{f}$ and $\overline{f}'$; therefore, the predicted distributions are based on the measured values of these moments at each condition considered.

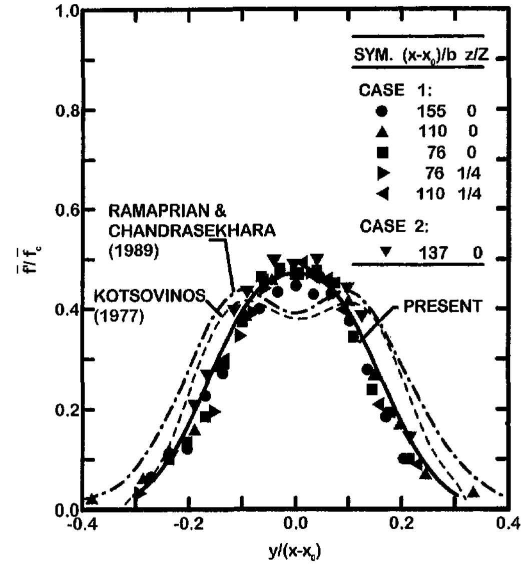

Fig. 3 Cross-stream distributions of rms mixture fraction fluctuations in plane self-preserving buoyant turbulent plumes. Measurements of Kotsovinos (1977), Ramaprian and Chandrasekhara (1989), and the present investigation.

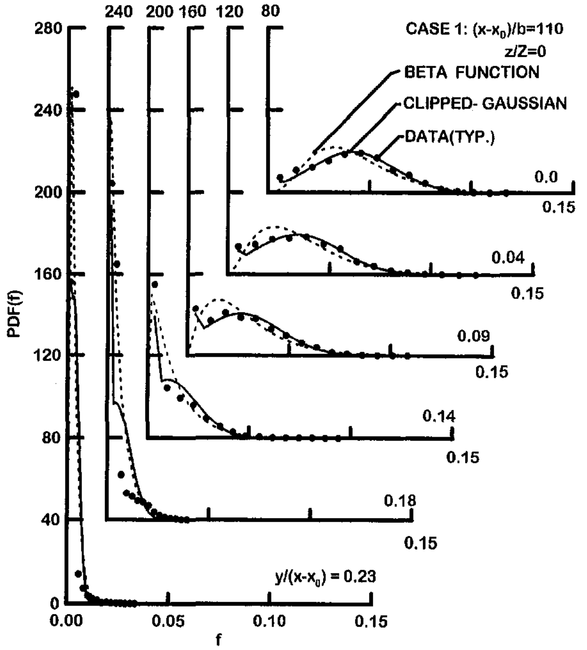

Fig. 4 Typical probability density functions in plane self-preserving buoyant turbulent plumes: Case 1 flow at $(x-x_o)/b = 110$

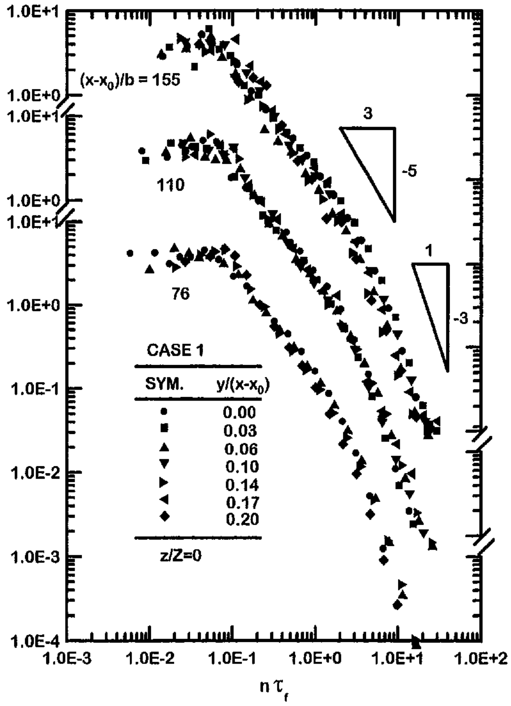

Fig. 5 Typical temporal power spectral densities of mixture fraction fluctuations in plane self-preserving buoyant turbulent plumes: Case 1 flow at $(x - x_o)/b$ = 76, 110, and 155

The measured PDF(f) illustrated in Fig. 4 are similar to earlier measurements in flames, round plumes and jets (Kounalakis et al., 1991; Papanicolaou and List, 1987, 1988; Dai et al., 1994; Becker et al., 1967). At the axis, the PDF(f) is nearly Gaussian, although the distribution is truncated while having a finite value at $f = 0$ indicating the presence of conditions where unmixed ambient fluid reaches the plane of symmetry. Finite values of PDF(0) near the axis or plane of symmetry are typical of self-preserving buoyant turbulent plumes but this behavior for nonbuoyant turbulent mixing processes is much less prominant than the results illustrated in Fig. 4 (Dai et al., 1994). The value of PDF(0) increases in magnitude with increasing cross stream distance and becomes spike-like and eventually dominates the mixture fraction distribution as the edge of the flow is approached where the observation point is mainly in ambient fluid. Similar to past observations of the PDF(f) in self-preserving round buoyant turbulent plumes due to Dai et al. (1994), both the clipped-Gaussian and beta function PDF's provide reasonably good fits of the measurements. The beta function distribution probably will be preferred for most practical calculations of scalar plume properties, however, because it is easier to use than the clipped-Gaussian function (Lockwood and Naguib, 1975).

Temporal Power Spectral Densities. Temporal power spectral densities are of interest to illustrate the signal-to-noise ratios of the present mixture fraction measurements, to study aspects of buoyancy/turbulence interactions, and to provide information needed to understand the temporal properties of radiation fluctuations in buoyant turbulent plumes. Some typical measurements of temporal power spectra for the present self-preserving plane buoyant turbulent plumes are illustrated in Fig. 5. These results are for the case 1 plume with $76 \leq (x - x_o)/b \leq 155$, considering cross-stream positions over the full width of the flow at each streamwise position. The measurements are normalized by local turbulence properties, τ_f and $\bar{f}'$, in the usual manner as described by Hinze (1975). The present spectra are qualitatively similar to earlier results for round plumes reported by Dai et al. (1994) and Papanicolaou and List (1987, 1988). The normalized spectra are relatively independent of cross-stream position at each streamwise location when scaled in the manner of Fig. 5, which provides a convenient summary of the data. Similarly, the low-frequency portion of the spectra are relatively independent of streamwise position when normalized in the manner of Fig. 5.

The spectra illustrated in Fig. 5 initially decay according to the $-\frac{5}{3}$ power of frequency; this behavior is typical of the inertial region of the turbulence spectrum of velocity fluctuations which has been called the inertial-convective region for scalar property fluctuations where effects of molecular diffusion are small (Tennekes and Lumley, 1972). This is followed by a prominent region where the spectrum decays roughly according to the -3 power of frequency, which has been termed the inertial-diffusive subrange by Papanicolaou and List (1987). This region is not observed in nonbuoyant flows and is thought to be caused by variations of the local rate of dissipation of mixture fraction fluctuations due to buoyancy-generated inertial forces. Thus, the -3 decay region of the temporal spectra merits additional study as an important buoyancy/turbulence interaction. The mixture fraction microscale, where temporal power spectral densities rapidly become small, should be observed at larger frequencies than the -3 decay region. Unfortunately, present measurements did not have the spatial and temporal resolution needed for observations at these conditions. Present measurements were able to resolve nearly five decades of the temporal power spectra, however, which provides the good signal-to-noise ratios needed to resolve mixture fraction fluctuations with the experimental uncertainties mentioned earlier.

Temporal Integral Scales. The properties of the temporal power spectra are completed by the temporal integral scales. Present measurements of the temporal integral scales are plotted as a function of cross-stream distance in Fig. 6. The measurements are limited to the self-preserving region, $76 \leq (x - x_o)/b \leq 155$, for the case 1 source; however, effects of streamwise distance are relatively small when plotted in the manner of Fig. 6.

The temporal integral scales in Fig. 6 have been plotted by combining Taylor's hypothesis and the requirements of a self-preserving streamwise velocity field for plane buoyant turbulent jets. This implies that $\tau_f \bar{u}/l_u$ should be a universal function of $y/(x - x_o)$ within the self-preserving region of the flow, yielding the normalized variables of Fig. 6 after adopting the self-pre-

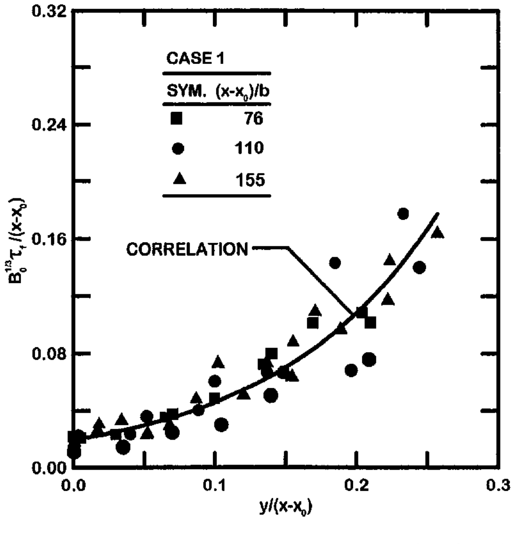

Fig. 6 Cross-stream distributions of temporal integral scales of mixture fraction fluctuations in plane self-preserving buoyant turbulent plumes

serving velocity scale for plane buoyant turbulent plumes from Eq. (6). This approach provides a somewhat scattered but reasonable correlation of τ_f for self-preserving plane plumes, similar to earlier findings for self-preserving round turbulent plumes (Dai et al., 1994). The similarities of the behavior of τ_f for round and plane buoyant turbulent plumes suggest that streamwise spatial integral scales of mixture fraction fluctuations are relatively constant over the flow cross section for the present plane buoyant turbulent plumes. Then the increase of τ_f as the edge of the flow is approached results from the reduced values of $\bar{u}$ in this region through Taylor's hypothesis. Measurements of the velocity properties of the present plumes are needed, however, in order to properly establish the behavior of spatial integral scales for these flows.

Conclusions

Mixture fraction statistics were measured in plane buoyant turbulent plumes in still air, emphasizing fully developed (self-preserving) conditions where effects of source disturbances are lost and flow properties scale in a relatively simple manner. The test conditions consisted of buoyant jet sources of helium and air to give ρ_o/ρ_∞ of 0.500 and 0.770 and source Froude numbers of 3.39 and 3.78, respectively, with $(x - x_o)/b$ in the range 76–155 and $(x - x_o)/l_M$ in the range 9–21. The major conclusions of the study are as follows:

1 The present measurements yielded distributions of mean mixture fractions that were self-preserving for $(x - x_o)/b \geq 76$. In this region, distributions of mean mixture fractions were up to 36 percent narrower, with scaled values at the plane of symmetry up to 24 percent smaller, than earlier results using buoyant jet sources in the literature. The earlier measurements generally were obtained for $(x - x_o)/b \leq 65$ which does not appear to be sufficiently far from the source to reach self-preserving conditions for the conditions of the earlier measurements, while also involving problems of accurately determining the value of the buoyancy flux needed to scale self-preserving properties, in some instances.

2 Cross-stream distributions of mixture fraction fluctuations in the self-preserving region of plane buoyant turbulent plumes do not exhibit reduced values near the plane of symmetry, similar to plane nonbuoyant jets. Instead, effects of buoyancy cause mixture fraction fluctuations to reach a maximum at the plane of symmetry, to yield intensities of roughly 47 percent. These values are comparable to results observed in the self-preserving round buoyant turbulent plumes, 45 percent, and provide strong evidence of significant effects of buoyancy/turbulence interactions in both of these flows.

3 The probability density functions of mixture fractions in self-preserving plane buoyant turbulent plumes can be approximated reasonably well by either clipped-Gaussian and beta function distributions, and exhibit finite levels of intermittency at the plane of symmetry, similar to self-preserving round buoyant turbulent plumes.

4 The low-frequency portion of the temporal spectra of mixture fraction fluctuations scale in a relatively universal manner. The spectra exhibit the well known $-\frac{5}{3}$ power inertial decay region but this is followed by a prominent -3 power inertial-diffusive decay region. These properties are very similar to observations in self-preserving round buoyant turbulent plumes. The -3 power inertial-diffusive region has been observed by others in buoyant turbulent flows but is not observed in nonbuoyant turbulent flows; therefore, this spectral region represents an interesting buoyancy/turbulence interaction that merits further study.

5 Temporal integral scales could be correlated in a relatively universal manner in terms of self-preserving parameters. The temporal integral scales were smallest at the plane of symmetry. This behavior follows (based on similar behavior for round buoyant turbulent plumes) according to Taylor's hypothesis, noting that mean streamwise velocities reach a maximum at the plane of symmetry.

Acknowledgments

This research was supported by the United States Department of Commerce, National Institute of Standards and Technology, Grant No. 60NANB4D1696, with H. R. Baum of the Building and Fire Research Laboratory serving as Scientific Officer.

References

Anwar, H. O., 1969, "Experiment on an Effluent Discharging from a Slot into Stationary or Slow Moving Fluid of Greater Density," *J. Hydr. Res.*, Vol. 7, pp. 411–430.

Becker, H. A., Hottel, H. C., and Williams, G. C., 1967, "The Nozzle-Fluid Concentration Field of the Round, Turbulent, Free Jet," *J. Fluid Mech.*, Vol. 30, pp. 285–303.

Bird, R. B., Stewart, W. E., and Lightfoot, E. N., 1960, *Transport Phenomena*, John Wiley and Sons, New York, pp. 502–513.

Dai, Z., and Faeth, G. M., 1996, "Measurements of the Structure of Self-Preserving Round Buoyant Turbulent Plumes," ASME JOURNAL OF HEAT TRANSFER, Vol. 118, pp. 493–495.

Dai, Z., Tseng, L.-K., and Faeth, G. M., 1994, "Structure of Round, Fully-Developed, Buoyant Turbulent Plumes," ASME JOURNAL OF HEAT TRANSFER, Vol. 116, pp. 409–417.

Dai, Z., Tseng, L.-K., and Faeth, G. M., 1995a, "Velocity Statistics of Round, Fully-Developed Buoyant Turbulent Plumes," ASME JOURNAL OF HEAT TRANSFER, Vol. 117, pp. 138–145.

Dai, Z., Tseng, L.-K., and Faeth, G. M., 1995b, "Velocity/Mixture-Fraction Statistics of Round, Self-Preserving Buoyant Turbulent Plumes," ASME JOURNAL OF HEAT TRANSFER, Vol. 117, pp. 918–926.

Faeth, G. M., Gore, J. P., Chuech, S. G., and Jeng, S.-M., 1989, "Radiation from Turbulent Diffusion Flames," *Annual Review of Numerical Fluid Mechanics and Heat Transfer*, Vol. 2, Hemisphere, Washington, DC, pp. 1–38.

George, W. K., Jr., Alpert, R. L., and Tamanini, F., 1977, "Turbulence Measurements in an Axisymmetric Buoyant Plume," *Int. J. Heat Mass Transfer*, Vol. 20, pp. 1145–1154.

Grella, J. J., and Faeth, G. M., 1975, "Measurements in a Two-Dimensional Thermal Plume Along a Vertical Adiabatic Wall," *J. Fluid Mech.*, Vol. 71, pp. 701–710.

Gutmark, E., and Wygnanski, I., 1976, "The Plane Turbulent Jet," *J. Fluid Mech.*, Vol. 73, pp. 465–495.

Harris, P. R., 1967, "The Densimetric Flows Caused by the Discharge of Heated Two-Dimensional Jets Beneath a Free Surface," Ph.D. thesis, University of Bristol, Bristol, UK.

Hinze, J. O., 1975, *Turbulence*, 2nd Ed., McGraw-Hill, New York, pp. 175–319.

Kotsovinos, N. E., 1975, "A Study of the Entrainment and Turbulence in a Plane Buoyant Jet," Ph.D. thesis, California Institute of Technology, Pasadena, CA.

Kotsovinos, N. E., 1977, "Plane Turbulent Buoyant Jets. Part 2. Turbulence Structure," *J. Fluid Mech.*, Vol. 81, pp. 45–62.

Kotsovinos, N. E., 1985, "Temperature Measurements in a Turbulent Round Plume," *Int. J. Heat Mass Trans.*, Vol. 28, pp. 771–777.

Kotsovinos, N. E., and List, E. J., 1977, "Plane Turbulent Buoyant Jets. Part 1. Integral Properties," *J. Fluid Mech.*, Vol. 81, pp. 25–44.

Kounalakis, M. E., Sivathanu, Y. R., and Faeth, G. M., 1991, "Infrared Radiation Statistics of Nonluminous Turbulent Diffusion Flames," ASME JOURNAL OF HEAT TRANSFER, Vol. 113, pp. 437–445.

Lai, M.-C., and Faeth, G. M., 1987a, "Turbulence Structure of Vertical Adiabatic Wall Plumes," ASME JOURNAL OF HEAT TRANSFER, Vol. 109, pp. 663–670.

Lai, M.-C., and Faeth, G. M., 1987b, "A Combined Laser-Doppler Anemometer/Laser-Induced Fluorescence System for Turbulent Transport Measurements," ASME JOURNAL OF HEAT TRANSFER, Vol. 109, pp. 254–256.

Lai, M.-C., Jeng, S.-M., and Faeth, G. M., 1986, "Structure of Turbulent Adiabatic Wall Plumes," ASME JOURNAL OF HEAT TRANSFER, Vol. 108, pp. 827–834.

Lee, S. L., and Emmons, H. W., 1961, "A Study of Natural Convection Above a Line Fire," *J. Fluid Mech.*, Vol. 11, pp. 353–368.

Liburdy, J. A., and Faeth, G. M., 1978, "Heat Transfer and Mean Structure of a Turbulent Thermal Plume Along Vertical Isothermal Walls," ASME JOURNAL OF HEAT TRANSFER, Vol. 100, pp. 177–183.

Liburdy, J. A., Groff, E. G., and Faeth, G. M., 1979, "Structure of a Turbulent Thermal Plume Rising Along an Isothermal Wall," ASME JOURNAL OF HEAT TRANSFER, Vol. 101, pp. 299–355.

List, E. J., 1982, "Turbulent Jets and Plumes," *Ann. Rev. Fluid Mech.*, Vol. 14, pp. 189–212.

Lockwood, F. C., and Naguib, A. S., 1975, "The Prediction of Fluctuations in the Properties of Free, Round-Jet Turbulent Diffusion Flames," *Combust. Flame*, Vol. 24, pp. 109–124.

Moffat, R. J., 1982, "Contribution to the Theory of Single-Sample Uncertainty Analysis," *J. Fluids Engr.*, Vol. 104, pp. 250–258.

Panchapakesan, N. R., and Lumley, J. L., 1993, "Turbulence Measurements in Axisymmetric Jets of Air and Helium. Part 2. Helium Jet," *J. Fluid Mech.*, Vol. 246, pp. 225–247.

Papanicolaou, P. N., and List, E. J., 1987, "Statistical and Spectral Properties of Tracer Concentration in Round Buoyant Jets," *Int. J. Heat Mass Trans.*, Vol. 30, pp. 2059–2071.

Papanicolaou, P. N., and List, E. J., 1988, "Investigation of Round Vertical Turbulent Buoyant Jets," *J. Fluid Mech.*, Vol. 195, pp. 341–391.

Ramaprian, B. R., and Chandrasekhara, M. S., 1985, "LDA Measurements in Plane Turbulent Jets," *J. Fluids Engr.*, Vol. 107, pp. 264–271.

Ramaprian, B. R., and Chandrasekhara, M. S., 1989, "Measurements in Vertical Plane Turbulent Plumes," *J. Fluids Engr.*, Vol. 111, pp. 69–77.

Rouse, H., Yih, C. S., and Humphreys, H. W., 1952, "Gravitational Convection from a Boundary Source," *Tellus*, Vol. 4, pp. 201–210.

Stårner, S. H., and Bilger, R. W., 1983, "Differential Diffusion Effects on Measurements in Turbulent Diffusion Flames by the Mie Scattering Technique," *Prog. Astro. and Aero.*, Vol. 88, pp. 81–104.

Tennekes, H., and Lumley, J. L., 1972, *A First Course in Turbulence*, MIT Press, Cambridge, MA, pp. 113–124.

Liang-Han Chien
Assistant Professor,
Department of Mechanical Engineering,
Chang-Gung University,
Kwei-Shan, Taiwan, ROC
Assoc. Mem. ASME

R. L. Webb
Professor,
Department of Mechanical Engineering,
The Pennsylvania State University,
University Park, PA 16802
e-mail: r5w@psu.edu
Fellow ASME

A Parametric Study of Nucleate Boiling on Structured Surfaces, Part I: Effect of Tunnel Dimensions

This two-part experimental work identifies the effect of geometric dimensions on the boiling performance of "tunneled" enhanced boiling surfaces. The surface is formed on an integral-fin tube having a copper foil wrapped over the fin tips. Pores of known diameter and pitch are pierced in the foil cover. Tests were performed on a 19.1-mm diameter horizontal tube using R-11 and R-123 at 26.7°C for heat fluxes from 2 to 70 kW/m^2. The first part of the study defines the effect of the tunnel dimensions. The data show that greater tunnel height and smaller tunnel pitch are preferred. Sharp tunnel corners provides greater enhancement.

Introduction

Enhanced boiling tubes are used in the refrigeration and process industries. Pais and Webb (1991) survey the data for refrigerants on enhanced boiling surfaces. As stated in this study, "structured surfaces" are made by reforming the base surface to make fins of a standard or special configuration. Webb (1994) and Thome (1990) have surveyed the techniques used to develop enhanced boiling surfaces, which include the Hitachi Thermoexel-E (Fig. 1(*a*)) surface, Wolverine Turbo-B surface, Wieland GEWA-TW tube, and Trane bent fin surface. The structured surfaces all consist of interconnected tunnels and pores (or narrow gaps at the surface). The present authors propose that the Thermoexel-E, Turbo-B, and Turbo-B II geometries having surface pores operate by the same mechanism. It is probable that the mechanism of the GEWA-TW and bent fin geometries having narrow fin gap s_g operate by a closely related mechanism. Two key geometric characteristics of the surfaces are the (1) subsurface tunnels and (2) surface pores or fin gaps. These key features may be further defined by the following dimensional parameters:

1 subsurface tunnels: tunnel pitch (P_t), tunnel height (H_t), tunnel width (W_t), tunnel base radius (R_b), and tunnel shape.
2 surface pores (or gaps): pore diameter (d_p), and pore pitch (P_p).

Thus, a geometry having surface pores has six geometrical dimensions, plus the tunnel shape. Figure 1(*b*) illustrates a generic surface having subsurface tunnels and surface pores, which may be defined by the above dimensions.

Nakayama et al. (1980b, 1982) tested a Fig. 1(*b*) type surface which was made by soldering a thin copper sheet onto a horizontal finned plate. Pores were made in the copper sheet above the rectangular tunnels. The pore and tunnel sizes in their tests are listed in Table 1. Water, R-11, and liquid nitrogen were used as working fluids. Nakayama et al. (1982) compared surfaces having pores of uniform pore size and mixed pore size (d_p = 0.05 to 0.15 mm). They found that the surface pores having a uniform pore diameter (d_p = 0.1 mm) had the best boiling performance for R-11. The effect of pore pitch, tunnel size, and tunnel shapes were not investigated.

Arshad and Thome (1983) tested a planar surface similar to the Nakayama et al. (1980b) surface, for which they also varied the tunnel cross-section shape. They soldered micro-drilled cover plates on top of grooved surfaces to form the test surfaces. They tested circular, rectangular, and triangular shape tunnels. The range of pore and tunnel dimensions are listed in Table 1. They found the surface having 0.25-mm pore diameter had the best boiling performance. Circular tunnels generally required a larger incipient superheat. Triangular tunnels had high performance at low heat flux, but they dried out at intermediate heat flux.

Ma et al. (1986) boiled water and methanol on a copper plate having (*a*) parallel grooves covered by fine mesh screens, and (*b*) parallel grooves with a 40-mesh screen, and a brass cover plate having rows of pores. The tunnel and pore geometric parameters used in their study are listed in Table 1. They varied the groove size and the cross-section shape of the grooves (rectangular, triangular, and pentagonal shapes). They found that the triangular shaped tunnels have the highest boiling performance. They found the optimum pore diameter (d_p) is 0.16 mm for water. For methanol, the optimum d_p was between 0.16 and 0.22 mm. Because the pores of the covering mesh were not necessarily located on top of a groove (or a fin tip), the exact pore pitch is not known. They did not vary the pore pitch.

The authors have performed a systematic test series to define the effect of the pore and tunnel dimensions, and the tunnel shape on the surface performance. The experiments were performed by boiling R-11, R-123, R-134a, or R-22 on a low integral-fin tube which was wrapped with a copper foil. The pores were made by piercing the copper foil using a needle. Tunnels were created by the copper foil and the fins. The tunnel pitch and the tunnel height are equal to the fin pitch and height, respectively. Pores of specific diameters (d_p) were pierced in the foil at a specific pore pitch (P_p). The tunnel dimensions were varied by using integral-fin tubes of different fin pitch and fin height. This paper presents the effects of the tunnel width, height, and fin base shape using R-11 and R-123. Chien and Webb (1998a) reports the effect of pore diameter and pore pitch.

Chien and Webb (1998b) also performed visualization experiments, and found that evaporation in the tunnel is the dominant boiling mechanism. Chien and Webb (1998c) proposed a boiling model based on the findings of their visualization and para-

---

Contributed by the Heat Transfer Division for publication in the JOURNAL OF HEAT TRANSFER and presented at the '96 NHTC. Manuscript received by the Heat Transfer Division, Dec. 2, 1996; revision received, Mar. 10, 1998. Keywords: Boiling, Enhancement, Experimental, Heat Transfer. Associate Technical Editor: J. Howell.

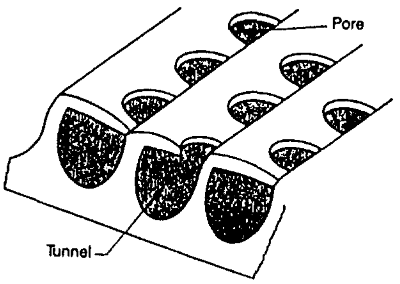

Fig. 1(*a*) Hitachi Thermoexcel-E

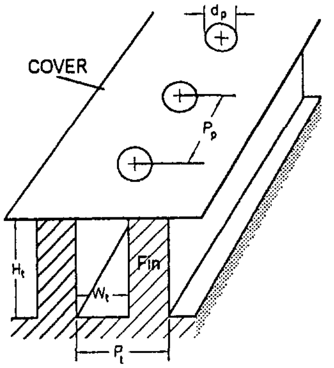

Fig. 1(*b*) Surface geometry studied

Fig. 1 Illustration of enhanced nucleate boiling surfaces

metric experiments. Their model stated that the liquid is drawn into the tunnel by inertia force after a bubble departs from a surface pore. Surface tension force acts to spread the liquid along the tunnel walls and pull it into the corners. The evaporation occurs mainly on the liquid menisci in the corners, plus a small portion of liquid film on the side walls. The pore diameter and pore pitch control the amount of liquid that flows into the tunnels. The liquid film distribution within the tunnel is controlled by surface tension and the tunnel geometry.

Experimental Program

Scope of Data. This paper provides data to define the effect of the tunnel dimensions and shape. The companion paper by Chien and Webb (1998a) reports the effect of the pore diameter and the pore pitch. Table 2 summarizes the geometric parameters and test ranges investigated in this paper and by Chien and Webb (1998a). Figure 2 defines the tunnel dimensions (P_t, H_t, and W_t) and illustrates the two tunnel base shapes investigated—rectangular and circular. For a circular fin base, the tunnel width is defined as the fin spacing measured at the half fin height as shown in Fig. 2(*b*). Table 3 lists the tunnel shapes investigated. This paper addresses the effect of the tunnel dimensions and shape. The pore pitches used are 0.75, 1.5, and 3.0 mm and the pore diameters are 0.12, 0.18, 0.23, and 0.28 mm. Chien and Webb (1998a) report the effect of pore pitch and pore diameter for the first two series of Table 2. Chien (1996) provides additional data on the Table 2 cases for R-22. Note that the present investigation is the first to apply pierced copper foil on the fin tips of a horizontal tube.

Table 1 Tunnel and pore size used in the literature for copper foiled surfaces

Authors	Nakayama et al. (1980, 1982)			Arshad & Thome (1983)	Ma et al. (1986)
Fluid	water	R-11	liquid nitrogen	water	water, methanol
Tunnel Shape	rect.	rect.	rect.	cir., rect., tri.	rect., tri., pent.
P_t (mm)	0.5-0.6	0.55	0.4	0.6, 1.2	0.6-0.9
H_t (mm)	0.5-0.62	0.4	0.4-0.56	0.5	0.4-0.6
d_p (mm)	0.08-0.20	0.04-0.15	0.03-0.2	0.15-0.25	0.07-0.15
P_p (mm)	0.6-0.72	0.7	0.72	0.6	NA

Table 3 summarizes the geometries tested. The first column of Table 3 shows the tube code used to describe the test results. The first number is the fins/m and second is the fin height (mm). The second column shows the fin base shape. The rectangular and circular fin base shapes are shown on Fig. 2(*a*) and Fig. 2(*b*), respectively. The surface code in the figure legends indicates the tube code followed by the pore diameter and pore pitch. For example, 1969-0.9-0.23-1.5 means a surface, made on a 1969 fins/m and 0.9-mm fin height tube, having 0.23-mm diameter surface pores (d_p) on 1.5-mm pitch (P_p).

Apparatus. The test apparatus is similar to that used by Webb and Pais (1992). As shown in Fig. 3, the single-tube pool boiling test cell consists of a 101.6 mm (4.0 in.) outside diameter, 203.2-mm (8.0 in.) long cylindrical glass cell and two brass end flanges. This apparatus allows visualization and photography of the boiling details. One end of the glass cell was held in place by an annular flange. The other end of the glass cell was clamped with a circular end flange. Neoprene gaskets were put between the end flanges and the two ends of the glass cell.

The test tube section was soldered to a 50.8-mm (2 in.) diameter circular brass flange. Two 0.25-mm diameter iron-constantan sheathed thermocouples located below the tube wall at 180 deg opposite positions sensed the tube wall temperature. The brass flange, to which the tube was attached, allowed the test section to be rotated inside the annular end flange. An O-ring seal was used between the two flanges. This design allowed measurement of the wall temperature as a function of circumferential angle. The vapor was condensed in an external water-cooled condenser. The test cell pressure was read on a manometer. Two 1.59-mm diameter iron-constantan sheathed thermocouples measured the saturation temperature in the glass boiling vessel. The apparatus also had a charging line, and an evacuation line connected to a positive displacement vacuum pump.

Nomenclature

CHF = critical heat flux, kW/m^2
cir. = circular
DHF = dry-out heat flux, kW/m^2
d_p = pore diameter, mm
h = heat transfer coefficient, W/(m^2 K)
H_f = fin height, mm
H_t = tunnel height, mm
pent. = pentagonal
P_f = fin pitch, mm
P_p = pore pitch, mm
P_t = tunnel pitch, mm
q'' = heat flux, W/m^2
R_b = tunnel base radius (Fig. 2(*b*)), mm
rect. = rectangular
s_g = fin gap, mm
tri. = triangular
T_s = saturation temperature, °C
T_w = wall temperature, °C
W_t = tunnel width, mm

Table 2 Investigated parameters in the present parametric study

Test Series	Parameter Studied	Test Range
Series I	Pore diameter (d_p)	0.12-0.28 (mm)
Series II	Pore pitch (P_p)	0.75-3.0 (mm)
Series III	Fin height (H_f)	0.5-0.15 (mm)
Series IV	Fins/m, Tun. Width (W_t)	1378-1969 fins/m 0.25-0.4 (mm)
Series V	Fin base shape	Circ., Rect.
Series VI	Fluid prop.	R-11, R-123

The test tubes were 140 mm long, 9.53 mm inside diameter, and 18 to 19.5 mm outside diameter. A 500-W electric cartridge heater of 9.52 mm diameter and 129 mm length was inserted into the copper tube. Its electric power was controlled by an auto-transformer and measured using a precision voltmeter and ammeter. The heater contains one continuous 101.6-mm long heated section, and two 12.7-mm long unheated sections at each ends. The heater was coated with a silicone-based heat sink compound to enhance thermal contact with the tube.

Two different tube designs (Fig. 4) were used in this work. The different designs were necessary, because different methods were used to make the test tubes. The Method-1 design (Fig. 4(*a*)) consisted of a thin wall integral-fin tube and a thick copper sleeve inside the tube. The 15.875-mm inside diameter integral-fin tube had 0.7-mm tube wall thickness. The outside diameter of the copper sleeve is 0.025 mm larger than the inside diameter of the outside tube. The copper sleeve had two 0.51 mm (0.02″) wide 0.38 mm (0.15″) deep axial thermocouple grooves diametrically opposite in the outer diameter of the copper sleeve. The sleeve was shrink fitted on the tube by cooling it with liquid nitrogen, and then pressing into the outside tube. The Method-1 design was used for the 1378 fins/m tube.

Method-2 (Fig. 4(*b*)) used a special thick wall tube of 9.52-mm diameter, in which two 0.4-mm wide thermocouple grooves were made by EDM (electric discharging machining). A 0.25-mm sheathed thermocouples were installed in each groove. A 0.3-mm thick copper strip was inserted between the thermocouple and the heater to insure that the thermocouple was located at the base of the groove. The base of the groove is approximately 1.0 mm beneath the root of fins. The measured temperature was corrected for the conduction temperature drop to the tube root diameter. The Method-2 design was used for the 1575 and 1969 fins/m tubes.

Fabrication of the Enhanced Surface. A 50-μm (0.002″) thick copper sheet was tinned using solder having 165°C melting temperature. This solder coating was approximately 50 μm (0.002″) thick. The integral-fin tube was first soldered to the end flange using a higher melting point silver-solder. This finned tube was then wrapped (2.0 to 3.0 mm overlap region) with the solder coated copper foil, and tied by fiberglass cords. The tube surface was deoxidized with a commercial cleaner (TARN-X), and cleaned with acetone before wrapping the copper foil. The tube was heated to the solder melting temperature using a 500-W cartridge heater inside the tube. During the heating process, the tube wall temperature was controlled carefully by observing the thermocouples inserted in the thermocouple grooves near the tube wall at two different axial locations. The tube was kept at 190°C and rotated slowly for five minutes to make sure that the solder melted and distributed uniformly. After completion of the tests and removal of the copper foil, inspection by a direct measurement microscope showed that the foil was joined to the fin tips over the entire tube surface area.

The tube surface was again cleaned by acetone after the copper foil was attached. Then, pores were made in the copper foil by a needle attached to a special tool that controlled the desired pore diameter. As shown in Fig. 5(*a*), the pore making tool used a sharp needle that extended out of the flat end of the pen-like body. The diameter of the pores depended on the extension length of the needle. A 3.18-mm diameter end screw controlled the needle extension length. Two small screws on the side of the tool fixed the desired position of the needle and the end screw. The pore pitch was measured by a dial caliper having 0.02-mm subdivisions, and marked on a bare foil surface before making pores. During the process of making surface pores, the pore size was frequently checked by a direct measurement microscope. This microscope has a reticle having 0.02-mm division and 50 power magnification. Figure 5(*b*) shows a photo of the pores taken from the back of the surface. The edge of the pores protrudes approximately 0.06 mm into the tunnel and form a re-entrant like pore shape.

Experimental Procedure. The system was evacuated by a vacuum pump before charging the test fluid. The working fluid was charged in the system according to the procedures described by Webb and Pais (1992). The data were taken in order of decreasing power input, starting at 470 W. The tube was tested using the following procedure.

1 Boil at maximum heat flux for one hour and keep the pool temperature at 26.7°C.

2 Control the pool temperature by adjusting the cooling water flow rate. Wait for the pool temperature to attain a constant value (less than 0.1°K variation).

3 When the system approaches steady state and is maintained at 26.7°C, measure: (*a*) electrical current and voltage through the heater; (*b*) saturation temperature and tube wall temperature; (*c*) system pressure.

4 Decrease the heat flux and repeat steps 2 and 3.

5 The reported data are the averages of three runs, obtained using three different thermocouple angular locations. Two wall temperatures are measured by the two diametrically opposite thermocouples, and the heat transfer coefficient is evaluated by averaging the thermocouple readings at the six angular locations. The thermocouple angular location was changed by rotating the inner disk shown in Fig. 3.

Data Reduction and Uncertainty

The heat transfer coefficient (h) is determined by the heat flux (q'') over wall superheat ($T_w - T_s$). Calculations of q'' and h are based on the envelope area, defined by the heated length (101.6 mm) multiplied by tube outside perimeter. The input power of the heater was calculated by multiplying the voltage and current through the heater. The thermocouples were connected to the Omega data logger (OM-480), which was calibrated for the reference zero point prior to the experiments. The calculated accuracy of the temperature measurements is ±0.1°C. The tube wall temperature was determined by extrapolating the thermocouple temperatures to the tube wall using Fourier's law. The output of a pressure transducer was also connected to the data logger. The transducer and thermocouples were calibrated and checked for repeatability. The geometric parameters were measured by the aforementioned direct measurement micro-

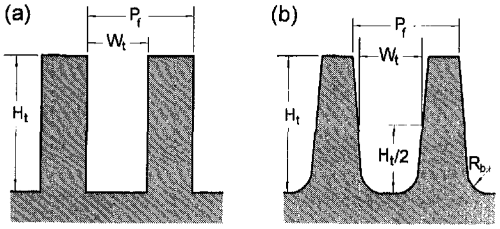

Fig. 2 Fin base shape of rectangular tunnels (*a*) Rectangular fin base (*b*) Circular fin base

Table 3 Tube code and specifications

Tube code	Fin base shape	Fins/m	P_f (mm)	W_t (mm)	H_t (mm)
1378-0.9	Circ.	1378	0.73	0.40	0.90
1378-0.5	Circ.	1378	0.73	0.40	0.50
1575-1.5	Circ.	1575	0.64	0.33	1.50
1575-0.8	Circ.	1575	0.64	0.33	0.80
1575-0.6	Circ.	1575	0.64	0.33	0.60
1575r-0.6	Rect.	1575	0.64	0.33	0.60
1969-0.9	Circ.	1969	0.51	0.25	0.95

scope and a dial caliper. The largest uncertainty of the geometric parameters is the pore diameter (±10 percent).

An error analysis was made taking into account the uncertainty of the measuring devices. The uncertainty in the heat transfer coefficient is estimated to be within ±5 percent at maximum heat flux and within ±10 percent at low heat flux ($q'' \approx 10$ kW/m^2). As described in the test procedure, each surface geometry was tested three times. Each data set is based on averaging data for three circumferential thermocouple locations. The average of the two thermocouples were repeatable within ±10 percent in the three independent tests. In two cases, the copper foil was removed from the tube after the test. Then, the same pore diameter and pore pitch were made on a new copper foil on the same tube. The boiling heat transfer curves of the surfaces agreed within ±10 percent.

Results and Discussion

Effect of Fin Height. The effect of tunnel height is shown by Figs. 6 and 7 for R-123 and R-11, respectively. The three enhanced surfaces in Fig. 6 are made on 1575 fins/m tubes having 0.6, 0.8, and 1.5-mm fin heights. The pore diameters and pore pitches are identical (d_p = 0.23 mm and P_p = 1.5 mm) for the three enhanced surfaces. Each curve in Figs. 6 and 7 shows a peak h-value. The heat flux corresponding to this peak h-value is called "dry-out heat flux" (DHF), which is defined as the heat flux, at which the liquid flow into the tunnel is just enough to sustain the evaporation in the tunnel. The liquid thickness approaches a minimum value, which results in a maximum heat transfer coefficient. In Figs. 6 and 7, the greater fin height yields higher heat transfer coefficients for $q'' <$ DHF. However, smaller fin height gives higher heat transfer coefficient for $q'' >$ DHF. The 1575-0.8 tubes have 33 percent larger fin area than the 1575-0.6 tube. Its heat transfer coefficient is 10 to 20 percent greater than for the 1575-0.6 tube at $2.9 \leq q'' \leq 9.4$ kW/m^2 for the same pore diameter and pore pitch. However, the 1575-1.5 tube having 150 percent larger fin area than the 1575-0.6 tube gains only 17 to 34 percent greater h-value.

The Webb and Pais (1992) data for the Turbo-B tube (1654 fins/and 0.6 mm fin height) is shown in Fig. 6 for comparison purposes. The pore diameter and pore pitch for Turbo-B are approximately 0.2 and 0.7 mm, respectively. Comparison of the data shows that the 1575 fins/m, 0.23-mm diameter pore diameter, 1.5-mm pore pitch surface provides higher performance than Turbo-B. However, the data suggest that Turbo-B will have a higher DHF. This is because its pore pitch is smaller.

Figure 7 compares 0.5 mm and 0.9-mm fin height on a 1378 fins/m tube having 0.12, 0.23, or 0.28-mm pore diameters. All the data in Fig. 7 used the same pore pitch (P_p = 1.5 mm) for R-11. Additional data for different pore pitches and pore diameters for the 1378 fins/m tubes are presented in Chien and Webb (1998a). Similar to the results in Fig. 6, for the same pore diameter and pore pitch, higher fin height gives higher h, except the smallest pores (d_p = 0.12 mm) at high heat flux. For d_p = 0.12 mm, no evaporation happens in the tunnel because tunnels are dry.

Comparison of the Figs. 6 and 7 data shows that a greater fin height is favorable for low fins ($H_f \leq 0.9$ mm). As dis-

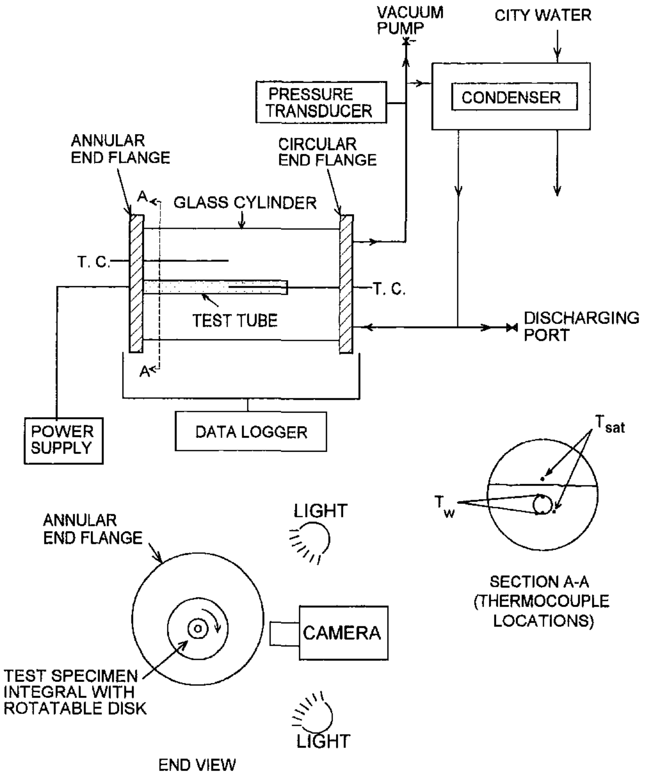

Fig. 3 Schematic of the low pressure boiling test apparatus

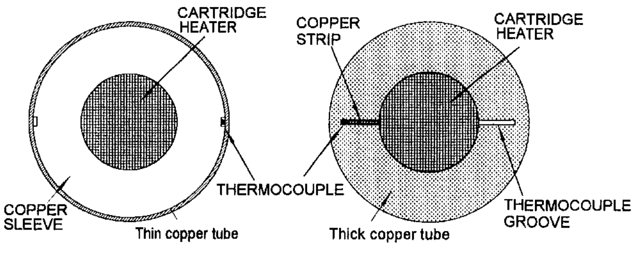

(a) METHOD (1) (b) METHOD (2)

Fig. 4 Thermocouple grooves in tubes

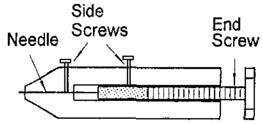

Fig. 5(*a*) Pore making tool

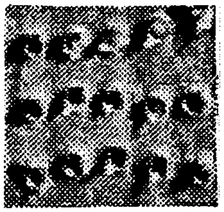

Fig. 5(*b*) Photo of the pores

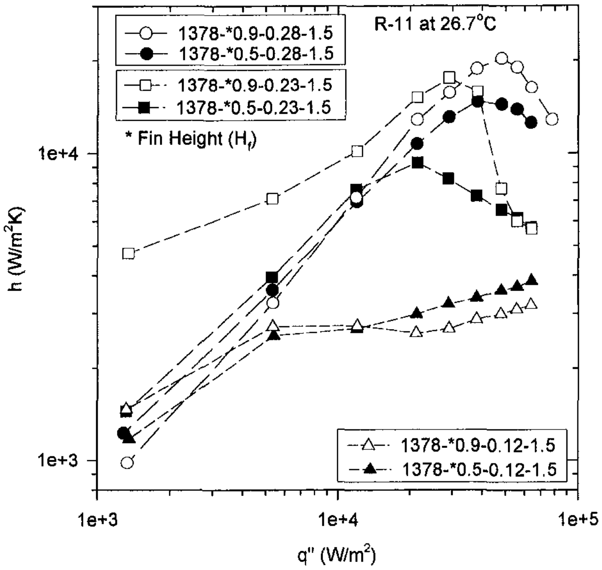

Fig. 7 Effect of fin height for various pore diameters using R-11

cussed in Chien and Webb (1998c), the evaporation mainly occurs on the menisci in the corners, plus a small portion of evaporation from the liquid film on the side walls. The evaporation surface area in the tunnel increases as the fin height increases, and is expected to yield greater *h*-values. However, the data shows that increasing fin height will not yield significant enhancement for high fins ($H_f \cong 1.5$ mm). This is because the surface tension force is not enough to sustain the liquid film on the entire side wall when the fin is too high. From the present data, the fin height = 0.7 to 1.0 mm is recommended.

Effect of Fin Pitch and Tunnel Width. Data for two identical pore pitch/pore diameter surfaces for 1575 and 1969 fins/m tubes are compared in Fig. 8. All data are for R-123 having 0.23-mm pore diameter and 1.5 pore pitch. The 1969 fins/m tube has 0.9 mm fin height. Data for the identical fin height is not available for the 1575 fins/m tube. Therefore, two 1575 fins/m fin heights (0.8 and 1.5 mm) are shown in Fig. 8. The 1969-0.9 tube gives about ten percent higher *h* than the 1575-0.8 tube for the same pore dimensions and test fluids. The total surface area inside the tunnels of the 1575-1.5 tube is 22 percent greater than for the 1969-0.9 tube. However, the 1575-1.5 tube and the 1969-0.9 tube have about the same heat transfer coefficients at high heat flux ($10 \leq q'' \leq 40$ kW/m^2). The 1969-0.9 tube provides approximately the same boiling performance as the 1575-1.5 tube by using smaller fin height. From these curves, we conclude that the fin pitch has only a secondary effect on boiling performance. However, the 1969 fins/m tubes may give slightly better performance than the 1575 fins/m tubes for the same fin height. The pore size and pore pitch are the primary factors for the boiling heat transfer performance, as discussed by Chien and Webb (1998a).

Effect of Fin Base Shape. Figure 9 compares two surfaces having circular and rectangular fin base using the same pore and tunnel dimensions. Surface 1575r-0.6-0.23-1.5 was made on a 1575 fins/m tube having rectangular fin base as shown in Fig. 2(*a*). This was made from cutting rectangular grooves on a 5.0 mm wall thickness plain tube. Surface 1575-0.6-0.23-1.5 was made on a 1575 fins/m tube having circular fin base shape. This tube was made by a finning machine having a smooth fin surface and circular fin base as shown by Fig. 2(*b*). Both sur-

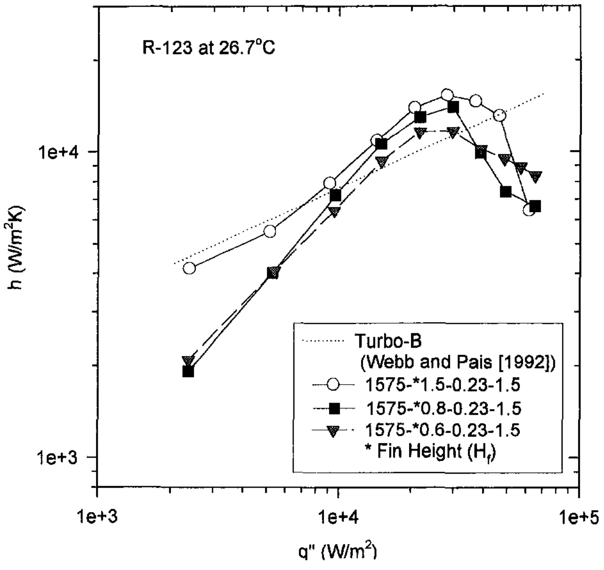

Fig. 6 Effect of fin height on the 1575 fins/m tubes for R-123

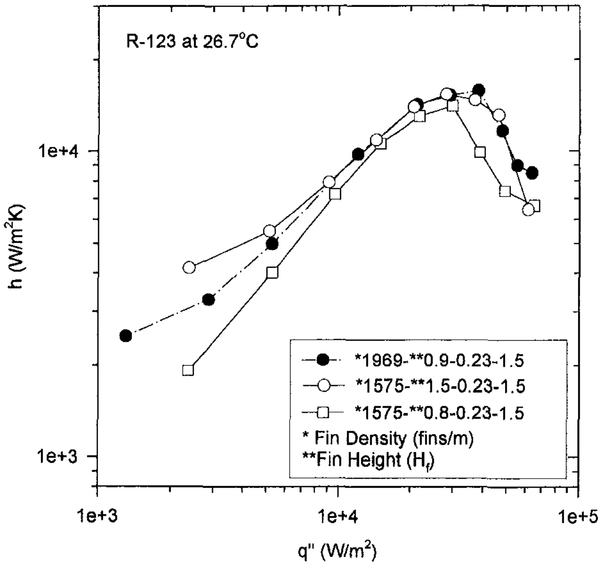

Fig. 8 Fin pitch effect for R-123 on 1575 and 1969 fins/m tubes

faces have the same pore diameter (0.23 mm), pore pitch (1.5 mm) and fin height (0.6 mm). As shown in Fig. 9, the heat transfer coefficient of surface 1575r-0.6-0.23-1.5 having a rectangular fin base is approximately 20 percent higher than one having a circular fin base. The authors propose that the rectangular fin base provides a higher *h*-value because of the greater thin film surface area provided by menisci in the sharp corners. As analyzed by Chien and Webb (1998c), smaller corner radius yields stronger surface tension force near the corners and increased evaporation area by retaining more liquid. Therefore, rectangular fin base is expected to yield greater boiling heat transfer rate than a circular fin base. Chien (1996) provides additional discussion of the proposed mechanism.

Comparison of R-11 and R-123. The properties of R-11 and R-123 are similar at the same saturation temperature. Therefore, their boiling performances are expected to be nearly equal. Figure 10 shows the boiling performance for two surfaces (1969-0.9-0.23-1.5 and 1575-0.8-0.2-1.5) using R-11 and R-123. For both surfaces, the two fluids have approximately equal boiling heat transfer coefficients at $q'' <$ DHF. However, R-11 yields approximately 10 to 20 percent higher boiling performance than R-123 for $q'' >$ DHF.

Webb and Pais (1992) tested R-11 and R-123 on five enhanced tube geometries. They found the difference of boiling heat transfer coefficients on the two fluids is within ten percent for all tubes, except Turbo-B. Their R-11 data are 40 percent greater than their R-123 data, and they considered this unexpected result as an anomaly. However, the authors tested the same Turbo-B tube and found the Turbo-B tube boiling performances for R-11 and R-123 were approximately equal in the present test. For R-123, Webb and Pais's Turbo-B data are in good agreement with the present test results. Hence, we conclude, R-11 and R-123 yield similar boiling performance on all surfaces.

Conclusions

From our experiments, the following conclusions are drawn:

1 For 1378 to 1969 fins/m, use of $d_p = 0.23$ and $P_p = 1.5$ mm provides good boiling performance and high DHF. For a smaller pore diameter, a smaller pore pitch should be used.

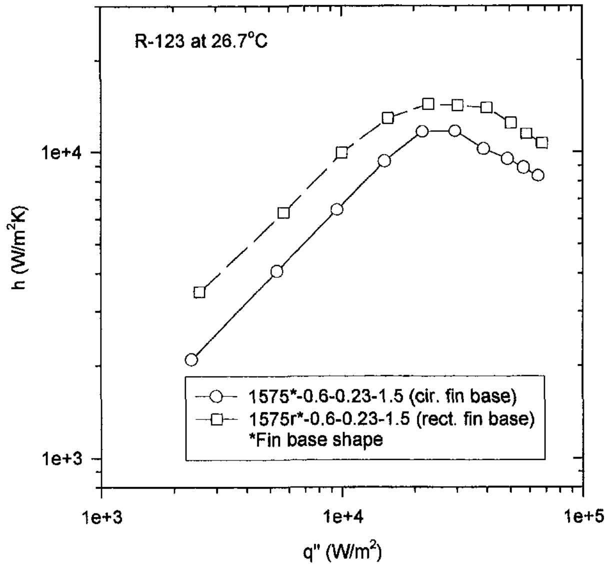

Fig. 9 Effect of fin base shapes on R-123

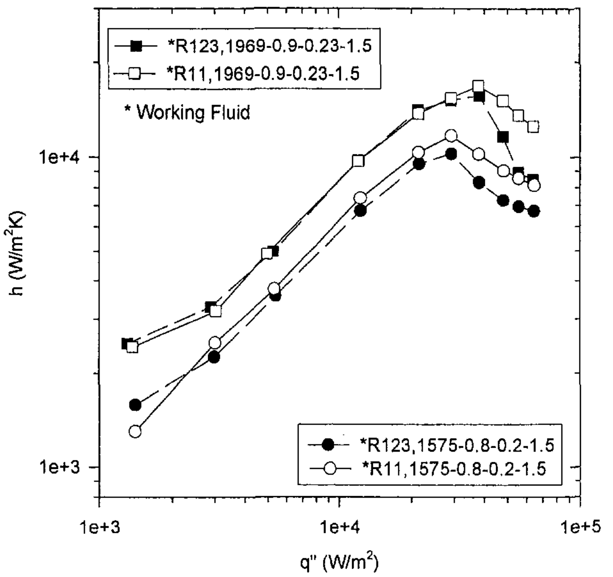

Fig. 10 Comparison of boiling performance for R-11 and R-123

2 Increasing the fin height from 0.5 to 0.9 will significantly increase the heat transfer coefficient on 1378 and 1575 fins/m tubes. However, for high fins, increasing fin height from 0.8 to 1.5 does not significantly increase the boiling performance. Therefore, the recommended fin height is between 0.7 and 1.0 mm.

3 The 1969-0.9 tube has smaller fin height and performance similar to the 1575-1.5 tube for $d_p = 0.23$ and $P_p = 1.5$ mm surface pores. Therefore, the 1969 fins/m tube is preferred. However, the effect of fin pitch is not as significant as the combination of pore diameter and pore pitch.

4 A tube having a small fin base radius results in higher boiling heat transfer performance. This is because of evaporation from menisci at the fin base.

5 At the same saturation temperature, R-11 and R-123 yield nearly equal boiling heat transfer performance on the Turbo-B and the present enhanced surfaces.

Acknowledgment

This work was supported by a consortium of industrial companies. The consortium members are Wolverine Tube, Carrier Corp., The Trane Co., York International, Olin Brass Corp., UOP Corp., and Wieland-Werke AG. Special thanks is given to Wieland-Werke and Wolverine Tube companies for providing test sections used in this work.

References

Arshad, J., and Thome, J. R., 1983, "Enhanced Boiling Surfaces: Heat Transfer Mechanism Mixture Boiling," *Proc. ASME-JSME Therm. Eng. Joint Conf.*, Vol. 1, pp. 191–197.

Chien, L.-H., 1996, "Mechanism and Analysis of Nucleate Boiling on Structured Surfaces," PH.D. dissertation, The Pennsylvania State University, University Park, PA.

Chien, L.-H., and Webb, R. L., 1998a, "Parametric Studies of Nucleate Pool Boiling on Structured Surfaces, Part II: Effect of Pore Diameter and Pore Pitch," ASME JOURNAL OF HEAT TRANSFER, Vol. 120, pp. 1049–1054.

Chien, L.-H., and Webb, R. L., 1998b, "Visualization of Pool Boiling on Enhanced Surfaces," *Experimental Thermal and Fluid Science*, Vol. 16, pp. 332–341.

Chien, L.-H., and Webb, R. L., 1998c, "A Nucleate Boiling Model for Structured Enhanced Surfaces," *International Journal of Heat and Mass Transfer*, Vol. 41, No. 14, pp. 2183–2195.

Nakayama, W., Daikoku, T., Kuwahara, H., and Nakajima, T., 1980a, "Dynamic Model of Enhanced Boiling Heat Transfer on Porous Surfaces, Part I:

Experimental Investigation," ASME JOURNAL OF HEAT TRANSFER, Vol. 102, pp. 445–450.

Nakayama, W., Daikoku, T., Kuwahara, H., and Nakajima, T., 1980b, "Dynamic Model of Enhanced Boiling Heat Transfer on Porous Surfaces Part II: Analytical Modeling," ASME JOURNAL OF HEAT TRANSFER, Vol. 102, pp. 451–456.

Nakayama, W., Daikoku, T., and Nakajima, T., 1982, "Effects of Pore Diameters and System Pressure on Saturated Pool Nucleate Boiling Heat Transfer From Porous Surfaces," ASME JOURNAL OF HEAT TRANSFER, Vol. 104, pp. 286–291.

Ma, T., Liu, X., Wu, J., and Li, H., 1986, "Effects of Geometrical Shapes and Parameters of Reentrant Grooves on Nucleate Pool Boiling Heat Transfer from Porous Surfaces," *Heat Transfer 1986, Proceedings of the 8th International Heat Transfer Conference,* Vol. 4, pp. 2013–2018.

Pais, C., and Webb, R. L., 1991, "Literature Survey of Pool Boiling on Enhanced Surfaces," *ASHRAE Transactions,* Vol. 97, pp. 79–89.

Thome, J. R., 1990, *Enhanced Boiling Heat Transfer,* Hemisphere Publishing Corp., New York.

Webb, R. L., 1994, *Principles of Enhanced Heat Transfer,* Wiley Interscience, New York, Chapter.

Webb, R. L., and Pais, C., 1992, "Nucleate Boiling Data for Five Refrigerants on Plain, Integral-Fin and Enhanced Tube Geometries," *International Journal of Heat and Mass Transfer,* Vol. 35, No. 8, pp. 1893–1904.

Liang-Han Chien
Assistant Professor,
Department of Mechanical Engineering,
Chang-Gung University,
Kwei-Shan, Taiwan, ROC
Assoc. Mem. ASME

R. L. Webb
Professor,
Department of Mechanical Engineering,
The Pennsylvania State University,
University Park, PA 16802
e-mail: r5w@psu.edu
Fellow ASME

A Parametric Study of Nucleate Boiling on Structured Surfaces, Part II: Effect of Pore Diameter and Pore Pitch

This two-part experimental work identifies the effect of geometric dimensions on the boiling performance of "tunneled" enhanced boiling surfaces, which is similar to the Hitachi Thermoexcel-E surface. Tests were performed on a horizontal tube using R-11 and R-123 at 26.7°C for heat fluxes from 2 to 70 kW/m². This second part of the study defines the effect of the pore dimensions (pore diameter and pore pitch). The pore diameters are 0.12, 0.18, 0.23, and 0.28 mm and the pore pitches are 0.75, 1.5, and 3.0 mm. The results are interpreted to explain the relationship between pore diameter and pore pitch on the boiling performance.

Introduction

This paper is concerned with boiling on enhanced surfaces having subsurface tunnels and surface pores. The surface geometric characteristics are defined by the (1) subsurface tunnels and (2) surface pores or gaps. These key features may be further defined by the following dimensional parameters:

1 subsurface tunnels: Tunnel pitch (P_t), tunnel height (H_t), tunnel width (W_t), tunnel base radius, and tunnel shape.
2 surface pores (or gaps): pore diameter (d_p) and pore pitch (P_p).

This is the second part of a two-part paper intended to define the effect of the geometric parameters. Chien and Webb (1998a) report on the effect of the tunnel width, height, and shape for a limited range of pore diameters and pore pitches. This paper presents the results of a detailed parametric study to define the effect of the pore diameter and pore pitch. The tests were performed using R-11 boiling on a standard, 1378 fins/m integral-fin tube that was wrapped with a 0.05-mm thick copper foil. The foil was soldered to the fin tips. Pores of specific diameters ($d_p = 0.12$, 0.18, 0.23, and 0.28 mm) were pierced in the foil at specific pore pitches ($P_p = 0.75$, 1.5, and 3.0 mm). A description of the test apparatus and a survey of prior work to investigate the effects of pore pitch and pore diameter are given by Chien and Webb (1998a).

Boiling Mechanism

The boiling visualization experiments of Chien and Webb (1998b) support the existence of the "suction-evaporation model," which was initially proposed by Nakayama et al. (1982). In this model, liquid is sucked in the tunnel through inactive pores by the pumping action of bubbles departing from the active pores. It then spreads along the tunnels and evaporates from menisci at the corners of the tunnel.

Xin and Chao (1985) proposed a boiling model for a plane T-finned surface. The model assumed a steady-state evaporation of a thin film in the T-shape tunnel. They extended their model to the planar Thermoexcel-E surface by fitting empirical constants from Nakayama et al. (1980) data. Contrary to the observations by Chien and Webb (1998b), the Xin and Chao model appears to be based on a physically unrealistic assumption, because the bubble evolution and liquid film evaporation processes are periodic.

Chien and Webb (1998b) observed that active tunnels are vapor filled except for liquid menisci in the corners. The liquid menisci are illustrated in Figs. 1(*a*) and 1(*b*) for the tunnels of rectangular fin base and circular fin base, respectively. Four menisci exist in the corners of the tunnel having a rectangular fin base (Fig. 1(*a*)). For the circular fin base, the liquid is pulled into the corners near the fin tips by surface tension force because the corners near the fin tip have much smaller radius than at the fin base. The evaporation rate in the tunnel depends on the thickness of the liquid meniscus. Chien and Webb (1998b) observations support the proposal of Nakayama et al. (1980) that the total heat flux is the sum of the following two parts:

1 latent heat flux in the tunnel (q''_{tun}) due to the evaporation inside the tunnels of the enhanced surface.
2 sensible heat flux (q''_{ex}) due to the external convection induced by bubble agitation.

Both of the heat fluxes are based on the projected surface area. Thus, the total heat flux is given by

$$q'' = q''_{\text{tun}} + q''_{\text{ex}} . \tag{1}$$

A higher heat transfer coefficient will exist if the liquid film thickness is smaller. However, at a certain heat flux, the liquid menisci will dry out. This is called the "dry-out heat flux," (DHF). The DHF is different from the conventional "critical heat flux," (CHF), which is controlled by the hydrodynamic stability of the vapor columns rising from the boiling surface. The DHF occurs when the tunnel walls become dry. We find that the DHF is dependent on the "total open area" (A_{pt}) of the tunnel, which is defined as the sum of the pore areas that feed liquid into and vapor from the tunnels. The $A_{pt} = A_pL/P_p$, where $A_p = \pi d_p^2/4$, L is the tunnel length, and P_p is the pore pitch. Hence A_{pt}/L is given by

$$\frac{A_{pt}}{L} = \frac{\pi d_p^2}{4P_p} . \tag{2}$$

As A_{pt} increases, more liquid can get in the tunnel, and a higher heat flux can be supported before the DHF occurs. Above

---

Contributed by the Heat Transfer Division for publication in the JOURNAL OF HEAT TRANSFER and presented at the '96 NHTC. Manuscript received by the Heat Transfer Division, Dec. 2, 1996; revision received, June 7, 1998. Keywords: Boiling, Enhancement, Experimental, Heat Transfer. Associate Technical Editor: J. Howell.

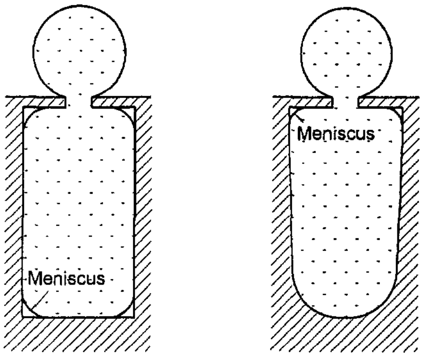

(a) Rectangular Fin Base (b) Circular Fin Base

Fig. 1 Tunnel cross section showing menisci in the corners

the DHF, the evaporation rate in the tunnel exceeds the available liquid supply rate and the "dried-up mode," as described by Nakayama et al. (1982), will exist. Then, the tunnel is completely filled with vapor and vaporization into bubbles takes place outside the tunnels. Thus, $q''_{\rm tun} \cong 0$, and $q'' \cong q''_{\rm ex}$.

At low heat flux the A_{pt} is too large and the liquid supply rate will exceed the evaporation rate, so intermittent regions of the tunnel will flood with liquid. Then, the liquid menisci regions will not exist in the flooded tunnel regions.

The highest performance will occur when just enough liquid flows into the tunnel to sustain the liquid menisci in the corners. At higher heat flux the DHF condition will occur. By increasing the pore diameter, or decreasing the pore pitch, the liquid supply rate will be increased and a higher DHF can be sustained. Therefore, an optimum total open area exists, which is dependent on heat flux. For a fixed pore pitch a surface having larger pores will display a greater heat transfer coefficient at high heat flux.

Based on the results of the present study and Chien and Webb (1998a, 1998b), the authors have proposed an analytical model (Chien and Webb, 1998c). The temporal variation is important in considering the periodic nature of boiling process; however, this was not addressed in the Nakayama et al. (1980) and Xin and Chao models. The Chien and Webb (1998c) model accounts for the temporal evaporation rate variation during a bubble cycle, and predicts the present data within ±30 percent.

Experimental Program

Scope of Data. The authors have performed a systematic test series to define the effect of the pore diameter and pore pitch formed in the cover foil of a 1378 fins/m, standard integral-fin tube. The experiments were performed by boiling R-11 or R-123 at 26.7°C. The pores were made by piercing the 50 μm (0.002 in.) thick copper foil using a needle illustrated in Fig. 5(*a*) of Chien and Webb (1998a). Pores of specific diameters (d_p) were pierced in the foil at a specific pore pitch (P_p). Figure 1(*b*) of Chien and Webb (1998a) defines the tunnel dimensions (P_t, H_t, and W_t), the pore diameter (d_p), and the pore pitch (P_t). Data were taken for pore diameters of 0.12, 0.18, 0.23, and 0.28 mm, and for pore pitches of 0.75, 1.5, and 3.0 mm.

Table 1 Tube code and specifications

Tube code	Fin base shape	Fins/m	P_f (mm)	W_t (mm)	H_t (mm)
1378-0.9	Circular	1378	0.73	0.40	0.90
1378-0.5	Circular	1378	0.73	0.40	0.50
1969-0.9	Circular	1969	0.51	0.25	0.95

Table 1 lists the tubes used in the present study and their dimensions. The first column of Table 1 shows the tube code used to describe the test results. The first number is the fins/m and second is the fin height (mm). The second column defines the fin base shape as "circular." This standard integral-fin geometry has 0.15 mm radius at the fin root, as illustrated in Fig. 1(*b*). The surface code used in the figure legends indicates the tube code followed by the pore diameter and pore pitch. For example, 1378-0.9-0.23-1.5 means a surface made on a 1378 fins/m (35 fins/in.) tube having 0.9-mm fin height and 0.23-mm diameter (d_p) surface pores on 1.5-mm pitch (P_p).

Test Apparatus. As illustrated by Fig. 3 of Chien and Webb (1998a) the single-tube pool boiling test cell consists of a 101.6-mm (4.0 in.) outside diameter, 203.2-mm (8.0 in.) long cylindrical glass cell and two brass end flanges. The test surface was formed on an integral fin tube having a copper foil wrapped over the fin tips. A 500 W, 9.52-mm diameter electric cartridge heater was inserted into the tube. The heater contains one continuous 101.6-mm long heated section and a 12.7-mm long unheated section at each end. Sheathed iron-constantan thermocouples 0.25-mm (0.01 in.) diameter were inserted in each of two 0.5-mm wide thermocouple grooves to measure the tube wall temperature. Details of this apparatus are described in Chien and Webb (1998a).

Tests were performed on a 19.1-mm diameter horizontal tube using R-11 and R-123 at 26.7°C. The experimental procedures are the same as described by Chien and Webb (1998a). Each tube was tested three times, with the wall thermocouples in a specific angular location. After each test, the tube was rotated 120 deg and the test repeated. The final test results are average values from the three angular position tests. Chien (1996) describe the data reduction and uncertainty in detail. The pore diameter has the largest uncertainty (within ±10 percent) among the geometric parameters. The uncertainty in the heat transfer coefficient is estimated to be within ±5 percent at maximum heat flux and within ±10 percent at low heat flux ($q'' \cong 10$ kW/m^2). By retesting some surfaces, the present data were found repeatable within ±10 percent.

Test Results

Pore Diameter. Figure 2 shows boiling curves for different pore diameters using a fixed pore pitch (P_p = 1.5 mm) on a

Nomenclature

A_p = open area of a pore, m^2
A_{pt} = total pore open area per unit tunnel length, m^2
DHF = dry-out heat flux, kW/m^2
d_p = surface pore diameter*, mm
h = heat transfer coefficient, W/(m^2 K)
H_t = tunnel height*, mm
L = tunnel length, mm
P_f = fin pitch, mm
P_p = pore pitch*, mm
P_t = tunnel pitch*, mm
q'' = heat flux based on projected area ($= q''_{\rm tun} + q''_{\rm ex}$), W/m^2
$q''_{\rm ex}$ = external (to tunnel) heat flux component, W/m^2
$q''_{\rm tun}$ = heat flux component based on evaporation in tunnels, W/m^2
s_g = gap width for "continuous fin gap" type surface, mm
T_s = saturation temperature, °C
T_w = wall temperature, °C
W_t = tunnel width, mm

* see Fig. 1(*b*) of Chien and Webb (1998a).

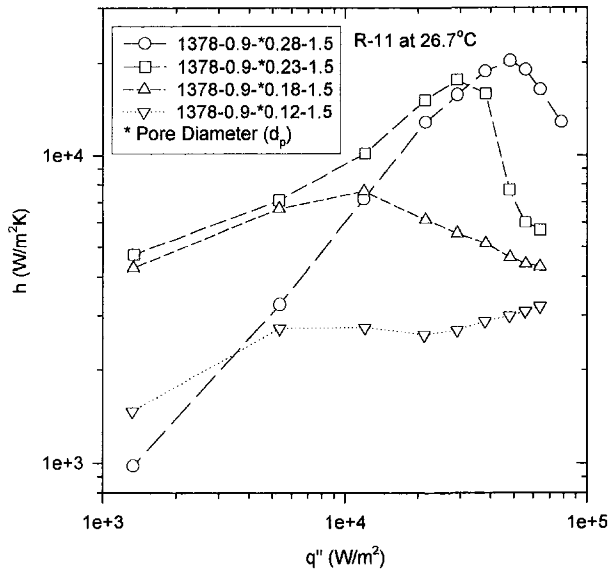

Fig. 2 Effect of pore diameter for fixed pore pitch (1.5 mm) on tube 1378-0.9

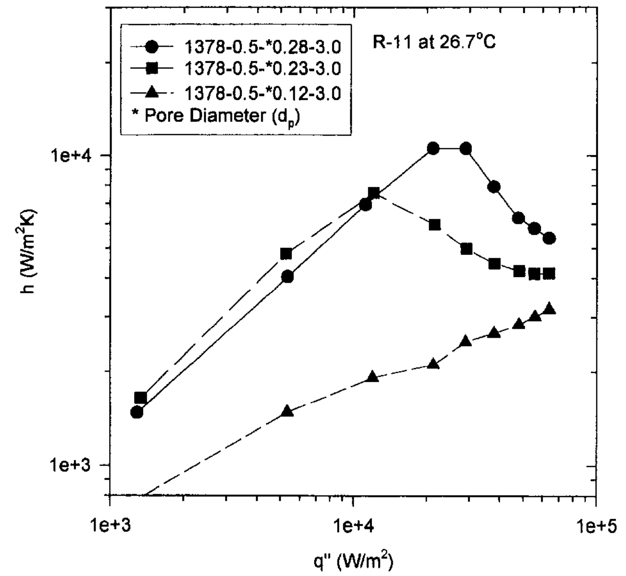

Fig. 3 Effect of pore diameter for fixed pore pitch (3.0 mm) on tube 1378-0.5

0.9 mm fin height, 1378 fins/m tube. The surfaces having $d_p = 0.18$, 0.23, and 0.28 mm give high performance at low heat flux. However, all show a maximum, which indicates the dry-out heat flux (DHF) and the heat transfer coefficients decrease drastically above their DHF. The DHF is defined as the maximum heat transfer coefficient, which occurs when liquid is depleted in the tunnel. Above the DHF, evaporation does not occur in the tunnels, and the vapor in the tunnels causes high thermal resistance. The boiling curves are strongly influenced by the pore diameter. As the pore diameter increases, the boiling curves shift upward and to the right. The dry-out heat flux (DHF) increases with the increase of the pore diameter. The surface having the largest pores ($d_p = 0.28$ mm) has the greatest heat transfer coefficient at high heat flux and greater DHF. However, the performance of this surface drops rapidly at heat fluxes greater than the DHF. The 0.23-mm pore diameter is the best for $q'' < 35$ kW/m^2.

The same qualitative effects of pore diameter are observed for a fixed $P_p = 3.0$ for the tests on the 1378-0.5 tube as shown in Fig. 3. The surface having $d_p = 0.23$ mm has the highest boiling heat transfer coefficient for $q'' < 10$ kW/m^2. The largest pore diameter ($d_p = 0.28$ mm) has higher DHF, but a lower h-value than for the 0.23 mm pore diameter surface at low heat flux.

Figure 4 shows similar effect of pore diameter (d_p) on the 1969-0.9 tube using R-123. Surfaces having $d_p = 0.18$ and 0.23 and $P_p = 0.75$ and 1.5 mm are compared. For a fixed pore pitch ($P_p = 1.5$ mm), the surface having larger pores ($d_p = 0.23$ mm) has higher h-value at $q'' > 10$ kW/m^2 and greater DHF (dry-out heat flux) than the surface having $d_p = 0.18$ mm pores. The smaller pores cannot provide sufficient liquid into the tunnel at high heat flux. For a smaller pore pitch $P_p = 0.75$ mm, the surface having larger pores ($d_p = 0.23$ mm) has greater DHF, but yields lower heat transfer coefficient at $q'' <$ DHF. This is because the tunnels contain regions, which are partially flooded.

Pore Pitch. Figure 5 shows the effect of pore pitch on the 1378-0.9 tube using fixed pore diameter ($d_p = 0.28$ and 0.12 mm). The pore pitch was varied from 0.75 to 3.0 mm. For comparison purposes, the standard 1378-0.9 tube (without copper cover and surface pores) was also tested and the results are shown in Fig. 5. All three curves for $d_p = 0.28$ mm have much higher heat transfer coefficient than the 1378-0.9 tube without copper cover. For $d_p = 0.28$ mm, the surface having the largest pore pitch ($P_p = 3.0$ mm) has the highest heat transfer coefficient for $q'' < 30$ kW/m^2.

The Fig. 5 data are plotted as h versus P_p in Fig. 6 with heat flux as the parameter. As shown in Fig. 6, the largest P_p (3.0 mm) has the highest h-value at low heat flux ($q'' = 12$, 21 and 29 kW/m^2). For high heat fluxes ($q'' = 55$ and 64 kW/m^2), the heat transfer coefficient is highest when the smallest pore pitch ($P_p = 0.75$ mm) is used. For $P_p = 1.5$ mm, the surface has high heat transfer coefficient over a wide range of heat fluxes. These trends are expected, because the total open area (A_{pt}) increases as the pore pitch is reduced. Hence, the liquid supply rate to the tunnels increases as the total open area increases. According to the suction-evaporation mode model of Nakayama et al. (1982), the evaporation rate in the tunnel depends on the liquid menisci in the corners. The surface has the highest heat transfer coefficient when just enough liquid flows into the tunnels to sustain the liquid menisci in the tunnel. At low heat flux, less total open area is required to sustain the

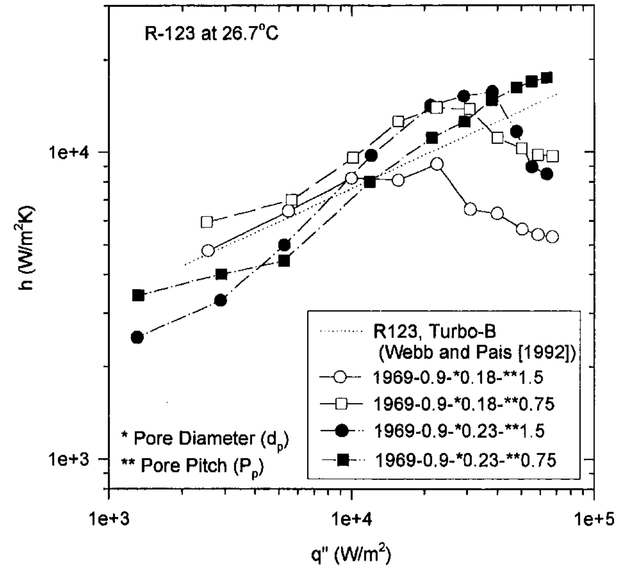

Fig. 4 Effect of pore diameter and pore pitch on tube 1969-0.9 for R-123

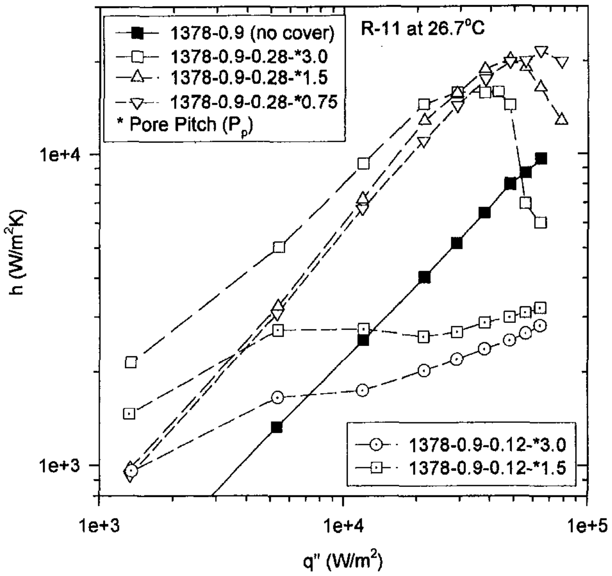

Fig. 5 Effect of pore pitch for fixed pore diameters (0.12 and 0.28 mm) on tube 1378-0.9

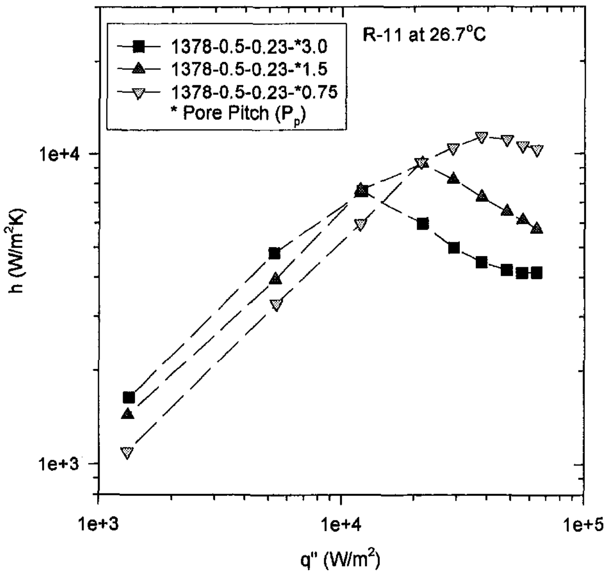

Fig. 7 Effect of pore pitch for fixed pore diameter (0.12 and 0.28 mm) on tube 1378-0.5

liquid menisci. If the A_{pt} is too large the tunnels will become partially flooded. Hence, for operation at low heat fluxes, one desires smaller A_{pt}. As shown in Fig. 5, for the small pores (d_p = 0.12 mm), smaller pore pitch has higher heat transfer coefficient for all heat fluxes.

Figure 7 shows the effect of pore pitch for 0.5-mm fin height (Tube 1378-0.5) with fixed pore diameter (d_p = 0.28 mm). The trends are the same as shown in Fig. 5 for 0.9-mm fin height. The smaller pore pitch has higher h-values at high heat flux, and has lower h-values at low heat flux. For the smallest pore pitch P_p = 0.75 mm, the DHF was not yet attained at the highest heat flux. However, its heat transfer coefficient is much lower than the other two surfaces at reduced heat fluxes. This is because the total open area for this combination is too large, and part of the tunnel is flooded at any heat flux. For smaller pore diameter (d_p = 0.12 mm), the heat transfer coefficient increases as the pore pitch decreases for all heat fluxes. Because the pore diameter d_p = 0.12 is small, decreasing the pore pitch improves the liquid supply and increases the heat transfer coefficient. At $q'' > 8$ kW/m^2, it is possible that the tunnels are nearly dry. In this case, evaporation does not occur inside the tunnel. The decrease of P_p may increase the number of nucleation sites and increases the external evaporation rate. This may explain the low heat transfer coefficient for the smallest pore diameters.

Figure 8 shows the boiling curves for 0.5-mm fin height (Tube 1378-0.5) with fixed pore diameter (d_p = 0.23 mm). As expected, the larger pore pitch yields higher heat transfer coefficient at low heat flux, and a smaller DHF.

Discussion

The previously presented data show that the liquid supply rate to the tunnel is established by the total open area. This is a function of the pore diameter and pore pitch. Consider, for example, use of 1.5-mm pore pitch. Figure 2 shows that the

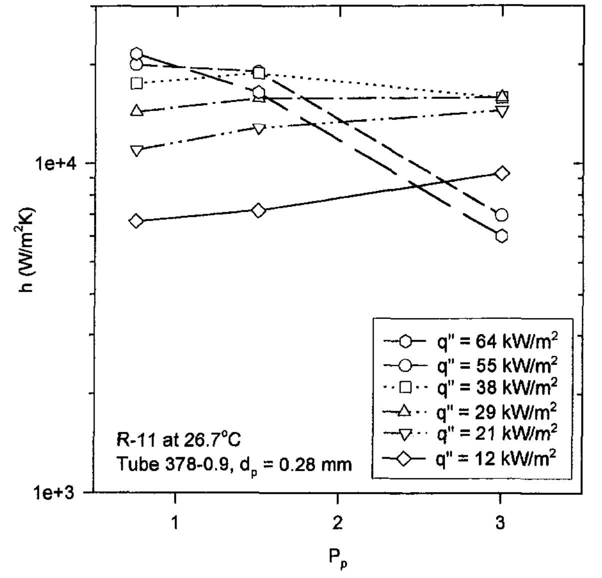

Fig. 6 Heat transfer coefficient (h) versus pore pitch (P_p) for fixed pore diameter (0.28 mm)

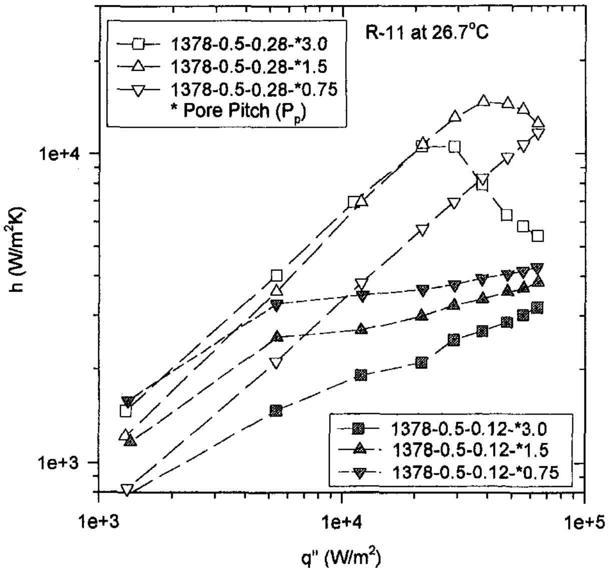

Fig. 8 Effect of pore pitch for fixed pore diameter (0.23 mm) on tube 1378-0.5

highest boiling coefficient is obtained by use of the largest pore diameter. However, a smaller pore diameter is preferred for low heat fluxes. The large pore diameter may result in too much liquid supply to the tunnel at low heat flux. This may result in a situation that will decrease the evaporation in the tunnel. Part of the tunnel may be flooded with liquid as shown in Fig. 9. Then, the evaporation area in the tunnel is reduced.

Figure 9 was sketched based on observations from Chien and Webb (1998b) visualization experiment, at low heat flux (5 kW/m^2). As shown in Fig. 9, all the tunnels are internally connected. At low heat flux, part of the tunnel was filled with liquid as shown by the darker region in Fig. 9. Oscillating liquid menisci were observed at the two ends of each vapor region. Bubbles emerged from the vapor-filled regions, and the liquid-filled regions were nonactive. The overall heat transfer coefficient decreases because the total evaporation area decreases.

The total open area (A_{pt}) acts to supply liquid to the tunnel. Because $A_{pt} \propto d_p^2/P_p$, the same A_{pt} may exist using closely spaced small pores, or widely spaced large pores. The effect of d_p and P_p are qualitatively explained in Fig. 10 for R-11 boiling on an integral-fin tube having 1378 fins/m and 0.9 mm fin height. Figure 10 was prepared to illustrate the separate and combined effects of pore pitch (P_p) and pore diameter (d_p). There are two families of curves in Fig. 10:

1 The solid lines are for fixed pore pitch (P_p = 1.5 mm) with increasing pore diameter (d_p). These curves are based on the same data shown in Fig. 2 for P_p = 1.5 mm for the 1378-0.9 tube.

2 The dashed lines show the effect of pore pitch ($0.75 \le P_p \le 4.0$ mm) for fixed pore diameter (d_p = 0.23 mm). Data were obtained only for the d_p = 0.23 mm, P_p = 1.5 and 3.0 mm cases. Based on the data in Figs. 4 to 8, the dashed lines are the authors qualitative estimates of the effect of pore pitch.

The salient features shown on Fig. 10 are as follows.

1 As shown by the solid curves for fixed P_p, the DHF increases as the pore diameter increases. A lower DHF occurs for the smaller pore diameters, because they cannot supply enough liquid to the tunnel at high heat flux. So, the smaller pores become dry and the DHF occurs at a lower heat flux. Conceivably, a higher DHF would be observed for $d_p > 0.28$ mm. However, the maximum possible pore diameter is limited by the fin pitch, 0.5 mm.

2 For fixed P_p and heat fluxes less than the DHF (e.g., 50 percent of the DHF), the heat transfer coefficient increases as d_p increases, except for the largest d_p (0.28 mm). The lower heat transfer coefficient for the largest d_p occurs because too much liquid is supplied to the tunnels. The tunnel becomes flooded in intermittent regions. Hence, there is an optimum pore diameter for operation at low-to-moderate heat flux.

3 For fixed d_p (0.23 mm), the DHF decreases as the P_p increases. This is because the tunnel needs greater liquid supply at the higher heat flux. However, the more widely spaced pores are unable to supply the liquid.

4 For low heat flux at fixed d_p (0.23 mm), increasing P_p causes the heat transfer coefficient to increase. At the lower heat flux condition, a smaller liquid supply to the tunnel will prevent tunnel flooding and result in thin liquid films in the tunnel.

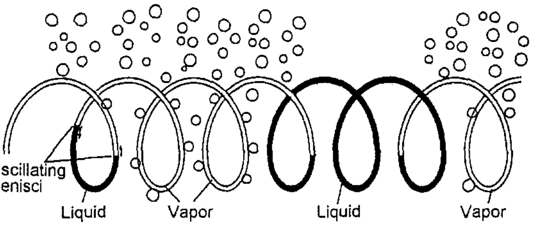

Fig. 9 Boiling mechanism for a horizontal tube at low heat flux

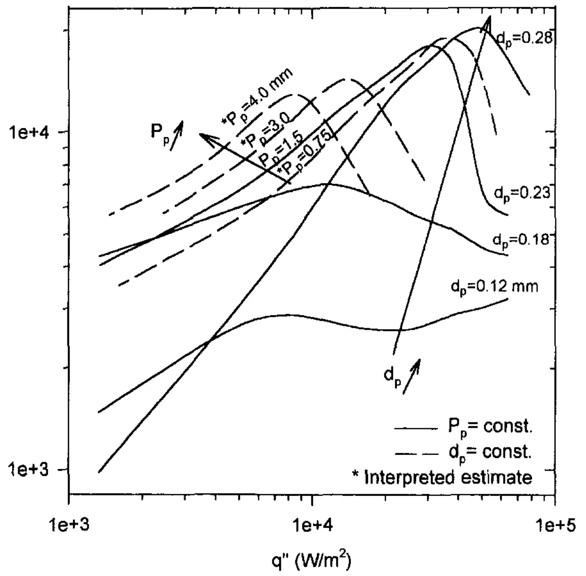

Fig. 10 Combined effect of pore diameter (d_p) and pore pitch (P_p)

At high heat flux, the boiling surface will benefit from increased pore size. However, at reduced heat flux, the same surface may experience liquid flooding in the tunnel. It is possible to optimize the surface performance for operation within a specific heat flux range (below the DHF). This is equivalent to being able to change the slope of the boiling curve.

The "total open area" (A_{pt}) is the parameter that defines the potential liquid supply rate. A larger A_{pt} is needed at higher heat flux than at lower heat flux. If the liquid supply rate exceeds the evaporation rate, the performance will be reduced, because of tunnel flooding. Hence, the preferred pore diameter and pitch depend on the design heat flux range. Although it may be possible to select a d_p and P_p combination that will show a high DHF, this would not be preferred if one desires to operate at a somewhat lower heat flux range. Use of increased pore pitch would yield higher performance at the lower heat flux condition.

The GEWA-TW and bent fin surfaces have continuous open gaps at the fin tips, as opposed to the surface pores of Turbo-B, Turbo-BII, Thermoexcel-E surfaces (described by Webb, 1994) and the present studied geometry. Although comparable data have not been taken on the "continuous fin gap" structures, the authors propose that the understanding developed for the "pored" surfaces can be extended to the "continuous fin gap" structures. The equivalence is found in the total open area, A_{pt}. For the continuous open gap structures, the total open area is given by

$$\frac{A_{pt}}{L} = s_g. \tag{3}$$

Webb (1972) found that the optimum fin gap for the bent fin surface is between 0.004 and 0.09 mm for R-11. Assuming the optimum design for the bent fin surface has the same total open area as for the pored surface, the optimum gap width (s_g) of bent fin can be found by setting Eq. (2) and Eq. (3) equal giving

$$s_g = \frac{\pi d_p^2}{4P_p}. \tag{4}$$

The present tests suggest that the optimum combination is d_p = 0.23 and P_p = 1.5 mm for the pored surface. Substituting these values for d_p and P_p in Eq. (4) yields s_g = 0.028 mm, which is within the range recommended by Webb (1972).

Conclusions

Based on our experimental data, the following conclusions are drawn:

1 The dry-out heat flux increases with the increase of total open area. For a given pore pitch, a higher dry out heat flux will be obtained using larger, rather than smaller, pore sizes.

2 At a certain reduced heat flux, part of the tunnel will become flooded and the performance will be reduced. Smaller pore size will inhibit flooding at reduced heat fluxes.

3 It is possible to select the preferred pore diameter and pore pitch for operation over a specific heat flux range.

4 The boiling coefficient is strongly controlled by the pore size at a given heat flux. The optimum pore diameter is $d_p \cong 0.23$ mm for 1378 fins/m tubes at $q'' < 30$ kW/m^2.

5 The boiling heat transfer rate decreases as the tunnel height reduces.

6 The relationship between the fin gap and pore diameter is defined in terms of the "total open area, A_{pt}."

Acknowledgment

This work was supported by a consortium of industrial companies. The consortium members are Wolverine Tube, Carrier Corp., The Trane Co., York International, Olin Brass Corp., UOP Corp., and Wieland-Werke AG. Special thanks is given to Wieland-Werke and Wolverine Tube companies for providing test sections used in this work.

References

Chien, L.-H., 1996, "Mechanism and Analysis of Nucleate Boiling on Structured Surfaces," Ph.D. dissertation, The Pennsylvania State University, University Park, PA.

Chien, L.-H., and Webb, R. L., 1998a, "Parametric Studies of Nucleate Pool Boiling on Structured Surfaces, Part I: Effect of Tunnel Dimensions," ASME JOURNAL OF HEAT TRANSFER, Vol. 120, pp. 1042–1048.

Chien, L.-H., and Webb, R. L., 1998b, "Visualization of Pool Boiling on Enhanced Surfaces," *Experimental Thermal and Fluid Science*, Vol. 16, pp. 332–341.

Chien, L.-H., and Webb, R. L., 1998c, "A Nucleate Boiling Model for Structured Enhanced Surfaces," *International Journal of Heat and Mass Transfer*, Vol. 41, No. 14, pp. 2183–2195.

Nakayama, W., Daikoku, T., Kuwahara, H., and Nakajima, T., 1980, "Dynamic Model of Enhanced Boiling Heat Transfer on Porous Surfaces, Part I: Experimental Investigation," ASME JOURNAL OF HEAT TRANSFER, Vol. 102, pp. 445–450.

Nakayama, W., Daikoku, T., and Nakajima, T., 1982, "Effects of Pore Diameters and System Pressure on Saturated Pool Nucleate Boiling Heat Transfer From Porous Surfaces," ASME JOURNAL OF HEAT TRANSFER, Vol. 104, pp. 286–291.

Webb, R. L., 1972, "Heat Transfer Surface Having a High Boiling Heat Transfer Coefficient," U.S. Patent 3,696,861 assigned to The Trane Company.

Webb, R. L., 1994, *Principles of Enhanced Heat Transfer*, Wiley Interscience, New York, Chapter 11.

Xin, M., and Chao, Y., 1985, "Analysis and Experiment of Boiling Heat Transfer on T-shaped Finned Surfaces," AIChE paper, 23rd National Heat Transfer Conference, Denver, CO.

Numerical Simulation of Combustion and Extinction of a Solid Cylinder in Low-Speed Cross Flow

Chin Tien Yang

J. S. T'ien
Professor of Engineering,
e-mail: jst2@po.cwru.edu,
Mem. ASME.

Department of Mechanical
and Aerospace Engineering,
Case Western Reserve University,
Cleveland, OH 44106-7222

The combustion and extinction behavior of a diffusion flame around a solid fuel cylinder (PMMA) in low-speed forced flow in zero gravity was studied numerically using a quasi-steady gas phase model. This model includes two-dimensional continuity, full Navier Stokes' momentum, energy, and species equations with a one-step overall chemical reaction and second-order finite-rate Arrhenius kinetics. Surface radiation and Arrhenius pyrolysis kinetics are included on the solid fuel surface description and a parameter Φ, representing the percentage of gas-phase conductive heat flux going into the solid, is introduced into the interfacial energy balance boundary condition to complete the description for the quasi-steady gas-phase system. The model was solved numerically using a body-fitted coordinate transformation and the SIMPLE algorithm. The effects of varying freestream velocity and Φ were studied. These parameters have a significant effect on the flame structure and extinction limits. Two flame modes were identified: envelope flame and wake flame. Two kinds of flammability limits were found: quenching at low-flow speeds due to radiative loss and blow-off at high flow speeds due to insufficient gas residence time. A flammability map was constructed showing the existence of maximum Φ above which the solid is not flammable at any freestream velocity.

1 Introduction

Combustion phenomena in a microgravity environment can be very different from those in normal gravity because of the absence of buoyancy. Research in the past decade has shown that in subbuoyant low-speed flows, a flame can behave qualitatively different from one in high-speed flows typically encountered in normal gravity (e.g., T'ien, 1986; Olson et al., 1988; Bhattacharjee and Altenkirch, 1990; Chen and Cheng, 1994; Grayson et al., 1994; Ferkul and T'ien, 1994). In low-speed flow, radiative loss becomes important since convection is reduced.

In addition to fundamental scientific interest, the flame behavior in low-speed flow can be important to spacecraft fire safety, especially for the combustion of solids. Most of the microgravity experiments on solid burning used thin specimen because of the limitations on microgravity test duration and the long thermal response time of a thick sample. However, the slow heat-up and conduction processes which occur inside a bulk solid introduces additional factors in characterizing material flammability (Fernandez-Pello, 1995). In this theoretical study, we use the combustion of two-dimensional solid cylinders in a forced flow to illustrate this complication.

To simplify the numerical simulation, instead of a single cylinder placed in an unbounded air stream, a column of identical cylinders with equal separation distance is placed perpendicular to the incoming flow. This way, we only have to solve for one cylinder with a domain of *finite* height (perpendicular to the flow).

There are a number of studies on droplet combustion in a convective flow (see Dwyer and Sanders, 1986, for example), but very limited work on a solid cylinder. The well-known experiment by Tsuji and Yamaoka (1967) used a porous cylinder with a gaseous fuel injected from the upstream half of the cylinder. Their measurements and subsequent theoretical studies by others focused, however, only on the forward stagnation-point part of the flame. One exception was the work by Chen and Weng (1990a), who solved the whole field around the porous cylinder and studied the wake flame and blowoff phenomena around the cylinder.

In the present work, the combustion and extinction phenomena of a solid fuel cylinder in a forced convective air stream is modeled. Although geometrically similar to the porous cylinder, there are several important differences in this work on solid fuel. First, the fuel burning rate is not controlled by the experimenter, as in Tsuji's experiment. The solid fuel burning rate is coupled to the heat feedback from the gas flame. Second, surface radiative loss is included in the model since we are interested in combustion behavior in low-speed flows. Third, we clarify an ambiguous point regarding the flammability limit for a thick solid by specifying an additional parameter (the percentage of gas conductive heat flux into solid) in the gas-solid interface energy balance equation. This will be elaborated in later sections.

Despite the differences, the gas-phase governing equations in the present work are similar to those by Chen and Weng. Consequently, their numerical scheme and computer program were adopted and modified for this problem.

2 Mathematical Model

2.1 The Question of Steady-State Burning. A solid cylinder burning in a cross flow will never reach a steady state. This is because of two reasons: The first is that as the solid burns, the cylinder/diameter shrinks with time. The second is related to the temperature profile inside the solid cylinder. Until the solid reaches a uniform temperature, its interior thermal profile continuously evolves with time. However, a quasi-steady

---

Contributed by the Heat Transfer Division for publication in the JOURNAL OF HEAT TRANSFER and presented at NHTC '97, Baltimore. Manuscript received by the Heat Transfer Division, Oct. 6, 1997; revision received, Mar. 30, 1998. Keywords: Combustion, Cylinder, Flame, Heat Transfer, Microgravity. Associate Technical Editor: P. Menguc.

state can often be established in the gas phase if relevant parameters are in the proper ranges. These are detailed in the next section.

2.2 Quasi-Steady State Gas Phase Approximation. Although quasi-steady gas phase may seem to be obvious in the burning of a solid, the low-speed flow complicates the situation since it lengthens the gas-phase time scale. In this section, several relevant time scales will be estimated to establish the approximation of quasi-steady gas phase. The gas residence time in the neighborhood of the cylinder can be estimated by $2R/U_\infty$, where U_∞ is the free-stream gas velocity and R the radius of the cylinder. The gas residence time in the whole flame zone is l_f/U_∞, where l_f is the flame length. The gas diffusion time across the flame is δ^2/D, where δ is the flame standoff distance or flame thickness and D is an average diffusion coefficient. If we use the forward stagnation-point flow to estimate δ then the diffusion time is δ/U_∞. For a reasonable large solid cylinder (thermally thick), we expect $2R > \delta$ and therefore gas residence time is greater than the diffusion time. Comparing the two residence times, it is found that although $l_f/U_\infty > 2R/U_\infty$ when $l_f > 2R$, the longest time is when $l_f < 2R$ at minimum U_∞, given by $2R/U_\infty$. For the sample cylinder used in this computation, $R = 0.95$ cm and the minimum U_∞ is 0.8 cm/s (below this value the flame is quenched) and this gives a gas residence time of less than three seconds.

The rate of shrinkage of a cylinder radius is estimated based on the available experimental data (T'ien et al., 1978). The linear burning rate of PMMA is approximately 4.7×10^{-3} cm/s for the fastest burning condition examined in this work. Thus, within one gas-phase time scale, the cylinder radius shrinks less than 0.014 cm. For a cylinder radius of 0.95 cm, used in our present calculation, the percentage of radius shrinkage in one gas-phase time is less than 1.5 percent (a very conservative estimate). Thus, in the gas-phase analysis the radius can be approximated as a constant.

The rate of variation of the temperature profile in the solid, especially the rate of change of the surface temperature gradient, will depend on the process that drives the unsteady change. The most common and perhaps the most important situation is related to the solid conduction and heat-up processes. For example, when the solid cylinder is ignited, the subsurface solid temperature gradient is relatively steep and only a portion of the surface layer is heated up. As time progresses, the temperature wave reaches the center and the whole cylinder begins to heat up. The time constant for the surface gradient variation can be estimated by δ_s^2/α_s, where α_s is the thermal diffusivity of the solid and δ_s is the surface layer thickness that the solid temperature has penetrated. Clearly, this timescale can be very small if δ_s approaches zero. But as we shall see later, the solid is not flammable in such a situation. For $R = 0.95$ cm (used in the present calculation) and $\delta_s/R = 20$ percent (i.e., thermal wave reaches a surface layer of $\frac{1}{5}$ of the cylinder radius), the solid thermal time is 30 seconds, one order of magnitude greater than the gas-phase time. Indeed, experiments performed in low gravity show a relatively long period of ignition delay time in low-speed flow (Goldmeer, 1996). After ignition, the surface gradient will change more slowly as δ_s increases. When $\delta_s \rightarrow R$, the solid time approaches 700 seconds.

As a result of these estimates, a quasi-steady gas-phase approximation is employed in our model. The quasi-steady model requires the specification of cylinder radius and the solid boundary conditions. In this work, a cylinder radius is fixed at 0.95 cm and the ratio of the conductive heat flux from the gas phase to the conductive heat flux into the solid (Φ) will be specified and treated as a parameter in the boundary condition. For brevity, this parameter will be referred to as "the percentage of heat flux into solid." The derivation of this term will be given in the interfacial boundary condition. Note that in a fully coupled problem with a transient solid, the magnitude of Φ can be computed as a function of time. However, the results of the unsteady computations are restricted by the specific transient process. For example, an unsteady computation has been performed for a depressurization transient proposed for the space station fire fighting scenario (Goldmeer, 1996). Treating Φ as a parameter, while losing the specifics, does provide a broader appreciation of the energy coupling at the solid-gas interface on gas flame behavior.

2.3 Assumptions. In addition to the quasi-steady gas phase, several assumptions were made to make this problem tractable. The assumptions are as follows:

- The cross-section of the fuel cylinder is circular.
- Prandtl number and Lewis number are set to be constants (equal to 0.7 and 1.0, respectively).
- Viscosity is assumed to be proportional to temperature to the power of 0.75.
- C_p is assumed to be a constant. Mass diffusivity is assumed to be proportional to the temperature to the power of 1.75. Thermal conductivity is assumed to be proportional to temperature to the power of 0.75.

Nomenclature

B = frequency factor in gas-phase combustion process
b = pre-exponential factor of pyrolysis process
C_p = constant-pressure specific heat of gas
C_s = specific heat of solid fuel
D = diffusion coefficient
Da = Damkohler number
E = activation energy in gas-phase combustion process
E_s = activation energy in pyrolysis process
f = stoichiometric oxidizer/fuel mass ratio
L = latent heat in pyrolysis process
$\dot{m}$ = fuel mass burning rate
P = pressure
Q = heat of combustion per unit mass of fuel
Q_R = surface radiation heat loss per unit area per unit time
R = cylinder radius
R^o = universal gas constant
S = surface radiation loss parameter
T = temperature
u = velocity in the x-direction
U_∞ = freestream velocity
v = velocity in the y-direction
v_n = velocity normal to cylinder surface
$\dot{w}_f$ = reaction rate of fuel
x = distance along the x-direction
y = distance along the y-direction
Y_i = mass fraction of species i

Greek

ϵ = solid emissivity
Φ = ratio of conductive heat flux going into the solid to that from the gas phase at the solid surface
λ = coefficient of heat conduction
μ = viscosity
ρ = density
σ = Stefan Boltzmann constant

Superscript

$*$ = reference state

Subscript

f = fuel
in = in-flow position
n = outward normal to the cylinder
o = oxidizer
out = out-flow position
s = surface of the cylinder
t = tangential to the cylinder
∞ = ambient

- One-step overall chemical reaction and second-order finite rate Arrhenius kinetics are assumed for the gas-phase chemical reaction.
- Flow is two-dimensional and laminar at zero gravity. Ideal gas law is applied.
- Gas phase radiation is neglected. The consequence of this simplification will be discussed in the Conclusion.
- Zeroth-order Arrhenius pyrolysis law is applied to the solid surface.

2.4 Flow and Cylinder Configuration. A column of identical, infinitely long solid-fuel cylinders at equal distance between their neighbors are placed in a cross flow with upstream velocity U_∞. The upstream flow is perpendicular to the column. Since the cylinders are of the same radius, the burning of this column of cylinders is reduced to the study of one unit as shown in Fig. 1 with proper symmetric boundary conditions. In the present work, the cylinder radius is assumed to be 0.95 cm and the separation distance between neighboring cylinders is eight times that of this radius (7.6 cm.)

2.5 Governing Equations. The dimensional governing equations and boundary conditions are listed as follows:

Continuity Equation.

$$\frac{\partial(\rho u)}{\partial x} + \frac{\partial(\rho v)}{\partial y} = 0$$

x-Momentum Equation.

$$\rho u \frac{\partial u}{\partial x} + \rho v \frac{\partial u}{\partial y} = -\frac{\partial P}{\partial x} + \frac{\partial}{\partial y}\left[\mu\left(\frac{\partial u}{\partial y} + \frac{\partial v}{\partial x}\right)\right] + \frac{\partial}{\partial x}\left\{\mu\left[2\frac{\partial u}{\partial x} - \frac{2}{3}\left(\frac{\partial u}{\partial x} + \frac{\partial v}{\partial y}\right)\right]\right\}$$

y-Momentum Equation.

$$\rho u \frac{\partial v}{\partial x} + \rho v \frac{\partial v}{\partial y} = -\frac{\partial P}{\partial y} + \frac{\partial}{\partial x}\left[\mu\left(\frac{\partial u}{\partial y} + \frac{\partial v}{\partial x}\right)\right] + \frac{\partial}{\partial y}\left\{\mu\left[2\frac{\partial v}{\partial y} - \frac{2}{3}\left(\frac{\partial u}{\partial x} + \frac{\partial v}{\partial y}\right)\right]\right\}$$

Energy Equation.

$$\left(\rho u \frac{\partial T}{\partial x} + \rho v \frac{\partial T}{\partial y}\right) C_p = \left[\frac{\partial}{\partial x}\left(\lambda_g \frac{\partial T}{\partial x}\right) + \frac{\partial}{\partial y}\left(\lambda_g \frac{\partial T}{\partial y}\right)\right] - Q\dot{w}_f$$

where Q represents the heat of combustion per unit mass of fuel, and $\dot{w}_f$ is the fuel reaction rate given by Arrhenius kinetics and is assumed to be of second order (first order with respect to fuel and oxygen, respectively).

$$\dot{w}_f = -BT\rho^2(Y_f)(Y_o)\exp(-E/R^oT)$$

where B represents the pre-exponential factor and E represents the activation energy.

Fuel Species Equation.

$$\rho u \frac{\partial Y_f}{\partial x} + \rho v \frac{\partial Y_f}{\partial y} = \frac{\partial}{\partial x}\left(\rho D \frac{\partial Y_f}{\partial x}\right) + \frac{\partial}{\partial y}\left(\rho D \frac{\partial Y_f}{\partial y}\right) + \dot{w}_f$$

Oxidizer Species Equation.

$$\rho u \frac{\partial Y_o}{\partial x} + \rho v \frac{\partial Y_o}{\partial y} = \frac{\partial}{\partial x}\left(\rho D \frac{\partial Y_o}{\partial x}\right) + \frac{\partial}{\partial y}\left(\rho D \frac{\partial Y_o}{\partial y}\right) + f\dot{w}_f$$

where f is the stoichiometric oxidizer/fuel mass ratio.

Equation of State.

$$\rho = P/R^oT$$

Viscosity Variation With Temperature.

$$\mu = \mu^*(T/T^*)^{0.75}$$

Boundary Conditions.

When $x = x_{\text{in}}$ (upstream)

$$u = U_\infty, \quad v = 0, \quad T = T_\infty, \quad Y_f = 0, \quad Yo = Yo_\infty.$$

When $x = x_{\text{out}}$ (downstream)

$$\frac{\partial u}{\partial x} = \frac{\partial v}{\partial x} = 0, \quad \frac{\partial T}{\partial x} = \frac{\partial Y_f}{\partial x} = \frac{\partial Y_o}{\partial x} = 0.$$

When $y = y_{\text{top}}$ (top of the domain)

$$\frac{\partial u}{\partial y} = 0, \quad v = 0, \quad \frac{\partial T}{\partial y} = \frac{\partial Y_f}{\partial y} = \frac{\partial Y_o}{\partial y} = 0.$$

When $y = 0$, $x_{\text{in}} \le x < -R$ or $R < x \le x_{\text{out}}$ (symmetry line)

$$\frac{\partial u}{\partial y} = 0, \quad v = 0, \quad \frac{\partial T}{\partial y} = \frac{\partial Y_f}{\partial y} = \frac{\partial Y_o}{\partial y} = 0.$$

When $\sqrt{x^2 + y^2} = R$ (on the cylinder)

$$v_t = 0, \quad v_n = \frac{\dot{m}}{\rho_w}$$

$$\dot{m}Y_f = \dot{m} + \rho D \left.\frac{\partial Y_f}{\partial n}\right|_g$$

$$\dot{m}Y_o = \rho D \left.\frac{\partial Y_o}{\partial n}\right|_g$$

$$(\lambda_g)\left.\frac{\partial T}{\partial n}\right|_g = (\lambda_s)\left.\frac{\partial T}{\partial n}\right|_s + \dot{m}L + Q_R$$

where $(\lambda_s)(\partial T/\partial n)|_s$ is the heat flux into the solid and $(\lambda_g)(\partial T/\partial n)|_g$ is the heat flux from the gas phase. The solid to gas phase heat flux ratio is the percentage of gas phase heat flux into the solid (called percentage of heat flux into solid, Φ). That is

$$\Phi = (\lambda_s)\left.\frac{\partial T}{\partial n}\right|_s \Big/ (\lambda_g)\left.\frac{\partial T}{\partial n}\right|_g.$$

This ratio will be treated as a parameter in our model. Note that the portion of gas phase heat flux not going into the solid is used to pyrolyze the solid (latent heat) or is re-radiated.

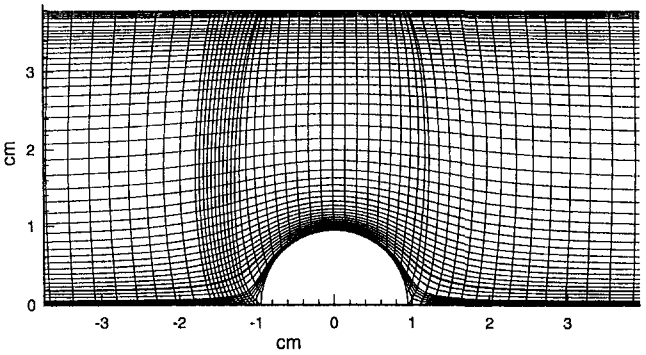

Fig. 1 The grid distribution near the cylinder (radius = 0.95 cm)

Table 1 Numerical values used

Gas Phase			Solid Phase		
Symbol	Value	Unit	Symbol	Value	Unit
R	0.95	cm	b	1.966E+6	cm/s
U_∞	parameter	cm/s	σ	5.695E-12	J/cm^2 K^4 s
T^*	1350	K	λ_s	2.09E-3	J/cm s
C_p	1.254	J/gK	C_s	1.463	J/gK
E	113000	J/mole	L	1050	J/g
B	1.43E+8	cm^3/g sK	ϵ	0.9	N/A
Q	25957	J/g	ρ_s	1.18	g/cm^3
R^o	8.313	J/mole K	E_s	125600	J/mole
ρ^*	2.61E-4	g/cm^3			
μ^*	5.716E-4	g/cm s			
λg^*	6.02E-4	J/cm s K			

Script "s" is the solid phase on the boundary and "g" is the gas phase. In the above equations, subscript "n" is the unit vector normal to the cylinder surface and is positive into the gas. "$\dot{m}$," the fuel burning rate, is related to surface temperature T_s by the Arrhenius law: $\dot{m} = b\rho_s \exp(-E_s/R^oT_s)$ where "b" is the pre-exponential factor of pyrolysis process and "E_s" is the activation energy in the solid pyrolysis process. Assuming a grey body in a nonparticipating medium, the solid surface radiative heat loss, Q_R, is defined as $Q_R = \epsilon\sigma(T_s^4 - T_\infty^4)$, where ϵ is the surface emissivity. Radiation for neighboring cylinders has been neglected. The maximum error which occurs at the shoulder region ($\theta = 90°$) is 16 percent.

The above set of differential equations and boundary conditions is first nondimensionalized (see Yang, 1994, for details) and then solved numerically. The two nondimensional parameters, Damkohler number, Da, and surface radiation loss parameter, S, that will be used in the discussion of results are defined here:

$$\mathrm{Da} = \rho^* B T^* \exp(-E/R^oT^*)/(U_\infty/R)$$

$$S = \epsilon\sigma T_s^{*4}/C_p T^* \rho^* U_\infty .$$

It should be noted that both of these two parameters are inversely proportional to the freestream velocity U_∞. The Damkohler number decreases when U_∞ increases and the surface radiation loss parameter increases when U_∞ decreases.

3 Numerical Scheme

The computer program developed by Chen and Weng (1990a, b) was adopted and modified for this problem. Grid distribution is selected utilizing the grid generation technique developed in Thomas and Middecoff (1980). A body-fitted coordinate system is used to transform the physical domain (Fig. 1) into a rectangular computational domain with uniform meshes (140 × 55 grids are used). With transformed equations and boundary conditions, this problem is solved using the SIMPLE algorithm (Patankar, 1980).

Validation of the numerical code was originally performed in Chen and Wang (1990b) where detailed comparison with experimental results have been made in nonreacting low Reynolds number flow around cylinders. Validation has also been made with Tsuji's porous cylinder burner in the combustion case (Chen and Wang, 1990a). In the present application of the same numerical code, care has been taken to make certain that there is enough grid points within the smallest physical scale to capture the essential physics.

Figure 1 shows the grid distribution near the cylinder surface in the physical domain. The grids are most dense near the cylinder surface and stagnation point region where the flame standoff distance is the smallest. Grids expand both in the downstream and upstream directions so that the boundary conditions are specified far enough from the cylinder and the flame to simulate infinity.

In the present computation, the incoming flow is air ($Y_{o\infty} = 0.23$) at one atmospheric pressure and the solid emissivity is 0.9. The separation distance between adjacent cylinders (from center to center) is fixed at 7.6 cm and cylinder radius at 0.95 cm so that $y_{\mathrm{top}} = 3.8$ cm and $y_{\mathrm{top}}/R = 4$. The property data are listed in Table 1 and are taken from Foutch and T'ien (1987).

4 Results

In this series of computations, freestream velocity and the percentage of heat flux into solid, Φ, are used as parameters. Figure 2 shows the flammability map. The flammability boundary is divided into a quenching and a blowoff branch. Within the flammable domain, two types of flames are identified: envelope flame and wake flame. To illustrate the differences between these two flames, some selected flame structures for two representative cases will be shown next.

Envelope Flame. Figure 3 shows the fuel vapor reaction rate contours w_f, the nondimensional temperature distribution, and the velocity vectors for an envelope flame ($U_\infty = 10$ cm/s and $\Phi = 0.3$). In models using one-step global reaction, the fuel reaction rate contours give the best indication of the flame shape. Based on our previous comparison (Grayson et al., 1994), we take $\dot{w}_f = 10^{-4}$ g/cm^{3}s as the contour of the visible blue flame. As can be seen in Fig. 3(a), the flame starts in the upstream, wraps around the cylinder, and becomes elongated in the downstream direction. Figure 3(b) shows the nondimensional temperature distributions ($T = 1$ is 1350 K) and their relative position with respect to the reaction zone. Figure 3(c)

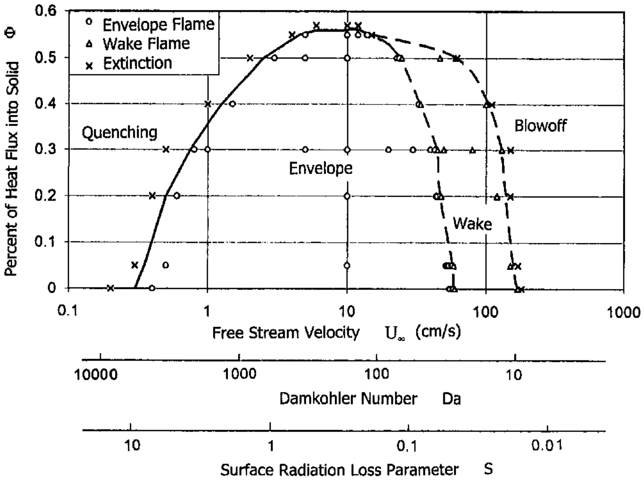

Fig. 2 Flammability map at 1.0 atm

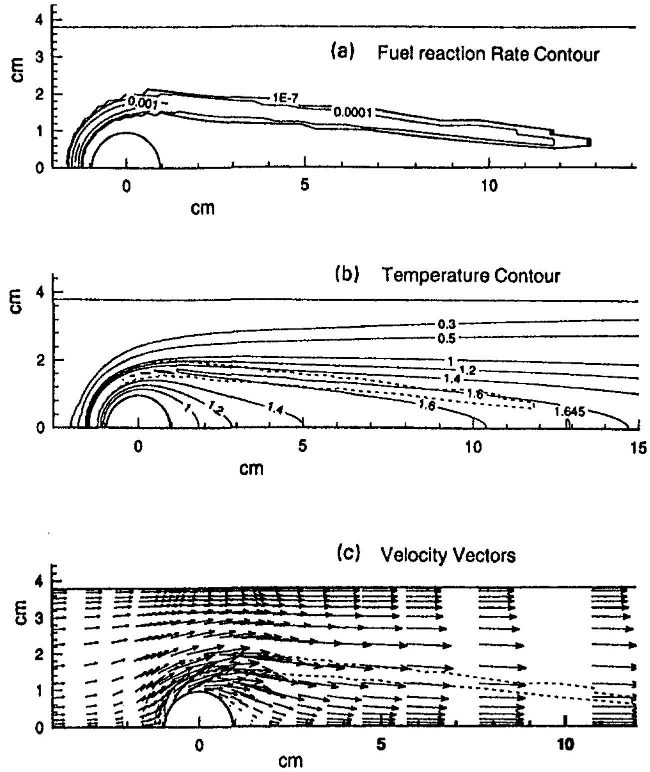

Fig. 3 Envelope flame at 10 cm/s, Φ = 30 percent, and p = 1 atm. (*a*) fuel reaction rate contour, (*b*) nondimensional temperature (T = 1 corresponds to 1350 K), (*c*) velocity vector. Dash lines in (*b*) and (*c*) are $\dot{w}_f = 10^{-4}$ g/cm^{3}s.

shows that the velocity increases downstream due to heat release (thermal expansion). It appears that the closeness of the cylinders ($y_{\text{top}}/R = 4$) promotes this velocity acceleration which makes the flame longer. However, we did not vary the cylinder separation distance to quantify this influence.

Figure 4 presents the surface temperature, local burning rate, gas-phase heat flux, and surface radiative flux along the cylinder surface as a function of angle θ (zero degree is along the forward stagnation streamline) for the above case. The surface temperature is highest at $\theta = 0°$ (715 K) and it decreases toward downstream gradually until at about $\theta = 100°$, after which the rate of surface temperature decrease accelerates and at $\theta = 180°$, $T_w = 615$ K. The local burning rate shows a similar trend, but with more drastic variation. In the wake zone ($\theta > 140°$), the burning rate is only about five percent of that at the forward stagnation point region. This drastic reduction is the consequence of the gas temperature distribution in the rear part of the cylinder (see Fig. 3(*b*)). Figure 4(*b*) shows the large decrease in the surface heat flux from the gas phase as θ increases. This, plus the nearly constant surface radiative loss, results in a large drop of net heat flux reaching the surface in the wake region, hence the local burning rate decrease. This large burning rate difference between the front and the rear parts of the cylinder has been observed experimentally in Rees (1981) albeit in a higher speed mixed forced and buoyant flow.

Wake Flame. Figure 5 gives the corresponding features for a wake flame (U_∞ = 45 cm/s, Φ = 0.3). Figure 5(*a*) shows that, in this case, the reaction zone only exists downstream of the cylinder. The fuel reaction rate contour is I-shaped (due to symmetry, only one-half is shown). The temperature distribution in this case is drastically different from that in the envelope flame, as shown in Fig. 4(*b*). The velocity plot in Fig. 4(*c*) shows the existence of a low-speed long recirculation zone.

Because the reaction and the high-temperature zones exist only downstream of the fuel cylinder, only the rear portion of the cylinder surface is heated to a high temperature and significant solid pyrolysis occurs only in the region $\theta > 130°$ as shown in Fig. 6(*a*). Figure 6(*b*) gives the gas-phase heat flux and radiative flux levels on the surface. It should be noted that the wake flame behind a pyrolyzing solid is qualitatively different from that predicted by Chen and Weng (1990a) for the porous cylinder. In the latter case, the gaseous fuel is ejected from the front half of the cylinder. The flame anchors itself near the flow separation point near the surface and the reaction zone spreads downstream much like a stabilized premixed flame behind a bluff body. In the present case, the needed coupling between the flame and the solid dictates that the reaction zone stays close to the surface in the flow-reversal zone. This type of wake flame is relatively short and has been observed experimentally in low-pressure burning of a PMMA cylinder in buoyant normal gravity conditions (Goldmeer, 1996). We are not aware of any experimental data in purely forced flow in this velocity range.

Another observation from this calculation concerns the length of the flow reversal zone behind the cylinder. Figure 5(*c*) shows a long reversal zone, extending to x = 4.5 cm (the ratio of the reversal zone length to cylinder diameter is 1.87). While in both the porous cylinder case (Chen and Weng, 1990a) and the envelope flame case (Fig. 3(*c*)), the reversal zone length is short,—less than the cylinder diameter. It appears that the presence of the flame immediately behind the cylinder modifies the pressure distribution and causes this elongation of the flow-reversal zone. It should also be noted that the flow-reversal zone in a burning solid is not a *closed* recirculation bubble, such as that behind an inert cylinder. This is because a burning solid always adds mass into the region.

Effect of Freestream Velocity and Φ. To illustrate the evolution of the envelope and wake flames and the ways they approach extinction, we plot the contour of $\dot{w}_f = 10^{-4}$ g/cm^{3}s as a function of freestream velocity at Φ = 0.3 in Fig. 7. Starting at U_∞ = 30 cm/s, we have a very long flame (indicating the

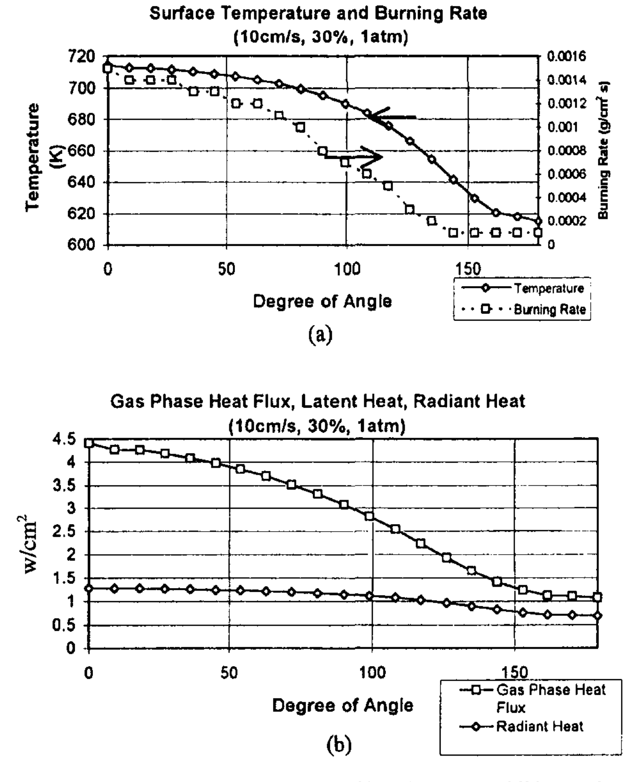

Fig. 4(*a*) Surface temperature and local burning rate and (*b*) gas-phase heat flux and surface radiative heat flux as a function of angle along the solid cylinder surface. U_∞ = 10 cm/s, Φ = 0.3, 1 atm.

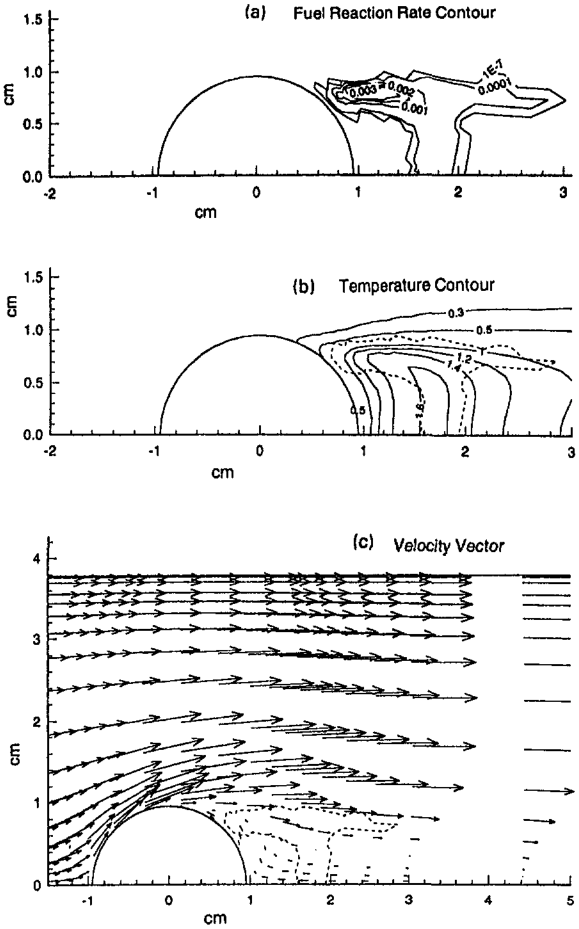

Fig. 5 Wake flame at 45 cm/s, $\Phi = 30$ percent, and $p = 1$ atm. (*a*) fuel reaction rate contour, (*b*) nondimensional temperature, (*c*) velocity vector. Dash lines in (*b*) and (*c*) are $\dot{w}_f = 10^{-4}$ g/cm^{3}s.

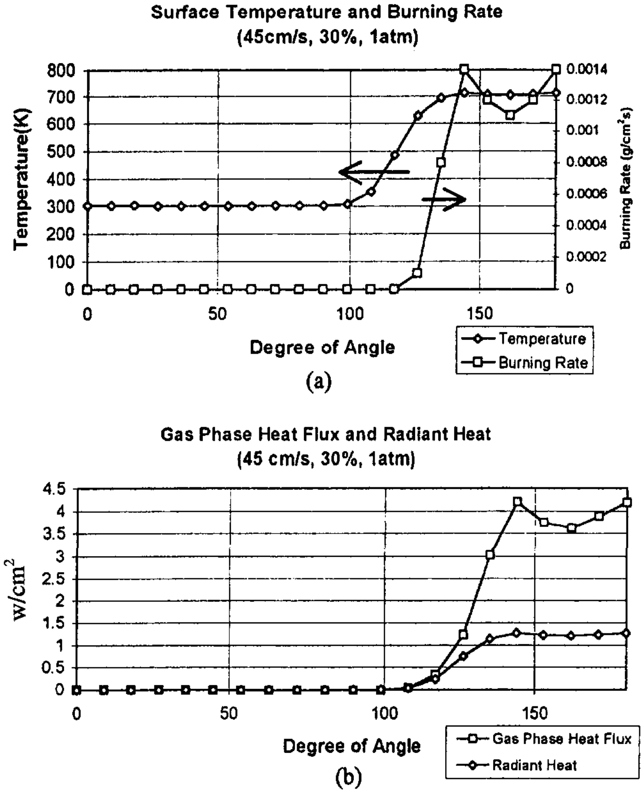

Fig. 6(*a*) Surface temperature and local burning rate and (*b*) gas-phase heat flux and surface radiative heat flux as a function of angle along the solid cylinder surface. U_∞ = 45 cm/s, Φ = 0.3, 1 atm.

shape of visible flame). As we decrease the free-stream velocity, the flame becomes shorter. When U_∞ = 0.8 cm/s, flame exists only near the forward stagnation region. At a further decrease of U_∞ to 0.5 cm/s the flame goes out. This extinction mode, at the low-velocity limit, is the result of radiative loss and is referred to as quenching. This is similar to those found previously in other flame geometries (T'ien, 1986; Olson et al., 1988; Bhattacharjee and Altenkirch, 1990; Chen and Cheng, 1994; Grayson et al., 1994; Ferkul and T'ien, 1994), but this is the first work for a blunt body. Note from Figs. 7 and 8 that the flame standoff distance at the forward stagnation point (defined as the distance from the maximum flame temperature location to the solid surface) increases drastically at low-flow velocities. This increase decreases the conduction heat feedback, hence the solid burning rate. Therefore the percentage of radiative heat loss to heat generation increases at low speed, which causes the quenching. This trend can be seen more analytically by examining the surface radiation loss parameter S, which is plotted in Fig. 2 (using $T_s^* = 700$ K). S, as defined, is the ratio between the rate of surface radiative loss to the rate of heat convection. In the forward stagnation zone, convection balances conduction for a stabilized flame (Peclet number is of the order unity). So, S is also the ratio of the rate of surface radiative loss to the rate of heat conduction from the flame to the solid. Decreasing U_∞ increases S, which amplifies the influence of radiative loss relative to the rate of combustion heat generation.

As U_∞ increases from 30 cm/s to 40 cm/s, the flame length increases but the flame is pushed very close to the surface at the forward stagnation point. Between 40 to 45 cm/s, a local flame blowoff occurs, the flame can no longer be stabilized in the upstream region of the cylinder and a wake flame is established. Further increase of U_∞ (e.g., at 80 cm/s) does not appreciably increase the wake flame length. Instead, a portion of the reaction zone comes closer to the rear surface of the cylinder

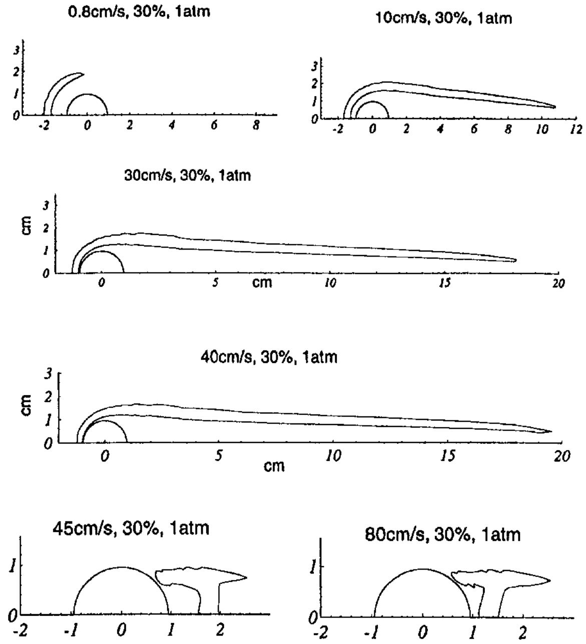

Fig. 7 Visible flame zone ($\dot{w}_f = 10^{-4}$ g/cm^{3}s): effect of freestream velocity (Φ = 30 percent, 1 atm). Flame quenches at U_∞ = 0.5 cm/s and total blowoffs at 150 cm/s.

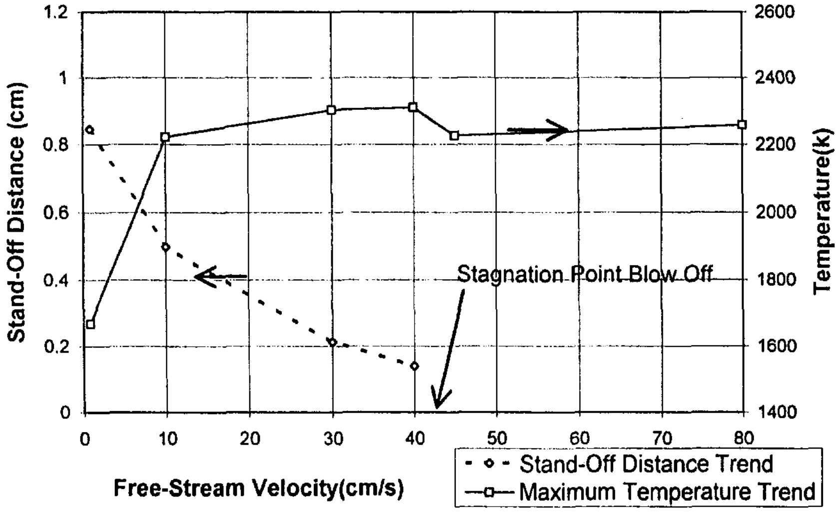

Fig. 8 Flame standoff distance at the forward stagnation region and maximum flame temperature as a function of freestream velocity. Φ = 0.3 and 1 atm.

as a result of increased reverse velocity in the recirculation region. Wake flame is blown off when U_∞ is above 150 cm/s.

Local flame blowoff in the front part of the cylinder can be a stagnation-point extinction phenomena. In classical theory the latter is analyzed with Damkohler number in which the flow parameter is the stretch or strain rate. The Damkohler number defined in this paper is consistent with the stagnation-point Damkohler number since the stretch rate at the forward stagnation point for a cylinder is $2U_\infty/R$. Damkohler number is plotted in Fig. 2 to show that for a given Φ there is a minimum Da below which an envelope flame can no longer exist. We note that the critical Damkohler number dividing the envelope flame and the wake flame is not only a function of Φ but may also have a weak dependence on the radiative loss (especially in the low velocity region, see T'ien, 1986). It should also be pointed out that the value of Da plotted in Fig. 2 depends on the choice of the temperature T^* used. In this calculation $T^* = 1350$ K. A different choice of T^* may shift the absolute magnitude of Da but its dependence on U_∞ is the same.

To further verify the connection between the envelope flame/wake flame boundary and the stagnation-point extinction, we compare our results with those from Foutch and T'ien (1987) where the same physical/chemical properties were used, except for the value of the surface radiation emissivity ϵ.

In their steady burning problem in air, the extinction stretch rate was 80 1/s with $\epsilon = 1$ and $\Phi = 0.23$. In the present work, the transition stretch rate is 90 1/s with $\epsilon = 0.9$ and $\Phi = 0.25$. The agreement between the two pieces of work appears to be very good.

Figure 8 presents both the flame standoff distance in the forward stagnation region and the maximum flame temperature as a function of freestream velocity for the cases shown in Fig. 7. Flame standoff distance decreases monotonically when velocity increases until local flame blowoff at $U_\infty = 42$ cm/s. The maximum flame temperatures, however, are approximately constant (varying between 2200 K and 2300 K) when the freestream velocities are greater than 10 cm/s. It should be noted that the locations of maximum flame temperature can shift with freestream velocities. But these rather high and fair constant temperatures suggest that both the flame blowoffs at the forward stagnation region and in the wake are flame stabilization phenomena related to the insufficient flow residence time in their particular stabilization zone. On the other hand, when the freestream velocity is less than 10 cm/s, the flame temperature drops significantly in spite of long residence times (small velocity and larger standoff distance). Radiative loss becomes a significant portion of the total combustion heat release in this low-speed region which decreases the flame temperature and eventually quenches the flame. Consistent with the large flame standoff distance, computed results indeed show a quick drop of the solid burning rate in this very low-speed regime (Yang, 1994).

Figure 9 gives the evolution of flame shape at $U_\infty = 10$ cm/s when the percentage of gas conductive flux to solid, Φ, is varying. $\Phi = 0$ (solid interior temperature is uniform) has the longest flame. As Φ decreases, the flame lengths decrease monotonically. The flame goes out when Φ is above 0.57. Note that from Fig. 2, at higher freestream velocities, it is possible to have a wake flame-envelope flame transition when Φ decreases.

Flammability Limit. Figure 2 clearly shows that for a given freestream velocity there exists a maximum Φ above which the solid is not flammable. Basically too much of the

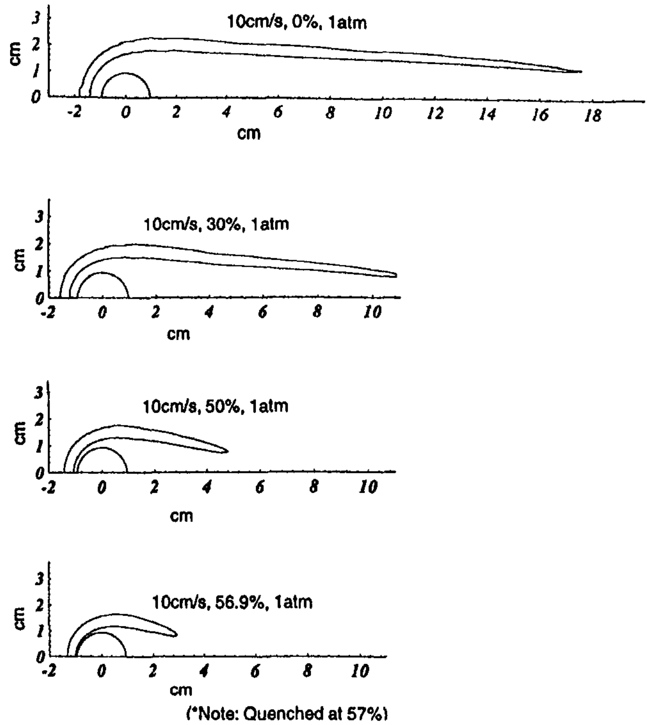

Fig. 9 Visible flame zone ($\dot{w}_f = 10^{-4}$ g/cm^{3}s): effect of Φ, percentage of heat conductive flux into solid. $U_\infty = 10$ cm/s, 1 atm.

gas-phase heat flux goes into the solid interior for the fuel to make the solid nonflammable. This is, of course, consistent with our laboratory experience: We need to apply the ignition source for sufficiently long periods of time to a thick solid to establish a self-sustained flame. That is, a solid surface layer needs to be heated sufficiently so that Φ is below this limiting value. With the inclusion of surface radiative loss Fig. 2 shows that there is a critical Φ above which we cannot have a flame for *any freestream velocities.* In Fig. 2 this occurs at $U_\infty \approx 10$ cm/s, and the limiting value for Φ is around 0.57. In the sense of having the maximum flammable Φ, 10 cm/s is the most flammable velocity for the present solid.

In the burning of a thick solid, Φ may change continuously with time. Typically, Φ may start at a higher value at ignition and decrease its magnitude as the temperature profile propagates further into the solid interior. Therefore, as time goes on the solid becomes more flammable in the sense that the gas flame travels more and more into the flammable domain and away from the flammability boundary. It is clear that from Fig. 2, even at a given environmental and flow condition, the flammability limit of a thick solid cannot be rigorously defined unless Φ, the percentage of gas conductive flux into the solid, is specified. The most flammable condition for a given flow velocity is at $\Phi = 0$, i.e., the solid has been heated up uniformly to the pyrolysis surface temperature. It is also clear that we cannot equate ignitability (which normally occurs for $\Phi > 0$) to flammability (which *can* occur at $\Phi = 0$).

5 Conclusion

Combustion and extinction of a two-dimensional circular solid cylinder in a forced laminar cross flow in zero gravity is modeled and solved. The gas-phase model consists of steady Navier-Stokes' momentum, energy and species equations with a one-step finite rate Arrhenius chemical kinetics. On the solid surface, radiative loss is included in the interfacial energy balance and a nondimensional surface parameter Φ, the ratio of conductive heat flux into the solid to that from the gas phase, is specified in order to complete the description for the quasi-steady gas-phase system.

Numerical solutions started with a body-fitted mapping scheme which transformed the gas domain into a rectangular one. The transformed equations were then solved using the SIMPLE algorithm.

Two parameters in this program were systematically varied and their effects on flame and extinction were investigated. These two parameters were freestream velocity and the percentage of heat flux into the solid. Two types of flames were identified: envelope flame in which the reaction starts upstream at the forward stagnation-point region and the wake flame in which reaction is restricted to the wake zone only. Two types of extinction limits were observed: quenching due to radiative loss and blowoff due to insufficient gas residence time.

Starting with an envelope flame, as freestream velocity decreases, the flame length shrinks until it exists only in the forward stagnation-point region before quench extinction occurs. As freestream velocity increases, the envelope flame length increases until a local flame blowoff occurs at the forward stagnation-point region. This results in a transition to a wake flame. This abrupt transition produces a much shorter flame and a much smaller solid cylinder burning rate. Further increases of freestream velocity produce little change in flame length until finally a total flame blowoff is reached.

The velocity ranges where envelope and wake flames exist depend strongly on the percentage of heat flux going into the solid. The flammable range shrinks as the percentage of heat flux into the solid increases and there is a maximum value of this parameter above which the solid is nonflammable at any flow velocity. For the properties used in this computation, the most flammable flame occurs at a freestream velocity of approximately 10 cm/s, which is below the buoyancy-induced value in normal gravity (20 cm/s and above).

While the effect of freestream velocity has been noted in other flame problems, it is important to emphasize the importance of the other parameter investigated in this work: the percentage of gas-phase conductive heat flux going into the solid, Φ. Since solid surface pyrolysis temperature is generally much higher than the ambient temperature (e.g., 700 K versus 298 K), heatup of the solid fuel is necessary to establish a flame. For a thick solid, heat up of the whole sample may take a long time (after the whole sample is heated up to uniform temperature, $\Phi \rightarrow 0$) and the solid fuel may spend a substantial amount of its burning time with varying the percentage of heat flux going into the solid. The model clearly shows that without specifying this parameter, the flammability limit of a thick solid is not well defined. The most flammable condition is when the percentage of heat flux going into the solid vanishes, which is the thin fuel limit.

While this work includes surface radiative loss, partly due to complexity, gas-phase radiation has been neglected. Recent works on simpler configurations (Bhattacharjee and Altenkirch, 1990; Chen and Cheng, 1994; Jiang, 1995; Rhatigan, et al., 1997) show that gas radiation reduces flame temperature and flame length, but for solid fuel its effect on extinction is limited (since surface radiative loss dominates). While we will include gas radiation in future work, the essential feature of solid flammability is expected to be similar to the one presented in this work.

The present work also assumes a laminar flow. Using the reference temperature to evaluate gas density and viscosity, the Reynolds number based on cylinder diameter is found to be 43.5 at a freestream velocity of 100 cm/s. This shows that most of the cases covered in Fig. 2 are indeed laminar. For those cases near the wake flame blowoff limit with a small value of Φ, the possibility of unsteadiness in the downstream wake region exists. Its influence on the extinction limit may require further investigation.

Acknowledgment

We are indebted to Prof. Chiun-Hsun Chen and Dr. Fang-Bor Weng who provided us with the computer program in Chen and Weng (1990a) on which our numerical program was based and to Dr. Jeffrey Goldmeer for his advice and consultation. This work is partially supported by NASA Grant NAG3-1046.

References

Bhattacharjee, S., and Altenkirch, R. A., 1990, "Radiation-Controlled, Opposed-Flow Flame Spread in a Microgravity Environment," *Twenty-Third Symposium (International) on Combustion,* The Combustion Institute, pp. 1627–1633.

Chen, C. H., and Cheng, M. C., 1994, "Gas-Phase Radiative Effects in Downward Flame Spread in Low Gravity," *Combustion Science and Technology,* Vol. 97, pp. 63–83.

Chen, C. H., and Weng, F. B., 1990a, "Flame Stabilization and Blowoff Over a Porous Cylinder," *Combustion Science and Technology,* Vol. 73, pp. 427–446.

Chen, C. H., and Weng, F. B., 1990b, "Heat Transfer for Incompressible and Compressible Fluid Flows over a Heated Cylinder," *Numerical Heat Transfer,* Part A, Vol. 18, pp. 325–342.

Dwyer, H. A., and Sanders, B. R., 1986, "A Detailed Study of Burning Fuel Droplets," *Twenty-First Symposium (International) on Combustion,* The Combustion Institute, pp. 633–639.

Ferkul, P. V., and T'ien, J. S., 1994, "A Model of Low-Speed Concurrent Flow Flame Spread Over a Thin Solid," *Combustion Science and Technology,* Vol. 99, pp. 345–370.

Fernandez-Pello, A. C., 1995, "The Solid Phase," *Combustion Fundamentals of Fire,* G. Cox, ed., Academic Press, San Diego, CA, Chapter 2.

Foutch, D. W., and T'ien, J. S., "Extinction of a Stagnation-Point Diffusion Flame at Reduced Gravity," *AIAA J.,* Vol. 25, No. 7, pp. 972–976.

Goldmeer, J. S., 1996, "Extinguishment of a Diffusion Flame over a PMMA Cylinder by Depressurization in Reduced Gravity," Ph.D. thesis, Department of Mechanical and Aerospace Engineering, Case Western Reserve University, Cleveland, OH.

Grayson, G., Sacksteder, K., Ferkul, P. V., and T'ien, J. S., 1994, "Flame Spreading Over a Thin Fuel in Low Speed Concurrent Flow: Droptower Experimental Results and Comparison with Theory," *Microgravity Science and Technology,* pp. 187–196.

Jiang, C.-B., 1995, "A Model of Flame Spread over a Thin Solid in Concurrent Flow with Flame Radiation," Ph.D. thesis, Department of Mechanical and Aerospace Engineering, Case Western Reserve University, Cleveland, OH.

Olson, S. L., Ferkul, P. V., and T'ien, J. S., 1988, "Near-Limit Flame Spread Over a Thin Solid Fuel in Microgravity," *Twenty-Second Symposium (International) on Combustion,* The Combustion Institute, pp. 1213–1222.

Patankar, S. V., 1980, *Numerical Heat Transfer and Fluid Flow,* McGraw-Hill, New York.

Rees, G. W., 1981, "Gasification and Burning of a Fuel Particle," M.S. Project Report, Mechanical Engineering Department, University of California, Berkeley, Berkeley, CA.

Rhatigan, J. L., Bedir, H., and T'ien, J. S., 1998, "Gas-Phase Radiative Effects on the Burning and Extinction of a Solid Fuel," *Combustion and Flame,* Vol. 112, pp. 241.

Thomas, P. D., and Middecoff, J. F., 1980, "Direct Control of the Grid Point Distribution in Meshes Generated by Elliptic Equations," *AIAA J.,* Vol. 18, No. 6, pp. 652–656.

T'ien, J. S., 1986, "Diffusion Flame Extinction at Small Stretch Rates: The Mechanism of Radiation Loss," *Combustion and Flame,* Vol. 65, pp. 31–34.

T'ien, J. S., Singhal, S. N., Harrold, D. P., and Prahl, J. M., 1978, "Combustion and Extinction in the Stagnation Point Boundary Layer of a Condensed Fuel," *Combustion and Flame,* Vol. 33, pp. 55–68.

Tsuji, H., and Yamaoka, I., 1967, "The Counterflow Diffusion Flame in the Forward Stagnation Region of a Porous Cylinder," *Eleventh Symposium (International) on Combustion,* The Combustion Institute, p. 979.

Yang, C.-T., 1994, "Numerical Simulation of the Combustion of a Solid Cylinder in Low-Speed Flows," M.S. thesis, Department of Mechanical and Aerospace Engineering, Case Western Reserve University, Cleveland, OH.

The Heat Transport Capacity of Micro Heat Pipes

J. M. Ha
Graduate Research Assistant

G. P. Peterson[1]
Tenneco Professor and Head,
Fellow ASME

Department of Mechanical Engineering,
Texas A&M University,
College, TX 77843-3123

The original analytical model for predicting the maximum heat transport capacity in micro heat pipes, as developed by Cotter, has been re-evaluated in light of the currently available experimental data. As is the case for most models, the original model assumed a fixed evaporator region and while it yields trends that are consistent with the experimental results, it significantly overpredicts the maximum heat transport capacity. In an effort to provide a more accurate predictive tool, a semi-empirical correlation has been developed. This modified model incorporates the effects of the temporal intrusion of the evaporating region into the adiabatic section of the heat pipe, which occurs as the heat pipe approaches dryout conditions. In so doing, the current model provides a more realistic picture of the actual physical situation. In addition to incorporating these effects, Cotter's original expression for the liquid flow shape factor has been modified. These modifications are then incorporated into the original model and the results compared with the available experimental data. The results of this comparison indicate that the new semiempirical model significantly improves the correlation between the experimental and predicted results and more accurately represents the actual physical behavior of these devices.

Introduction

The high effective thermal conductivity resulting from the utilization of the latent heat of the working fluid in heat pipes has resulted in their application in a wide range of thermal control applications ranging from protection of the permafrost layer under the Alaska pipeline to the thermal control of optical surfaces in spacecraft (Peterson and Ortega, 1990). More recently, the miniaturization of electronic components has necessitated the development of novel heat rejection techniques, some of which have incorporated very small "micro" heat pipes or micro heat spreaders fabricated as an integral part of the silicon wafer or substrate. Use of these devices facilitates removal of the ever increasing heat fluxes, while at the same time providing a uniform temperature distribution across the entire wafer.

The concept of micro heat pipes fabricated in silicon wafers was first introduced by Cotter (1984), but the first experimental test results on these devices were not published until somewhat later by Peterson et al. (1993). As an intermediary step in the development process, experimental tests were conducted by Babin et al. (1990) on micro heat pipes approximately 1 mm in diameter, fabricated from silver or copper and charged with distilled, deionized water. While larger than originally conceived, these individual micro heat pipes (now typically referred to as miniature heat pipes) fit the fundamental criteria as posed by Cotter

$$\frac{1}{r_c} \approx \frac{1}{r_h}. \tag{1}$$

Using conventional steady-state modeling techniques as outlined by Chi (1976), the maximum heat transport capacity of the trapezoidal heat pipes were evaluated and showed a reasonably good agreement with the experimental results. Because the dimensions were fairly large when compared to those originally proposed, conventional modeling methods could be applied and did not require the development of new techniques.

Shortly thereafter, Chen et al. (1992) carried out visualization experiments for a glass micro heat pipe of approximately the same dimensions, and constructed a flow pattern map. In addition, a micro heat pipe model, which employed the concept of two-phase flow in porous media with modified relative permeabilities and the Leverett function, was developed to calculate the maximum heat transport capacity. The predicted results were compared with Babin et al.'s experimental data and while the results were again fairly good, a constant in the capillary pressure term of the governing equation was used to compensate for the discrepancy with the experimental data.

More recently, Khrustalev and Faghri (1994) proposed a numerical model of the heat and mass transfer occurring in a micro heat pipe to include the effects of shear stresses at the liquid-vapor interface. This model demonstrated that the shear stresses due to liquid vapor frictional interaction could significantly influence the maximum heat transfer capacity; however, several semi-empirical equations used in the model make it difficult to grasp the physical relationship between the model and the actual conditions in an operating micro heat pipe.

These and several other models have been summarized in detail and the results compared by Peterson (1992) and more recently by Peterson et al. (1996). In essence, while all of these models provide reasonably accurate predictions of the maximum heat transport capacity, none provide the type of insight to the physical phenomena that govern the operation of these devices as well as the original model proposed by Cotter. For this reason, the approximate analytical approach of Cotter (1984) has been reevaluated in light of the currently available experimental data in an attempt to modify it to better predict the actual operating conditions and maximum heat transport capacity. Building upon the fundamental work of Wang et al. (1994) this new model better approximates the physical behavior of the liquid-vapor interface in the dryout region.

Comparison of Cotter's Model to Experimental Data

Cotter's Model. When the first analytical model for micro heat pipes was introduced by Cotter (1984), several simplifying assumptions were made.

(i) The capillary pressure gradient resulting from the variation in the radius of curvature was assumed to be the driving force for the liquid flow.

---

[1] To whom correspondence should be addressed.

Contributed by the Heat Transfer Division for publication in the JOURNAL OF HEAT TRANSFER. Manuscript received by the Heat Transfer Division, Apr. 4, 1996; revision received, May 29, 1998. Keywords: Heat Transfer, Heat Pipes, Microscale, Surface Tension, Thermocapillary. Associate Technical Editor: M. Modest.

(ii) The liquid-vapor interface velocity was assumed to be zero.

(iii) The vapor flow regime was assumed to be both laminar and incompressible.

Utilizing these three assumptions and simplifying the momentum equation for steady-state incompressible gravity-free parallel flow yields

$$\mu\left(\frac{\partial^2 w}{\partial x^2} + \frac{\partial^2 w}{\partial y^2}\right) = \frac{dP}{dz}. \tag{2}$$

(iv) Assuming a uniform cross-sectional area and no slip conditions at the boundaries, this expression was transformed to

$$\frac{\partial^2 w'}{\partial x'^2} + \frac{\partial^2 w'}{\partial y'^2} = -1 \tag{3}$$

where

$$x = A^{0.5}x', \quad y = A^{0.5}y', \quad w = -\frac{A}{\mu}\frac{dP}{dz}w'. \tag{4}$$

Substituting these variables into the local mass flow equation, which is then integrated over the area A, yields

$$\dot m = \rho \iint w dx dy = -\frac{K\rho A^2}{8\pi\mu}\frac{dP}{dz}. \tag{5}$$

Here K is a dimensionless shape factor given by

$$K = 8\pi \iint w' dx' dy'. \tag{6}$$

The value of K is one for a circular disk and is less than one for any other shape as shown in Table 1, which summarizes the data for several shapes, as determined by Polya and Szego (1951).

Table 1 Values of the flow shape factor (Polya and Szego, 1951)

Shape	K
circle	1.000
square	0.883
triangle, 60 deg − 60 deg − 60 deg	0.725
triangle, 30 deg − 60 deg − 90 deg	0.597

The relationship between the capillary pressure that drives the liquid flow and the liquid-vapor pressure difference can be expressed as

$$P_v - P_l = \frac{\sigma}{r} \tag{7}$$

where r is the mean radius of curvature. Differentiating Eq. (7) with respect to z, and using Eq. (5) yields

$$\frac{8\pi\nu_v \dot m_v}{K_v A_v^2} = \frac{8\pi\nu_l \dot m_l}{K_l A_l^2} - \frac{d}{dz}\left(\frac{\sigma}{r}\right). \tag{8}$$

Realizing that at steady state the local liquid and vapor mass flow rates are equal in magnitude and proportional to the local heat flux, the mass flow rate can be calculated as

$$\dot m_v(z) = -\dot m_l(z) = \frac{\dot Q}{h_{fg}} h(z/L) \tag{9}$$

where $h(z/L)$ is a fraction of the total heat transport and $A(z) = A_l(z) + A_v(z)$ is the total area. Here, A_l can be related to r by a geometrically determined dimensionless variable β as

$$A_l = \beta^2 r^2. \tag{10}$$

Substituting Eqs. (9) and (10) into Eq. (8) and solving, results in a first-order ordinary differential equation, which relates the radius of curvature to the axial position along the pipe, or

$$\frac{dr}{dz} = \frac{8\pi Q r^2 h(z/L)}{\sigma h_{fg}}\left(\frac{\nu_v}{K_v(A - \beta^2 r^2)^2} + \frac{\nu_l}{K_l \beta^4 r^4}\right). \tag{11}$$

If the cross-sectional area A is constant, this equation is separable and therefore solvable.

For constant values of A, K_v, K_l, and β, the solution of Eq. (11) depends only on four dimensionless parameters; the distance along the pipe, ζ, the interface radius of curvature, ϕ, the kinematic viscosity and the heat flux parameters, γ, defined by

$$\zeta = z/L, \quad \phi = \beta A^{-1/2} r, \quad \alpha = \frac{K_l \nu_v}{K_v \nu_l}, \quad \text{and}$$

$$\gamma = \frac{8\pi Q \nu_l L}{\beta \sigma h_{fg} K_l A^{3/2}}. \tag{12}$$

Nomenclature

A = cross-section area
c, c_1 = parameters in Eq. (39)
cf = correction factor in Eq. (31)
d = hydraulic diameter in Eq. (27)
G = interface curvature integral in Eq. (15)
H = integral of h in Eq. (15)
h = fraction of total heat transport in Eq. (9)
h_{fg} = latent heat of vaporization
L = length of micro heat pipe
K = dimensionless shape factor in Eq. (6)
$\dot m$ = local mass flow rate
P = pressure
$\dot Q$ = maximum heat transport capacity of the micro heat pipe
QL = heat transport factor in Eq. (34)
$r(z)$ = radius of curvature in the intrinsic meniscus at z
w = z-component of velocity
x = coordinate orthogonal to z, or length of dried out region in Fig. 5
y = coordinate orthogonal to z, or length of the new evaporating region in Fig. 5
z = coordinate measured along the axial direction of the micro heat pipe

Greek Symbols

α = kinematic viscosity parameter in Eq. (12)
β = liquid geometric shape parameter in Eq. (10)
Γ = mass flow rate per cross section along only one groove in Eq. (38)
γ = heat transport parameter in Eq. (12)
κ = parameter in Eq. (38)
μ = dynamic viscosity
ν = kinematic viscosity
ϕ = dimensionless radius of curvature in Eq. (12)
ζ = dimensionless axial distance in Eq. (12)
ρ = density
σ = surface tension
θ = groove half-angle

Superscript

$'$ = newly determined value with excess heat input in Eqs. (33), (35)

Subscripts

a = adiabatic
c = capillary in Eq. (1), or condenser
e = evaporator
h = hydraulic in Eq. (1)
l = liquid
max = maximum
v = vapor

Using the dimensionless parameters in Eq. (12), Eq. (11) reduces to the dimensionless form

$$\frac{d\phi}{d\zeta} = \gamma h(\zeta)\left\{\frac{\alpha\phi^2}{(1-\phi^2)^2} + \frac{1}{\phi^2}\right\}. \tag{13}$$

Separating the variables and integrating, the solution of the above equation can be written as

$$\gamma H(\zeta) = G(\phi, \alpha) - G(\phi_0, \alpha) \tag{14}$$

where

$$H(\zeta) = \int_0^\zeta h(\zeta)d\zeta, \quad \text{and}$$

$$G(\phi, \alpha) = \int_0^\phi \frac{\phi^2(1-\phi^2)^2}{\alpha\phi^4 + (1-\phi^2)^2}d\phi. \tag{15}$$

A family of curves on the function $G(\phi, \alpha)$ is an asymptotically increasing function of ϕ. Thus, the maximum of γ in Eq. (14) can be represented as

$$\gamma_{\max} = [G(\phi_{\max}, \alpha) - G(\phi_{\min}, \alpha)]/H(1). \tag{16}$$

By having $G(\phi_{\max}, \alpha)$ only slightly smaller than $G(1, \alpha)$, and $G(\phi_{\min}, \alpha)$ only slightly larger than zero, Eq. (16) can be reduced to

$$\gamma_{\max} = G(1, \alpha)/H(1). \tag{17}$$

For further simplification, $G(1, \alpha)$ is assumed to be approximately equal to $0.16\alpha^{-1/2}$. In the range of $5 < \alpha < 200$, the error caused by this assumption is less than ten percent. Returning to the physical quantities, Eq. (17) yields

$$\dot{Q}_{\max} = \frac{0.16\beta\sqrt{K_l K_v}}{8\pi H(1)}\frac{\sigma h_{fg}}{\nu_l}\sqrt{\frac{\nu_l}{\nu_v}}\frac{A^{3/2}}{L}. \tag{18}$$

Comparison With Experimental Data. The derived final equation for the maximum heat transport capacity, Eq. (18), requires some careful treatment due to the imposed restrictions assumed in the derivation. For this reason, before going to the application of Cotter's prediction, it is necessary to discuss some subtle points which are not immediately apparent in the original reference of Cotter.

First, the mass balance requirement in Eq. (9) can hold only in the regions where phase changes occur. In the dryout region of the evaporator or in the flooded region of the condenser, Eq. (9) cannot be applied because the local liquid and vapor flows in those regions are not proportional to the local heat flux. Therefore, both the dryout region in the evaporator and the flooded region in the condenser should be excluded from the foregoing analytical procedures.

Second, the requirement of $\phi_{\min} = 0$ for the maximum heat transport capacity is one of essential points in understanding Cotter's model. First of all, Eq. (14) can be derived from

$$\begin{aligned}\gamma H(\zeta) &= \int_{\phi_0}^\phi \frac{\phi^2(1-\phi^2)^2}{\alpha\phi^4 + (1-\phi^2)^2}d\phi \\ &= \int_0^\phi \frac{\phi^2(1-\phi^2)^2}{\alpha\phi^4 + (1-\phi^2)^2}d\phi \\ &\quad - \int_0^{\phi_0} \frac{\phi^2(1-\phi^2)^2}{\alpha\phi^4 + (1-\phi^2)^2}d\phi \\ &= G(\phi, \alpha) - G(\phi_0, \alpha).\end{aligned} \tag{19}$$

Once a micro heat pipe filled with liquid works, the radius of curvature at the beginning of the evaporator (at $\zeta = 0$ in Fig. 1) will start small within the corners, and then in the condenser region will pass through a maximum value (at $\zeta = 1$ in Fig. 1) with the vapor located in a liquid-enclosed bubble. Beyond the cross section where $\zeta > 1$, the radius diminishes as the liquid fills the entire cavity. The maximum value of the mean radius of curvature at $\zeta = 1$, which depends only on the size and shape of the cavity, is a useful capillary characteristic dimension.

In a normal operating state without any dryout region, ϕ_0 in Eqs. (14) or (19) generally has a certain value larger than zero at $\zeta = 0$. When $\phi_0 > 0$, the liquid does not reach the capillary limit under the given heat flux because the evaporating liquid will permit a greater heat load, until the radius of curvature reaches the smallest value. Namely, for attaining the maximum heat transport, ϕ_0 should have the value of zero at $\zeta = 0$. This physical fact was used and satisfied in Eq. (17). $\phi_{\min} = 0$ results in the minimum value of G; i.e., $G(\phi_{\min}, \alpha) = G(0, \alpha)$ is zero from the definition of G in Eq. (15). Meanwhile, the value of $\phi_{\max}$ corresponding to the maximum radius of curvature at $\zeta = 1$ is one, from the definition in Eq. (12) and results in the maximum value of G. Note that for the maximum heat transport capacity, unflooded heat pipe behavior is assumed. In summary, in Eq. (17) for the maximum heat transport, it has already been assumed that the evaporation takes place at the capillary limit state; in other words, the radius of curvature starts from zero at the beginning of the evaporator with no dryout and ends at the maximum radius in the condenser.

Third, a clear understanding of $H(1)$ will lead to a better understanding of the physical significance and can avoid some confusion in the use of Eq. (18). Babin et al. (1990) and Chen et al. (1993) both stated that $H(1)$ must be known a priori to predict the maximum transport capacity and that in this sense, it behaves as a correction factor which can be varied to better simulate the experimental results. They tried, based on this

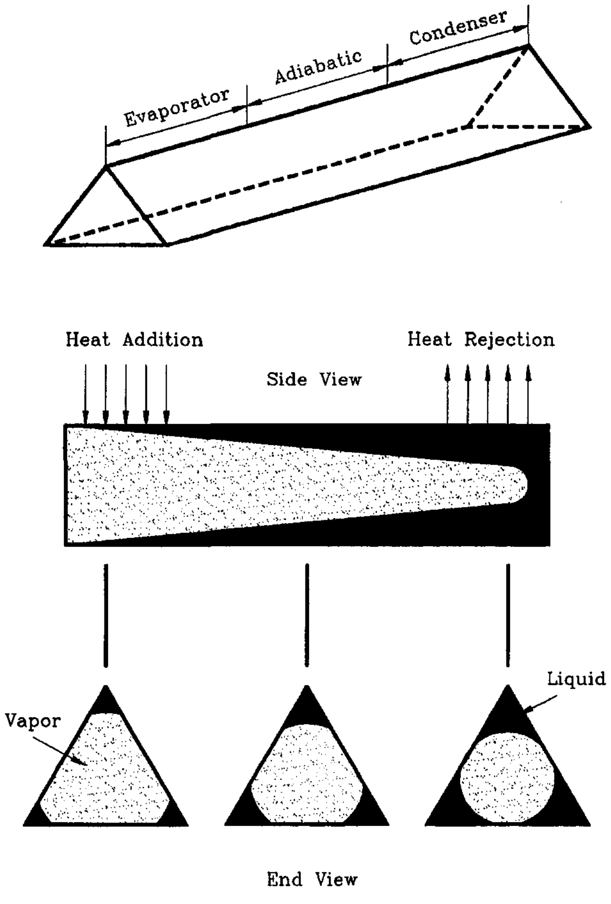

Fig. 1 Micro heat pipe operation

argument, to determine the effect of $H(1)$ on the capillary limit. However, as will be shown here that $H(1)$ is not a correction factor, but rather has a physical meaning, the value of which can be obtained as follows.

If a micro heat pipe has a uniform heat flux distribution along its evaporator and condenser sections, the axial heat transport distribution will be

$$\text{at } 0 \le z < L_e, \quad \dot{Q} = \frac{z}{L_e}\dot{Q}_{\max} \tag{20}$$

$$\text{at } L_e \le z \le L_e + L_a \quad \dot{Q} = \dot{Q}_{\max} \tag{21}$$

$$\text{at } L_e + L_a < z \le L \quad \dot{Q} = \frac{L - z}{L_c}\dot{Q}_{\max}. \tag{22}$$

Consequently, from the definition, $H(1)$ can be calculated as follows:

$$\begin{aligned} H(1) &= \int_0^1 h(\zeta)d\zeta \\ &= \int_0^{L_e/L} \frac{L}{L_e}\zeta d\zeta + \int_{L_e/L}^{(L_e+L_a)/L} d\zeta \\ &\quad + \int_{(L_e+L_a)/L}^{1} \frac{L}{L_c}(1-\zeta)d\zeta \\ &= \frac{0.5L_e + L_a + 0.5L_c}{L_e + L_a + L_c}. \end{aligned} \tag{23}$$

Once the lengths of each region are specified, $H(1)$ is automatically calculated for each region. As with Eq. (23), Eq. (18) can be written in an alternative form as

$$\dot{Q}_{\max} = \frac{0.16\beta\sqrt{K_l K_v}}{8\pi(0.5L_e + L_a + 0.5L_c)}\,\frac{\sigma h_{fg}}{\nu_l}\sqrt{\frac{\nu_l}{\nu_v}}\,A^{3/2}. \tag{24}$$

Note that in the above equation, the total length, L, does not appear, and that the condenser region, L_c, only designates the region where phase change occurs.

To date, very little experimental data has been reported for micro heat pipes. Babin et al. (1990) conducted an experimental investigation with a relatively small trapezoidal heat pipe whose shape and size are given in Fig. 2 and Table 2. They applied Cotter's prediction for the comparison with the obtained experimental data, but the rationale for selection of specific values for some of the parameters was not clear. In the current investigation, the values of $H(1)$, K_v, K_l, β are determined in such a manner that they have a clear physical meaning.

In Eq. (23) for $H(1)$, $L_e = 12.7$ mm, $L_a = 57.0 - 12.7 - 12.7 = 31.6$ mm. As mentioned previously, L_c is not the total condenser length, but rather the length from the junction of the adiabatic region and condenser to the location where the maximum radius of curvature exists. Generally, there is no guarantee that the maximum radius exists at the end of the condenser. In the micro heat pipe used in the experiment, the charge of 0.0032 gm fills a length of approximately 8.03 mm of the condenser region without the wicking action because the calculated core area is $0.707^2 - 4 \times 0.02536 = 0.3985$ mm^2. This length should be omitted in the calculated length of the condenser. Namely, $12.7 - 8.03 = 4.67$ mm is the approximate proper length for the value of L_c. Thus, the calculated value of $H(1)$ is 0.82265 from Eq. (23).

Table 2 Micro heat pipe dimensions of Babin et al. (1990)

total length	57.0 mm
evaporator length	12.7 mm
condenser length	12.7 mm
inner vapor channel diameter	0.6 mm
outer vapor channel diameter	1.0 mm
charged liquid amount	0.0032 g

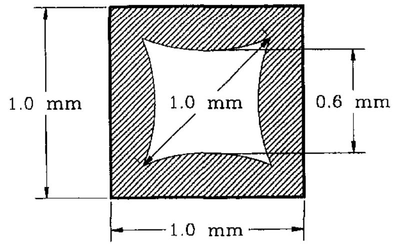

Fig. 2 Cross-sectional dimensions of Babin et al.'s micro heat pipe

As seen in Fig. 2, the shape of the cross section is not a regular edged polygon. So, the following treatment is introduced for K_v:

$$K_v = \frac{2r_i r_c}{r_i^2 + r_c^2} \tag{25}$$

where r_i is radius of the inscribed circle and r_c is radius of the circumscribed circle. Using the above definition, 0.88 is the value of K_v at the beginning location of the evaporator, where only vapor fills the core with $r_i = 0.3$ mm, and $r_c = 0.5$ mm. The final value of K_v becomes

$$K_v = \frac{1 + 0.88}{2} = 0.94. \tag{26}$$

The value of 1 in the numerator in Eq. (26) represents K_v at the location where the maximum radius exists because the value of the flow shape factor of a circle is unity. (See Table 1.) A simple arithmetic average can be adopted to determine the final value of K_v for the entire vapor space. However, estimating the value of K_l is somewhat difficult because determining the dimensions of the liquid region in the corner is difficult. According to Cotter's treatment, a rough approximation of 0.5 is assumed.

For β, the cross section where the maximum radius exists can be used because Cotter's prediction of Eq. (18) was derived under the assumption that the shape of the liquid in the corner is similar along the entire region, which means β is constant. The definition of $A_l = \beta^2 r^2$ produces $\beta = 1.1343$ with $A_l = 0.1158$ mm^2 and $r = 0.3$ mm.

In Table 3, the calculated results are tabulated and compared to those of Babin et al. Usually small changes of the shape factor K_v, and K_l do not seriously affect Eq. (18) or Eq. (24) because the product is raised to the $\frac{1}{2}$ power. However, small errors in $H(1)$, and β can have a relatively large effect on Eq. (18) or Eq. (24).

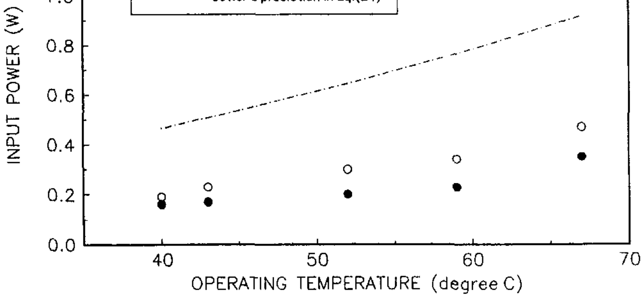

Fig. 3 Comparison of the maximum heat transport capacity of a trapezoidal micro heat pipe as a function of the operating temperature (copper-water)

Table 3 Dimensionless constants

Parameters	Babin	Current
$H(1)$	0.5	0.8226
K_v	0.975	0.94
K_l	0.6	0.5
β	2.044	1.1343

Cotter's prediction with the above values is compared to Babin et al.'s experimental data, in Fig. 3 for the copper-water micro heat pipe. The points of the onset of dryout correspond to the situation for the maximum heat transport capacity, and the termination of dryout represents the situation where dryout occurs throughout the entire evaporator. Although the trend is correct, the absolute values of the prediction are about three times higher than those of the data, which go further than even those of the termination of dryout.

At this point it is useful to consider the model presented by Gerner et al. (1992). That was a simple analytical model developed to predict the maximum heat transport capacity using the hydraulic diameter. In the resulting procedure, the average film thickness was treated simply as one quarter of the hydraulic diameter, d, and the following formula was proposed:

$$\dot{Q}_{\max} = c\,\frac{3\pi}{2048}\,\frac{\sigma h_{fg} d^3}{\nu_v L} \tag{27}$$

A correction factor, c, was introduced and the value was determined to be 2.38 from the experimental data of Babin et al. In this model, the correction factor, c, simply compensates for the deviation between the predicted and experimental data. However, it should be noted that Cotter's model, even in case where only liquid properties are used, shows a more interesting parametric relationship than that of Gerner et al.

Without taking into account vapor flow, Eq. (13) reduces to

$$\frac{d\phi}{d\zeta} = \gamma h(\zeta)\,\frac{1}{\phi^2}\,. \tag{28}$$

Using separation of variables, the integrated solution becomes

$$\gamma H(1) = \tfrac{1}{3}[\phi^3]_0^1. \tag{29}$$

Returning to the physical quantities without any approximation results in

$$\dot{Q}_{\max} = \frac{\beta \sigma h_{fg} k_l A^{3/2}}{24 H(1) \pi \nu_l L}\,. \tag{30}$$

Comparing Eq. (30) to Eq. (27), it is clear that even if only fluid properties are considered, Eq. (30) includes more parameters, such as the effects of shape and the length of each of the regions than Eq. (27). Thus, Cotter's model, Eq. (18), when modified to include parameters for the effect of vapor flow is more generally applicable.

While Cotter's model is of value, it over predicts the maximum heat transport capacity as seen Fig. 3. So, if a correction factor, cf, is introduced, the following semi-empirical correlation for $\dot{Q}_{\max}$ can be proposed:

$$\dot{Q}_{\max} = cf\,\frac{0.16\beta\sqrt{K_l K_v}}{8\pi(0.5L_e + L_a + 0.5L_c)}\,\frac{\sigma h_{fg}}{\nu_l}\sqrt{\frac{\nu_l}{\nu_v}}\,A^{3/2}. \tag{31}$$

Comparing Babin et al.'s data, cf is found to be 0.33 for a copper-water micro heat pipe, and 0.37 for a silver-water micro heat pipe. The slight difference of cf comes from the interaction of the different material and the working fluid caused by the contact angle. Equation (31) can be rearranged in terms of physical terms

$$\frac{\dot{Q}_{\max}\nu_l L}{\sigma h_{fg} A^{3/2}} = cf\,\frac{0.16\beta\sqrt{K_l K_v}}{8\pi H(1)}\sqrt{\frac{\nu_l}{\nu_v}}\,. \tag{32}$$

The nondimensional term in the left-hand side represents the ratio of maximum heat transport capacity to the product of the characteristic heat flux, $\sigma h_{fg}/\nu_l$, and a characteristic area, $A\sqrt{A/L}$. The second factor represents the geometric shape of the liquid and vapor flow and the effect of the length of each region. The third factor depends on the kinematic viscosity ratio, which varies mainly with the vapor density. The graphical representation of Eq. (32) with respect to the operating temperatures is given in Fig. 4. Data for the two cases, copper and silver, are in good agreement with the averaged value of $cf = 0.35$ in the range above 35°C.

Though the significance of Cotter's model has been recognized, the problem of overprediction still remains. It is believed that the overprediction is due to the assumption of zero velocity at the liquid-vapor interface. The vapor and liquid each flow in opposite directions, so the interface velocity will ordinarily be small compared to the mean velocity of either phase. In this context, Cotter assumed the interface velocity was zero for the purpose of simplicity, because this treatment permits the use of the scaling law which introduced the shape factors, K_v and K_l. In a real device, however, the vapor velocity is much larger than the liquid velocity since the diameter of the cross section is very small compared to the length of micro heat pipe. When the vapor velocity becomes very large, the resistance on the liquid-vapor interface due to the counter flow retards the liquid velocity. This frictional effect reduces the heat transport capacity. The effect of shear stress in the liquid vapor interface was investigated by Ma and Peterson (1994) and also in the numerical model of Khrustalev and Faghri (1994). In both of these investigations, it was demonstrated that neglecting the shear stress at the interface can lead to an overestimation of the maximum heat transport capacity. In addition to the effect of the interfacial shear stress, the effects of the disjoining pressure may need to be considered if the diameter approaches very small values (Swanson and Peterson, 1994). Methods by which these factors can be incorporated into the current model are currently underway.

Length of the Evaporating Region

In an operating heat pipe, vaporization takes place in the entire evaporator region until the applied heat load reaches the maximum heat transport capacity, $\dot{Q}_{\max}$. If the heat load exceeds the limit of $\dot{Q}_{\max}$, then dryout occurs beginning at the end of the evaporator. Once dryout begins, the wall temperature in the adiabatic section increases and a small part of what was formerly the adiabatic section begins to act as an evaporator. As the power continues to increase, the dryout in the evaporator

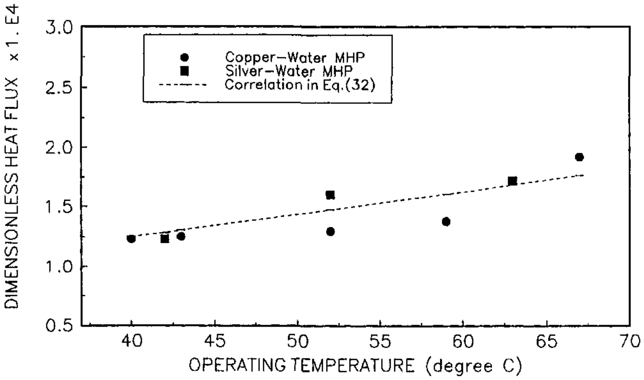

Fig. 4 Dimensionless heat flux with respect to the operating temperature

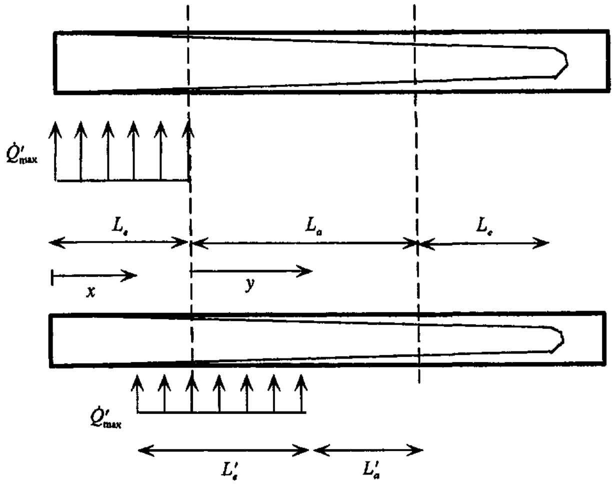

Fig. 5 Coordinates for the length of evaporating region with dryout

spreads and the portion of the adiabatic section that behaves as an evaporator expands. In the extreme case where complete dryout of the former evaporator section occurs, a large portion of the adiabatic section may behave as an evaporator and may even begin to dry out at the end furthest from the condenser.

When dryout occurs it is difficult, as mentioned by Babin et al. (1990), to measure how far the evaporating length has advanced into the adiabatic region. However, if two heat inputs and the corresponding dryout length in the evaporator are known, it can be determined how far the end of the evaporating length has intruded into the adiabatic region by use of Cotter's model.

Let $\dot{Q}'_{\max}$ denote a heat input larger than $\dot{Q}_{\max}$. The heat flux of $\dot{Q}'_{\max}$ supplied from the outside of the micro heat pipe case is redistributed again on the liquid inside of the wall. In the dryout region, there is no heat transfer. Here, it will be assumed for simplicity that the new heat flux distribution on the active evaporator region is nearly uniform. Let the dryout length be x, and the length of new evaporating region intruding into what was formerly the adiabatic region by y as shown in Fig. 5. Then, with the new uniform distribution of $\dot{Q}'_{\max}$, the lengths of the resultant evaporating and resultant adiabatic regions are

$$L'_e = L_e - x + y, \quad L'_a = L_a - y. \tag{33}$$

Meanwhile, in Eq. (31), the magnitude of $\dot{Q}_{\max}(0.5L_e + L_a + 0.5L_c)$ is constant as long as it is at the same operating temperature, whether dryout occurs or not.

$$\begin{aligned} QL &\equiv \dot{Q}_{\max}(0.5L_e + L_a + 0.5L_c) \\ &= cf\frac{0.16\beta\sqrt{K_l K_v}}{8\pi}\frac{\sigma h_{fg}}{\nu_l}\sqrt{\frac{\nu_l}{\nu_v}}A^{3/2} \end{aligned} \tag{34}$$

Though dryout has occurred at the beginning of the evaporator due to excess heat, the heat transport factor denoted by QL will remain constant under the same operating temperature because the right-hand side in Eq. (34) depends only on the fluid properties, the cross-sectional area, and the shape of the vapor and liquid flow regions. Then, although dryout occurs, the transport factor, QL, remains constant with the following value:

$$\begin{aligned} \mathrm{QL} &= \dot{Q}'_{\max}(0.5L'_e + L'_a + 0.5L_c) \\ &= \dot{Q}'_{\max}\{0.5(L_e - x + y) + (L_a - y) + 0.5L_c\}. \end{aligned} \tag{35}$$

Combining Eqs. (34) and (35) gives

$$y = -x + 2H(1)L\left(1 - \frac{\dot{Q}_{\max}}{\dot{Q}'_{\max}}\right). \tag{36}$$

From the above result y can be determined from x and $\dot{Q}_{\max}$, $\dot{Q}'_{\max}$, which are all obtained from the experimental data. For example, consider Babin et al.'s experimental data for the copper-water micro heat pipe. $\dot{Q}_{\max}$, $\dot{Q}'_{\max}$, and calculated y are plotted with respect to operating temperature in Fig. 6. Data for the onset of dryout correspond to $\dot{Q}_{\max}$ at each operating temperature, and the curve fitted values are used to determine $\dot{Q}_{\max}$ in Eq. (36). Data for the termination of dryout correspond to $\dot{Q}'_{\max}$ at each operating temperature, and the curve fitted values can be used for $\dot{Q}'_{\max}$ in Eq. (36). For each case x is 12.7 mm because the entire length of the former evaporator region is dried out in this situation. Figure 6 shows that the active evaporating length becomes shorter at an operating temperature of 40°C as $y = L'_e = 5$ mm, $L'_a = 31.6 - 5 = 26.6$ mm; up to an operating temperature of 67°C, the new evaporator length, $y = 15$ mm, intrudes a little less than half of the original adiabatic length. In other words, under the same length of dryout, more heat transport capacity is available at a higher operating temperature, but causes dryout to intrude further into the evaporating region. Though Eq. (36) only provides an approximate prediction technique, it does provide excellent physical insight into the relationship between the heat amount and the various lengths.

Modified Cotter's Model

Cotter's original model has provided considerable insight into the operation of micro heat pipes and while the work of Wang et al. (1994) has helped to clarify the fundamental aspects of this model, it still requires some additional refinement. First, it significantly overpredicts the heat transport performance. Second, determination of the value of K_l is not clearly described. Third, the effect of contact angle was not included. If these drawbacks can be removed or at least alleviated, Cotter's model will be more useful and will more accurately represent the actual physical operation of these devices.

For this purpose, consider a simple triangular shape for the edge of a micro heat pipe. Using the same assumptions and approach as Cotter, Eq. (8) becomes

$$\frac{d}{dz}\left(\frac{\sigma}{r}\right) = \frac{8\pi\nu_l\dot{m}_l}{K_l A_l^2} - \frac{8\pi\nu_y\dot{m}_v}{K_v A_v^2}. \tag{37}$$

Here the first term in the right-hand side for the liquid flow will be modified to include an alternative method for determining K_l.

Xu and Carey (1990) developed a model for the axial variation of intrinsic meniscus in a triangular micro groove, by assuming that the liquid flow along a groove is driven by the

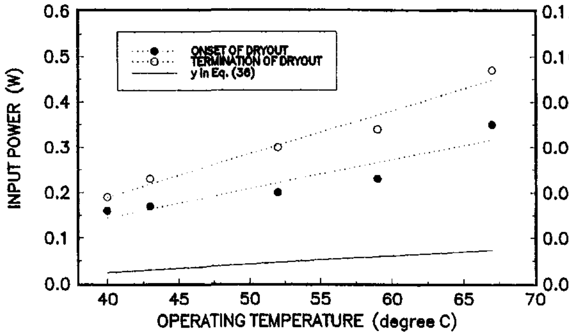

Fig. 6 The maximum heat transport capacity and the evaporating length intruding to adiabatic region as a function of the operating temperature

capillary pressure difference due to the receding of the meniscus. Ha and Peterson (1994) approximated this value in order to obtain an analytical solution for the location of the axial dryout point. Xu and Carey's (1990) governing equation for the intrinsic meniscus is

$$\frac{d}{dz}\left(\frac{\sigma}{r(z)}\right) = \frac{2\kappa\nu_l}{cr(z)^4}\Gamma + \rho_l g \sin\psi \qquad (38)$$

where

$$c = 4c_1^3 \tan^2\theta, \quad \text{and} \quad c_1 = \frac{1}{\tan\theta} + \theta - \frac{\pi}{2}. \qquad (39)$$

The parameter κ originally determined by Ayyaswamy et al. (1974) is a function of the groove half-angle, θ, and the contact angle. The parameter, Γ, is the mass flow rate through the cross-sectional liquid area, and ψ is the inclination angle against gravity. In Eq. (38), the vapor pressure was assumed to be constant so the vapor flow term was neglected. Comparing Eq. (37) with Eq. (38), the following equivalence will be possible between the corresponding liquid flow terms:

$$\frac{8\pi\nu_l}{K_l A_l^2}\dot{m}_l = \frac{2\kappa\nu_l}{cr^4} n\Gamma. \qquad (40)$$

Note that Γ in Eq. (38) is the mass flow rate through one channel. Thus, the value of $\dot{m}_l$ must include the entire amount of liquid flowing through all the channels, that is, $\dot{m}_l = n\Gamma$. For a triangular micro heat pipe, the value of n is three. Thus,

$$\dot{m}_l(z) = n\Gamma(z) = -\frac{\dot{Q}}{h_{fg}} h(z/L). \qquad (41)$$

As a result, combining Eqs. (37), (40), and (41) produces the following expression:

$$\frac{dr}{dz} = \frac{8\pi\dot{Q}r^2 h(z/L)}{\sigma h_{fg}}\left\{\frac{\nu_v}{K_v(A-\beta^2 r^2)^2} + \frac{\kappa\nu_l}{4\pi c r^4}\right\}. \qquad (42)$$

Previously, β was defined in Eq. (10), but β now can be redefined as

$$\beta = \sqrt{nc_1} \qquad (43)$$

since $A_l = nc_1 r^2$ and Eq. (42) can be rewritten as

$$\frac{dr}{dz} = \frac{8\pi\dot{Q}r^2 h(z/L)}{\sigma h_{fg}}\left\{\frac{\nu_v}{K_v(A-\beta^2 r^2)^2} + \frac{\nu_l}{K_l \beta^4 r^4}\right\} \qquad (44)$$

with the modified definition of K_l

$$K_l = \frac{4\pi c}{\kappa\beta^4} = \frac{16\pi c_1 \tan^2\theta}{n^2\kappa}. \qquad (45)$$

Table 4 Dimensionless constants

$H(1)$	0.666
K_v	0.86
K_l	0.135
β	1.433

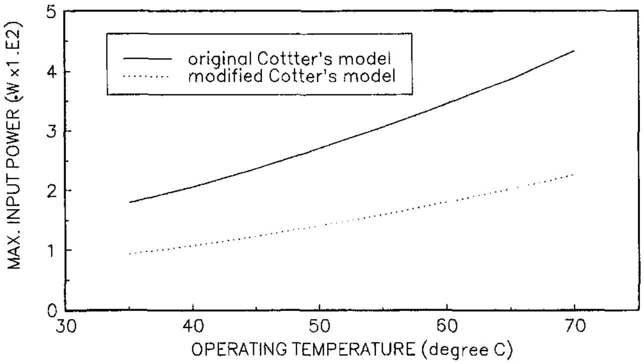

Fig. 7 Comparison of maximum heat transport capacity of a triangular micro heat pipe as a function of operating temperature

The form of Eq. (44) is exactly the same as that of Eq. (11) except for the definition of K_l, the liquid flow shape factor or the dimensionless mass flow rate of the liquid flow. Thus the rest of Cotter's procedure can be applied to Eq. (44), and yields the following expression for the maximum heat transport capacity:

$$\dot{Q}_{\max} = \frac{0.16\beta\sqrt{K_l K_v}}{8\pi H(1)}\frac{\sigma h_{fg}}{\nu_l}\sqrt{\frac{\nu_l}{\nu_v}}\frac{A^{3/2}}{L} \qquad (46)$$

which is identical to that of Cotter, with the exception of the definition of K_l. This change has several advantages which are not included in Cotter's original model. First, the determination of K_l is clearly defined. Second, the effect of the contact angle is included with the aid of κ. The best evaluation, however, is to determine if this new expression for K_l can more accurately predict the maximum heat transfer capacity. It should be noted here that the model of Xu and Carey (1990) again neglects the effect of the shear stress occurring at the liquid-vapor interface.

For this purpose, consider a micro heat pipe of equilateral triangular cross section shown in Fig. 1, and filled with an optimum amount of water, designed to operate in the range 30°C to 80°C with a uniformly heated evaporator and uniformly cooled condenser. The triangular pipe has a side of 0.2 mm and total length of 15 mm; the length of each region, evaporator, adiabatic region, and condenser, is 5 mm. For this triangular micro heat pipe $n = 3$ in Eqs. (43) and (45). Note that for all equilateral triangular micro heat pipes, the values of K_v, K_l, and β in Eq. (46) are always constant as shown in Table 4.

The calculated maximum heat transport capacity with respect to the operating temperature is illustrated in Fig. 7. The prediction of the modified model is about half that of Cotter's original model. This result is due to $K_l = 0.135$ from Eq. (45), while $K_l = 0.5$ from Cotter's method. This implies that in reality, the mass flow rate of the liquid is not nearly as large as originally estimated by Cotter.

Conclusions

The original analytical model for predicting the maximum heat transport capacity in micro heat pipes as developed by Cotter has been re-evaluated in light of the currently available experimental data and the fundamental work of Wang et al. (1994). As is the case for most heat pipe models, the original model assumed a fixed evaporator length, failing to compensate for the growth of the evaporator region resulting from conduction through the heat pipe wall. While the initial model resulted in trends that are consistent with more recent experimental results, it significantly overpredicts the maximum heat transport capacity. In an effort to provide a more accurate predictive tool, a semi-empirical correlation has been developed analytically using the available experimental data. This modified model, which is described in detail, incorporates the effects of the intrusion of the evaporator length into the adiabatic region that occurs as the heat pipe approaches dryout conditions, and thereby provides a more realistic picture of the actual physical situation. In addition to these effects, Cotter's original expression for the liquid flow shape factor has been modified to include a new analytical derivation of the dimensionless shape factor

K_l, which has been shown to provide a more reliable prediction than that of the original model of Cotter.

When these modifications are incorporated into the original model and the results compared with the available experimental data, the resulting new semi-empirical model is shown to significantly improve the correlation between the experimental and predicted results and more accurately represents the actual physical behavior of these devices.

References

Ayyaswamy, P. S., Catton, I., and Edwards, D. K., 1974, "Capillary Flow in Triangular Grooves," ASME *Journal of Applied Mechanics,* Vol. 41, pp. 332–336.

Babin, B. R., Peterson, G. P., and Wu, D., 1990, "Steady-State Modeling and Testing of a Micro Heat Pipe," ASME JOURNAL OF HEAT TRANSFER, Vol. 112, pp. 595–601.

Chen, H., Groll, M., and Rosler, S., 1992, "Micro Heap Pipes: Experimental Investigation and Theoretical Modelling," *Proceedings the 8th International Heat Pipe Conference,* Beijing, China.

Cotter, T. P., 1984, "Principles and Prospects of the Micro Heat Pipes," *Proceedings the 5th International Heat Pipe Conference,* Tsukuba, Japan, pp. 328–335.

Gerner, F. M., Longtin, J. P., Henderson, H. T., Hsieh, W. M., Ramadas, P., and Chang, W. S., 1992, "Flow and Heat Transfer Limitations in Micro Heat Pipes," ASME HTD-Vol. 206-3, ASME, New York, pp. 99–105.

Ha, J. M., and Peterson, G. P., 1994, "Analytical Prediction of the Axial Dryout Point for Evaporating Liquids in Triangular Microgrooves," ASME JOURNAL OF HEAT TRANSFER, Vol. 116, pp. 498–503.

Khrustalev, D., and Faghri, A., 1994, "Thermal Analysis of a Micro Heat Pipe," ASME JOURNAL OF HEAT TRANSFER, Vol. 116, pp. 189–198.

Ma, H. B., Peterson, G. P., and Lu, X. J., 1993, "The Influence of Vapor-Liquid Interactions on the Liquid Pressure Drop in Triangular Microgrooves," *Int. J. Heat & Mass Transfer,* Vol. 37, No. 15, pp. 2211–2219.

Peterson, G. P., Swanson, L. W., and Gerner, F. M., 1998, "Micro Heat Pipes," *Microscale Energy Transport,* C. L. Tien, A. Majumdar, and F. M. Gerner, eds. Taylor-Francis, Washington, DC, in press.

Peterson, G. P., 1992, "An Overview of Micro Heat Pipe Research," invited review article, ASME *Applied Mechanics Review,* Vol. 45, pp. 175–189.

Peterson, G. P., 1996, "Modeling Fabrication and Testing of Micro Heat Pipes: An Update," ASME *Applied Mechanics Reviews,* Vol. 49, No. 10, Pt. 2, pp. 175–183.

Peterson, G. P., Duncan, A. B., and Weichold, M. H., 1993, "Experimental Investigation of Micro Heat Pipes Fabricated in Silicon Wafers," ASME JOURNAL OF HEAT TRANSFER, Vol. 115, pp. 751–756.

Peterson, G. P., and Ortega, A., 1990, "Thermal Control of Electronic Equipment and Devices," *Advances in Heat Transfer,* Vol. 20, J. P. Hartnett and T. F. Irvine, eds., Pergamon, New York, pp. 181–314.

Polya, G., and Szego, G., 1951, *Isoperimetric Inequalities in Mathematical Physics,* Princeton University Press, Princeton, NJ.

Swanson, L., and Peterson, G. P., 1994, "The Evaporating Extended Meniscus in a *V*-Shaped Channel," *AIAA J. of Thermophysics and Heat Transfer,* Vol. 8, No. 1, pp. 172–181.

Wang, C. Y., Groll, M., Rösler, S., and Tu, C. J., 1994, "Porous Medium Model for Two-Phase Flow in Mini Channels with Applications to Micro Heat Pipes," *Heat Recovery Systems & CHP,* Vol. 14, No. 4, pp. 377–389.

Xu, X., and Carey, V. P., 1990, "Film Evaporation from a Micro-Grooved Surface—An Approximate Heat Transfer Model and its Comparison with Experimental Data," *AIAA J. of Thermophysics and Heat Transfer,* Vol. 4, No. 4, pp. 512–520.

Thermal and Hydraulic Performance of a Rectangular Duct With Multiple V-Shaped Ribs

C.-O. Olsson
Department of Thermo and Fluid Dynamics,
Chalmers University of Technology,
412 96 Goteborg, Sweden

B. Sunden
Division of Heat Transfer,
Lund Institute of Technology,
Box 118,
221 00 Lund, Sweden
e-mail: bengts@emvox2.vok.th.se
Mem. ASME

Experiments have been carried out to investigate the performance of a new swirl flow duct which is suitable for compact heat exchangers such as radiators. The ducts tested have rectangular cross sections with aspect ratio 1 to 8, and multiple V-shaped ribs are attached to the wide walls in a staggered arrangement such that square secondary flow cells are established. A previous investigation has shown that multiple V-shaped ribs may provide greater heat transfer enhancement than angled straight ribs and V-shaped ribs at Reynolds numbers below 2000. The data are presented as j and f factors for Reynolds numbers from 500 to 15,000, and correlations are obtained for the influence of rib height ($0.1 < e/H < 0.2$), rib pitch ($3 < p/H < 7$), and rib angle ($15 \text{ deg} < \phi < 45 \text{ deg}$). It was found that a rib angle of 45 deg provided the highest j/f ratio, while increasing the rib height or decreasing the rib pitch lowers the j/f ratio.

Introduction

This investigation is concerned with an improved surface roughness geometry for enhancement of convective heat transfer with application to laminar and turbulent flow in rectangular ducts. Rectangular ducts or tubes are frequently employed in heat exchangers such as radiators and charge air coolers, and in order to reduce the size of the heat exchangers the ducts are often made rib-roughened or dimpled. The roughness increases the heat transfer coefficient, but as it also increases the pressure drop it is of interest to find a roughness geometry that will yield a given heat transfer augmentation with minimum pressure drop increase. The particular roughness type considered in the present investigation is related to angled and V-shaped rib-roughnesses, on which extensive work has been performed and presented in the open literature. The basic idea of the heat transfer augmentation is to not only disturb the velocity and temperature profiles close to the walls, but also to create a secondary flow that will exchange heat and momentum between the wall regions and the core region.

In Olsson and Sundén (1997a) the flow fields in ducts with different rib configurations were studied using smoke-wire visualization and Laser Doppler Anemometry. The rib configurations tested were parallel ribs, cross ribs, parallel V-ribs, cross V-ribs, and multiple V-ribs. At Reynolds numbers below 2000 the secondary flow patterns were found to be more stable when confined in square cells as in the swirl flow duct than confined in rectangular cells. Convective motion in the direction normal to the wide walls was present in a greater fraction of the cross section in the swirl flow duct than in the other tubes or ducts. Therefore it was speculated that more heat transfer augmentation would be provided by the swirl flow duct than by the other ducts. j and f factors for the same ducts were reported in Olsson and Sundén (1997b) where rib height, rib pitch, and rib angle were identical for the ducts and thus only the rib configuration was varied. It was found that the swirl flow duct provided a significant increase in the j factor at $\text{Re} < 2000$ as compared to the other ducts, while both j and f factors were of the same order of magnitude for most of the ducts at larger Reynolds numbers. It was concluded that the swirl flow duct is preferable and suitable when a high heat transfer coefficient is required at Reynolds numbers below 2000 and only a modest pressure drop can be accepted at higher Reynolds numbers.

No previous reports on multiple V-shaped rib-roughened ducts are known to the authors. However, extensive work has been reported concerning rib-roughened ducts with angled and V-shaped ribs. For instance, Taslim et al. (1996) conducted experiments using liquid crystal thermography to determine local Nusselt numbers in a square channel with angled, V-shaped, and discrete ribs on two opposite walls. The distribution of local Nusselt numbers at $\text{Re} = 15{,}500$ indicated that high heat transfer is obtained where the secondary flow transports fluid toward a wall, while the heat transfer is low where the secondary flow is directed away from a wall. Han et al. (1978) investigated rib-roughened surfaces to determine the effects of rib-shape, angle of attack, and pitch-to-height ratio on friction and heat transfer in a parallel plate geometry at Reynolds numbers from 3000 to 30,000. Ribs at a 45 deg angle of attack were found to have superior heat transfer performance at a given friction power when compared to ribs at 90 deg angle of attack or when compared to sand-grain roughness. Han et al. (1991) reported heat transfer and friction data for square channels with parallel, crossed, and V-shaped ribs at Reynolds numbers from 15,000 to 90,000. They found the best heat transfer performance for V-shaped ribs pointing upstream. Rib-roughened circular tubes were investigated by Gee and Webb (1980) at Reynolds numbers from 6000 to 65,000, and they concluded that the preferred helix angle is approximately 45 deg.

There also exist some investigations on the thermal and hydraulic performance of commercial radiator tubes; see, e.g., Farrell et al. (1991) and Olsson and Sundén (1996a). In the latter report rib-roughened, dimpled, and offset strip fin tubes were investigated. It was found that the rib-roughened tubes provided the largest heat transfer increase per unit pressure drop increase.

Contributed by the Heat Transfer Division for publication in the JOURNAL OF HEAT TRANSFER. Manuscript received by the Heat Transfer Division, Sept. 25, 1996; revision received, June 1, 1998. Keywords: Augmentation and Enhancement, Forced Convection, Heat Exchangers. Associate Technical Editor: S. Ramadhyani.

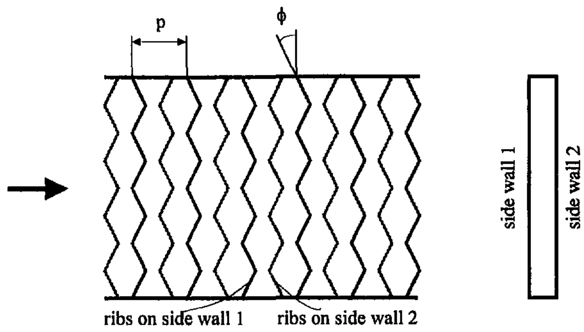

Fig. 1 Schematic drawing of the swirl flow duct. In the cross-sectional plane the ribs are not shown.

Table 1 Rib dimensions of the ducts

Duct	e/H	ϕ deg	p/H
SFD1	0.1	30	5
SFD2	0.2	30	5
SFD3	0.14	30	5
SFD4	0.1	15	5
SFD5	0.1	45	5
SFD6	0.1	30	3
SFD7	0.1	30	7
SFD8	0.1	45	3
SFD9	0.2	45	5
SFD10	0.1	45	5

Experimental Arrangement

The ducts tested are made in copper and have an internal cross section of 5 × 40 mm which yields a hydraulic diameter equal to 8.89 mm. The ducts are 500 mm long and they are manufactured in two parts—a 10 × 50 mm bar with a 5 mm deep and 40 mm wide milled slot and a 5 × 50 mm planar bar. The two parts are screwed together and sealed with an O-ring gasket. The multiple V-ribs are made of copper wires which are soldered on the wide walls in the ducts. Figure 1 shows a schematic drawing of the swirl flow duct geometry. Each set of four V-ribs is formed with one continuous copper wire so that there is a small radius of curvature at the rib corners. The soldering tin ensures thermal contact between the ribs and the wall, and it also fills up the crevices on each side of the wire which makes the rib shape very similar to what would be obtained if the ribs were formed through rolling or hobbing of the walls. To ensure that the chosen procedure was sufficiently accurate, sample pieces were inspected under a microscope. The rib height, the rib angle, and the rib pitch of the ducts tested are found in Table 1. The rib height is varied from 0.5 to 1.0 mm ($0.1 < e/H < 0.2$), the rib angle from 15 deg to 45 deg, and the rib pitch from 15 to 35 mm ($3 < p/H < 7$). The duct SFD 10 has the same geometrical parameters as SFD5, but it has a 1.0 mm slot between each rib element, which means that a set of multiple V-shaped ribs are not continuously connected. Due to the manufacturing process employed in the industry it may be difficult to realize continuous ribs, and it may be necessary to allow a small spacing between the rib elements. The duct SFD 5 is converted to SFD 10 through milling off the copper wire corners. This process results in sharp ends for all rib elements.

The pressure drop and heat transfer investigations were performed separately. Air was used in both tests and the pressure drop measurements were performed at isothermal conditions. The pressure drop rig consists of a fan, three rotameters to measure the flow rate (Krohne, flow ranges 0.12–1.2 m^3/h, 1.2–8 m^3/h, and 3–30 m^3/h, respectively), and a by-pass arrangement to control the flow. The air is sucked into the tested duct from the quiescent room. No bellmouth is used since the purpose is to simulate the real situation in radiators. The quiescent room corresponds to the big manifolds of the radiator. To enable pressure drop measurements the ducts are equipped with 10 pressure taps with 0.5 mm hole diameter. The distance between the pressure taps is 50 mm for all ducts except for SFD 6, 7, and 8 for which it is 45 mm, 35 mm, and 45 mm, respectively. The pressure taps are placed symmetrically over the duct length. By using the p/H-values in Table 1, the precise positions of the pressure taps in relation to the ribs can be found. As the presure drop is analyzed according to Eq. (1) no particular problem is envisaged in these measurements. The pressure drops are measured with a micromanometer, FCO14 Furness Controls Ltd., and the signals are recorded by a Macintosh II using a MacADIOS card.

The heat transfer test rig consists of a fan and the same flow rate control system as in the pressure drop test rig. In addition, there is a heating chamber upstream of the tested duct. Air is sucked into the duct from the heating chamber and no bellmouth contraction is used here either, since the objective is to simulate real inlet conditions in the radiator. In order to obtain constant temperature at the duct wall, the duct is mounted on a so-called water table. Water flows over the duct in cross flow with a speed of approximately 1 m/s, and a two-dimensional contraction is placed upstream the duct to make the water flow uniform. This provides the outer duct wall with a heat transfer coefficient that is much larger than the inside wall heat transfer coefficient. By using empirical formulas for the cross flow of water it may be estimated that the heat transfer coefficient on the water side is at least 35 times that of the air side. This will be considered in the section on estimation of uncertainty. The thermal resistance on the outer side is thus much less than that on the inside of the duct and is assumed negligible. Under the prevailing circumstances also the thermal resistance in the duct wall is negligible. It can therefore be assumed that the inside wall

Nomenclature

A = heat transfer area
A_c = duct cross-sectional area
c_p = specific heat
D_h = hydraulic diameter
e = rib height
f = Fanning friction factor
H = duct height
j = Colburn heat transfer factor ($=\mathrm{St}\,\mathrm{Pr}^{2/3}$)
K_c = inlet loss coefficient
L = duct length
Nu = average Nusselt number ($=\alpha D_h/\lambda$)
Pr = Prandtl number
p = rib pitch
Re = Reynolds number ($=u_m D_h/\nu$)
St = Stanton number (=Nu/Re Pr)
T = temperature
U = local axial mean velocity at LDV-measurements
u' = root-mean-square value of axial velocity fluctuations at LDV-measurements ($=u'$)
u_m = mean velocity
x = coordinate in the main flow direction

Greek Symbols

α = heat transfer coefficient
Δp = pressure drop
λ = thermal conductivity
ν = kinematic viscosity
ρ = density
ϕ = rib angle

Subscripts

fd = fully developed conditions
in = duct inlet
out = duct outlet
wall = duct wall

temperature is the same as the temperature of the water. Since the water flow rate is high and the heat flux modest, the water temperature can be considered as constant and uniform. The temperature difference (wall-air) at the inlet is approximately 70°C and the temperature difference at the outlet is 2–20°C depending on the flow rate and the rib-roughness in the duct.

The air temperatures are measured using 0.25 mm copper-constantan thermocouples, and the voltages are recorded by a Keithley 199 System DMM/Scanner. At the duct inlet and outlet two thermocouples are used. In the determination of the heat transfer coefficient the mean temperatures at the inlet and outlet are used. At the outlet there is a large difference between the maximum and the minimum temperature. To obtain the outlet bulk temperature accurately, the duct outlet is connected to an insulated enclosure where mixing takes place. The air leaves the enclosure through two circular holes in which the thermocouples are placed.

An additional thermocouple is used to measure the temperature at the flow meters. The water temperature is taken by a mercury thermometer. In the heat transfer rig no pressure drop measurements are carried out. Only the pressures downstream the duct and at the flow meters are taken so that the air density can be determined.

Data Evaluation

The pressure drop data are evaluated using the Fanning friction factor, f, and the inlet loss coefficient, K_c. These parameters are determined from the nondimensional pressure drop equation; see, e.g., Kakaç et al. (1987) and Eckert and Drake (1972),

$$\frac{\Delta p}{\rho u_m^2/2} = K_c + (f\ \mathrm{Re})_{\mathrm{fd}} \frac{4x}{D_h\,\mathrm{Re}}, \tag{1}$$

by performing a least-squares fit of a line to the straight part of the plot of $\Delta p/(\rho u_m^2/2)$ versus $x/(D_h\ \mathrm{Re})$. The slope is equal to $4(f\ \mathrm{Re})_{\mathrm{fd}}$, and the intercept is equal to K_c. The velocity u_m is the mean velocity calculated from the mass flow rate divided by the density and cross-sectional area of the duct. The cross-sectional area is measured at the base of the roughness elements. The Reynolds number is determined from

$$\mathrm{Re} = \frac{u_m D_h}{\nu}. \tag{2}$$

The heat transfer data are presented as Colburn heat transfer factor, j, versus Reynolds number. The j factor is defined as

$$j = \mathrm{St}\,\mathrm{Pr}^{2/3} = \frac{\alpha}{c_p \rho u_m}\mathrm{Pr}^{2/3} = \frac{\mathrm{Nu}}{\mathrm{Re}\,\mathrm{Pr}^{1/3}}. \tag{3}$$

The fluid properties are determined from the mean values of temperature and pressure upstream and downstream of the duct. The heat transfer coefficient is obtained as

$$\alpha = \frac{\rho u_m A_c c_p}{A} \ln \left| \frac{T_{\mathrm{in}} - T_{\mathrm{wall}}}{T_{\mathrm{out}} - T_{\mathrm{wall}}} \right| \tag{4}$$

where A_c is the cross-sectional area and A the heat transfer area. The ratio of these areas can be expressed as

$$\frac{A_c}{A} = \frac{D_h}{4L} \tag{5}$$

where L is the length of the duct.

Estimation of Uncertainty

The uncertainties of the components in the experiments have been estimated. The micromanometer has been calibrated to give a maximum error of less than ±1 percent. An important contribution to the pressure drop uncertainty is the error due to the scatter in the pressure drop data for each least-squares fit. This scatter is due to uncontrolled parameters such as the exact shape of the pressure tap holes, secondary flows, etc. The maximum errors in the slope $(4f\ \mathrm{Re})_{\mathrm{fd}}$ have been estimated with the maximum likelihood method and 95 percent confidence to be within ±5 percent; see, e.g., Box et al. (1978).

The thermocouples used in the heat transfer test rig are calibrated individually, and the maximum error is estimated to be ±0.05°C. This estimate also holds for the mercury thermometer used for measuring the water temperature. The inlet air temperature controlled by the heater varies up to ±0.5°C.

The rotameters have been calibrated and the error is less than ±1 percent. Corrections are also made to allow for changes in ambient temperature and pressure during the tests. The geometric quantities of the ducts have been determined within ±0.05 mm and the fluid properties are estimated to be within ±1 percent.

A root-sum-square combination of the effects of each of the individual sources of error (see, e.g., Moffat, 1988) yields the following estimates of the uncertainties: $f \pm 6$ percent, Re ± 2 percent, $j \pm 4$ percent. In general, the measurements showed to be reproducible well within these limits. However, it has not been possible to estimate the deviation between the measured outlet temperature and the true outlet bulk temperature. This problem may therefore give rise to an additional error in the heat transfer data.

An additional error in the j factor is due to finite values of the thermal resistances of heat conduction in the duct wall and forced convection on the outer side of the duct. The heat transfer coefficient on the water side is constant in these experiments while the inside air heat transfer coefficient (which is to be determined) is dependent on the flow rate. Thus the maximum error occurs at the highest air flow rate. This error is estimated to be less than −1 percent for laminar flow. For the highest flow rate this error is less than −5 percent. The negative sign means that the true values are greater than the measured and reported ones. There may also be an underestimation of the Nusselt number due to the sealings at the duct ends. The sealings cover less than 10 mm of each duct end, which for a 500 mm long duct may give an error up to 4 percent.

Results and Discussion

Figures 2(a) and 2(b), from Olsson and Sundén (1997a), show some features of the flow in one of the swirl flow ducts. Panel 1, in Fig. 2(a), shows a sketch of the conjectured secondary flow pattern that is expected to occur in the duct. A smoke wire visualization of the flow at Reynolds number equal to 1100 is presented in panel 2 of Fig. 2(a). The third panel provides the secondary flow velocity field. There is a good agreement between the visualization and the schematic pattern, which consists of eight longitudinal vortices which will exchange momentum and heat between the core region and the wide walls. In Fig. 2(b) contour plots of the axial mean velocity distribution and the r.m.s. axial velocity fluctuations are provided. Panel 3 in Fig. 2(a) and the two panels in Fig. 2(b) are obtained from LDV measurements at a Reynolds number equal to 3000 in a duct with $e/H = 0.1$, $p/H = 5$, and $\phi = 30$ deg. The cross section of the LDV measurements is located at a distance $p/4$ downstream of a set of ribs on the right-hand wall and a distance $p/4$ upstream of a set of ribs on the left hand wall. The effect of the secondary flow on the axial velociy, U/U_m, and axial turbulence intensity, u'/U_m, is shown by the contour plots in Fig. 2(b). High momentum fluid is convected either to the right or to the left by the secondary flow. In the regions of low momentum fluid, the axial velocity fluctuations are approximately twice those in the high momentum regions. Although the secondary flow is weak at the considered Reynolds number, it has a significant influence on the axial mean velocity and

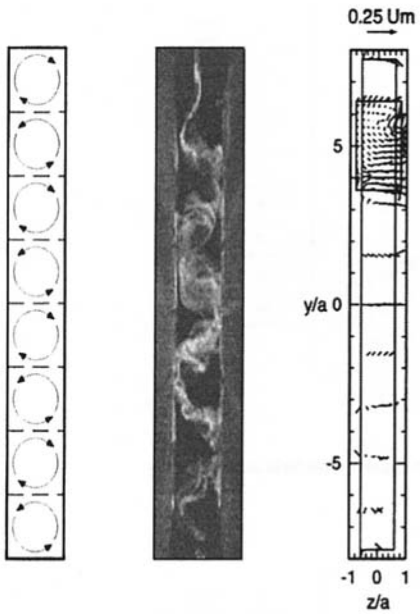

Fig. 2(*a*) **Secondary flow in a swirl flow duct. Panel 1: Conjectured flow pattern, Panel 2: Smoke wire visualization at Re = 1100, Panel 3: Secondary flow velocity vectors (Re = 3000).**

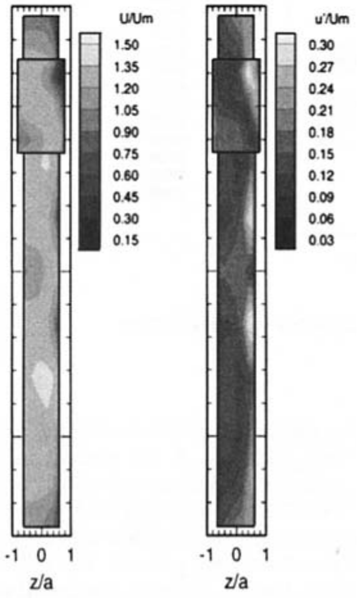

Fig. 2(*b*) **Contour plots of axial flow velocities. Panel 1: Mean velocity distribution, Panel 2: r.m.s. axial fluctuating velocity distribution (turbulence intensity). Re = 3000.**

velocity fluctuations, as is obvious in the contour plots in Fig. 2(*b*). According to Taslim et al. (1996) it is expected that high heat transfer coefficients will be obtained where fluid is transported towards the walls while low heat transfer coefficients will be obtained where fluid is transported away from the walls.

Figures 3 and 4 show the j and f factors, respectively, for the ducts investigated. The markers represent experimental data and the lines represent geometry-based correlations. In order to capture the different trends at laminar and turbulent flow, two sets of correlations are determined through least-squares fits to the data by using available MATLAB routines. The expressions are as follows:

$500 < \mathrm{Re} < 1500$:

$$f = 20.82\,\mathrm{Re}^{-0.5306}\left(\frac{e}{H}\right)^{0.9212}\left(\frac{p}{H}\right)^{-0.3513}\left(\frac{\phi}{90}\right)^{0.1886} \tag{6}$$

$$j = 2.313\,\mathrm{Re}^{-0.4948}\left(\frac{e}{H}\right)^{0.5275}\left(\frac{p}{H}\right)^{-0.2387}\left(\frac{\phi}{90}\right)^{0.2389} \tag{7}$$

$$\frac{j}{f} = 0.1111\,\mathrm{Re}^{0.0358}\left(\frac{e}{H}\right)^{-0.3937}\left(\frac{p}{H}\right)^{0.1126}\left(\frac{\phi}{90}\right)^{0.0503} \tag{8}$$

$2000 < \mathrm{Re} < 15{,}000$:

$$f = 1.028\,\mathrm{Re}^{0.0000}\left(\frac{e}{H}\right)^{1.2982}\left(\frac{p}{H}\right)^{-0.6108}\left(\frac{\phi}{90}\right)^{-0.0987} \tag{9}$$

(independent of Re)

$$j = 0.3221\,\mathrm{Re}^{-0.2457}\left(\frac{e}{H}\right)^{0.5160}\left(\frac{p}{H}\right)^{-0.3143}\left(\frac{\phi}{90}\right)^{0.0000} \tag{10}$$

(independent of ϕ)

$$\frac{j}{f} = 0.3133\,\mathrm{Re}^{-0.2457}\left(\frac{e}{H}\right)^{-0.7822}\left(\frac{p}{H}\right)^{0.2965}\left(\frac{\phi}{90}\right)^{0.0987} \tag{11}$$

The correlations are valid for $0.1 < e/H < 0.2$, $3 < p/H < 7$, and $0.167 < \phi/90 < 0.5$. For angles larger than 45 deg it is expected that the j and f factors will decrease with increasing angle; see, e.g., Gee and Webb (1980). It should be noted that the suggested correlations do not cover the Reynolds number range 1500–2000 which may be referred to as a transitional region as the measurement points indicate. For the friction factor, ducts SFD 3 and SFD 7 were most difficult to incorporate in the correlations. The maximum difference between the correlations and the experimental data is about ten percent. The correlations for the j-factor were generally closer with a maximum difference of at most five percent.

500 < Re < 1500. In the low Reynolds number range the slope of the j factor curves is close to -0.5 which is different from the slope of -1.0 for thermally developed conditions in a smooth duct. Hence, in addition to laminar diffusion another heat transfer mechanism is present in the flow, i.e., the secondary flow which redistributes warm and cold fluid and thereby enhances the heat transfer. This mechanism is intensified with increasing Reynolds number according to the slope of the curves. It can be noted from Fig. 3 that SFD 4, which takes the lowest position for Re < 1500, exhibits a steeper slope than the other ducts, indicating that the secondary flow is weaker than for the other ducts.

The f factors at this Reynolds number interval show a similar behavior as the j factors, and the slope of the curves is also close to -0.5, which implies that the j/f ratio is almost independent of Reynolds number. Increasing the rib height results in an increase in the j factor, but the accompanying increase in the f factor is greater which causes the j/f ratio to decrease. The effect of decreasing the rib pitch is similar to increasing the rib height. However, increasing the j factor ten percent through increasing the rib height with 19.8 percent results in a decrease in j/f of 6.9 percent, while the same j factor increase can be accomplished through decreasing the rib pitch with 30.8 percent which results in a decrease in j/f of only 4.1 percent. Increasing the rib angle increases both the j and the f factor and also the j/f ratio is increased, which points out that a 45 deg rib angle is the best choice of the rib angles included in the investigation.

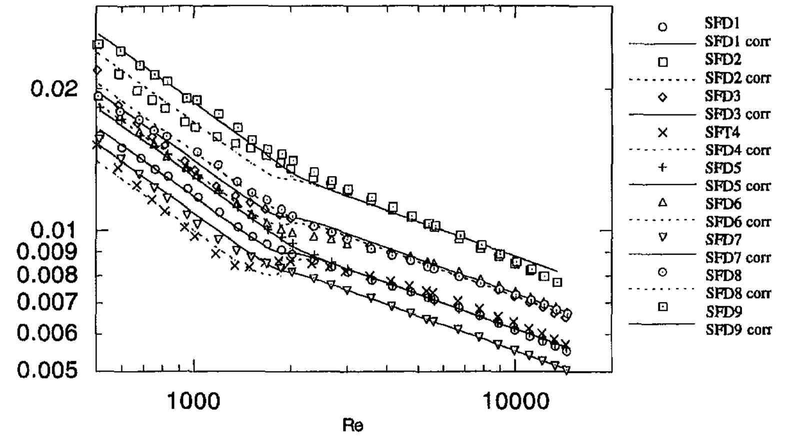

Fig. 3 *j* **factors versus Reynolds number. The markers are experimental data and the lines are given by Eqs. (7) and (10).**

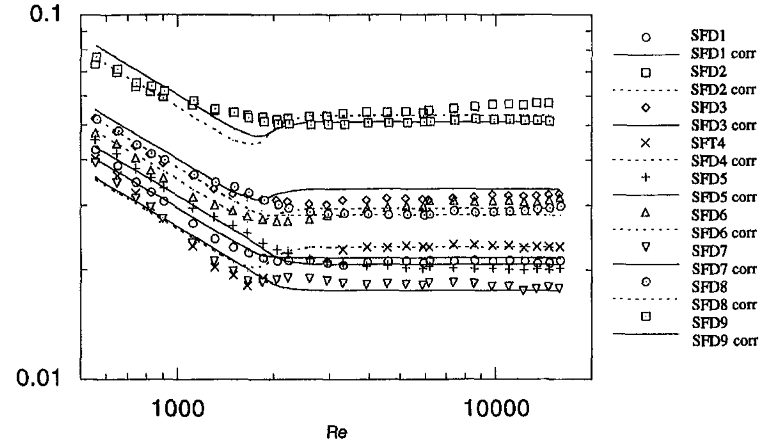

Fig. 4 *f* **factors versus Reynolds number. The markers are experimental data and the lines are given by Eqs. (6) and (9).**

2000 < Re < 15,000. For Reynolds numbers above 2000 the slope of the *j* factor curves is −0.25, which is in accordance with the Hausen correlation for smooth ducts and close to −0.2 as for the Dittus-Boelter correlation, see Kakaç et al. (1987). Therefore it seems likely that the same mechanism is dominating the heat transfer process for smooth ducts and for the swirl flow duct. The ribs are creating a secondary flow and increase the turbulent fluctuations which increases the heat transfer. However, the variation of the *j* factor with Reynolds number is similar to that for smooth ducts which indicates that the induced secondary flow has a limited influence on the heat transfer. The fact that the secondary flow is less important for Re > 2000 is seen in the correlation for the *j* factor, Eq. (10), which is independent of the rib angle. One may expect five different levels of the curves in Fig. 3 since there are five different combinations of e/H and p/H. However, SFD 3 and SFD 6 happen to provide almost the same level of the *j* factor.

The *f* factors at this Reynolds number interval do not show a similar behavior as the *j* factors. The data fall on almost horizontal lines, and the least-squares fit resulting in the *f* factor correlation, Eq. (11), produced an exponent of the Reynolds number equal to zero. This indicates that the flow is in the fully rough regime according to the Moody chart for pipe friction; see, e.g., White (1994). This means that the form drag of the ribs is the dominating contribution to the pressure drop, and this process is not connected with any heat transfer mechanism. Hence, the j/f ratio decreases with increasing Reynolds number with the same exponent as the *j* factor.

Increasing the rib height or decreasing the rib pitch results in increased *j* and *f* factors. A ten percent increase of the *j* factor may be achieved by increasing the rib height with 20.3 percent which will decrease j/f with 13.5 percent. It may also be achieved by decreasing the rib pitch with 26.2 percent which will decrease j/f with only 8.6 percent. The *j* factor is independent of the rib angle, but the *f* factor is decreased with increasing rib angle according to Fig. 4. Thus, the j/f ratio is increased with increasing rib angle, and accordingly the 45 deg rib angle produces the best results.

Performance Comparison. Figure 5 shows the j/f ratios obtained from the correlations, Eqs. (8) and (10), together with corresponding curves for a smooth duct. The smooth duct curves are obtained using $\mathrm{Nu} = 5.59$, $\mathrm{Pr} = 0.72$, and $f\ \mathrm{Re} = 20.6$, for laminar flow (see Shah and London, 1978) and the Dittus-Boelter correlation together with the Blasius relation for turbulent flow (see e.g., Kakaç et al., 1987). In laminar flow the j/f ratio for the smooth duct is a constant while in turbulent flow it is increasing slightly with increasing Reynolds number. In contrast to the smooth duct curves, the curves for the swirl flow ducts have a small positive slope at Reynolds numbers below 2000 while they have a negative slope for larger Reynolds numbers. It is also seen that all swirl flow ducts provide higher j/f ratios for Re < 2000 while they provide lower j/f ratios for Re > 2000. The shape of the curves reflects the different heat transfer and pressure drop mechanisms that are present. For Re < 2000 convection due to the secondary flow is added

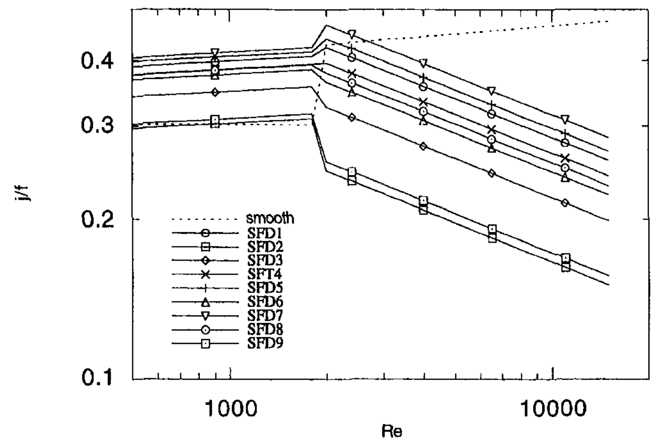

Fig. 5 Flow area goodness factor, j/f, versus Reynolds number. From Eqs. (8) and (11).

to the laminar diffusion of energy and momentum, and according to Fig. 5 the transport of energy is increased more than the transport of momentum. However, increasing the rib height or decreasing the rib pitch adds form drag and effects of recirculation and reattachment zones close to the ribs become more important which lower the j/f ratio. A maximum in j/f ratio is therefore expected, but it must occur at smaller e/H or larger p/H than those included in this investigation.

Discontinuous Ribs. The differences in j and f-factors between SFD 10 (with a 1 mm wide slot between each rib element) and SFD 5 were found to be very small. The actual shape of the rib corners is thus not important for the performance of the swirl flow duct.

Conclusions

The thermal and hydraulic performance of one to eight aspect ratio rectangular ducts with multiple V-shaped ribs has been investigated for Reynolds numbers from 500 to 15,000. Correlations based on the Reynolds number, the rib height ($0.1 < e/H < 0.2$), the rib pitch ($3 < p/H < 7$), and the rib angle ($15 \text{ deg} < \phi < 45 \text{ deg}$) have been presented.

Increasing the rib height or decreasing the rib pitch increases the j and f factors while the j/f ratio is decreased.

A 45 deg rib angle proved to be superior to smaller rib angles.

At $500 < \text{Re} < 1500$ the j/f ratio increases with Reynolds number, while at $\text{Re} > 2000$ the j/f ratio decreases with increasing Reynolds number.

At $\text{Re} > 2000$, the f factor is independent of the Reynolds number and the j factor is independent of the rib angle.

Acknowledgments

This work was accomplished under the sponsorship of AB Volvo and Valeo Engine Cooling AB.

References

Box, G. E. P., Hunter, W. G., and Hunter, J. S., 1978, *Statistics for Experimenters*, John Wiley and Sons, New York.

Eckert, E. R. G., and Drake, R. M., 1972, *Analysis of Heat and Mass Transfer*, McGraw-Hill, New York.

Farrell, P., Wert, K., and Webb, R. L., 1991, "Heat Transfer and Friction Characteristics of Turbulator Radiator Tubes," *SAE Transactions*, Vol. 100, Sect. 5, 910197, pp. 218–230.

Han, J. C., Glicksman, L. R., and Rohsenow, W. M., 1978, "An Investigation of Heat Transfer and Friction for Rib-Roughened Surfaces," *Int. J. Heat Mass Transfer*, Vol. 21, pp. 1143–1156.

Han, J. C., Zhang, Y. M., and Lee, C. P., 1991, "Augmented Heat Transfer in Square Channels With Parallel, Crossed, and V-Shaped Angled Ribs," ASME Journal of Heat Transfer, Vol. 113, pp. 590–596.

Kakaç, S., Shah, R. K., and Aung, W., *Handbook of Single-Phase Convective Heat Transfer*, John Wiley and Sons, New York, Chapters 3 and 4.

Gee, D. L., and Webb, R. L., 1980, "Forced Convection Heat Transfer in Helically Rib-Roughened Tubes," *Int. J. Heat Mass Transfer*, Vol. 23, pp. 1127–1136.

Moffat, R. J., 1988, "Describing the Uncertainties in Experimental Results," *Exp. Thermal Fluid Sci.*, Vol. 1, pp. 3–17.

Olsson, C. O., and Sundén, B., 1996a, "Heat Transfer and Pressure Drop Characteristics of Ten Radiator Tubes," *Int. J. Heat Mass Transfer*, Vol. 39, pp. 3211–3220.

Olsson, C. O., and Sundén, B., 1997a, "Experimental Study of Flow and Heat Transfer in Rib-Roughened Channels," *Exp. Thermal Fluid Sci.*, Vol. 16, pp. 349–365.

Olsson, C. O., and Sundén, B., 1997b, "Fluid Flow and Heat Transfer in Rib-Roughened Tubes," *Experimental Heat Transfer, Fluid Mechanics and Thermodynamics 1997*, Vol. 3, Edizioni ETS, Pisa, pp. 1655–1662.

Shah, R. K., and London, A. L., 1978, "Laminar Flow Forced Convection in Ducts," *Adv. in Heat Transfer*, Supplement 1, Academic Press, New York.

Taslim, M. E., Li, T., and Kercher, D. M., 1996, "Experimental Heat Transfer and Friction in Channels Roughened With Angled, V-Shaped, and Discrete Ribs on Two Opposite Walls," ASME *Journal of Turbomachinery*, Vol. 118, pp. 20–28.

White, F. M., 1994, *Fluid Mechanics*, 3rd Ed., McGraw-Hill, New York.

Journal of Heat Transfer

Technical Notes

This section contains shorter technical papers. These shorter papers will be subjected to the same review process as that for full papers.

Size Effects on the Thermodynamic Properties of Thin Solid Films

R. S. Prasher[1,3] **and P. E. Phelan**[2,3]

Introduction

In crystalline solids, the evaluation of internal energy (U), dependent on the wave characteristics of the vibrations of a lattice structure, under the Debye assumption is given by (Ashcroft and Mermin, 1976),

$$U = 3 \sum_{k} \frac{\hbar c k}{\exp\left(\frac{\hbar c k}{k_b T}\right) - 1}, \qquad (1)$$

where c is the Debye speed, k the wave vector, T the temperature, $\hbar$ the Planck constant, and k_b the Boltzmann constant. The summation is taken over all possible values of k. The allowed values of k in terms of its components are given by (Ashcroft and Mermin, 1976),

$$k_x = 0, \pm \frac{2\pi}{L_x}, \pm \frac{4\pi}{L_x} \ldots \pm \frac{N_x \pi}{L_x}, \quad \Delta k_x = \frac{2\pi}{L_x} = \frac{2\pi}{N_x a}, \qquad (2)$$

where Δk_x is the difference in consecutive wave vectors in a particular direction. Similar relations hold for the components of k in other directions.

In a bulk solid Eq. (1) reduces to

$$u_{\text{bulk}} = 9 n k_b T \left(\frac{T}{\theta}\right)^3 \int_0^{X_d} \frac{X^3}{\exp(X) - 1} dX, \qquad (3)$$

where u_{bulk} is U per unit volume for a bulk solid. The above expression of u only gives the contribution from the bulk phonon modes, which means that the surface contribution is neglected. In a bulk solid the contribution from the surface phonon modes is negligible. In the analysis to follow, the size effects on the thermodynamic properties, dependent only on the bulk phonon mode, are considered for a thin-film structure. Although there have been quite a good number of experimental and theoretical studies on the heat capacity of small particles (Zally and Mochel, 1972; Allen and De Wette, 1969; Novotny and Meincke, 1973), the size effect on the heat capacity due to bulk phonon modes has been neglected. Most of the work on the heat capacity of small particles has been done for approximately spherical particles of the dimension of the order of 20 Å (Novotny and Meincke, 1973), where the contribution of the surface modes becomes very prominent as the surface-to-volume ratio is very large. But a thin-film structure is semi-infinite in two directions and it is reasonable to expect that the heat-holding capacity of the structure is primarily due to the excitation of the bulk phonon modes. Size effects on bulk lattice properties have also been described in the past (Grille et al., 1996), but in general these results are not in a form that is useful for engineering calculations. In this paper, any thermodynamic property of the bulk solid or of the thin film refers only to that originating from the contribution of the bulk phonon modes.

It is well known that as the dimension of a specimen decreases the evaluation of u, and heat capacity per unit volume, C, by the usual integral method Eq. (3) is not valid; rather, the original summation of Eq. (1) has to be retained. Accordingly, here an approximate procedure for calculating u and C by summation (that is, for very thin films) is presented, in which it is shown that the value of the Debye wave vector (k_d) remains almost unchanged, even at these short length scales. Furthermore, a novel nondimensional parameter is introduced which accurately captures the microscale effects on the thermodynamic properties, caused by both small length scales as well as low temperatures. Use of this nondimensional parameter allows the thermodynamic properties of any thin film to be easily calculated from the present results, provided the bulk thermodynamic properties at the temperature of interest are already known.

If the number of atoms in any one dimension is very small compared to the other two, e.g., $N_x \ll N_y$, and N_z, then the change in k, Δk, will not be negligibly small compared to the total allowed values of k (Rosenberg, 1988). As a result, k in that direction will increase in fairly large discrete steps on the scale of $2\pi/L$, making the use of an integral to approximate the discrete summation in Eq. (3) suspect. Here N_x is assumed to be much smaller than N_y and N_z. In this case the usual method for calculating the number of states (N) in the k space cannot be used (Prasher and Phelan, 1998), as evident from Fig. 1 for an equivalent inverse two-dimensional lattice. The area of each rectangle is too large to give the exact number of points inside the circle of radius k. There are two opposing effects taking place: (i) the exact number of points in the k space is not the same as that for a bulk solid and (ii) the volume Ω of the k

---

[1] Graduate Student

[2] Assistant Professor. Corresponding author e-mail: phelan@asu.edu.

[3] Department of Mechanical and Aerospace Engineering, Arizona State University, Tempe, AZ 85287-6106.

Contributed by the Heat Transfer Division for publication in the JOURNAL OF HEAT TRANSFER and presented at the '98 NHTC, Albuquerque. Manuscript received by the Heat Transfer Division, Dec. 30, 1997; revision received, July 22, 1998. Keywords: Heat Transfer, Low Temperature, Thermophysical, Thin Films. Associate Technical Editor: A. Majumdar.

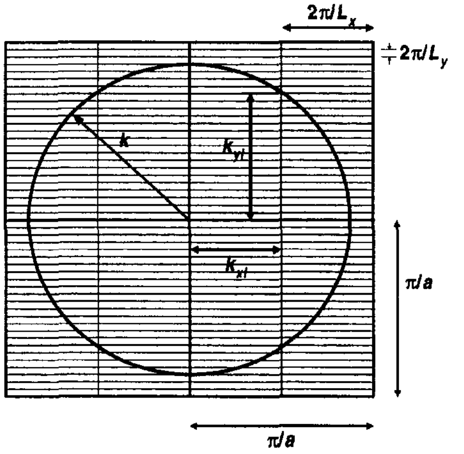

Fig. 1 Inverse two-dimensional lattice with much fewer number of atoms in the *x*-direction compared to the *y*-direction

space has to be evaluated using summation (Rosenberg, 1988). The exact evaluation of the number of points within a region in k space therefore has to be determined by evaluating the discrete summation directly. A method is developed in Section 3 to observe this effect on the value of N. The details of the analysis to follow are given in the article by Prasher and Phelan (1998).

Internal Energy and Heat Capacity for $N_x \ll N_y$ and $N_x \ll N_z$

Lattice. The initial analysis is performed for a two-dimensional lattice for simplicity, i.e., with N_x and N_y atoms in the x and y-directions, respectively, and is extended later to a three-dimensional lattice. First a quantity ϵ is defined as the ratio of the exact number of points within the k space (N_{exact}) to the number of points given for a k region of circular shape (N_{circular}), which is valid for a bulk solid:

$$\epsilon = \frac{N_{\text{exact}}}{N_{\text{circular}}} \tag{4}$$

where for a two-dimensional lattice N_{circular} is given by

$$N_{\text{circular}} = \frac{Ak^2}{4\pi} \tag{5}$$

where $A = L_x L_y$ is the area of the two-dimensional lattice.

The quantity ϵ will approach unity for large values of N_x and N_y, but will be greater than one if N_x or N_y is relatively small. In general ϵ will be a function of k and will be comparatively larger than unity for a small k than for a large k, because as k decreases the area of the circle decreases, and the area of each rectangle becomes comparable to the area of the circle (Fig. 1). In order to simplify the calculation, ϵ is determined only for a k equal to the Brillouin zone. Strictly speaking this only gives a very conservative estimate of ϵ.

Now N_{circular} can be easily reduced to the following form for $k = \pi/a$ (the first Brillouin zone):

$$N_{\text{circular}} = \frac{\pi}{4} N_x N_y. \tag{6}$$

For the calculation of N_{exact}, k_x and k_y for the first quadrant are given by

$$k_{x_i} = \left(\frac{2\pi}{L_x}\right) i, \quad i = 0 \ldots \frac{N_x}{2} \tag{7}$$

$$k_{y_i} = \left(\frac{\pi}{a}\right) \frac{1}{N_x} \sqrt{N_x^2 - 4i^2}. \tag{8}$$

Therefore the total number of points in the k space is given as

$$N_{\text{exact}} = 4 \sum_{i=0}^{N_x/2} \frac{k_{y_i}}{2\pi/L_y} = \frac{2N_y}{N_x} \sum_{i=0}^{N_x/2} \sqrt{N_x^2 - 4i^2}. \tag{9}$$

From its definition in Eqs. (4) and (6), and employing Eq. (9), ϵ becomes

$$\epsilon = \frac{8}{\pi N_x^2} \sum_{i=0}^{N_x/2} \sqrt{N_x^2 - 4i^2}. \tag{10}$$

Three-Dimensional Lattice. Until this point, for simplicity the analysis has been described for a two-dimensional lattice. In real materials, of course, three-dimensional lattices are the norm. A similar procedure for a three-dimensional lattice yields (Prasher and Phelan, 1998)

$$\epsilon = \frac{3}{N_x^3} \sum_{i=0}^{N_x/2} (N_x^2 - 4i^2). \tag{11}$$

The value of ϵ is greater than 1 and Ω for a thin film is less than that for a bulk solid, resulting in two opposing effects. These two opposing effects keep k_d effectively a constant. Therefore, to simplify the analysis to follow k_d will be taken as the classical value, and hence the Debye temperature remains unchanged. If ϵ is not taken into consideration then k_d will increase leading to an increase in the Debye temperature (Grille et al., 1996).

Now after including ϵ, the number of states (ΔN) in the k space of small volume $\Delta\Omega$ is given by

$$\Delta N = \frac{V\epsilon}{(2\pi)^3} \Delta\Omega \tag{12}$$

where $\Delta\Omega = \Delta k_x \Delta k_y \Delta k_y$ and V is the volume of the solid. Using Eq. (12), U from Eq. (1) can be written as

$$\frac{U}{V} = u = 3 \frac{\epsilon \hbar c}{(2\pi)^3} \sum_{k_x} \sum_{k_y} \sum_{k_z} \frac{\sqrt{k_x^2 + k_y^2 + k_z^2}}{\exp\left(\frac{\hbar c \sqrt{k_x^2 + k_y^2 + k_z^2}}{k_b T}\right) - 1} \times \Delta k_x \Delta k_y \Delta k_z. \tag{13}$$

The quantity ϵ has been taken out of the summation in Eq. (13) as it has been treated as a constant, but strictly speaking it should be kept inside the summation, as it is actually a function of k, as mentioned earlier.

The values of Δk_y and Δk_z are sufficiently small to replace them by dk_y and dk_x and the summation over k_y and k_z in Eq. (13) by integrals, reducing it to

$$u_{\text{micro}} = \frac{24\epsilon\hbar c}{(2\pi)^3} \times \sum_{k_x} \left[\int_0^{\sqrt{k_d^2 - k_x^2}} \int_0^{\sqrt{k_d^2 - k_x^2 - k_y^2}} \frac{\sqrt{k_x^2 + k_y^2 + k_z^2}\, dk_z dk_y}{\exp\left(\frac{\hbar c \sqrt{k_x^2 + k_y^2 + k_z^2}}{k_b T}\right) - 1} \right] \times \Delta k_x \tag{14}$$

where u_{micro} denotes the internal energy calculated by summation, i.e., the microscale internal energy. The heat capacity at constant volume is simply $(\partial u/\partial T)_{V=\text{constant}}$. Therefore taking this analysis one step further, the heat capacity can be calculated.

Nondimensionalization of Results

Calculations utilizing the analysis of the preceding section are performed for materials used in the semiconductor industry to emphasize the importance of thickness on the thermal properties of thin films. Only the result on the size effects on C is

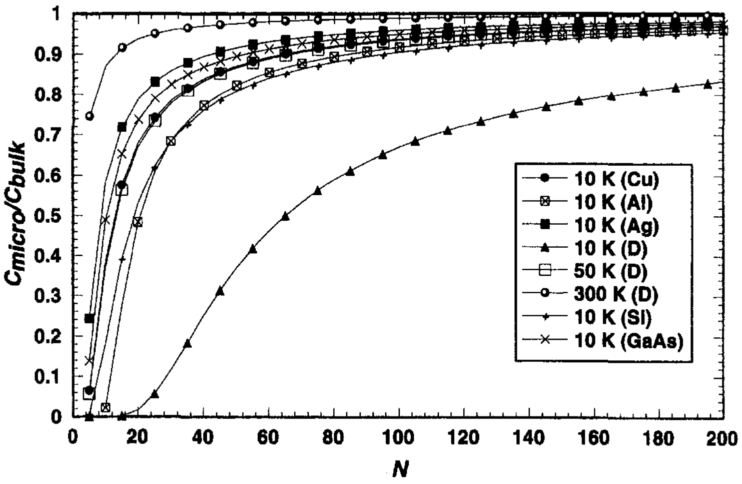

Fig. 2 Ratio of C_{micro} and C_{bulk} versus the number of atomic layers. The symbol "*D*" refers to diamond.

shown and it can be analogously applied for u. The low temperature values of θ are utilized, as the size effects are prominent mainly at low temperatures. The initial result is shown in Fig. 2. In Fig. 2 the ratio of the microscopic and the bulk values of C versus the number of atomic layers, for fixed values of temperature, are plotted for six materials. The purpose of Fig. 2 is to show the effects of temperature and number of atomic layers on the thermal properties of thin films. Figure 2 demonstrates that at low temperatures, the thermal properties calculated by summation are less than the bulk values for fewer atomic layers, or equivalently, for smaller film thickness. The physics of this behavior of the thermal properties of thin films are quite apparent. From Eq. (2) it can be seen that for small values of N_x, Δk_x is large, leading to high values of k_x and thereby increasing the magnitude of the wave vector k. At low temperatures, however, only the oscillators having small k are excited. So the number of oscillators excited per unit volume for a thin film is less than that for a bulk lattice.

The number of excited phonon modes of wave vector k, if the Debye approximation used, is given by

$$n = \frac{1}{\exp\left(\frac{\hbar c k}{k_b T}\right) - 1} = \frac{1}{\exp\left(\frac{1}{Y}\right) - 1} \tag{15}$$

where $Y = k_b T/\hbar c k$. It was shown by Prasher and Phelan (1998) that size effects are prominent only in the low-temperature regime where the bulk C is proportional to T^3. In this regime only long wavelength acoustic modes are excited, i.e., modes with $\hbar c k \ll k_b T$. The excitation of these modes is approximately classical in nature as shown below. Thus for the bulk case $Y \gg 1$, making $1/Y \ll 1$. Therefore by the expansion of the exponential function, Eq. (15) can be reduced to (Kittel, 1986)

$$n = \frac{1}{1/Y + 1/2Y^2 + \dots} \cong Y = \frac{k_b T}{\hbar c k} \tag{16}$$

where the second-order and above terms are neglected. Thus the excitation of these modes is approximately classical (Kittel, 1986). Of the allowed volume in k space, the fraction occupied by the excited modes is of the order of $(k_T/k_d)^3$, where k_T is a thermal wave vector (Kittel, 1986) which yields a macroscopic heat capacity that varies as

$$C_{\text{bulk}} \propto \left(\frac{T}{\theta}\right)^3 . \tag{17}$$

For the microscopic case $Y \gtrsim 1$ as k is relatively large compared to the macroscopic case. Thus the second-order term in Eq. (16) is retained and again a thermal wave vector, $k_{T_{\text{micro}}}$, analogous to k_T, can be defined:

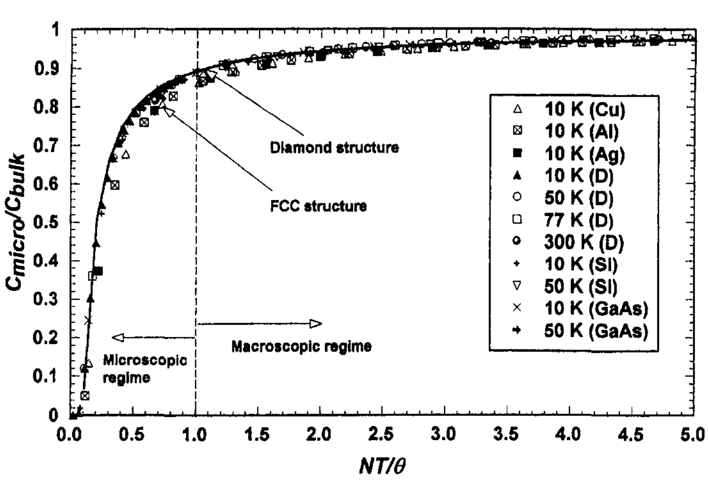

Fig. 3 Ratio of C_{micro} and C_{bulk} versus the nondimensional parameter NT/θ. The solid line indicates the analytical fit for a diamond lattice.

$$\hbar c k_{T_{\text{micro}}} = \frac{2(k_b T)^2}{2k_b T + \hbar c k}, \tag{18}$$

which after some simplifications, gives

$$\left(\frac{k_{T_{\text{micro}}}}{k_d}\right)^3 = \left(\frac{T}{\theta}\right)^3 \left(1 - 3\frac{\hbar c k}{k_b T}\right) = \left(\frac{T}{\theta}\right)^3 \left(1 - 3\frac{k\theta}{Tk_d}\right) \tag{19}$$

where k in Eq. (19) can be conveniently replaced by Δk_x because the maximum contribution to the excited modes will come from $k_x = \Delta k_x = 2\pi/N_x a$. Therefore

$$C_{\text{micro}} \propto \left(\frac{k_{T_{\text{micro}}}}{k_d}\right)^3 = \left(\frac{T}{\theta}\right)^3 \left(1 - 3\frac{k\theta}{2Tk_d}\right)$$

$$= \left(\frac{T}{\theta}\right)^3 \left(1 - 3\frac{2\pi\theta}{2N_x a T k_d}\right) = \left(\frac{T}{\theta}\right)^3 \left(1 - \frac{H\theta}{N_x T}\right) \tag{20}$$

where H is a constant.

Thus with the aid of Eqs. (17) and (20) the ratio of the microscopic and the bulk heat capacities is given by

$$\frac{C_{\text{micro}}}{C_{\text{bulk}}} = \left(1 - \frac{H\theta}{N_x T}\right). \tag{21}$$

Thus Eq. (21) clearly depicts the dependence of $C_{\text{micro}}/C_{\text{bulk}}$ on a nondimensional parameter, NT/θ.

Using Eq. (21), and realizing that heat capacity is of more practical interest than internal energy, a curve fit of the following form is employed for the heat capacity and is shown in Fig. 3, which gives

$$\frac{C_{\text{micro}}}{C_{\text{macro}}} = \alpha - \frac{\beta}{NT/\theta} \tag{22}$$

where α and β are constants. The values of α and β are found to be $\alpha = 0.9932$, $\beta = 0.102$ for a diamond lattice structure and $\alpha = 0.9850$, $\beta = 0.1177$ for an FCC lattice structure. Equation (22) can be conveniently used to calculate the microscopic values of the heat capacity from the known values of the bulk heat capacity, for any film thickness and temperature.

Figure 3 also shows that $NT/\theta = 1$ is the demarcation between the microscopic and macroscopic thermodynamic regimes. Thus $NT/\theta = 1$ marks the boundary between the *macroscopic* and the *microscopic* regimes of thermal properties. For $NT/\theta > 1$, the bulk (macroscopic) values of the thermal properties can be applied with little error. For $NT/\theta < 1$ the microscopic values must be considered.

The temperature where the onset to the microscopic regime occurs, T_{on}, is defined from

$$\frac{NT_{on}}{\theta} = 1 \text{ (start of microscopic regime)} \tag{23}$$

which can also be written as

$$LT_{on} = a\theta \tag{24}$$

where L is the film thickness. For any $LT < LT_{on}$ the microscopic value of the thermal properties must be considered. Thus LT_{on} denoting the onset of the microscopic regime is a property of a given material, and can be easily determined from Eq. (24). As an example, $LT_{on} = 8000$ ÅK for diamond.

Since θ is also a function of the lattice structure, the curves for different lattice structures are not exactly the same, as indicated in Fig. 3, which shows two distinct (but close) groupings: materials having a diamond structure (diamond, silicon, and GaAs), and those having an FCC structure (copper, aluminum, and silver).

Conclusions

The analysis presented here presents a simplified procedure for calculating size effects on the thermodynamic properties of thin films. These size effects are most important at cryogenic temperatures, where the heat capacity of bulk materials is proportional to T^3. A nondimensional parameter that combines the effects of temperature and film thickness is presented that accurately defines the onset of the microscopic regime. This parameter allows the heat capacity and the internal energy of any thin film to be easily determined for any temperature and film thickness. A convenient form for finding the onset of the microscopic regime is also given in terms of the actual thickness and temperature of the films.

Acknowledgments

The authors would like to acknowledge the help of Sashishekara S. Talya in evaluating the integrals. P.E.P. gratefully acknowledges the support of the National Science Foundation through a CAREER Award (Grant No CTS-9696003).

References

Allen, R. F., and De Wette, F. W., 1969, "Calculation of Dynamical Surface Properties of Noble-Gas Crystals. I. The Quasiharmonic Approximation," *Physical Review*, Vol. 179, pp. 873–886.

Ashcroft, N. W., Mermin, N. D., 1976, *Solid State Physics*, W. B. Saunders, Philadelphia, PA, pp. 415–450.

Grille, H., Karch, K., and Bechstedt, F., 1996, "Thermal Properties of $(\text{GaAs})_N$-$(\text{Ga}_{1-x}\text{Al}_x\text{As})_N$(001) Superlattices," *Physica B*, Vol. 219 and 220, pp. 690–692.

Kittel, C., 1986, *Introduction to Solid State Physics*, John Wiley and Sons (SEA) PTE LTD, Singapore, pp. 80–124.

Novotny, V., and Meincke, P. P. M., 1973, "Thermodynamic Lattice and Electronic Properties of Small Particles," *Physical Review B*, Vol. 8, pp. 4186–4199.

Prasher, R. S., and Phelan, P. E., 1998, "Size Effects on the Thermodynamic Properties of Thin Films," *AIAA/ASME Joint Thermophysics and Heat Transfer Conference*, Albuquerque, NM, pp. 195–203.

Rosenberg, H. M., 1988, *The Solid State*, Oxford University Press, New York, pp. 95–105.

Zally, G. D., and Mochel, J. M., 1972, "Fluctuation Contribution to the Heat Capacity of Amorphous Superconducting Films," *Physical Review B*, Vol. 6, pp. 4142–4150.

A Conservative Numerical Scheme for the Energy Equation

J. Y. Murthy[1,2] and S. R. Mathur[1,2]

Nomenclature

C_p = specific heat
E = total energy ($=U + u_i u_i/2$)
g = acceleration due to gravity
J = mass flow rate
$\mathcal{H}$ = total enthalpy
k = thermal conductivity
Nu = Nusselt number ($=qL/k(T_h - T_c)$)
p = static pressure
Pr = Prandtl number
q = mean heat flux
S_h = energy source per unit volume
t = time

---

[1] Fluent, Inc., 10 Cavendish Court, Lebanon, NH 03766.

[2] Mem. ASME.

Contributed by the Heat Transfer Division for publication in the JOURNAL OF HEAT TRANSFER. Manuscript received by the Heat Transfer Division, June 9, 1997; revision received, May 20, 1998. Keywords: Conduction, Numerical Methods, Transient and Unsteady Heat Transfer. Associate Technical Editor: R. Douglass.

$$\hbar c k_{T_{\text{micro}}} = \frac{2(k_b T)^2}{2k_b T + \hbar c k}, \tag{18}$$

which after some simplifications, gives

$$\left(\frac{k_{T_{\text{micro}}}}{k_d}\right)^3 = \left(\frac{T}{\theta}\right)^3 \left(1 - 3\frac{\hbar c k}{k_b T}\right) = \left(\frac{T}{\theta}\right)^3 \left(1 - 3\frac{k\theta}{Tk_d}\right) \tag{19}$$

where k in Eq. (19) can be conveniently replaced by Δk_x because the maximum contribution to the excited modes will come from $k_x = \Delta k_x = 2\pi/N_x a$. Therefore

$$C_{\text{micro}} \propto \left(\frac{k_{T_{\text{micro}}}}{k_d}\right)^3 = \left(\frac{T}{\theta}\right)^3 \left(1 - 3\frac{k\theta}{2Tk_d}\right)$$

$$= \left(\frac{T}{\theta}\right)^3 \left(1 - 3\frac{2\pi\theta}{2N_x a T k_d}\right) = \left(\frac{T}{\theta}\right)^3 \left(1 - \frac{H\theta}{N_x T}\right) \tag{20}$$

where H is a constant.

Thus with the aid of Eqs. (17) and (20) the ratio of the microscopic and the bulk heat capacities is given by

$$\frac{C_{\text{micro}}}{C_{\text{bulk}}} = \left(1 - \frac{H\theta}{N_x T}\right). \tag{21}$$

Thus Eq. (21) clearly depicts the dependence of $C_{\text{micro}}/C_{\text{bulk}}$ on a nondimensional parameter, NT/θ.

Using Eq. (21), and realizing that heat capacity is of more practical interest than internal energy, a curve fit of the following form is employed for the heat capacity and is shown in Fig. 3, which gives

$$\frac{C_{\text{micro}}}{C_{\text{macro}}} = \alpha - \frac{\beta}{NT/\theta} \tag{22}$$

where α and β are constants. The values of α and β are found to be $\alpha = 0.9932$, $\beta = 0.102$ for a diamond lattice structure and $\alpha = 0.9850$, $\beta = 0.1177$ for an FCC lattice structure. Equation (22) can be conveniently used to calculate the microscopic values of the heat capacity from the known values of the bulk heat capacity, for any film thickness and temperature.

Figure 3 also shows that $NT/\theta = 1$ is the demarcation between the microscopic and macroscopic thermodynamic regimes. Thus $NT/\theta = 1$ marks the boundary between the *macroscopic* and the *microscopic* regimes of thermal properties. For $NT/\theta > 1$, the bulk (macroscopic) values of the thermal properties can be applied with little error. For $NT/\theta < 1$ the microscopic values must be considered.

The temperature where the onset to the microscopic regime occurs, T_{on}, is defined from

$$\frac{NT_{on}}{\theta} = 1 \text{ (start of microscopic regime)} \tag{23}$$

which can also be written as

$$LT_{on} = a\theta \tag{24}$$

where L is the film thickness. For any $LT < LT_{on}$ the microscopic value of the thermal properties must be considered. Thus LT_{on} denoting the onset of the microscopic regime is a property of a given material, and can be easily determined from Eq. (24). As an example, $LT_{on} = 8000$ ÅK for diamond.

Since θ is also a function of the lattice structure, the curves for different lattice structures are not exactly the same, as indicated in Fig. 3, which shows two distinct (but close) groupings: materials having a diamond structure (diamond, silicon, and GaAs), and those having an FCC structure (copper, aluminum, and silver).

Conclusions

The analysis presented here presents a simplified procedure for calculating size effects on the thermodynamic properties of thin films. These size effects are most important at cryogenic temperatures, where the heat capacity of bulk materials is proportional to T^3. A nondimensional parameter that combines the effects of temperature and film thickness is presented that accurately defines the onset of the microscopic regime. This parameter allows the heat capacity and the internal energy of any thin film to be easily determined for any temperature and film thickness. A convenient form for finding the onset of the microscopic regime is also given in terms of the actual thickness and temperature of the films.

Acknowledgments

The authors would like to acknowledge the help of Sashishekara S. Talya in evaluating the integrals. P.E.P. gratefully acknowledges the support of the National Science Foundation through a CAREER Award (Grant No CTS-9696003).

References

Allen, R. F., and De Wette, F. W., 1969, "Calculation of Dynamical Surface Properties of Noble-Gas Crystals. I. The Quasiharmonic Approximation," *Physical Review*, Vol. 179, pp. 873–886.

Ashcroft, N. W., Mermin, N. D., 1976, *Solid State Physics*, W. B. Saunders, Philadelphia, PA, pp. 415–450.

Grille, H., Karch, K., and Bechstedt, F., 1996, "Thermal Properties of $(\mathrm{GaAs})_N$-$(\mathrm{Ga}_{1-x}\mathrm{Al}_x\mathrm{As})_N(001)$ Superlattices," *Physica B*, Vol. 219 and 220, pp. 690–692.

Kittel, C., 1986, *Introduction to Solid State Physics*, John Wiley and Sons (SEA) PTE LTD, Singapore, pp. 80–124.

Novotny, V., and Meincke, P. P. M., 1973, "Thermodynamic Lattice and Electronic Properties of Small Particles," *Physical Review B*, Vol. 8, pp. 4186–4199.

Prasher, R. S., and Phelan, P. E., 1998, "Size Effects on the Thermodynamic Properties of Thin Films," *AIAA/ASME Joint Thermophysics and Heat Transfer Conference*, Albuquerque, NM, pp. 195–203.

Rosenberg, H. M., 1988, *The Solid State*, Oxford University Press, New York, pp. 95–105.

Zally, G. D., and Mochel, J. M., 1972, "Fluctuation Contribution to the Heat Capacity of Amorphous Superconducting Films," *Physical Review B*, Vol. 6, pp. 4142–4150.

A Conservative Numerical Scheme for the Energy Equation

J. Y. Murthy[1,2] and S. R. Mathur[1,2]

Nomenclature

C_p = specific heat
E = total energy ($=U + u_i u_i/2$)
g = acceleration due to gravity
J = mass flow rate
$\mathscr{H}$ = total enthalpy
k = thermal conductivity
Nu = Nusselt number ($=qL/k(T_h - T_c)$)
p = static pressure
Pr = Prandtl number
q = mean heat flux
S_h = energy source per unit volume
t = time

---

[1] Fluent, Inc., 10 Cavendish Court, Lebanon, NH 03766.

[2] Mem. ASME.

Contributed by the Heat Transfer Division for publication in the JOURNAL OF HEAT TRANSFER. Manuscript received by the Heat Transfer Division, June 9, 1997; revision received, May 20, 1998. Keywords: Conduction, Numerical Methods, Transient and Unsteady Heat Transfer. Associate Technical Editor: R. Douglass.

T = temperature
U = internal energy
u_i = velocity component in i direction
x_i = coordinate direction
α = thermal diffusivity
$\Delta \mathscr{V}$ = volume of control volume
ρ = density
τ_{ij} = stress tensor

Introduction

Conservative numerical methods for solving transport problems have been in existence for over three decades now. Implicit schemes for the solution of the convection-diffusion equation for a transported scalar have been described by Patankar (1980) and others (Peric, 1985; Mathur and Murthy, 1997). These schemes have been applied to fluid flow, heat transfer, combustion, and other areas, and successful numerical simulations of complex industrial problems are now routinely being obtained.

Though these methods are applicable to the energy equation (and indeed, are routinely used), care must be taken in obtaining robust *conservative* formulations, especially in the presence of temperature-dependent properties, viscous dissipation, chemical reaction, compressibility, and other complications. The primary difficulty lies is the fact that the convective and unsteady terms in the energy equation are most conveniently written in terms of total enthalpy or energy, whereas the diffusion terms are most naturally written in terms of gradients of temperature. However, if implicit numerical schemes are to be used (see, for example, Patankar 1980), it is desirable to have both the right and left-hand sides of the equation expressed in terms of the same dependent variable, either total enthalpy or temperature. It is possible to write the diffusion terms in terms of enthalpy, but this not desirable for conjugate heat transfer problems where step jumps in C_p make the enthalpy double-valued on fluid-solid boundaries. Also, boundary conditions are most naturally written in terms of temperature; conversion to enthalpy form of complex boundary conditions, such as for radiation or surface reaction, is not convenient. On the other hand, writing the convective side in terms of temperature renders the equation nonconservative if C_p is variable, and even conservative numerical schemes cannot guarantee the conservation of total enthalpy in adiabatic flows.

The objective of this paper is to devise an iterative numerical method which allows a robust implicit solution of the energy equation while guaranteeing complete conservation at convergence. Temperature is used as the primary dependent variable. The development is done using unstructured meshes composed of arbitrary polyhedra (Mathur and Murthy, 1997), though the basic idea can be used with more conventional finite volume discretizations as well. Details of the discretization of the governing equations and boundary conditions may be found may be found in Mathur and Murthy (1997) and Murthy and Mathur (1997) and are not repeated here.

Total Energy, Total Enthalpy, and Temperature Equations

The equation for the conservation of energy for compressible variable property flow of a Newtonian fluid may be written in terms of the total energy E as

$$\frac{\partial}{\partial t}(\rho E) + \frac{\partial}{\partial x_i}(\rho u_i E) = \frac{\partial}{\partial x_i}\left(k \frac{\partial T}{\partial x_i}\right) + \frac{\partial \tau_{ij} u_j}{\partial x_i} - \frac{\partial p u_i}{\partial x_i} + S_h. \quad (1)$$

Here τ_{ij} is the stress tensor given by

$$\tau_{ij} = \mu\left(\frac{\partial u_i}{\partial x_j} + \frac{\partial u_j}{\partial x_i}\right) - \frac{2}{3}\mu \frac{\partial u_l}{\partial x_l}\delta_{ij}. \quad (2)$$

The same equation may be written in terms of the total enthalpy $\mathscr{H}$, defined as

$$\mathscr{H} = E + \frac{p}{\rho} = h_{\text{ref}} + \int_{T_{\text{ref}}}^{T} C_p dT + \frac{u_i u_i}{2} \quad (3)$$

where h_{ref} is the reference enthalpy at the reference temperature T_{ref}. For incompressible flows, we assume $\mathscr{H} \approx E \approx U$. Defining

$$H = \begin{array}{ll} \mathscr{H} + \dfrac{p}{\rho} & \text{for incompressible flow} \\ \mathscr{H} & \text{otherwise} \end{array} \quad (4)$$

we may write Eq. (1) as

$$\frac{\partial}{\partial t}(\rho H) + \frac{\partial}{\partial x_i}(\rho u_i H) = \frac{\partial}{\partial x_i}\left(k \frac{\partial T}{\partial x_i}\right) + \frac{\partial \tau_{ij} u_j}{\partial x_i} + \frac{\partial p}{\partial t} + S_h. \quad (5)$$

The term $\partial p / \partial t$ is set equal to zero for incompressible flows. In solid regions the convective terms, the viscous work, and the unsteady pressure term drop out.

The temperature form of energy equation, widely used in the literature, is given by (Bird et al., 1960)

$$\frac{\partial}{\partial t}(\rho C_p T) + \frac{\partial}{\partial x_i}(\rho u_i C_p T) = \frac{\partial}{\partial x_i}\left(k \frac{\partial T}{\partial x_i}\right) + \tau_{ij}\frac{\partial u_i}{\partial x_j} + \left(\frac{\partial \ln (1/\rho)}{\partial \ln T}\right)_p \left(\frac{\partial p}{\partial t} + u_i \frac{\partial p}{\partial x_i}\right) + \rho T\left(\frac{\partial C_p}{\partial t} + u_i \frac{\partial C_p}{\partial x_i}\right). \quad (6)$$

Equation (1) is conservative in that for steady adiabatic flow, it may cast in the form

$$\frac{\partial \phi_i}{\partial x_i} = 0 \quad (7)$$

where ϕ_i are the components of a vector function Φ composed of the convection, diffusion, viscous dissipation, and pressure work terms. Equation (5) retains the conservative form of Eq. (7). Conservative finite volume schemes, such as that described by Patankar (1980), ensure conservation at the discrete level for equations which have the form of Eq. (7); this is true regardless of mesh size. Equation (6) does not have the conservative form for variable C_p or if compressibility or viscous dissipation effects are important. As a result, conservative finite volume solvers cannot guarantee perfect energy conservation for coarse meshes. Conservation is approached only in a limiting sense, for fine enough meshes. For the purposes of this paper, we focus on Eq. (5), though the energy form (Eq. (1)) is equivalent and may be used as well.

Iterative Scheme

Our objective is to solve Eq. (5) numerically, using an iterative approach similar to that outlined in Patankar (1980). We wish to retain temperature as the primary dependent variable, while ensuring that a conservative discretization of Eq. (5) is satisfied at convergence. To this end, we rewrite Eq. (5) as

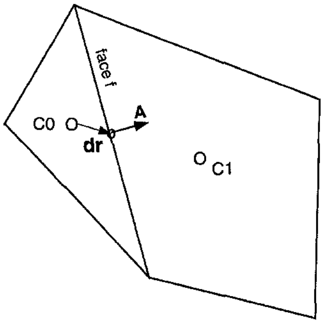

Fig. 1 Control volume

$$\frac{\partial}{\partial t}(\rho C_p T) + \frac{\partial}{\partial x_i}(\rho u_i C_p T) = \frac{\partial}{\partial x_i}\left(k\frac{\partial T}{\partial x_i}\right) + \frac{\partial \tau_{ij} u_j}{\partial x_i} + \frac{\partial p}{\partial t} + S_h + \frac{\partial}{\partial t}\rho(C_pT^* - H^*) + \frac{\partial}{\partial x_i}\rho u_i(C_pT^* - H^*). \quad (8)$$

Here, T^* and H^* are the values of T and H at the current iteration. In the discretization process, we wish to treat the unsteady, convective, and diffusive terms in T implicitly, while absorbing the T^* and H^* terms explicitly. This leads to a (nominally) linear set of algebraic equations in T, similar in structure to that described in Patankar (1980), which may be solved using a variety of methods. The coefficients of the algebraic set as well as the nonlinear source terms are updated iteratively using prevailing values. At convergence, $T = T^*$; the unsteady and convective terms in T and T^* in Eq. (8) cancel and Eq. (5) is satisfied identically.

This iterative scheme has a number of advantages:

1 Though the computation is in terms of temperature, the formulation ensures complete energy conservation if conservative numerical schemes are used for discretization. This is true regardless of mesh size.

2 When C_p is constant and compressibility and viscous dissipation effects are not important, Eq. (8) reverts to the conventional temperature form of the energy equation, and behavior similar to conventional schemes is recovered. If properties are not a function of temperature, Eq. (8) is linear, and again, the conventional temperature form is recovered.

3 Temperature is continuous across conjugate boundaries. Therefore the evaluation of the diffusion terms poses no difficulty. This is in contrast to formulations using enthalpy, which must address the jump discontinuity in enthalpy at conjugate boundaries.

4 Formulations using enthalpy as the dependent variable must recover temperature from enthalpy after enthalpy is computed. For $C_p = C_p(T)$, this requires finding the roots of a nonlinear equation for each computational cell in the domain, and can be quite expensive. In the present approach, T is computed directly from Eq. (8); an evaluation of H is required using Eq. (4), but no root-finding.

5 Boundary conditions can be posed directly in terms of T and do not require a conversion to H.

It is important to note that unlike conventional enthalpy forms of the energy equation, the pressure work and dynamic head appear explicitly on the right-hand side of Eq. (8), in the H^* terms. In conventional enthalpy forms, these terms would in effect be included implicitly through the solution of H. However, they would appear explicitly in the recovery of T from H. Thus their inclusion in an explicit manner in the current formulation is not expected to cause any difficulties.

Discretization

A complete description of the discretization procedure may be found in Mathur and Murthy (1997) and Murthy and Mathur (1997). Essentially, the domain is discretized into arbitrary unstructured polyhedral cells, such as those shown in Fig. 1, over which energy balances are written. Temperature, H and all properties are stored at cell centers. T and H are also stored at the centroids of boundary faces.

Integration of Eq. (8) about the cell C0 with volume $\Delta \mathcal{V}$ yields

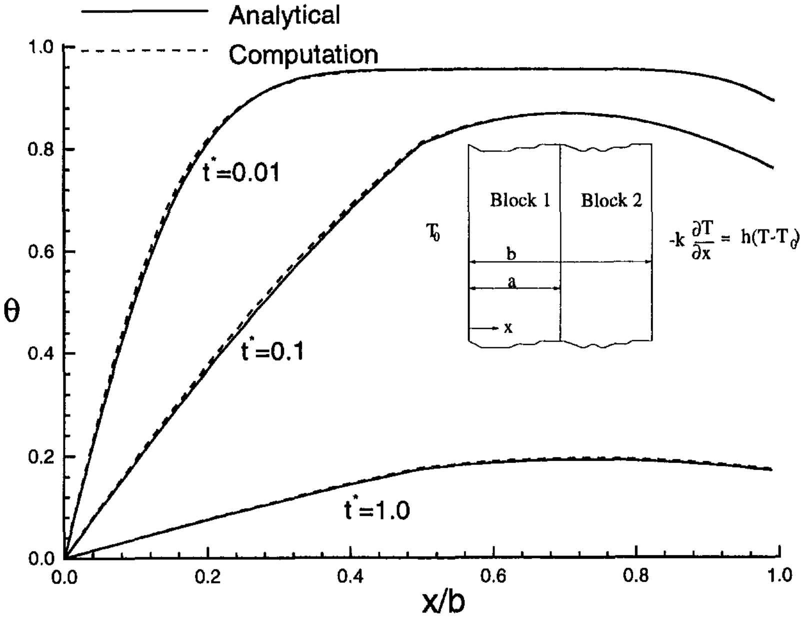

Fig. 2 Unsteady conduction in a composite block: temperature profiles

Table 1 Natural convection: accuracy and convergence behavior

	Constant C_p		$\Delta C_p/C_{pc} = 0.2$		$\Delta C_p/C_{pc} = 0.4$	
Mesh	% Error	Iterations	% Error	Iterations	% Error	Iterations
14 × 12	3.33	111	3.33	115	3.40	102
28 × 24	1.03	88	0.96	83	1.02	102
56 × 48	0.1	91	0.04	91	0.15	126

$$\frac{\rho C_p(T_0^{n+1} - T_0^n)\Delta\mathcal{V}_0}{\Delta t} + \sum_f J_f C_{pf} T_f$$
$$= \int_{\Delta\mathcal{V}_0} \left(\frac{\partial}{\partial x_i}\left(k \frac{\partial T}{\partial x_i}\right) + \frac{\partial \tau_{ij} u_j}{\partial x_i} + \frac{\partial p}{\partial t} + S_h \right) d\mathcal{V} + \mathcal{E}. \quad (9)$$

The summation on the left-hand side is over the faces f of the cell. J_f, C_{pf}, and T_f are the face values of the mass flow rate, specific heat, and temperature, respectively. The discretization of the quantities inside the integral is discussed in Mathur and Murthy (1997). T_0^{n+1} and T_0^n are temperatures in the C0 cell at the current and previous time-steps, respectively. The term $\mathcal{E}$ contains the extra unsteady and convective terms in T^* and H^* on the right-hand side of Eq. (8). A fully implicit scheme is used for time discretization (Patankar, 1980). Thus, the convective, diffusive, source, and viscous work terms in the above equation are computed at time-step $n + 1$. The time discretization is first-order accurate; generalization to second-order schemes is straightforward.

Discretization of Convection and E Term. The accuracy of the scheme is independent of the discretization of convective terms involving T. Consequently, we use the first-order approximation

$$T_f = T_{\text{upwind}} \quad (10)$$

in all convective terms involving T. Here T_{upwind} is the temperature of the cell upwind of the face f. The $\mathcal{E}$ term is discretized as

$$\mathcal{E} = \frac{\rho C_p(T_0^{*\,n+1} - T_0^n)\Delta\mathcal{V}_0}{\Delta t} - \frac{\rho(H_0^{*\,n+1} - H_0^n)\Delta\mathcal{V}_0}{\Delta t} + \sum_f J_f(C_{pf}T_f^* - H_f^*) \quad (11)$$

Here starred values represent current iterates. Note that the convective terms involving T are differenced identically on the left and right-hand sides of Eq. (9) so that they cancel identically at convergence. The accuracy of the H convection terms is critical to the overall accuracy of the scheme. Under a first-order approximation, the face value H_f is obtained as

$$H_f = H_{\text{upwind}} \quad (12)$$

where H_{upwind} is the value of H in the upwind cell. A second-order value at the face can be obtained as

$$H_f = H_{\text{upwind}} + \nabla H_{r\text{upwind}} \cdot \mathbf{dr} \quad (13)$$

where $\nabla H_{r\text{upwind}}$ is the reconstruction gradient at the upwind cell and $\mathbf{dr}$ is the vector directed from the centroid of the upwind cell to the centroid of the face. The computation of the reconstruction gradient is described in Mathur and Murthy (1997).

Discretization results in a set of nominally linear algebraic equations in temperature, which are solved using an algebraic multigrid method. An outer loop updates all nonlinearities (Mathur and Murthy, 1997).

Results

In this section, we apply the method developed above to three validation problems. All results presented have been obtained using the second-order discretization described previously. Convergence of the iterative process is considered achieved when the scaled residual (Mathur and Murthy, 1997) in the energy equation drops to 10^{-6}; when fluid flow is solved, the scaled continuity residual is required to drop to 10^{-4} in addition. The first problem tests the effect of the iterative procedure on unsteady composite conduction problems with temperature-depen-

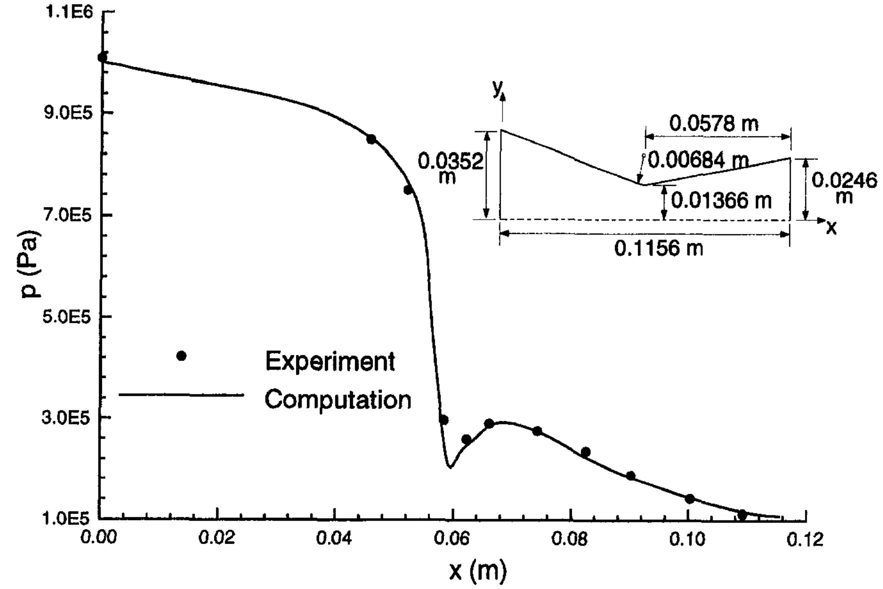

Fig. 3 Converging diverging nozzle: static pressure on nozzle wall

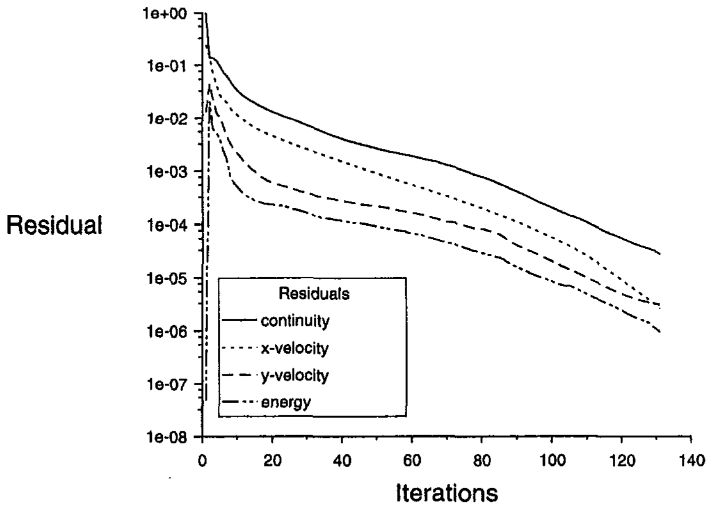

(a)

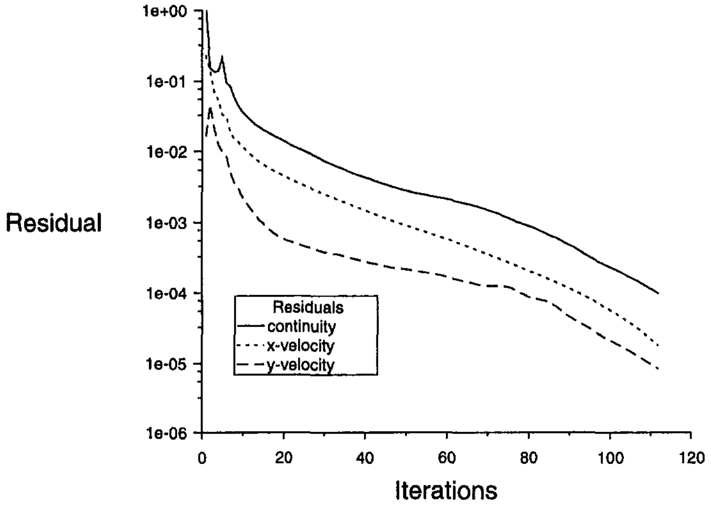

(b)

Fig. 4 *Converging diverging nozzle: convergence behavior (a) with present scheme, and (b) assuming constant total enthalpy*

dent C_p and a step jump in C_p at the composite interface. The second problem investigates the performance of the scheme in variable C_p convection problems. The last problem investigates the effect on convergence of explicit kinetic energy terms in compressible flow problems.

One-Dimensional Unsteady Conduction in a Composite Block. Here we consider two solid blocks 1 and 2 in thermal contact as shown in Fig. 2. The lengths a and b are chosen to be 1 and 2, respectively. Further, $C_{p1} = 1 + 0.1T$, $k_1 = 1 + 0.1T$, $C_{p2} = 4 + 0.4T$, and $k_2 = 2 + 0.2T$. For $t < 0$, both blocks are at $T_i = 0.95445$. At $t = 0$ the wall left of block 1 is set to $T = T_0$ and the wall right of block 2 is exposed to the condition

$$-k_2 \frac{\partial T}{\partial x} = h(T - T_0) \qquad (14)$$

with $h = (2 + 0.2T)$ and $T_0 = 0$. The objective is to compute the transient response of the composite block. An analytical solution using Kirchoff's transformation may be deduced from Ozisik (1980).

Computations were done with a mesh of 80 cells is used in the x-direction. Auxilliary computations with a 160-cell mesh show a maximum difference of less than one percent in temperature in steady-state. The nondimensional time-step, $\alpha_1 \Delta t/b^2$, is fixed at 10^{-2}. Figure 2 shows a plot of the dimensionless temperature $\theta = T/T_i$ versus x/b, the dimensionless distance along the slabs. Calculations are shown for $t^*(=\alpha_1 t/b^2) = 0.01$, 0.1, and 1.0. Also shown is the analytical result. The maximum error at each time instant is found to be under 1.5 percent. Approximately three to five iterations were required at each time-step to achieve convergence. If the properties of each block were constant, only one iteration per time-step would be required.

Natural Convection in a Rhomboidal Cavity. Here we consider variable-C_p natural convection in a 45 deg rhomboidal enclosure of side L. The left wall is hot and at T_h and the right wall is cold and at T_c; the top and bottom are adiabatic. Gravity points downwards. We compute buoyancy-driven natural convection using the Boussinesq approximation for $\mathrm{Ra} = g\beta(T_h - T_c)L^3/\nu\alpha = 10^6$ and $\mathrm{Pr} = 0.1$. Benchmark solutions for constant property flow have been published by Demirdzic et al. (1992) for these parameter values. Here, we compute both constant and variable C_p flow. For the latter case, we assume

$$\frac{C_p}{C_{pc}} = 1 + \frac{\Delta C_p}{C_{pc}}(T - T_c) \qquad (15)$$

with $\Delta C_p/C_{pc} = (C_{ph} - C_{pc})/C_{pc} = 0.2$ and 0.4. Here C_{pc} is the value of specific heat evaluated at T_c; C_{ph} is the corresponding value at T_h. For the variable property case, Ra and Pr are evaluated at T_c. Though no published benchmarks are available for variable C_p, a comparison of performance with the constant C_p case is instructive.

Computations are first done on a 14 × 12 mesh. The mesh is doubled consecutively and solutions are obtained at each mesh level using the previous solution as an initial guess. Table 1 shows the error in the mean Nusselt number Nu on the cold wall, along with incremental iterations to convergence. For the constant-C_p case, the error is defined with respect to the benchmark of Demirdzic et al. (1992). For the variable C_p case, the error is defined with respect to the solutions obtained on a 224 × 192 mesh; these are Nu = 6.2433 and 6.4807 for $\Delta C_p/C_{pc} = 0.2$ and 0.4, respectively. The variable-C_p cases exhibit approximately the same error levels as the constant-C_p case, and achieve convergence in approximately the same number of iterations.

Compressible Flow in a Converging-Diverging Nozzle. In this problem we examine the effect of explicitly included kinetic energy terms on the convergence of inviscid subsonic flow in the converging diverging nozzle shown in Fig. 3. The total pressure at the nozzle entrance is 1.01×10^6 Pa and the total temperature is 300 K. The static pressure at the exit is 1.14×10^5 Pa. The fluid is air; it is assumed to be a perfect gas and is inviscid and nonconducting, with a constant specific heat. Because of symmetry, only one-half of the domain is used in the calculation. Experimental measurements of the static pressure on the nozzle wall have been published by Mason et al. (1980). The flow is computed using the SIMPLE algorithm with a density correction term in the pressure correction equation (Mathur and Murthy, 1997; Karki and Patankar, 1989).

Calculations are done using an unstructured triangular mesh of 974 cells. Figure 3 compares the static pressure on the nozzle wall with experiment. The comparison is good, with a maximum difference of less than 2.5 percent. Figure 4(*a*) shows a plot of scaled continuity, momentum and energy residuals versus iteration number. Convergence is obtained in 128 iterations using the proposed formulation. Since the flow is adiabatic, the total enthalpy remains constant at the inlet value, and as such, no energy equation need be solved for this problem; the temperature may be deduced every iteration from the inlet total enthalpy and the local velocity field. Figure 4(*b*) shows a plot of the scaled continuity and momentum residuals computed in this manner. Convergence is obtained in 112 iterations, i.e., in about 12 percent fewer iterations. Thus, the explicit inclusion of the kinetic energy terms in the present formulation imposes a small overhead, but not a significant one. In more general problems involving viscous flow and heat transfer, an energy equation must of course be solved; for such cases the present formulation appears to offer an attractive alternative to conventional enthalpy formulations.

Acknowledgments

We wish to acknowledge the use of Fluent Inc.'s software, FLUENT/UNS, TGrid, and PreBFC, in this work.

References

Bird, R. B., Stewart, W. E., and Lightfoot, E. N., 1960, *Transport Phenomena*, John Wiley and Sons, New York.

Demirdzic, I., Lilek, Z., and Peric, M. 1992, "Fluid Flow and Heat Transfer Test Problems For Non-Orthogonal Grids: Bench-Mark Solutions," *International Journal for Numerical Methods in Fluids*, Vol. 15, pp. 329–354.

Karki, K. C., and Patankar, S. V., 1989, "Pressure Based Calculation Procedure for Viscous Flows at All Speeds in Arbitrary Configurations," *AIAA Journal*, Vol. 27, No. 9, pp. 1167–1174.

Mason, M. L., Putnam, L. E., and Re, R. J., 1980, "The Effect of Throat Contouring on Two-Dimensional Converging-Diverging Nozzles at Static Conditions," Technical Paper 1704, Aug., NASA.

Mathur, S. R., and Murthy, J. Y., 1997, "A Pressure Based Method for Unstructured Meshes," *Numer. Heat Transfer*, Vol. 31, No. 2, pp. 195–216.

Murthy, J. Y., and Mathur, S. R., 1997, "Computation of Anisotropic Conduction Using Unstructured Meshes," ASME JOURNAL OF HEAT TRANSFER, submitted for publication.

Ozisik, N., 1980, *Heat Conduction*, John Wiley and Sons, New York, Chapter 15.

Patankar, S. V., 1980, *Numerical Heat Transfer and Fluid Flow*, McGraw-Hill, New York.

Peric, M., 1985, "A Finite Volume Method for the Prediction of Three-Dimensional Fluid Flow in Complex Ducts," Ph.D. thesis, University of London, London UK.

Transition From Turbulent Natural to Turbulent Forced Convection

K. Patel,[1] B. F. Armaly,[1,2] and T. S. Chen[1,2]

Introduction

Turbulent mixed convection occurs in many engineering devices where the buoyancy force in the flow is as significant as the inertia force. These conditions occur in the cooling of electronic equipment and nuclear reactors, and in many other devices where heat exchangers are used. A great deal of work has been published on laminar and turbulent forced and natural convection flows and also on laminar mixed convection flow, but very limited results are available for the turbulent mixed convection flow. This study simulates the process of transition from turbulent natural convection to turbulent forced convection adjacent to a vertical heated plate. This is accomplished by starting with a turbulent natural convection flow adjacent to a heated vertical plate, followed by introducing different levels of freestream velocity until the turbulent forced convection regime is reached. At each velocity level, the steady-state convective flow condition is numerically simulated. The introduction of freestream velocity changes the flow regime from pure turbulent natural convection to a turbulent mixed convection regime where turbulence is suppressed and the heat transfer rate decreases. As the velocity increases further, the turbulent mixed convection regime changes to turbulent forced convection regime. To simulate these flow regimes, a low Reynolds number k-ϵ turbulence model equivalent to that proposed by Jones and Launder (1973) was used to predict the various flow regimes.

The problem of natural convection along an isothermal vertical flat plate has been thoroughly investigated in both the laminar and turbulent flow regimes. Ostrach (1952) provided a similarity solution for the laminar case. Plumb and Kennedy (1977), Lin and Churchill (1978), and To and Humphrey (1986) have analyzed turbulent natural convection along a vertical plate using a version of the k-ϵ turbulence model. Their results compared well in terms

---

[1] Department of Mechanical and Aerospace Engineering and Engineering Mechanics, University of Missouri, Rolla MO 65409-0050.

[2] Fellow ASME.

Contributed by the Heat Transfer Division for publication in the JOURNAL OF HEAT TRANSFER and presented at the '96 ASME/AICHE NHTC Houston. Manuscript received by the Heat Transfer Division, Sept. 9, 1996; revision received, June 1, 1998. Keywords: Flow Transition, Flow Visualization, Forced Convection, Mixed Convection, Natural Convection. Associate Technical Editor: S. Ramadhyani.

points downwards. We compute buoyancy-driven natural convection using the Boussinesq approximation for $\mathrm{Ra} = g\beta(T_h - T_c)L^3/\nu\alpha = 10^6$ and $\mathrm{Pr} = 0.1$. Benchmark solutions for constant property flow have been published by Demirdzic et al. (1992) for these parameter values. Here, we compute both constant and variable C_p flow. For the latter case, we assume

$$\frac{C_p}{C_{pc}} = 1 + \frac{\Delta C_p}{C_{pc}}(T - T_c) \tag{15}$$

with $\Delta C_p/C_{pc} = (C_{ph} - C_{pc})/C_{pc} = 0.2$ and 0.4. Here C_{pc} is the value of specific heat evaluated at T_c; C_{ph} is the corresponding value at T_h. For the variable property case, Ra and Pr are evaluated at T_c. Though no published benchmarks are available for variable C_p, a comparison of performance with the constant C_p case is instructive.

Computations are first done on a 14 × 12 mesh. The mesh is doubled consecutively and solutions are obtained at each mesh level using the previous solution as an initial guess. Table 1 shows the error in the mean Nusselt number Nu on the cold wall, along with incremental iterations to convergence. For the constant-C_p case, the error is defined with respect to the benchmark of Demirdzic et al. (1992). For the variable C_p case, the error is defined with respect to the solutions obtained on a 224 × 192 mesh; these are $\mathrm{Nu} = 6.2433$ and 6.4807 for $\Delta C_p/C_{pc} = 0.2$ and 0.4, respectively. The variable-C_p cases exhibit approximately the same error levels as the constant-C_p case, and achieve convergence in approximately the same number of iterations.

Compressible Flow in a Converging-Diverging Nozzle. In this problem we examine the effect of explicitly included kinetic energy terms on the convergence of inviscid subsonic flow in the converging diverging nozzle shown in Fig. 3. The total pressure at the nozzle entrance is 1.01×10^6 Pa and the total temperature is 300 K. The static pressure at the exit is 1.14×10^5 Pa. The fluid is air; it is assumed to be a perfect gas and is inviscid and nonconducting, with a constant specific heat. Because of symmetry, only one-half of the domain is used in the calculation. Experimental measurements of the static pressure on the nozzle wall have been published by Mason et al. (1980). The flow is computed using the SIMPLE algorithm with a density correction term in the pressure correction equation (Mathur and Murthy, 1997; Karki and Patankar, 1989).

Calculations are done using an unstructured triangular mesh of 974 cells. Figure 3 compares the static pressure on the nozzle wall with experiment. The comparison is good, with a maximum difference of less than 2.5 percent. Figure 4(*a*) shows a plot of scaled continuity, momentum and energy residuals versus iteration number. Convergence is obtained in 128 iterations using the proposed formulation. Since the flow is adiabatic, the total enthalpy remains constant at the inlet value, and as such, no energy equation need be solved for this problem; the temperature may be deduced every iteration from the inlet total enthalpy and the local velocity field. Figure 4(*b*) shows a plot of the scaled continuity and momentum residuals computed in this manner. Convergence is obtained in 112 iterations, i.e., in about 12 percent fewer iterations. Thus, the explicit inclusion of the kinetic energy terms in the present formulation imposes a small overhead, but not a significant one. In more general problems involving viscous flow and heat transfer, an energy equation must of course be solved; for such cases the present formulation appears to offer an attractive alternative to conventional enthalpy formulations.

Acknowledgments

We wish to acknowledge the use of Fluent Inc.'s software, FLUENT/UNS, TGrid, and PreBFC, in this work.

References

Bird, R. B., Stewart, W. E., and Lightfoot, E. N., 1960, *Transport Phenomena*, John Wiley and Sons, New York.

Demirdzic, I., Lilek, Z., and Peric, M. 1992, "Fluid Flow and Heat Transfer Test Problems For Non-Orthogonal Grids: Bench-Mark Solutions," *International Journal for Numerical Methods in Fluids*, Vol. 15, pp. 329–354.

Karki, K. C., and Patankar, S. V., 1989, "Pressure Based Calculation Procedure for Viscous Flows at All Speeds in Arbitrary Configurations," *AIAA Journal*, Vol. 27, No. 9, pp. 1167–1174.

Mason, M. L., Putnam, L. E., and Re, R. J., 1980, "The Effect of Throat Contouring on Two-Dimensional Converging-Diverging Nozzles at Static Conditions," Technical Paper 1704, Aug., NASA.

Mathur, S. R., and Murthy, J. Y., 1997, "A Pressure Based Method for Unstructured Meshes," *Numer. Heat Transfer*, Vol. 31, No. 2, pp. 195–216.

Murthy, J. Y., and Mathur, S. R., 1997, "Computation of Anisotropic Conduction Using Unstructured Meshes," ASME JOURNAL OF HEAT TRANSFER, submitted for publication.

Ozisik, N., 1980, *Heat Conduction*, John Wiley and Sons, New York, Chapter 15.

Patankar, S. V., 1980, *Numerical Heat Transfer and Fluid Flow*, McGraw-Hill, New York.

Peric, M., 1985, "A Finite Volume Method for the Prediction of Three-Dimensional Fluid Flow in Complex Ducts," Ph.D. thesis, University of London, London UK.

Transition From Turbulent Natural to Turbulent Forced Convection

K. Patel,[1] B. F. Armaly,[1,2] and T. S. Chen[1,2]

Introduction

Turbulent mixed convection occurs in many engineering devices where the buoyancy force in the flow is as significant as the inertia force. These conditions occur in the cooling of electronic equipment and nuclear reactors, and in many other devices where heat exchangers are used. A great deal of work has been published on laminar and turbulent forced and natural convection flows and also on laminar mixed convection flow, but very limited results are available for the turbulent mixed convection flow. This study simulates the process of transition from turbulent natural convection to turbulent forced convection adjacent to a vertical heated plate. This is accomplished by starting with a turbulent natural convection flow adjacent to a heated vertical plate, followed by introducing different levels of freestream velocity until the turbulent forced convection regime is reached. At each velocity level, the steady-state convective flow condition is numerically simulated. The introduction of freestream velocity changes the flow regime from pure turbulent natural convection to a turbulent mixed convection regime where turbulence is suppressed and the heat transfer rate decreases. As the velocity increases further, the turbulent mixed convection regime changes to turbulent forced convection regime. To simulate these flow regimes, a low Reynolds number k-ϵ turbulence model equivalent to that proposed by Jones and Launder (1973) was used to predict the various flow regimes.

The problem of natural convection along an isothermal vertical flat plate has been thoroughly investigated in both the laminar and turbulent flow regimes. Ostrach (1952) provided a similarity solution for the laminar case. Plumb and Kennedy (1977), Lin and Churchill (1978), and To and Humphrey (1986) have analyzed turbulent natural convection along a vertical plate using a version of the k-ϵ turbulence model. Their results compared well in terms

---

[1] Department of Mechanical and Aerospace Engineering and Engineering Mechanics, University of Missouri, Rolla MO 65409-0050.

[2] Fellow ASME.

Contributed by the Heat Transfer Division for publication in the JOURNAL OF HEAT TRANSFER and presented at the '96 ASME/AICHE NHTC Houston. Manuscript received by the Heat Transfer Division, Sept. 9, 1996; revision received, June 1, 1998. Keywords: Flow Transition, Flow Visualization, Forced Convection, Mixed Convection, Natural Convection. Associate Technical Editor: S. Ramadhyani.

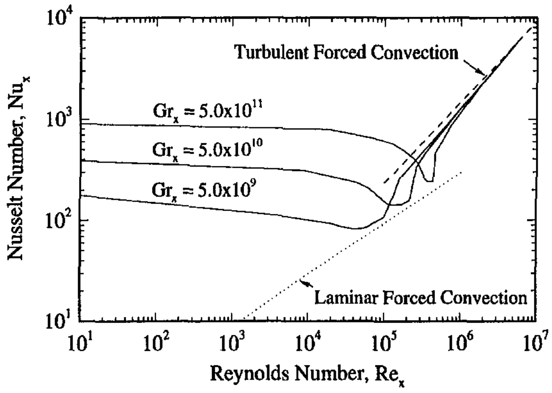

Fig. 1 Effect of freestream velocity on Nusselt number, Pr = 0.7

of predicting heat transfer along the plate. The case of turbulent natural convection along an isothermal vertical plate has also been investigated experimentally, for example, by Cheesewright (1968) and more recently by Tsuji and Nagano (1988).

The case of turbulent mixed convection from an isothermal vertical surface has received little attention. Hall and Price (1970) conducted experimental studies in a limited range of Grashof numbers, $10^{8.5} < \mathrm{Gr}_x < 10^{9.5}$, where $\mathrm{Gr}_x = g\beta(T_w - T_\infty)x^3/\upsilon^2$ is the local Grashof number; g is gravity; β is the coefficient of thermal expansion; T_w is the wall temperature; T_∞ is the freestream temperature; x is the distance along the plate from the leading edge; and υ is the kinematic viscosity. Krishnamurthy and Gebhart (1989) also conducted experiments on mixed convection flows but their interest was focused on studying the transition to turbulence in mixed convection from a vertical uniform-heat-flux (UHF) surface. They concluded that the beginning of both the thermal and velocity transition occurred when the laminar mixed convection parameter $\mathrm{Re}_x/(\mathrm{Gr}_x^*/5)^2$ reaches the value of 0.18, where $\mathrm{Gr}_x^* = g\beta q_w x^4/\kappa\upsilon^2$ is the modified Grashof number; $q_w = -\kappa(\partial T/\partial y)_{y=0}$ is the local heat transfer rate; κ is the thermal conductivity; T is the mean local air temperature; y is the distance normal to the plate; $\mathrm{Re}_x = u_\infty x/\upsilon$ is the local Reynolds number; and u_∞ is the freestream velocity. Oosthuizen (1974) investigated the problem analytically using a mixing-length model but the analysis was also limited to the same range of Grashof numbers as Hall and Price (1970). Chen et al. (1987) used a modified Van Driest mixing length model for the turbulent eddy-diffusivities to study turbulent mixed convection along an isothermal vertical surface for a wide range of Grashof and Reynolds numbers ($\mathrm{Gr}_x \leq 1.0 \times 10^{14}$ and $\mathrm{Re}_x \leq 1.0 \times 10^8$). They concluded that the local wall shear stress and the local surface heat flux increase with increasing values of the buoyancy parameter ($\mathrm{Gr}_x/\mathrm{Re}_x^2$). Their results also indicated that the model underpredicted the Nusselt number for mixed convection in the buoyancy-dominated regime by as much as 20 percent. Armaly et al. (1986) used a low Reynolds number k-ϵ turbulence model to study the turbulent mixed convection regime. The trends and results of this study agreed with those of Chen et al. (1987). In all of these studies, the focus was on the effect of buoyancy force on turbulent forced convection, while the focus of the present study is on the effect of the forced flow on turbulent natural convection. Results generated in this study are used to map the regions of the various convection flow regimes as a function of the Grashof and Reynolds numbers (Gr_x, Re_x) and also to develop correlations for calculating the heat transfer in these regimes.

Recently, Kitamura and Inagaki (1987) reported measurements of turbulent mixed convection along a vertical flat plate with water as the working fluid. They determined that the local Nusselt numbers in the turbulent mixed convection regime decreased by as much as 25 percent from those for the turbulent pure forced and the turbulent pure natural convection values. They concluded that the reduction in heat transfer is caused by turbulent suppression or relaminarization that is caused by the introduction of freestream velocity.

Results and Discussion

The same governing equations for the low Reynolds number k-ϵ turbulence model for two-dimensional boundary layer mixed convection flow adjacent to an isothermal vertical flat plate, that were used by Armaly et al. (1986) and initially proposed by Jones and Launder (1973), are used in this study. Details of the solution method that was used can be found in these references and also in Patel et al. (1996). Transition to turbulence is triggered by providing small initial values of the order of 10^{-4} for k and ϵ at whichever of the following criteria that was first satisfied by the flow, $\mathrm{Re}_x = 5.0 \times 10^4$ or $\mathrm{Gr}_x = 3.5 \times 10^8$. The transition Gr_x was chosen based on the experimental results of Black and Norris (1975). The solution domain used a nonuniform grid with 100 points in the cross-stream direction. Comparisons between solutions that use 50, 100, and 200 grid points revealed that solutions with 100 grid points are grid independent, and that was used in this study.

Numerical results were obtained for air flow with Prandtl number, Pr = 0.7. Some typical results from the present k-ϵ turbulence model calculations, such as velocity and turbulent kinetic energy profiles and Nusselt number, for turbulent natural convection compare well with those of Plumb and Kennedy (1977), as was presented by Patel et al. (1996). The predicted laminar flow regime compared very well with other published results. These favorable comparisons of predicted results with other published values validate the use of the numerical scheme.

The results reveal that starting with the case of turbulent natural convection (at $\mathrm{Gr}_x = 1.0 \times 10^{11}$, $x = 3.15$ m, and $\Delta T = 20°\mathrm{C}$), an increase in the freestream velocity to 0.05 m/s decreases the turbulent kinetic energy levels and the heat transfer. A further reduction in the turbulent kinetic energy and the heat transfer is seen as the freestream velocity increases to 0.25 and 0.75 m/s. The results for the turbulent kinetic energy are not presented in this Note due to space limitations, but can be observed in Patel et al. (1996). The freestream velocity serves to dampen turbulence, causing the heat transfer to decrease. At $u_\infty = 0.75$ m/s, the turbulence is almost completely damped out to a very small magnitude and for that reason this velocity produces the lowest heat transfer rate as compared to other velocities examined in this study. A further increase in the freestream velocity to $u_\infty = 2.00$ m/s causes the turbulent kinetic energy to increase due to the higher Reynolds number of the flow, and this leads to an increase in heat transfer rate and transition to turbulent forced convection. The effects of fre-

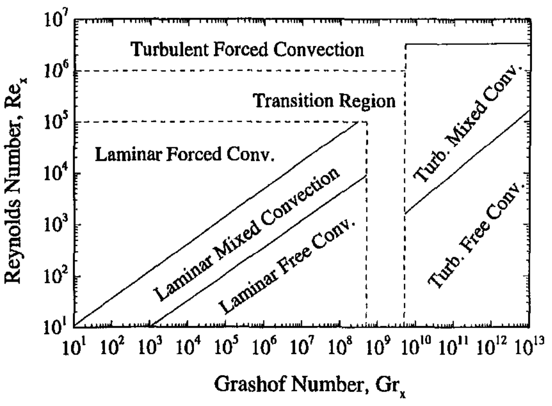

Fig. 2 Regimes of convective heat transfer, Pr = 0.7

estream velocity on the velocity, temperature, turbulent kinetic energy, and turbulent dissipation distributions in the boundary layer were presented by Patel et al. (1996).

The effects of increasing freestream velocity (u_∞) on the heat transfer rate (Nu_x) for various Grashof numbers, Gr_x, are presented in Fig. 1. Introducing a freestream velocity on a turbulent natural convection flow appears to suppress turbulence and results in decreasing heat transfer. At high values of the Reynolds number (i.e., high freestream velocity), the heat transfer rates begin to increase and approach the predicted values for turbulent forced convection flow.

By utilizing the numerical model and the predicted results, a map of the various convection flow regimes (laminar, turbulent, mixed, natural, and forced) as a function of the Reynold and Grashof numbers was developed and the results are presented in Fig. 2. The mapping of these mixed convection regimes is based on comparing the predicted heat transfer rate for that regime with those predicted for pure forced or pure natural convection flow. The axis for Gr_x represents pure natural convection while the axis for Re_x represents pure forced convection. The boundary separating the laminar mixed convection from the laminar free convection is obtained in the following manner. For a given Grashof number, Gr_x, the Nusselt number, Nu_x, is predicted for increasing Reynolds number, Re_x. When the Nusselt number, Nu_x, deviates more than five percent from that predicted for laminar natural convection at the specified Grashof number, the point (Re_x, Gr_x) is noted as the boundary point separating laminar free convection from laminar mixed convection. This procedure is performed for a range of Grashof numbers to obtain the line describing this boundary. The line separating the laminar mixed convection from laminar forced convection is obtained in a similar fashion. At this boundary, however, the predicted Nusselt number is compared to those predicted for pure laminar forced convection for the specified Grashof and Reynolds numbers. The turbulent mixed convection flow regime is established in a manner similar to that used for the laminar mixed convection region. Starting with a Grashof number for turbulent natural convection ($Gr_x > 5.0 \times 10^9$), one determines the Reynolds number for which the predicted heat transfer rate differs by more than five percent from the value predicted for pure turbulent natural convection. In the turbulent mixed convection regime, turbulence is suppressed causing the heat transfer rate to be lower than that predicted by either the pure forced or the pure free turbulent convective flow results. This is different than the laminar mixed convection regime where the reverse trend occurs. This decrease in the heat transfer rate in the turbulent mixed convection regime was also observed experimentally by Kitamura and Inagaki (1987).

Correlations that can be used to calculate the Nusselt number in the various convection flow regimes are given below:

For Laminar Natural Convection:

$$Nu_{x1} = 0.351\, Gr_x^{1/4} \tag{1}$$

For Laminar Forced Convection:

$$Nu_{x2} = 0.295\, Re_x^{1/2} \tag{2}$$

For Laminar Mixed Convection:

$$Nu_{x3} = (Nu_{x1}^3 + Nu_{x2}^3)^{1/3} \tag{3}$$

For Turbulent Natural Convection:

$$Nu_{x\mathrm{Free}} = 0.0219\, Gr_x^{2/5} \tag{4}$$

For Turbulent Forced Convection:

$$Nu_{x\mathrm{Forced}} = Re_x^{0.8}[0.0201/(-0.1555\, Re_x^{-0.1} + 0.9)] \tag{5}$$

For Turbulent Mixed Convection:

For the region where $Gr_x \geq 5.0 \times 10^9$ and $Re_x/Gr_x < 8.13 \times 10^{-6}$

$$\frac{Nu_x}{Nu_{x\mathrm{Free}}} = -0.0553\, Gr_x^{-0.382}\, Re_x + 0.491\, Gr_x^{0.0231}. \tag{6}$$

For the region where $Gr_x \geq 5.0 \times 10^9$ and $Re_x/Gr_x > 8.13 \times 10^{-6}$

$$\frac{Nu_x}{Nu_{x\mathrm{Free}}} = 0.0224\, Gr_x^{-0.365}\, Re_x + 2.205 \times 10^5\, Gr_x^{-0.614}. \tag{7}$$

Using these correlations, the Nusselt number can be calculated to within five percent of the predicted values. The region covered by $5 \times 10^8 < Gr_x < 5 \times 10^9$ and $1 \times 10^5 < Re_x < 1 \times 10^6$ corresponds to the transition regime and the predictions in this region have a higher degree of uncertainty.

The boundary lines separating the various convective flow regimes are given below:

Laminar Regions. For a given Grashof number, $Gr_x < 5.0 \times 10^8$:

1 if $Re_x < Re_{xm1}$, where $Re_{xm1} = 0.276 Gr_x^{0.520}$, use laminar free convection,

2 if $Re_x > Re_{xm2}$, where $Re_{xm2} = 3.15\, Gr_x^{0.533}$, use laminar forced convection, and

3 if $Re_{xm1} < Re_x < Re_{xm2}$, use laminar mixed convection.

Turbulent Regions: For a given Grashof number, $Gr_x > 5.0 \times 10^9$:

1 if $Re_x < Re_{xm3}$, where $Re_{xm3} = 1.74 \times 10^{-3}\, Gr_x^{0.615}$, use turbulent free convection,

2 if $Re_x > Re_{xm4}$, where $Re_{xm4} = 2.84 \times 10^6$, use turbulent forced convection, and

3 if $Re_{xm3} < Re_x < Re_{xm4}$, use turbulent mixed convection.

In the laminar mixed convection regime the Nusselt number is larger than that predicted by the pure laminar natural or the pure laminar forced convection correlations. In the turbulent mixed convection regime the Nusselt number is smaller than that predicted by the pure turbulent natural or the turbulent forced convection correlations.

Conclusions

Different convection flow regimes for fluids with Pr = 0.7 are identified and mapped as a function of Grashof and Reynolds numbers (Gr_x, Re_x) and correlations are developed to estimate the heat transfer rate in each of these regimes. When a freestream velocity is introduced to a turbulent natural convection flow, turbulence is suppressed and therefore the heat transfer rate decreases. As the freestream velocity continues to increase the turbulent forced convection regime is reached. These trends are supported by the experimental observations of Kitamura and Inagaki (1987).

Acknowledgments

The present study was supported partially by a grant from the National Science Foundation (NSF CTS-9304485).

References

Armaly, B. F., Ramachandran, N., and Chen, T. S., 1986, "Prediction of Turbulent Mixed Convection Along a Vertical Plate," *Proc. of the 8th Int. Heat Transfer Conf.*, Vol. 3, pp. 1445–1450.

Black, W. Z., and Norris, J. K., 1975, "The Thermal Structure of Free Convection Turbulence from Inclined Isothermal Surfaces and its Influence on Heat Transfer," *Int. J. of Heat and Mass Transfer*, Vol. 18, pp. 43–50.

Cheesewright, R., 1968, "Turbulent Natural Convection From a Vertical Plane Surface," ASME JOURNAL OF HEAT TRANSFER, Vol. 99, pp. 1–8.

Chen, T. S., Armaly, B. F., and Ali, M. M., 1987, "Mixed Convection in Turbulent Boundary Layer Flow Along a Vertical Plate," ASME JOURNAL OF HEAT TRANSFER, Vol. 109, pp. 251–253.

Gebhart, B., and Krishnamurthy, R., 1989, "An Experimental Study of Transition to Turbulence in Vertical Mixed Convection Flows," ASME JOURNAL OF HEAT TRANSFER, Vol. 111, pp. 121–130.

Hall, W. B., and Price, P. H., 1970, "Mixed Forced and Free Convection From a Vertical Heated Plate to Air," *Proc. of the 4th Int. Heat Transfer Conf.*, Vol. 4, Paper No. NC3.3.

Jones, W. P., and Launder, B. E., 1973, "The Prediction of Laminarization with a Two-Equation Model of Turbulence," *Int. J. of Heat and Mass Transfer*, Vol. 15, pp. 301–314.

Kitamura, K., and Inagaki, T., 1987, "Turbulent Heat and Momentum Transfer of Combined Forced and Natural Convection Along a Vertical Flat Plate-Aiding Flow," *Int. J. Heat and Mass Transfer*, Vol. 30, pp. 23–41.

Lin, S. J., and Churchill, S. W., 1978, "Turbulent Free Convection From a Vertical, Isothermal Plate," *Numerical Heat Transfer*, Vol. 1, pp. 129–145.

Oosthuizen, P. H., 1974, "Turbulent Combined Convective Flow Over a Vertical Plane Surface," *Proc. of the 5th Int. Heat Transfer Conf.*, Vol. 3, pp. 129–133.

Ostrach, S., 1952, "An Analysis of Laminar Natural Convection Flow and Heat Transfer About a Flat Plate Parallel to the Direction of the Generating Body Force," NACA TN 2635.

Patankar, S. V., and Spalding, D. B., 1970, *Heat and Mass Transfer in Boundary Layers*, Intertext Books, London. 2nd Ed.,

Patel, K., Armaly, B. F., and Chen, T. S., 1996, "Transition from Turbulent Natural to Turbulent Forced Convection Adjacent to an Isothermal Vertical Plate," ASME-HTD-Vol. 342-2, pp. 51–56.

Plumb, O. A., and Kennedy, L. A., 1977, "Application of a k-ϵ Turbulence Model to Natural Convection From a Vertical Isothermal Surface," ASME JOURNAL OF HEAT TRANSFER, Vol. 99, pp. 79–85.

Spalding, D. B., 1977, *Genmix-A General Computer Program for Two-Dimensional Parabolic Phenomena*, Pergamon Press, New York.

To, W. M., and Humphrey, J. A. C., 1986, "Numerical Simulation of Buoyant, Turbulent Flow–I. Free Convection along a Heated Vertical Flat Plate," *Int. J. Heat and Mass Transfer*, Vol. 29, pp. 573–592.

Tsuji, T., and Nagano, Y., 1988, "Characteristics of a Turbulent Natural Convection Boundary Layer Along a Vertical Flat Plate," *Int. J. Heat Mass Transfer*, Vol. 31, pp. 1723–1734.

Entropy Generation due to Laminar Natural Convection From a Horizontal Isothermal Cylinder

B. A/K Abu-Hijleh,[1,2] M. Abu-Qudais,[1] and E. Abu Nada[1]

Introduction

The use of computational fluid dynamics (CFD) as a design tool has increased dramatically in the last two decades. CFD has been used extensively in the evaluation and optimization of the overall performance of heat exchangers and turbomachinery (Bejan, 1994). In search of better system designs, researchers turned to the idea of component rather than system optimization. To achieve this, researchers shifted to the study of entropy generation in order to locate regions of high irreversibility and search for ways to minimizes or avoid such regions. Recent work on entropy generation due to natural convection included convection from a fluid impinging on a heated wall (Drost and White, 1991) and laminar mixed convection in a vertical channel with transverse fins (Cheng et al., 1994). The current work focuses on entropy generation due to laminar natural convection from a heated horizontal isothermal cylinder. Natural convection from a heated horizontal cylinder is the basic building block in many types of heat exchangers. Heat exchangers are an integral part of many thermal systems and any reduction in the irreversibility in the heat exchanger will lead to better system efficiency.

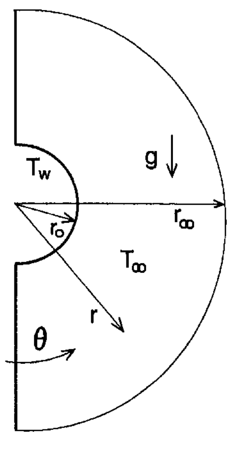

Fig. 1 Schematic of the flow field

Entropy Calculation

Figure 1 shows a schematic of the flow field under investigation, including the effect of the plan of symmetry. The nondimensional form of the local entropy generation equation in two-dimensional cylindrical coordinates can be written as (Bejan, 1994)

$$S''_{\text{gen}} = \frac{1}{(\phi + \bar{T})^2}\left[\left(\frac{\partial\phi}{\partial R}\right)^2 + \left(\frac{1}{R}\frac{\partial\phi}{\partial\theta}\right)^2\right] + \frac{\sigma}{(\phi + \bar{T})}\left\{2\left[\left(\frac{\partial U}{\partial R}\right)^2 + \frac{1}{R}\left(\frac{\partial V}{\partial\theta} + U\right)^2\right] + \left[\frac{1}{R}\frac{\partial U}{\partial\theta} + R\frac{\partial}{\partial R}\left(\frac{V}{R}\right)^2\right]\right\} \quad (1)$$

where

$$U = \frac{ur_0}{\alpha}, \quad V = \frac{vr_0}{\alpha}, \quad R = \frac{r}{r_0}, \quad \phi = \frac{T - T_\infty}{T_w - T_\infty},$$

$$\bar{T} = \frac{T_\infty}{T_w - T_\infty}, \quad \sigma = \frac{\alpha^2\mu}{r_0^2 k(T_w - T_\infty)}, \quad S''_{\text{gen}} = \frac{s''_{\text{gen}} r_0^2}{k}.$$

The total nondimensional entropy generation is calculated by integrating the S''_{gen} over the entire flow file,

$$S_{\text{gen}} = \int_1^{R_\infty}\int_0^{\pi} S''_{\text{gen}}(R, \theta)\, d\theta dR. \quad (2)$$

There are two components in the entropy generation equation: the conduction part and the viscous dissipation part, the first and second terms on the right-hand side of Eq. (1), respectively. Dimensional analysis of Eq. (1) for air, the fluid under consideration, reviled that the viscous dissipation part was negligible for all combinations of Rayleigh number (Ra_D) and cylinder radius (r_0) considered in this study. This was also confirmed by actual calculations of the value of the contribution of both components. The Rayleigh number is defined as

$$\text{Ra}_D = \frac{g\beta(2r_0)^3(T_w - T_\infty)}{\alpha\nu}. \quad (3)$$

In order to calculate the entropy generation, the local velocity a temperature profiles must first be obtained. This was done by solving the coupled continuity, momentum, and energy equations for a two-dimensional laminar incompressible flow with the Boussinesq approximation in cylindrical coordinates

---

[1] Mechanical Engineering Department, Jordan University of Science and Technology, P.O. Box 3030, Irbid 22110, Jordan.

[2] Assoc. Mem. ASME. e-mail: bassam@just.edu.jo.

Contributed by the Heat Transfer Division for publication in the JOURNAL OF HEAT TRANSFER. Manuscript received by the Heat Transfer Division, June 27, 1997; revision received, Jan. 30, 1998. Keywords: Natural Convection, Numerical Methods, Thermodynamics and Second Law. Associate Technical Editor: J. Howell.

Jones, W. P., and Launder, B. E., 1973, "The Prediction of Laminarization with a Two-Equation Model of Turbulence," *Int. J. of Heat and Mass Transfer*, Vol. 15, pp. 301–314.

Kitamura, K., and Inagaki, T., 1987, "Turbulent Heat and Momentum Transfer of Combined Forced and Natural Convection Along a Vertical Flat Plate-Aiding Flow," *Int. J. Heat and Mass Transfer*, Vol. 30, pp. 23–41.

Lin, S. J., and Churchill, S. W., 1978, "Turbulent Free Convection From a Vertical, Isothermal Plate," *Numerical Heat Transfer*, Vol. 1, pp. 129–145.

Oosthuizen, P. H., 1974, "Turbulent Combined Convective Flow Over a Vertical Plane Surface," *Proc. of the 5th Int. Heat Transfer Conf.*, Vol. 3, pp. 129–133.

Ostrach, S., 1952, "An Analysis of Laminar Natural Convection Flow and Heat Transfer About a Flat Plate Parallel to the Direction of the Generating Body Force," NACA TN 2635.

Patankar, S. V., and Spalding, D. B., 1970, *Heat and Mass Transfer in Boundary Layers*, Intertext Books, London. 2nd Ed.,

Patel, K., Armaly, B. F., and Chen, T. S., 1996, "Transition from Turbulent Natural to Turbulent Forced Convection Adjacent to an Isothermal Vertical Plate," ASME-HTD-Vol. 342-2, pp. 51–56.

Plumb, O. A., and Kennedy, L. A., 1977, "Application of a k-ϵ Turbulence Model to Natural Convection From a Vertical Isothermal Surface," ASME JOURNAL OF HEAT TRANSFER, Vol. 99, pp. 79–85.

Spalding, D. B., 1977, *Genmix-A General Computer Program for Two-Dimensional Parabolic Phenomena*, Pergamon Press, New York.

To, W. M., and Humphrey, J. A. C., 1986, "Numerical Simulation of Buoyant, Turbulent Flow–I. Free Convection along a Heated Vertical Flat Plate," *Int. J. Heat and Mass Transfer*, Vol. 29, pp. 573–592.

Tsuji, T., and Nagano, Y., 1988, "Characteristics of a Turbulent Natural Convection Boundary Layer Along a Vertical Flat Plate," *Int. J. Heat Mass Transfer*, Vol. 31, pp. 1723–1734.

Entropy Generation due to Laminar Natural Convection From a Horizontal Isothermal Cylinder

B. A/K Abu-Hijleh,[1,2] **M. Abu-Qudais,**[1] **and E. Abu Nada**[1]

Introduction

The use of computational fluid dynamics (CFD) as a design tool has increased dramatically in the last two decades. CFD has been used extensively in the evaluation and optimization of the overall performance of heat exchangers and turbomachinery (Bejan, 1994). In search of better system designs, researchers turned to the idea of component rather than system optimization. To achieve this, researchers shifted to the study of entropy generation in order to locate regions of high irreversibility and search for ways to minimizes or avoid such regions. Recent work on entropy generation due to natural convection included convection from a fluid impinging on a heated wall (Drost and White, 1991) and laminar mixed convection in a vertical channel with transverse fins (Cheng et al., 1994). The current work focuses on entropy generation due to laminar natural convection from a heated horizontal isothermal cylinder. Natural convection from a heated horizontal cylinder is the basic building block in many types of heat exchangers. Heat exchangers are an integral part of many thermal systems and any reduction in the irreversibility in the heat exchanger will lead to better system efficiency.

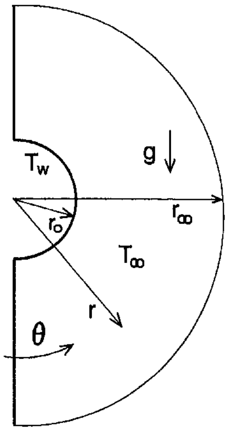

Fig. 1 Schematic of the flow field

Entropy Calculation

Figure 1 shows a schematic of the flow field under investigation, including the effect of the plan of symmetry. The nondimensional form of the local entropy generation equation in two-dimensional cylindrical coordinates can be written as (Bejan, 1994)

$$S''_{\text{gen}} = \frac{1}{(\phi + \bar{T})^2}\left[\left(\frac{\partial\phi}{\partial R}\right)^2 + \left(\frac{1}{R}\frac{\partial\phi}{\partial\theta}\right)^2\right] + \frac{\sigma}{(\phi + \bar{T})}\left\{2\left[\left(\frac{\partial U}{\partial R}\right)^2 + \frac{1}{R}\left(\frac{\partial V}{\partial\theta} + U\right)^2\right] + \left[\frac{1}{R}\frac{\partial U}{\partial\theta} + R\frac{\partial}{\partial R}\left(\frac{V}{R}\right)^2\right]\right\} \quad (1)$$

where

$$U = \frac{ur_0}{\alpha}, \quad V = \frac{vr_0}{\alpha}, \quad R = \frac{r}{r_0}, \quad \phi = \frac{T - T_\infty}{T_w - T_\infty},$$

$$\bar{T} = \frac{T_\infty}{T_w - T_\infty}, \quad \sigma = \frac{\alpha^2\mu}{r_0^2 k(T_w - T_\infty)}, \quad S''_{\text{gen}} = \frac{s''_{\text{gen}} r_0^2}{k}.$$

The total nondimensional entropy generation is calculated by integrating the S''_{gen} over the entire flow file,

$$S_{\text{gen}} = \int_1^{R_\infty}\int_0^{\pi} S''_{\text{gen}}(R, \theta)\, d\theta dR. \quad (2)$$

There are two components in the entropy generation equation: the conduction part and the viscous dissipation part, the first and second terms on the right-hand side of Eq. (1), respectively. Dimensional analysis of Eq. (1) for air, the fluid under consideration, reviled that the viscous dissipation part was negligible for all combinations of Rayleigh number (Ra_D) and cylinder radius (r_0) considered in this study. This was also confirmed by actual calculations of the value of the contribution of both components. The Rayleigh number is defined as

$$\text{Ra}_D = \frac{g\beta(2r_0)^3(T_w - T_\infty)}{\alpha\nu}. \quad (3)$$

In order to calculate the entropy generation, the local velocity a temperature profiles must first be obtained. This was done by solving the coupled continuity, momentum, and energy equations for a two-dimensional laminar incompressible flow with the Boussinesq approximation in cylindrical coordinates

---

[1] Mechanical Engineering Department, Jordan University of Science and Technology, P.O. Box 3030, Irbid 22110, Jordan.

[2] Assoc. Mem. ASME. e-mail: bassam@just.edu.jo.

Contributed by the Heat Transfer Division for publication in the JOURNAL OF HEAT TRANSFER. Manuscript received by the Heat Transfer Division, June 27, 1997; revision received, Jan. 30, 1998. Keywords: Natural Convection, Numerical Methods, Thermodynamics and Second Law. Associate Technical Editor: J. Howell.

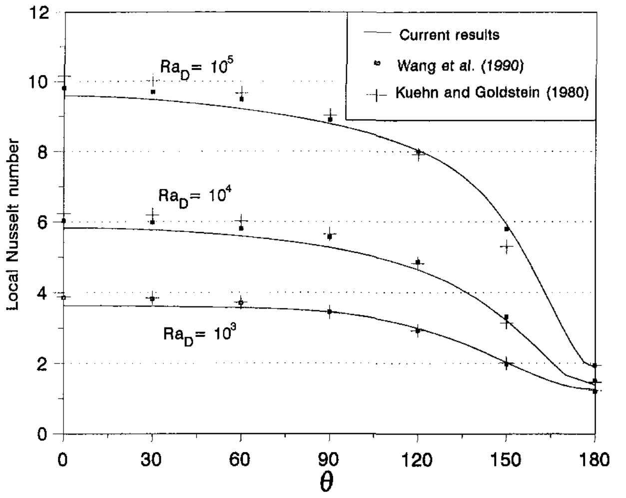

Fig. 2 Local Nusselt number comparison at different values of Rayleigh number

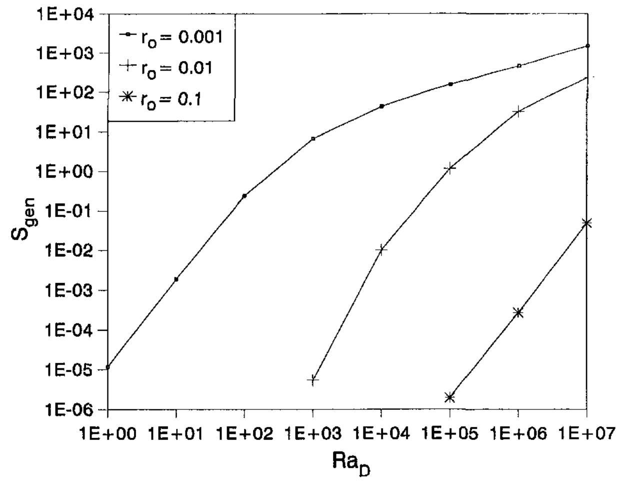

Fig. 3 Change in total entropy generation as a function of Rayleigh number and cylindrical radius

(White, 1991). The equations were solved using the finite difference numerical method and the stream-function vorticity formulation on a stretched grid in the radial direction (Qureshi and Ahmad, 1987). The code was checked for result independence from grid size, tolerance value, and outer boundary location. The calculated values of average Nusselt number based on cylinder diameter (Nu_D) over a wide range of Rayleigh numbers were in excellent agreement with published data. The accuracy of the local Nusselt values were important to insure the accuracy of the local entropy generation calculations. Figure 2 shows very good agreement between the profiles of the local Nusselt number at three different values of Rayleigh number as calculated by the current code and the data reported by Wang et al. (1990) and Kuehn and Goldstein (1980).

Results

The local and total entropy generation were calculated for eight Rayleigh numbers ($Ra_D = 1$ to 10^7) and three cylinder radii ($r_0 = 10^{-3}$ to 10^{-1}) at each Rayleigh number. The values of total entropy generation at low Rayleigh numbers and large cylinder radius were very small. In order to make Fig. 3 more readable, these low values were excluded from the figure. Figure 3 shows the change in the calculated total entropy as a function of Rayleigh number and cylinder radius. As expected, an increase in Rayleigh number, and thus higher temperature difference between the cylinder and surroundings, results in an increase in the value of total entropy generation. The main conclusion from Fig. 3 is that the use of larger size cylinders results in significantly lower entropy generation for the same value of Rayleigh number. A larger size cylinder results in lower temperature difference, as per Eq. (3). A larger cylinder also reduces the tangential temperature gradient which in turn reduces the contribution from the second component in the conduction part of the entropy generation equation, Eq. (1). Increased cylinder size results in increased viscous dissipation and an increase in the contribution of the second part of Eq. (1). But the second term of Eq. (1) was negligible even at the largest cylinder radius at the highest Rayleigh number. Thus, there is no problem in increased irreversibility due to increased viscous dissipation. The analysis of the local entropy generation profiles revealed that the location of maximum entropy generation was dependent on the size of the cylinder. For a cylinder radius $\leq 10^{-3}$ m, maximum entropy generation occurred in the plum region, top of the cylinder. For a cylinder size $\geq 10^{-1}$ m, maximum entropy generation occurred in the inflow region, bottom of the cylinder. For $10^{-1} > r_0 > 10^{-3}$, the contributions from both inflow and plum regions were of the same order. Determining the conditions and regions of high entropy generation is the first phase of an ongoing research in entropy generation minimization. One can try to manipulate the flow in regions of low entropy generation with little effect on the total irreversibility of the component. Ideas under investigation include localized flow suction or blowing and/or fin placement. The interaction between cylinders in a multicylinder bank arrangements can also be used to manipulate regions of high entropy generation.

References

Bejan, A., 1994, *Entropy Generation Through Heat and Fluid Flow,* Wiley Interscience, New York.

Cheng, C. H., Ma, W. P., and Huang, W. H., 1994, "Numerical Prediction of Entropy Generation for Mixed Convection Flows in a Vertical Channel with Transverse Fin Arrays," *International Communications in Heat and Mass Transfer,* Vol. 21, No. 4, pp. 519–530.

Drost, M. K., and White, M. D., 1991, "Numerical Prediction of Local Entropy Generation in an Impinging Jet," ASME JOURNAL OF HEAT TRANSFER, Vol. 113, pp. 823–829.

Kuehn, T. H., and Goldstein, R. J., 1980, "Numerical Solution to the Navier-Stokes Equations for Laminar Natural Convection About a Horizontal Isothermal Circular Cylinder," *International Journal of Heat and Mass Transfer,* Vol. 23, No. 6, pp. 971–979.

Qureshi, Z. H., and Ahmad, R., 1987, "Natural Convection a Uniform Heat Flux from Horizontal Cylinder at Moderate Rayleigh Number," *Numerical Heat Transfer,* Vol. 11, No. 2, pp. 199–212.

Wang, P., Kahawita, R., and Nguyen, T. H., 1990, "Numerical Computation of the Natural Convection Flow About a Horizontal Cylinder Using Splines," *Numerical Heat Transfer,* Vol. 17, No. 2, pp. 191–215.

White, F. M., 1991, *Viscous Fluid Flow,* McGraw-Hill, New York.

Study on Interpolation Schemes of the Discrete Ordinates Interpolation Method for Three-Dimensional Radiative Transfer With Nonorthogonal Grids

Seok-Ho Seo[1] and Tae-Kuk Kim[2]

1 Introduction

Recent developments in the radiative transfer analyses using nonorthogonal grids are very promising. Chui and Raithby (1993) were successful analyzing the radiative transfer within two-dimensional trapezoidal, annular and J-shaped regions filled with an absorbing, emitting, and scattering medium by using the finite volume method (FVM). Chai et al. (1994) were also successful in analyzing the radiative transfer within complicated two-dimensional regions by applying the FVM using orthogonal grid systems. Liu et al. (1997) applied the discrete ordinate method (DOM) and FVM for the two and three-dimensional radiation problems in general body fitted coordinates. All the methods explained above use control volumes to check the radiative energy balance within them. However, the discrete ordinate interpolation method (DOIM) proposed by Cheong and Song (1997) does not use the control volume concept.

This study is an extension of the DOIM by Cheong and Song (1997) to three-dimensional radiative transfer analyses. To do this we are proposing a simple but accurate interpolation method for determining the upstream intensities and source terms required for the analysis.

2 Radiative Transfer Equation

For an absorbing, emitting, and scattering medium, the radiative transfer equation can be expressed for an infinitesimal path length Δs as shown in Fig. 1. Assuming $\beta(s) \fallingdotseq \beta_P =$ constant over the path length Δs, the source function $S(s, \Omega)$ is expanded by the Taylor series around the location P and the higher-order terms are neglected. The resulting radiative transfer equation can be expressed in the following approximate form (Raithby and Chui, 1990; Chui and Raithby, 1993):

$$I_P(\Omega) \fallingdotseq I_u(\Omega)e^{-\beta_P\Delta s} + \frac{S_P(\Omega)}{\beta_P}(1 - e^{-\beta_P\Delta s}) - \frac{1}{\beta_P^2}\left(\frac{\partial S(s, \Omega)}{\partial s}\right)_P \{1 - e^{-\beta_P\Delta s}(1 + \beta_P\Delta s)\}. \quad (1)$$

Equation (1) can be used to evaluate the intensity at a node P where the unknown intensity I_u and source term S_u should be determined by a suitable interpolation using the known intensities and source terms at the upstream nodes in a marching fashion. The source function for an absorbing, emitting, and anisotropically scattering medium is considered as

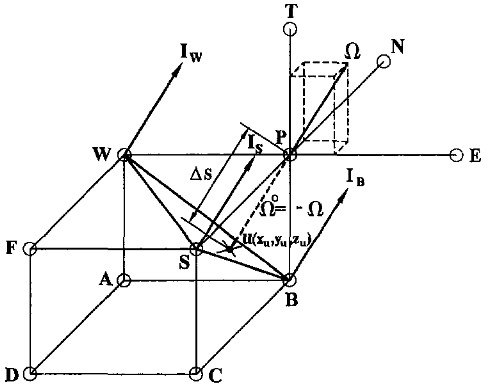

Fig. 1 Nodes shown with a triangular interpolation plane

$$S_P(\Omega) = x_P I_{bP} + \frac{\sigma_{sP}}{4\pi}\int_{4\pi} I_P(\Omega')\Phi(\Omega'; \Omega)d\Omega'. \quad (2)$$

β_P in Eq. (1) is the extinction coefficient which is the sum of the absorption coefficient x_P and the scattering coefficient σ_{sP}. I_{bP} is the black body intensity at point P and $\Phi(\Omega'; \Omega)$ is the medium scattering phase function.

For a diffusely reflecting opaque wall the radiative intensity leaving from the wall is uniformly distributed and can be expressed by the following equation (Siegel and Howell, 1992):

$$I_w(s_w, \Omega) = \epsilon_w(s_w)I_{bw} + \frac{\rho_w(s_w)}{\pi}\int_{\mathbf{n}\cdot\Omega'<0} |\mathbf{n}\cdot\Omega'|I_w(s_w, \Omega')d\Omega' \quad (3)$$

where $\mathbf{n}$ is the unit normal vector to the wall.

3 Interpolation Schemes

The DOIM considered in this study is proved to suffer less false scattering (Cheong and Song, 1997) than the standard S-N method since the one follows the line of radiative transfer more accurately than the other. Figure 1 shows a typical node arrangement in an arbitrary three-dimensional space where seven nodes marked with the symbols P, E, W, N, S, T, and B, respectively, are shown to divide the three-dimensional space into eight regions. Prior to obtaining the intensity I_P using Eq. (1), the intensity at the upstream point (I_u) should be determined. For this purpose, two possible schemes are studied. The following two interpolation schemes proposed by this work compute the intensity in marching fashion without using the unwanted step approximation which is frequently used in the FVM. And the original DOIM by Cheong and Song (1997) performs interpolations only on the horizontal plane to determine the ϕ_u's, but the currently proposed method uses the diagonal plane (LMS) and the horizontal or vertical plane (RMS) for the interpolation.

3.1 Interpolation on Diagonal Triangular Plane (LMS). Using the three known edge values of an arbitrary variable ϕ (ϕ_W, ϕ_S, ϕ_B) on the upstream triangular interpolation plane ΔWSB, the value at a point u on ΔWSB in Fig. 1 can be estimated by a linear interpolation as shown in Fig. 2. The resulting interpolation equation is expressed as

$$\phi_u = \left(1 - \frac{d_w}{S_w}\right)\phi_W + \left(1 - \frac{d_s}{S_s}\right)\phi_S + \left(1 - \frac{d_b}{S_b}\right)\phi_B. \quad (4)$$

---

[1] Graduate School, Chung Ang University, Seoul, Korea. Currently at HyoSung Industries Co., Ltd.

[2] To whom correspondence should be addressed. Department of Mechanical Engineering, Chung Ang University 221 Huk-Suk Dong, Dong-Jak Ku, Seoul, Korea 156-756. e-mail: kimtk@cau.ac.kr.

Contributed by the Heat Transfer Division for publication in the JOURNAL OF HEAT TRANSFER. Manuscript received by the Heat Transfer Division, Oct. 18, 1996; revision received, June 1, 1998. Keywords: Numerical Methods, Radiation, Radiation Interactions. Associate Technical Editor: T. Tong.

3.2 Interpolation on Rectangular Planes (RMS). This scheme uses the rectangular interpolation planes to estimate the I_u's and S_u's. According to the direction Ω selected, the upstream u point can be placed either on □ABCD, □CDFS or □ADFW shown in Fig. 1. A linear interpolation is then applied on the selected plane to determine ϕ_u as

$$\phi_u = a_0 + a_1 x_u + a_2 y_u + a_3 z_u . \tag{5}$$

The second method indicated by RMS is a similar method as the two-dimensional interpolation scheme by Cheong and Song (1997). But the RMS needs an additional process of selecting the interpolation plane. Also the RMS has to use the corner value at the system boundary where a discontinuous boundary condition may be imposed.

4 Results and Discussions

To solve the radiative transfer equation with suitable boundary conditions, intensities at all nodes and directions are computed by using Eq. (1) with predetermined I_u's and S_u's. The computation is followed by the eight sweeping groups of the directions which are also considered in the standard S-N method for better convergence (Kim et al., 1994). To assess the interpolation schemes discussed in the previous section, some numerical experiments are made for the radiative heat transfer problems in three dimensional enclosures. The problems considered here include a pure radiation problem and some heat generation problems.

4.1 Pure Radiation in a Cubical Enclosure. The pure radiation within a cubical enclosure is studied to demonstrate the performance of the interpolation methods proposed in the previous section. The bottom wall of the cubical enclosure is maintained at a temperature of 1000 K, and all other walls and the medium are maintained at 500 K. The system has a dimension of 1 m and all of the walls are assumed to be black ($\epsilon_w = 1.0$). A purely absorbing medium with an extinction coefficient of $\beta = \kappa = 1.0\ \mathrm{m}^{-1}$ is considered as the participating medium.

Figure 3 shows a comparison of the average intensities obtained from different methods. The results indicated by LMS-16 or RMS-16 are obtained from the linear interpolation scheme on a triangular or rectangular plane, respectively. The standard S-16 results shown in Fig. 3 are obtained by using the CCRHT^{3D} program (Kim et al., 1994). All of the results compared in Fig. 3 are obtained by using the same quadrature set as that used in the standard S-16 method. Figure 3 indicates that the LMS-16 results show a better agreement with the standard S-16 as compared to the RMS-16. For a small number of angular directions the RMS method may result in a severe error due to the effect of the discontinuous boundary condition at the system edges while the S-N and the LMS show a reasonable results since they do not use the system edge conditions.

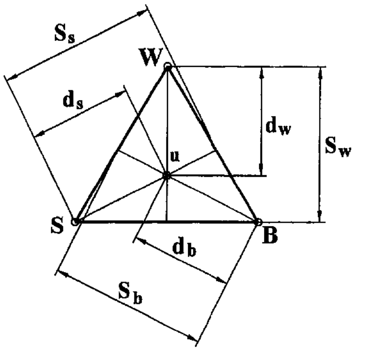

Fig. 2 The linear interpolation on a triangular element

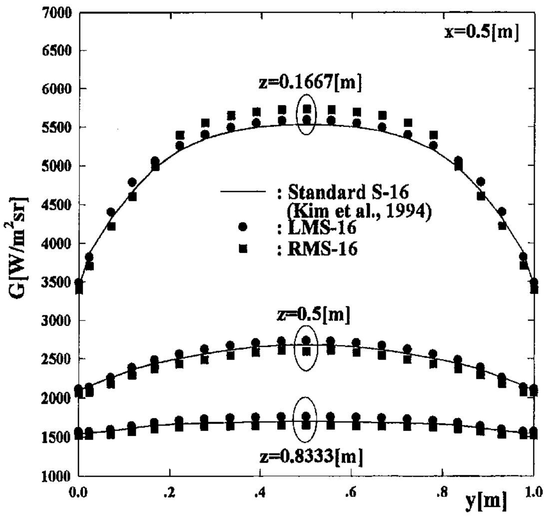

Fig. 3 Comparison of average intensities obtained from various methods

4.2 Three-Dimensional Heat Generation Problems. For a given volumetric heat generation rate $\dot{q}$, we may write a simple energy balance equation as

$$\nabla \cdot \mathbf{Q}_r = \dot{q} . \tag{6}$$

To solve the energy equation, the radiative transfer equation shown in Eq. (1) needs to be solved simultaneously.

4.2.1 Regular Bar-Shaped System. For a bar-shaped three-dimensional system worked by Mengüc and Viskanta (1985) the DOIM with a linear interpolation on the triangular plane is applied. The system dimensions and the conditions used are the same as in Mengüc and Viskanta (1985).

In Fig. 4, current results (LMS-8, 17 × 17 × 17 grids) are compared with the results obtained from the Zone method (Mengüc and Viskanta, 1985), P-3 method (Mengüc and Viskanta, 1985), standard S-8 method (17 × 17 × 17 grids, Kim et al., 1994), and FVM (11 × 11 × 21 grids, angular directions 10 × 12, Kim and Baek, 1996). The resulting wall radiative heat flux profiles are shown in Fig. 4 and the current LMS-8 results are appeared to be well matched with the Zonal results, which are considered to be accurate, as compared to the others. The reason why the LMS-8 results are better than the

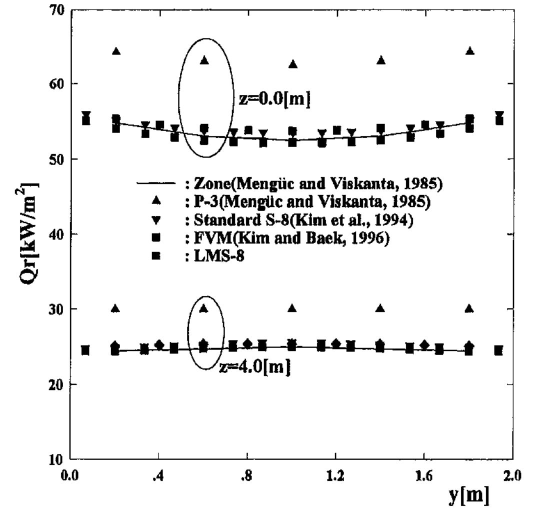

Fig. 4 Comparison of wall heat flux profiles obtained from various methods at $x = 1.0$ m

Table 1 Comparison of typical temperatures and wall heat fluxes

	Zone	LMS-8	Standard S-8	FVM	P-3
		Error	Error	Error	Error
T [K] x=y=1.0[m]	z=0.4 [m]	1057.40	1052.50	1049.96	1039.00
	1060.00	-0.25%	-0.71%	-0.95%	-1.98%
	z=2.0 [m]	953.62	952.53	952.79	957.00
	953.00	0.07%	-0.05%	-0.02%	0.42%
	z=3.6 [m]	873.26	877.84	878.27	890.00
	871.00	0.26%	0.79%	0.83%	2.18%
Q_r [kW/m^2] x=y=1.0[m]	z=0.0 [m]	52.18	53.50	53.70	62.5
	52.50	-0.61%	1.90%	2.29%	19.05%
	z=4.0 [m]	25.01	25.53	25.38	30.00
	25.00	0.04%	2.12%	1.52%	20%

FVM results can be explained by recognizing that the FVM results compared here were obtained by using the inaccurate step approximation and the uniformly divided angular quadrature sets. By comparing the relative error from the zone results, accuracy of each method is shown quantitatively in Table 1 where the current LMS-8 results appear to be best matched with the zone results.

4.2.2. Complicated System. For a more complicated system (Kim and Baek, 1996) shown in Fig. 5, where the conditions of the hot, cold, and all other walls are the same as the bar-shaped enclosure considered by Mengüc and Viskanta (1985), the three-dimensional heat generation problem is considered again with $\dot{q} = 5.0$ kW/m^3. Typical dimensions of the complicated system are $x_o = x_e = 2$ m, $y_o = 1$ m, $y_e = 1.423$ m, $y_h = 3.78$ m, and $z_o = 7.6$ m. The Mie-anisotropic scattering medium ($\beta = 0.5$ m^{-1} and $\omega = 0.7$) is considered to examine the effect of the anisotropies of scattering phase functions (Kim and Lee, 1988).

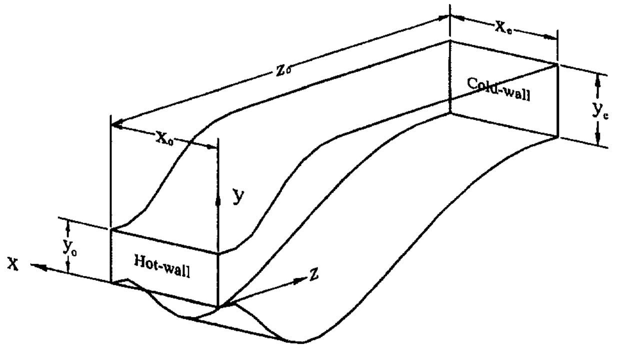

a) System outlines

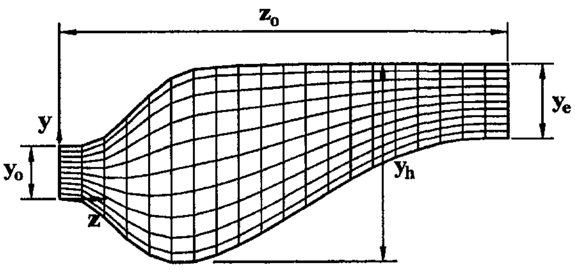

b) Computational grids on y-z plane

Fig. 5 Schematic diagram of a three-dimensional irregular shaped enclosure

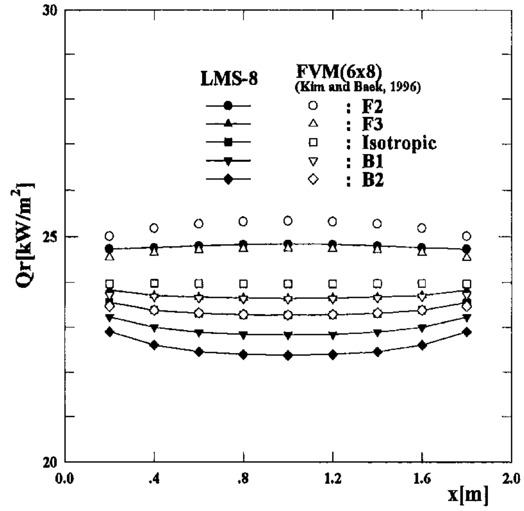

Fig. 6 Effect of the scattering phase functions on wall heat fluxes ($z = z_o$, $y = 0.5y_e$)

Figure 6 shows the computed wall heat fluxes on cold wall which are shown with the FVM results obtained by using the inaccurate step approximation (Kim and Baek, 1996). The current LMS-8 results are obtained by using the S-8 Gaussian quadrature (80 directions) with a linear interpolation on the triangular plane and the FVM results are obtained by using the uniformly distributed 48 directions. By examination of the results shown in Fig. 6, Kim and Baek (1996)'s FVM, using the step approximation, overestimates the wall heat fluxes. The overestimation of the wall heat fluxes by the FVM reaches up to 4.6 percent on the cold wall for the F3 phase function as compared to the respective LMS-8 results.

5 Conclusions

The proposed interpolation scheme (LMS) using a linear interpolation on the diagonally placed triangular plane was proven to be a simple yet accurate scheme for three-dimensional radiative heat transfer analyses. Also the proposed DOIM, using a linear interpolation on the triangular plane, was effectively applied to nonorthogonal grid systems. Generally, the proposed method showed a similar or better overall performance as compared to the standard S-N and FVM.

Acknowledgments

This work was supported in part by the Chung Ang University Research Fund and the R&D Management Center for Energy and Resources (subsidiary of the Korean Ministry of the Commerce and Industry) and is much appreciated.

References

Chai, J. C., Lee, H. S., and Patankar, S. V., 1994, "Treatment of Irregular Geometries Using a Cartesian Coordinates Finite-Volume Radiation Heat Transfer Procedure," *Num. Heat Trans.*, Part B, Vol. 26, pp. 225–235.

Cheong, K. B., and Song, T. H., 1997, "An Alternative Discrete Ordinate Method with Interpolation and Source Differencing for Two-Dimensional Radiative Transfer Problems," *Num. Heat Trans.*, Part B, Vol. 32, pp. 107–125.

Raithby, G. D., and Chui, E. H., 1990, "A Finite-Volume Method for Predicting a Radiant Heat Transfer in Enclosures with Participating Media," ASME JOURNAL OF HEAT TRANSFER, Vol. 112, pp. 415–423.

Chui, E. H., and Raithby, G. D., 1993, "Computation of Radiant Heat Transfer on a Nonorthogonal Mesh Using the Finite-Volume Method," *Num. Heat Trans.*, Part B, Vol. 23, pp. 269–288.

Liu, J., Shang, H. M., and Chen, Y. S., 1997, "Prediction of Radiative Transfer in General Body-Fitted Coordinates," 35th Aerospace Sciences Meeting & Exhibit, AIAA-97-0811, Reno, NV, Jan. 6–10.

Kim, M. Y., and Baek, S. W., 1996, "Prediction of Radiative Heat Transfer in a Three-Dimensional Gas Turbine Combustor with the Finite-Volume Method," *Proc. 96' KSME Spring Annual Meeting,* Part B, pp. 610–615.

Kim, T. K., and Lee, H. S., 1988, "Effect of Anisotropic Scattering on Radiative Heat Transfer in Two-Dimensional Rectangular Enclosures," *Int. J. of Heat and Mass Trans.,* Vol. 31, No. 8, pp. 1711–1721.

Kim, T. K., Sim, D. G., Kim, C. H., Min., D. H., and Han, K. I., 1994, "Development of a Computer Program ($CCRHT^{3D}$) for Combined Conduction-Convection-Radiation Heat Transfer in 3-D Enclosures with Absorbing-Emitting-Scattering Media," ITS# 94-04-03, ITSCAU, Korea (in Korean).

Mengüc, M. P., and Viskanta, R., 1985, "Radiative Transfer In Three-Dimensional rectangular Enclosures Containing Inhomogeneous, Anisotropically Scattering Media," *J. of Quan. Spectro. and Radiative Trans.,* Vol. 33, No. 6, pp. 533–549.

Siegel, R., and Howell, J. R., 1992, *Thermal Radiation Heat Transfer,* 3rd Ed., Hemisphere, Bristol, PA.

Journal of
Heat Transfer

Discussion

Convective Condensation of Superheated Vapor[1]

A. F. Mills[2]. Webb (1998) has proposed a method for calculating the effect of vapor superheat on condensation heat transfer that is "theoretically based" and generally applicable. The purpose of this discussion is to show that the proposed method is an ad hoc model that is not based on theory, does not have correct limiting behavior, and is not generally applicable.

A theoretically sound method to account for vapor superheat was proposed more than 60 years ago by Ackermann (1937), and subsequently has been presented in textbooks such as those by Spalding (1963) and Mills (1995). This method is reviewed first as a basis for evaluating the Webb proposal. Convective heat transfer from the superheated vapor to the condensate surface is given by

$$q_{\text{conv}} = k \left. \frac{\partial T}{\partial y} \right|_s = h_c (T_b - T_s) \tag{1}$$

where T_s is the condensate surface temperature and T_b is the bulk or freestream vapor temperature. Equation (1) defines the heat transfer coefficient h_c. The Ackermann analysis is based on a stagnant film model (or equivalently, a Couette flow or Reynolds flux model) of the vapor flow, in lieu of solving exact conservation equations governing the vapor flow. For a pure vapor the result is

$$\frac{h_c}{h_c^0} = \frac{B_h}{\exp B_h - 1}\,; \; B_h = \frac{\dot m'' c_{pv}}{h_c^0} \tag{2}$$

where $\dot m''$ [kg/m^{2}s] is the mass transfer rate and is negative for condensation, and h_c^0 is the limiting value of h_c as $\dot m''$ goes to zero: h_c^0 is estimated from an appropriate impermeable surface convection correlation. B_h is usually termed a "blowing parameter." The Ackermann method is theoretically sound in the sense that, for the implied Couette flow model, the effect of mass transfer is mathematically correct. Of course, applications involve approximations related to true nature of the vapor flow, including the effects of the liquid film on the vapor flow.

The use of Eqs. (1) and (2) depends on the particular problem, and any further approximations that may be warranted. In particular, the two asymptotic limits of Eq. (2) are useful. First, for high condensation rates (strong suction limit), $B_h \to -\infty$, and

$$h_c = -\dot m'' c_{pv} \tag{3}$$

$$q_{\text{conv}} = -\dot m'' c_{pv} (T_b - T_s) \tag{4}$$

Secondly, for low condensation rates, $B_h \to 0$,

$$\frac{h_c}{h_c^0} = 1 - \frac{1}{2} B_h + O(B_h^2). \tag{5}$$

Notice that Webb's Eq. (13) results from the use of Eq. (4) in Nusselt's analysis for condensation on a vertical wall, as shown in Section 7.2.4 of Mills (1995). For condensation of refrigerants inside tubes at relatively low condensation rates, as considered in some detail by Webb, Eq. (5) applies and then Eq. (1) gives

$$q_{\text{conv}} = h_c^0 (T_b - T_s) - \tfrac{1}{2} \dot m'' c_{pv} (T_b - T_s). \tag{6}$$

Turning now to Webb's proposed method, the essential element is his Eq. (7), which in the current notation, is

$$q_{\text{conv}} = h_c^0 (T_b - T_s) - \dot m'' c_{pv} (T_b - T_s). \tag{7}$$

Comparing Eq. (7) to Eq. (6) we see that Eq. (7) is incorrect in the limit case of low condensation rates, overestimating the effect of mass transfer by 100 percent. Also, comparing to Eqs. (2) and (4) we see that Eq. (7) is not generally valid, and in the limit of high condensation rates overestimates q_{conv} by $h_c^0(T_b - T_s)$. It is important to recognize that Eq. (2) is based on a model that is a limit form of exact conservation equations, and it is well established in the literature that Eq. (2) is a good approximation to more exact solutions of the conservation equations for various types of forced flow. Since Webb's method is ad hoc and contradicts Eq. (2) it should be rejected as incorrect and unnecessary.

Other elements in Webb's development require comment.

1 Webb's Eqs. (1) and (2) are also ad hoc. They are good approximations for forced convection condensation in horizontal tubes, but are invalid for gravity dominated condensation in vertical tubes and on external surfaces.

2 Webb's Eq. (9) is not "identical" to the Colburn-Hougen model for condensation in the presence of a noncondensable gas. The Colburn-Hougen method accounts for sensible and latent heat gas phase resistances in parallel, implicitly in series with the liquid film thermal resistance, and is generally valid (see, for example, Example 10.9 of Mills (1995)). Webb's Eq. (9) cannot be given an equivalent circuit interpretation: It represents neither resistances in parallel or series. It is valid only if the thermal resistance of the condensate film is independent of superheat (which is generally not true) and is a consequence of the resulting linearity of the thermal problem.

3 Webb's relation $\dot m_v''/A = q_{\text{lat}}/i_{fg}$ is also generally invalid: It is untrue if the condensate film resistance depends on vapor superheat.

4 Webb's claim that the mass transfer correction would be significantly smaller for steam than for R-22 is also not generally valid. From his Eq. (9), or equivalently Eq. (2) of this discussion, the appropriate parameter scaling the effect of mass transfer is $B_h = \dot m'' c_{pv}/h_c^0$. Condensation of steam in practice

---

[1] By R. L. Webb, published in the May 1998 issue of the ASME JOURNAL OF HEAT TRANSFER, Vol. 120, pp. 418–421.

[2] School of Engineering and Applied Science, University of California, Los Angeles, CA 90097.

usually occurs at low pressures for which h_c^0 is small, and with thin condensate films for which $\dot{m}''$ is large. The aforementioned Example 10.9 of Mills (1995) shows a value of $B_h = -6.77$ and $h_c/h_c^0 = 6.78$, which is not significantly lower than 1.4 as suggested by Webb. Of course, the effect of vapor superheat on the condensation rate remains small.

5 Webb's Fig. 1 shows a comparison of his model predictions with experimental data. There is no similar evaluation of the well-established Ackermann model. However, given the expected uncertainty in the experimental data due to random and bias error, and the scatter shown in Fig. 1, it is doubtful if any conclusion could be drawn from this comparison.

References

Ackermann, G., 1937, "Heat Transfer and Molecular Mass Transfer in the Same Field at High Temperatures and Large Partial Pressure Differences," *Forsch. Ing. Wes. VDI, Forschungesheft,* Vol. 8, p. 232.

Mills, A. F., 1995, *Heat and Mass Transfer,* Richard D. Irwin, Chicago, IL.

Spalding, D. B., 1963, *Convective Mass Transfer,* McGraw-Hill, New York.

Author's Closure[1]

Prior to addressing Professor Mills comments it is helpful to review the chronology of the analysis methods referenced by Mills and in the present work. The 1934 Colburn and Haugen analysis was the first to address the effect of noncondensible gas on condensation. They proposed that the heat transfer rate is the sum of the latent (condensation) and sensible load (cooling of vapor to saturation temperature), which is the same as Eq. (2) in the present work. They worked an example for gas condensing on the outside of tubes. Their analysis did not include a correction for the effect of mass transfer on the sensible heat term. The 1937 analysis of Ackermann formulated a correction factor to account for the effect of mass transfer on the sensible heat term. Present day analysis (e.g., Collier and Thome (1994) and Hewitt et al. (1994)) of the noncondensible gas problem typically includes use of the "Ackermann correction factor" in the Colburn and Hougen equation.

We were not aware of Mills analysis of vapor velocity effect, which he references in his discussion. It appears that the Mills analysis is intended to treat the fundamentals of the problem by giving the differential equation that is to be solved, as opposed to giving a *solution* as is done in the present work. Mills analysis derives the Colburn and Haugen differential equation with the Ackermann correction factor.

There are two basic ways to solve convective heat transfer problems: one is to solve a differential equation (for a given flow geometry) by integrating the temperature profile across the flow field to obtain the temperature profile. Then, one calculates the heat flux by calculating $k(dT/dy)$ at the wall. This is the approach described by Mills, although he did not actually solve the differential equation. The other approach is to use heat transfer coefficients and thus calculate the heat flux using $q = h(T_{\text{sat}} - T_w)$, as is done in the present work. We have formulated a composite heat transfer coefficient using Eq. (2) and have given a generalized solution method (Eq. (9)) that is applicable for any flow geometry.

Equation (2) properly states the underlying theory of the Colburn-Haugen equation as stated on page 1179 of the Colburn and Haugen paper, or the present Eq. (2). However, as noted above, Colburn and Haugen did not correct h_{fc} for mass transfer. We have included a correction factor for mass transfer as is included in Eq. (7).

It appears that the principal concern expressed by Professor Mills relates to our use of a different formulation to obtain the correction factor to the single-phase heat transfer coefficient to account for mass transfer. Our formulation could have been developed using the "Ackermann correction factor." However, we chose not to use the Ackermann formulation, which is based on the *assumption* of Couette (laminar between two parallel plates with the upper plate moving at a specified velocity). The present formulation is more general and is applicable to laminar or turbulent flow and is applicable to any geometry. The present formulation uses an energy balance to: (1) determine the mass flux to the interface, (2) write the bulk convection of sensible heat in terms of a heat transfer coefficient, and (3) define a composite heat transfer coefficient (h_{fc}^*) to include the effect of bulk convection to the single-phase term in Eq. (2). The result is Eq. (8). One may manipulate Eq. (8), which I will call Eq. (8*a*) here to yield

$$\frac{h_{fc}^*}{h_{fc}} = 1 + \frac{c_{pv} q_{\text{lat}}}{i_{fg} h_{fc}} . \tag{8a}$$

Equation (8*a*) is equivalent in concept to the Akermann correction factor (Mills, Eq. (2)). Mills argues that Eq. (8*a*) does not have the same asymptotes as his Eq. (2). I agree that it is not asymptotic to his Eq. (2), because the detailed formulation leading to Eq. (8*a*) is different. There is no reason why it should have the asymptotes of his Eq. (2), because it is not based on the same assumptions or restrictions (e.g., the laminar flow model of Ackermann). Should the reader be interested in the Ackermann analysis, it is given in detail on p. 604 of Hewitt et al. (1994).

If one prefers, they could use the Akermann correction factor (Mills, Eq. (2)), rather than Eq. (8) to account mass transfer effects on the q_{sens} term in Eq. (2). Because the latent heat term dominates Eq. (2), it is possible that one would see little practical difference between the two formulations. However, I have not performed a sample calculation to evaluate the difference between the two formulations.

Mills item 3 criticism states that "the relation $(m_v/A) = q_{\text{lat}}/i_{fg}$ is generally invalid; it is untrue if the condensate film resistance depends on vapor superheat." We do not argue that the condensate film resistance should depend on superheat. Nothing in the present model says that.

Professor Mills is critical of the predictive ability of the Lee (1991) model, and he further implies that the Lee data are not very good. We feel that his criticism is unjustified. The predictive ability of the model is shown in Fig. 1 and is good. Professor Mills admits that "there is no similar evaluation of the well-established Akermann model."

In summary, we have presented a formulation based on use of heat transfer coefficients for condensation and single-phase heat transfer that is applicable to any flow geometry. If one prefers to use the Ackermann correction factor (rather than Eq. (8*a*) above), one may do so. We have shown that the predicted results are in good agreement with the convective condensation data of Lee.

---

[1] Professor Ralph Webb, Department of Mechanical Engineering, Pennsylvania State University, University Park PA 16802.

usually occurs at low pressures for which h_c^0 is small, and with thin condensate films for which $\dot{m}''$ is large. The aforementioned Example 10.9 of Mills (1995) shows a value of $B_h = -6.77$ and $h_c/h_c^0 = 6.78$, which is not significantly lower than 1.4 as suggested by Webb. Of course, the effect of vapor superheat on the condensation rate remains small.

5 Webb's Fig. 1 shows a comparison of his model predictions with experimental data. There is no similar evaluation of the well-established Ackermann model. However, given the expected uncertainty in the experimental data due to random and bias error, and the scatter shown in Fig. 1, it is doubtful if any conclusion could be drawn from this comparison.

References

Ackermann, G., 1937, "Heat Transfer and Molecular Mass Transfer in the Same Field at High Temperatures and Large Partial Pressure Differences," *Forsch. Ing. Wes. VDI, Forschungesheft,* Vol. 8, p. 232.

Mills, A. F., 1995, *Heat and Mass Transfer,* Richard D. Irwin, Chicago, IL.

Spalding, D. B., 1963, *Convective Mass Transfer,* McGraw-Hill, New York.

Author's Closure[1]

Prior to addressing Professor Mills comments it is helpful to review the chronology of the analysis methods referenced by Mills and in the present work. The 1934 Colburn and Haugen analysis was the first to address the effect of noncondensible gas on condensation. They proposed that the heat transfer rate is the sum of the latent (condensation) and sensible load (cooling of vapor to saturation temperature), which is the same as Eq. (2) in the present work. They worked an example for gas condensing on the outside of tubes. Their analysis did not include a correction for the effect of mass transfer on the sensible heat term. The 1937 analysis of Ackermann formulated a correction factor to account for the effect of mass transfer on the sensible heat term. Present day analysis (e.g., Collier and Thome (1994) and Hewitt et al. (1994)) of the noncondensible gas problem typically includes use of the "Ackermann correction factor" in the Colburn and Hougen equation.

We were not aware of Mills analysis of vapor velocity effect, which he references in his discussion. It appears that the Mills analysis is intended to treat the fundamentals of the problem by giving the differential equation that is to be solved, as opposed to giving a *solution* as is done in the present work. Mills analysis derives the Colburn and Haugen differential equation with the Ackermann correction factor.

There are two basic ways to solve convective heat transfer problems: one is to solve a differential equation (for a given flow geometry) by integrating the temperature profile across the flow field to obtain the temperature profile. Then, one calculates the heat flux by calculating $k(dT/dy)$ at the wall. This is the approach described by Mills, although he did not actually solve the differential equation. The other approach is to use heat transfer coefficients and thus calculate the heat flux using $q = h(T_{\text{sat}} - T_w)$, as is done in the present work. We have formulated a composite heat transfer coefficient using Eq. (2) and have given a generalized solution method (Eq. (9)) that is applicable for any flow geometry.

Equation (2) properly states the underlying theory of the Colburn-Haugen equation as stated on page 1179 of the Colburn and Haugen paper, or the present Eq. (2). However, as noted above, Colburn and Haugen did not correct h_{fc} for mass transfer. We have included a correction factor for mass transfer as is included in Eq. (7).

It appears that the principal concern expressed by Professor Mills relates to our use of a different formulation to obtain the correction factor to the single-phase heat transfer coefficient to account for mass transfer. Our formulation could have been developed using the "Ackermann correction factor." However, we chose not to use the Ackermann formulation, which is based on the *assumption* of Couette (laminar between two parallel plates with the upper plate moving at a specified velocity). The present formulation is more general and is applicable to laminar or turbulent flow and is applicable to any geometry. The present formulation uses an energy balance to: (1) determine the mass flux to the interface, (2) write the bulk convection of sensible heat in terms of a heat transfer coefficient, and (3) define a composite heat transfer coefficient (h_{fc}^*) to include the effect of bulk convection to the single-phase term in Eq. (2). The result is Eq. (8). One may manipulate Eq. (8), which I will call Eq. (8*a*) here to yield

$$\frac{h_{fc}^*}{h_{fc}} = 1 + \frac{c_{pv}q_{\text{lat}}}{i_{fg}h_{fc}}. \tag{8a}$$

Equation (8*a*) is equivalent in concept to the Akermann correction factor (Mills, Eq. (2)). Mills argues that Eq. (8*a*) does not have the same asymptotes as his Eq. (2). I agree that it is not asymptotic to his Eq. (2), because the detailed formulation leading to Eq. (8*a*) is different. There is no reason why it should have the asymptotes of his Eq. (2), because it is not based on the same assumptions or restrictions (e.g., the laminar flow model of Ackermann). Should the reader be interested in the Ackermann analysis, it is given in detail on p. 604 of Hewitt et al. (1994).

If one prefers, they could use the Akermann correction factor (Mills, Eq. (2)), rather than Eq. (8) to account mass transfer effects on the q_{sens} term in Eq. (2). Because the latent heat term dominates Eq. (2), it is possible that one would see little practical difference between the two formulations. However, I have not performed a sample calculation to evaluate the difference between the two formulations.

Mills item 3 criticism states that "the relation $(m_v/A) = q_{\text{lat}}/i_{fg}$ is generally invalid; it is untrue if the condensate film resistance depends on vapor superheat." We do not argue that the condensate film resistance should depend on superheat. Nothing in the present model says that.

Professor Mills is critical of the predictive ability of the Lee (1991) model, and he further implies that the Lee data are not very good. We feel that his criticism is unjustified. The predictive ability of the model is shown in Fig. 1 and is good. Professor Mills admits that "there is no similar evaluation of the well-established Akermann model."

In summary, we have presented a formulation based on use of heat transfer coefficients for condensation and single-phase heat transfer that is applicable to any flow geometry. If one prefers to use the Ackermann correction factor (rather than Eq. (8*a*) above), one may do so. We have shown that the predicted results are in good agreement with the convective condensation data of Lee.

---

[1] Professor Ralph Webb, Department of Mechanical Engineering, Pennsylvania State University, University Park PA 16802.